STAB 2018

Stability of Ships and Ocean Vehicles

13th International Conference

Kobe, Japan

16-21 September 2018

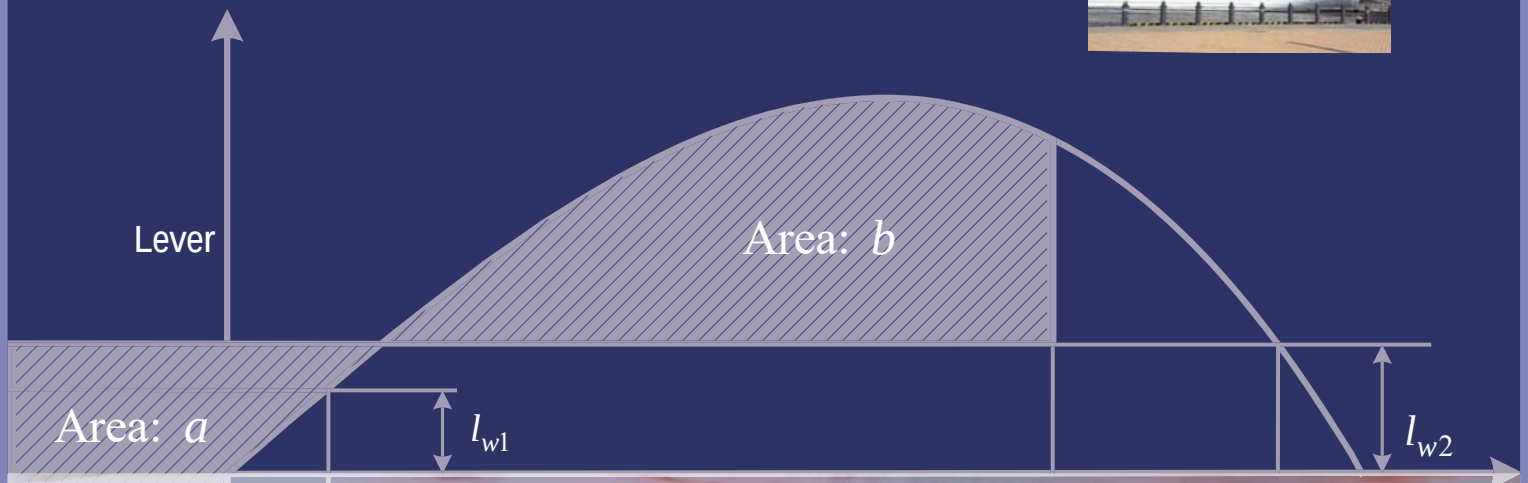

Osaka University
Osaka Prefecture University
MLIT, JPN

Edited by
Naoya UMEDA
Toru KATAYAMA
Atsuo MAKI

Designed by
M graphic
Miyuki NAKAYAMA

PREFACE

The international Conference on Stability of Ships and Ocean Vehicles started in 1975 at the University of Strathclyde in Scotland under the initiative of Professor Chengi Kuo with the UK's Department of Trade. Responding to its success, the second conference was held in Tokyo, Japan in 1982 organised by the Society of Naval Architects of Japan, Japan's Ministry of Transport and the Japan Ship Building Industry Foundation under the leadership of Professor Seizo Motora as "STABILITY 82", which had 55 papers with participants from 16 countries. Following these two very successful conferences, nine conferences were held in various countries keeping their high standard in science and crucial importance in regulation and industry so far and then the conference finally returned to Scotland in 2015 and to Japan this year.

Japan opened a country to foreign trade and diplomatic relation because of the arrival of Commodore Perry and his two wooden paddle steamers in 1852. Then we learned cultures, science and technology from western countries, particularly naval architecture mainly from Scotland. After its training period, some novel ideas emerged also in Japan. One of typical examples is the invention of fin stabilizer for reducing ship roll motion at sea by Dr. Shintaro Motora in 1923[1]. On the other hand, Japan experienced two tragic stability accidents: one is the capsize of a torpedo boat "Tomozuru" in following waves and the other is the capsize of a passenger train ferry "Toya Maru" with accumulated water on the wagon deck in 1954[2]. Such tragic accidents forced Japan to establish domestic stability standard in 1956[3]. Part of this standard is known as the "weather criterion", and was adopted by the IMO (International Maritime Organization) in 1985 by merging with USSR's calculation method of ship roll amplitude. This means that STABILITY 82 was held during the hot discussion on the weather criterion at the IMO so that interests of stability experts at that time focused on stability in wind and waves.

After STABILITY 82, there is no doubt that stability conferences had important roles to develop new ideas and make decisions in regulation. Some examples can be listed as the probabilistic damage stability criteria in the SOLAS convention, the MODU code, the guidance for ship masters in following seas, the safe return to port and so on. Here in Japan this time, we have several discussion items, which include the second generation intact stability criteria and responses to the capsizing of a flooded large cruise ship "Costa Concordia". We can easily suppose that this conference in Kobe, which has 62 papers from 19 countries, would provide innovative ideas for making wise decisions at the IMO in very near future on these critical items.

---

[1] This was published in the Journal of the Society of Naval Architects of Japan in Japanese. Later, this patent was sold to Denny Brown Co.

[2] The presentations for revisiting these accidents are invited at the historical review session of this conference.

[3] This domestic standard was introduced in the paper published in the Transaction of RINA in1959 by M. Yamagata et al.

On this opportunity I would like to express my deep appreciation to the main sponsor, the ClassNK and other sponsors, i.e. Tsutomu Nakauchi Foundation, Kobe Convention Bureau, US Office of Naval Research Global. I am indebted to The Chairman of the International Standing Committee Prof. Kostas Spyrou and all members of the committee for their effective guidance and patient support for preparing this conference.

I particularly extend my gratitude to the reviewers of the papers. These voluntary works enable all papers, except for invited keynote papers, to be reviewed by at least two peers for making quality of this conference high.

Special thanks to the local organising committee members, particularly, Dr. Atsuo Maki, Prof. Toru Katayama, Dr. Hirotada Hashimoto, Prof. Masahiko Fujikubo, Mr. Akihiko Matsuda, Dr. Takako Kuroda and Dr. Daisuke Terada for their unlimited help.

I wish that this week in Kobe, Japan would be memorable for all of you by finding and/or confirming future directions in your professional activities in ship stability.

Naoya Umeda
Chairman of the local organizing committee of STAB 2018
17 September 2018

COMMITTEE STRUCTURE

The International Standing Committee

Prof. Kostas Spyrou (Chairman)	National Technical University of Athens
Dr. Vadim L. Belenky	David Taylor Model Basin
Mr. Hendrik Bruhns	Herbert Software Solutions
Dr. Gabriele Bulian	University of Trieste
Prof. Alexander B. Degtyarev	St.Petersburg State University
Prof. Alberto Francescutto	University of Trieste
Dr. Jan Otto de Kat	American Bureau of Shipping
Dr. Toru Katayama	Osaka Prefecture University
Prof. Luis Perez-Rojas	Universidad Politécnica de Madrid
Mr. William S. Peters	U.S. Coast Guard
Prof. Marcelo Santos Neves	Universidade Federal do Rio de Janeiro
Prof. Naoya Umeda	Osaka University
Prof. Dracos Vassalos	University of Strathclyde
Dr. Frans van Walree (Secretary)	Maritime Research Institute Netherlands

The Local Organising Committee

Prof. N. Umeda (Chairman)	Osaka Univ.
Prof. T. Katayama	Osaka Pref. Univ.
Dr. H. Hashimoto	Kobe Univ.
Mr. J. Hirata	Class NK
Mr. A. Ishihara	Maritime Bureau, Japanese Govt.
Mr. Y. Mori	Maritime Bureau, Japanese Govt.
Dr. A. Maki	Osaka Univ.
Mr. A. Matsuda	NRIFE
Dr. D. Terada	Nat. Defense Academy, Japan
Dr. H. Taguchi	NMRI
Dr. T. Kuroda	NMRI

The History of the conferences

1975 - Glasgow, UK	by Prof. C. Kuo
1982 - Tokyo, Japan	by Prof. S. Motora
1987 - Gdansk, Poland	by Prof. L. Kobylinski
1990 - Naples, Italy	by. Prof. P. Cassella

1994 - Melbourne (Florida), USA	by Prof. W. Cleary
1997 - Varna, Bulgaria	by Prof. A. Bogdanov
2000 - Launceston (Tasmania), Australia	by Dr. M. Renilson
2003 - Madrid, Spain	by Prof. L. Perez-Rojas
2006 - Rio de Janeiro, Brazil	by Prof. M. Neves
2009 - St Petersburg, Russia	by Prof. A. Degtyarev
2012 - Athens, Greece	by Prof. K. Spyrou
2015 - Glasgow, UK	by Profs. D. Vassalos and C. Kuo

Stability Awardees

Prof. R. Pauling	Univ. Of California, USA
Prof. S. Motora	Univ. of Tokyo, Japan
Prof. M. Hamamoto	Osaka Univ., Japan
Prof. C. Kuo	Univ. of Strathclyde, UK
Prof. Y. Nechaev	St. Petersburg State Marine Technical Univ., Russia
Prof. L. Kobylinski	Technical Univ. of Gdansk, Poland
Prof. Y. Odabasi	Istanbul Technical Univ., Turkey
Dr. T. Allan	MCA, UK

TABLE OF CONTENTS

The papers marked with * in the Table of Contents are invited papers.

Keynote Lectures

Historical Reviews

Manoeuvring (STAB)

2nd Generation Intact Stability Criteria (1)

2nd Generation Intact Stability Criteria (2)

2nd Generation Intact Stability Criteria (3)

2nd Generation Intact Stability Criteria (4)

2nd Generation Intact Stability Criteria (5)

2nd Generation Intact Stability Criteria (6)

2nd Generation Intact Stability Criteria (7)

2nd Generation Intact Stability Criteria (8)

Roll Damping (1)

Roll Damping (2)

Roll Damping (3)

Roll Motion (1)

Roll Motion (2)

Roll Motion (3)

Multi-Hull Vessels

Accident

Monitoring

Probability (1)

Probability (2)

Probability (3)

Probability (4)

Damage Stability (1)

Damage Stability (2)

Securing Ship Safety by Digitalization with Digital Platform

Hirofumi Takano

Senior Corporate Officer

Director of Innovation Development Division

ClassNK

ABSTRACT

The global trend in shipping is increasingly inclined to digitalization. Big data analytics will play crucial role for digitalization of shipping. To realize the full potential of big data for the maritime industry, the industry needs to work on a digital open platform where multiple stakeholders could co-create new values from the big data with a holistic approach to data sharing with appropriate rules, mutual agreement and confidentiality and professionalism. These new values are important while ensuring ship safety with digitalization. . The immediate challenges are big data from maritime industry storing and establishment its framework within which data sharing could be done efficiently and in safe manner.

1. INTRODUCTION

The Global trends involving digitalization are quite visible in many industries, especially in the manufacturing industry. The maritime industry is no exception. Ship owners, ship managers, shipyards, makers, etc. observe IoT 4.0 as the strategic tool to not only improve the operational efficiency but also use it to maintain a competitive advantage.

ClassNK has been carefully taking a lead towards maritime ICT with introducing technology trends such as Cloud Computing, Big Data Analytics and so on to some projects, which started in 2007 including the inventory development system for Ship Recycling Convention. To add, we established the maritime industry`s first data centre (Ship Data Centre) to provide the infrastructure to the marine industry for smooth transition to the era of IoT 4.0. The centre is fast evolving to be a leader for industrial Big Data related activities in Japan and the world with initiatives such as “IoS (Internet of Ships) Open Platform” named today.

2. GLOBAL TRENDS AND CHALLENGES

2.1 Global Trends

Internet of Things (IoT) – Due to better connectivity between the ship and shore more and more machinery will start interacting with each other. Advanced cloud technologies will radically change the way data is managed today. The big data open platform will foster innovation and co-create new value through interaction between stakeholders such as shipping companies, manufacturers, shipyards, etc.

The concept of Digital Twin - Digital twin refers to a digital replica of physical assets (physical twin), processes and systems that are used for various purposes. A Digital Twin is a virtual space where actual events appear in real time. It allows an integrated outlook, which will enable coordinated effort among multiple

stakeholders. In the present day the concept of the `Digital Twin,` could be seen for the specific operations only such as for voyage optimization where on real-time basis information is available in the virtual place or condition based monitoring where the data from the machinery is captured continuously and analyzed.

The autonomous ships – The evolution of the fully autonomous ships will take in a phased manner. In the first phase, we will see more and more `connected ships`. Such ships will have their machinery and equipment connected to the network ashore. Simple decisions support such as optimizing route, adjusting rpm of the main engine, etc. based on big data analytics shall be available to the ship staff. In the next phase, we will see `semi-autonomous ship` where actual feedbacks from the shore network to seafarers, including action proposal such as taking collision avoiding maneuver, etc., if the seafarer approved so, will be introduced. Finally, in the third phase, the `autonomous ship`shall cover all standard operation tasks such as collision avoidance, the optimum running of M/E, etc. with the high level of autonomy.

2.2 Challenges

Big Data - The immediate challenge for the maritime industry is to utilize the data that is already available in an efficient way as well as to explore additional opportunities to use it. However, there is also the need for strategies and methods to ensure data quality and integrity and to acknowledge the impact of the reliance on data about the human element as well as external interferences.

Framework for data sharing – The challenge will be for the data distribution, the rules which will govern the data sharing with the stakeholders and legal issues for the data ownership.

Automation and remote operations - The challenge will be to assess the level of automation that still enables a safe and secure operation of a vessel, while also acknowledging the risks that might be associated with autonomous ships with regard to cybersecurity issues as well as the potential division of authority that more autonomous shipping entails.

2.3 Regulations and Policies

The discussion about MASS (Maritime Autonomous Surface Ship) is initiated at the IMO/MSC99 in May 2018. As the debate on MASS is developing, the big data issue could be raised in the light of cyber security/ maritime safety in future sessions.

The Ministry of Land, Infrastructure, Transport, and Tourism (MLIT), Japan and the Japanese Government is pushing for the further utilization of big data. The law for enhancement of exchange and utilization of big data between industries prepared by Ministry of Economy, Trade, and Industry (METI), Japan was passed in the diet.

ClassNK issued guidelines for the autonomous ships and related ICT technologies, and is preparing a guideline for maritime cyber security.

3. THE SHIPPING INDUSTRY IN THE LAST DECADE

In the last decade, we have seen two significant signs of progress in the hardware and software aspects of the ships. Regarding hardware, substantial improvements are seen in the ship designs and machinery for more economical ships. These ships could navigate better, consume less fuel and could travel faster. Regarding software, significant progress was made by analyzing the `static` and `dynamic` data of the ships to predict potential damage to the machinery, minimize downtime, reduce

reports and simplifies surveys for class, also to optimize the voyage leading to fuel saving with the transparency of voyage. Fuel saving up to 7.0% was reportedly achieved during full-scale trials by one of the software service providers.

Though this progress has a significant impact on the ships which are using these services, however, the approach to capture data and transmission is still fragmented with redundant data sent by several software service providers. Further, the analysis of the data is carried out almost entirely on a ship-by-ship which restricts benefits to the individual vessels and the ship owners.

4. FUTURE OF THE DIGITALIZATION IN SHIPPING

The future we are rapidly approaching is where the operators/ owners/managers could know the performance of every ship in their fleet. Where the redundant information from service providers could be avoided and where the marine community could interact with each other on one platform. To make more significant gains, we will need to centralize this data in onshore data-centers, making it available to service providers and end users for big data analysis. This way, e.g. the engine manufacturers will know the performance of every one of their engines around the world on the real-time basis which will help them to improvise the engines. Similarly, the ship designers will able to monitor each of its ship`s behavior which will help them to bring innovation in the ship design. Big Data open platform and `Digital Twin` will play a critical role in the realizing the next generation ship designs and enhance ship safety.

The Big Data Center (open platform) - The future of the digitalization of the maritime industry lies in the `Big Data` center which shall provide an open platform to access data from ships safely, easily and efficiently. This platform makes use of ship data at an onshore location much easier and will help further enhance development and operation of ship services. The big data open platform will harmonize the data capture and transmission from the ships by converting the specific data format of a software service provider or system into a standardized ISO format. A `Big Data` center for the maritime industry will allow the industry stakeholders such as ship operators, shipowner, ship management companies, weather information companies, remote maintenance companies, shipyards, ship design companies, ship machinery manufacturers, etc. These stakeholders could share the data from the ships for creating new values as per their specific requirements. As an example, the quality of the ship operations could be improved by data analytics and ensure that shore managers, the ship staff, the ship owners could assess the same information at the same time for taking a more informed decision. In designing and building, it is possible to compare such actual operational data and design data, and by feeding back to the model such as computational fluid dynamic (CFD) in the research and development phase, it is possible to design a ship that can demonstrate its power in actual operation. If this design data is sent back to the ship manager or operator, then a better voyage optimization could be achieved. The remote monitoring of the ship may allow the inspection to be waved off based on the analysis of the data or to carry out a survey based on the actual condition of the vessels rather than the mandatory periodical inspections by the classification societies.

It will not be a distant dream to carry out remote repairs or to predict accurately when the machinery may fail which will allow the ship owners and managers to keep minimum spares on board and plan their repairs well in advance to avoid costly repairs or stoppages or deviation to nearest port necessary to carry out repairs.

By sharing data, we can automatically benefit from synergistic effects. It will be

possible to aim for better ships and ship operations in a way that is truly meaningful.

The concept of the Digital Twin - A digital twin continuously learns and updates itself from multiple sources to represent its near real-time status, working condition or position

Today`s digital products provided by software service providers are in principle aligned with the concept of the digital twin. As an example, for the voyage planning of the ship the digital twin could be the voyage optimization software. For ship designing companies offering integrated 3D model from the beginning of the design process and a consistent database for multiple design aspects as compartments are part of the same model. For the machinery the service providers services for the condition monitoring and automatic diagnostic of machinery.

Digital twin concept could also be used for increased safety while constructing a ship by building an `advanced comprehensive inspection system`. The new shipbuilding could be pursued after digitizing various data on design and construction, analyzing and utilizing the data obtained, rationalizing the inspection and rationalizing the building process. Furthermore, the rule conformity judgment could be made directly by using digital design data, which may lead to faster and more accurate judgment work. The innovation of inspection by digitization like this could be realized with the common understanding and cooperation among the shipyards, marine makers, shipowner and management companies and classification bodies. The broader benefits will be possible when such services are available on the big data open platform.

5. ROADMAP FOR FUTURE

If the open platform for the big data is like plowing the land, the data is like a seed which if nurtured well will bear fruits in the future. We cannot merely bear fruits if we cannot exchange data (put seeds) in the big data open platform with confidence and within in a robust legal framework. It is therefore essential to make a roadmap for the future.

Since the first verified data under European Union Monitoring Reporting and Verification regulation will be made public by June 2019 and verified data in the IMO Data Collection System by June 2020, therefore, let’s assume in another two years, i.e., by 2020 we aim to get reasonable quality data from ships. The various software service providers such as ClassNK CMAXS or ClassNK NAPA GREEN shall be able to give feedback for the operation of ships with reasonable accuracy. We see this stage as the start of the data usage by feeding the operational data not only for ship performance but also for the safety aspects of the ship, such as structure and design. In another two years, i.e., by 2022, it could be possible to have an optimum design in which ship design and operation are in harmony. In this situation, we can say the flowers are bloom!

By 2024, necessary support technologies such as new technical standards using data, evaluation method and construction technology have to be created to align with the new design ships. Advancement of such technology shall be possible by exchange of data using the big data open platform, where each stakeholder will use the data for co-creating new values and highly innovative ship. At this point, we can say that fruit from the flowers is achieved.

The success of the roadmap will depend on how strong the foundation (big data open platform) have we lay. If the foundation is weak, the roadmaps will not bear the fruits. It is therefore in the interest of the maritime industry that more and more stakeholders should join the big data open platform.

6. CONCLUSION

Digitalization in shipping is the upcoming trend now. In the near future, we see more and more `Connected Ships` which will provide a strategic advantage to shipping companies for enhancing ship safety.

The concept of the "Digital Twin" is already prevalent in shipping as many software service provider`s services are closely aligned with the concept of the `Digital Twin`. However, such services are fragmented and restricted to few ship owners.

If the marine industry wants to maximize the outcome from big data analysis, then the industry needs to join a big data open platform where multiple stakeholders who can co-create new value and foster innovation by data sharing.

To ensure fairness, transparency and data security it is essential that strict due diligence shall be carried out for the rules and legalities for the data sharing both at the national level and international level.

7. REMARKS

In recent year, ClassNK has aimed not just at improving the productivity of our operations, but also at supporting our clients through the development of new software and services. The most recent major software and services developed from these efforts are as follows.

• H-CSR software: The world's first powerful advanced calculation software package for use with the IACS Common Structural Rules for Bulk Carriers and Oil Tankers (CSR BC & OT)

• Hull Maintenance: A specially designed information service created to organize and categorize information collected from classification surveys to provide owners and managers with hull maintenance information for individual ships.

• Condition Based Maintenance: "ClassNK CMAXS" analyzes ship data from onboard sensors using sophisticated algorithms to monitor ship machinery conditions

• GBS-SCF onshore data center: "ClassNK Archive Center (NKAC)" is the maritime industry's first onshore digital archive center that fully complies with IMO Goal-Based Standards (GBS) and the related Industry Standard

• Online solution for EU-MRV: Service which helps lower costs associated with creating the Emission Reports (ER) required by the EU MRV regulations

• Inventory of Hazardous Materials: Service for smooth development and maintenance of the IHM, the list of the amount and location of hazardous substances onboard vessels

• Electronic Certificate: World's first class-developed service to issue and provide Full-term (Final) certificate(s) of Class /Installations Registration and each Statutory with Secured Electronic file (PDF) in place of traditional paper certificates

• Voyage Optimization: A total solution for planning, monitoring and follow-up of ship operations, helping its users to realize operational savings through increased awareness, trim and voyage optimization and performance analysis

• Big Data Platform: ClassNK subsidiary "Ship Data Center Co., Ltd." was established to provide a secure platform through which ship-related Big Data can be fully utilized

• Ship Data Center Co. Ltd. is an independently operated database for Internet of Ships (IoS) initiatives

Historic Review of Ikeda's Prediction Method for Ship Roll Damping and it's Future

Yoshiho, Ikeda, *Osaka University of Economics and Law* tyi00716@osakafu-u.ac.jp

ABSTRACT

Histric review of Ikeda's Prediction Method for the ship roll damping is carried out at first part of the present paper. Following the original method for conventional general cargo ships, several modifications to the original method have been carried out to meet various kinds of ships. Secondly, the simplified mehod of Ikeda's method which is recommended to use in Second Generation Intact Stability Criteria of SOLAS is intoduced, and some wornings to use it are pointed out. Finally, future works to be needed in the field is proposed.

Keywords: *SHIP ROLL DAMPING, IKEDA'S PREDICTION METHOD, IMO, SIMPLIFIED METHOD*

1. INTRODUCTION

In 1970's, strip methods for predicting ship motions in 5-degree of freedoms in waves have been established. The methods are based on potential flow theories, and can predict pitch, heave, sway and yaw motions of ships in fairly good accuracy. In roll motion, however, the strip methods do not work well because of significant viscous effects on the roll damping. Therefore, some empirical formulas or experimental data are used to predict the roll damping in the strip methods.

To improve the prediction of ship motions by these strip methods, one of the authors carried out a research project to establish a roll damping prediction method which has the same concept and the same order of accuracy as the strip methods which are based on hydrodynamic forces acting on strips, or cross sections of a ship. The prediction method, which is now called Ikeda's method, divides the roll damping into the wave, friction, eddy and bilge keel components at zero forward speed, and at forward speed the lift component is added and the increases of wave and friction components with forward speed are corrected on the basis of experimental results.

At zero forward speed, each component except the friction component is predicted for each cross section, and the vales are summed up along the ship length. The friction component is predicted by Kato's formula, and a prediction formula was developed for a three-dimensional ship shape. Modification functions for predicting the forward speed effects on the roll damping components are developed for the friction, wave and eddy components. The computer program of the method was published, and the method has been widely used.

For these thirty years, the original Ikeda's method developed for conventional cargo ships has been improved to apply many kinds of ships, for examples, more slender and rounder ships, fishing boats with hard chines, flat barges, small ships with skegs, and so on.

The original method has been also widely used. However, sometimes, different conclusions of roll motions were derived even though the same Ikeda's method was used in the calculations. Then, to check the accuracy of the computer programs of the same method, a simpler prediction method with the same accuracy as the Ikeda's original one has been expected to be developed. It is said that in initial design stages of ships, Ikeda's method is too complicated to use. To meet these needs, a simple roll damping prediction method is deduced by using regression analysis.

2. IKEDA'S ORIGINAL METHOD FOR CONVENTIONAL CARGO SHIPS

2.1 How was Ikeda's Original Method made?

The method is composed by five components, friction, wave, eddy, lift and bilge keel components, on the basis of physical origins. The prediction methods for these components were published in four papers by Ikeda et al. (1976, 1977a, 1977b, 1978a), and English translated versions of these papers are available as Reports of Department of Naval Architecture, University of Osaka Prefecture, No. 401-404. The total feature of the method was summarized by Ikeda et al. (1978b) with the computer code, and Himeno (1981) made a comprehensive review on the roll damping prediction method.

The most different points from other prediction methods is that the method is not a simple empirical method based on experimental results. Each component was investigated from the physical point of view. The frictional component was theoretically calculated by using unsteady boundary layer theory to validate an existing empirical formula. It was confirmed by measurements of generated waves by rolling hulls that the wave component can be accurately calculated by existing linear potential theory.

The most difficult problems in the roll damping prediction are to clarify physical characteristics of vortex-shedding and to identify these effects on the roll damping. At the moment, CFD methods solving NS equation could not be used yet. Vortex shedding flows around rolling hulls are comprehensively investigated by using flow visualizations, pressure measurements and force measurements. From the experimental works, it was found that the vortices created by a bare hull is different from those created by a bilge keel. The former is a thin separation bubble created on the hull surface at bilge corner, but the latter are shedding vortex created at the edge of a bilge keel and have significant dependence on Keulegan Carpenter number which shows the relative amplitude of the motion of the blunt body. They are called the eddy component of a bare hull and the bilge keel component, respectively. Both components are generated by vortices created by a hull and a bilge keel. On the basis on the measured pressure for various hulls, the simple pressure distributions are assumed. By integrating the pressure over the hull or the bilge keel, the roll moment of each component can be obtained in Ikeda's method.

The advance speed effects on the roll damping are also important factors. The effects of each component were separately investigated. The effect on the frictional component was revealed by using unsteady boundary layer theory. The effect on the wave component was calculated a very simple potential theory and a fundamental characteristics of the effect are deduced on the basis on the calculated results.

A new component, lift component, was confirmed by the new experimental method. The method was carried out in a circulating water channel. The free surface in the channel was covered by a horizontal flat plate and a ship model was floating in the middle of it with very slight gap between the model and the cover plate. Then the wave component may be deleted. The experiment demonstrated that a component linearly increasing with advance speed exists. It is the lift component, and a prediction method was developed by using the lift coefficient of a hull which is also used in ship manoeuvring prediction. After then, Ikeda found a paper in which Yumuro already pointed out the lift component of the roll damping.

The experimental results also revealed the advance speed effect on the eddy component of a hull. As the advanced speed increases, the nonlinear eddy component gradually changes the linear lift component. A modified coefficient for the advanced speed effect on the component was developed. It should be noted that the method is an empirical one and should be revised by CFD calculation. Vortices created by roll motion changes from two-dimensional ones to three-dimensional ones with increasing advanced speed.

Using the components of the roll damping, the original method for predicting the roll damping of ships was developed for conventional hull shapes of cargo ships, whose block coefficient, Cb, is around 0.56-0.85, and Froude number is up to 0.25. It should be noted that for easy practical application the hull shape is assumed to be a simple one in the method, for example, the mid-ship section is assumed to be a cross section composed by a flat bottom, vertical side walls and quadrant bilge circles. Bilge keels are located at the centre of the bilge circles.

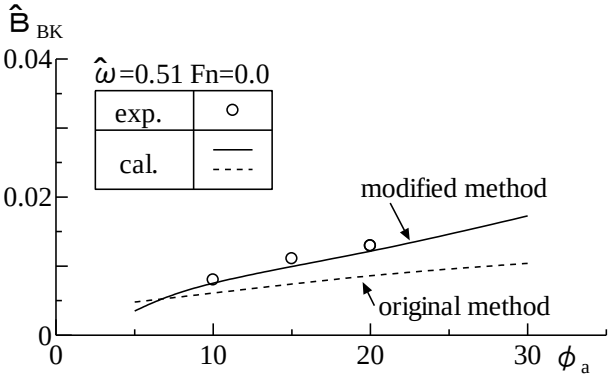

Fig.1 Improvement of accuracy of prediction due to adoption of exact hull shape and exact location of bilge keels.

2.2 Modified Methods

Hull Shape Effect on Bilge Keel Component

In the original method, for simplification, a simple mid-ship cross section (horizontal bottom, vertical sides and quadrant-bilge) and the location of bilge keels were assumed to be the centre of the quadrant-bilge, and the pressure on hull surface was integrated over the simply assumed hull shape. For a slender ship with bilge keels, however, the assumptions were found to cause large error because the cross section and the location of bilge keels sometimes significantly differ from the simple assumption. Therefore, the prediction method was improved to be able to take into account the exact shape of the cross sections and the exact location of bilge keels. Since the pressure distribution on and around a bilge keels are given in the original method, the pressure distributions are integrated over bilge-keels and hull surface to get the roll damping generated by bilge keels. To use the modified prediction method, detailed offset data of each hull section and the location of bilge keel must be input although only breadth-draft ratio and cross area coefficient of each section are needed for the original method. Fig. 1 shows the difference of the predicted result between by original and modified methods for a frigate hull with very slender hull shape.

Forward Speed Effect on Bilge Keel Component

In the original method, the forward speed effect on the bilge keel components was neglected. For wide bilge keels with relatively large aspect ratio, however, the lift force acting on bilge keels increases the roll damping at high speed. Using Jones theory for small aspect ratio wing, the roll damping generated by the lift force acting on bilge keels can be predicted as follows,

$$\hat{B}_{BKL} = \frac{\pi r^2 b_{BK}{}^2 U}{B^2 \nabla} \sqrt{\frac{B}{2g}} \qquad (1)$$

where r denotes distance between roll axis and centre of a bilge keel, ∇, U and B are the displaced volume, forward speed and breadth of a ship, respectively.

In Fig. 2, measured bilge keel component of the roll damping for a frigate with advanced speed are compared with the predicted results by the original method and the modified method using Jones theory. We can see that the predicted result is slightly improved by the modification. In very fast speed, however, some discrepancy from experimental result can be seen. More detailed studies on forward speed effects on bilge keel effects should be done.

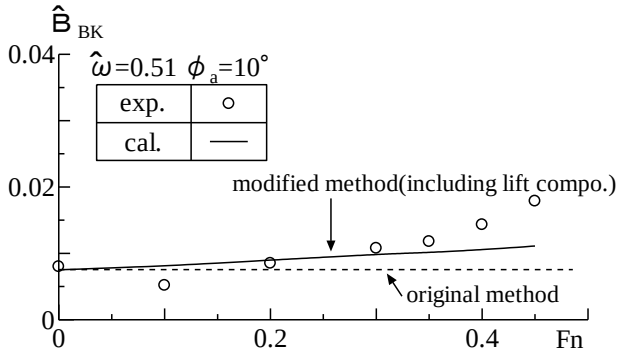

Fig.2 Forward speed effect on bilge keel component of larger bilge keels of a frigate.

Non-linear Effect on Hull Lift Component

The lift component for a hull in the original prediction method of the roll damping was predicted using the Inoue's prediction formula for lift coefficients of obliquely-towed hulls. If the Inoue's formula overestimates or underestimates the lift, a more accurate lift coefficient, like measured one, is recommended to replace the value of lift coefficient by Inoue's formula used in the original method.

Fig. 3 is an example of the lift coefficient for a slender frigate hull with big bulbous bow. The coefficient shows a significant non-linearity, and Inoue's formula cannot predict it accurately.

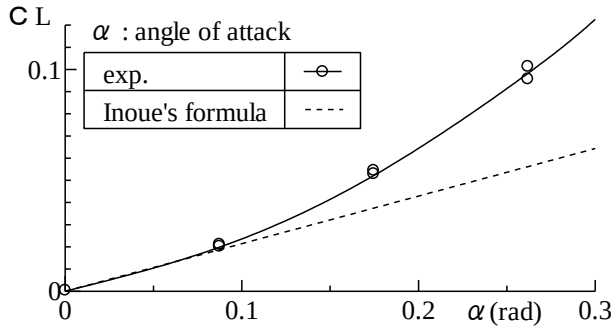

Fig. 3 Non-linearity of lift coefficient for a frigate hull.

For a fast ship with significant running trim like semi-planing and planing hulls, increase of running trim induces the large lift component of the roll damping, too. Fig. 4 shows an example of measured roll damping for a fast fishing boat. We can see rapid increase of the roll damping due to increase of running trim at high speed (Fn > 0.4).

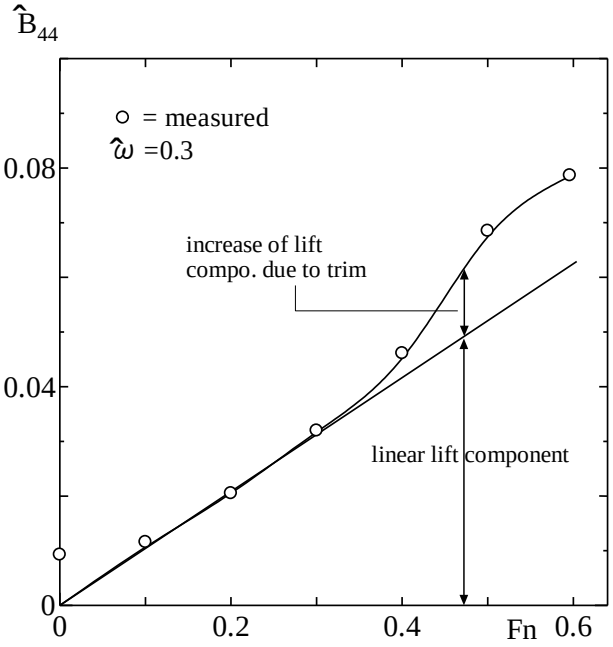

Fig. 4 Increase of roll damping due to increase of running trim of a fast fishing boat with skeg.

Barge with Sharp Corners

The original prediction method covered a sharp-cornered box hull with normal breadth-beam ratio, but not a very flat hull. Yamashita confirmed that the method gives good result for a very flat ship when the roll axis is located in water surface level (Yamashita S and Katagiri T, 1980). Standing (1991), however, pointed out that the original Ikeda's method underestimates the roll damping of a barge model. To confirm the contradictions, Ikeda et al. (1993) carried out experimental study on the roll damping of a very flat barge model. In the paper, they proposed a simplified formula for predicting the eddy component of the roll damping of a flat barge as follows,

$$B_e = \frac{2}{\pi}\rho L d^4 \left(H_0 + 1 - \frac{OG}{d}\right)\left(H_0^2 + \left(1 - \frac{OG}{d}\right)^2\right)\phi_a \omega \qquad (2)$$

As shown in Figs. 5 through 7, the experiments revealed that the simple formula expressed by Eq. (2) gives much better results

than the original method when the centre of gravity is located above water surface. It should be also noted that it was also confirmed that the formula is valid only when roll amplitude is smaller than about five degrees. Above five degrees of roll amplitude, the simple formula underestimates the roll damping of a barge as shown in these figures. This may be because interaction between water surface and shedding vortices from the edge cannot be neglected at larger roll angle.

In order to confirm the reliability of experimental results, the roll damping was measured by three different test methods, free decay test, forced roll test, and ship motion and wave excitation. In Fig.7, experimental results obtained by the three methods are shown. We can see that the three methods give almost same results and the predicted roll damping of a flat barge significantly overestimate in larger roll angle although the predicted one is in fairly good agreement with the measured ones below 5 degree.

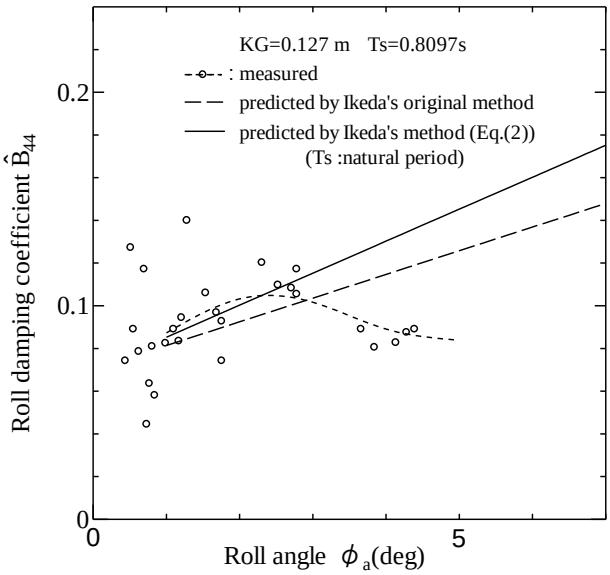

Fig. 5 Comparison between measured and predicted roll damping of flat barge model (1.662m long and 0.549m wide).

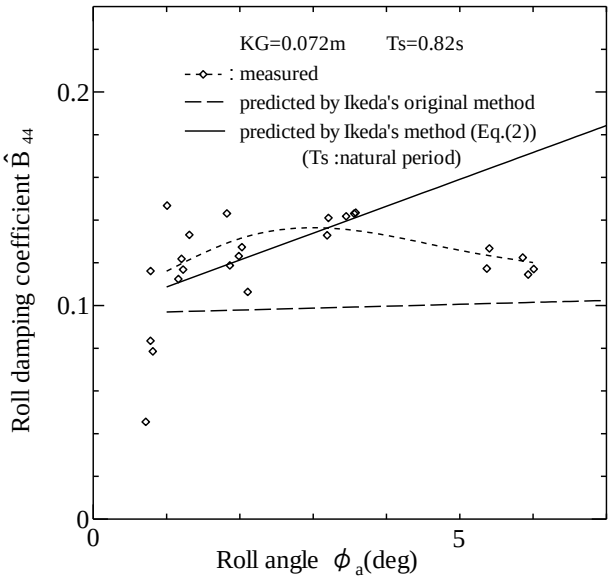

Fig. 6 Comparison between measured and predicted roll damping of flat barge model.

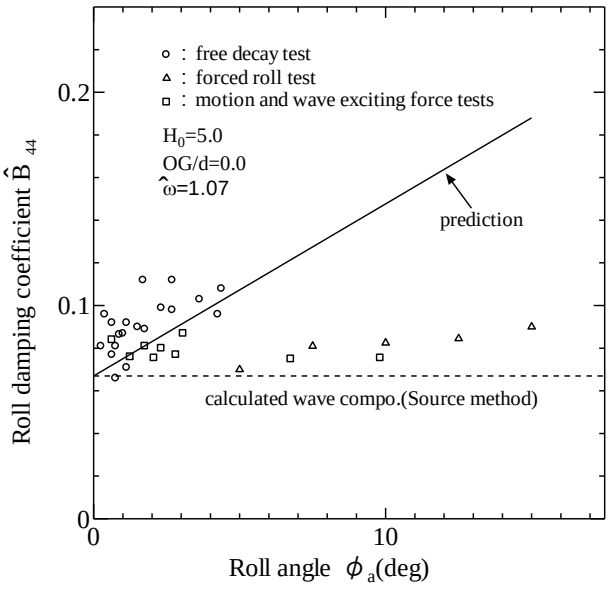

Fig.7 Comparison between results by three experimental ways and predicted results by Ikeda's original methods and modified one for flat barge model.

Small Craft with Hard-Chine Hull and Skeg

A hard-chine hull of a small craft increases the roll damping by strong vortices generating at the hard-chine. A skeg also increases the roll damping like bilge keels, but its efficiency for the roll damping significantly depends on rise of floor of the hull bottom. When a ship has a flat bottom, the pressure component, which is created by vortices shed

from the edge of a skeg on bottom surface of the hull, becomes to be negative.

A Prediction method for the roll damping of such a hard-chine hull with a skeg was proposed by Tanaka and Ikeda (1985), and was improved by Ikeda and Umeda (1990a). Forward speed effect on the roll damping was investigated by Ikeda et al. (1988) and Umeda et. al. (1988).

Flat Planing Craft

A planing craft has generally a flat hull. For such flat hulls, the asymmetrical vertical lift force acting the hull bottom in each side creates much larger roll damping than horizontal lift force acting on side of the hull, and the lift component due to vertical lift force is dominant in the roll damping at very fast speed. A prediction method of the roll damping component due to vertical lift was proposed by Ikeda et al. (2000). Fig.8 shows the comparison between measured and predicted roll damping at very high speed. In the method, the measured steady lift coefficient for vertical lift force is used. It was also confirmed that good prediction results can be obtained by using Savisky's formula for prediction of the vertical lift coefficient.

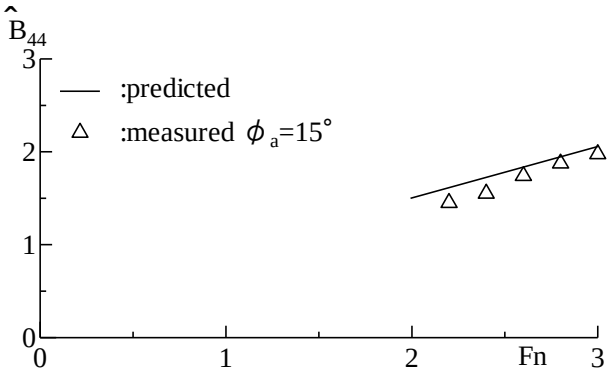

Fig.8 Comparison between predicted and measured roll damping of a hard-chine planing craft with very flat cross sections at very high speed.

Reduction of Bilge Keel Effect for Shallow Draft Ship

For a shallow draft and round ship like a high speed escort boat, it was found that the large bilge keels can give only a little increase of the roll damping (Tanaka and Ikeda, 1981) . It was experimentally revealed that interaction effects between generated waves and vortex shedding from the bilge keels cause the unexpected reduction of the roll damping of the ship. Phenomena of the interaction between shedding vortices and the free surface may be very complex, the CFD including viscous effect may be only proper tool to solve the problem. Recently, Yildiz et al. (2016) calculated the interaction effects between the shedding vortices and the generated waves by using CFD, and compared the calculated and the Ikeda's empirical pressures on the hull surface created by bilge keels.

Other Problems

Other problems concerning to the roll damping were investigated in the laboratory of the author as follows; increase of the roll damping by a large sonar dome(1994), interaction effects between fin stabilizers and bilge keels(1994), roll damping of bilge keel with fixed fins(1990b), vertical oscillating anti-rolling plates(1993), the roll damping for a twin-skeg ferry(1990b) and effects of a flume-type anti-rolling tank(1991).

3. SIMPLE FORMULA

After 40years since Ikeda's prediction method developed, the author met strange results in several papers on the roll problem even though the same prediction method was used in them, as mentioned before. The author considered that a simple method may be needed to easily validate the computer program of the Ikeda's method. Then a simplified Ikeda's method (Kawahara et.al. 2009, 2012) was developed as follows.

Key factors for each roll damping component may be different. For the wave component of two-dimensional section, the cross sectional area coefficient and the breadth/draft ratio are important factors. Since the component is linear, the roll damping coefficient, B_{44}, depends on only frequency, and not on roll amplitude. For the eddy component, the bilge circle radius and the distance from roll axis to the separation points

on the hull surface are important. For the bilge keel component, the same key factors as the eddy damping component are also important, and in addition to them the Kuelegan-Carpenter number, Kc, is also an important factor. Therefore, in developing the simplified method the regression formula of each component was deduced.

After deep considerations on the characteristic of each component, following factors are chosen as parameters for the simple prediction formula. The ship shape is created by using Taylor's series. The ship hull shape is determined when the five factors, the length, beam, draft, mid-ship sectional coefficient and longitudinal prismatic coefficient, are given. For each ship shape with various factors, components of the roll damping are calculated by using Ikeda's original method. The predicted each component is approximated by each simple prediction formula as will be explained.

Frictional Component

In the Ikeda's original method, the frictional component is predicted by using Kato's formula at Fn=0 and Tamiya's modification factor for advanced speed effect on it. The formula uses only Cb and main dimensions, L, B and d as the imput data of a ship shape for calculation of the component. Therefore, the prediction method of the frictional component in the original method is used without any modification.

Wave component

In the original Ikeda's method, the wave component is not included and should be added to the predicted roll damping. As well known, the wave component of the roll damping for a two-dimensional cross section can be calculated by potential flow theories in fairly good accuracy and the roll damping for a three-dimensional ship can be obtained by integrating the roll damping of cross sections over the ship length. For various hull shapes of the Taylor's series created by systematically changing the factors, the wave component of the roll damping was calculated. A prediction formula for predicting the wave component was deduced by fitting the results. It should be noted that in the original Ikeda's prediction method the wave component is not included, but in the simplified method the wave component is included.

Eddy Component

The eddy component of the roll damping is created by small separation bubble or small shedding vortices generated at the bilge part or at the relatively sharp bottom of bow or stern sections. Although vortex shedding flow from oscillating bluff bodies is usually govern by Keulegan-Carpenter number, Kc, it was found by Ikeda et. al. that the viscous forces created by such small separation bubbles or small shedding vortices do not depend on Kc. In Ikeda's prediction method, the distribution of the pressure created on a hull surface by such separation bubble is assumed as a simple shape for each shape of cross sections on the basis of experimental results of pressure distribution on hull surfaces. The pressure value was determined as the calculated eddy components of the roll damping for various cross sections are in good agreement with measured ones. By fitting these predicted eddy components of the Taylor's series the simple prediction formula is deduced. It should be noted that the component is nonlinear and the roll damping coefficient B_{44} is a linear function of roll amplitude.

Bilge Keel Component

The bilge keel component is usually the largest one in the roll damping. Usually the component creates 50-80% of the total roll damping. The component is created by shedding vortices from the sharp edges of bilge keels due to roll motion. The component can be divided into two components, the normal force component and the hull pressure component. Both components are created by the same vortices from the edge of a bilge keel. The former one is created by the force acting a bilge keel, and the latter by the pressure on the hull surfaces in front of and behind the bilge keel.

In Ikeda's method, the pressure distributions in front of and behind a bilge keel are assumed on the basis of the measured ones, and are integrated over the hull surface. This

means that the method may be available for any shape of cross section. Ikeda et. at. experimentally found that the magnitude and distribution of the pressure created by a bilge keel significantly depends on Kc which corresponds to relative amplitude of roll motion. The bilge keel components of the series ship shapes are calculated for various size and aspect ratio of bilge keels by Ikeda's original method. Fitting the predicted results, a following prediction formula for the roll damping is derived . It should be noted that the component is a nonlinear function of roll amplitude.

Limitation of Simple Formula

By using the simple prediction method the roll damping of a ship can be approximately predicted. Detailed hull data like a body plan which is needed for the Ikeda's original prediction method is not needed. Only B/d, C_b, C_m, OG/d, ω, b_{BK}/B, l_{BK}/L_{pp} and φa are needed for the calculation. As hull shapes are automatically generated in Taylor's Series by using the data, some discrepancies between the created hull shape and the real hull shape. These cause some error of the roll damping.

It should be noted that the simple formula was deduced in the following limitations,

Block coefficient: $0.5 < C_b < 0.85$

Breadth/draft: $2.5 < B/d < 4.5$

Height of CG/d: $-0.5 < OG/d < 0.2$

Mid-ship coefficient: $0.9 < C_m < 0.99$

Breadth of bilge keel: $0.01 < b_{BK} < 0.06$

Length of bilge keel: $0.15 < l_{BK}/L_{pp} < 0.4$

The formula was recommended to use in the Second Generation Intact Stability Criteria (see, e.g. IMO,2016). Several reports pointed out some defects for some types of ships. For an example, Rudakovic et.al. (2017) pointed out that the Ikeda's simple formula gives negative eddy making component for a European inland vessel with 0.84 of C_b.

4. CONCLUDING REMARKS

When I was a student in master and doctor courses of Osaka Prefecture University, I selected the studies on the roll damping of a ship. At that moment, most of the clever researchers in seakeeping research field concentrated to studies on wave problems to make full use of a potential flow theory. A lot of valuable results have been published. Meanwhile, I determined to focus on another remained problem in seakeeping field. It was the roll damping generated by vortex shedding problems.

At first, I divided the roll damping into components, and investigated the characteristics of each component. Only theoretical tools which we could use were a potential flow theory and a boundary layer theory, and we were obliged to depend on experimental works in those days. To know characteristics of shedding vortices, I carefully watched vortex flow around a rolling hull by using flow visualization methods, measured velocities of the vortex flows and measured the pressure distributions on the hull. Then I built rational assumptions of the pressure distribution created vortex shedding flow, and got a prediction method by integrating the assumed pressure over the rolling hull.

Nowadays, you can use CFD to calculate the roll damping of a ship. I hope you will get deep understanding on vortex shedding flows around a rolling hull by using CFD. An example can be seen as Miyake's paper (2014). He calculated vortex-shedding flow from a oscillating bilge keel by CFD, and compared the results of pressure distributions with the assumed ones used in Ikeda's method. Yildiz et al (2016) calculated the interaction between vortices generated from bilge keels of a shallow-draft ship and free surface by CFD. Using CFD, you will be able to make a new rational prediction method of the roll damping of a ship in near future.

5. ACKNOWLEDMENTS

The author appreciates the late Prof. Norio Tanaka and Prof. Yoji Himeno who

advised the author in the graduate school as supervisers. All students of the author who worked hard in experimental studies and supported the author in writing many papers on roll damping of a ship.

6. REFERENCES

Fujiwara, T., Ikeda, Y. and Umeda, N. (1994), Determination of the Capability of Roll Damping Devices Using Capsizing Probability, Proc. Of 5th International Conf. On Stability of Ship and Ocean Vehicles, Vol.2

Himeno, Y., 1981, Prediction of Ship Roll Damping –State of the Art, Report of NA & ME, The University of Michigan, No.239

Ikeda, Y., Himeno, Y. and Tanaka, N., 1976, On Roll Damping Force of Ship – Effects of Friction on Hull and Normal Force of Bilge Keels, Jour. of Kansai Society of Naval Architects, Japan, No.161, pp.41-49, in Japanese

Ikeda, Y., Komatsu, K., Himeno, Y. and Tanaka, N., 1977a, On Roll Damping Force of Ship – Effects of Hull Surface Pressure Created by Bilge Keels, Jour. of Kansai Society of Naval Architects, Japan, No.165, pp.31-40, in Japanese

Ikeda, Y., Himeno, Y. and Tanaka, N., 1977b, On Eddy-Making Component of Roll Damping Force on Naked Hull, Jour. of Japan Society of Naval Architects,Vol.142, pp.59-69, in Japanese

Ikeda, Y., Himeno, Y. and Tanaka, N., 1978a, Components of Roll Damping of Ship at Forward Speed, Jour. of Japan Society of Naval Architects, Vol.143, pp.121-133, in Japanese

Ikeda, Y., Himeno, Y. and Tanaka, N., 1978b, A Prediction Method for Ship Roll Damping, Report of Department of Naval Architecture, University of Osaka Prefecture, No.405

Ikeda, Y., Umeda, N. and Tanaka, N., 1988, Effect of Forward Speed on Roll Damping of a High-Speed Craft, Jour. of Kansai Society of Naval Architects, Japan, No.208, pp.27-34, in Japanese

Ikeda, Y. and Umeda, N., 1990a, A Prediction Method of Roll Damping of a Hardchine Boat at Zero Forward Speed, Jour. of Kansai Society of Naval Architects, Japan, No.213, pp.57-62, in Japanese

Ikeda, Y., Takata, H. and Tanaka, N., 1990b, An Experimental Study on Roll Damping of a Car Ferry with Twin-Skeg Hull, Jour. of Kansai Society of Naval Architects, Japan, No.213, pp.51-56, in Japanese

Ikeda, Y. and Yoshiyama, T., 1991, A Study on Flume-Type Anti-Rolling Tank, Jour. of Kansai Society of Naval Architects, Japan, No.216, pp.111-119, in Japanese

Ikeda, Y. et al., 1993, Roll Damping of a Sharp-Cornered Barge and Roll Control by a New-Type Stabilizer, Proc. of the 3rd ISOPE, Vol.3, pp.634-639

Ikeda, Y., Katayama, T., Hasegawa,. Y and Segawa, M., Roll Damping of High Speed Slender Vessels, Jour. of Kansai Society of Naval Architects, Japan, No.222, pp.73-81, in Japanese

Ikeda, Y. and Katayama, T., 2000, Roll Damping Prediction Method for a High-Speed Planing Craft, Proc. of 7th International Conference on Stability of Ships and Ocean Vehicles, Feb., 2000, pp.532-541

IMO SDC 4/5/1 Add.3-Annex 4., 2016, Draft Explanatory Notes on the vulnerability of ships to the dead ship stability failure mode

Kawahara Y., Maekawa K. and Ikeda Y., 2009 and 2012, A Simple Prediction Formula of Roll Damping of Conventional Cargo Ships on the Basis of Ikeda's Method and Its limitation, Proc. Of 10th International Conf. On Stability

of Ships and Ocean Vehicles, 387-398, and Journal of Shipping and Ocean Engineering, 2, 201-210

Miyake, T. and Ikeda, Y., 2014,), A Validation of Ikeda's Prediction Method of Bilge Keel Component of Roll Damping of a Ship, Proc. of JASNAOE, 18, pp.363-366

Rudakovic, S. and Backkalov, I., 2017, On Application of Standard Methods for Roll Damping Prediction to Inland Vessels, Proc. of the 16th International Ship Stability Workshop, pp.159-166

Tanaka, N, Himeno, Y., Ikeda, Y. and Isomura, K., Experimental Study on Bilge-Keel Effect for Shallow-Draft Ship, Jour. of Kansai Society of Naval Architects, Japan, No.180, pp.69-75, in Japanese

Standing, RG., 1991, Prediction of Viscous Roll Damping and Response of Transportation Barges in Waves, Proc. of 1st ISOPE, Vol.3

Tanaka, N. and Ikeda, Y., 1985, Study on Roll Characteristics of Small Fishing Vessel (Part 4) – Effect of Skeg and Hardchine on Roll Damping, Jour. of Kansai Society of Naval Architects, Japan, No.196, pp.31-37, in Japanese

Umeda, N. and Ikeda, Y., 1988, Application of Slender Body Theory to Rolling Motion of a Moving Ship with Bilge Keels, Jour. of Society of Naval Architects of Japan, Vol. 163, pp.193-205

Yamashita, S. and Katagiri, T., 1980, The Results of a Systematic Series of Tests on Rolling Motion of a Box-Shaped Floating Structure of Shallow Draft, Tran. of West-Japan Society of Naval Architects, No.60, pp.77-86

Yildiz, B., Cakici F., Katayama T., and Yilmaz H., 2016, URAN prediction of roll damping for a ship hull section at shallow draft, J. Mar.Sci. Technol, 21,48-56

Model Experiments carried out by Prof. Seizo Motora on the Disaster of the Train Ferry "Toya Maru"

Naoji, TOKI, Ehime University toki.naoji.mz@ehime-u.ac.jp

PREFACE

Prof. Seizo Motora, now aged 96, recently told several of his students including the author that the model experiments carried out by him on the disaster of "Toya Maru" around 60 years ago is still quite memorable to him. Knowing that he published a paper on the matter, the author asked Prof. Naoya Umeda for his opinion on the paper. He replied after checking the paper again, "I believe it is a remarkable accomplishment which should attract more attention. It is almost surprising to know Prof. Motora carried out such model experiments more than 60 years ago and brought very important findings. How about introducing the summary of his accomplishment on the occasion of Stability 2018? I hope it would be appreciated by the attendees."

Based on the original Japanese paper and its English translation, the author prepared this paper to explain mainstream of the papers and summarize the results within limited pages. The two papers with big volumes of 23 and 35 pages contain the detailed explanations on what happened on the major 7 ferries under typhoon, the results of model experiments carried out for their representative ferries "Toya Maru" and "Tokachi Maru". However, this paper concentrates mainly on "Toya Maru". Please refer to the original papers for more detailed information.

Keywords: *Capsizing Model Experiment, Seikan Ferry, Flooding of Car Deck in Head Waves*

1. INTRODUCTION

Typhoon Marie (the 15th in the year of 1954) landed on southern Kyushu in the early morning of September 26 and took course north-eastward through the Sea of Japan. She developed into a very strong one after the landing, which is different from the usual typhoon. And she created violent storm in the night of the same day when she hit Hokkaido, and capsized five railway ferries of "Seikan Ferry" including "Toya Maru" and wrecked many other ships. Until 1988, "Seikan Ferry" operated between Aomori and Hakodate stations on Honshu and Hokkaido Islands, to transport passenger and freight trains accommodated on the car deck.

In the case of "Toya Maru", the disaster is the worst since the tragedy of "Titanic", as it claimed the lives of 1,172 people out of 1,198 passengers and 133 crewmembers. Naturally, it invited a strong cry for investigations into the cause of the disaster. In accordance with the request of the Marine Disaster Inquiry Agency, Kato, Sato and Motora (1957) jointly conducted model experiments to clarify the technical causes of the tragedy and published the results in Japanese. Afterwards, Tamiya and Motora (1960) published its English translation.

2. THE DISASTER OF "TOYA MARU"

2.1 The typhoon which brought the disaster

The course of Typhoon Marie ("Toya Maru Typhoon" is more popular name in Japan) is illustrated in Fig. 1. Around Noon, she headed

northeast with high speed around 100km/h, as if she might cross the north of Honshu island into the Pacific Ocean until 18 o'clock. It means she would be in the east of Hakodate bay. However, in the afternoon, she lost her speed gradually and changed her course to northward. As the results, she continued to stay in the west of Hakodate bay. This change of course and speed made the wind and wave condition at Hakodate bay worse and caused the tragedy.

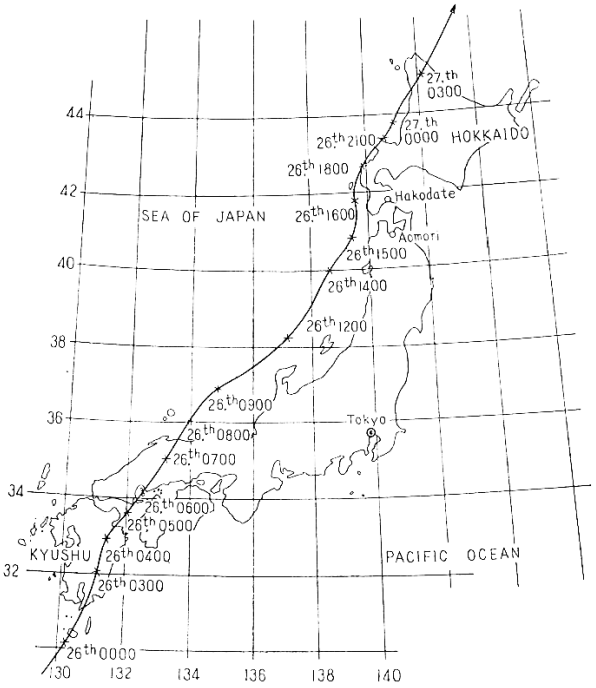

Fig. 1 Course of Typhoon Marie (No. 15)

Since typhoons swirl anticlockwise in the northern hemi-sphere, the III and IV quadrants in Fig. 2 would be the dangerous area where the advance speed of typhoon is cumulative to the velocity of swirling wind.

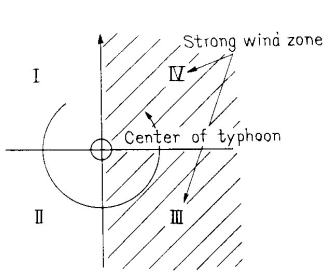

Fig. 2 Dangerous

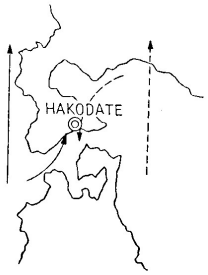

Fig.3 Two passes of Typhoon for Hakodate, Dangerous and Safe

If Typhoon Marie passes west of Hakodate bay as shown by the solid arrow in Fig.3, the bay is not only included in the dangerous quadrants but also wind from southwest continue to blow and the grown up waves attack the bay. On the contrary, when she passes east of Hakodate bay as shown by a broken arrow in Fig.3, the bay is included in comparatively safer zone and receive wind from northeast, to which the bay is screened by mountains.

2.2 Wave condition at Hakodate Bay on the night of disaster

As for the value of wave height, 6 m is considered a fair value, when the information from the crewmembers of "Toya Maru" and witness ashore are summarized. Since, in cases of visual observation, attention is apt to be drawn to comparatively high waves, this value may be considered close to the significant wave height.

As there are no observed values of wave length and period, Prof. Motora computed the characteristics of the waves on the assumption that the wind with average velocity of 25 m/s had been blowing for 5 hours over the Tsugaru straight. The results are shown in the Table 1.

Table 1. Computed wave characteristics

	Sverdrup-Munk's theory	Bretschneider's theory
Significant wave height	5.8 m	5.7 m
Wave length	62.3 m	137 m
Wave period	6.3 sec.	9.4 sec

Accordingly, the wave condition at the night is supposed as wave height = 6m and wave period is from 6 to 9 seconds.

2.3 Sequential record of what happened on "Toya Maru"

Followings are the summary of information obtained mainly by the statements of the survived crewmembers about what happened on "Toya Maru". Fig.4 illustrates the movements of "Toya Maru" and other ships in Hakodate bay.

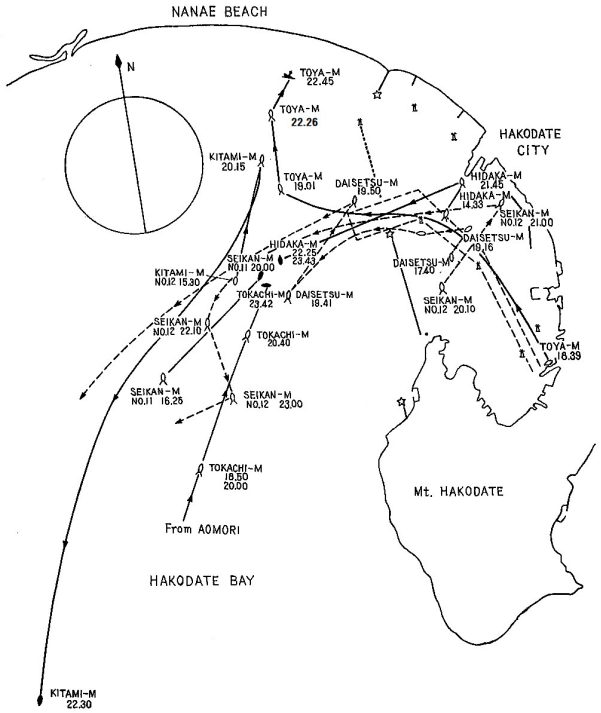

Fig. 4 Movement of "Toya Maru" together with the other ships in Hakodate bay

At 18:39 on September 26th, "Toya Maru" left Hakodate pier for Aomori and passed the lighthouse at the breakwater bank at 18:55.

At 19:01, because the wave and wind were unexpectedly strong, starboard side anchor was dropped at the place 0.85 mile from the lighthouse in the direction of 300 degrees. However, as the anchor dragged, the port side anchor was also dropped. As the results, the ship was anchored with the heading angle around 180 degrees in head or bow wave condition.

At about 19:30, crewmembers recognized the flooding of water upon the wagon deck from the stern opening. From 20 to 21 o'clock, wind was at its strongest, and maximum instantaneous velocity was 58m/s.

At about 20:40, the flooded water began to leak into the engine and boiler rooms from the skylight. At about 22:00, the centrifugal pump and circulating pump in the port side were flooded and failed to operate. Then, port side engine stopped. At about the same time, the list changed from port to starboard.

At 22:08, the list reached 20 to 30 degrees to starboard. The centrifugal pump in starboard side also failed to operate due to flooding. The ship sent out the signal: "Unable to operate the main engines". By this time, the ship became parallel to the coastline and rolled considerably in beam waves, while wind came athwart ship.

At 22:13, the ship sent out the signal: "Being drifted due to failure of main engines". The engines completely stopped. All the personnel in engine and boiler rooms were evacuated, because those rooms were considerably flooded. Up to this time, the ship had tried to keep an anchorage with the help of propeller thrust, however, as the engines stopped, it became inevitable to drag anchors.

At 22:27, all the lights went out. Sea water had been poured into the third-class passenger room (beneath the wagon deck) through a stairway like a waterfall. At 22:29, the ship sent out the signal: "Stranded at 22:26". Crewmembers felt shock at the bottom of ship several times. At 22:40, the ship sent out SOS signal. The list of the ship reached about 40 to 50 degrees to starboard, and it was never recovered. The list gradually increased and the ship finally overturned at the point about 500 meters from the coast (Nanae-beach). There was no sign of the falling of freight cars up to the list grew about 40 degrees. But loud noises of falling cars were heard while the ship overturned.

In spite of considerable flooding, "Toya Maru" did not overturn when she could stay in head wind and waves with the help of

anchoring and propeller thrust, while the other 4 freight train ferries overturned in the anchored or heave-to condition. "Toya Maru" overturned after approaching near the shore where she had wind and waves athwart ship. Therefore, it was caused indirectly due to the loss of propeller thrust, which had helped the anchors to avoid being dragged.

The sequence of the overturn of "Toya Maru" is supposed to be as follows. She listed considerably to starboard with an angle of 40 to 45 degrees and halted a while, and then gradually increased her list until she finally lay on her side. A survivor who had been in the third-class passenger room reported that the overturn happened shortly after the time when water had been poured in through a stairway like a waterfall. From the report, it is believed that with a large list the promenade deck dipped in water and a large amount of water came aboard through stairway openings, non-water-tight doors and windows, resulting in a complete loss of stability. Based on the above fact, it is considered that her stability was null at a larger angle than about 40 degrees where her promenade deck would dip in water.

Although it is commonly said that the falling of freight cars might cause overturning of ferries, in these cases of Seikan ferries, the freight cars began to fall down after the ships had started to overturn (at the larger list angle than 60 degrees).

2.4 The Problems raised for the investigation

After summarizing the records as explained above, Prof. Motora concluded that, the problems to be investigated by model experiments are the following two items.

1) To study the mechanism of water flooding to the wagon deck through the stern opening and to measure the volume of water, while the ship is anchored, heave-to, or advanced slowly conditions in head waves.

2) To study the effect of bottom contact on the stability of the ship.

Original two papers also contain the results of huge amount of stability calculations, however they are omitted to save the pages.

3. THE RAILWAY FERRY "TOYA MARU" AND THE MODEL SHIP

The fleet of Seikan ferries was composed of passenger train ferries and freight train ferries, the both have almost the same length, breadth and depth. They were equipped with twin propellers each of which was driven by a set of boilers and steam turbine. Among 5 ferries sunken under the typhoon, "Toya Maru" only is the passenger train ferry (the other 4 are freight train ferries). Principal particulars and the values related to the load condition of "Toya Maru" on the day of disaster are as follows.

$L_{PP} \times B_{MD} \times d_F \times d_A$ =113.20×15.85×4.56×5.05 m
Disp. =5,173.5 t, KG×GM=6.139×1.198 m
The estimated rolling natural period =12.5 sec.

General arrangement of "Toya Maru" is shown in Fig. 5.

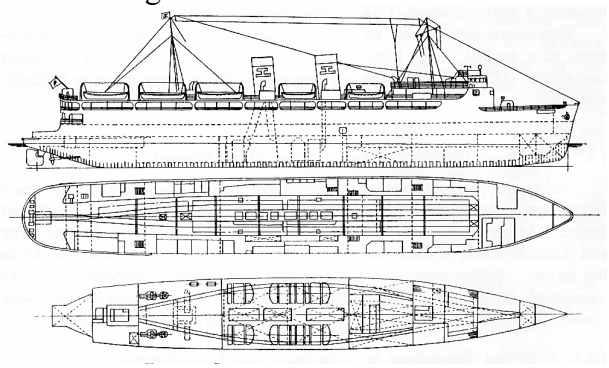

Fig. 5 General arrangement of "Toya Maru"

L_{PP}=2.00 m wooden model was made, which is 1/56.6 scale of the actual ship. Photo of the model is shown in Fig. 6. Compartments were provided under the wagon deck, so that a desired amount of water could be poured in the

engine and boiler rooms. Upper structures on the wagon deck were made precisely with brass sheet and openings were provided at the places of non-watertight windows, doors and openings, so that water could come aboard through them.

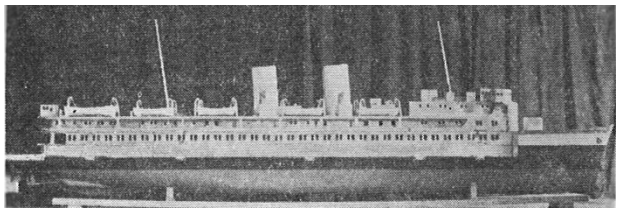

Fig. 6 2.00 m model of "Toya Maru"

To examine water flooding in head waves, another 2.00 m model was prepared, of which the sidewall of the wagon deckhouse was made of transparent plastic as shown in Fig. 7.

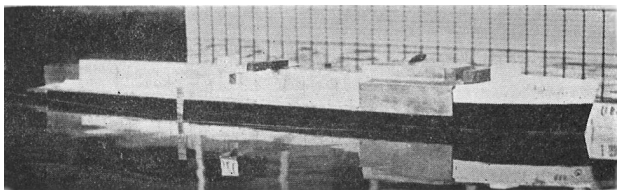

Fig. 7 Another 2.00 m model of "Toya Maru"

4. MODEL EXPERIMENTS ON WAGON DECK FLOODING

4.1 Purpose and set up of model ship

While "Toya Maru" was anchoring outside of Hakodate port in head or bow wave condition, seawater came aboard of the wagon deck through the stern opening and stagnant on the deck. Some portion of the water thus drained came into the engine and the boiler rooms through the skylights of these rooms and the hatchways of the coalbunkers, resulting in the stop of the engines. Therefore, the wagon deck flooding is considered an important indirect cause of capsize, and the mechanism of flooding and how much water could be stagnant in certain wave conditions must be investigated by model experiments.

For the anchored condition, the ship was supposed to drop the port and starboard anchors to the seabed of 20m water depth. For heave-to and advancing slowly conditions, the model was set up as shown in Fig. 8.

The model was pulled by weights for the slowly advancing condition, and nylon gut was fixed to the carriage for heave-to condition. The amount of flooded water saturated after several encounters to waves. Then, the stern of the model was picked up and water was pumped up for the measurement.

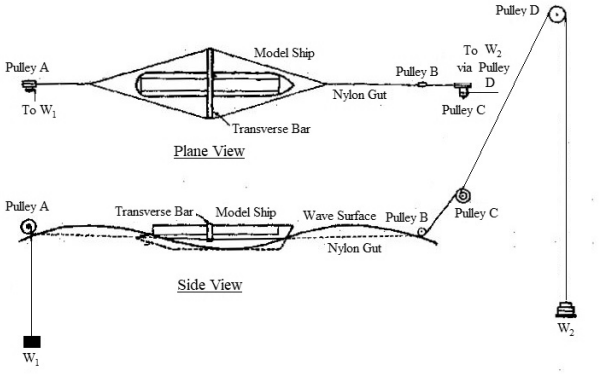

Fig. 8 The model ship set up in the tank

4.2 Results of experiments

As a result, it was found that water is taken up when the stern apron lowered by pitching motion and wave crest passing at the stern occur almost at the same time. Fig. 9 shows two photos of stern apron in motion. Next moment when the ship lowered her bow, the taken water flows forward on the wagon deck.

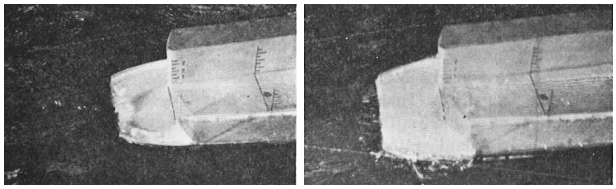

Fig. 9 Water is taken up by the stern apron

This motion of water is well illustrated by Tanaka (1998) as shown in Fig. 10.

.

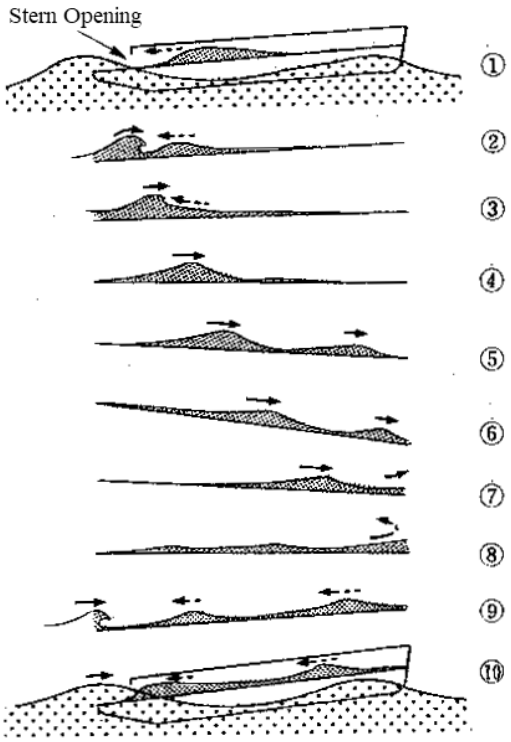

Fig. 10 The motion of water on the wagon deck when the flooding occurred

Relation between the amount of stagnant water on wagon deck and wave period in anchored condition is shown in Fig. 11 for some values of wave height. In the cases of wave height is 6 m, there is no water stagnant for wave period up to 7 seconds. After that, amount of water increases with the increase of wave period, and gets maximum at wave period of 9 seconds, then decrease at the longer period. There is no water stagnant for wave height of 4m or lower, and then amount of water increases with the increase of wave height

In the cases of wave period = 9 sec., the amount of stagnant water is maximum at head wave condition as shown in Fig.12. It gradually decreases with the change of encounter angle, and at 120 degrees, no flooding occurs.

In the cases of wave period = 9 sec. and wave height = 4 to 7 m, the amount of stagnant water is maximum in heave-to condition and gradually decreases with the increase of ship speed, as shown in Fig. 13.

It is noteworthy that water flooding does not happen unless the wave height became larger than 5m. It was also noticed that a model of the freight train ferry might overturn with a certain combination of wave length and wave height due to the free water effect of the stagnant water on the wagon deck, however "Toya Maru" could withstand. Prof. Motora's model experiments could reproduce the characteristics of the disaster, as the results coincide with what happened actually.

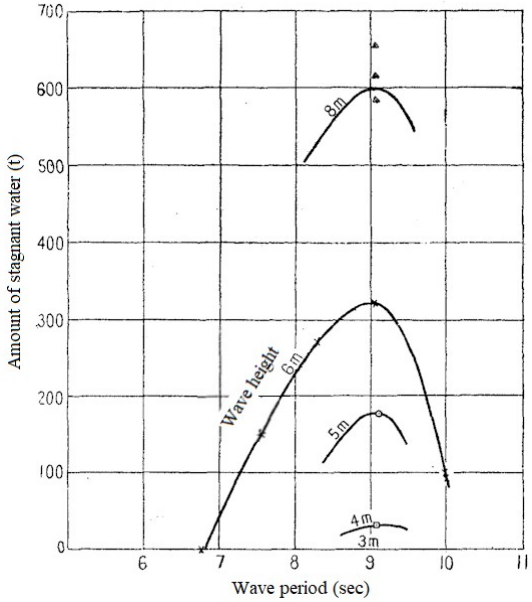

Fig. 11 Relation between the amount of stagnant water and wave period in anchored condition

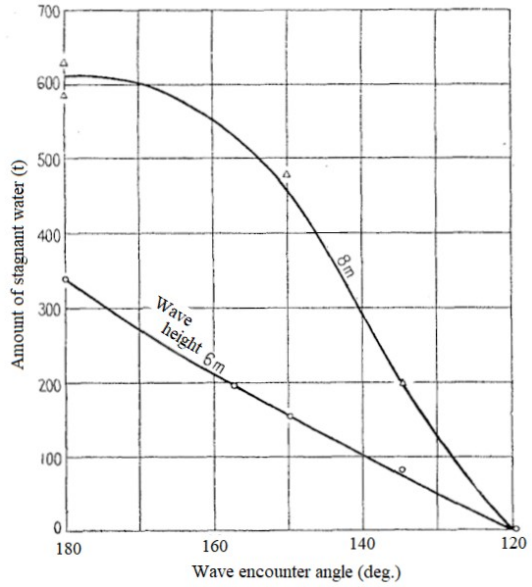

Fig. 12 Relation between the amount of stagnant water and wave encounter angle for wave period of 9 sec. in anchored condition

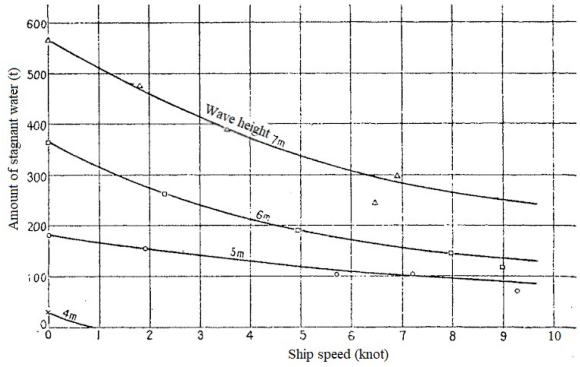

Fig. 13 Relation between the amount of stagnant water and ship speed for wave period of 9 sec. in heave-to and slowly advancing conditions

The reason of the difference of the two types of ferries can be explained as follows. Toya Maru type passenger train ferry has passenger accommodations on the both sides of wagon deck, while Tokachi Maru type freight train ferry has no accommodations. Therefore, the width of the deck space of freight train ferries where trains are actually accommodated is greater than that of passenger train ferry. It resulted in the difference of free surface effect of flooded water on the wagon deck, and brought null or negative GM to freight train ferries while "Toya Maru" could keep positive GM in the same condition.

It had been generally believed among sailors that the ship should stay in head wind and waves as the best safety measure in a heavy storm. However, it had to be changed after the model experiments because it was found that head wave condition is the most dangerous for this type of ships with an opening at her stern.

5. MODEL EXPERIMENTS ON THE EFFECT OF BOTTOM CONTACT ON CAPSIZING

Since "Toya Maru" capsized soon after bottom contacts on the Nanae Beech, it is quite natural to suspect that the bottom contact and surfs which are common in stormy beech might have some strong effects to cause the capsize.

In order to investigate the effects of bottom contact and surfs, the experiments were carried out in the tank provided with a temporary bottom, which is 1/56.6 scale model of the Nanae Beech where she finally capsized.

The model ship was set in beam sea condition and carried to shallows by the effect of upcoming waves, as shown in Fig. 14. The movement of the model ship during each experiment was recorded by 16mm movie film. The supposed amount of flooding water for the experiments was 500 tons in engine and boiler rooms and that of stagnant water on the wagon deck was 1,000 tons.

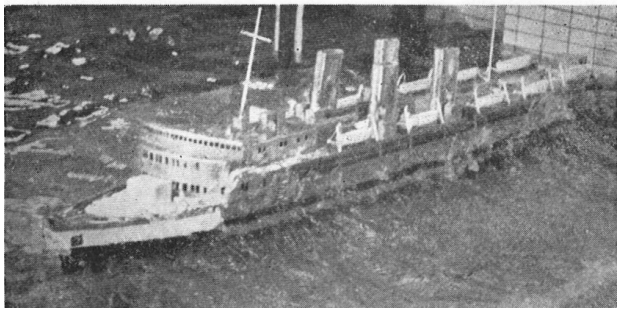

Fig. 14 The model ship was carried to shallows while she floats upright

5.1 Place of bottom contact

The water depth at the spot where the bottom contact began after the ship had drifted to shallows by wind and waves with period of 9 sec. is 8 m to 10 m when wave height is 6 m, and 10 m to 12 m when wave height is 8 m. These results are approximately consistent with the place where the ship sank. As the draft of lower side is 6.75 m when the ship heeled by 15 degrees and heaving amplitude is close to a half of wave height, the above values of water depth are considered appropriate.

5.2 Reaction of the hull to bottom contact

The reaction of the hull to bottom contact may vary as the cases. In model experiment, the results were such that the ship sometimes capsized and sometimes stranded safely. These

two different results were due to the slight difference of conditions.

Case 1). The sea bottom is smooth and the hull is not restrained by chain cables

In this case, at first, the ship drifts to shoreside on the crest of waves with the list to shoreside due to wind blowing to the shore as shown in Fig 15 (a), and afterwards when the ship is drifting to offshore on the trough of waves as shown in Fig 15 (b) the bottom contact generally took place. Accordingly, the list tends rather reduced by the forces due to the bottom contact. After repeating the process several times, the model tends to sit on shallows safely in upright condition. The last scene is almost the same as shown in Fig. 14.

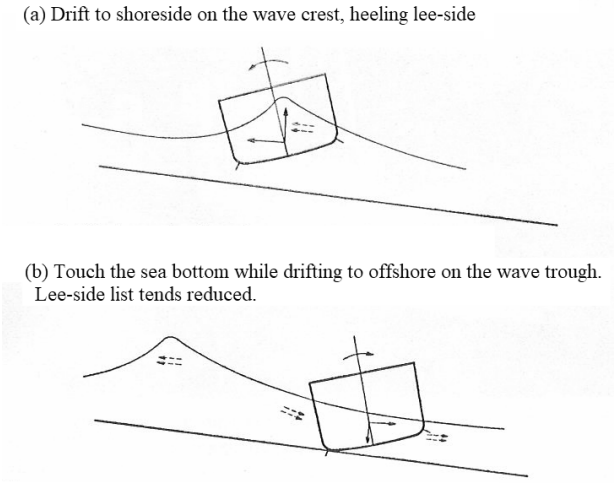

Fig. 15 Movements of the model ship when bottom contact does not result in capsizing

However, under certain delicate combinations among ship draft, water depth and list of the ship at an instant, bilge keel is caught by the sea bottom while she is pushed toward the shore by wave crest as shown in Fig. 16, then the ship overturns as shown in Fig. 17.

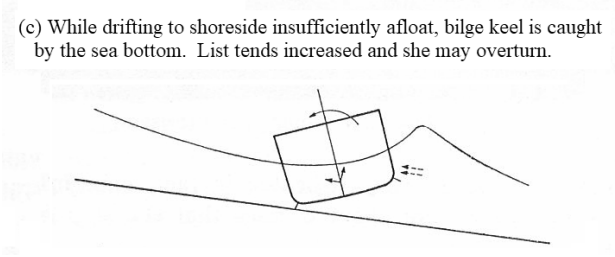

Fig. 16 Movement of the model ship when bottom contact results in capsizing

This combination is very delicate; in fact, the experiments show out of 10 cases there are about 8 cases where the ship stranded in safe and about 2 cases where the ship overturned.

If drifting is not restrained by chain cables, the ship can move to shallows smoothly and it would increase the possibility where she runs aground the shallows safely.

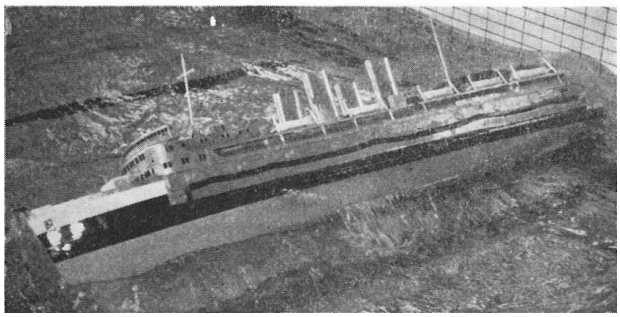

Fig. 17 The model ship overturned and then capsized

Case 2). The sea bottom is smooth and the hull is restrained by chain cables

The results show similar tendency to the case 1), however because the drifting of the hull is restrained, the ship cannot move to shallows and there is relatively bigger possibility that she is driven to the dangerous condition mentioned above.

Case 3). The sea bottom is not smooth

In this case, bilge keel would tend to stick in the projected part of the sea bottom when the ship is drifting toward the shore on the crest of waves, and the possibility of the ship to overturn would surely increase when compared to the case 1).

6. CONCLUSIONS

Prof. Motora tried to clarify two key points among what had happened on “Toya Maru” by carrying out model experiments based on the information collected after the tragedy, as explained above. When the results of the model experiments are compared with the

sequence of the tragedy, it can be concluded that the following points are almost confirmed.

1) It was found that water flooding on the wagon deck in head wave condition is caused by the stern apron, which takes water up onto the deck. Water is taken only in rare conditions when the stern apron lowered by pitching motion and wave crest passing at the stern occur almost at the same time and wave height is greater than 4 m.

2) Water flooding on the wagon deck from the stern opening in head waves happened for the first time in the history of Seikan ferry. The first reason why it had never happened is suspected that there had been no attack of such big typhoon ever, and the second one is that the flooding occurs in the cases of Seikan ferry only when the length of incoming wave is close to ship length.

3) Although it had been believed that the ship should stay in head wind and waves as the best safety measure in a heavy storm. However, it was found by the model experiments that head wave condition in the above case is the most dangerous for this type of ships with an opening at her stern.

4) In the disaster, "Toya Maru" could keep her stability in anchored condition in spite of heavy flooding on the wagon deck, while the other 4 freight train ferries overturned in anchored or heave-to condition in head waves. Comparative model experiments could reproduce the difference successfully.

5) The causes of the overturning and capsize of "Toya Maru" are considered as follows. Although she could withstand the free water effect of heavy flooding on the wagon deck, the flooded water leaked into the engine and boiler rooms, which resulted in complete, stop of main engines. Up to the engine stop, the anchored condition in head waves could be kept with the help of propeller thrust; after that it is inevitable for "Toya Maru" to drift and change the heading parallel to the shore line. It means the change from head waves to beam waves. "Toya Maru" drifted to the shore and several contacts of ship bottom and sea bottom happened, and she overturned. Model experiments show that even in this occasion there is much greater possibility of stranded safely than overturning. It has to be said that the overturning was brought by really unfortunate coincidence.

7. ACKNOWLEDMENTS

The author expresses his sincere thanks to Prof. Motora who gave the permission to publish the summarized version of the two papers on his model experiments. In addition, special thanks to Prof. Umeda who gave the author a chance to read two papers intensively and prepare this summary to revive the record of old but remarkable experiments.

8. REFERENCES

Kato H., Sato M. and Motora S., 1957: On the Disaster of the Ferry-Boat "Toya Maru" (in Japanese), Journal of The Society of Naval Architects of Japan, Vol. 101, pp. 107-129.

Tamiya S. and Motora, S., 1960, Problems of Capsizing with Special Reference to the Toya Maru Disaster, Advances in Research on Stability and Rolling of Ships, The Society of Naval Architects of Japan 60th Anniversary Series., Vol. 6, Chapter 7, pp. 159-192.

Tanaka S., 1998: Mystery on Capsizing of Seikan Ferry "Toya Maru" (in Japanese), Seizando-Shoten Publishing Co. Ltd., p.154.

Capsize of a torpedo boat in following waves in 1930'

Atsuo, MAKI, *Osaka University* maki@naoe.eng.osaka-u.ac.jp

Naoya, UMEDA, *Osaka University* umeda@naoe.eng.osaka-u.ac.jp

Haruka, NAGATO, *Osaka University* haruka_nagato@naoe.eng.osaka-u.ac.jp

Akihiko, MATSUDA, *NRIFE* amatsuda@fra.affrc.go.jp

ABSTRACT

Dr. Takaishi (he passed away in 2012) made presentations at the first STAB conference (1975, Glasgow) and the second STAB conference (1982, Tokyo). Then, in his STAB1982 paper, the risk of navigation in following/quartering seas was considered from the aspect of the encounter waves. In his similar report presented in 1978, Tomozuru incident (Matsumoto, 1954) was introduced as one of the typical accidents happened in the encounter wave condition. Although Takaishi concluded that the primary reason of her accidents is the shortage of restoring moment, but simultaneously he emphasized the decrease in restoring moments in following/quartering seas. From here onwards, Japan research community of naval architecture has partly believed that the restoring variation in following/quartering seas could result in this accident. In this research, the authors attempt to uncover the actual reason of her capsizing accident based on extensive tank tests and numerical simulations.

Due to the London Naval treaty of 1930, Imperial Japanese Navy (IJN) which was outnumbered on the destroyers, tried to excessively arm the vessel lesser than 600 tons. It is because the treaty did not limit this category. As a result, IJN built and commissioned the torpedo boat “IJN Chidori-class” which armament surprisingly reacheed over 20 percent weight in the total. This excessive armament led to the top heavy, so the first boat experienced steeply inclining in the turning tests in the sea trial. Therefore, soon after the commission of the first boat of this class, IJN decided to add the bulges to the hull of every IJN Chidori class torpedo boat in an attempt to recover the dynamical stability. However, in 1934, the third boat “IJN Tomozuru” joined in 21st torpedo flotilla capsized out of Sasebo port after night torpedo attack exercise. The research report on this accident made by IJN was released in public domain after the end of the WWII, and it is noteworthy that this report was mentioning the dangerous decrease in restoring moments due to bulge exposure from the water (Matsumoto, 1954). On the other hand, Kawashima (1978) and Takaishi (1978) reported that increase of restoring moment due to lowering the position of the center of gravity is more effective than that due to the attachment of budges on the hull. However, as mentioned above, Takaishi (1978) simultaneously emphasized the decrease in restoring moments in following/quartering seas. Therefore, in order to investigate the decisive factor of her capsizing accident, the authors conducted the captive model experiments for her model with/without bulges, which included CMT (circular motion tests) and restoring variation measurement tests in waves. Furthermore, 4 DoF (surge-sway-yaw-roll) numerical simulations were extensively carried out by using hydrodynamic coefficients obtained from the experiments. Then, we finally uncovered that the effect of bulges on the restoring variation was existing indeed, but it was limited in actual. Instead of that, centrifugal force acting on the hull in the yaw-roll coupling motion (Ikenaga, 2018) greatly contributed to catastrophic roll and her capsizing. In other words, the presence or absence of bulges on the hull was not a decisive factor in her accident, but the range of the dynamical stability in each state decided the issue. These results

obtained here almost agree with the facts pointed out in the accident report of IJN. This fact supports the outstanding research level and contribution of IJN on the ship stability research in waves.

Keywords: *Yoshifumi TAKAISHI, IJN Tomozuru, Pure loss of stability, Resorting variation*

2. REFERENCES

Ikenaga, Y., 2018, "Relationship between pure loss of stability and Broaching -Model experiment and numerical simulation about an ocean research vessel in irregular quartering sea- (in Japanese)", Bachelor Thesis (Osaka University).

Kawashima, R., Takaishi, Y., Morimura, S., Yoshino, T. and Sasaki, H., 1978, "Model Experiments on Capsize and Its Prevention for a Small Fishing Boat in Waves (in Japanese)" Journal of the Japan Society of Naval Architects and Ocean Engineers, Vol. 143, pp.153-169.

Matsumoto, K., 1954, "Some Problems in Naval Shipbuilding Technology: Part IV (in Japanese)" Ship Magazine, Vol. 27, No.1, pp.1009-1021.

Takaishi, Y., 1975, "Experimental Technique for Studying Stability of Ships Achieved in Ship Research Institute", Proceedings of the International Conference on Stability of Ships and Ocean Vehicles, Glasgow.

Takaishi, Y., 1978, "Present Status and Future Aspects of the Research on Stability of Ships (in Japanese)" Bulletin of the Society of Naval Architects of Japan, Vol. 594, pp.571-578.

Takaishi, Y., 1982, "Consideration on the Dangerous Situations Leading to Capsize of Ships in Waves", Proceedings of the International Conference on Stability of Ships and Ocean Vehicles, Tokyo, pp.243-253.

An overview of the current research on stability of ships and ocean vehicles

Nikolaos Themelis, *Chairman of the Stability R&D Committee*, n.themelis77@gmail.com

Teemu Manderbacka, *NAPA Ltd*, teemu.manderbacka@napa.fi

Igor Bačkalov, *University of Belgrade, Faculty of Mechanical Engineering* ibackalov@mas.bg.ac.rs

Evangelos Boulougouris, *MSRC, University of Strathclyde*, evangelos.boulougouris@strath.ac.uk

Eleftheria Eliopoulou, *National Technical University of Athens*, eli@deslab.ntua.gr

Hirotada Hashimoto, *Kobe University*, hashimoto@port.kobe-u.ac.jp

Marcos Míguez González, *University of A Coruña*, mmiguez@udc.es

Dimitris Konovessis, *Singapore Institute of Technology,*

Dimitrios.Konovessis@SingaporeTech.edu.sg

Jean-François Leguen, *DGA Hydrodynamics*, jean-francois.leguen@intradef.gouv.fr

Claudio A. Rodríguez, *Universidade Federal do Rio deJaneiro,*

claudiorc@laoboceano.coppe.ufrj.br

Anders Rosén, *KTH Royal Institute of Technology*, aro@kth.se

Pekka Ruponen, *NAPA Ltd*, pekka.ruponen@napa.fi

Vladimir Shigunov, *DNV GL SE, Hamburg*, vladimir.shigunov@dnvgl.com

Martin Schreuder, *Chalmers University of Technology*, martin.schreuder@chalmers.se

Daisuke Terada, *National Defense Academy, Japan*, dterada@nda.ac.jp

ABSTRACT

The paper analyses the state-of-the-art and future perspectives by reviewing a selection of papers published in STAB2015, ISSW2016 & 2017. These works have been organized in different sections, according to the main thematic areas of research, covering intact and damage stability, regulatory issues including probabilistic approaches, advanced numerical methods for ship motion and stability failure prediction including roll damping, operational issues related to ship stability and environmental modelling. Furthermore, the challenges of feeding back to the educational process the research conducted are discussed. This review paper is a joint effort within the SRDC (Stability R&D Committee).

Keywords: *ship stability; ocean vehicles; ship dynamics; ship safety; STAB; ISSW; review*

1. INTRODUCTION

Ship stability is an area of vital importance for the design and operation of ships and other floating structures. Thus, it is a subject of continuous and extensive research aiming at enhancing safety. A series of STAB Conferences and ISSW workshops cover the key research topics related to the stability of ships, providing significant contributions to the

maritime community. Bačkalov et al. (2016) have reviewed the most relevant contributions reported in the STAB and ISSW proceedings of the period 2009-2014, identified and analysed the trends of research in ship stability. In the present work, a review of the research presented in STAB conferences and ISSW workshops in the period 2015 – 2017 (STAB 2015, ISSW 2016 and ISSW 2017) is done, and categorised in the following sections covering all major aspects of ship stability.

2. INTACT STABILITY

Regarding intact stability, in the period under review, the IMO work on preparing the Second Generation Intact Stability Criteria (SGISC, SDC 3/WP.5, annex 1) dominated the research agenda. In fact, the vast majority of presented papers is related either directly to the Criteria or to some of the five failure modes which are dealt with in SGISC. Within the works directly related to SGISC, the first group includes papers which focus on analysing the simplified stability failure assessment methods used in the current Level 1 (L1) and Level 2 (L2) criteria of the SGISC (Umeda and Francescutto, 2016). The second group focuses on studying the more advanced methodologies which constitute the Direct Stability Assessment (DSA), representing the third tier criteria in SGISC. The third group of papers involves studies of the main five dynamic stability failure modes, i.e. parametric roll resonance, pure loss of stability, surf-riding and broaching, dead ship condition and excessive accelerations, but from a perspective outside of the SGISC's framework. Finally, the fourth category includes papers dealing with probabilistic approaches for prediction of extreme events and capsizing. In the following subsections, the most relevant contributions in each of the previous four categories are described.

2.1 Simplified dynamic stability failure assessment methodologies

Considering that in the years under review a draft version of the first two tiers of the IMO SGISC has been accomplished, a very representative effort has been directed at testing the applicability and consistency of these two first levels in the stability evaluation process set up in these regulations. These studies consider many ship types, including for example Ro-Pax and container ships (Krueger et al., 2015a), the well-known C11 class container ship (Liu et al., 2015, Tompuri et al., 2017), cruise ships (Tompuri et al., 2017), a whole set of 17 vessels of different types (Schrøter et al., 2017), a patrol vessel (Ariffin et al., 2015) and fishing vessels (Mata-Álvarez-Santullano and Pérez-Rojas, 2015, Míguez González et al., 2015) and naval vessels (Petacco et al., 2017), despite not being considered within the scope of SGISC.

The need for this type of studies, that could be used for benchmarking of the user – implemented codes especially in L1 and L2, is highlighted in Reed (2016, 2017), where the process of verification, validation and accreditation of numerical tools is explained for L1 and L2 of the SGISC. Apart from the applicability and consistency studies described above, some other authors have focused their work on studying more in depth the numerical methodologies proposed for the L1 and L2 criteria for different failure modes.

Broaching and surf riding failure mode is tackled in Feng et al. (2015) and Umeda et al. (2015a). Although the former work focuses on fishing boats and small-size high speed vessels, and the latter investigates larger ships (container ships, RoRo, PCC and naval vessels), both studies conclude that surf-riding probability is greatly affected by the accuracy of calm-water resistance and the wave-induced surge force, particularly with respect to the diffraction effects. Additionally, Feng et al. (2015) find that surf-riding probability index is not sensitive to uncertainties in the propeller

thrust coefficient, wake fraction and thrust deduction coefficients, while wave force calculation and especially the diffraction effect affect significantly the probability index.

Regarding parametric roll resonance, Grinnaert et al. (2016a) assess the effect of the duration of the one-degree-of-freedom roll simulation, initial roll angle and linearization of GZ curve in the computation of maximum KG associated to L2 stability criteria for this failure mode. Their numerical results for two container ships, a RoRo vessel and a tanker show that ten roll cycles are sufficient to achieve steady parametric roll amplitudes, that initial roll angles greater than 5° have no influence on the maximum KG, and that the linearization of GZ curve has little effect on the parametric rolling L2 vulnerability index, especially when the GZ curve is close to linear up to 25° heel.

Peters and Belenky (2016) study the consistency of pure loss of stability L1 and L2 criteria for large *B/d* ratio vessels using a large cruise vessel as a test case. The inconsistency found between the two levels is eliminated by including the weathertight superstructures within the vessel buoyant volume in the GZ computation, which seems to be a reasonable solution for the case under analysis. However, the authors also suggest the inclusion of some operator model that would lead to a more realistic L2 standard that, otherwise, could be largely conservative.

Peters and Belenky (2017) analyze L1 and L2 vulnerability criteria for dead ship condition and point out that the different mathematical models used in these criteria frequently lead to inconsistency, i.e. stricter L2 than L1. A methodology is proposed to allow some controlled level of probability of inconsistency. Besides, the issue of integrity is raised: because L1 is based on the Weather Criterion, making L2 less restrictive than L1, as usually, may lead to situations that loading conditions failing the Weather Criterion are recognized as safe by SGISC.

2.2 Direct stability assessment (DSA) and operational guidance (OG) methodologies

Shigunov (2016) studies two approaches to solve the problem of rarity in DSA, extrapolation of the time to stability failure over wave height and reducing assessment to few selected combinations of wave height, period and direction and ship speed (design situations). Whereas the former method works well, the latter one shows significant scatter, therefore, it is suggested to use different design situations for different stability failure modes. Shigunov (2017) tests this suggestion for stability failures in beam seaway and confirms the suitability of the design situations method. Several approaches to select design situations are proposed and compared. Besides, a quicker solution, combining design situations with non-probabilistic safety criteria is tested but shows very poor performance.

Hashimoto et al. (2017) tackle the influence of operational limitations on navigation when a vessel is vulnerable to a stability failure. The authors investigate the influence of operational limitations on the routing of C11 container ship in trade between Japan and US, using parametric roll criterion, and consider effects of wave height, period and encounter angle and ship speed on the vessel motions.

2.3 Analysis of dynamic stability failure modes

The third main group of papers comprises the studies of the five dynamic stability failure modes from a perspective outside the framework of SGISC.

Regarding surge dynamics and broaching, Themelis et al. (2015) examine surf-riding in random sea through the concept of “high-runs’ events which are defined as the time periods where a ship attains abnormally high speed due to waves’ effect, thus they are defined as a speed crossing problem. Instantaneous wave celerity is used as a threshold value and its

correlation with mean ship speed is examined. The statistics of high-runs occurrence are investigated by direct counting based on numerical simulations. From another viewpoint, Kontolefas and Spyrou (2015) study the problem of time-dependence of nonlinear dynamics of surge motion in a multi-chromatic wave environment, by identifying phase-space objects, the so-called hyperbolic Lagrangian Coherent Structures. Spyrou et al. (2016) use this technique along with extended numerical simulations for the identification of new bifurcation phenomena of ship surge dynamics as more frequencies are added in the wave excitation. De Jong et al. (2015) perform extended numerical simulations of a 6 d.o.f. numerical simulation model targeting broaching behaviour in following and stern-quartering regular waves and examine the effect of ship speed, wave heading and steepness. Broaching zones are estimated, however the issue of their utilisation in real wave environment remains open. Belenky et al. (2015a, 2015b) use the concept of split-time method for the estimation of the probability of surf-riding and capsize due to pure loss of stability in irregular waves. By this concept, two problems are set: non-rare and rare, where a metric of the danger of the rare event is defined and computed utilising data from the non-rare problem (exceedances of an intermediate threshold) and statistical extrapolation techniques. Problems arising from the nature of each stability failure in irregular seas, such as the time dependence of phase-space and roll stiffness, are discussed.

Most of the works dealing with the parametric roll resonance have focused on the reliability of various mathematical models in predicting the phenomenon occurrence and on the accuracy of estimating the roll amplitudes. Umeda et al. (2015b) propose a 5 d.o.f. mathematical model considering maneuvering forces for numerical prediction of parametric roll resonance in regular oblique waves and compare the results with the free-running model tests. A 6 d.o.f. mathematical model is used by Liu and Papanikolaou (2015) to predict parametric roll in regular and triple-frequency head waves; the results are compared with semi-captive model tests. Ma et al. (2015) compare results obtained by a 3 d.o.f. mathematical model with model tests for parametric roll in regular head waves. Lu and Gu (2016) employ a 1 d.o.f. mathematical model, whereby the calculated instantaneous wetted surface due to heave and pitch motions is considered in the calculation of restoring variation. The numerical results are compared with free-running model experiments, with emphasis on the influence of radiation and diffraction forces on restoring variation. Rodríguez et al. (2015) develop a pre-calculated derivative model for fast parametric roll prediction in irregular head waves which, in contrast to full hydrodynamic codes, does not require high computational capacity.

With respect to stability in beam seas, Anastopoulos and Spyrou (2015) propose a stability assessment method based on the “realistic wave groups” (sequences of waves with high probability of occurrence in a given sea state). In another study of stability in beam waves, Anastopoulos and Spyrou (2017) estimate the probability of exceedance of a critical roll angle, by assessing the probability of encountering wave sequences exceeding previously identified critical wave groups. Hinz (2015) utilize risk analysis to estimate the safety of a RoPax ship based on the number of fatalities due to capsize in dead ship condition, and compare the results of the analysis with the stability assessment carried out with the presently used procedures (i.e. minimum *GM*).

Regarding pure loss of stability, Umeda et al. (2017) compare the performance of a coupled 4 d.o.f nonlinear model with model tests for a research vessel that sank while sailing in stern-quartering waves. Results show a good correlation between the model and the experiments and confirm that the accident could be due to pure loss of stability. The authors highlight the possibility to use this tool for the direct stability assessment of pure loss of stability under SGISC framework and

confirm that, similarly to Peters and Belenky (2016), the bulwark and weathertight superstructures should be included within buoyant hull due to the transient characteristics of the phenomenon under analysis. Borisov et al. (2015) suggest a L1 vulnerability criterion for excessive accelerations, which uses the roll amplitude from the IMO Weather Criterion, and examine a set of measures that could be implemented in the proposed criterion to improve its accuracy.

2.4 Probabilistic approaches to ship stability

Campbell et al. (2015) further develop the envelope peaks over threshold (POT) method for the extrapolation of the probability of occurrence of extreme events over the response amplitude from limited time series, including application of the generalized Pareto (GP) distribution to approximate the tail of the roll amplitudes probability density function, recommendations for the definition of the threshold and for estimation of the shape and scale parameter of GP, and uncertainty estimates of the probability of exceedance obtained by extrapolation. Smith and Zuzick (2015) apply statistical extrapolation of the exceedance probability over response amplitude to large-amplitude roll and pitch motions and vertical and lateral accelerations, using the GP distribution. For validation, the extrapolated values based on a subset of a time history are compared to the directly computed values. Belenky (2015) summarizes the known mathematical methods to account for data dependency in computing the variances of the estimates of mean and variance and proposes methods for their computation for an ensemble of independent records of different durations. Belenky et al. (2016) study the tail of the probability density distribution of large roll amplitudes, concluding that the tail is heavy until close to the unstable equilibrium and then becomes light with the right bound at the unstable equilibrium. It is shown that the tail structure is related to the shape of the stiffness curve. Weems and Belenky (2017) perform perturbed motion simulations with a high-fidelity potential code as an input for the solution of the rare problem of critical roll rate as a part of the split-time method for the example of pure loss of stability.

3. DAMAGE STABILITY

The main categories of studies are related with numerical methods for damage stability, including validation studies using model tests, as well as accident analyses. In addition, the survivability and safety assessment of damaged ships were studied.

3.1 Numerical and Experimental Methods

A series of model experiments to assess the flooding process in a ship like structure is presented by Lorkowski et al. (2015), together with a validation of a numerical simulation method. The test model has adjustable bulkheads and multiple external and internal openings that could be closed to test different flooding scenarios. Motions and floodwater levels are measured during the calm water experiments. The numerical model assesses floating positions in a quasi-static manner and employs a Bernoulli type flood rate calculation with discharge coefficients, determined experimentally. Two of the tested flooding scenarios are used to validate the method, while some limitations of the numerical model are discussed. Lim et al. (2015) present results for free-running model tests of a damaged ship, both in head and following seas. The focus is on the propulsion and manoeuvring performance of a flooded ship, related to the Safe Return to Port (SRtP) requirements. It is noted that in damaged condition the distinguishable roll period is identical to the wave encounter period, whereas in intact condition resonance in the natural roll period is observed. Dankowski and Krüger (2015) present an extension to a numerical time-

domain flooding simulation method to properly deal with the roll dynamics during the transient flooding in calm water. Validation results with model tests are also presented. Manderbacka and Ruponen (2015) study the effects of the breach size and internal openings on the roll motion during the transient flooding stage using dynamic simulation with lumped mass method. Furthermore, the effect of the inflow momentum flux is studied. It is concluded that a quasi-static approach is applicable when there are large internal obstacles in the flooded compartment. On the other hand, when the breach is large and internal obstacles are small, accounting for the inflow momentum flux becomes more important. Lee (2015) introduces a new simulation method for progressive flooding, based on a dynamic orifice equation, whereas the common practice is to use quasi-static Bernoulli method. The new approach is shown to avoid numerical stability problems, and it is demonstrated with the simulation of the Sewol accident. A CFD approach using URANS to a zero-speed damaged ship in calm water and in waves is presented by Sadat-Hosseini et al. (2015). This paper includes extensive validation of both flooding and roll damping characteristics against model test.

3.2 Accident Analyses

Krueger (2016) present an overview of using time-domain flooding simulation in the analysis of accidents. Several cases are briefly presented, including the Costa Concordia and Sewol. The main conclusion is that current time-domain flooding simulation tools, based on Bernoulli's theorem, are very useful for investigation of marine casualties. However, it is also pointed out that the main challenge is obtaining accurate data on the damage, actual loading condition, possible cargo shift and environmental factors. The flooding of the Sewol ferry is also studied by Lee (2015), as an example of using the dynamic orifice equation for flooding simulation.

3.3 Survivability Assessment

SOLAS 2009 does not explicitly address the accumulation of water on car deck spaces. Thus, many concerns have been raised regarding the level of safety required by SOLAS 2009 damage stability regulations and the one provided by Stockholm Agreement. The SDC sub-committee of IMO proposed amendments to SOLAS chapter II-1, including the survivability assessment of RoPax ships. Among others, a new s-factor concerning the RoRo spaces has been adopted in the new SOLAS 2020.

The particular s-factor formulation is investigated in Skoupas (2015). Calculations were performed for two large RoPax ships. The results show that the revised formulation seems to account the water on deck effect satisfactory but a more systematic investigation is needed in order to drawn consistent conclusions. Bergholtz et al. (2016) review existing, as well as proposed amendments, to Ro-Ro passenger ship safety regulations from a holistic perspective. Operational issues, decision support systems and emergency safety procedures are significant contributors of ship safety and need to be addressed in a systematic way.

Krueger et al. (2015b) investigate the effect on entrapped water in vehicle deck spaces of RoPax ships. Given the fact that the majority of relevant ship accidents happened in an intact ship condition with respect to the watertight subdivision, water on deck is formulated as an intact stability criterion and it is proposed to be regulated by the intact stability regulatory framework. The proposed methodology is quite simple in principle and can be also applied on calculations pertaining water accumulation due to firefighting. However, further development is needed with respect to the amount of water and the resulting roll period as well as to the proposed criteria.

As naval vessels are designed and built to support high-end combat operations,

survivability as well as ability to 'fight hurt' is a vital design objective. A new probabilistic approach on estimating the level of survivability of a surface combatant is presented in Boulougouris et al. (2015). The proposed approach is applied in a generic frigate and the results are compared to the current in force semi-empirical deterministic criteria. The assumed damage length is also discussed and proposed to be refined in a more rational way in order to account current weapon threats.

An alternative formulation of the critical wave height, derived in the GOALDS project, is presented by Cichowicz and Murphy (2016). The formulation includes the damage GZ curve properties (GM, GZ area and range), as well as the total residual buoyancy of the ship. The formulation from the HARDER project (and implicitly SOLAS 2009) is based on GZ_{max} and positive range of stability. A better agreement, compared to that of the HARDER formulation, between predictions of the GOALDS formulation and measurements from model tests is presented. Furthermore, the physical rationale behind the alternative formulation is outlined, as well as examples of how it could be utilized in the design of ships.

The starting point of Paterson et al. (2017) is that the wave height distribution behind the s-factor formulation of SOLAS 2009, derived from recorded accident sea states at the time of collision, cannot distinguish between either operational area or ship type, and that new formulations are needed to rectify this. A new s-factor formulation is thus proposed based on 129 accidents involving passenger ships only, between 2005 and 2016. New s-factor formulations based on wave height data of different key operational areas is presented. Finally, a large container ship is used to determine an attained index for all the presented s-factor formulations, and it is concluded that all new methods rendered a lower index than that of SOLAS 2009, in particular, the proposed formulation of the new accident database.

4. SHIP SAFETY IN OPERATION

Stability during ship's operational phase is influenced by various operational parameters such as environmental or loading conditions that could lead to various instabilities. Human reactions in emergency cases are very crucial and operational guidance is considered essential in all circumstances.

In the framework of IMO's SGISC, the use of operational guidance/limitations will be a necessity for the vessel which does not pass the different three tiers of the criteria. Under these conditions, some authors have focused their work in this field. For example, Terada et al. (2017b), using data from towing tank experiments and from a real vessel, test a methodology based on the use of a GPS with motion measurement capabilities to obtain, applying Wave Buoy Analogy, the incident wave spectra, which could be straightforwardly applied for predicting ship motions and thus, generating operational information. In investigating suitable signal processing methods for analysing non-stationary stochastic ship motions, as part of the development of guidance systems for heavy weather operation, Iseki (2015) reports the development and application of Discrete Wavelet Transform. The results were compared with Discrete Fourier Transform and a Time-Varying coefficient Vector Auto Regressive model and it is concluded that it is a powerful tool for analysing non-stationary ship motion data.

The rationale and development status of the assessment framework for manoeuvrability in adverse conditions is presented in Shigunov et al. (2016). The same authors have earlier proposed criteria for manoeuvrability in adverse conditions and a comprehensive assessment procedure, based on a simple mathematical model and allowing alternative methods (model tests, numerical simulations or empirical formulae, depending on designer's needs) for components of forces. Two additional procedures with reduced level of complexity were developed to determine the

required installed power as a function of ship's deadweight, windage area, rudder area, propeller characteristics and engine type.

Operational guidance is also important to prevent accidents related to stability failures. In this respect, an investigation of a safety level regarding excessive acceleration is presented in Ogawa (2015) based on a very serious marine casualty of a 8,750 TEU container ship during ballast transit. A technical investigation of a capsizing accident of a Japanese pusher tug is reported in Taguchi et al. (2015). At the time of the accident the tug was travelling without the box barge, and the investigation included an at-sea experiment and stability calculations in order to confirm the capsize mechanism. In order to prevent similar accidents, the operating company was instructed to prepare a manual, which explains precautions for pusher tug boats in navigating solely, limitations on loaded fuel oil and wind and wave conditions, as well as appropriate way of steering. Operational stability of car carriers is discussed in Huss (2016) as experienced by a shipping company and in relation to corresponding rule development and compliance. In order to maintain safe and efficient shipping, the sensitivity of this type of ships to stability variations in waves is highlighted, noting that the existing requirements in the Intact Stability Code and other IMO regulations and guidelines so far give very limited operational guidance. Stability management activities discussed include design measures, decision support systems on board, training and monitoring.

Modern passenger ships are equipped with loading computer as a statutory requirement. Following a flooding accident, the loading computer can produce information on the final equilibrium of the damaged ship for decision support. However, the timeline of the propagation of the flooding including the estimation of events, e.g. submergence time of non-watertight openings and time to capsize, is not assessed. More advanced decision support systems capable of assessing the timeline are available but not yet in wide use. In this respect, Pennanen et al. (2017) compare the outcome and performance of loading computer and advanced decision support system in accident. Possible crew response and statutory requirements to the decision support systems are also discussed. The Vessel TRIAGE method, intended for on-board use for assessing and communicating the safety status of the vessel in accidents is described together with a demonstration of its use in a collision damage of a large passenger ship by Pennanen et al. (2016). The safety status is determined by the most severe of similarly labelled threat factors of which two, related to damage stability, are presented. In the demonstration case it is shown that the predictions were influenced by crew actions, e.g. closure of an open watertight door. Another method of assessing ship's survivability on-board of a damaged ship is presented in Ruponen et al. (2015). Floodwater level sensors are used to detect the hull breach and then calculations of progressive flooding in time-domain are performed. Critical factors, such as stability of the ship and the evacuation time are accounted for. The proposed method is tested with two realistic damage scenarios for a large passenger ship. As an effective means to reduce the risk of losing lives in case of a flooding accident, Karolius and Vassalos (2017) discuss methods on improving active measures to reduce flooding and prolong the time to capsize, such as closing of external/internal openings, counter-ballasting and recovery of buoyancy with deployable emergency floating devices.

Fishing vessels have been historically characterized by a very large number of stability-related accidents. Simplified stability guidance systems have been proposed by many authors as one of the feasible solutions for providing stability information to the masters under the main premises of simplicity of use and low cost. Scarponi (2017) presents application examples of the so-called Wolfson simplified stability guidance, taking as a basis minimum freeboard and maximum sea state and displaying the level of safety of the vessel in a color-coded poster. Examples of two sank

vessels show that they were operating in dangerous conditions under the criteria of this method. Míguez González et al. (2016, 2017) describe a methodology to determine the natural roll frequency of the vessel and use it in a simplified computer stability guidance system. This method, based on sequential spectral analysis of the vessel roll motion, is applied to a stern trawler in regular and irregular head and beam waves, showing promising results.

5. ROLL DAMPING, ADVANCED NUMERICAL METHODS AND SPECIAL STABILITY PROBLEMS

Development and improvement of models used in seakeeping codes concerned roll damping (contributions due to bilge keels and wind, memory effect, stall effect for anti-roll fins and scale effect corrections), nonlinear wave-induced forces and nonlinear models of anti-roll tanks. Simulations based on direct numerical solution of flow equations are becoming a practical tool for the investigation of complex phenomena: apart from the establishing as the industry standard for definition of roll damping, such simulations proved their applicability to the simulation of fluid motions in anti-roll tanks (ART), severe green-water events, parametric roll, behaviour of granulated cargo and fluidisation of particle cargo.

5.1 Modelling of roll damping

Handschel at al. (2015) compare simulation results of free roll decay and harmonically excited roll motion for the definition of roll damping and recommend the Froude energy conservation approach and Fourier transform for the post-processing of roll decay and harmonic excitation simulations, respectively. Katayama and Umeda (2015) propose a ‘memory effect’ correction to Ikeda method for the bilge keel component of roll damping. The memory effect depends on the difference between the Keulegan-Carpenter (KC) number in the previous and current swings. RANS and experimental results are presented for forced irregular roll motions. Söder et al. (2015) formulate an approach for the estimation of aerodynamic roll damping and show that aerodynamic roll damping associated to wind, ship forward speed and roll motion is of the same order of magnitude as the hydrodynamic roll damping. Yıldız et al. (2016) numerically investigate the effect of vortex shedding and its interaction with free surface on roll damping due to bilge keel. A decrease in roll damping is observed at large roll motions due to proximity of bilge keels to the free surface, which is not predicted by the Ikeda method. Söder and Rosén (2016) propose a framework for holistic multi-tier roll damping prediction. A scale effect correction is proposed for roll damping due to bilge keels based on RANS simulation results.

Wassermann et al. (2016) applied RANS to simulate flow due to forced roll motion of an ellipsoid equipped with normal plates at varied flow speeds, roll frequencies and amplitudes and plate dimensions. The results compare well with available experiments. An improvement is proposed for the empirical formula of Ikeda for roll damping due to bilge keels, applicable in a wider range of KC numbers. Besides, an improved procedure is proposed to extrapolate the frictional component of roll damping from model to full scale. Rudaković and Bačkalov (2017) investigate the applicability of the Ikeda methods for roll damping prediction to typical European inland vessels and show that the simplified Ikeda method may considerably under-estimate the eddy-making component of roll damping or even provide negative values for full hull form vessels even with block coefficient within its applicability limits.

5.2 Anti-roll devices

Cercos-Pita et al. (2015) combine a 6 DOF simulation code of ship motions with an SPH (smoothed-particle hydrodynamics) numerical

method for fluid motions in the tank to investigate nonlinear dynamics of the system in regular beam waves. The SPH solver is validated using available experimental data. The results of simulations indicate nonlinear effects, e.g. decreasing efficiency of the tank with increasing wave steepness. Besides, bending of the response curves was observed with and without the tank due to the hardening restoring of the vessel. Fernandes et al. (2016) simulate two-dimensional flow around a wing profile with harmonically oscillating angle of attack using RANS to study the behavior of lift and drag with changing angle of attack and improve models of anti-roll fins in seakeeping codes. Sensitivity to turbulence model, time step and grid density is studied. The results agree well with cases available in the literature. Comparison to a typical seakeeping code shows a big improvement potential in predicting stall of fin sections: whereas models for upstroke motion are comparable to RANS results, they vastly under-estimate the stall effect for down stroke.

To enable efficient direct simulations of responses of an anti-roll tank (ART), Carette (2016) proposes to use amplitude-dependent retardation functions based on harmonic ART response data and Hilbert transform for time-dependent interpolations to capture the non-linearity in the tank response. The results of tests show good accuracy and efficiency. Using the effective gravity angle (EGA) as excitation parameter greatly improves the prediction when sway motion is significant.

5.3 Application of CFD in ship stability

Hashimoto et al. (2015) combine RANS solver, overset multi-block structured grids to tackle heave and pitch motions and a level set method for the free surface, to investigate the wave-induced surge force in following waves. The approach is validated against model tests and applied to a series of ship hulls to investigate the influence of main ship particulars, heave and pitch motions and heel angle on the wave-induced surge force and validate the empirical formula used in the SGISC pure loss criterion. Zhou et al. (2015) study parametric roll with a potential-theory solver where roll damping coefficients are provided with various methods (RANS simulations of roll decay and forced roll in calm water, roll decay tests and Ikeda method) and direct RANS simulations of ship motions in waves. The methods are compared with experiments. Galbraith and Boulougouris (2015) study parametric roll in regular head waves using a RANS solver combined with an overset grid method.

Kawamura et al. (2015) develop a numerical method based on SPH flow solver to predict 6 DOF ship motions in waves including severe water shipping (green water) events and validate it against model tests for a simplified model of a fishing vessel, captive or fully unrestrained, in following and stern-quartering regular waves. Reasonable agreement with tests is achieved, worsening for sway force and roll moment (for captive model) and sway and roll motions (for free sailing model). Gu et al. (2015a) simulate roll decay at zero speed with a RANS solver to compare roll damping between various positions of the bilge keels along a two-dimensional section of an FPSO. Gu et al. (2015b) simulate forced roll of a two-dimensional section and free roll decay of a three-dimensional container ship at zero speed using RANS. Good agreement with experiments is achieved for the forced roll, whereas free roll decay simulations of the three-dimensional ship compare less favourably with experiments, under-estimating the measured roll damping. Begovic et al. (2015) simulate free roll decay at zero speed to define roll damping of DTMB 5415 naval ship in intact and two-compartment damage conditions. Sensitivity to time step, turbulence model and grid refinement is studied. Comparison with experiments shows small error for the roll period and poorer agreement for roll damping in both intact and damage cases. Gu et al. (2016) compare two methods to tackle ship motions, sliding grid interface and

overset grid, to simulate roll decay at zero speed with a RANS solver of a pure car carrier and 2792 naval ship and compare numerical results with model experiments. Both approaches demonstrate a better accuracy than the simplified Ikeda method. For the pure car carrier, the overset grid method better predicts roll period, whereas the sliding interface method better predicts roll damping. For the 2792 hull, both roll period and roll damping are better predicted with the overset grid method.

5.4 Advanced cargo behaviour modelling

Ju and Vassalos (2015) apply a numerical FEM-based method to simulate fluidization of particle cargo. The method is validated vs. experiments for three-axial compression and cyclic direct simple shear (DSS). The influence of various factors (frequency and amplitude of oscillations and the initial degree of saturation of cargo) on the liquefaction onset is studied in simulations of a centrifuge test and a shaking table test. Spandonidis and Spyrou (2015) study a two-dimensional problem of coupled motion of dry granular cargo with ship roll motion in regular beam waves to identify the critical parameters affecting response. The cargo is modelled as individual particles, interacting through nonlinear elastic and frictional forces. The results show that a resonance of roll motion exists both with and without granular cargo. If wave excitation is below a certain limit, the presence of dry cargo reduces roll amplitudes, whereas for larger wave excitation, the vessel can show larger roll motions or even capsize in certain excitation frequency regions due to cargo movement.

6. STABILITY OF SPECIFIC SHIP TYPES

Recognising the particular challenges faced by specific ship types, a number of researchers have submitted papers focusing on their distinct stability issues. The types addressed during the review period included fishing and naval vessels, high speed crafts, multipurpose ships, offshore support vessels (OSVs), as well as river-sea ships and sailing yachts.

6.1 Fishing vessels

Stability related issues, both static and dynamic, mainly leading to capsizing, are among the most common causes of accidents involving fishing vessels. In addition, flooding, especially of the main fish holds and engine room, is also usually pointed out as another major reason. However, in both cases, accidents occur in a sudden way, preventing the crew from taking any corrective action or even being able to escape from the vessel. These statements are proven for the case of the Spanish fishing fleet in Mata-Álvarez-Santullano (2015), through an extensive analysis of more than 300 accidents occurring between 2008 and 2014. In Matsuda et al. (2017), another extensive analysis, in this case using towing tank experiments of 17 different vessels, shows that the Japanese fishing fleet is prone to experiencing dynamic stability failures. These include pure loss of stability, broaching and bow diving, thus also highlighting the importance of dynamic stability related accidents within the fishing fleet. The issue of flooding is tackled in Atzampos et al. (2017), where the authors propose the use of a high expansion foam system (Damage Stability Recovery System, DSRS) to reduce the flooding volume in high risk compartments, and thus increase the vessel survivability in critical flooding scenarios. A test case using a coastal UK fishing vessel is presented, showing a large reduction of risk by protecting the high-risk compartments (which, among others, include engine room and fish storage areas) with this system.

6.2 Naval Vessels

Naval ship stability papers mainly focus on two topics linked to the improvement of naval and merchant ship stability rules. The improvements of the Naval Ship Code, based

partially on similar to IMO's Goal-Based Standards underline the need for these two directions of work. The first is to find the justification of current rules in order to know if they are to be changed or not. The second is related to the associated tolerable risk and the probability of capsizing, similar to level 3 of IMO's SGISC.

Hayes et al. (2015) study the wind speed parameters used in merchant and naval intact stability analysis. In particular the nominal wind speed and gust factor used is investigated. It is noted that there are no clear and obvious justification for some of the values used. The authors explain the two philosophies that lead to very different nominal wind speed and they propose the introduction of a standardised set of wind speeds for stability analyses, which would make both naval and merchant rules more transparent. Luquet et al. (2015) show that numerical aerodynamic calculations (CFD) could be used in a near future to check or adjust the rules. Creismeas et al. (2017) compare the naval and commercial approaches on the impact of ice accretion on the stability of ships, a topic of great significance given the increasing importance of polar navigation and patrolling in polar areas.

Regarding the estimation of the operational capsizing risk, a number of researchers have utilised numerical dynamic stability tools to investigate the performance of naval vessels. Verboom and van Walree (2015) compare the accuracy of two time-domain, panel method, 6 d.o.f. codes to simulate the large amplitude motions of a frigate operating in stern quartering seas. The first method is partially body exact while the second method utilised is fully body exact. The comparison with model tests proves the significant improvement achieved by using the second method. On the other hand, Le Pivert et al. (2015) select a simpler solution and use one degree of freedom to derive analytically the probability density function of roll angle, roll speed and roll excitation moment and estimate the probability of capsize introducing a suitable criterion. A more sophisticated seakeeping code, namely FREDYN is used in Perrault (2015, 2016) to estimate the probability of exceeding a critical roll angle. A study is performed to find the most accurate correlation parameters to this probability. A list of regressors are suggested where GZ parameters showed always strong correlations over the set of ships tested (8 frigate-type ships).

Attempts to check some naval ships against SGISC is performed in Kahramanoğlu et al. (2015), Grinnaert et al. (2016) and Petacco et al. (2017). Some inconsistencies are pointed between L1 and L2 criteria. It is also pointed that the request of a maximum value of KG requested by the four other failure modes and the minimum value for excessive acceleration, contradict in some cases.

6.3 High-speed craft

Depending on the prevailing conditions in the market, high-speed craft (other than surface combatants) may not get sufficient attention at the STAB and ISSW events. During the review period considered in this paper only a handful of papers on high-speed craft has been presented. Nevertheless, high-speed craft in planning mode are subject to numerous hazardous, and from a modelling point of view challenging, dynamic stability phenomena.

Katayama and Amano (2015) present model experiments with three different high-speed craft hulls in regular and irregular head seas. Various aspects of the experimental setup, such as sampling frequency, are discussed. The longitudinal distribution of the vertical accelerations and the vertical acceleration stochastic process in irregular seas are characterized. Rosén et al. (2017) consider vertical accelerations for high-speed craft in irregular head waves, both through model experiments and time-domain simulations with a non-linear strip method. The results are discussed in relation to the prevailing safety philosophy and semi-empirical design methods

in the IMO HSC Code and classification rules. A number of questions are raised regarding the validity of these methods and the possibility of introducing direct methods is discussed. Also van Walree and Thomas (2017) present simulations and model experiments with a high-speed boat which is free-running in different relative angles towards the waves. Various operating limits, such as excessive accelerations, water ingress and surf riding, are investigated. The simulations are performed with a non-linear panel method, where very good correlation to measured motions is presented, and also the accelerations correlate fairly well. Terada et al. (2017a) present a method which could be used on-board high-speed craft for automatic avoidance of dangerous situations related to the craft vertical impact accelerations. It is based on recursive fitting of a time series model to real time measurement of the vertical accelerations on-board. The method is validated and the influence of various modelling parameters is investigated based on pre-recorded acceleration time series. Also de Alwis and Garme (2017) consider the situation on-board high-speed craft. A field study is presented where both subjective data in terms of the crews' experience of the operational environment and various pain and fatigue symptoms, and objective data in terms of vertical accelerations measured on-board, are collected. Clear correlation between subjective and objective data is found and the methods used for the data collection are concluded feasible for further studies.

6.4 Other ship types

Lübcke (2015) presents the investigation results for the accident of the multipurpose ship MV ROSEBURG, which occurred in the Bay of Kiel, in 2013. As a consequence of improper loading and subsequent incorrect on board stability management, the ship with the timber cargo on deck heeled due to wind gusts. This initial heel caused the sliding of cargo and failure of cargo securing equipment, which in turn, increased the heel. As a result, the ship lost some 75% of the cargo, but managed to avoid capsize. Chopra (2015) analyses the existing stability criteria of several offshore support vessels through their limiting KG for several conditions and/or operational modes. Oliveira et al. (2015) propose an alternative method to carry out inclining tests for offshore vessels in their operational location, taking into account the environmental conditions and the effects of mooring and risers. The method has been validated through model tests experiments and full scale tests using a semisubmersible unit. Wang et al. (2015) analyse the response of taut mooring lines subjected to single and bi-frequency parametric excitation. It is observed that, depending on the damping level and the amplitude of the harmonic excitation components, the safe regions of the stability chart may greatly change compared to those of single parametric excitation. Mazarakos et al. (2015) investigate the dynamics of a TLP platform supporting three oscillating water column (OWC) devices and a wind energy turbine using frequency and time domain numerical models. Umeda et al. (2016) address the occurrence of "false negatives" in the application of Level 2 of pure loss SGISC to offshore supply vessels (OSV), through model tests and numerical simulations.

The river-sea ships are inland vessels suitable for restricted navigation at sea. Chatelier et al. (2017) present research on the development of appropriate classification rules for river-sea ships that would take into account stability in waves and seakeeping of inland vessels. Angelou and Spyrou (2015) present a mathematical model intended for sailing yachts behaviour prediction. The model aims to estimate the variation of forces and moments acting on sails, caused by the wind-induced sails deformation and recognize the influence of these variations on the course-keeping instabilities in downwind sailing.

7. MODELLING OF ENVIROMENT

Studies related with the modelling of ocean waves are those of Gankevich and Degtyarev (2015) and Reed et al. (2016). Gankevich and Degtyarev (2015) present a theoretical method to estimate velocity and wave pressures of potential flow under given information of a wavy surface elevation. This work proposes a new method for the efficient calculation of the velocity and the wave pressures of potential flow in actual sea, which cannot be handled by numerical calculation of elliptic equation. In particular, it is demonstrated that the velocity and the wave pressures of potential flow in the actual sea state can be reproduced by the wavy surface elevation generated by an autoregressive model. This method can use the real time evaluation with respect to waves around a ship.

Reed et al. (2016) present a new modelling procedure with respect to incident irregular waves for use in a time-domain numerical ship-motion simulation code, using an autoregressive modelling procedure, which is a type of the statistical modelling procedure. The procedure appears to have several significant advantages compared with the classical Fourier series modelling, such as the Longuet-Higgins model, where the most important presented to be the computational time.

Regarding to an evaluation method of the wind force, Ariffin et al. (2016) examine several assumptions of the weather criterion code based on a new wind tunnel experiment method considering the effect of roll motion. Two models are used; a merchant ship with simple geometry and a naval ship. It appeared that experimental values of roll angle are lower than those predicted by the criterion.

Concerning the monitoring of the ocean waves, Susaki et al. (2017) propose to estimate the crests of incident waves in real time using radar. Specifically, the wave period can be estimated with an error of 7.0% and error of 6.6% compared with the wave buoy data by the radar mounted on the actual ship. It is also mentioned that it is possible to predict the wave profile of the incident wave to encounter, but verified results exist for wave heights below 3 m.

8. EDUCATION

In the previous reviews of papers presented at STAB conferences and ISSW events (Bačkalov et al., 2015 and Bačkalov et al., 2016), a growing concern was expressed that the contemporary research on ship stability and engineering education on this subject do not advance at the same pace. As a consequence, the research and the educational process become increasingly disconnected and the implementation of research results in university courses on ship stability turns into a challenging task. The papers highlighted the potential deficiencies of “classic” ship stability education, which could result in lack of knowledge necessary for proper understanding of complex stability problems that are nowadays gradually becoming an integral part of engineering practice. The papers also indicated some possibilities for facilitating these difficulties in teaching process. Yet the question how to attain the required level of ship stability knowledge through university education remained open, which in turn instigated the initiative to include this topic in the present review paper as well.

Therefore, a number of papers presented during the review period helping in bridging the gap between the research and the education on ship stability, have been identified. This includes papers that could assist in understanding of the future (or even present) stability rules on a conceptual level; papers that could help in implementation of advanced computational methods; and papers that put the well-established methods and approaches to test and re-examine the boundaries of their application.

An overview of the process of development and the current status of the SGISC is presented in Umeda and Francescutto (2016), offering an insight into the underlying assumptions and reasoning behind the formulation of standards to be used in novel regulatory requirements, provides information necessary for proper understanding and, consequently, successful implementation of rules. The paper of Peters and Belenky (2016) has a similar significance for the educational process. Focusing on pure loss of stability failure mode, the authors discuss the consistency of vulnerability levels of SGISC and consider the options for resolving such issues. Moreover, the paper offers a broader view of requirements that intact stability criteria should comply with in order to be successfully applied.

The implications of use of different mathematical models of the same phenomenon in analysis of ship stability in waves are the subject of Peters et al. (2015). Shigunov (2016) addresses the problem of rarity of stability failures and deliberates upon accuracy and suitability of two possible approaches that could be used in probabilistic direct stability assessment of ship stability. Both papers treat novel methods, typically above the scope of classis ship stability courses, and offer lessons on importance of proper mathematical modelling of stability phenomena and thorough understanding of underlying assumptions and boundaries of models' application, which students often fail to take into account.

While presenting a procedure implemented in software intended for decision support in flooding events, Pennanen et al. (2016) reintroduce the concept of floodable lengths curve to safety of passenger ships. Although this could unintentionally create some confusion in the classroom over the role of floodable lengths in the present subdivision and damage stability regulations, the paper is interesting from the educational point of view, as it invokes this somewhat neglected tool which is still taught in ship stability courses. On the other hand, Smith and Silva (2017) propose a method for assessment of applicability of linear strip-theory seakeeping approach in high sea states. In both cases, the papers deal with the revaluation of well-known methods that are standard parts of the naval architecture curricula.

As a final point, the authors of papers that are going to be presented in the future STAB and ISSW events are invited to take into account the importance of their work for education of prospect generations of engineers and, where applicable, to strive to present their results in a pedagogical manner. The teachers, on the other hand, are invited to embrace the abundance of knowledge on the subject, contained in the proceedings of ship stability conferences and workshops and to join and take active part in the work of international ship stability community gathered around STAB and ISSW.

9. FINAL REMARKS

Following the previous review work of Stability R&D Committee (Bačkalov et al. 2015), the current paper attempts to identify and synopsize the key directions of stability research as published in STAB and ISSW proceedings since 2015. Most of the works presented are driven by the forthcoming SGISC regulations, treatment of the nonlinear dynamics in a realistic sea environment, survivability assessment in damage conditions, advances in numerical codes for direct stability assessment as well as the increased focus on operational stability issues and stability of special vessels. Furthermore, it is highlighted that STAB Conference is playing a significant role in the education of young professionals as there is a need to bridge the gap between the research and the educational process.

10. ACKNOWLEDGMENTS

This collaborative effort has been undertaken by a group of members of the "Stability R&D Committee" (www.shipstab.org/stability-r-d-committee-srdc/) .

11. REFERENCES

Anastopoulos, P.A., Spyrou, K.J., 2015, "Assessing the Stability of Ships under the Effect of Realistic Wave Groups", Proceedings of STAB 2015, pp. 489-498.

Anastopoulos, P.A., Spyrou, K.J., 2017, "Evaluation of the critical wave groups method for calculating the probability of extreme ship responses in beam seas", Proceedings of ISSW 2017, pp. 131-138.

Angelou, E., Spyrou, K.J., 2015, "Modeling Sailing Yachts' Course Instabilities Considering Sail Shape Deformations", Proceedings of STAB 2015, pp. 1063-1073.

Ariffin, A., Mansor, S., Laurens, J-M., 2015, "A Numerical Study for Level 1 Second Generation Intact Stability Criteria", Proceedings of STAB 2015, pp. 183-193.

Ariffin A., Mansor S., Laurens J.-M., 2016, "Conduction of a wind tunnel experiment to investigate the ship stability weather criterion", Proceedings of ISSW 2016, pp. 245-252.

Atzampos, G., Vassalos, D., Boulougouris, E., Paterson, D., 2017, "A new era of fishing vessel safety emerges", Proceedings of ISSW 2017, pp. 193-198.

Bačkalov, I., Bulian, G., Cichowicz, J., Eliopoulou, E., Konovessis, D., Leguen, J.F., Rosén, A., Themelis, N., 2016, "Ship stability, dynamics and safety: Status and perspectives from a review of recent STAB conferences and ISSW events", Ocean Engineering, Vol. 116, pp. 312-349.

Bačkalov, I., Bulian, G., Cichowicz, J., Eliopoulou, E., Konovessis, D., Leguen, J.F., Rosén, A., Themelis, N., 2015, "Ship stability, dynamics and safety: status and perspectives", Proceedings of STAB 2015, pp. 99-141.

Begovic, E., Day, A.H., Incecik, A., Mancini, S., Pizzirusso, D., 2015, "Roll damping assessment of intact and damaged ship by CFD and EFD methods", Proceedings of STAB 2015, pp. 501-511.

Belenky, V., 2015, "Statistical Uncertainty of Ship Motion Data", Proceedings of STAB 2015, pp. 891-902.

Belenky, V., Weems, K., Spyrou, K., 2015a, "Toward a Split-Time Method for Estimation of Probability of Surf-Riding in Irregular Seas", Proceedings of STAB 2015, pp. 1087-1102.

Belenky, V., Weems, K., Woei-Min L., 2015b, "Split-time Method for Estimation of Probability of Capsizing Caused by Pure Loss of Stability", Proceedings of STAB 2015, pp. 821-840.

Belenky, V., Glotzer, D., Sapsis, T., 2016, "On the tail of nonlinear roll motions", Proceedings of ISSW 2016, pp. 109-114.

Bergholtz, J., Ahlman, T., Schreuder, M., Hanzén, R., Winby, P., Rosenqvist, S., 2016, "Holistic Perspective on Damage Stability Standards for RoPax Ships", Proceedings of ISSW 2016, pp. 121-128.

Borisov, R., Luzyanin, A., Kuteynikov, M., Samoylov, V., 2015, "An Approach to Assess the Excessive Acceleration Based on Defining Roll Amplitude by Weather Criterion Formula with Modified Applicability Range", Proceedings of STAB 2015, pp. 601-612.

Boulougouris, E., Winnie, S., Papanikolaou A., 2015, "Advanced Damage Stability Assessment for Surface Combatants", Proceedings of STAB 2015, pp. 967-978.

Carette, N.F.A.J., 2016 "Fast time domain calculations with non-linear anti-roll tank coupling using retardation functions", Proceedings of ISSW 2016, pp. 59-66.

Campbell, B., Belenky, V., Pipiras, V., 2015, "Application of the envelope peaks over threshold (EPOT) method for probabilistic assessment of dynamic stability", Proceedings of STAB 2015, pp. 809-820.

Cercos-Pita, J.L., Bulian, G., Pérez-Rojas, L., Francescutto, A., 2015, "Coupled simulation of nonlinear ship motions and free surface tanks", Proceedings of STAB 2015, pp. 1049-1061.

Chatelier, J.M., Nzengu, W.N., Cocito, R., 2017, "Stability and seakeeping of river-sea vessels – classification rules", Proceedings of ISSW 2017, pp. 149-158.

Chopra, G. H., 2015, "Modified Dynamic Stability Criteria for Offshore Vessels", Proceedings of STAB 2015, pp. 411-424.

Cichowicz, J., Murphy, A., 2016. "On damaged ship survivability assessment in design and operation of passenger ships", Proceedings of ISSW 2016, pp. 135-140.

Creismeas P., Lannel G., Leguen J;-F., 2017, "Iced maritime routes, impact on stability for naval ships", Proceedings of ISSW 2017, pp. 97-102.

Dankowski, H., Krüger, S., 2015. "Dynamic Extension of a Numerical Flooding Simulation in the Time-Domain", Proceedings of STAB 2015, pp. 383-391.

de Alwis, M P., Garme K., 2017, "Adverse health effects and reduced work ability due to vertical accelerations in high-performance marine craft personnel", Proceedings of ISSW 2017, pp. 103-108.

de Jong, P., Renilson, M.R., van Walree, F., 2015, "The Effect of Ship Speed, Heading Angle and Wave Steepness on the Likelihood of Broaching-To in Astern Quartering Seas", Proceedings of STAB 2015, pp. 1103-1114.

Feng, P., Fan,S., Liu, X., 2015, "Study on the Second Generation Intact Stability Criteria of Broaching Failure Mode", Proceedings of STAB 2015, pp. 195-202.

Fernandes, G., Kapsenberg, G., Kerkvliet, M., van Walree, F., 2016, "Towards accurate computations of active stabiliser fins, focusing on dynamic stall", Proceedings of ISSW 2016, pp. 51-58.

Galbraith, A., Boulougouris, E., 2015, "Parametric rolling of the tumblehome hull using CFD", Proceedings of STAB 2015, pp. 535-543.

Gankevich, I. and Degtyarev, A. B. (2015) Computational of pressures in inverse problem in hydrodynamics of potential flow, Proceedings of STAB 2015, pp. 1117-1122.

Grinnaert, F., Billard, J-Y., Laurens, J-M., 2016a, "Different computations of parametric roll level 2 criterion", Proceedings of ISSW 2016, pp. 33-39.

Grinnaert F., Gualeni P., Billard J.-Y., Laurens J.-M., Petacco N., 2016, "Application of 2nd generation intact stability criteria on naval ships", Proceedings of ISSW 2016, pp. 239-243.

Gu, Y., Day, S., Boulougouris, E., 2015a, "A study on the effects of bilge keels on roll damping coefficient", Proceedings of STAB 2015, pp. 775-783.

Gu, M., Lu, J., Bu, S., Wu, C., Qiu, G., 2015b, "Numerical simulation of the ship roll

damping", Proceedings of STAB 2015, pp. 341-348.

Gu, M., Bu, S., Qiu, G., Zeng, K., Wu, C., Lu, J., 2016, "Validation of CFD simulation for ship roll damping using one pure car carrier and one standard model", Proceedings of ISSW 2016, pp. 165-172.

Handschel, S., Feder, D.F., Abdel-Maksoud, M., 2015, "Estimation of ship roll damping - A comparison of the decay and the harmonic excited roll motion technique for a post panamax container ship", Proceedings of STAB 2015, pp. 475-488.

Hashimoto, H., Yoneda, S., Tahara, Y., Kobayashi, E., 2015, "Prediction of wave-induced surge force using overset grid RANS solver", Proceedings of STAB 2015, pp. 623-632.

Hashimoto, H., Taniguchi, Y., and Fujii, M., 2017, "A case study on operational limitations by means of navigation simulation", Proceedings of ISSW 2017, pp. 41-48.

Hayes P., Smith W., Renilson M., Cannon S., 2015, "A Reassessment of Wind Speeds used for Intact Stability Analysis", Proceedings of STAB 2015, pp. 441-450.

Hinz, T., 2015, "Risk Analysis of a Stability Failure for the Dead Ship Condition", Proceedings of STAB 2015, pp. 799-807.

Huss, M., 2016, "Operational stability beyond rule compliance", Proceedings of ISSW 2016, pp. 193-200.

Iseki, T., 2015, "Non-stationary Ship Motion Analysis Using Discrete Wavelet Transform", Proceedings of STAB 2015, pp. 673-680.

Ju, L., Vassalos, D., 2015, "Potential assessment of cargo fluidization based on an UBC3D-PLM model", Proceedings of STAB 2015, pp. 1123-1131.

Kahramanoğlu E., Yılmaz H., Yıldız B., 2015, "Comparative Stability Analysis of a Frigate According to the Different Navy Rules in Waves", Proceedings of STAB 2015, pp. 869-877.

Karolius, K. B. and Vassalos, D., 2017, "How to buy time following a flooding incident – incident – intelligent quantification of emergency response measures", Proceedings of ISSW 2017, pp. 67-72.

Katayama T., Amano R., 2015, "An Experimental Study on the Characteristics of Vertical Acceleration on Small High Speed Craft in Head Waves", Proceedings of STAB 2015, pp. 587-597.

Katayama, T., Umeda, J., 2015, "A study on roll damping time domain estimation for non periodic motion", Proceedings of STAB 2015, pp. 691-700.

Kawamura, K., Hashimoto, H., Matsuda, A., Terada, D., 2015, "SPH simulation of ship behaviour in severe water-shipping situations", Proceedings of STAB 2015, pp. 433-440.

Kontolefas, I., Spyrou, K.J., 2015, "Coherent Phase-Space Structures Governing Surge Dynamics in Astern Seas", Proceedings of STAB 2015, pp. 1077-1085.

Krueger, S., Hatecke, H., Gualeni, P., Di Donato, L., 2015a, "On the application of the 2nd Generation Intact Stability Criteria to Ro-Pax and Container Vessels", Proceedings of STAB 2015, pp. 453-463.

Krueger, S., Nafouti, O., Mains, C., 2015b, "A New Approach for the Water-On-Deck Problem of RoRo-Passenger Ships", Proceedings of STAB 2015, pp. 215-225.

Krueger, S., 2016, "Numerical flooding simulations - a useful tool for marine

casualty investigations", Proceedings of ISSW 2016, pp. 147-153.

Le Pivert F., Tizaoui A., Radjesvarane A., Billard J-Y, 2015, "Analytical Study of the Capsize Probability of a Frigate", Proceedings of STAB 2015, pp. 725-733.

Lee, GJ., 2015. "Flow Model for Flooding Simulation of a Damaged Ship", Proceedings of STAB 2015, pp. 931-951.

Lim, T., Seo, J., Park, S.T., Rhee, S.H., 2015. "Free-Running Model Tests of a Damaged Ship in Head and Following Seas", Proceedings of STAB 2015, pp. 643-652.

Liu, H., Turan, O., Boulougouris, E., 2015, "Investigation of the 2nd Generation of Intact Stability Criteria in Parametric Rolling and Pure loss of Stability", Proceedings of STAB 2015, pp. 701-710.

Liu, S., Papanikolaou, A., 2015, "Prediction of Parametric Rolling of Ships in Single Frequency Regular and Group Waves", Proceedings of STAB 2015, pp. 1029-1039.

Lorkowski, O., Kluwe, F., Dankowski, H., 2015, "A Numerical and Experimental Analysis of the Dynamic Water Propagation in Ship-Like Structures", Proceedings of STAB 2015 pp. 373-382.

Lu, J., Gu, M., 2016, "Validation of one numerical method for parametric roll criteria with experiments", Proceedings of ISSW 2016, pp. 41-47.

Luquet R., Vonier P., Prior A., Leguen J. F., 2015, "Aerodynamics Loads on a Heeled Ship", Proceedings of STAB 2015, pp. 735-744.

Lübcke, A., 2015, "Investigation of the intact stability accident of the multipurpose vessel MS ROSEBURG", Proceedings of STAB 2015, pp. 271-279.

Ma, S., Wang, R., Duan, W., Zhang, J., 2015, "Numerical Simulation of Ship Parametric Roll Motion in Regular Waves Using Consistent Strip Theory in Time Domain", Proceedings of STAB 2015, pp. 1145-1156.

Manderbacka, T., Ruponen, P. 2015. "The Impact of the Inflow Momentum on the Transient Roll Response of a Damaged Ship", Proceedings of STAB 2015, pp. 227-237.

Mata-Álvarez-Santullano, F., 2015, "Main Contributing Factors to the Stability Accidents in the Spanish Fishing Fleet", Proceedings of STAB 2015, pp. 653-660.

Mata-Álvarez-Santullano, F., Pérez-Rojas, L., 2015, "Application of IMO Second Generation Intact Stability Criteria for Dead Ship Condition to Small Fishing Vessels", Proceedings of STAB 2015, pp. 261-270.

Matsuda, A., Terada, D., Hashimoto, H., 2017, "The characteristics of capsizing phenomena of Japanese fishing vessels", Proceedings of ISSW 2017, pp. 199-206.

Mazarakos, T. P., Konispoliatis, D.N., Manolas, D.I., Mavrakos, S.A., Voutsinas, S.G., 2015, "Coupled Hydro – Aero – Elastic Analysis of a Multi – Purpose Floating Structure for Offshore Wind and Wave Energy Sources Exploitation", Proceedings of STAB 2015, pp. 1171-1181.

Míguez González, M., Díaz Casás, V., Pérez Rojas, L., Pena Agras, D., Junco Ocampo, F., 2015, "Investigation of the Applicability of the IMO Second Generation Intact Stability Criteria to Fishing Vessels, Proceedings of STAB 2015, pp. 441-450.

Míguez González, M., Santiago Caamaño, L., Díaz Casás, V., 2016, "Real-time stability assessment in mid-sized fishing vessels", Proceedings of ISSW 2016, pp. 201-208.

Míguez González, M., Bulian, G., Santiago

Caamaño, L. and Díaz Casás, V., 2017, "Towards real-time identification of initial stability from ship roll motion analysis", Proceedings of ISSW 2017, pp. 221-230.

Ogawa, Y., 2015, "An Investigation of a Safety Level in Terms of Excessive Acceleration in Rough Seas", Proceedings of STAB 2015, pp. 251-259.

Oliveira, M. C., Barreira, R.A., Porciúncula, I.N., 2015, "Offshore Inclining Test", Proceedings of STAB 2015, pp. 557-574.

Paterson, D., Atzampos, G., Vassalos, D., Boulougouris, E., 2017, "Impact assessment of wave statistics on ship survivability", Proceedings of ISSW 2017, pp. 73-80.

Pennanen, P., Ruponen, P., Nordström, J., Goerlandt, F., 2016, "Application of vessel TRIAGE for a damaged passenger ship", Proceedings of ISSW 2016, pp. 141-146.

Pennanen, P., Manderbacka, T. and Ruponen, P., 2017, "Implications of different alternatives for damage stability analysis in decision support", Proceedings of ISSW 2017, pp. 81-86.

Perrault D., 2015, "Exploration of the Probabilities of Extreme Roll of Naval Vessels", Proceedings of STAB 2015, pp. 855-868.

Perrault D., 2015, "Correlations of GZ curve parameters", Proceedings of ISSW 2016, pp. 229-238.

Petacco, N., Gualeni, P., Billard, J-V. and Grinnaert, F., 2017, "An integration of present navy ships intact stability criteria in the perspective of ship performance assessment in a seaway", Proceedings of ISSW 2017, pp. 89-96.

Peters, W. S., Belenky, V., 2016, "Regulatory aspects of implementation of second generation IMO intact stability criteria", Proceedings of ISSW 2016, pp. 27-32.

Peters, W. S., Belenky, V., 2017, "Challenges of Dead Ship condition vulnerability criteria development", Proceedings of ISSW 2017, pp. 15-20.

Peters, W., Belenky, V., Chouliaras, S., Spyrou, K., 2015, "Requirements for computational methods to be used for the IMO Second Generation Intact Stability Criteria", Proceedings of STAB 2015, pp. 711-721.

Reed, A. M., 2016, "Specific intended uses: Establishing verification, validation and accreditation objectives", Proceedings of ISSW 2016, pp. 67-72.

Reed, A. M., Degtyarev, A. B., Gankevich, I. and Weems, K., 2016, "New models of irregular waves - way forward", Proceedings of ISSW 2016 pp. 95-102.

Reed, A. M., 2017, "Verification and validation aspects of development and implementation of the Second Generation Intact Stability Criteria", Proceedings of ISSW 2017, pp. 169-174.

Rodríguez, C.A., Neves, M.A.S., Polo, J.C.F., 2015, "A Time-Efficient Approach for Nonlinear Hydrostatic and Froude-Krylov Forces for Parametric Roll Assessment in Irregular Seas", Proceedings of STAB 2015, pp. 663-671.

Rosén A., Begovic E., Razola M., Garme K., 2017, "High-speed craft dynamics in waves: challenges and opportunities related to the current safety philosophy", Proceedings of ISSW 2017, pp. 239-248.

Rudaković, S., Bačkalov, I., 2017, "On application of standard methods for roll damping prediction to inland vessels", Proceedings of ISSW 2017, pp. 159-166.

Ruponen, P., Lindroth, D., and Pennanen, P.,

2015, "Prediction of Survivability for Decision Support in Ship Flooding Emergency", Proceedings of STAB 2015, pp. 987-997.

Sadat-Hosseini, H., Kim, DH., Carrica, P., Rhee, S.H., Stern, F., 2015. "URANS Simulations for a Flooded Ship in Calm Water and Regular Beam Waves", Proceedings of STAB 2015 pp. 393-407.

Scarponi, M., 2017, "Use of the Wolfson stability guidance for appraising the operational stability of small fishing vessels", Proceedings of ISSW 2017, pp. 213-220.

Schrøter, C., Lützen, M., Erichsen, H., Jensen, J. J., Kristensen, H. O., Lauridsen, P. H., Tunccan, O., Baltsersen, J. P., 2017, "Sample applications of the Second Generation Intact Stability Criteria – robustness and consistency analysis", Proceedings of ISSW 2017, pp. 9-14.

Shigunov, V., 2016, "Probabilistic direct stability assessment", Proceedings of ISSW 2016, pp. 17-26.

Shigunov, V., Papanikolaou, A., and Chroni, D., 2016, "Maneuverability in adverse conditions: assessment framework and examples", Proceedings of ISSW 2016, pp. 217-226.

Shigunov, V., 2017, "Possible simplifications of direct stability assessment", Proceedings of ISSW 2017, pp. 27-38.

Skoupas, S., 2015, "Investigation of the Impact of the Amended s-factor Formulation on ROPAX Ships", Proceedings of STAB 2015, pp. 513-519.

Smith, T., Zuzick, A., 2015, "Validation of Statistical Extrapolation Methods for Large Motion Prediction", Proceedings of STAB 2015, pp. 1157-1170.

Smith, T. C., Silva, K. M., 2017, "Linear seakeeping high sea state applicability", Proceedings of ISSW 2017, pp. 111-116.

Spandonidis, C.C., Spyrou, K.J., 2015, "Coupled granular material and vessel motion in regular beam seas", Proceedings of STAB 2015, pp. 1133-1141

Spyrou, K.J., Kontolefas, I., Themelis, N., 2016, "Towards a theory of surf-riding in two-frequency and multi-frequency waves", Proceedings of ISSW 2016, pp. 75-81.

Söder, C.J., Ovegård, E., Rosén, A., 2015, "On aerodynamic roll damping", Proceedings of STAB 2015, pp. 425-431.

Söder, C.J., Rosén, A., 2016, "A framework for holistic roll damping prediction", Proceedings of ISSW 2016, pp. 183-189.

Susaki, H., Hirakawa, Y., Takayama,T., and Hirayama, T., 2017 "Acquisition and prediction of wave surface by marine radar for the safety of small ships", Proceedings of ISSW 2017 , pp. 49-56.

Taguchi, H., Haraguchi, T., Minami, M., and Houtani, H., 2015, "An Investigation into the Capsizing Accident of a Pusher Tug Boat", Proceedings of STAB 2015, pp. 903-910.

Terada, D., Amano, R., and Katayama, T., 2017a, "A motion estimation method of high speed craft in irregular sea by using onboard monitoring motion time series data for motion control", Proceedings of ISSW 2017, pp. 233-238.

Terada, D., Tamashima, M., Nakao, I., and Matsuda, A., 2017b, "On safe navigation support system using GPS compass", Proceedings of ISSW 2017, pp. 57-64.

Themelis, N., Spyrou, K.J., Belenky, V., 2015, "Surf-Riding in Multi-Chromatic Seas: 'High-Runs' and the Role of Instantaneous

Celerity", Proceedings of STAB 2015, pp. 757-767.

Tompuri, M., Ruponen, P., Lindroth, D., 2017, "On the consistency of the level 1 and 2 vulnerability criteria in the Second Generation Intact Stability", Proceedings of ISSW 2017, pp. 3-8.

Umeda, N., Ihara, T., Usada, S., 2015a, "An Investigation into the Factors Affecting Probabilistic Criterion for Surf-Riding", Proceedings of STAB 2015, pp. 319-329.

Umeda, N., Fujita, N., Morimoto, A., Sakai, M., Terada, D., Matsuda, A., 2015b, "Numerical Prediction of Parametric Roll Resonance in Oblique Waves", Proceedings of STAB 2015, pp. 331-339.

Umeda, N., Francescutto, A., 2016, "Current state of the second generation intact stability criteria - achievements and remaining issues", Proceedings of ISSW 2016, pp. 3-9.

Umeda, N., Alway, A., Usada, S., Matsuda, A., Terada, D., 2016, "Model experiment of an offshore supply vessel running in astern waves", Proceedings of ISSW 2016, pp. 11-16.

Umeda, N., Osugi, M., Sakai, M., Matsuda, A., Terada, D., 2017, "Model experiment on pure loss of stability for a ship in astern waves and its relationship with the Second Generation Intact Stability Criteria", Proceedings of ISSW 2017, pp. 21-26.

van Walree F., Thomas W L., 2017, "Validation of simulation tools for a RHIB operating in heavy seas", Proceedings of ISSW 2017", pp. 249-258.

Verboom E., van Walree F., 2015, "Validation of Time Domain Panel Codes for Prediction of Large Amplitude Motions of Ships", Proceedings of STAB 2015, pp. 745-754.

Wang, A., Yang, H., Barltrop, N., Huang, S., 2015, "Dynamic Instability of Taut Mooring Lines Subjected to Bi-frequency Parametric Excitation", Proceedings of STAB 2015, pp. 923-928.

Wassermann, S., Krambs, G., Abdel-Maksoud, M., 2016, "Estimation of force coefficients for normal forces on bilge keels and skin friction roll damping of ships by CFD", Proceedings of ISSW 2016, pp. 157-163.

Weems, K., Belenky, V., 2017, "Including diffraction and radiation into probabilistic description of capsizing", Proceedings of ISSW 2017, pp. 117-124.

Yıldız, B., Yurtseven, A., Katayama, T., 2016, "Effect of vortex shedding and free surface interaction on roll damping due to large amplitude roll motion", Proceedings of ISSW 2016, pp. 173-181.

Zhou, Y-H., Ma, N., Lu, J., Gu, X-C., 2015, "A study on applicability of CFD approach for predicting ship parametric rolling", Proceedings of STAB 2015, pp. 465-473.

Mathematical Models of Maneuvering in Waves: Historical Perspectives and the State of the Art

Arthur M. Reed, *David Taylor Model Basin, Carderock Division, Naval Surface Warfare Center*, arthur.reed@navy.mil
Robert F. Beck, *University of Michigan*, rbeck@umich.edu

The historical development and state-of-the-art in ship-motion computations for ships maneuvering in a large seaway are discussed. The paper goes beyond discussing a list of requirements for a computationally fast tool should meet, it presents, on a component by component basis, those functionalities that a maneuvering-in-waves program should incorporate with detailed citations. It is believed that the main focus areas in this development should be body exact computations of the hydrodynamic (radiation and diffraction) forces, and true integration of the maneuvering and seakeeping model rather than superimposing separate models on top of one another.

1 INTRODUCTION

Because of the complexity of hydrodynamic computations for ships operating in a seaway, computations have traditionally been separated into seakeeping, maneuvering, resistance, and propulsion. Modern advances in computational methods and computers have allowed these separate areas to slowly come together into the unified field of ship dynamics. In order to properly simulate maneuvering-in-waves (MiW), it is necessary to consider all aspects of seakeeping, maneuvering, resistance, and propulsion as one. Waves and wave loads drive a ship's motions, but they also affect added resistance, propeller thrust and torque, and rudder forces, all of which in turn alter a ship's maneuvering characteristics.

The mathematical modeling of ship maneuvering-in-waves has been challenging as it has a dual background: conventional seakeeping and calm-water maneuvering. The historical development of these two disciplines, while describing the same object, differ in how the fluid-body interaction is described. For example, traditional seakeeping theories put a significant emphasis of the dependence of added masses on wave frequency, while maneuvering in calm water used (for a good reason) added mass at zero-frequency. The differences in the approaches to these two problems have created difficulty in developing an adequate mathematical model of MiW that can be successfully validated against model-test data. The transition of numerical seakeeping approaches from the linear frequency domain to the nonlinear time domain has been a significant step forward but has not fully solved the problem of predicting MiW, unless full-blown computational fluid dynamics (CFD) approaches are used. The latter, however, are too computationally expensive to produce a statistically significant quantity of data in a practical amount time. Thus, a practical solution has to be built based on a potential flow solver embedding results from relatively short time CFD simulations. This paper presents a review of works done in this area—with specific attention given to adding cross-flow drag and other relevant terms to each station of a ship hull, so the "maneuvering terms" can be integrated along with the hydrostatic, Froude-Krylov, diffraction and radiation

forces considered in seakeeping.

In the discussion that follows, we shall first provide a historical review of various computational approaches to the maneuvering-in-waves problem; then we shall summarize what we believe to be the state-of-the-art in fast computational approaches and provide a comparison of this proposed approach to that of other contemporary approaches.

2 MANEUVERING IN WAVES

2.1 The Maneuvering-in-Waves Problem Defined

Traditionally, seakeeping assessments and intact stability assessments of vessels have been separate processes. Seakeeping assessments have been performed using linear assumptions, with a wave spectrum being combined with a response amplitude operator (RAO) to produce a response spectrum. This response spectrum is then used to determine whether the vessel's motions are acceptable for a commercial ship or are used to determine the percent time operable for a naval vessel.

Historically, the intact stability of commercial vessels has been evaluated using *prescriptive* criteria based on the work of Rahola (1939) as incorporated in the International Code on Intact Stability, the 2008 IS Code (IMO MSC 85/26/Add.1 2008). The history of this development is described by Kobylinski and Kastner (2003) and IMO MSC.1/Circ.1281 (2008). Similar criteria for naval vessels are provided by Sarchin and Goldberg (1962) and NAVSEA (2016).

Beginning in the early 2000's, IMO initiated efforts to develop *performance-based* stability criteria for commercial vessels (cf., Francescutto 2004, 2007; Peters et al. 2011). In the same time frame, NATO initiated an effort to develop a goal-based standard for naval vessels that could guide navies and classification societies in the development of rules for naval vessels (Rudgley et al. 2005; NATO 2007a,b). More complete summaries of the development of the IMO intact-stability standards and the Naval Ship Code can be found in Reed (2009) and Reed and Zuzick (2015).

Under the IMO umbrella, there are several levels of assessment with both complexity and fidelity increasing in parallel. The highest level of fidelity is that of direct assessment, where a computational tool is used to predict the responses of a vessel in a seaway using an accurate model of the seas and the ship.

Computational tools that support direct assessment against stability criteria are simulating a ship-motion problem that is different from a traditional seakeeping problem. In a traditional "seakeeping" framework, the ship's speed and heading are considered known or prescribed—the solution of the seakeeping problem is the characterization of the motions about this nominally constant speed and heading. This framework is adequate and appropriate for determining non-rare motion statistics, such as the root mean-squared (RMS) or significant single-amplitude (SSA) values for vessels in moderate to high seas.

In the characterization of the large-amplitude, or rare-motion problem for a vessel in extreme seas, it is necessary to consider the forces and responses that arise from large deviations from the constant speed-heading assumption. These may include, but are not limited to, surf-riding and broaching. As such, the physical problem is best characterized as a *maneuvering-in-waves* problem.

At the highest level, the MiW problem can be described by the ambient environment, the ship-control condition, and the forces acting on the ship. Figure 1 illustrates the physical problem to be modeled.

In solving MiW problems, one may think that superimposing a seakeeping code "on top of" a maneuvering code is all that is necessary. This is what de Kat and Paulling (1989), de Kat (1994), and de Kat, Brouwer, et al. (1994) did; they literally superimposed a seakeeping model on a maneuvering model. A more formal way of performing this superposition is to separate the problem into a low-frequency portion (maneuvering) and a high-frequency portion (seakeep-

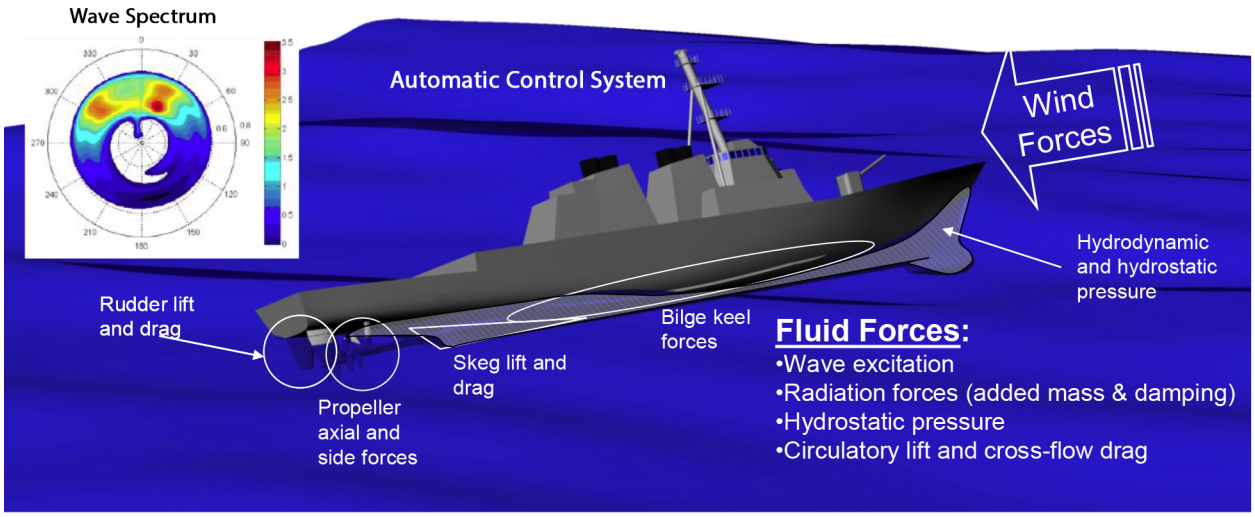

Fig. 1 Illustration of the maneuvering-in-waves problem to be simulated. (From Belknap and Reed 2010)

ing), an approach which has been employed by many authors studying MiW (cf., Yasukawa and Nakayama 2009; Skejic and Faltinsen 2013, for just two examples). As will be shown, this does not appear to be a satisfactory decomposition for extreme seas.

Figure 2 shows a series of measured turning circles for a model at a Froude number, F_N of 0.3, with a rudder angle of δ of 20° in calm water, and for an approach in head waves of length, λ/L of 1.0, for increasing steepnesses. In waves of smaller steepness, H/λ 1/90 and 1/60, the turning circles in waves lie on top of the calm-water turning circles, although for a steepness of 1/60, the circles in waves are starting to drift relative to the calm-water turning circles. However, for the maximum steepness, $H/\lambda = 1/30$, there is significant divergence, with the model in waves showing significant drift and the diameter of the circles increasing. Cura-Hochbaum and Uharek (2016) and Papanikolaou et al. (2016) show similar drift for turning circles in steep waves from experiments at MARINTEK (Sprenger et al. 2016) and RANS calculations. Thus one must conclude that for steep waves, the physics to be simulated in MiW is not just a simple superposition of seakeeping upon a maneuvering problem.

Yasukawa and Nakayama (2009) presented the results from another set of regular wave MiW experiments, as well as computations based on the low-frequency/high-frequency decomposition to separate the maneuvering problem from the seakeeping one. These experiments were performed at a constant wave amplitude, so that as the frequency of the regular waves increased, the wave steepness also increased. The results of the experiments and computations for four wavelengths are shown in Figure 3. The results for the shortest/steepest waves are on the left and the results for the longest/least steep waves are on the right. As can be seen, the predictions for all but the shortest and steepest are in reasonably good agreement with the experiments. Yasukawa and Nakayama (2009) attribute the poor agreement in the left-most plot on the shortness of the wave length, but in fact, there is no way to tell if it is due to the shortness of the waves or to their steepness. The results from a Force Study, (Telste and Belknap 2008; Belknap and Telste 2008), would indicate that it is the steepness rather than the wavelength that is most important.

The turning-circles-in-waves performance of another computational model, a classic blended code that computes the exact hydrostatic and Froude-Krylov forces with linear radiation and diffraction forces superimposed on

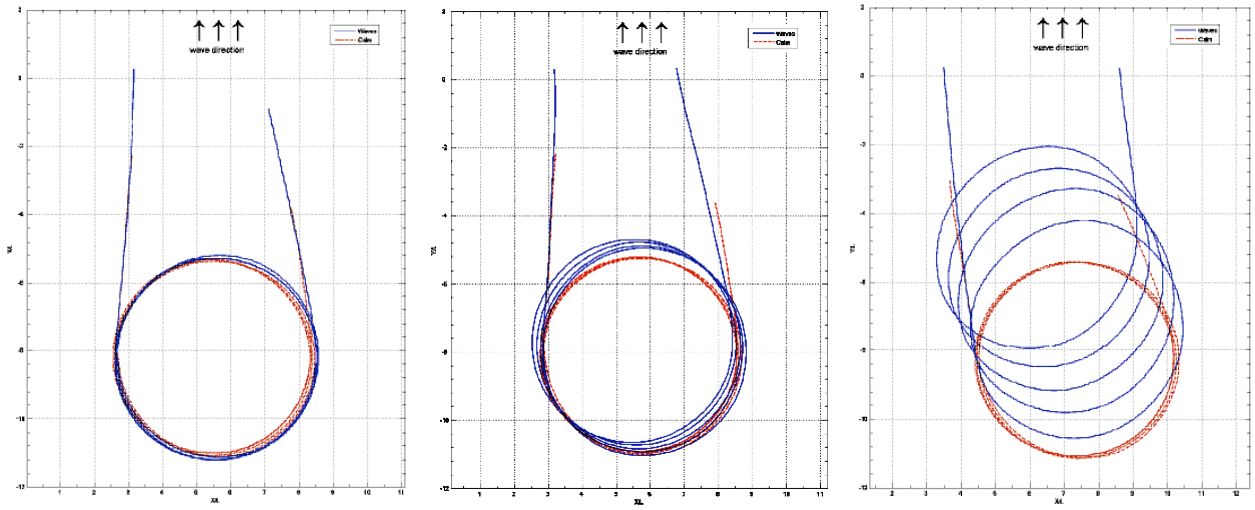

Fig. 2 Measured turning circles in waves (approaching in head waves), $F_N = 0.3$, $\delta = 20°$, $\lambda/L = 1$, left: $H/\lambda = 1/90$, center: $H/\lambda = 1/60$, right: $H/\lambda = 1/30$; red dashed line in calm water, solid blue line in waves. (Courtesy of Bob Bachman)

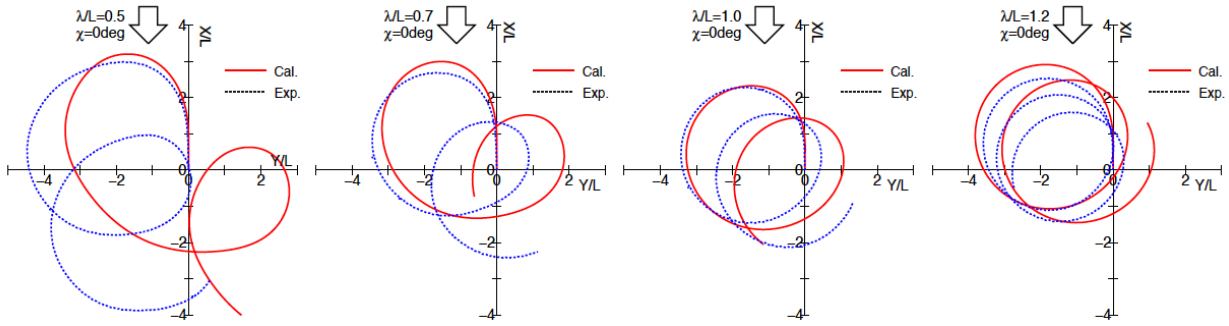

Fig. 3 Turning circles in waves for S-175 container ship for constant wave amplitude (approaching in head waves), $F_N = 0.15$, $\delta = -35°$, $\lambda/L = 0.5$ $(H/\lambda = 1/25), 0.7$ $(H/\lambda = 1/30), 1.0$ $(H/\lambda = 1/50), 1.2$ $(H/\lambda = 1/60)$; solid red line calculated, dashed blue line experiment. (From Yasukawa and Nakayama 2009)

a coefficient based maneuvering model is shown in Figure 4. The small red circles are experimental results for steep regular waves with $\lambda/L = 1.0$ and $H/\lambda = 1/30$, the vessel is drifting in the direction of wave travel. The large dark blue trajectory moving toward the top of the figure is a maneuvering model tuned to replicate the turning circle of the model in calm water. The light blue trajectory moving diagonally in the direction of wave travel and toward the top of the page is a model that has been tuned to best replicate the performance of the physical model in waves, but does not do at all well at predicting calm-water turning circles. Neither of the maneuvering models does well at replicating either the turning circle diameter or drift direction of the physical model in the steep regular waves.

Subramanian (2012) and Subramanian and Beck (2015) have performed MiW calculations using body-exact strip-theory to predict radiation and diffraction forces, Froude-Krylov forces, and hydrostatic forces for a case which correspond to Yasukawa and Nakayama's (2009) experiment where $\lambda/L = 1$ for $H/\lambda = 1/50$. The result of Subramanian's calculations is shown in Figure 5 which does not compare with the model experiments nearly as well as Yasukawa and Nakayama's calculations do. The Force Study, (Telste and Belknap 2008; Belknap and Telste 2008), suggests that the

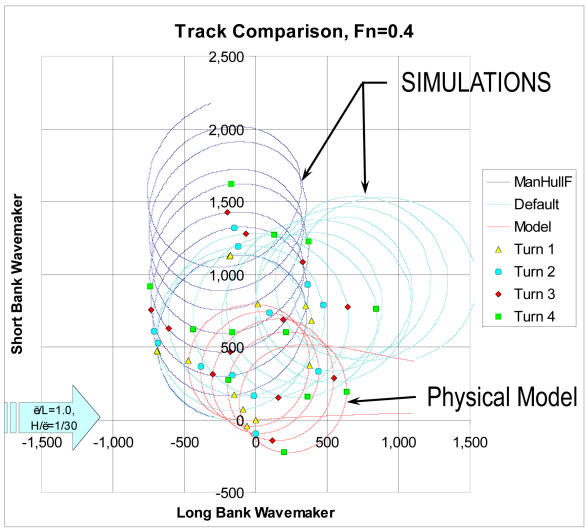

Fig. 4 Performance of Coefficient-based Maneuvering Model in Steep Regular waves, $F_N = 0.40$, $\delta = -30°$ (turning to port), $\lambda/L = 1.0$, $H/\lambda = 1/30$; light and dark blue lines calculated with two different coefficient based models, red line experiment. (Courtesy of Tim Smith and Paul Kopp)

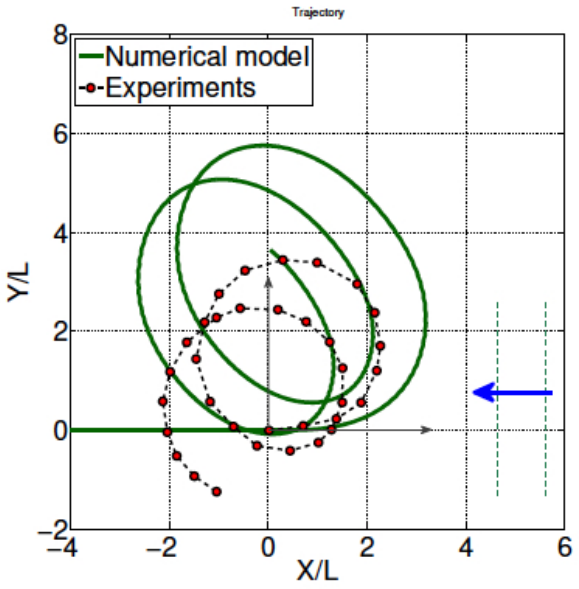

Fig. 5 Time-history turning circle in waves for S-175 container ship (approaching in head waves), $F_N = 0.15$, $\delta = 20°$, $\lambda/L = 1$, $H/\lambda = 1/50$; solid green line computations, black dashed line with red dots experiments. (From Subramanian 2012)

body-exact strip-theory radiation and diffraction forces, Froude-Krylov forces, and hydrostatic forces are calculated quite accurately. The poor over-all agreement may reflect deficiencies in the maneuvering-force, rudder-force, and propulsor-force models.

Finally, Figure 6, from Yasukawa and Nakayama (2009), shows calculated and measured time histories of speed, drift angle (yaw), yaw rate, heave, heel+roll, and pitch during one complete circle for the case of the S-175 model at $F_N = 0.15$, $\delta = -35°$, $\lambda/L = 0.7$, $H/\lambda = 1/60$, approaching in beam waves from starboard and turning to port. When comparing these time histories one should examine the envelopes of motions, not the actual time histories, as the wave traces are not synchronized. The envelopes of motions show that the experimental model was turning faster than indicated by the calculations. This is an indication of either an error in the calculated speed or in the calculated turning-circle diameter. The calculated and measured speed losses are quite comparable, although it appears that the calculated speed is slightly greater than the calculated measurement, which would indicate that motion-history calculations should be leading, not lagging behind actual measurements. Thus, it should be expected that the turning diameters are over predicted, which is indeed the case as shown in Figure 3, although it is for a different wave-approach direction than Figure 6.

The discussion and figures shown above indicate that the MiW in extreme seas problem is one of the most complex ship-hydrodynamics problems one will encounter. It combines all of the hydrodynamic problems that a naval architect might encounter into one problem—resistance, propulsion, seakeeping, and maneuvering. The remainder of this section will discuss how the problem may be addressed in a computationally efficient manner.

2.2 Historical Background

There are two basic approaches for solving the maneuvering-in-waves problem: blended methods and CFD (Beck and Reed 2001). Blended methods use a mixture of linear and nonlinear theories. The forces are often com-

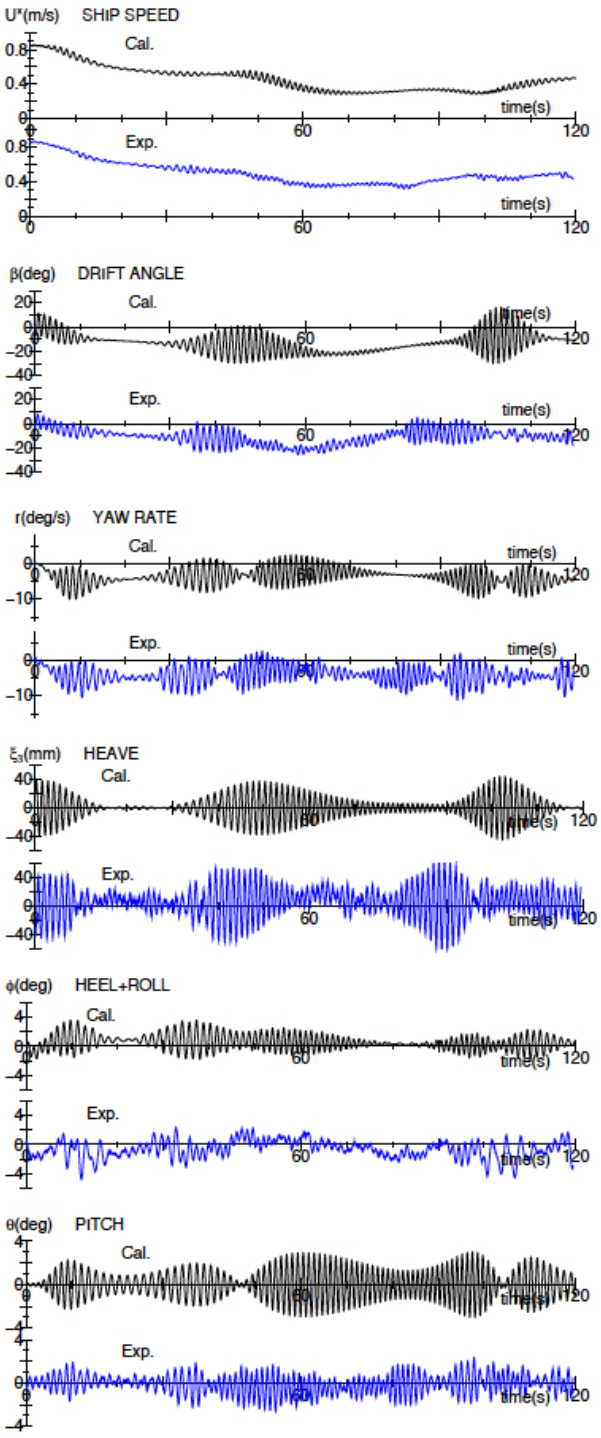

Fig. 6 Time histories for turning circle in waves for S-175 container ship (approaching in beam waves from starboard), $F_N = 0.15$, $\delta = -35°$ (turning to port), $\lambda/L = 0.7$, $H/\lambda = 1/60$; black line (top) calculated, blue line (bottom) experiment. (From Yasukawa and Nakayama 2009)

puted with the hydrostatic and Froude-Krylov forces integrated over the exact wetted surface, the added mass and damping found using a linear theory such as a strip approach, and viscous damping is treated empirically. The blended methods are computationally very fast (on the order of minutes of computer time). On the other hand, unsteady CFD methods can handle viscous effects such as flow separation and flow into a propeller, and thus are more realistic but require hours of computer time. Depending on the type of free-surface boundary conditions used, some CFD codes can also compute breaking waves and green-water-on-deck.

Whether a blended method or a CFD method is used depends on the purpose of the computations, the desired outcomes and the available computational time. Typically, because of their speed, blended methods are used for general design studies and real-time ship-motion computations. For detailed design studies such as stern-shape optimization, CFD computations are used. As computational power increases and numerical methods improve, it is expected the CFD will eventually be used for all types of MiW problems.

Regardless of the method used, the first step in solving a MiW problem starts with time integration of the rigid-body equations of motion. The rigid-body equations of motion that must be solved to determine ship motions equate the forces and moments acting on a body to the accelerations times the mass matrix for the six degrees-of-freedom. The equations themselves are six, coupled, nonlinear, first-order differential equations for the six unknowns: 3 translation velocities (surge, sway and heave) and 3 rotational velocities (roll, pitch and yaw). One also needs to know the orientation of the body relative to the inertial (or earth-fixed) axis, which leads to six more differential equations for the three translations along the axes and three Euler angles for the rotations. The difficult part of solving the equations of motion is finding the forces acting on a body. These forces are a function of: the accelerations (added mass), velocity (damping) and orientations (spring constants),

wave and wind loads, propeller forces, rudder forces, etc.

Blended/Potential Flow Methods

The complete ship MiW problem is extremely difficult to solve and approximations must be made. Depending on the approximations, very different mathematical problems result, which is why solving maneuvering, seakeeping, calm-water resistance, and propulsion problems went in different directions. For example, equations of motion and orientation can be linearized differently to simplify each of the above problems. For seakeeping problems, one can work in the time or frequency domain and neglect rudder and propeller forces. For MiW problems, the time domain is required because ship responses and maneuvers are generally not sinusoidal and vessel speed is not constant. Because rudder forces are critical, some type of autopilot is needed to keep a vessel on a desired course. For MiW, the solution to the 12 equations above is typically found by time-stepping. At each time step, the forces acting on a vessel must be determined, the equations of motion solved, and finally the orientation at the new time step determined. To determine the forces at each time step, one can use a purely theoretical analysis such as slender-body theory, blended methods or CFD.

Blended methods cover a large range of different techniques depending on the approximations that are made. The simplest blended methods employ linear equations of motion with linear-hydrodynamic coefficients. Typically, these approaches are based on the linear-convolution theory of Cummins (1962) or Ogilvie (1964). Fossen (1994, 2005) and Bailey et al. (1997) are examples of this type of approach. In order to obtain acceptable results, linear potential-flow computations need to be blended with empirical corrections to account for viscous effects, propulsion performance, rudders, and bilge keels. Viscous corrections typically take the form of maneuvering coefficients (both linear and nonlinear) used in normal calm-water maneuvering-equations of motion. A next level of complexity is to add in nonlinearities that are easily computed. Three nonlinearities are usually included at this level: equations of motion are no longer linearized; the velocity-squared term in the Bernoulli equation is included in calculating hydrodynamic pressure; and nonlinear hydrostatic and Froude-Krylov exciting-force terms are included. Nonlinear hydrostatic and Froude-Krylov terms are found by integrating hydrostatic pressure and incident-wave pressure over an exact-hull wetted surface. Normally, an exact wetted-surface is taken as the intersection of an incident-wave-free surface with an exact-hull surface (including motion effects), neglecting changes in free-surface height due to calm-water, radiated, and diffracted waves.

As with pure seakeeping problems, incorporating further nonlinearities becomes more difficult since the potential-flow hydrodynamic problems are no longer linear. Nonlinear behavior arises from both a changing-body shape due to vessel motions and nonlinear free-surface boundary conditions. Body-exact and weak-scatterer approaches use a linearization of the free-surface boundary condition; these approaches also use the instantaneous wetted surface to solve the potential-flow problem at each time step. The solutions must still be combined with empirical corrections in order to obtain accurate solutions. Nonaka (1990b,a) and Skejic and Faltinsen (2008, 2013) and others use a two time-scale approach. High-frequency motions due to waves are considered separately from low-frequency or maneuvering motions. At each time step, the seakeeping problem is solved normally assuming constant velocity along a straight-line path. Mean second-order force and slowing varying forces due to waves are also computed. Next, the maneuvering problem is solved including the mean drift and slowly varying forces which gives a new path and vessel speed for the next time step, then the process can be repeated.

The two time-scale approach to the MiW problem is appropriate for head seas when the frequency of encounter is relatively high, but the

proponents of this separation do not discuss following seas where the frequency of encounter can become quite small and there is little separation in the time/frequency scales for the maneuvering and seakeeping problems.

Separating the two time scales is not always necessary. As discussed in the remainder of this paper (or see Subramanian and Beck 2015), it is possible to combine all the forces acting on a vessel and solve the equations of motions for the seakeeping motions and the maneuvering path simultaneously. To obtain accurate answers, good models for nonlinear wave loads, propellers, rudder, calm-water resistance, and viscous forces are necessary.

CFD Methods

The other possibility for solving MiW problems is to use CFD methods. As previously stated, CFD can give the most comprehensive solution with a minimum amount of approximations, and viscous effects are automatically included; thus, no empirical corrections are necessary. Depending on the code, breaking waves can be accounted for properly. Varying thrust, torque, side load and cavitation on a propeller can also be accounted for if one can make extensive calculations that are extremely large and long. The disadvantage of using CFD methods rather than blended methods is that CFD computations require large amounts of computer time, which for extensive calculations can be on the order of many days.

At the present time, CFD computations for MiW are not routine because of difficulties involved in setting up grids and because of the large amounts of computer time involved. Larsson et al. (2014), Chapter 4, "Evaluation of Seakeeping Predictions" provide a good overview of the accuracy of CFD computations in seakeeping for steady-forward speeds compared with experiments.

Three different models were used in Larsson's study: KVLCC2, a modern tanker with a bulbous bow and a stern bulb; KCS, a container ship; and 5415, a naval-combatant hull form. Test cases were given for: regular head waves; diffraction at forward speed with fixed sinkage and trim; and roll decay for free-to-roll only. The errors between predictions and experiments ranged widely depending on the case, wavelength and speed. The total average error was 23-percent, but for ship motions, the first harmonic errors for amplitude and phase were 13-percent. Compared with potential flow, the CFD calculations showed larger errors for medium and long wavelengths, but were much better in small motions at short wavelengths.

Guo et al. (2012) also investigated CFD computations for the KVLCC2 in head waves. The theoretical predictions for ship motions and added resistance agreed well for the wavelength range tested ($0.44 < \lambda/L < 1.6$). Comparisons with strip-theory predictions for ship motions showed that CFD had no advantage. However, added-resistance predictions of CFD were substantially better than the Radiated Energy Method (REM) as proposed by Gerritsma and Beukelman (1972), especially in short waves. For powering-in-waves computations, both added resistance and the effects of waves and ship motions on propeller performance were important. Guo et al. (2012) showed that the nominal wake flow into a propeller was significantly modified by a ship operating in waves, *i.e.*, both the 0th- and 1st-order axial-flow velocities were changed by the waves. The authors found maximum changes in the propeller-in-flow velocity of approximately 35-percent of the free-stream value. These changes in the nominal wake were surprisingly strong and their effects on propeller performance need to be investigated further.

Sadat-Hosseini, Toxopeus, et al. (2015) studied a model of the naval-surface combatant 5415M, both experimentally and analytically. The experiments were carried out in the MARIN Seakeeping and Maneuvering Basin with a free-running model fitted out with twin propellers and rudders, anti-roll fins, and split-bilge keels. Automatic controls were used for both the rudders and the anti-roll fins. The cases studied included: roll decay in calm water; forced roll in calm water; regular head- and beam-

waves with active roll fins; and stern-quartering bi-chromatic waves with active roll fins. The CFD results are from CFDShip-Iowa. For comparison, the blended method codes FREDYN, SWAN, and LAMP were run. System-based codes, SurSim and FreSim were run for calm-water roll damping cases and forced-roll cases. It was concluded that the blended-method codes produced good results, but that the high-fidelity CFD results generally had better agreement with experiments.

The performance of the ONR tumble-home topside model (Bishop et al. 2005) in following seas was studied by Sadat-Hosseini, Carrica, et al. (2011). The model was tested both fixed to a carriage, and free-running with constant RPM propellers and an autopilot to hold a desired heading in the free-running tests. Depending on the Froude number, the course relative to the waves, and transverse GM, different responses of periodic motion, surf-riding and broaching were obtained. Two sets of analytic results were given. The first set of results gave complete stability boundaries using a simplified, four-degrees-of-freedom maneuvering model with coefficients obtained by running CFDShip-Iowa v4 RANS code. The surge-exciting force due to waves was obtained by three methods: Froude-Krylov force computations; measurements from captive-model tests; and CFD computations. Figures showed that the stability boundaries between the three types of responses were insensitive to the wave-surge-force calculation method. Comparisons were also given for selected experimental results and complete CFD calculations using CFDShip-Iowa v4. Predictions for a free-running model using CFD computations for $Fn = 0.4$ were shown. The authors reported similar results at other Froude numbers. For the case of $Fn = 0.4$ and a heading less than 30° from the waves, the boundaries between periodic motion and surf-riding/broaching were accurately predicted by the CFD computations.

Nonlinear effects of above-water hull form in extreme seas were studied by Furukawa et al. (2012). They performed free-running model tests and analytical computations, for the ONR tumble-home-topside and the ONR flared-topside hull forms (Bishop et al. 2005). The two hull forms had identical underwater-hull forms but different topsides. Performance of the two hulls in stern-quartering seas was compared for periodic motions, surf-riding, and broaching as a function of heading and Froude number. These experiments were conducted in the seakeeping and maneuvering basin of the National Research Institute of Fisheries Engineering of Japan. The analytical calculations were performed using a simplified, four-degrees-of-freedom maneuvering model (similar to the one presented by Sadat-Hosseini, Carrica, et al. 2011) with coefficients obtained by running the CFDShip-Iowa v4 RANS code. The agreement between the experiments and theory was reasonable, and showed that the above-water hull form changed the behavior of ships in extreme stern-quartering seas.

3 APPROACH FOR PREDICTING MANEUVERING-IN-WAVES

A simulation tool for MiW needs to include the physical phenomena that are relevant to a full-scale problem. As such, the first step in developing a computational tool is to identify the physical problem and break it down in a manner that can be modeled. At the highest level, the physical problem can be described by the ambient environment, the ship-control condition, and the forces acting on the ship. Figure 1 illustrates the physical problem to be modeled.

At a high level, Belknap and Reed (2010) outlined the features and physics that a model of MiW needed to incorporate. In addition, they discussed features that such a model would need to incorporate in order to have the fidelity to produce sufficiently accurate response predictions and still be fast enough computationally to be able to simulate the thousands, if not millions of full-scale hours required to characterize the rare motion responses of a design as it changes and evolves through the design cycle.

Reed and Beck (2016) pick up where Belknap and Reed (2010) leave off, further elaborat-

ing on the computational speed and fidelity issues. Then based on the desirable characteristics of a reasonably fast and reasonably accurate model for use in assessing ship responses in extreme seas, they defined the details of a model that meets these requirements. The philosophy driving the selection of the proposed solution approach was to include all aspects of the MiW physical problem and model these components such that they capture the important nonlinearities. Doing this in detail is a formidable task that would take far more pages than are reasonable for this paper. Therefore, this section is confined to a brief description of each of the models that make up the Environment, Ship Control Condition, and Force components of the overall model. These descriptions will consist of a brief statement along with citations to references that detail the proposed theory.

3.1 Environment

A model for the environment consists of models for both wind and waves. The wind environment must account for the earth's boundary layer and also include wind gusts. Ideally, the wind environment should be coupled to the wave environment, but that is more complex than is reasonable to do for a fast model at the present time.

The ambient-wave environment must be capable of representing an arbitrary wave spectra, and must be nonlinear, at least to the extent that pressure under the waves must be zero at the air-water interface, something that classic linear theory does not do. Reed and Telste (2014) provides a means of decomposing a spectrum into its Fourier components. Gudmestad (1993), Stansberg (1998), Forristall (2000), Grue et al. (2003), and Stansberg et al. (2008) provide the details of several techniques for describing second-order waves and deriving the pressure under these waves. If linear-wave theory is employed, then a technique such as Wheeler Stretching should be employed (Wheeler 1970; Zelt et al. 1995).

A challenge to modeling wind is when there are separated flow conditions and a vessel is in a wave trough so that the hull and lower portion of the superstructure are in a wave shadow, or even experiencing a back flow. This condition leads to the need to couple both wind and wave models for extreme-sea states. Given this, a modeling decision that remains is to choose the most appropriate wind-velocity profile to use when modeling a complex wind field. Fullerton et al. (2012) provides a description of a model for the wind environment.

3.2 Ship Control Condition

As was discussed earlier in this paper, MiW requires that both an autopilot to control heading and a model of the propulsion system be provided, as it is very unlikely that a ship operating in extreme seas will be capable of maintaining the ordered speed and it may well not be capable of maintaining the ordered heading. A Proportional-Integral-Derivative (PID) controllers (Fossen 2003) can provide the necessary autopilot function.

It should be noted that a PID controller does not always act like a human. For example, during model testing in extreme seas, it has been noticed that the rudder motion is often in phase with large roll excursions—rudder excitation of resonant roll, and at capsize the rudder was often hard over in the direction that would increase the roll angle. A well trained helmsperson would have put the rudder over in the opposite direction in order to mitigate the roll rather than trying to stay on course. Because rudder deflection can have a substantial influence on roll amplitude, in the long run it would be desirable to have a controller that mimics a well-trained human.

For propulsion, it is sufficient to specify that the propulsor(s) operate at constant RPM or that the model accurately reflects machinery dynamics. Either way, it is necessary to computationally model the thrust force from a propulsor operating on a vessel whose resistance is varying with time, along with the propulsor inflow velocity and direction. This will be discussed further in the next section.

3.3 Forces and Moments

Hydrostatic Restoring Forces

Hydrostatic restoring forces and moments[1] are one of the two most significant forces in MiW problem. As a consequence, they must be calculated as accurately as possible. This is accomplished by integrating the gz term in Bernoulli's equation over the instantaneous wetted surface of a vessel (de Kat and Paulling 1989).

Wave Excitation Forces

In the absence of a ship, the other significant forces that must be computed accurately are the Froude-Krylov[2] exciting forces, which result from evaluation of the pressure on a hull due to incident waves (de Kat and Paulling 1989). (The diffraction forces, which will be discussed next, account for the presence of a ship in waves.) The Froude-Krylov forces are obtained by integrating the dynamic terms from Bernoulli's equation (ϕ_{It} and $|\nabla\phi_I|^2$, where ϕ_I is the incident wave potential) over the instantaneous wetted surface of a hull. The incident wave pressure must be computed to the second order so the total pressure—hydrostatic plus dynamic—is zero on the free surface. Alternatively, Wheeler Stretching (Wheeler 1970) can be used to compute the pressure for linear waves, and the Froude-Krylov forces can be obtained by integrating the dynamic Wheeler stretched pressure over the instantaneous wetted surface of the vessel.

The other wave-exciting forces are diffraction forces, representing forces from the waves generated to counter incident waves attempting to "flow" through a hull. Based on the results of the Force Study (Telste and Belknap 2008; Belknap and Telste 2008), these diffraction forces must be computed for an instantaneous wetted hull. For reasons of computational speed, diffraction forces are computed using body-exact strip theory. A technique such as that of P. Bandyk (2009) is employed to compute the diffraction potential. The forces are computed by integrating the dynamic terms (ϕ_{Dt} and $|\nabla\phi_D|^2$, where ϕ_D is the diffraction potential) of Bernoulli's equation over the instantaneous wetted surface of a hull.

The dynamic terms in Bernoulli's equation contain a time derivative of the diffraction potential (ϕ_{Dt}). This term can be computed from successive calculations of the diffraction potential using finite-difference techniques. However, using a finite-difference technique is complicated by the changing immersed surface of a ship. To aleviate this difficulty, it is proposed to compute the acceleration potential, *i.e.*, $\partial\phi/\partial t$ on the instantaneous wetted surface of a hull, providing the time derivative directly (P. J. Bandyk and Beck 2011; Subramanian and Beck 2015). Computing the acceleration potential turns out to be computationally efficient, as it involves solving the same boundary-value problem required to compute the diffraction potential, but with a different body-boundary condition, *i.e.*, with a different right-hand side of the matrix equation.

Wave Radiation Forces

Wave-radiation forces are those forces analogous to added mass and damping in linearized seakeeping theory, resulting from the motions of a ship, and thus acting as a wave maker in six-degrees-of-freedom. Like the diffraction force, wave-radiation forces must be computed for an instantaneous wetted hull, and for reasons of computational speed, they are computed using body-exact strip theory (P. Bandyk 2009). The forces are computed by integrating the dynamic terms (ϕ_{Rt} and $|\nabla\phi_R|^2$, where ϕ_R is the radiation potential) of Bernoulli's equation over the instantaneous wetted surface of a hull. The ϕ_{Rt} term in Bernoulli's equation is computed using the acceleration potential (P. J. Bandyk and Beck 2011).

[1] Hence forth, we shall use the term "force" in its most general interpretation to mean both forces and moments.

[2] The Froude-Krylov forces are named for William Froude and Aleksey Krylov, who used the forces named after them in a attempt to model the rolling and pitching (in the case of Krylov) of ships (Froude 1861; Krylov 1896, 1898)

Green Water on Deck

The mass of green-water-on-deck and its dynamics can have a significant impact on the motions of a vessel. There are three distinct phases to this problem: the shipping-water phase by which water comes aboard; the deck-in-water phase which is the time when a deck is totally immersed; and the freeing phase when water is leaving the deck. Grochowalski et al. (1998) provides a detailed description of these processes.

It is possible to treat the shipping-of water-problem rigorously—it is either a one-dimensional or two-dimensional shallow-water-flow problem. This problem has been solved with quite good correlation with experimental results by Zhou et al. (1999) and others. Buchner (1995, 1996) and Buchner and Cozijn (1997) provide analysis of the time history of shipping water, and based on analysis, give some simplified models for loading on the deck, which compares quite satisfactorily with experimental data. From these simple models one can estimate the mass of water that is accumulating on deck.

The deck-in-water portion of the problem is straight forward to deal with: the hydrostatic, Froude-Krylov, diffraction, and radiation problems can all be solved for a totally immersed section. However, the solution of the diffraction and radiation problems can become numerically unstable when there is little depth to the water over the deck. For the deck-in-water problem, the most satisfactory treatment is to compute only the hydrostatic and Froude-Krylov loads on the immersed deck, and to calculate the hydrodynamic components as though the hull extends vertically up from the deck edge, avoiding any issues with shallow-water hydrodynamics above the wetted deck.

The complexity of the freeing problem depends upon whether the vessel has a bulwark or not. If there is no bulwark, the problem is simply the inverse of the shipping-water problem, which is solved using a shallow-water-flow solver (cf., Zhou et al. 1999). The solution of the water-freeing problem when there is a bulwark is a simple water "draining from a tank" problem driven by the area of the scuppers and the hydrostatic head. The only wrinkle in this solution is that gravitational acceleration must be adjusted for the vertical acceleration of the water on deck due to movement of the vessel.

For the freeing-of-water problem on a deck without bulwarks, continuing the hydrostatic and Froude-Krylov forces only approach to the water-on-deck forces seems the most robust, as the inverse of Buchner's impulsive loading of the deck makes no physical sense.

Resistance

Resistance force, which is critical to determining ship speed in a seaway, is composed of two components: calm-water resistance forces; and second-order forces which include added resistance in waves. Two approaches to calm-water resistance are viable, the total resistance approach or the component approach. In either approach, data over the speed range from zero to the maximum expected speed is input with sufficient resolution for accurate interpolation for speeds between the input data points.[3] However, the preferred approach is the component one, where the residual-resistance coefficient and the correlation allowance are provided, because the instantaneous wetted surface can be used to compute frictional drag. The component approach also facilitates making resistance predictions for both a model-scale ship and a full-scale ship, with minimal effort.

Second-order longitudinal forces in waves is another critical component required to determine a ship's speed that can be achieved in waves. It is also the most difficult one and one for which at the present time, there is no known formulation for predicting second-order forces in waves in the time domain. The instantaneous Froude-Krylov force in some sense captures this second-order force, but there are still significant radiation-related forces that are not captured, which can lead to a significant under-

[3] In situations where surf riding into broaching is to be modelled, it is necessary to take the resistance data up to speeds approaching the high Froude number hump, even for displacement vessels.

estimation of speed loss, particularly in more extreme seas. The second-order side force and yawing moment must also be computed, as they can have a significant effect on the maneuvering performance of the ship.

Circulatory Lift and Cross-Flow Drag on the Hull

A ship in a turn experiences forces in the direction normal to its center plane. These forces are a combination of lift and cross-flow drag, where lift is the greatest contributor for small angles of attack and cross flow becomes a greater contributor as the angle of attack becomes larger. In the extreme case of a vessel moving sideways, lift goes to zero and all of the force is due to cross-flow drag.

Given that, at angles of attack, a ship behaves like a low-aspect-ratio lifting surface, it is reasonable to use a low-aspect-ratio-lifting surface model to estimate hull-lift force and moment. Works such as those of Oltmann and Sharma (1984), Hooft and Nienhuis (1994), and Hughes, Kopp, et al. (2011) provide the models to be employed. Because these models are coefficient based, there is a need to obtain the lift coefficients from an empirical model, a physical model experiment, or from a viscous-flow numerical tool, such as RANS. Depending on the formulation and the hydrodynamic reference frame used, transverse-wave drag or other lateral-plane-steady forces may be captured by a potential-flow model when a ship is in a turning condition and/or has a drift angle; this can result in the possibility of "double counting" forces. To avoid these issues, RANS, with a rigid-free surface, should be employed. Finally, once suitable hull-lift coefficients are obtained, they must be adjusted for the changing draft of a ship, because this is the driving feature of low-aspect-ratio lifting theory.

Cross-flow drag models are generally tied to a hull-lift model in that the coefficients are often attenuated going aft (cf. Hooft 1994; Hooft and Nienhuis 1994) to be consistent with the hull-lift force at drift angles less than 90 degrees. The cross-flow-drag coefficients can be obtained in three ways: empirically; directly from physical-model experiments; or from 2-D RANS calculations. The model needs to adjust these coefficients or modify the force to account for changing draft which can be done on a section-by-section basis. While quasi-steady assumptions are the norm, higher-fidelity models such as those of Greeley and Willemann (2012) incorporate Keulegan-Carpenter (KC) number dependency (see: Keulegan and Carpenter 1958) in the cross-flow drag coefficients.

Ross (2008) provides the details of a model such as is proposed above by Hooft and Nienhuis (1994) and Hughes, Kopp, et al. (2011). Greeley and Willemann (2012) propose an excellent computational model. Although it is much faster than CFD techniques such as RANS, it is still too slow to meet the present requirements for computational speed.

Damping Forces

Traditionally, roll is the mode of motion that has been most dependent on empirical relationships for accurate predictions.

For a ship, the beam is roughly twice the draft, resulting in little contribution to hydrodynamic forces by wave radiation—and thus little damping. The major forces are from Froude-Krylov exciting forces, which oppose hydrostatic restoring forces. The damping is largely from viscous forces generated by friction and vortex shedding from bilge keels or "sharp" bilges of high-block coefficient vessels, and frictional damping is generally small. There is no simple model for roll damping in the time domain.

Traditionally, in the frequency domain, the component models of Ikeda, Himeno, et al. (1978c), Ikeda, Komatsu, et al. (1978), Ikeda, Himeno, et al. (1978b,a), and Himeno (1981) have been employed. Ikeda decomposes the equivalent linear roll damping, B_e as $B_e = B_F + B_E + B_L + B_W + B_{BK}$, where B_F is friction damping, B_E hull-eddy damping, B_L hull-lift damping, B_W hull wave-making damping, and B_{BK} bilge-keel damping. Bilge-keel damping is further decomposed as $B_{BK} = B_{BKN} +$

$B_{BKH} + B_{BKW}$ where B_{BKN} is the bilge-keel normal force, B_{BKH} the bilge-keel-hull interaction force and B_{BKW} the bilge-keel wave-making damping force. The models for the damping components include both empirical (B_F, B_E and B_W) and semi-empirical (B_L, B_{BKN} and B_{BKH}) formulations. The hull wave-making damping, B_W, is computed rigorously as part of the radiation force calculations, and the bilge-keel wave-making component, B_{BKW}, is neglected.

Ikeda's frequency-domain component roll damping is a function of both frequency and roll amplitude—*i.e.*, roll velocity, which must be determined iteratively, because the amount of damping influences the amplitude of the roll motion, and thus the roll velocity. To convert Ikeda's frequency-domain model to the time domain, the problem is worked in reverse. The velocity and roll amplitude from recent history are known, so these values can be used to determine an instantaneous frequency that can be substituted into Ikeda's component formulations to obtain updated component drags.

A more rigorous force model to predict the forces on bilge keels has been developed by Greeley and Petersen (2010). Their bilge-keel force model follows the hull-lift and cross-flow drag-force model of Greeley and Willemann (2012). However, because of the simple geometry of bilge keels, the problem is simpler, following the low-aspect-ratio lifting-surface theory and cross-flow drag models for flat plates. It contains Keulegan-Carpenter, KC number dependency. Greeley's bilge-keel model uses lifting-surface techniques to solve the potential-flow boundary-value problem, but it is not clear that this level of fidelity is required. Even though Greeley's approach is relatively slow, it is still significantly faster than RANS.

Whether using the Ikeda component model or the Greeley lifting-surface model, inflow velocities to the bilge-keel model need to consider not just body motion, but also wave-orbital velocity, particularly the contribution from longer wave lengths.

Propulsor

Propeller thrust is required to overcome the resistance of a ship operating in a seaway. Inflow to the propeller will oscillate about some mean value, where the oscillation is due to the cyclic variation caused by the orbital velocities of the waves as they pass a ship or a ship passes the waves. A number of researchers have shown that this oscillation causes the nondimensional-propeller thrust and torque to move up and down the K_T and K_Q curve of the propeller open-water curves (cf. McCarthy et al. 1961; Tasaki 1975). For very high thrust loading, and a low advance coefficient, J, Tasaki (1975) shows that thrust and torque cease following the open-water curves when the propeller operates at an immersion typical of that which would occur for a propeller on a ship. This is likely due to ventilation of the propeller as waves pass, decreasing the immersion yet further relative to that which would occur in calm water.

Although we have some qualitative understanding of how a propeller performs in open water in waves, we have little understanding of how hull-propeller-interaction coefficients behave in extreme seas. As a result, we must assume that the hull-propulsor-interaction coefficients are unaffected by operation in a seaway, even though we know that to be in error. Nakamura and Naito (1977) provide some insight into how hull-propulsor-interaction coefficients behave as functions of vessel speed, wavelength over ship length, λ/L, and wave steepness, H/λ. Tasaki (1975) provides similar data. Nakamura and Naito (1977) shows that there is significant variation in the hull-propulsor-interaction coefficients with λ/L. These two sets of data do not provide enough insight as to how the variations in hull-propulsor-interaction coefficients should behave in a seaway, especially considering that the data in both Tasaki (1975) and Nakamura and Naito (1977) are for a single-screw container ship.

Another effect related to propeller force is that a propeller operating in a non-uniform or oblique inflow can produce significant "side

forces"[4]—up to 70 percent or more of the propeller thrust. Fuhs and Dai (2007) provide an empirical model for estimating the side forces given an inclination angle and an axial force prediction. The difficulty in predicting these forces arises in establishing the inflow velocity, which can vary between port and starboard propellers. For a computationally efficient model, the only tractable solution is to provide the inflow velocity via an empirical model that accounts for the local drift angle and possibly the heel angle. The added velocity due to rigid-body motions and wave-orbital velocities should also be included.

Rudder Force

The rudder-force model is relatively straight forward. A computationally efficient model with sufficient fidelity can be obtained by treating a rudder as a lifting surface and supplying appropriate inflow. Inflow is determined in the same manner as propeller inflow, but an adjustment needs to be made for the acceleration of flow from the propeller. The thrust provided by the propeller can be used to determine the increase in velocity.

Because a full range of inflow conditions is possible, a stall model must be included to capture loss-of-lift at large angles of attack. Hughes and Shen (2014) provide a simple model that allows the rudder-stall angle to be calculated based on two-dimensional airfoil data. This simple model also accounts for scale effects between a model and a full-scale ship, because it is well known that a lifting foil stalls at a lower angle of attack at a low Reynolds number than when at a high Reynolds number. Similarly, due to the inherent unsteadiness of the outflow from a propeller, a rudder behind a propeller stalls at a higher ange of attack than a rudder in a steady flow at the same Reynolds number (Collar 1941).

Wind Force

The final force model is the wind-force model In general, although wind forces are insignificant relative to hydrodynamic forces, there are some conditions where wind forces cannot be neglected. In conditions where a vessel is operating at the peak of, or beyond, the peak of the righting-arm curve, very little additional heeling moment can result in significant increases in the roll angle. This situation can be particularly critical for a vessel at zero speed in beam seas, *i.e.*, a vessel in a dead-ship condition. Wind forces can also have a significant effect on the response of a vessel suffering pure loss of stability, where the righting arm goes to zero.

Isherwood (1972) and Blendermann (1993) have proposed coefficient-based models to predict wind loads. Blendermann (1994) provided the coefficients for a broad spectrum of vessel-topside shapes. Haddara and Guedes Soares (1999) provided an assessment of several coefficient-based models for a tanker-like shape and found that in general, the best model performed relatively well against experimental data. However, this does not mean that one has the best model for a vessel when one does not know what the answer should be. Haddara and Guedes Soares (1999) find that the best results can be obtained from a neural-net-based model[5], but again, one must have a significant amount of data in order to train the neural net.

As discussed in the environment section, a modeling decision that remains is determining what is the most appropriate wind-velocity profile to use with the wind-force model when dealing with a complex wind environment. It is not obvious that the coefficient-based models, which are based on a presumed boundary-layer profile, are valid when the environmental model includes separated-flow conditions. Blendermann (1995) proposed a partial solution to this dilemma, but it is not the complete answer.

4 MANEUVERING-IN-WAVES THEORY IMPLEMENTATION

The nonlinear body-exact strip theory based model just described has been implemented in a computational model for MiW in extreme

[4]Non-axial propeller forces with components in the lateral and/or vertical directions.

[5]Neural nets are an artificial intelligence technique.

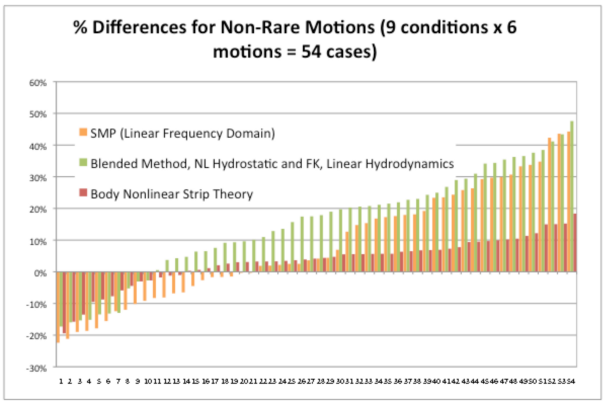

Fig. 7 SSA Accuracy Comparison between experiments and three computational models: Ship Motion Program (SMP); time-domain blended code with nonlinear hydrostatic and Froude-Krylov forces, and linear radiation and diffraction; and fully nonlinear body-exact strip theory based model.

seas. The performance of this new model is shown in Figure 7. The figure shows the errors in significant-single amplitude (SSA) motions resulting from the use of three computational models. The first is the US Navy's Ship Motion Program (SMP), which is a linear frequency-domain code, which predicts motions in irregular seas by "multiplying" the frequency domain response amplitude operator by the appropriate wave spectrum for each of the seaways. The second code is a classic time-domain blended code which computes the nonlinear hydrostatic restoring forces and moments, and the Froude-Krylov exciting forces and moments using the instantaneous wetted surface of the vessel in waves; the diffraction and radiation forces and moments are calculated linearly. The third code is the nonlinear body-exact strip theory based model.

The figure shows the percent difference between model tests and predictions for motions in extreme seas by the three computational models, ordered by percent error from greatest under-prediction on the left to greatest over-prediction on the right. The experiments were for nine environmental conditions covering three significant wave heights between 7.5 m and 15 m, and three wave modal periods from 10 s to 24 s; high significant-wave-height seas of modest steepnesses to extreme steepnesses were covered. The motions that were compared were roll, pitch, yaw rate, and the vertical, lateral and longitudinal accelerations at the center of gravity. The combination of 9 environmental conditions and 6 motions, means that there were 54 SSA results to compare.

It has been noted that there is little difference in the error in the predictions by linear strip theory (SMP) and the blended code—why is there such little difference? Two reasons are hypothesized for these small differences between the linear strip theory and the blended code errors. The first is that, as discussed in Telste and Belknap (2008) and Belknap and Telste (2008), in extreme seas such as these, the hydrostatic and Froude-Krylov forces are close to 180 degrees out of phase, producing a nearly constant force equal to the weight the vessel, so that the primary forces contributing to the motions are the linear radiation and diffraction forces that are computed in a similar manner in both codes. The second reason is that the linear strip-theory predictions were made at the achieved speed of the model, not the ordered speed. If the linear SMP predictions had been made at the ordered speed, then the differences between SMP and the blended code would have been significantly larger, with SMP performance expected to be much worse than what is reflected in the figure.

5 CONCLUSIONS AND RECOMMENDATIONS

There are pieces of the maneuvering-in-waves problem that still require substantial research. In the area of the environment, there is a need for an accurate and fast method for predicting nonlinear waves of an extreme random seaway, and the flow and pressure beneath those waves. There is also a need to predict unsteady wind over a random seaway—currently unsteady-wind models are uncorrelated with the seas, but it is well known that there is air-flow separation over the waves which contributes to gustiness and back flows that will affect the aerodynamic loads on a vessel.

From a hydrodynamic perspective, an Abkowitz type coefficient-based maneuvering model has been shown to not perform well in extreme seas. The topics of maneuvering; and roll, sway, and yaw damping need significant investigation. So far there has been little work on the prediction of these quantities in the time domain for extreme seas, except by using "brute force" CFD methods. Greeley and Petersen (2010) have shown progress in the area of bilge-keel forces for roll damping, but significant work remains before truly fast approaches are viable. Significant work remains regarding the prediction of maneuvering forces. Greeley and Willemann (2012) have shown that progress has been made in this area, but substantial work remains. Because both of Greeley, et al.'s approaches are potential-flow-based approaches, they do not contain any purely viscous effects; therefore, viscous forces have to be accounted for in an empirical manner.

In the area of resistance and propulsion in waves, there is a need for understanding second-order forces and moments in waves, *in the time domain*. Additionally, there is little understanding of the effects of extreme seas on propulsor thrust, hull-propulsor interaction and rudder performance. Because little research has been done in the area of resistance and propulsion in waves in the last 40 years, there are many opportunities for further research.

ACKNOWLEDGMENTS

The authors appreciate the many researchers in the hydrodynamics community, with whom they have discussed the subject of maneuvering-in-waves over the years. Some of those individuals are: Dr. Bill Belknap, Mr. Brad Campbell, Dr. Dave Greeley, Dr. Mike Hughes, Dr. Chris Kent, Dr. John O'Dea, Prof. Randy Paulling, Prof. Paul Sclavounos, Dr. Young Shen, Mr. John Telste and Prof. Armin Troesch. We offer our apologies to those whose names have been missed.

The authors also appreciate the comments and suggestions by the anonymous reviewers of this paper.

References

Bailey, P. A., W. G. Price, and P. Temarel (1997). "A Unified Mathematical Model Describing the Maneuvering of a Ship Travelling in a Seaway". In: *Transactions of the Royal Institution of Naval Architects*. Vol. 140, pp. 131–149.

Bandyk, Piotr (2009). "A body-exact strip theory approach to ship motion computations". Doctoral Thesis. Ann Arbor, MI: University of Michigan, Dept. of Naval Architecture and Marine Engineering, pp. xii+122.

Bandyk, Piotr J. and Robert F. Beck (2011). "The acceleration potential in fluid-body interaction problems". In: *Journal of Engineering Mathematics* 70 (1), pp. 147–163.

Beck, Robert F. and Arthur M. Reed (2001). "Modern Computational Methods for Ships in a Seaway". In: *Transactions of SNAME*. Vol. 109, pp. 1–51.

Belknap, William F. and Arthur M. Reed (2010). "TEMPEST—A New Computationally Efficient Dynamic Stability Prediction Tool". In: *Proceedings 11th International Ship Stability Workshop* (Wageningen, The Netherlands). Ed. by Frans van Walree.

Belknap, William F. and John G. Telste (2008). "Identification of Leading Order Nonlinearities from Numerical Forced Motion Experiment Results". In: *Proceedings 27th Symposium on Naval Hydrodynamics*. Seoul, Korea, p. 18.

Bishop, Richard C., William F. Belknap, Charles Turner, Beverly Simon, and Joseph H. Kim (2005). *Parametric Investigation on the Influence of GM, Roll Damping, and Above-Water Form on the Roll Response of Model 5613*. report NSWCCD-50-TR-2005/027. Carderock Division, Naval Surface Warfare Center. 185 pp.

Blendermann, Werner (1993). "Wind loads on moored and manoeuvring vessels". In: *Proceedings 12th International Conference on Offshore Mechanics and Arctic Engineer-*

ing (OMAE'93). Vol. 1. New York, NY, pp. 183–189.

— (1994). "Parameter identification of wind loads on ships". In: *Journal of Wind Engineering and Industrial Aerodynamics* 51, pp. 339–351.

— (1995). "Estimation of wind loads on ships in wind with a strong gradient". In: *Proceedings 14th International Conference on Offshore Mechanics and Arctic Engineering (OMAE'95)*. Vol. 1-A. Copenhagen, Denmark, pp. 271–277.

Buchner, Bas (1995). "The Impact of Green Water on FPSO Design". In: *Proceedings of the 27th Offshore Technology Conference*, pp. 45–57.

— (1996). "The Influence of the Bow Shape of FPSOS on Drift Forces and Green Water". In: *Proceedings of the 28th Offshore Technology Conference* (Houston, TX). OTC 8073, pp. 389–400.

Buchner, Bas and J. L. Cozijn (1997). "An Investigation into the Numerical Simulation of Green Water". In: *BOSS8* (Delft, The Netherlands). Vol. 2, pp. 113–125.

Collar, A. R. (1941). *On the Static Thrust of Contra-Rotating Airscrews*. Reports & Memoranda NACA R & M 1994. Washington DC: National Advisory Committee for Aeronautics, pp. 87–91.

Cummins, William E. (1962). "The Impulse Response Function and Ship Motions". In: *Schiffstechnik* 9.47, pp. 101–109.

Cura-Hochbaum, Andrés and Sebastian Uharek (2016). "Prediction of Ship Manoeuvrability in Waves Based on RANS Simulations". In: *Proceedings 31th Symposium on Naval Hydrodynamics* (Monterey, CA).

De Kat, Jan O. (1994). "Irregular Waves and their Influence on Extreme Ship Motions". In: *Proceedings 20th Symposium on Naval Hydrodynamics* (Santa Barbara, CA), pp. 48–67.

De Kat, Jan O., R. Brouwer, Kevin A. McTaggart, and Wiliam L. Thomas III (1994). "Intact Ship Survivability in Extreme Waves: New Criteria from a Research and Navy Perspec-tive". In: *Proceedings 5th International Conference on the Stability of Ships and Ocean Vehicles (STAB'94)* (Melbourne, FL). Vol. 1. 6 vols. Melbourne, FL: Florida Institute of Technology.

De Kat, Jan O. and J. Randolph Paulling (1989). "The Simulation of Ship Motions and Capsizing in Severe Seas". In: *Transactions of SNAME*. Vol. 97. Jersey City, NJ: Society of Naval Architects and Marine Engineers, pp. 139–168.

Forristall, George Z. (2000). "Wave Crest Distributions: Observations and Second-Order Theory". In: *Journal of Physical Oceanography* 30.8, pp. 1931–1943.

Fossen, Thor I. (1994). *Guidance and Control of Ocean Vehicles*. John Wiley and Sons Ltd.

— (2003). *Marine control systems*. Trondheim, Norway: Marine Cybernetics AS, pp. xiv+570.

— (2005). "A nonlinear unified state-space model for ship maneuvering and control in a seaway". In: *Journal of Bifurcation and Chaos* 15.9, pp. 2717–2746.

Francescutto, Alberto (2004). "Intact Ship Stability—The Way Ahead". In: *Marine Technology* 41, pp. 31–37.

— (2007). "Intact Stability of Ships-Recent Developments and Trends". In: *Proceedings 10th International Symposium on Practical Design in Shipbuilding & Other Floating Structures (PRADS'07)*. Ed. by Vadim Belenke. Vol. 1. Houston, TX, pp. 487–496.

Froude, William E. (1861). "On the rolling of ships". In: *Transactions of the Institution of Naval Architects* 2, pp. 180–229.

Fuhs, D. and C. Dai (2007). *Effect of cross flow on propeller forces*. Report NSWCCD-50-TR 2007/046. Carderock Division, Naval Surface Warfare Center.

Fullerton, Anne M., Kristine L. C. Beale, Eric Terrill, and Douglas Dommermuth (2012). "An Extended Wind Boundary Layer Profile". In: *Proceedings 29th Symposium on Naval Hydrodynamics*.

Furukawa, Tomohiro, Naoya Umeda, Akihiko Matsuda, Daisuke Terada, Hirotada Hashimoto, Frederick Stern, et al. (2012). "Effect of Hull Form above Calm Water Plane on Extreme Ship Motions in Stern Quartering Waves". In: *Proceedings 29th Symposium on Naval Hydrodynamics* (Gothenburg, Sweden).

Gerritsma, Jelle and Wim Beukelman (1972). "Analysis of the resistance increase in waves of a fast cargo ship". In: *International Shipbuilding Progress* 19.217, pp. 285–301.

Greeley, David S. and B. J. Petersen (2010). "Efficient Time-Domain Computation of Bilge Keel Forces". In: *Proceedings 28th Symposium on Naval Hydrodynamics* (Pasadena, CA). Arlington, VA: Office of Naval research.

Greeley, David S. and Simmy D. Willemann (2012). "Surface Ship Maneuvering Forces in Calm Water and Waves". In: *Proceedings 29th Symposium on Naval Hydrodynamics* (Gothenburg, Sweden).

Grochowalski, Stefan, Chi-Chao Hsiung, Z. J. Huang, and L. Z. Cong (1998). "Theoretical modeling of ship motions and capsizing in large and steep waves". In: *Transactions of SNAME*. Vol. 106, pp. 241–67.

Grue, John, Didier Clamond, Morten Huseby, and Atle Jensen (2003). "Kinematics of extreme waves in deep water". In: *Applied Ocean Research* 25.6, pp. 355–366.

Gudmestad, Ove T. (1993). "Measured and Predicted Deep Water Wave Kinematics in Regular and Irregular Seas". In: *Marine Structures* 6.1, pp. 1–73.

Guo, Bing-Jie, Sverre Steen, and G. B. Deng (2012). "Seakeeping prediction of KVLCC2 in head waves with RANS". In: *Applied Ocean Research* 35, pp. 56–67.

Haddara, Mahmoud R. and Carlos Guedes Soares (1999). "Wind loads on marine structures". In: *Marine Structures* 12.3, pp. 199–209.

Himeno, Yoji (1981). *Prediction of Ship Roll Damping-State of the Art*. Report 239. Department of Naval Architecture and Marine Engineering, University of Michigan, pp. xiii+74.

Hooft, J. P. (1994). "The cross flow drag on a manoeuvering ship". In: *Ocean Engineering* 21.3, pp. 329–342.

Hooft, J. P. and U. Nienhuis (1994). "The prediction of the ship's maneuverability in the design stage". In: *Transactions of SNAME*. Vol. 102. New York, NY, pp. 419–445.

Hughes, Michael J., Paul J. Kopp, and Ronald W. Miller (2011). "Modeling of hull lift and cross flow drag forces in large waves in a computationally efficient dynamic stability prediction tool". In: *Proceedings 12th International Ship Stability Workshop* (Washington, DC).

Hughes, Michael J. and Young T. Shen (2014). "A Method to Predict Rudder Stall Inception from Two-dimensional Airfoil Data". In: *Journal of Ship Research* 58.1, pp. 1–19.

Ikeda, Yoshiho, Yoji Himeno, and Norio Tanaka (1978a). *Components of roll damping of ship at forward speed*. Report 00404. University of Osaka Prefecture, Dept. of Naval Architecture, pp. ii+14.

— (1978b). *On eddy making component of roll damping force on naked hull*. Report 00403. University of Osaka Prefecture, Dept. of Naval Architecture, pp. ii+12.

— (1978c). *On roll damping force of ship-effect of friction on hull and normal force of bilge keels*. Report 00401. University of Osaka Prefecture, Dept. of Naval Architecture, pp. ii+10.

Ikeda, Yoshiho, Kiyoshi Komatsu, Yoji Himeno, and Norio Tanaka (1978). *On roll damping force of ship-effect of hull surface pressure created by bilge keels*. Report 00402. University of Osaka Prefecture, Dept. of Naval Architecture, pp. ii+10.

IMO MSC 85/26/Add.1 (2008). *International Code on Intact Stability, 2008 (2008 IS Code)*. London, UK. 96 pp.

IMO MSC.1/Circ.1281 (2008). *Explanatory Notes to the International Code on Intact Stability, 2008*. London, UK. 30 pp.

Isherwood, R. M. (1972). "Wind resistance of merchant ships". In: *Transactions of the Royal Institution of Naval Architects*. Vol. 115, pp. 327–338.

Keulegan, G. M. and L. H. Carpenter (1958). "Forces on cylinders and plates in an oscillating fluid". In: *Journal of Research of the National Bureau of Standards* 60.5, pp. 423–440.

Kobylinski, Lech K. and Sigismund Kastner (2003). *Stability and Safety of Ships: Regulation and Operation*. Amsterdam, The Netherlands: Elsevier. 454 pp.

Krylov, Aleksey Nikolaevich (1896). "A new theory of the pitching motion of ships on waves and of the stresses produced by this motion". In: *Transactions of the Institution of Naval Architects*. Vol. 38. In the original publication, the author's family name was spelled "Kriloff", consistent with the German transliteration of that time; "Krylov" is the modern English transliteration., pp. 326–368.

— (1898). "A General Theory of the Oscillations of a Ship on Waves". In: *Transactions of the Institution of Naval Architects*. Vol. 40. In the original publication, the author's family name was spelled "Kriloff", consistent with the German transliteration of that time; "Krylov" is the modern English transliteration., pp. 135–202.

Larsson, Lars, Frederick Stern, and Michel Visonneau, eds. (2014). *Numerical Ship Hydrodynamics. An assessment of the Gothenburg 2010 Workshop*. Dordrecht: Springer, pp. ix+318.

McCarthy, Justin H., W. H. Norley, and G. L. Ober (1961). *The performance of a fully submerged propeller in regular waves*. Hydromechanics Laboratory Research and Development Report 1440. Carderock, Maryland: David Taylor Model Basin. 38 pp.

Nakamura, Shoichi and Shigeru Naito (1977). "3. Propulsive Performance of a Container Ship in Waves". In: *Journal of the Society of Naval Architects of Japan* 15, pp. 24–48.

NATO (2007a). *Buoyancy, Stability and Controllability. Chapter III of Naval Ship Code*. Allied Naval Engineering Publication ANEP-77. NATO Naval Armaments Group, Maritime Capability Group 6, Specialist Team on Naval Ship Safety and Classification, pp. vii+121.

— (2007b). *Guidance on NSC Chapter III Buoyancy and Stability, Part B: Application. Chapter 3, Guide to the Naval Ship Code*. NATO Naval Armaments Group, Maritime Capability Group 6, Specialist Team on Naval Ship Safety and Classification. 91 pp.

NAVSEA (2016). *Design Practices And Criteria For U.S. Navy Surface Ship Stability And Reserve Buoyancy*. T9070-AF-DPC-010/079-1. NAVSEA Technical Publication. Naval Sea Systems Command. 175 pp.

Nonaka, Koji (1990a). "Manoeuvring Motion of a Ship in Waves". In: *Proceedings Joint International Conference on Marine Simulation and Ship Manoeuvrability (MARSIM & ICSM 90)* (Tokyo, Japan). Society of Naval Architects of Japan. Tokyo, Japan: Japan Shipbuilding Industry Foundation, pp. 421–427.

— (1990b). "On the Manoeuvring Motion of a Ship in Waves". Japanese. In: *Transactions of the West-Japan Society of Naval Architects* 80, pp. 73–86.

Ogilvie, T. Francis (1964). "Recent Progress Toward the Understanding and Prediction of Ship Motion". In: *Proceedings 5th Symposium on Naval Hydrodynamics* (Bergen, Norway), pp. 3–128.

Oltmann, Peter and Som Deo Sharma (1984). "Simulation of Combined Engine and Rudder Maneuvers Using an Improved Model of Hull-Propeller-Rudder Interactions". In: *Proceedings 15th Symposium on Naval Hydrodynamics* (Hamburg, Germany). Washington, DC: National Academy Press, pp. 83–108.

Papanikolaou, Apostolos, Nikos Fournarakis, Dionysia Chroni, Shukui Liu, Timoleon Plessas, and Florian Sprenger (2016). "Simulation of the Maneuvering Behavior of Ships in Adverse Weather Conditions". In: *Proceedings 31th Symposium on Naval Hydrodynamics* (Monterey, CA).

Peters, William, Vadim Belenky, Christopher Bassler, Kostas Spyrou, Naoya Umeda, G. Bulian, et al. (2011). "The Second Generation Intact Stability Criteria: An Overview of Development". In: *Transactions of SNAME*. Vol. 119, pp. 225–264.

Rahola, J. (1939). "The judging of the stability of ships and the determination of the minimum amount of stability especially considering the vessel navigating Finnish waters". PhD Thesis. Helsinki, Finland: Technical University of Finland, pp. viii+232.

Reed, Arthur M. (2009). "A Naval Perspective on Ship Stability". In: *Proceedings 10th International Conference on the Stability of Ships and Ocean Vehicles (STAB'09)* (St. Petersburg, Russia), pp. 21–44.

Reed, Arthur M. and Robert F. Beck (2016). "Advances in the Predictive Capability for Ship Dynamics in Extreme Waves". In: *Transactions of SNAME* (Belevue, WA). Vol. 124, pp. 2–39.

Reed, Arthur M. and John G. Telste (2014). "Deriving the linear-wave spectrum from a nonlinear spectrum". In: *Proceedings 14th International Ship Stability Workshop* (Kuala Lumpur, Malaysia), pp. 236–241.

Reed, Arthur M. and Aurore V. Zuzick (2015). "Direct Assessment Will Require Accreditation—What This Means". In: *Proceedings 12th International Conference on the Stability of Ships and Ocean Vehicles (STAB'15)*. Ed. by STAB2015 Secretariat. Glasgow, UK, pp. 49–78.

Ross, A. (2008). "Nonlinear manoeuvering models for ships: A Lagrangian approach". Doctoral Dissertation. Trondheim, Norway: Norwegian University of Science and Technology. 114 pp.

Rudgley, G., E. C. A. ter Bekke, P. Boxall, and R. Humphrey (2005). "Development of a NATO 'Naval Ship Code'". In: *Proceedings RINA Conference on Safety Regulations and Naval Class II*. Ed. by RINA. London, UK: RINA.

Sadat-Hosseini, Hamid, Pablo Carrica, Frederick Stern, Naoya Umeda, Hirotada Hashimoto, Shinya Yamamura, et al. (2011). "CFD, system-based and EFD study of ship dynamic instability events: Surf-riding, periodic motion, and broaching". In: *Ocean Engineering* 38.1, pp. 88–110.

Sadat-Hosseini, Hamid, Serge Toxopeus, Michel Visonneau, Emmanuel Guilmineau, Tin-Guen Yen, Woei-Min Lin, et al. (2015). "CFD, Potential Flow and System-Based Simulations of Fully Appended Free Running 5415M in Calm Water and Waves". In: *Proceedings of VI International Conference on Computational Methods in Marine Engineering, MARINE 2015* (Rome, Italy). Ed. by Francesco Salvatore, Riccardo Broglia, and Roberto Muscari, pp. 306–326.

Sarchin, Theodore H. and L. L. Goldberg (1962). "Stability and buoyancy criteria for U. S. Naval surface ships". In: *Transactions of SNAME*. Vol. 72, pp. 418–458.

Skejic, Renato and Odd M. Faltinsen (2008). "A unified seakeeping and maneuvering analysis of ships in regular waves". In: *Journal Marine Science and Technology* 13.4, pp. 371–394.

— (2013). "A Unified Seakeeping and Maneuvering Analysis of Two Interacting Ships". In: *Proceedings 32nd International Conference on Offshore Mechanics and Arctic Engineering (OMAE'13)*. Nantes, France, pp. 209–218.

Sprenger, Florian, Vahid Hassani, Adolfo Maron, Guillaume Delefortrie, Thibaut Van Zwijnsvoorde, Andrés Cura-Hochbaum, et al. (2016). "Establishment of a Validation and Benchmark Database for the Assessment of Ship Operation in Adverse Conditions". In: *Proceedings 35rd International Conference on Offshore Mechanics and Arctic Engineering (OMAE'16)* (Busan, South Korea). OMAE2016-54865.

Stansberg, Carl Trygve (1998). "Non-Gaussian Extremes in Numerically Generated Second-Order Random Waves on Deep Water". In: *Proceedings of the Eighth International Offshore and Polar Engineering Conference (ISOPE)* (Montreal, Canada). Vol. 3, pp. 103–110.

Stansberg, Carl Trygve, Ove T. Gudmestad, and Sverre K. Haver (2008). "Kinematics Under Extreme Waves". In: *Journal of Offshore Mechanics and Arctic Engineering* 130.2.

Subramanian, Rahul (2012). "A Time Domain Strip Theory Approach to Predict Maneuvering in a Seaway". Doctoral Thesis. Ann Arbor, MI: University of Michigan, Dept. of Naval Architecture and Marine Engineering, pp. xii+104.

Subramanian, Rahul and Robert F. Beck (2015). "A time-domain strip theory approach to maneuvering in a seaway". In: *Ocean Engineering* 104, pp. 107–118.

Tasaki, Ryo (1975). "Propulsion Factors and Fluctuating Propeller Load in Waves". In: *Proceedings 14th International Towing Tank Conference* (Ottawa, Canada), pp. 225–236.

Telste, John G. and William F. Belknap (2008). *Potential Flow Forces and Moments from Selected Ship Flow Codes in a Set of Numerical Experiments*. NSWCCD Report NSWCCD-50-TR-2008/040. Carderock Division, Naval Surface Warfare Center, pp. 15, 240.

Wheeler, J. D. (1970). "Method for calculating forces produced by irregular waves". In: *Journal of Petroleum Technology* 22.3, pp. 359–367.

Yasukawa, H. and Y. Nakayama (2009). "6-DOF Motion Simulations of a Turning Ship in Regular Waves". In: *International Conference on Marine Simulation and Ship Manoeuvrability 2009 (MARSIM' 09)* (Panama City, Panama), pp. 508–517.

Zelt, Jeffrey A., Ove T. Gudmestad, and James E. Skjelbreia (1995). "Fluid accelerations under irregular waves". In: *Applied Ocean Research* 17.1, pp. 43–54.

Zhou, Z. Q., Jan O. de Kat, and Bas Buchner (1999). "A Nonlinear 3-D Approach to Simulate Green Water Dynamics on Deck". In: *Proceedings 7th International Conference on Numerical Ship Hydrodynamics* (Nantes, France), pp. 5.1-1–5.1-15.

Generation of Hydrodynamic Derivatives for ONR Topside Series Using Computational Fluid Dynamics

Kevin M. Silva, *Naval Surface Warfare Center Carderock Division* kevin.m.silva1@navy.mil

Shawn Aram, *Naval Surface Warfare Center Carderock Division* shawn.aram@navy.mil

ABSTRACT

Maneuvering models often require captive model tests to provide hydrodynamic derivatives of hullforms under desired conditions. The use of Computational Fluid Dynamics (CFD) as a substitute for these captive model tests has been previously investigated and provides an attractive alternative. CFD simulations are able to calculate model or full scale values for input into maneuvering models. The presented study utilizes a methodology for the Office of Naval Research Tumblehome (ONRTH) to generate hydrodynamic derivatives for maneuvering models using NavyFOAM. This could have implications for not only concept design, but also in the prediction of extreme events for current vessels.

Keywords: *CFD; RANS; Maneuvering*

1. INTRODUCTION

Maneuvering models have been implemented in a variety of applications including assessing a vessel's calm water maneuverability and also in the field of extreme event predictions. These maneuvering models are dependent on empirical inputs that drive the calculations and are both vessel and condition specific. These empirical inputs, referred to as hydrodynamic derivatives or coefficients, require data typically from a series of captive model tests, full-scale trials, or Computational Fluid Dynamics (CFD).

The ability to perform captive model tests and full-scale trials is often limited, and increasingly CFD has become an attractive alternative for performing captive tests. The presented study utilized the in-house CFD framework, NavyFOAM to perform captive model simulations of the Office of Naval Research Tumblehome (ONRTH) for various conditions. The ONRTH is the tumblehome variant of the ONR Topside Series hullforms developed for research applications. The current study provided an opportunity to report results that could be applicable to other ongoing research. The methodology used to perform the simulations will be presented as well as tabulated results of forces, moments, and hydrodynamic derivatives for a selected maneuvering model of interest.

2. BACKGROUND

Various maneuvering models have been proposed that utilize different hydrodynamic derivatives. When leveraging previously developed derivatives, it is imperative that knowledge of the maneuvering model and how the derivatives were non-dimensionalized is known. The maneuvering model used as the template for the present study and utilized in the work of Spyrou and Tigkas (2007) is shown in Equation (1), where the hydrodynamic reaction forces (X_H and Y_H) and moments (N_H and K_H) were approximated using the maneuvering derivatives based Taylor series expansion from Mikelis (1985).

$$
\begin{aligned}
X_H &= X_{\dot{u}}\dot{u} - Y_{\dot{v}}vr - Y_{\dot{r}}r^2 \\
&\quad + X_{vr}vr - Res(u) \\
Y_H &= Y_{\dot{v}}\dot{v} + Y_{\dot{r}}\dot{r} + Y_v vU + Y_r rU \\
&\quad + Y_{vv}v|v| \\
&\quad + Y_{vr}v|r| \\
&\quad + Y_{rr}r|r| \\
N_H &= N_{\dot{r}}\dot{r} + N_{\dot{v}}\dot{v} + N_r rU \\
&\quad + N_v vU + N_{rr}r|r| \\
&\quad + N_{rrv}\frac{r^2 v}{U} \\
&\quad + N_{vvr}\frac{v^2 r}{U} \\
&\quad + N_\phi \phi U^2 \\
&\quad + N_{v\phi}v|\phi|U \\
&\quad + N_{r\phi}r|\phi|U \\
K_H &= K_{\dot{p}}\dot{p} + K_p p + K_\phi \phi - Z_Y Y_H
\end{aligned}
\tag{1}
$$

Captive model tests are the most common method of extracting hydrodynamic derivatives for a particular vessel. Standard captive model tests include the static drift, rotating arm, rotating arm with drift tests, and horizontal planar motion mechanism. Static drift model tests are performed by fixing the vessel at a series of drift angles and towing at a constant resultant speed. Towing with constant forward speed at a series of drift angles allows for a direct relation between the force and moments on the hull and the lateral velocity, *v*.

Another common captive model test is the rotating arm, where the vessel is fixed at prescribed distances from a central rotational point. The vessel is oriented perpendicular to the moment arm between the center of rotation and the vessel. The vessel is then rotated around the center of rotation at a rate that corresponds to the desired resultant tangential forward speed. Performing the tests in this manner allows for a relationship to be developed for forces and moments with respect to the rotational velocity, *r*. Another captive model test that is typically performed is the rotating arm at a drift angle. This test combines the static drift and rotating arm where the model is rigged in the same manner as the rotating arm but is no longer oriented perpendicular to the moment arm. Performing the rotating arm with drift captive model test allows for cross-dependent derivatives to be developed using *u* and *v*. Horizontal planar motion mechanism tests are similar to static drift test but the model is oscillated horizontally on a prescribed path. With proper phasing between fore and aft actuators it is possible to develop maneuvering derivatives for *u*, *v*, and *r*.

Though model tests are still the primary method of calculating hydrodynamic derivatives, they have a major requirement that a physical model must be constructed and the test matrix may be limited due to equipment and/or time restrictions. CFD has increasingly been used to compliment model testing in many technical areas including captive model testing. CFD allows for numerous vessels and testing conditions to be analyzed in parallel and eliminates the burdens of constructing a scale model and rigging the model with instrumentation. Previous investigations such as Bhushan, et al. (2015) have explored the use of CFD to perform captive model simulations and have shown a positive correlation with model tests. CFD also offers the capability of simulating captive model tests using a single phase solver and neglecting any free surface effects that would be captured during a model test or in a multi-phase flow solver. Disregarding the free surface effects can be useful when maneuvering models are being implemented within a potential flow simulation framework that already attempts to account for these wavemaking effects. Double-counting these forces will result in an incorrect estimation of the derivatives used to calculate the reaction forces in the maneuvering model. There is no practical way of removing free surface effects during a traditional captive model test but CFD allows for this capability.

All the simulations conducted in the presented study utilized an in-house CFD framework, NavyFOAM (Gorski, et al. 2014, Kim, et al. 2017). NavyFOAM is a suite of CFD tools developed using OpenFOAM®, an

open source software library. OpenFOAM® uses object-oriented programming to allow others to re-use and re-purpose sections of the programming to adopt new numerical schemes, algorithms and physical models. NavyFOAM utilizes Navier-Stokes solvers that use a cell-centered finite-volume method that permits the use of unstructured polyhedral cells. Several top-level solvers for single and multi-phase flows have also been added in NavyFOAM aiming at marine applications including underwater vehicles, surface ships, and propulsors. Solvers have also been developed to replicate conditions experienced during captive model tests including static drift, rotating arm, and rotating arm at a drift angle.

3. METHODOLOGY

The objective of the study was to perform a series of captive model simulations of the ONRTH (Model 5613) shown in Figure 1 using NavyFOAM and generate hydrodynamic derivatives suitable for implementation in the maneuvering model in Equation (1). Table 1 demonstrates the principal characteristics of the ONRTH. All the simulations were performed to match the model scale Froude (*Fn*) and Reynolds Number (*Re*). Bilge keels, propellers, propeller shafts, and rudders were not included in the presented study. The only appendage considered was the skeg.

The simulation matrices in Table 2 and Table 3 were developed in order to capture the relationships needed to generate hydrodynamic derivatives. Table 2 shows the static drift and rotating arm cases that were used to calculate the hydrodynamic derivatives that were dependent on either v or r (eg. Y_{vv}, N_{rr}, etc.). Table 3 shows the simulation matrix used to generate cross-dependent hydrodynamic derivatives like Y_{vr} and N_{vvr}. The drift angle in the simulation matrices was represented by β, while the moment arm used for the rotating arm cases was referred to as R, and specified in terms of ship-lengths, L.

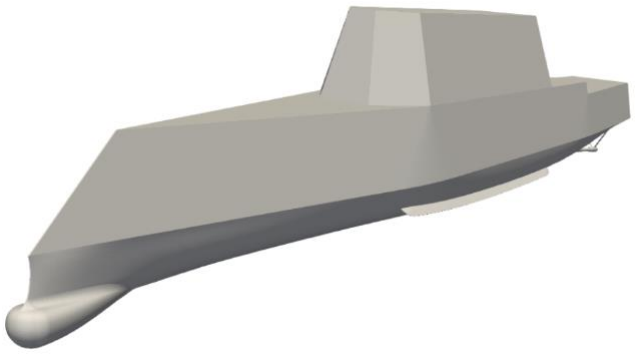

Figure 1. Complete geometry of ONR Tumblehome (ONRTH).

Table 1. Principal characteristics of ONR Tumblehome (ONRTH).

Dimension	Value
Waterline Length, L [m]	3.147
Waterline Beam, B [m]	0.384
Draft, T [m]	0.112
Wetted Surface Area, S [m^2]	1.500
Longitudinal Center of Gravity, LCG [m] (+Aft of FP)	1.625
Froude Number, Fn	0.20
Reynolds Number, Re	3.48×10^6

Table 2. Simulation matrix used to calculate coefficients that are dependent on either v or r but not both.

Type	β [deg]	R [m]	r [deg/s]	u [m/s]	v [m/s]
Static Drift	0	0	0.00	1.1100	0.0000
	2	0	0.00	1.1093	0.0387
	4	0	0.00	1.1073	0.0774
	6	0	0.00	1.1039	0.1160
	8	0	0.00	1.0992	0.1545
	10	0	0.00	1.0931	0.1927
Rotating Arm	0	2L	101.05	1.1100	0.0000
	0	3L	67.36	1.1100	0.0000
	0	4L	50.52	1.1100	0.0000
	0	5L	40.42	1.1100	0.0000
	0	10L	20.21	1.1100	0.0000

Table 3. Simulation matrix used to calculate coefficients that are dependent on both *v* and *r*.

Type	β [deg]	R [m]	r [deg/s]	u [m/s]	v [m/s]
Rotating Arm With Drift	2	3L	67.364	1.1093	0.0387
	6	3L	67.364	1.1039	0.1160
	2	4L	50.523	1.1093	0.0387
	6	4L	50.523	1.1039	0.1160
	2	5L	40.418	1.1093	0.0387
	6	5L	40.418	1.1039	0.1160

The results of the presented study were intended for implementation of a maneuvering model within a potential flow simulation framework in future work of predicting ship stability and extreme events. Therefore, ignoring the free surface effects was determined to be necessary for calculating hydrodynamic derivatives. Removing the free surface effects warranted utilizing a single-phase scheme that only considered the static submerged geometry. Only the underwater geometry shown in Figure 2 was considered in developing the hexahedra-dominant grid in Figure 3 and Figure 4. The domain size was set to 16L, 12.7L, and 3.17L in the x, y, and z directions respectively, where x is positive aft, y is positive starboard, and z is positive up. The domain size was set to be large enough to accommodate all of the simulation conditions and resulted in a cell count of 3 million. . A refinement region was used around the hull to increase the grid resolution in the vessel's wake region and allow for a smoother transition of cell sizing from the thin boundary layer cells with a y^+ (the average distance between the first cell center and vessel surface, in viscous unit) of 25 to the outer domain. Figure 4 shows the refinement regions as the cell density increases closer to the vessel. Since the simulations are only considering the underwater geometry, the free surface boundary utilizes a symmetry condition, also referred to as the "double-body" condition. Treating the free surface in this manner neglects the wavemaking effects and focuses on capturing the viscous contributions.

Figure 2. Underwater geometry of ONR Tumblehome (ONRTH).

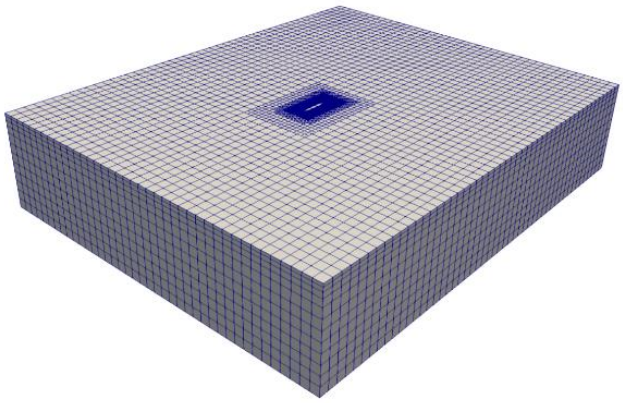

Figure 3. Isometric view of computational domain.

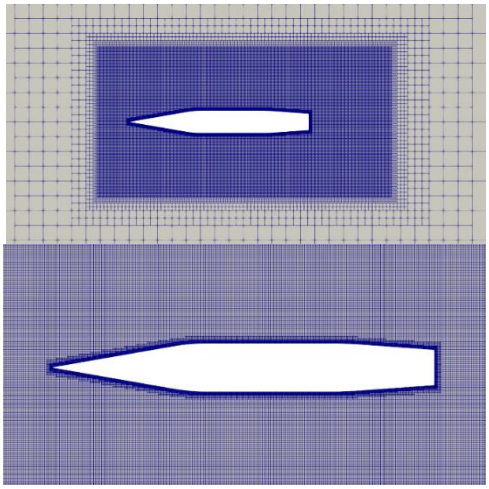

Figure 4. Depiction of the grid refinement regions around the ONRTH.

The static drift conditions were accomplished by setting the velocity inlet boundary condition to reflect the x and y axial-velocity components *u* and *v* needed to achieve the drift angle of interest, β, as shown in Figure 5.

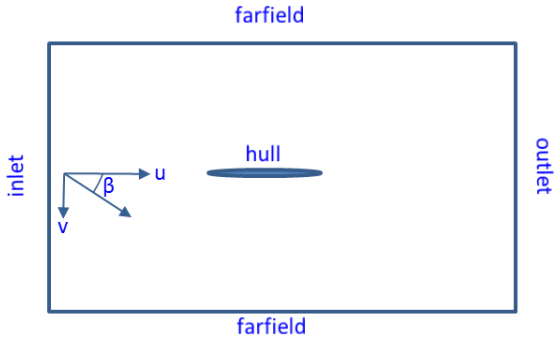

Figure 5. Illustration of boundary conditions for static drift cases.

The rotating arm captive model simulation was accomplished using a specialized solver that transforms the continuity and momentum equations from an inertial frame (*i*-frame) to a body-fixed frame (*b*-frame) as illustrated in Figure 6. The boundary conditions on the vessel surface are set to replicate the constant rotational rate the vessel would experience during a rotating arm test using the moment arm distance, R, and rotational velocity, r tabulated in Table 2. The rotating arm with drift cases in Table 3 were simulated using the solver used for rotating arm cases. To achieve the drift angle, the location on the vessel where it is rotated about the origin, O is translated from the center of gravity (CG) to a point forward. This geometric transformation allows the solver to mimic rotating arm with drift. Figure 7 shows the rotating arm and rotating with drift cases. The angle between the two moment arms in Figure 7 represents the drift angle. The presented methodology allowed for simulation of the static drift, rotating arm, and rotating arm with drift conditions using the same computational domain.

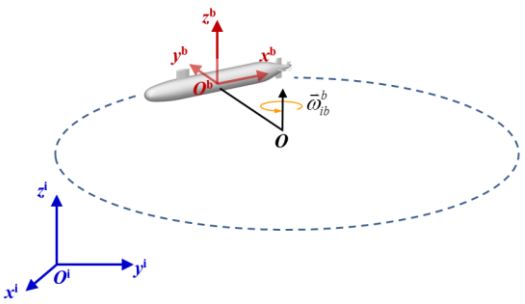

Figure 6. Illustration of coordinate system transformation from the inertial *i*-frame to the body-fixed *b*-frame.

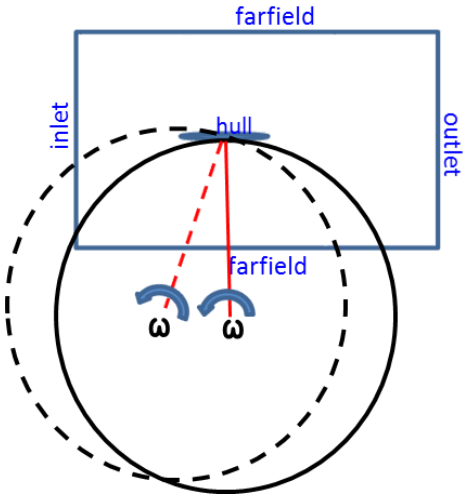

Figure 7. Illustration of rotating arm with drift case.

Ignoring the free surface effects by using a single phase solver makes it pivotal to model the turbulence correctly in the simulations. Selection of a suitable turbulence model is critical to ensure that the viscous contributions are being represented accurately. To investigate the dependence on turbulence model in the simulations, two different models were compared for the static drift portion of the matrix in Table 2. The turbulence models selected for investigation were the *k-ω* SST (Menter et al. 2003) and Wilcox's *k-ω* (Wilcox, 2008) for the static drift cases. Results of the comparison aided the decision of which turbulence model to use for the rotating arm and rotating arm with drift cases. Wall functions were used for both turbulence models to predict the behaviour in the viscous boundary layer.

To expedite the generation of the hydrodynamic derivatives, all the simulations were performed using a steady-state solver without any time dependence in the momentum equations. The use of a steady solver allowed for quicker simulation run times and also eliminated the numerical instability associated with unsteady solvers. To calculate the hydrodynamic reaction forces predicted in the simulations, Equation

(2) was used to calculate the pressure force and moment (F_p^b, M_p^b) and the viscous force and moment (F_v^b, M_v^b) in the body-fixed coordinate system. In Equation (2), n refers to the unit normal vector, ρ is the water density, p is the pressure, τ is the shear stress, and r - r_O is the location along the surface with respect to the center of gravity of the vessel.

$$\begin{aligned} F_p^b &= \int_S n^b p dS \\ F_v^b &= \int_S n^b \tau^b dS \\ M_p^b &= \int_S (r^b - r_O^b) \times n^b p dS \\ M_v^b &= \int_S (r^b - r_O^b) \times (n^b \cdot \tau^b) dS \end{aligned} \quad (2)$$

The implemented CFD methodology and simulation matrix limits the application of the generated hydrodynamic derivatives to the maneuvering model in Equation (1). Due to the CFD simulations all utilizing a steady-state solver, all the time-dependent terms are unavailable for extraction. The hydrodynamic reaction force calculations of X_H and K_H have also been ignored. The maneuvering model reduces to Equation (3) when the time-dependent terms, X_H and K_H are not included. Equation (3) was used in the calculation of hydrodynamic derivatives presented.

$$\begin{aligned} Y_H = {} & Y_v vU + Y_r rU + Y_{vv} v|v| \\ & + Y_{vr} v|r| + Y_{rr} r|r| \\ N_H = {} & rU + N_v vU + N_{rr} r|r| \\ & + N_{rrv} \frac{r^2 v}{U} + N_{vvr} \frac{v^2 r}{U} \end{aligned} \quad (3)$$

4. RESULTS

The static drift cases in Table 2 were simulated using the *k-ω* SST and Wilcox's *k-ω* turbulence models prior to beginning the rotating arm simulations. Figure 8 through Figure 13 compare the forces *X*, *Y*, and *Z* and the moments *K*, *M*, and *N* for each turbulence model at a series of drift angles. *Y*, *Z*, *K*, and *M* do not show any tangible difference in their results. The force *X* however, shows an inconsistency between the turbulence models. In terms of magnitude, the *X* force demonstrates the smallest values across the drift angles for any of the forces and moments. Though the small magnitude of the force may be a contributor to noticing differences, the *k-ω* SST model is resulting in a larger *X* that doesn't seem to follow any clear trend. The *X* at 10 degrees of drift also results in a 10% increase in comparison to Wilcox's *k-ω* model.

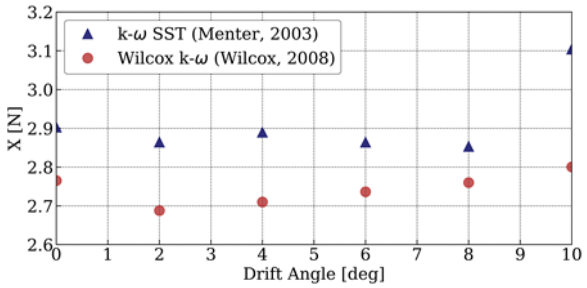

Figure 8. Comparison of X using different turbulence models in static drift.

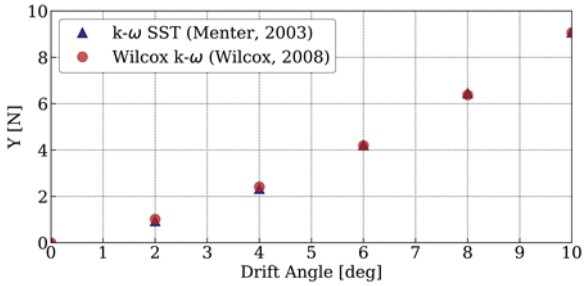

Figure 9. Comparison of Y using different turbulence models in static drift.

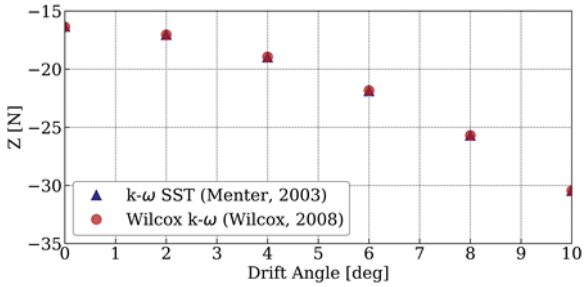

Figure 10. Comparison of Z using different turbulence models in static drift.

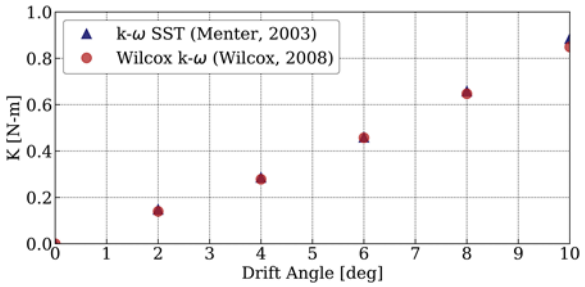

Figure 11. Comparison of K using different turbulence models in static drift.

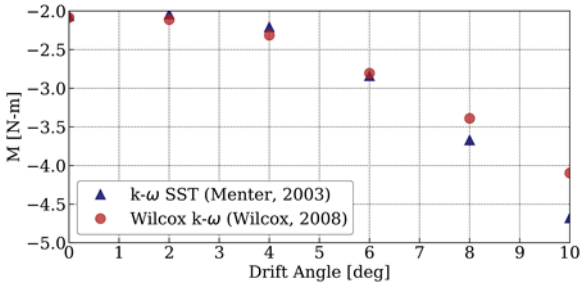

Figure 12. Comparison of M using different turbulence models in static drift.

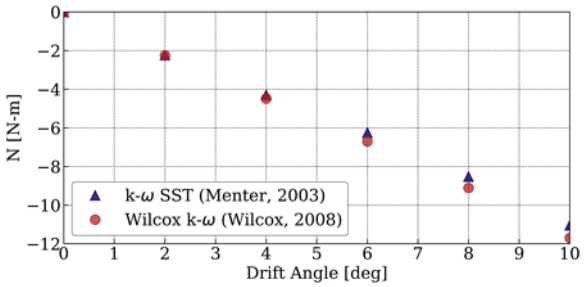

Figure 13. Comparison of N using different turbulence models in static drift.

Figure 14 shows the vortices shedding off the hull, colored by velocity magnitude (U), during the static drift simulations at 0 and 10 degrees of drift for both turbulence models. The vortices were identified using iso-surfaces of the Q-criterion (the second invariant of velocity deformation tensor). A clear distinction between 0 and 10 degrees of drift is shown as large vortices extend from the bulbous bow aft for the higher drift angle. The turbulent structures between both turbulence models look similar but the large vortices seem to extend slightly further downstream for Wilcox's *k-ω* turbulence model. Though the turbulence model demonstrated overall similar forces, moments, and vortices structures the lack of trend in *X* prompted the selection of Wilcox's *k-ω* turbulence model for the remaining rotating arm and rotating arm with drift simulations.

Figure 15 and Figure 16 show the results of the static drift cases Table 2 and the regression used to calculate the hydrodynamic coefficients Y_v, Y_{vv}, and N_v. Figure 17 and Figure 18 show the results of the rotating arm cases in Table 2 and the regression used to calculate Y_r, Y_{rr}, N_r, and N_{rr}. The *Y* force at higher rotational rates in Figure 17 demonstrated an unusual trend where the sign of the force switched from negative to positive possibly due to the ability of the grid resolution to handle the higher rates. To accommodate the sign change, only *r* from zero to five deg/s were used for the regression that calculated Y_v and Y_{vv}.

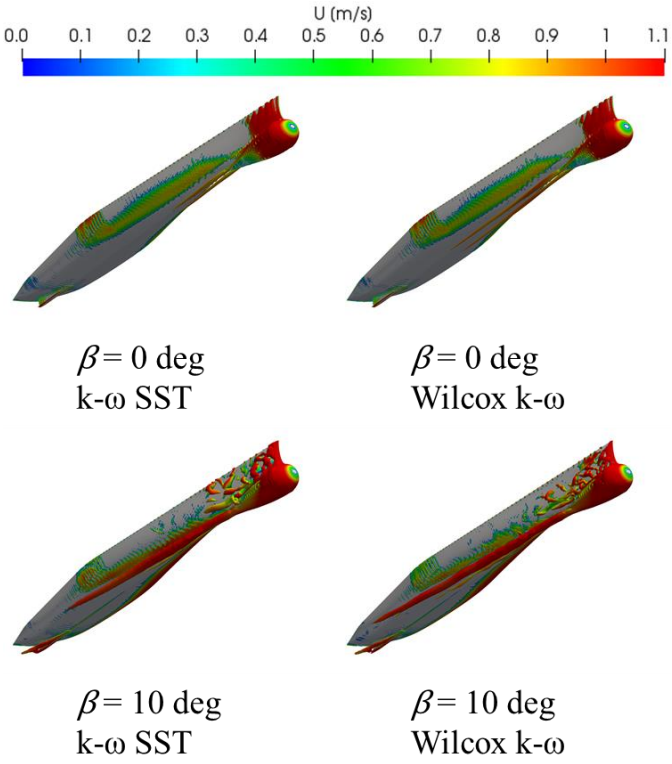

Figure 14. Iso-surfaces of Q=100 for drift angles of 0 and 10 degrees using different turbulence models.

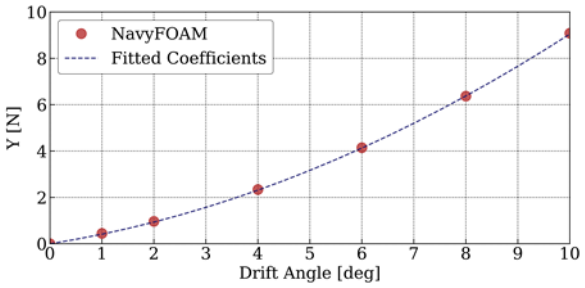

Figure 15. Regression of force Y from static drift cases at specified drift angles.

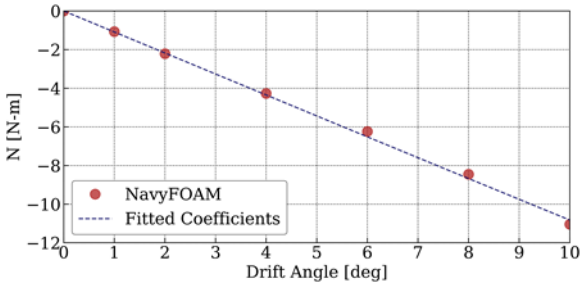

Figure 16. Regression of moment N from static drift cases at specified drift angles.

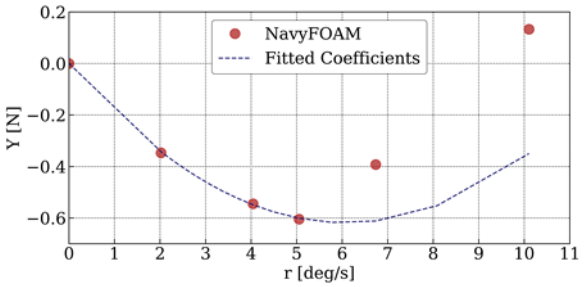

Figure 17. Regression of force Y from rotating arm cases at specified rotational rates.

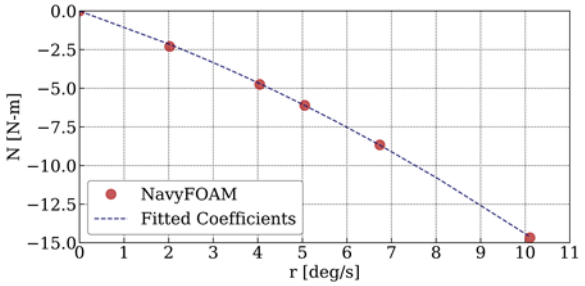

Figure 18. Regression of moment N from rotating arm cases at specified rotational rates.

Figure 19 and Figure 20 show the contours velocity magnitude and relative velocity, U_{rel}, throughout the domain for rotating arm and rotating arm with drift at R of 3L and β of 0 and 6 degrees. The wake of the vessel in Figure 19 shows how the flow reacts when a drift angle is introduced. Figure 20 shows how velocity relative to the center of rotation propagates throughout the domain. The contours of relative velocity also demonstrates the relocation of the center of rotation forward to achieve the rotating arm with drift condition.

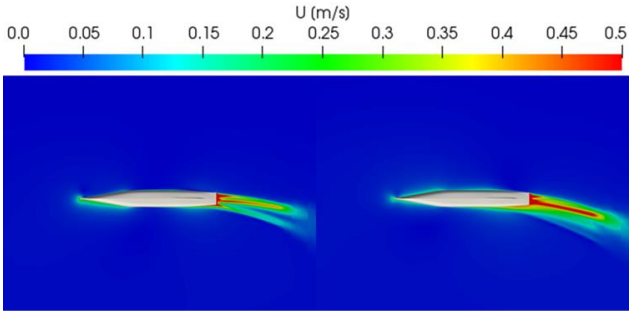

$R = 3L$ $\beta = 0$ deg $R = 3L$ $\beta = 6$ deg

Figure 19. Contours of velocity for rotating arm with and without drift at R = 3L and β = 0 and 6 degrees.

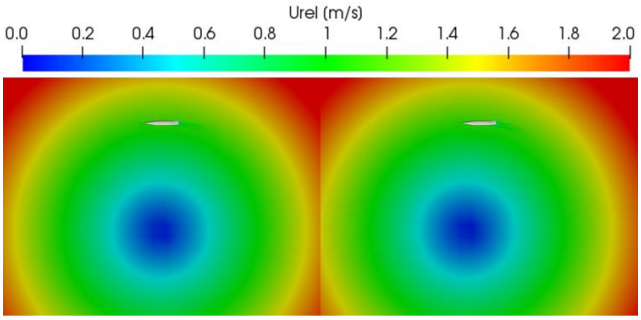

$R = 3L$ $\beta = 0$ deg $R = 3L$ $\beta = 6$ deg

Figure 20. Contours of relative velocity for rotating arm with and without drift at R = 3L and β = 0 and 6 degrees.

Figure 21 and Figure 22 show the comparison of the rotating arm with drift cases in Table 3 with the hydrodynamic derivatives calculated through multivariate linear regression. The NavyFOAM calculated Y force does not show dependence on the rotational rate at a particular drift angle. The calculated hydrodynamic derivatives however, show more of a dependence on r. The N moment shows a better correlation

between the NavyFOAM calculation and the calculated derivatives.

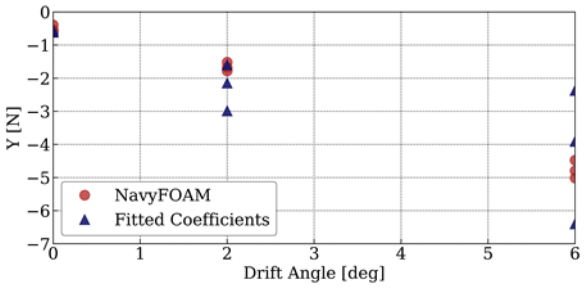

Figure 21. Multivariate regression of force Y for rotating arm with drift cases.

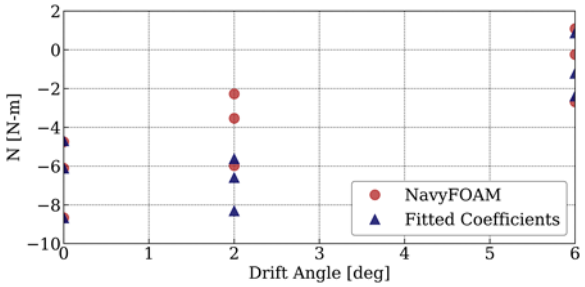

Figure 22. Multivariate regression of moment N for rotating arm with drift cases.

Table 4 and Table 5 show the hydrodynamic reaction forces and moments respectively for each condition. Table 6 summarizes the hydrodynamic derivatives calculated using the NavyFOAM simulations. Results of the current study only utilized the underwater geometry of the ONRTH, therefore are applicable to any of the ONR Topside Series hullforms. The computational expense to perform the simulations needed to develop Table 4 through Table 6 was around 15,000 CPU hours, relatively computationally inexpensive when it comes to CFD for naval applications. The proposed methodology could be applied to develop larger matrices of testing conditions as well numerous vessel configurations (eg. with and without certain appendages). The analysis performed can also be used for additional post-processing analysis such as extracting sectional cross-flow drag characteristics as proposed in Hughes, et al. (2011).

Table 4. Summary of hydrodynamic reaction forces *X*, *Y*, *Z*.

β **[deg]**	***R*** **[m]**	***X*** ***[N]***	***Y*** ***[N]***	***Z*** ***[N]***
0	0	2.7651	-0.0006	-16.3650
2	0	2.6878	1.0193	-17.0314
4	0	2.7098	2.4140	-18.9345
6	0	2.7365	4.1918	-21.8351
8	0	2.7602	6.3808	-25.6921
10	0	2.8004	9.0672	-30.4456
0	2L	3.7582	0.1328	-26.6258
0	3L	2.8911	-0.3923	-20.8048
0	4L	2.8943	-0.6044	-18.7771
0	5L	2.8860	-0.5446	-17.8384
0	10L	2.8898	-0.3469	-16.6248
2	3L	3.0654	-1.7818	-20.8338
6	3L	3.4965	-5.0118	-24.9104
2	4L	3.0617	-1.6742	-19.1770
6	4L	3.4561	-4.7944	-23.9433
2	5L	3.0314	-1.5188	-18.3521
6	5L	3.3597	-4.4743	-23.1226

Table 5. Summary of hydrodynamic reaction moments *K*, *M*, *N*.

β **[deg]**	***R*** **[m]**	***K*** ***[N-m]***	***M*** ***[N-m]***	***N*** ***[N-m]***
0	0	0.0000	-2.0843	0.0002
1	0	0.1398	-2.1121	-2.2466
2	0	0.2783	-2.3135	-4.4836
4	0	0.4575	-2.8051	-6.6995
6	0	0.6473	-3.3894	-9.1059
8	0	0.8490	-4.0971	-11.6986
10	0	0.0000	-2.0843	0.0002
0	2L	0.3786	-2.6463	-14.6665
0	3L	0.1214	-1.5517	-8.6653
0	4L	0.0884	-1.5208	-6.1098
0	5L	0.0785	-1.4935	-4.7476
0	10L	0.0408	-1.3945	-2.2919
2	3L	-0.0132	0.5904	-5.9749
6	3L	-0.2371	5.0314	-2.6838
2	4L	-0.0542	0.2902	-3.5350
6	4L	-0.3100	3.7828	-0.2441
2	5L	-0.0766	0.0144	-2.2733
6	5L	-0.3371	2.7357	1.0921

Table 6. Summary of calculated hydrodynamic derivatives.

Coefficient	Value
Yv	16.5790
Yvv	148.0097
Nv	-50.5872
Yr	-0.1830
Yrr	0.0167
Nr	-0.8772
Nrr	-0.0467
Yvr	-12.6867
Nrrv	0.7112
Nvvr	155.2880

5. CONCLUSIONS

Methodology and results from a series of captive model CFD simulations using NavyFOAM were presented for the ONRTH. The simulation methodology results in a simple, rapid, and effective manner of generating hydrodynamic derivatives for implementation of a maneuvering model within a potential flow simulation framework to supplement ongoing research in the field of ship stability and the prediction of extreme events. Since only the underwater geometry is considered in the methodology, the presented forces and moments should be applicable to any of the ONR Topside Series hullforms.

6. ACKNOWLEDGMENTS

The presented work was funded by the Naval Surface Warfare Center Carderock Division (NSWCCD) Independent Applied Research (IAR) Program under Dr. Jack Price. The authors would like to thank Dr. Sung-Eun Kim, Dr. Vadim Belenky, and Mr. Kenneth Weems for their guidance and support of this effort. The authors would also like to thank Dr. Kostas Spyrou for his insight into developing the simulation matrix.

7. REFERENCES

Bhushan, S., Yoon, H., Stern, F., Guilmineau, E., Visonneau, M., Toxopeus, S., Simonsen, C., Aram, S., Kim, S-E., and Grigoropoulos, G., 2015 “CFD Validation for Surface Combatant 5415 at Straight-Ahead and 20 degree Static Drift Conditions”, IIHR Technical Report #493, The University of Iowa, Iowa City, IA.

Gorski J., Kim S-E., Aram S., Rhee B., and Shan H., 2014, “Development of a CFD Framework for Prognoses of Resistance, Powering, Maneuvering, and Seakeeping of Surface Ships,” Proceedings of 30th Symposium of Naval Hydrodynamics, Tasmania, Australia.

Hughes, M.J., Kopp, P.J., and Miller, R.W., 2011, “Modelling of Hull Lift and Cross Flow Drag Forces in Large Waves in a Computationally Efficient Dynamic Stability Prediction Tool,” Proceedings of 12th International Ship Stability Workshop, ISSW2011, Washington, D.C.

Kim S-E., Shan, H., Miller, R., Rhee, B., Vargas, A., Aram S., and Gorski, J., “A Scalable and Extensible Computational Fluid Dynamics Software Framework for Ship Hydrodynamics Applications: NavyFOAM”, Computing in Science & Engineering, Vol. 19, No. 6, pp. 33-39.

Menter, F. R., Kuntz, M., and Langtry, R., 2003, "Ten Years of Industrial Experience with the SST Turbulence Model," Turbulence, Heat and Mass Transfer 4, Begell House, Inc., pp. 625 - 632.

Mikelis, N., 1985, “A procedure for the prediction of ship manoeuvring response for initial design,” Proceedings of International Conference of Shipyard Operation and Ship Design, ICCAS, Banda, P., and Kuo, C., Elsevier Publishers B.V., North Holland, pp. 437–446.

Spyrou, K.J. and Tigkas, I., 2007, “Dynamics of a ship steering win wind revisited,” Journal of Ship Research, Vol. 51, No. 2, pp. 160-173.

Wilcox, D. C., 2008, "Formulation of the k-omega Turbulence Model Revisited," AIAA Journal, Vol. 46, No. 11, pp. 2823-2838.

Numerical prediction of roll motion during ship turning using CFD-System based method

Haipeng Guo, *School of Naval Architecture, Ocean and Civil Engineering, Shanghai Jiao Tong University, China* guohaipeng@sjtu.edu.cn

Zaojian Zou, *State Key Laboratory of Ocean Engineering, Shanghai Jiao Tong University, China* zjzou@sjtu.edu.cn

Yi Liu, *School of Naval Architecture, Ocean and Civil Engineering, Shanghai Jiao Tong University, China* lucy261@sjtu.edu.cn

Xianrui Hou, *College of Ocean Science and Engineering, Shanghai Maritime University, China* xrhou@shmtu.edu.cn

ABSTRACT

This paper focuses on the prediction of roll motion during ship maneuvers with CFD-System based method. RANS simulations of free roll decay test with forward speed is performed for the ONR tumblehome ship model using STAR-CCM+. The influence of appendages is presented with the decay curves and flow field. The inertia term and damping term are obtained by analyzing the numerical data. Furthermore, a 4-DOF system based simulation of turning circle test is performed. The results show good agreement with the published experimental dada, demonstrating the reliability of the method in the prediction of ship rolling during maneuvers.

Keywords: *ship rolling; turning circle test; RANS method; 4-DOF MMG model*

1. INTRODUCTION

The roll motion during ship tight maneuvers is remarkable for the vessels with high service speed and small metacentric height, such as warships, large container and passenger ships. The change of ship attitude may result in capsizing of the vessel. Hence, the roll-coupled ship maneuvers should be paid more attention. Aiming at this subject, some researches are carried out based on the system-based method, which is a widely used approach in the ship maneuverability prediction. Several 4 DOF mathematical models have been proposed, such as the MMG model of Hirano & Takashina (1980), Son & Nomoto (1982), and Umeda & Hashimoto (2002). The reliability of these models highly depends on the accurately prediction of the hydrodynamic and hydrostatic

forces acting on the ship under rolling condition.

Large amounts of researches on ship roll motion are carried out in the physical basin. Aloisio & Felice (2006), de Oliveira et al (2012, 2014), and Kristiansen et al (2014) carried out a series of experiments to study the effect of bilge keel on the roll damping, and the flow field around the bilge keel is analyzed using PIV technology. Fullerton et al (2006, 2008), and Atsavapranee et al (2007) measured the hydrodynamic force acting on the ship models during free and forced roll motion. Broglia et al (2009) studied the roll motion coefficients at different Froude number and Reynolds number though full scale and model scale free roll decay tests.

Apart from the experimental approach, the computational fluid dynamics (CFD) technology has drawn more and more attention. Irkal et al (2016a, 2006b), Yu & Kinnas (2009), Bangun et al (2010), Jaouen et al (2011), Avalos et al (2014), Chen et al (2016), Yildiz et al (2016), and Yildiz & Katayama (2017) performed 2-dimension CFD simulations for the middle section of hull-like body to investigate the effect of ship type and bilge keel on the roll damping. Further, several researches are performed for actual ship models. Wilson et al (2006), Yang et al (2013), Zhou et al (2015), and Gu et al (2015) carried out numerical simulation of free decay and forced roll tests at various forward speeds and amplitudes for different ship models. Gao & Vassalos (2011) and Begovic et al (2015) performed an assessment of the roll damping for both intact and damaged ship models at zero and forward speed to explore the effect of flooding and sloshing on the ship roll motions. Overall, the CFD method shows promising reliability in the prediction of roll damping.

In this study, ship maneuvers considering the roll-coupling effect is investigated based on the CFD-System based method. An improved MMG model is employed to describe the 4-DOF ship motions. Taking the ONR tumblehome (ONRT) ship model as the study subject, the free roll decay test with a forward speed is simulated using Reynolds-Averaged Navier-Stokes (RANS) method. The influence of bilge keels and shaft brackets on the dynamic response of ship model is presented with the decay curves, and the mechanism is analyzed with the local flow field. The added moment of inertia and roll damping is obtained by the regression of the numerical data. Moreover, the system-based simulation of turning circle test is performed with the coefficients in the mathematical model derived from CFD data. The trajectory of turning motion and the time history of roll angle are compared with the published free sailing model test data to validate the proposed numerical prediction method.

2. MATHEMATICAL MODEL

Using the coordinate systems (Hamamoto & Kim, 1993) shown in Fig. 1, the 4-DOF ship motion can be described with an improved MMG model, as presented in Eqs. (1)-(4).

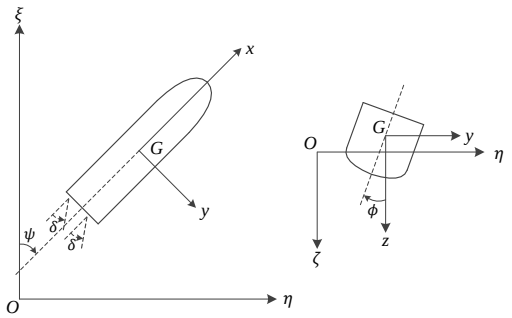

Figure 1 The coordinate systems for 4-DOF mathematical model

$$(m+m_x)\dot{u}-(m+m_y)vr=X_H(u,v,r)+X_P(u,n)+X_R(u,v,r,\delta) \quad (1)$$

$$(m+m_y)\dot{v}+(m+m_x)ur=Y_H(u,v,r,\phi)+Y_P(u,v,r)+Y_R(u,v,r,\delta) \quad (2)$$

$$(I_x + J_x)\dot{p} - m_x z_H ur = K_H(u,v,r,p,\phi) + K_P(u,v,r) + K_R(u,v,r,\delta) \quad (3)$$

$$(I_z + J_z)\dot{r} = N_H(u,v,r,\phi) + N_P(u,v,r) + N_R(u,v,r,\delta) \quad (4)$$

where m is the mass of the ship. I_x and I_y are the moments of inertia. m_x, m_y, J_x, and J_y are the added masses and added moments of inertia. u and v are the velocity components in the longitudinal and transverse directions, p and r are the angular velocities of roll and yaw motions. ϕ is the roll angle. n is the propeller revolutions. δ is the rudder angle. X, Y, K, and N with the subscripts 'H', 'P', and 'R' denote the force and moment components on the hull, propeller, and rudder, separately. z_H denotes the z-coordinate of the acting point of the lateral force.

The module relating to the roll motion can be represented as Eqs. (5)-(7). The hydrodynamic derivatives relating to roll angle ϕ can be derived from the static heel test. Besides, the roll damping K_p, as well as the added moment of inertia J_x in Eq. (3), can be obtained from the free roll decay test.

$$Y_H(\phi) = Y_\phi \phi \quad (5)$$

$$K_H(p,\phi) = K_p p + K_\phi \phi - mgGM\phi \quad (6)$$

$$N_H(\phi) = N_\phi \phi \quad (7)$$

where Y, K, and N with subscripts 'p' and 'ϕ' are the hydrodynamic derivatives relating to roll motion. g is the gravitational acceleration. GM is the metacentric height.

3. SUBJECT SHIP

The ONR Tumblehome ship published by the US Office of Naval Research is selected as subject ship. It is a kind of twin-screw surface combatant appended with bilge keels, skeg, and shaft brackets. Particularly, the ship type has a wave piercing hull design with 10° tumblehome sides and transom stern. The body-plan is shown in Fig. 2, and the principal particulars of the vessel model are given in Tab. 1 (Sadat-Hosseini et al, 2010).

In the study, the simulation of roll decay test are performed in the calm water under Fr = 0.2, and the initial heeling angle ϕ_0 = 25°. Three kinds of ship model are adopted, including bare hull, hull appended with bilge keels, and hull appended with bilge keels and shaft brackets. The parameter of k_x = 0.123 is questionable in the experiments, hence k_x = 0.1298 is adopted in present CFD simulation, which is in accordance with Sadat-Hosseini et al (Sadat-Hosseini et al, 2010).

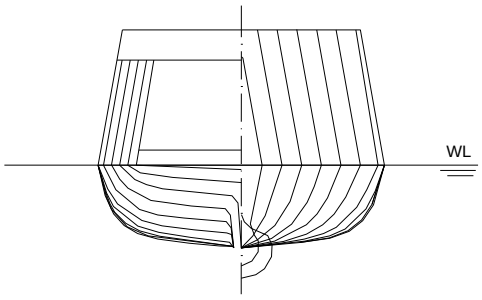

Figure 2 The body-plan of ONRT model

Table 1 The principal particulars of ONRT model

Item	Value
Length: L (m)	3.305
Breath: B (m)	0.403
Draft: d (m)	0.1201
Displacement: m (kg)	84.7
Meta-centric height: GM (m)	0.043
Roll radius of gyration: k_x (m)	0.123
Pitch and Yaw radius of gyration: k_y and k_z (m)	0.826

4. NUMERICAL METHOD

The CFD computations are performed using the RANS solver in STAR-CCM+, with

the isotropic blended SST k-ω turbulence model. The governing equations are discretized using Finite Volume method (FVM). The convective and viscous terms are discretized using a second-order schemes, while the temporal term is discretized using a first-order backwards Euler scheme. The pressure/velocity coupling is realized with the SIMPLE method. The two phase volume of fluid (VOF) technique is adopted for capturing the free surface. The Dynamic Fluid Body Interaction (DFBI) module is employed to simulate the dynamic response of ship model during roll decay test, and the dynamic overset mesh technology is used to realize the movement of ship model.

A cuboid computational domain is adopted in CFD simulation. The dimension of the computational domain and setup of boundary condition are presented in Fig. 3. The computational domain is discretized using an unstructured hexahedral grid. As shown in Fig. 4, the grid points around the ship and waterline are increased to capture the flow and wave features during ship motion, and the surface mesh on the appendages is refined to capture the geometric feature sufficiently. On the surfaces of ship model, prismatic cells are used to achieve better resolution of the near wall flow. The alignment of these cells is in accordance with the targeted non-dimensional distance from the wall Y^+ ranging from 30 to 60 for the ship model under water line.

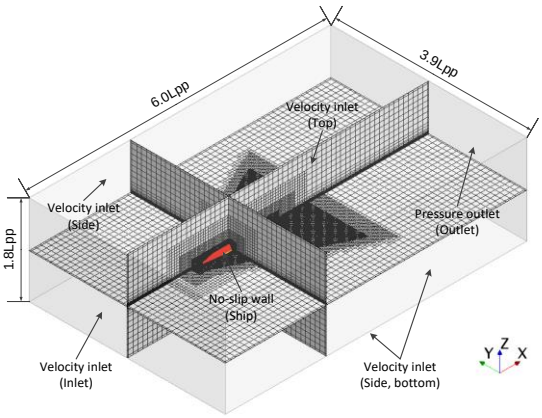

Figure 3 Dimension of the computational domain and boundary condition

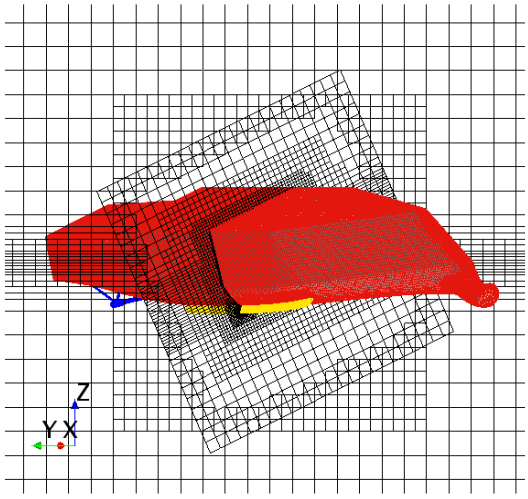

Figure 4 Grid generation around the ship model

5. CONVERGENCE STUDY

The convergence study of grid spacing and time step is performed for the free roll decay test with the bare hull at Fr = 0.2, based on the methodology proposed by Stern et al (1999). Referring to Wilson et al (2006), the uncertainty is investigated for the deviation of roll angle during the period of $0 < t < 1.58$s, which is represented as a L2 norm form. Three grid points of 1.78×10^6 (S_{G1}), 0.88×10^6 (S_{G2}), and 0.49×10^6 (S_{G3}) are generated based on the refinement ratio of $\sqrt{2}$, and three time steps of 0.005s (S_{T1}), 0.01s (S_{T2}), and 0.02s (S_{T3}) are selected based on refinement ratio of 2. Grid convergence study is carried out with the minimum time step Δt=0.005s, and time-step convergence study is carried out with the maximum grid points of 1.78×10^6.

The results of convergence study are given in Tab. 2, where 'Mon.', 'Osc.', and 'Div.' denote monotonic convergence, oscillatory convergence, and divergence, respectively. According to the spatial and temporal discretization scheme, the theoretical order of accuracy P_{est} = 2 and 1 is adopted for the grid and time step convergence study.

Table 2 Grid and time-step convergence of free roll decay simulation with ϕ_0=25°

	Grid (G)	Time step (T)
R	-0.533	-3.453
Con.	Osc.	Osc.
P	-	-
C	-	-
$U\%S_1$	0.533	1.025

As shown in Tab. 2, the grid and time-step convergence can be achieved with $R < 1$, although both of them show oscillatory convergence. Overall, the numerical result is slightly influenced by grid and time step due to the reasonably small uncertainty $U\%S_1$. In the following simulation, the grid of maximum density S_{G1} and the minimum time step S_{T1} are used for spatial and temporal discretization.

6. NUMERICAL RESULT

6.1 Roll decay simulation

The time histories of roll angle during free roll decay simulation are presented in Fig. 5. Correspondingly, the time histories of roll angular velocity and roll angular acceleration during free roll decay simulation are presented in Fig. 6 and the time histories of roll moments is plotted in Fig. 7. For the case of bare hull, the amplitude and period show good agreement with the experimental data at the initial stage. With the growth of the time, there is a slight difference of phase due to the accumulation of errors. In addition, the time histories of roll motion present obvious change for the case with appendages. Compared with the case of bare hull, the amplitude of roll decay is smaller while the period is larger. Besides, the effect of shaft brackets is negligible small according to the comparison of the cases with different appendages. Hence, the bilge keels play a primary role in the roll damping, and further affect the ship roll motion.

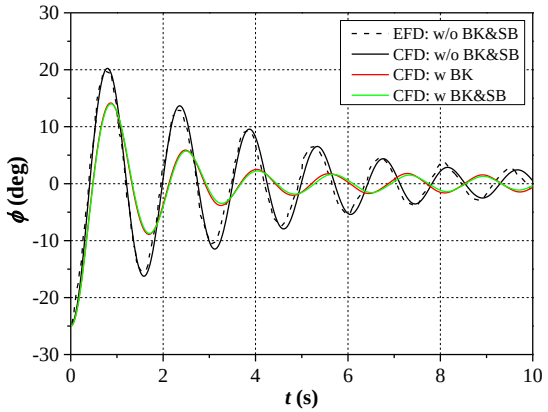

Figure 5 Time history of roll angle under different condition

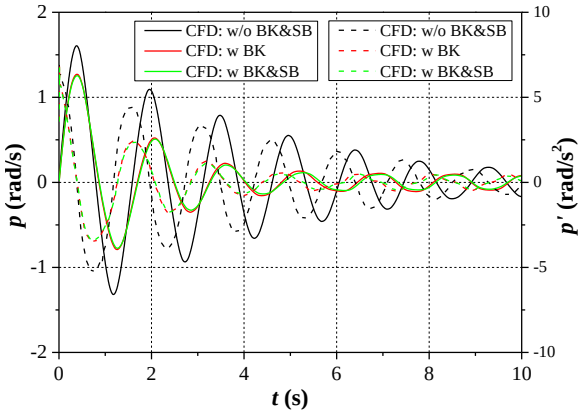

Figure 6 Time histories of kinematics parameters (solid: roll angular velocity; dash: roll angular acceleration)

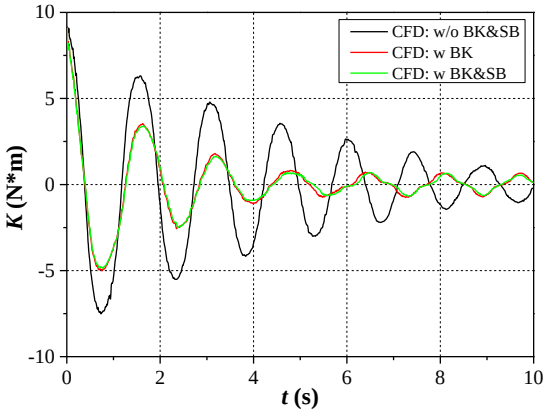

Figure 7 Time history of roll moments

In order to provide deeper insight into the free roll decay simulation, the qualitative analysis of the local flow field is presented for the case with bilge keels and shaft brackets. Three instants of t = 0.48s, 0.88s, and 1.33s are

selected. With nine cross-sections uniformly spaced within -0.4 < *x/L* < 0.4, the contours of axial velocity *u* and axial vortex ω_x are plotted in Figs. 8-10. The main features of the flow along the ship model are clearly captured, especially the flow around the appendages of bilge keels and shaft brackets.

At *t* = 0.48s, the ship model is rotating counter clockwise seen from stern with zero heeling angle and maximum roll angular velocity. A series of clockwise vortex are generated at the tip of bilge keels. The vortex results in a high momentum flow around the boundary layer of hull surface on the left of bilge keel while low momentum flow near the boundary layer of hull surface on the right of bilge keels. As a consequence, the boundary layer on the hull surface is thinner on the left side of bilge keels while thicker on the right side of bilge keels. Besides, the boundary layer develops along the longitudinal direction. As for the flow field around stern, it is shown that the vortex shedding from the shaft brackets is rather weak, demonstrating the negligible effect of shaft brackets on the roll damping.

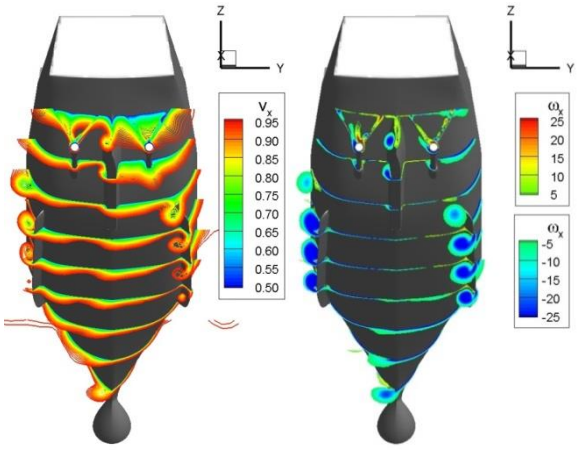

Figure 8 The contours of axial velocity and axial vortex at *t* = 0.48s

At *t* = 0.88s, the ship model is with the max heeling angle and zero roll angular velocity. The clockwise rotating vortex is weakened and a smaller anticlockwise rotating vortex appears at the tip of bilge keels. At *t* = 1.33s, the ship model return to the zero heeling angle condition. A series of anticlockwise rotating vortex develop at the tip of bilge keels. The flow field is more complicated at the after body due to previously generating vortex system, which is with opposite rotational direction. With the growth of time, the roll motion decays due to the impact of roll damping, leading to a weaker vortex system.

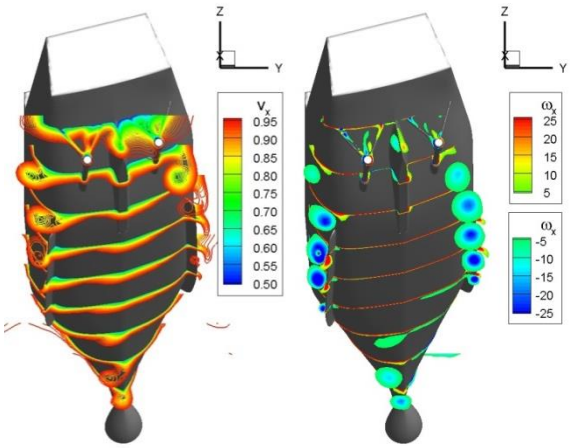

Figure 9 The contours of axial velocity and axial vortex at *t*=0.88s

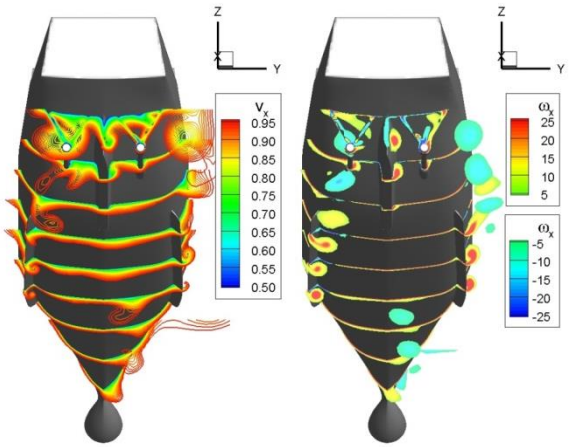

Figure 10 The contours of axial velocity and axial vortex at *t* =1.33s

6.2 Inertia term and damping term

According to the 1-DOF uncoupled free roll decay function given in Eq. (8), the roll moment acting on the ship model can be represented as a linear expression relating to roll angle, roll angular velocity, and roll

angular acceleration.

$$(I_x + J_x)\dot{p} + K_p p + K_\phi \phi - mgGM\phi = 0 \qquad (8)$$

A least squares fitting is performed with time histories of roll angle, roll angular velocity, roll angular acceleration, and roll moment plotted in Fig. 5, Fig. 6, and Fig. 7. In order to reduce the fitting error, the dimensionless coefficient of K'_ϕ is set as 0.0073, which is obtained from the CFD simulation of static heel test in the previous work (Guo & Zou, 2017). The computed added inertia of moment and linear damping coefficient are given in Tab. 3, and the coefficients are normalized according to Eq. (9). From Tab. 3, it can be seen that the bilge keels have a remarkable effect on enhancement of the added moment of inertia and linear damping coefficient. Meanwhile, the shaft brackets have negligible effect on the computed coefficients, taking the fitting error into account.

$$J'_x = \frac{J_x}{0.5\rho L^4 d}, \quad K'_p = \frac{K_p}{0.5\rho V L^3 d}, \quad K'_\phi = \frac{K_\phi}{0.5\rho V^2 L^2 d} \qquad (9)$$

where ρ is the fluid density. V is the speed of ship model.

Table 3 The dimensionless added inertia of moment and linear damping coefficient

Cases	J'_x	K'_p
w/o BK&SB	4.803×10^{-5}	-3.589×10^{-4}
w BK	8.547×10^{-5}	-9.892×10^{-4}
w BK&SB	8.977×10^{-5}	-1.029×10^{-4}

6.3 Turning circle simulation

The system-based simulation of turning circle test is performed using a 4-DOF MMG model in Araki et al (2012). Apart from the added moment of inertia J_x and linear damping coefficient K_p computed in present work, the rest of hydrodynamic coefficients are taken from Guo & Zou (2017). The trajectory of the turning circle simulation with δ = -35° at Fr = 0.2 is presented in Fig. 11. The present simulation shows good agreement with the published experimental data. The turning diameter is slightly underestimated with the error of 2.45%, demonstrating a satisfactory accuracy in the prediction of ship maneuverability.

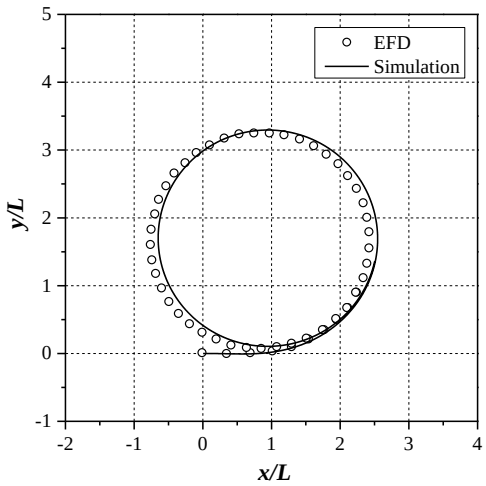

Figure 11 Trajectory of turning circle simulation

The corresponding time history of roll angle is depicted in Fig. 12. It is shown that an inward heeling angle appears at the initial stage of turning due to the deflection of the rudder. The phenomenon is detected accurately by the present simulation. During the turning, the roll angle changes to be windward and remarkable oscillation can be observed. The peak value of the windward heeling angle is underestimated by the simulation. The roll angle tends to be a constant value at the state of steady turning, and good agreement is achieved between the EFD data and the simulation results with the deviation of 5.07%. Overall, the prediction of roll motion shows satisfactory accuracy in view of the rather small magnitude of roll angle.

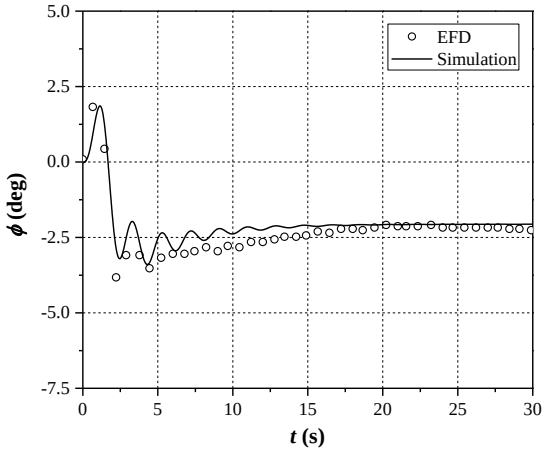

Figure 12 Time history of roll angle during turning simulation

7. CONCLUSIONS

The present work focuses on the prediction of roll motion during ship tight maneuvers with the CFD-System based method. A 4-DOF MMG mathematical model is adopted to describe ship maneuvers coupled with roll motion. Taking the ONR tumblehome ship model as study subject, a series of free roll decay simulation in calm water with forward speed is performed with the RANS solver of STAR-CCM+. The computed free roll decay curve is compared with the published experimental data, and satisfactory agreement is achieved. The influence of the appendages of bilge keels, shaft brackets on the roll motion is analyzed macroscopically with the decay curves. The flow fields at different longitudinal sections of hull are plotted to gain a deeper insight into the flow around the appendages during ship rolling. Besides, the added moment of inertia and linear damping coefficient is estimated based on the computed kinematic and dynamic quantities relating to ship rolling. It is shown that the bilge keels play a primary role in the roll damping, while the effect of shaft brackets is negligible small. Furthermore, a system-based simulation of turning circle test is performed with the data of hydrodynamic coefficients obtained from previous and present CFD computation. The trajectories of turning motion and the time histories of roll motion show good agreement with the available experimental data, demonstrating the reliability of the CFD-System based method in the prediction of ship rolling during manoeuvres.

8. ACKNOWLEDGEMENTS

This work is financially supported by the National Natural Science Foundation of China [Grant number 51779140] and the Fund of the State Key Laboratory of Ocean Engineering of Shanghai Jiao Tong University for Independent Researches [Grant number GKZD010068].

9. REFERENCE

Atsavapranee, P., Carneal, J.B., Grant, D., and Percival, A.S., 2007, "Experimental Investigation of Viscous Roll Damping on the DTMB Model 5617 Hull Form", 26th International Conference on Offshore Mechanics and Arctic Engineering. California, USA.

Aloisio, G. and Felice, F., 2006, "PIV Analysis around the Bilge Keel of a Ship Model in a Free Roll Decay", XIV Congresso Nazionale AI VE. LA., Rome, Italy, pp. 6-7.

Araki, M., Sadat-Hosseini, H., Sanada, Y., Tanimoto, K., Umeda, N., and Stern, F., 2012, "Estimating Maneuvering Coefficients Using System Identification Methods with Experimental, System-Based, and CFD Free-Running Trial Data", Ocean Engineering, Vol. 51, pp. 63-84.

Avalos, G.O.G., Wanderley, J.B.V., Fernandes, A.C., and Oliveira, A.C., 2014, "Roll Damping Decay of a FPSO with Bilge Keel", Ocean Engineering, Vol. 87, pp. 111-120.

Broglia, R., Bouscasse, B., Di Mascio, A.,

Lugni, C., and Atsavapranee, P., 2009, "Experimental and Numerical Analysis of the Roll Decay Motion for a Patrol Boat", 19th International Offshore and Polar Engineering Conference, Osaka, Japan.

Begovic, E., Day, A.H., Incecik, A., Mancini, S., and Pizzirusso, D., 2015, "Roll Damping Assessment of Intact and Damaged Ship by CFD and EFD Methods", 12th International Conference on the Stability of Ships and Ocean Vehicles, Glasgow, UK.

Bangun, E.P., Wang, C.M., and Utsunomiya, T., 2010, "Hydrodynamic Forces on a Rolling Barge with Bilge Keels", Applied Ocean Research, Vol. 32(2), pp. 219-232.

Chen, L., Sun, L., Zang, J., Hillis, A., and Plummer, A., 2016, "Numerical Study of Roll Motion of a 2-D Floating Structure in Viscous Flow", Journal of Hydrodynamics, Ser. B, Vol. 28(4), pp. 544-563.

Hamamoto, M. and Kim, Y.S., 1993, "A New Coordinate System and the Equations Describing Maneuvering Motion of a Ship in Waves", Journal of the Society of Naval Architects of Japan, Vol. (173), pp. 209-220.

Hirano, M. and Takashina, J., 1980, "A Calculation of Ship Turning Motion Taking Coupling Effect Due to Heel into Consideration", The Japan Society of Naval Architects and Ocean Engineers, Vol. (59), pp. 71-81.

Irkal, M.A.R., Nallayarasu, S., and Bhattacharyya, S.K., 2016a, "CFD Approach to Roll Damping of Ship with Bilge Keel with Experimental Validation", Applied Ocean Research, Vol. 55, pp. 1-17.

Irkal, M.A.R., Nallayarasu, S., and Bhattacharyya, S.K., 2016b, "CFD Simulation of Roll Damping Characteristics of a Ship Mid-Section with Bilge Keel", 35th International Conference on Ocean, Offshore and Arctic Engineering, Busan, South Korea.

Jaouen, F., Koop, A., and Vaz, G., 2011, "Predicting Roll Added Mass and Damping of a Ship Hull Section Using CFD", 30th International Conference on Ocean, Offshore and Arctic Engineering, Rotterdam, Netherlands.

Kristiansen, T., Ruth, E., Firoozkoohi, R., Borgen, H., and Ola Berge, B., 2014, "Experimental and Numerical Investigation of Ship Roll Damping with and without Bilge Keels". 33rd International Conference on Ocean, Offshore and Arctic Engineering, California, USA.

Fullerton, A.M., Fu, T.C., and Hong, Y.S., 2006, "The Induced Forces and Motions of a Tumblehome Hullform Undergoing Forced Roll", 26th Symposium on Naval Hydrodynamics, Rome, Italy.

Fullerton, A.M., Fu, T.C., and Reed, A.M., 2008, "The Moments on a Tumblehome Hull Form Undergoing Forced Roll", 27th Symposium on Naval Hydrodynamics, Seoul, Korea.

Gu, M., Lu, J., Bu, S., Wu, C., and Qiu, G., 2015, "Numerical Simulation of the Ship Roll Damping", 12th International Conference on the Stability of Ships and Ocean Vehicles, Glasgow, UK.

Gao, Q. and Vassalos, D., 2011, "Numerical Study of The Roll Decay of Intact and Damaged Ships", 12th International Ship Stability Workshop, Virginia, USA.

Guo, H. and Zou, Z., 2017, "System-Based Investigation on 4-DOF Ship Maneuvering with Hydrodynamic Derivatives Determined by RANS Simulation of Captive Model Tests", Applied Ocean Research, Vol. 68, pp. 11-25.

Oliveira, A.C. and Fernandes, A.C., 2012, "An Empirical Nonlinear Model to Estimate FPSO with Extended Bilge Keel Roll Linear Equivalent Damping in Extreme Seas", 31st International Conference on Ocean, Offshore and Arctic Engineering, Rio de Janeiro, Brazil.

Oliveira, A.C. and Fernandes, A.C., 2014, "The Nonlinear Roll Damping of a FPSO Hull", Journal of Offshore Mechanics and Arctic Engineering, Vol. 136(1), pp. 011106.

Son, K.H. and Nomoto, K., 1982, "On the Coupled Motion of Steering and Rolling of a High-Speed Container Ship", Naval Architecture and Ocean Engineering, Vol. 20, pp. 73-83.

Sadat-Hosseini, H., Stern, F., Olivieri, A., Campana, E.F., Hashimoto, H., Umeda, N., Bulian, G., and Francescutto, A., 2010, "Head-Wave Parametric Rolling of a Surface Combatant", Ocean Engineering, Vol. 37(10), pp. 859-878.

Stern, F., Wilson, R.V., Coleman, H.W., and Paterson, E.G., 1999, "Verification and Validation of CFD Simulations", IIHR Report 407, Iowa Institute of Hydraulic Research, the University of Iowa.

Umeda, N. and Hashimoto, H., 2002, "Qualitative Aspects of Nonlinear Ship Motions in Following and Quartering Seas with High Forward Velocity", Journal of Marine Science and Technology, Vol. 6(3), pp. 111-121.

Wilson, R.V., Carrica, P.M., and Stern, F., 2006, "Unsteady RANS Method for Ship Motions with Application to Roll for a Surface Combatant", Computers & fluids, Vol. 35(5), pp. 501-524.

Yildiz, B., Çakici, F., Katayama, T., and Yilmaz, H., 2016, "URANS Prediction of Roll Damping for a Ship Hull Section at Shallow Draft", Journal of Marine Science and Technology, Vol. 21(1), pp. 48-56.

Yildiz, B. and Katayama, T., 2017, "Bilge Keel-Free Surface Interaction and Vortex Shedding Effect on Roll Damping", Journal of Marine Science and Technology, Vol. 22(3), pp. 432-446.

Yu, Y. and Kinnas, S., 2009, "Roll Response of Various Hull Sectional Shapes Using a Navier-Stokes Solver", International Journal of Offshore and Polar Engineering, Vol. 19(1), pp. 46-51.

Yang, C., Zhu, R., Miao, G., and Fang, J., 2013, "Numerical Simulation of Rolling for 3-D Ship with Forward Speed and Nonlinear Damping Analysis", Journal of Hydrodynamics, Ser. B, Vol. 25(1), pp. 148-155.

Zhou, Y., Ma, N., Shi, X., and Zhang, C., 2015, "Direct Calculation Method of Roll Damping Based on Three-Dimensional CFD Approach", Journal of Hydrodynamics, Ser. B, Vol. 27(2), pp. 176-186.

Improvement of Broaching Prediction Method by System Identification Using CFD

Kentaro Mizumoto, *Osaka University, Japan* kentaro08260331@gmail.com

Motoki Araki, *National Maritime Research Institute, Japan* araki@nmri.go.jp

Frederick Stern, *The University of Iowa, USA* frederick-stern@uiowa.edu

Hirotada Hashimoto, *Kobe University, Japan* hashimoto@port.kobe-u.ac.jp

Naoya Umeda, *Osaka University, Japan* umeda@naoe.eng.osaka-u.ac.jp

ABSTRACT

A broaching prediction method based on modular manoeuvring model with linear potential flow theory (Umeda et al., 2016) was available but it requires limited scaled captive model tests for determining some parameters. To overcome this drawback, Araki et al. (2013) proposed a system identification technique using limited number of time histories from CFD (computational fluid dynamics) in waves and validated this technique at least for moderate sea states. As a next step, we apply this technique to severe sea states which could result in typical broaching. Thus, we use the CFD time history including broaching for this technique and provide reasonable agreement in broaching probability with free-running model experiment in irregular astern waves.

Keywords: *broaching, CFD, system identification,*

1. INTRODUCTION

Broaching is well known as a dangerous phenomenon when a ship navigates in oblique waves with high speed and accurate prediction of broaching occurrence is an issue for safe operation. However, estimation of wave force in oblique waves shows discrepancy between numerical simulations based on a slender theory and experiments. Meanwhile, with remarkable developments of computer technology, computational fluid dynamics (CFD) has become a practical tool for naval architecture. CFD can provide us wave force data during its free-running test. Therefore, CFD free-running test is conducted in this study, and wave forces obtained from CFD was compared with experimental results. Then, modification for mathematical model by using system identification was conducted. At the same time, time history of modified system based model for estimation of broaching in regular waves is compared with original model. Finally, modified system based on the model evaluates the probability of occurrence of broaching by applying theoretical estimation method (Umeda et al. 2016) using deterministic ship dynamics and stochastic wave theory.

2. CFD SIMULATION

2.1 CFDSHIP-IOWA v4.5

The code CFDSHIP-IOWA v4.5 (Carrica, 2010) is used for the CFD computations. The CFDSHIP-IOWA is an overset, block structured CFD solver. Turbulence models include blended k-ε/k-ω based RANS, and DES approaches with near wall or wall functions. A single-phase level-set method is used for free-surface capturing. Captive, semi-captive, and full 6DoF capabilities for multi-objects with parent/child hierarchy are

available. Body force propeller is employed for this calculation. Rudder and propeller are defined as child and controlled by PID values. For simulation, ONR-flare topside vessel was used. The used grids are shown in Table 1 and Figs. 1-4. By using this grid, it was confirmed that the calm-water resistance and the extinction curve of this vessel can be accurately predicted as shown in Figs. 5-6, respectively.

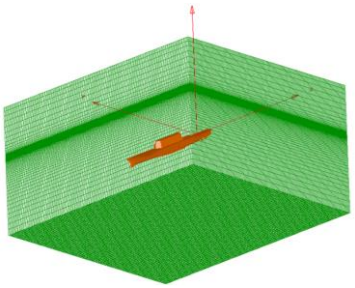

Fig 1 Snapshot of Ship hull and background grids.

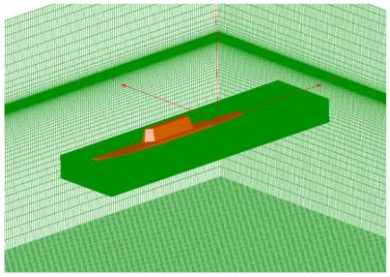

Fig.2 Refinement grid around ship hull

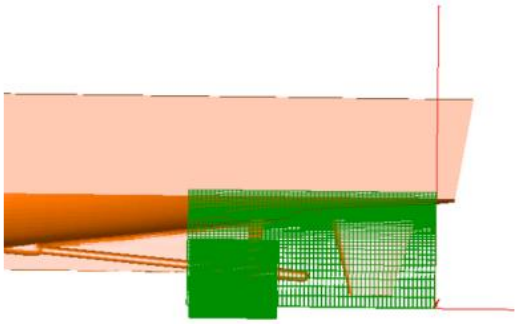

Fig.3 Refinement mesh around propeller shafts and rudders

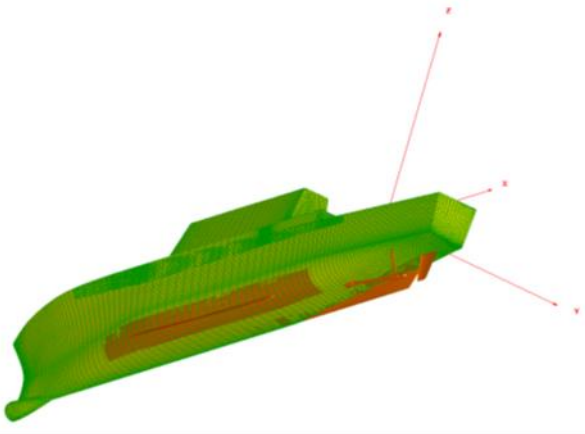

Fig.4 Snapshot of all ship's appendages.

2.2 CFD free-running simulation in regular waves

CFD free-running simulation in regular waves is conducted and the CFD result is compared with experiment (EFD) by Umeda et al. (2016) as shown in Fig. 7. 6DoF Initial condition is obtained from EFD data as a reference and the transient part is finally recreated by trial and error. The surge speed, pithing angle and yaw angle agree quantitatively with EFD.

Table 1 Details of all the grids including refinement grids.

ONR-Flare(regular waves)	
Hull-P/S	480256 *2
SS_P/S	355320 *2
Skeg_P/S	119136 *2
BK_P/S	119556 *2
Prop_trus_Pin	117300
Prop_trus_Pout	117300
Prop_trus_Sin	117300
Prop_trus_Sout	117300
ShaftEnd_P/S	111150 *2
Shaft_refine_P/S	503152 *2
Shaft_P/S	112258 *2
BossCap_P/S	120000 *2
Rudder_ref_P/S	155382 *2
Rudder_Pin	120048
Rudder_Pout	120048
Rudder_Sin	120048
Rudder_Sout	120048
BG	3620487
HullRefinement	4004154
Total	12.72645 M

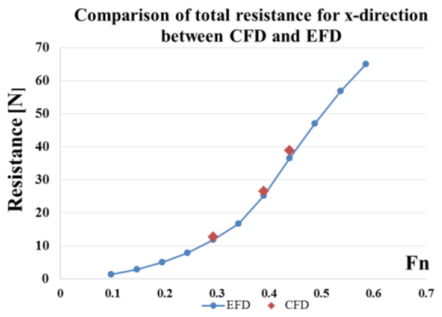

Fig.5 Comparison of total calm-water resistance between CFD and EFD

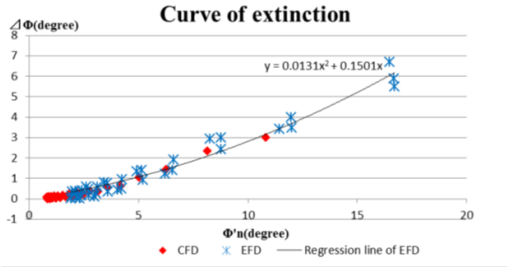

Fig.6 Comparison of curve of extinctions between CFD and EFD

3. SYSTEM IDENTIFICATION

System identification (SI) is used with the system based a mathematical model from CFD trials to obtain wave forces as shown in Equations (1-13). Wave force is obtained by subtracting CFD forces under free-running in calm water from those in waves. Herein constrained least square system identification techniques are used (Araki et al., 2013). The fitting of the wave forces are shown in Fig. 8.
It is noteworthy here that the wave forces and moments are functions of not only incident wave but also sway velocity and yaw angular velocity. This means that the current modelling takes the wave effects on manoeuvring coefficients into account, while Umeda et al. (2016) ignored them as higher order terms.

$$Optimize: y(x_i) = \min\left[\sum_{t=0}^{t}\left\{X_{outi} - Xesti(x_i)\right\}^2\right] \qquad i = 1...4 \tag{1}$$

$$X_{out1} = X_{w-CFD} \tag{2}$$

$$X_{out2} = Y_{w-CFD} \tag{3}$$

$$X_{out3} = N_{w-CFD} \tag{4}$$

$$X_{out4} = K_{w-CFD} \tag{5}$$

$$\begin{aligned} X_{est1}(x_1) &= a_1 X_w{}^{FK} \sin(k\xi_G + \varepsilon_{a1}) \\ &+ k\zeta_w(a_2 \sin(k\xi_G + \varepsilon_{a2}) \cdot X_{vv} \cdot v^2 + a_3 \sin(k\xi_G + \varepsilon_{a3}) \cdot X_{rr} \cdot r^2 + a_4 \sin(k\xi_G + \varepsilon_{a4}) \cdot X_{vr} \cdot vr) \end{aligned} \tag{6}$$

$$\begin{aligned} X_{est2}(x_2) &= b_1 Yw^{FK} \sin(k\xi_G + \varepsilon_{b1}) + b_2 Y^{Diff} \sin(k\xi_G + \varepsilon_{b2}) \\ &+ k\zeta_w(b_3 \sin(k\xi_G + \varepsilon_{b3}) \cdot Y_v \cdot v + b_4 \sin(k\xi_G + \varepsilon_{b4}) \cdot Y_r \cdot r) \end{aligned} \tag{7}$$

$$\begin{aligned} X_{est3}(x_3) &= d_1 Nw^{FK} \sin(k\xi_G + \varepsilon_{d1}) + d_2 N_w{}^{Diff} \sin(k\xi_G + \varepsilon_{d2}) \\ &+ k\zeta_w(d_3 \sin(k\xi_G + \varepsilon_{d3}) \cdot N_v \cdot v + d_4 \sin(k\xi_G + \varepsilon_{d4}) \cdot N_r \cdot r) \end{aligned} \tag{8}$$

$$\begin{aligned} X_{est4}(x_4) &= c_1 Kw^{FK} \sin(k\xi_G + \varepsilon_{c1}) + c_2 K_w{}^{Diff} \sin(k\xi_G + \varepsilon_{c2}) \\ &+ k\zeta_w(c_3 \sin(k\xi_G + \varepsilon_{c3}) \cdot K_v \cdot v + c_4 \sin(k\xi_G + \varepsilon_{c4}) \cdot K_r \cdot r) + OG \cdot Y_w \end{aligned} \tag{9}$$

$$x_1 = \begin{bmatrix} a_1 & a_2 & a_3 & a_4 & \varepsilon_{a1} & \varepsilon_{a2} & \varepsilon_{a3} & \varepsilon_{a4} \end{bmatrix}^T \tag{10}$$

$$x_2 = \begin{bmatrix} b_1 & b_2 & b_3 & b_4 & \varepsilon_{b1} & \varepsilon_{b2} & \varepsilon_{b3} & \varepsilon_{b4} \end{bmatrix}^T \tag{11}$$

$$x_3 = [c_1 \quad c_2 \quad c_3 \quad c_4 \quad \varepsilon_{c1} \quad \varepsilon_{c2} \quad \varepsilon_{c3} \quad \varepsilon_{c4}]^T \tag{12}$$

$$x_4 = [d_1 \quad d_2 \quad d_3 \quad d_4 \quad \varepsilon_{d1} \quad \varepsilon_{d2} \quad \varepsilon_{d3} \quad \varepsilon_{d4}]^T \tag{13}$$

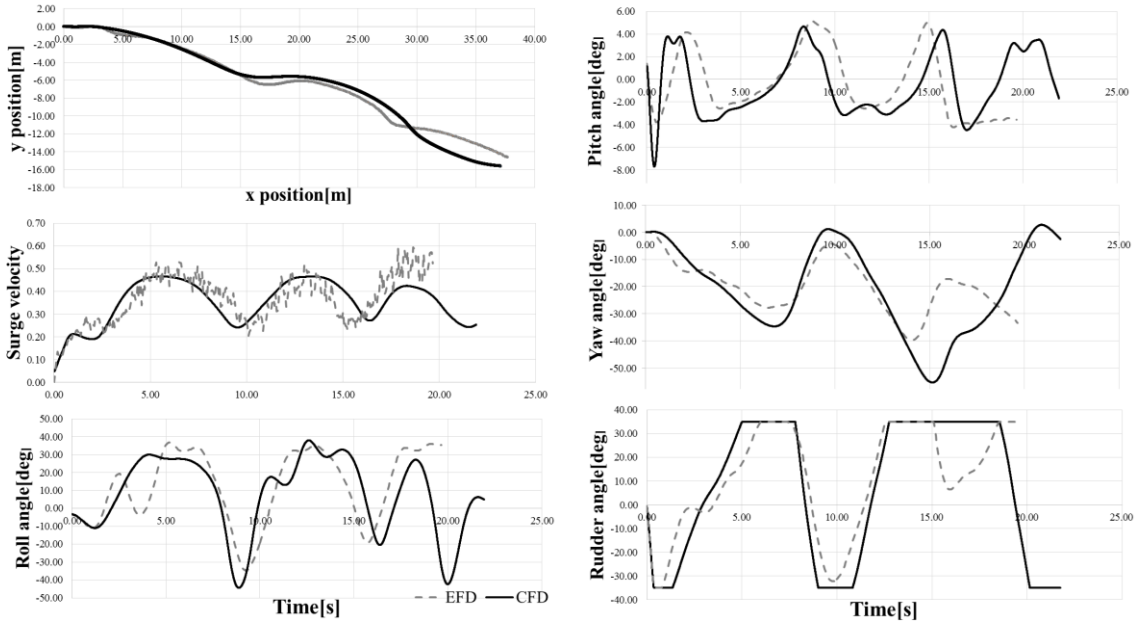

Fig.7 Comparison of motions between CFD and EFD *(Fn*=0.41, *H/λ*=0.05*λ/L*=1.25 *χc=-15 degrees, Kp=3.0, GM=0.768m at model scale).*

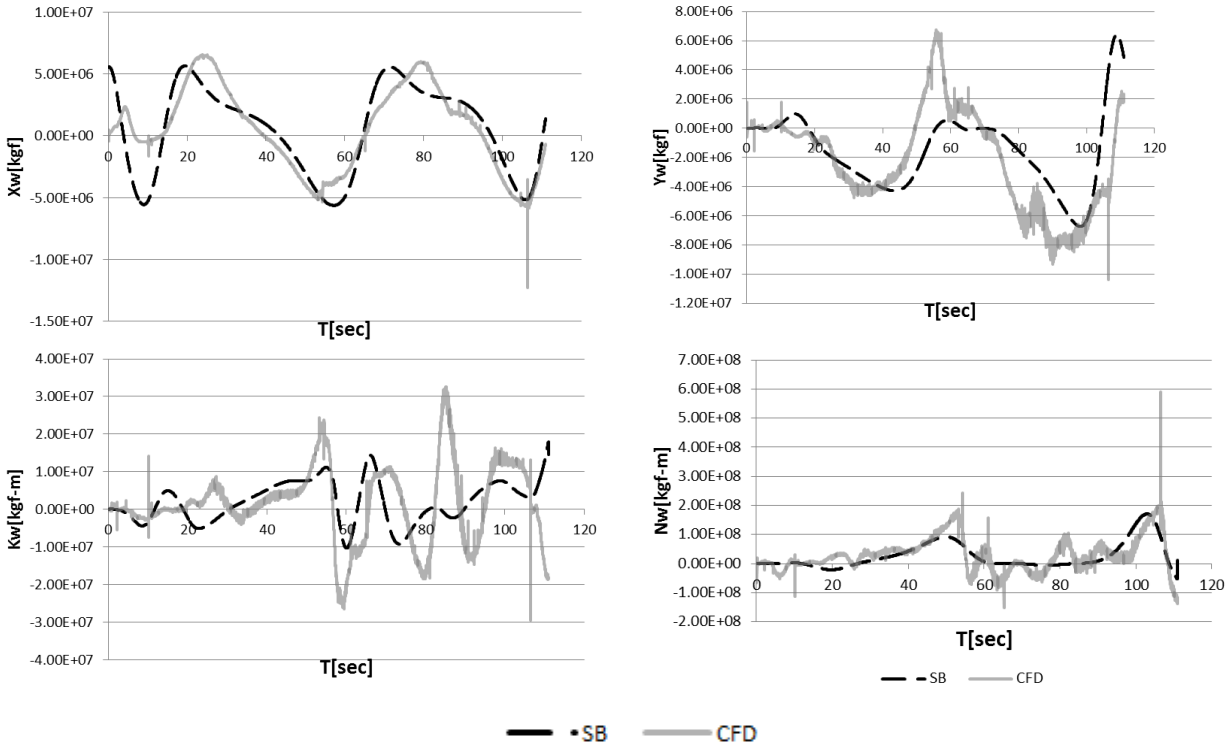

Fig.8 Comparison of wave force between CFD and modified system based model.

Table3.3 Details of parameters for tuning wave induced forces.

a_1	1. 00000	b_1	1.00000	c_1	1.00000	d_1	1.00000
ε_{a1}	−6. 29400	ε_{b1}	1.91241	ε_{c1}	4.20971	ε_{d1}	-3.14000
a_2	3. 00000	b_2	0.13194	c_2	23.34624	d_2	1.38454
ε_{a2}	5. 08820	ε_{b2}	-0.13751	ε_{c2}	0.49627	ε_{d2}	-3.11060
a_3	3. 00000	b_3	0.10000	c_3	35.40626	d_3	10.00000
ε_{a3}	−4. 78288	ε_{b3}	1.88012	ε_{c3}	-2.76155	ε_{d3}	0.46771
a_4	3. 00000	b_4	0.10000	c_4	0.71099	d_4	0.79467
ε_{a4}	−1. 06424	ε_{b4}	-1.27629	ε_{c4}	-2.55445	ε_{d4}	3.84860

4. APPLICATION FOR SYSTEM-BASED MATHEMATICAL MODEL

4.1 Time domain simulation

Time domain simulation program (TDS) with modified system based model is used for predicting the time history. Fig. 9 shows the comparison of the time history between modified-TDS and EFD. From this figure, it is observed that the modified model result reasonably well agrees with the experimental result. Both the TDS and EFD shows that yaw angular velocity increases despite the application of the maximum opposite rudder deflection. This can be regarded as a typical broaching.

4.2 Stochastic evaluation of broaching occurrence

The numerical results from the theoretical method were compared with free-running model experiments in irregular stern quartering waves (Umeda et al., 2016) as shown in Fig.10. The modified estimation of broaching probability when the ship meets a zero-crossing wave is closer to experimental result than original estimation method. Here, H_S: the significant wave height, T_{01}: the mead wave period.

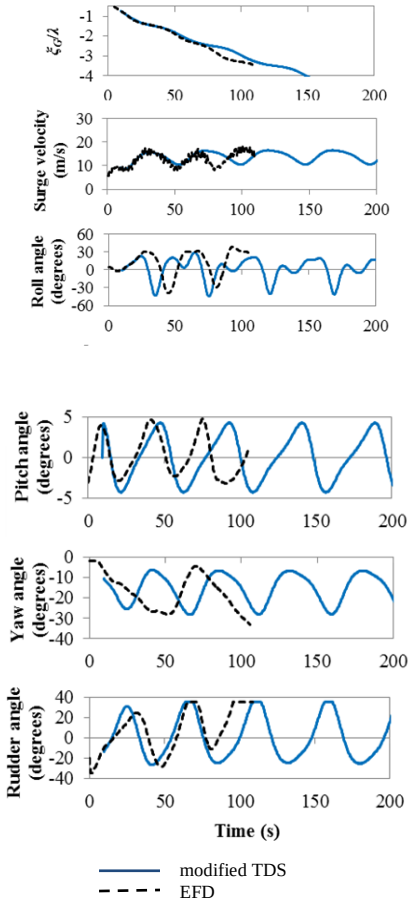

Fig.9 Comparison of time history (λ/L=1.25, H/λ=0.05, Fn=0.39, Kp=3.0, χ_C=-15 degrees at full scale)

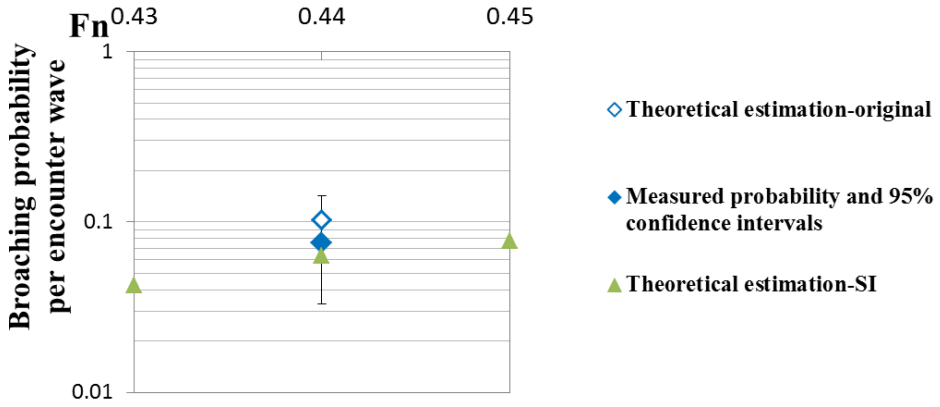

Fig.10 Comparison of the broaching probability(H_s=9.64m, T_{01}=11.1s, Fn=0.44, χ_C=15degrees, K_P=3.0 at full scale

5. CONCLUSIONS

By using CFD, a broaching phenomenon observed in EFD was well predicted. By applying SI to wave forces from CFD, the present simulation model was improved. Moreover, broaching probability estimation in stationary irregular waves is also improved by the wave force modification.

6. ACKNOWLEDGEMENTS

This work was supported by the US Office of Naval Research Global grant No. N62909-13-1-N257 under the administration of Dr. Woei-Min Lin and a Grant-in Aid for Scientific Research from the Japan Society for Promotion of Science (JSPS KAKENHI Grant Number 15H02327). The authors thanks Messrs. Shota Yoneda, Tomoyuki Ohmura and Yuki Banno for their help on CFD runs.

7. REFERENCES

Araki, M., Sadat-Hosseini, H., Sanada, Y., Umeda, N., and Stern, F., 2013, System Identification using CFD Captive and Free Running Tests in Severe Stern Waves, Proceedings of the 13th International Ship Stability Workshop, Brest, pp. 165-177.

Carrica, P M, Castro, A M, Stern, F, 2010, Self-propulsion computations using a speed controller and a discretized propeller with dynamic overset grids, Journal of Marine Science and Technology, 15 (4), 316-330.

Umeda N, Usada S, Mizumoto K., and Matsuda A, 2016, Broaching probability for a ship in irregular stern-quartering waves: theoretical prediction and experimental validation. Journal of Marine Science and Technology, 21 (1), 23-37.

Nomenclature

F_n	Nominal Froude number
GM	Metacentric height
H	Wave height
H_S	Significant wave height
k	Wave number
K_r	Derivative of roll moment with respect to yaw rate
K_P	Rudder gain
K_v	Derivative of roll moment with respect to sway velocity
K_W	Wave-induced roll moment
$K_{W\text{-}CFD}$	Wave-induced roll moment estimated by CFD
K_W^{Diff}	Wave-induced diffraction roll moment
K_W^{FK}	Wave-induced Froude-Krylov roll moment
L	Ship length between perpendiculars
N_r	Derivative of yaw moment with respect to yaw rate
N_v	Derivative of yaw moment with respect to sway velocity
N_W	Wave-induced yaw moment
$N_{W\text{-}CFD}$	Wave-induced yaw moment estimated by CFD
N_W^{Diff}	Wave-induced diffraction yaw moment
N_W^{FK}	Wave-induced Froude-Krylov yaw moment
OG	Height of gravitational centre of ship above calm water plane
t	Time
T_{01}	Mean wave period
v	Sway velocity
X_{rr}	Derivative of surge force with respect to the square of yaw angular velocity
X_{vr}	Derivative of surge force with respect to the product of sway velocity and yaw angular velocities
X_{vv}	Derivative of surge force with respect to the square of sway velocity
X_W	Wave-induced surge force
$X_{W\text{-}CFD}$	Wave-induced surge force estimated by CFD
X_W^{FK}	Wave-induced Froude-Krylov surge force
Y_r	Derivative of sway force with respect to yaw rate
Y_v	Derivative of sway force with respect to sway velocity
Y_W	Wave-induced sway force
$Y_{W\text{-}CFD}$	Wave-induced sway force estimated by CFD
Y_W^{Diff}	Wave-induced diffraction sway force
Y_W^{FK}	Wave-induced Froude-Krylov sway force
ξ_G	Horizontal position of ship gravitational centre from a wave trough
ζ_w	Wave amplitude
λ	Wavelength
χ_C	Desired heading angle from wave direction

CFD prediction of wave-induced forces on ships running in irregular stern quartering seas

Hirotada Hashimoto, *Kobe University*, hashimoto@port.kobe-u.ac.jp

Shota Yoneda, *Kobe University*

Tomoyuki Omura, *Kobe University*

Naoya Umeda, *Osaka University*, umeda@naoe.eng.osaka-u.ac.jp

Akihiko Matsuda, *National Research Institute of Fisheries Engineering*, amatsuda@fra.affrc.go.jp

Frederick Stern, *The University of Iowa*, frstern@iowa.uiowa.edu

Yusuke Tahara, *National Maritime Research Institute*, tahara@nmri.go.jp

ABSTRACT

Surf-riding/broaching is one of the great threats to high-speed ships running in stern quartering seas. Theoretical methods are still in qualitative level for the prediction of wave-induced forces on ships in surf-riding and broaching situations. Therefore an URaNS CFD solver is applied to predict the wave-induced forces on ships in irregular stern quartering seas. To validate the CFD method, a model experiment was conducted and the wave-induced forces were measured to be direct compared with CFD prediction using the same irregular waves encountered. As a result, the CFD results show good agreement with EFD except for the wave-induced roll moment.

Keywords: *Stern quartering seas, Irregular seas, Wave-induced force, CFD, EFD, Broaching/surf-riding*

1. INTRODUCTION

Numerical prediction of wave-induced forces acting on a slender ship running in stern quartering seas is an important issue to realize the quantitative prediction of surf-riding/broaching phenomenon. The surf-riding/broaching is one of the five stability failure modes in the second generation intact stability criteria (SGISC) discussed at the International Maritime Organization (IMO). Theoretical methods, like the slender body theory or similar, are practically useful because their calculation cost is quite low. However, the accuracy has not reached to the quantitative level until now [Hashimoto, et al., 2011][Umeda et al., 2016]. It is obvious that the prediction accuracy of surf-riding/broaching strongly depends on the prediction accuracy of wave-induced forces. Therefore the inaccurate prediction could lead to the misjudgement of occurrence of surf-riding and broaching. In order to realize the quantitative prediction of wave-induced forces in following and stern quartering seas, an unsteady Reynolds-averaged Navier–Stokes (URaNS) solver has been applied to the problem of regular seas as one of the most advanced measures and it was demonstrated that the computational fluid dynamics (CFD) simulation showed promising results [Hashimoto et al., 2016][Yoneda et al., 2016].

In this study, we use the same URaNS CFD solver for the prediction of wave-induced forces in irregular stern quartering seas, which

is most relevant environment for the safety assessment of surf-riding/broaching. The computational domain is discretized using multi-block structured grids with the method for treatment of overset grids. In order to generate the same irregular waves encountered in experimental fluid dynamics (EFD), the measured irregular wave is decomposed to a finite number of elementary waves using the fast Fourier transform (FFT) analysis. Then the determined amplitude and phase of the elementary waves are used as the input for the wave boundary condition of the CFD solver to reproduce the same irregular wave profile.

Then the CFD simulation is performed and is validated deterministically through comparisons with a semi-captive towing test in irregular seas for a high-speed slender ship known as ONR tumblehome. For the reproduction of irregular waves, finer grids are necessary to keep the wave profile, in terms of numerical dissipation, compared to cases in regular seas. As a result of validation studies, URaNS CFD simulations show good agreement with the EFD results in the prediction of wave-induced hydrodynamic forces as well as ship vertical motions in irregular stern quartering seas.

Because it is a strong demand to reduce the computational cost/time from a practical view point, grid coarsening is attempted and its influence on the prediction accuracy is discussed. Lastly similar CFD prediction of wave induced-force in irregular seas is performed for ONR-flare that has the almost same under-water hull form with ONR-tumblehome but has the significantly different above-water hull form. By comparing the CFD result with the EFD one, it is demonstrated the URaNS CFD solver can capture the influence of above-water hull form on the wave-induced force.

These results well demonstrate the possibility to replace the time- and cost-consuming semi-captive model experiments by CFD simulation.

2. EFD MEHTOD

2.1 Subject ship

The subject ship is the ONR-tumblehome known as a high-speed slender vessel with a wave-piercing bow. It is know that high-speed slender ships are prone to suffer surf-riding and broaching due to the small hull resistance. This face was demonstrated by a free-running model experiment in regular stern quartering seas [Umeda et al., 2008] and in irregular stern quartering seas [Umeda et al., 2016], and by CFD in regular stern quartering seas [Carrica, et al., 2008].

Table 1 Principal particulars of subject ship

	Actual	Scaled
Waterline length (m)	154.0	3.147
Breadth (m)	18.8	0.384
Draught (m)	5.5	0.112
Mass (kg)		73.0
Appendage: skeg, bilge keels, rudders, shaft brackets		

2.2 EFD setup

A model experiment was conducted at the Marine Dynamic Basin of National Research Institute of Fisheries Engineering (NRIFE) (see Fig.1). In the model experiment, all appendages except for twin propellers and their shafts were attached to keep the experimental condition to be similar to actual one because the exclusion of appendages results in the slight overestimation of wave-induced hydrodynamic forces [Yoneda et al., 2016].

The ship model was attached to a towing sub carriage through a heaving rod. A load cell to measure hydrodynamic forces is attached between the ship model and the heaving rod as shown in Figs.2-3. Then the ship model was towed in oblique direction by the combination of main and sub towing carriages. Here the ship model was free in heave and pitch. For the purpose of direct comparison of wave-induced

hydrodynamic forces in irregular waves, the encountered irregular waves in the experiment need to be reproduced in CFD simulation. For the confirmation of the accuracy of wave reproduction, two wave probes were attached to the sub carriage as shown in Fig.4. Here the longitudinal positions of two wave probes are midship and bow and their transversal positions are the end of sub carriage to be outside of ship-generated waves.

Fig.1 Model basin

Fig.2 Ship model

Fig.3 Towing rod and measurement system

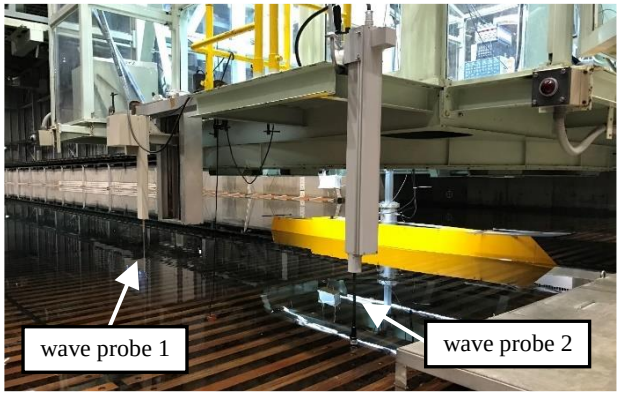

Fig.4 Wave probes at midship and bow

2.3 FED procedure

Prior to the oblique towing test in irregular waves, wave measurement without the ship model was executed. In this measurement, time history of wave elevation at the position of two wave probes was measured for 10 minutes from the timing when all the elementary waves reached to the measurement point. The input wave condition is shown in Table 2. Here the mean wave period was selected to be similar with a free-running model test in past [Umeda et al., 2016]. The ITTC wave spectrum from 0.3 Hz to 3.0 Hz was used to generate elementary waves in the experiment. The measured wave elevation at the midship position is shown in Fig.6.

Table 2 Wave condition

Significant wave height: $H_{1/3}$	0.1 m
Mean wave period: T_1	1.6 s

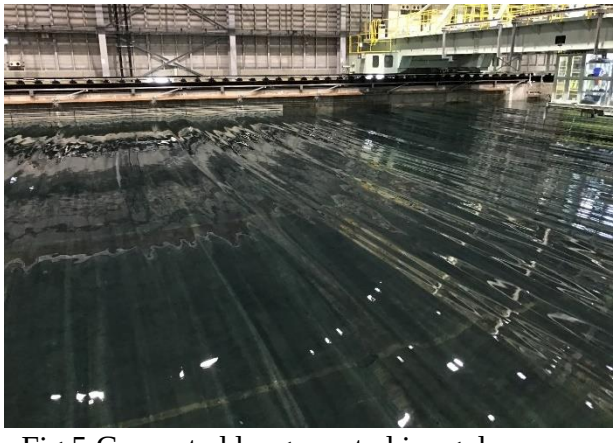

Fig.5 Generated long-crested irregular waves

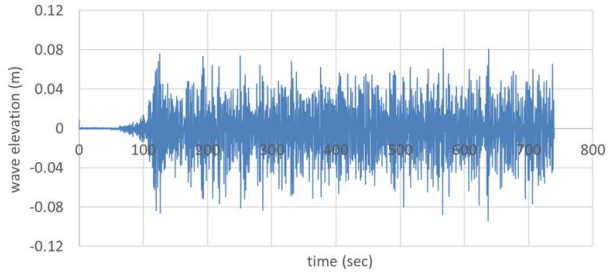

Fig.6 Measured wave elevation at a fixed point without ship model

The oblique towing test in long-crested irregular waves was conducted. The towing condition is shown in Table 3. Here the Froude number is calculated using the water plane length as the representative length. The coordinate system used in the analyses in the following sections can be found in Fig.9 appeared later. In the experiment, the ship model was running in irregular stern quartering seas as shown in Fig.7. During the towing test, the wave-induced surge force, sway force, roll moment and yaw moment were measured by a load cell on a gimbal, and the heave and pitch motions were measured by potentiometers. In addition, the wave elevation at two positions, i.e. midship and bow, was also measured by wave probes.

Table 3 Towing condition

Towing speed: U	1.667 m/s
Froude number: Fn	0.3
Encounter angle: χ	-30 deg

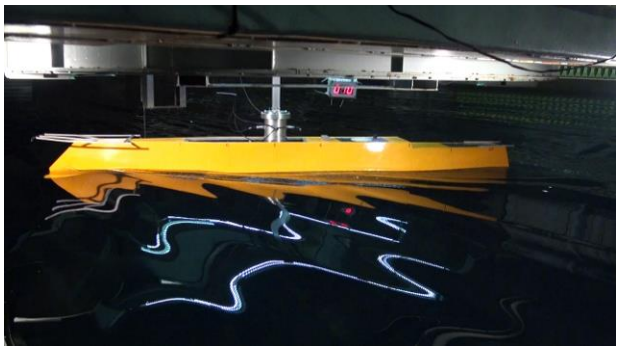

Fig.7 Oblique towing test in long-crested irregular waves

3. CFD METHOD

3.1 URaNS solver and grids

For the accurate prediction of wave-induced forces, CFD approach solving the Navier-Stokes equation computationally is most straightforward nowadays. An URaNS solver of CFDShip-Iowa V4.5 [Huang et al., 2008] developed by IIHR of The University of Iowa is used for CFD simulations. The latest applications of CFDShip-Iowa to ship hydrodynamics can be found in a literature [Stern et al., 2015]. CFDShip-Iowa is a block structured overset CFD solver designed for the applications to naval architecture and ocean engineering problems using either absolute or relative inertial non-orthogonal curvilinear coordinate system for arbitrarily moving control volumes. Turbulence models include bended k-ε/k-ω based isotropic and anisotropic RaNS, and DES approaches with near-wall or wall functions. A single-phase level-set method is used for capturing complex free-surface. The SUGGAR [Noack, 2007] is used to obtain the overset interpolation information. It was already confirmed that the prediction of wave-induced surge force using CFDShip-Iowa shows quantitative agreement with EFD in regular following and stern quartering seas [Hashimoto et al., 2016].

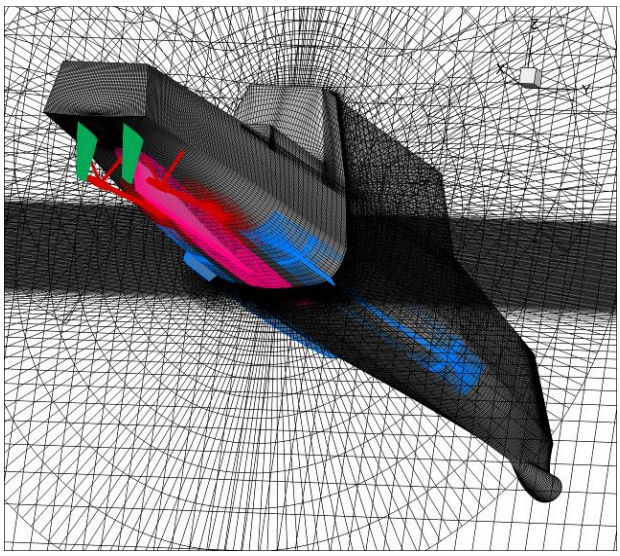

Fig.8 Grids around the hull

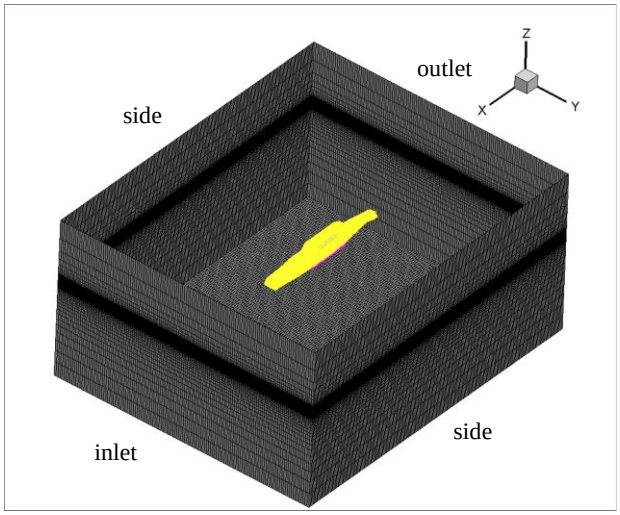

Fig.9 Overview of grids

Table 4 Number of grids

Hull	Refinement	Background
9.13 M	4.42 M	7.18 M
Total 20.73 M		

Table 5 CFD condition (model scale)

Reynolds number	6.995E+6
Time step	0.00354 s
Level set solver	Liner
Turbulence model	Blended k-ε/k-ω
Pressure solver	Projection
6DOF integration	Explicit first order with 8-point smoothing

The grid design for the CFD computation is shown in Figs.8-9 and the coordinate system used in this study can be found in Fig.9. The number of grid points is shown in Table 4. In order to obtain a comparable CFD result with EFD one, all the appendages in the experiment, i.e. skeg, bilge keels, rudders and shaft brackets, are included in the CFD grids. To enhance the connectivity between the moving grids and the background grids, several refinement grids are additionally introduced. The quality of the grid was verified for a calm water resistance problem [Furukawa et al., 2012]. Here it should be noted that relatively short elementary waves disappear easily if sufficiently dense background grids are not used. The condition set for CFD computation are presented in Table 5. These conditions were used as in past for the prediction of wave-induced forces [Hashimoto et al., 2016][Yoneda et al., 2016].

3.2 Irregular wave generation

For the generation of irregular waves in CFD, the measured irregular waves are decomposed to a finite number of elementary waves under the hypothesis of linear wave superposition. Therefore frequency components of measured wave data shown in Fig.6 are analysed by the Fast Fourier Transform (FFT). The FFT result of the amplitude and phase with respect to angular frequency is shown in Fig.10. Then wave frequencies, wave numbers, wave amplitudes, wave phase of 1000 elementary waves are prepared as input files for the wave boundary condition in CFD. Here the ship is running in stern quartering seas, where the ship is generally overtaken by wave at the tested Froude number, so the inversed time is used for the FFT analysis of the wave phase. An example of snap shot of the simulated wave-pattern around the ship is shown in Fig.11.

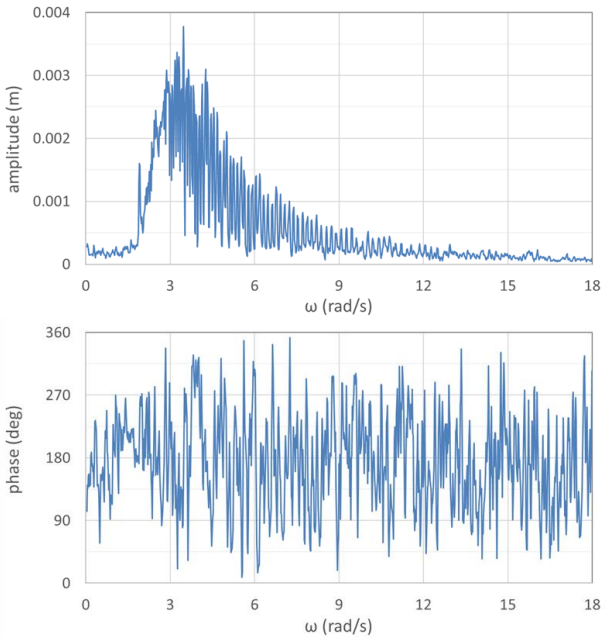

Fig.10 FFT analysis of measured wave data

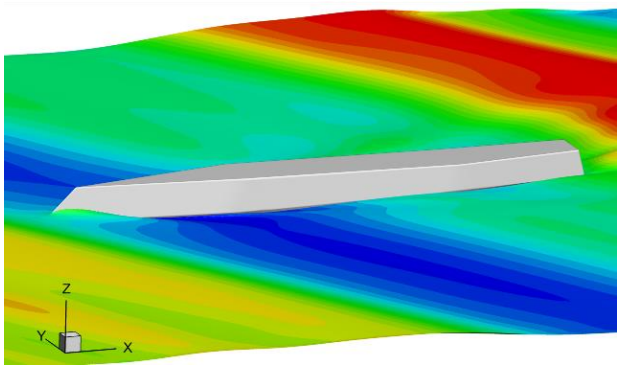

Fig.11 CFD result of wave pattern in irregular stern quartering seas

4. RESULTS AND DISCUSSION

4.1 Irregular wave elevation

Firstly, the accuracy of reproduced encountering irregular waves is investigated. The comparison of the water elevation at the position of wave probe 1 between EFD and CFD is shown in Fig.12. Here the speed of the towing carriage became constant from 128 seconds till 140 seconds. Before and after this range, the towing carriage is accelerated or decelerated. For the constant speed range, the irregular wave surface can be well reproduced by CFD for relatively long waves which are dominant components for the wave-induced forces in stern quartering seas.

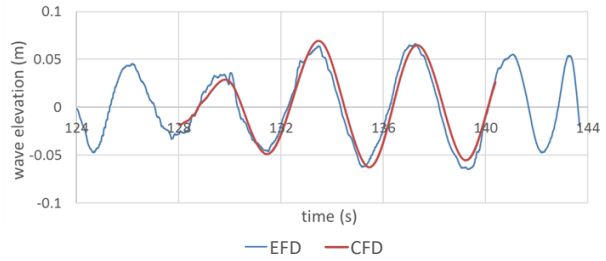

Fig.12 Comparison of wave elevation at midship position

4.2 Heave and pitch

Secondly, the prediction accuracy of ship motions in irregular stern quartering seas is investigated. The comparison of the heave and pitch motions is shown in Fig.13. Good agreement between EFD and CFD can be found for ship vertical motions as well as the irregular wave elevation. There is a certain unstable behaviour at the beginning of CFD result. This is natural tendency of CFD, which does not start from the state of rest, because the flow field and ship attitude do not correspond to those of EFD for the first several time steps.

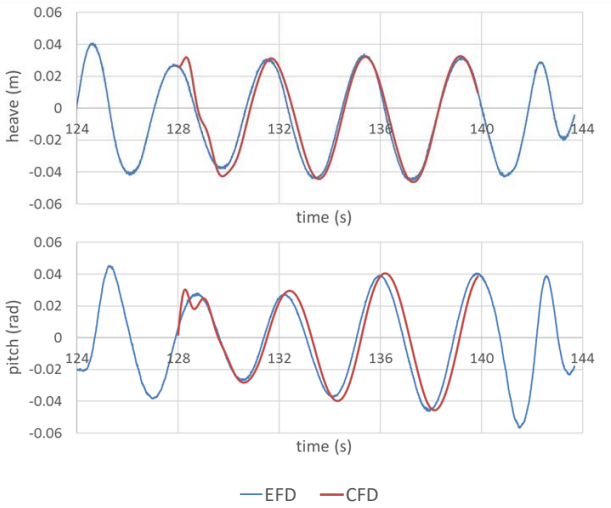

Fig.13 Comparison of heave and pitch

4.3 Wave-induced Force

Lastly, the prediction accuracy of wave-induced forces on the subject ship running in irregular stern quartering seas is investigated. The comparison of the surge force, sway force, roll moment and yaw moment is shown in Fig.14. Here the centre of roll moment is assumed to be two times higher than the draught, and then the measured and calculated roll moments were converted from the original heights of each measurement centre. The centre of yaw moment is assumed to be midship. The surge force includes the calm water resistance component both in EFD and CFD, so the mean value of the variation is not zero. Nevertheless the agreement in surge is quite good, so the both of wave component and calm water resistance component are well predicted by CFD. The sway force and the yaw moment are also predicted with sufficient accuracy. The irregularity of yaw moment is most prominent

than others and this trend can be also well captured by CFD. The agreement in the roll moment is worse than other modes. This is possibly because the magnitude of the roll moment is much smaller than the yaw moment so that more accuracy is required for CFD for roll mode.

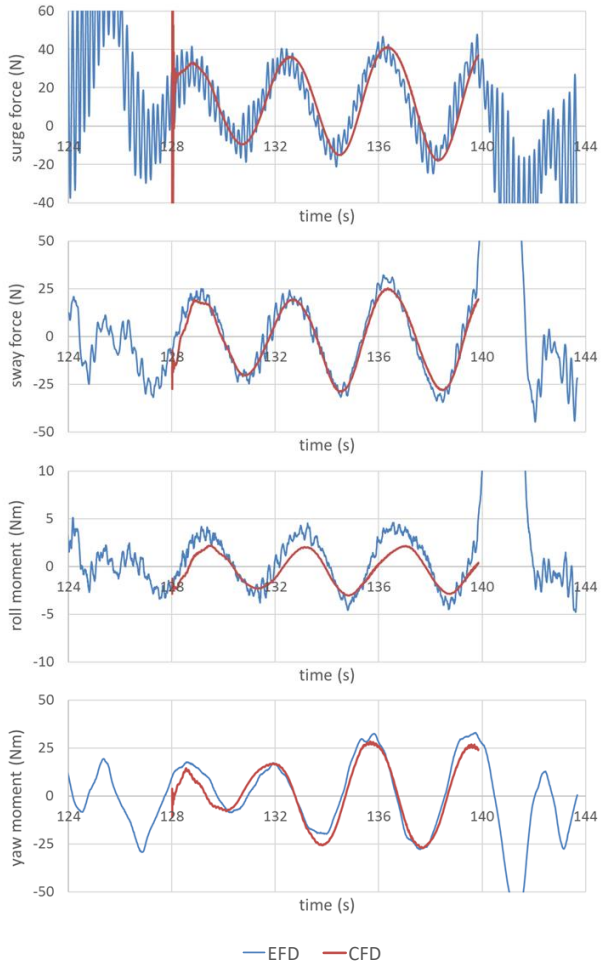

Fig.14 Comparison of wave-induced forces and moments

5. FURTHER DISCUSSION

5.1 Grid coarsening

It was well demonstrated the URaNS CFD simulation can well predict the wave-induced forces on ships running in irregular stern quartering seas, in general. However larger number of grid points and longer computation time are required for irregular seas compared to regular seas. Therefore, the grid coarsening is attempted to reveal the required spatial resolution to capture the wave-induced forces in irregular stern quartering seas. The coarsened grids are shown in Fig.15 and the number of grid points is presented in Table.6. The CFD conditions are same as the dense grids case. Here, the shaft brackets are intentionally removed for the sake of simplicity. The background grids are also coarsened but not so much, to keep the accuracy of irregular wave reproduction and propagation as appropriate.

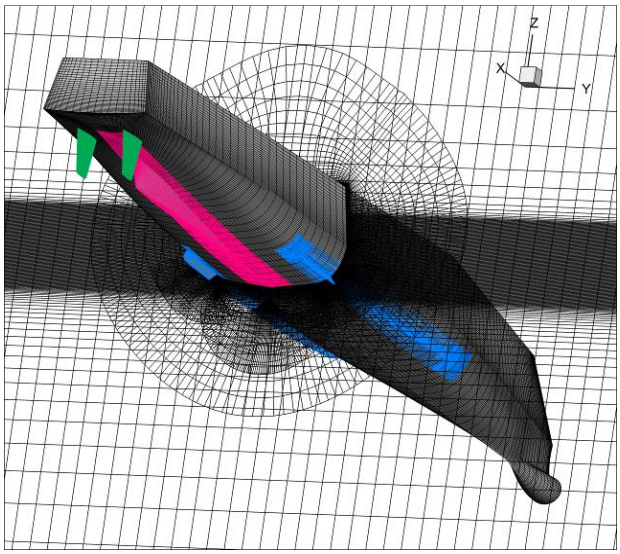

Fig.15 Coarsened grid

Table 6 Number of grids

Hull	Refinement	Background
3.00 M	0.60 M	5.05 M
Total 8.65 M		

The comparison of CFD results using the dense and coarsened grids are shown in Fig.16 together with the EFD result. There is small difference in sway and yaw around the third positive peak between the dense and coarse grids. However in general, the difference between two results seems to be negligibly small so that the coarsened grid tested here can be practically acceptable for several discussions in the following.

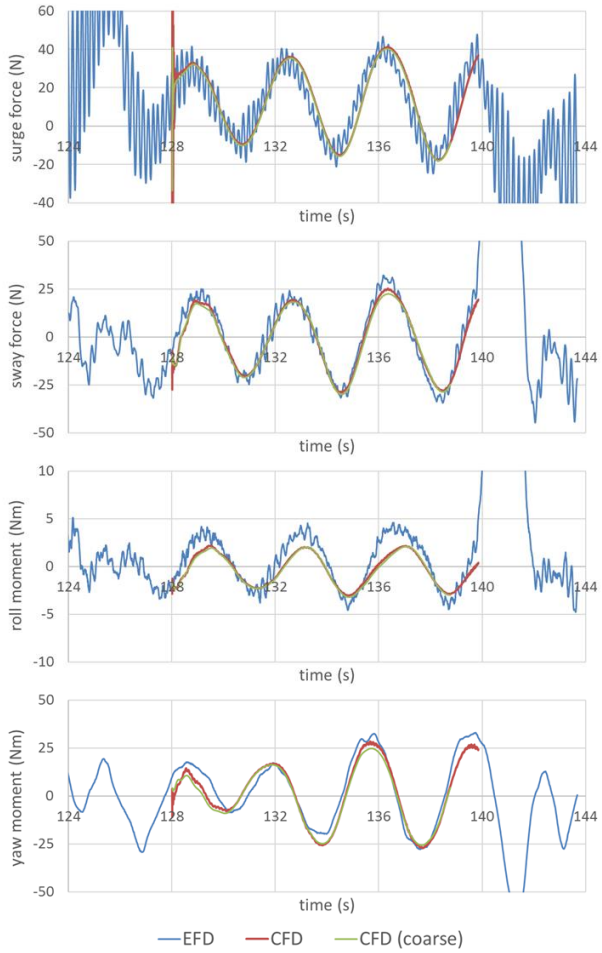

Fig.16 Wave-induced forces using coarsened grids

5.2 ONR-flare

To collect more examples of CFD prediction of wave-induced forces in irregular stern quartering seas, the similar validation study is executed for the ONR-flare, which has the almost same under-water hull with the ONR-tumblehome but its topside has outward inclination while the ONR-tumblehome has inward inclination. Fig.17 shows the ship model used for EFD analysis. For the direct comparison between the ONR-tumblehome and the ONR-flare, the random seed for the wave phases in the experiment was not changed so that the same irregular waves can be generated. Also the same start timing, the same towing speed and the same heading angle were used as the ONR-tumblehome.

Fig.17 ONR-flare ship model

The grid design for the ONR-flare is shown in Fig.18 and the number of grid points is presented in Table.7. Here the shaft brackets are neglected as same as in section 5.1. It should be noted that the completely same background grids are used with the CFD for the ONR-tumblehome so that the incident irregular waves in each CFD runs are the same.

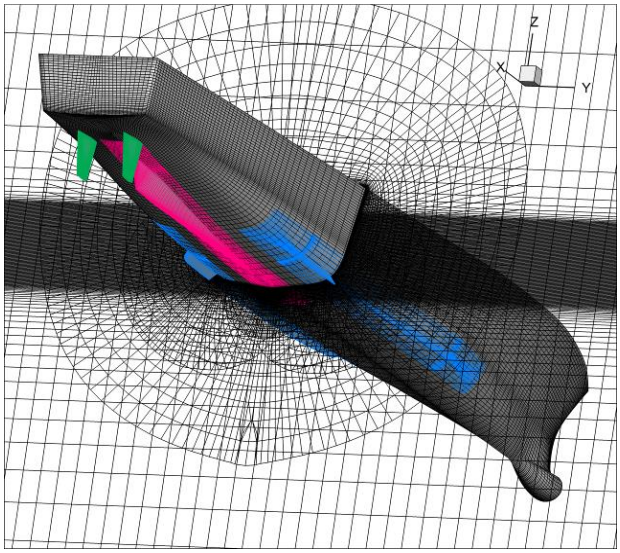

Fig.18 Grids around the hull

Table 7 Number of grids

Hull	Refinement	Background
1.92 M	0.36 M	5.05 M
Total 7.33 M		

The measured and calculated results of wave-induced forces are compared as in Fig.19. The CFD result agrees well in the surge force but does not agree in the roll moment as same as the ONR-tumblehome case. On the other hand, the agreement becomes worse in the

sway force and the yaw moment. This might be because the spatial resolution of the hull, using 1.92 M grid points, is insufficient to obtain the appropriate pressure distribution on the hull. Regarding the inaccuracy of the roll moment, the improving rate with respect to grid points seems to be not so high as presumed from Fig.16. Therefore the required grid points for the quantitative prediction of the wave-induced roll moment could be tremendous. Further grid studies are expected to conclude this discussion.

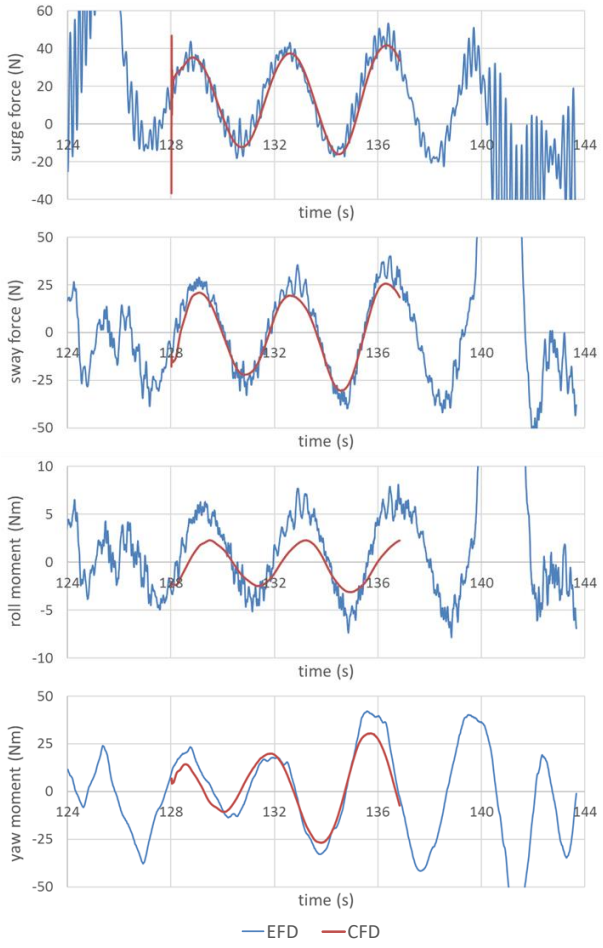

Fig.19 Comparison of wave-induced forces of ONR-flare

5.3 Influence of above-water hull form

The EFD results for the ONR-flare and the ONR-tumblehome are compared. As already mentioned, the major difference between two ships is inclination direction of the topside. Therefore the influence of the topside inclination can be discussed. From Fig.19, it seems that the effect of above-water hull form does not appear in the surge force, while it appears in sway, roll and yaw. More precisely, the amplitudes of sway force, roll and yaw moments of the ONR-flare are larger than those of the ONR-tumblehome. This EFD trend can be captured by the CFD calculation.

Based on all the comparison results in this paper, it could be concluded that URaNS CFD methods have high-possibility to replace conventional captive model experiments in a future for the prediction of wave-induced surge, sway forces and yaw moment. Further investigations are expected for the prediction of wave-induced roll moment.

6. CONCLUSIONS

A captive model experiment was conducted for the ONR-tumblehome in irregular stern quartering seas. To realize the quantitative prediction of wave-induced forces, URaNS CFD simulation is performed using the same condition with the model experiment. The encountered irregular waves are successfully reproduced in the CFD simulation. Then, CFD results of wave-induced force on ships are compared with EFD ones. As the result, it is well demonstrated that the CFD results show fairly good agreement with EFD in irregular stern quartering seas, except for the roll moment. Similar investigation for more severe waves, including wave breaking and over topping phenomena, is expected towards the quantitative assessment of safety of high-speed ships against surf-riding/broaching.

7. ACKNOWLEDMENTS

This work was supported by the US Office of Naval Research Global grant No. N62909-13-1-N257 under the administration of Dr. Woei-Min Lin and JSPS KAKENHI Grant numbers 15H02327, 17H03493. The authors express sincere gratitude to Dr. Hamid Sadat-

Hosseini and Dr. Motoki Araki for their technical advice on CFDShip-Iowa.

8. REFERENCES

Carrica, P.M., Paik, K-J., Hosseini H.S., Stern, F., URANS., 2008, "analysis of a broaching event in irregular quartering seas", Journal of Marine Science and Technology, 13(4), 395-407.

Furukawa, T., Umeda, N., Matsuda, A., Terada, D., Hashimoto, H., Stern, F., Araki, M., Sadat-Hosseini, H., 2012, "Effect of Hull Form above Calm Water Plane on Extreme Ship Motions in Stern Quartering Waves", Proceedings of the 29th Symposium on Naval Hydrodynamics.

Hashimoto, H., Umeda, N., Matsuda, A., 2011, "Broaching prediction of a wave-piercing tumblehome vessel with twin screws and twin rudders", Journal of Marine Science and Technology, 16(4), 448-461.

Hashimoto, H., Yoneda, S., Tahara, Y., Kobayashi, E., 2016, "CFD-based study on the prediction of wave-induced surge force, Ocean Engineering", 120(1), 389-397.

Huang, J., Carrica, P. M. and Stern, F., 2008, "Semi-coupled air/water immersed boundary approach for curvilinear dynamic overset grids with application to ship hydrodynamics", International Journal for Numerical Methods in Fluids, 58(6), 591-624.

Noack, R., 2007, "Enabling Large Amplitude and Relative Motions Through Overlapping Grids", Proceedings of 9th International Conference on Numerical Ship Hydrodynamics.

Stern, F., Wang, Z., Yang, J. et al., 2015, "Recent progress in CFD for naval architecture and ocean engineering", Journal of Hydrodynamics, 27(1), 1-23.

Umeda, N., Yamamura, S., Matsuda, A., Maki, A., Hashimoto, H., 2008, "Model Experiments on Extreme Motions of a Wave-Piercing Tumblehome Vessel in Following and Quartering Waves", Journal of the Japan Society of Naval Architects and Ocean Engineers, 8, 123-129.

Umeda, N., Usada, S., Mizumoto, K., Matsuda, A., 2016, " Broaching probability for a ship in irregular stern-quartering waves: theoretical prediction and experimental validation" , Journal of Marine Science and Technology, 21(1), 23-37.

Yoneda, S., Hashimoto, H., Tahara, Y., Kobayashi, E., Umeda, N., Stern, F., 2016, "CFD-based captive tests for the wave-exciting force acting on a ship running in stern quartering waves", Proceedings of 3rd International Conference on Violent Flows.

Effect of Propeller Thrust Reduction on Ship Surf-riding/Broaching Prediction

Tinghao Wang, *School of Naval Architecture, Ocean and Civil Engineering, Shanghai Jiao Tong University (SJTU),* bruceorpigeon@sjtu.edu.cn

Ning Ma*, *State Key Laboratory of Ocean Engineering, Collaborative Innovation Center for Advanced Ship and Deep-Sea Exploration, SJTU,* ningma@sjtu.edu.cn

Xiechong Gu, *State Key Laboratory of Ocean Engineering, Collaborative Innovation Center for Advanced Ship and Deep-Sea Exploration, SJTU,* xcgu@sjtu.edu.cn

Peiyuan Feng, *Marine Design & Research Institute of China (MARIC),* pyfeng23@163.com

ABSTRACT

To explore the effect of propeller thrust reduction on ship's surf-riding and broaching events, a modified 6-DOF weakly nonlinear unified model considering sea-keeping motion and maneuvering motion is developed. In the modified model, the influence of propeller thrust reduction on surf-riding/broaching prediction is taken into account by incorporating the effect of wave orbital velocity and the propeller submergence depth. By using this modified model, the numerical simulations of a fishing vessel (ITTC ship A2) are performed and comparison study is conducted with the original model. Consequently, it is shown that propeller submergence ratio decreases and propeller thrust drops dramatically when surf-riding happens, and simulation result shows better agreement with published experiment results.

Keywords: *Surf-riding, Broaching, Unified model, Propeller thrust reduction*

1. INTRODUCTION

Surf-riding and broaching is recognized as a major cause for ship stability failure events in adverse longitudinal waves, and such phenomena have been included in the second-generation intact stability criteria by the International Maritime Organization (IMO). Surf-riding happens when ships are overtaken by astern waves and forced to sail with wave celerity. Broaching occurs when ships suffer large wave-induced yaw moment and finally lose course-keeping ability despite maximum steering efforts. Both phenomena usually happen on small fishing vessels sailing with a large Froude number in following and quartering seas.

Since early 1950s, researches on surf-riding and broaching have been conducted theoretically mainly focusing on the surf-riding occurrence by applying uncoupled surge equation (Grim 1951, Ananiev 1966, Makov 1969, Umeda & Kohyama 1990, Maki et al. 2014). To realize precise prediction, numerical simulations (Spyrou 1996, Umeda & Hamamoto 2000, Umeda & Hashimoto 2002, Yu, Ma & Gu 2014) and model experiments (Kan et al. 1990, Umeda et al. 1999, Umeda et al. 2006) were conducted. And as a result, propeller thrust was believed to be a key factor for the occurrence of surf-riding/broaching.

As one of strongly nonlinear phenomena, surf-riding and broaching can be influenced by many factors. In previous research, rudder and propeller emersion were observed in free running model experiments when broaching occurred (Araki et al. 2012), and loss of rudder effectiveness due to emersion were regarded as a key factor for the occurrence of broaching. However, the effect of propeller emersion and propeller hydrodynamics in waves on surf-riding/broaching prediction is rarely discussed. Hashimoto, Umeda and Matsuda (2004) pointed out the wave effect on propeller was not negligible for predicting broaching event in heavy following and quartering waves. But only wave particle velocity was implemented in the mathematical model and thrust reduction was still underestimated in contrast with experiment data. Sadat-Hosseini et al. (2011) used CFD and system-based simulation method to predict surf-riding and broaching event for an ONR tumblehome model with twin propeller/rudder. And emergence of propeller and rudder out of water is presumed to be the cause for the overestimation in roll angle and underestimation in yaw deviation.

During numerical simulation, most propeller model developed before hypothetically assumed propeller thrust same with that in calm water. And their simulation results showed the risk of surf-riding and broaching event were overestimated in different level (Umeda & Hamamoto 2000, Yu, Ma & Gu 2014). Actually, propeller thrust dramatically decrease when propeller is close to the free surface or even emerges from water, and ship's horizontal motion could be significantly influenced.

Therefore, in order to investigate the effect of propeller thrust reduction due to propeller submergence, a modified 6-DOF weakly nonlinear unified model considering sea-keeping motion and maneuvering motion is applied for the simulation of surf-riding and broaching event. And an approximate hydrodynamic model of the propeller is proposed to account for the effect of wave orbital velocity and the propeller submergence depth. Through comparison study with the original propeller model, the propeller thrust reduction due to propeller submergence is presented and its effect on surf-riding and broaching prediction are investigated.

2. MATHEMATICAL MODEL

The model is originated from the 6-DOF weakly nonlinear model developed by Yu, Ma & Gu (2014). And the propeller model is modified to take the effect of propeller submergence into account.

2.1 6-DOF weakly nonlinear unified model

In this model, the maneuvering motion is simulated by using a 3-DOF surge-sway-yaw MMG model:

$$\begin{cases} (m+m_x)\dot{u}-(m+m_y)vr = X_W + X_H + X_\delta + T - R \\ (m+m_y)\dot{v}+(m+m_x)uv = Y_W + Y_H + Y_\delta \\ (I_{zz}+J_{zz})\dot{r} = N_W + N_H + N_\delta \end{cases} \quad (1)$$

where m, m_x, m_y represent the ship mass and added mass in surge and sway, I_{zz} , J_{zz} represent moment of inertia and added moment of inertia in yaw, and X_δ, Y_δ, N_δ are defined as rudder force or moment; R and T are resistance and propeller thrust. X_H, Y_H, N_H are hull hydrodynamic forces as expressed as follows.

$$\begin{cases} X_H = X_{vv}v^2 + X_{vr}vr + X_{rr}r^2 \\ Y_H = -Y_v v - Y_r r - Y_{vvr}v^2 r - Y_{vrr}vr^2 \\ \qquad - Y_{vvv}v^3 - Y_{rrr}r^3 \\ N_H = -N_v v - N_r r - N_{vvr}v^2 r - N_{vrr}vr^2 \\ \qquad - N_{vvv}v^3 - N_{rrr}r^3 \end{cases} \quad (2)$$

In equation (1), X_W, Y_W, N_W represent the wave-induced forces, mainly consist of restoring and F-K forces (F^{res} & F^{FK}), which are calculated nonlinearly by conducting pressure integration on instantaneous wetted

surfaces. Recent study (Feng, Fan & Ma 2017) shows the diffraction effect is not negligible in surge wave exciting force model. Therefore, the wave-induced surge force is corrected empirically:

$$\begin{cases} X_W = F_1^{res}(t) + \mu_x F_1^{FK}(t) \\ Y_W = F_2^{res}(t) + F_2^{FK}(t) \\ N_W = F_6^{res}(t) + F_6^{FK}(t) \end{cases} \tag{3}$$

where μ_x is diffraction correction coefficient, and it can be solved by using following formula (SDC 2/INF.10 2014):

$$\mu_x = \begin{cases} 1.46C_B - 0.05 & C_M < 0.86 \\ (5.76 - 5C_M)C_B - 0.05 & 0.86 < C_M < 0.94 \\ 1.06C_B - 0.05 & C_M \geq 0.94 \end{cases} \tag{4}$$

The seakeeping motion is simulated by using a 5-DOF sway-heave-roll-pitch-yaw model.

$$\begin{aligned} &\sum_{j=2}^{6}\left[\left(m_{ij} + \mu_{ij}(\infty)\right)\dot{v}_j(t) + \int_0^t R_{ij}(t-\tau)v_j(\tau)d\tau\right] \\ &+\left[F_i^{res}(t),\ \textit{for motion } i=3,4,5\right] \\ &+\left(B_v v_4,\ \textit{for motion } i=4\right) \\ &=\left[F_i^{FK}(t),\ \textit{for motion } i=3,4,5\right] + F_i^{dif}(t) \\ &+\left(K_\delta - z_H Y_H,\ \textit{for motion } i=4\right) \\ &(i = 2,\ldots,6) \end{aligned} \tag{5}$$

where m_{ij} and μ_{ij} represent ship mass and add mass with infinite frequency. B_v is viscous roll damping coefficient which can be obtained experimentally. F^{dif} is diffraction forces. According to Impuse Response Function (IRF) approach, radiation and diffraction forces are calculated in frequency domain by the strip theory and transferred into time domain by using retardation function R_{ij}. (Cummins 1962, Yu 2016). K_δ is rudder roll moment, and z_H is vertical distance between acting point of Y_H (hull hydrodynamic forces in sway direction) and center of gravity.

According to unified theory, the total ship motion is calculated by combining the maneuvering motion and seakeeping motion together:

$$\begin{aligned} &[u_T, v_T, w_T, p_T, q_T, r_T] = [0, v_S, w_S, p_S, q_S, r_S] \\ &\qquad + [u_M, v_M, 0, 0, 0, r_M] \\ &[x_T, y_T, z_T, \phi_T, \theta_T, \psi_T] = [x_{T0}, y_{T0}, z_{T0}, \phi_{T0}, \theta_{T0}, \psi_{T0}] \\ &+\left[\int_0^t u_T dt, \int_0^t v_T dt, \int_0^t w_T dt, \int_0^t p_T dt, \int_0^t q_T dt, \int_0^t r_T dt\right] \end{aligned} \tag{6}$$

where the subscript *T*, *S*, *M* stand for the total motion, seakeeping motion and maneuvering motion respectively, and subscript *T0* indicates the initial value for ship motion.

2.2 Submerged Propeller Model

In our previous research, the loss of rudder effectiveness due to emersion has been considered in the numerical model (Yu, Ma & Gu 2015). Therefore, only propeller thrust model with submergence is introduced in this paper.

The propeller thrust are calculated by the following empirical formula:

$$\begin{cases} T = \rho K_T D_P^4 n^2 \\ J = \dfrac{(1-\omega_p)U\cos\beta}{nD_P} \\ K_T = a_0 + a_1 J + a_2 J^2 \end{cases} \tag{7}$$

where ρ, D_p, n, donate the water density, propeller diameter and rotation rate. K_T, J, U, β are thrust coefficient, advanced coefficient, propeller inflow velocity and drift angle. a_0, a_1 and a_2 are the equivalent linear, quadratic and cubic thrust coefficient depending on J.

To evaluate the wave effect, this model can be modified to incorporate wave orbital velocity (Naito & Nakamura 1979).

$$\begin{cases} \Delta T_1 = -\kappa \bar{u}_p \\ u_p = C_w k A_w e^{kz} \cos(kx - \omega t) \\ \kappa = \rho D_p^2 (a_1 D_p n + 2 a_2 U) \end{cases} \quad (8)$$

where ΔT_1 denotes the thrust reduction due to wave orbital velocity. C_w, k, A_w, ω, κ are wave phase velocity, wave number, wave amplitude, frequency and thrust reduction coefficient. $\bar{u}_p$ represents mean value of wave orbital velocity around propeller as shown in Figure 1:

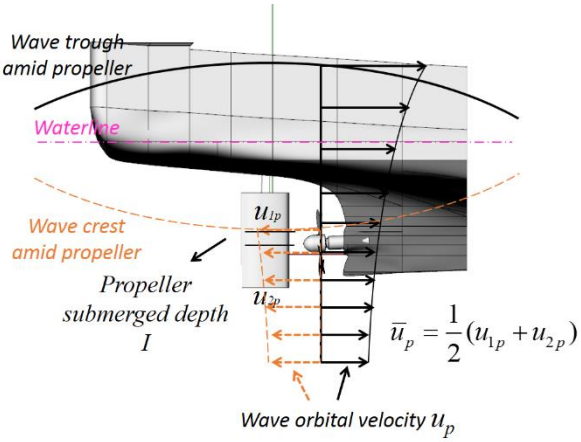

Figure 1 Wave orbital velocity around propeller and propeller submergence depth

Furthermore, the variation of propeller submergence depth is taken into consideration. As a preliminary assumption, ratio of propeller load at shallow submergence to that at deep one is regarded as linearly dependent on submergence depth. Thus, the propeller model can be modified as follow:

$$\begin{cases} \Delta T_2 = T - T_\infty \\ T/T_\infty = a \cdot \mathrm{SDR} + b \quad (\mathrm{SDR} \le A) \\ \qquad = 1 \qquad\qquad (\mathrm{SDR} > A) \end{cases} \quad (9)$$

where ΔT_2, T_∞ denotes the thrust reduction due to propeller submergence and thrust at deep submergence, SDR represents submergence ratio, defined as the ratio of submergence depth I to propeller radius R. A denotes the critical maximum submergence ratio, under which propeller load is linearly dependent on submergence depth, A and its equivalent linear and quadratic coefficient a, b depending on SDR can be solved experimentally.

However, the shallow submergence assumption is no longer applicable when most part of propeller emerges from water. Accordingly, the SDR is approximately regarded as constant (SDR=0.5) when SDR<0.5, and such approximation are applied in the following simulation.

Thus, the thrust reduction can be regarded as the summation of both above effects:

$$\Delta T = \Delta T_1 + \Delta T_2 \quad (10)$$

3. MODEL VALIDATIONS

3.1 Ship Model

A 135GT Japanese purse seiner (ITTC ship A2, NAOE Osaka University, 2017) is adopted for numerical simulation in this study. Figure 2 shows the hull surfaces of the ITTC ship A2, and the main particulars of the ship are shown in Table 1.

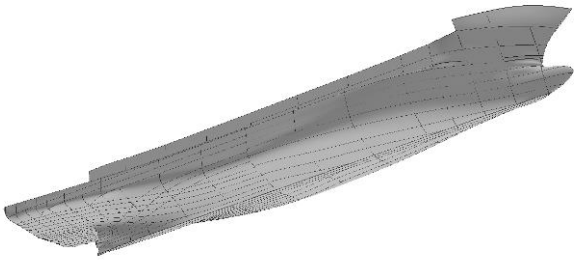

Figure 2 Hull surfaces of the ITTC ship A2

Table 1 Main particulars of ITTC ship A2

Ship	Value
Length between Perpendiculars, L_{pp}(m)	34.5
Breadth, B(m)	7.60
Depth, D(m)	3.07
Fore draught, d_f (m)	2.5
Aft draught, d_a (m)	2.8
Mean draught, d (m)	2.65
Block coefficient, C_B	0.597

Natural roll period, T_R (s)	7.4
Max rudder angle(deg)	35
Radius of gyration, roll, k_{xx}/Lpp	0.108
Radius of gyration, yaw, pitch, k_{yy}/L_{pp}, k_{zz}/L_{pp}	0.302
Propeller	
Number of blades	3
Diameter (m)	2.6
Pitch Ratio	0.5778
Expanded blade area ratio	0.5439
Boss ratio	0.1259

3.2 Validation of Propeller Model

The 6-DOF weakly nonlinear unified model has been validated qualitatively based on experiment data of ITTC ship A2 in Yu, Ma & Gu (2014). Thus, only the submerged propeller model is further validated. Since the propeller submergence data of ITTC ship A2 test is not available, the model is firstly applied to a 5-blade propeller (Naito & Nakamura 1979). The comparison result with experiment data is demonstrated in Figure 3.

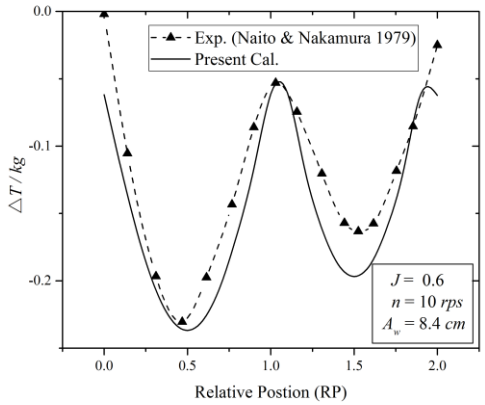

Figure 3 Comparison of thrust reduction of open water test in wave between experiment and calculation

In Figure 3, J, n and A_w donates advanced coefficient, propeller rotation rate and wave amplitude in experiment. The ship stays in the trough of wave when RP(relative position)=0.5 and crest when RP=1.5.The agreement between calculation and experiment data is quite acceptable. Therefore, the submerged propeller model is proved to be effective in predicting propeller thrust reduction.

Furthermore, the modified 6-DOF weakly nonlinear unified model is validated by comparison with the original model and the result of comparison is shown in Figure 4. In Figure4, (a), (b), (c) and (h) represent ship pitch, roll, yaw motion and speed in wave direction. (d) demonstrates ship's relative position in wave, which means ship stays in the trough of wave when RP=0.5 and crest when RP=0 or 1. (e), (f) and (g) represent mean value of wave orbital velocity around propeller, propeller submergence ratio and propeller thrust. The solid line is the result for modified model with the effect of propeller submergence, and the dash line is result for original model.

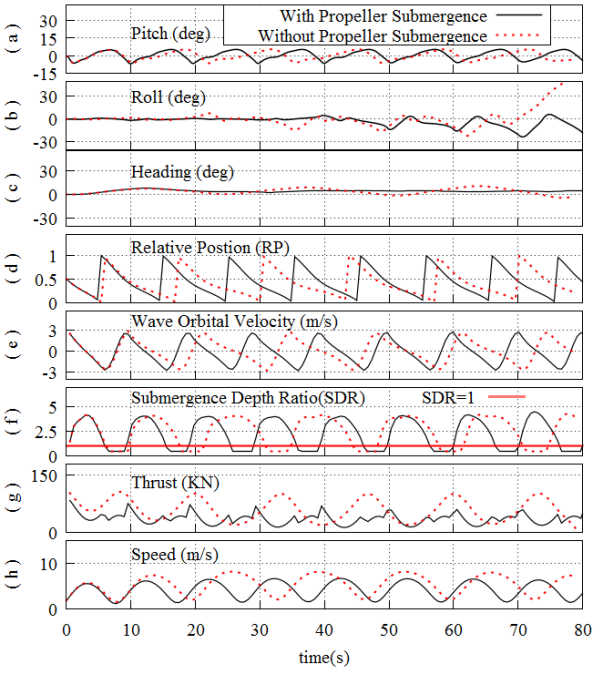

Figure 4 Comparison of ship motion between with and without the effect of propeller submergence (H/λ=1/10.0, λ/L_{pp}=1.637, Fn=0.30 and χ=-5 deg)

From Figure 4, ship ITTC A2 can be regarded as doing periodic motion with and without the effect of propeller submergence. However, difference in ship speed and propeller thrust can be easily observed, which

can be concluded as the effect of propeller submergence. In (e) and (f), wave orbital velocity and propeller submergence ratio oscillate periodically during the simulation. When ship reach the wave downslope (*RP*=1~0.5), propeller even emerges from water (SDR<1). After several times of oscillation, ship speed in modified model becomes smaller than the original model owing to propeller reduction effect.

Accordingly, the proposed submerged propeller model is regarded to be effective to account for the effect of propeller thrust reduction qualitatively. And its effect on surf-riding/broaching prediction is discussed in next section.

4. SIMULATION RESULTS

4.1 Simulation Condition

The modified 6-DOF weakly nonlinear unified model is applied to ship ITTC A2 with different auto pilot course and ship speed. To decrease the interference of initial condition, the ship is set to sail with its auto pilot course but start with a smaller initial speed (*Fn*=0.1). To investigate the effect of propeller thrust reduction on ship surf-riding/broaching prediction, simulation with the original model are also conducted with the same condition. In these cases, periodic motion, capsizing on wave crest, capsizing due to broaching and surf-riding with oscillation are identified. For each model, two cases for typical surf-riding/broaching motion in both models are chosen and they are listed in Table 2.

Table 2 Part of Simulation Condition of ITTC ship A2

No.	*Fn*	H/λ	λ/L_{pp}	χ (*deg*)
1	0.37	1/10.0	1.637	-10
2#	0.37	1/10.0	1.637	-10
3	0.40	1/10.0	1.637	-5
4#	0.40	1/10.0	1.637	-5

where case number with # represents the simulation is conducted with original model.

4.2 Results and Discussions

For case with autopilot speed Fn=0.37, numerical simulation results in full scale are demonstrated in Figure 5. In Figure 5(Left), ship speed accelerates and reaches to wave phase velocity swiftly in the first 20s. From 20s to 50s, ship relative position in wave, pitch and heave motion keep almost constant, which indicate surf-riding occurs. Meanwhile, the rudder angle largely increases and finally loses its course-keeping ability. In Figure 5(Right), when the effect of propeller submergence is taken into consideration, propeller thrust reduction occurs (marked by '(g)'). When ship reaches to the wave downslope (RP=1~0.5), propeller reaches to the surface of water or even emerges from water, and the propeller thrust drops dramatically. As a result, ship speed accelerates gently and keeps periodic motion ever since. And the threshold between surf-riding and periodic motion are influenced.

For cases with autopilot speed Fn=0.4, simulation results are demonstrated in Figure 6. In the original model (left), rudder angle rises to the maximum but still cannot control heading direction around 45s, which should be categorized as broaching. Meanwhile, ship motion in the modified model (right) can be categorized as surf-riding with oscillation. In this case, surf-riding motion can be observed in both model (20~40s in original model and 30~50s in modified model). However, the occurrence of surf-riding delays nearly 10s in the modified model. And that could be regarded as the effect of propeller submergence. When ship keeps surf-riding motion, propeller submergence ratio remains low, and thrust reduction is significant. Since surf-riding motion can be regarded as an equilibria position formed by wave-induced surge force, thrust and resistance, it can be presumed that ship relative position in waves when surf-riding occurs will leave away from wave trough, where wave- induced yaw moment will be smaller. As a result, ship instability in yaw motion is slightly reduced. Therefore, the amplitude for yaw oscillation is smaller as can

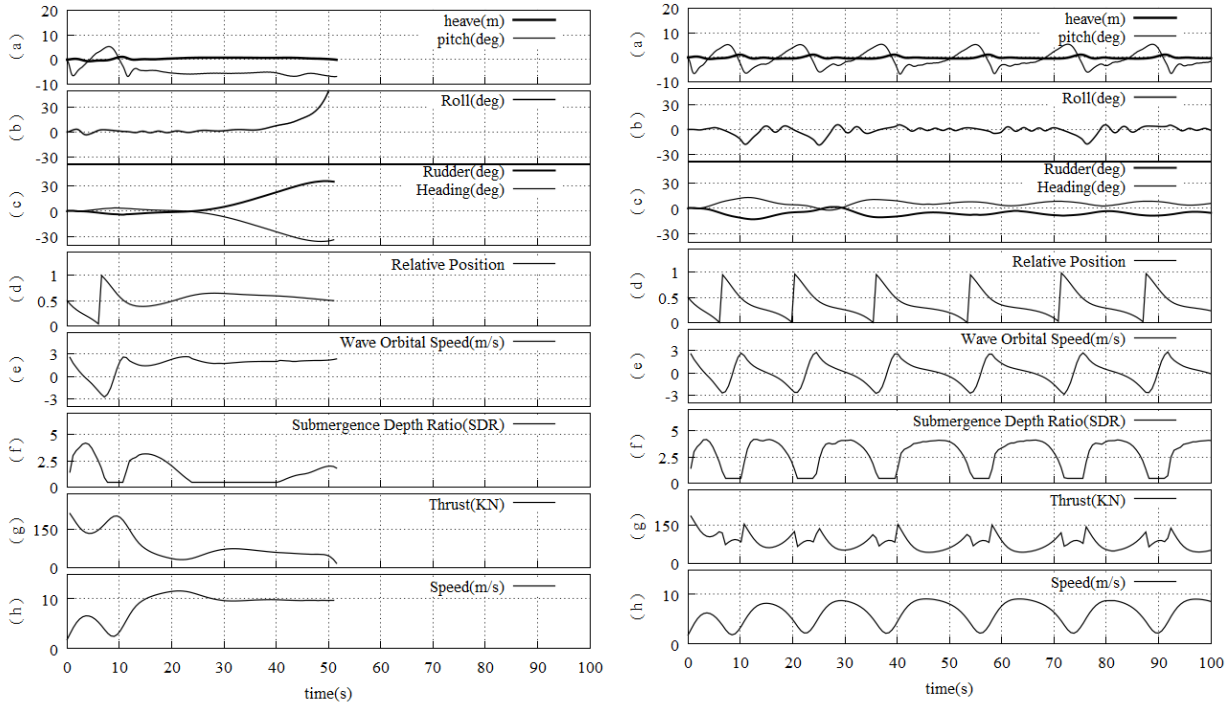

Figure 5 Simulation results of ship motion for case 1 & 2#.
(H/λ=1/10.0, λ/L_{pp}=1.637, Fn=0.37 and χ=-10 deg
Left: Original model, Capsize due to Broaching;
Right: Modified model, Periodic Motion)

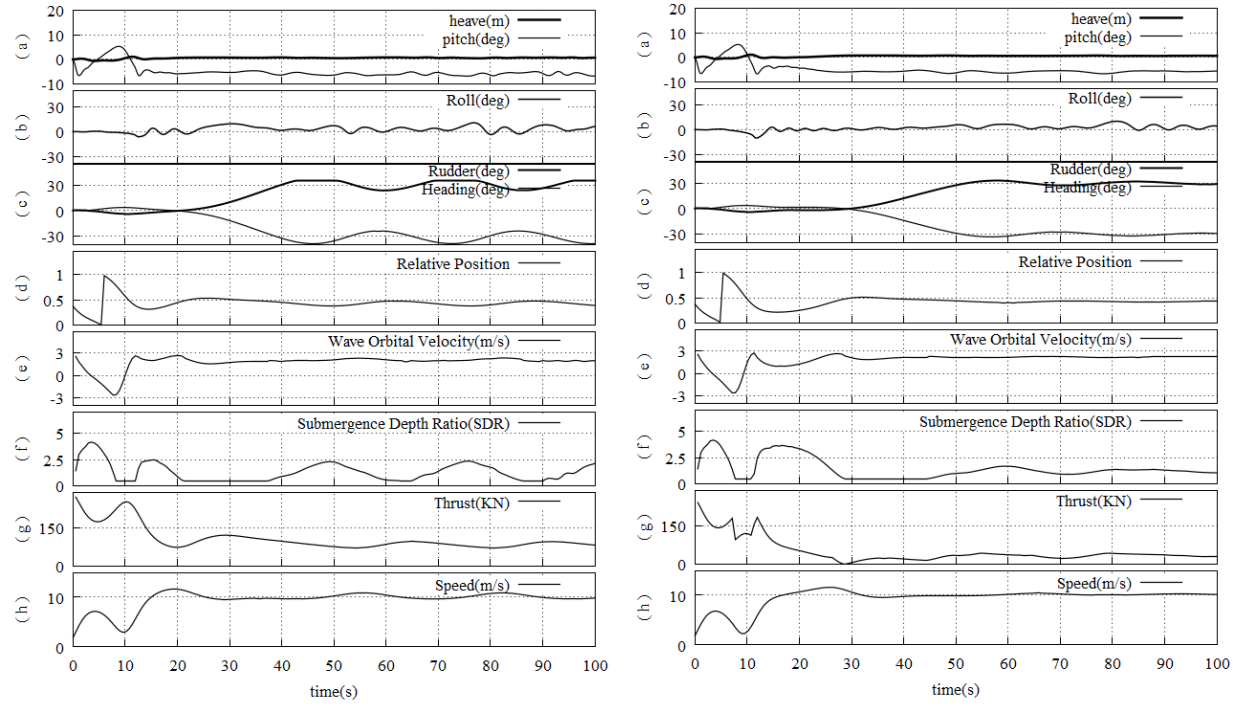

Figure 6 Simulation results of ship motion for case 3 & 4#.
(H/λ=1/10.0, λ/L_{pp}=1.637, Fn=0.40 and χ=-5 deg
Left: Original model, Broaching without Capsize;
Right: Modified model, Surf-riding with Oscillation)

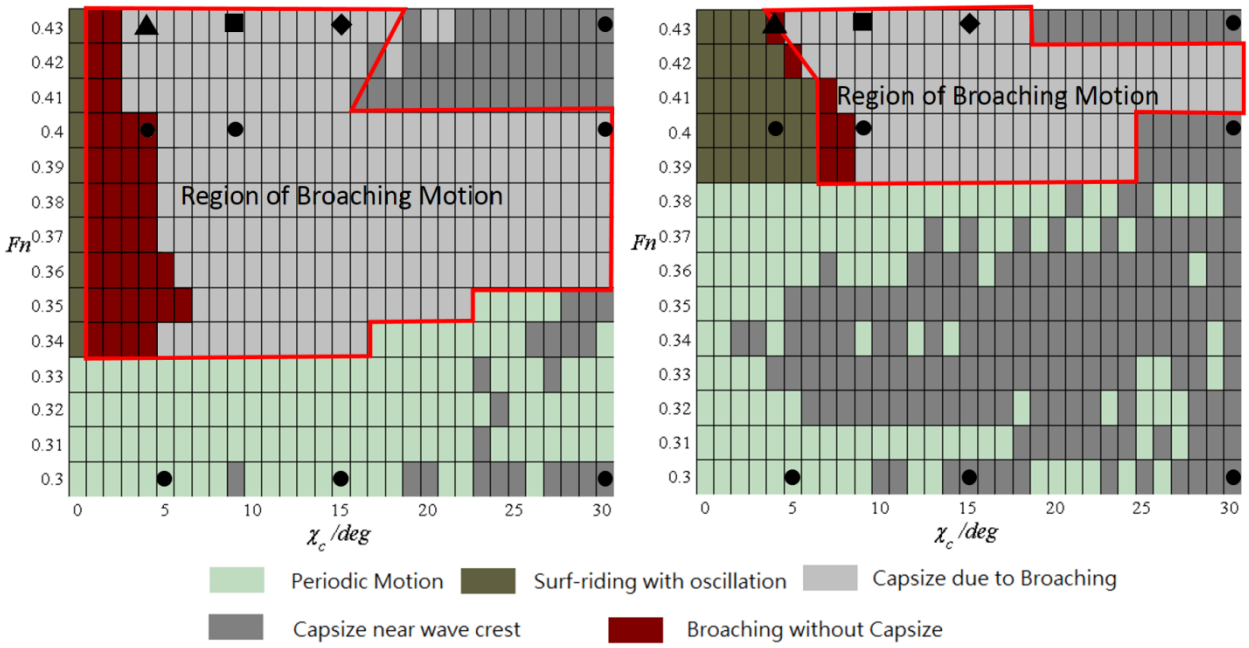

Figure 7 Comparison of measured ship motions (Umeda et al. 1999) and calculated ones with and without the effect of propeller submergence.
(H/λ=1/10.0, λ/L_{pp}=1.637 and Fn=0.40
Left: Original model; *Right*: Modified model
Square, Experimental, Capsize due to Broaching;
Diamond, Experimental, Capsize without Broaching;
Triangle, Experimental, Surf-riding;
Circles, Experimental, Periodic Motion)

be seen by comparing (c) "Heading (deg)" in two figures, and ship motion transforms from broaching to surf-riding with oscillation.

In Figure 7, all simulation results with different Froude number and autopilot courses and comparison with experiment results (Umeda et al. 1999) are presented. From these results, it can be concluded that ship tends to do surf-riding and broaching motion with high Froude number. Taking thrust reduction effect into consideration, the threshold between periodic motion and surf-riding/broaching rises from Fn=0.335 to Fn=0.385, which is much closer to the experiment.

For cases with Froude number larger than surf-riding/broaching threshold, 4 typical ship motions can be observed from the experiments. When modified model is applied, the region of broaching slightly decreased and move to the region with larger heading angle, which indicated propeller thrust reduction could reduce ship instability in yaw motion. However, it should be noted the influence on thrust reduction in transversal direction of the region is negligibly small, where other factors such as rudder emersion could be more effective for precise prediction.

5. CONCLUSION

In this paper, a modified 6-DOF weakly nonlinear unified model considering propeller submergence is developed. By numerically reproducing open water test in waves and conducting comparative study with the original model, the modified model is well validated. Furthermore, numerical simulation with different Froude number and autopilot course are conducted. And following concluding remarks can be drawn:

(1) Propeller thrust reduction occurs

remarkably when ship reaches wave downslope and surf-riding motion occurs.

(2) For surf-riding prediction, owing to thrust reduction, the autopilot Froude number for surf-riding/broaching threshold will increase, and the occurrence of surf-riding motion will delay.

(3) For broaching prediction, thrust reduction will slightly reduce ship instability in yaw motion and the region for broaching occurrence become smaller. However, the influence on broaching prediction is negligibly small comparing with that on surf-riding prediction.

However, this weakly nonlinear model still needs to be validated experimentally and other factors such as the coupled effect of rudder and propeller and effect of trapped water on deck should be investigated quantitatively in the future.

6. ACKNOWLEDMENTS

This research is supported by the National Natural Science Foundation of China (NSFC) research projects: No. 51579144 and No.51709240, the China Ministry of Education Key Research Project KSHIP-II Project (Knowledge-based Ship Design Hyper-Integrated Platform) No. GKZY010004 and the China Ministry of Industry and Information Technology Research Project: No. K24352. Authors express their sincerely thanks to Dr. Liwei Yu and Prof. Sheming Fan for their valuable advice and support during this research.

7. REFERENCES

Anaiev, D.M., 1966. “On surf-riding in following seas”. Transaction of Krylov Society, 13: 169-176.

Araki, M., Umeda, N., Hashimoto, H., and Matsuda, A., 2012. “An improvement of broaching prediction with a nonlinear 6 degrees of freedom model”. Journal of the Japan Society of Naval Architects and Ocean Engineers, 14, 85–96.

Cummins W E., 1962. “The impulse response function and ship motions”. Schiffstechnik, 57(9): 101–109.

Feng P., Fan S., and Ma N., 2017. “Correction of wave surge forces to improve surf-riding/broaching vulnerability criterion check accuracy”. Journal of Shanghai Jiaotong University, 22(5):549-554.

Grim, O., 1951. “Das Schiff in von Achtern Auflaufender See”. Jahrbuch Schiffbautechnishe Gesellschaft, 4: 264-287.

Hashimoto H., Umeda N., and Matsuda A., 2004. “Importance of several nonlinear factors on broaching prediction”. Journal of Marine Science & Technology, 9(2):80-93.

Kan, M., Saruta, T., Taguchi, H. et al., 1990, “Capsizing of a ship in quartering seas, part 1: model experiments on mechanism of capsizing”, Journal of the Society of Naval Architects of Japan, 167(167):81-90.

Maki, A., Umeda, N., Renilson, M., and Ueta, T., 2014. “Analytical methods to predict the surf-riding threshold and the wave-blocking threshold in astern seas”. Journal of Marine Science and Technology, 19 (4) :415-424.

Makov, Y., 1969. “Some results of theoretical analysis of surf-riding in following seas”. Transaction of Krylov Society, 126: 124-128.

Naito S. and Nakamura S., 1979. “Open Water Characteristics and Load Fluctuation of Propeller at Racing Condition in Waves”. Journal of the Kansai Society of Naval Architects, 51-63.

NAOE Osaka University. 2017. Sample ship data sheet: ITTC A2 fishing vessel. Retrieved from http://www.naoe.eng.osaka-u.ac.jp/imo/a2.

Sadat-Hosseini H., Carrica P., Stern F., et al., 2011. "CFD, system-based and EFD study of ship dynamic instability events: Surf-riding, periodic motion, and broaching". Ocean Engineering, 38(1):88-110.

SDC 2/INF.10, 2014, "Development of Second Generation Intact Stability Criteria", Subcommittee on Ship Design and Construction, 2nd session, Agenda item 5, Annex 32.

Spyrou, K. J., 1996. "Dynamic instability in quartering seas: The behavior of a ship during broaching". Journal of Ship Research, 40 (1) :46-59.

Umeda, N. and Hamamoto, M., 2000. "Capsize of ship models in following/quartering waves: physical experiments and nonlinear dynamics". Philosophical Transactions of the Royal Society of London. Series A: Mathematical, Physical and Engineering Sciences, 358(1771), 1883–1904.

Umeda, N. and Hashimoto, H., 2002. "Qualitative aspects of nonlinear ship motions in following and quartering seas with high forward velocity". Journal of Marine Science and Technology, 6(3) : 111–121.

Umeda, N. and Kohyama, T., 1990. "Surf-riding of a ship in regular seas". Journal of Kansai Society of Naval Architects. 213: 63-74

Umeda, N., Maki, A., and Hashimoto, H., 2006. "Maneuvering and control of a high-speed slender vessel with twin screws and twin rudders in following and quartering seas". Journal of the Japan Society of Naval Architects & Ocean Engineers, 4:155-164.

Umeda, N., Matsuda, A., Hamamoto, M., and Suzuki, S., 1999. "Stability assessment for intact ships in the light of model experiments". Journal of Marine Science and Technology, 4(2), 45–57.

Yu, L., Ma, N., and Gu, X., 2014. "Numerical investigation into ship stability failure events in quartering seas based on time domain weakly nonlinear unified model". In Proceedings of the 14th International Ship Stability Workshop. Kuala Lumpur, Malaysia. pp. 229–235.

Yu L., Ma N., and Gu X., 2015. "Influence of rudder emersion on ship broaching prediction". In Proceedings of the 12th International Conference on the Stability of Ships and Ocean Vehicles, Glasgow, UK. pp. 547-556

Yu L., 2016. "Prediction and prevention of ship transverse stability failure events in longitudinal seaway based on the unified model". Ph.D. Thesis, Shanghai Jiao Tong University, Shanghai.

On the direct assessment of broaching-to vulnerability of a high speed craft

Matteo Bonci, Delft University of Technology m.bonci@tudelft.nl

Martin Renilson, University of Tasmania, martin@renilson-marine.com

Pepijn De Jong, MARIN Wageningen, p.d.jong@marin.nl

Frans Van Walree, MARIN Wageningen, F.v.Walree@marin.nl

Riaan Van't Veer, Delft University of Technology, Riaan.vantVeer@tudelft.nl

ABSTRACT

Small high-speed craft sailing in following and stern-quartering waves are more exposed than other larger vessels to violent and uncontrollable motions. Surf-riding, broaching-to and in general loss of course stability are recognized to be one of the most dangerous scenarios by operators and on-board crews.

This paper analyses the vulnerability of a high-speed craft to broaching-to by means of time domain numerical simulations in irregular sea states. The mathematical model is based on the potential flow boundary element method theory. The results of this risk assessment are compared with a simpler stochastic method based on regular waves scenarios simulations. The differences between the two methods are presented and the future implications are discussed.

Keywords: *dynamic stability, broaching-to, high-speed craft*

1. INTRODUCTION

The following sea is one of the most critical conditions for a vessel sailing in a seaway. Every mariner, operator or designer is aware of the great risk that a ship can experience when navigating in following and stern quartering waves. The danger is represented by the difficulty of steering the vessel when sailing during these conditions. And the consequences can be dramatic: the ship becomes suddenly uncontrollable without any foreseeable signal. The consequences can be particularly severe for small and fast vessels. High speed craft are often subjected to large relative motions, and the inception of dynamic instabilities are extremely quick and unavoidable. Many authors (Renilson & Tuite, 1998), (Spyrou, 1996), (Umeda, 1999), tried to describe these events and the physical mechanisms behind them. In the most common situations, a broach is described as a two-step process. The ship is captured by the incoming stern wave and starts to surf on it traveling at the same speed as the wave (surf-riding). At that point the yaw moment from the wave on the vessel becomes large. The vessel then starts to turn driven by the yawing moment of the wave, which in the case of a broach cannot be counter-acted by the rudder. This makes it impossible to keep the vessel on a straight course (broaching-to). Surf-riding and broaching-to are dynamic phenomena strictly connected to each other.

The International Maritime Organization (IMO) is currently developing criteria to assess the liability of ships to dynamic instability inceptions. The mechanisms involved in these phenomena are complex: their prediction can be very challenging, even with the most advanced experimental and numerical techniques. For this reason they are more

conveniently treated in a statistical fashion (Peters et al., 2011), (Umeda et al., 2016), (IMO, 2015). The characterization of these instabilities is then reduced to the estimation of their probability of occurrence. The criteria developed at IMO are constituted by simple formulations that can be used in an early design stage. In the cases where the ship is vulnerable to dynamic instability according to the simpler criteria, the direct assessment of the probability of occurrence is then needed. This consists of model experiments, such as free running model tests, or of numerical simulations.

IMO vulnerability criterions are addressed only to the occurrence of surf-riding. The assessment of the risk connected to broaching-to unfortunately is not a straightforward task. Past work on the topic (Renilson, 1982), (De Jong et al., 2013), (De Jong, 2015) is often based only on regular wave scenarios, since understanding the physics in irregular waves can be extremely complex. From an experimental point of view, open water or ship model basin self-propelled model experiments are the most common way to estimate the vulnerability of a ship to broaching in realistic sea state conditions. However, free running model tests can become very expensive and time consuming.

Broaching-to in following waves is a rarely occurring event. This means that an enormous effort must be spent to encounter a high enough number of waves to ensure a reliable statistical description of the phenomenon.

In recent years numerical investigations are increasingly becoming popular in the study of these problems. Advanced numerical techniques, like RANSE solvers, are in principle able to model these effects, although an extensive use of those tools in such problems is still impractical. The great complexity of the physical phenomena involved demands too high a computational time which makes the statistical characterization of broaching unrealistic. Simpler mathematical tools seem to be the most suitable means for the problem of the ship in waves.

Panel methods represent, for example, an appealing compromise between broadness of applicability and accuracy of results. These models can be applied extensively to the problem of the ship in following waves, and they can even be used to provide statistical data for the probability of occurrence of dynamic instability events. The only drawback of those mathematical models is that they need validation of the computation of the hydrodynamic loads in order to reproduce the physical reality correctly. This means that they must often be tuned according to the results of experimental investigations.

In 2016 Umeda (Umeda, 2016) proposed a simplified stochastic method to the direct assessment the probability of broaching-to in realistic sea state conditions by means of numerical simulations in regular waves. The same method is also presented in this paper (see Section 4). The method was validated by means of free-running model tests in irregular waves in a model basin.

In the present work, the probability estimated using the simplified stochastic method is compared to that obtained directly from time domain simulations in irregular sea state conditions.

The mathematical model considered is a time domain potential flow boundary element method. The particulars of the mathematical tool are presented in Section 3.

2. TEST CASE DEFINITION

In this work, a panel method was employed to assess the broaching-to liability of a small high speed craft. High speed craft are the most problematic case for this type of investigation. They are subjected to relatively large motions and consequently the inception of dynamic instability is more likely than for other kind of vessels (Renilson, 2007). The rescue boat SAR NH-1816 of the Royal Netherlands Sea Rescue

Institution (KNRM) was chosen for this study. The vessel hull is derived from the axe-bow concept (Keuning, 2006) for the first time applied to a fast and small rescue craft. The hull lines and the model particulars are shown in Figure 1 and Table 1 respectively.

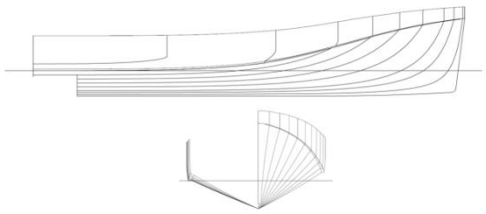

Figure 1 SAR NH-1816 Hull lines

Table 1 SAR-NH1816 particulars. Data are also available on www.knrm.nl.

NH-1816 model properties	*SU*	*Values*
Overall Length	[m]	19.3
Length between Perpendiculars	[m]	18.4
Overall Breadth	[m]	5.60
Draft	[m]	1.10
Weight	[t]	34.4
Longitudinal Centre of Gravity	[m]	6.00
Wetted Surface at Zero Speed	[m^2]	78

Past researchers investigated the liability of this vessel to broaching-to (De Jong et al., 2013), and its manoeuvrability characteristics (Bonci et al., 2017a, 2017b), by means of static captive model tests in calm water. The manoeuvrability of a high speed craft plays an important role in following seas, because the vessel must be able to counteract the destabilizing moment from the incoming wave. Furthermore, the vessel is also exposed to large relative vertical motions due to the large waves, and this can influence its manoeuvrability due to large variations in submerged geometry.

3. NUMERICAL METHOD

The numerical method was developed in the past years as a reliable and relatively fast tool for the characterization of ship behaviour at sea. Originally conceived for high speed craft seakeeping applications (Van Walree, 1999), (De Jong, 2011), (De Jong et al. 2007), (Van Walree, 2002), (De Jong & Van Walree, 2009, 2008), it was also recently validated for following and stern-quartering wave scenarios (Van Walree & De Jong, 2011). Manoeuvrability in following and stern-quartering waves is particularly important for small high-speed vessels, thus its accurate prediction is fundamental for dynamic course stability analysis.

The model is based on potential flow theory. A boundary value problem is solved to obtain the disturbed flow potential caused by the ship body moving on the free surface of the water. The problem domain is the body and the free water surface. The fluid is assumed to be homogeneous, incompressible, inviscid, irrotational and without surface tension. The Laplace equation is solved in the interior of the fluid assuming dynamic and kinematic conditions on the free surface, and zero normal flow speed on the body surface. The disturbance potential is set to vanish at a great distance from the body surface.

The hull surface is discretized by planar quadrilateral panels. This geometry is cut at the flat waterline intersection, dividing the geometry into above water and below water panels. The free surface boundary conditions are linearized around this flat waterline. The waterline intersection is defined by the running equilibrium position of the craft at speed. On the linearized submerged geometry a transient Green function is specified. The Green function expresses the influence of the ship hull on the free surface (memory effect), eliminating the need for an additional discretization of the free surface. This function is exact for each forward speed and submerged geometry.

Static loads (buoyancy) and Froude-Krylov wave loads are specified on the actual submerged geometry, i.e. on the instantaneous wavy free surface. Potential dynamic pressures due to the flow regime originated by the incoming (undisturbed) wave, ship diffraction

and radiation are evaluated only on the fixed below water geometry. Once the disturbance potential is known, the hydrodynamic pressures acting on the submerged hull are calculated by means of the Bernoulli theorem. The viscous forces are obtained from the actual submerged geometry, and they are determined by semi-empirical formulations. The linearization of the boundary conditions and the Green function around the flat waterline results in a less accurate prediction than their computation on the actual wavy free surface. However, the linearization drastically reduces the computational effort, permitting a wider range of utilization of the method.

Figure 2 shows the reference frame by which are defined all the significant quantities of the simulations.

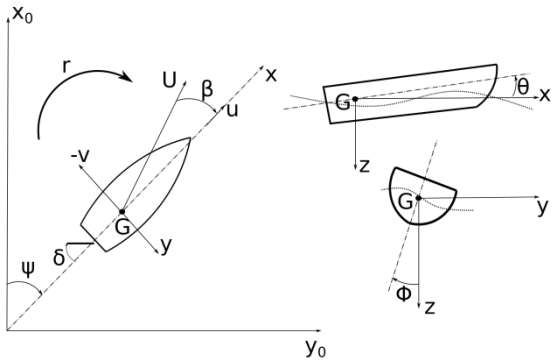

Figure 2 Ship reference axis system.

In the following the mathematical method will be applied to a free running ship sailing in following and stern-quartering seas, both regular and irregular. The ship is free to move in six degrees of freedom in the seaway. The initial positions in terms of heave and pitch were set to ensure the vertical state of equilibrium in calm water conditions for each of the speed considered. Similarly, the thrust propulsion rate was set to match the calm water resistance, and kept constant during the entire time loop of the simulation. The initial conditions are summarized in Table 1. Heave is given as the position of the centre of gravity over the calm water line: it is positive under the waterline (sink), and negative above (rise).

Table 2 Initial conditions of the simulations.

Fr	Z_0/L	ϑ [rad]	RPM
0.38	-0.024	+0.016	939
0.48	-0.025	+0.029	1196
0.58	-0.031	+0.032	1468

The steering angle was set by an autopilot with a control algorithm given in Equation 1. The autopilot coefficients and steering nozzle limits are shown in Table 2. The autopilot is meant to simulate a response by the helmsman during a normal operation; it is aimed to counteract a certain change of heading and turning rate bringing the ship back again on a straight course. The values are taken from the work of (De Jong et al., 2013).

$$\delta = b_{\delta\psi}\Delta\dot{\psi} + c_{\delta\psi}\Delta\psi \quad (1)$$

Table 3 Autopilot and steering characteristics used in the mathematical model

Description	Symbol	Unit	Value
Damping coefficient	$b_{\delta\psi}$	deg/(deg/s)	9.49
Proportional coefficient	$c_{\delta\psi}$	deg/deg	3.00
Max deflection angle	δ_M	deg	23
Max deflection speed	$\dot{\delta}_M$	deg/s	10

4. BROACHING-TO RISK ASSESMENT

4.1 Procedure

The risk assessment of ship dynamic instability in following seas is currently under development at IMO (IMO, 2015), (Peters et al., 2011). The procedure for the estimation of the liability of a ship to these events is treated by means of three subsequent levels of vulnerability checks. If a ship does not satisfy one of these criteria then the subsequent level must be examined.

IMO criteria focus on the liability of a vessel to surf-riding, since surf-riding is considered to be the first sign of a loss of dynamic stability. The first stage is a simple

threshold of the ship susceptibility to surf-riding. This criterion represents a threshold based on phase-plane analyses for a number of ships using a wave steepness of 1/10, which indicates the susceptibility of a ship to be surf-ridden by the incoming waves. Level 1 excludes from the subsequent checks ships longer than $200m$ with $Fr \leq 0.3$.

Level 2 is based on a statistical approach to evaluate the risk of surf-riding in a certain sea state. This criterion estimates the probability of occurrence of a surf-riding event in a certain irregular sea state, using the Melnikov analysis for determining the surf-riding threshold. Each of those probabilities are summed together and weighted according to the number of occurrences of each of the individual sea states over 100.000 observations. These values are given on wave scatter diagrams (IACS, 2001).

The third and final level is the direct assessment of the probability of occurrence of a dynamic stability event in time in irregular waves. As IMO proposes, this direct assessment can be alternatively conducted by experimental tests, typically free sailing model tests, or by time domain numerical simulations.

The final level of the vulnerability criteria is investigated in this work. As a first method, a stochastic approach is used to determine the probability, P, of broaching-to. According to IMO regulation (IMO, 2015) this probability can be discretized as in Equation 2.

$$P(T_0, H_{1/3}) = \sum_i \sum_j C(l_i, s_j)\, p^*(l_i, s_j) \Delta l \Delta s \tag{2}$$

This probability is associated with the probability of encountering a local regular wave that causes a dynamic instability, given a certain sea state. The term $p^*(l_i, s_j)$ (see Equation 3) is a joint probability function defined in the domain of the i-th non dimensional wave length, l_i, and j-th wave steepness, s_j. This originates from the Longuet-Higgins' theory (Longuet-Higgins, 1983), based on the wave envelope theory. This function represents the probability of having locally a certain wave length l_i and steepness s_j during a short-time realization of an irregular sea state. The probability is weighted according to the value $C(l_i, s_j)$ defined in Equation 4. This term is alternatively 1 or 0 whether a broach occurs or not for a certain l_i - s_j case.

$$p^*(l_i, s_j) = \frac{4\sqrt{g}}{\pi v} \frac{L^{5/2} T_{01}}{(H_{1/3})^3} s_j^2 l_i^{3/2} \left(\frac{\sqrt{1+v^2}}{1+\sqrt{1+v^2}} \right) \times$$
$$exp\left[-2 \left(\frac{L s_j l_i}{H_{1/3}} \right)^2 \left\{ 1 + \frac{1}{v^2} \left(1 - \sqrt{\frac{T_{01}^2}{2\pi L l_i}} \right)^2 \right\} \right] \tag{3}$$

$$C(l_i, s_j) = \begin{cases} 1 & yes\ broaching \\ 2 & no\ broaching \end{cases} \tag{4}$$

The value $P(T_0, H_{1/3})$ in Equation 2 is obtained by summation of the product of the density function p^* and C over the regular wave domain discretized by the wave length interval Δl and wave steepness interval Δs. P represents the probability of having a broach in a certain short-term sea state characterized by the significant wave height H_s and mean wave period T_0.

The results from this method are compared with those from a second method, which is based on counting the broaching events occurring during a number of time realizations of a sea spectrum. Time domain irregular waves were simulated by means of the panel method described in Section 3. The required test duration for assessing the probability of rarely occurring events is recommended by ITTC (ITTC, 2011) as $N = 100$ wave encounters, corresponding to one hour of full scale run duration. $N = 400$ or over is considered to be excellent practice. The probability of broaching-to occurrence is evaluated dividing the number of broaches by the total number of zero-crossing wave encounters, as shown in Equation 5. This is the easiest and most direct way to estimate a probability of a broach occurrence.

Note that each wave realisation is terminated when a broaching-to event is identified.

This approach was used also by Umeda (Umeda, 2016).

$$P_{BROACH} = \frac{N_{BROACH}}{N_{WAVES}} \quad (5)$$

4.2 Definition of broaching-to

In order to estimate the probability of the inception of broaching-to, it is necessary to define a broach in a quantitative manner. Many authors in other studies gave a definition of broaching-to. (Renilson & Tuite, 1998) defined as a broach the situation in which the yaw rate, r, and yaw acceleration rate, $\dot{r}$, are of the same sign, the steering angle, δ, is at the maximum value in the direction opposite to the yaw, and the ship's heading angle is greater or equal to 20 degrees. This is expressed in Equations 6 and 7.

$$\delta = \delta_M, r > 0, \dot{r} > 0 \; and \; \psi \geq 20° \quad (6)$$
$$broach\ to\ starboard$$

$$\delta = -\delta_M, r < 0, \dot{r} < 0 \; and \; \psi \leq 20° \quad (7)$$
$$broach\ to\ port$$

In a past study (Umeda et al., 1999), a qualitative definition of broaching-to was given, without including the threshold on the ship heading.

In the present study the first definition has been used. It is clear that different broaching-to definitions can lead to significant differences in the risk assessment.

In the present work also surf-riding was detected and defined, in order to distinguish the case where surf-riding is occurring from the broaching events. The definition of surf-riding is simpler: the vessel, which is initially travelling slower than the waves, is captured by the following wave and thus accelerated to its celerity. A surf-riding event is detected when the vessel forward speed U is greater or equal than the wave celerity c.

4.3 Method 1: Regular wave simulations

For the regular wave case, different ranges of non-dimensional wave length and wave steepness were considered. The main parameters are reported in Table 4.

Three speeds were considered at this stage. For each of these speeds simulations were conducted for a range of wave lengths and steepness's, creating $a(l_i, s_j)$ matrix of regular wave conditions. Each condition corresponded to a simulation. $C(l_i, s_j)$ was then calculated for each simulation depending on whether the vessel broached or not according to the definition given in Section 4.2.

Simulations in regular stern-quartering waves were carried out considering the discretized domain of regular non-dimensional wave length and wave steepness; the waves were considered to be linear, so the non-linear effects which can arise at high wave steepness were neglected. Similarly, the calculation of $p^*(l_i, s_j)$ is straightforward using Equation 3. Note that a matrix $p^*(l_i, s_j)$ exists for every sea state in the wave scatter diagram.

Table 4 Parameters of the simulations in regular stern quartering waves

Quantity	Symbol	Units	Range
Speed	Fr	[-]	0.38,0.48,0.58
Non-dimensional wave length	l_i	[-]	1 - 3
Wave steepness	s_j	[-]	0.03 – 0.15
Wave length interval	Δl	[-]	0.1
Wave steepness interval	Δs	[-]	0.03
Wave heading	ψ_W	[deg]	15

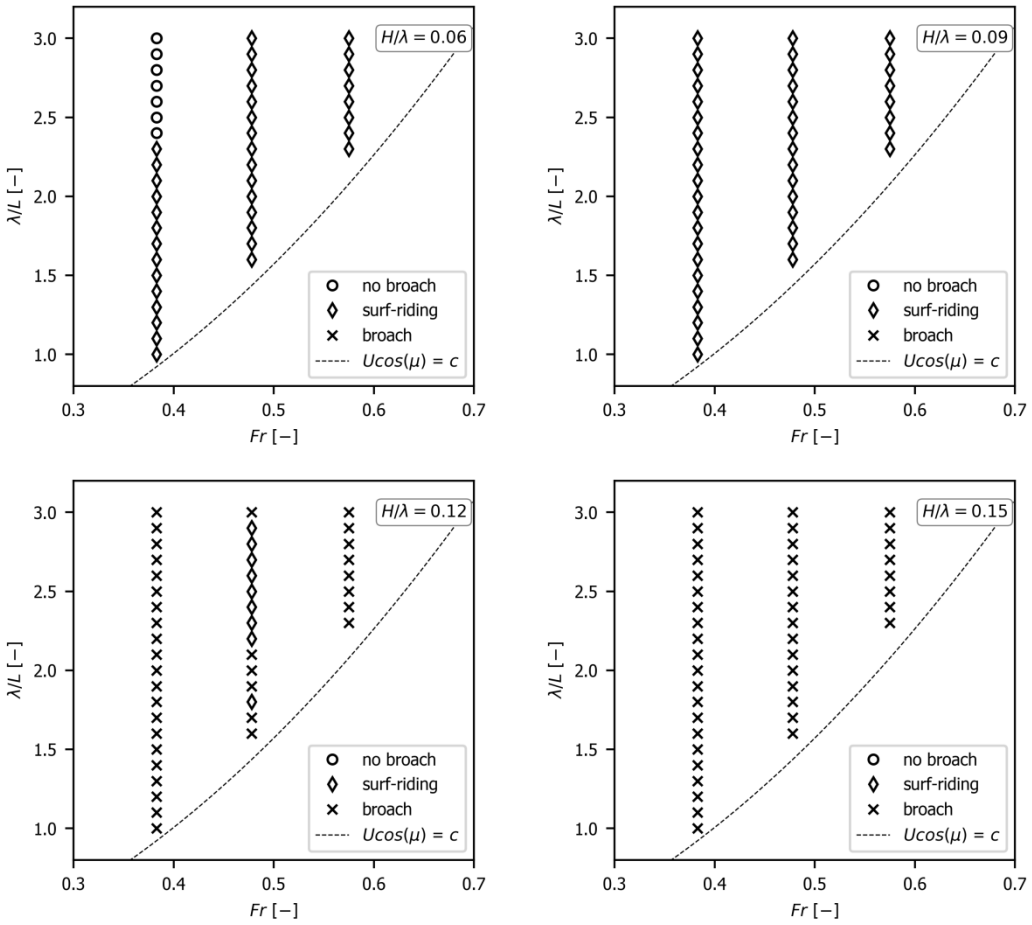

Figure 3 Simulations in regular waves given four different wave steepness's. No broaching occurs at steepness less than 0.12.

Figure 3 shows the results of the simulations for the four different values for the wave steepness considered in regular waves. The x-axis is the vessel speed, defined by its Froude number and the y-axis is the wave length, made non-dimensional by the vessel length. The dotted line shows the situation where the component of the vessel speed in the wave direction is the same as the wave speed. Above this line corresponds to the wave overtaking the vessel, and below this line corresponds to the vessel overtaking the wave. The crosses indicate cases where a broach occurs, and the diamonds indicate cases where the vessel was caused to surf-ride, without a broach.

Note that the range of wave lengths was restricted to the longer waves, i.e. the ones faster than the vessel in order to have a proper following sea situation. Outside this range the waves are slower than the vessel. In these conditions C is automatically zero, so they do not influence the probability computation.

Although not shown in Figure 3, the simulations were extended to λ/L = 4.0 for the larger steepness's where broaches were identified at λ/L = 3.0.

Using Equation 2 it is possible to calculate the probability, $P(T_0, H_{1/3})$. Figure 4 shows the probability, $P(T_0, H_{1/3})$, as a function of period, T_0, for different significant wave heights, $H_{1/3}$, evaluated by means of the Level 2 criterion.

The probability, P, was normalized by dividing it by the maximum probability, P_{MAX}, evaluated among the cases investigated. The highest probability of broaching-to was for a wave mean period of around 4 to 8 seconds, close to the component of vessel speed in the wave direction. The significant wave heights

with the greatest probabilities are between 4.5 to 10.5 m. This is because the heights tested in the simulations are more likely to occur in those sea states at intermediate wave heights.

Figure 5 shows the probability, $P(T_0, H_{1/3})$, as a function of period, T_0, for different Froude numbers, Fr. As the period increases, the wave steepness decreases since the significant wave height is constant. This explain the low probabilities at high wave periods. Furthermore, for greater speeds the probability of broaching is lower. This is unexpected and needs further study.

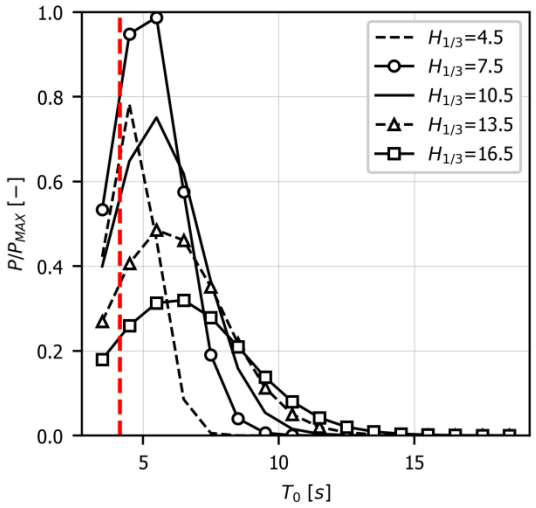

Figure 4 Plot of the probability of broaching-to as function of wave mean period for different significant wave heights. The vertical dotted line indicates the waves which travel at the same speed as the vessel in the wave direction $\mu = 15deg,\ Fr = 0.5$.

4.4 Method 2: Direct simulation in irregular waves

In this section the results of the time domain simulation in irregular waves are shown, in terms of the probability of broaching. The results are presented and compared with the simpler stochastic method in regular waves.

For the purpose of this work, only one sea state was considered. The probability evaluated in this sea state was compared with the correspondent probability, $P(T_0, H_{1/3})$, evaluated by means of Method 1. The parameters of the simulations are summarized in Table 5.

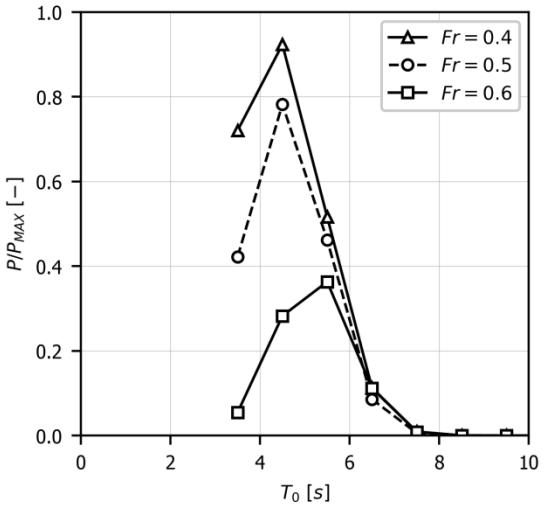

Figure 5 Plot of the probability of broaching-to as functions of wave mean period for different speeds. The significant wave height is fixed: $H_{1/3} = 4.5m.\ \mu = 15deg.$

Table 5 Parameters of the simulations in irregular seas.

Fr [-]	$H_{1/3}$ [m]	T_0 [s]	N_{WAVES} [-]
0.38			583
0.48	4.5	4.5	552
0.58			459

In order to achieve a reliable number of waves encountered during the time domain simulations, different realizations of the spectrum, N_{REAL}, were considered and simulated. Since broaching-to is considered as a single wave event, the probability of broaching was calculated easily by means of Equation 7, i.e. dividing the number of occurrences of a broach by the number of waves encountered. Note that when a broach occurred the simulation was terminated and started again with the next wave realisation.

Figure 6 is an example of the results from a typical simulation showing a broach occurring.

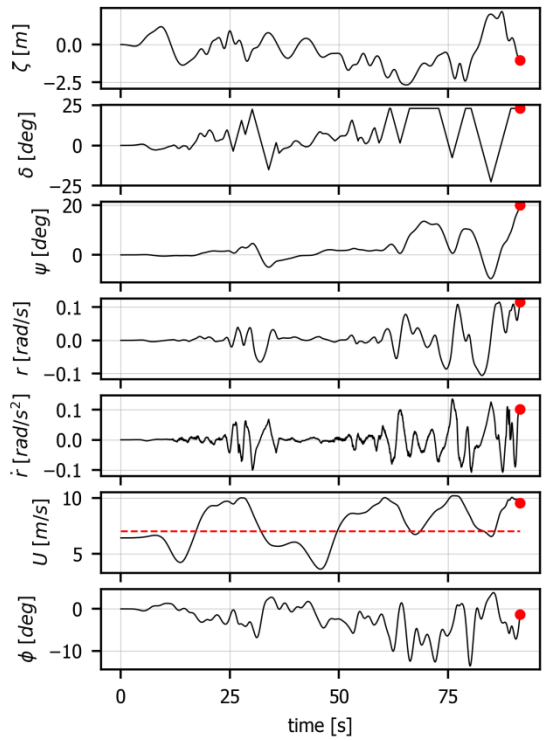

Figure 6 Time histories of a typical simulation event in irregular following sea. The red dashed line refers to the mean sea speed. At the red dots broaching occurs.

Figure 7 shows the predicted probability of a broach occurring using the two methods, as a function of ship speed in a single sea state.

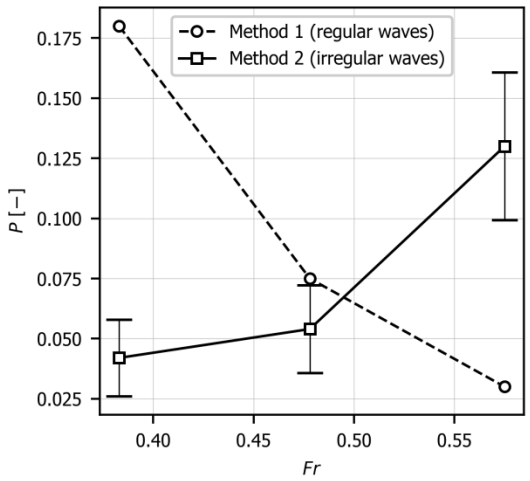

Figure 7 Comparison of the probability of broaching-to evaluated with the two different criteria levels, for the three speeds investigated.

As can be seen, the probability estimated using Method 1 decreases with increasing speed, whereas the probability estimated using Method 2 increases with increasing speed. The confidence intervals for Method 2 are calculated according to the procedure in (ITTC, 2008).

5. FINAL REMARKS AND DISCUSSION

In this paper a numerical technique has been used to determine the vulnerability of a high speed craft to inceptions of broaching-to in following waves.

Two methods were used to estimate the probability of broaching-to. The first was based on a regular wave stochastic approach: the probability of occurrence of broaching-to is connected with probability of encountering a local regular wave that causes a broach given a certain sea state.

The second used time domain simulation with a direct assessment of the number of broaches occurring during a time realization of the sea spectrum.

The two methods investigated gave different results, as shown in Figure 6. This is different to that found by Umeda in his work (Umeda, 2016).

According to Method 1, the instability events decrease in number with the increase of speed. This because at higher ship speeds less waves are able to overtake the model, thus possibly causing surf-riding or broaching-to. This causes a drop in the probability estimation. In irregular waves (Method 2) the trend is opposite: at this stage it is not understood why this is the case, since the ship dynamic is different and much more complicated than the regular waves case. The understanding of this difference will be the subject of ongoing investigations.

However, the numerical technique made it possible to realize an excellent statistical description of the phenomenon in irregular seas. It was possible to simulate more than 400 wave encounters for each of the speeds considered. This number is unfeasible for experiments in a ship model basin with free

running model tests. The mathematical tool can be then also utilized to investigate other issues, such as: different vessel designs; different appendage configurations; and different sea states.

The probability values estimated using these two methods should be related to more practical operational quantities. For example, the probability of broaching should perhaps be evaluated in terms of operational time before an instability event could occur, rather than based on the number of wave encounters.

Also, it is important to establish an agreed quantitative definition of what is meant by a broach. This will make it possible to compare work conducted by different researchers in this field.

6. ACKOWLEDGMENT

The authors would like to acknowledge KNRM and DAMEN to having made the information of the NH-1816 rescue boat used as model in this study available, as owner and designer of the vessel.

7. NOMENCLATURE

$\boldsymbol{b_{\delta\psi}}$	Autopilot damping coefficient
$\boldsymbol{c_{\delta\psi}}$	Autopilot proportional coefficient
$\boldsymbol{Fr}$	Length based Froude number
$\boldsymbol{L}$	Ship length
$\boldsymbol{l_i}$	Non-dimensional wave length λ/L
$\boldsymbol{H_{1/3}}$	Significant wave height
$\boldsymbol{N_{WAVES}}$	Number of waves encountered
$\boldsymbol{r}$	Yaw rate
$\boldsymbol{\dot{r}}$	Yaw acceleration rate
$\boldsymbol{s_i}$	Wave steepness H/λ
$\boldsymbol{T_0}$	Mean wave period
$\boldsymbol{T_{01}}$	$1.083\boldsymbol{T_0}$
$\boldsymbol{\delta}$	Steering angle
$\boldsymbol{\delta_M}$	Maximum steering angle
$\boldsymbol{\dot{\delta}_M}$	Maximum steering speed
$\boldsymbol{\Delta\psi}$	Deviation from desired course heading
$\boldsymbol{\psi}$	Course heading
ζ	Wave elevation
$\boldsymbol{v}$	Spectrum band parameter
ϑ	Ship pitch
Z_0	Ship sink/rise

8. REFERENCES

Bonci, M., Renilson, M. R., Jong, P., Walree, F., Keuning, A. J., & Huijsmans, R., 2017, "Experimental and numerical investigation on the heel and drift induced hydrodynamic loads of a high speed vessel", 14th Conference on Fast Sea Transportation, Nantes.

Bonci, M., Renilson, M., De Jong, P., Van Walree, F., Keuning, A. J., and Huijsmans, R., 2017, "Heel-sway-yaw coupling hydrodynamic loads on a high speed vessel", 11th Symposium on High Speed Marine Vehicles, Naples.

De Jong, P., 2011, "Seakeeping behaviour of high speed ships - An experimental and numerical study", Ph.D. thesis, Technical University of Delft.

De Jong, P. and Van Walree, F., 2008, "Hydrodynamic lift in a time-domain panel method for the seakeeping on high speed ships", 6th International Conference on High-Performance Marine Vehicles, Naples.

De Jong, P. and Van Walree, F., 2009, "The development and validation of a time-domain panel method for the seakeeping of high speed ships", 10th International Conference on Fast Sea Transportation, Athens.

De Jong, P., Renilson, M., and Van Walree, F., 2015, "The effect of ship speed, heading angle and wave steepness on the likelihood of broaching-to in astern quartering seas", 12th International Conference on the Stability of Ships and Ocean Vehicles, Glasgow.

De Jong, P., Van Walree, F., and Renilson, M., 2013, "The broaching of a fast rescue craft in following seas", 12th International Conference on Fast Sea Transportation, Amsterdam.

De Jong, P., Van Walree, F., Keuning, J. A., and Huijsmans, R., 2007, "Evaluation

of the free surface elevation in a time-domain panel method for the seakeeping of high speed ships", 17th International Offshore and Polar Engineering, Lisbon.

IACS, 2001, "Standard wave data. Recommendation No.34, Rev.1".

IMO, 2015, "Report of the working group (part 1), SDC 2/WP.4, Annex 3".

ITTC, 2008, "Testing and Extrapolation Methods Loads and Responses, Stability Model Tests on Intact Stability no. 7.5-02 07-04.1".

Keuning, J. A., 2006, "Grinding the bow", International Shipbuilding Progress, 281-310.

Longuet-Higgins, M. S., 1983, "On the joint distribution of wave periods and amplitudes in a random wave field", Proceedings of the Royal Society of London, A, 241-258.

Peters, W., Belenky, V., Bassler, C., Spyrou, K., Umeda, N., Bulian, G., 2011. "The Second Generation Intact Stability Criteria: An Overview of Development", Transactions-Society of Naval Architects and Marine Engineers, SNAME.

Renilson, M., 2007, "Predicting the Hydrodynamic Performance of Very High Speed Craft - A Note on Some of the Problems", International Journal of Small Craft Technology.

Renilson, M. R., 1982, "An investigation into the factors affecting the likelihood of broaching-to in following seas", 2nd International Conference on Stability of Ships and Ocean Vehicles, No.4 p.17, Tokyo.

Renilson, M. R. and Tuite, A. J., 1998, "Broaching-to - a proposed definition and analysis method", Twenty-Fifth American Towing Tank Conference, Iowa.

Spyrou, K. J., 1996, "Dynamic Instability in Quartering Seas: The Behavior of a Ship During Broaching", Journal of Ship Research, 40, 46-59.

Umeda, N., 1999, "Nonlinear dynamics of ship capsizing due to broaching in following and quartering seas", Journal of Marine Science and Technology, 4, 16-26.

Umeda, N., Matsuda, A., and Takagi, M., 1991, "Model Experiment on Anti-Broaching Steering System", Journal of Naval Architects of Japan, 185, 41-48.

Umeda, N., Usada, S., Mizumoto, K., and Matsuda, A., 2016, "Broaching probability for a ship in irregular stern-quartering waves: theoretical prediction and experimental validation". Journal of Marine Science and Technology, 21, 23-37.

Van Walree, F., 2002, "Development, validation and application of a time domain seakeeping method for high speed crafts with a ride control system", 24th Symposium on Naval Hydrodynamics, Fukoka.

Van Walree, F. and De Jong, P., 2011, "Validation of a time domain panel code for high speed craft operating in stern and quartering seas", 11th International Conference on Fast Sea Transportation, Honolulu.

Van Walree, F., 1999, "Computational methods for hydrofoil craft in steady and unsteady flow", Ph.D. thesis, Technical University of Delft.

Validation of a Time Domain Panel Code for Predicting the Behaviour of a RHIB Towed Alongside a Patrol Boat

Frans van Walree, *Maritime Research Institute Netherlands*, f.v.walree@marin.nl

Daniel Sgarioto, *Defence Science & Technology Group*, daniel.sgarioto@dst.defence.gov.au

Terry Turner, *Defence Science & Technology Group*, terry.turner@dst.defence.gov.au

Nicolas Carette, *Maritime Research Institute Netherlands*, N.C. Carette@marin.nl

ABSTRACT

The paper describes the validation of a numerical simulation method for predicting the dynamic behaviour of a Rigid Hull Inflatable Boat (RHIB) in waves when towed alongside a patrol boat. An overview of a multi-vessel interaction model testing program is provided and several hydrodynamic phenomenon observed during these experiments are also discussed. A number of validation cases are presented, based on a comparison between simulated and experimental results. Results obtained indicate that the simulation method is capable of providing representative motion and tow line force predictions for a RHIB when towed alongside a patrol boat for a variety of conditions.

Keywords: *side-by-side operation, launch & recovery, hydrodynamic interaction, model tests, simulation, validation*

1. INTRODUCTION

Vessels such as Rigid Hull Inflatable Boats (RHIBs) have been widely adopted as the preferred small boat platform for navies, coast guards and lifeboat organisations. For navies in particular, RHIBs provide major fleet units with a versatile and rapidly deployable small boat capability for operations ranging from search and rescue to high speed interception and boarding operations. In support of naval and coast guard operations, RHIBs are launched and recovered from a larger patrol boat or frigate and often operate in harsh seaway environments. Ever-present during Launch and Recovery (L&R) operations are considerable risks to materiel and personnel, arising from RHIB capsizing or severe impacts between the RHIB and the parent vessel.

This has resulted in the requirement to better understand the seakeeping behaviour of RHIBs when operating in close proximity to parent vessels. Numerical simulation methods provide a cost effective means of predicting towing loads and small boat seakeeping during L&R operations. A major challenge when employing numerical simulation methods is verifying that the developed models are representative and meaningful results are obtained. In the absence of full-scale trials data, which is usually costly and difficult to procure, the use of model test data is often relied upon for the validation of simulation-based methods (Carette et al. 2016). Once validated, these tools can be used to establish safe operational limits and provide rational operability guidance tools to small boat operators (van Walree and Thomas 2017).

This paper outlines the validation of a numerical simulation method for examining the dynamic behaviour of a RHIB when towed alongside a patrol boat in waves. The code, PanShip, is a time domain panel method for predicting hydrodynamic loads and seakeeping behaviour of single and multiple vessels operating in a seaway (van Walree 2002, de Jong 2011, van Walree et al. 2016, van Walree and Thomas 2017). A brief description of the

simulation method is given first, followed by an overview of the model scale experiments. Notable hydrodynamic phenomena observed during these experiments are also discussed, upon which a number of validation cases are presented. Comparisons are shown between model test and simulation results for the main motion components of interest, as well as towing line tensions.

2. MODEL TESTS

2.1 Overview

A series of model tests (1:10 scale) were performed at the Maritime Research Institute of the Netherlands (MARIN) Seakeeping and Manoeuvring Basin (SMB) using a model of a 7.2 m RHIB towed alongside a 55 m patrol boat model (see Figure 1). The objective of this model testing program was to investigate the influence that vessel speed, wave direction and various towing configurations have on the motion and towing forces of the RHIB during L&R operations. These experiments also provide suitable validation material to facilitate the development of numerical simulation capabilities.

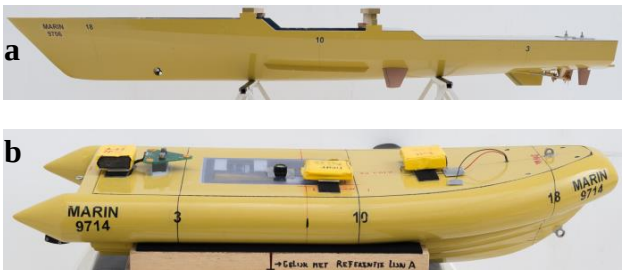

Figure 1 Multi-vessel interaction models; (a) 55 m patrol boat (b) 7.2 m RHIB.

The patrol boat model was equipped with a pair of propellers, two controllable rudders, passive fins and bilge keels, whilst the RHIB model contained a waterjet with a steerable nozzle. The patrol boat was free sailing, controlled by an autopilot based on yaw angle and yaw rate control. The speed of the patrol boat ranged from 4 to 10 knots. The RHIB was passively towed alongside the patrol boat on the leeward side with a rope attached to a spring and force transducer. The patrol boat was tested at two headings; starboard bow quartering and port stern quartering, since these headings provide a suitable lee for RHIB L&R operations.

A total of four towing connection configurations were tested, but only two are the subject of the validation study presented here. These configurations are the Stag Horn Organically connected to the patrol boat (SH/O) and the Bow Ring connected to the patrol boat via a boat rope Boom (BR/B). Figure 2a shows the Organic connection and the boat rope Boom on the patrol boat, whilst Figure 2b shows the Stag Horn connection and the Bow Ring on the RHIB. Figure 2a also shows the RHIB in the BR/B condition.

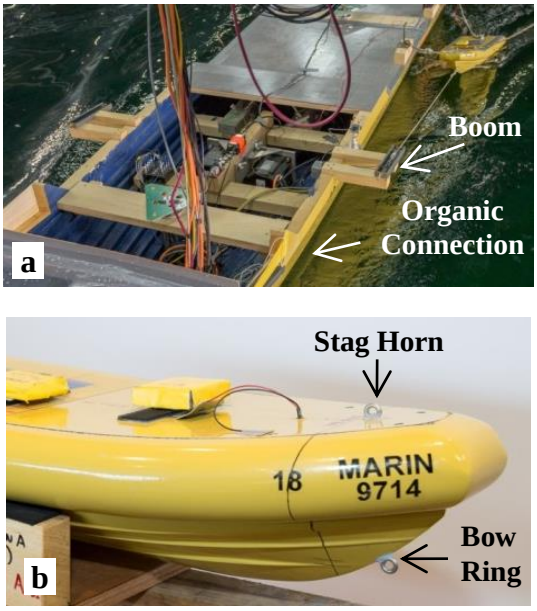

Figure 2 Towing configurations; (a) patrol boat connections (b) RHIB connections.

Experiments were performed using two different loading conditions for the RHIB, termed Light and Heavy. The Heavy load condition represents the maximum limiting displacement of the RHIB, The Light load condition is the lightship condition of the RHIB plus two nominal personnel (coxswain and bowman). The majority of the model test experiments were undertaken in irregular seas using a JONSWAP spectrum with a peak

enhancement factor of 3.3. The significant wave height and peak wave period for each of these tests was 1.88 m and 7.7 s respectively (middle of Sea State 4). The test duration was sufficient for 180 wave encounters with a maximum of 1800 s (full scale). Figure 3 provides an example of the experimental set-up employed during the model testing program.

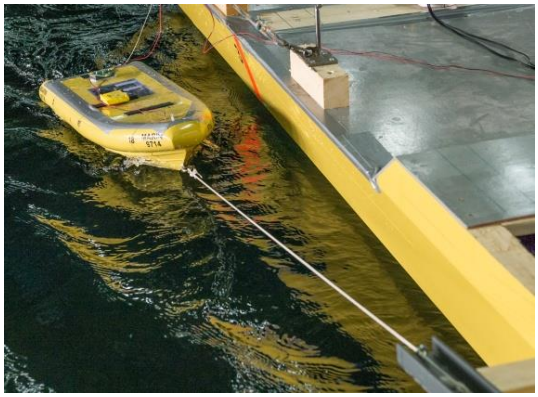

Figure 3 RHIB towed alongside the patrol boat in the Bow Ring-Boom configuration.

2.2 Findings

The patrol boat heading relative to the waves was found to influence the motions of the RHIB, with RHIB motions lower in stern quartering seas. At low speeds, the RHIB experienced significant yawing motions. Tow line forces were largest at low speed in stern quartering seas. In bow quartering seas, the maximum load in the tow line increased with increasing vessel speed. Maximum towing loads were found to be due to snap loads within the tow line, caused by the seaway inducing large relative motions between the patrol boat and the RHIB.

The RHIB often encountered a low yet steep wave originating from the patrol boat stabilising fin, an example of which is shown in Figure 4. This wave developed from the same location on the patrol boat, irrespective of speed or fin angle setting, but impacted the RHIB at a variety of locations, depending on the vessel speed and towing configuration. The steepness of the wave was dependent on the fin angle.

Figure 4 Example of the wave originating from the patrol boat roll stabilisation fin.

As a result, a number of calm water runs were performed where the angle of the patrol boat roll stabilisation fin was varied. Figure 5 and 6 provide a series of still images derived from the video recordings of moderate and high speed, Light load, Stag Horn/Boom (SH/B) towing runs where the angle of the patrol boat fin was varied through an approximate range of ±19°.

The short wave radiating from the patrol boat hull, induced by the fin, can be clearly seen in front of the RHIB bow in Figure 5b and 5d. At 6 knots, this wave is stable, oscillating inboard and outboard of the RHIB bow, dependent on the fin angle setting. As a result, the wave induces sway, roll and yawing motions on the RHIB. Consequently, frequent contact between the RHIB and the patrol boat hull occurs as a result of the hydrodynamic interactions.

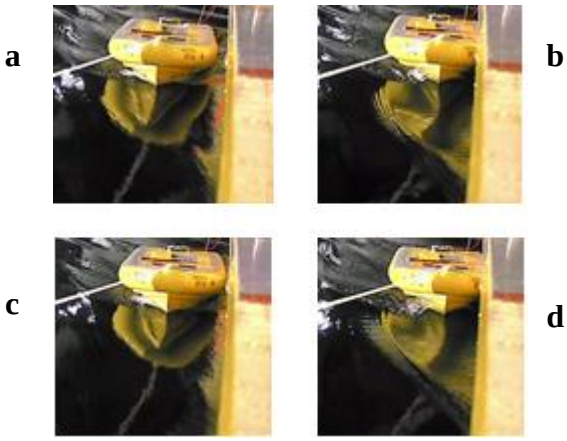

Figure 5 Effect of patrol boat fin on RHIB motions: moderate speed (6 knots); (a) t = 200s (b) t = 270s (c) t = 340s (d) t = 361s.

Even with passive fins as used during the model tests the fin incidence varies due to the motions of the patrol boat. The RHIB encounters the wave originating from the patrol boat fin directly at the bow stem in Figure 6a. Shortly afterwards, as the fin angle setting is varied, the wave front moves inboard, impacting the RHIB hull further aft towards amidships (Figure 6b). As a result, the RHIB is yawed to starboard and sways further away from the patrol boat. At higher speed, the wave is steep enough to break and this breaking wave action inboard of the RHIB bow produces large sway and yaw motions (Figure 6c). After the wave has broken, Figure 6d shows that the RHIB stern is drawn towards the patrol boat and sizable yawing is maintained as the wave system dissipates.

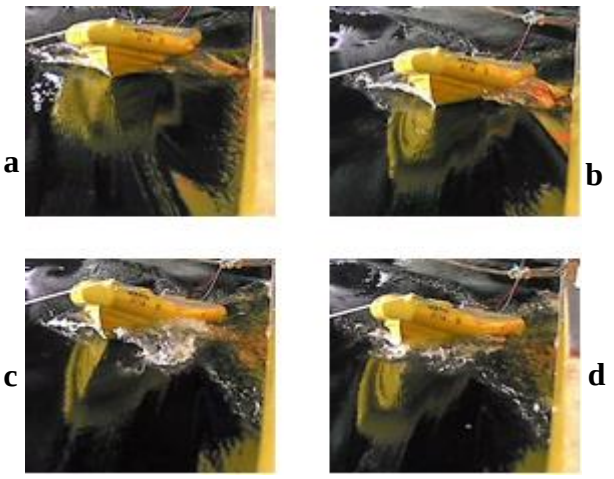

Figure 6 Effect of patrol boat fin on RHIB motions: high speed (10 knots); (a) t = 170s (b) t = 220s (c) t = 230s (d) t = 240s.

3. SIMULATION METHOD

PanShip is a time domain panel code for predicting seakeeping responses and impulsive loads for single and multiple vessels operating in waves. The method is characterised by:

- 3D transient Green function to account for linearised free surface effects, exact forward speed effects on radiation and diffraction forces and a Kutta condition at ventilated transom sterns of ship hulls;
- 3D panel method to account for Froude-Krylov forces on the instantaneous submerged body;
- Constant source strength panels on ship hulls and combined constant source and doublet strength panels on lifting surfaces;
- Cross flow drag method for viscosity effects in both the vertical and horizontal planes;
- Resistance (in waves) is obtained from pressure integration at each time step and the viscous resistance of the actual wetted surface;
- Propulsion and steering using propeller open water characteristics, semi-empirical lifting-surface characteristics and propeller-rudder interaction coefficients. Also a semi-empirical waterjet propulsion and steering method is incorporated;
- Empirical viscous roll damping by either the Fast Displacement Ship or Ikeda methods;
- Autopilot steering;
- Linear elastic tow line and impact (stiff fender) models.

The radiation and diffraction method used assumes that the motions of the craft are small, i.e. the submerged geometry does not change in time. The speed and heading are assumed to be constant so that the Green functions can be computed a priori for use at each time step in the simulation. The wave excitation and restoring forces are treated in a nonlinear way by using the actual submerged hull geometry under the disturbed incident wave.

For the present multi-body problem, impulse response functions are determined for the mean relative position of the two vessels. The hydrodynamic interaction is strictly speaking valid only for this mean position. It is more accurate to determine the interaction for the actual relative position but this requires determining the Green functions at each time step which is impractical when a large amount of conditions need to be simulated.

During the simulations, the patrol boat was free running and self-propelled and kept on course through an autopilot. The propeller RPM was set such that the mean speed in

waves was approximately equal to that of the model tests. The autopilot gains were the same as used for the model tests. The patrol boat fins were passive for the tests considered here.

The RHIB was towed by the patrol boat and free running as well, but without propulsion and course control, i.e. inactive waterjet. The tow line was modeled as a linear spring which could yield snap loads when under sudden tension after being slack.

For all simulations the effect of forward speed on sinkage and trim was taken into account by determining the calm water equilibrium position a priori and adapting the hull mesh accordingly. The effects of the tow line force on the trim and sinkage of the RHIB was included.

4. VALIDATION

The validation work focuses on the motions of the RHIB when towed alongside the patrol boat in waves. Obviously the motions of the RHIB are affected by the presence and motions of the patrol boat (wave shielding and radiation, tow line forces). Before examining the RHIB motions two aspects of the patrol boat hydrodynamics are discussed first: the wave shielding and fin generated wave.

4.1 Wave shielding

The data from a different test program are used here, see Carette et al 2016. Figure 7 shows a comparison between experimental and simulated wave amplitude amplification factors at the windward and leeward sides of the patrol boat aft body. The wave direction of 135 degrees denotes bow quartering waves on the starboard side. No stabilising fins are present. The circles show the experimental values while the PanShip result is shown through the contour plot in the area around the patrol boat. The wave amplitude amplification and reduction on the starboard and port sides respectively are well predicted, except that the wave amplification close to the starboard side is somewhat under-predicted by PanShip.

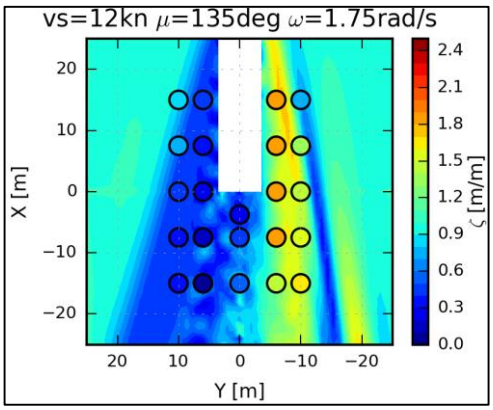

Figure 7 Comparison of simulated and experimental wave amplification and shielding.

4.2 Fin generated wave

It was shown in the previous section that the wave generated by the patrol boat stabilising fin has a marked effect on the RHIB motions. This aspect of hydrodynamic interaction can be included in the PanShip simulations by modelling the fin as a lifting surface shedding a trailing edge wake sheet with a time varying vortex strength. Figure 8 shows the wave pattern around the patrol boat aft body with and without the presence of the stabilising fin. For this case the speed was 10 knots and the fin had a zero incidence angle setting. The flow incidence was approximately 1°. Despite this low incidence angle the wave making effect of the fin is clear.

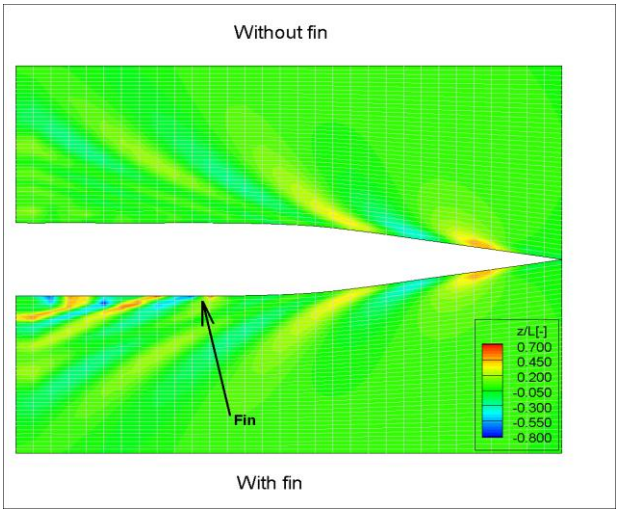

Figure 8 Wave pattern with and without fin.

Another way to show the effect of the fin is by inspecting the radiation forces exerted on the RHIB by the patrol boat. Figures 9 and 10 show the roll and yaw moment acting on the RHIB due to an impulsive patrol boat roll velocity, with and without the presence of the fin.

The roll and yaw excitation due to the patrol boat roll velocity, which results in fin lift forces and thereby flow disturbances, are clearly much larger due to the presence of the fin.

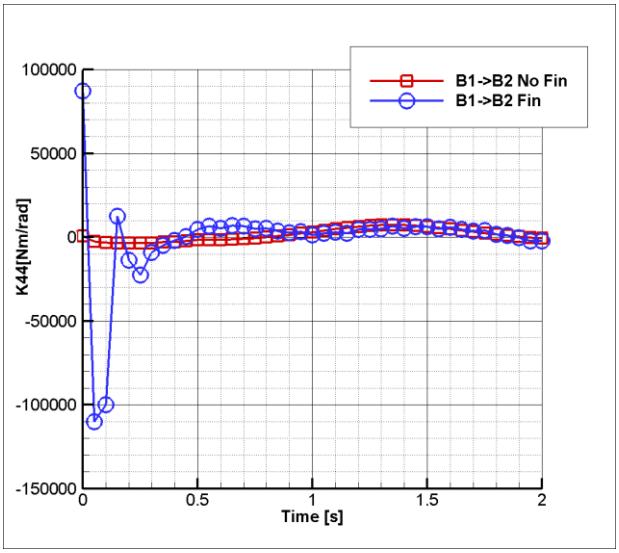

Figure 9 Roll moment on RHIB due to patrol boat roll velocity.

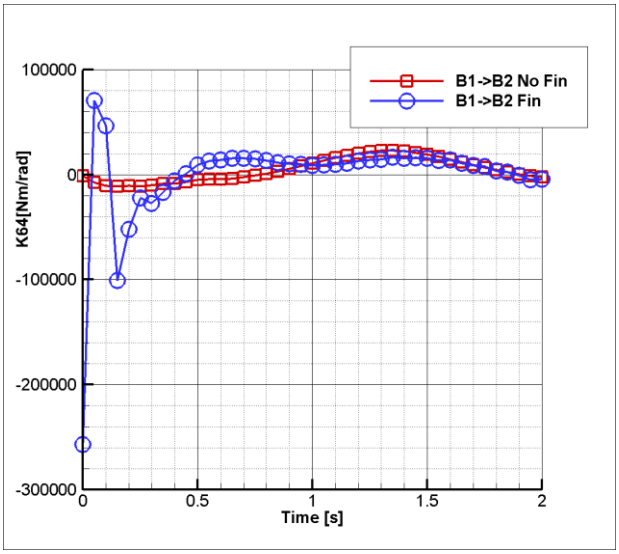

Figure 10 Yawing moment on RHIB due to patrol boat roll velocity.

4.3 RHIB manoeuvring coefficients

The problem of predicting the motions of an un-steered towed vessel in waves is a combined seakeeping and manoeuvring problem. The first part of the validation consists of comparing calculated manoeuvring coefficients with those obtained from Planar Motion Mechanism (PMM) model tests. The second part deals with the combined seakeeping and manoeuvring problem. Validation of PanShip for seakeeping of RHIBs is dealt with by Bird et al. 2017 and van Walree and Thomas 2017.

In PanShip the principal forces due to manoeuvring are obtained from the potential flow method by considering the hull as a low aspect ratio lifting surface. This is complemented by a cross-flow drag method to account for viscosity effects. Experience shows that this approach yields reasonably good results as long as there is no significant flow separation, i.e. the drift angle is limited in magnitude.

Figures 11 and 12 show a comparison between experimental and simulated manoeuvring coefficients for the RHIB whereby the following notation is used:

- Xuv: Longitudinal force at forward speed u due to drift velocity v.
- Xur: Longitudinal force at forward speed u due to yaw velocity r.
- Yuv: Transverse force at forward speed u due to drift velocity v.
- Yur: Transverse force at forward speed u due to yaw velocity r.
- Kuv: Heeling moment at forward speed u due to drift velocity v.
- Kur: Heeling moment at forward speed u due to yaw velocity r.
- Nuv: Yawing moment at forward speed u due to drift velocity v.
- Nur: Yawing moment at forward speed u due to yaw velocity r.

Forces and moments have been made non-dimensional on basis of:

- ½ρuvLT for Xuv and Yuv.
- ½ρuvL^{2}T for Kuv and Nuv.
- ½ρu^{2}rLT for Xur and Yur.
- ½ρu^{2}rL^{2}T for Kur and Nur.

L and T denote the hull length and draft, respectively. The forward speed is 8 knots (Froude number 0.54) and LL stands for the Light Load condition.

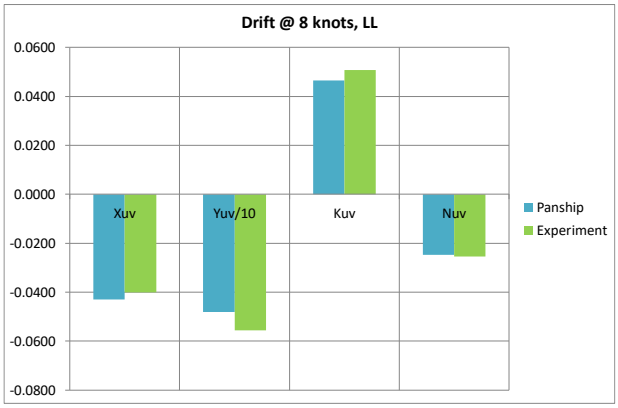

Figure 11 Comparison of force and moment coefficients due to drift angle

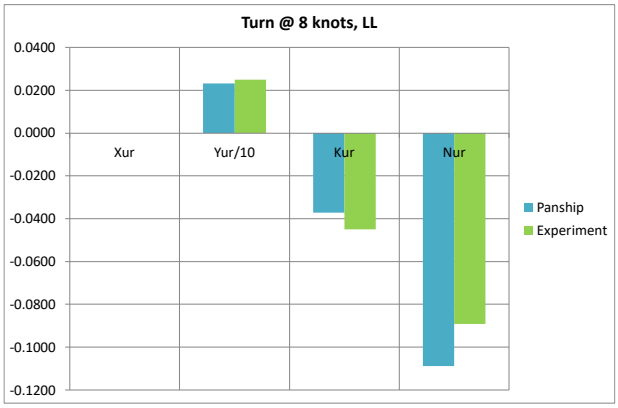

Figure 12 Comparison of force and moment coefficients due to yawing velocity

PanShip is seen to provide representative predictions for manoeuvring force and moment coefficients. It should be noted that the cross-flow drag coefficient has been tuned to obtain a good fit against the experimental data.

4.4 Validation for towed RHIB in waves

The problem of hydrodynamic interaction between two ships operating side-by-side is essentially a non-linear problem: when the separation of the two ships changes the hydrodynamic interaction changes as well. This means that the hydrodynamic properties should be updated each simulation time step. This is in principle possible, but requires a large amount of computing time. When the number of simulations is large such an approach would be impractical. In order to perform simulations within a reasonable amount of time, the impulse response option was used in PanShip. This means that retardation functions for hydrodynamic damping and wave diffraction were pre-computed and stored in a database for use in the time domain, together with body-exact wave excitation and restoring forces. The retardation functions were computed for the mean position of the two ships and for a constant (mean) speed.

A number of validation cases are presented here where results from PanShip side-by-side simulations are compared to model test data. The comparison includes the standard deviation of roll, pitch and yaw motions for two speeds and headings. A 20 degree heading means stern-quartering waves while 160 degrees means bow-quartering waves. For all cases the RHIB was positioned at the port side of the patrol boat, i.e. the leeward side.

The first configuration concerns the Stag Horn with Organic connection (SH/O), Full Load condition in SS4. Figures 13 through 15 show the standard deviations of the RHIB roll, pitch and yaw respectively for two speeds and headings.

The second configuration is the Bow Ring with Boom (BR/B), Full Load condition in SS4. Figures 16 through 18 show the roll, pitch and yaw standard deviations for the same conditions as described previously.

The plots show that the trends in standard deviation with speed and wave direction are generally well predicted by PanShip. The experimental and simulated yaw angles significantly reduce with increasing speed. This is due to the relatively high wave excitation forces at low speed. Except for the higher speed and 20 degrees heading, the BR/B configuration shows clearly higher yaw angle

standard deviations compared to the SH/O configuration. Differences in roll and pitch for the two towing configurations are less clear.

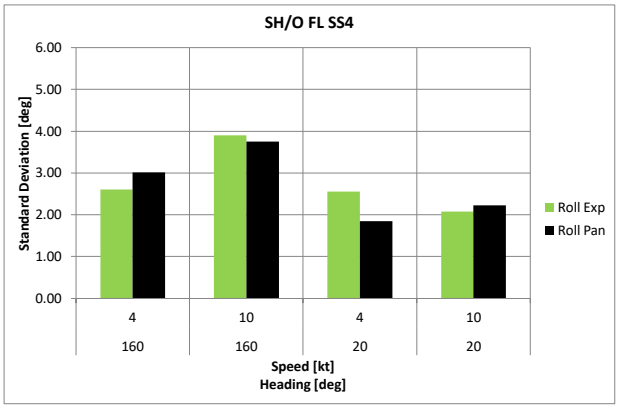

Figure 13 Comparison of roll

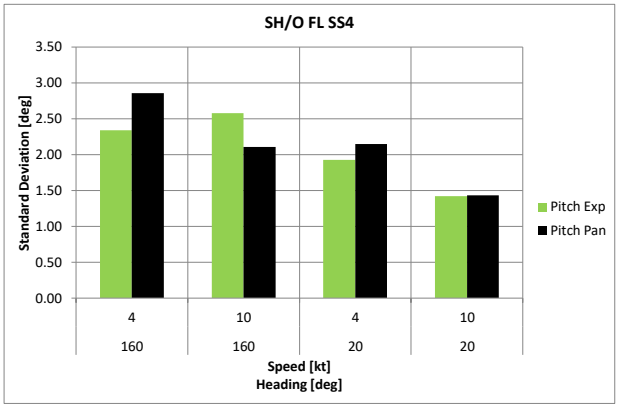

Figure 14 Comparison of pitch

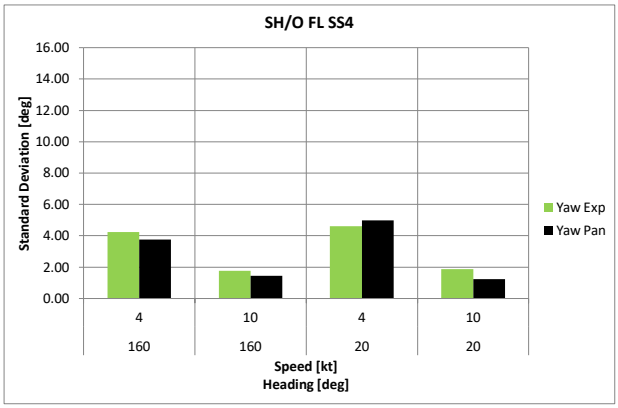

Figure 15 Comparison of yaw

The absolute values of the predicted standard deviation sometimes deviate from the experimental value. This is most likely a consequence of the linearisation applied to the hydrodynamic interaction problem whereby the RHIB is assumed to have a constant position relative to the ACPB. When the surge, sway and yaw motions of the towed RHIB are large this assumption is violated, particularly when considering the effect of the patrol boat fin, which is especially position-dependent.

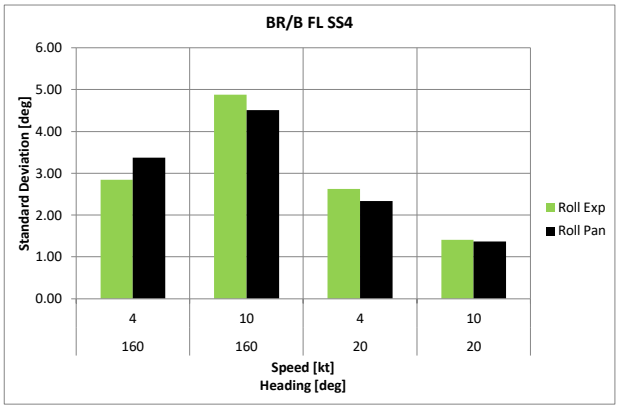

Figure 16 Comparison of roll

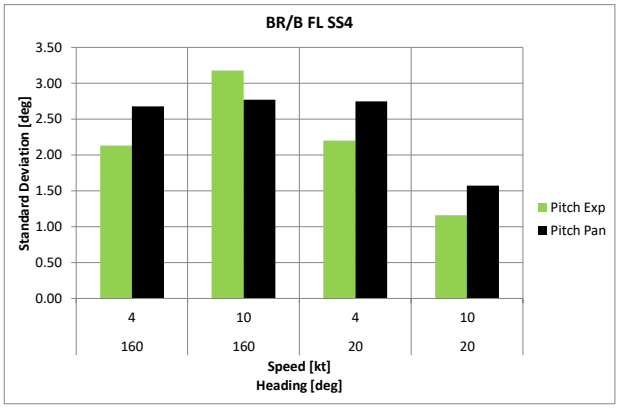

Figure 17 Comparison of pitch

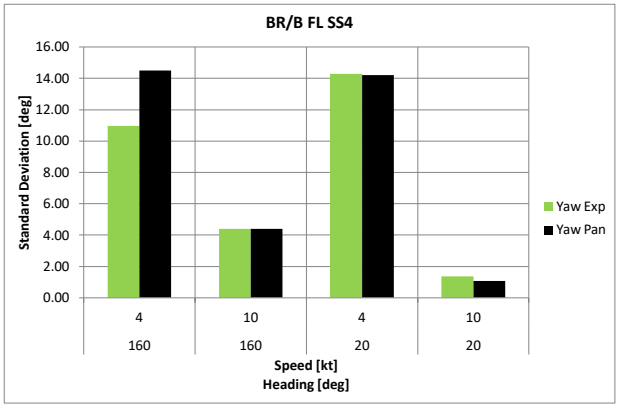

Figure 18 Comparison of yaw

Additional comparison data are provided for the RHIB forward speed and towline load (Ftow) standard deviation and the maximum towline load (Ftow-max). Figures 19 through 24 show the Full Load condition results for both tow configurations in SS4. It is seen that PanShip predicts the forward speed variations reasonably well. The forward speed variations are largest at a low speed, where the disturbing

wave effects are relatively large. Tow line load standard deviations and maximum values tend to be under-predicted by PanShip for the SH/O and BR/B towing configurations in bow quartering seas. The line loads are more difficult to predict than motions since highly non-linear snap loads frequently occur.

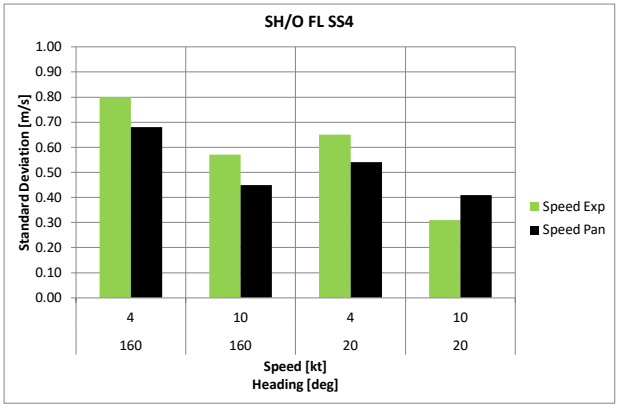

Figure 19 Comparison of speed variations

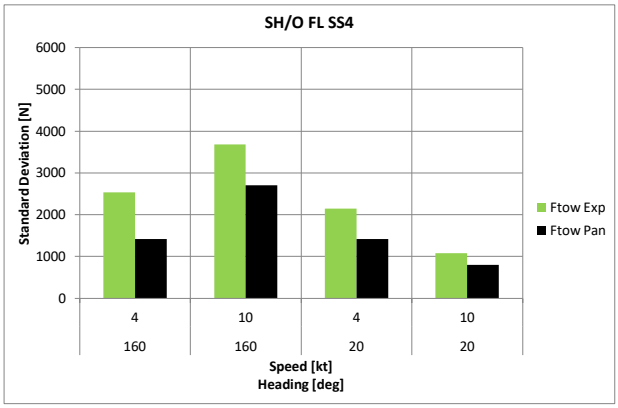

Figure 20 Comparison of tow line load variation

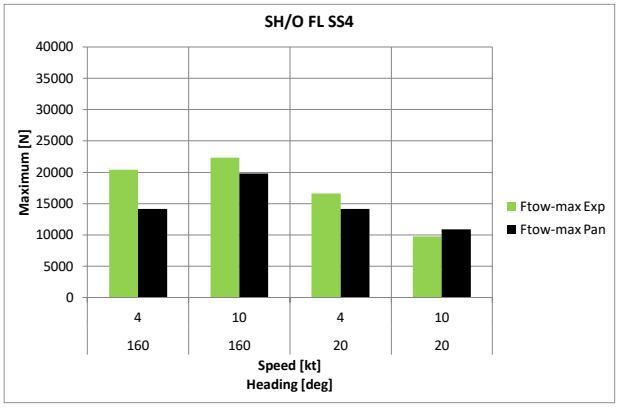

Figure 21 Comparison of maximum tow line load

The second configuration is the BR/B, Full Load condition in SS4, shown in Figures 22 through 24.

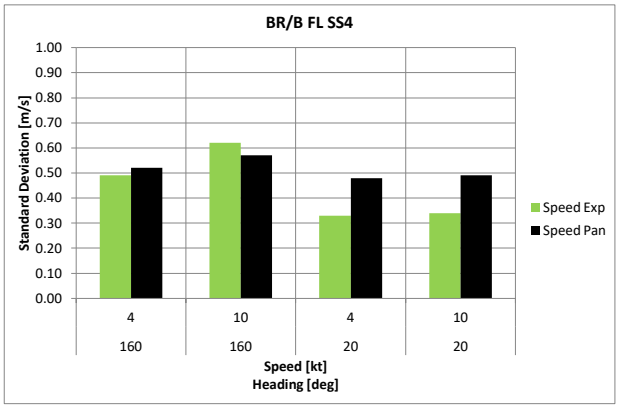

Figure 22 Comparison of speed variations

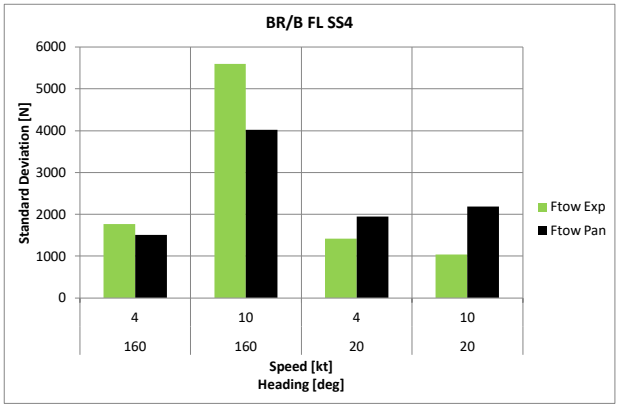

Figure 23 Comparison of tow line load variation

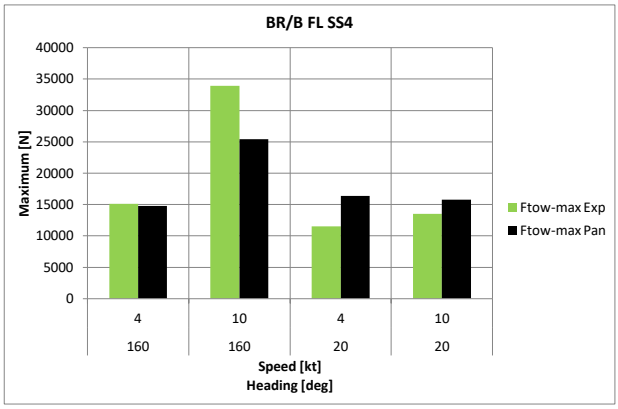

Figure 24 Comparison of maximum tow line load

5. CONCLUSIONS

A validation study on the time domain panel method PanShip has shown that:

- a potential flow approach, in combination with a tuned cross-flow drag method, can provide representative RHIB manoeuvring coefficients;
- Wave shielding and patrol boat fin

interaction effects can be included in the PanShip method;
- PanShip can provide representative predictions for standard deviations of roll, pitch and yaw motions for the two towing configurations analysed. The trends with forward speed and wave direction are generally well predicted.
- Predictions for tow line loads show larger differences with experimental values. This is thought to be caused by the influence of strongly non-linear snap loads.

6. ACKNOWLEDGEMENTS

The model test program was undertaken as part of the LAURA JIP (LAUnch and Recovery system for Any small navy craft Joint Industry Project). The authors acknowledge the permission granted by the consortium to utilise the experimental data.

7. REFERENCES

Bird, C., Walree F. van, Sgarioto, D., Thomas, W.L., and Turner T., 2017, "Validation of a Time Domain Panel Code for Predicting the Seakeeping Behaviour of a Rigid Hull Inflatable Boat", Proceedings of 14th International Conference of High Speed Sea Transportation, FAST'2017, Nantes, France.

Carette, N., Turner T., Mathew, J., Sgarioto, D., Hallmann, R., Walree F. van, Duffy, J., Denehy, S., and Macfarlane, G., 2016, "Physical Testing of Rigid Hull Inflatable Boat and Mothership Interactions for Launch and Recovery Simulation Validation", Proceedings of the Launch and Recovery Symposium 2016, LR'2016, Linthicum Heights, USA.

Jong P. de, 2011, "Seakeeping Behaviour of High Speed Ships", Ph.D. Thesis, Delft University of Technology, Netherlands.

Walree F. van, 2002, "Development, validation and application of a time domain seakeeping method for high-speed craft with a ride control system", Proceedings of 24th Symposium on Naval Hydrodynamics, Fukuoka, Japan.

Walree F. van, Sgarioto, D. and Turner T., 2016, "Validation of a Time Domain Panel Code for Prediction of Impulsive Loads on High Speed Ships", Proceedings of 31st Symposium on Naval Hydrodynamics, SNH'2016, Monterey, USA.

Walree F. van and Thomas W.L., 2017, "Development and Validation of a Time Domain panel Code for Prediction of Hydrodynamic Loads on High Speed Craft", Proceedings of 16th International Ship Stability Workshop, ISSW'2017, Belgrade, Serbia.

Capsizing phenomena due to water on deck with stern trim fishing vessel

Akihiko Matsuda, *National Research Institute of Fisheries Engineering* amatsuda@fra.affrc.go.jp

Yoshiaki Hirakawa, *Yokohama National University* hirakawa-yoshiaki-jd@ynu.ac.jp

Yuya Hara, *Yokohama National University*

Ko Taguchi, *Yokohama National University*

Yo Nambu, *Yokohama National University* nambu.yoh.desu@gmail.com

Ryuzo Takahashi, *National Research Institute of Fisheries Engineering* takahashiryuzo@affrc.go.jp

ABSTRACT

The second generation intact stability criteria are discussed at the International Maritime Organization (IMO). The criteria consist in 5 failure modes which are parametric roll, pure loss of stability, dead ship condition, broaching-to and excessive acceleration. Parametric roll and excessive acceleration are occurred by harmonizing between ship roll motion and wave. Pure loss of stability and broaching-to are occurred mainly with high speed voyage at the following and quartering seas. Naturally, dead ship condition is occurred with zero speed. In this study, we conducted free running model experiments by using over 20 Japanese fishing vessels to examine the causes of the capsizing. Mostly, the main causes of the capsizing are pure loss of stability, broaching-to and bow-diving because of characteristics of Japanese fishing vessels which are a high speed, a soft spring GZ curve and a low freeboard. However, a Japanese purse seiner of stern trim is capsized by water on deck with middle speed and not capsized with high speed and zero speed. Finally, we show the results of model experiments and discuss the capsizing phenomena.

Keywords: *at least 3 suitable keywords for indexing purposes*

1. INTRODUCTION

In 2008, 135GT Japanese purse seiner was capsized at anchoring with parachute anchor (JTSB, 2011a). In 2009, 135GT Japanese purse seiner was capsized at quartering heavy seas (JTSB, 2010). In 2010, Japanese trawler was capsized at head seas (JTSB, 2011b). More than 30 fishermen's lives were lost in these accidents. Therefore, we consider it is necessary to examine the cause of the capsizing phenomena to reduce the number of these accidents.

The second generation intact stability criteria are discussed at the International Maritime Organization (IMO). The criteria consist in 5 failure modes which are parametric roll, pure loss of stability, dead ship condition, broaching-to and excessive acceleration (IMO (2015), (2016)). Parametric roll and excessive acceleration are occurred by harmonizing between ship roll motion and wave. Pure loss of stability and broaching-to are occurred mainly with high speed voyage at the following and quartering seas. Naturally, dead ship condition is occurred with zero speed.

On the other hand, small fishing vessels have low free board and large bulwark. It is considered that water on deck is one of the most dangerous phenomena for small fishing vessels. Safety and stability of small fishing vessels due to water on deck are phenomena of strong non-linearity. There are many experimental and theoretical studies. (Grochowalski, (1989), Huang et.al. (1995), Francescutto et.al. (2009))

In this study, we conducted free running model experiments by using over 20 Japanese fishing vessels to clarify the cause of the capsizing. Mostly, the main causes of the capsizing are pure loss of stability, broaching-to and bow-diving because of characteristics of Japanese fishing vessels which are a high speed, a soft spring GZ curve and a low freeboard. (Matsuda et.al. (2017)) However, a Japanese purse seiner of stern trim is capsized by water on deck with middle speed and not capsized with high speed and zero speed. Finally, we show the results of model experiments and discuss the capsizing phenomena.

2. FREE RUNNING MODEL EXPERIMENTS

2.1 Experimental system

Free running model experiments are conducted in Marine Dynamics Basin at NRIFE shown in Fig.1.

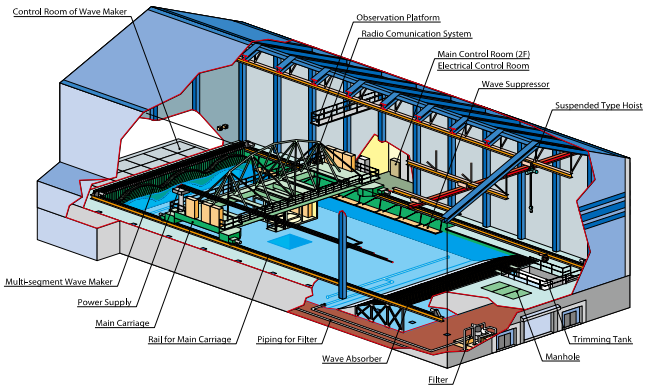

Figure1 Marine Dynamics Basin in NRIFE

The basin is a tank of 60m long, 25m wide, with a depth of 3.2m. The tank includes 80 segmented plunger type wave makers.

The model was controlled by "Model Motion Tracking System" (Matsuda et.al. (2016)).

Principal particulars of subject model ship are shown in Table.1 and the photo of model is shown in Fig. 2. GZ curve is shown in Fig.3. The characteristics of GZ curve is a soft spring type.

Table.1 Principal Particulars of model ship

Lpp	2.313m
B	0.494m
D	0.202m
Draft(fore)	0.062m
Draft(midship)	0.184m
Draft(aft)	0.215m
Displacement	$0.124m^3$
GM	0.093m

Figure 2 Model ship

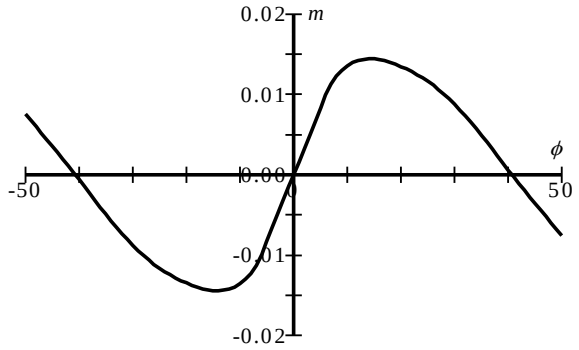

Figure 3 GZ curve

2.2 Experimental results and discussion

Experimental conditions are shown in Table 2 and experimental results are shown in Figures 4-6. Coordinate system is shown in Fig.7.

In λ/L=1.0 case, capsizing phenomena did not occur. In λ/L=1.25 and 1.5 cases, the model ship capsized at low speed with water on deck. On the other hand, capsizing phenomena did not occur with high speed more than Fn=0.3. A bow-diving phenomena occurs at Fn=0.405. However, this type of Japanese purse seiner cannot speed up over 13knots (Fn=0.35), and usually there is no dangerous phenomena with high speed. In these wave conditions, there was no dangerous phenomena occurred at dead ship conditions.

Table.2 Experimental Conditions

Model Speed	Fn=0.405, 0.351, 0.270, 0.216, 0.135
Wave Length	λ/L=1.0, 1.25, 1.5
Wave Height	H/ λ=1/10
Heading	χ=-5, -15, -30 degrees

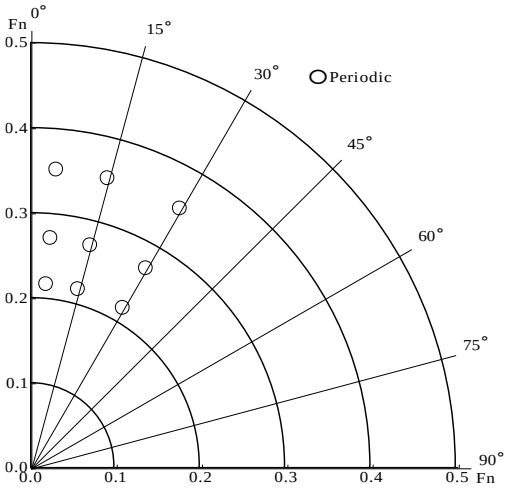

Figure 4 Experimental Results (λ/L=1.0)

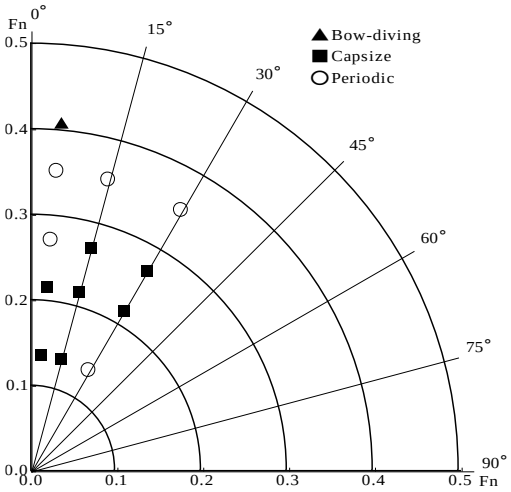

Figure 5 Experimental Results (λ/L=1.25)

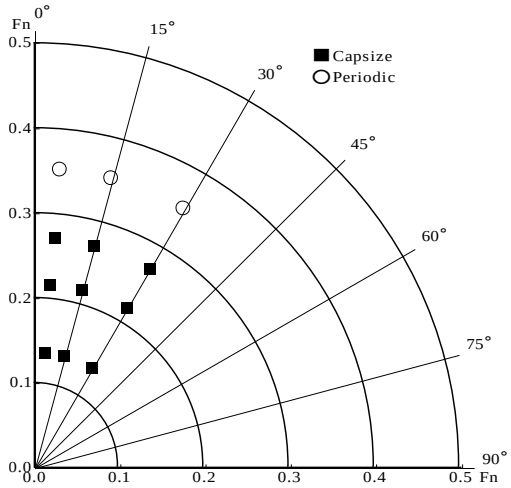

Figure 6 Experimental Results (λ/L=1.5)

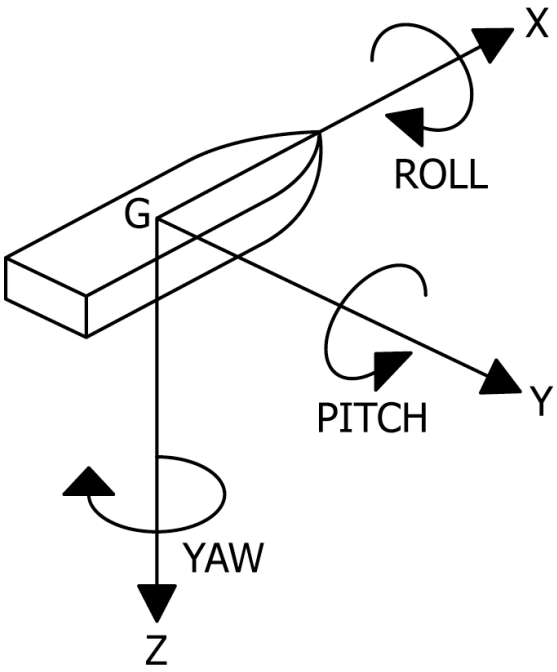

Figure 7 Coordinate system

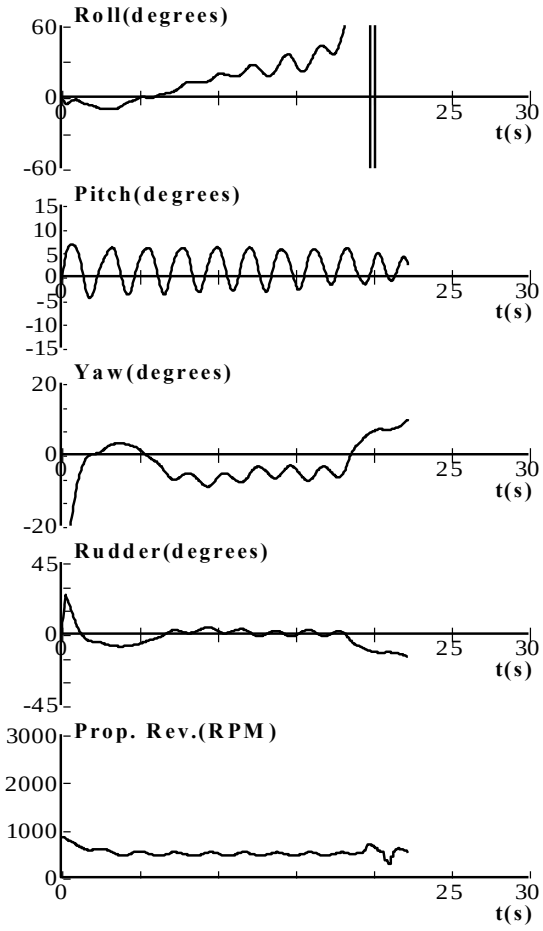

Figure 8 Time series (λ/L=1.25, H/ λ=1/10, Fn=0.270, χ=-5 degrees)

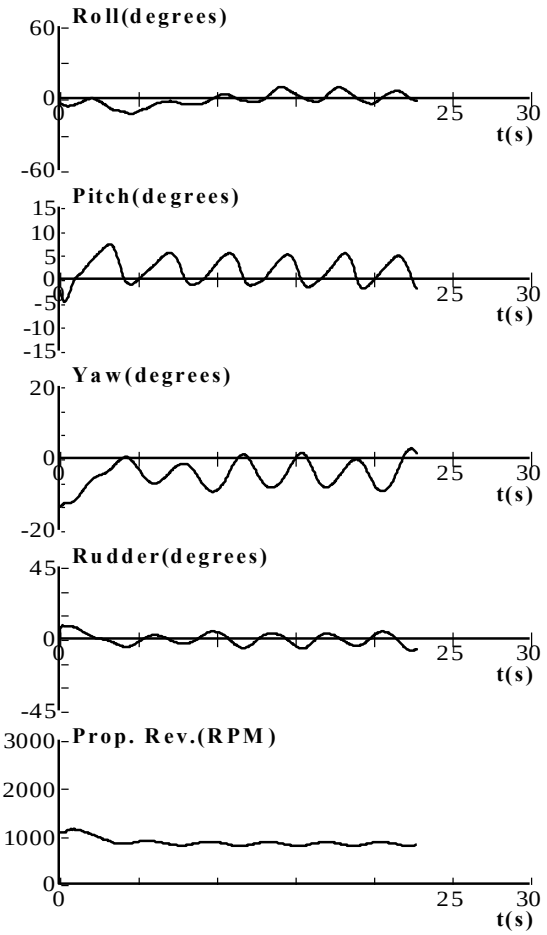

Figure 9 Time series (λ/L=1.25, H/ λ=1/10, Fn=0.351, χ=-5 degrees)

Time Series of capsizing is shown in Fig.8 and the ship motion is shown in Photo 1. It shows monotonic increasing of roll angle was caused by water on deck from stern and finally, the model was capsized. However, by changing speed as Fn= 0.270 to 0.351, the model was able to avoid a capsizing. Time series of attitude due to ship speed is shown in Fig.9 and the ship motion is shown in Photo 2. There was no water on deck and she was able to avoid capsizing.

To investigate the water on deck, the attitude of model was measured in calm water. The result is shown in Fig.10. The data shows that pitch angle and heave are approximately constant. However both of them changed to stern up and it avoided water on deck due to the wave from stern except pitch angle at

Fn=0.351. Time series of pitch angles are shown in Fig.11. Pitch angles were constant after 30 seconds. Our model basin does not have enough length at Fn=0.351. It is considered that the stable pitch angle at Fn=0.351 decreases.

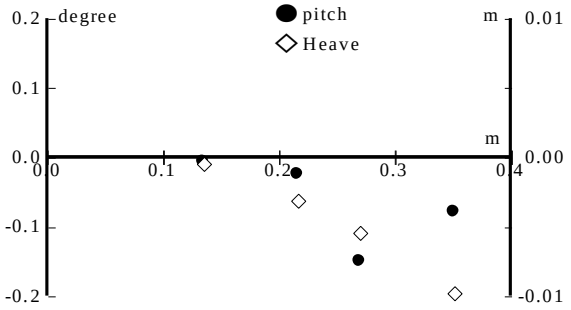

Figure 10 Attitude due to ship speed in calm water

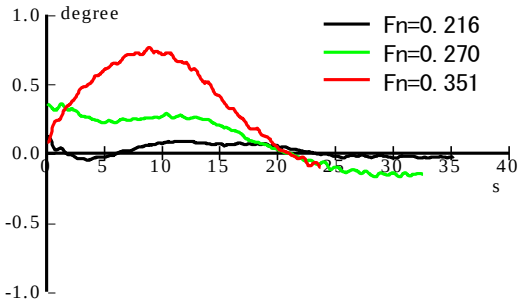

Figure 11 Time Series of pitch angles in calm water

3. CONCLUSION

In this study we conclude as follows.

1. A Japanese purse seiner of stern trim was capsized by water on deck with middle speed and did not capsize with high speed and zero speed.

2. The cause of capsizing was water on deck due to small freeboard at stern.

3. Attitude of heave and pitch due to high speed avoided water on deck at stern.

4. REFERENCES

Francescutto, A., Bulian, G., Larios, M., U., and Ulloa, M., A., "Stability and dynamical effects of water on deck on the survivability of small fishing vessels", Ship Science & Technology, 2009.

Grochowalski, S., "Investigation into the physics of ship capsizing by combined captive and free-running model tests", Transaction of SNAME, Vol.97, 1989.

Huang, J., Cong, L., Grochowalski, S., and Hsiung, C.-C., "Capsize analysis for ships with water shipping on and off the deck", Twenty-Second Symposium on Naval Hydrodynamics, Washington, D.C., 1999.

IMO, 2015, SDC 2/WP.4, Development of Second Generation Intact Stability Criteria. Report of the Working Group, London, UK.

IMO, 2016, SDC 3/WP.5, Development of Second Generation Intact Stability Criteria. Report of the Working Group, London, UK.

JTSB (Japan Transport Safety Board) (2010) "Capsize of FV Daiei Maru No.11", Marine Accident Investigation Report, MA-2010-5, Vol. 2, May 2010, pp.1-54, http://www.mlit.go.jp/jtsb/ship/rep-acci/2010/MA2010-5-2_2009tk0006.pdf, (downloaded on 27 July 2018), (in Japanese)

JTSB (Japan Transport Safety Board) (2011a) "Sunk of FV Suwa Maru No.58", Marine Accident Investigation Report, MA-2011-4, Vol. 2, Apr. 2011, pp.1-108, http://www.mlit.go.jp/jtsb/ship/rep-acci/2011/MA2011-4-2_2008tk0002.pdf, (downloaded on 27 July 2018), (in Japanese).

JTSB (Japan Transport Safety Board) (2011b) "Sunk of FV Yamada Maru No.2", Marine Accident Investigation Report, MA-2011-11, Vol. 8, Nov. 2011, pp.1-55,

http://www.mlit.go.jp/jtsb/ship/rep-acci/2011/MA2011-11-8_2010tk0001.pdf, (downloaded on 27 July 2018), (in Japanese).

Matsuda, A., Hashimoto, H., Terada, D. and Taniguchi, Y., 2016, "Validation of Free running Model Experiments in Heavy Seas", Proceedings of 3rd International Conference on Violent Flows(VF-2016), Osaka, Japan

Matsuda, A., Terada, D. and Hashimoto, H., 2017, "The Characterisitics of Capsizing Phenomena of Japanese Fishing Vessels", Proceedings of the 16th International Ship Stability Workshop, Belgrade, Serbia

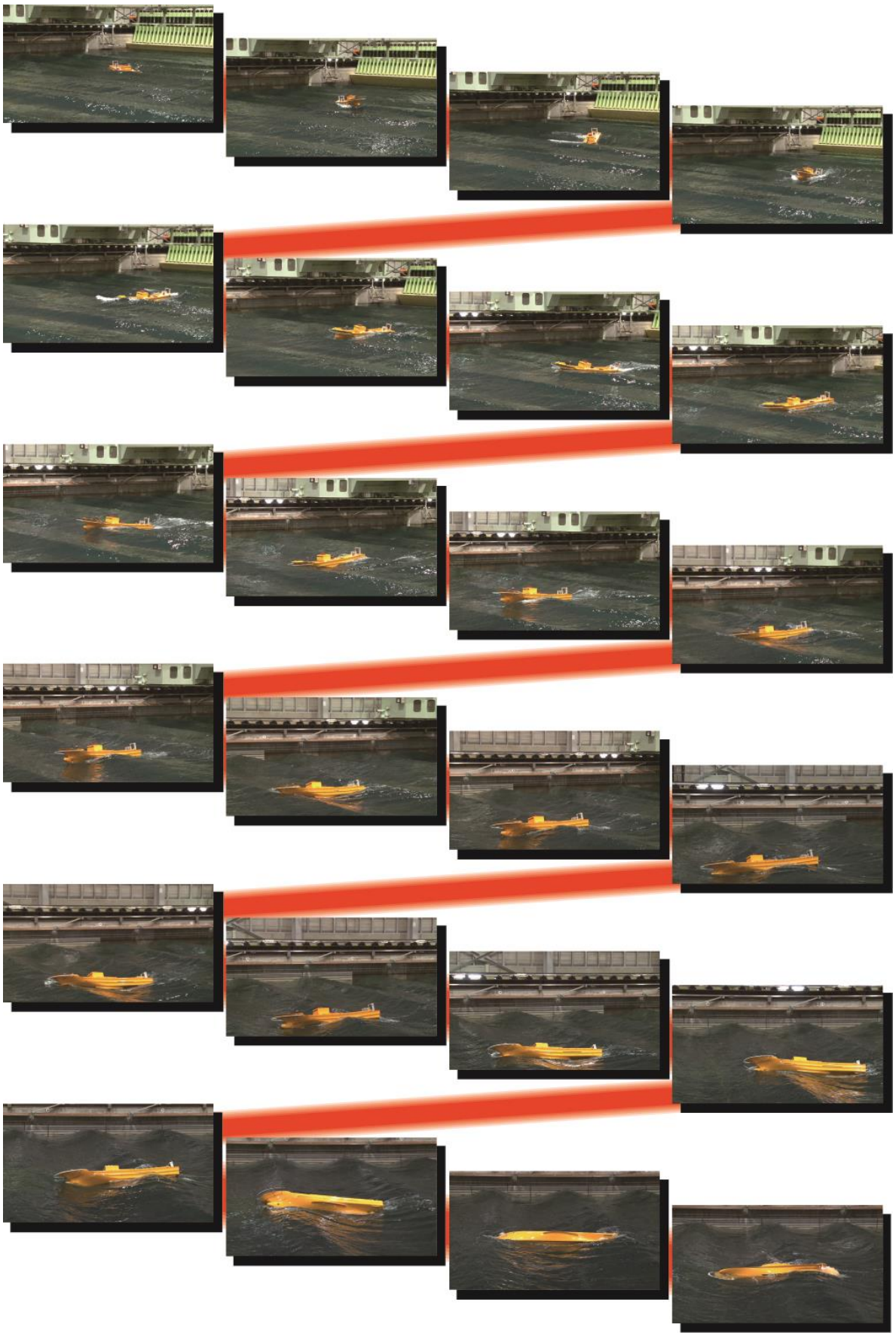

Photo 1 Experimental Results (λ/L=1.25, H/ λ=1/10, Fn=0.270, χ=-5 degrees)

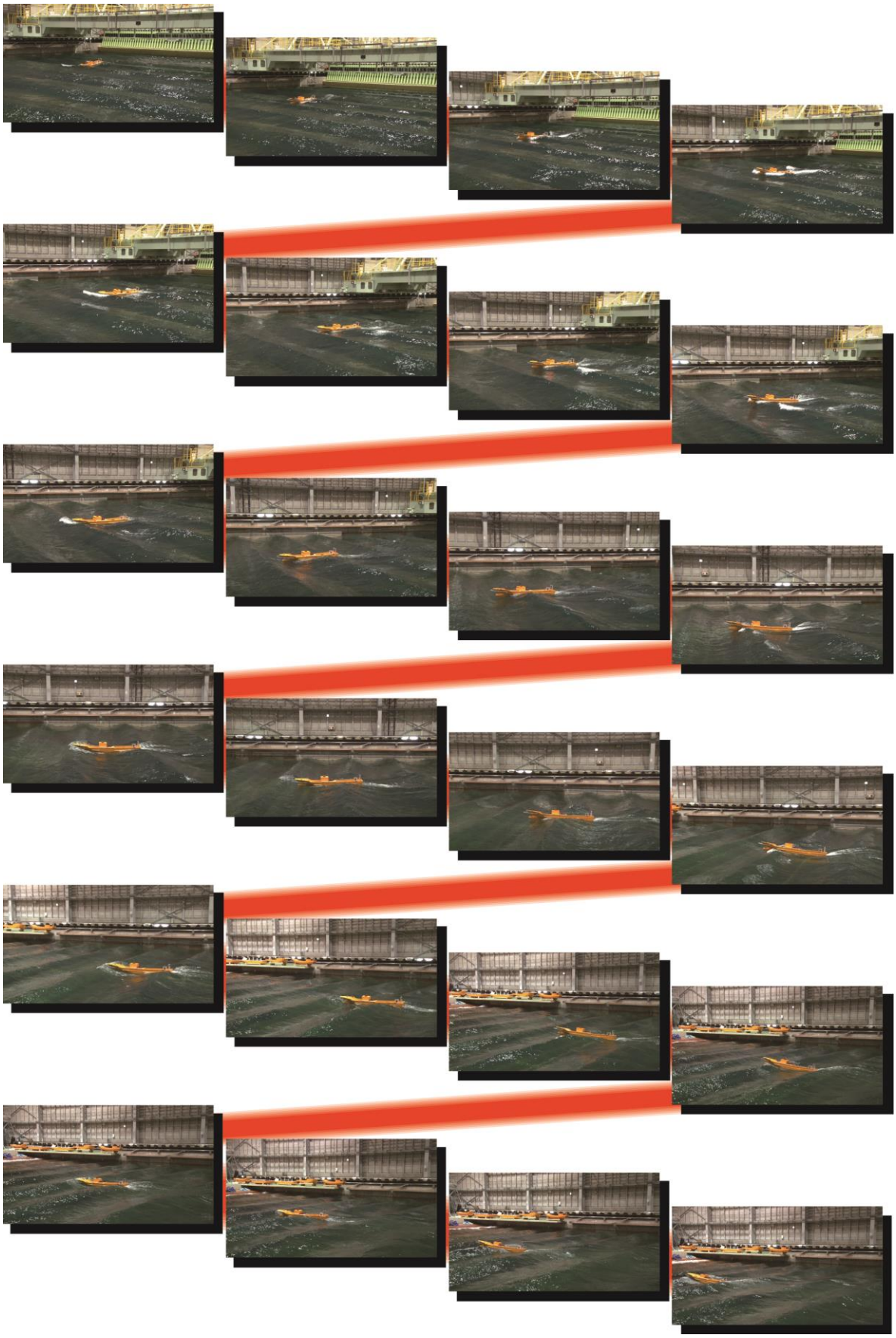

Photo 2 Experimental Results (λ/L=1.25, H/ λ=1/10, Fn=0.351, χ=-5 degrees)

Water-on-Deck Effects on Roll Motions of an Offshore Supply Vessel in Regular Stern Quartering Waves

Su Sandy Htun, *Osaka University* su_sandy_htun@naoe.eng.osaka-u.ac.jp

Naoya Umeda, *Osaka University* umeda@naoe.eng.osaka-u.ac.jp

Masahiro Sakai, *Osaka University* masahiro_sakai@naoe.eng.osaka-u.ac.jp

Akihiko Matsuda, *National Research Institute of Fisheries Engineering* amatsuda@fra.affrc.go.jp

Daisuke Terada, *National Research Institute of Fisheries Engineering* dterada@fra.affrc.go.jp

ABSTRACT

The applicability of the second generation intact stability criteria for preventing pure loss of stability in astern waves to offshore supply vessels (OSV) is investigated. OSVs show an inconsistency problem in the first and second level criteria. Thus, free-running model experiments of an OSV by changing its length of low weather deck in regular stern quartering waves were conducted and were compared with numerical simulation used for pure loss of stability so far. As a result, it was confirmed that the effects of water on deck (WOD) on the behaviour of OSV could prevent the occurrence of typical pure loss of stability for the cases of long low weather deck. One is its effects is the increase of roll damping due to WOD and the other is the loss of static stability due to WOD.

Keywords: *offshore supply vessel, water on deck, pure loss of stability, roll damping, bulwark*

1. INTRODUCTION

At the International Maritime Organization (IMO), the second generation intact stability criteria are currently under development. These criteria are physics-based, consisting of two-levelled vulnerability criteria and direct stability assessment. They are designed to cover five major failure modes such as pure loss of stability, parametric roll, surfing and broaching, dead ship condition and excessive acceleration.

For pure loss of stability failure mode, the level 1 and level 2 criteria developed at the IMO utilize the metacentric height (GM) and righting arm (GZ) in longitudinal waves, respectively (IMO, 2015). The sample calculations performed by two delegations (Japan, 2018) indicate that offshore supply vessels easily pass the lowest level (level 1) criteria but often fail to pass the second level (level 2). This suggests that draft criteria may overlook some physics. Thus, the current vulnerability criteria are allowed not to be applied to a vessel with extended low weather deck due to increased likelihood of water on deck or deck-in water. However, the definition of the extended low weather deck was not yet established until now. Therefore, one of the remaining issues is the applicability of criteria for preventing pure loss of stability in astern waves to offshore supply vessels (OSV).

OSVs are essential needs in the offshore oilfield business and these vessels are required to operate and work in the harsh environments. OSVs often have extended low weather decks about half the ship length which is surrounded by bulwarks with freeing ports. Among the

different types of OSVs, some often have no bulwarks at stern end because of operational purpose such as anchor handling and towing. Thus, in heavy seas, large amount of water can be trapped on the weather deck. This may be one of factors that the draft criteria overlook. There are some reports of accidents of offshore supply vessels such as M/V Sabine Seashore and M/V Laverne Herbert which include capsizing and loss of ship where water on deck could have been one of the causes (NTSB 1978 & 1983).

Many researchers studied the effect of water on deck concerning with fishing vessels and OSVs. Dillingham (1981) performed numerical simulation of 2D flow of water on deck of a fishing vessel in beam seas. Falzarano et al (2002) improved this method to apply to 3D flow of water on deck of an OSV in beam seas. Both concluded by numerical simulations that the water on deck reduces the roll but not always. Umeda, Aqmil et al (2016) performed a model experiment of an OSV in regular stern quartering waves and compared it with numerical model proposed by Kubo et al (2012). They found that there were no severe roll at high speed but there was large heel at low speed. These results cannot be explained by the simulation which does not take into account of the water on deck.

In this research, the effect of low weather deck length and the effect of WOD on the behaviour of OSV in regular stern quartering seas are investigated. Free running model experiments of OSVs are performed with models having the same hull form but with different low weather deck lengths. Also, the experiment results are compared with numerical simulation which considers the WOD effect.

2. MODEL EXPERIMENT

2.1 Subject Ship

Free running model experiment was performed at the seakeeping and manoeuvring basin at the National Research Institute of Fishery Engineering. The ship model used is the same one as in Umeda, Aqmil et al (2016). Principal particulars of the OSV are shown in Table 1. The vessel has a deck house in the bow part and a low weather deck from its midship to aft end. It has twin propellers and twin rudders. Model scale of 1:30 is used for the model experiment.

Table 1 Principal particulars of the OSV

	Ship scale	Model scale
Length, Lpp	60.00 m	2.00 m
Breadth, B	16.40 m	0.546 m
Depth, D	7.20 m	0.24 m
Moulded draught, d	6.00 m	0.20 m
Metacentric height, GM	1.45 m	0.048 m
Natural roll period, T_φ	11.5 s	2.1 s

2.2 Experiment Condition

The experiment procedures were based on the ITTC (International Towing Tank Committee) recommended procedures for intact stability model test (ITTC, 2008). Propulsion power was supplied from the rechargeable batteries which were placed inside the model hull. The ship model was equipped with an optical fibre gyroscope to get the roll angle, pitch angle, and yaw angle, propeller rate and rudder angle, steering gear and a PD autopilot for course keeping. Water surface elevation was measured by a servo-needle type wave probe attached to the towing carriage of the basin near wave maker. Instantaneous position of the model relative to the basin was measured with total station system.

To modify the length of low weather deck of original vessel, three additional decks are added systematically. Each additional deck has equal length of 14.73 meters and is watertight. They have the same width as width between bulwarks and same height as bulwark height. Based on the mode of addition, the ship model was modified into four cases as shown in Table 2. Here, *l* refers to the length of low weather deck measured from AP.

Table 2 Lengths of low weather deck and GMs of four model cases (ship scale)

	Length of low weather deck, *l*	l/L_{pp}	GM
Original OSV	39.94 m	0.67	1.45 m
Case 1	0 m	0.0	1.45 m
Case 2	10.48 m	0.17	1.45 m
Case 3	25.21 m	0.42	1.45 m
Case 4	25.21 m	0.42	1.053 m

For Case 1, all three additional decks are added. For Case 2, two additional decks are added. For Case 3, only one additional deck is added. The metacentric heights of models of Case 1, Case 2 and Case 3 are kept the same as that of original model. For Case 4, the condition is the same as Case 3 but the metacentric height is reduced from 1.45m to 1.053m, with which the ship marginally complies with IS Code 2008, to exclude the additional buoyancy due to extended superstructure. The displacements of all model cases are kept the same as that of original model. Model ships of all four cases are shown in Figure 1.

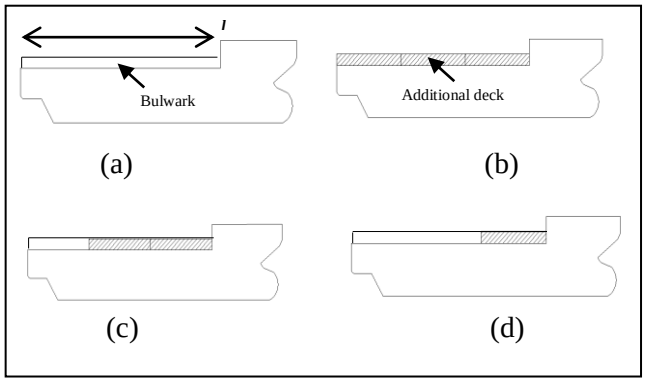

Figure 1 Deck layouts of (a) original model, (b) Case 1 model, (c) Case 2 model, (d) Case 3 and Case 4 model

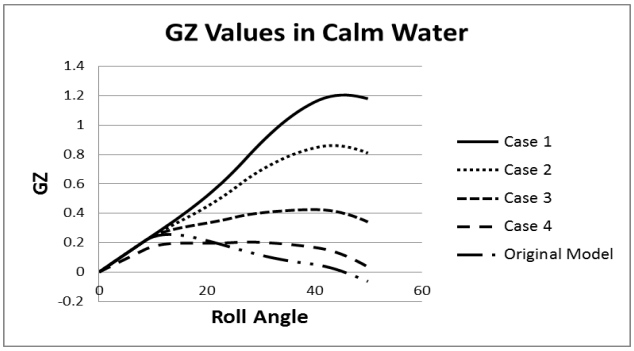

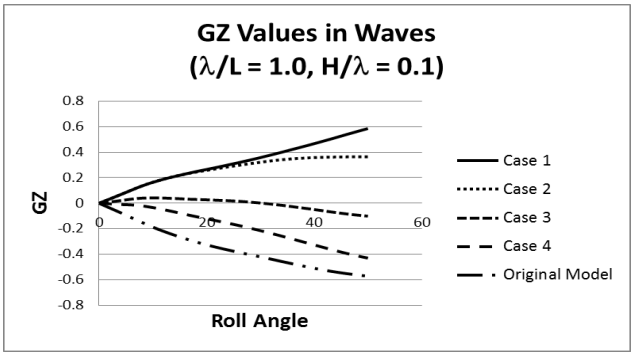

Figure 2 Righting arm curves in calm water and in waves.

Free running model experiments were conducted for regular waves of two wave cases: one is the wavelength to ship length ratio, λ/L, of 1.0, and the wave steepness, H/λ, of 0.1; the other is λ/L of 1.5 and H/λ of 0.1. The heading angle was 30 degrees from the wave direction and the tested Froude numbers ranged from 0.15 to 0.37.

The model was situated near the wave maker first. After the wave train propagated enough in

the model basin, the model propeller revolutions were increased to the specified value to achieve the required speed and the steering system activated. Several runs were performed with possible combinations of wave conditions and speeds.

The righting arm curves of all four model cases in calm water and in waves with λ/L of 1.0 and H/λ of 0.1 are shown in Figure 2. For comparison sake, the righting arm curve of the original model (Umeda, Aqmil et al, 2016) is also included.

3. EXPERIMENT RESULTS AND DISCUSSION

3.1 Pure Loss Level 2 Criteria Check

First of all, Case 1, Case 2 and Case 3 models are checked with draft pure loss level 2 criteria (IMO, 2015). In level 2 criteria, there are two criteria values: CR1 and CR2. CR1 is a criterion based on the calculation of the angle of vanishing stability. CR2 is a criterion based on the calculation of the angle of heel under the action of heeling lever.

The results are shown in Figure 3 which shows the relationship between the lengths of low weather deck and the level 2 index values. When the length of low weather deck increases, the index values increase. This is because more GZ values are reduced in waves when the model has longer low weather deck. Even negative righting arms can appear when a wave crest is at amidships for models with larger lengths of low weather decks. It is obvious from Figure 3 that the restoring moment can be decreased and the cases were judged as dangerous by the level 2 criteria when the low weather deck length is longer than 0.4 L_{pp}. This means that Case 1 and Case 2 models are safe for pure loss while Case 3 and original design can be vulnerable to pure loss.

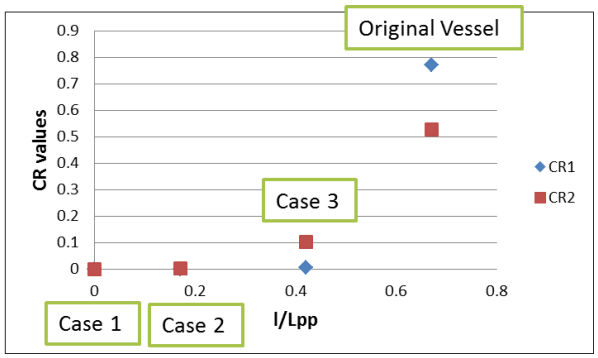

Figure 3 Level 2 criteria check results

3.2 Model Experiment Results

The results from the model experiment for the wave case of λ/L of 1.5 and H/λ of 0.1 are shown in Figure 4. Here, the maximum roll angles recorded in the free running experiment for different Froude number are shown. For comparison sake, the experiment result of the original model (Umeda, Aqmil et al., 2016) is also included.

For Case 1, Case 2 and Case 3 models, the roll angles are not so large and also no tendency of pure loss of stability. In a typical pure loss of stability phenomenon, the roll amplitude usually increases with increasing speed. The level 2 criteria check, however, indicates that the model of Case 3 can be vulnerable to pure loss. There are some contradictions between the level 2 criteria result and the experiment results. For Case 4, large roll angles are found for the Froude number smaller than 0.25. This behaviour is similar to that of the original model. During the experiment, it was found that a large amount of water entered from the stern end for this case and despite the egress through the freeing ports, the ingress from the stern was much larger. Thus, this large roll angles can be considered due to the static heeling moment of large volume of trapped water on deck.

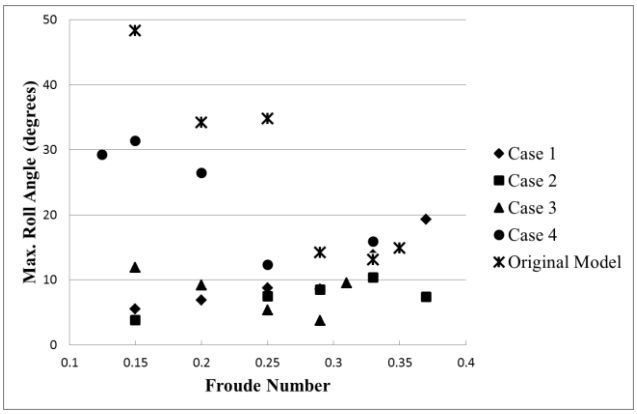

Figure 4 Experiment results of all four model cases compared with original model result (λ/L = 1.5 and H/λ = 0.1)

4. NUMERICAL SIMULATION

4.1 Simulation without WOD

Numerical simulation using a coupled surge-sway-yaw-roll (4DOF) model developed by Kubo et al. (2012) which is based on the manoeuvring model for ships in calm water by Hirano and Takashima is applied. The linear wave-induced forces and moments are calculated by a slender body theory with low encounter frequency assumption (Umeda et al., 1995). The roll restoring arm variation is estimated with Grim's effective wave concept.

The comparison between the experiment results and simulation results are shown in Figure 5. Here, the wave condition is λ/L of 1.5 and H/λ of 0.1. Froude number, Fn, is 0.15 for Case 1, 0.29 for Case 2 and Case 3 and 0.15 for Case 4. For Case 1, the model has no low weather deck so that also no WOD. There is good agreement in the amplitudes between the simulation result and the experiment result. For Case 2 and Case 3, it can be seen that the simulation result overestimates the roll motion. The models in both cases have low weather deck and therefore a certain amount of water can enter and be trapped. If some phase lag exists between the trapped water and the ship roll motion, the water may act as anti-rolling device. Nevertheless, this simulation does not take into account of this effect. For Case 4, the simulation result and the experiment result are even qualitatively different. A certain mean heel angle exists due to the static heeling moment of trapped water which might be in phase with the ship roll motion. Also, here, the simulation does not take into account of this heeling moment.

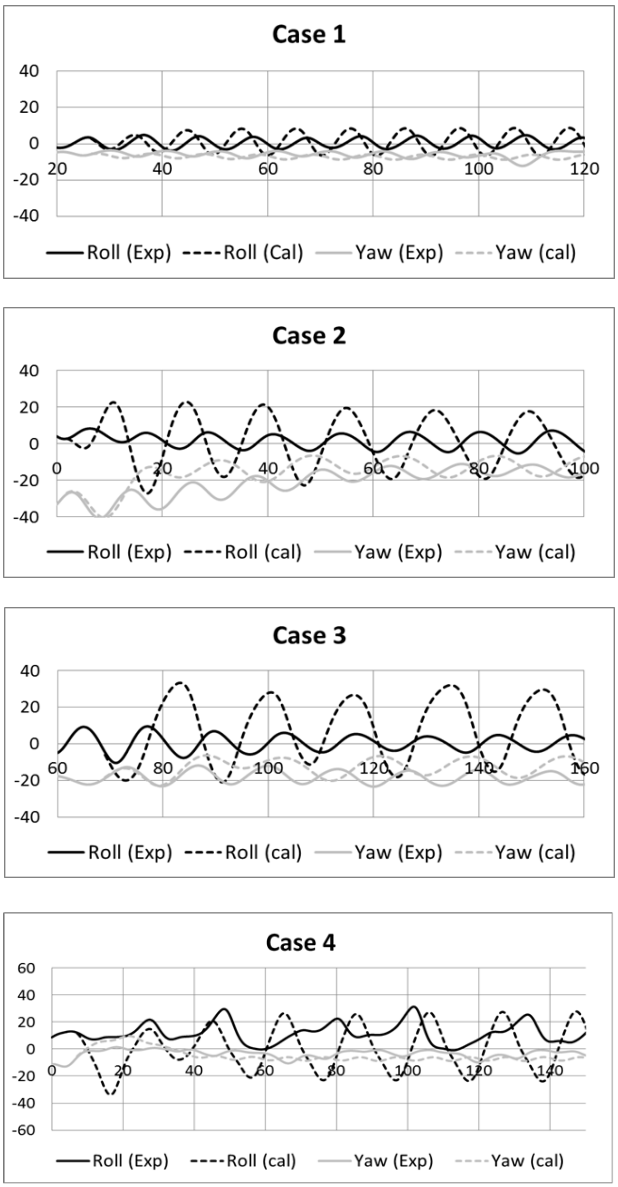

Figure 5 Comparison of simulation results without WOD effect and experiment results (λ/L=1.5 and H/λ=0.1)

4.2 Water on Deck Effect

Water trapped on deck may sometimes act as an anti-rolling mechanism when there is a phase lag between the trapped water natural frequency and ship roll motion frequency. To examine if this is the case, two roll decay tests were performed during the experiment: small angel roll decay tests and large angle roll decay tests. For the small angle tests, an initial heel angle of about 10 degrees was given to the model and then released. No water entered from the freeing ports. This can be considered as roll damping due to hull only. For the large angle tests, an initial heel angle of about 25 degrees was given to the model and released. Some water entered from the freeing ports. So, the latter test results included the WOD effect. The roll extinction curves of these two kinds of tests are shown in Figure 6. It can be seen that the damping with WOD increases compared with the one without WOD. Generally, it can be concluded that WOD plays a somewhat important role in the roll damping of this ship model. Therefore, roll damping of this OSV should be provided as the sum of the damping due to hull only and the damping due to WOD. For the hull only damping, the data from the small angle roll decay tests can be used.

For the damping due to WOD, the ITTC recommended formula (ITTC 7.5-02-07-04.5, 2011) for the equivalent linear roll damping due to flooded water, as shown in (1), is attempted to use. The estimation formula is based on the database obtained from a systematic model experiment by Katayama et al. (2009) and Ikeda et al. (2008).

$$B_{44IW} = A\left(\frac{h}{B_{comp}}, \phi_a, \frac{OG}{B}\right) \times C\left(\omega_E, \frac{h}{B_{comp}}\right)^{B\left(\frac{h}{Bcomp}, \phi_a\right)} \times \exp\left\{-C\left(\omega_E, \frac{h}{B_{comp}}\right)^{B\left(\frac{h}{Bcomp}, \phi_a\right)}\right\} \times \frac{l_{comp}}{B_{comp}} \rho B_{comp}^5 \sqrt{\frac{2g}{B_{comp}}} \quad (1)$$

where h is the water depth, l_{comp} and B_{comp} are the length and the breadth of flooding compartment, respectively. ρ and g are the density of fluid and the acceleration of gravity, respectively. ω_E is the roll frequency and ϕ_a is the roll amplitude.

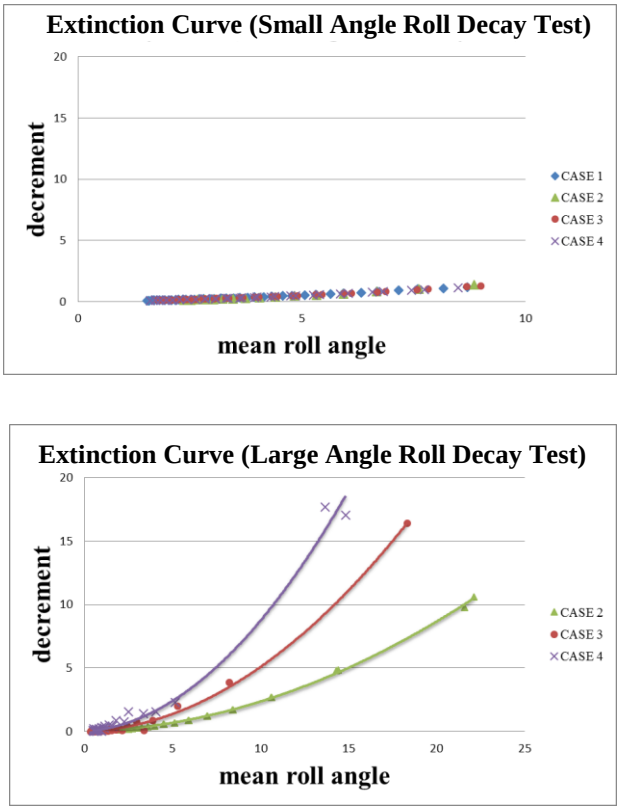

Figure 6 Roll extinction curves of free roll tests with and without water on deck

In applying this equation to the ship model, the deck is considered as a tank with the length equal to the length of low weather deck, the breadth equal to the width between bulwarks and the height equal to the bulwark height. This estimation equation is used to calculate the additional damping due to WOD. The feasible range of water that can be trapped on deck is first estimated for a particular speed and for an average roll angle for that condition. Then, a certain depth of water is assumed to be trapped within the bulwarks of ship, the freeing ports are assumed to be closed and then the numerical simulation is again performed.

For the static heeling arm due to accumulated water which is obvious in Case 4 is calculated using hydrostatics. Here, the amount of water on deck, which was not measured in the experiments, is systematically changed for realizing good agreements in the numerical simulation. For the heeling arm calculation, the movement of CG is calculated assuming that the shape of free surface is horizontal and the dynamic effect of water is not considered. The freeing ports are assumed to be closed and the flow of water is considered only over the bulwark.

4.3 Simulation with WOD

The numerical simulation model is extended to take account of the above roll damping effect and the heel moment effect of the WOD and then applied to the experiment cases. The results, as shown in Figure 7, indicate the reasonably better agreements between the experiment and the simulation.

The roll amplitudes in the numerical simulation for Case 2 and Case 3 are reduced because of roll damping effect due to water on deck. Here, the used water depth on deck is around 0.3m while the bulwark height is 2.7m. The ratio of the frequency of roll motion to the natural roll frequency of water is about 1. The mean roll angle in the simulation for Case 4 increases because of hydrostatic heeling moment due to accumulated water on deck. Here, the used water depth is 0.5m while the bulwark height is 2.7m. The ratio of frequency of roll motion to the natural roll frequency of water is smaller than 1. The mutual importance of these two different effects of WOD could depend on the magnitude of hull restoring moment.

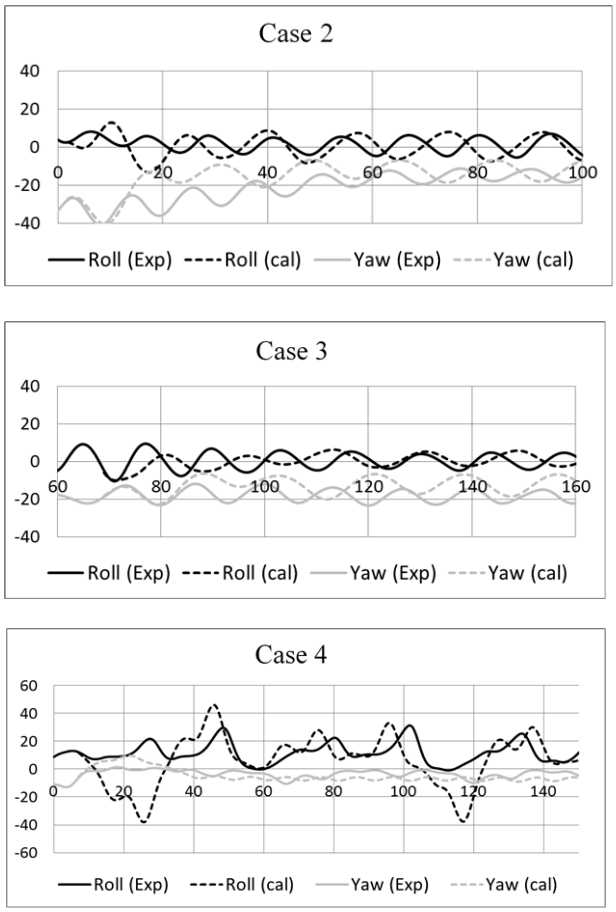

Figure 7 Comparison of simulation results with WOD effect and experiment results (λ/L=1.5 and H/λ=0.1)

Also, the comparison of the maximum roll angles obtained from the model experiments and the simulation (with and without WOD effect) is shown in Figure 8. The results from the simulation with WOD effect are relatively comparable to those of model experiments. For Case 4, the simulation results without WOD effect for Fn=0.25 and Fn=0.27 are plotted as 90 degrees as the simulation indicates the vessel to be capsized.

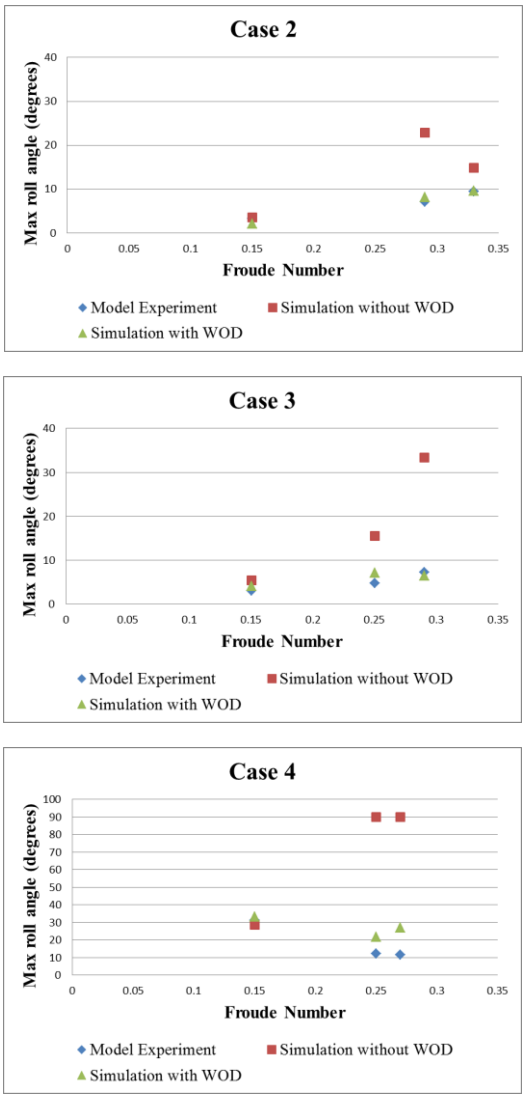

Figure 8 Comparison of experiment results with simulation results (with and without WOD effect)

5. CONCLUSION

It is confirmed experimentally that the level 2 pure loss of stability criteria cannot be applied to ships with low weather deck length greater than 0.4 L_{pp} and which is not completely surrounded by bulwarks. The presence of WOD is important for the stability of the OSV. For high metacentric height, the presence of WOD reduces the roll motion like Case 2 and Case 3. In contrast, when metacentric height is reduced, the heeling moment due to accumulated water becomes more relevant like Case 4.

6. ACKNOWLEDMENTS

This work was supported by a Grant-in Aid for Scientific Research from the Japan Society for Promotion of Science (JSPS KAKENHI Grant Number 15H02327). It was partly carried out as a research activity of Goal-based Stability Criteria Project of Japan Ship Technology Research Association in the fiscal years of 2016 funded by the Nippon Foundation.

7. REFERENCES

Dillingham, J.T., 1981, “Motion Studies of a Vessel with Water on Deck”, Marine Technology, Vol. 18, No. 1.

Falzarano. J.M., Laranjinha. M., Soares. C.G., 2002, “Analysis of the Dynamical Behaviour of an Offshore Supply Vessel”, Proceedings of International Ship Stability Workshop, New York.

Ikeda. Y., Kawahara. Y., 2008, “A Proposal of Guidance to the Master of a Damaged Passenger Ship for Deciding to Return to Port”, Journal of the Japan Society of Naval Architects and Ocean Engineers, Vol. 7, pp. 115-122.

IMO, 2015, “Report of the working group (Part 1)”, SDC 2/WP.4, IMO.

Japan, 2018, “Information collected by the Correspondence Group on Intact Stability”, SDC 5/6/INF.4, IMO.

Katayama. T., Kotaki. M., Katsui. T., Matsuda. A., 2009, “A Study on Roll Motion Estimation of Fishing Vessels with Water on Deck”, Journal of the Japan Society of Naval Architects and Ocean Engineers, Vol. 9, pp. 115-125.

Kubo. H., Umeda. N., Yamane. K., Matsuda. A., 2012, “Pure Loss of Stability in Astern Seas – Is it Really Pure?”, Proceedings of the 6th Asia-Pacific Workshop on Marine

Hydrodynamics, Johor, pp. 307-312

Umeda. N., Aqmil. A., Usada. S., Matsuda. A., Terada. D., 2016, "Model Experiment of an Offshore Supply Vessel Running in Astern Waves", Proceedings of the 15th International Ship Stability Workshop, Washington DC.

ITTC, 2008, Recommended Procedures, Model Tests on Intact Stability, 7.5-02-07-04.

ITTC, 2011, Recommendation Procedures, Numerical Estimation of Roll Damping, 7.5-02-07-04.5.

NTSB, "Sinking of the Offshore Supply Vessel M/V Sabine Seashore in the Gulf of Mexico, Jan. 1978, NTSB/MAR-79/10

NTSB, "Marine Accident Report Capsizing of US Offshore Vessel Laverene Herbet in the Texas Coast", Nov. 1983, NTSB/MAR-84/06

Investigation of the Effect of Parametric Variation on the Pure Loss of Stability Criteria

Tianhua Wang, China Ship Scientific Research Center, Wuxi , China tianhua_wang@126.com

Min Gu, *China Ship Scientific Research Center, Wuxi, China* gumin702@163.com

Ke Zeng, China Ship Scientific Research Center, Wuxi, China398638829@qq.com

Jiang Lu, *China Ship Scientific Research Center, Wuxi,China* lujiang1980@aliyun.com

*Zhailiu Hao, China Ship Scientific Research Center, Wuxi, China*aghaozhailiu@163.com

ABSTRACT

Pure loss of stability is one of the five stability failure modes, which vulnerability criteria are agreed in general by International Maritime Organization (IMO) in the second generation intact stability criteria. For giving out some guideline on ship safety design, firstly, a series of transformed hulls are designed on the basis lines of the standard model C11 containership according to an optimization method, and all the sample hulls are calculated on the pure loss of stability failure mode. Secondly, The criteria values are calculated through different parametric variations, the effects of which are evaluated for the vulnerability criteria. Finally, the problem of inconsistency between the levels of vulnerability criteria is discussed with design parameter's transformation. The weight factors of different parameters are obtained through regression analysis for the vulnerability criteria, which could be used for ship safety design for the vulnerability criteria for pure loss of stability and promote the application of the second generation intact stability criteria.

Keywords: *pure loss of stability; parametric variation; regression analysis; second generation intact stability*

1. INTRODUCTION

Pure loss of stability was firstly named by Paulling as a kind of capsizing mode(1961) and afterwards was under research and realization. Germany proposed pure loss of stability to be part of the stability criteria in the development of IMO in the second generation intact stability criteria. Especially for containerships and RORO ships, initial metacnetric height(GM) is generally much bigger, that could be strongly changed because of the small transform of the hull modeled lines or a little of heel angle.

Some ships that fully satisfy the 2008 IS Code, may be susceptible to different modes of stability failures. Vulnerability criteria would check for this susceptibility and should be based on simplified models, simple mathematical formulations, analytical solutions or statistical data. Vulnerability criteria can be probabilistic or deterministic in nature. These criteria will likely require separate development for different failure modes. Pure loss of stability is one of the five stability failure modes, which vulnerability criteria are agreed in general by IMO in the second generation intact stability criteria.

The stability criteria should be assessed at the design stage, but single parametric variation may not be appreciable for satisfy pure loss of stability criteria owing to diversification of the design parameters. The researches on design optimization for ship stability are few. Therefore multi-objective optimization

algorithm is able to adopt during design phase involved coupling design objection, which optimal solution is Pareto front. And it should have an even distribution to avoid accumulative stack. Pareto front is able to be obtained based on physical programming with Multi-objective optimization algorithm .

Total of 80 projects are obtained with multi-objective optimization algorithm based on physical programming an even distribution of Pareto front, and five variables are transformed with single equivalent distance in view of a pattern form C11 containership. All the sample hulls are calculated for the pure loss of stability failure mode. The criteria values are calculated through different parametric variation, the effect of which are evaluated for the vulnerability criteria. Finally, the weight factors of different parameter are obtained through regression analysis for the vulnerability criteria, which supply for the security optimization of the new-designed hulls for the second generation intact stability criteria and speed and application of the vulnerability criteria for pure loss of stability.

2. PARAMETRIC MODEL

2.1 Physical Programming

Physical Programming is a new method for multi-objective optimization problem. The dimensionless parameters with the same order of magnitude are transformed from design variables of different physical meaning.The optimization model is structured based on physical programming, that is solved by using suitable optimization algorithm.

The target values are normalized for contrast of the calculation results after physical programming. The normalization method of the i-th element is:

$$F_i^{'} = \left(F_i - F_{i\min}\right) / \left(F_{i\max} - F_{i\min}\right) \qquad (1)$$

where, F_i' is the normalized target value, F_i is the original value, F_{imax} and F_{imin} are respectively the maximum and minimal values of the target matrix.

2.2 Design Procedure

The five characteristic parameters are selected based on a parent ship C11 containership, which principal particulars is listed in Table 1. The even distribution of Pareto front is acquired with equivalent distance of the five parameters, including length, breadth, draft, prismatic coefficient and longitudinal variation centre of buoyancy which range are listed in Table 2, and the transform tendency of breadth and draft of all sample ships are displayed in Figure 2. Total of 80 projects are generated and their projection of 2 variables is shown in Figure 1. Hull geometry of some sample ships are shown in Figure 3.

Table1 Principal particulars of the C11 containership

Variable	Items	Ship
L	Length	262.0m
d	Draft	11.5m
B	Breadth	40.0m
D	Depth	24.45m
W	Displ.	67508ton
C_B	C_B	0.560
GM	GM	1.928m
T_φ	Period	24.68s

Table 2 Range of the five parameters

Variable	Items	Range
L	Length	-15%~15%
B	Breadth	-10%~10%
d	Draft	-10%~10%
C_p	Prismatic coefficient	-5%~5%
Δ XCB	Longitudinal variation centre of buoyancy	-5%~5%

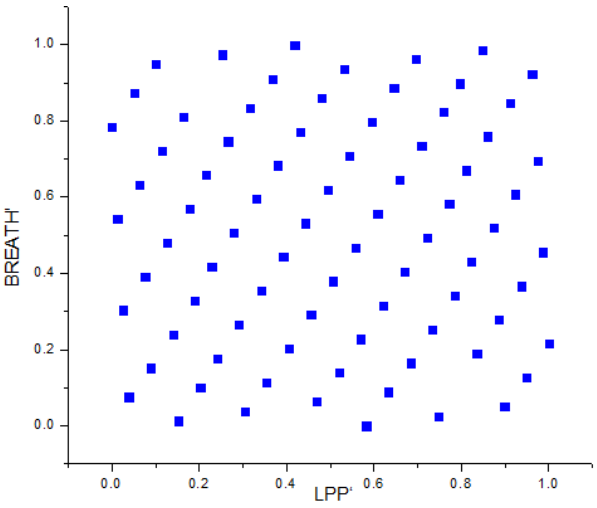

Figure 1 Projection of 2 variables

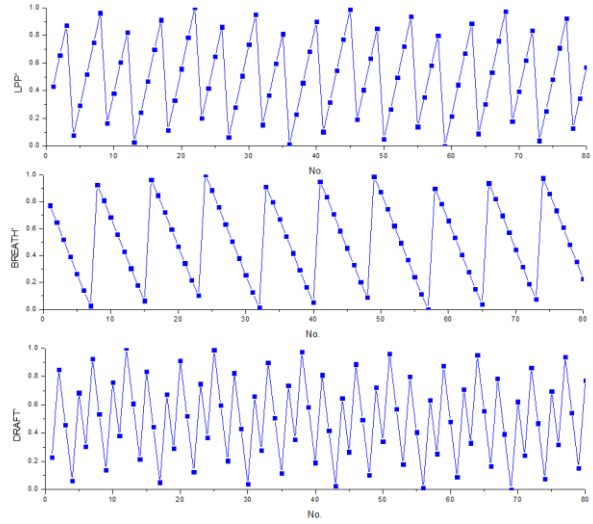

Figure 2 Tendency of length breadth and draft

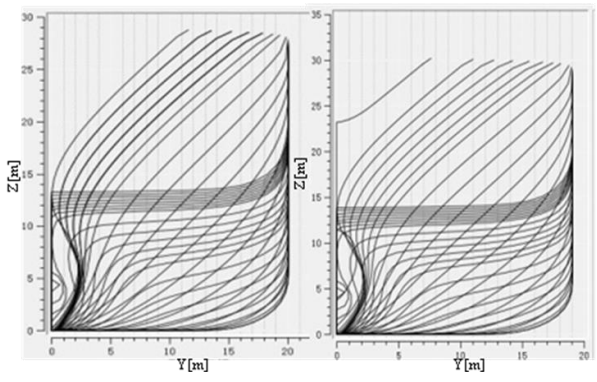

Figure 3 Hull geometry of some sample ships

3. MATHEMATICAL METHOD

3.1 Vulnerability Criteria

The Level 1 assessment of the vulnerability to pure loss of stability is performed by the smallest GM value computed during the wave pass. The wave length λ is taken equal to the ship length and the wave height H is calculated as:

$$H = 0.0334 \cdot \lambda \tag{2}$$

A ship is considered not vulnerable to pure loss of stability if

$$GM_{\min} > R_{PLA} \tag{3}$$

The Level 2 assessment of the vulnerability to pure loss of stability is done using the actual GZ curves in waves computed for 10 different waves. The length λ of all the waves equals to ship length. The wave height H for these 10 waves is computed as:

$$H_i = i \cdot 0.01 \cdot \lambda \quad i = 1, 2, ..., 10 \tag{4}$$

The first short-term criteria C1i is computed for each wave height H_{Wi} as:

$$C1_i = \begin{cases} 1 & \varphi_{V\min i} < 30 \\ 0 & otherwise \end{cases} \tag{5}$$

The second short-term criteria C2i is computed for each wave height λ_i as:

$$C2_i = \begin{cases} 1 & \varphi_{SAi} < 15 \\ 0 & otherwise \end{cases} \tag{6}$$

Both short term criteria C1i and C2i are averaged over the wave scatter diagram, producing the long term criteria CR1 and CR2, respectively. The ship is considered not to be vulnerable if the largest value among CR1 and CR2 does not exceed the standard value 0.06.

The calculation formula for wave height in the Level 2 vulnerability criteria to pure loss of stability is as follows:

$$H_{3\%}^{eff}\left(L_{PP}\right)=5.9725\sqrt{m_0} \tag{7}$$

$$\begin{aligned} m_0 = &\int_{0.01\omega_L}^{\omega_L}\left\{\frac{\frac{\omega^2 L}{g}\sin\left(\frac{\omega^2 L}{2g}\right)}{\pi^2-\left(\frac{\omega^2 L}{2g}\right)^2}\right\}^2 A\omega^{-5}\exp\left(-B\omega^{-4}\right)d\omega \\ &+\int_{\omega_L}^{3\omega_L}\left\{\frac{\frac{\omega^2 L}{g}\sin\left(\frac{\omega^2 L}{2g}\right)}{\pi^2-\left(\frac{\omega^2 L}{2g}\right)^2}\right\}^2 A\omega^{-5}\exp\left(-B\omega^{-4}\right)d\omega \end{aligned} \tag{8}$$

where,

$A=173H_s^2T_{01}^{-4}$, $B=691T_{01}^{-4}$, $T_{01}=1.086T_z$, $\omega_L=\sqrt{\frac{2g\pi}{L}}$.

L(m): length of the ship, H_s (m) : the significant wave height, and T_Z (s), : the average zero-crossing mean wave period. If H_i> *0.1L*, H_i should be set as H_i=*0.1L*.

The detail of the vulnerability criteria for pure loss of stability can be referred in the reference IMO SDC 4(2017).

3.2 Multivariable Regression Analysis Method

The effect of different factors on criteria is undefined.Sensitivity analysis for design variables on the Level 1 and 2 assessment of the vulnerability to pure loss of stability is performed with the help of regression techniques.

Multivariable regression modelling refers to techniques for the modelling and analysis of numerical data consisting of values of a dependent variable and of one or more independent variables. The dependent variable in the multivariable regression equation is modelled as a function of the independent variables, corresponding parameters, and an error term. The error term is treated as a random variable and represents unexplained variation in the dependent variable. Parameters are estimated to give a best fit of the data. Most commonly the best fit is evaluated by using the least squares method, but other criteria have also been used. The linear model under the multivariate setup is

$$y=\beta_0+\beta_1x_1+...+\beta_mx_m+\varepsilon \tag{9}$$

where,ε~N(0,σ^2),,y is a dependent variable, x_1, x_2,…, x_m are independent variables, and n observations on each of the m independent variables are available. The regression coefficients associated with x_1, x_2,…, x_m are β_1, β_2,…, β_m, respectively, and β_0 is the involved intercept term in the model. The random error component ε takes care of all the random factors affecting y not included in the model and is assumed to be identically and independently distributed following a normal distribution with mean and constant variance. Once a regression analysis model is obtained, statistical analysis techniques can be used to check the fitness of the model. The coefficient R^2 is defined as:

$$R^2=\frac{S_R}{S_T} \tag{10}$$

where,

$$\begin{aligned} S_R &= \sum_{i=1}^{n}\left(\hat{y}_i-\bar{y}\right)^2 \\ S_T &\hat{=} \frac{1}{n}\sum_{i=1}^{n}\left(y_i-\bar{y}\right)^2 \end{aligned} \tag{11}$$

Obviously, The coefficient R^2 is much closer to 1,illustrated the fitness of the model is better. Regression equations are found out using software for statistical analysis called MATLAB. The regression equation helps to get the relation between different response variables and the input parameters. The software required the input conditions and the observations of the experiments and developed the regression equations for each desired output.

4. RESULTS AND ANALYSIS

4.1 The First Level Assessment Results

Sample calculation on the first level vulnerability criteria of pure loss of stability are done by using 80 ships. All ships have service Froude number a little larger than 0.24,and the GM values are same to the parent ship C11 containership.

To be specific, the calculation results for levels 1 vulnerability criteria are shown in Figure 4. The verification results of level 1 criteria of pure loss of stability indicated that 42 ships were judged as vulnerable and it presented a failure rate of 52.5%.

Because different characteristic parameters of 80 sample ships, the first level criteria results do not have apparent regular pattern with single parameter as displayed in Figure 5.

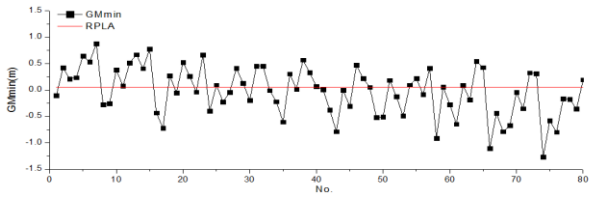

Figure 4 The first level criteria results of 80 sample ships

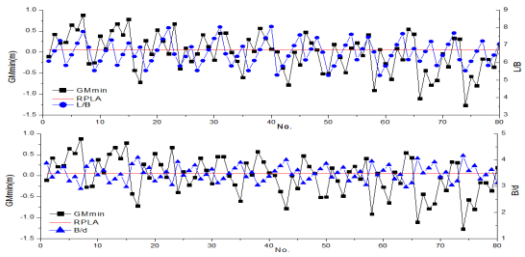

Figure 5 The curves of first level criteria results and different characteristic parameters

4.2 The Second Level Assessment Results

Sample calculations on the second level vulnerability criteria of pure loss of stability are done based on the short term criteria C1i and C2i. Taking a ship as an example, GZ curves in different waves were calculated as shown in Figure 6 and it could be gained that $MAX(CR_1,CR_2)=0.1673>0.06$, that indicated the ship was vulnerable to the second level vulnerability criteria.

As shown in Figure 7, the sample calculation results of level 2 indicated the following: 11 ships were judged as vulnerable and it presented a failure rate of 13.75%. We consider that the proposed levels 1 and 2 criteria should be kept consistent and all sample are under the satisfaction.

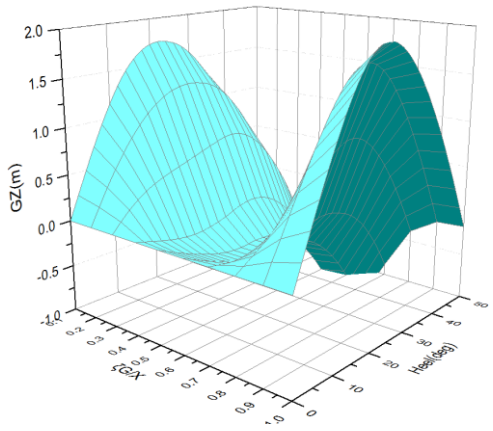

Figure 6 The GZ curves in different waves for second level criteria

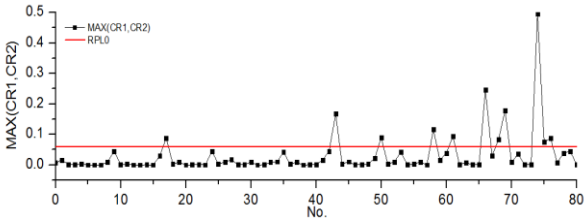

Figure 7 The second level criteria results of 80 sample ships

4.3 Discussions of the Regression Results

Based on the design parameters and the first level assessment method of the vulnerability to pure loss of stability, seven variables were chosen for the regression analysis, as listed in Table 3.They are separately length/breadth、

breadth/draft、depth/draft、the ratio of center of buoyancy and length and three coefficients including prismatic coefficient 、 block coefficient and midship section coefficient.

The first level assessment results GM_{min} in the multivariable regression equation is modelled as a function of the seven variables, and the coefficient of regression equation were obtained. The bigger absolute value of regression coefficients is the more sensitive first level assessment results GM_{min}. The regression coefficient is positive, that indicated the criteria value are identically interrelated with the variable. While regression coefficient is negative, that indicated the criteria value are adversely interrelated with the variable.

As we can see from Figure 8, D/d and X_C/L_{PP} have the greatest impact on the first level criteria results of pure loss of stability. L/B 、 B/d and X_C/L_{PP} are adversely interrelated with the first level criteria results and D/d、C_p、C_B and C_M are identically interrelated with the GM_{min}. For checking the fitness of the model, the coefficient R^2 is obtained,R^2=0.9641,that illustrated the accuracy of the regression model was high.

Similarly, seven variables were chosen for the regression analysis based on the design parameters and the second level assessment method of the vulnerability to pure loss of stability, as listed in Table 4.They are separately length、 breadth、depth、draft、 prismatic coefficient 、 longitudinal variation centre of buoyancy and the first level assessment results GM_{min}.

Table 3 The regression coefficients of first level results

No.	Variable	Coefficient
X1	L/B	-0.1096
X2	B/d	-1.4351
X3	D/d	12.0314
X4	X_C/L_{PP}	-5.4494
X5	C_p	1.3519
X6	C_B	0.5865
X7	C_M	3.9721

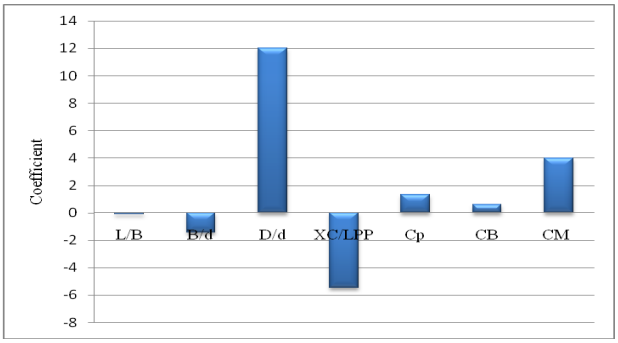

Figure 8 The regression coefficients of first level assessment

As we can see from Figure 9, ΔXCB and C_p have the greatest impact on the second level criteria results for pure loss of stability, and the next are draft and $GM_{min.}$ L、B、d、ΔXCB and GM_{min} are adversely interrelated with criteria results and D and C_p are identically interrelated with the criteria results. For checking the fitness of the model, the coefficient R^2 is obtained,R^2=0.7687,that illustrated the accuracy of the regression model was acceptable. For security purposes design characteristic parameters could be modified to satisfy the first and second level for pure loss of stability on the basis of the regression results.

Table 4 The regression coefficients of second level results

No.	Variable	Coefficient
X1	L	-0.0029
X2	B	-0.0719
X3	D	0.5607
X4	d	-1.0686
X5	C_p	1.098
X6	ΔXCB	-2.6631
X7	GM_{min}	-0.6623

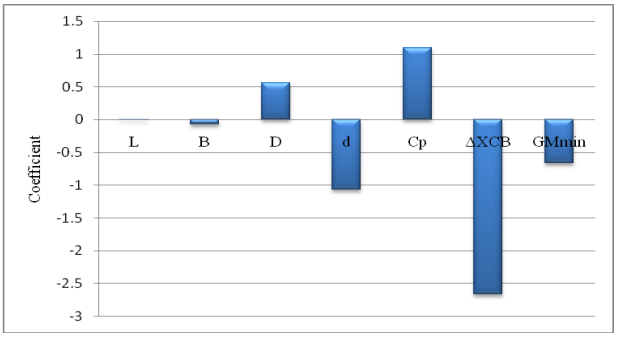

Figure 9 The regression coefficients of second level assessment

5. CONCLUSIONS

Total of 80 projects were obtained with multi-objective optimization algorithm based on a pattern form C11 containership. The results of first and second level criteria of pure loss of stability were calculated, that were modelled with the multivariable regression equation as a function of the different variables. Sensitivity analysis for different variables on the criteria results was performed and through research we have reached the following conclusions.

(1) The first and second level criteria results do not have apparent regular patterns with single parameter and the linear coefficients of variables and criteria calculation values were gained with multivariable regression equation.

(2) Regression results showed that D/d and X_C/L_{PP} have the greatest impact on the first level criteria and ΔXCB and Cp have the greatest impact on the second level criteria. It may be because the location of the centre of buoyancy was considerable for GZ curves in waves during criteria assessment of pure loss of stability.

(3) More variables would be analysis during the design stage and the regression analysis method would be fitted for the other four stability failure modes for the vulnerability criteria and promote the application of the second generation intact stability criteria.

6. ACKNOWLEDMENTS

The research is supported by Ministry of Industry and Information Technology of China (No. [2016] 26; [2017]614) These supports are gratefully acknowledged.

7. REFERENCES

Ayla S. ,Ahmet D.A., Onur G., 2010, "Nonlinear meta-models for conceptual seakeeping design of fishing vessels",Ocean Engineering,Vol.37, pp.730-741.

IMO, 2017, Finalization Second Generation Intact Stability Criteria, SDC 4/WP.4.

Justin A. Harper, Robert M. Scher, John J. Mcmullen., 2001,"Improvements in the Prediction of Maneuvering Characteristics of Ships Using Regression Analysis",The Proceedings of the 26th American Towing Tank Conference, Glen Cove, New York.

Jiang Lu, Min Gu, Tianhua Wang, 2015, "The Application on vulnerability criteria of IMO Second Generation Intact Stability Criteria", Proceedings of the 12th International Marine Design Conference.

Messac A., Mattson C.A., 2002,"Generating well-distributed sets of pareto points for engineering design using physical programming",Optimization and Engineering, Vol.3,pp.431-450.

N.C. Nguyen, J. Peraire., 2015, "Gaussian functional regression for linear partial differential equations", Comput. Methods Appl. Mech. Engrg. Vol.287, pp.69–89.

Robert G., Hekkenberg., 2010,"Barges of Tomorrow,New Design Rules of Thumb for Inland Ships", The Proceedings of 11th International Symposium on Practical Design of Ships and Other Floating Structures.

Tianhua Wang, Min Gu, Jiang Lu,2013, "Application assessment on vulnerability criteria of pure loss of stability", Proceedings of the 5th International Marine Conference on Design for Safety.

Zhailiu Hao, Zhipeng Wang, Chengsheng WU et al., 2017,"Bow Optimization of A Polar Tanker Based on Approximate Technology", Proceedings of the 24th International Conference on Port and Ocean Engineering under Arctic Conditions.

Experimental and Numerical Study on Standard Mathematical Model for Pure Loss of Stability

Jiang, Lu, *China Ship Scientific Research Center*lujiang1980@aliyun.com

Min, Gu, *China Ship Scientific Research Center*gumin702@163.com

Tianhua, Wang, *China Ship Scientific Research Center*thwang@163.com

Chao, Shi, *China Ship Scientific Research Center*shichao840409@163.com

ABSTRACT

The guidelines for direct stability assessment of pure loss of stability are currently under development at the International Maritime Organization (IMO) for the second generation intact stability criteria. For providing a standard mathematical model of pure loss of stability with sufficient accuracy and practically useful, firstly, one standard mathematical model for pure loss of stability is presented base on one Maneuvering Modeling Group (MMG) standard method for ship maneuvering predictions and existing mathematical models for broaching predictions. Secondly, model tests are carried out for pure loss of stability in following and stern-quartering waves. Thirdly, the effect of some crucial terms, such as the higher order coefficients, the different degrees of freedom (DOF) motions, the diffraction forces, heel-induced hydrodynamic forces and the roll damping on predicting pure loss of stability are studied with the ONR tumblehome vessel. Finally, the types of roll motions are identified during pure loss of stability. The result shows that the 2 DOF surge-roll coupled motion is appropriate for pure loss of stability in following waves while not appropriate for that in stern-quartering waves due to not 'pure' loss of stability , and the 4 DOF surge-roll-sway-yaw coupled motion is necessary in stern-quartering waves. The stable periodic roll motion, unstable roll motion, capsizing due to pure loss of stability and capsizing due to coupled pure loss of stability and broaching are newly idendified.

Keywords:*Pure loss of stability, second generation intact stability criteria, ONR tumblehome*

LIST OF SYMBOLS

a_H Rudder force increase factor

AE, FE After section and forward section

A_R Rudder area

A_{RP}, A_{RS} The port and starboard rudder area

$B(x)$ Sectional breadth

C_T Total resistance coefficient in calm water

d Ship draft

$d(x)$ Sectional draught

D_P Propeller diameter

$D(p)$ Roll damping moment

F_N Rudder normal force

F_n Froude number based on ship length

f_α Rudder lifting slope coefficient

g Gravitational acceleration

GM Metacentric height

GZ_W Righting arm in waves

H_R Rudder span length

I_{xx}, J_{xx} Moment and addd moment of inertia in roll

I_{zz}, J_{zz} Moment and addd momentof inertia in yaw

J_P Propeller advanced ratio

k Wave number

K_r, N_r, Y_r Derivative of roll moment,yaw moment and sway force with respect to yaw rate, their nondimensional K_r', N_r', Y_r'

$K_{rrr}, N_{rrr}, Y_{rrr}$ Derivative of roll moment, yaw moment and sway force with respect to cubic yaw rate, their nondimensional $K_{rrr}', N_{rrr}', Y_{rrr}'$

$K_{r|\varphi|}, N_{r|\varphi|}, Y_{r|\varphi|}$ Derivative of rollmoment, yaw moment and sway force with respect to yaw rate and heeling angle, their nondimensional $K'_{r|\varphi|}, N'_{r|\varphi|}, Y'_{r|\varphi|}$

$K_{vvr}, N_{vvr}, Y_{vvr}$ Derivative of roll moment, yaw moment and sway force with respect to squared yaw rate and sway velocity, their nondimensional $K'_{vvr}, N'_{vvr}, Y'_{vvr}$

$K_{vvr}, N_{vvr}, Y_{vvr}$ Derivative of roll moment, yaw moment and sway force with respect to squared yaw rate and sway velocity, their nondimensional $K'_{vvr}, N'_{vvr}, Y'_{vvr}$

K_v, N_v, Y_v Derivative of roll moment, yaw moment and sway force with respect to sway velocity, their nondimensional K'_v, N'_v, Y'_v

$K_{vvv}, N_{vvv}, Y_{vvv}$ Derivative of roll moment, yaw moment and sway force with respect to cubic sway velocity, their nondimensional $K'_{vvv}, N'_{vvv}, Y'_{vvv}$

$K_{v|\varphi|}, N_{v|\varphi|}, Y_{v|\varphi|}$ Derivative of roll moment, yaw moment and sway force with respect to sway velocity and heeling angle, their nondimensional $K'_{v|\varphi|}, N'_{v|\varphi|}, Y'_{v|\varphi|}$

$K_\varphi, N_\varphi, Y_\varphi$ Derivative of roll moment, yaw moment and sway force with respect to roll angle, their nondimensional $K'_\varphi, N'_\varphi, Y'_\varphi$

K_P Rudder gain

K_T Thrust coefficient of propeller

L_{PP} Ship length between perpendiculars

ℓ_R' Correction factor for flow-straightening due to yaw

m Ship mass

m_x, m_y Added mass in surge and sway

n_P Propeller revolution number

OG Vertical distance between center of gravity and waterline

p Roll rate

r Yaw rate

R Ship resistance

$S(x)$ Sectional area

$S_y(x)$ Added mass of one section at sway direction

$S_y l_\eta(x)$ Added moment of one section at roll direction

S_F Wetted hull surface area

t_P Thrust deduction factor

t_R Steering resistance deduction factor

T Propeller thrust

T_E Time constant for steering gear

T_D Time constant for differential control

T_φ Natual roll period

u, v Surge and sway velocity

u_R Longitudinal inflow velocity component to rudder

U Ship forward velocity

w_P Wake fraction at propeller positon

w_R Wake fraction at rudder position

W Ship weight

x_{HR} Longitudinal position of additional sway force due to rudder

x_R Longitudinal position of rudder

X_H, Y_H, N_H, K_H Surge force, sway force, yaw moment and roll moment aroud center of ship gravity acting on ship hull

X_P Surge force due to propeller

X_R, Y_R, N_R, K_R Surge force, sway force, yaw moment and roll moment around center of ship gravity by steering

X_{rr} Derivative of surge force with respect to squared yawrate, its nondimensional X'_{rr}

X_{vr} Derivative of surge force with respect to sway velocity and yaw rate, its nondimensional X'_{vr}

X_{vv} Derivative of surge force with respect to squared sway velocity, its nondimensional X'_{vv}

X_{vvvv} Derivative of surge force with respect to 4th order sway velocity, its nondimensional X'_{vvvv}

X_W, Y_W, N_W, K_W Surge force, sway force, yaw moment and roll moment around center of ship gravity acting on ship hull induced by waves

Z_H Vertical position of center of sway force due to sway motion

z_{HR} Vertical position of of additional sway force due to rudder

z_R Vertical position of center of rudder

α Linear roll damping coefficient

α_R Effective inflow angle to rudder

β Hull drift angle

δ Rudder angle

η Ratio of propeller diameter to rudder span

ε Ratio of wake fraction at propeller and rudder position

κ Propeller-induced flow velocity factor

λ Wave length

Λ Ruder aspect ratio
φ Roll angle
γ Cubic nonlinear roll damping coefficient
γ_R Flow-straightening effect coefficient
θ Pitch angle
χ Yaw angle from wave direction
χ_c Yaw angle of auto pilot course
ρ Water density
ω Wave frequency
ω_e Averaged encounter frequency
ξ_G Longitudinal position of center of ship gravity from a wave trough
(ξ_G, η_G, ζ_G) Position of center of ship gravity in the space-fixed coordinate system
ζ_w Wave amplitude

1. INTRODUCTION

The guidelines for direct stability assessment of five stability failure models including pure loss of stability are under development at the International Maritime Organization (IMO) for the second generation intact stability criteria (IMO SDC 4, 2017). Once the crest of the large wave passes the midship section of a ship with a slightly higher speed than ship speed, the state of stability loss at the crest may exist long enough to evolve a large heel angle, or even capsizing. It is urgently required to establish a standard mathematical model which is sufficient accuracy and practically useful for predicting pure loss of stability.

Without external heel moment, once the wave crest passes the ship, the ship will finally return to the upright position with regained stability except for cases that the ship already heel too far or the metacentric height in the wave is negative. Initial heel moments induced by cargo shift or winds in following waves and roll moment excited by oblique waves and heel moments induced by a centrifugal force due to ship maneuvering motions are the relevent external moments. Several freely running experiments also prove that coupling with maneuvering motion is essential for explaining the forward speed effect on pure loss of stability in stern-quartering waves (IMO SDC 3，2016).

Pure loss of stability in stern-quartering waves is a nonlinear phenomenon involving large amplitude roll motion and it is still difficult to be predicted quantitatively. Japan delegation (IMO SLF55， 2013) notes that predicting pure loss of stability with their newly 4 degrees of freedom (DOF) mathematical model is more accuracy than the 2 DOF mathematical model (Kubo et al., 2012).The delegations for the second generation intact stability criteria at IMO SDC 4 gave to priority to discussing the guidelines for direct stability assessment and the 4 DOF for predicting pure loss of stability has been agreed at the current stage (IMO SDC 4, 2017).

Though the 4 DOF mathematical model for predicting pure loss of stability has not been investigated widely with simulations and experiments, a 4 DOF mathematical model for broaching prediction (Umeda, 1999) has been investigated for many years. For providing a accurate mathematical model for broaching prediction, Umeda and Hashimoto had investigated essential terms in the 4 DOF mathematical model one by one by utilizing fishing vessels. Nonlinear maneuvering forces in calm water (Umeda & Hashimoto, 2002), wave effect on linear maneuvering forces, roll restoring and rudder force (Umeda et al., 2003), and several nonlinear factors were also investigated, such as nonlinear wave forces, nonlinear sway-yaw coupling, wave effect on propeller thrust, heel-induced hydrodynamic forces for large heel angle in calm water (Hashimoto et al., 2004), and wave effect on heel-induced hydrodynamic forces for large heel angle. A simplified mathematical model was proposed for more practically useful (Hashimoto et al., 2011a). Existing 4 DOF mathematical model was used for broaching predicton of the ONR tumblehome vessel, and a fair quantitative prediction was realized (Hashimoto et al., 2011b). Broaching is a nonlinear phenomena related to ship maneuvering in the wave, and above 4 DOF mathematical models are based on a

Maneuvering Modeling Group (MMG) model, but simulation methods without standard expressions could not be used in general. Therefore a MMG standard method for ship maneuvering predictions was introduced (Yasukawa & Yoshimura, 2015). A 4 DOF mathematical model was refined for broaching prediction of the ONR flare topside vessel (Umeda et al., 2016).

For drafting guidelines for direct stability assessment, several crucial elements for predicting parametric roll were investigated with simulations and experiments by the authors (Lu et al., 2017), and some crucial terms in the 4 DOF mathematical for predicting pure loss of stability still require further experimental and numerical studies with more examples. The physical mechanism of pure loss of stability is different from that of broaching and a 4 DOF standard mathematical model for predicting pure loss of stability has not been established widely. Therefore, systematic studies on the 4 DOF mathematical model for predicting pure loss of stability are hot tasks at this stage. Also IMO is calling for the validation of numerical methods or guidelines for the finalization of second generation intact stability with examples.

Based on the MMG standard method and existing mathematical model for broaching and pure loss of stability, the authors tried to provide a 4 DOF standard mathematical model only with numerical study (Lu & Gu, 2017), and the present study intends to provide a 4 DOF and a 2 DOF standard mathematical models with experimental and numerical study for the prediction of pure loss of stability in stern-quartering and following waves. Some crucial terms in the mathematical models were investigated using one standard ship.

2. MATHEMATICAL MODEL

2.1 Coordinate systems

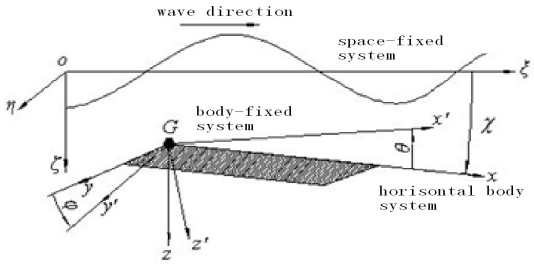

Fig. 1: Coordinate systems

A space-fixed coordinate system $O-\xi\eta\zeta$ with the origin at a wave trough, a body-fixed system $G-x'y'z'$ with the origin at the center of gravity of the ship, and a horizontal body coordinate system (Hamamoto & Kim, 1993) $G-xyz$ which has the same origin with the body-fixed system but does not rotated around the x-axis and y-axis are adopted as shown in Fig. 1.

The relationships between the horizontal body coordinate system $G-xyz$, the body-fixed system $G-x'y'z'$ and the space-fixed system $O-\xi\eta\zeta$ are shown in Eq. (1) and Eq. (2), respectively.

$$\begin{bmatrix} x \\ y \\ z \end{bmatrix} = \begin{bmatrix} \cos\theta & \sin\phi\sin\theta & \cos\phi\sin\theta \\ 0 & \cos\varphi & -\sin\varphi \\ -\sin\theta & \sin\varphi\cos\theta & \cos\varphi\cos\theta \end{bmatrix} \begin{bmatrix} x' \\ y' \\ z' \end{bmatrix} \quad (1)$$

$$\begin{bmatrix} \xi-\xi_G \\ \eta-\eta_G \\ \zeta-\zeta_G \end{bmatrix} = \begin{bmatrix} \cos\theta\cos\chi & \sin\varphi\sin\theta\cos\chi & \cos\varphi\sin\theta\cos\chi \\ & -\cos\varphi\sin\chi & +\sin\varphi\sin\chi \\ \cos\theta\sin\chi & \sin\varphi\sin\theta\sin\chi & \cos\varphi\sin\theta\sin\chi \\ & +\cos\varphi\cos\chi & -\sin\varphi\cos\chi \\ -\sin\theta & \sin\varphi\cos\theta & \cos\varphi\cos\theta \end{bmatrix} \begin{bmatrix} x' \\ y' \\ z' \end{bmatrix} \quad (2)$$

2.2 Mathematical model

Heave and pitch response will be dynamic or static depending on the encounter frequency In case of following and astern waves, the encounter frequency is much lower than the natural frequencies of heave and pitch so that coupling with heave and pitch is almost static (Matsuda & Umeda, 1997). The 4 DOF mathematical model are expressed by surge, sway, yaw and roll motions as shown in Eq. (3) to Eq. (6), respectively. Control equation for keeping course by steering is added in the 4 DOF mathematical model as shown in Eq. (7).

$$(m+m_x)\dot{u}-(m+m_y)vr=X_H+X_R+X_P+X_W \quad (3)$$

$$(m+m_y)\dot{v}+(m+m_x)ur=Y_H+Y_R+Y_W \quad (4)$$

$$(I_{zz}+J_{zz})\dot{r} \qquad =N_H+N_R+N_W \quad (5)$$

$$(I_{xx}+J_{xx})\dot{p}-m_x z_H ur-m_y z_H \dot{v}=K_H+K_R+K_W \quad (6)$$
$$-D(\dot{\varphi})-WGZ_W(\xi_G/\lambda,\chi,\varphi)$$

$$\dot{\delta}=\{-\delta-K_P(\chi-\chi_C)-K_P T_D r\}/T_E \quad (7)$$

The subscript H, R, P and W refer to hull, rudder, propeller and wave, respectively. The mathematical model only with surge-roll coupled motion and control equation is named 2 DOF.

2.3 Hydrodynamic forces acting on ship hull

Hydrodynamic forces acting on a ship hull of a MMG standard method (Yasukawa & Yoshimura, 2015) is referenced with the roll motion and heel-induced hydrodynamic forces taken into account.

The hull forces in still water X_H, Y_H, N_H and K_H are expressed as follows:

$$X_H=-R(u)+\frac{1}{2}\rho L_{pp}dU^2(X'_{vv}\cdot v'^2+X'_{vr}\cdot v'r' +X'_{rr}\cdot r'^2+X'_{vvv}\cdot v'^4) \quad (8)$$

$$Y_H=\frac{1}{2}\rho L_{pp}dU^2(Y'_v\cdot v'+Y'_r\cdot r' +Y'_{vvv}\cdot v'^3+Y'_{vvr}\cdot v'^2r'+Y'_{vrr}\cdot v'r'^2+Y'_{rrr}\cdot r'^3 +Y'_\varphi\cdot\varphi+Y'_{v|\varphi|}\cdot v'|\varphi|+Y'_{r|\varphi|}\cdot r'|\varphi|) \quad (9)$$

$$N_H=\frac{1}{2}\rho L_{pp}^2dU^2(N'_v\cdot v'+N'_r\cdot r' +N'_{vv}\cdot v'^3+N'_{vr}\cdot v'^2r'+N'_{vrr}\cdot v'r'^2+N'_{rrr}\cdot r'^3 +N'_\varphi\cdot\varphi+N'_{v|\varphi|}\cdot v'|\varphi|+N'_{r|\varphi|}\cdot r'|\varphi|) \quad (10)$$

$$K_H=\frac{1}{2}\rho L_{pp}d^2U^2(K'_v\cdot v'+K'_r\cdot r' +K'_{vv}\cdot v'^3+K'_{vr}\cdot v'^2r'+K'_{vrr}\cdot v'r'^2+K'_{rrr}\cdot r'^3 +K'_\phi\cdot\phi+K'_{v|\varphi|}\cdot v'|\varphi|+K'_{r|\varphi|}\cdot r'|\varphi|) \quad (11)$$
$$=Y_H\times Z_H$$

where v', r' denote nondimentioanl sway velocity, and yaw rate, respectively and are expressed as follows:

$$v'=\frac{v}{U} \quad ,r'=\frac{rL_{pp}}{U} \quad (12)$$

Each maneuvering coefficient can be determined by circular motion test , or oblique towing test (OTT). For providing unified expressions, the nondimentinal maneuvering coefficients are rewritten as follows:

$$X'_{vv}=\frac{X_{vv}}{\frac{1}{2}\rho L_{PP}d} \quad ,X'_{vr}=\frac{X_{vr}}{\frac{1}{2}\rho L_{PP}^2d} \quad (13)$$

$$X'_{rr}=\frac{X_{rr}}{\frac{1}{2}\rho L_{PP}^3d} \quad ,X'_{vvvv}=\frac{X_{vvvv}}{\frac{1}{2}\rho L_{PP}d/U^2} \quad (14)$$

$$Y'_v=\frac{Y_v}{\frac{1}{2}\rho L_{PP}dU},Y'_r=\frac{Y_r}{\frac{1}{2}\rho L_{PP}^2dU},Y'_\varphi=\frac{Y_\varphi}{\frac{1}{2}\rho L_{PP}dU^2} \quad (15)$$

$$Y'_{vv}=\frac{Y_{vv}}{\frac{1}{2}\rho L_{PP}d/U},Y'_{vr}=\frac{Y_{vr}}{\frac{1}{2}\rho L_{PP}^2d/U},Y'_{vr}=\frac{Y_{vr}}{\frac{1}{2}\rho L_{PP}^3d/U} \quad (16)$$

$$Y'_{rr}=\frac{Y_{rr}}{\frac{1}{2}\rho L_{PP}^4d/U},Y'_{v|\varphi|}=\frac{Y_{v|\varphi|}}{\frac{1}{2}\rho L_{PP}dU},Y'_{r|\varphi|}=\frac{Y_{r|\varphi|}}{\frac{1}{2}\rho L_{PP}^2dU} \quad (17)$$

$$N'_v=\frac{N_v}{\frac{1}{2}\rho L_{PP}^2dU},N'_r=\frac{N_r}{\frac{1}{2}\rho L_{PP}^3dU},N'_\varphi=\frac{N_\varphi}{\frac{1}{2}\rho L_{PP}^2dU^2} \quad (18)$$

$$N'_{vv}=\frac{N_{vv}}{\frac{1}{2}\rho L_{PP}^2d/U},N'_{vr}=\frac{N_{vr}}{\frac{1}{2}\rho L_{PP}^3d/U},N'_{vr}=\frac{N_{vr}}{\frac{1}{2}\rho L_{PP}^4d/U} \quad (19)$$

$$N'_{rr}=\frac{N_{rr}}{\frac{1}{2}\rho L_{PP}^5d/U},N'_{v|\varphi|}=\frac{N_{v|\varphi|}}{\frac{1}{2}\rho L_{PP}^2dU},N'_{r|\varphi|}=\frac{N_{r|\varphi|}}{\frac{1}{2}\rho L_{PP}^3dU} \quad (20)$$

$$K'_v=\frac{K_v}{\frac{1}{2}\rho L_{PP}d^2U},K'_r=\frac{K_r}{\frac{1}{2}\rho L_{PP}^2d^2U},K'_\varphi=\frac{K_\varphi}{\frac{1}{2}\rho L_{PP}d^2U^2} \quad (21)$$

$$K'_{vv}=\frac{K_{vv}}{\frac{1}{2}\rho L_{H}d^2/U},K'_{vr}=\frac{K_{vr}}{\frac{1}{2}\rho L_{H}^3d^2/U},K'_{rr}=\frac{K_{rr}}{\frac{1}{2}\rho L_{H}^4d^2/U} \quad (22)$$

2.4 Propeller thrust and the hull resistance in still water

The surge force due to propeller thrust X_P with twin propellers is expressed as follows:

$$X_P=2\times(1-t_P)T \quad (23)$$

$$T=\rho n_P^2D_P^4K_T(J_P) \quad (24)$$

$$J_P=\frac{(1-w_P)u}{n_PD_P} \quad (25)$$

The hull resistance in still water R in the surge motion is expressed asfollows:

$$R=\frac{1}{2}\rho S_F u^2 C_T(\frac{u}{\sqrt{gL_{PP}}}) \quad (26)$$

2.5 Hydrodynamic force by steering

Hydrodynamic forces acting on a ship hull of a MMG standard method (Yasukawa & Yoshimura, 2015) is referenced

The steering rudder forces components X_R, Y_R, N_R and K_R with twin rudders (Khanfir, et al., 2011) are refernced and expressed as follows (S:starboard; P:port). The averge values of $\bar{\gamma}_R$, $\bar{\ell}_R$ are used in this paper.

$$X_R=-(1-t_R)F_N\sin\delta \quad (27)$$

$$Y_R=-(1+a_H)F_N\cos\delta \quad (28)$$

$$N_R=-(x_R+a_H x_{HR})F_N\cos\delta \quad (29)$$

$$K_R=(z_R+a_H z_{HR})F_N\cos\delta \quad (30)$$

where

$$F_N=\frac{1}{2}\rho(A_{R(S)}+A_{R(P)})u_R^2 f_\alpha\sin\alpha_R \quad (31)$$

$$u_R=\varepsilon(1-w_p)u\sqrt{\eta\left\{1+\kappa\left(\sqrt{1+\frac{8K_T(J_P)}{\pi J_P^2}}-1\right)\right\}^2+1-\eta} \quad (32)$$

$$\alpha_R=\delta-\bar{\gamma}_R\frac{U}{u_R}(\beta-\bar{\ell}_R r') \quad (33)$$

$$\bar{\gamma}_R=\frac{1}{2}(\gamma_{R(s)}+\gamma_{R(P)})$$

$$\bar{\ell}_R=\frac{1}{2}(\ell'_{R(s)}+\ell'_{R(P)})$$

$$f_\alpha=\frac{6.13\Lambda}{2.25+\Lambda}\quad,\varepsilon=\frac{1-w_R}{1-w_P} \quad (34)$$

$$\eta=\frac{D_P}{H_R},\beta=\arctan(\frac{-v}{u}),U=\sqrt{u^2+v^2} \quad (35)$$

2.5Excited wave force

The wave-induced forces as the sum of the Froude-Krylov force (W_FK) and the diffraction force (W_Dif) including hydrodynamic lift forces acting on the hull are rewitten as follows. The rudder forces due to wave particle velocity which are considered for broaching prediction (Umeda & Hashimoto, 2002) are not taken into account for predicting pure loss of stability. The Froude-Krylov roll moment is taken into account for calculating the roll restoring force variation, so that only the diffraction force is used in Eq. (39).

$$X_W(\xi_G/\lambda,u,\chi)=X_{W\_FK}(\xi_G/\lambda,u,\chi)$$
$$=-\rho g\zeta_w k\cos\chi\int_{AE}^{FE}C_1(x)S(x)e^{-kd(x)/2}\sin k(\xi_G+x\cos\chi)dx \quad (36)$$

$$Y_W(\xi_G/\lambda,u,\chi)=Y_{W\_FK}(\xi_G/\lambda,u,\chi)+Y_{W\_Diff}(\xi_G/\lambda,u,\chi)$$
$$=\rho g\zeta_w k\sin\chi\int_{AE}^{FE}C_1(x)S(x)e^{-kd(x)/2}\sin k(\xi_G+x\cos\chi)dx$$
$$+\zeta_w\omega\omega_e\sin\chi\int_{AE}^{FE}\rho S_y(x)e^{-kd(x)/2}\sin k(\xi_G+x\cos\chi)dx \quad (37)$$
$$-\zeta_w\omega u\sin\chi\left[\rho S_y(x)e^{-kd(x)/2}\cos k(\xi_G+x\cos\chi)\right]_{AE}^{FE}$$

$$N_W(\xi_G/\lambda,\chi)=N_{W\_FK}(\xi_G/\lambda,u,\chi)+N_{W\_Diff}(\xi_G/\lambda,u,\chi)$$
$$=\rho g\zeta_w k\sin\chi\int_{AE}^{FE}C_1(x)S(x)e^{-kd(x)/2}x\sin k(\xi_G+x\cos\chi)dx$$
$$+\zeta_w\omega\omega_e\sin\chi\int_{AE}^{FE}\rho S_y(x)e^{-kd(x)/2}x\sin k(\xi_G+x\cos\chi)dx \quad (38)$$
$$+\zeta_w\omega u\sin\chi\int_{AE}^{FE}\rho S_y(x)e^{-kd(x)/2}\cos k(\xi_G+x\cos\chi)dx$$
$$-\zeta_w\omega u\sin\chi\left[\rho S_y(x)e^{-kd(x)/2}x\cos k(\xi_G+x\cos\chi)\right]_{AE}^{FE}$$

$$K_W(\xi_G/\lambda,u,\chi)=K_{W\_FK}(\xi_G/\lambda,u,\chi)+K_{W\_Diff}(\xi_G/\lambda,u,\chi)$$
$$=-\rho g\zeta_w k\sin\chi\int_{AE}^{FE}C_1(x)\frac{B(x)}{2}\{d(x)\}^2e^{-kd(x)/2}\sin k(\xi_G+x\cos\chi)dx$$
$$-\rho g\zeta_w k^2\sin\chi\int_{AE}^{FE}C_4(x)\left\{\frac{B(x)}{2}\right\}^3d(x)e^{-kd(x)/2}\sin k(\xi_G+x\cos\chi)dx \quad (39)$$
$$-\zeta_w\omega\omega_e\sin\chi\int_{AE}^{FE}\rho S_y l_\eta(x)e^{-kd(x)/2}\sin k(\xi_G+x\cos\chi)dx$$
$$+\zeta_w\omega u\sin\chi\left[\rho S_y l_\eta(x)e^{-kd(x)/2}\cos k(\xi_G+x\cos\chi)\right]_{AE}^{FE}$$
$$+Y_w(\xi_G/\lambda,u,\chi)\cdot\overline{OG}$$

$$C_1=\frac{\sin(k\sin\chi\cdot B(x)/2)}{k\sin\chi\cdot B(x)/2} \quad (40)$$

$$C_4=\{k\sin\chi\cdot B(x)/2\}^{-3}\left[2\sin\{k\sin\chi\cdot B(x)/2\}\right. \quad (41)$$
$$\left.-k\sin\chi\cdot B(x)\cos\{k\sin\chi\cdot B(x)/2\}\right]$$

2.6 Roll restoring force variation

Pure loss of stability is one of the problems related to the roll restoring force variation. The restoring force variation in oblique waves can be calculated by integrating the pressure around the instantaneously wetted hull surface with static balance of heave and pitch as show in Eq.(42) which is base on Froude-Krylov assumption (Lu et al., 2017). The Froude-Krylov roll moment is taken into account in Eq. (42) in oblique waves, while the effect of wave heading is converted into the change of the

effective wave height in longitudinal waves by using Grim's effective wave concept in the references (Umeda &Yamakoshi, 1994; Kubo et al., 2012). For avoiding double counting of the Froude-Krylov roll moment in case of oblique waves, only the diffraction force is used in Eq. (39).

$$W\cdot GZ_W=\rho g\int_{AE}^{FE} y(x,\xi_G/\lambda)\cdot A(x,\xi_G/\lambda)\,dx+\rho g\sin\chi\cdot \int_{AE}^{FE} z(x,\xi_G/\lambda)\cdot F(x)\cdot A(x,\xi_G/\lambda)\cdot\sin(\xi_G+x\cos\chi)dx \quad (42)$$

$$F(x)=\zeta_w k\frac{\sin(k\frac{B(x)}{2}\sin\chi)}{k\frac{B(x)}{2}\sin\chi}e^{-kd(x)} \quad (43)$$

where, $A(x,\xi_G/\lambda)$ is the submerged area of local section of the ship. $y(x,\xi_G/\lambda)$ is the transverse position of buoyancy centre of local section. $z(x,\xi_G/\lambda)$ is the vertical position of buoyancy centre of local section.

2.7 Roll damping force

Roll damping is one of essential terms for predicting roll motion, especialy large amplitude roll motion. Linear and cubic nonlinear roll damping coefficients are used for predicting parametric roll and linear and squared nonlinear roll damping coefficients are used for predicting dead ship stability in the vulnerability criteria (IMO SDC 4, 2017). Linear and cubic nonlinear roll damping coefficients are adopted as shown in Eq.(44) for predicting pure loss of stability, which could lead to large amplitude roll motion, or even capsizing,in following and stern-quartering waves.

$$D(p)=(I_{xx}+J_{xx})(\alpha\cdot p+\gamma\cdot p^3) \quad (44)$$

3. EXPERIMENTS

The free running experiment with a 1/40.526 scaled model of the ONR tumblehome vessel were newly conducted in the seakeeping basin (length: 69 m, breadth: 46 m, depth: 4 m) of China Ship Scientific Research Center, which is equipped with flap wave makers at the two adjacent sides of the basin.

The ship model was used to study stability under dead ship condition (Gu et al., 2015), and here the standard bilge, rudders and propellers are added. The ship model was driven by twin propellers in regular following and stern-quartering seas in the free running experiment. The roll angle, pitch angle and yaw angle were measured by the MEMS (Micro Electro-Mechanical System)-based gyroscope placed on the ship model and the roll angle, pitch angle, yaw angle, rudder angle and propeller rate were recorded by an on-board system which is connected with an on-shore control computer by a wireless. The wave elevation was measured at the middle position of the basin by a servo-needle wave height sensor attached to a steel bridge which is 78 m length and spans over the basin.

Roll damping is very important for predicting pure loss of stability which is often accompanied with large roll motions, and here free roll decay tests with different initial roll angles in calm water are conducted to obtain roll damping coefficients. The speed is a key factor for pure loss of stability, and here the nominal Froude number (Fn) is used for the experiment of pure loss of stability in following and stern-quartering waves by using the same specified propeller rate in calm water. The specified propeller rate corresponding one nominal speed in calm water is determined by measuring instantaneous position of the model ship with a total station system, and the total station system is consists of a theodolite and a prism attached on the model ship as shown in Fig. 2.

First the model is kept near the wave maker by hands of two workmen sitting on the carriage and the initial heading of the model is kept referring to the steel bridge which can rotate about its center, up to 45 degree. Next, the wave-making system starts to generate waves. Then the propeller revolutions increase up to specified value after receiving the order from the on-shore control computer by a wireless. When the wave train propagates far enough, the model is released free near one wave crest with its initial heading, and then the model automatically runs in following or

quartering waves with its specified propeller rate and auto pilot course.

Fig. 2 The theodolite and the prism attached on the model ship

The subject ship is the ONR tumblehome vessel which is one of standard ships for the second generation intact stability criteria provided by the coordinator of corresponding group. The principal particulars and the lines of the ONR tumblehome vessel are shown in Table 1 and Fig. 3, respectively. The system parameters of the ONR tumblehome used in this standard mathematical model refer to (Umeda et al., 2016) as shown in Table 2.

Table 1 Principal particulars of the ONR tumblehome

Items	Ship	Model
Length:L	154.0m	3.800m
Draft:d	5.494m	0.136m
Breadth:B	18.8m	0.463m
Depth:D	14.5m	0.358m
Displ.:W	8507ton	127.8kg
C_B	0.535	0.535
GM	1.48m	0.037m
OG	-2.729m	-0.067m
L_{CB}	-2.569m	-0.063m
T_φ	14.0s	2.199s
κ_{yy}	0.25L	0.25L
K_{zz}	0.25L	0.25L
$2\times A_R$	$2\times23.74m^2$	$2\times0.0145\ m^2$
D_P	5.22m	0.129m
δ_{max}	35degs	35degs

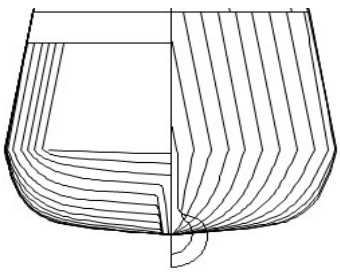

Fig. 3 The ONR Tumblehome lines

Table 2 System parameters of the ONR tumblehome used in this standard mathematical model

Items	Ship	Items	Ship
m_x/m	0.015	$1-t_R$	0.323
m_y/m	0.680	$1+a_H$	1.312
J_{ZZ}/I_{ZZ}	0.676	$x_R+a_H x_{HR}$	-88.3
K_P	3.0	$z_R+a_H z_{HR}$	7.02
T_D	0.0	κ	0.647
T_E	0.1	ε	0.932
t_P	0.25	$\bar{\gamma}_R$	0.472
w_P	0.15	$\bar{\ell}'_R$	-0.709
z_H/d	0.852	Λ	1.18
		η	0.982

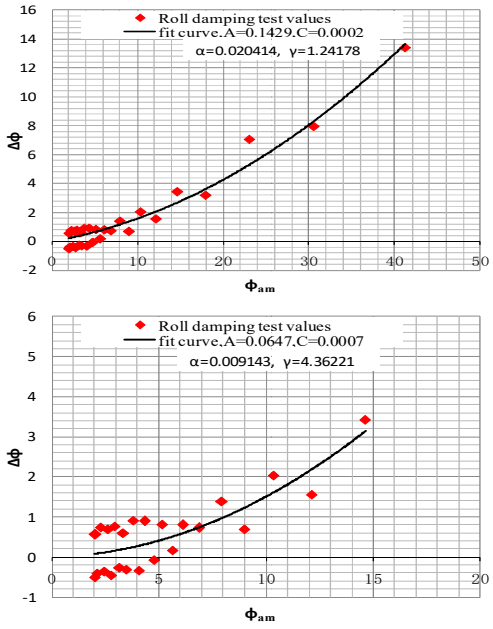

Fig. 4 Extinction curve with different initial roll amplitudes (A, C are linear and cubic extinction coefficients and α, γ are their non-dimensional coefficients)

The nonlinear roll damping coefficients are obtained from free roll decay tests with different initial roll amplitudes and the damping coefficients are also different as shown in Fig. 4.

The type of roll motions at different conditions of speed during pure loss of stability, such as the stable periodic roll motion, the unstable roll motion and the capsizing due to pure loss of stability are captured in the experiments as shown in Fig. 5 (a), (b) and (c), respectively.

(a) Snapshot of the stable periodic roll motion far from the critical speed of pure loss of stability

(b) Snapshot of the unstable roll motion near the critical speed of pure loss of stability

(c) Snapshot of the capsizing due to pure loss of stability

Fig. 5 The type of roll motions at different conditions of speed during pure loss of stability

4. SIMULATIONSAND DISCUSSIONS

4.1 The effect of high order coefficients

The higher order maneuvering coefficients for hydrodynamic force acting on ship hull in the surge motion are taken into accout in the MMG standard method for ship maneuvering prediction (Yasukawa & Yoshimura, 2015), and the higher order maneuvering coefficients without X_{vvv} are also recommended for predicting pure loss of stability by Japan (IMO SLF55，2013; Kubo et al., 2012), while these higher order maneuvering coefficients are ignored for broaching prediction (Umeda et al., 2016). For investigating the effect of higher order maneuvering coefficients in the surge motion on predicting pure loss of stability, the following value X'_{vv}=-0.1194, X'_{vr}=-0.0649, X'_{rr}=0.0084,1 X'_{vvv}=0.4323 are used based on databases of ships.

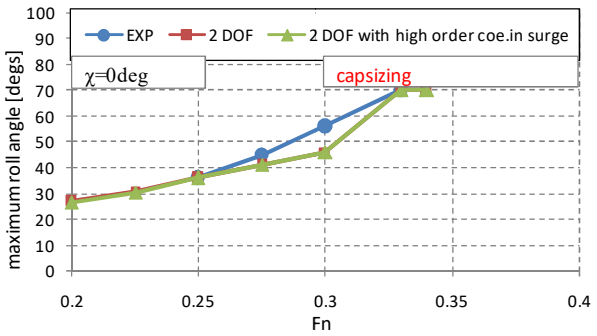

Fig. 6 Comparison of maximum roll angle as function of the Froude number between the experimental results and calculated results with the 2 DOF without and with higher order coefficients in the surge motion with *λ/Lpp*=1.25, *H/Lpp*=0.05, and $\chi=0^0$, and the initial heel angle is set 8.6 degrees by cargo shift.

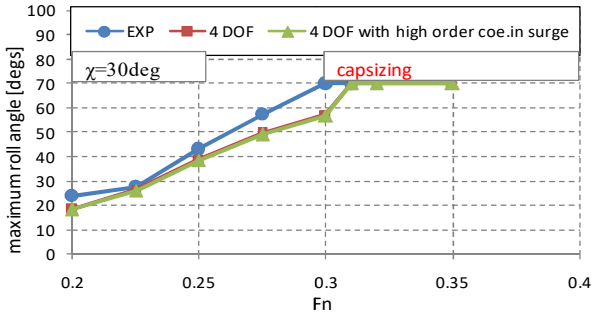

Fig. 7 Comparison of maximum roll angle as function of the Froude number between the experimental results and calculated results with the 4 DOF without and with higher order coefficients in the surge motion with *λ/Lpp*=1.25, *H/Lpp*=0.05, and $\chi=30^0$.

A comparison of maximum roll angle as function of the Froude number between the experimental results and calculated results with 2 DOF without and with higher order coefficients in the surge motion of *λ/Lpp*=1.25, *H/ Lpp*=0.05, and $\chi=0^0$ are carried out as shown in Fig.6, while the similar comparison with the 4 DOF in stern-quartering waves are shown in Fig.7. The results indicate that the effect of higher order maneuvering coefficients in the surge motion on predicting pure loss of stability is very small. The higher order maneuvering coefficients in the surge motion are ignored in following simulations.

The higher order maneuvering coefficients of heel-induced hydrodynamic forces are not considered in this study due to lack of referenced databases of ships. The other

maneuvering coefficients mentioned in the references (Hashimoto et al., 2011b; Umeda et al., 2016) are used in this study.

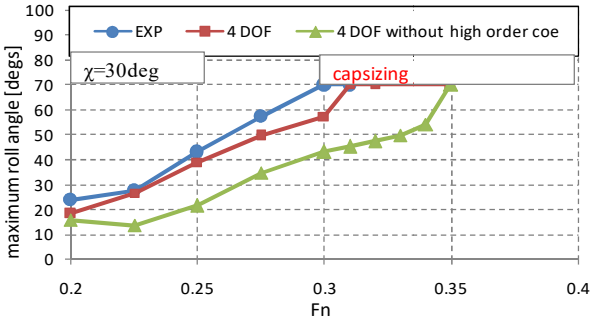

Fig. 8 Comparison of maximum roll angle as function of the Froude number between the experimental results and calculated results with the 4 DOF with and without higher order maneuvering coefficients in sway, roll and yaw motions with λ/Lpp=1.25, H/Lpp=0.05, and χ=30^0.

The higher order maneuvering coefficients in sway, roll and yaw motions for hydrodynamic force acting on ship hull could affect predicting pure loss of stability, and a comparison of maximum roll angle between the experimental results and calculated results with 4 DOF with and without high order coefficients in sway, roll and yaw motions under the conditon of λ/Lpp=1.25, H/Lpp=0.05, and χ=30^0 are carried out as shown in Fig.8. The results indicate that the mathematical model of 4 DOF without higher order maneuvering coefficients in sway, roll and yaw motions could predict capsizing due to pure loss of stability, but it underestimates the roll angle and capsizing range of critical ship speeds.

4.2 The effect of different DOF

For investigating the effect of different mathematical models on predicting pure loss of stability, a comparison of maximum roll angle as function of the Froude number between mathematical models with different DOF are conducted.

A comparison of maximum roll angle as function of the Froude number between the 4 DOF and the 2 DOF under the condition of λ/Lpp=1.25, H/Lpp=0.05, and χ=0^0 are carried out as shown in Fig.9, while the similar comparison in stern-quartering waves are shown in Fig.10.

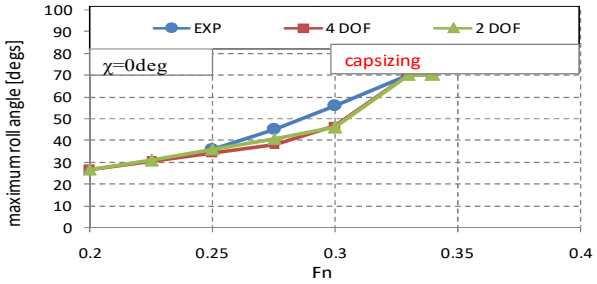

Fig. 9 Comparison of maximum roll angle as function of the Froude number between the experimental results and calculated results with 4 DOF and 2 DOF models with λ/Lpp=1.25, H/Lpp=0.05, and χ=0^0, and the initial heel angle is set 8.6 degrees by cargo shift.

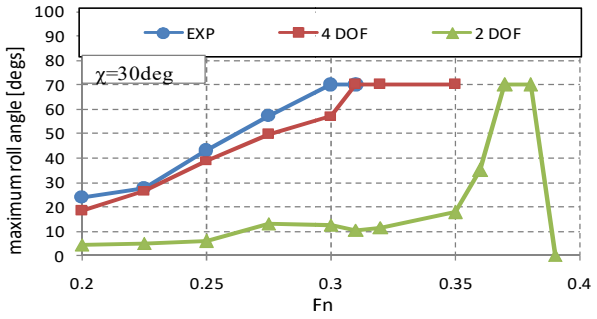

Fig. 10 Comparison of maximum roll angle as function of the Froude number between the experimental results and calculated results with 4 DOF and 2 DOF models with λ/Lpp=1.25, H/Lpp=0.05, and χ=30^0.

The results indicate that both the mathematical with the 2 DOF and 4 DOF coupled motions could appropriately estimate the pure loss of stability in following waves. The results also show that the mathematical model with the 2 DOF coupled motion could fail to predict pure loss of stability in stern-quartering waves, while the 4 DOF coupled motion could appropriately estimate the pure loss of stability instern-quartering waves.

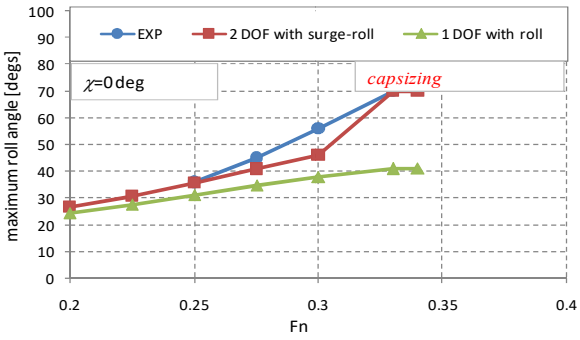

Fig. 11 Comparison of maximum roll angle as function of the Froude number between the experimental results and calculated results with mathematical models of different DOF with λ/Lpp=1.25, H/Lpp=0.05, and χ=0^0, and the initial heel angle is 8.6 deg due to cargo shift.

As shown in Fig.11, the mathematical model with 1 DOF of roll motion fails to predict capsizing due to pure loss of stability in following waves while that with 2 DOF of surge-roll coupled motions could appropriately estimate the pure loss of stability in following waves. Therefore, the surge motion is important for predicting pure loss of stability in following waves.

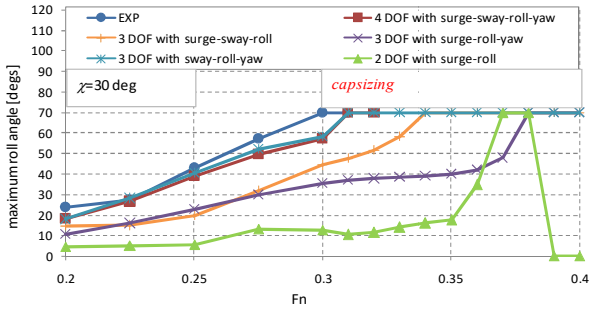

Fig. 12 Comparison of maximum roll angle as function of the Froude number between the experimental results and calculated results with mathematical models of different DOF with λ/Lpp=1.25, H/Lpp=0.05, and χ=30^0.

As shown in Fig.12, the mathematical models with the 3 DOF and the 2 DOF coupled motions could underestimate the roll angle in stern-quartering waves except the 3DOF with sway-roll-yaw coupled motions. This means not only the surge motion, but also the centrifugal force due to sway and yaw motions are very important for predicting pure loss of stability in stern-quartering waves.

The mathematical model with 4 DOF of surge-roll-sway-yaw coupled motions could predict roll angle and appropriately estimate capsizing due to pure loss of stability, and pure loss of stability in stern-quartering waves could not "pure". This also supports the conclusion in the reference (Kubo et al., 2012) that the centrifugal force due to sway and yaw motions, other than the restoring reduction on a wave crest, are indispensable for explaining "pure" loss of stability on a wave crest. Therefore, both the sway and yaw motions should be considered in the mathematical model for predicting pure loss of stability in stern-quartering waves.

4.3 The effect of diffraction forces

Diffraction forces are very important for predicting ship motions in waves, and for investigating the effect of diffraction forces on predicting pure loss of stability in stern-quartering waves, simulations with diffraction forces, without diffraction forces and only without diffraction forces in the roll motion are carried out as shown in Fig.13.

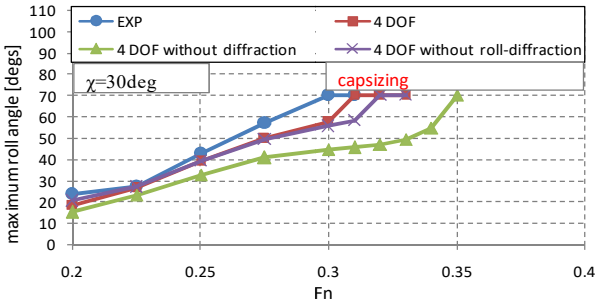

Fig. 13 Comparison of maximum roll angle as function of the Froude number between the experimental results and calculated results with the 4 DOF with and without diffraction force and only without diffraction force in the roll motion with λ/Lpp=1.25, H/Lpp=0.05, and χ=30^0.

The mathematical model of 4 DOF without diffraction forces could underestimate roll angle due to indirectly reducing the effect of maneuvering motions on the roll and it also fails to correctly predict capsizing range of critical ship speeds. The mathematical model of 4 DOF only without diffraction forces in the roll motion could predict roll angle, but it could underestimate the capsizing range of critical ship speeds. This means diffraction forces should be taken into account for predicting pure loss of stability in stern-quartering waves.

4.4 The effect of heel-induced hydrodynamic forces for large heel angle in calm water

Pure loss of stability is accompanied with large roll. The heel-induced hydrodynamic forces for large heel angle in calm water, which are hydrodynamic lift due to underwater non-symmetry induced by heel angle with forward velocity, could affect the prediction of pure loss of stability. The linear heel-induced hydrodynamic forces in calm water are investigated as shown in Fig.14. The effect of the linear heel-induced hydrodynamic forces, such as $Y_{\varphi}^{'}\cdot\varphi, N_{\varphi}^{'}\cdot\varphi, K_{\varphi}^{'}\cdot\varphi$, on pure loss of stability is not significant at this presented condition. However, the 4 DOF mathematical

model without linear heel-induced hydrodynamic forces could fail to predict capsizing at critical ship speed due to pure loss of stabiltity in previous study (Lu& Gu, 2017). The effect of heel-induced hydrodynamic forces on pure loss of stability should be further studied and if this effect is not significant, the complicated procedure and time can be ignored for obtained these coefficients, and also a seekeeping model could be condsidered because the maneuvering model needs so many maneuvering coefficients which should be obtained from experiments and also changed with ship speed.

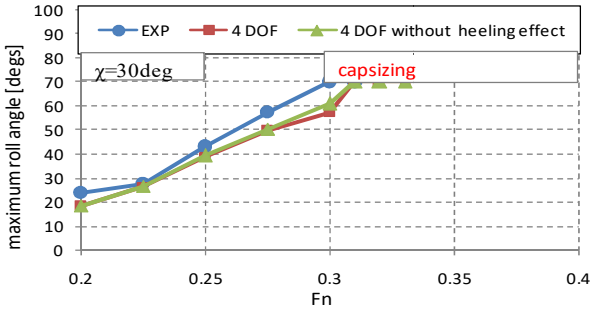

Fig. 14 Comparison of maximum roll angle as function of the Froude number between the experimental results and calculated results with the 4 DOF with and without linear heeling effect with λ/Lpp=1.25, H/Lpp=0.05, and χ=30^0.

4.5 The effect of roll damping

Roll damping is one of essential terms for predicting large amplitude roll motions, such as parametric roll, roll under dead ship condition and roll due to pure loss of stability. Linear and cubic nonlinear roll damping coefficients are adopted for predicting parametric roll (IMO SDC 4, 2017). However, the roll damping coefficients obtained from the roll decay with different initial roll amplitudes could be different , and could result in a significant difference of roll angle for predicting large amplitude roll motions.

The effects of nonlinear damping coefficient obtained from the roll decay with different initial roll amplitudes on predicting pure loss of stability are investigated as shown Fig. 15. It shows that the calculated results of 4 DOF mathematical model with the damping coefficients from the roll decay up to 40 degrees is better than that up to 15 degrees. Therefore, for predicting large amplitue roll motions, the roll decay with a large initial roll amplitue is necessary.

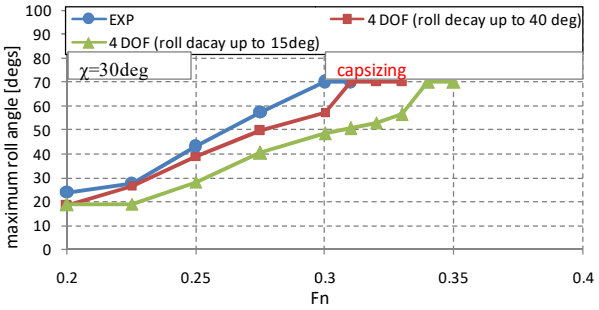

Fig. 15 Comparison of maximum roll angle as function of the Froude number between the experimental results and calculated results with the 4 DOF with roll damping coefficients from different initial roll amplitudes of roll decay with λ/Lpp=1.25, H/Lpp=0.05, andχ=30^0.

4.6 The type of roll motions during pure loss of stability

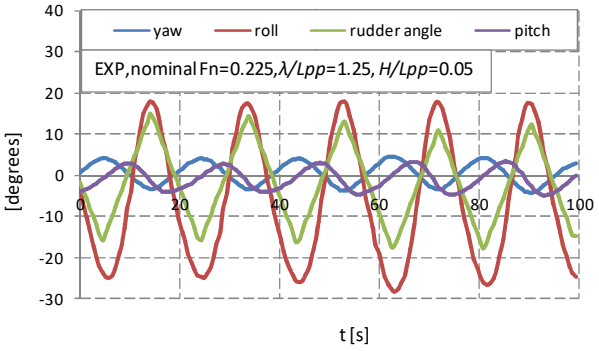

(a) stable roll motion far from the critical speed of pure loss of stability

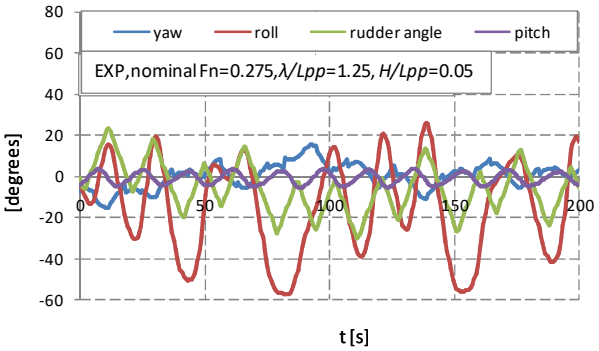

(b) unstable roll motion near the critical speed of pure loss of stability

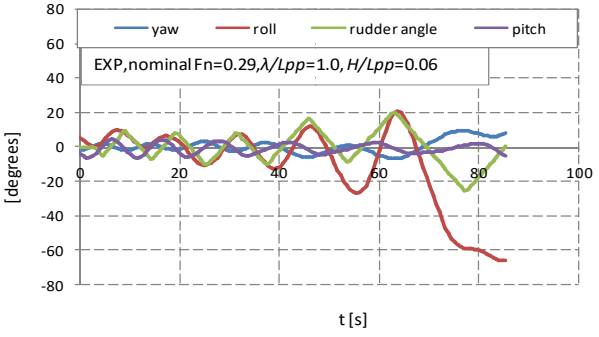

(c) capsizing due to pure loss of stability

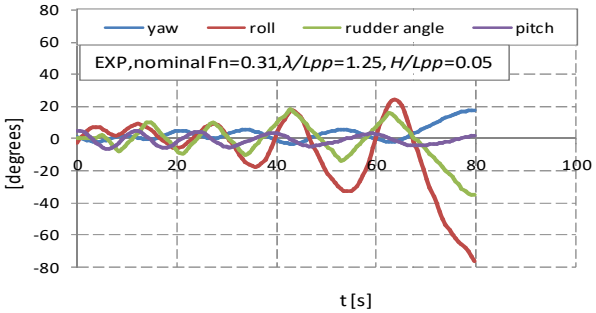

(d) capsizing due to coupled pure loss of stability and broaching

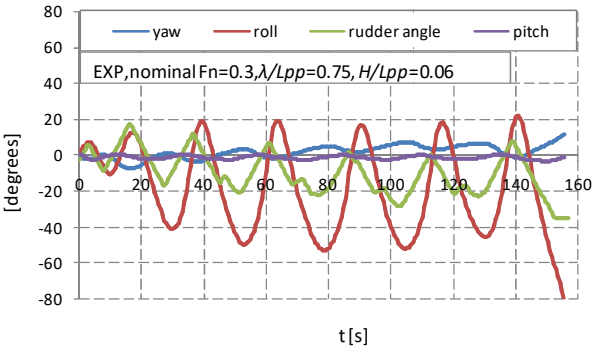

(e) capsizing due to coupled pure loss of stability and broaching

Fig. 16 Yaw, roll, pitch motions and rudder angle in the free running experiment with χ=30^0.

The experimental results of yaw, roll, pitch motions and rudder angle in stern-quartering waves are shown in Fig. 16. A stable periodic roll motion can be found when the ship speed is far from the critical speed of pure loss of stability as shown in Fig.16(a), while an unstable roll motion can be found when the ship speed is close to the critical speed as shown in Fig.16(b). The capsizing due to pure loss of stability is shown in Fig.16(c). The yaw angle reaches to 20 degrees and the rudder angle reaches to the maximum 35 degrees when ship capsizes as shown in Fig.16(d). The yaw angle reaches to 12 degrees and the rudder angle reaches to the maximum 35 degrees to correct the course, but the capsizing occurs due to pure loss of stability before developing a more larger yaw angle, that is too say, the maximum rudder angle cannot correct course and obvious broaching is stopped due to capsizing as shown in Fig.16(e). This could be a new phenomenal of capsizing due to coupled pure loss of stability and broaching.

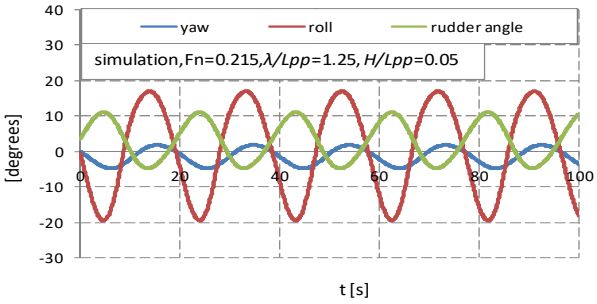

(a) stable periodic roll motion far from the critical speed of pure loss of stability

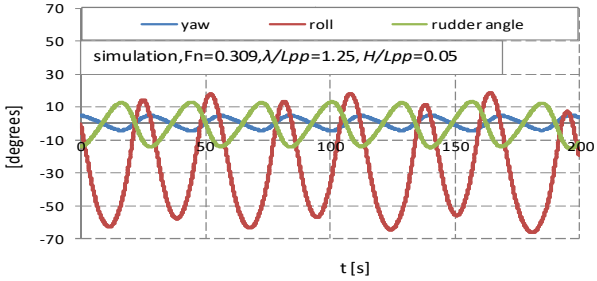

(b) unstable roll motion near the critical speed of pure loss of stability

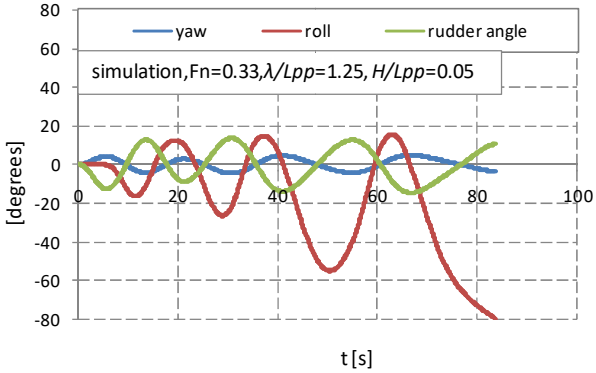

(c) capsizing due to pure loss of stability

Fig. 17 Yaw, roll motions and rudder angle in the simulation with the 4 DOF mathematical model with *λ/Lpp*=1.25, *H/Lpp*=0.05 and χ=30^0.

The calculated results of yaw, roll motions and rudder angle in stern-quartering waves are shown in Fig.17. A stable periodic roll motion when the ship speed is far from the critical speed of pure loss of stability, an unstable roll motion when the ship speed is close to the critical speed and the capsizing due to pure loss of stability also can be found in the simulations with the 4 DOF mathematical model as shown in Fig.17 (a), (b) and (c), respectively. However, the new phenomenal of capsizing due to coupled pure loss of stability and broaching in the experiment cannot be recurred by the simulations at this stage, while a difference of the phase of the yaw motion is still existed and the unstable roll motion also

cannot be completely repeated in the simulations. Pure loss of stability in stern-quartering waves is more complicated than our previous understanding, although the roll angle and capsizing due to pure loss of stability can be predicted.

5. CONCLUSIONS

On the basis of the experimental and numerical study on standard mathematical model of pure loss of stability with the ONR tumblehome vessel, the following remarks can be made:

1) The effect of surge motion with varied forward speed effect on pure loss of stability in following and stern-quartering waves should be considered while the higher order maneuvering coefficients in the surge motion can be ignored.

2) The 2 DOF coupled motion could appropriately estimate pure loss of stability in following waves while could fail to predict pure loss of stability in stern-quartering waves, and the 4 DOF coupled motion could appropriately estimate pure loss of stability in stern-quartering waves.

2) The centrifugal force due to sway and yaw motions and maneuvering motions with higher order maneuvering coefficientss should be considered in the 4 DOF standard mathematical model of pure loss of stability.

3) The effect of diffraction forces on pure loss of stability in stern-quartering waves should be taken into account.

4) Nonlinear roll damping coefficients obtained from the roll decay with large initial roll amplitudes should be considered for predicting pure loss of stability.

5) Pure loss of stability is not pure in stern-quartering waves. Unstable roll motions and capsizing due to coupled pure loss of stability and broaching could be existed during pure loss of stability.

6. AKNOWLEDMENTS

Some contents used in this research were once guided by Prof. Naoya Umeda during the first author's Ph.D course at Osaka University supported by China Scholarship Council [No. 2008606031]. The research is supported by Ministry of Industry and Information Technology of China (No. [2016] 25, 26; [2017] 614) and China research fund (No. B2420132001; No. 51509124). These supports are gratefully acknowledged.

7. REFERENCES

Gu M., Lu J. and Wang T.H., 2015, "Stability of a Tumblehome Hull under Dead Ship Condition", Journal of Hydrodynamics, Vol. 27 (3), pp. 452-457.

Hamamoto M. and Kim Y.S., 1993, "A New Coordinate System and the Equations Describing Manovering Motion of a Ship in Waves", Journal of the Society of Naval Architects of Japan, Vol. 173, pp. 209-220.

Hashimoto H., Umeda N. and Matsuda A.,2004, "Importance of Several Nonlinear Factors on Broaching Prediction", Journal of Marine Science and Technology, Vol. 9, pp. 80-93.

Hashimoto H., Umeda N. and Matsuda A., 2011a, "Model Experiment on Heel-Induced Hydrodynamics Force in Waves for Realising Quantitative Prediction of Broaching", M.A.S. Neves et al. (eds.), Contemporary Ideas on Ship Stability and Capsizing in Waves, Fluid Mechanics and Its Application 96, pp. 379-397.

Hashimoto H., Umeda N. and Matsuda A., 2011b, "Broaching Prediction of a Wave-piercing Tumblehome Vessel with Twin screws and Twin Rudders", Journal of Marine Science and Technology, Vol. 16, pp. 448-461.

IMO 2013, Development of Second Generation Intact Stability Criteria, SLF55/INF.15. Annex 12

IMO 2016, Finalization Second Generation Intact Stability Criteria, SDC 3/WP.5. Annex 3

IMO 2017, Finalization Second Generation Intact Stability Criteria, SDC4/WP.4.

Khanfir S., Hasegawa K., Nagarajan V., Shouji K. and Lee S.K., 2011, "Manoeuvring Characteristics of Twin-rudder systems: Rudder-hull Interaction Effect on the Manoeuvrability of Twin-rudder Ships", Journal of Marine Science and Technology, Vol. 16, pp. 472-490.

Kubo H., Umeda N., Yamane K. and Matsuda A., 2012, "Pure Loss of Stability in Astern Seas -Is It Really Pure?", Proceedings of the 6th Asia-Pacific Workshop on Marine Hydrodynamics, pp. 307-312.

Lu J., Gu M. and Umeda N., 2017, "Experimental and Numerical Study on Several Crucial Elements for Predicting Parametric Roll in Regular Head Seas", Journal of Marine Science and Technology, Vol. 22, pp. 25-37.

Lu J. and Gu M., 2017, "Study on Standard Mathematical Model of Pure Loss of Stability in Stern-quartering Waves", 16th International Ship Stability Workshop, 5-7 June 2017, Belgrade, Serbia

Matsuda A. and Umeda N., 1997, "Vertical Motions of a Ship Runing in Folloqing and Quartering Seas", Naval Architecture and Ocean Engineering, No.227, pp. 47-55 (in Japanese).

Umeda N., 1999, "Nonlinear Dynamics of Ship Capsizing due to Broaching in Following and Quartering Seas", Journal of Marine Science and Technology, Vol. 4, pp. 16-26.

Umeda N. and Hashimoto H., 2002, "Qualitative Aspects of Nonlinear Ship Motions in Following and Quartering Seas with High Forward Velocity", Journal of Marine Science and Technology, Vol. 6, pp. 111-121.

Umeda N. and Hashimoto H., 2003, "Broaching Prediction in the Light of an Enhanced Mathematical Model, with High-order Terms Taken into Account", Journal of Marine Science and Technology, Vol. 7, pp. 145-155.

Umeda N., Usada S., Mizumoto K., and Matsuda A., 2016, "Broaching Probability for a Ship in Irregular Stern-quartering Waves: Theoretical Prediction and Experimental Validation", Journal of Marine Science and Technology, Vol. 21, pp. 23-37.

Umeda N. and Yamakoshi Y., 1994, "Probability of Ship Capsizing due to Pure Loss of Stability in Quartering Seas", Naval Architecture and Ocean Engineering, Vol.30, pp.73-85.

Umeda N., Furukawa T., Matsuda A. and Usada S., 2014, "Rudder Normal Force during Broaching of a Ship in Stern Quartering Waves", 30th Symposium on Naval Hydrodynamics, Hobart, Tasmania, Australia, 2-7 November 2014.

Yasukawa H. and Yoshimura Y., 2015, "Introduction of MMG Standard Method for Ship Maneuvering Predictions", Journal of Marine Science and Technology, Vol. 20, pp. 37-52.

Empirical and experimental roll damping estimates for an oil tanker in the context of the 2nd generation intact stability criteria

Mauro Costa de Oliveira, *Petrobras* mauro@petrobras.com.br

Bruno Barros de Mendes Kassar, *PUC-Rio* bkassar@tecgraf.puc-rio.br

Luiz Cristovão Gomes Coelho, *PUC-Rio* lula@tecgraf.puc-rio.br

Flávia Vieira Monteiro, *UFRJ* flaviamonteiro@poli.ufrj.br

Rafael Torres de Santis, *UFRJ* rafaeltorres@poli.ufrj.br

Claudio Alexis Rodriguez Castillo, *UFRJ* claudiorc@oceanica.ufrj.br

Marcelo de Almeida Santos Neves, *UFRJ* masn@laboceano.coppe.ufrj.br

Júlio Cézar F. Polo, *UFRJ* jcf.polo@gmail.com

Paulo de Tarso Themistocles Esperança, *UFRJ* ptarso@laboceano.coppe.ufrj.br

ABSTRACT

This paper assesses the prediction approaches for the roll damping coefficients based on experimental decay tests, Ikeda's original method (Himeno, 1981) and the simplified approach (Kawahara et al., 2009) that has been proposed for the second generation intact stability criteria. The damping coefficients obtained from these procedures have been applied in a time domain nonlinear model for the simulation of ship motions in waves, developed to perform direct stability assessments. Furthermore, a set of model test results with a VLCC oil tanker in decay, regular and irregular wave tests have been used as benchmark to assess the accuracy of the damping estimates. A single degree of freedom numerical model has also been implemented to allow second-level intact stability calculations and compare their results with those of the 6-dof direct assessment simulations.

Keywords: *roll damping, Ikeda, 2nd generation, stability criteria, decay tests*

1. INTRODUCTION

The 2nd Generation Intact Stability Criteria has been under development in the IMO for around 15 years (IMO-SLF, 2006). This new set of rules consists of five stability vulnerability modes to be evaluated in up-to-three levels. In this new approach a more physical and rational analysis is required compared to the prescriptive nature of the current 2009 IS Code (IMO, 2009). The assessment of vulnerability in the second and third levels requires time domain simulations for some of the failure modes, for instance, parametric rolling. Therefore, roll damping coefficients estimates are necessary to perform the numerical predictions. The Explanatory Notes developed by IMO subcommittee recommend the use of the simplified Ikeda empirical procedure (Kawahara et al, 2009) to estimate the roll damping coefficients. To verify the applicability of this approach, the

present work have performed a detailed comparison of those results with those from the more complete (original) Ikeda formulation (Himeno, 1981) and from experimental results using a VLCC type oil tanker as case study.

2. ESTIMATION OF ROLL DAMPING COEFFICIENTS FROM DECAY TESTS

The roll motion of a ship in wave can be expressed as a one degree of freedom equation defined as:

$$(I_{44}+a_{44})\ddot{\phi}(t)+B\dot{\phi}(t)+c_{44}\phi(t)=M_{\phi} \quad (1)$$

Where $\phi(t)$ represents roll, I_{44} is the roll inertia, a_{44} and c_{44} denote the added mass and hydrostatic restoring coefficients, respectively, and M_ϕ is the exciting moment.

Dividing by $(I_{44}+a_{44})$:

$$\ddot{\phi}+\frac{B}{(I_{44}+a_{44})}\dot{\phi}+\frac{mg\overline{GM}}{(I_{44}+a_{44})}\phi=\hat{M}_{\phi} \quad (2)$$

The natural damped frequency ω_n is given by

$$\frac{mg\overline{GM}}{(I_{44}+a_{44})}=\omega_n^2 \quad (3)$$

And the normalized damping p is

$$p=\frac{B}{(I_{44}+a_{44})}, \quad (4)$$

So that, the normalized roll equation is

$$\ddot{\phi}+p\dot{\phi}+\omega_n{}^2\phi=\hat{M}_{\phi} \quad (5)$$

Defining the damping term as linear and quadratic, such that:

$$p\dot{\phi}=p_1\dot{\phi}+p_2\dot{\phi}\left|\dot{\phi}\right| \quad (6)$$

Three procedures have been applied to obtain the damping coefficients p_1 and p_2 from the decay tests: the logarithmic decrement method, the Froude energy method (quadratic form), and a least-squares iterative method.

2.1 Logarithmic decrement method

If the exciting moment in eq. (5) is a harmonic function, then the resulting roll motion takes the following form:

$$\phi(t)=\phi_0\cos(\omega t). \quad (7)$$

Then, in the quadratic damping term of eq.(6) we get:

$$\dot{\phi}\left|\dot{\phi}\right|=-\phi_0^2.\omega^2.\sin(\omega t)\left|\sin(\omega t)\right| \quad (8)$$

It is possible to describe the function sin(ωt) |sin(ωt)| as a Fourier series:

$$\sin(\omega.t)\left|\sin(\omega.t)\right|=\frac{8}{3\pi}\sin(\omega.t)+\sum_{n=3,5,\ldots}^{\infty}\frac{8}{\pi(n+2)n(n-2)}\sin(n\omega.t) \quad (9)$$

Taking only the first term, eq.(9) becomes

$$\sin(\omega.t)\left|\sin(\omega.t)\right|\approx\frac{8}{3\pi}\sin(\omega.t) \quad (10)$$

Introducing T_k as the measured damped period $T_k=2\pi/\omega$ and ϕ_k as the initial amplitude of each cycle, eq.(8) results in

$$\dot{\phi}\left|\dot{\phi}\right|\approx-\frac{8}{3\pi}\phi_k^2\omega^2\sin(\omega t)=\frac{8}{3\pi}\phi_k\omega\,\dot{\phi}(t)=\frac{16}{3T_k}\phi_k\dot{\phi}(t) \quad (11)$$

Using eq.(11), the quadratic damping term can be simplified to

$$p\dot{\phi}(t)=\left(p_1+p_2\frac{16}{3T_k}\phi_k\right)\dot{\phi}(t). \quad (12)$$

For decay tests, without external exciting moment, the problem is described by the following homogeneous equation:

$$\ddot{\phi}(t)+p\dot{\phi}(t)+\omega_n{}^2\phi(t)=0. \quad (13)$$

The solution of eq.(13) is

$$\phi(t)=\phi_0\,e^{\frac{-pt}{2}}\cos\left[\sqrt{\omega_n^2-\left(\frac{p}{2}\right)^2}\;t+\beta\right]. \quad (14)$$

Analyzing the exponential decay term in eq.(14), we define the logarithmic decrement in cycle k as

$$\delta_k=\ln\left(\frac{\phi_k}{\phi_{k+2}}\right)=\ln\left(e^{\frac{p}{2}T_k}\right)=\frac{p}{2}T_k, \quad (15)$$

Where ϕ_k and ϕ_{k+2} are respectively the magnitudes of the roll angles at times t_k and t_k+T_k. Then, it is possible to find the equivalent linear damping:

$$p = \frac{2\delta_k}{T_k} \tag{16}$$

For each cycle, p versus $(16/(3T_k))\ \phi_k$ will be plotted, where ϕ_k is the initial angle for each cycle. By linear regression on p data and eq.(6), p_1 and p_2 can be obtained, as shown in Fig. 1.

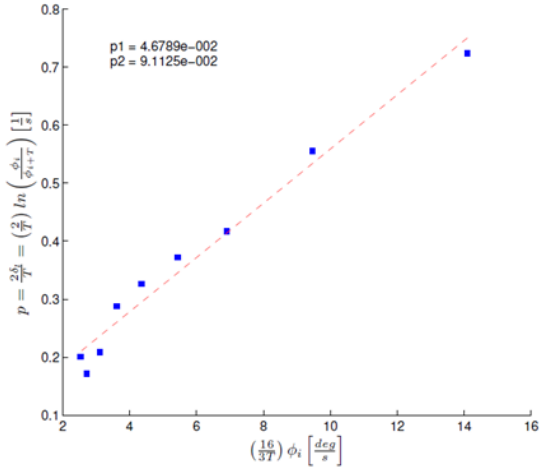

Figure 1 Typical fit of decay test data for the logarithmic decrement method

2.2 Froude's energy method

This method is based on the energy balance which assumes that the dissipated energy by the damping term in half cycle is equal to the variation of the potential energy, as the kinetic energy at the initial and final positions are zero. In the roll decay equation assuming linear plus quadratic damping, the energy balance gives:

$$\int_0^{t=T/2} [\ddot{\phi} + p_1\dot{\phi} + p_2\dot{\phi}|\dot{\phi}| + \omega_n{}^2\phi]d\phi = 0 \tag{17}$$

As $\frac{d\phi}{dt} = \dot{\phi}$ then $d\phi = \dot{\phi}dt$, then:

$$\int_0^{t=T/2} [\ddot{\phi} + p_1\dot{\phi} + p_2\dot{\phi}|\dot{\phi}|]\dot{\phi}dt + \int_{\phi_k}^{\phi_{k+1}} \omega_n{}^2\phi\dot{\phi}dt = 0 \tag{18}$$

Integrating, and considering k=1:

$$\int_0^{t=T/2} \ddot{\phi}(t)\dot{\phi}(t)dt = 0 \tag{19}$$

$$\int_0^{t=T/2} p_1\dot{\phi}(t)\dot{\phi}(t)dt = p_1\frac{\pi^2}{T}\phi_0^2 \tag{20}$$

$$\int_0^{t=T/2} p_2\dot{\phi}(t)|\dot{\phi}(t)|\dot{\phi}(t)dt = p_2\frac{16\pi^2}{3T^2}\phi_0^3 \tag{21}$$

$$\int_{\phi_1}^{\phi_2} \omega_n{}^2\phi(t)\dot{\phi}(t)dt = \omega_n{}^2(\phi_1 - \phi_2)\frac{(\phi_1 + \phi_2)}{2} \tag{22}$$

So for the energy balance equation:

$$p_1\frac{\pi^2}{T}\phi_0^2 + p_2\frac{16\pi^2}{3T^2}\phi_0^3 = \omega_n{}^2(\phi_1 - \phi_2)\frac{(\phi_1 + \phi_2)}{2} \tag{23}$$

With: $\omega_n = \frac{2\pi}{T}$ and $\phi_0 = \frac{(\phi_1 + \phi_2)}{2}$. Then, dividing by $4\pi^2/T^2$, we get:

$$p_1\frac{T}{4}\phi_0 + p_2\frac{4}{3}\phi_0^2 = (\phi_1 - \phi_2)\phi_0 \tag{24}$$

If we also define $\delta\phi = (\phi_1 - \phi_2)$, then:

$$\delta\phi = p_1\frac{T}{4}\phi_0 + p_2\frac{4}{3}\phi_0^2 \tag{25}$$

Eq. (25) denotes a quadratic (parabolic) function for $\delta\phi$ against ϕ_0. Figure 2 illustrates a typical fitting for decay data using the energy method.

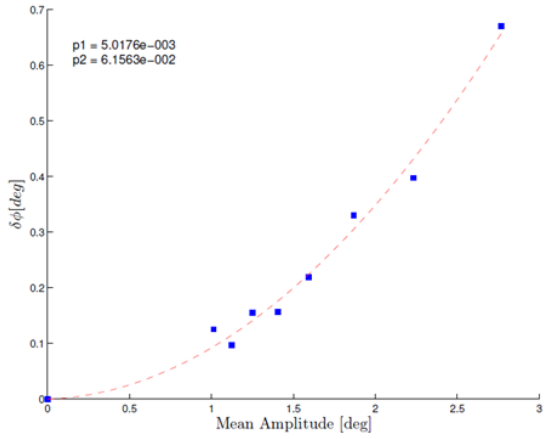

Figure 2 Quadratic fit of decay test data

2.3 Least-squares iterative method

This method, here called K method, is based on the fitting of the numerical solution of the roll decay equation (eq. 13) to the time series of the decay test. The fitting process is iterative and based on the least-squares method using the damping coefficients in the roll decay equation as parameters.

3. VLCC TANKER DATA

The ship selected for this study is a Very Large Crude Carrier (VLCC) oil tanker. Its main characteristics at the full loading condition are shown in Table 1. A 1/70-scaled model has been tested at the Ocean Technology Laboratory (LabOceano) of the Federal University of Rio de Janeiro. The tests included decay tests, regular wave and irregular wave tests.

Table 1. VLCC characteristics

LBP	320.00	m
Breadth	54.50	m
Depth	27.80	m
Condition	Full loading	
Draft	21.00	m
Displ.	311,046.00	t
I44	1.092E+08	$t.m^2$
VCG	14.34	m
GM	7.90	m

3.1 Decay tests results

The results of B_1 and B_2 have been obtained based on three sets of decay tests, with initial heel angles of 5º (T18-00300), 10º (T18-00303) and 15º (T18-00306). A typical decay test is illustrated in figure 3.

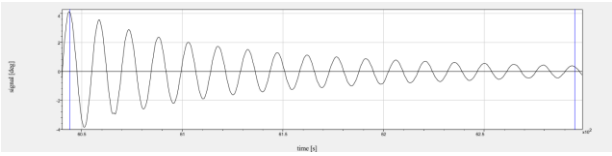

Figure 3 Decay test

Tables 2 to 4 show the results of the analyses of the decay tests for the VLCC using the methods described earlier for the three initial conditions. B_1 and B_2 represent the dimensional coefficients corresponding to p_1 and p_2.

Table 2. T18-00300 Damping coefficients for 5º

	B_1 [ton.m²/s]	B_2 [ton.m²/s²]
Logarithmic	2.01E+06	6.26E+07
Energy	2.52E+06	3.30E+07
K-method	1.97E+06	6.62E+07

Table 3. T18-00303 Damping coefficients for 10º

	B_1 [ton.m²/s]	B_2 [ton.m²/s²]
Logarithmic	2.20E+06	7.01E+07
Energy	2.03E+06	7.87E+07
K-method	1.78E+06	9.03E+07

Table 4. T18-00306 Damping coefficients for 15º

	B_1 [ton.m²/s]	B_2 [ton.m²/s²]
Logarithmic	2.70E+06	5.66E+07
Energy	2.03E+06	7.87E+07
K-method	1.81E+06	9.05E+07

Tables 5 to 7 summarize the results for each method.

Table 5. Damping coefficients - Energy method

Test condition	B_1 [ton.m²/s]	B_2 [ton.m²/s²]
Test 5°	2.61E+06	2.93E+07
Test 10°	2.02E+06	7.76E+07
Test 15°	1.91E+06	8.23E+07
Average	2.18E+06	6.31E+07

Table 6. Damping coefficients - Logarithmic method

Test condition	B_1 [ton.m²/s]	B_2 [ton.m²/s²]
Test 5°	2.00E+06	6.23E+07
Test 10°	2.27E+06	6.49E+07
Test 15°	2.47E+06	6.45E+07
Average	2.25E+06	6.39E+07

Table 7. Damping coefficients - K method

Test condition	B_1 [ton.m²/s]	B_2 [ton.m²/s²]
Test 5°	1.92E+06	7.15E+07
Test 10°	1.82E+06	8.68E+07
Test 15°	1.80E+06	8.94E+07
Average	1.85E+06	8.26E+07

4. IKEDA'S METHOD

4.1 Context and Development

The equation of roll motion can be expressed as:

$$\ddot{\phi} + B_1\dot{\phi} + B_2\left|\dot{\phi}\right|\dot{\phi} + C_1\phi = M \qquad (26)$$

A empirical method for roll damping prediction of ships has been proposed by Ikeda et al. (1978b) Later, Himeno (1981) made a comprehensive review of Ikeda's method and also presented a computer code for numerical application. The method is based on the assumption that roll damping can be separated in components that can computed independently according to various kinds of fluid flow phenomena, namely, skin friction of the hull, eddy shedding from the hull, free-surface waves, etc. It was also pointed out that roll damping may be strongly affected by the presence of bilge-keels, rudder and other appendages.

In Ikeda's method the total roll-damping coefficient for an ordinary ship hull form can be divided into five components, namely, friction, eddy, lift and wave damping for the naked hull, plus bilge keels damping., i.e.:

$$B_e = B_F + B_E + B_L + B_W + B_{BK} \qquad (27)$$

$$B_{BK} = B_{BKN} + B_{BKH} + B_{BKW} \qquad (28)$$

Friction damping B_F is caused by the skin-friction stress on the hull in roll motion. The eddy damping B_E is caused by the pressure variation on the naked hull due the formation of eddies. B_L represents the lift damping which is associated to the lifting effect of the hull itself in roll motion due to ship forward speed. The wave damping, B_W, denotes the increment of the hull-pressure due to the presence of free surface waves.

Bilge keel damping B_{BK} represents the increment of pressure damping due to the presence of bilge keels. This term can be divided in three components: B_{BKN} due to the normal force on the bilge keels themselves, B_{BKH} which represents the damping due to the pressure change on the hull when bilge keels are installed, i.e., accounts for the interaction between hull and bilge keels, and B_{BKW} which is the wave damping due to the presence of bilge keels. In summary, according to Ikeda's method, B_L, B_W, and B_{BKW} account for non-viscous damping whereas, B_F, B_E, B_{BKN}, B_{BKH} represent the viscous effects.

Recently, Kawahara et al. (2009) have proposed a simplified procedure for roll damping estimation based on Ikeda's original method. This simplified approach only requires main ship dimensions and coefficients as input data instead of the detailed hull geometry data as in the original Ikeda's method.

4.2 Numerical tool

Based on the original Ikeda's method (Himeno, 1981), a script for the numerical prediction of roll damping and the corresponding damping coefficients B_1 and B_2 have been implemented. Additionally, an option for the calculation of the simplified Ikeda's method has been included.

4.3 Input data for Ikeda's method

Tables 8 to 10 present the data of the VLCC tanker that was used as input for the damping prediction script based on Ikeda's method.

Table 8. Fluid data

water kinematic viscosity [m²/s]	0.000001188
water specific mass [t/m³]	1.025

Table 9. Bilge keel data

length [m]	127.2
width [m]	1.0

Table 10. Ship Data

Main Parameters	**Full loading**
Draft [m]	21
Froude number	0
Volume [m³]	303461
Wetted Area [m²]	27196
Block coeff. [0.5,0.85]	0.809
Midship coeff. [0.9,0.99]	0.996
KG [m]	16.8
Bilge keel pos. X1 [m]	-45.37
Bilge keel pos. X2 [m]	81.83
OG	4.200

4.4 Damping coefficients results

The components of the roll damping moment, its total value, and the corresponding damping coefficients have been computed for

the natural period of the VLCC tanker at its full loading condition (14.7 s). Results for the simplified and original approaches of the Ikeda's method are displayed in graphical form in figures 4 to 7.

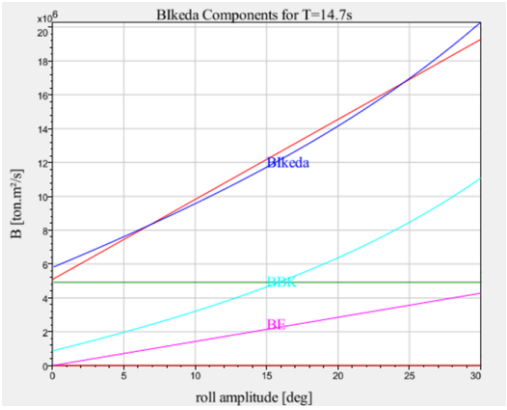

Figure 4 Damping components – simplified Ikeda

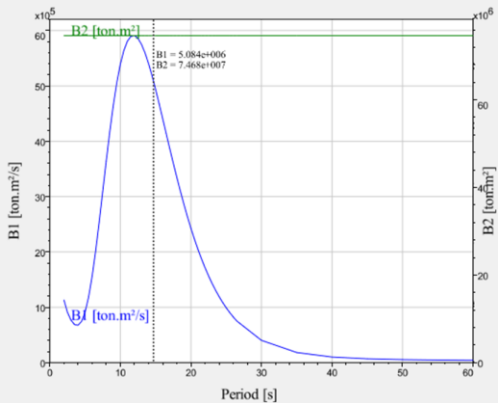

Figure 5 Damping coefficients – simplified Ikeda

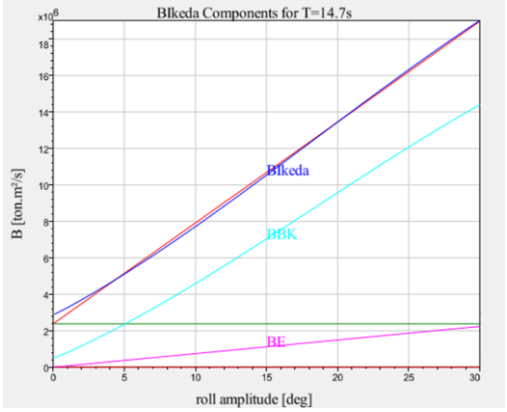

Figure 6 Damping components – original Ikeda

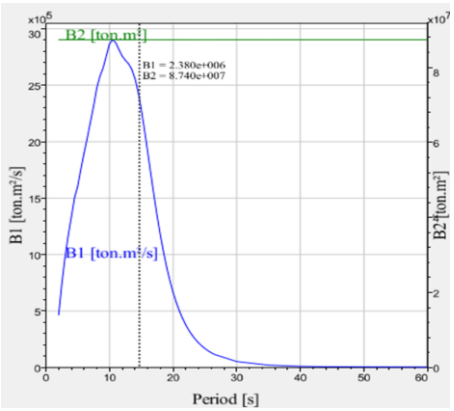

Figure 7 Damping coefficients – original Ikeda

Table 11. Ikeda damping coefficients

Ikeda	Period [s]	B1 [ton.m²/s]	B2 [ton.m²]
Original	14.70	2379988	87396943
Simplified	14.70	5083557	74683077

5. TIME DOMAIN VALIDATIONS

In this section the influence of the damping coefficients are presented comparing the numerical simulations with model test results, for decay tests, regular wave and irregular wave tests. The numerical results have been performed with the in-house code DSSTAB, developed by Tecgraf-PUC, Laboceano-UFRJ on behalf of CENPES-Petrobras. DSSTAB is a nonlinear time-domain numerical tool for the simulation of ship motions and offshore structures in waves. DSSTAB computes Froude-Krylov and hydrostatics actions up to the actual free-surface, while diffraction and radiation forces are based on linear frequency domain hydrodynamic data from Wamit®. Memory effects and mooring are also included.

All the following results belong to the VLCC tanker at is full loading condition.

5.1 Decay tests

Figures 8 to 10 present the time series of the decay tests for the initial conditions of 5º, 10º and 15º, respectively. Besides the experimental time series (TEST), two sets of numerical time series are presented in each figure: numerical simulations using the damping coefficients obtained from

experiments (F: energy method, K: K-method, L: logarithmic method) and numerical predictions using the damping coefficients obtained from Ikeda's method (IKS: simplified, IKC: original).

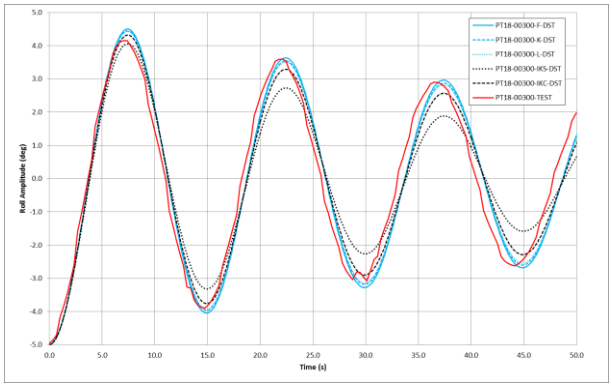

Figure 8 PT18-00300 Decay test time series

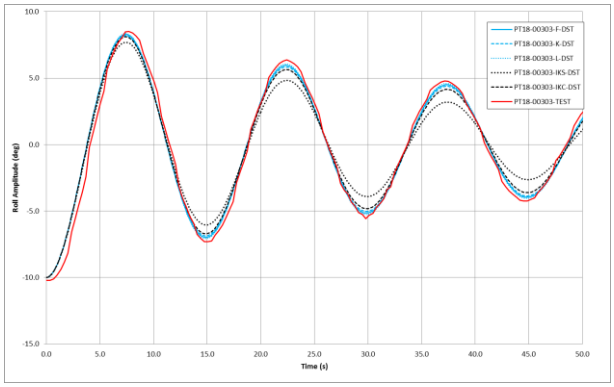

Figure 9 PT18-00303 Decay test time series

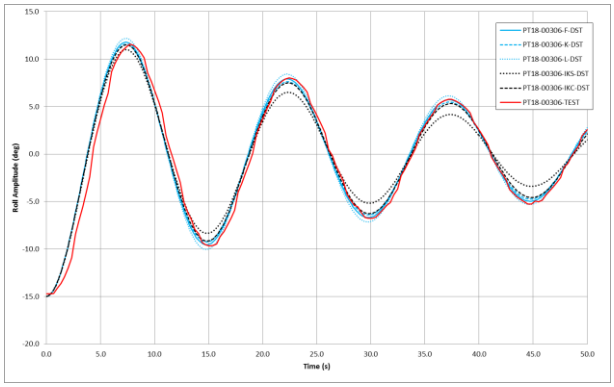

Figure 10 PT18-00306 Decay test time series

To analyse the quality of the numerical simulations in relation to model test results, the absolute value of the difference between the instantaneous roll motion in each time step has been calculated, summed up, averaged by the number of points and divided by the initial amplitude, resulting in a relative error.

Table 12. Error PT18-00300

	Accumulated Absolute Error (deg)	Average Abs. Error (deg)	Relative error
F	1466.84	0.489	0.098
K	1500.77	0.500	0.100
L	1460.27	0.486	0.097
IKS	1607.19	0.535	0.107
IKC	1442.52	0.481	0.096

Table 13. Error PT18-00303

	Accumulated Absolute Error (deg)	Average Abs. Error (deg)	Relative Error
F	1435.35	0.478	0.048
K	1480.96	0.493	0.049
L	1406.31	0.468	0.047
IKS	2148.42	0.716	0.072
IKC	1557.90	0.519	0.052

Table 14. Error PT18-00306

	Accumulated absolute error (deg)	Average abs. error (deg)	Relative error
F	1482.78	0.494	0.033
K	1555.20	0.518	0.035
L	1481.98	0.494	0.033
IKS	2403.60	0.801	0.053
IKC	1745.63	0.581	0.039

5.2 Regular wave tests

Figures 11 to 13 display the time series of the regular wave conditions from model tests and numerical simulations. The nomenclature for time series identification is the same adopted for decay tests in the previous section. The test conditions corresponded to waves of period around the roll natural period, beam incidence, and three wave heights.

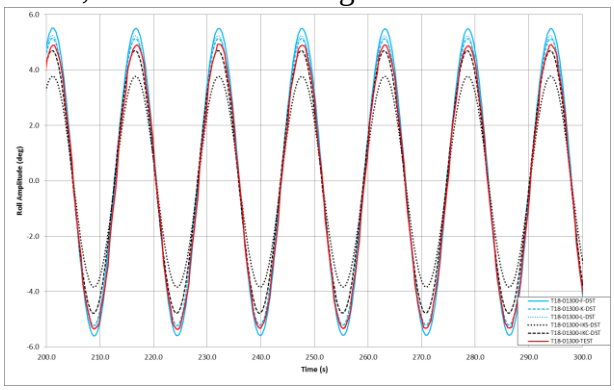

Figure 11 T18-01300 time series (H = 3.5 m).

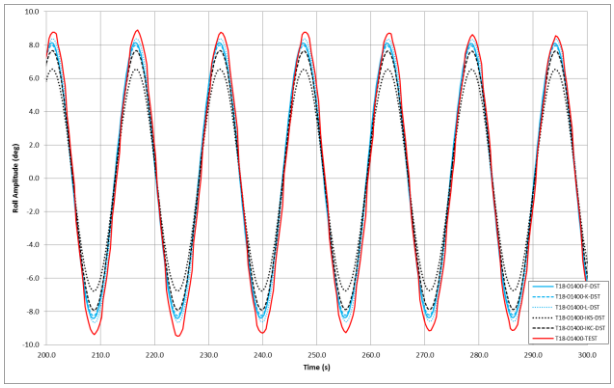

Figure 12 T18-01400 time series (H = 7.0 m).

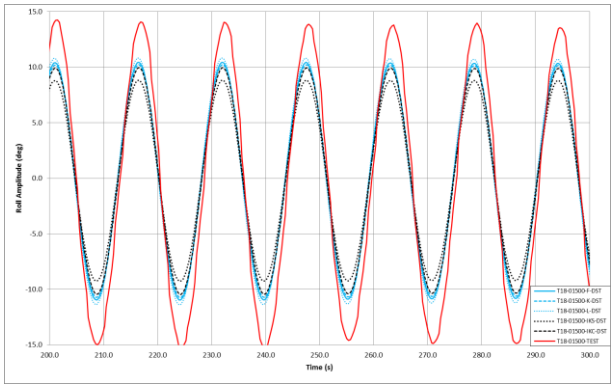

Figure 13 T18-01500 time series (H = 10.5 m).

Table 15. Error evaluation of regular wave tests simulations

		Standard Deviation (deg)		Error in relation to test %
Test	Procedure	MODEL TEST	DSSTAB	DSSTAB
T18-01300	L	3.79	3.63	-4.3%
T18-01300	F	3.79	3.81	0.6%
T18-01300	K	3.79	3.55	-6.2%
T18-01300	IKS	3.79	2.61	-31.2%
T18-01300	IKC	3.79	3.25	-14.2%
T18-01400	L	6.22	5.87	-5.6%
T18-01400	F	6.22	5.70	-8.3%
T18-01400	K	6.22	5.60	-10.0%
T18-01400	IKS	6.22	4.59	-26.2%
T18-01400	IKC	6.22	5.37	-13.7%
T18-01500	L	9.25	7.68	-16.9%
T18-01500	F	9.25	7.40	-20.0%
T18-01500	K	9.25	7.25	-21.6%
T18-01500	IKS	9.25	6.26	-32.3%
T18-01500	IKC	9.25	7.06	-23.7%

5.3 Irregular wave tests

The comparison has been performed with the irregular wave test T18-001600, which is based on a JONSWAP wave spectrum, with H_s=7.84 m and T_p=15.45 s. Figure 14 presents the time series of roll motion in the long-crested irregular wave, beam incidence.

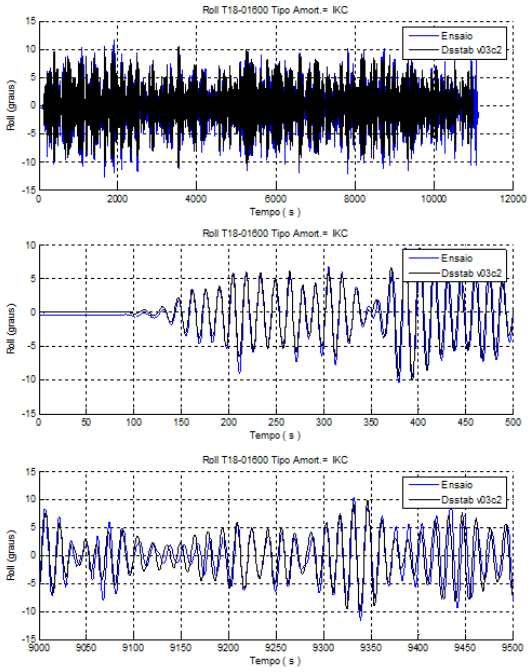

Figure 14 T18-01600 time series

Figures 15 shows the roll response spectra computed from experimental and numerical time series, using 5000 harmonic components. The nomenclature is the same adopted for regular wave tests. Figure 16 depicts the root mean square value computed from each of the roll motion (experimental and numerical) time series.

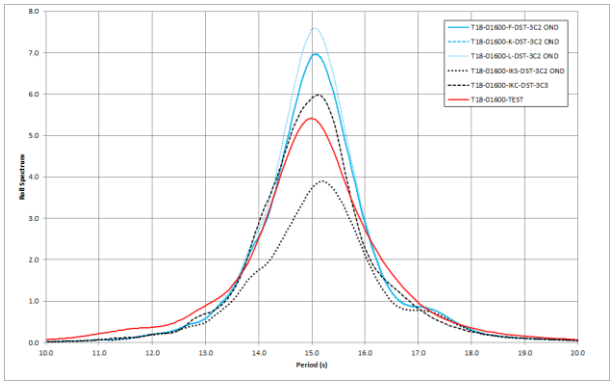

Figure 15 T18-01600 response spectra

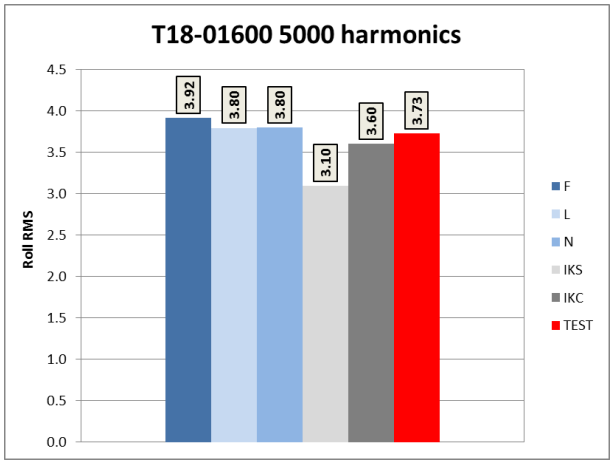

Figure 16 T18-01600 time series

Finally, figure 17 shows the error of the numerical time simulations taking as reference the experimental time series.

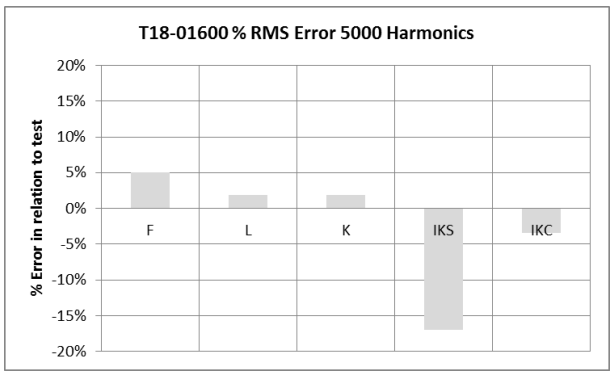

Figure 17 Error for the irregular wave test

6. LINEARIZATION PROCEDURE

In order to verify if the damping terms prediction procedures can be linearized and used in linear frequency domain programs, the following linearization scheme has been used. Considering the non-linear roll equation:

$$\ddot{\phi}+b_1\dot{\phi}+b_2\left|\dot{\phi}\right|\dot{\phi}+c_1\phi+c_3\phi^3=M \qquad (29)$$

Proceeding to the statistical linearization and applying the minimization of: $E\left[e(t)^2\right]$, where the error $e(t)=b_1\dot{\phi}+b_2\left|\dot{\phi}\right|\dot{\phi}-b_L\dot{\phi}+c_1\phi+c_3\phi^3-c_L\phi$. Being b_L and c_L variables, the minimum of $E\left[e(t)^2\right]$ satisfies:

$$\frac{\partial\{E\left[e(t)^2\right]\}}{\partial b_L}=0 \text{ and } \frac{\partial\{E\left[e(t)^2\right]\}}{\partial c_L}=0$$

which are equivalent to: $E\left[2e(t)(-\dot{\phi})\right]=0$ and $E\left[2e(t)(-\phi)\right]=0$, or $E\left[\dot{\phi}e(t)\right]=E\left[\phi e(t)\right]=0$

Applying the due substitutions, we get the following expressions:

$$E[\dot{\phi}e(t)]=E[b_1\dot{\phi}^2+b_2\left|\dot{\phi}\right|\dot{\phi}^2-b_L\dot{\phi}^2+c_1\phi\dot{\phi}+c_3\phi^3\dot{\phi}-c_L\phi\dot{\phi}]=0 \qquad (30)$$

$$E[\phi e(t)]=E[b_1\dot{\phi}\phi+b_2\left|\dot{\phi}\right|\dot{\phi}\phi-b_L\dot{\phi}\phi+c_1\phi^2+c_3\phi^4-c_L\phi^2]=0 \qquad (31)$$

Observing that if all statistical expected values contained on the right hand side were known, explicit expressions for the coefficients b_L e c_L can be set up in function of these statistical expected values. Considering that the roll displacement and velocity expected values are zero and retaining the most relevant terms, we get:

$$b_L\cong b_1+b_2\frac{E(\dot{\phi}^2\left|\dot{\phi}\right|)}{E(\dot{\phi}^2)}+c_3\frac{E(\phi^3\dot{\phi})}{E(\dot{\phi}^2)} \qquad (32)$$

$$c_L\cong c_1+c_3\frac{E(\phi^4)}{E(\phi^2)} \qquad (33)$$

Using eqs.(32) and (33) and choosing initial values for the expected values of b_L and c_L, it is possible to write an iterative procedure to obtain b_L, which is the linear equivalent damping. The equivalent linear equation follows:

$$\ddot{\phi}+b_L\dot{\phi}++c_L\phi=M \qquad (34)$$

Once eq.(34) is linear, the roll RAO can be determined in the frequency domain. Besides, the response spectra of the displacement and velocity can be determined respectively as follows:

$$S_{\phi\phi}(\omega)=\left|H(\omega)\right|^2S_{MM}(\omega) \qquad (35)$$

$$S_{\dot{\phi}\dot{\phi}}(\omega)=\omega^2\left|H(\omega)\right|^2S_{MM}(\omega) \qquad (36)$$

Where $S_{MM}(\omega)$ is the spectrum of the stochastic excitation M. From (35) and (36) the variances can be determined as below:

Roll variance:

$$\sigma_{\phi}^2 = \int_0^{\infty} |H(\omega)|^2 S_{MM}(\omega) d\omega \qquad (37)$$

Roll angular velocity variance:

$$\sigma_{\dot{\phi}}^2 = \int_0^{\infty} \omega^2 |H(\omega)|^2 S_{MM}(\omega) d\omega \qquad (38)$$

Inside the iterative process, the results obtained in (35) and (36) are compared, in each iteration, with the previous values to determine b_L and c_L, as indicated in (32) and (33).

If we consider a linear restoration ($c_3 = 0$), equations (32) and (33) simplify to:

$$b_L \cong b_1 + b_2 \frac{E(\dot{\phi}^2 |\dot{\phi}|)}{E(\dot{\phi}^2)} \qquad (39)$$

$$c_L \cong c_1$$

As the process is Gaussian, the statistical averages defined in (30) can be written as:

$$E(\dot{\phi}^2 |\dot{\phi}|) = 2\int_0^{\infty} \dot{\phi}^3 f(\dot{\phi}) d\dot{\phi} \qquad (40)$$

$$E(\dot{\phi}^2) = \int_{-\infty}^{\infty} \dot{\phi}^2 f(\dot{\phi}) d\dot{\phi} \qquad (41)$$

where (Gauss):

$$f(\dot{\phi}) = \frac{\exp[-\frac{\dot{\phi}^2}{2\sigma_{\dot{\phi}}^2}]}{\sigma_{\dot{\phi}}\sqrt{2\pi}} \qquad (42)$$

Calculating the integrals in (40) and (41) results in:

$$\frac{E(\dot{\phi}^2 |\dot{\phi}|)}{E(\dot{\phi}^2)} = \sqrt{\frac{8}{\pi}} \sigma_{\dot{\phi}} \qquad (43)$$

And finally:

$$b_L \cong b_1 + b_2 \sqrt{\frac{8}{\pi}} \sigma_{\dot{\phi}} \qquad (44)$$

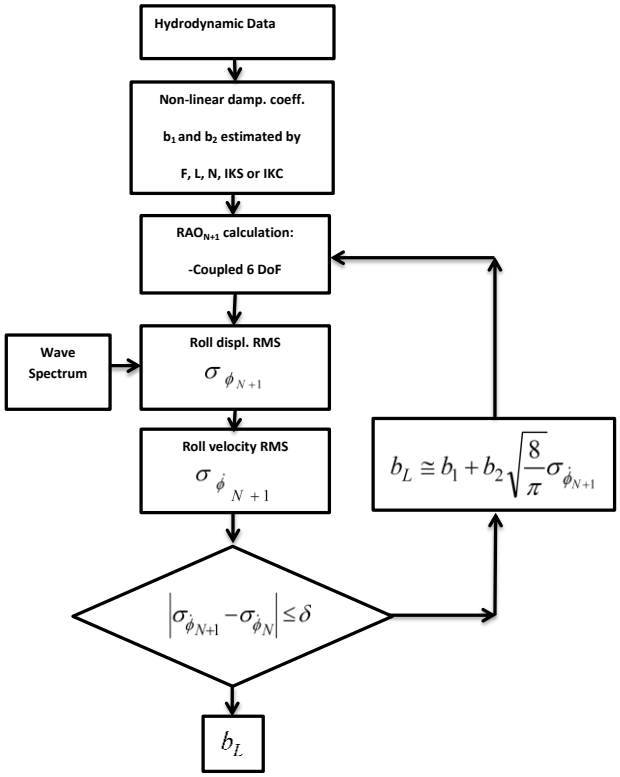

Figure 18 Linearization Procedure

6.1 Results

The linearization iterative procedure has been applied for the 5 pairs of damping coefficients calculated by the 5 different numerical procedures. Also the roll RAO has been calculated by the uncoupled single degree of freedom roll motion equation and with the 6 degrees of freedom equation, leading to the following results:

Table 16. Non-linear Damping Coefficients All Decay Tests All methods

Method	Roll Nat. Period [s]	B1 [ton.m²/s]	B2 [ton.m²]
F	14.7	2,180,220	63,073,200
L	14.7	2,247,150	63,901,300
K	14.7	1,846,560	82,594,600
IKS	14.7	5083,560	74,683,100
IKC	14.7	2,380,020	87,396,900

Table 17. Linearized Damping Coefficient B_{lin} – Uncoupled roll equation

Met.	Step	σ_{ϕ}	$\sigma_{\dot{\phi}}$	B_{linear} total [ton.m²/s]	B_{lin} total /crit
F	18	0.138	0.058	8,033,700	7.0%
L	18	0.137	0.058	8,130,200	7.1%

K	21	0.128	0.054	8,964,000	7.8%
IKS	13	0.113	0.048	10,755,000	9.4%
IKC	20	0.123	0.052	9,576,900	8.4%

Table 18. Linearized Damping Coefficient B_{lin} – Coupled roll equation

Method	Step	σ_ϕ	$\sigma_{\dot{\phi}}$	$B_{linear\ total}$ [ton.m²/s]	$B_{lin\ total}$ /crit
F	22	0.105	0.045	6,692,700	5.8%
L	21	0.104	0.044	6,774,200	5.9%
K	26	0.098	0.042	7,335,200	6.4%
IKS	12	0.081	0.035	9,224,200	8.3%
IKC	22	0.092	0.039	7,870,900	6.9%

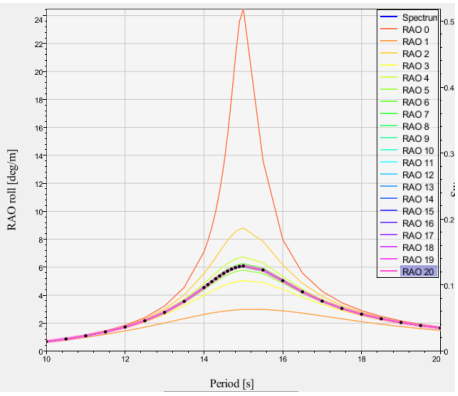

Figure 19 T18-01600 Irregular Wave Test Linearization Process Uncoupled 1 DoF Equation IKC Method with 20 steps

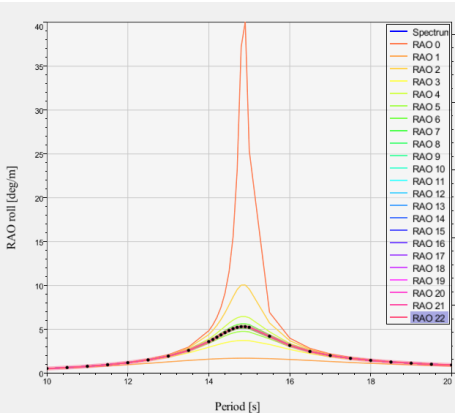

Figure 20 T18-01600 Irregular Wave Test Linearization Process with Coupled 6 DoF Equations IKC Method with 22 steps

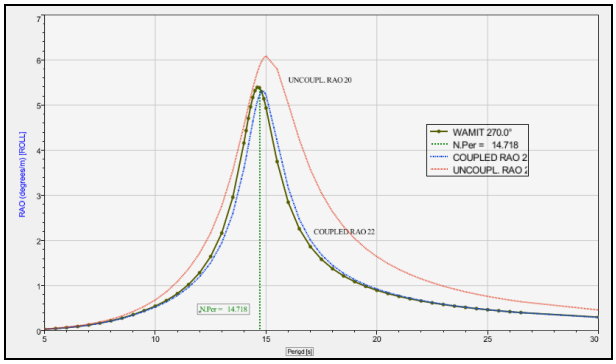

Figure 21 Comparison of RAOs T18-01600 Irregular Wave Test IKC Method generated by Coupled, Uncoupled and Wamit

Table 19. Linearized Damping Coefficient B_{lin} without the Potential Damping parcel – Uncoupled roll equation

Method	B lin - B44 [ton.m²/s]	(B lin - B44) /Bcrit
F	5,658,176	5.0%
L	5,754,676	5.1%
K	6,588,476	5.8%
IKS	8,379,476	7.3%
IKC	7,201,376	6.3%

Table 20. Linearized Damping Coefficient B_{lin} without the Potential Damping parcel – Coupled roll equation

Method	B lin - B44 [ton.m²/s]	(B lin - B44) /Bcrit
F	4,317,176	3.8%
L	4,398,676	3.9%
K	4,959,676	4.4%
IKS	6,848,676	8.0%
IKC	5,495,376	4.8%

Including the linearized damping coefficient in the frequency domain analysis using the computer program Wamit® and the same model test sea state (T18-001600) it is possible to determine the roll motion RMS and to compare with the model test RMS.

Table 21. Comparison of Roll RMS in Frequency Domain x Model Test – Uncoupled roll equation

Damping Estimation Method	RMS Roll (deg)	Error % test
F	5.26	41.1%
L	5.21	39.8%
K	4.83	29.4%
IKS	4.18	12.1%
IKC	4.58	22.8%
Model Test	3.73	

Table 22. Comparison of Roll RMS in Frequency Domain x Model Test – Coupled roll equations

Damping Estimation Method	rms roll (deg)	Error % test
F	6.09	63.3%
L	6.03	61.7%
K	5.66	51.7%
IKS	4.72	26.5%
IKC	5.35	43.4%
Test	3.73	

Observing Table 17 and Table 18 one can conclude that the linearized damping coefficient doesn't predict the roll response in the frequency domain method. The errors range from 12% to 63% overprediction. Bearing this in mind we calibrate a B2 coefficient in order to attain the correct RMS of the model test (3.73 degrees). It should also be noted the Ikeda Original (Complete) prediction of the B1 coefficient is exactly the potential damping coefficient.

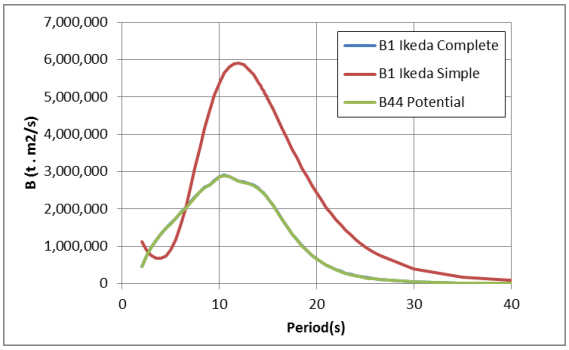

Figure 22 Linear B1 and B44 damping terms

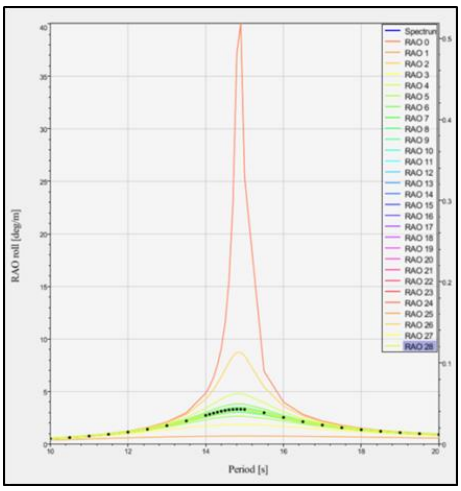

Figure 23 T18-01600 Irregular Wave Test Linearization Process Coupled 6 DoF Equation calibrated B2 with 28 steps

Table 23. Calibrated Linearized Damping Coefficient B_{lin} – Coupled roll equation

B1 [ton.m²/s]	B2 calibrated [ton.m²]	Blin total [ton.m²/s]	Blin total/ Bcrit
2,379,990	200,000,000	11,630,000	10.0%

Table 24. Calibrated Linearized Damping Coefficient B_{lin} without the Potential Damping parcel – Coupled roll equation

	B44 [ton.m²/s]	Blin - B44 [ton.m²/s]	(Blin - B44) /Bcrit
Calibration based on model test	2,379,990	9,250,010	7.9%

7. CONCLUSIONS

Although some differences were observed in the damping coefficients among the three methods of decay tests analyses, all of them, in general, reproduced well the decay time series. The initial angle on decay tests, at least, for the tested VLCC tanker, has a small influence on the obtained damping coefficients.

Regarding the assessment of damping coefficients in simulation of decay tests, regular and irregular wave tests, the conclusions have been summarized in the form of tables and organized by method and type of

test, using the following colours code to assess the roll motion prediction:

Blue: results of the numerical simulations using each method's predicted damping coefficients are greater than the model test series,

Green: simulations agree with model tests.

Red: simulations are below the model tests.

Table 25. Roll Decay Simulation x Model Tests Analysis

Damping coeff. from:	Decay Test 5º	Decay Test 10º	Decay Test 15º
Exp decay – F			
Exp decay – L			
Exp decay – K			
Ikeda Simple			
Ikeda Original			

Table 26. Reg. Wave Simulation x Model Tests Analysis

Damping coeff. from:	Reg. Wave 3.5 m	Reg. Wave 7 m	Reg. wave 10.5 m
Exp decay – F			
Exp decay – L			
Exp decay – K			
Ikeda Simple			
Ikeda Original			

Table 27. Irreg. wave time domain simulations x Model Tests Analysis

Damping coeff. from:	Irreg. Wave Time Domain
Exp decay – F	
Exp decay – L	
Exp decay – K	
Ikeda Simple	
Ikeda Original	

Table 28. Irreg. wave freq. domain simulations x Model Tests Analysis

Damping coeff. from:	Irreg. Wave Freq. Domain Uncoupled	Irreg. Wave Freq. Domain Coupled
Exp decay – F		
Exp decay – L		
Exp decay – K		
Ikeda Simple		
Ikeda Original		

In general, Ikeda's original approach performed better than the simplified approach. Indeed, in some of the studied conditions, the simplified approach failed, while the original approach did quite well. As the simplified approach is currently the recommended procedure for roll estimation in the context of second generation intact stability criteria, it is suggested that to improve the numerical simulations, Ikeda's original method should be considered, especially for direct assessment calculations.

The roll RMS predicted in the time domain simulations for irregular waves predicted by the original Ikeda's method were within 5% of the model tests results. The simplified approach showed excessive damping, leading to small roll angle predictions.

When linearized damping coefficients are used for frequency domain simulations for irregular waves, both, damping coefficients from decays tests and form Ikeda's prediction showed higher roll RMS compared to the irregular wave tests, i.e., damping was under-predicted.

8. ACKNOWLEDMENTS

The authors acknowledge the significant contribution from Petrobras in the development of the research to write this paper.

9. REFERENCES

Ikeda, Y. H., 1981, "*Prediction of Ship Roll Damping – State of the Art",* MI, USA.: Technical Report 239, Naval architecture and Marine Engineering, University of Michigan, Ann Harbor.

Ikeda, Y., Himeno, Y., & Tanaka, N., 1978, "Components of Roll Damping of Ship at Forward Speed", JSNA Japan, Vol. 143.

IMO-SLF. 2006, "Revision Of The Intact Stability Code" - Report of the Working Group on Intact Stability at SLF 49 (part 2). London, UK: IMO.

Kawahara, Y., Maekama K., Ikeda, Y., 2009, "A Simple Prediction Formula of Roll Damping of Conventional Cargo Ships on the basis of Ikedas Method and its Limitation", 10th International Conference on Stability of Ships and Ocean Vehicles (STAB'2009).

IMO. 2009. The International Code On Intact Stability. CPI Books Limited.

Study of the Properties of the Parametric Roll Stochastic Process of a Containership

Julio Cesar, Polo, LHEAA – Ecole Central de Nantes, Francejcf.polo@gmail.com

Marcelo, Neves, LabOceano - COPPE/UFRJ, Brazil masn@oceanica.ufrj.br

ABSTRACT

In the present paper the ergodicity and stationarity of the parametric roll motion under stochastic conditions were studied on a typical modern containership. This was done collecting data from numerical simulations using a new, very fast numerical model. Two wave conditions were studied. The results show that the roll process under parametric conditions seems to be a stationary process. Additionally, the recognized non-ergodic behaviour of the roll process seems to change according to the wave intensity.

Keywords:*Head seas; Parametric rolling; Irregular seas; Second generation stability criteria*

1. INTRODUCTION

Safety must be one of the main priorities in the process of designing ocean projects. For the purpose of guiding naval architects, international organizations and classification societies have developed norms and rules that designs must comply. Despite that, nowadays it is acknowledged that the norms and rules designed to ensure intact stability are not accurate enough to avoid some dangerous dynamic instabilities in ships. For this reason, the international community is currently working to consolidate a second generation of intact stability criteria, Peters et al. (2012). This new criteria is a three level tier based criteria for several dynamic instabilities. The first level is a vulnerability level based purely on basic geometric properties of designs. The second level is a check level, based on simplified models that represent the physics of each instability considered. The final level is a complete stability analysis under realistic wave conditions. The first two levels of the new criteria are in their final phase of development and soon shall be ready for implementation. Meanwhile, the third level is still in an early development stage. Nevertheless, it is clear that this level must be based on statistical analysis performed with the responses obtained with state of the art simulation algorithms. Possibly, the third level could be a reliability or risk analysis level, where the probability distribution of the responses for all the environmental conditions in which a specific design may encounter needs to be taken into account; see Kobylinski (1997) and McTaggart and de Kat (2000). This procedure could measure the total capsizing risk that a design may undergo during a single route or its entire lifetime.

One of the instabilities been considered in the new criteria is the Parametric Roll resonance. The Parametric Roll phenomenon is well known and it has been studied vastly by many researchers, for a review, see Neves (2016). Nevertheless, almost all approaches have been developed to study Parametric Roll under deterministic conditions. Since in real life those conditions are rarely encountered at sea by a ship, a complete intact stability study must take into consideration the wave excitation as a stochastic process. The main

issue that must be addressed in modelling the Parametric Roll as a stochastic process is that the Parametric Roll is a highly nonlinear phenomenon; therefore, spectral and statistical techniques employed in linear systems cannot be freely applied. This is caused by the non-ergodic character of the roll response under parametric conditions. Significant works regarding the non-ergodicity of roll responses are Belenky et al. (1998), Belenky et al. (2003), Bulian et al. (2006), Hashimoto et al. (2006a) and Rodríguez et al. (2016). The lack of practical ergodicity (See Bulian et al. 2006) in the roll responses prevents the characterization of the roll stochastic process by a single realization of the process. This makes compulsory the generation of several realizations of the roll process for a given wave condition in order to perform any statistical analysis. One of the statistical approaches used to obtain probability distributions of the roll process is the Extreme Value Theory (EVT); see McTaggart and de Kat (2000) and Kim et al. (2014). The EVT in its current state was formally presented in Gumbel (1959) for random variables. Later it was extended to stationary random processes by Leadbetter (1971). However, no mention about the stationarity of the roll process under parametric conditions was discussed in previous works.

In the present work, an analysis of the stochastic characteristics of the roll process was performed in a typical modern containership. The data for the analysis was taken from several realizations of the roll stochastic process obtained with a very fast simulation code; see more details in Polo et al. (2017).

2. MATHEMATICAL MODEL

The model used is a heave-roll-pitch coupled derivative model, in which the hydrostatic and wave-induced actions are represented in a Taylor series fashion up to the third order; see Neves and Rodríguez (2006a). For the wave-induced action, its periodic nature is taken as an advantage to build nonlinear oscillatory terms which are characterized by Fourier series up to second harmonic term. For stochastics conditions, these terms could be expressed as functions of high order response operators (which are an expansion of the RAO concept employed for the first order oscillatory terms) and the input spectrum. Then time domain realizations of the wave-induced actions could be obtained. Added mass and damping in the directly excited modes (heave and pitch) may be computed using convolution integrals (Cummins, 1962). However, based on Celis (2008), which reports small influence of memory effects on the development of parametric rolling in regular waves; added mass and damping are computed at the frequency value corresponding to the peak value of the input spectrum, as done by many authors. The roll damping action is approximate as a quadratic function where the linear (potential and linear skin friction effects) and nonlinear (viscous effects) terms may be computed using the formulae giving in Himeno (1981), or maybe estimated from data of roll decaying tests.

The motion equations for irregular heads seas are given by the following equations, Polo et al (2016):

$$
\begin{aligned}
&(m + A_{33})\ddot{z} + A_{35}\ddot{\theta} + B_{33}\dot{z} + B_{35}\dot{\theta} + Z_z z \\
&+ z_\theta \theta + \frac{1}{2}Z_{zz}z^2 + \frac{1}{2}Z_{\phi\phi}\phi^2 + \frac{1}{2}Z_{\theta\theta}\theta^2 \\
&+ Z_{z\theta}z\theta + \frac{1}{6}Z_{zzz}z^3 + \frac{1}{2}Z_{zz\theta}z^2\theta + \\
&\frac{1}{2}Z_{\phi\phi z}\phi^2 z + \frac{1}{2}Z_{\phi\phi\theta}\phi^2\theta + \frac{1}{2}Z_{\theta\theta z}\theta^2 z + \\
&\frac{1}{6}Z_{\theta\theta\theta}\theta^3 + \sum_{n=1}^{R}\tilde{Z}_{\zeta z0}z + \sum_{n=1}^{R}\tilde{Z}_{\zeta z}z + \\
&\sum_{n=1}^{R}\tilde{Z}_{\zeta\zeta z}z + \sum_{n=1}^{R}\tilde{Z}_{\zeta\theta 0}\theta + \sum_{n=1}^{R}\tilde{Z}_{\zeta\theta}\theta + \\
&\sum_{n=1}^{R}\tilde{Z}_{\zeta\zeta\theta}\theta + \frac{1}{2}\sum_{n=1}^{R}\tilde{Z}_{\zeta zz0}z^2 + \frac{1}{2}\sum_{n=1}^{R}\tilde{Z}_{\zeta zz}z^2
\end{aligned}
\tag{1}
$$

$$+\sum_{n=1}^{R}\tilde{Z}_{\zeta z\theta_0 z\theta}+\sum_{n=1}^{R}\tilde{Z}_{\zeta z\theta}z\theta+$$
$$\frac{1}{2}\sum_{n=1}^{R}\tilde{Z}_{\zeta\phi\phi_0\phi^2}+\frac{1}{2}\sum_{n=1}^{R}\tilde{Z}_{\zeta\phi\phi}\phi^2+$$
$$\frac{1}{2}\sum_{n=1}^{R}\tilde{Z}_{\zeta\theta\theta_0\theta^2}+\frac{1}{2}\sum_{n=1}^{R}\tilde{Z}_{\zeta\theta\theta}\theta^2=Z_w(t)$$

$$(J_{xx}+A_{44})\ddot{\phi}+B_{14}\dot{\phi}+B_{24}\dot{\phi}|\dot{\phi}|+K_{\phi}\phi$$
$$+K_{z\phi}+K_{\phi\theta}\phi\theta+\frac{1}{2}K_{zz}z^2\phi+\frac{1}{6}K_{\phi\phi\phi}\phi^3$$
$$+\frac{1}{2}K_{\theta\theta\phi}\theta^2\phi+K_{z\phi\theta}z\phi\theta+\sum_{n=1}^{R}\tilde{K}_{\zeta\phi_0}\phi+$$
$$\sum_{n=1}^{R}\tilde{K}_{\zeta\phi}\phi+\sum_{n=1}^{R}\tilde{K}_{\zeta\zeta\phi}\phi+\sum_{n=1}^{R}\tilde{K}_{\zeta z\phi_0}z\phi+$$
$$\sum_{n=1}^{R}\tilde{K}_{\zeta\zeta z\phi}z\phi+\sum_{n=1}^{R}\tilde{K}_{\zeta\phi\theta_0}\phi\theta+$$
$$\sum_{n=1}^{R}\tilde{K}_{\zeta\phi\theta}\phi\theta=0 \qquad (2)$$

$$(J_{yy}+A_{55})\ddot{\theta}+A_{53}\ddot{z}+B_{53}\dot{z}+B_{55}\dot{\theta}$$
$$+M_z z+M_\theta\theta+\frac{1}{2}M_{zz}z^2+\frac{1}{2}M_{\phi\phi}\phi^2+$$
$$\frac{1}{2}M_{\theta\theta}\theta^2+M_{z\theta}z\theta+\frac{1}{6}M_{zzz}z^3+$$
$$\frac{1}{2}M_{zz\theta}z^2\theta+\frac{1}{2}M_{\phi\phi z}\phi^2 z+\frac{1}{2}M_{\phi\phi\theta}\phi^2\theta+$$
$$\frac{1}{2}M_{\theta\theta z}\theta^2 z+\frac{1}{6}M_{\theta\theta\theta}\theta^3+\sum_{n=1}^{R}\tilde{M}_{\zeta z_0}z+$$
$$\sum_{n=1}^{R}\tilde{M}_{\zeta_z}z+\sum_{n=1}^{R}\tilde{M}_{\zeta\zeta z}z+\sum_{n=1}^{R}\tilde{M}_{\zeta\theta_0}\theta+$$
$$\sum_{n=1}^{R}\tilde{M}_{\zeta\theta}\theta+\sum_{n=1}^{R}\tilde{M}_{\zeta\zeta\theta}\theta+\frac{1}{2}\sum_{n=1}^{R}\tilde{M}_{\zeta zz_0}z^2+$$
$$\frac{1}{2}\sum_{n=1}^{R}\tilde{M}_{\zeta zz}z^2+\sum_{n=1}^{R}\tilde{M}_{\zeta z\theta_0}z\theta+\sum_{n=1}^{R}\tilde{M}_{\zeta z\theta}z\theta$$
$$+\frac{1}{2}\sum_{n=1}^{R}\tilde{M}_{\zeta\phi\phi_0}\phi^2+\frac{1}{2}\sum_{n=1}^{R}\tilde{M}_{\zeta\phi\phi}\phi^2+$$
$$\frac{1}{2}\sum_{n=1}^{R}\tilde{M}_{\zeta\theta\theta_0}\theta^2+\frac{1}{2}\sum_{n=1}^{R}\tilde{M}_{\zeta\theta\theta}\theta^2=Z_w(t) \qquad (3)$$

In the above equations m, J_{xx} and J_{yy} represent body mass, roll and pitch moments of inertia, respectively. Coefficients with upper double dots nomenclature $(\ddot{z},\ddot{\phi},\ddot{\theta})$ are accelerations in the heave, roll and pitch directions. Coefficients with upper dots nomenclature $(\dot{z},\dot{\phi},\dot{\theta})$ are velocities in the same directions. Meanwhile, the coefficients with subscripts representing purely displacements (z,ϕ,θ) are the derivatives of the Taylor series expansions up to the third order, which models the hydrostatic restoring actions; see details in Neves and Rodriguez (2006a). The effects of the interactions between non-linear motions and incident waves are represented by the coefficients that includes the wave symbol "ζ" in the subscript (e.g.$\tilde{K}_{\zeta\phi}$). These coefficients describe the changes in the restoring actions of the vessel due to the periodic changes in the wave-induced pressure alongside the hull surface; they are computed as the derivatives of the Froude-Krylov force with respect to the body motions in heave, roll and pitch. In the other hand, coefficients with the double wave symbol "$\zeta\zeta$" represent the nonlinear contributions due to the instantaneous wave elevation, those derivatives are computed using the second harmonic terms from Fourier analysis of the time series of the wave-induced terms. Finally, the terms $Z_w(t)$ and $M_w(t)$ represent the linear wave-induced exciting force (linear Froude-Krylov + linear diffraction). The wave-induced coefficients have the following form for each frequency component ω_n and wave elevation A_{wn}:

$$\tilde{K}_{\zeta\phi 0_n}=K_{\zeta\phi 0}(\omega_n,A_{w_n}) \qquad (4)$$
$$\tilde{K}_{\zeta\phi_n}(\omega_n,A_{w_n})=K_{\zeta\phi}(\omega_n,A_{w_n})\cos[\omega_n t-\epsilon(\omega_n)+\varphi_1(\omega_n)] \qquad (5)$$
$$\tilde{K}_{\zeta\zeta\phi_n}(t)=K_{\zeta\zeta\phi}(\omega_n,A_{w_n})\cdot\cos[2\omega_n t-2\epsilon(\omega_n)+\varphi_2(\omega_n)] \qquad (6)$$

It should be noted that each harmonic wave-induced coefficient in the motion equations have its own unique phase which is the result of each transfer function phase (e.g.$\varphi_1(\omega_n)$) plus the random generated phase of each frequency component (e.g. $\epsilon(\omega_n)$) of

the input spectrum.The model presented here is very time-efficient when compared against more complex hybrid methods which compute the hydrostatic and wave-induced action iteratively at each time-step of the simulation. This feature makes it feasible to use a Monte Carlo approach to perform a stochastic study with the results generated with this model.

3. SIMULATIONS

The stochastic characteristics of the roll process under parametric conditions were studied on a typical containership, denoted as NTU containership (see Table 1 and Figure 1). Two wave conditions were studied. In order to guarantee parametric resonance, the peak period of encounter was selected to satisfy the Mathieu's ratio of encounter frequency equal to twice the roll natural frequency. The waves conditions are given by the Jonswap spectrum with the parameters of significant height, peak period and ship velocity shown in table 2.

Table 1 Mesh of NTU Containership.

Property	*Symbol*	*Value (Unit)*
Length	L	293.51 (m)
Depth	D	24.51 (m)
Draft	T	11.71 (m)
Weight	m	76332.29 (ton)
Metacentric height	GM_T	1.84 (m)
Roll natural period	T_{44}	21.0 (s)
Roll moment of inertia	J_{44}	1.77x10^7 (ton×m^2)
Pitch moment of inertia	J_{55}	4.47x10^8 (ton×m^2)

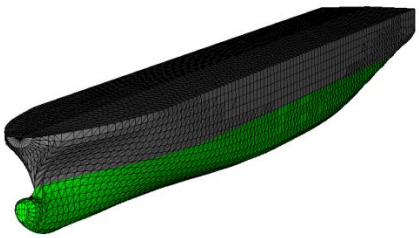

Figure 1 Mesh of NTU Containership.

Table 2 Mesh of NTU Containership.

$H_s\ [m]$	$T_P\ [s]$	$V\ [knot]$
7.0	13.54	11.7
10.0	13.54	11.7

For each wave condition it was generated 500 realizations with 3 hour of duration of the heave, roll and pitch stochastic processes. Figure 2 shows several realizations of the roll process for the wave condition with $H_S = 7.0m$.

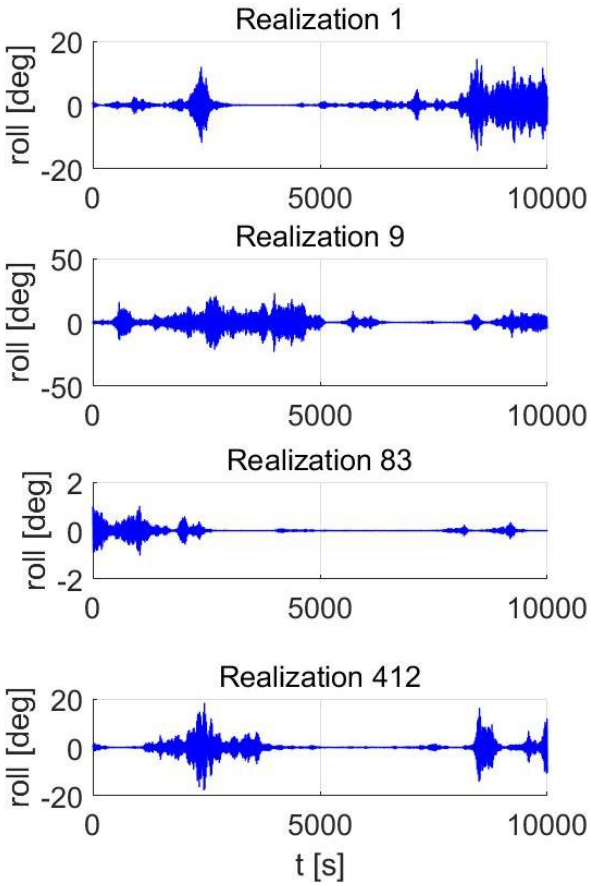

Figure 2 Realizations of the rol stochastic process. Jonswap $H_S = 7.0m$ and $T_P = 13.54s$.

From Figure 2, it can be seen that the parametric resonance occurs at different times with different maximum amplitudes and in some cases the amplification doesn't develop beyond the initial condition (2º). Also, it appears that the roll amplification occurs in well-defined isolated groups. No capsizes were registered in this wave condition. Meanwhile, Figure 3 shows several realizations of the roll process for the wave with $H_S = 10.0m$. As in

the previous case, the roll amplifications occur at different times and with different amplitudes. Nevertheless, the amplifications occur in much closer groups which are difficult to isolate. For this wave condition, it was registered 222 capsizing scenarios.

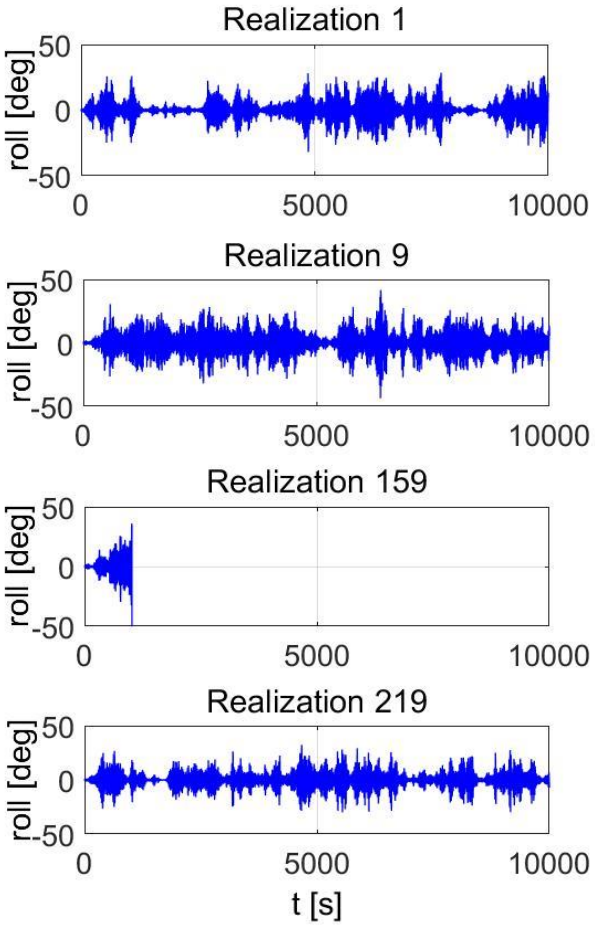

Figure 3 Realizations of the roll stochastic process. Jonswap $H_S = 10.0m$ and $T_P = 13.54s$.

4. RESULTS

It must be remembered that a stochastic process is a sequence of random variables. This sequence of random variables could represent the time progression of a given variable of a system (e.g. roll motion); these random variables can be obtained fixing the time and collecting the data of each realization in that time. The relation between those random variables establishes the stochastic nature of a process. An ergodic process is a process where each random variable within a process have the same statistical properties, which is also the same for each realization of the process. A common technique to evaluate the practical ergodicity of a process is to analyse the convergence of the variance of each realization. In the other hand, a stationary process is a process where all the statistical properties of the random variables within the process don't change with time. For engineering applications, it is common to evaluate only the probability function and the bivariate joint probability function of the random variables, see Peebles (2001). If a process is stationary, all probability functions of the random variables must be the same. As well as, all the bivariate joint distributions must depend only of the separation in time of the joint random variables. This also can be expressed as that the autocorrelation function of two random variables within the process only depends on the separation τ between the random variables. The easiest way to evaluate this feature is using the correlation coefficient ρ, given by:

$$COV = \frac{1}{N}\left[\sum_{i=1}^{N} x_i \cdot x_{i+\tau} - \frac{1}{N}\sum_{i=1}^{N} x_i \cdot \sum_{i=1}^{N} x_{i+\tau}\right] \quad (7)$$

$$\rho = \frac{COV}{\sigma(x_i)\sigma(x_{i+\tau})} \quad (8)$$

where x_i are the values of a random variable X_i in place i of a sequence of random variables, $\sigma(x_i)$ is the standard deviation of that random variable and N is the number of realizations. Therefore, if a stochastic process is stationary, ρ must converge to an unique value for different values of τ. It is clear to see that all ergodic process are also stationaty process.

For the wave condition given by significant height of $H_S = 7.0m$, Figure 4 shows the probability density function of the roll process generated. Figure 5 shows the variance in time of several realizations. Meanwhile, Figure 6

shows the cumulative distribution function (CDF) of several realizations of the stochastic process. It is clear that the roll probability distribution doesn't fit the Gaussian distribution and that the statistical properties of all realizations don't converge to the same value. This means that the roll process under this wave condition is not ergodic.

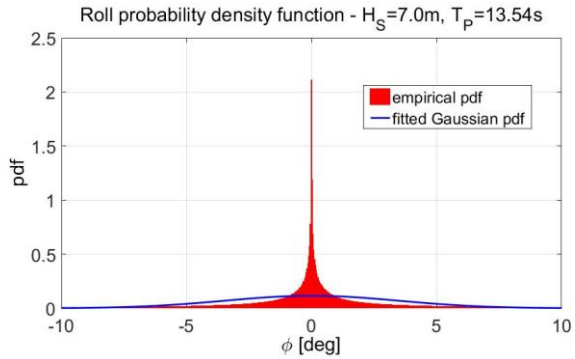

Figure 4 pdf of the roll stochastic process. Jonswap $H_S = 7.0m$ and $T_P = 13.54s$.

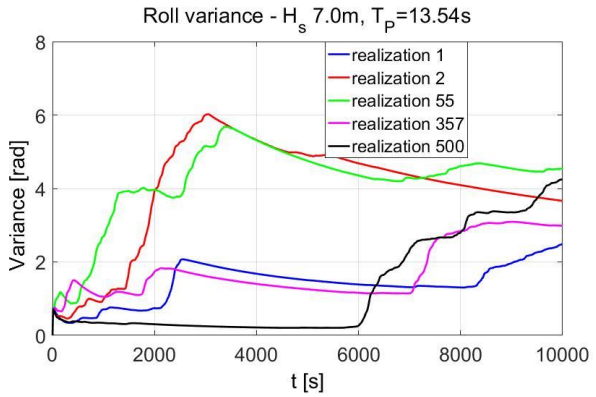

Figure 5 Variance of the roll stochastic process. Jonswap $H_S = 7.0m$ and $T_P = 13.54s$.

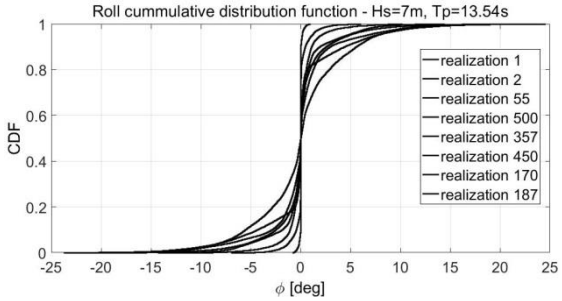

Figure 6 Roll CDF for serveral realizations. Jonswap $H_S = 7.0m$ and $T_P = 13.54s$.

Figures 7 and 8 show the mean and the standard deviation of all the random variables of the roll process. From those figures it can be seen that there is a convergence time (around 1000 seconds). Figure 9 shows the cumulative distribution function of several random variables of the roll process before the convergence time. Meanwhile, Figure 10 shows the cumulative distribution function of several random variables of the roll process after the convergence time.

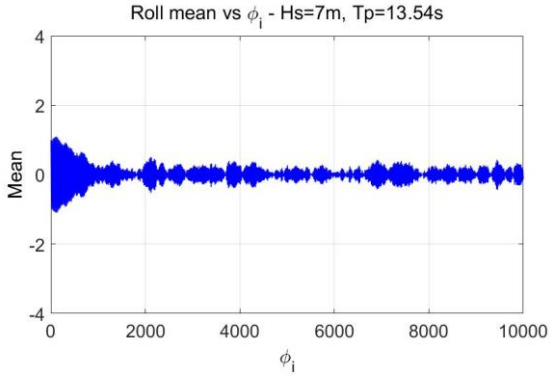

Figure 7 Mean of the random variables of the roll stochastic process. Jonswap $H_S = 7.0m$ and $T_P = 13.54s$.

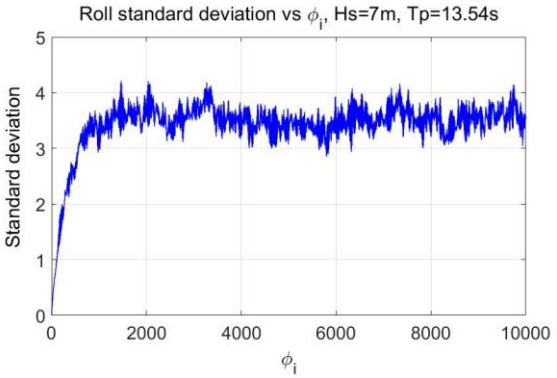

Figure 8 Standard deviation of the random variables of the roll stochastic process. Jonswap $H_S = 7.0m$ and $T_P = 13.54s$.

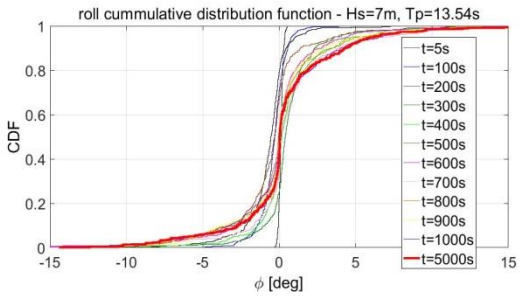

Figure 9 CDFof several random varaibles of the roll stochastic process before 1000s. Jonswap $H_S = 7.0m$ and $T_P = 13.54s$.

From Figures 9 and 10 it can be concluded that after some convergence time the random variables, within the roll process, appear to have the same probability distribution for this wave condition.

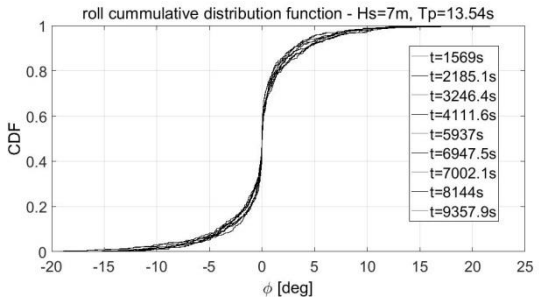

Figure 10 CDF of several random varaibles of the roll stochastic process after 1000s. Jonswap $H_S = 7.0m$ and $T_P = 13.54s$.

The correlation coefficient, for different separation τ between variables, for all the random variables within the roll process generated with the wave condition with significant height of $H_S = 7.0m$ is shown in Figure 11.

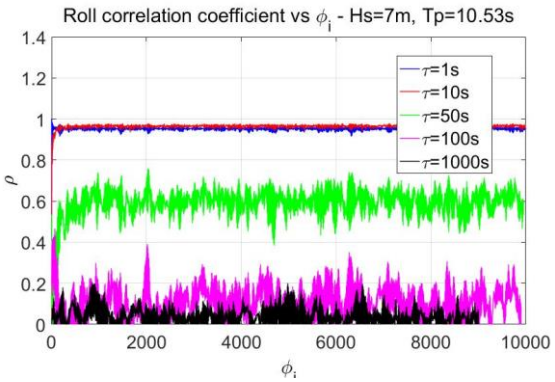

Figure 11 Correlation coefficient of the roll stochastic process. Jonswap $H_S = 7.0m$ and $T_P = 13.54s$.

It is shown that for different separation times the correlation coefficient seems to converge with certain degree of randomness. Therefore, it could be concluded that the roll process under this specific wave condition is a stationary process. Additionally, Figure 11 shows that random variables with small separation (τ=1s) are highly correlated and random variables with large separation (τ=1000s) are almost independent of each other. This behaviour is in concordance with the condition established in Leadbetter (1971) for applying the Extreme Theorem (Fisher-Tippett-Gnedenko Theorem) to stochastic processes. Although this process is a non-ergodic process as shown previously, it can be considered a stationary process.

On the other hand, for the wave condition given by the significant height of $H_S = 10.0m$, Figure 12 shows the probability density function of the roll process generated. It is interesting to see that in this case, the probability density function of the roll process fits much closer to the Gaussian distribution than in the case with less wave intensity. Figure 13 shows the variance in time of several realizations of the roll process. Here, it seems that the convergence of the variance is much better than the in previous case. Figure 14 shows the probability function of several realizations of the process. From Figure 14, it is clear that the probability function of the realizations tend to converge to a one distribution. Figures 15 and 16 show the mean and the standard deviation of all the random variables of the roll process. Figure 16 shows that the standard deviation of the random variables still has a convergence time. Nevertheless, the mean of the random variables appear to be random and doesn't stay closer to zero. Figure 17 shows the cumulative distribution function of several random variables after the convergence time of the standard deviation.

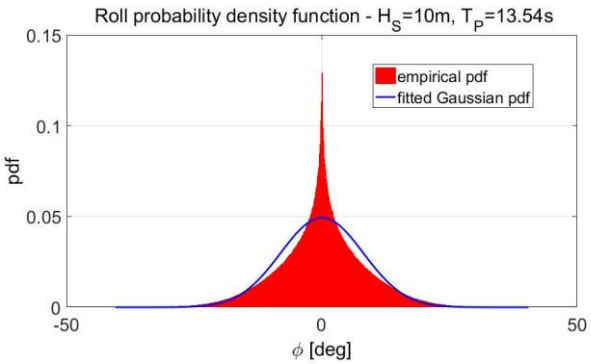

Figure 12 pdf of the roll stochastic process. Jonswap $H_S = 10.0m$ and $T_P = 13.54s$.

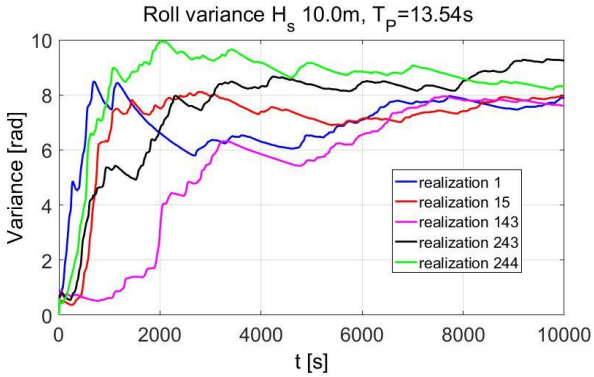

Figure 13 Variance of the roll stochastic process. Jonswap $H_S = 10.0m$ and $T_P = 13.54s$.

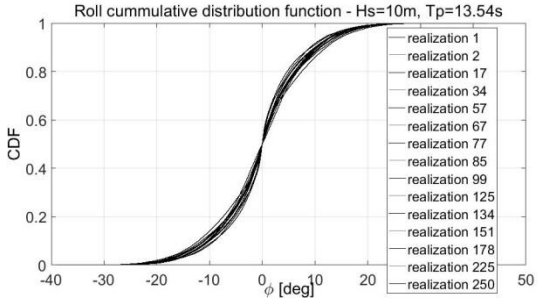

Figure 14 Roll CDF for serveral realizations. Jonswap $H_S = 10.0m$ and $T_P = 13.54s$.

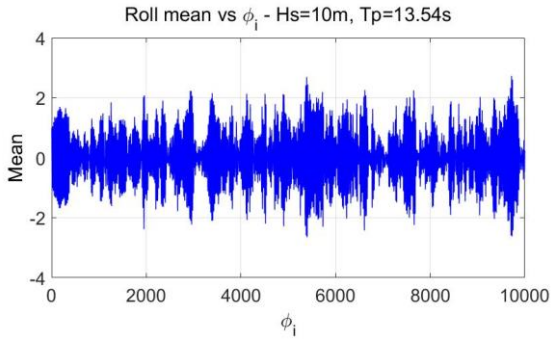

Figure 15 Mean of the random variables of the roll stochastic process. Jonswap $H_S = 10.0m$ and $T_P = 13.54s$.

Finally, Figure 18 shows the correlation coefficient, for different separations τ between variables, for all the random variables within the roll process generated with the wave condition with the significant height of $H_S = 10.0m$. It is shown that randomness of the convergence is more significant than the case with less wave intensity. Nevertheless, random variables with small separation (τ=1s) are still highly correlated and random variables with large separation (τ=1000s) are still almost independent of each other. Conditions to use the Extreme Theorem are still satisfied.

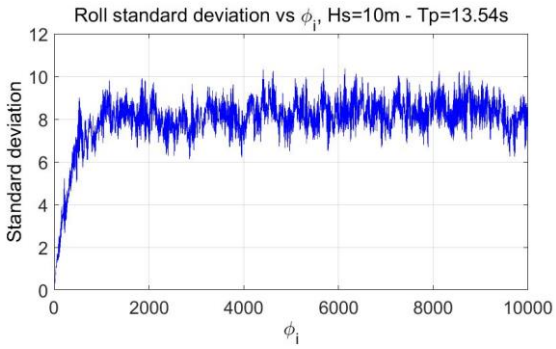

Figure 16 Standard deviation of the random variables of the roll stochastic process. Jonswap $H_S = 7.0m$ and $T_P = 13.54s$.

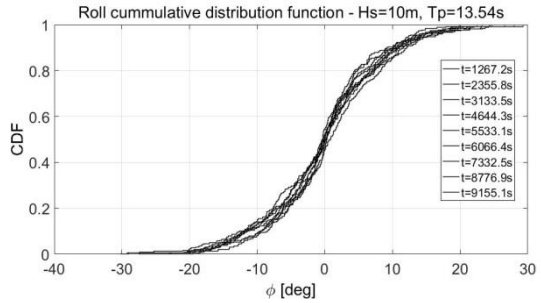

Figure 17 Realizations of the rol stochastic process. Jonswap $H_S = 7.0m$ and $T_P = 13.54s$.

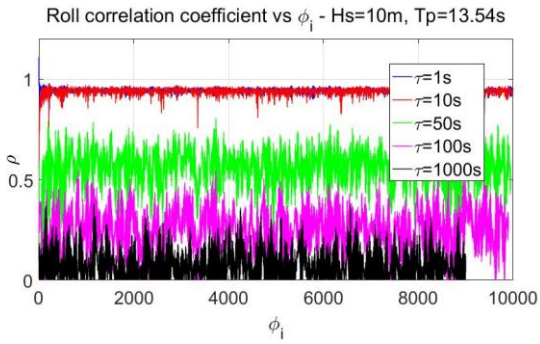

Figure 18 Realizations of the rol stochastic process. Jonswap $H_S = 7.0m$ and $T_P = 13.54s$.

5. CONCLUSIONS

A study of the stochastic properties of the roll process of a modern containership was carried under parametric resonance conditions. Results show that the roll process is not ergodic, as reported in previous works.

However, the practical non-ergodicity seems to decrease when the wave intensity is increased. Regarding stationarity, results show that the roll process under roll parametric condition can be approximately considered a stationary process for this particular containership. Future works with several containerships must confirm the stochastic nature of the roll process under roll parametric conditions. Additionally, the stochastic properties of different types of vessels must be studied. Knowledge of the stochastic properties of the motion processes of vessels could lead to the implementation of a stability based on risk analysis.

6. ACKNOWLEDMENTS

The present investigation has been supported by PETROBRAS. Authors greatly acknowledge this crucial support. The support of the Sustain-T project of the ERASMUS program is also acknowledged.

7. REFERENCES

Belenky, V.L., Degtyarev, A.B., Boukhanovsky, A.V., 1998,"Probabilistic qualities of nonlinear stochastic rolling", Ocean Engineering 25 (1), pp 1–25

Belenky,V.L.,Weems,K.M.,Lin,W.,Paulling,J.R .,2003, "Probabilistic Analysis of Roll Parametric Resonance in Head Seas", Proceedings of the 8th International Conference on Stability of Ships and OceanVehicles (STAB2003), Madrid, pp.325–340.

Bulian, G., Francescutto, A., Lugni, C., 2006, "Theoretical, numerical and experimental study on the problem of ergodicity and 'practical ergodicity' with an application to parametric roll in longitudinal long crested irregular sea", Ocean Engineering 33, pp 1007–1043.

Celis, M.A.C., 2008, "Dynamic Stability of Ships: Influence of Memory Effects on Parametric Rolling", M.Sc. Dissertation, COPPE – Ocean Engineering Department. Federal University of Rio de Janeiro.

Cummins, E., 1962, "The impulse response function and ship motions", Proceedings of the International Symposiumon on Ship Theory, no.8, Hamburg, Germany, pp. 101–109.

Gumbel, E. J.,1958,"Statistics of Extremes", Columbia University Press, New York.

Hashimoto, H., Umeda, N., Matsuda, A., 2006, "Experimental and Numerical Studies on Parametric Roll of a Post-Panamax Container Ship in Irregular Waves", Proceedings of the 9th International Conference on the Stability of Ships and Ocean Vehicles (STAB2006), Rio de Janeiro, Brazil.

Himeno, Y.,1981, "Prediction of ship roll damping - state of the art", Report No.239, Department of Naval Architecture and Marine Engineering. The University of Michigan, Michigan

Kim, D., Belenky, V., Campbell, B., Troesch, A., 2014, "Statistical Estimation of Extreme Roll in Head Seas", Proceedings of the 33rd International Conference on Ocean, Offshore and Artic Engineering (OMAE2014), San Francisco, USA.

Kobylinski, L.K. 1997, "Rational Approach to Ship Safety Requirements", Proceedings of the Second International Conference on Marine Technology, Szczecin, Poland.

Leadbetter, M.R., 1971,"Extremes and Related Properties of Random Sequences and Processes", Springer, New York.

McTaggart, K., de Kat, J.O., 2000, "Rational Approach to Ship Safety Requirements", Transactions, Society of Naval Architects and Marine Engineers (SNAME). 108, pp.

147-177.

Neves, M. A. S., Rodríguez, C. A., 2006, "On Unstable Ship Motions Resulting from Strong Non-Linear Coupling", Ocean Engineering, 33, pp. 1853-1883.

Neves, M.A.S., 2016, "Dynamic stability of ships in regular and irregular seas - An overview", Ocean Engineering, 120, pp. 362-370.

Peebles, P., 2001, "Probability, Random Variables and Random Signal Principles", McGraw-Hill.

Peters, W., Belenky, V., Bassler, C., Spyrou., K., Umeda, N., Bulian, G., Almayer, B., 2012, "The Second Generation of Intact Stability Criteria: An Overview of Development", Transactions, Society of Naval Architects and Marine Engineers (SNAME).

Polo, J.C.F., Troesch, A., and Neves, M.A.S., 2017, "Second order wave induced actions for parametric rolling", Proceedings of 32th International Workshop on Water Waves and Floating Bodies, Dalian, China.

Rodríguez, C.A., Polo, J., Neves M.A.S., 2016, "A Time-Efficient Approach for Nonlinear Hydrostatic and Froude-Krylov Forces for Parametric Roll Assessment in Irregular Seas", Ocean Engineering, 120, pp 246–255.

Investigation on IMO Second Level Vulnerability Criteria of Parametric Rolling

Clève WANDJI, *Bureau Veritas*, cleve.wandji@bureauveritas.com

ABSTRACT

This paper describes the application of level 2 vulnerability criteria of parametric roll as outlined in the current state of development, by the International Maritime Organisation, of the second generation intact stability criteria. In order to identify and understand possible sources of inconsistencies in level 2 vulnerability criteria for parametric rolling, an investigation regarding environmental and operational conditions used in the two checks is carried out. Numerical tools (simplified and 3D hydrodynamic potential flow code) able to compute parametric roll prediction have been developed and tested on large number of ships, covering a wide range of ship type, size and speed. These tools are used in this study. In addition comment on the applicability of these criteria from a regulatory and approval perspective, are presented.

Keywords: *parametric roll, second level vulnerability criteria, direct stability assessment*

1. INTRODUCTION

The International Maritime Organisation (IMO) Sub-Committee on Ship Design and Construction (SDC) is developing Second Generation Intact Stability Criteria (SGISC) to assess the dynamic stability of ships in waves. Five stability failure modes are considered: Pure loss of stability, Parametric roll, Loss of stability under dead ship condition, Surf-riding/broaching and Excessive accelerations.

These SGISC are based on a multi-tiered assessment approach structured in three levels. The first two levels are called vulnerability criteria Level 1 and Level 2. The third level is called Direct Stability Assessment (DSA). In the framework of SGISC development, Level i+1 should be more complex and less conservative than Level i criteria. The ship design should comply for each realistic loading condition with one of the three criteria for each stability failure mode. Alternatively, Operational Limitations or Operational Guidance can be developed, based on results of Level 2 or Level 3 assessment, respectively.

Amongst the identified dynamic stability failure modes, parametric roll is probably the most emblematic and the most known. Parametric roll (short of parametric resonance) is an amplification of roll motions caused by periodic variation of transverse stability in waves (IMO 2017 – SDC 4/5/1/Add.1). It is well known that parametric roll is mostly expected to occur in head, following, bow and stern quartering seas, when the wave encounter frequency is approximately the double of natural roll frequency and roll damping of the ship is not sufficient to dissipate additional energy (accumulated because of the parametric resonance). Therefore, many studies which are mainly focused on the periodic change of the restoring force as the ship advances through waves, have been carried out to analyse this phenomenon, and could be found in several sources like for example in Belenky et al. (2006), Hashimoto et al. (2006), KangHyun et

al. (2013), Bulian and Francescutto (2010). Following this trend, the IMO SDC (former SLF: Stability Load Lines and on Fishing Vessel) subcommittee has developed parametric roll vulnerability criteria.

Hard work was done intersessionally between SLF 51 and SDC 4 with active participation of many delegations. As a result, several methodologies have been submitted and tested (e.g., Wandji and Corrignan 2012, 2013). During SLF 54, significant work was done to harmonize draft vulnerability criteria Levels 1&2 for parametric roll and others stability failure (especially pure loss of stability and broaching). The guideline of DSA are under development and Level 1 and Level 2 vulnerability criteria are close to finalization. One of the remaining issue to close completely vulnerability criteria, is the consistency problem. Consistency is one of the cornerstones of the framework of SGISC. In this context consistency means that if a ship comply Level i requirement, it should also fulfil Level i+1 requirement.

Based on this background, numerical study has been carried out using a tool implemented to perform IMO vulnerability criteria and a 3D seakeeping nonlinear time domain numerical code, in order to investigate possible source of inconsistencies in parametric roll. The study is focused especially on Level 2 vulnerability criteria of parametric roll. The next section of this paper describes briefly the tools used to perform this investigation, their application on a sample ship and finally some comments on the applicability from a regulatory/approval point of view.

2. PARAMETRIC ROLL LEVEL 2 VULNERABILITY CRITERIA

The Level 2 vulnerability criterion is subdivided into two checks. If the first check criterion detects the vessel as vulnerable to, the second check assessment should be carried out. Therefore the first check should be more conservative than the second check requirements.

2.1 First Check

The first check requires the assessment of the variation of metacentric height (GM) and the parametric roll resonance speed in a series of 16 longitudinal regular waves. For each wave case, the loading condition is considered as non-vulnerable to parametric roll according to the first check if one of the following sub-criteria are meet. The first sub-criterion is fulfilled if the ratio of the amplitude of the variation of GM to the average GM in wave is smaller than the Level 1 threshold (R_{PR}) and if the average GM is positive. The threshold R_{PR} (or standard) is function of the roll damping and includes an empirical formulation to take into account bilge keels. The second sub-criterion is fulfilled if the service speed of the vessel is smaller than the parametric roll resonance speed V_{PRi}.

$$V_{PRi} = \left| \frac{2\lambda_i}{T_\phi} \sqrt{\frac{GM(H_i,\lambda_i)}{GM}} - \sqrt{\frac{g\lambda_i}{2\pi}} \right| \quad (1)$$

In this equation (1), λi, Hi, Tϕ, GM(Hi,λi), GM and g are respectively wave length, wave height, natural roll period in calm water, average metacentric height for different position of the crest along the ship, metacentric height in calm water and gravity acceleration.

After assessing each particular wave case, the final criterion (C1) is obtained as a weighted average by using the probability of occurrence of each wave cases. A vessel is judged to be vulnerable to parametric roll according to the first check if C1 is greater than a standard R_{PR0} = 0.06 (IMO 2015 – SDC 2/WP.4).

The environmental conditions used in this check, is a series of 16 waves with the wave length associated with the zero up-crossing period, and the wave height is assumed to be the conditional average significant wave height multiplied by a factor k_{PR} set to 0.7 (IMO 2017 – SDC 4/5/1/Add.1).

2.2 Second Check

The second check assesses the roll motion in head and following seas for 4 ship speeds in a series of regular "effective" waves. These four ship speeds are 0%, 50%, 86.6% and 100% of service speed. For each combination of "effective" wave cases and speed cases, the failure index is set to 1 if the roll angle is larger than 25 degrees and 0 otherwise. After assessing each combination of "effective" wave cases and speed cases, the final criterion (C2) is obtained as a weighted average by using the probability of occurrence of "effective" wave in the scatter table and assuming that the speed is uniformly distributed. A vessel is considered to be vulnerable to parametric roll according to the second check if C2 is larger than R_{PR0} (IMO SDC 2/WP.4 Annex 2). In this work, the roll angle is obtained by solving the uncoupled roll motion using numerical simulation technique in time domain.

The environmental conditions used in this check i.e. "effective wave" are computed by using Grim's effective wave height concept (Grim 1961). The wave length used to obtain the "effective" wave height is equal to ship length in all cases. Assuming a wave spectrum, the corresponding wave height is computed for the entire scatter diagram, precisely where the probability of occurrence is different to zero. For example using wave scatter diagram from IACS Recommendation No 34, 197 "effective" waves are computed on 306 possibilities.

3. COMPUTATION TOOLS

Numerical simulation tools have been developed to perform dynamic stability especially parametric rolling, these tools contain the SGISC and there are updated after each SDC session. At this stage in Bureau Veritas, most of the stability failure mode is covered by some numerical tools. Figure 1 shows the SGISC covered by numerical simulation tools at this moment (the shading part in green on the Figure 1).

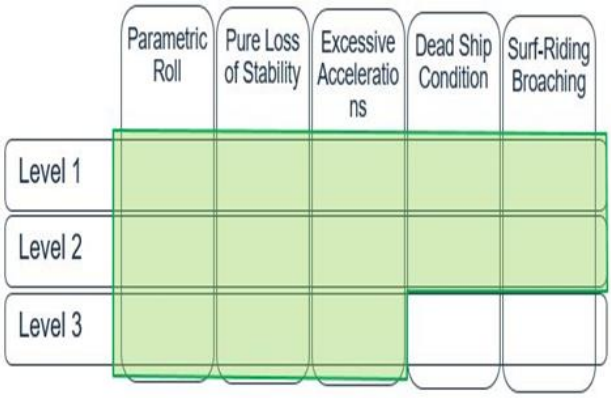

Figure 1: Matrix structure of SGISC and numerical simulation tools availability.

3.1 Level 2 Numerical Simulation Tool for Parametric Rolling

The description of the numerical simulation tool in this section is the one located in the second line and first column in the matrix of Figure 1. Both checks require computation of hydrostatics in longitudinal sinusoidal waves, in order to derive GM and GZ for different position of the wave crest along the ship length. In the stability assessment, the ship is balanced in pitch and heave quasi-statically. The vessel is modelled using the stations, which are a list of (Y transversal and Z vertical coordinate) points with the same longitudinal coordinate X. In addition, the hydrostatic in waves are computed following the procedure describes in SLF 52/INF.2 Annex 6. The area at each station and its moment relative to the vertical axis are expressed as function of the local draft and taking into account sinkage and trim. Therefore, the local draft at each station comes from the formula, describing wave elevations along the hull, and depends on sinkage and trim. The wave profile along the ship hull is evaluated by satisfying equilibrium conditions. Once sinkage and trim are found, the wave profile is found and the moment of inertia of the waterplane and other hydrostatic terms are computed. An accurate estimation of roll restoring term is very important for the representation of parametric roll, because one of the main factor which drives the apparition of the parametric roll is

the variation of the transversal stability in waves. In this tool, the restoring term in waves is modelled by the calm water GZ "modulated" by the GM in waves as presented in SDC 4/5/1/Add.1.

For the second check, the roll damping has been estimated using Ikeda simplified method (Ikeda 1978 and Kawahara 2009). Amongst the roll damping components there is also included the lift component, in order to take into account the effect of the forward speed on roll damping.

In the second check, the maximum roll angle resulting from parametric roll is obtained by solving an equation of uncoupled roll motion. The uncoupled roll motion equation is a differential equation. The solution is obtained using a numerical simulation technique in time domain. Note that another option to solve the equation is to use the averaging method as fully described in SDC 5/6/2.

3.2 Level 3 Numerical Simulation Tool for Parametric Rolling

The tool describes in this part is located in the third line and first column in the matrix of Figure 1. In the present study, ship motions are computed by means of the time domain seakeeping software, namely HydroStar++ developed by Bureau Veritas. HydroStar++ is the time domain version of the 3D panel code HydroStar (frequency domain code) also developed by Bureau Veritas. Resolution in HydroStar is based on boundary element method. HydroStar computes all first order quantities (fluid kinematics, ship motion, pressure on hull, hull girder loads) and can assess second order loads. In addition, HydroStar is able to solve the hydrodynamic problem on user defined modes. This is an important step towards hydro-elastic calculation included in Bureau Veritas hydro-structure tool HOMER.

The calculations start with the linear frequency domain analysis. The result of these calculations are the linear hydrodynamic coefficients (added mass, damping, diffraction). From these, frequency dependent coefficient are transferred to time domain using the method proposed by Cummins (1962). The advantages of time domain method lies in the possibility to introduce the nonlinear components in the excitation forces. The Froude-Krylov force, which has considerable effect on the nonlinearity of ship motions, is estimated by the integration of the hydrostatic and hydrodynamic wave pressure along the instantaneous wetted surface of the hull at each time step, instead along the mean wetted surface as it is done within the linear model. In this way the metacentric height variation is implicitly taken into account at each time step and all quantities which influence GM (heave, pitch, roll, wave elevation, …) are included. This procedure implies the meshing of the hydrodynamic model up to the intersection of the ship with the incident wave elevation at each time step. The roll damping is estimated using various empirical formulations such as Ikeda method.

Finally, the equations of motion are integrated in time domain using the Runge-Kutta 4th order or Adams-Bashforth scheme. HydrosStar++ has been widely and intensively validated. Moreover, HydroStar++ has been validated for Parametric rolling and the results can be found in Malenica et al. (2006).

4. INVESTIGATIONS

In this section we will try to identify the possible sources of inconsistency between the two checks of parametric roll on one side and between Level 2 outcome and DSA on another side.

For these investigations, the sample ship used to perform all calculations results presented in this paper is the C11-class post-Panamax containership. A body plan of the vessel is presented in Figure 2, while Table 1 contains the main characteristics of the vessel.

Table 1: Main particular of C11 containership

Length	262.0 m
Breath	40.0 m
Draught	11.5 m
Service speed	12.0 m/s
Block coefficient	0.562
Metacentric height	1.96 m
Natural roll period	25.1 s
Bilge keel area	61.2 m^2

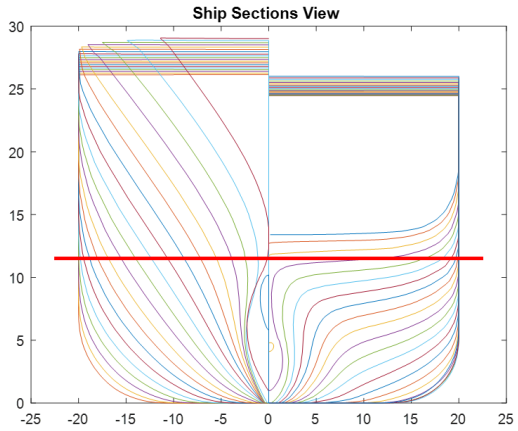

Figure 2: Body plan of C11 containership

4.1 Ship Speeds Investigations

In this section different aspects of the ship speed will be investigated especially for the second check such as the zero forward speed case and the speed discretisation.

Zero Forward Speed. In the current draft vulnerability criteria (SDC 2/WP.4 Annex 2), for the 2nd check, it's proposed to compute for zero speed case the roll angle only in head waves. The results in Figure 3 (following waves) and Figure 4 (head waves) show that for zero speed, the roll angle could be different in some cases, especially when using a tool like HydroStar++ (In these Figures, negative ship speed means following waves).

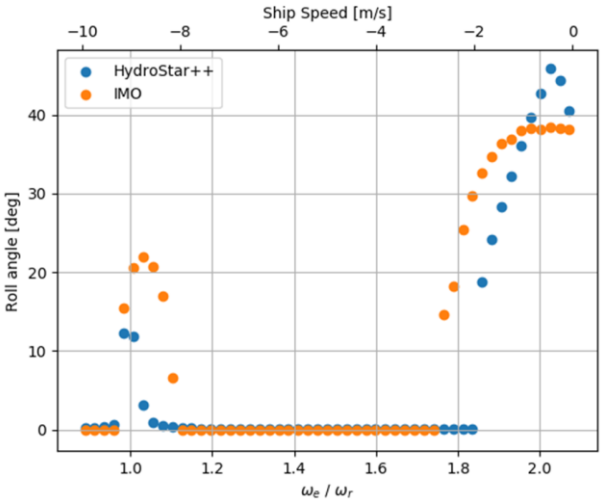

Figure 3: Following wave results with λ/Lpp = 0.75 and H/λ = 0.02

In this example, the roll angle is assessed to 41 degrees for following waves and 47 degrees for head waves. This could create a possible inconsistency between Level 2 – 2nd check and DSA in which calculations should be carried out for many heading (including head and following seas) and for many ship speeds (including zero ship speed). To avoid this inconsistency a solution could be in Level 2 check 2, for zero ship speed, to assess the roll angle both for following and head waves and take the mean of these two values.

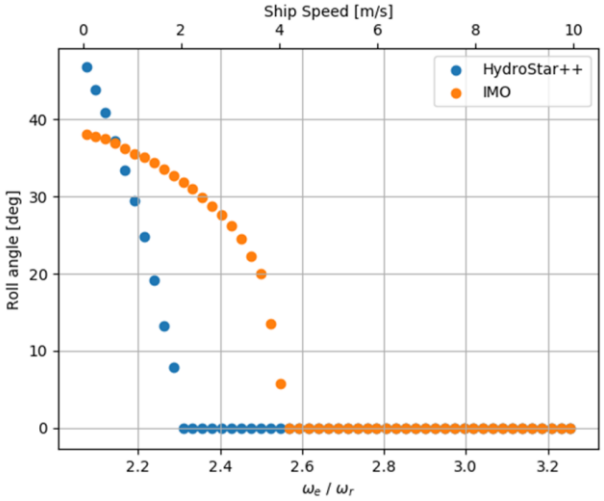

Figure 4: Head wave results with λ/Lpp = 0.75 and H/λ = 0.02

It's interesting to note from Figure 3 and Figure 4 that, the tool based on IMO vulnerability criteria (named IMO in these figures) in general predicts larger parametric roll angle than Level 3 tool (HydroStar++).

Looking at the ratio between the encounter frequency and the natural roll frequency (ωe/ωr), it's interesting to see in Figure 3 that both tools are able to catch the principal parametric resonance (ωe/ωr ≈ 2) and the fundamental parametric resonance (ωe/ωr ≈ 1).

The 1st check vulnerability criteria (also the Level 1 vulnerability criterion) are associated only to the principal parametric resonance. Thus, a possible source of inconsistency may occur between the 1st check and the 2nd check because 2nd check could identify more critical situations (fundamental parametric resonance cases) than 1st check.

Speed Discretisation. In the current draft vulnerability criteria (SDC 2/WP.4 Annex 2), for the 2nd check, the repartition of ship speeds is made using a cosine law described in equation (2).

$$V_i = V_s * \cos\left[\frac{(i-1)\pi}{2N}\right] \quad (2)$$

In this formula (2), Vs is the service speed and N is the number of nonzero forward speed cases. In the current draft vulnerability criteria (SDC 2/WP.4 Annex 2), N = 3 has been used and this provides the ship speed cases presented in section 2.2 of this paper (for i = 1, 2, and 3).

Using a cosine law for ship speed repartition means that more ship speeds are concentrated above 0.5*Vs. Therefore, according to this subdivision, parametric resonance is most likely to occur when ship speeds is above 0.5*Vs. But this is not always the case as shown in Figures 3 and 4, where parametric roll occurred mostly for ship speed lower than 0.5*Vs.

This situation could create a possible inconsistency between Level 2 – 2nd check outcome and DSA in which computations should be carried out for many ship speeds especially for lower speeds.

Using the ship speed subdivision contained in the current draft vulnerability criteria (SDC 2/WP.4 Annex 2), the outcome for the 2nd check is C2 = 0.052, while using an evenly distributed ship speeds i.e. constant speed step, the result is C2 = 0.071. This means that, in the first case, the ship is regarded as safe to parametric roll (since C2 = 0.052 < 0.06), while in the second case, the ship is judged as vulnerable to parametric roll (since C2 = 0.071 > 0.06). These results show that the positions and number of ship speed have an impact on the final outcome of the criteria.

A possible way to solve this issue could be to use more ship speed sample and evenly distributed, but this will require may be to adjust the standard of the 2nd check, since the standard was determined using 3 sample ship speeds (which leads to a total of 7 sample ship speeds = 3 ship speeds for head waves + 3 ship speeds for following waves + 1 zero speed) and a cosine distribution.

4.2 Waves Investigations

Waves used in both checks of Level 2 vulnerability criteria are regular waves. The first check uses 16 different regular waves, while the second check uses 197 regular waves having the same wave length.

Waves Weight in the First Check. The wave weight used in the 1st check is obtained from the wave scatter diagram as the probability associated to the spectral period. Figure 5 shows the weight corresponding to the 16 wave cases.

In Figure 5, the threshold RPR0 (0.06) of the 1st check is also plotted (red line). The weight of each wave case from 4 to 9 is greater

than the standard RPR0. Consequently, the ship is vulnerable to parametric rolling according to the 1st check if it's vulnerable to one wave in this group.

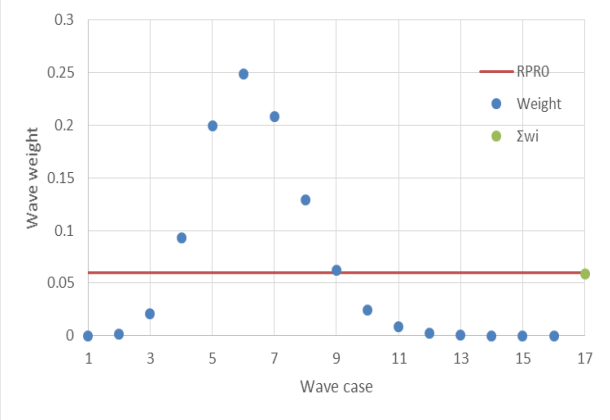

Figure 5: Wave cases weight used in the first check Level 2 criteria for parametric roll

In addition, the green point in Figure 6 (case number 17) represents the sum of wave cases from 1 to 3 and from 10 to 16. This sum (0.59066) is under the standard. Thus, none wave in this group and none of their combinations can trigger the vulnerability of the vessel. Therefore, these 10 wave cases (from 1 to 3 and from 10 to 16) are useless in the view of the detection of vulnerability to parametric rolling according to the 1st check.

Wave Length in the Second Check. In the second check all waves have the same length, precisely they are equal to the ship length. This choice is justified by the fact that in general, the maximum righting lever variation occurs when the wave length is nearly the same as the ship length.

But to trigger parametric roll, not only the maximum excitation is necessary, the resonance zone (frequency area) should also be targeted.

For example, Figure 6 shows the results of roll amplitude in head waves using a wave length equal to ship length where no parametric roll is observed. While Figure 7 shows the results of roll amplitude in the same condition but with a different wave length. Parametric resonance occurs in this case, because the resonance frequency has been captured.

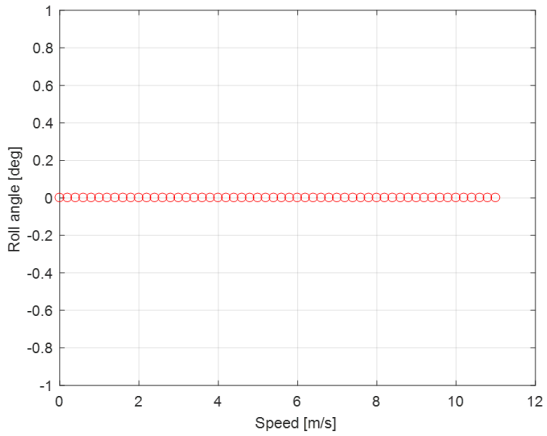

Figure 6: Roll amplitude in head waves – λ/Lpp = 1 and 1.0 m wave amplitude

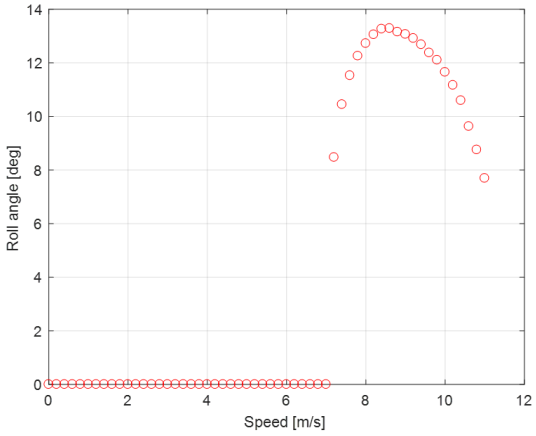

Figure 7: Roll amplitude in head waves – λ/Lpp = 0.75 and 1.0 m wave amplitude

The results in Figures 6 and 7 show that parametric roll occurs when righting lever variation is larger than a certain threshold and the resonance condition is meet. Both conditions are necessary for parametric rolling occurrence, having only the righting lever variation even if it is the maximum is not sufficient to assess properly parametric resonance.

In the 2nd check, the resonance zone is not captured properly on one hand because the wave length is constant during all computations

and on another hand because the 4 ship speeds (including the zero speed) are not necessary the resonance speed like those used in the 1st check.

This situation could be a possible source of inconsistency between the 2nd check and DSA, because in the 2nd check some parametric roll cases in longitudinal waves are missing due the fact that the resonance is not assessed appropriately, while DSA will assess all these cases.

Wave direction. In Level 2 vulnerability criteria, only longitudinal waves (following and head waves) are used. But parametric rolling could occur also in bow quartering and stern quartering seas as shown in Figure 8.

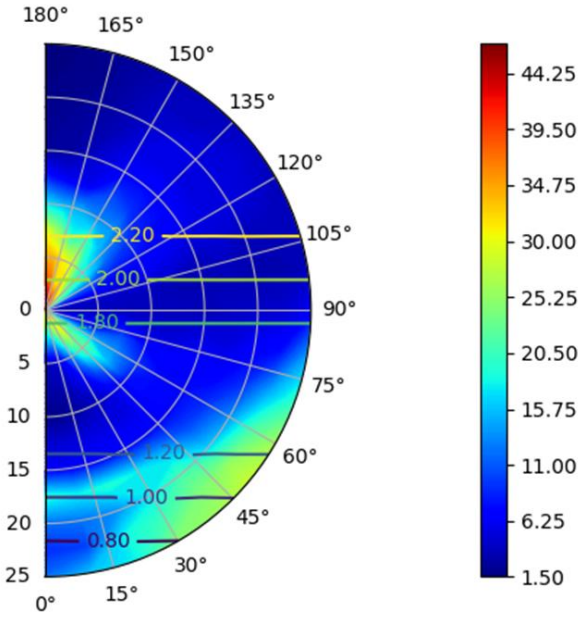

Figure 8: Polar plot of rolling in irregular short crested waves (Hs = 6.0 m and Tp = 12.5 s)

Figure 8 shows a polar plot of roll motion in irregular waves computed using Hydro-Star++. In the calculations, irregular and short crested waves are used (6.0 m significant wave height and 12.5 sec for peak period). To take into account the non-ergodicity of parametric roll, ten realisation of 3 hours of the same sea state is performed, but for each realisation a different set of random phases, frequencies and directions of the wave components composing the sea state is used. At the end, the average of the maximum roll angle of these ten realisation is computed.

In Figure 8, the radial direction represents the ship speed in knots, the rotational direction represents the wave encounter angle (180 degrees for head seas and 0 degree for following seas), and the horizontal lines represent iso-frequency lines, i.e. lines where the ratio encounter frequency and natural roll frequency is constant.

We can see that for this sea state, in stern quartering seas, parametric roll ($\omega e/\omega r \approx 2$) occurs for lower speed (under 5 knots), while for higher speed (above 20 knots) it is synchronous resonance ($\omega e/\omega r \approx 1$). Parametric roll occurs also in bow quartering seas at lower speed ($\omega e/\omega r \approx 2$).

Since in both checks of Level 2 vulnerability criteria (also in Level 1 vulnerability criteria) for parametric roll only head and following waves are used, and we have seen from Figure 8 that parametric roll could occur also in other wave direction, this may result in a possible source of inconsistency between Level 2 outcomes and the results of DSA (Level 3) if the standards and/or the environmental conditions used in these levels (Level 2 and Level 3) are not selected properly.

4.3 Roll Damping Investigations

Roll damping is an important parameter for the development of the parametric resonance. Therefore, a correct modelling of roll damping is essential in vulnerability criteria. In the first check (and also in Level 1 vulnerability criterion), linear roll damping defines the threshold for parametric excitation, and it is embedded in the standard through the bilge keels area and the midship section coefficient. For the second check the roll damping is assessed using the simplified Ikeda method. From these values, one can derive the linear, quadratic and cubic roll damping coefficient. The impact of ship

speed and vertical position of centre of gravity (KG) on these two models of roll damping are investigated in this section.

Speed Variation. Using simplified Ikeda method, linear roll damping coefficient has been computed for different ship speeds, in order to compare second check roll damping to the first check roll damping. The results in Figure 9 show the non-dimensional linear total roll damping coefficient (ratio between the linear total roll damping and the critical roll damping). The maximum roll angle used in Ikeda's simplified model to obtain these results was 20 degrees as suggested in the draft explanatory notes (SDC 4/5/1/Add.1 – Annex 2). The results in Figure 9 show that below 12 knots, the second check roll damping is smaller than first check roll damping.

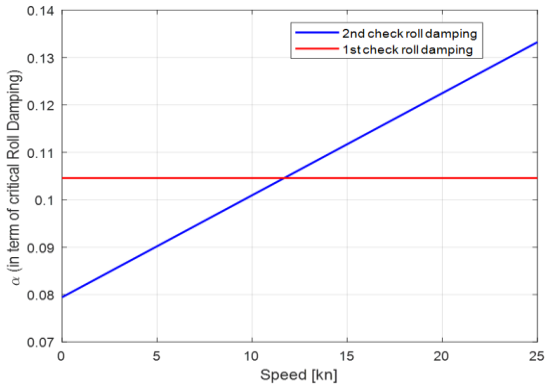

Figure 9: Comparison of linear total roll damping used in the 1st and 2nd check for different ship speed

Therefore, this result may indicate parametric roll for the second check in a case (Vs < 12 knots) in which the first check does not. This could be a potential source of inconsistency.

Centre of Gravity Height Variation. Using simplified Ikeda method, linear roll damping coefficient has been computed for different KG, in order to compare second check roll damping to the first check roll damping. The results in Figure 10 show the non-dimensional linear total roll damping coefficient (ratio between the linear total roll damping and the critical roll damping). The maximum roll angle used in Ikeda's simplified model to obtain these results was 20 degrees as suggested in the draft explanatory notes. The results in Figure 10 show that below a KG value of 17.6 m, we could have a non-conservative value since the second check roll damping is smaller than the first check roll damping.

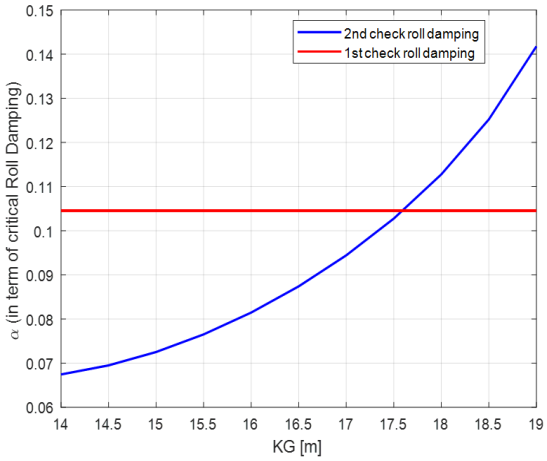

Figure 10: Comparison of roll damping used in the 1st and 2nd check for different KG

Hence, in this case (KG < 17.6 m), the assessment may indicate parametric roll for a loading condition in which the first check does not. This could be also a potential source of inconsistency.

5. CRITERIA APPLICABILITY

The second level vulnerability criteria for parametric roll requires the computations of righting lever variation in regular waves in both checks. These calculations are straight forward, they need computer software (there are also included in many hydrostatics or stability commercial software) and time to prepare the geometric input.

Regarding the first check, computing the final criterion (C1) requires some time because the metacentric height in waves needs to be evaluated for at least ten positions of wave crest along the ship length, and these calcula-

tions are repeated for all 16 wave cases. From an approval perspective, to make a decision on the vulnerability of a ship according to the 1st, it is sufficient to perform the calculations only in 6 wave cases (wave case 4 to 9).

Regarding the second check, the assessment of the final criterion (C2) is time consuming because, the metacentric height in waves needs to be evaluated for at least ten positions of wave crest along the ship length, and these calculations are repeated for all wave cases where the probability of occurrence is different from zero in scatter diagram, 196 if using for example wave scatter diagram from IACS Recommendation No 34. Having assessed the righting lever variation in waves, the next step is to compute the roll angle for different ship speeds in head and following waves. From an approval perspective, the user should be sure that the roll angle used in the criterion are steady roll angle or the roll cut-off angle. The roll cut-off angle should be specified carefully in accordance with the GZ curve range angle and also the down flooding angle.

Direct Stability Assessment (Level 3) is expected to consider all the relevant physics of the phenomenon in the most accurate way. Therefore it's expected to be the most accurate and the most comprehensive procedure or methodologies in the SGISC. Consequently, tools used for DSA are time consuming and require more computational time than those used for Level 2 assessment. To perform properly DSA the user should have some knowledge in hydrodynamics and statistics.

In the framework of the development of SGISC, consistency is one of the cornerstones. Regarding parametric roll, consistencies issues between 1st check and 2nd check should be addressed on one hand, and in another hand the development of DSA should be addressed in order to avoid inconsistencies issues between the 2nd check and DSA.

6. CONCLUSIONS

This paper presents an investigation into the second level vulnerability criteria for parametric rolling, as defined in the current state of development, by the International Maritime Organisation in SDC sub-committee and under the name of the Second Generation Intact Stability Criteria.

The tools used to perform the sample calculations results presented in this paper have been described. They are on one side a tool implemented to check vulnerability of the ships according to IMO requirements and in other side a DSA tool (HydroStar++). Figure 11 shows a table which summarizes the main characteristics of the models used in this work. In this table $H_{1/3}$ is the significant wave height, T_z the zero crossing period, L_{bp} the length between perpendiculars, δGM the amplitude of variation of metacentric height and $E(H_{1/3}|T_z)$ the conditional average significant wave height.

	Level 2 - check 1	Level 2 - check 2	Level 3 (DSA)
Waves Type	Regular waves	Regular waves	Irregular sea states
Wave Period	Tz	$(2\pi L_{bp}/g)^{0.5}$	Tz
Wave Height	$0.7*E(H_{1/3}\|Tz)$	$H_{1/3}$ using Grim	$H_{1/3}$
Wave Heading	Head and Following	Head and Following	All
Balance	Quasi-static Equilibrium	Quasi-static Equilibrium	Dynamic Balance
Wave Pressure	Hydrostatic	Hydrostatic	Froude-Krylov
Restoring Term	GM in waves	Calm water GZ modulated by GM in waves	Froude-Krylov
Degree of Freedom	-	1 dof	6 dof
Roll Damping	Constant and Linear No speed effect No KG effect	Linear and Cubic obtained using Ikeda	Linear and Quadratic obtained using Ikeda
Speed discretisation	-	Cosine law	Constant speed step
Criteria per sea state	$\delta GM/GM > R_{PR}$ and $V_{PRi} < V_S$	Roll angle > 25 degrees	Not defined yet
Overall criteria threshold	0.06	0.06	Not defined yet

Figure 11: Main features of the models used in Level 2 (in both checks) and Level 3

Possible inconsistencies between both checks and between the second check and DSA have been identified and presented. Moreover, comments on the applicability of these criteria from regulatory/approval point of view were presented. However, additional work remains to define the DSA guidelines and criteria.

7. REFERENCES

Belenky V., Yu H., and Weems K., 2006, "Numerical Procedures and Practical Experience of Assessment of Parametric Roll of a Container Carrier", Proceedings of 9th International Conference on Stability of Ships and Ocean Vehicles, pp. 119-130.

Bulian G. and Francescutto A., 2010, "A Simplified Regulatory-oriented Method for Relative Assessment of Susceptibility to Parametric Roll Inception at the Early Design Stage", Proceedings of 4th International Maritime Conference on Design for Safety and 3rd Workshop on Risk-Based Approaches in the Marine Industries, Part I pp. 93-106.

Cummins W. E., 1962, "The Impulse Reponse function and Ship Motions", Schiffstechnik 47(9), pp 101-109

Grim, O., 1961, "Beitrag zu dem Problem der Sicher heit des Schiffes im Seegang", Schiff und Hafen.

Hashimoto H., Umeda N., Matsuda A., and Nakamura S., 2006, "Experimental and Numerical Studies on Parametric Roll of a Post-Panamax Container Ship in Irregular Waves", Proceedings of 9th International Conference on Stability of Ships and Ocean Vehicles, pp. 181-190.

Ikeda Y., Himeno Y. and Tanaka N., 1978, "Components of roll damping of ship at forward speed", Journal of Society of Naval Architects of Japan No. 143, pp 121-133

IMO SDC 2/WP.4 Annex 2, 2015, "Development of Second Generation Intact Stability Criteria", Report of the working group (part 1).

IMO SDC 4/5/1/Add.1, 2017, "Finalization of Second Generation Intact Stability Criteria". Report of the correspondence group (part 2), Submitted by Japan

IMO SDC 5/6/2, 2018, "Finalization of Second Generation Intact Stability Criteria: Comments on the Calculation Method for Parametric Rolling Failure Mode", Submitted by Japan

IMO SLF 52/INF.2 Annex 6, 2009, "Development of New Generation Intact Stability Criteria", Information collected by intersessional correspondence group on Intact Stability, submitted by Japan (Annex 6 submitted by the United States).

KangHyun S., DongMin P., YongHwan K., and GangHyun L., 2013, "A New Guidance for the Quantitative Analysis of Parametric Roll in Random Seaways", Proceedings of the PRADS2013, pp. 625-633.

Kawahara Y., Maekawa K., and Ikeda Y., 2009, "A Simple Prediction Formula of Roll Damping of Conventional Cargo Ships on the Basis of Ikeda's Method and its Limitation", Proceedings of 10th International Conference on Stability of Ships and Ocean Vehicles, pp. 387-398

Malenica S., Chen X. B., Orozco J. M., and Xia J., 2006, "Parametric Roll – Validation of a Numerical Model", Proceedings of 7th International Conference on Hydrodynamics, pp. 147-152

Wandji C. and Corrignan P., 2012, "Test Application of Second Generation IMO Intact Stability Criteria on a Large Sample of Ships", Proceedings of 11th International Conference on the Stability of Ships and Ocean Vehicles, pp. 129-139

Wandji C. and Corrignan P., 2013, "Sample Application of Second Generation IMO Intact Stability Criteria as Updated during SLF 55", Proceedings of 13th International Ship Stability Workshop, pp. 121-129

Variation in Ship Parametric Roll Amplitude with Forward Speed and Heading Angle

Hongxia Li, *School of Naval Architecture, Dalian University of Technology* li_hx@dlut.edu.cn

Bohai Zhu, *School of Naval Architecture, Dalian University of Technology* 952669372@qq.com

Xiaoyu Zhou, *School of Naval Architecture, Dalian University of Technology* 479138249@qq.com

Jiyue Zhang, *School of Naval Architecture, Dalian University of Technology* 1273831423@qq.com

Zhongyao Dong, *School of Naval Architecture, Dalian University of Technology* 917637129@qq.com

ABSTRACT

Prediction of ship parametric roll can provide valuable reference for navigation. In this study, simulations of ship parametric roll in waves were conducted, and the results of numerical calculation are compared with the results of model test. The Froude-Krylov forces and restoring forces were calculated by integrating the pressure over the instantaneous wet surface of the ship. Coefficients of the damping moment were obtained from free decay model tests. The study confirmed that roll amplitude varies with forward speed and heading angle.

Keywords: *Parametric roll, Forward speed, Heading angle*

1. INTRODUCTION

Ship rolling is generated by forced and parametric excitations, which are mainly induced by sea waves. When a ship sails in rough sea conditions, the captain tends to steer the ship away from beam waves and toward head waves. As is often the case, ships sail in bow and quarter waves. Hashimoto (2004) studied ship parametric rolling in regular and irregular waves in the head and oblique direction and found variations in the ship's restoring moment. Bulian (2004) used time-domain simulation model to analyze the ship's non-linear parametric rolling in regular and irregular longitudinal waves. Sayed (2011) established the non-linear coupled motion equation of rolling and pitching and analyzed the response and stability of parametric rolling. Hashimoto (2011) conducted a self-propulsion test of post Panamax container. Parametric rolling in regular waves, irregular long-crested waves and irregular short-crested waves were tested, and the influence of such factors as wave steepness, speed, and course angle were analyzed. Li (2014) proposed a new method to calculate the restoring force and coupled motion response. This method considers the effects induced by the relative position of the waves and ship, as well as the coupling motions of heave, pitch, and roll. The results demonstrated that ship motion in regular bow or quarter waves is nonlinear. Bu (2014) proposed three numerical methods for analyzing parametric rolling under longitudinal wave conditions. The interactions among parametric roll, heave and pitch are studied, and simulation results were compared with the test results.

The C11 container ship was selected as a representative example for the study. By using the numerical simulation method, the effects of speed, heading angle, wave length and such factors are studied, and the range of sea conditions in which ship may experience intense parametric rolling is obtained. Finally, three conclusions related to the ship's

parametric rolling under head sea and oblique sea conditions were drawn from this study.

2. NUMERICAL SIMULATION METHOD AND RESULTS

2.1 Mathematical Model

The mathematical model includes: the coupling effects of heave, pitch, and roll; calculation of the incident wave force and hydrostatic pressure are calculated by considering the integral of water pressure over the instantaneous wet-surface, and nonlinear damping force, as shown in equation(1).

$$\begin{bmatrix} m+\delta m_{33} & \delta m_{34} & \delta m_{35} \\ \delta m_{43} & I_{44}+\delta m_{44} & \delta m_{45} \\ \delta m_{53} & \delta m_{54} & I_{55}+\delta m_{55} \end{bmatrix} \cdot \begin{bmatrix} \ddot{x}_3 \\ \ddot{x}_4 \\ \ddot{x}_5 \end{bmatrix} + \begin{bmatrix} c_{33}\dot{x}_3+c_{34}\dot{x}_4+c_{35}\dot{x}_5 \\ A\cdot\dot{x}_4+C\cdot\dot{x}_4^3 \\ c_{53}\dot{x}_3+c_{54}\dot{x}_4+c_{55}\dot{x}_5 \end{bmatrix} + \begin{bmatrix} F_{res3}(x_3,x_4,x_5,t) \\ F_{res4}(x_3,x_4,x_5,t) \\ F_{res5}(x_3,x_4,x_5,t) \end{bmatrix} = \begin{bmatrix} F_{FK3} \\ F_{FK4} \\ F_{FK5} \end{bmatrix} + \begin{bmatrix} F_{diff3} \\ F_{diff4} \\ F_{diff5} \end{bmatrix} \quad (1)$$

where x_3, x_4, x_5 represent heave, roll, and pitch motion, respectively; $m_{ij}\,(i,j=3,4,5)$ are mass coefficients; $\delta m_{ij}\,(i,j=3,4,5)$ are added mass coefficients; A, C are the linear and nonlinear damping coefficients for ship rolling; c_{ij} $(i,j=3,4,5)$ are linear damping coefficients; and F_{resi}, F_{FKi}, F_{diffi} $(i=3,4,5)$ are the restoring forces, Froude-Krylov (FK) forces and diffraction forces, respectively, of the heave, roll, and pitch motions.

2.2 Simulation Results

The response of C11 container ship is simulated, and the parameters which may lead to intense parametric roll are analyzed. Table 1 lists the main characteristics of the C11 container ship.

Roll motions in bow wave and quartering wave are described as in figure 1~4.

Table 1 Main Characteristics of the C11 Container Ship

Item	Ship	Item	Ship
Length between Perpendiculars *Lpp*/m	262	Molded Breadth *B*/m	40.0
raught *T*/m	11.5	Molded Depth *D*/m	24.45
Metacentric Height $\overline{GM}$ /m	1.95	Rolling Natural Frequency ω_n / rad•s^{-1}	0.25
Transverse Inertia Radius *Kxx*/m	16.73	Longitudinal Inertia Radius *Kyy*/m	62.55
Longitudinal Centre of Gravity *LCG*/m(to the 0 station)	125.52	Vertical Centre of Gravity *KG*/m(to the base line)	17.54

(1) Speed 5.0m/s, course angle 60° and wave amplitude 3.4m.

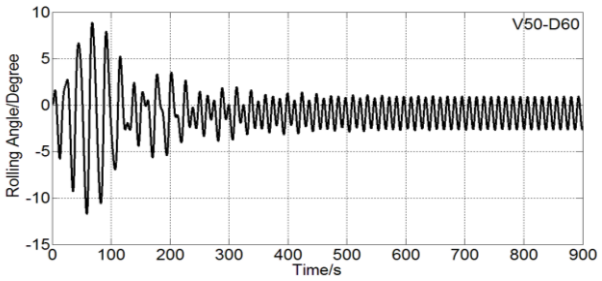

Figure 1 Time History of Roll

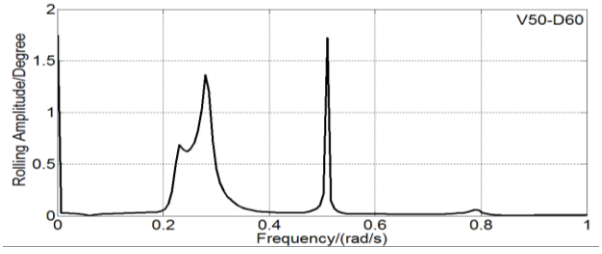

Figure 2 Roll Spectral Density

(2) Speed 5.0m/s, course angle 150° and wave amplitude 6.7m.

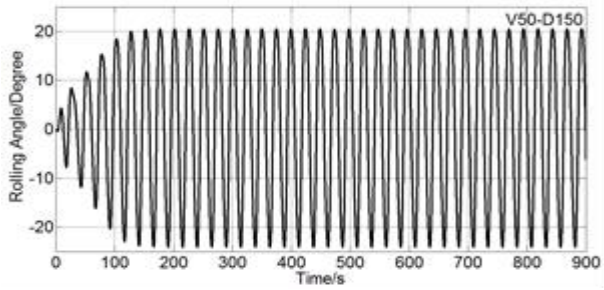

Figure 3 Time History of Roll

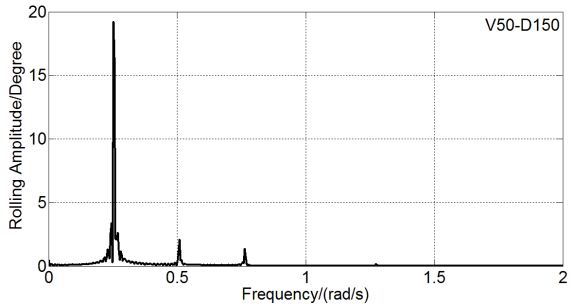

Figure 4 Roll Spectral Density

Figure 2 shows that the energy of the rolling motion is highest at 0.28 rad/s and 0.47 rad/s with the latter having the greatest concentration of energy. Therefore, the roll motion in this case is mainly generated by forced excitation. In Fig. 4, the energy of rolling motion is mainly concentrated at 0.26 rad/s with a value that is nearly half that of the encounter frequency, a clear sign of parametric rolling.

2.3 Comparison Between Model Test and Numerical Simulation

In the numerical simulation, the rolling time history of the C11 container ship was calculated with a course angle of 150°, wave amplitude of 3.93 m, and wave frequency of 0.485 rad/s. A self-propelled ship model at the China Ship Scientific Research Center was used to conduct a test based on the mathematical model with a scaled ratio of 1:65.6 and heading angle of 150°.

Figure 5 shows a comparison between the model test and the numerical simulation.

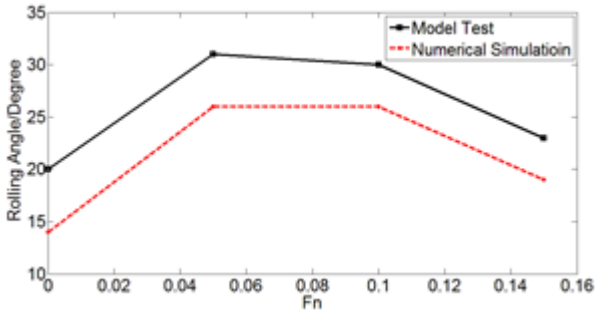

Figure 5 Comparison between Model Test and Numerical Simulation

As Fig.5 shows, the shape of the plot line for the numerical simulation accords with that of the model test result. In both of the cases, when the Froude number (*Fn*) equals 0.05 and 0.1, the rolling motion is shown to be more violent, because the ratio of rolling natural period to encounter period is 2.06 and 2.26(nearly to 2) in that condition, and parametric rolling tends to happen.

3. SEA CONDITIONS THAT MAY LEAD TO PARAMETRIC ROLLING

When encounter frequency is twice that of natural frequency, the ship may experience parametric roll. Encounter frequency is dependent on speed and course angle as expressed in Eq. (2).

$$\omega_e = \left| \omega - \frac{\omega^2 V}{g} \cos(\mu) \right| \tag{2}$$

where ω_e represents encounter frequency, V represents speed, μ represents course angle and ω represents wave frequency.

When $\omega - \frac{\omega^2 V}{g}\cos(\mu) > 0$, Eq. (1) turns into:

$$\frac{\omega^2 V}{g}\cos(\mu) - \omega + \omega_e = 0 \tag{3}$$

When $\omega - \frac{\omega^2 V}{g}\cos(\mu) < 0$, Eq.1 turns into:

$$\frac{\omega^2 V}{g}\cos(\mu) - \omega - \omega_e = 0 \qquad (4)$$

The wave frequency ω in Eq.3 and Eq.4 are solved by a series of speed and course angle conditions:

(1) Navigation speed is smaller than the component of wave speed in the direction of navigation in head waves or in long-period following waves, as shown in curve 1 of Fig.6 and expressed as:

$$\omega = (g - \sqrt{g^2 - 4gv\omega_e \cos\mu}) / (2v\cos\mu) \qquad (5)$$

(2) Navigation speed is smaller than the component of wave speed in the direction of navigation in short-period following waves, as shown in curve 2 of Fig.6 and expressed as:

$$\omega = (g + \sqrt{g^2 - 4gv\omega_e \cos\mu}) / (2v\cos\mu) \qquad (6)$$

(3) Navigation speed is larger than the component of wave speed in the direction of navigation in short-period following waves, as shown in Curve 3 of Fig.6 and expressed as:

$$\omega = (g + \sqrt{g^2 + 4gv\omega_e \cos\mu}) / (2v\cos\mu) \qquad (7)$$

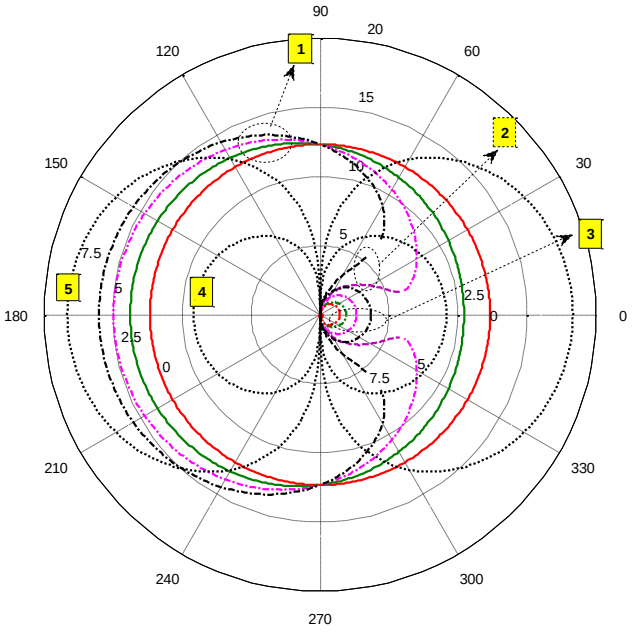

Figure 6 Conditions Tending to Induce Parametric Rolling

Figure 6 shows the system of polar coordinates. The polar diameter represents the wave period, and the polar angle represents the heading angle. Curves 1, 2, and 3 in Figure 6 are a combination of wave period, course angle and ship speed when ω_e is equal to $2\omega_\phi$. Different speeds are distinguished by different colors: black represent 7.5 m/s, pink represent 5 m/s, green represent 2.5 m/s, red represent 0 m/s.

Generally, when the wave length λ is around 0.5*Lpp* to 2*Lpp* in longitudinal waves, ships may experience parametric rolling. Hence, the wave length in bow or quarter waves is given as follows:

$$\frac{Lpp}{2}\cos\mu < \lambda < 2Lpp\cos\mu \qquad (8)$$

Curves 4 and 5 in Fig.6 are the critical wave lengths that represent parametric rolling.

In conclusion, the inner part of curve 1, 2, 3 bounded by curve 4, 5 is the sea conditions where the C11 container ship may experience parametric rolling in Figure 6.

4. ANALYSIS RESULTS

Choose a series of sea conditions in the region where parametric roll may happen in Figure 6 (Tab.2). The wave frequency for each sea condition was calculated according Eqs.(5)-(7), and the wave height was set at 4% *Lpp*, 3% *Lpp* and 2% *Lpp*. The total number of sea conditions calculated within the scope of this particular study was 3 × 20. And the roll time history curve was obtained by the above numerical simulation method.

Table 2 Simulated Operational Conditions of C11 Container Ship

No.	Course Angle(degree)	Speed(m/s)
1	0	0,2.5
2	30	0,2.5
3	60	0,2.5,5,7.5
4	90	0,2.5,5,7.5
5	150	0,2.5,5,7.5
6	180	0,2.5,5,7.5

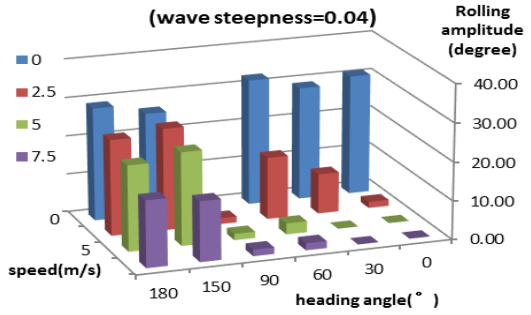

Figure.7 Rolling amplitude (wave steepness equals 0.04)

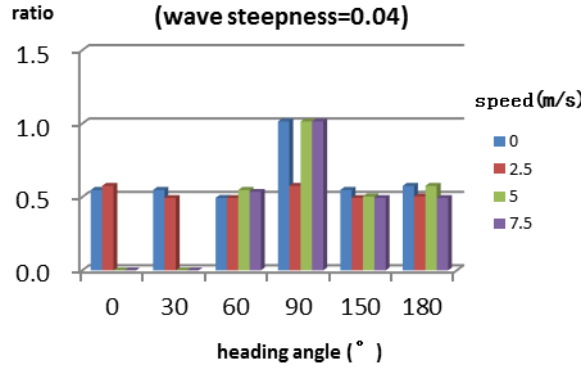

Figure.8 Ratio of roll frequency to encounter frequency (wave steepness equals 0.04)

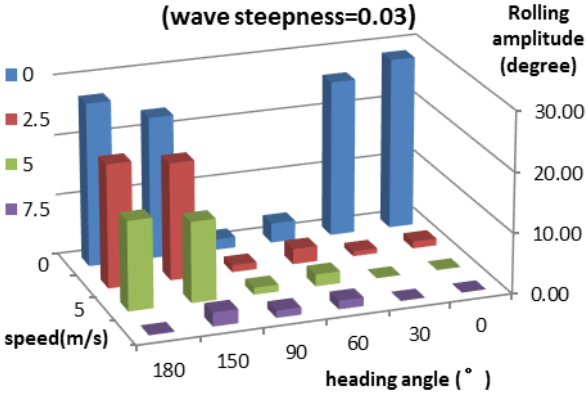

Figure.9 Rolling amplitude (wave steepness equals 0.03)

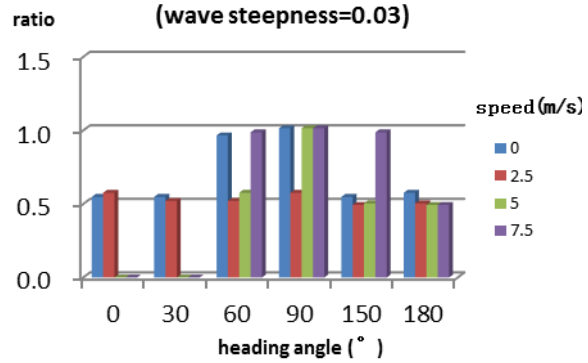

Figure.10 Ratio of roll frequency to encounter frequency (wave steepness equals 0.03)

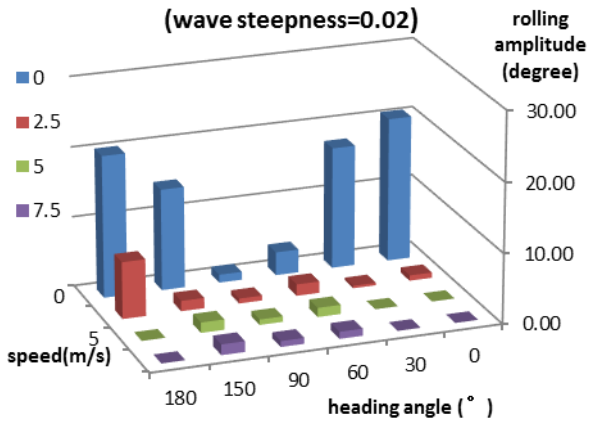

Figure.11 Rolling amplitude (wave steepness equals 0.02)

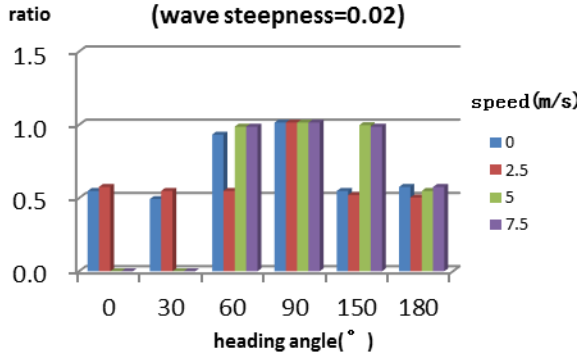

Figure.12 Ratio of roll frequency to encounter frequency (wave steepness equals 0.02)

Figures 7, 9, and 10 are bar charts of the roll amplitude at a wave steepness of 0.04, 0.03, and 0.02, respectively. Figures 8, 10 and 12 are bar graphs of the ratio of roll frequency to encounter frequency at a wave steepness of 0.04, 0.03 and 0.02, respectively. When the ratio of roll frequency to encounter frequency approximates 0.5, parametric rolling occurs; when the ratio of roll frequency to encounter frequency equals 1, harmonic roll occurs.

Figures 8, 10, and 12 show that ship rolling in longitudinal waves is mainly parametric, and ship rolling in beam waves is mainly harmonic. Under longitudinal or bow wave conditions, wave amplitude increases and the range of speed at which the ship may experience parametric rolling increases.

Figures 7, 9, and 11 show that large amplitude parametric rolling mainly occurs in low speed conditions under longitudinal waves or 150° bow waves. The roll amplitude in beam

waves is small. In 60° quarter wave conditions, only large amplitude waves can induce intense parametric rolling. In conditions with following waves, parametric rolling is the primary form but its amplitude is not as large.

Figure 13 shows the roll amplitude at two different course angles and four different speeds. At close to a 0.5 ratio of roll frequency to encounter frequency, parametric rolling occurs. The numerical simulation results demonstrate that the C11 container ship may experience large parametric roll in bow waves (e.g., 150°bow waves), and the roll amplitude nearly equals that in the head waves.

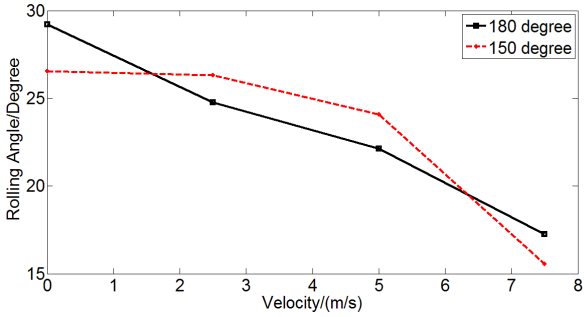

Fig. 13 Comparison between Bow Waves Conditions and Heading Waves Conditions

5. CONCLUSIONS

In this study, the C11 container ship was selected as a representative sample for determining the parametric conditions in which the ship may experience parametric rolling. According to results of the simulation analysis, three conclusions are obtained.

(1) Ship parametric rolling occurs in bow and quarter waves when the encounter frequency is about twice that of the natural frequency. The energy of the rolling motion is mainly concentrates at the encounter frequency and at half the encounter frequency. At the encounter frequency, energy increases when sea waves are more like beam waves.

(2) When the encounter frequency nearly equals twice of the natural frequency and the wave amplitude is increased, then the speed will increase to within the range where parametric rolling occurs.

(3) The ship rolling amplitude in bow waves when the heading angle is 150° is similar to the amplitude for longitudinal waves.

6. ACKNOWLEDGMENTS

This work is supported by the Ministry of Industry and Information Technology of China (No. [2016] 25) and the National Natural Science Foundation of China (project no. 51779042).

7. REFERENCES

Bu Shuxia, Lu Jiang, Gu Min, and Wang Tianhua, 2014, “Numerical Prediction of Parametric Rolling in Regular Head Seas”, Shipbuilding of China, Vol. 55, No.2, pp. 1-7.

Bulian G., Francescutto A., and Lugni C., 2004, “On the nonlinear modeling of parametric rolling in regular and irregular waves”, International shipbuilding progress, Vol. 51, No. 2-3, pp. 173-203.

Hashimoto H., Umeda N., and Matsuda A., 2011, “Experimental Study on Parametric Roll of a Post-Panamax Containership in Short-Crested Irregular Waves”, Fluid Mechanics & Its Applications, pp. 267-276.

Hashimoto H., Umeda N. et al., 2004, “Nonlinear analysis of parametric rolling in longitudinal and quartering seas with realistic modeling of roll-restoring moment”, Journal of Marine Science and Technology, Vol. 9, No. 3, pp. 117-126.

Li Hongxia, Peng Dongsheng, and Huang Yi, CHU Ji-long, 2014, “Parametric rolling analysis in oblique seas”, Journal of Ship Mechanics, Vol. 18, No.1-2, pp. 62-67.

Sayed M., Hamed Y.S., 2011, “Stability and response of a nonlinear coupled pitch-roll ship model under parametric and harmonic excitations”, Nonlinear Dynamics, Vol. 64, No. 3, pp.207-220.

Free running model experiment and numerical simulation on the occurrence and early detection of KCS parametric roll in head waves

Liwei, Yu, *Shandong Provincial Key Laboratory of Ocean Engineering, Ocean University of China*

yuliwei@ouc.edu.cn

Ning, Ma, *State Key Laboratory of Ocean Engineering, Collaborative Innovation Center for Advanced Ship and Deep-Sea Exploration (CISSE), Shanghai Jiao Tong University, Institute of Advanced Sciences, Yokohama National University,* ningma@sjtu.edu.cn

Yoshiaki, Hirakawa, *Systems Design for Ocean-Space, Yokohama National University,*

hirakawa-yoshiaki-jd@ynu.ac.jp

Ko, Taguchi, *Systems Design for Ocean-Space, Yokohama National University,*

taguchi-ko-rm@ynu.jp

Kenta, Akagi, *Systems Design for Ocean-Space, Yokohama National University,*

akagi-kenta-wv@ynu.jp

ABSTRACT

Under the collaborative research between Shanghai Jiao Tong University (SJTU) and Yokohama National University (YNU), the free running model experiments and numerical simulations on the occurrence and early detection of KCS (KRISO Container Ship) parametric roll in regular head waves are conducted. The occurrence of parametric roll under various ship speeds and wave lengths in regular heading waves are realized using the free running model experiments. The real-time parametric roll early detection algorithm are validated through the model experiment to be able to detect parametric roll while its amplitude is still small. Then, the occurrence of KCS parametric roll in regular head waves is simulated using the 5-DOF seakeeping model and the Unified model. Through comparison with experimental results, it is found that the 5-DOF seakeeping model overestimates the occurrence of parametric roll. The influence of manoeuvring motion like speed and heading changes on parametric roll is investigated using the Unified model. The overestimation of parametric roll is not improve.

Keywords: *Parametric roll; Parametric roll early detection; Hilbert-Huang transform; Unified model*

1. INTRODUCTION

When a ship sails in heavy longitudinal seas, large variations of water plane area and roll restoring forces may induce extreme self-resonant roll motion, i.e. Parametric roll. It is a very dangerous nonlinear phenomenon which causes severe damages. Severe parametric roll

was reported on containerships (France et al., 2003), small fishing vessels (Neves et al., 1999), cruise ship and PCTC (Ovegård et al., 2012).

The study on the parametric roll phenomenon were conducted through numerical simulations (Bulian, 2005; Hashimoto and Umeda, 2010; Neves et al., 1999; Spanos and Papanikolaou, 2007; Terada, 2018) and model experiments (Hashimoto et al., 2007; Neves et al., 2002; Taguchi et al., 2011). The International Maritime Organization Sub-Committee on Ship Design and Construction (IMO SDC) is finalizing the multilevel second generation intact stability criteria on parametric roll (IMO SDC4/WP.4, 2017).

Study on the stabilization of parametric roll in the operational stage is also very important. It was pointed out by Yu et al. (2012) that the parametric roll stabilization techniques was effective when the parametric roll amplitude was still small and anti-roll control was activated early. Thus, in order to achieve a good performance on parametric roll stabilization, an on-board real-time parametric roll early detection system is needed to detect the parametric roll and activate the rudder anti-roll control when the roll amplitude is still small. For the early detection of parametric roll, Galeazzi et al. (2015, 2013) proposed a signal-based parametric roll detection method combining a spectral correlation detector in the frequency domain with a phase synchronization detector in the time domain. The proposed detection schemes are fully validated to be effective and robust using the full-scale long-term voyage data. Yu et al. (2017, 2016) developed an alternative signal-based detection method using the incremental real-time Hilbert-Huang Transform (IR-HHT) technique. The detection algorithm based on the IR-HHT approach is proved by both numerical simulations and model experiments to be capable of detecting the frequency shift and amplitude growth during the initial stage of parametric rolling.

In this paper, model experiments and numerical simulations on the occurrence and early detection of parametric roll of a KCS containership model in regular head waves are conducted under the collaborative research between Shanghai Jiao Tong University (SJTU) and Yokohama National University (YNU). The effectiveness of the real-time parametric roll early detection algorithm proposed by Yu et al. (2016) are proved using the model experiment. Meanwhile, the proposed numerical model for parametric roll simulation is validated by the model experiment.

2. MODEL EXPERIMENTS

2.1 Experiment setup

The free-running model experiments in regular head waves are conducted in the towing tank of Yokohama National University, which is 100m long, 8m wide and 3.5m deep. Results on the model experiments are fully reported in Yu et al. (2017), and results on occurrence and detection in regular waves are chosen from Yu et al. (2017) and introduced in this paper. The model ship used in the experiment is a 1/100 scale KCS (KRISO Container Ship) containership (Simman2008, 2008). The KCS model ship is presented in Fig.6. Main particulars of the model ship are shown in Table 1. Roll and pitch natural periods are measured by roll and pitch decay tests in calm water with zero forward speed.

Table 1 Main particulars of the KCS model

Ship	Model (1/100)
Length, L_{pp}(m)	2.300
Breadth, B(m)	0.322
Depth, D(m)	0.190
draft, d(m)	0.108
Displacement(m^3)	0.05203
Mass(kg)	52.31
Longitudinal COB, LCB(m)	1.116 from AP
Height of COG, KG(m)	0.1366
Metacentric height, GM(m)	0.0127

k_{xx}/B	0.3242
k_{yy}/L_{pp}(k_{zz}/L_{pp})	0.2495(0.2465)
Roll natural period, T_{roll} (s)	2.160
Pitch natural period, T_{pitch} (s)	0.772
Rudder	Model
Area, A_R(m^2)	0.0055
Rudder aspect ratio, □	1.8
Rudder height, h(m)	0.099
Bilge Keel	Model
Position of fore end(m)	0.285 forward from midship
Position of aft end(m)	0.288 backward from midship
Thickness(m)	0.0026
Span, b_{BK} (m)	0.0122

Figure 1 The KCS model ship

The self-propelled model ship is made by FRP and equipped with rudder and propeller. The model is driven by a DC motor and steered by a servo motor. The setup of all the experimental equipment is presented in Fig.9. The roll and pitch angles are measured by an inclining&gyro sensor and the rudder angle is measured by a potentiometer all with a sample rate of 50Hz. The heading angle, speed and trajectory of the model ship are measured by the 2D motion capturing system. The parametric roll detection algorithm and the autopilot program are all embedded in the onboard single board computer Raspberry-Pi.

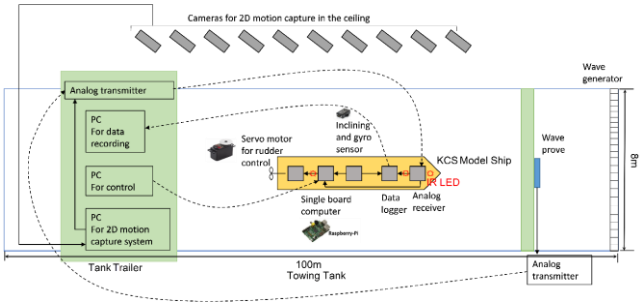

Figure 2 Setup of all the experimental equipment in the towing tank(arrows with dashed lines: wireless transmission, arrows with solid lines: wire transmission)

During the experiment, two setups (No. I and II) with or without the bilge keel are established. In table 2, natural roll periods and viscous roll damping coefficients obtained from roll decay tests are shown. During the experiments, cases with different ship speeds and wave lengths are selected. The test cases of regular head waves are presented in Table 3. In Table 3 for the regular wave cases, T_e/T_{roll} indicates the relationship between the encounter period T_e and the natural roll period T_{roll} which is critical to the onset of parametric roll. In the experiment, each case is repeated several times to ensure the repeatability and validate the parametric roll early detection algorithm.

Table 2 Natural roll periods and viscous roll damping coefficients (model scale)

No.	*GM [m]*	*Bilge Keel*	T_{roll}*[s]*	*a**	*b**
I	0.0127	Yes	2.160	0.1164	0.0101
II	0.0127	No	1.997	0.0336	0.0067

*The damping coefficients, a and b, are defined as follows: $\delta\phi = a\phi_m + b\phi_m^2$ where $\delta\phi$ and ϕ_m indicate decrement and mean swing angle of roll decay tests without forward speed.

Table 3 Experimental cases for regular head waves (model scale)

No.	Planned speed V_m[m/s]	Wave Period T[s]	Wave Length λ/L_{pp}	Wave Frequency ω_0[rad/s]	Encounter Frequency ω_e[rad/s]	T_e/T_{roll} (Setup No.I)
1	0.100	1.214	1.000	5.176	5.449	0.534

2	0.200				5.722	0.508
3	0.300				5.995	0.485
4	0.400				6.268	0.464
5	0.500				6.541	0.445
6	0.600				6.814	0.427
7	0.200	1.302	1.150	4.826	5.301	0.549
8	0.300				5.538	0.525
9	0.400				5.775	0.504
10	0.500				6.013	0.484
11	0.600				6.250	0.465
12	0.700				6.488	0.448
13	0.800				6.725	0.433
14	0.900				6.962	0.418
15	0.400	1.384	1.300	4.540	5.380	0.541
16	0.500				5.590	0.520
17	0.600				5.800	0.501
18	0.700				6.011	0.484
19	0.800				6.221	0.468
20	0.900				6.431	0.452

Table 4 Parametric roll in regular head waves for Setup No.I with BK and Setup No.II (without BK)

No.	Planned speed V_m[m/s]	Wave Length λ/L_{pp}	T_e/T_{roll} (Setup No.I)	Setup No.I (With BK)			Setup No.II (Without BK)		
				P.R.	Roll Amp.	Amp. Detected Φ_p	P.R.	Roll Amp.	Amp. Detected Φ_p
1	0.100	1.000	0.534	×	-	-	×	-	-
2	0.200		0.508	○	6.894	1.953	×	-	-
3	0.300		0.485	○	11.175	1.758	○	12.921	4.526
4	0.400		0.464	○	7.448	6.278	○	24.680	4.938
5	0.500		0.445	×	-	-	○	24.823	10.211
6	0.600		0.427	×	-	-	○	25.795	6.283
7	0.200	1.150	0.549	×	-	-	×	-	-
8	0.300		0.525	○	8.116	2.286	×	-	-
9	0.400		0.504	○	11.274	3.047	○	9.339	3.918
10	0.500		0.484	○	12.243	2.475	○	16.635	6.065
11	0.600		0.465	○	8.883	5.928	○	17.259	14.585
12	0.700		0.448	○	5.409	2.606	○	20.750	4.832
13	0.800		0.433	×	-	-	○	21.009	4.939
14	0.900		0.418	×	-	-	×	-	-
15	0.400	1.300	0.541	×	-	-	×	-	-
16	0.500		0.520	×	-	-	×	-	-
17	0.600		0.501	○	5.592	2.907	○	13.962	4.035
18	0.700		0.484	○	1.718	1.386	○	16.302	6.070
19	0.800		0.468	×	-	-	○	17.196	5.307
20	0.900		0.452	×	-	-	○	16.767	8.513

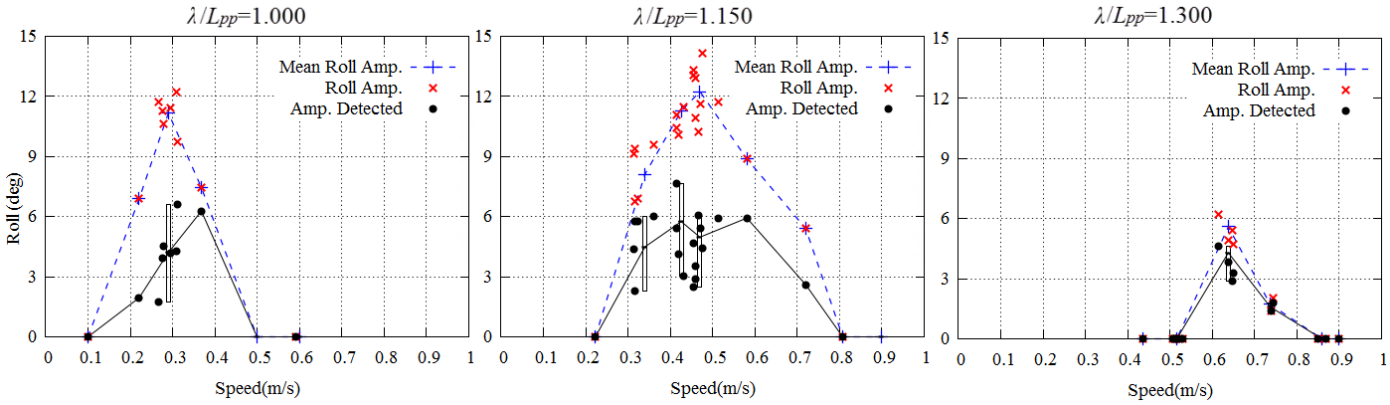

Figure 3. Occurrence and detection amplitude Φ_p of parametric roll in regular head waves with Bilge Keel

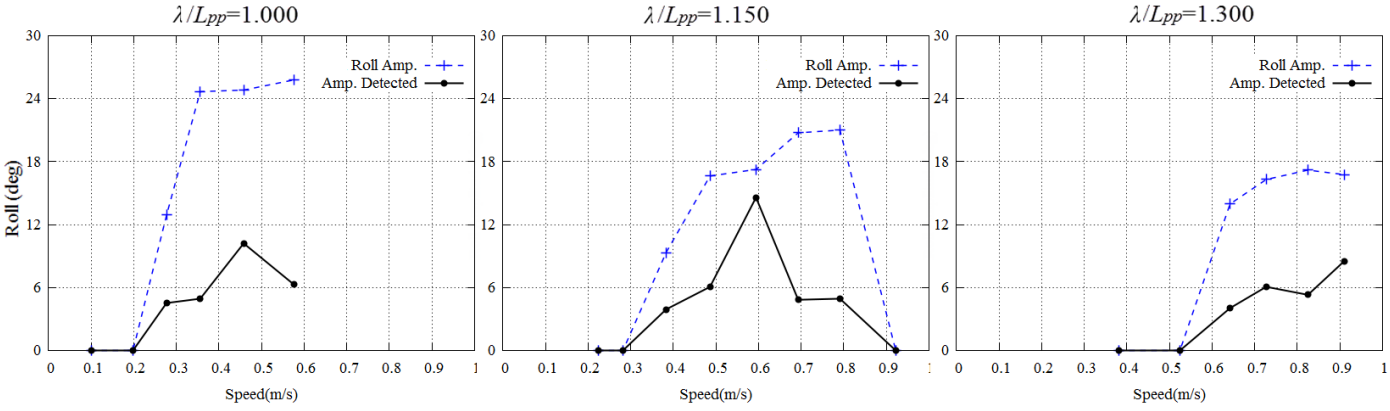

Figure 4. Occurrence and detection amplitude Φ_p of parametric roll in regular head waves without Bilge Keel

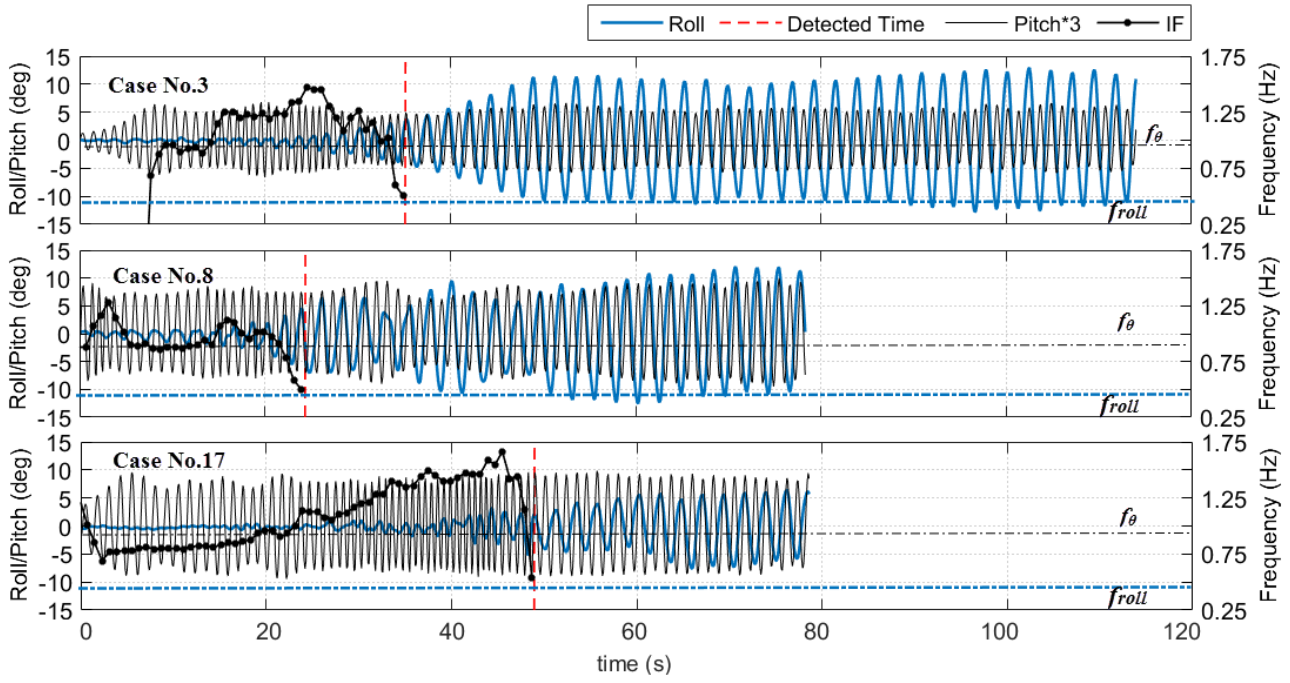

Figure 5. Time series of parametric roll early detection in regular waves for Setup No.I (with BK)

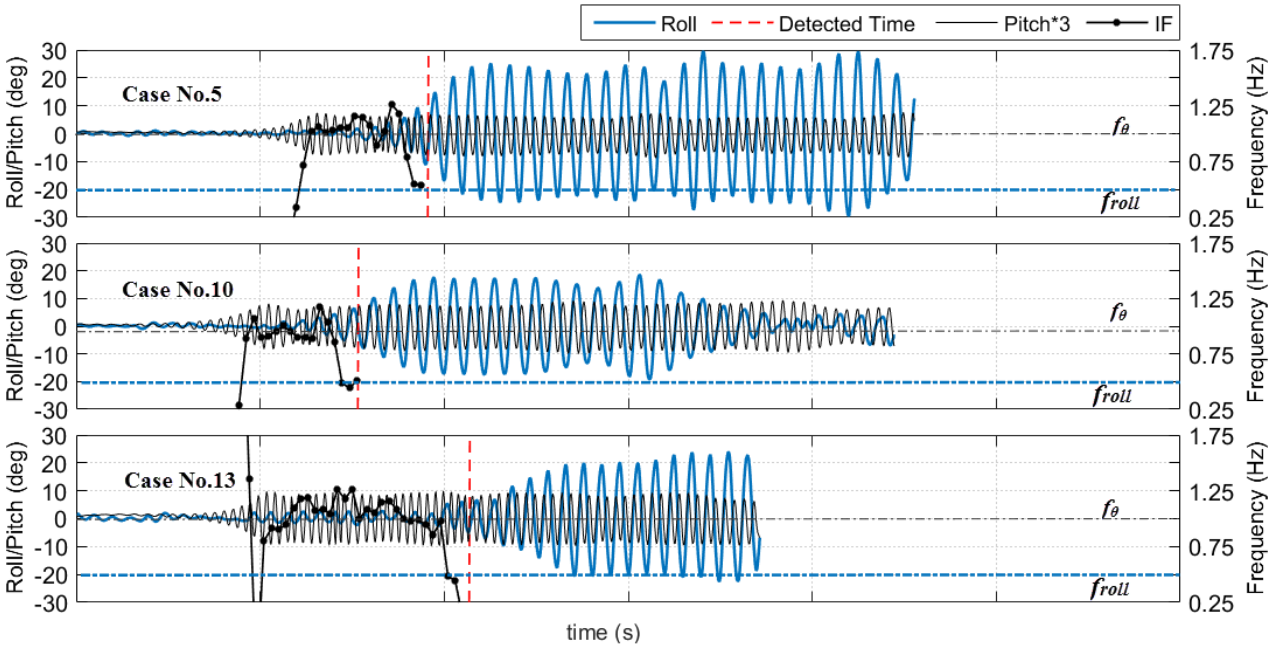

Figure 6 Time series of parametric roll early detection in regular waves for Setup No.II (without BK)

2.2 Occurrence of KCS Parametric Roll

The occurrence and detection results of parametric roll in regular head waves for Setup No.I with BK and Setup No.II without BK are summarized in Table 4 and Fig.3&4. In Table 4, "×" indicates that parametric roll (P.R.) doesn't occur, while "◯" indicates that parametric roll occurs. "Roll Amp." stands for the steady parametric roll amplitude without rudder stabilization. "Amp. Detected" Φ_p is the roll amplitude when parametric roll is detected at time t_p. "Amp. Stabilized" is the steady parametric roll amplitude after rudder parametric roll stabilization. The results of Table 4 are plotted in Fig.3 and 4. In the free running experiments, the ship speeds and roll amplitudes can be slightly different among repeated runs under the same case due to the uncertainty in initial conditions, ship heading and course. Thus 6-8 times of repeated runs are conducted for each case in Setup No.I. In Fig.3, the roll amplitudes and ship speeds of all the runs are shown as red cross points "×". The blue crisscross points "+" connecting by the dashed line are plotted based on the average roll amplitude and ship speed of red cross points "×".

From the occurrence of parametric roll shown in Fig. 3 and 4 (dashed line with crisscross points), it is found that parametric roll occurs when T_e/T_{roll} is around 0.5 for the specific vessel and loading condition under analysis. Comparing between Fig.3 and 4, it can be found that the roll damping provided by the bilge keel can reduce significantly the steady parametric roll amplitude.

Moreover, the roll and pitch time series of several cases are presented in Fig.5 and 6. In the figures, roll and pitch angles are represented by the thick blue solid line and the thin black solid line. The pitch angle in the figures is three times of its actual value to make it more distinguishable. It can be observed that roll angle (thick blue solid line) becomes large and the roll period is about twice of the pitch period(thin black solid line) when parametric roll occurs.

2.3 Detection of KCS Parametric Roll

The effectiveness of the real-time parametric roll early detection algorithm based on IR-HHT technique proposed by Yu et al. (2016) are validated through model

experiments. Results are presented in Fig.5 and 6. In the figures, the instantaneous frequency(IF) [Hz] of the pitch and roll combined time series obtained by the real-time detection algorithm is shown as the line with round dot. The P.R. detected time t_p are shown as the dashed vertical line. The pitch frequency f_θ and the roll natural frequency f_{roll} are plotted as the thin black horizontal dash-dot line and the thick blue horizontal dash-dot line.

In the figures, at the beginning when no parametric roll occurs, the pitch motion is dominant in the pitch and roll combined time series. Thus, the instantaneous frequency of the combined time series (line with round dot) is about the pitch frequency f_θ (thin black horizontal dash-dot line) i.e., wave encounter frequency. When parametric roll occurs, the roll motion is dominant. Therefore, the instantaneous frequency (line with round dot) drops to the value around the roll natural frequency f_{roll} (thick blue horizontal dash-dot line). Based on the frequency drops, parametric roll events are successfully detected at time t_p (dashed vertical line) when the roll amplitudes are still small for all the cases in Fig.5 and 6.

Furthermore, the amplitude detected Φ_p for all the cases are summarized in Table 4 and Fig.3&4 (solid line with round dot and rectangle). In order to fully validate the parametric roll early detection algorithm, some cases with bilge keel are repeated by 6 to 8 times and all the amplitudes detected Φ_p are plotted as round dot in Fig.3. The rectangle is the statistical plot of repeated runs under the same case where the upper limit of the rectangle is the maximum Φ_p, the lower limit is the minimum Φ_p and the solid line is the average Φ_p. For the cases with only one run, the amplitude detected Φ_p is represented as one round dot.

According to the amplitude detected Φ_p presented in Table 4 and Fig.3&4, parametric roll is successfully detected in all the cases and no false alarm is generated. Parametric roll events in all the cases and runs are detected when Φ_p is less than 6 deg except for case No.5 and 11 without bilge keel. Thus, it is concluded that the detection algorithm can successfully detect parametric roll at its early stage in regular head waves. The effectiveness of the parametric roll early detection algorithm based on the IR-HHT technique in regular head waves is verified through model experiments.

3. NUMERICAL SIMULATIONS

Numerical simulations of the KCS parametric roll in regular waves are conducted using two different numerical models, one is 5-DOF seakeeping model, the other is a unified model coupling manoeuvring and seakeeping motion. With these two models, a better agreement with experiment results is attempted.

3.1 Simulations by the Seakeeping Model

5DOF Seakeeping Model. The seakeeping model is a 5-DOF sway-heave-roll-pitch-yaw weakly-nonlinear model based on the Impulse Response Function (IRF) approach. The equation of motion can be written as:

$$m_i\dot{v}_i(t)+\sum_{j=2}^{6}\left[\mu_{ij}(\infty)\dot{v}_j(t)+C_{ij}\eta_j(t)+\int_0^t R_{ij}(t-\tau)v_j(\tau)d\tau\right]$$
$$+F_i^{res}(t)+B_v(v_4)=F_i^{FK}(t)+F_i^{dif}(t)\quad(i=2,...,6) \tag{1}$$

According to the IRF approach, the added mass μ_{ij}, infinite-frequency added mass $\mu_{ij}(\infty)$, damping coefficient λ_{ij}, and diffraction force $F_i^{dif}(t)$ are calculated in the frequency domain by the STF method and transferred into time domain using the retardation function $R_{ij}(\tau)$ and $Q_i(\tau)$. Details on the numerical model can be found in Yu et al. (2012). In the model, the nonlinear restoring $F_i^{res}(t)$ and Froude-Krylov $F_i^{FK}(t)$ forces are calculated through pressure integration on the instantaneous wetted surfaces which is detailed in Yu et al. (2017a). The roll viscous damping B_v are obtained from roll decay tests in zero forward speed with linear and cubic damping coefficients.

$$B_v(v_4) = Av_4 + Cv_4^3 \qquad (2)$$

The viscous damping with a forward speed is estimated as: $A=A_0+k\mathrm{Fn}$, where k is a empirical coefficient, Fn is the Froude number. The 5-DOF time domain model is verified through comparison with motion RAOs obtained by the frequency domain STF method (wave angle 135 deg) and model experiment (wave angle 180deg). The comparison results are presented in Figure 7.

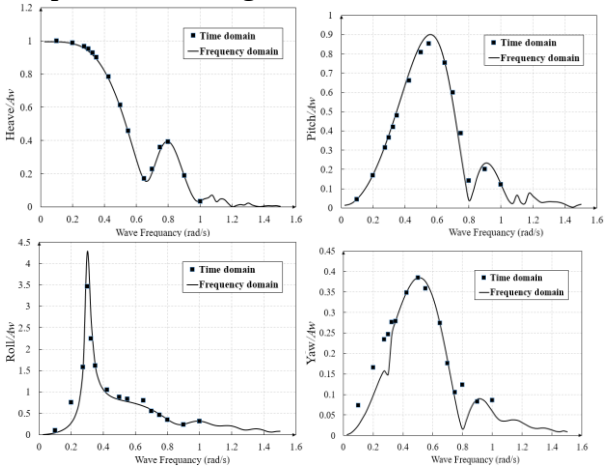

Figure 7 Comparison on heave, pitch, roll and yaw RAOs between time and frequency domain (wave angle 135deg)

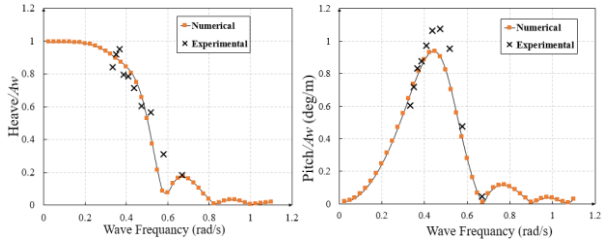

Figure 8 Comparison on heave, pitch RAOs with experiment results (wave angle 180deg)

Simulation Results. Numerical simulations of the KCS parametric roll using the 5-DOF seakeeping model are conducted under the similar cases as model experiments. The ship speed are chosen as 0.2~0.8 m/s. λ/L_{pp} equals to 1.00, 1.15 and 1.30. The wave steepness is 0.02. Cases with and without bilge keel are simulated. The simulation results are presented in Fig.9~12.

From Fig.9 and 10, the phenomenon of parametric roll can be observed with the pitch period half of the roll period. The steady parametric roll amplitudes of all the cases with and without bilge keel are presented in Fig.11 and 12. From the figures, it is found that the roll damping provided by the bilge keel can reduce significantly the steady parametric roll amplitude. The roll amplitude decreases as the speed growing high, which is caused by the larger roll damping under higher speed.

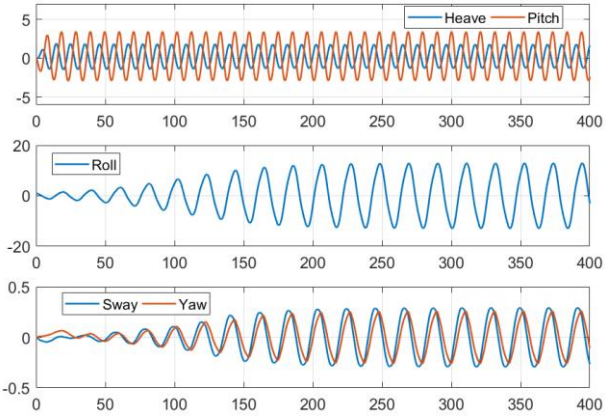

Figure 9 Results under V=0.7m/s, λ/L_{pp}=1.15 with Bilge Keel

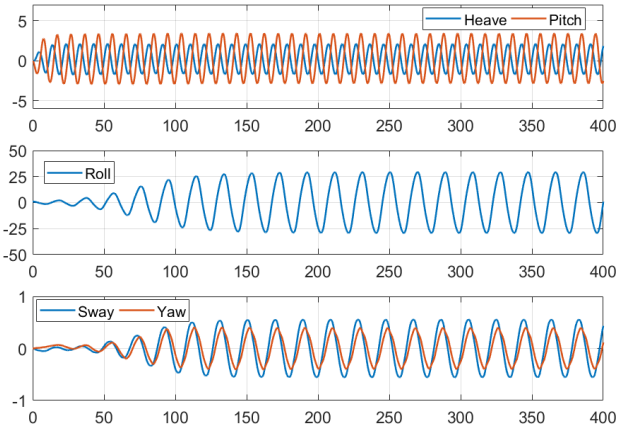

Figure 10 Results under V=0.7m/s, λ/L_{pp}=1.15 without Bilge Keel

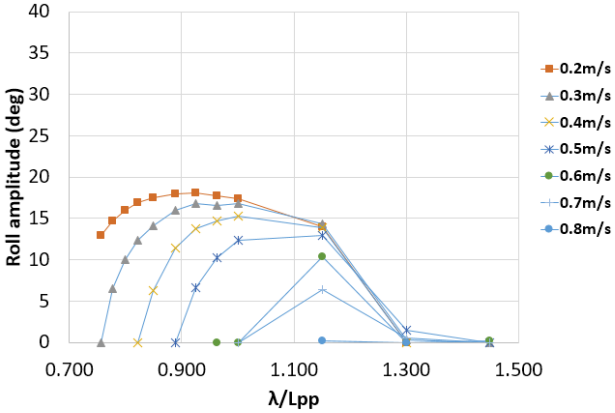

Figure 11 Roll amplitudes with Bilge Keel

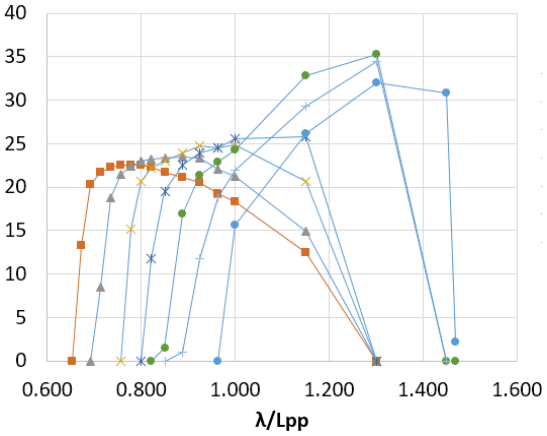

Figure 12 Roll amplitudes without Bilge Keel

Comparison between numerical simulations and model experiments are presented in Fig.13 and 14. From the comparison results, it is found that roll amplitudes are overestimated by the numerical model for the cases with and without bilge keel. In order to improve the overestimation, the unified model is proposed in the next section.

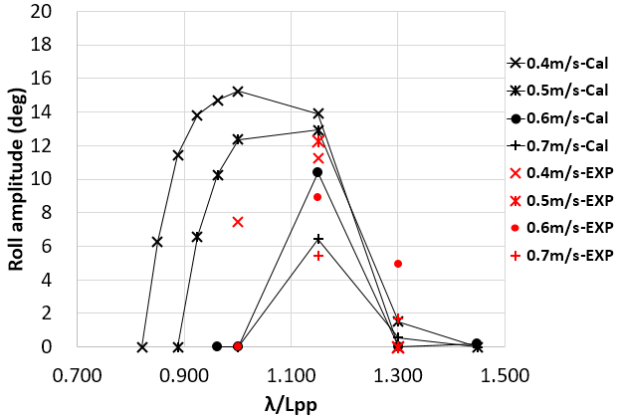

Figure 13 Comparison with experiment results (with bilge keel)

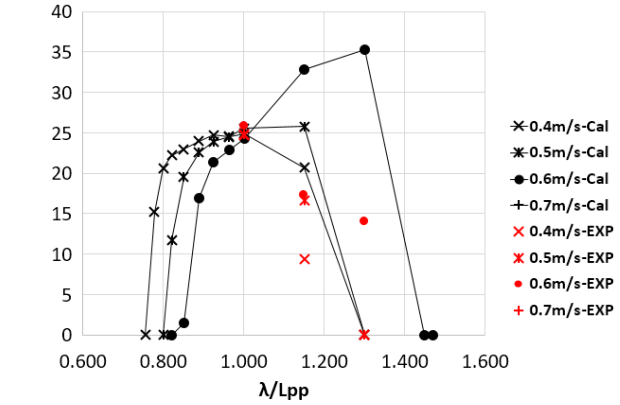

Figure 14 Comparison with experiment results (without bilge keel)

3.2 Simulations by the Unified Model

Unified Model. In order to improve the overestimation of the 5-DOF seakeeping model, the unified model coupling between maneuvering and seakeeping model is proposed. Details on the unified model can by found in Yu et al. (2012). In the model, the seakeeping model is the same as the 5-DOF seakeeping model in the last section. The maneuvering model is a 3-DOF MMG model. In the unified model, the maneuvering and seakeeping models are solved in different time scale. As a slowly varying motion, the maneuvering motion is simulated using larger time step than the seakeeping motion. The seakeeping motion is simulated within each time step of the maneuvering simulation assuming that the maneuvering motion is constant. Then the total motion of the ship is calculated by combining the two motions referring to different coordinate system together.

In order to verify the proposed model, the simulation result of 35 deg turning circle in calm water is compared with the experiment result provided by Yasukawa and Sano (2008) as shown in Fig.15. Moreover, the 35 deg turning circle in the regular wave are simulated. The turning circle, heading angle, roll and pitch time histories as ship turning in the wave are plotted in Fig.16. It can be found that the model can simulate the drifting of turning circles and the variations on amplitudes and frequencies of seakeeping motions while ship turning. The coupling between maneuvering and seakeeping motion is well reproduced.

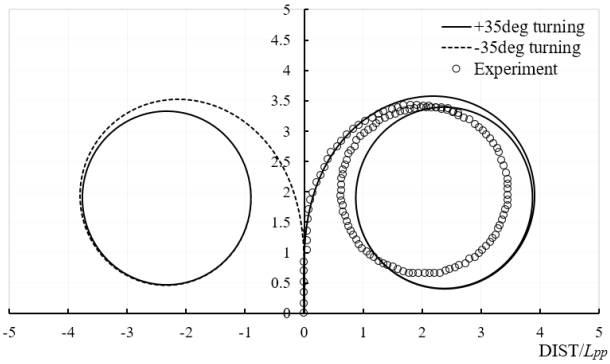

Figure 15 Comparison with experiment results of 35 deg turning circle in calm water

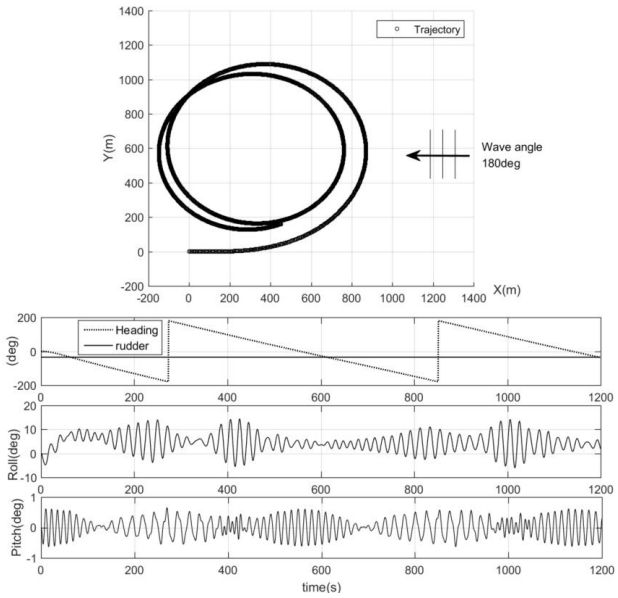

Figure 16 Simulation results of 35 deg turning circle in regular wave

Simulation Results. Numerical simulations using the unified model are conducted under the same cases as the 5-DOF seakeeping model. Only the cases with bilge keel are simulated. During the simulation, the heading angle measured in the experiment is taken as the heading angle of the simulation in order to reproduce the exact experimental scenario. The simulation results are shown in Fig.17~19. In the figures, the roll, heading, speed and trajectory of the simulation (black solid line) and experiment (red dashed line) are plotted. The headings of the simulation and experiment are same. The roll time histories of the 5-DOF seakeeping model (blue thin line) are also plotted. It can be found that although there is improvement on the simulation results comparing to the results of the seakeeping model, the overestimation is not improved. In Fig.20, comparison on steady parametric roll amplitudes with results of seakeeping model and experiment are presented. It is confirmed that the results of the unified model is almost the same as those of the seakeeping model. The overestimation is not improved by the unified model.

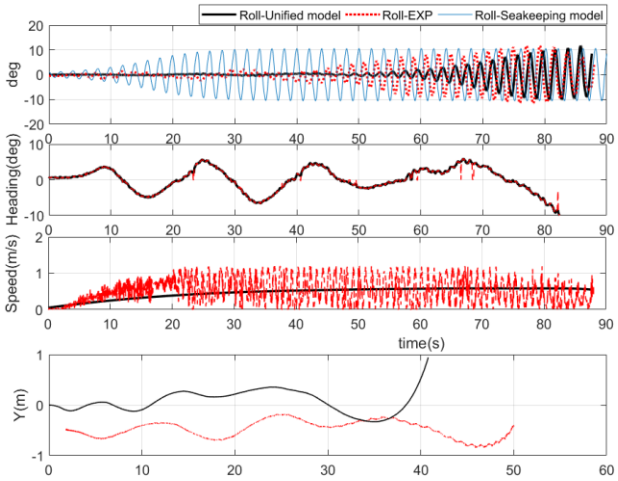

Figure 17 Simulation results under V=0.6m/s, λ/L_{pp}=1.150

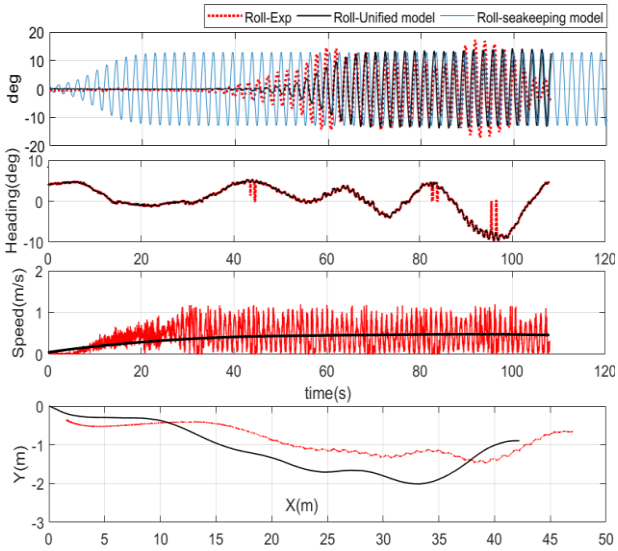

Figure 18 Simulation results under V=0.5m/s, λ/L_{pp}=1.150

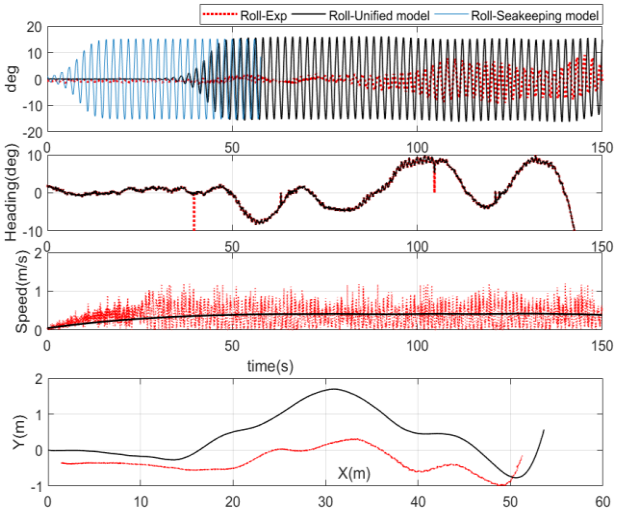

Figure 19 Simulation results under V=0.4m/s, λ/L_{pp}=1.000

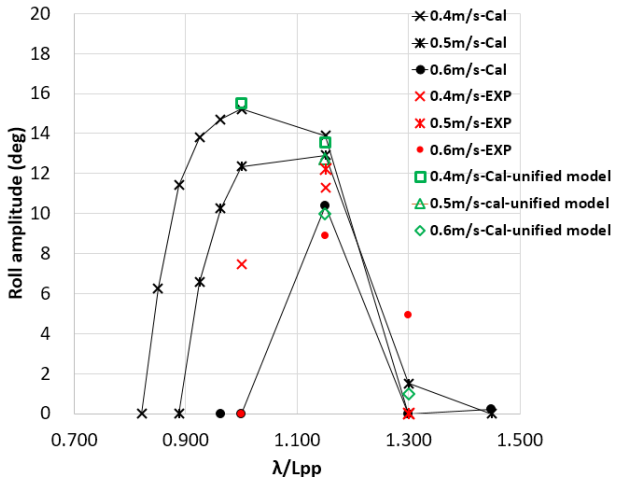

Figure 20 Comparison with results of seakeeping model and experiment (with bilge keel)

4. CONCLUSIONS

In this paper, model experiments and numerical simulations on the occurrence and early detection of parametric roll of a KCS containership model in regular head waves are conducted under the collaborative research between Shanghai Jiao Tong University (SJTU) and Yokohama National University (YNU). The following conclusions are drawn.

The occurrence of parametric roll under various ship speeds and wave lengths in regular heading waves are realized using the free running model experiments.

The real-time parametric roll early detection algorithm are validated through the model experiment to be able to detect parametric roll while its amplitude is still small.

The occurrence of KCS parametric roll in regular head waves is predicted using the 5-DOF seakeeping model and the Unified model. The simulation results are compared with the experimental results. It is found that the 5-DOF seakeeping model overestimates the occurrence of parametric roll. The influence of manoeuvring motion like speed and heading changes on parametric roll is investigated using the Unified model. The overestimation of parametric roll is not improve.

Further improvement on the Unified model will be conducted in the future work.

5. ACKNOWLEDMENTS

The present study is supported by the Institute of Advanced Sciences in Yokohama National University and the National Natural Science Foundation of China (NSFC) research project: No. 51579144, the Natural Science Foundation of Shandong Province (ZR2018BEE049).

6. REFERENCES

Bulian, G., 2005. Nonlinear parametric rolling in regular waves—a general procedure for the analytical approximation of the GZ curve and its use in time domain simulations. Ocean Eng. 32, 309–330.

France, W.N., Levadou, M., Treakle, T.W., Paulling, J.R., Michel, R.K., Moore, C., 2003. An investigation of head-sea parametric rolling and its influence on container lashing systems. Mar. Technol. 40, 1–19.

Galeazzi, R., Blanke, M., Falkenberg, T., Poulsen, N.K., Violaris, N., Storhaug, G., Huss, M., 2015. Parametric roll resonance monitoring using signal-based detection. Ocean Eng. 109, 355–371. doi:http://dx.doi.org/10.1016/j.oceaneng.2015.08.037

Galeazzi, R., Blanke, M., Poulsen, N.K., 2013. Early Detection of Parametric Roll Resonance on Container Ships. Control Syst. Technol. IEEE Trans. doi:10.1109/TCST.2012.2189399

Hashimoto, H., Umeda, N., 2010. A study on Quantitative Prediction of Parametric Roll

in Regular Waves, in: 11th International Ship Stability Workshop. Wageningen, Netherlands, pp. 295–301.

Hashimoto, H., Umeda, N., Sakamoto, G., 2007. Head-sea parametric rolling of a car carrier, in: Proceedings of the 9th International Ship Stability Workshop, Hamburg, Germany. pp. 30–31.

IMO SDC4/WP.4, 2017. Finalization of Second Generation Intact Stability Criteria.

Neves, M.A.S., Perez, N.A., Lorca, O.M., 2002. Experimental analysis on parametric resonance for two fishing vessels in head seas, in: 6th International Ship Stability Workshop. New York.

Neves, M.A.S., Pérez, N.A., Valerio, L., 1999. Stability of small fishing vessels in longitudinal waves. Ocean Eng. 26, 1389–1419.

Ovegård, E., Rosén, A., Palmquist, M., Huss, M., 2012. Operational Guidance with Respect to Pure Loss of Stability and Parametric Rolling, in: Proceedings of the 11th International Conference on the Stability of Ships and Ocean Vehicles (STAB2012) : pp. 655–668.

Simman2008, 2008. MOERI Container Ship (KCS) [WWW Document]. URL http://www.simman2008.dk/KCS/container.html

Spanos, D., Papanikolaou, A., 2007. Numerical simulation of parametric roll in head seas. Int. Shipbuild. Prog. 54, 249–267.

Taguchi, H., Ishida, S., Sawada, H., Minami, M., 2011. Model experiment on parametric rolling of a post-panamax containership in head waves, in: Contemporary Ideas on Ship Stability and Capsizing in Waves. Springer, pp. 277–294.

Terada, D., Hashimoto, H., Matsuda, A., "Novel Statistical Prediction on Parametric Roll Resonance by Using Onboard Monitoring Data for Officers", in: 12th Internationalconference on the Stability of Ships and Ocean Vehicles. UK, 2015, pp. 1007-1015.

Yasukawa, H., Sano, M., 2008. Maneuvering simulation of MOERI container ship, in: SIMMAN 2008. pp. 68–73.

Yu, L., Ma, N., Gu, X., 2017a. On the mitigation of surf-riding by adjusting center of buoyancy in design stage. Int. J. Nav. Archit. Ocean Eng. 9, 292–304. doi:http://dx.doi.org/10.1016/j.ijnaoe.2016.10.008

Yu, L., Ma, N., Gu, X., 2016. Early detection of parametric roll by application of the incremental real-time Hilbert-Huang Transform. Ocean Eng. 224–236.

Yu, L., Ma, N., Gu, X., 2012. Study on Parametric Roll and Its Rudder Stabilization Based on Unified Seakeeping and Maneuvering Model, in: 11th Internationalconference on the Stability of Ships and Ocean Vehicles. Greece, pp. 159–170.

Yu, L., Taguchi, K., Kenta, A., Ma, N., Yoshiaki Hirakawa, 2017b. Model experiments on the early detection and rudder stabilization of KCS parametric roll in head waves. J. Mar. Sci. Technol.

On the Parametric Resonance of the Deep Draft Semisubmersible using the Partially Non-Linear Time Domain Model

Liwei, Yu, *Shandong Provincial Key Laboratory of Ocean Engineering, Ocean University of China*, yuliwei@ouc.edu.cn

Shuqing, Wang, *Shandong Provincial Key Laboratory of Ocean Engineering, Ocean University of China*, shuqing@ouc.edu.cn

Xiancang, Song, *Ocean University of China*, songxiancang@163.com

Xiaowen, Qu, *Ocean University of China*, 1016317268@qq.com

Binzhou, Wang, *Ocean University of China*, Wbz@stu.ouc.edu.cn

ABSTRACT

The deep draft semisubmersible (DDS) is designed to improve the heave performance of the traditional semisubmersible, while maintaining its advantages. However, increasing draft may cause severe parametric resonance between pitch and heave motion under certain conditions. In the present study, a 6-DOF partially nonlinear time domain is developed to investigate the parametric resonance of a DDS platform. In the model, three methods for the calculation of restoring forces are used to investigate the importance of nonlinear restoring force on the occurrence of parametric resonance. From the simulation results, it is found that only the time domain method with fully nonlinear restoring forces is able to simulate parametric resonance of the DDS platform among the three methods for he calculation of restoring forces. Parametric resonance occurs when the wave period is half of the pitch natural period.

Keywords: *Parametric resonance; Deep draft semi-submersible; Partially nonlinear model*

1. INTRODUCTION

The semi-submersible platform are developed to maintain good stability and seakeeping performance for offshore tasks such as drilling and oil production under various sea states. In recent years, the semi-submersible with deep draft, i.e. deep draft semi-submersible (DDS), are designed to further improve the heave performance of the traditional semisubmersible for the possible installation of the economic Dry Tree system. However, with increasing draft, the heave motion can induce nonlinear variation on the pitch metacentric height. Thus, the parametric resonance between pitch and heave motion may occur under certain conditions.

Parametric resonance is a self-resonance phenomenon which can be explained by the nonlinear damping Mathieu equation. It happens on ship and offshore structures with unexpected large motion and huge loss. Parametric resonance on ships is normally referred as parametric roll. Researches on the ship parametric roll emerge after the well-

known APL-China accident (France et al., 2003). Until now, its mechanism has been well addressed through numerical simulations (Bulian, 2005; Hashimoto and Umeda, 2010; Neves et al., 1999; Spanos and Papanikolaou, 2007) and model experiments (Hashimoto et al., 2007; Neves et al., 2002; Taguchi et al., 2011). The IMO Sub-Committee on Ship Design and Construction (IMO SDC) is finalizing the multilevel second generation intact stability criteria on parametric roll (IMO SDC4/WP.4, 2017).

Parametric resonance on offshore structures is often observed on the spar platform. Haslum and Faltinsen (1999) investigated the parametric pitch motion of spar platform under large heave motion through model experiments and the Mathieu equation. Rho et al. (2003) and Rho and Choi (2002) found by model experiments that parametric resonance occurs when the pitch natural period is twice of the heave period and the heave motion is large. Koo et al. (2004) developed a numerical model incorporating riser and mooring system for the simulation of parametric resonance of the spar platform. The influence of pitch viscous damping on parametric resonance is investigated using the numerical model. Abe and Utsunomiya (2012) investigated the parametric resonance of a spar type wind turbine using Mathieu equation, and proposed design suggestions for avoiding parametric resonance.

Parametric resonance also happens on semi-submersibles, especially the DDS platform. Mao and Yang (2016) used the damping Mathieu equation to simulate the parametric resonance of a DDS platform. The governing factors for parametric resonance were identified. Wei et al. (2016) reproduced the parametric resonance of a semi-submersible in regular and irregular waves through both numerical simulation and model experiment.

In order to improve the design of DDS platform for the avoidance of parametric resonance, a 6-DOF partially nonlinear numerical model considering only the nonlinearity of restoring forces using pressure integration over instantaneous wetted surfaces are developed. The parametric resonance of a prototype DDS platform in various regular heading waves are simulated using the proposed model.

2. PARTIALLY NONLINEAR NUMERICAL MODEL

2.1 Coordinate System

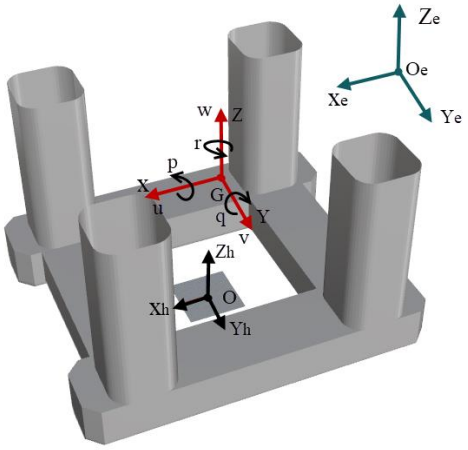

Figure 1 Definition of coordinate system and ship motions

In the model, three coordinate systems, the earth fixed coordinate O_e-$X_eY_eZ_e$, the body fixed coordinate G-XYZ and the horizontal body axes coordinate O-$X_hY_hZ_h$ are used as shown in Figure 1. The O-$X_hY_hZ_h$ coordinate moves with the ship with the x axe pointing from ship stern to stem, the y axe pointing from starboard to port, the z axe pointing upwards. The origin O is chosen at the bottom of the ship. The displacement and velocity vectors are defined as:

$$\boldsymbol{\eta} = [x, y, z, \phi, \theta, \psi]^T$$
$$\boldsymbol{\nu} = [u, v, w, p, q, r]^T \quad (1)$$

2.2 Seakeeping Model

The 6-DOF seakeeping model is defined in the horizontal body axes coordinate O_h-$X_hY_hZ_h$. The model is based on the Impulse

Response Function (IRF) approach. The equation of motion can be written as:

$$m_i\dot{v}_i(t)+F_i^{rad}(t)+F_i^{res}(t)+\left(B_{vi}v_i,\text{for } i=3,4,5\right) = F_i^{ext}(t) \quad (i=1,...,6) \tag{2}$$

According to the IRF approach, the linear radiation and wave excitation forces (F-K and diffraction force) are calculated in the frequency domain by the 3D boundary element method and transferred into time domain using the retardation function $R_{ij}(\tau)$ and $Q_i(\tau)$.

$$F_i^{rad}(t)=\sum_{j=1}^{6}\left[\begin{array}{l}\mu_{ij}(\infty)\dot{v}_j(t)+C_{ij}\eta_j(t)\\+\int_0^t R_{ij}(t-\tau)v_j(\tau)d\tau\end{array}\right] \tag{3}$$

$$F_i^{ext}(t)=\int_{-\infty}^{t}Q_i(t-\tau)\alpha(\tau)d\tau$$

Where $\alpha(\tau)$ is the wave elevation, the retardation functions R_{ij} and Q_i are calculated as:

$$\begin{aligned}R_{ij}(t)&=\frac{2}{\pi}\int_0^\infty\lambda_{ij}(\omega_e)\cos(\omega_e t)d\omega_e\\&=-\frac{2}{\pi}\int_0^\infty\omega_e\left[\mu_{ij}(\omega_e)-\mu_{ij}(\infty)\right]\sin(\omega_e t)d\omega_e\end{aligned} \tag{4}$$

$$Q_i(t)=\frac{1}{\pi}\int_0^\infty\left[d_i^R(\omega_e)\cos(\omega_e t)-d_i^I(\omega_e)\sin(\omega_e t)\right]d\omega_e$$

$$C_{ij}=\omega_e{}^2\left[\mu_{ij}(\infty)-\mu_{ij}(\omega_e)\right]-\omega_e\int_0^\infty R_{ij}(\tau)\sin(\omega_e\tau)d\tau$$

The added mass μ_{ij}, infinite-frequency added mass $\mu_{ij}(\infty)$, damping coefficient λ_{ij}, the real and maginary part of diffraction forces d_i^R , d_i^I in the frequency domain are calculated by the boundary element method. B_{vi} stands for the viscous damping coefficient of heave, roll and pitch.

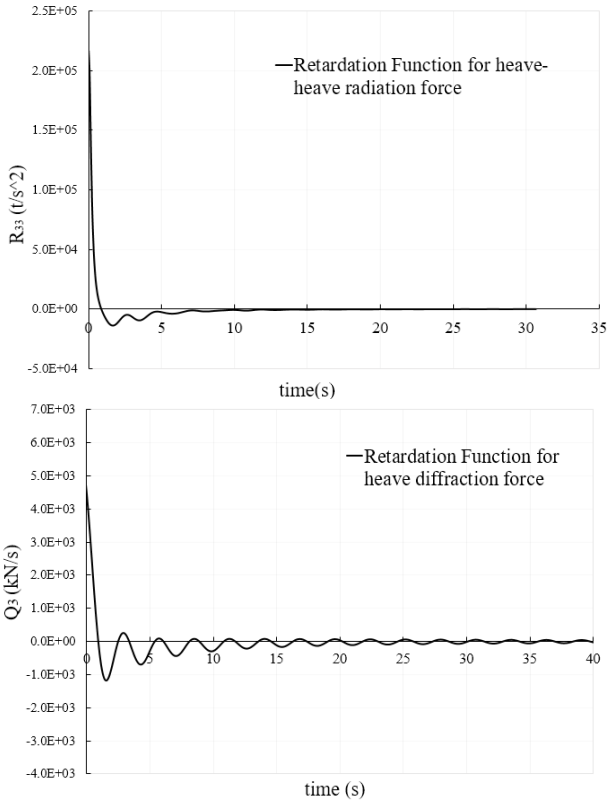

Figure 2 Retardation functions for heave-heave radiation force and heave diffraction force

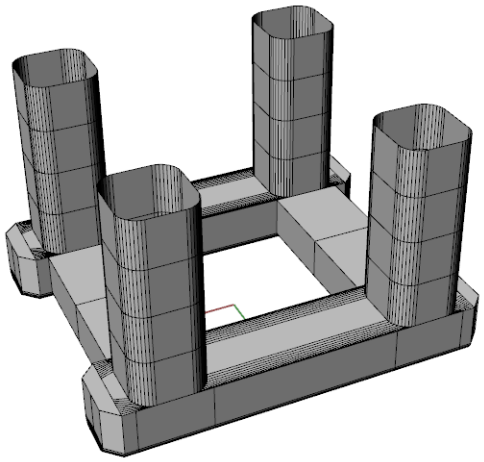

Figure 3 Hull NURBS surfaces of the DDS platform

2.3 Nonlinear Restoring Forces

The nonlinear restoring forces are calculated through pressure integration on the instantaneous wetted surfaces(Yu et al., 2017). During the calculation, the hull and upper deck consist of several Non-Uniform Rational B-Splines (NURBS) surfaces as demonstrated in Figure 3. Each surface has an area of A_i, a

central point $\boldsymbol{r}_i=(x_i,y_i,z_i)$ with a normal vector $\boldsymbol{n}_i=(n_{1i},n_{2i},n_{3i})$ in body-fixed axis. The restoring and Froude-Krylov forces are calculated as:

$$\begin{aligned} F_j^{res} &= \sum_{i=1}^{N^*} A_i P_{res}(\boldsymbol{r}_i) n_{ji}^h - mg\cos\theta\cos\phi \quad (j=3) \\ F_j^{res} &= \sum_{i=1}^{N^*} A_i P_{res}(\boldsymbol{r}_i) n_{ji}^h \times (r_G - \boldsymbol{r}_i^h) \quad (j=4,5) \end{aligned} \tag{5}$$

Where the restoring pressure $P_{res}(r_i^h)$ are given by:

$$P_{res}(\boldsymbol{r}_i) = \rho g(d(x_i^e,t) - z_i^e) \tag{6}$$

Where the instantaneous draft $d(x_i,t)$ is calculated as:

$$\begin{aligned} d(x_i^e,t) &= d_0 + \alpha(t) \\ &= d_0 + A_w \cos\left(\omega_e t - k(x_i^e\cos\chi + y_i^e\sin\chi)\right) \end{aligned} \tag{7}$$

Superscript (h) and (e) indicates vectors in the horizontal body axes coordinate O-$X_hY_hZ_h$ and the earth-fixed coordinate O_e-$X_eY_eZ_e$. The relationships between the three coordinates are defined as Eq.(8).

$$\begin{aligned} \boldsymbol{r}_i^h &= \Re_{3\times3}\boldsymbol{r}_i \\ \Re_{3\times3} &= \begin{bmatrix} \cos\theta & \sin\theta\sin\phi & \sin\theta\cos\phi \\ 0 & \cos\phi & -\sin\phi \\ -\sin\theta & \cos\theta\sin\phi & \cos\theta\cos\phi \end{bmatrix} \end{aligned} \tag{8}$$

$$\begin{aligned} \boldsymbol{r}_i^e &= \aleph_{3\times3}\boldsymbol{r}_i^h \\ \aleph_{3\times3} &= \begin{bmatrix} \cos\psi & -\sin\psi & 0 \\ \sin\psi & \cos\psi & 0 \\ 0 & 0 & 1 \end{bmatrix} \end{aligned}$$

Because the dynamics of mooring lines are not considered in the numerical model, the concept of soft spring is adopted for the surge, sway and yaw motion to prevent the unstable monotonously changing motion. The spring stiffness can be calculated as follows:

$$C_{ii} = \left(m_i + \mu_{ii}(\infty)\right) \times \left(\frac{2\pi}{T_i}\right)^2, i = 1,2,6 \tag{9}$$

Where T_i is the artificial natural period.

3. CALCULATION CASES

In the numerical simulation of parametric resonance, a DDS platform prototype in model scale is chosen. Its main particulars are demonstrated in Table 1.

During the numerical simulation, the calculation cases in the regular wave with different wave frequencies are chosen. The wave circular frequencies are set from 0.2~4 rad/s. The wave heading and wave amplitude is 180 degrees and 0.02m respectively. The viscous damping of heave, roll and pitch (B_{v3}, B_{v4}, B_{v5}) are chosen empirically as 15%, 4% and 6% of the critical damping according to the data of a similar semi-submersible. The artificial natural periods of surge, sway and yaw (T_1, T_2, T_6) are set as 100, 100, 120s.

Table 1 Main particulars of the DDS platform

Item	*Unit*	*Model*
Length(L_{pp})	m	0.820
Breadth(B)	m	0.712
Draft(d)	m	0.360
Displacement(∇)	m^3	0.06572
K_{xx}	m	0.307
K_{yy}	m	0.329
K_{zz}	m	0.329
Center of Gravity(OG)	m	0.200
Long. metacentric height(GML)	m	0.045
Trans. metacentric height(GMB)	m	0.036
Waterline area(A_w)	m^2	0.1010
Heave natural period wetted(T_{heave})	s	2.3
Roll natural period wetted(T_{roll})	s	4.0
Pitch natural period wetted(T_{pitch})	s	3.8

4. SIMULATION RESULTS

Regarding the nonlinearity of restoring forces, the simulations in the time domain are conducted with the following three different numerical methods:

a) Linear restoring forces;

The restoring forces and moments in time domain are calculated linearly, which is the same with the frequency domain.

b) Body exact nonlinear restoring forces;

The restoring forces and moments in time domain are calculated using pressure integration over instantaneous wetted surface considering only the 6-DOF body motion, while ignoring the nonlinearity caused by the wave elevation. Therefore, the wave elevation $\alpha(\tau)$ in Eq.(7) is set to 0 during the calculation.

c) Fully nonlinear restoring forces

The restoring forces and moments in time domain are calculated using pressure integration over instantaneous wetted surface considering both the 6-DOF body motion and the wave elevation as shown in Eq.(7).

Through these three methods, the importance of nonlinear restoring forces on the simulation of DDS parametric resonance can be investigated. The heave and pitch RAOs calculated by the numerical models with linear, body exact and fully nonlinear restoring forces are presented in figure 4 and 5. In the figures, the RAOs calculated in the frequency domain using the 3D boundary element method are also presented.

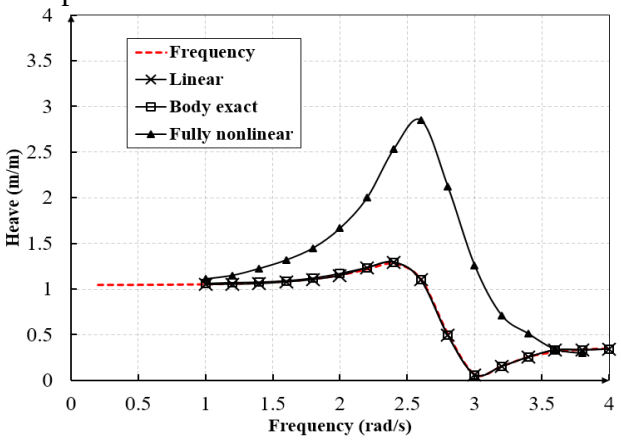

Figure 4 Heave RAOs of the DDS platform using different methods

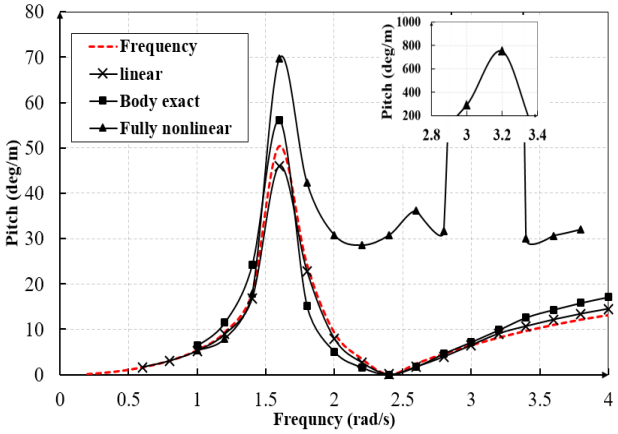

Figure 5 Pitch RAOs of the DDS platform using different methods

From the figures, it can be found that heave and pitch RAOs calculated by the frequency domain method and the time domain method with linear restoring forces are almost the same. Therefore, the linear time domain model proposed in this research is verified. The RAOs calculated by the time domain method with body exact nonlinear restoring forces also agree quite well with the results of the frequency domain method. This is mainly because the ship motion amplitudes are relatively small under 0.02m wave amplitude. The nonlinearity of restoring forces caused by body exact pressure integration is small.

However, the heave and pitch RAOs calculated by the time domain method with fully nonlinear restoring forces differ significantly with the results of other methods, especially at the frequency range 1.5~3.5 rad/s. Moreover, the phenomenon of parametric resonance is observed when circular frequency equals to 3.0 and 3.2 rad/s. In figure 5, the pitch motion RAO grows very large at 3.0 and 3.2 rad/s. The heave and pitch time histories under 3.0 and 3.2 rad/s are plotted in figure 7 and 8. According to the two figures, the period of pitch becomes twice of the period of heave and the pitch amplitudes grows very large, which indicates that parametric resonance of heave and pitch motion occurs.

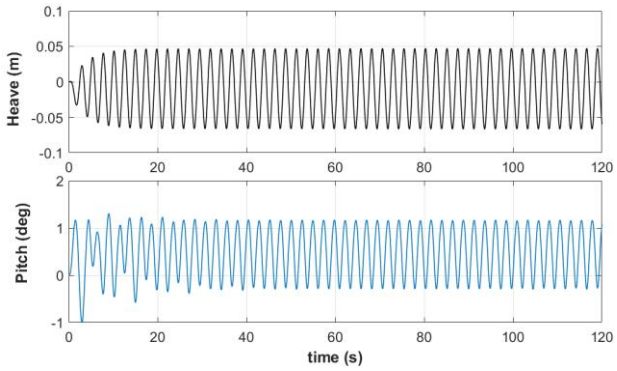

Figure 6 Heave and pitch time histories at 2.6 rad/s

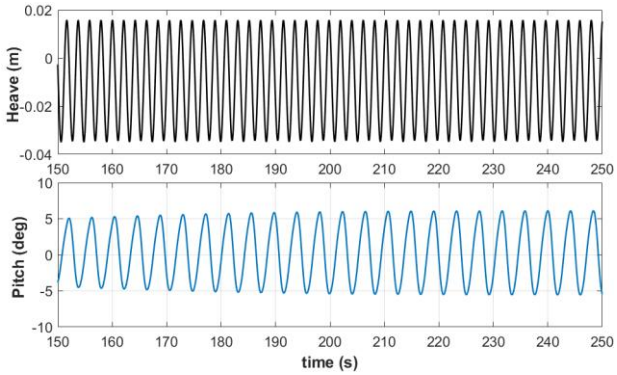

Figure 7 Heave and pitch time histories at 3.0 rad/s

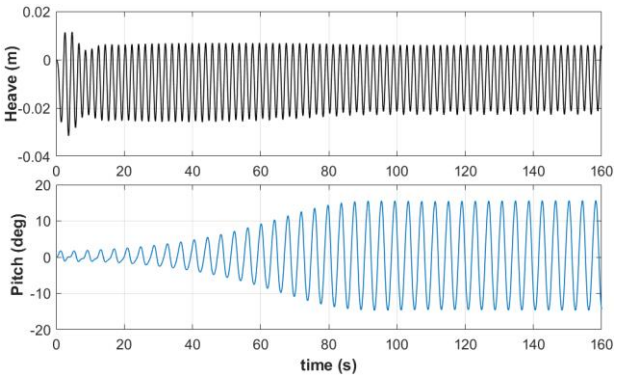

Figure 8 Heave and pitch time histories at 3.2 rad/s

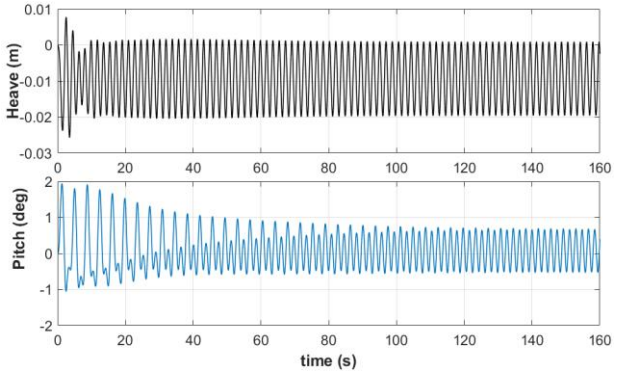

Figure 9 Heave and pitch time histories at 3.4 rad/s

Furthermore, it is found that the wave periods under 3.0 and 3.2 rad/s are 2.10s and 1.96s which are close to the half of the pitch natural period, 3.8s. This conclusion agrees with the mechanism of parametric resonance which generally occurs when the wave period is half of the pitch natural period. When the wave period is away from half of the pitch natural period, the phenomenon of parametric resonance disappears and the pitch amplitudes get small as shown in figure 6 and 9 under 2.6 and 3.4 rad/s.

5. MODEL EXPERIMENTS

The model experiments on the parametric resonance of the deep draft semisubmersible (DDS) are conducted in the wave flume (30m×1.0m×1.2m) of the Ocean University of China (OUC). The flap type wave generator is install at the end of the wave flume.

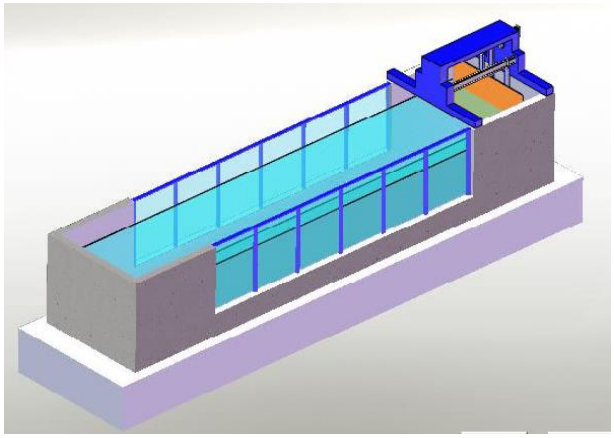

Figure 10 Wave flume in OUC

Figure 11 Model of the DDS platform

The main particulars of the DDS model are shown in Table 1. A gyroscope is fitted on the model for the measurement of pitch angle and heave acceleration. The generated wave is measured by the wave height gauge. The experiment cases in the regular wave with different wave periods are chosen. The wave periods are set from 1~3s. The wave heading and wave amplitude is 180 degrees and 0.04m respectively.

The pitch RAO are plotted in Figure 12. It can be found from the figure that the pitch amplitudes get very large when the frequency is around 2.4 rad/s (i.e. wave period 2.6s). This indicates the occurrence of the parametric resonance. The time history of the pitch angle when the wave period is 2.6s is shown in Figure 13. It is found that parametric resonance occurs after t=70s. After t=70s, the pitch period is twice of the wave period and pitch amplitude gets very large.

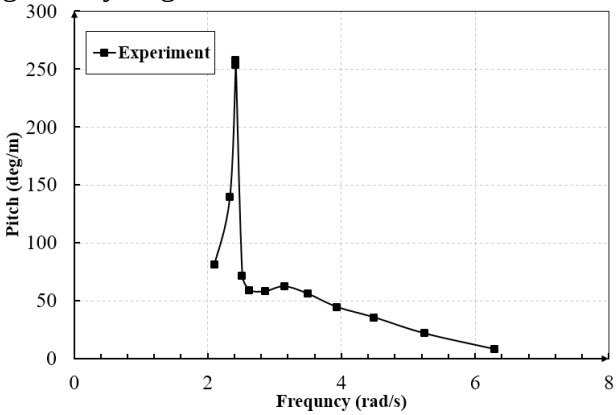

Figure 12 Pitch RAO of the model experiment

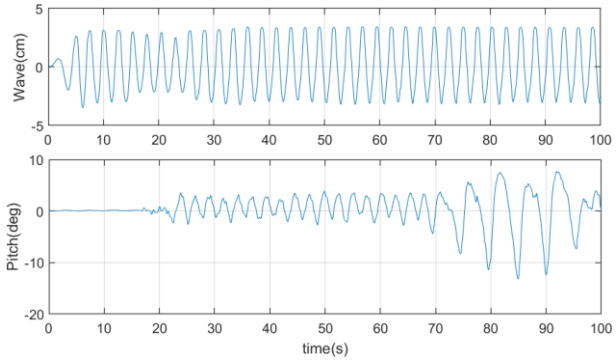

Figure 13 Pitch RAO of the model experiment

6. CONCLUSIONS

In this research, the parametric resonance of the deep draft semisubmersible (DDS) is investigated using the proposed partially nonlinear time domain model. Numerical simulation under various wave frequencies are conduct. Three methods for the calculation of restoring forces are used to investigate the importance of nonlinear restoring force on the occurrence of parametric resonance. The following conclusions are drawn.

Among the three methods for the calculation of restoring forces, only the time domain method with fully nonlinear restoring forces is able to simulate parametric resonance of the DDS platform.

For the DDS platform, parametric resonance occurs when the wave period is half of the pitch natural period.

Model experiments on the parametric resonance of the DDS platform are conducted. Parametric resonance is observed in the model experiment.

Further verification of the numerical model based on the model experiment results will be conducted in the future.

7. ACKNOWLEDMENTS

The authors acknowledge the support by the Natural Science Foundation of Shandong Province (ZR2018BEE049), the National Key R&D Program of China (2016YFE0200100), the Fundamental Research Funds for the Central Universities (841713045).

8. REFERENCES

Abe, K., Utsunomiya, T., 2012. Study on Parametric Excitation of a Spar Platform. J. Appl. Mech. 68, I_813-I_822.

Bulian, G., 2005. Nonlinear parametric rolling in regular waves—a general procedure for the analytical approximation of the GZ curve and its use in time domain simulations. Ocean Eng. 32, 309–330.

France, W.N., Levadou, M., Treakle, T.W., Paulling, J.R., Michel, R.K., Moore, C., 2003. An investigation of head-sea parametric rolling and its influence on container lashing systems. Mar. Technol. 40, 1–19.

Hashimoto, H., Umeda, N., 2010. A study on Quantitative Prediction of Parametric Roll in Regular Waves, in: 11th International Ship Stability Workshop. Wageningen, Netherlands, pp. 295–301.

Hashimoto, H., Umeda, N., Sakamoto, G., 2007. Head-sea parametric rolling of a car carrier, in: Proceedings of the 9th International Ship Stability Workshop, Hamburg, Germany. pp. 30–31.

Haslum, H., Faltinsen, O., 1999. Alternative Shape of Spar Platforms for Use in Hostile Areas, in: Offshore Technology Conference.

IMO SDC4/WP.4, 2017. Finalization of Second Generation Intact Stability Criteria.

Koo, B.J., Kim, M.H., Randall, R.E., 2004. Mathieu instability of a spar platform with mooring and risers. Ocean Eng. 31, 2175–2208.

Mao, Y., Yang, H., 2016. Study on parametric resonance of a deep draft semi-submersible platform. Ocean Eng. 34, 18–24.

Neves, M.A.S., Perez, N.A., Lorca, O.M., 2002.Experimental analysis on parametric resonance for two fishing vessels in head seas, in: 6th International Ship Stability Workshop. New York.

Neves, M.A.S., Pérez, N.A., Valerio, L., 1999. Stability of small fishing vessels in longitudinal waves. Ocean Eng. 26, 1389–1419.

Rho, J.B., Choi, H.S., 2002. Heave and Pitch Motions of a Spar Platform with Damping Plate, in: Proceedings of The Twelfth (2002) International Offshore and Polar Engineering Conference. pp. 198–201.

Rho, J.B., Hang, S.C., Shin, H.S., Park, I.K., 2003. An Experimental Study for Mooring Effects on the Stability of Spar Platform.

Spanos, D., Papanikolaou, A., 2007. Numerical simulation of parametric roll in head seas. Int. Shipbuild. Prog. 54, 249–267.

Taguchi, H., Ishida, S., Sawada, H., Minami, M., 2011. Model experiment on parametric rolling of a post-panamax containership in head waves, in: Contemporary Ideas on Ship Stability and Capsizing in Waves. Springer, pp. 277–294.

Wei, H., Xiao, L., Tian, X.B.T.-T.I.O. and P.E.C., 2016. Nonlinear Coupling of Heave and Pitch for a Semi-submersible Platform with Bracings.

Yu, L., Ma, N., Gu, X., 2017. On the mitigation of surf-riding by adjusting center of buoyancy in design stage. Int. J. Nav. Archit. Ocean Eng. 9, 292–304.

The statistical analysis of the parametric rolling for C11 containership in the irregular wave experiment

Shan Ma, *Harbin engineering university* mashan01@ hrbeu.edu.cn

Wenhao Xu, *Harbin engineering university* xwhao@hrbeu.edu.cn

Qiang He, *Harbin engineering university* heqiang@hrbeu.edu.cn

Wenyang Duan, *Harbin engineering university* duanwenyang@hrbeu.edu.cn

ABSTRACT

The parametric excited rolling is a nonlinear ship motions phenomenon, which happens in special sea conditions. Previous studies have shown that statistical characteristics of the parametric rolling in random seas is quite non-ergodic. The motion responses highly depend on the incident wave realizations or the wave group effects. Even though for given sea states, the statistical value like standard deviation, maximum value under different random wave realizations could be quite scattered.

In order to have a more understanding of the motion characteristics of the parametric rolling motion in random seas, the experiments of the parametric rolling for C11 containership are conducted by a free running ship model at the towing tank basin of CSSRC. At each forward speed, the experiments are conducted at certain sea states. In order to study the statistics of the parametric rolling at instant sea states, the experiments have been tested under multiple runs in random head sea. During the experiments, the significant parametric rolling is found especially at zero forward speed.

Based on the experimental measurement, the statistical characteristics of the motion responses including the pitch, parametric rolling are studied in this paper.

According to the statistical analysis, the statistical quantity like the standard deviation, the estimated probability density functions (PDFs), the estimated cumulative distribution functions (CDFs), the single significant amplitude (SSA) with 95% confidence bands for the parametric rolling from independent runs of different random wave realizations are presented in head seas. Furthermore, the statistical quantities from the ensemble of multiple random realizations of the parametric rolling are studied. The influences of the number of the time history records on these statistical values are investigated.

Based on the above experimental study, the particular statistical feature for parametric rolling is deeply investigated.

Keywords: *Parametric rolling; random seas; experiments; statistical analysis*

1. INTRODUCTION

The ship parametric rolling can lead to large amplitude roll angles, which could happen after encountering several successive waves when the encounter wave period is about one half of the natural roll period for the ships. The parametric rolling phenomenon was first found

in the model test. Because of its sensitivity and reliability, the experimental measurement is widely used in the study of parametric rolling in random waves. Bulian et al. (2004) found that the parametric rolling in random waves rapidly increases and is more dangerous via the model test. At the same time, it was also pointed out that the forward speed has a great influence on standard deviation of roll motion. Taguchi et al. (2007) found that the maximum roll amplitude of the parametric rolling increases with the increase of the significant wave height and the head-sea parametric rolling is the most dangerous state. Bulian et al. (2006) discussed the problem of ergodicity of stochastic processes and showed that temporal averages can be associated to very large coefficients of variation, even if they are a theoretically correct tool for the estimation of ensemble averages. They proved that the process in itself is ergodic, but in the tested conditions the parametric rolling should be considered as 'practically not ergodic'. For a small confidence interval for temporal averages, it needs a very long run length. Bulian et al. (2008) studied the influence of the initial conditions and found that the uncertainty in the statistical estimation from the time history of rolling motion can be significantly larger than those for pitch motion and incident wave. Schumacher et al. (2016) found that the roll amplitude is highly dependent on the time and space position of random waves. Lu et al. (2016) performed the parametric model test for C11 containership in head regular waves, where the free running model experiments, partially restrained model experiments with and without surge motions were conducted. Via the model test and numerical simulations, several elements required for numerical modelling of the parametric rolling in head waves were investigated.

In the past years, there are many publications and discussions on the statistical analysis for the parametric rolling. Belenky et al. (2003) discussed the probabilistic analysis of parametric roll response in irregular head seas using numerical simulation. The authors demonstrate that the roll motions are evidently non-ergodic and do not have a normal distribution, which is different with the large amplitude pitch and heave motions. The ITTC Expert Committee on Stability in Waves (2011) conducted a benchmark of numerical simulation methods for the prediction of the parametric rolling in heads seas. Via the benchmark study, it was found that there is evident difference in the variance of the various records, the physical reason is analysed and the numerical convergence for the variance of the ensemble is provided as a function of the number of the records. Park et al. (2013) performed the numerical simulation of parametric roll for two containerships using two different time domain potential flow methods. The authors discussed the sensitivity of the computation results to some parameters that can affect the analysis. Belenky et al. (2013) revisits the derivation of the formula for the variance of the variance of a stationary stochastic process. The authors showed that the assumption of the Gaussian distribution of the process is not necessary if one can estimate a covariance function of the centered squares of the process. Belenky et al. (2015) proposes the mathematical methods to compute the mean, variance of the mean, the variance of the variance estimate from the records of the nonlinear ship motions with the purpose of quantifying the statistical uncertainty of the estimate.

In this paper, the statistical analysis of the parametric rolling for C11 containership is conducted through experiments in irregular head seas. Presently the direct evidence and detailed investigation about the statistical analysis of the parametric rolling based only on experiment is insufficient. Based on our recent study, the physical experiments for parametric rolling in multiple independent random wave realization are studied, the quantitative results are provided, which provides the physical insight to understand this highly nonlinear phenomena.

2. MODEL TEST INFORMATION

2.1 The Introduction of the ship model

The ship model of C11 containership was manufactured on a scale 1:65.5, and its principal particulars are presented in Table 1.

Table 1 Main particular of the C11 containership

Principal particular	data
Length between perpendiculars, L_{PP} (m)	262.00
Breadth, B (m)	40.00
Depth, d (m)	24.45
Mean draught, D (m)	11.80
Block coefficient, C_b	0.566
Displacement, ∇(m^3)	69957.96
vertical center of gravity, KG (m)	18.436
Longitudinal center of gravity relative to amidship (m)	5.7681
Metacentric height (GM/m)	1.90
Radius of gyration, roll, K_{xx}	0.38B
Radius of gyration, pitch, K_{yy}	0.24L_{PP}
Natural roll period, T/s	24.5

2.2 The measurements in the experiment

In the experiment, the random wave spectrum is modelled using the ITTC two-parameter spectrum with the significant wave height of 7.5 m and the spectral peak period of 14.4 s. The experiments are conducted at 0 knots, 5 knots, and 10 knots respectively according to the full scale ranges. At each forward speed case, the parametric rolling experiments are performed under multiple random wave realizations to study the statistical characteristics of parametrically excited rolling motion. Presently, the statistical analysis is focused on the zero speed case in head seas, the following Tab. 2 shows the measurement duration time under the ten different random wave realizations in the experiments.

Table 2 The measurement duration under ten different random wave realizations (Fn=0.0)

Random wave Record #	measurement time duration in Model scale (s)	measurement time duration in Full scale (s)
Record 1	613.12	4962.12
Record 2	614.52	4973.44
Record 3	519.46	4204.10
Record 4	659.36	5336.34
Record 5	646.18	5229.67
Record 6	570.82	4619.76
Record 7	631.08	5107.46
Record 8	614.82	4975.87
Record 9	624.60	5055.02
Record 10	633.18	5124.46

In the experiment, the free running model is used, where the ship model is propelled by a propeller and the automatic rudder is used to control the heading of the ship. In the experiment, the typical parametric rolling scenario is shown in Fig. 1. It is seen that the phenomenon of ship's parametric rolling is obvious.

Fig. 1. (a) The parametric motion of the model at one time moment

Fig. 1. (b) The parametric motion of the model

at the other time moment

Fig. 1 The typical parametric rolling motion in irregular wave at zero forward speed

3. WAVE SPECTRUM ANALYSIS

One of the most direct causes of parametric rolling is related to the properties of the encountered wave. In the following Figs. 2-4, the wave spectrum of the selected three random wave realizations are analysed and compared with the target wave spectrum.

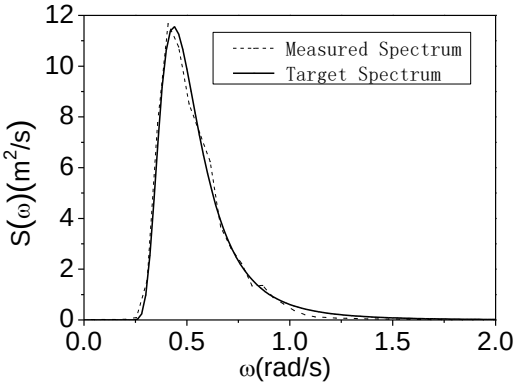

Fig. 2 The comparison of the wave spectrum from measured wave for No. 1 random wave realization with the target wave spectrum

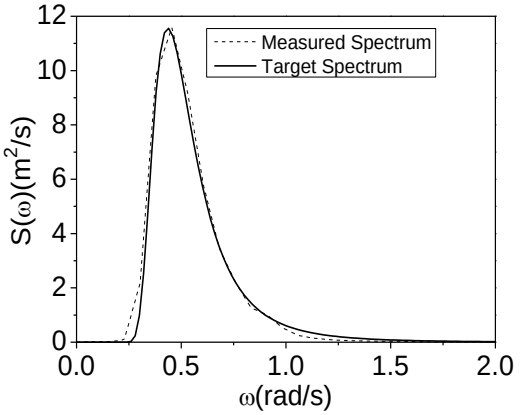

Fig. 3 The comparison of the wave spectrum from measured wave for No. 2 random wave realization with the target wave spectrum

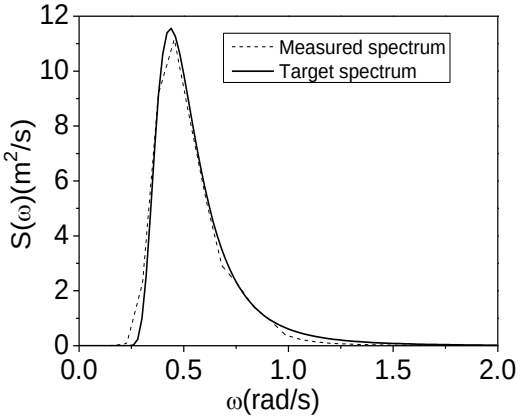

Fig. 4 The comparison of the wave spectrum from measured wave for No. 3 random wave realization with the target wave spectrum

It can be seen that the spectral density of the encountered wave in the experiment has a good repeatability with the target spectrum. The good quality of the wave generaton is garuanted.

4. THE STATISTICAL ANALYSIS OF THE PARAMETRIC ROLLING

Fig. 5 shows the comparisons of the time history of the incoming waves, pitch motion and roll motion under three different random wave realization at the zero forward speed. It is seen that the incoming wave signal and the pitch motions among different random waves have similar time variation characteristics, while the parametric roll motions shows obvious different amplitude variation characteristics under different random wave realization.

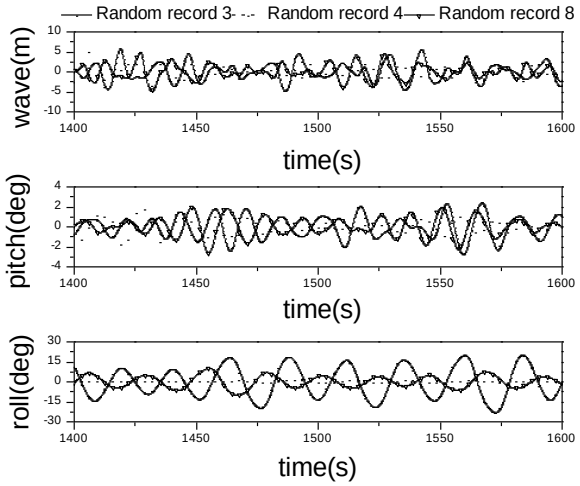

Fig. 5 The comparison of the incoming waves, pitch and roll motions under three random wave realizations.

In order to further investigate the difference quantitatively, the maximum amplitudes of the roll motion from different random wave realizations are given in Fig. 6. It's seen that the difference of the maximum amplitudes of the different random wave realizations are significant, there is a difference of 15.59^o between the largest and the smallest parametric rolling amplitude among different measurement runs, which shows that the parametric rolling in different wave realizations have strong uncertainty even though in the same sea state.

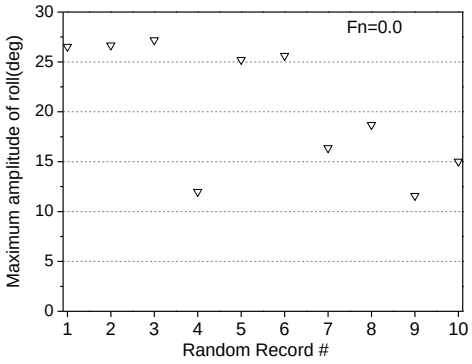

Fig. 6 The measured maximum amplitude of roll angles from 10 independent wave realizations runs in head seas

4.1 Gaussian Examination

The Kurtosis coefficient is an important parameter to measure the random variables, which is used to describe the shape characteristics of random variable probability distribution. If the kurtosis coefficient of the statistical distribution of random signals is about 3, it is a sufficient condition that the estimated probability distribution belongs to the Gaussian distribution. The greater the kurtosis coefficient, the higher the probability of the fluctuations for the random data.

The average and standard deviation of roll motion can be written as follows:

$$\bar{\phi} = \frac{1}{N}\sum_{i=1}^{N}\phi_i \tag{1}$$

$$S = \sqrt{\frac{1}{N-1}\sum_{i=1}^{N}(\phi_i - \overline{\phi_m})^2} \tag{2}$$

Where N is the total number of the sample points in the whole time series of the roll motion signal. The Kurtosis coefficient can be written as follows:

$$g_1 = \frac{\sum_{i=1}^{N}(\phi_i - \overline{\phi_m})^4}{N \bullet S^4} \tag{3}$$

The kurtosis coefficients of the parametric roll motion from 10 different random records at zero forward speed are shown in Fig. 7.

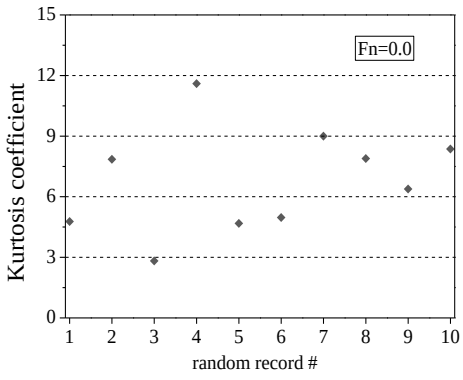

Fig. 7 Kurtosis coefficient of parametric roll

As can be seen from Fig. 7, the kurtosis coefficient obtained from the random parametric roll motion of different random

waves looks quite scattered and most of the kurtosis coefficient are larger than 3. Thus, it can be preliminarily analysed that there is a large fluctuation for the probability distribution of the parametric roll motion compared to the normal distribution relative to the random Gaussian process.

4.2 Probability Distribution Analysis

In the above analysis, it is seen that the parametric rolling from different random records deviates from the normal distribution based on the estimation of the kurtosis coefficient. In order to further investigate the statistical property of the ship motions in random seas, the probability density histograms of the typical motions signals are analysed and compared with the corresponding normal distribution density functions.

The following measured signals are investigated:

(1) the incoming wave elevation at the servo probe (positive for wave crest);

(2) the pitch motion (positive for bow down);

(3) the roll motion (positive when heeling to starboard).

The normalized probability density function (PDF) can be written as follows:

$$f(x)=\frac{1}{\sqrt{2\pi}\sigma}e^{-\frac{1}{2}(\frac{x-\mu}{\sigma})^2} \quad (4)$$

where μ is the mean value and σ is the standard deviation of the random process.

The histograms in the Figs. 8-10 are the probability density distribution histograms estimated from the measured records of waves, pitch motion and roll motion, while the solid line is the theoretical normal distribution probability density function estimated based on the standard deviation and the mean value of the time histories according to Eqs. (1), (2) and (4). In Fig. 8, the probability density of wave, pitch and roll motions under the wave conditions of one single random record are provided. In Fig. 9 and Fig. 10, the probability density of wave, pitch and roll motions from the ensemble of five and ten records are provided respectively.

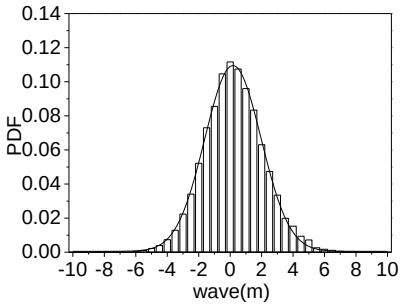

Fig. 8. (a) the estimated PDF for the incident wave

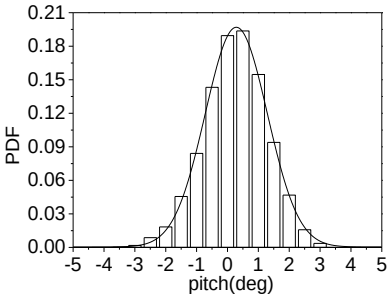

Fig. 8. (b) the estimated PDF for the pitch motion

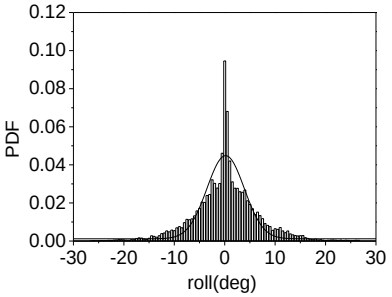

Fig. 8. (c) the estimated PDF for the roll motion

Fig. 8 the PDFs of wave, pitch and roll motions from one random record

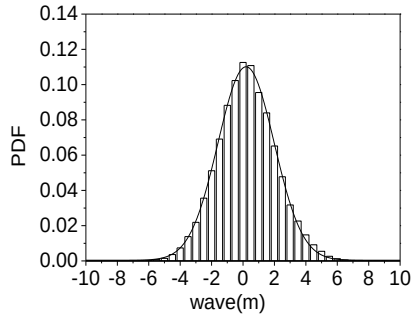

Fig. 9. (a) the estimated PDF for the incident wave

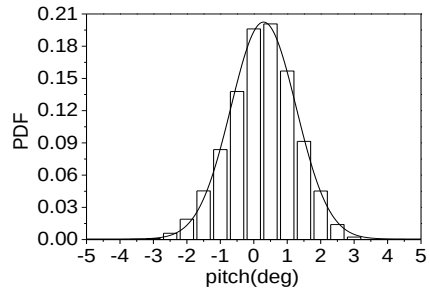

Fig. 9. (b) the estimated PDF for the pitch motion

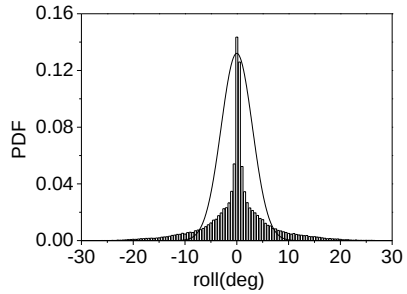

Fig. 9. (c) the estimated PDF for the roll motion

Fig. 9 the PDFs of wave, pitch and roll motions from the ensemble of five separate random records

It can be seen that regardless of the cumulative number of the random records, the probability densities of wave and pitch motions follows the normal distribution, while that of the roll motion is not. With the increase of the statistical time for the roll motions, the probability density of roll motion close to zero degree is close to the normal distribution, while the probability density of the roll motions, which is in the range of 0^o and 8^o, is in general smaller than the probability density of the normal distribution. It is also interesting to find that the probability density of the roll motions, which is larger than about 8^o, is larger than the probability density of the normal distribution. This means that the probability of large amplitude parametric roll motion is larger when the ships experience parametric rolling. In other words, ships tend to experience larger amplitude parametric roll for a longer period. Besides, it is also observed that there is evident quantitative difference for the estimated PDF of the parametric rolling from the ensemble of the random records with different length.

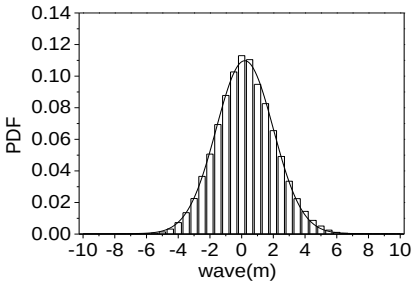

Fig. 10. (a) the estimated PDF for the incident wave

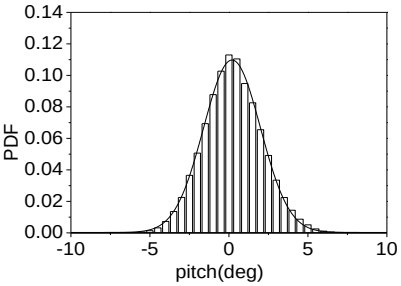

Fig. 10. (b) the estimated PDF for the pitch motion

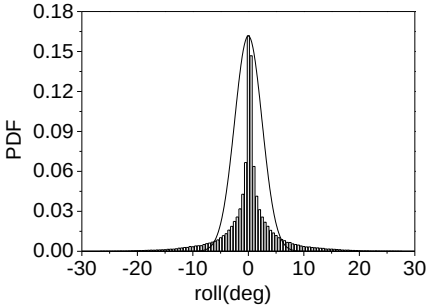

Fig. 10. (c) the estimated PDF for the roll

motion

Fig. 10 the PDFs of wave, pitch and roll motions from the ensemble of ten separate random records

Besides the probablity density statistics for the time history of the ship motions, the statistical property of the sampled peak/trough values from the successive measured random signal are often used to study the extreme value of the ship motion in severe sea state. In the traditional ship seakeeping analysis, the Rayleigh distribution curve is often used to approximate the probability density function of the peak/trough values fo the ship motions in waves, which is shown in the following Eq. (5):

$$f(x) = \frac{x}{\sigma^2} e^{-\frac{x^2}{2\sigma^2}} \qquad (5)$$

where σ is the standard deviation of the random process.

Figs 11-13 present the estimated cumulative distribution functions (CDFs) of the peak and trough values of waves, roll, and pitch under one single random wave run and the ensemble of five and ten random wave runs respectively. The theoretical probability distribution obtained by the integration of Eq. (5) is also given, which is shown as "Rayleigh distribution".

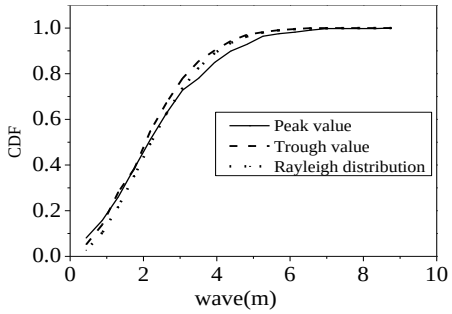

Fig. 11. (a) The estimated CDF of peak/trough values for the incident wave

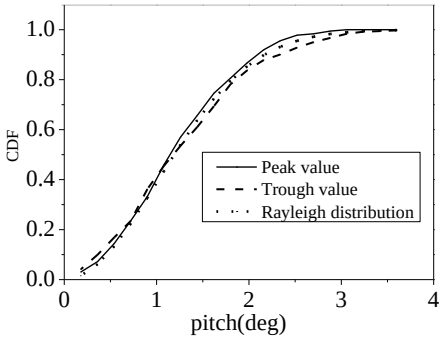

Fig. 11. (b) The estimated CDF of peak/trough values for pitch

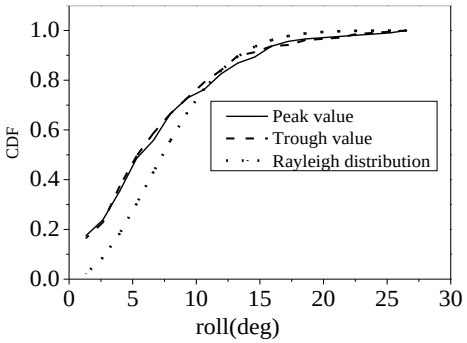

Fig. 11. (c) The estimated CDF of peak/trough values for roll

Fig. 11 The estimated CDFs of peak/trough values of wave, roll and pitch motions from one random record

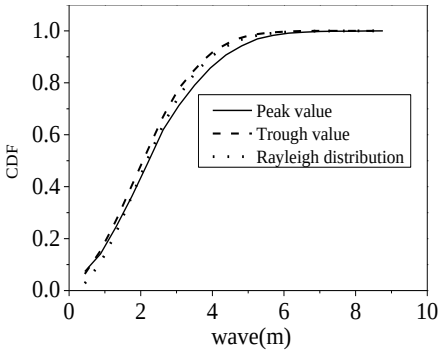

Fig. 12. (a) The estimated CDF of peak/trough values for the incident wave

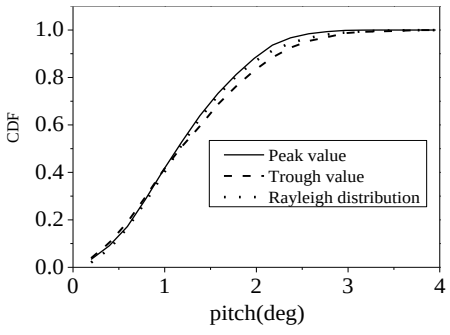

Fig. 12. (b) The estimated CDF of

peak/trough values for the pitch motion

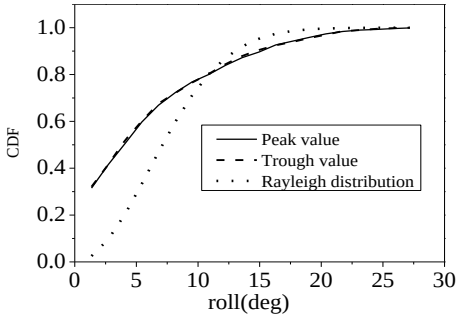

Fig. 12. (c) The estimated CDF of peak/trough values for the roll motion

Fig. 12 The estimated CDFs of peak/trough values of wave, roll and pitch motions from the ensemble of five separate random records

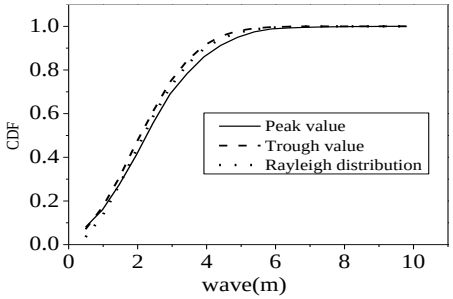

Fig. 13. (a) The estimated CDF of peak/trough values for the incident wave

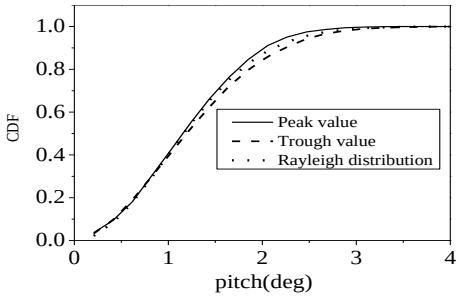

Fig. 13. (b) The estimated CDF of peak/trough values for the pitch motion

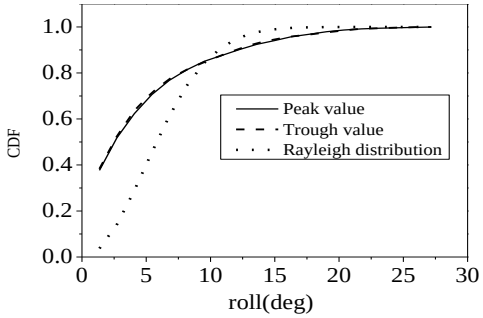

Fig. 13. (c) The estimated CDF of peak/trough values for the roll motion

Fig. 13 The estimated CDFs of peak/trough values of wave, roll and pitch motions from the ensemble of ten separate random records

It can be seen from Fig. 11 that the probability distributions of the peak and trough value for the respective waves, pitch and roll motions are quite close. The estimated peak and trough values probability distributions of the measured wave and pitch motion agrees quite well to the Rayleigh distribution, while the probability distribution of the parametric roll motion does not agree with the Rayleigh distribution characteristics. When the amplitude of the peak and trough values are small, the probability for the parametric rolling are larger than the value given by the Rayleigh distribution. Whe the ampiltude of the peak and trough value are larger, the cumulative probablity for the parametric rolling is a little smaller than the value given by the Rayleigh distribution. The statistical results in Figs. 11-13 demonstrate that when the parametric rolling occurs in ranmom seas during navigation, The ship tends to experience either the low-amplitude state without parametric rolling or the large-amplitude state with evident parametric rolling.

5. UNCERTAINTY ANALYSIS OF MODEL EXPERIMENTAL RESULTS

In section 4, the statistical property of the parametric rolling is discussed, it shows that there is evident statistical difference for the parametric rolling based on the analysis of the maximum value and the probability distribution among the various separate random record or from different length of the random records. It means that there exists significant statistical uncertainty for the parametric rolling. In this section, a quantitative estimation of the uncertainty for the parametric rolling is performed using the ITTC recommended procedure for stochastic processes (2017). Using the procedure, the single significant amplitude (SSA) of the random process and its confidence interval can be estimated by the direct counting of the motion time series.

5.1 Single Significant Amplitude and Its Uncertainty Analysis

In this section, the procedure of getting the SSA and its confidence interval for one ensemble of several records is shortly introduced, the detailes can be found in the above mentioned ITTC RP (2017).

Firstly the concerned sample like parametric motion is represented as a set of independent records of different lengths. A nested matrix is a convenient way to describe this type of data:

$$X = \{x_j\}_i; \quad j = 1,...,N_i; \quad i = 1,...,Nr \tag{6}$$

where Nr is the number of records in the sample. Ni is the number of data points of ith record.

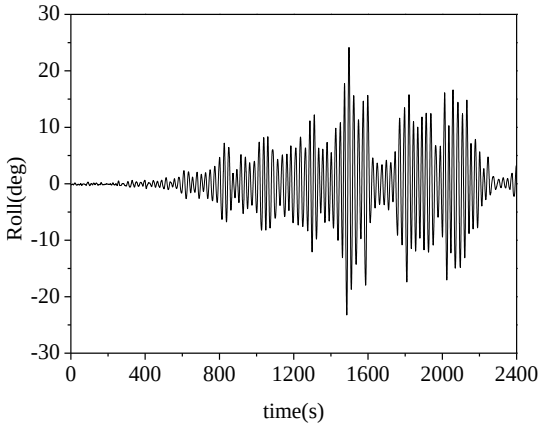

Fig. 14 The time history of parametric roll motion for one random record

The estimate of single significant amplitude (SSA) can be evaluated as follows:

$$\hat{SSA} = \hat{E}(Ps^{<3>}) = \frac{1}{Ns}\sum_{i=1}^{Ns} Ps_{l,3} \tag{7}$$

where Ns is the number of sample peaks above the 1/3rd-quantity from the integrated sample.

As an example, the peak values of roll motion from the record in Fig. 14 are shown in Fig. 15, where the dash line is the estimate of SSA.

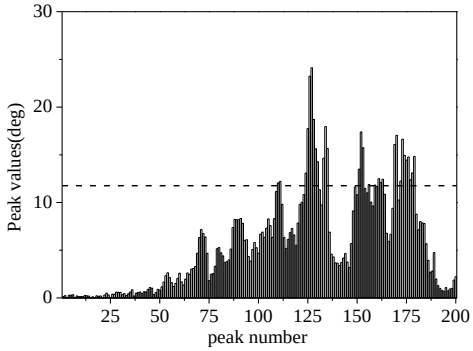

Fig. 15 Peak values of parametric roll motion

The confidence interval of SSA for the entire sample can be expressed as:

$$\hat{SSA}_{Low,Hi} = \hat{SSA} \pm K_\beta \sqrt{Var(\hat{SSA})} \tag{8}$$

where K_β is about 1.96, when the specified level is 0.95. $\mathrm{Var}(\hat{SSA})$ is the variance of SSA estimate.

Following the mentioned procedure, the SSA and its confidence interval for the concerned random sample can be estimated. The following Fig. 16 gives the SSA and its confidence interval estimation of the parametric roll motion for only one record corresponding to the time history in Fig. 14.

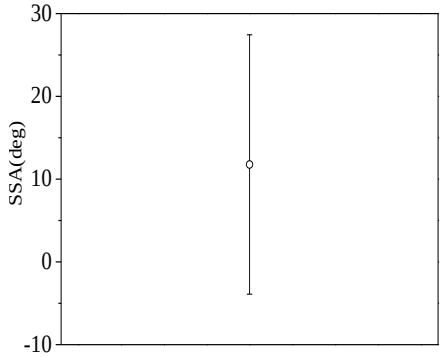

Fig. 16 SSA and its confidence interval estimation of roll motion for only one record

5.2 Uncertainty Analysis of Experimental Parametric Rolling in Random Seas

Based on the uncertainty analysis method,

the SSA and its confidence interval for the incident wave, pitch and roll motions are calculated and analysed. In the calculations, the results are obtained from the different length of the sample, whose length varied with the ensemble of different number of independent records. By this way, the uncertainty analysis is carried out to study the convergence of the SSA and its confidence interval with the number of records increasing.

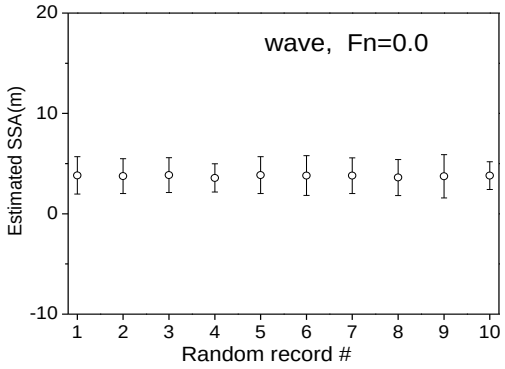

Fig. 17. (a) The SSA of the incident wave with 95% confidence bands from 10 different independant records

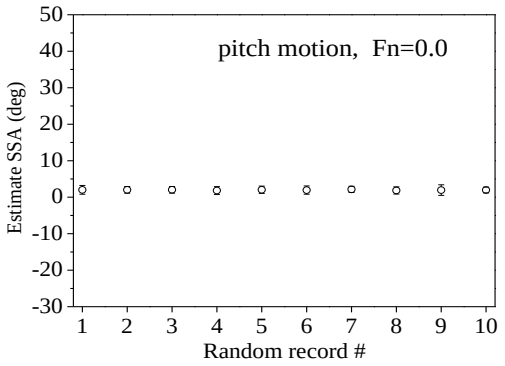

Fig. 17. (b) The SSA of the pitch angle with 95% confidence bands for 10 different independent records

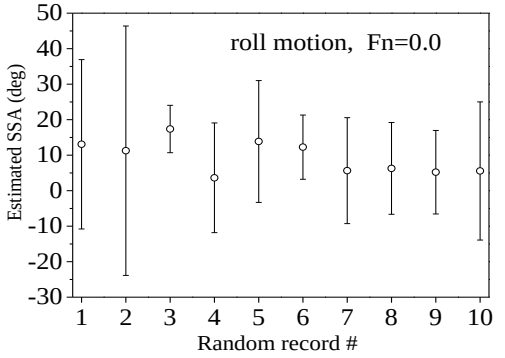

Fig. 17. (c) The SSA of the roll angle with 95% confidence bands for 10 different independent records

Fig. 17 SSA and its confidence interval estimate of incident wave, pitch and roll angles from the 10 different independant record respectively

It can be seen from Fig. 17 that the SSA estimate of the wave elevation and pitch angle from the 10 independent random records almost equals to each other and the confidence interval is quite small. However, there is a big difference for the estimate of SSA and confidence interval among the parametric roll angle from the 10 random records. In some records, the value of the confidence intervals for the roll angle is negative. Actually, the estimate of SSA was assumed to be normal distribution. When the confidence of the single significant amplitude is 95%, the estimated value of the SSA within the confidence interval following normal distribution can be expressed as followed:

$$(\bar{X} - 1.96\frac{\delta}{\sqrt{n}}, \bar{X} + 1.96\frac{\delta}{\sqrt{n}}) \qquad (9)$$

where $\bar{X}$ is the mean value, δ^2 is the variance, n is the sample number. The confidence interval is symmetrical and related to the variance, it leads to the impression that the confidence interval of SSA is negative in some cases.

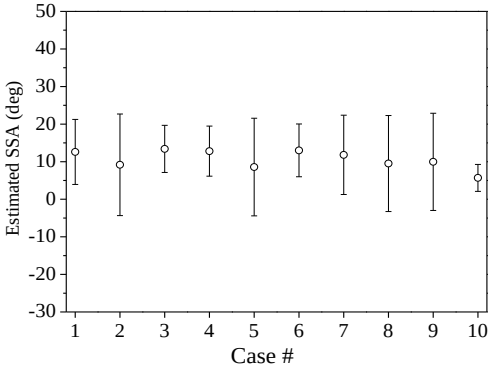

Fig. 18. (a) The SSA of the roll angle with 95% confidence bands from the ensemble of arbitray selected 4 records

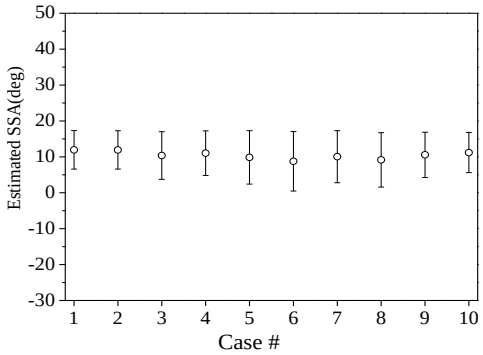

Fig. 18. (b) The SSA of the roll angle with 95% confidence bands from the ensemble of arbitray selected 7 records.

Fig. 18 SSA and its confidence interval estimation of parametric roll angle from the ensemble of multiple records (Fn=0.0)

From Fig. 17, it is shown that there is significant uncertainty for the parametric rolling angle from the different records. In Tab. 2, it is found that the time duration for each random record is about 5000 seconds. We further investigate the convergence of SSA and its confidence interval with the increasing of the total length for the parametric rolling amplitude. In Fig. 18, the total length of the roll angle is increased by the ensemble of different records. In Fig. 18 (a, b), the SSA of the roll angle with 95% confidence bands for the data sample from the ensemble of arbitray selected 4 and 7 records are provided respectively.

It can be seen from Fig. 18 that the difference of the SSA estimation of roll motion decreases with the increase of the number of the records. In Fig. 18(b), the SSA for the roll angle from different sample tends to converge to a certain value, the corresponding confidence bands also gets relatively narrower. It is indicated that the SSA and its confidence bands for the roll angle from the ensemble of 7 records tends to converge in the present forward speed and wave conditions. In order to check the final convergence, longer length of the sample is needed for the further analysis of the SSA and its confidence bands.

6. CONCLUSIONS

Based on the experimental data and its statistical analysis for the parametric roll of C11 containership in irregular head seas at zero forward speed, the following conclusions can be drawn:

(1) The probability distributions of the incident waves and pitch motion closely follows the normal distribution, while the probability distribution of the parametric roll motion is not, which verifies that the parametric roll motion is a non-Gaussian process.

(2) There is evident quantitative difference for the estimated probability distribution of the parametric rolling from the ensemble of the random records with different length. Based on the CDF analysis for ship parametric rolling, it is found that the ship tends to experience either the low-amplitude state without parametric rolling or the large-amplitude state with evident parametric rolling, which deviates from the Rayleigh distribution.

(3) The difference of the SSA of the wave and pitch motion among different random records is not significant, and the range of confidence interval is small. However, the SSA of the parametric roll motion is quite significant among different records and the confidence interval is accordingly larger. At zero forward speed, the SSA of the parametric rolling and its confidence interval gradually converge with the increase of the total length of the sample data. The ensemble of 7 random records (about 35000s) in the present wave conditions shows the converging tendancy.

7. ACKNOWLEDMENTS

In this work, the experimental study for C11 containership is jointly carried out by HEU and CSSRC. The model test data of parametric rolling is provided by Prof. Gu M.

and Dr. Lu J. from China Ship Scientific Research Center (CSSRC). Their help is gratefully acknowledged. The present work is supported by the National Natural Science Foundation of China (Grant No. 51379045) and The National Defense Basic Scientific Research Foundation (Grant No. B2420132001).

8. REFERENCES

Belenky, V. L, Weems, K.M., Lin W.M., and Paulling J.R., 2003, "Probabilistic Analysis of Roll Parametric Resonance in Head Seas", 8th International Conference on the Stability of Ships and Ocean Vehicles, pp. 325-340.

Belenky, V., Pipiras, V., Kent, C., Hughes, M., Campbell, B., and Smith T., 2013, "On the Statistical Uncertainties of Time-domain-based Assessment of Stability Failures: Confidence Interval for the Mean and Variance of a Time Series", Proc. 13th Int'l. Ship Stability Workshop, Breast 23-26, September pp. 251–258.

Belenky, V., Pipiras, V., and Weems, K., 2015, "Statistical Uncertainty of Ship Motion Data", Proceedings of the 12th International Conference on the Stability of Ships and Ocean Vehicles, 14-19, June 2015, Glasgow, U.K., pp. 891-902.

Bulian, G., and Francescutto, A., 2004, "On the Nonlinear Modeling of Parametric Rolling in Regular and Irregular Waves", International Shipbuilding Progress, 51 (2), pp.173-203.

Bulian, G., Francescutto, A., and Lugni, C., 2006, "Theoretical, Numerical and Experimental Study on the Problem of Ergodicity and 'Practical Ergodicity' with an Application to Parametric Roll in Longitudinal Long Crested Irregular Sea", Ocean Engineering, Vol. 33, pp. 1007-1043.

Bulian, G., Francescutto, A., Umeda, N., and Hashimoto, H., 2008, "Qualitative and Quantitative Characteristics of Parametric Ship Rolling in Random Waves in the Light of Physical Model Experiments", Ocean Engineering, Vol. 35, pp. 1661-1675.

ITTC-Recommended Procedures, 2017, "Single Significant Amplitude and Confidence Intervals for Stochastic Processes", 7.5-02-01-08, Revision 00, pp. 1-16.

Lu, J., Gu, M., and Umeda, N., 2017, "Experimental and Numerical Study on Several Crucial Elements for Predicting Parametric Roll in Regular Head Seas", Journal of Marine Science & Technology, Vol. 22, No.1, pp. 25-37.

Park, D. M., Kim, Y.W., and Song, K.H., 2013, "Sensitivity in Numerical Analysis of Parametric Roll", Ocean Engineering, Vol. 67(2), pp. 1-12.

Schumacher, A., Ribeiro e Silva, S., and Guedes Soares, C., 2016, "Experimental and Numerical Study of a Containership Under Parametric Rolling Conditions in Waves", Ocean Engineering, Vol. 124, pp. 385-403.

Taguchi, H., Ishida, S., Sawada, H., and Minami, M., 2007, "2007S-OS8-7 Parametric Rolling of a Ship in Head and Bow Seas: Part 3. A Model Experiment in Irregular Waves", The Japan Society of Naval Architects and Ocean Engineers, pp. 185-188.

The Specialist Committee on Stability in Waves, 2011, "Parametric Roll Benchmark Study", Proceedings of the 26th ITTC-Volume 2, Rio de Janeiro, Brazil, pp. 534-542.

Encounter Frequency Effect on the Simplified Design Criteria against Parametric Roll

Masahiro Sakai, *Osaka University* masahiro_sakai@naoe.eng.osaka-u.ac.jp

Naoya Umeda, *Osaka University* umeda@naoe.eng.osaka-u.ac.jp

Atsuo Maki, *Osaka University* maki@naoe.eng.osaka-u.ac.jp

ABSTRACT

The second generation intact stability criteria are under developing in the International Maritime Organization and the level 1 and 2 criteria are almost agreed. However, validation/verification studies about the level 2 criteria do not appear to be completely sufficient. We use mean frequencies of Grim's effective waves and compare them with the draft second check of the level 2 criteria for parametric roll. As a result, we verify the encounter frequency assumption used in the draft second check. In addition, it is shown that number of samples of operational conditions should be at least 24.

Keywords: *parametric roll, Grim's effective wave, mean frequency of Grim's effective waves, the second check of the level 2, second generation intact stability criteria*

1. INTRODUCTION

The International Maritime Organization (IMO) has been developing the second generation intact stability criteria and the level 1 and 2 criteria have been almost agreed for pure loss of stability, parametric roll, surf-riding/broaching and dead ship condition. Recent studies for the second generation intact stability criteria have focused on the four topics: consistency between the level 1 and 2 criteria, numerical modelling and possible simplification for the direct stability assessment, operational limitation/guidance and standards of excessive acceleration. It can be said that these four are regarded as critical issues for establishing the second generation intact stability criteria. In addition to these, the authors consider that validations/verifications of the level 2 criteria are also an important and remained issue.

Parametric roll is one of the dangerous roll phenomena that are to be covered with the second generation intact stability criteria. This roll phenomenon is induced by periodic change of a roll restoring coefficient mainly in longitudinal waves and could lead to loss and damage of cargoes; a C11-class post-Panamax container ship lost more than 400 units in 1998 (France et al., 2003) and an 8,160 TEU container ship lost 517 units in 2014 (Danish Maritime Accident Investigation Board, 2014). A phenomenon which is excited by a periodic change of a restoring coefficient, such as parametric roll, is classified in a parametric oscillation and it can be estimated by the Mathieu-type equation. The Mathieu equation admits a periodic solution with an infinite amplitude when a restoring variation exceeds a threshold. Using this method, the level 1 criteria against parametric roll require that a roll restoring variation should not exceed the threshold.

In case of the level 2 criteria for parametric roll, the vulnerability is examined by occurrence probability of unsafe wave conditions. There are two checks to judge the likelihood of dangerous parametric roll. The first check employs the same idea as the level 1 but explicitly takes wave-profile effect on a restoring variation into account. The draft second check employs the Mathieu-type equation with nonlinear restoring and damping moments, estimates parametric roll amplitudes with various ship forward speed in longitudinal waves and judges a condition as dangerous when the amplitude exceeds 25° (IMO, 2015). In order to estimate parametric roll amplitude, Umeda et al. proposed the Mathieu-type equation with quintic restoring, cubic damping and direct wave excitation as an uncoupled roll model and applied an averaging method to it (Umeda et al., 2004). This approach is a base of the draft second check of the level 2 criteria for parametric roll (IMO, 2016).

The amplitude of the wave-induced GM variation does not increase in proportion to the incident wave height so that Grim's effective concept (Grim, 1961) was introduced to the current draft second check, thereby GM variation in irregular waves is converted to that in equivalent regular waves. By using this concept, the vulnerability for parametric roll is estimated in regular longitudinal waves by changing sinusoidally her speed. For the sake of making criteria simple, the GM variation frequency is assumed to be equal to that of a wave whose length is equal to the ship length by using the dispersion relationship of deep water waves. However, the Grim's effective waves cannot be regarded as propagating waves but are just a variation of water surface along the ship whose instantaneous profile follows always a cosine function. Thus, the dispersion relationship cannot be simply applied to Grim's effective wave so that its wave frequency should be calculated from Grim's effective wave spectrum. In order to examine this point, we estimate parametric roll amplitudes by using mean frequencies of Grim's effective waves and compare the vulnerabilities derived by using the mean frequency and the current draft. Finally, the results show good agreement, therefore the appropriateness of the assumption is shown in this study. In addition, it is shown that number of samples of operational conditions for ship courses should be at least 24.

2. MATHEMATICAL MODEL

2.1 Uncoupled Roll Model

The level 2 criteria for parametric roll in the draft second generation intact stability criteria employ an uncoupled roll model to estimate parametric roll amplitudes. The time-varying restoring moments in waves are represented by the sum of calm-water restoring and GM variation in waves as shown in eq. (1) (Umeda et al., 2004):

$$\ddot{\phi}+2\alpha\dot{\phi}+\gamma\dot{\phi}^3+\omega_\phi^{\,2}\left(\frac{GM_{mean}}{GM}+\frac{GM_{amp}}{GM}\cos\omega_e t\right)\left\{\phi-\left(1/\pi^2\right)\phi^3\right\}+\omega_\phi^{\,2}\left(\phi+l_3\phi^3+l_5\phi^5\right)=0. \quad (1)$$

Here, α and γ are the damping coefficients estimated by Ikeda's simplified method (Kawahara et al., 2012) with the lift component of Ikeda's original method (Ikeda, 2004). The symbol ω is the wave frequency and the subscripts ϕ and e indicate the natural roll frequency and the wave encounter frequency, respectively. GM_{mean} and GM_{amp} are the mean and amplitude of the wave-induced GM variation, respectively. l_3 and l_5 are the cubic and quintic coefficients of the hydrostatically calculated calm-water GZ curve divided by GM.

2.2 Grim's Effective Wave

Grim's effective wave (Grim, 1961) is briefly explained in this subsection. Although this concept was extended to the case in short-crested quartering waves by Umeda et al. (1991), the detailed derivations of the formula

equations are shown in the appendix. Grim's effective wave was proposed in order to stochastically deal with nonlinear variations of GM in irregular waves. To transfer irregular waves to longitudinal waves whose length is equal to the ship length, the least squares method was applied and the wave profile along the ship was approximated by a cosine curve. Here, it is assumed that GM variation amplitude has the largest value in longitudinal waves whose length is equal to a ship length and GM has a maximum and minimum value when the amidship is at a wave trough and crest, respectively. An amplitude of a single oblique wave with frequency of ω is converted into an effective amplitude of a longitudinal wave as eq. (2):

$$\begin{aligned} &\zeta_{ae} = G\left(\omega, L_{pp}, \chi\right) \cdot \zeta_a, \\ &G\left(\omega, L_{pp}, \chi\right) \equiv \frac{\frac{\omega^2}{g} L_{pp} \cos(\chi) \sin\left(\frac{\omega^2}{2g} L_{pp} \cos(\chi)\right)}{\pi^2 - \left(\frac{\omega^2}{2g} L_{pp} \cos(\chi)\right)^2}, \end{aligned} \tag{2}$$

where χ is an angle formed by a ship course and a wave propagating direction, g is the gravitational acceleration, L_{pp} is the ship length, ζ_a is the incident wave amplitude and ζ_{ae} is the effective wave amplitude. Then, a spectrum of irregular waves is converted as eq. (3):

$$S\eta_{eff}\left(\omega, L_{pp}, \alpha\right) = \left[G\left(\omega, L_{pp}, \chi\right)\right]^2 S\left(\omega, \alpha\right) \tag{3}$$

where α is a wave propagating direction for each individual wave and $S(\omega, \alpha)$ and $S\eta_{eff}(\omega, L_{pp}, \alpha)$ are an incident wave spectrum and Grim's effective wave spectrum, respectively. Here, we derive the significant effective wave height based on ITTC spectrum as eq. (4) (IMO, 2016):

$$\begin{aligned} &H_{eff} = 4.0043\sqrt{m_0}, \\ &m_n = \int_{\alpha=-\pi/2}^{\alpha=\pi/2} \int_{\omega=0}^{\omega=\infty} \omega^n S\eta_{eff}\left(\omega, L_{pp}, \alpha\right) d\omega d\alpha, \\ &S\left(\omega\right) = A\omega^{-5} \exp\left(-B\omega^{-4}\right), \\ &A = 173 H_s{}^2 T_{01}{}^{-4}, \quad B = 691 T_{01}{}^{-4}, \\ &T_{01} = 1.086 T_z, \end{aligned} \tag{4}$$

where H_{eff} is the Grim's effective wave height, m_n is n-th moment of Grim's effective wave spectrum, H_s is a significant wave height [m] and T_z is a zero-crossing mean wave period [s]. H_s and T_z are given from a wave scatter diagram in the North Atlantic Ocean. The mean wave encounter frequency, ω_e, is defined as a zero-upcrossing mean frequency as eq. (5):

$$\omega_e = \sqrt{\frac{\int_0^\infty \left(\omega - \frac{\omega^2}{g} u \cos\chi\right)^2 S\eta_{eff}\left(\omega, L_{pp}, \chi\right) d\omega}{\int_0^\infty S\eta_{eff}\left(\omega, L_{pp}, \chi\right) d\omega}}, \tag{5}$$

where u is the ship speed. On the other hand, the current draft uses eq. (6) instead of eq. (5):

$$\begin{aligned} &\omega_e = \omega_L - \frac{\omega_L{}^2}{g} u \cos\chi, \\ &\text{where} \quad \omega_L = \sqrt{\frac{2\pi g}{L_{pp}}}, \end{aligned} \tag{6}$$

and ω_L is the frequency of waves whose length is equal to the ship length derived by using the dispersion relationship for deep water waves.

2.3 Current Draft Criteria

We explain briefly the basic idea and procedure of the current draft second check. Parametric roll is one of the roll resonance so that the wave encounter frequency governs the amplitude, which depends on the ship speed and course. Therefore, the magnitude of parametric roll should be examined with several ship speeds. Then, the encounter frequencies are estimated in the current draft second check based on the assumption that a ship runs with her service speed in different directions and each course is chosen with the same probability. As a result, the ship speeds to be calculated are determined by the encounter frequencies. Here, it is implicitly assumed that GM variation due to waves has its maximum value in longitudinal waves. The longitudinal waves' properties are estimated by Grim's effective wave concept as shown in subsection 2.2. Therefore, vulnerability for parametric roll

is examined in regular longitudinal waves by systematically changing her speed as eqs. (7)-(9) (IMO, 2015):

$$C2 = \frac{1}{n}\sum_{k=1}^{n} C2_k\left(u_k\right), \tag{7}$$

$$u_k = u_{max}\cos\left(\frac{k}{n}\pi\right)\ \left(k = 0,1,2,...,n\right), \tag{8}$$

$$C2_k\left(u_k\right) = \sum_{i=1}^{n} W_i\, C_i\left(u_k\right), \tag{9}$$

where $C2$ is the dangerous wave occurrence probability to be used for examining the vulnerability. n is number of samples of operational conditions. u_k is calculated ship speed and u_{max} is the ship maximum speed. A positive/negative u_k indicates that the ship runs in following/heading waves, respectively. W_i is the occurrence probability of i-th waves case and N is the number of wave cases. $C_i(u_k)$ has value of one when the parametric roll amplitude exceeds 25° under i-th case waves with ship speed u_k, otherwise it is zero.

3. AVERAGING METHOD

We employ an averaging method (Hayashi, 1985) to obtain the parametric roll amplitude from eq. (1). Discretised numerical methods, such as Runge-Kutta method, provides quite reliable solutions but it is not straightforward to obtain all solutions. An averaging method is one of widely known methods to obtain periodic solutions of nonlinear differential equations. An averaging method was applied to eq. (1) by Umeda et al. (2004), Maki et al. (2011) and Sakai et al. (2017).

3.1 Applying Averaging Method

We rewrite eq. (1) as the form of eq. (10) with a perturbation parameter, ε:

$$\ddot{\phi} + \hat{\omega}^2\,\phi = \varepsilon\, f\left(\phi,\dot{\phi},t\right). \tag{10}$$

This form is based on an assumption that the natural roll frequency is almost the same as parametric roll frequency, $\hat{\omega}$, and the damping and nonlinear components can be regarded as sufficiently small. We assume the periodic form of solutions based on the general solutions with ε of zero as eq. (11):

$$\begin{aligned}\phi &= A\cos(\hat{\omega}t - \xi),\\ \dot{\phi} &= -\hat{\omega}A\sin(\hat{\omega}t - \xi).\end{aligned} \tag{11}$$

Then, differential equations of A and ξ are derived as eq. (12) and (13):

$$\dot{A} = -\alpha A - \frac{3}{8}\gamma\hat{\omega}^2 A^3 - \frac{1}{4}\frac{\omega_\varphi^2}{\hat{\omega}} M A\left(1 - \frac{1}{2\pi^2}A^2\right)\sin(2\xi), \tag{12}$$

$$\begin{aligned}\dot{\xi} = \frac{\hat{\omega}}{2} - \frac{1}{2}\frac{\omega_\varphi^2}{\hat{\omega}}\Bigg\{1 + F\left(1 - \frac{3}{4\pi^2}A^2\right) + \frac{3}{4}l_3 A^2\\ + \frac{5}{8}l_5 A^4\Bigg\} - \frac{1}{4}\frac{\omega_\varphi^2}{\hat{\omega}} M\left(1 - \frac{1}{\pi^2}A^2\right)\cos(2\xi),\end{aligned} \tag{13}$$

where

$$\begin{aligned}F &= \frac{GM_{mean}}{GM},\\ M &= \frac{GM_{amp}}{GM}.\end{aligned} \tag{14}$$

By solving eq. (10) and (11) by setting the time derivatives to zero, the parameters, A and ξ, can be determined.

4. CALCULATION

We estimate the parametric roll amplitudes by using the averaging method by using two different methods for the wave encounter frequencies and verify the draft second check criteria.

4.1 Subject Ship and Calculation Conditions

A C11-class post-Panamax container ship is used as a subject ship. This ship experienced heavy roll in actual seas due to parametric roll

(France et al., 2003), thereby being used to determine the standard of vulnerability indexes in the second generation intact stability criteria for parametric roll. Additionally, her GZ curve in calm water is well approximated by quintic equation as shown in Fig. 1. Her principal particulars are shown in Table 1.

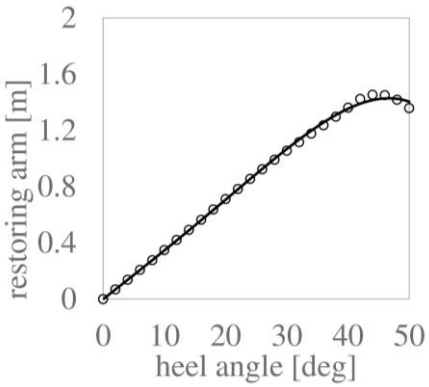

Fig. 1 Hydrostatically calculated calm-water GZ curve and its quintic approximation of C11-class post-Panamax container ship.

Table 1 Principal particulars.

item	value	unit
Length	262	[m]
Breath	40	[m]
Draught	12.34	[m]
Block coefficient	0.56	
GM	1.965	[m]
Natural roll period	25.7	[s]
Service speed	25.0	[knot]

4.2 Results

Figs. 2 and 3 show the comparison of $C2_k(u_k)$ in eq. (9) and $C2$ in eq. (7) derived by using the mean frequency of Grim's effective wave and the wave frequency used in the draft second check. Here, the white circles indicate results derived by using the mean frequency of Grim's effective wave and the crosses do those derived by using the current draft second check. Fig. 2 shows a slight shift of the peak of the current draft second check towards higher speed in following waves but it can be said that the difference between the two is not significant. Fig. 3 shows also the similar results between the two and clarifies that n = 6, which was tentatively adopted by at the IMO (IMO, 2015), is not sufficient, n should be at least 24 for $C2$ and in this case the index of 0.06 for $C2$ should be reduced.

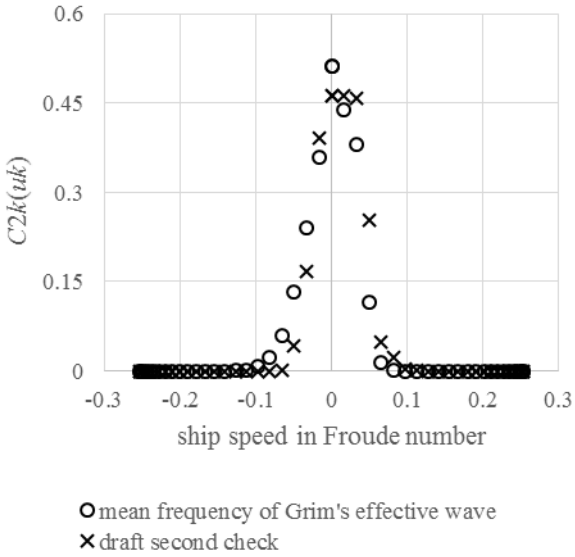

Fig. 2 Comparison of $C2_k(u_k)$ when n = 48.

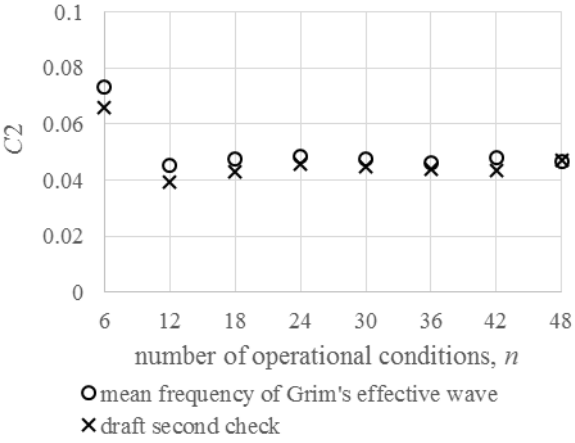

Fig. 3 Comparison of $C2$ with number of samples of operational conditions.

5. DISCUSSION

In order to investigate why such a simple assumption provides satisfactory approximations shown in Figs. 2 and 3, we compare the mean frequencies of Grim's effective waves and the frequency assumed in the draft second check in Figs. 4-6. Here, the significant wave heights and mean wave frequencies of Grim's effective waves are calculated for all sea states appearing in the

North Atlantic. Calculated conditions in Figs. 4-6 are zero forward speed, the service speed in heading waves and the service speed in following waves. The horizontal axis indicates the nondimensionalized frequency with the encounter frequency assumed in the draft second check for each calculated condition. So, the black chain line, which is located at one in the horizontal axis, indicates the frequency assumed in the draft second check. For more than 2.0 [m] height effective waves in Figs. 4-6, the mean frequency is distributed only near that of the draft second check. This guarantees that the simple assumption that the wave frequency of λ/L_{pp} = 1 can represent the GM variation frequency. The reason of the agreement shown in Fig. 4 can be easily understood in Fig. 7. Fig. 7 indicates that the transfer function, $[G(\omega, L_{pp}, \chi)]^2$, has the largest peak around the wave frequency of λ/L_{pp} = 1 and can also explain the groups around nondimensionalized wave encounter frequencies of 1.5, 2.0, and 2.5 in Fig. 4.

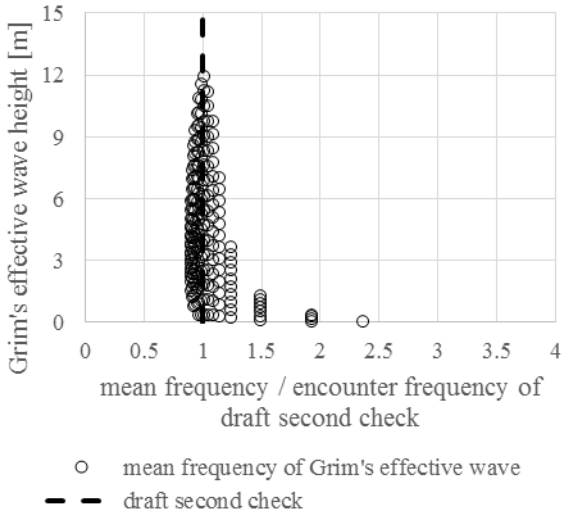

Fig. 4 The relationship between the mean wave frequency and wave height of Grim's effective wave with zero forward speed.

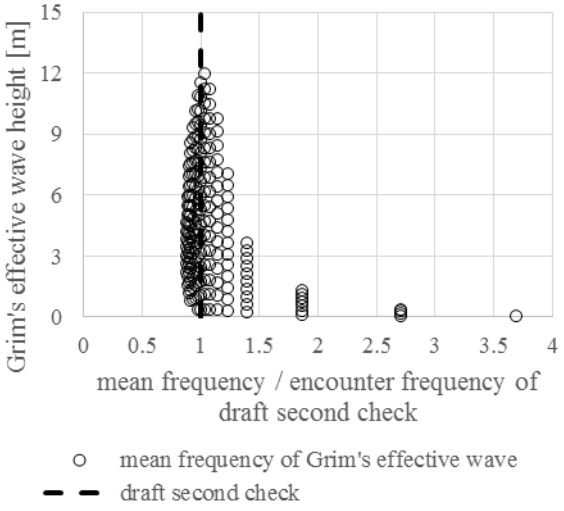

Fig. 5 The relationship between the mean wave frequency and wave height of Grim's effective wave with service speed in heading waves.

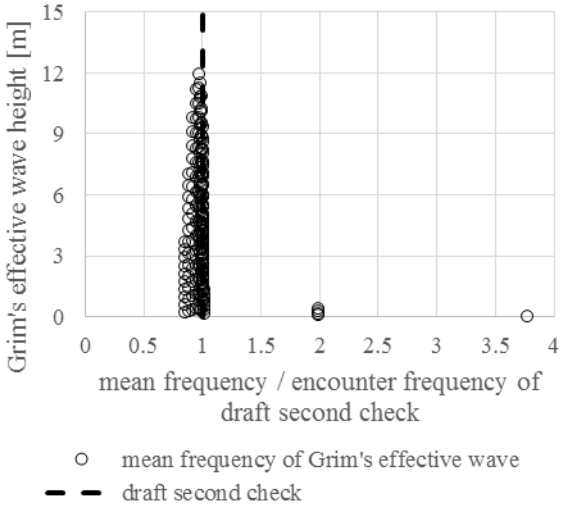

Fig. 6 The relationship between the mean wave frequency and wave height of Grim's effective wave with service speed in following waves.

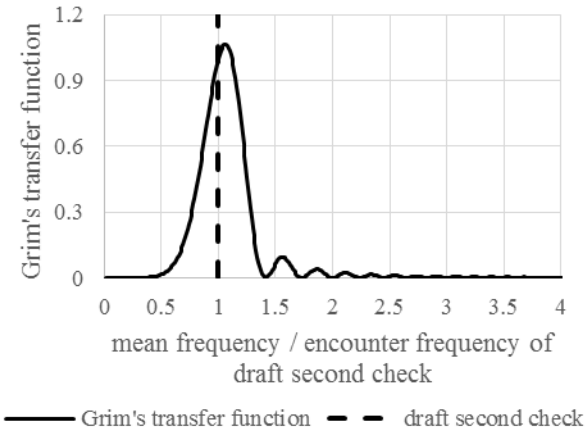

Fig. 7 Transfer function of Grim's effective wave spectrum.

6. CONCLUSIONS

The encounter frequency effect on the draft second check for parametric roll is well verified by using a more rigorous approach with the mean frequencies of Grim's effective waves. It appears appropriate that the GM variation frequency is assumed as the same as the one of waves of $\lambda/L_{pp} = 1$. In addition, it is clarified that the number of samples of operational conditions should be at least $n = 24$ for obtaining a reliable value of $C2$.

7. ACKNOWLEDGEMENT

This work was supported by a Grant-in-Aid for Scientific Research from the Japan Society for the Promotion of Science (JSPS KAKENHI Grant No. 15H02327).

8. APPENDIX

The detailed derivation of eqs. (2), (3) and (5) are shown in this section as following Grim's concept (Grim, 1961 and Umeda et al. 1991). The wave profile of irregular waves, ζ_w, is expressed by using the wave spectrum as eq. (A-1):

$$\begin{aligned}&\zeta_w(\xi,\eta,t)\\&=\int_{\alpha=-\pi/2}^{\alpha=\pi/2}\int_{\omega=0}^{\omega=\infty}\left\{\sqrt{2S(\omega,\alpha)d\omega d\alpha}\right.\\&\left.\cdot\cos\left[\omega t\pm\frac{\omega^2}{g}(\xi\cos\alpha+\eta\sin\alpha)+\psi\right]\right\},\end{aligned}\tag{A-1}$$

where, O-ξ, η is a space-fixed coordinate system and ψ is a random number between 0 and 2π. The sign "±" is determined by the wave propagating direction. The wave profile along the ship, ζ_s, is expressed as eq. (A-2);

$$\begin{aligned}&\zeta_s(x,t)\\&=\int_{\alpha=-\pi/2}^{\alpha=\pi/2}\int_{\omega=0}^{\omega=\infty}\left\{\sqrt{2S(\omega,\alpha)d\omega d\alpha}\right.\\&\left.\cdot\cos\left[\omega t\pm\frac{\omega^2}{g}(\xi_0\cos\alpha+\eta_0\sin\alpha+x\cos\chi)+\psi\right]\right\},\end{aligned}\tag{A-2}$$

where

$$\chi=\bar{\chi}-\alpha.\tag{A-3}$$

x is the ship-fixed coordinate system along the longitudinal direction and the midship is set to zero. $\bar{\chi}$ is a ship course and ξ_0 and η_0 express the midship position in the space fixed coordinate. To approximate ζ_s as a cosine function, we introduce a square of the residual as eq. (A-4):

$$\Delta=\int_{-L_{pp}/2}^{L_{pp}/2}\left[\zeta_s(x,t)-\zeta_{ae}\cos\left(\frac{2\pi}{L_{pp}}x\right)\right]^2dx.\tag{A-4}$$

And the derivative is

$$\begin{aligned}&\frac{d\Delta}{d\zeta_{ae}}\\&=\int_{-L_{pp}/2}^{L_{pp}/2}-2\cos\left(\frac{2\pi}{L_{pp}}x\right)\\&\quad\cdot\left[\zeta_s(x,t)-\zeta_{ae}\cos\left(\frac{2\pi}{L_{pp}}x\right)\right]dx\\&=L_{pp}\,\zeta_{ae}-\int_{-L_{pp}/2}^{L_{pp}/2}2\cos\left(\frac{2\pi}{L_{pp}}x\right)\zeta_s(x,t)\,dx.\end{aligned}\tag{A-5}$$

Since the least squares method requires that the derivative should be zero, we obtain

$$\zeta_{ae} = \frac{1}{L_{pp}} \int_{-L_{pp}/2}^{L_{pp}/2} 2\cos\left(\frac{2\pi}{L_{pp}} x\right) \zeta_s(x,t)\, dx$$

$$= \frac{1}{L_{pp}} \int_{-L_{pp}/2}^{L_{pp}/2} \left\{ 2\cos\left(\frac{2\pi}{L_{pp}} x\right) \cdot \left[\int_{\alpha=-\pi/2}^{\alpha=\pi/2} \int_{\omega=0}^{\omega=\infty} \sqrt{2S(\omega,\alpha)\, d\omega\, d\alpha} \cdot \cos\left(\omega t \pm \frac{\omega^2}{g} (\xi_0 \cos\alpha + \eta_0 \sin\alpha) + \psi \pm \frac{\omega^2}{g} \cos\chi \cdot x \right) \right] \right\} dx$$

$$= \int_{\alpha=-\pi/2}^{\alpha=\pi/2} \int_{\omega=0}^{\omega=\infty} \left\{ \sqrt{2S(\omega,\alpha)\, d\omega\, d\alpha} \cdot \frac{1}{L_{pp}} \cos\left[\omega t \pm \frac{\omega^2}{g} (\xi_0 \cos\alpha + \eta_0 \sin\alpha) + \psi \right] \cdot \int_{-L_{pp}/2}^{L_{pp}/2} \left[2\cos\left(\frac{2\pi}{L_{pp}} x\right) \cdot \cos\left(\frac{\omega^2}{g} \cos\chi \cdot x\right) \right] dx \right\}$$

$$= \int_{\alpha=-\pi/2}^{\alpha=\pi/2} \int_{\omega=0}^{\omega=\infty} \left\{ \sqrt{2S(\omega,\alpha)\, d\omega\, d\alpha} \cdot \left[G(\omega, L_{pp}, \chi) \right] \cdot \cos\left[\omega t \pm \frac{\omega^2}{g} (\xi_0 \cos\alpha + \eta_0 \sin\alpha) + \psi \right] \right\}. \quad \text{(A-6)}$$

Eq. (A-6) shows that Grim's effective amplitude is estimated by eq. (2) and Grim's effective wave spectrum follows eq. (3). Moreover, the zero-upcrossing mean frequency, ω_{mean}, is derived by eq. (A-7):

$$\omega_{mean} = \sqrt{\frac{m_2}{m_0}}. \quad \text{(A-7)}$$

According to eq. (A-7), we obtain the mean wave encounter frequency as eq. (5).

9. REFERENCES

Danish Maritime Accident Investigation Board, 2014, "Marine Accident Report September 2014".

France WN, Levadou M, Treakle TW, Paulling JR, Michel RK, and Moore C, 2003, "An Investigation of Head-Sea Parametric Rolling and its Influence on Container Lashing System", Mar Technol 40(1): 1-19.

Grim O, 1961, "Beitrag zu dem Problem der Sicherheit des Schiffes in Seegang", Schiff und Hafen 6: 490-497 (in German).

Hayashi C, 1985, "Nonlinear Oscillations in Physical Systems", Princeton University Press.

Ikeda Y, 2004, "Prediction Method of Roll Damping of Ships and Their Application to Determine Optimum Stabilization Devices", Mar Technol 41(2): 89-93.

IMO, 2015, "Report of the working group (part 1)", SDC 2/WP.4.

IMO, 2016, "Report of the working group (part 1)", SDC 3/WP.5.

Kawahara Y, Maekawa K and Ikeda Y, 2012, "A Simple Prediction Formula of Roll Damping of Conventional Cargo Ships on the Basis of Ikeda's Method and Its Limitation", J Shipping and Ocean Eng: 201-210.

Maki A, Umeda N, Shiotani S, Kobayashi E, 2011, "Parametric Rolling Prediction in Irregular Seas Using Combination of Deterministic Ship Dynamics and Probabilistic Wave Theory", Journal of Marine Science and Technology 16: 294-310.

Sakai M, Umeda N, Yano T, Maki A, Yamashita N, Matsuda A, Terada D, 2017, Averaging Methods for Estimating Parametric Roll in Longitudinal and Oblique Waves, Journal of Marine Science and Technology, published online.

Umeda N, Hashimoto H, Vassalos D, Urano S and Okou K, 2004, "Nonlinear Dynamics on Parametric Roll Resonance with Realistic Numerical Modelling" International shipbuilding Progress, 51 (2): 205-220.

Umeda N and Yamakoshi Y, 1991, "Assessment for Probability of Ship Capsizing due to Pure Loss of Stability in Quartering Seas", Journal of the Society of Naval Architects of Japan, 169: 15-25 (in Japanese).

A System Approach for Second Generation Intact Stability criteria compliance

Nicola Petacco, *University of Genoa,* nicola.petacco@edu.unige.it

Paola Gualeni, *University of Genoa,* paola.gualeni@unige.it

ABSTRACT

In the context of Second Generation Intact Stability Criteria (SGISC), a need for a comprehensive analysis among the different stability failures has been identified, to improve a balanced final design result in terms of ship stability performance. In this paper, the first vulnerability level criteria are analysed and a system approach (Design Structure Matrix) has been employed to observe comprehensively all stability failures. SGISC criteria have been applied to a set of Megayacht unit parent hulls and results are analysed in order to quantify the effect of some specific parameters on the whole ship stability performance at once.

Keywords: *Second Generation Intact Stability criteria, Ship Design, Design Structure Matrix*

1. INTRODUCTION

In the latest ten years, the development of the so-called Second Generation Intact Stability Criteria has been one of the important topics addressed by the Sub-Committee on Safety Design and Construction (SDC) of the International Maritime Organization regarding the intact stability of vessels. The Intact Stability code (IMO, 2008) states the need of new criteria that are able to assess the stability of a ship in seaway. This approach requires the study of the ship behaviour in terms of intact stability as a consequence of interactions with waves. The SDC Sub-Committee decided to tackle this issue considering a physical point of view, so four different phenomena are identified:

- Righting arm variation problem due to waves;
- Stability under dead ship condition;
- Manoeuvring-related failures in waves;
- Excessive lateral acceleration.

As a result of an long and complex job on these topics, five stability failure modes are defined and regulated by different specific criteria organized on two levels of vulnerability. A significant literature is available describing in details the physic of these phenomena (Belenky *et al*., 2008 and Belenky *et al*., 2011), therefore it will not be addressed within this paper. As already mentioned, unlike the traditional stability criteria, a multi-layered approach is adopted. It consists actually of three different assessment levels with an increasing level of accuracy for each stability failures. It is very simple and fast to apply the first level (L1) but it might give too conservative results; on the other hand, Level 2 (L2) requires more information and calculations but its outcomes are more accurate. Finally, at the third and last level, the Direct Stability Assessment is the most accurate, based in principle on non-linear seakeeping numerical tools but also the most time and money consuming.

On the top of that, as a very last option, an Operational Guidance is also allowed in case the vessel appears to be vulnerable in relation with the previously described assessment criteria.

In 2015, at SDC 2 meeting, the rule texts of criteria for Parametric Roll, Pure Loss of Stability and Surf-Riding/Broaching have been presented (IMO, 2015). While the last versions of criteria for Dead Ship condition and Excessive Acceleration failures have been delivered at the end of the SDC 3 session (IMO, 2016).

During the latest decade, such criteria have been further refined and modelled in their present version; at the same time, they have been applied to several ship typologies in order to gain further insight on their adequacy and to give a feedback to the community of experts. Many papers present the outcome of intense applications on a huge set of ships (Schrøter *et al*, 2017). Often, comparisons between the results of the first two levels of each stability failure are discussed. These valuable works enhance the tuning of the LV1 against LV2 and their reliability as assessment tools. Unfortunately, a cross comparison of the outcomes from the different stability failures criteria is not carried out. In some cases, stability failures under investigation are tightly connected from the underlying physical phenomena at their origin, such as Parametric Roll with Pure Loss of Stability as well as Parametric Roll with Excessive Acceleration. From a designer's point of view, it is useful to know how the criteria are linked together and in which way a modification of a parameter may influences all of them, improving some and/or making other worse. At the end of the day, the very same ship is requested to fulfil all the criteria at the same time.

This paper is structured in two distinct sections: the first part introduces the Design Structure Matrix as a tool for a comprehensive analysis to identify the main parameters common to all the criteria. It will not be surprising that all of them belong to the well-known domain of parameters able to characterise the ship stability performances of the ship. The interesting point is to observe the restricted selection that has been made about them. In the second section, application on a family of parent hulls is carried out. The choice of hull parameters for the parent hulls set generation is derived from the outcomes of the first part.

One of the main targets of the investigation is also to check the ability of the second generation intact stability criteria to be sensitive to ship parameter modifications, i.e. the real ability to improve ship safety, during the design process.

2. DESIGN STRUCTURE MATRIX: A POWERFUL DESIGN TOOL

A generic description of Design Structure Matrix (DSM) and all its features is given in this section. A DSM is a simple technique that describes in a compact and efficient way a set of design activities or a flow of information. The use of DSM in both industrial and research practice increased greatly in 90's. The tool has been applied in the real estate development, aerospace industries, small-scale manufacturing, automotive and building construction (Pektas & Pultar, 2006 or Qiao & Ryan, 2015). Some strong points of this kind of approach are:

– Strong visual asset is provided, by means of matrixes. They show clearly the relationships among each activity and they also may reveal possible interactions, i.e. how a parameter influences or may be influenced by another one in a clear and rapid way.

– Possibility to represent a huge amount of activities, data or parameters and their relationships in a compact way, to be read easily.

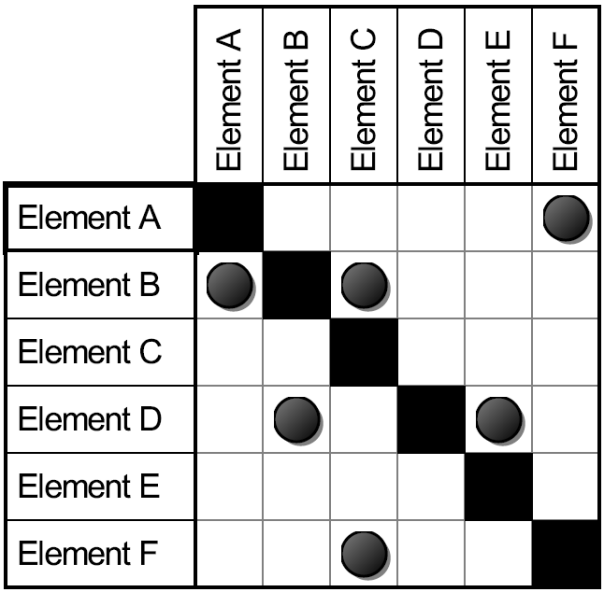

Figure 1 : Example of a generic Design Structure Matrix.

DSM is a square matrix with the same number of rows and columns. The cells on the main diagonal represent the elements or activities selected to model the system, while the off-diagonal cells depict the dependency among these elements. Exactly this last concept is the useful feature that makes different DSM from the previous project management tools such as PERT (Program Evaluation and Review Technique). In Figure 1 an example of a simple DSM is given. A dot in a cell means that the output of that column is required to process/elaborate the element identified by that specific row. On the contrary, reading by column, marked (by dots) rows mean that are influenced by the parameter selected in the considered column. According to Eppinger & Browning (2012), this kind of reading is conventionally called IC/FBD where IC means "Input in Column" and FBD means "Feedback Below Diagonal". It is worthwhile to mention that there is also the other convention that reads DSMs in the reverse order and it is called "Input in Row / Feedback Above Diagonal" (IR/FAD).

There are three different representation types to describe the relationship between two tasks of the system: sequential (or dependent), parallel (or concurrent) and coupled (or

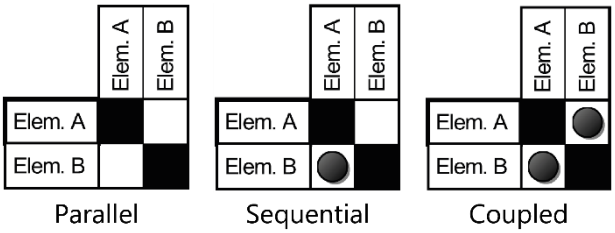

Figure 2 : Relationships between elements of a Design Structure Matrix.

interdependent). In the first configuration, the main element influences the outcome of the following task in a unidirectional flow. The dependent element may be performed only after the previous one. In the concurrency configuration, the elements do not interact with each other, so it is possible to perform the two task in parallel. In the last one, the elements depend on each other, therefore the related tasks should be solved in an iterative working flow. The respective representations in a DSM are listed in Figure 2. The application of a DSM to a project allows to quickly understand which parameters feed or need for what. In this way, the order of tasks may be organized to be more efficient and incisive. Taking for example the DSM in Figure 1, it is clear that the tasks could be manipulated in order to reduce the feedback marks above the main diagonal. In Figure 3 is shown the proper order to process easily and quickly the flow of

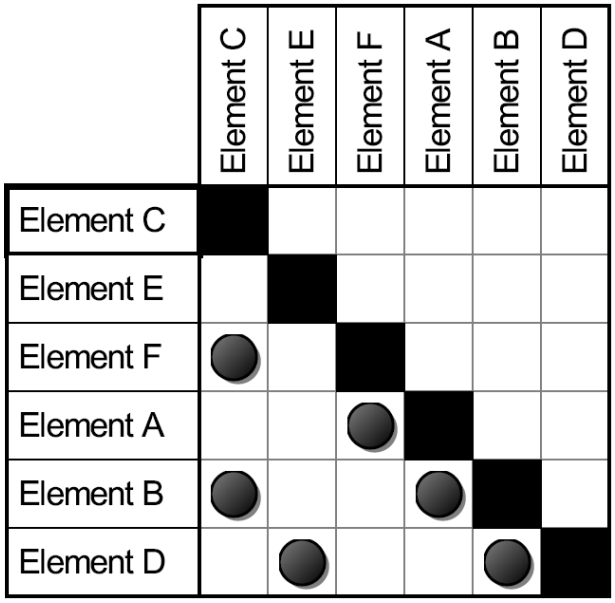

Figure 3 : Design Structure Matrix manipulated with the partitioning process.

information represented by the DSM. This process is called partitioning, it is one of the tools available to manipulate design structure matrix. A detailed description of each tool is given by Yassine (2002).

It is worthwhile to mention that all the DSMs presented in this paper, have been modelled thanks to the software CAM (Cambridge Advanced Modeller) developed by Wynn *et al*. (2010).

3. DSM APPLICATION FOR A CROSS-CHECKED DESIGN

In this part of the paper the Design Structure Method has been applied to the second generation intact stability criteria. In particular only the first levels of all stability failures have been considered. The procedure to evaluate a criterion is rendered into a set of specific data and derived parameters, which are logically ordered into a DSM. The DSMs developed in this perspective are graphically represented in Appendix 1 at the end of the paper. Beginning from the rule text of each stability failure (IMO, 2015 and IMO, 2016), data required by the rule for the assessment are identified. Then, they have been organized into the matrix according to the order of appearance within the criteria. Thereafter, by virtue of the properties of DSM, the set of parameters has been rearranged applying the partitioning method described above. Thanks to the new arrangement of the DSM, it is straightforward to subdivide the set of elements in three main categories: *Design parameters* (blue), *Dependent parameters* (white) and *Output* (green). It is considered *Design parameter* each element that does not directly depend on another one. The *Design parameters* category is subdivided in two other sub-category. Main elements and Secondary elements. The first sub-category consists of all those parameters that may be set directly by the designer or defined by the agreement between the ship owner and the yard, i.e. length between perpendicular, service speed, as well as, bilge keel dimension and vertical position of the center of gravity. The secondary elements can generally derive from the first ones, such as hull overall geometry or can even be independent like environmental conditions. *Dependent parameters* are those parameter that should be evaluated according to the formulas defined by the rule. They deterministically depend on the *Design parameters* and they cannot be tuned by the designer. Finally, the *Output* category is made up of two elements: the criterion that evaluates the vulnerability of the vessel and the standard that is the threshold against which to compare the calculated criterion.

Once the DSM is created and its elements are categorized, the *Design parameters* common to every stability failures have been highlighted. As shown in Appendix 1, the Main elements common to all the criteria are listed in Table 1.

Table 1: Main elements obtained by DSM

Main elements		
Breadth	B	(m)
Draught	d	(m)
Bilge keel area	A_{BK}	(m^2)
Service speed	V_S	(m/sec)
Vertical position of Centre of Gravity	KG	(m)
Length between perpendicular	L_{PP}	(m)
Depth	D	(m)

To better understand how strong is the relationship between a parameter and the final criterion, a selection of Main elements has been done. In this paper the effects due to a modification of breadth, draught and bilge keel area are analysed.

4. APPLICATION CASE

The investigated ship typology is representative of a megayacht unit. The main dimension of the hull are indicated in Table 2.

Table 2 : Main dimension of the analysed megayacht unit

Megayacht – Main dimensions		
L_{PP}	64.94	(m)
B_{WL}	12.97	(m)
d	3.30	(m)
D	7.50	(m)
B_{WL}/d	3.930	(-)
C_B	0.586	(-)
C_m	0.935	(-)
$A_{bilge\ keel}$	4.14	(m^2)
$A_{lateral}$	658.0	(m^2)
T_{roll}	8.09	(sec)

Moreover, since the Excessive Acceleration criterion requires the definition of the vertical coordinate of the highest location where crew or passengers may be present, this has been located on the Sun Deck at 15.70 (m) from keel line while its longitudinal relative position is 0.40 (-).

A set of systematic modifications have been done, in order to appreciate the direction and the intensity of the link between the main parameters selected in Section 3 and the criterion outcome. Five B_{WL}/d values (3.5, 3.6, 3.75, 3.85, 4.00) have been selected and for each ratio, two different hulls are modelled, for a total of ten different units. The block coefficients has remained the same for all the configurations. Modified hulls may be collected in two main groups: in the first group, only the breadth has been modified for each unit (Table 3), while in the other one only the underwater depth has been changed (Table 4). The influence of a modification on breadth or draught on the stability failures addressed by the SCGIS criteria has been evaluated. As regards the other Main elements listed in Table *1*, there is no need to change the original hull geometry to assess their influence on the final criteria. Their impact on the outcome can be simply evaluated changing the input value within the formula of each criterion.

Table 3 : Main dimensions of the new hulls keeping constant the draught (d=3.3 m)

(*) Hull family – Main dimensions						
B_{WL}/d	-	4.00	3.85	3.75	3.60	3.50
B_{WL}	m	13.20	12.71	12.38	11.88	11.55
d	m	3.30	3.30	3.30	3.30	3.30
D	m	7.50	7.50	7.50	7.50	7.50
T_{roll}	s	7.74	8.56	9.28	10.79	12.32

Table 4 : Main dimensions of the new hulls keeping constant the breadth (B_{WL}=12.97 m)

(#) Hull – Main dimensions						
B_{WL}/d	-	4.00	3.85	3.75	3.60	3.50
B_{WL}	m	12.97	12.97	12.97	12.97	12.97
d	m	3.24	3.37	3.46	3.60	3.71
D	m	7.44	7.57	7.66	7.80	7.91
T_{roll}	s	7.99	8.21	8.36	8.58	8.76

The following aspects have been taken into account:

– Bilge keels are represented within the criteria by means of their projected area. Therefore, it has been decided to change the bilge keel span in order to assess their influence on the final result. The bilge keel span has been changed from –10% to +40% of the design bilge keel span, step 10%;

– As regard the 1st level of each stability failure, service speed is a common parameter only between Pure Loss of Stability and Surf-Riding/Broaching. Due to the binary nature of its influence on the criteria, it has been disregarded in the sensitivity assessment;

– The effects of the vertical position of centre of gravity on SGIS criteria is well evident in literature. Nevertheless it is not addressed in this paper and the various sensitivity assessment are made with constant KG;

– The effects of a modification on length does not affect effectively the final values of criteria, as shown in Petacco & Gualeni (2016) also in the case of wave profile sensitive stability failures like pure loss of stability and parametric roll where the relation between the ship and the wave lengths, together with the wave height, is deemed to be relevant.

5. RESULTS AND COMMENTS

Criteria outcomes for each stability failures and hulls family are shown in Figure 4. On the vertical axis the criterion values divided by the criterion value computed for the baseline condition (Table 2) are represented. A very quick recapture of the main features for the different stability failure, first level of vulnerability, is given in the following. A detailed description about calculation procedures is given in IMO (2015 and 2016).

For pure loss of stability, the criterion evaluates the minimum metacentric height considering the ship balanced in draft and trim on a set of waves with the same length and height but a different wave crest position. In parametric roll the ratio between the variation of metacentric height in waves and the GM in calm water is calculated. For dead ship condition, the ratio between the areas under the GZ curve is taken into consideration. Finally, for excessive acceleration, the criterion computes a lateral acceleration in the highest point of the ship where crew and passenger may be present.

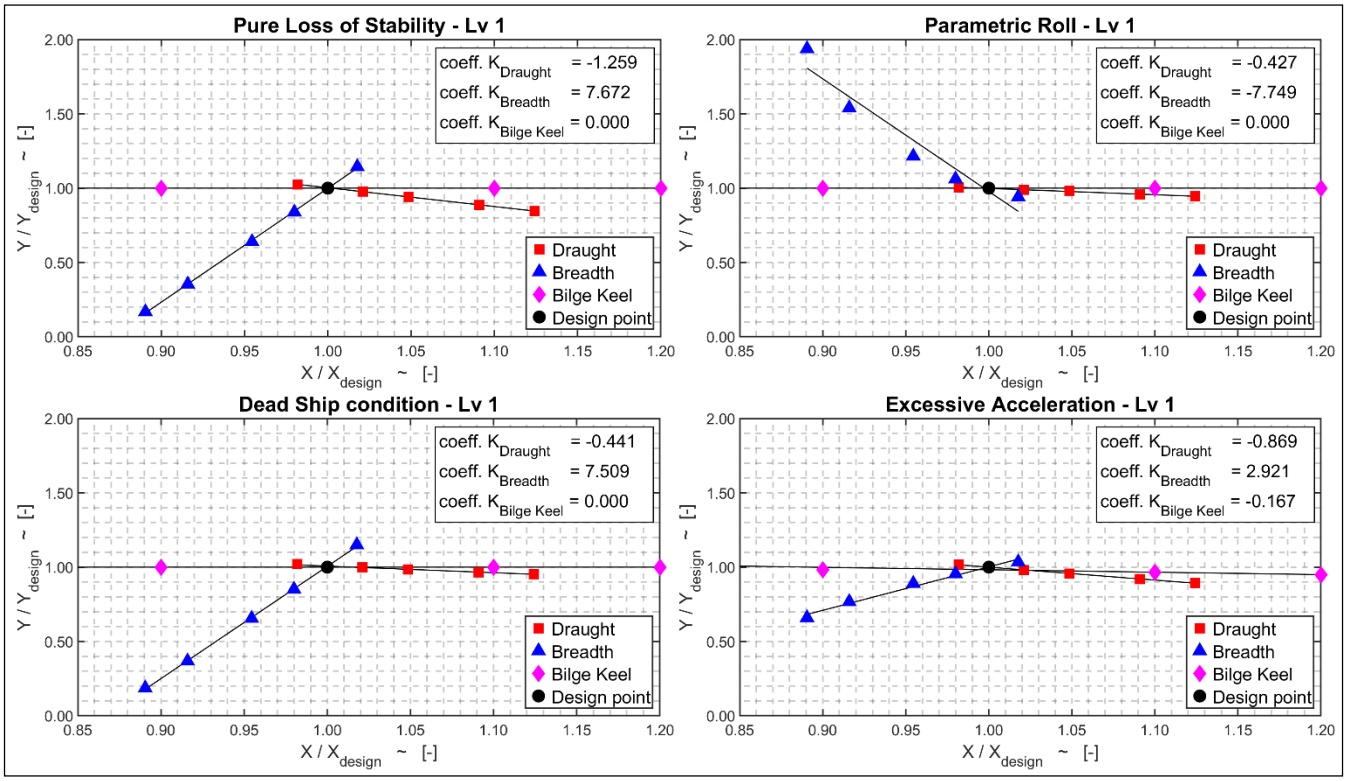

Figure 4: Effects of a change in Draught, Breadth and Bilge keel Area on first vulnerability levels for each stability failure.

In order to compare, in the same graphic, the results obtained by changing each parameter, on the horizontal axis are reported the values of the assessed parameter divided by the corresponding design value. The square red markers represent the draught influence, the blue triangles stand for the sensitivity to breadth changing while the pink diamonds show the effect of bilge keel area variation. To better represent the points and regression lines calculated, the x-axis has been limited. Due to this, some sample points have been cut off from the graphs for the bilge keel case.

In addition, to show the trend within each outcomes family, continuous lines are represented in the graphs. They are obtained by means of linear regression analysis. Calculating the slope of the regression line is a first attempt to express the link between the parameter and the final criterion by a numerical coefficient.

In order to overcome the regression line slope dependency on the criterion unit of measurement, the K-index is proposed. Its formulation is given below:

$$K = \frac{\Delta Y_{\%}}{\Delta X_{\%}} = \frac{\frac{Y - Y_{ref}}{Y_{ref}}}{\frac{X - X_{ref}}{X_{ref}}} =$$

$$K = \frac{(Y - Y_{ref})}{(X - X_{ref})} \cdot \frac{X_{ref}}{Y_{ref}} \qquad (1)$$

Where X_{ref} is the design value of the considered parameter; Y_{ref} is the relevant outcome value of the criterion referred to the design condition according to the linear regression; X and Y are the coordinates of the assessed parameter along the regression line. K - index does not depend on the specific unit of measurement of each criterion, so it can be assumed as a good coefficient for a comparison among all stability failures. As it is formulated, the coefficient K is based on the assumption of a linear relationship between the criterion and the parameter considered. This is valid if the parameter is changed in a limited neighbourhood of the design value. Moreover, the value of K is strictly related to the selected point of reference as baseline, in this paper it is chosen the parameter and criteria referred to the initial design condition.

The sign of K-index represents the direction of the relationship between a main parameter and the criterion; a positive sign means there is a direct relationship, so increasing the parameter increases the criterion, vice versa for negative signs. Instead, the strength of the relationship is evaluated by the numerical value of the K-index. A high value of K corresponds to a strong link, which means that a limited variation of the parameter produces a large variation of the criterion. A null value of K means no relationship exists between the parameter and the final criterion. In Table 5 the corresponding values for each main parameter and stability failures are reported.

Table 5: K-index values for each stability failures and parameters assessed

	Draught	**Breadth**	**Bilge keel Area**
PLS	-1.259	+7.672	0.000
PR	-0.427	-7.749	0.000
DS	-0.441	+7.509	0.000
EA	-0.869	+2.921	-0.167

As a further information, K-index of each failure mode has been highlighted also into the relevant DSM (**Error! Reference source not found.** to Figure 8). It is put into the cell created by the intersection between the criterion row and the considered parameter column.

Thanks to the outcomes summarized in Figure 4 and Table 5, as expected, it is evident how the most important parameter is the breadth; in all cases the criterion values present the regression line with the highest slope, this is also confirmed by the K - index which is up to seven time more than the other coefficients.

The influence of breadth on the final criterion value is less pronounced only for excessive acceleration phenomenon. As regards the variations of draught, pure loss of stability is the most influenced by this parameter. A particular explanation is needed when the bilge keel area variation is considered: results show a weak influence only on the excessive acceleration failure, while the other failures appear not to be linked with this parameter. It is necessary to highlight that, as far as parametric roll and dead ship condition failure modes, the bilge keel area affects only the standards. The criterion for pure loss of stability assessment does not include this parameter at all.

Focusing on the direction of the relationship between main parameters and criteria values, it is possible to deduce the following considerations: an increment of hull draught lead to a decrement of criteria outcomes for all the failure modes considered; this decrement is also confirmed between bilge keel area variations for the excessive acceleration phenomenon. As far as the breadth variation is concerned, the results points out that a direct relationship exists for all the failures excepting parametric roll.

It is worthwhile to remind that, to judge a ship vulnerable or not to a stability failure, the criterion should be compared with the standard. For parametric roll and excessive acceleration, a ship is considered to be not vulnerable if the criterion is lower than the standard; for pure loss of stability and dead ship condition it is the opposite.

6. CONCLUSION

In this paper, the first vulnerability levels of the Second Generation Intact Stability criteria have been considered excepting surf riding phenomenon. Thanks to the application of Design Structure Matrix, each failure has been systematically analysed and a set of main influencing parameter has been selected, also in a transversal perspective among the different stability failures. By means of a set of parent hull for a megayacht unit, the effects of a variation in breadth, draught and bilge keel area on the final criteria results have been studied. In order to quantify and compare each influence magnitude, a coefficient has been proposed, the so called K-index. As expected, it resulted that the modification in breadth is the most significant for all the phenomena assessed, with the lower influence on the excessive acceleration phenomenon. Regarding the draught and bilge keel area, their influences on the criteria in terms of absolute values is limited, but the outcomes point out the inverse relationship between these parameters and the criteria.

As a final comment to get advantage of such approach, it is important to keep in mind what follows: the criterion value, therefore the trend pointed out by the K-index, should be framed in the logic of comparison with the standard; e.g. for excessive acceleration, since the criterion should be lower than the standard to consider the ship not vulnerable, a negative sign of K-index means the ship improvement in her stability performance.

7. REFERENCES

Belenky, V., de Kat, J.O., Umeda, N., 2008, "Toward Performance-Based Criteria for Intact Stability", Marine Technology 45.

Belenky, V., Bassler, C.C., Spyrou, K.J., 2011, "Development of Second Generation Intact Stability Criteria", Hydromechanics Department Report, Naval Warfare Center Carderock Division, USA.

Eppinger, S.D. and Browning, T.R., 2012, "Design structure matrix methods and applications", MIT press, USA.

IMO, 2008, "Adoption of the International Code on Intact Stability", MSC Resolution MSC.267 (85).

IMO, 2015, "Development of Second Generation Intact Stability Criteria", SDC 2 / WP. 4.

IMO, 2016, "Finalization of Second Generation Intact Stability Criteria", SDC 3 / WP. 5.

Petacco, N. and Gualeni, P., 2016, "Second Generation Intact Stability criteria for mega-yachts: application and design consideration", Proceedings of 3rd International Conference on Maritime Technology and Engineering, Lisbon, PT.

Petkaş, Ş.T. and Pultar, M., 2006, "Modelling detailed information flows in building design with the parameter-based design structure matrix", Design Studies 27(1).

Qiao, L. and Ryan, M., 2015, "Applying the Design Structure Matrix (DSM) to SAR Satellite Formation Flying Design", Proceedings of System Engineering and Test & Evaluation conference (SETE), Canberra, AUS.

Schrøter, C., Lützen, M., Erichsen, H., Jensen, J.J., Kristensen, H.O., Lauridsen, P.H., Tunccan, O. and Terada, D., 2017, "Sample applications of the Second Generation Intact Stability Criteria – robustness and consistency analysis", Proceedings of the 16th International Ship Stability Workshop (ISSW), Belgrade, SRB.

Wynn, D.C., Wyatt, D.F., Nair, S.M.T. and Clarkson, P.J., 2010, "An Introduction to the Cambridge Advanced Modeller", Proceedings of 1st International Conference on Modelling ans Management of Engineering Processes (MMEP), Cambridge, UK.

Yassine, A.A., 2002, "An Introduction to Modelling and Analyzing Complex Product Development Processes Using the Design Structure Matrix (DSM) Method", Maine IEEE/PMI joint meeting, USA.

8. APPENDIX

Hereinafter, the Design Structure Matrices for the first vulnerability level of all stability failure are shown, excepting for Surf Riding/Broaching failure.

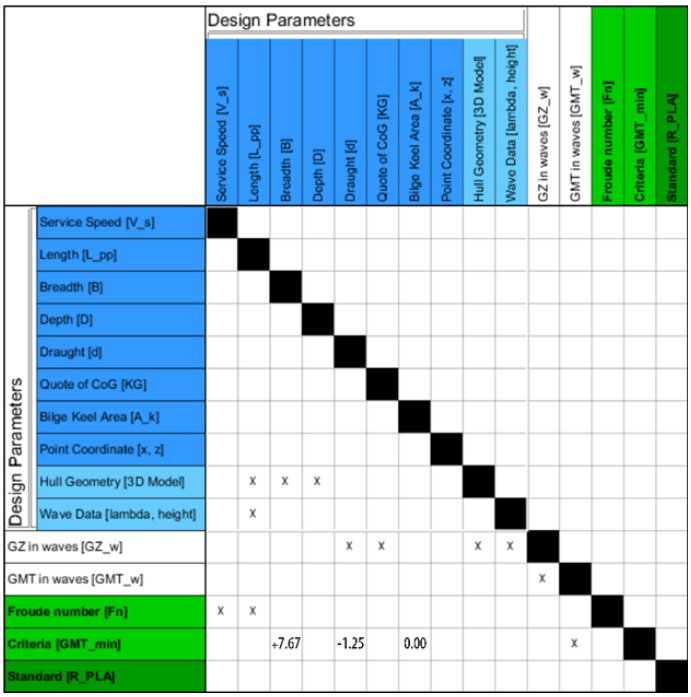

Figure 5: Design Structure Matrix of Pure loss of stability failure.

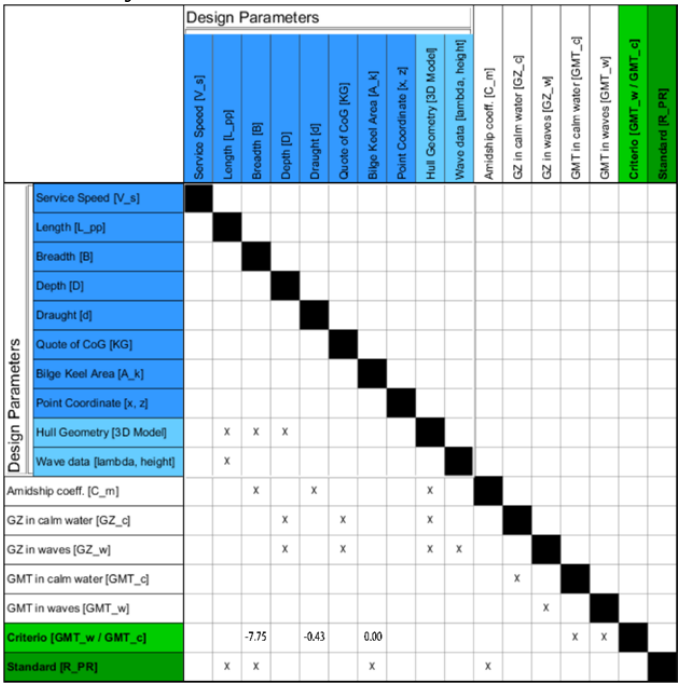

Figure 6: Design Structure Matrix of Parametric roll failure.

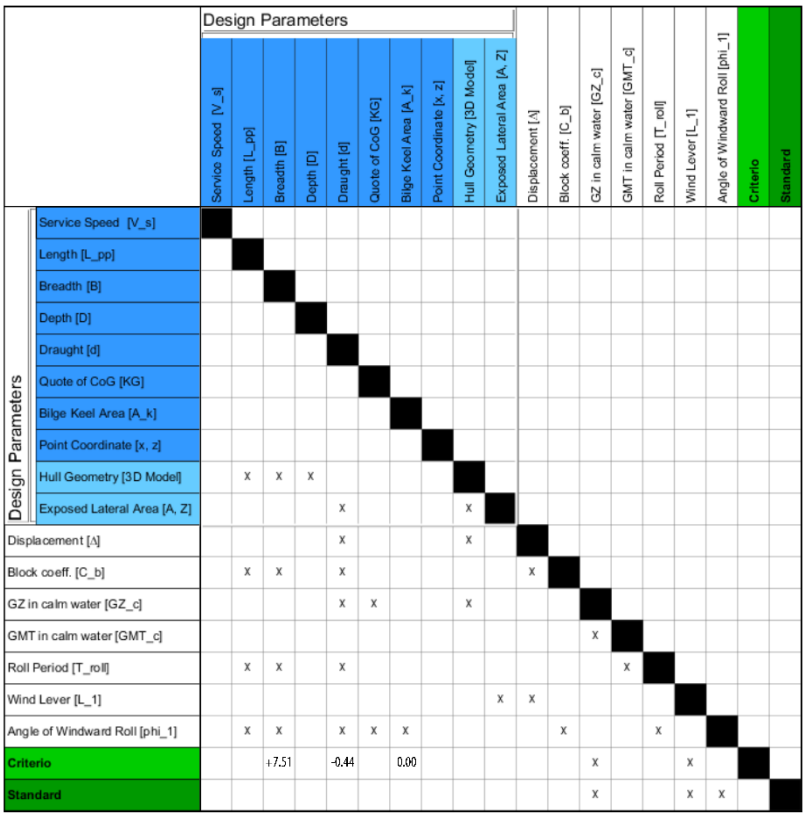

Figure 7: Design Structure Matrix of Dead ship condition failure.

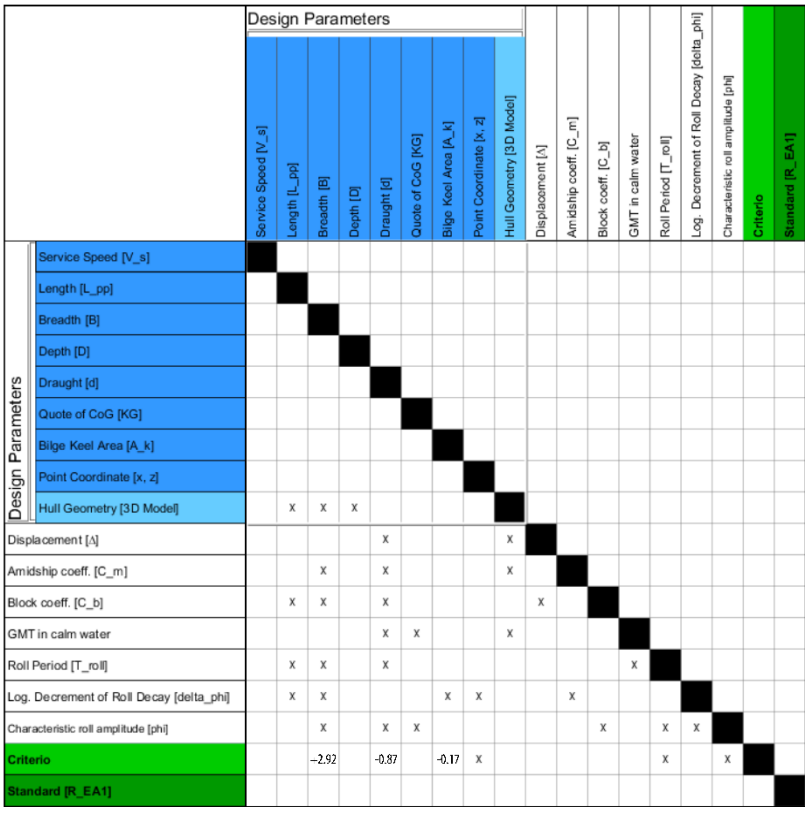

Figure 8: Design Structure Matrix of Excessive acceleration failure.

Operational Limitations of River-Sea Ships in the Framework of the Second Generation Intact Stability Criteria

Stefan Rudaković,
University of Belgrade, Faculty of Mechanical Engineering, Department of Naval Architecture
srudakovic@mas.bg.ac.rs

Igor Bačkalov,
University of Belgrade, Faculty of Mechanical Engineering, Department of Naval Architecture
ibackalov@mas.bg.ac.rs

ABSTRACT

The paper examines the possibilities for using the Second Generation Intact Stability Criteria (SGISC) framework in stability assessment and calculation of operational limitations of the river-sea ships. The level 2 vulnerability assessment procedures for dead ship condition and excessive accelerations are used to derive the operational limitations of a typical European inland container vessel in the North Sea coastal zone. The results are in good agreement with the operational experience in the designated area, but provide additional insights into safety of river-sea ships that could not have been observed by the classic stability analysis. It is shown that the approach used by the SGISC could be successfully applied to river-sea ships, provided that appropriate modifications of the Criteria are introduced.

Keywords: *river-sea ships, Second Generation Intact Stability Criteria, operational limitations, dead-ship condition, excessive accelerations*

1. INTRODUCTION

The river-sea ships are primarily inland vessels which are supposed to make short sea trips in coastal zones on a regular basis, provided that certain technical and environmental conditions are met. Such vessels are in operation in coastal areas of France, Belgium, Russia, India, China, etc. A particular concept of operational limitations is very well-known in the river-sea navigation. The existing regulations limit operation of river-sea ships in seaway by taking into account ship stability, seakeeping criteria and hull strength. The operational limitations of river-sea ships imposed by such regulations are typically related to wave height.

However, the common international regulatory framework for river-sea ships does not exist, not even on the European level. Instead, the national regulations and classification rules employing very dissimilar approaches are being used throughout the world, see Bačkalov (2012) and Chatelier et al (2017). Such regulations, being location-specific, are inevitably semi-empirical and tailored so as to take into account the design features of typical ships used in the designated navigation area, as well as the particular operational experience with such ships. In other words, the regulations successfully applied in one coastal zone may not

be appropriate for different ships sailing in another area.

On the other hand, the Second Generation Intact Stability Criteria (SGISC) framework foresees the introduction of operational limitations (OL) which could be regarded as limitations on the overall operability of the vessel in specific loading conditions (Bačkalov et al, 2016). While there is still no precise definition of operational limitations, there is a general agreement that OL could be developed using either vulnerability assessment level 2 (L2) or direct stability assessment (IMO, 2016a).

Furthermore, considering that the river-sea ships are unconventional both in terms of design and operation, the SGISC could represent a suitable option for stability assessment of such vessels. Therefore, the present paper explores the possibilities for using the SGISC framework as a basis for a coherent approach to calculation of operational limitations of river-sea ships, independent of their area-specific design features and in line with the current developments of ship stability criteria.

2. SAMPLE SHIP

The present investigation is conducted on a typical European inland container vessel, sailing along the Belgian shoreline, in the Southern North Sea coastal zone. The main particulars of the ship, corresponding to the design draught, are given in Table 1.

Table 1. Main particulars of the sample ship

length, L [m]	109.7
beam, B [m]	11.4
draught, d [m]	2.46
depth, D [m]	3.7
block coefficient, C_B [-]	0.868
mid-ship coefficient, C_M [-]	0.996
above water lateral area, AL [m^2]	646.9
wind moment lever, Z [m]	5.205
height of the wheelhouse above keel [m]	12.5
length of bilge keels, l_{bk} [m]	40
width of bilge keels, b_{bk} [m]	0.18

The body plan of the vessel is presented in Fig. 1. The cross sections are equally spaced at 500 mm distance whereby "0" represents the aftmost station. The ship has a single, box-shaped cargo hold without hatch covers, and a hydraulically operated, retractable wheelhouse. When fully loaded, the ship carries 192 TEUs in four tiers, four rows and 12 bays.

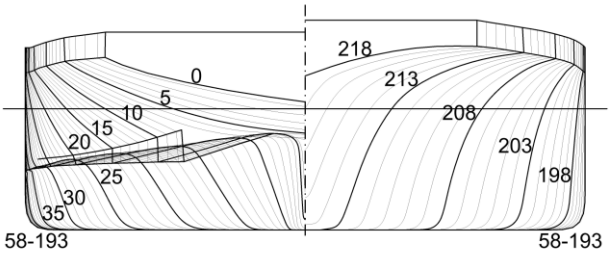

Fig. 1 The body plan of the sample ship

3. ISSUES IN APPLICATION OF THE SGISC FRAMEWORK TO RIVER-SEA SHIPS

The operational limitations are calculated taking into account stability failure modes relevant for the examined river-sea ship. Due to low Froude numbers at which they operate, the river-sea ships are not vulnerable to surf-riding and broaching. Considering the hull form features of the typical river-sea ships, the large variations of the righting arm in longitudinal waves which could lead to parametric roll or pure loss of stability are not to be expected, either.

It should be noted that most of the existing safety regulations for river-sea ships require assessment of stability in beam wind and waves (i.e. in the weather criterion scenario), and that some regulations pay particular attention to the level of lateral accelerations. For instance, according to the rules of the Russian River Register (RRR), the navigation area of

river-sea ships is determined by the so called "acceleration criterion" which requires verification of lateral accelerations and imposes 0.3*g* (where *g* stands for gravitational acceleration of 9.81 m/s^2) as the limiting value. In fact, the concept of excessive accelerations has been long known in the RRR regulations for the river-sea ships (see Lesyukov, 1974).

From the point of view of the SGISC, the draft regulations for excessive accelerations vulnerability assessment (IMO, 2016b) foresee that the stability of a ship should be checked with respect to this stability failure mode, in case that:

- the distance from the waterline to the highest location along the length of the ship where passengers or crew may be present exceeds 70% of the breadth of the ship; and
- the metacentric height exceeds 8% of the breadth of the ship.

Both conditions are satisfied for the examined ship at design draught, given that the helmsman position in the wheelhouse is around 10 m above the waterline (≈88% of the ship's breadth), while the realistic metacentric heights are in range of 15% ÷ 26% of the ship's breadth.

Therefore, the focus of the present investigation is on the large amplitudes of roll that could be attained in beam wind and waves (i.e. in the dead ship condition) and on excessive lateral accelerations in beam seas. The vulnerability to these two stability failure modes is assessed by calculating the capsize index (*CI*) and the exceedance index (*EI*), respectively. In order to derive the *CI* and the *EI* for the sample ship, the SGISC formulas and procedures were used as far as it was possible. However, this was not a straightforward process, due to a range of issues related to both the design and the operational features of the river-sea ships. The issues encountered in application of the SGISC to river-sea ships are herein discussed.

3.1 Roll Damping of River-Sea Ships

Within the SGISC framework, the use of simplified Ikeda's method for roll damping assessment is recommended in absence of either experimental data or another, more suitable method. Such approach would also apply to inland vessels, for which the available experimental data are scarce and unreliable. On the other hand, the sample ship falls out of scope of application of the simplified Ikeda's method due to high values of *B/d*, C_B and C_M. In addition, *OG/d* values may also be out of range of method application. In general, this is valid for almost all inland vessels. The applicability of simplified Ikeda's method on inland vessels was the subject of the study by Rudaković & Bačkalov (2017), where an adjustment of the eddy-making damping component was proposed in order to deal with the inaccuracies in roll damping prediction that arise at $C_B > 0.74$. Thus, in the present paper, the "modified" simplified Ikeda's method, as proposed by Rudaković & Bačkalov (2017), was adopted. Nevertheless, the problem of appropriate roll damping assessment of river-sea ships is not completely resolved and deserves more attention.

3.2 The Wind and Wave Climate

The SGISC define the "standard environmental conditions" that ought to be applied in stability assessment, but make provisions for using "alternative environmental conditions", that is, other data that are deemed to be more appropriate in the case of restricted navigation or operational limitations (IMO, 2016c). For the purposes of the present analysis, the use was made of the available wind and wave measurements in Belgian coastal zone (see Chatelier et al, 2017). The wave scatter diagram is given in Appendix to this paper. Furthermore, for the purposes of this paper, the following relation between the mean wind speed U_w and significant wave height H_s was established:

$$U_w = 11.75 \cdot H_s^{0.375} . \quad (1)$$

In Fig. 2, equation (1) is compared to the wind-wave relation as given in the draft vulnerability criteria of level 2 for the dead ship condition stability failure mode (IMO, 2015). It may be noticed that the same significant wave height in the coastal zone is associated with stronger winds than in the open sea.

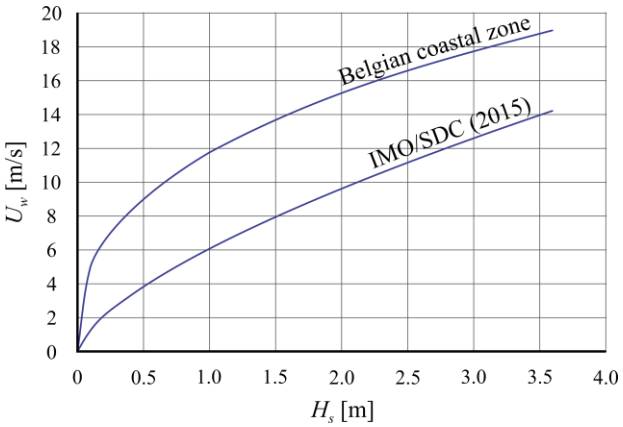

Fig. 2 Adopted relation between mean wind speed and significant wave height in Belgian coastal zone

The JONSWAP wave spectrum was adopted as the alternative to the standard spectrum foreseen by vulnerability criteria IMO (2015). This approach has proved to be successful in other studies of the North Sea coastal environment, see van Essen and Peters (2017), Chatelier et al (2017) and Verwaest et al (2008).

3.3 Applicability of Standards and Acceptable Safety Levels

The subject of the relevant stability failures and acceptable probability of their occurrence is probably the most delicate issue in this analysis.

For inland container vessels, which do not have hatch covers, the critical stability failure is usually the heeling to the angle of submergence of the hatch coaming. Thus, in such cases, the capsize index (which could be regarded as the long-term probability of attaining critical angle of heel) is actually the index of flooding of unprotected cargo hold. Concerning the limiting value of *CI* within the SGISC framework, acceptable safety level for the dead ship condition has been sought upon the grounds of consistency between the vulnerability levels 1 and 2, see Umeda and Francescutto (2016). In that case, the Severe wind and rolling criterion (Weather Criterion), as given in Intact Stability (IS) Code part A/2.3, but with the modified wave steepness factor *s*, forms the vulnerability level 1. Although the final value of *CI* is still not adopted, 0.04 and 0.06 are presently being discussed as possible safety levels.

It was already pointed out that the existing safety regulations for river-sea ships contain mandatory assessment of dynamic stability which follows the concept of the IS Code Weather Criterion (see Bačkalov, 2012). Nevertheless, although the scenario of these weather criteria is for the most part the same as in the IS Code, some specific aspects, such as wind pressure, resonant roll amplitude assessment, etc. may differ. Moreover, the weather criteria used are not uniform across the regulations for river-sea ships. This is not surprising because the rules are area-specific. Therefore, establishing the acceptable capsize index of river-sea ships based on consistency of two vulnerability levels could be a challenging task.

With respect to excessive accelerations, presently, the proposed L2 standard is derived based on the *Chicago Express* accident during which lateral accelerations in the wheelhouse attained 1*g* (BSU, 2009). The long-term attained exceedance index (which could be regarded as the long-term probability of attaining lateral acceleration of 1*g*) calculated for *Chicago Express* in the loading condition at the time of accident is $EI = 1.094 \cdot 10^{-4}$.

Although the same standards and safety levels developed for the seagoing ships may not be applicable to inland vessels in maritime operations, $CI = 0.04$ and $EI = 1 \cdot 10^{-4}$ are maintained in the current investigation. Their influence on the outcome of the analysis will be discussed later in the paper.

3.4 Other Issues

Some other practical issues may also arise in application of the SGISC framework to the river-sea ships. For instance, the estimation of the natural roll period of the sample ship depends on the roll radius of gyration, which is presently calculated using the formula prescribed by the Weather Criterion and developed for the seagoing ships. Similarly, the effective wave slope function is calculated using the "standard methodology" as given in the draft explanatory notes IMO (2016c), although the suitability of this method for inland vessels is yet to be ascertained.

4. DISCUSSION OF RESULTS

The capsize index *CI* and exceedance index *EI* of the sample ship are determined as weighted averages of short-term indices CI_S and EI_S which are calculated for each sea state in the wave scatter diagram:

$$CI = \sum_{i=1}^{N} W_i \cdot CI_{S,i}\,, \tag{2}$$

$$EI = \sum_{i=1}^{N} W_i \cdot EI_{S,i}\,, \tag{3}$$

where W_i represents the probability of occurrence of a sea state. It is considered that the procedures for calculation of *CI* and *EI* are well described in explanatory notes IMO (2016c) and IMO (2016b) and therefore need not to be reproduced here. The calculations are carried out for the complete scatter diagram (up to H_s = 3.6 m) as well as for the scatter diagram limited by the following wave heights: 3.0 m, 2.5 m, 2.0 m, 1.5 m, 1.0 m and 0.5 m. Whenever the wave height limitation is introduced, the wave scatter diagram is re-normalised in such way that the total probability of occurrence of sea states is equal to 1. Both *CI* and *EI* are calculated for a series of metacentric heights. The goal is to determine a range of loading conditions for which both *CI* and *EI* are below the limiting values in navigation up to a given significant wave height. For instance, if indices *CI* and *EI* calculated for the examined ship in a given loading condition do not exceed critical levels in waves up to H_s = 3.6 m, then the navigation in the designated area would be unrestricted in the loading case considered. Conversely, if either *CI* or *EI* are above the limiting values in e.g. waves up to H_s = 2 m, the navigation should not be permitted if weather conditions exceed this significant wave height.

The efficiency of the following options for improvement of operability of river-sea ships is examined: the addition of bilge keels, as a cost-effective design measure, as well as the lowering of metacentric height and the reduction of the draught, as possible operational measures in sea voyages.

4.1 The Influence of Bilge Keels

As inland vessels typically do not have bilge keels, *CI* and *EI* are calculated for the sample vessel both without and with bilge keels. The results are given in Fig. 3 ÷ 6, where each curve corresponds to a limiting significant wave height. The shaded areas in the charts correspond to $CI \geq 0.04$ and $EI \geq 1 \cdot 10^{-4}$. The angle of flooding of cargo hold is 21.3°. The calculations are performed in range $GM = 0 \div 3$ m, whereby it should be noted that the metacentric heights above GM = 3 m are virtually unrealistic for loading cases with four container tiers, while GM = 1.7 m corresponds to a uniform vertical distribution of cargo weight (i.e. a case in which loaded containers have equal weight). Therefore, GM = 1.7 m (marked in Fig. 3 ÷ 6 with a dashed vertical line) could be regarded as the minimal metacentric height from the point of view of the conventional loading practice.

As expected, the bilge keels have a positive effect on safety of the sample ship. For instance, the capsize index for GM = 1.7 m in waves up to H_s = 2 m decreases from $CI = 9 \cdot 10^{-3}$ for the ship without bilge keels (Fig. 3) to $CI = 9 \cdot 10^{-5}$ for the ship equipped with bilge keels (Fig. 4). If the navigation is limited to H_s = 2 m, the

range of "safe" metacentric heights, for which $CI < 0.04$, increases from $\Delta GM = 0.3$ m (Fig. 3) to $\Delta GM = 0.8$ m (Fig. 4) thanks to addition of bilge keels.

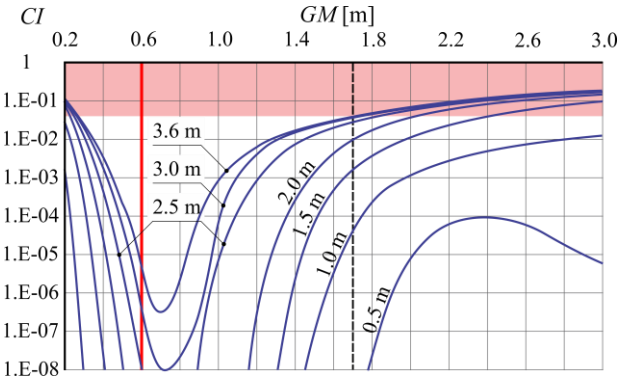

Fig. 3 Capsize indices of the sample ship without bilge keels, at $d = 2.46$ m. Each curve corresponds to a limiting H_s.

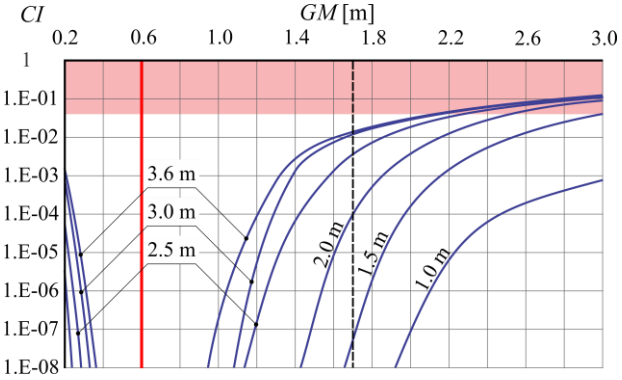

Fig. 4 Capsize indices of the sample ship with bilge keels, at $d = 2.46$ m. Each curve corresponds to a limiting H_s.

The similar conclusions are valid for excessive accelerations vulnerability assessment. In waves up to $H_s = 2$ m the ship equipped with bilge keels could be considered as safe from excessive accelerations in the complete range of possible metacentric heights (Fig. 6). Within the same range of weather conditions, the maximal metacentric height of the ship without bilge keels would be limited to 2.2 m (Fig. 5).

The unrestricted service in the area (i.e. in waves up to $H_s = 3.6$ m) would require that the metacentric height of the ship without bilge keels does not exceed 1.6 m (Fig. 5), which is below the value that could be attained by uniform vertical distribution of cargo weight. If the bilge keels are installed, the unrestricted service becomes possible for metacentric heights below ≈2.2 m.

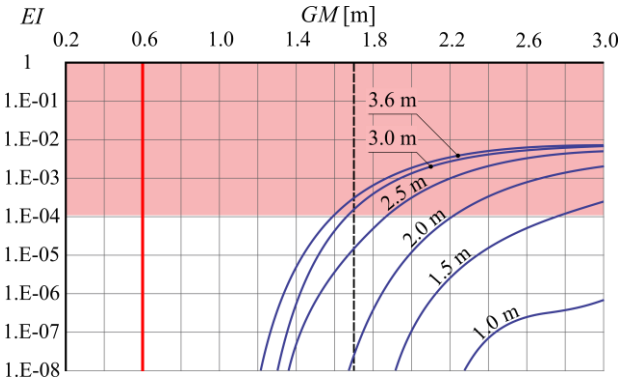

Fig. 5 Exceedance indices of the sample ship without bilge keels, at $d = 2.46$ m. Each curve corresponds to a limiting H_s.

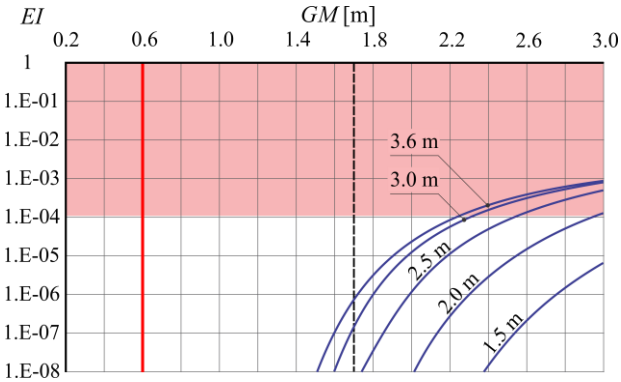

Fig. 6 Exceedance indices of the sample ship with bilge keels, at $d = 2.46$ m. Each curve corresponds to a limiting H_s.

4.2 The Influence of Reduced *GM*

The performed analysis indicates that the OL of the vessel could be further expanded by employing an operational measure quite different from the ones anticipated. Namely, Fig. 3 ÷ 6 show that the optimal metacentric height, from the point of view of ship stability in waves, would be around $GM = 0.7$ m. This value is far below the usual metacentric heights

for inland container vessels of this class with four container tiers at the design draught. Indeed, the metacentric heights below 1.7 m could not be attained unless heavier containers are loaded atop of lighter ones. The very minimal metacentric height that could be achieved by placing heavier containers in top tiers is *GM* = 0.6 m. This metacentric height is marked by the full red vertical line in Fig. 3 ÷ 6. Although such unconventional vertical distribution of cargo contradicts standard loading practices, it would be clearly beneficial for the stability of the examined river-sea ship in seaway.

The contribution of bilge keels and reduced metacentric heights to safety of the sample ship in sea voyages is evident from the OL given in Fig. 7 and 8. The shaded areas in the Figures represent the range of attainable and acceptable metacentric heights (for which both *CI* and *EI* are below the adopted safety levels) plotted as a function of H_s. As in the Fig. 3 ÷ 6, the dashed line corresponds to minimal metacentric height with respect to the usual loading practices (*GM* = 1.7 m), while full red line represents the minimal metacentric height (*GM* = 0.6 m) that could be achieved by an unconventional vertical distribution of cargo weight. If, by a proper distribution of the container weights, the metacentric height is reduced below 1.6 m, the sample ship would be safe in all expected weather conditions, even without bilge keels.

It should be noted that the operational limitations derived from the dead ship condition vulnerability assessment are, in the present case, stricter in comparison to the limitations imposed by the excessive accelerations. This interesting outcome will be discussed later in more detail.

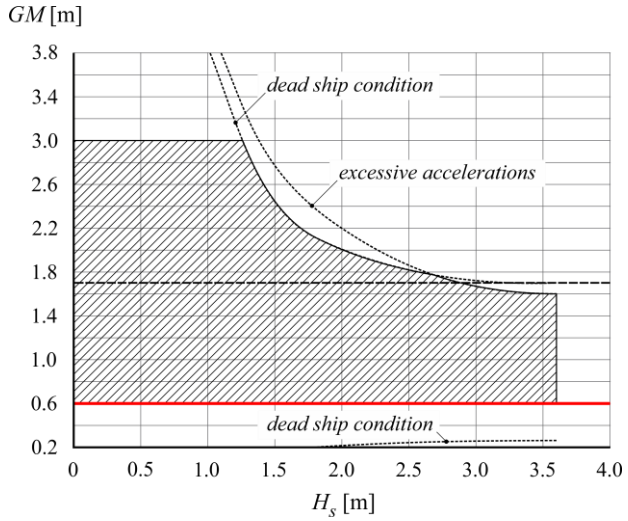

Fig. 7 Operational limitations of the sample ship without bilge keels, at *d* = 2.46 m

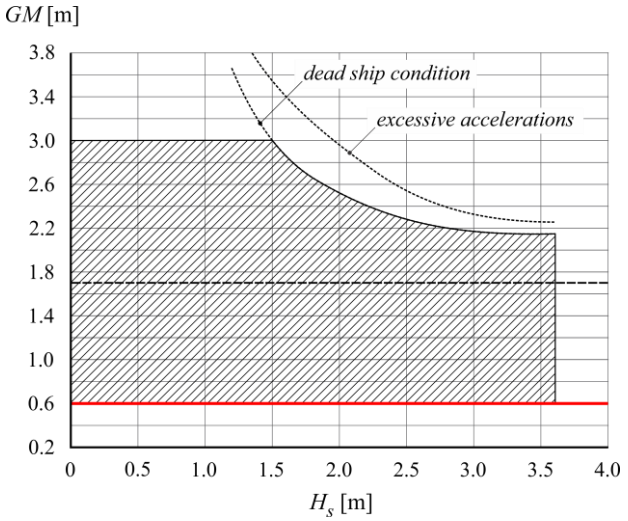

Fig. 8 Operational limitations of the sample ship with bilge keels, at *d* = 2.46 m

4.3 The Influence of Reduced Draught

Some regulations impose draught restrictions on inland vessels when operating in maritime stretches: the vessel is required to sail with the draught which is reduced in comparison to the (design) draught intended for inland navigation. To examine the effectiveness of such approach, *CI* and *EI* are calculated for the sample vessel, equipped with bilge keels, sailing at *d* = 2 m, loaded with four container tiers. In this case, the angle of flooding of cargo hold is 25.9°. The results are shown in Fig. 9 and 10. The capsize indices, as well as the exceedance indices of lateral accelerations, decrease in comparison to the design draught. Therefore, for any value of *GM*, the ship would be safer (from the stability point of view) at reduced draught than at the design draught.

However, the range of metacentric heights that could be attained by varying vertical distribution of cargo weight changes as well, to GM = 2.8 ÷ 3.8 m. Again, the lower value in the range is achieved by uniform distribution of container weight over the tiers. Thus, if the wave height reaches H_s = 2.5 m, the vessel with four container tiers at d = 2 m could be merely marginally safe, whereby this could be achieved only at quite specific loading case. The OL derived for the examined case (Fig. 11) show that even if the navigation is limited to waves up to H_s = 2 m, the range of acceptable metacentric heights would be less than 0.3 m, making stability of the vessel susceptible to e.g. loading errors.

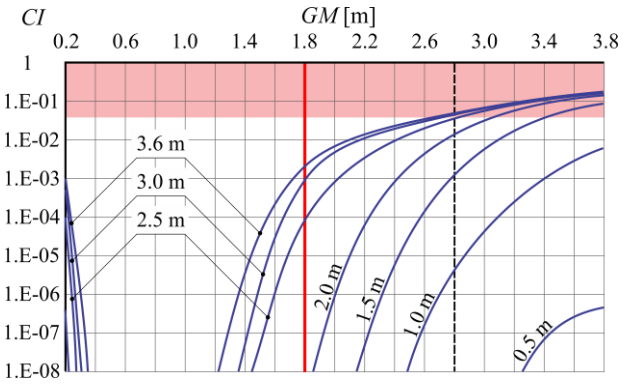

Fig. 9 Capsize indices for sample ship with bilge keels, at d = 2 m. Each curve corresponds to a limiting H_s.

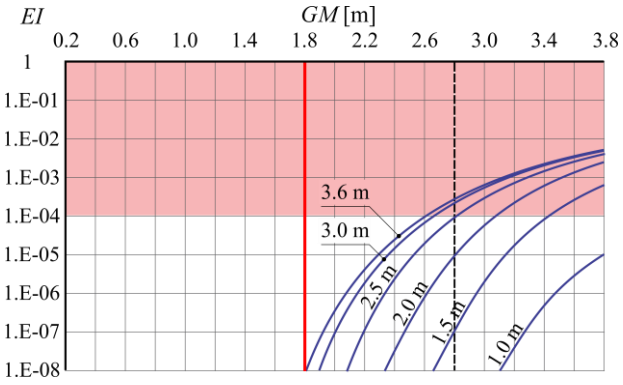

Fig. 10 Exceedance indices for sample ship with bilge keels, at d = 2 m. Each curve corresponds to a limiting H_s.

Further reduction of metacentric height is possible only if heavier containers are loaded in top tiers. The minimal metacentric height which could be attained in this way is GM = 1.8 m (full red line in Fig. 9 ÷ 11). This operational measure could indeed considerably expand the OL of the ship at reduced draught (Fig. 11) but it would not improve the operability in comparison to the navigation at the design draught (Fig. 8). Additionally, considering that the payload at d = 2 m would be decreased by some 500 t, the vessel would not benefit from the analysed draught restriction.

Although the dead ship condition could be formally considered as the prevailing stability failure mode at the reduced draught as well, the difference between the requirements of the two vulnerability criteria is practically negligible (Fig. 11).

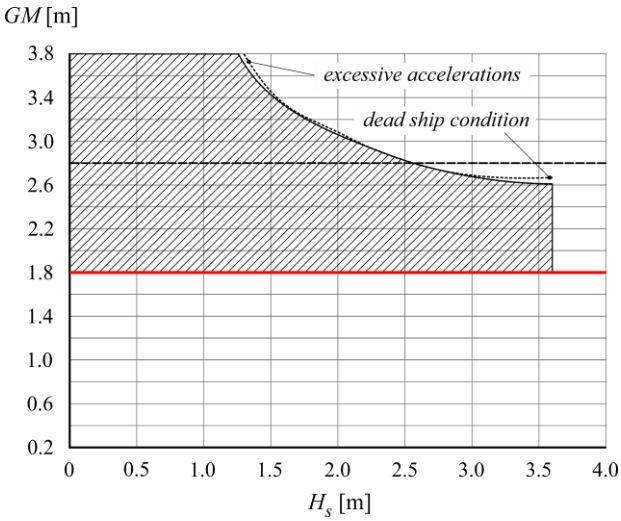

Fig. 11 Operational limitations of the sample ship with bilge keels, at d = 2 m

4.4 The Influence of Adopted Standards and Safety Levels

The results indicate that the lateral accelerations would not present the main limiting factor in operation of the sample ship (in particular at the design draught), if the same stability failure (i.e. the lateral acceleration of 1g) and related safety level (EI = $1 \cdot 10^{-4}$) as foreseen by the vulnerability criteria for the seagoing ships are adopted for the river-sea vessels too. Indeed, for most of the examined cases, the maximal metacentric heights, calculated using the excessive accelerations vulnerability criterion, is greater than the maximal GM value obtained by

the dead ship condition vulnerability assessment (see Fig. 7 and Fig. 8). In other words, the excessive accelerations criterion is generally less stringent when the examined ship is at design draught than the dead ship condition vulnerability criterion.

Such outcome is somewhat unexpected and in contrast with some regulations (e.g. the Russian River Register) which use the level of estimated lateral accelerations to define the operational limitations of river-sea ships. This potential inconsistency between the SGISC approach and operational experience with the examined type of vessels highlights the issue of appropriate stability standards and safety levels for river-sea ships. Thus, there are two possibilities. On one hand, it is possible that the adopted safety level for dead ship condition stability failure (CI = 0.04) is too stringent. Indeed, if a higher capsize index (e.g. CI = 0.06) is applied, the difference between the two examined vulnerability criteria would not be so pronounced and, in some cases, the excessive accelerations would be the dominant stability failure mode (Fig. 12).

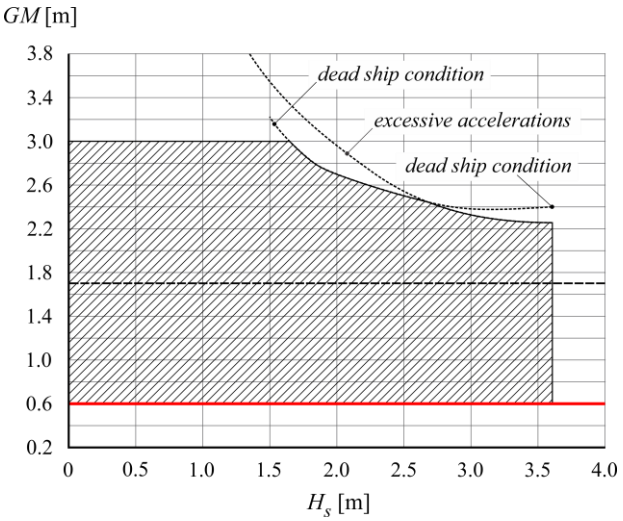

Fig. 12 Operational limitations of the sample ship with bilge keels, at d = 2.46 m, (CI = 0.06)

On the other hand, the question is whether accelerations of 1g could be too high for inland vessels and if a lower, more probable (and thus, more limiting) value could be more appropriate. Namely, the effect of lateral accelerations on people onboard is normally related to motion induced interruption (MII), i.e. sliding and tipping events. In the wheelhouse, such events could be prevented or diminished by design measures, that is, by appropriate bridge ergonomics, including sufficient number and a proper arrangement of handhelds. However, European technical standards for inland vessels (CESNI, 2015) do not contain particular requirements for bridge ergonomics that would address the safety of crew due to MII. On the other hand, as Bačkalov et al (2016) emphasized, the safety cannot be achieved by design measures only. In fact, the safety-by-design is complemented by skills, knowledge, appropriate training and experience of Master and crew, which is often referred to as "prudent seamanship". The question is, however, whether Masters and crews of inland vessels, which spend just a fraction of sailing time at sea, have a level of "prudent seamanship" sufficient to compensate for inadequate design. In addition, increased physical efforts required to maintain the posture due to vessel motion could lead to mental fatigue, decreased attention and cognitive performance of the crew. Therefore, it seems that neither suitable design nor appropriate operational safety measures are in place that would justify the same critical level of lateral accelerations as on the seagoing ships.

5. CONCLUSIONS

The present paper investigates the use of the Second Generation Intact Stability Criteria framework in calculation of operational limitations of river-sea ships from the stability point of view. The river-sea ships are actually "vessels intended for navigation on inland waterways and suitable for restricted navigation at sea" (Chatelier et al, 2017). As such, the river-sea ships in general do not comply with the major international safety regulations, such as SOLAS and ICLL. Consequently, the river-sea ships are unconventional from the design point of view, with respect to the typical hull-forms, main dimensions and their ratios, and compliance of the design with the maritime safety regulations. Furthermore, the river-sea ships

are unconventional from the operational point of view as well, with respect to the very notion of inland vessels sailing at sea and "prudent seamanship" of their crews. Hence, the authors believe that the safety assessment of inland vessels in maritime operations should be performed by methods taking into account, as far as practicable, ship dynamics in realistic weather conditions.

It is considered that a necessary balance of complexity of calculations and accuracy of physical modelling is achieved by the vulnerability assessment level 2 of the Second Generation Intact Stability Criteria. However, the application of the SGISC to the river-sea ships requires some modifications related to roll damping assessment, the use of location-specific environmental conditions, estimation of natural roll period, etc. Although the present analysis is performed on one sample vessel only, in a specific navigation area, the outlined approach, along with the dilemmas related to its use, apply to river-sea ships in general.

The results of the analysis are generally in good agreement with the operational experience in the Southern North Sea coastal zone, where river-sea ships nowadays operate in $H_s \approx 1.6 \div 2$ m. As expected, a modest modification of the hull such as addition of bilge keels, proved to be beneficial for the safety of the vessel. However, it was demonstrated that the draught reduction, which is sometimes imposed as an operational safety measure, would not expand the operational limitations of the vessel in realistic loading conditions. Furthermore, it was shown that an unconventional vertical distribution of cargo weight, i.e. loading of heavier containers in top tiers, resulting in lower metacentric heights, would have a positive effect on stability of the examined vessel in seaway. It should be emphasized that such results could not have been obtained by means of classic ship stability analysis, which is used in many existing regulations for river-sea ships.

The analysis indicated that the main limiting factor in operation of the sample ship, from the ship stability point of view, would be the large amplitudes of roll attained in beam wind and waves, that is, the dead ship condition vulnerability assessment would be the prevailing stability criterion. This outcome is the consequence of adopted stability failures and safety levels which correspond to the current proposals for seagoing ships. The critical stability failures and levels of corresponding indices that would be adequate for stability assessment of the river-sea ships need to be further investigated.

From the point of view of implementation in the regulatory framework, the examined approach could be classified as a "pre-computation and approval in the design stage" option for preparation of OL (see the proposal for guidelines for the preparation and approval of operational limitations IMO, 2017). A relatively large number of calculations that ought to be performed for a series of relevant loading cases, container arrangements and draughts could be a potential drawback of the approach. Additionally, unlike for seagoing ships, the verification of container mass prior to loading is still not mandatory for inland vessels. Therefore, there are uncertainties related to vertical centre of gravity and roll radius of gyration / natural roll period in a given loading condition, affecting the accuracy of stability assessment. Notwithstanding these practical yet solvable difficulties, the authors believe that the Second Generation Intact Stability Criteria could be a promising solution for a common approach to assessment of operational limitations of river-sea ships.

6. ACKNOWLEDMENTS

The paper is part of the project "Development of Next Generation of Safe, Efficient, Ecological (SE-ECO) Ships" executed by Department of Naval Architecture, Faculty of Mechanical Engineering University of Belgrade. The project is partly financed by Serbian Ministry of Education, Science and Technology Development, Contract No. TR35009.

The authors would like to thank Professor Milan Hofman (University of Belgrade) for valuable suggestions and comments in course of the study.

7. REFERENCES

Bačkalov, I., 2012, "A probabilistic analysis of stability regulations for river-sea ships", Proceedings of the 11th International Conference on the Stability of Ships and Ocean Vehicles (STAB 2012), Athens, pp. 67-77.

Bačkalov, I., Bulian, G., Rosén, A., Shigunov, V., Themelis, N., 2016, "Improvement of ship stability and safety in intact condition through operational measures: challenges and opportunities", Ocean Engineering, Vol. 120, pp. 353-361.

BSU (Bundesstelle für Seeunfalluntersuchung), 2009, "Very serious marine casualty: Fatal accident on board of CMV Chicago Express during typhoon 'Hagupit' on 24 September 2008 off the coast of Hong Kong", Investigation report, Hamburg.

CESNI (European Committee for drawing up Standards in the field of Inland Navigation), 2015, "European Standard laying down technical requirements for Inland Navigation vessels (ES-TRIN)", Strasbourg.

Chatelier, J.M., Nzengu, W.N., Cocito, R., 2017, "Stability and seakeeping of river-sea vessels – classification rules", Proceedings of the 16th International Ship Stability Workshop (ISSW 2017), Belgrade, pp. 149-158.

IMO, 2015, Sub-committee on Ship Design and Construction, 3rd session, Agenda item 6 (SDC 3/INF.10), "Information collected by the Correspondence Group on Intact Stability regarding second generation intact stability criteria", Submitted by Japan, London.

IMO, 2016a, Sub-committee on Ship Design and Construction, 4th session, Agenda item 5 (SDC 4/5), "Report of the working group at SDC 3 (part 2)", Submitted by the Chairman of the Working Group, London.

IMO, 2016b, Sub-committee on Ship Design and Construction, 4th session, Agenda item 5 (SDC 4/5/1/Add.4-Annex 5) "Draft Explanatory Notes on the vulnerability of ships to the excessive acceleration stability failure mode", Submitted by Japan, London.

IMO, 2016c, Sub-committee on Ship Design and Construction, 4th session, Agenda item 5 (SDC 4/5/1/Add.3-Annex 4) "Draft Explanatory Notes on the vulnerability of ships to the dead ship stability failure mode", Submitted by Japan, London.

IMO, 2017, Sub-committee on Ship Design and Construction, 5th session, Agenda item 6 (SDC 5/6/9), "Finalization of the draft guidelines for the specification of direct stability assessment, and for the preparation and approval of operational limitations and operational guidance", Submitted by Germany, London.

Lesyukov, V.A., 1974, "Theory and design of inland vessels" (In Russian), Transport, Moscow.

Rudaković, S., Bačkalov, I., 2017, "On application of standard methods for roll damping prediction to inland vessels", Proceedings of the 16th International Ship Stability Workshop (ISSW 2017), Belgrade, pp. 159-166.

Russian River Register, 2015, "Rules for classification of ships for inland and combined (river-sea) navigation", Moscow.

Umeda, N., Francescutto, A., 2016, "Current state of the second generation intact stability criteria – achievements and remaining issues", Proceedings of the 15th International Ship Stability Workshop (ISSW 2016), Stockholm, pp. 3-9.

van Essen, S., Peters, H., 2017, "Choosing the safest wave", The Naval Architect, October issue, pp. 49-53.

Verwaest, T., Doorme, S., Verelst, K., Trouw, K., 2008, "The wave climate in the Belgian coastal zone", Proceedings of the 9th Inter-

national Conference LITTORAL 2008, A Changing Coast: Challenge for the Environmental Policies, pp. 1-8.

APPENDIX

Table 2. Wave scatter diagram of the Belgian coastal zone (H_s is the significant wave height, T_p is the peak period)

Sum	0.01	0.70	5.73	16.96	27.61	20.58	13.83	7.48	3.87	1.83	0.84	0.50	0.07	0.000	100.0
3.6	0	0	0	0	0	0	0	0	0	0	0	0	0.01	0	0.01
3.5	0	0	0	0	0	0	0	0	0	0	0	0.03	0	0	0.03
3.4	0	0	0	0	0	0	0	0	0	0	0	0.01	0.01	0	0.02
3.3	0	0	0	0	0	0	0	0	0	0	0	0.01	0.01	0	0.02
3.2	0	0	0	0	0	0	0	0	0	0	0.01	0.03	0.01	0	0.05
3.1	0	0	0	0	0	0	0	0	0	0	0.04	0.05	0	0	0.09
3.0	0	0	0	0	0	0	0	0	0	0	0.04	0.1	0	0	0.14
2.9	0	0	0	0	0	0	0	0	0.01	0.02	0.04	0.1	0.01	0	0.18
2.8	0	0	0	0	0	0	0	0.01	0.03	0.02	0.09	0.07	0	0	0.22
2.7	0	0	0	0	0	0	0	0.03	0.01	0.07	0.09	0.03	0	0	0.23
2.6	0	0	0	0	0	0	0	0.02	0.04	0.15	0.11	0.01	0	0	0.33
2.5	0	0	0	0	0	0	0	0.07	0.1	0.08	0.07	0.01	0.01	0	0.34
2.4	0	0	0	0	0	0	0	0.07	0.07	0.21	0.1	0	0.01	0	0.46
2.3	0	0	0	0	0	0	0.04	0.06	0.14	0.18	0.07	0.02	0	0	0.51
2.2	0	0	0	0	0	0	0.04	0.05	0.15	0.12	0.02	0.01	0	0	0.39
2.1	0	0	0	0	0	0	0.1	0.12	0.17	0.14	0.01	0	0	0	0.54
2.0	0	0	0	0	0	0.02	0.07	0.17	0.13	0.1	0.02	0	0	0	0.51
1.9	0	0	0	0	0	0.03	0.26	0.22	0.2	0.07	0.01	0	0	0	0.79
1.8	0	0	0	0	0.01	0.13	0.33	0.33	0.27	0.09	0	0	0	0	1.16
1.7	0	0	0	0	0.01	0.18	0.44	0.53	0.3	0.07	0	0	0	0	1.53
1.6	0	0	0	0	0.01	0.42	0.7	0.63	0.22	0.01	0.01	0	0	0	2.00
1.5	0	0	0	0	0.11	0.58	0.79	0.57	0.14	0.01	0	0	0	0	2.20
1.4	0	0	0	0	0.24	0.61	0.87	0.36	0.15	0.02	0	0	0	0	2.25
1.3	0	0	0	0.01	0.41	0.84	1.11	0.45	0.18	0.06	0.01	0	0	0	3.07
1.2	0	0	0	0.07	0.93	1.38	1.16	0.42	0.16	0.05	0.04	0	0	0	4.21
1.1	0	0	0	0.24	1.31	1.65	1.12	0.41	0.11	0.03	0.03	0	0	0	4.90
1.0	0	0	0.02	0.62	1.93	1.85	0.92	0.26	0.02	0.03	0	0	0	0	5.65
0.9	0	0	0.08	0.98	2.53	1.72	0.72	0.15	0.09	0.01	0	0	0	0	6.28
0.8	0	0	0.25	1.56	3.36	1.9	0.63	0.18	0.1	0.02	0	0	0	0	8.00
0.7	0	0	0.6	2.29	3.42	2.12	0.55	0.32	0.18	0.04	0.01	0.01	0	0	9.54
0.6	0	0.03	1.16	2.68	3.18	1.56	0.77	0.33	0.24	0.07	0.01	0.01	0	0	10.04
0.5	0	0.27	1.32	3.36	3.1	2.03	1.15	0.8	0.32	0.1	0.01	0	0	0	12.46
0.4	0.01	0.35	1.45	3.13	3.76	2.21	1.31	0.65	0.3	0.04	0	0	0	0	13.21
0.3	0	0.05	0.85	2.02	3.3	1.35	0.75	0.27	0.04	0.02	0	0	0	0	8.65
H_s / T_p	3.0 – 3.5	3.5 – 4.0	4.0 – 4.5	4.5 – 5.0	5.0 – 5.5	5.5 – 6.0	6.0 – 6.5	6.5 – 7.0	7.0 – 7.5	7.5 – 8.0	8.0 – 8.5	8.5 – 9.0	9.0 – 9.5	9.5 – 10	Sum

Meta-model assessing the probability of exceeding the allowed acceleration limits, with the use of Bayesian network

Tomasz Hinz, Aalto University, Finland; Waterborne Transport Innovation, Poland; Deltamarin LTD, Poland; tomasz.hinz@aalto.fi

Maria Acanfora, Department of Industrial Engineering, University of Naples "FEDERICO II"; maria.acanfora@unina.it

Jakub Montewka, Faculty of Navigation, Gdynia Maritime University, Poland; j.montewka@wn.am.gdynia.pl

Krata Przemyslaw, Faculty of Navigation, Gdynia Maritime University, Poland; p.krata@wn.am.gdynia.pl

Jerzy Matusiak, Aalto University, Finland; jerzy.matusiak@aalto.fi

ABSTRACT

Two stability related accidents are especially relevant to container ships, mainly due to their flared hull shape and cargo stowing patterns. They are parametric roll and synchronous roll, both resulting in excessive acceleration. Moreover, the actual loading conditions, which often vary from the declared one, and the expected weather conditions, remain uncertain and thus difficult to describe in a deterministic manner. Therefore, we present a concept of a causal probabilistic model suitable for the stability-related safety assessment of a container ship. The two modes of resonant rolling are studied, accounting for the pertinent elements of uncertainty. The model structure is constructed on the basis of data obtained by means of a series of simulations with the use of 6 DoF the state-of-art ship motion model called LaiDyn. For a selected container ship type C11 we adopted typical loading case with the KG fluctuation. Subsequently, the obtained data are organized into a probabilistic meta-model with the use of Bayesian learning techniques. The model sensitivity is examined concerning the weather conditions, which bear a significant amount of uncertainty in the day-to-day operations of container ships.

Keywords: *excessive acceleration, Bayesian network, container vessel motion*

1. INTRODUCTION

In 1998 an accident related to resonance rolling took place, involving a C11 class container vessel. The incident triggered a significant development in researches regarding the parametric resonance phenomenon. Great deal of research has been conducted, in the aftermath of this accident, for example (Acanfora, Montewka, Hinz, & Matusiak, 2017a, 2017b; France et al., 2003; Levadou, Palazzi, & Belenky, 2003; Ribeiro e Silva, Guedes Soares, Turk, Prpic-Orsic, & Uzunoglu, 2010; Shin, Belenky, Lin, Weems,

& Engle, 2003; Uzunoglu, Silva, & Soares, 2015).

In the first generation of stability regulations in IS Code 2008, the criteria have a prescriptive character and are based on Reed's curve, (Rahola, 1939). These criteria examine the curve range, location of the maximum value and area under the curve. The limitations connected with the curve range are based on statistic data and experience gained from other stability accidents. Except for the weather criterion, these regulations are rather general. They are not based on any specific types of accident or types of ships. Only part B of the Code, which is not obligatory, contains requirements dedicated to particular types of ships.

Being aware of the insufficiency of Code regulations, the researchers took effort toward the development of the new generation of regulations. Therein five main issues are considered:

- dead ship condition,
- surf-riding, broaching,
- pure loss of stability,
- excessive acceleration,
- parametric resonance;

The so-called second generation of intact stability criteria, covering the above mentioned failure modes, have been planned to have a multi-tiered structure consisting of three levels.

Currently, the first two levels, based on the susceptibility analysis (Tompuri, 2016), have been extensively studied and refined. More information concerning these concepts might be found in Peters et al. (Peters et al., 2011). The criteria for the parametric resonance, that is the phenomenon mainly addressed in this paper, are also based on a two level susceptibility approach, (Grinnaert, 2017).

The third level of the second generation criteria is associated with a direct assessment of stability. The documents describing how this level should look like were presented during recent SDC 5. In that context, the participants launched the discussion regarding the provision of operational manuals and limiting instructions.

The criteria above mentioned, are intended to foster an increase in the ship safety affecting the design process. This aim at disclosing whether a newly designed ship is safe from the stability point of view. However, one cannot be sure what "safety" exactly means or how it is measured.

The second generation criteria may lead to noticeable progress compared to IS CODE 2008 standard. They are based on more extensive physical model of phenomena. Even though the scenarios currently opted by IMO still do not comprise all possible reasons of stability failure, the criteria structure enables to extend the regulations by further scenarios. The new regulations get rid of the passive, retroactive approach, moving towards proactive approaches. The latter are generated based on in-depth analysis of physical phenomena related to the behaviour of the ship in waves.

Ship stability issues are routinely considered at both the design stage and in the course of operation. Since the latter is directly linked to the safety of navigation, nowadays this matter involves wide efforts of scientists and international bodies. Nevertheless, the second generation criteria, being finalized soon, do not directly refer to the ship operation.

Therefore, in this paper, we present a causal probabilistic meta-model suitable for the assessment of the stability-related safety of a container ship. To avoid a misleading nomenclature we use the term "meta-model" for a Bayesian network based model gathering and processing input data, which need to be prepared separately prior BN feeding.

The meta-model at the present stage of its development focuses on two preselected types of accidents as follows: parametric roll and synchronous roll, together with the resulting excessive accelerations. The required model structure is constructed basing on input data obtained in the course of a series of simulations with the use of 6 DoF numerical model called LaiDyn. For the selected C11 type of container ship we adopted typical loading case. The weather conditions are described by the following parameters, referring to the irregular sea state: the relative direction, height and period of the waves. The Bayesian learning technique is utilized for organizing the obtained data into a probabilistic meta-model. This allows for model validation and sensitivity test execution.

It ought to be emphasized that authors' intention is to present the approach rather than final figures reflecting the probability of a stability related incident. The number of runs of the ship motion simulations so far is limited, enabling only for the concept presentation. However the method is complete and seems to be promising, thus, worthy to be discussed.

The remainder of the paper is organized as follows: in Section 2 methods used to develop the meta-model are presented and their overall idea is given. Section 3 elaborates on the meta-model and on the obtained results. Section 4 concludes.

2. METHODS

2.1 Probabilistic meta-models

The probabilistic meta-model here presented, turns the results obtained in the course of simulations, adopting the deterministic model of ship motion in waves, into probabilistic model, to support decision-making in presence of uncertainty. This is conducted by informing the potential end-users about the probability of exceeding acceleration threshold for a ship, due to the resonance motion and resultant non-linear gain of roll amplitude in the seaways, described by a set of environmental parameters. These are: wave height, wave period and wave encounter angle. The accelerations due to ship longitudinal and lateral motions are calculated for predefined locations on ship's deck. The threshold that is adopted comes from the LR rules (Lloyd's Register, 2014) and it is set equal to 0.5 gravity acceleration. Two types of accidents are considered, that are associated with high accelerations: parametric roll motion and synchronous roll of the C11 container ship. Figure 1 presents the profile of the C11 class ship and her particulars are tabulated in Table 1.

Ship motions are determined with the use of 6 DoF hybrid non-linear model called LaiDyn, that is described Section 2.3. The obtained set of data is organized into meta-model with the use of Bayesian learning techniques that are briefly elaborated in Section 2.2.

Figure 1 Typical representative of C11 class

Table 1 Principal particulars of the C11 hull

Dimension	Full scale
Length between perpendiculars, LBP (m)	262.00
Breadth, B (m)	40.00
Depth, D (m)	24.45
Draft molded on forward perpendicular, TF (m)	11.72
Draft molded on aft perpendicular, TA (m)	12.856
Displacement, D (tons)	76020
Center of gravity above keel, $\overline{KG}$ (m)	17.34
Transverse metacentric height, $\overline{GM_T}$ (m)	2.075
LCG measured from aft perpendicular (m)	122.78
Transverse radius of gyration, $\overline{k_{XX}}$ (m)	16.73
Longitudinal radius of gyration, $\overline{k_{YY}}$ (m)	62.55
Natural roll period, $\overline{T_n}$ (s)	25.2

2.2 Bayesian Networks

Bayesian networks have a number of favorable characteristics. They can contextualize of the occurrence of specific consequences through situational factors, which represent observable aspects of the studied system. They furthermore allow integration of different types of evidence through various types of probabilities and provide a means for performing sensitivity analysis. It is also rather straightforward to incorporate alternative hypotheses in a model.

Strictly speaking, BNs represent a class of probabilistic graphical models, defined as a pair Δ={G (V,A),P}. (Koller & Friedman, 2009), where G (V,A) is the graphical component and P the probabilistic component of the model. G (V,A) is in the form of a directed acyclic graph (DAG), where the nodes represent the variables V={V1,…,Vn}, while the arcs (A) represent the conditional (in)dependence relationships between them. P consists of a set of conditional probability tables (CPTs) P (Vi|Pa (Vi)) for each variable Vi, i=1,…,n in the network. Pa (Vi) signifies the set of parents of V1 in G: Pa (V1)={Y∈V| (Y,Vi)}. A BN encodes a factorization of the joint probability distribution (JDP) over all variables in V:

$$P(V)=\prod_{i=1}^{n} P\left(V_i \mid \boldsymbol{Pa}\left(V_i\right)\right) \qquad (1)$$

With the use of BNs as modeling tools, probabilistic meta-models are established. BNs can perform forward (predictive) and backward (diagnostic) reasoning. The former allows propagating through the model from new information about causes (explanatory variables) to updated beliefs about the effects (response variables), following the directions of the network arcs. The latter type of reasoning moves from the effects of interest to the most probable causes, where the information in the model is propagated against the direction of the arcs, (Montewka, Goerlandt, & Zheng, 2015).

The structure of the Bayesian network, developed in this paper, has been constructed basing on background knowledge of experts on the phenomena analyzed, while the parameters were determined on data basis with the use of PC classifier. Bayesian network has been created with the use of GeNie program developed at University of Pittsburgh, (Druzdzel, 1999).

2.3 Ship motion model

The LaiDyn code has been developed for modelling the dynamics of a rigid ship in waves, forced to motion by complex hydrodynamic actions. The numerical model can be defined as a hybrid non-linear model, in 6 degrees of freedom, in the time domain (Matusiak, 2002, 2017). The radiation and diffraction forces are calculated by means of linear model, based on the assumption of small amplitude oscillatory motions (Journée & Massie, 2002). The non-linear part of the code includes hydrostatics (hull shape), Froude-Krylov actions and also maneuvering and propulsion (Matusiak, 2011). Thus, for instance non-linearities of the roll motion are present in the model as governed by the non-linear features of restoring moment.

LaiDyn code participated in the several benchmark studies (ITTC, 2002; Spanos & Papanikolaou, 2009) with positive evaluation result. The model validation was also supported by the model tests conducted in the towing and the multi-functional tanks at Aalto University (Matusiak, 2003; Matusiak & Stigler, 2012). Thus, LaiDyn may be found as a reliable simulation tool applicable for analysis of complex ship motion, accounting for all the pertinent non-linearities.

The input parameters of the simulations cover the following ranges:

wave direction: 0 – 180 deg;

significant wave height: 4.34 – 14.00 m;

peak period: 4.67 – 14.50 s.

These values refer to a previous study conducted on the C11 class container ship, where the authors addressed excessive

accelerations induced by synchronous and parametric roll (Acanfora et al., 2017b),

2.4 Acceleration evaluation and adopted thresholds

Container vessels are members of a rife group of ships and they are specific ones in terms of both the typical hull shape, with apparent flared parts, and the specificity of cargo and its lashing. The concomitance of these aspects creates real operational challenges. The main factor governing the probability of container shifting is the resultant acceleration generating mass force exceeding or not the strength of the lashing system (twist locks, lashing bars, etc.).

The use of LaiDyn enables to calculate the acceleration acting on every single box stowed on board from the time histories of all ship motions. For the sake of simplicity, the most vulnerable container positions are predefined to trace the acceleration during the ship rolling in a limited number of relevant points. All components of acceleration, including gravitational acceleration, are taken into account and then the resultant transverse a_T is calculated. The details can be found in (Acanfora et al, 2017b). The acceleration a_T is related to the co-ordinates system fixed to the ship's hull. So, it results from both: a) the large value of an angle of heel (the transverse component of the gravity acceleration is significant in such a case) and b) the excessive value of the ship angular motion and corresponding acceleration in waves. According to the cargo stowage manual, the commonly accepted threshold equals to 0.5g as in LR rules too (Lloyd's Register, 2014). When this threshold is exceeded, the rolling case is identified as an accident involving container shifting.

3. MODEL AND RESULTS

3.1 Bayesian model

The developed probabilistic meta-model is depicted in Figure . The input parameters are described as a distribution, likewise the output.

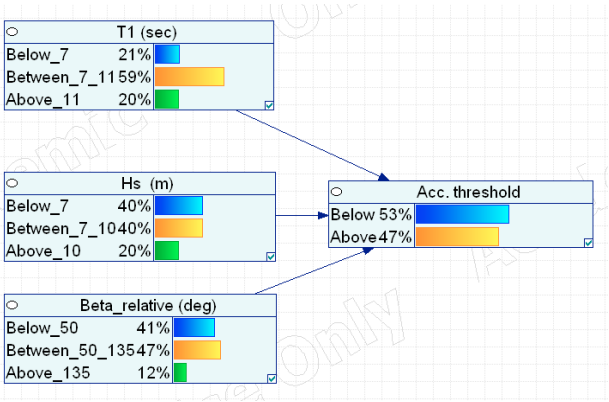

Figure 2 Probabilistic meta-model for excessive acceleration due to resonance motion for ship in seaway

3.2 Sensitivity analysis

The purpose of a sensitivity analysis is to investigate the effect of changes in the assigned probabilities of the network variables on the probabilities of a specific outcome variable. In a one-way sensitivity analysis, every conditional and prior probability in the network is varied, in turn, keeping the others unchanged. A sensitivity-value approach, presented by Coupé and van der Gaag (Coupé & van der Gaag, 2002) is applied. A sensitivity function is defined. It describes an outcome Y as a function of the parameter $z = p(Y = Y_i \mid \boldsymbol{\pi})$, where Yi is one state of the outcome, and π is a combination of states for the parent nodes of Y. For a network with no observations on any of the network variables, a linear sensitivity function is found:

$$f(z) = u_1 z + u_2 \qquad (2)$$

where the constants u_1 and u_2 are identified based on the model. The first derivative of the sensitivity function, at the base value, can be

considered as a numerical sensitivity indicator. It describes the effect that minor changes in the original parameter value have on the output value:

$$f'(z) = u_1 \qquad (3)$$

The sensitivity of an input parameter on the model outcome is considered by max $|u_1|$.

Numerical values of sensitivity functions are as follows: 0.045 for T_1 (wave period), 0.111 for H_s (wave height), 0.064 for Beta (wave encounter angle). This shows that the model is more sensitive to changes in H_s; however, the changes in other two variables are also relevant to the model outcome

3.3 Results

The presented method is twofold: first numerous simulations of ship dynamics are carried out with the use of LaiDyn program; then, the simulation results are used as input data to build the BN-based model. Table 2 introduces one sample set of input data. Figure 3 presents the time history of the ship roll motion for this case. **Error! Reference source not found.**4 shows the correspondent time history of the a_T acceleration: the orange line identifies the acceleration at the center of gravity of the ship (without gravitational effects); the blue line instead refers to the acceleration in a vulnerable point of the container stacks (including gravitational effects). Each container on board is exposed to a different local acceleration, resulting from the whole ship dynamics. The a_T values for inputting BN-based model, are calculated only in the most relevant and sensitive positions on board.

Table 2 Example case – parameter

Beta	30
Hs	11.0
T1	10.5
GM	2.075

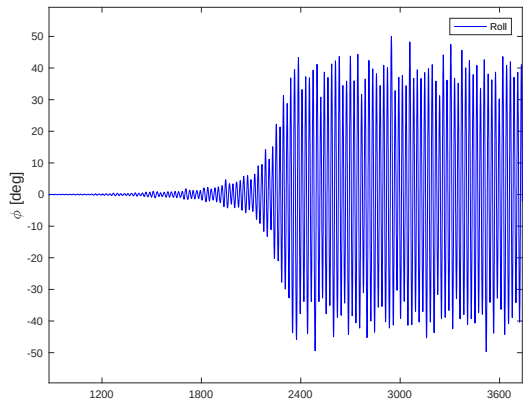

Figure 3 Sample history of roll motion

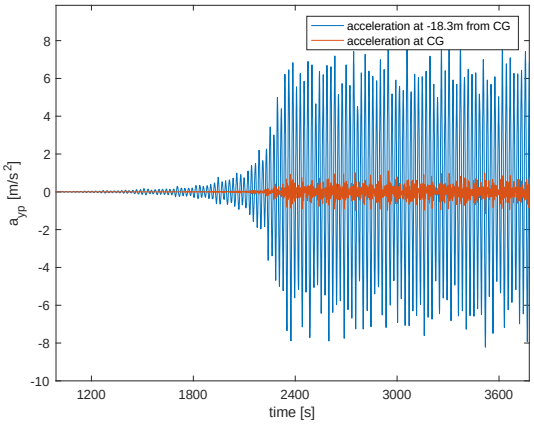

Figure 4 Sample history of transverse acceleration a_T

4. SUMMARY AND CONCLUSIONS

The contemporary stability regulations and the commonly used methods related to them, still depend on simple criteria associated with Reed's curve. The rules are applied in the procedures of determining the limiting maximum KG curves. At the first sight these curves come in handy at numerous stages of the ship operation. However, it seems that such a procedure consisting in application of limiting curves only, constitutes an insufficient solution when facing complex phenomena, like for instance strongly nonlinear ship motions during a voyage in high seas, or in case of uncertain and uncompleted information. The presented probabilistic approach is expected to overcome numerous shortcomings of the pending practice.

The Bayesian network-based method, introduced in the article, becomes a tool, definitely helpful in a routine sailing. The network is fed by the results of numerous simulations determining the ship response in various conditions. Then the outcome is obtained in the form of the probability of a predefined incident. In case of this research the incident is found at every acceleration threshold overrun. The method might be an alternative for aforementioned limiting curve-based evaluation.

The learning material utilized as a foundation for the network is preferably massive while in this research the number of simulated cases is limited. In spite of this fact, it is still sufficient to present the proposed procedure. So, the result of this study is rather elaboration and presentation of the approach not final figures describing the probability. In real situations, it would be advisable to extend the range of simulations each time changing the loading conditions, ship velocity and weather conditions.

Besides fostering the more informative stability-related safety assessment of a ship than it is done nowadays, the proposed approach based on the Bayesian network might be applied in the process of determining the optimal route. Having at disposal an extended and systematically prepared simulation database one may create the Bayesian network which constitutes a tool providing required information almost immediately. The output data from BN are treated as input data in the optimization process contributing to both the goal functions and the constraints. Thus, the method is considered promising especially thanks to the potentials for applications that are wider than typical stability assessment.

5. ACKNOWLEDGEMENTS

The Merenkulun säätiö – the Maritime Foundation - from Helsinki is appreciated for the travel grant provided.

6. REFERENCES

Acanfora, M., Montewka, J., Hinz, T., and Matusiak, J., 2017a. Towards realistic estimation of ship excessive motions in heavy weather. A case study of a containership in the Pacific Ocean. *Ocean Engineering*,*138*,140–150. https://doi.org/10.1016/j.oceaneng.2017.04.025

Acanfora, M., Montewka, J., Hinz, T., and Matusiak, J. E., 2017b. On the estimation of the design loads on container stacks due to excessive acceleration in adverse weather conditions. *Marine Structures*, *53*,105–123. https://doi.org/10.1016/j.marstruc.2017.01.003

Coupé, V. M. H. and van der Gaag, L. C., 2002. Properties of Sensitivity Analysis of Bayesian Belief Networks. *Annals of Mathematics and Artificial Intelligence*, *36*(4),323–356. https://doi.org/10.1023/A:1016398407857

Druzdzel, M. J., 1999. GeNIe: A Development Environment for Graphical Decision-analytic Models. In *In Proceedings of the 1999 Annual Symposium of the American Medical Informatics Association (AMIA-1999)* (p. 1206). Washington D.C.

France, W. N., Levadou, M., Treakle, T. W., Paulling, J. R., Michel, R. K., and Moore, C., 2003. An investigation of head-sea parametric rolling and its influence on container lashing systems. *Marine Technology*, *40*(1), 1–19. Retrieved from http://www.ingentaconnect.com/content/sname/mt/2003/00000040/00000001/art00001

Grinnaert, F., 2017. *Analysis and implementation of second generation criteria in a stability computer code*. *Universite de Bretagne*. Universite de Bretagne.Retrievedfrom https://tel.archives-ouvertes.fr/tel-01578973

ITTC., 2002. The Specialist Committee on Prediction of Extreme Ship Motions and Capsizing Final Report and Recommendations to the 23rd ITTC. In *23rd International Towing Tank Conference* (Vol. 2). International Towing Tank Conference.

Journée, J. M. J. and Massie, W. W., 2002.

OFFSHORE HYDROMECHANICS. *Delft University of Technology* (1st ed.). Delft, The Netherlands: Delft University of Technology. https://doi.org/10.1097/DCC.0b013e318276822f

Levadou, M., Palazzi, L., and Belenky, V., 2003. Assessment of operational risks of parametric roll. *Transactions - Society of Naval Architects and Marine Engineers*, *111*, 517–534.

Lloyd's Register., 2014. *Rules and regulations for the classification of ships*. *Lloyd's Register*.

Matusiak, J. E., 2002. Towards an unified theoretical model of ship dynamics. *Maritime Research Seminar*.

Matusiak, J. E., 2003. On the Effects of Wave Amplitude, Damping and Initial Conditions on the Parametric Roll Resonance. In *8th International Conference on the Stability of Ships and Ocean Vehicles*.

Matusiak, J. E., 2011. On the non-linearities of ship's restoring and the Froude-Krylov wave load part. *International Journal of Naval Architecture and Ocean Engineering*,*3*(1),111–115. https://doi.org/10.3744/JNAOE.2011.3.1.111

Matusiak, J. E., 2017. *Dynamics of Rigid Body*. *Aalto University* (II). Aalto University.

Matusiak, J. E. and Stigler, C., 2012. Ship Roll Motion in Irregular Waves During a Turning Circle Maneuver. In *11th International Conference on Stability of Ships and Ocean Vehicles* (pp. 307–313). Athens, Greece.

Montewka, J., Goerlandt, F., and Zheng, X., 2015. Probabilistic Meta-models Evaluating Accidental Oil Spill Size from Tankers. In A. Weintrit & T. Neumann (Eds.), *Information, Communication and Environment* (pp. 231–241). CRC Press. https://doi.org/10.1201/b18514-37

Peters, W., Belenky, V., Bassler, C., Spyrou, K., Umeda, N., Bulian, G., and Altmayer, B., 2011. The second generation intact stability criteria: An overview of development. *Transactions - Society of Naval Architects and Marine Engineers*, *121*.

Rahola, J., 1939. *The judging of the stability of ships and the determination of the minimum amount of stability - especially considering the vessels navigating Finnish waters*. Technical University of Finland.

Ribeiro e Silva, S., Guedes Soares, C., Turk, A., Prpic-Orsic, J., and Uzunoglu, E., 2010. Experimental Assessment of the Parametric Rolling On a C11 Class Container Ship. *HYDRALAB III Joint User Meeting*, (February), 267–270.

Shin, Y. S., Belenky, V., Lin, W.-M., Weems, K., and Engle, A. H., 2003. Nonlinear time domain simulation technology for seakeeping and wave-load analysis for modern ship design. *SNAME Transactions*, *111*, 557–583.

Spanos, D., and Papanikolaou, A., 2009. Benchmark Study on Numerical Simulation Methods for the Prediction of Parametric Roll of Ships in Waves. In *10th International Conference on Stability of Ships and Ocean Vehicles* (pp. 1–9). St. Petersburg, Russia.

Tompuri, M., 2016. Second generation intact stability criteria and operational limitations in initial ship design. In *PRADS*. Copenhagen, Denmark.

Uzunoglu, E., Silva, S., and Soares, C., 2015. Numerical and experimental study of parametric rolling of a container ship in regular and irregular head waves. In *Maritime Technology and Engineering* (pp. 1047–1056). CRC Press. https://doi.org/10.1201/b17494-140

Direct Stability Assessment for Excessive Acceleration Failure Mode and Validation by Model Test

Takako Kuroda, *National Maritime Research Institute* tkuroda@nmri.go.jp

Shoichi Hara, *National Maritime Research Institute* hara@nmri.go.jp

Hidetaka Houtani, *National Maritime Research Institute* houtani@nmri.go.jp

Daichi Ota, *National Maritime Research Institute* ota-d@nmri.go.jp

ABSTRACT

The excessive acceleration is one of five stability failure modes for intact stability being discussed at IMO. The trial calculation for Direct Stability Assessment (DSA) and the model test have been carried out. The ship motion in the short-crested irregular waves calculated by the linear superposition of frequency responses agrees well with the results of the model test. Using experimentally validated prediction method and wave scatter diagram of North Atlantic, DSA has been evaluated by long-term failure probability. DSA using time domain simulation was also carried out, and the assessment result is almost the same as that of the linear superposition method.

Keywords: *Direct Stability Assessment, Excessive Acceleration, Short-crested Irregular Wave, Time Domain Simulation*

1. INTRODUCTION

The excessive acceleration failure mode is one of five stability failure modes for the second-generation intact stability criteria. This is the critical standard of lateral acceleration acting on the place where passengers or crew may be present at the highest position in the residential area or at the bridge deck. This criterion is classified into 3 categories. Level 1 and Level 2 is simplified criteria, and Level 3 is Direct Stability Assessment (DSA).

In this study, the trial calculation of DSA for the excessive acceleration failure mode and the model test have been carried out using a container ship designed on the basis of "CMV CHICAGO EXPRESS" which caused an accident due to the excessive acceleration. The model test has been carried out to make a quantitative verification of two calculation methods for DSA. The ship motion in short-crested irregular waves has been calculated by both the linear superposition of frequency responses and developed time domain simulation. Those calculated results have been compared with the experimental results to validate the availability of two different calculation methods used for DSA. Using experimentally validated calculation method and wave scatter diagram of North Atlantic, DSA has been evaluated by long-term failure probability. Using the assessed results of DSA by both the linear superposition method and the time domain simulation, consistency between DSA and the vulnerability criterion of Level 2 has been confirmed.

2. SAMPLE SHIP

A sample ship was designed to reproduce an accident ship referring to the body plan shown in the investigation report (Federal Bureau of Maritime Casualty Investigation, 2009) of the container ship "CMV CHICAGO EXPRESS".

The general arrangement of the sample ship is shown in Fig. 1, and the principal particulars of the sample ship are shown in Table 1. Its displacement is within 1 % difference compared with that in the investigation report. The loading condition is the accident condition. Bilge keels are set referring to SLF 54/INF.7 (2011). Location of the bridge is estimated by both another container ship of the same length and photograph of CMV CHICAGO EXPRESS.

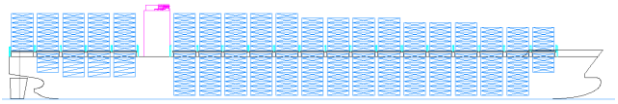

Fig. 1 General arrangement of sample ship referring to the investigation report (BSU, 2009)

Table 1 Principal particulars of the sample ship

Length between perpendiculars : L_{PP}	320.00 m
Breadth : B	42.800 m
Draught at A.P.	9.073 m
Draught at midship	8.078 m
Draught at F.P.	7.083 m
Metacentric height : GM	8.540 m
Breadth of bilge keel	0.600 m
Length of bilge keel	96.00 m
Longitudinal distance of bridge from A.P.	77.700 m
Height of bridge from base line	50.000 m

3. MODEL EXPERIMENT

3.1 Outline of Model Experiment

For validating the prediction method of ship motion in short-crested irregular waves, the model experiments for the sample ship were carried out in Actual Sea Model Basin of National Maritime Research Institute in Japan. The model test was done based on the ITTC recommended procedure 7.5-02-07-04 for intact stability model tests.

The model ship has a length overall of 3.5m and a scale of 1/96.054. Test condition of the model ship was set up on the accident condition. The dry pitch radius of gyration is 0.25L. The lateral acceleration was measured by installing an acceleration sensor at the height of bridge. Ship motions were free in six-degrees of freedom, and steady force is given by spring for each motion of surge, sway and yaw motions with no restoring force to avoid drifting due to wave.

Regular beam wave, long-crested and short-crested irregular waves were used in the model test. The frequency spectrum of long and short-crested irregular waves is the ITTC recommended unlimited fetch spectrum. The distribution of wave direction is fourth power of cosine function of which principal direction is beam wave. The used significant wave heights H_s are 5.5m and 7.5m in full scale and mean wave period T_{01} transformed from zero up-crossing period T_z corresponds to wave scattering diagram of IACS No. 34 by using equation (1). The waveform was expressed by the single summation method, and the initial phase and the direction were set by random numbers. The division number of wave frequencies is 150. The measurement time was 20 minutes which corresponds to approximate 3 hours in full scale.

$$T_{01} = 1.0864 T_Z \tag{1}$$

A roll decay test without advance speed was carried out and the roll damping coefficient μ and β expressed by $\ddot{\phi} + 2\mu\dot{\phi} + \beta\dot{\phi}|\dot{\phi}| + \omega_n^2\phi = M_\phi(\omega t)$ were obtained where ϕ , ω_n and M_ϕ are roll amplitude, roll natural frequency and roll moment divided by the inertia, respectively. μ is 0.0123(1/s) and β is 0.5208(1/rad) for the sample ship in model scale. Roll natural period is 1.112s, which corresponds to 10.89s in full scale.

3.2 Analysis of Short-Crested Irregular Waves in Model Test

Wave frequency and directional spectrum used for the model test are in advance analyzed. From the analysis results, the spectrum and its temporal variation of wave field generated in the basin are verified. The wave elevation to be analyzed is measured by the wave gauge array as shown in Fig. 2.

The wave condition is significant wave height of 5.73cm, mean wave period of 1.05s and principal wave direction of 90deg. The frequency spectrum is estimated by Fast Fourier Transform (FFT) and the directional spectrum is estimated by Extended Maximum Entropy Principle (EMEP) method (Hashimoto, 1994). The estimated frequency spectrum and directional distribution of wave energy are shown in Figs. 3 and 4, respectively. The directional distribution of wave energy is obtained by integrating directional spectrum with respect to frequency. The estimated frequency spectrum and the directional distribution of wave energy are in good agreement with the target values.

Regarding temporal variation of the wave field, the directional spectra are estimated for divided time series at every 5 minutes. The temporal variation of zero-moment of the directional spectrum (M_{00}) and mean wave direction (θ_m) are shown in Figs. 5 and 6, respectively. Each figure shows that neither M_{00} nor θ_m has significant temporal variation. The results indicate that the wave spectrum of the model test is in good agreement with the target one, and there is also no temporal variation in directional spectrum.

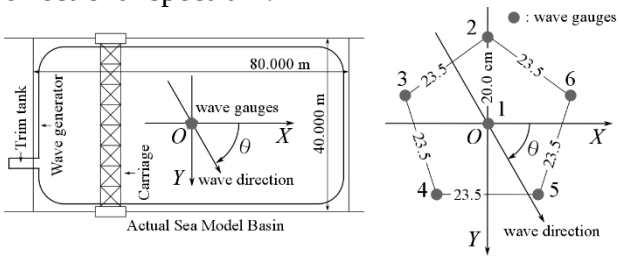

Fig. 2 Coordinate system of the basin and arrangement of wave gauge array.

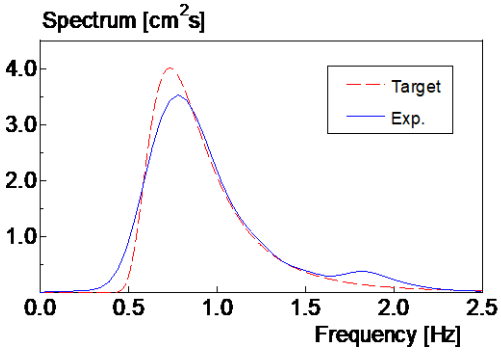

Fig. 3 Estimated frequency spectrum for experimental result.

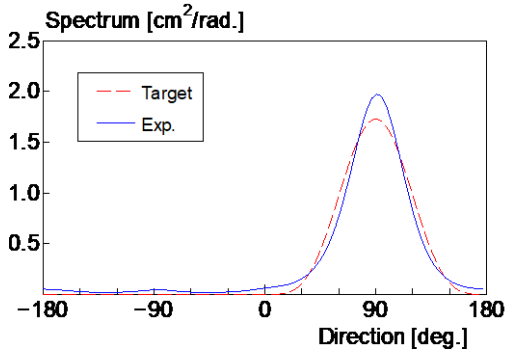

Fig. 4 Estimated directional distribution of wave energy for experimental result.

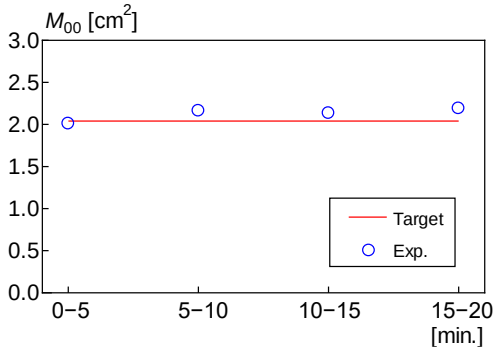

Fig. 5 Temporal variation of zero-moment of directional spectrum

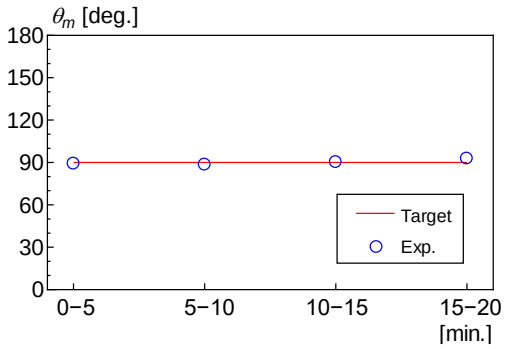

Fig. 6 Temporal variation of mean wave direction.

4. DIRECT STABILITY ASSESSMENT USING RESPONSE AMPLITUDE OPERATOR

Two prediction methods of the ship motions in irregular waves for obtaining DSA have been used in this study. In this section, DSA using Response Amplitude Operator (RAO) is described.

4.1 Prediction Method by using RAO

The used prediction method is the linear superposition method using RAO obtained by frequency domain calculation. The calculation tool in frequency domain is Salvesen-Tuck-Faltinsen (STF) method based on strip theory. The ship condition is 5 degrees of freedom with zero forward speed. Hydrodynamic force is calculated by using the 2-dimensional source distribution method. Roll damping coefficient was obtained by the roll decay model test. Roll damping force is estimated using equivalent linearization.

Using RAO of lateral acceleration and wave spectrum, the variance of lateral acceleration in long-crested irregular waves is obtained. Further, the variance of lateral acceleration in short-crested irregular waves is obtained using linear superposition of variance in long-crested irregular waves. Thus, the short-term probability can be calculated.

4.2 Predicted and Experimental Results in Regular and Irregular Waves

Examples of comparisons of roll and lateral acceleration in regular beam waves between numerical and experimental results are shown in Figs. 7 and 8, respectively. The numerical results agree well with the experimental results.

The one-third highest mean of lateral acceleration in long and short-crested irregular beam waves are compared between numerical and experimental results as shown in Fig. 9. The wave conditions of H_S and T_Z are 5.5m and 9.5s, respectively. 7 model test trials were carried out in short-crested irregular waves. Each test trial continued for 3 hours in full scale with initial phase of wave frequency and direction changed by random number. The numerical results for both long and short-crested irregular waves agree with those of model experiments. The results indicate that this prediction method can be used for DSA for excessive acceleration. Moreover, the numerical results in long and short-crested beam waves are smaller than the result of level 2 vulnerability criterion referring to SDC 3/WP.5 Annex 2 (2016). Thus this prediction method has consistency with Level 2 vulnerability criterion.

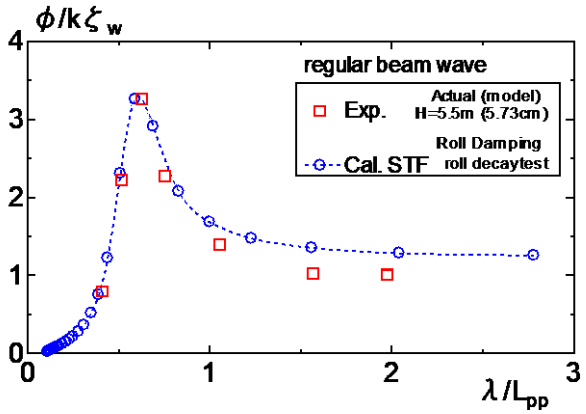

Fig. 7 Comparison of roll in regular beam waves between numerical and experimental results.

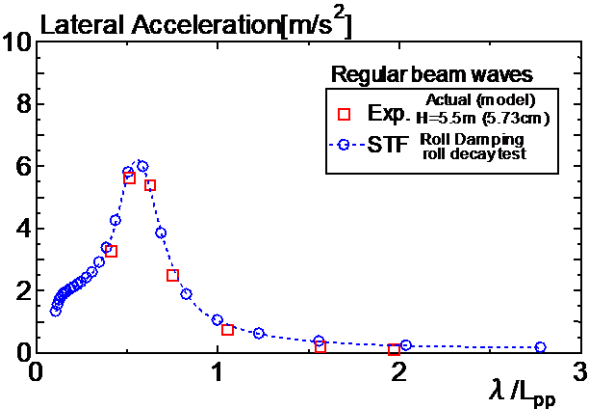

Fig. 8 Comparison of lateral acceleration in regular beam waves between numerical and experimental results.

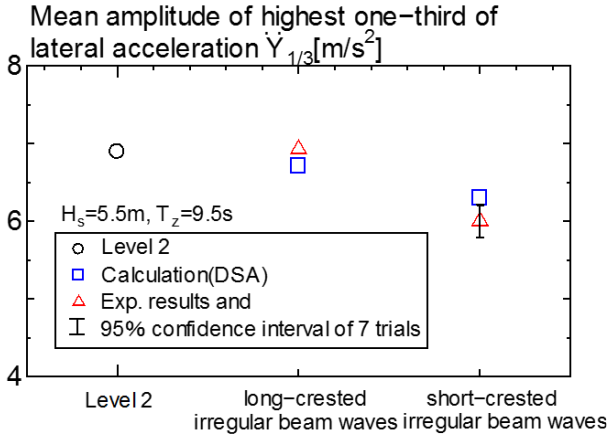

Fig. 9 Comparison of 1/3 highest mean of lateral acceleration in irregular waves between numerical and experimental results.

4.3 Long-Term Probability of Stability Failure for Excessive Acceleration

When the magnitude of crest to trough amplitudes of ship motion can be approximated by Rayleigh distribution, the short-term probability C_i exceeding threshold R is given by equation (2) where $\sigma^2$is variance. The statistical values of measured lateral acceleration in short-crested irregular waves are compared with relational formula assuming Rayleigh distribution as shown in Fig. 10. The statistical values of the model test and relational formula assuming Rayleigh distribution are in good agreement. On the basis of experimental results, the short-term probability of lateral acceleration can be obtained using standard deviation.

$$C_i = exp\{-R^2/2\sigma^2\} \qquad (2)$$

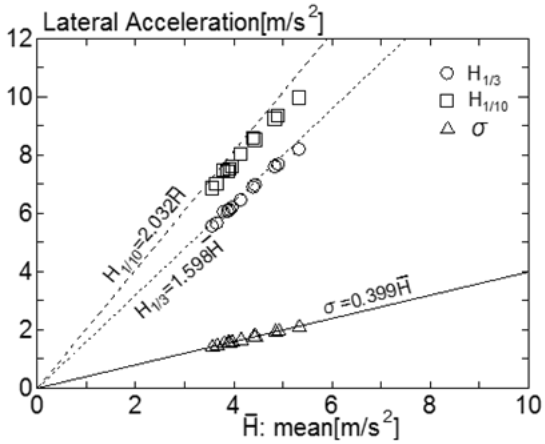

Fig. 10 Relation of statistical values of lateral acceleration between measured and relational formula assuming Rayleigh distribution

Fig. 11 shows the comparison of two exceedance probability obtained by different methods. One is obtained by dividing the number n exceeding the threshold by the total peak number N (direct counting method), and the other is obtained from the variance using equation (2). Table 2 shows the exceedance number n and exceedance probability obtained by direct counting method and variance value. It can be confirmed that the exceedance probability obtained by direct counting method and variance value are in good agreement. However, there is a difference when the exceedance number n is small. In order to obtain much more accurate exceedance probability by direct counting method, the exceedance number n for total number N should be more than a certain amount.

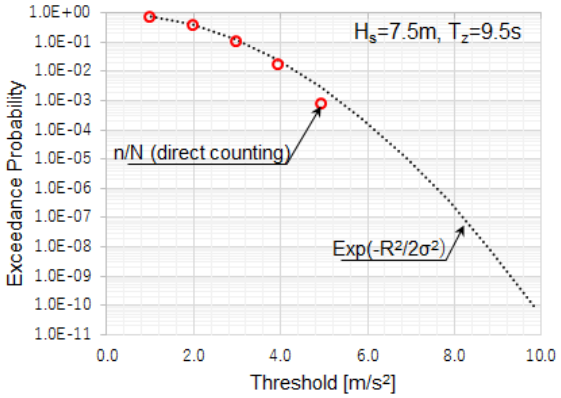

Fig. 11 Comparison of exceedance probability of lateral acceleration obtained by direct counting method and the variance.

Table 2 Exceedance number and exceedance probability of lateral acceleration obtained by direct counting method and the variance value.

standard deviation σ 2.095

Total num. of peak: N 2248

Level	Threshold [m/s^2]	Exceedance num. n	Direct Counting n/N	Probability Exp(-R^2/2σ^2)
1	9.81	0	0.00E+00	1.73E-05
0.9	8.83	0	0.00E+00	1.39E-04
0.8	7.85	0	0.00E+00	8.95E-04
0.7	6.87	0	0.00E+00	4.64E-03
0.6	5.89	20	8.90E-03	1.93E-02
0.5	4.91	122	5.43E-02	6.45E-02
0.4	3.92	405	1.80E-01	1.73E-01
0.3	2.94	893	3.97E-01	3.73E-01
0.2	1.96	1545	6.87E-01	6.45E-01
0.1	0.98	2018	8.98E-01	8.96E-01

By using this prediction method, short-term probability exceeding 9.81m/s^2 of the lateral acceleration in short-crested irregular beam waves is calculated for all wave conditions of IACS No.34.

DSA is assessed by the long-term failure probability. The long-term failure probability C is estimated using the short-term probability C_i exceeding lateral acceleration of 9.81 m/s^2 and the appearance frequency of each sea condition W_i as shown in equation (3). The obtained value C in short-crested irregular waves is 0.0000202.

The result of Level 2 vulnerability criterion which is assessed with the long-term failure probability by equation (3) for the sample ship is 0.00021. Thus, it is confirmed that DSA for excessive acceleration in the short-crested irregular waves calculated by the linear superposition method has consistency with Level 2 vulnerability criterion.

$$C = \frac{\sum_i W_i C_i}{\sum_i W_i} \tag{3}$$

Assuming that the ship encounters 1 wave per 10s., the average rate of stability failure per ship year S_{DSA} which is assessed results of DSA referring to SDC 4/WP.4 (2017) can be calculated by the following equation, and the calculation result is 1.00.

$$\begin{aligned} &S_{DSA} \\ &= 1 - (1 - 0.00002020)^{365\times24\times3600/10} \\ &= 1.00 \end{aligned} \tag{4}$$

5. DIRECT STABILITY ASSESSMENT USING TIME DOMAIN SIMULATION

5.1 Time Domain Simulation Method

Time domain simulation of ship motion without forward speed in short-crested irregular waves has been carried out. The ship motion is 6 degrees of freedom, and hydrodynamic force is calculated by the 3-dimensional panel method considering memory effect. Roll damping force coefficient is obtained by the roll decay model test.

The motion equation in time domain is derived from the velocity potential for impulse response as follows:

$$\begin{aligned} &\sum_j^6 \{(M_{kj} + m_{kj})\ddot{\eta}_j \\ &+ \int_{-\infty}^{t} K_{kj}(t-\tau)\,\dot{\eta}_j(\tau)d\tau + f_{kj} = E_k(t) \end{aligned} \tag{5}$$

$$k = 1\sim6$$

where m_{kj}, K_{kj}, $f_{kj}$and $E_k(t)$ are as follows:

m_{kj}: added mass in time domain
K_{kj}: memory effect function
f_{kj}: restoring force due to hydrostatic pressure
$E_k(t)$: external force (wave exciting force and drift force) (6)

The equation (5) is expressed by the general equation of ship motion as follows by arranging the inertia terms to the left side and the non-inertia term to the right side, respectively. The terms of right-hand of equation (7) indicate the summation of radiation force F_k^R, diffraction forceF_k^D, Froude-Krylov force F_k^{FK} and restoring force F_k^{REST} as shown in equation (8).

$$\sum_{j=1}^{6} M_{kj}\ddot{\eta}_j = F_k(t) \tag{7}$$

$$\begin{aligned} F_k(t) = F_k^R(t) + F_k^D(t) + F_k^{FK}(t) \\ + F_k^{REST}(t) \end{aligned} \tag{8}$$

Newmark-β method is used to solve the ship motion in time domain. If the displacement of j mode at a certain time is η_j^n, the displacement and velocity of the next step are expressed as follows:

$$\begin{aligned} \eta_j^{n+1} &= \eta_j^n + \Delta t\dot{\eta}_j^n + \frac{\Delta t^2}{2}\ddot{\eta}_j^n \\ &\quad + \beta\Delta t^2\left(\ddot{\eta}_j^{n+1} - \ddot{\eta}_j^n\right) \\ \dot{\eta}_j^{n+1} &= \dot{\eta}_j^n + \frac{\Delta t}{2}\left(\ddot{\eta}_j^{n+1} + \ddot{\eta}_j^n\right) \end{aligned} \tag{9}$$

The solution at time $t + \Delta t$ can be derived from that at time t. The equation (7) can be solved in the time domain by the convergent calculation for $\dot{\eta}_j^{n+1}$ using equation (9).1/4 is used for β value as an unconditionally stable coefficient. The convergence judgement during repeated calculation for the acceleration $\ddot{\eta}_i^{n+1}$ is as follows:

$$\frac{\left|\ddot{\eta}_j^{n+1} - \ddot{\eta}_j^{n}\right|}{\ddot{\eta}_j^{n+1}} \leq \frac{1}{100} \tag{10}$$

The radiation force $F_k^R(t)$ for each ship motion mode η_k considering the memory effect of hydrodynamic force is obtained by the following equation.

$$F_k^R(t) = \sum_{j=2}^{6}\left\{-m_{kj}(\infty)\,\ddot{\eta}_j - \int_{-\infty}^{t} K_{kj}(t-\tau)\dot{\eta}_j(\tau)d\tau\right\} \tag{11}$$

where m_{kj} is the added mass coefficient and $K_{kj}(t)$ is the memory effect function defined as shown in the equation (12).

$$K_{kj}(t) = \frac{2}{\pi}\int_0^{\infty} B_{kj}(\omega)\cos\omega t d\omega \tag{12}$$

where B_{kj} is the damping coefficient of wave making component calculated based on the linear potential theory.

The equation (11) for roll motion is expressed as follows;

$$\begin{aligned} F_4^R(t) = &\sum_{j=2}^{6}\left\{-m_{4j}(\infty)\,\ddot{\eta}_j\right\} \\ &- \int_{-\infty}^{t} K_{42}(t-\tau)\dot{\eta}_2(\tau)d\tau - \int_{-\infty}^{t} K_{43}(t-\tau)\dot{\eta}_3(\tau)d\tau \\ &- \int_{-\infty}^{t} K_{45}(t-\tau)\dot{\eta}_5(\tau)d\tau - \int_{-\infty}^{t} K_{46}(t-\tau)\dot{\eta}_6(\tau)d\tau \\ &-\{B_E(\dot{\eta}_4) - B_{44}(\dot{\eta}_4)\dot{\eta}_4\} - \int_{-\infty}^{t} K_{44}(t-\tau)\dot{\eta}_4(\tau)d\tau \end{aligned} \tag{13}$$

The 6th term on the right side of the equation (13) is the viscous effect of roll damping force. $B_E(\dot{\eta}_4)$ is expressed by the following equation obtained from the roll decay test of model ship. $B_{44}(\dot{\eta}_4)\dot{\eta}_4$ is the wave making component of roll damping force.

$$B_E(\dot{\eta}_4) = 2\mu\dot{\eta}_4 + \beta\dot{\eta}_4|\dot{\eta}_4| \tag{14}$$

The lateral acceleration at the bridge height position $\ddot{\eta}_p$ is calculated by considering the influence of sway η, roll ϕ and the lateral component of gravitational acceleration g due to roll motion using following equation.

$$\ddot{\eta}_p = \ddot{\eta} - (z_p - z_G)\ddot{\phi} - g\sin\phi \tag{15}$$

Wave conditions in this time domain simulation are short-crested irregular waves which are the same with the model test. The frequency spectrum is the ITTC spectrum. Distribution of wave direction of the fourth power of cosine function of which principal direction is beam wave. The waveform is expressed by the single summation method.

5.2 Simulation Condition

The relation between simulation time and simulated statistical values has been investigated to determine the optimum simulation time. The simulation of 1,000,000 steps has been done with time step of 0.01 second (about 2.8 hours). The division number of wave frequencies is 150. The significant wave height and the zero-up crossing period are 5.5m and 9.5s., respectively. The duration time for statistical values is increased by every 100,000 time steps (1000s). Each statistical value has been compared with that of the longest simulation time of 1,000,000 steps. The relative error of variance and one-third highest mean of roll motion for each duration time to those for the longest duration time is shown in Fig. 12. The simulation time needs at least 700,000 steps to keep relative error within 1%. Therefore, the simulation time is based on 3 hours in this study.

In order to investigate the influence of the division number of wave frequencies on the accuracy of simulation results, the simulation has been done varying the division number of wave frequencies by every 100 divisions from 50 to 350. The time step is 0.01s and the simulation time is 3 hours. As for wave condition, the significant wave height and the zero up-crossing period are 5.5m and 9.5s, respectively. The relation between statistical values of roll motion and the division number of wave frequencies is shown Fig. 13. When the

division number of wave frequencies becomes larger than 150, scattering is small. From this result, the division number of wave frequencies in time domain simulation is set 150. In the case of lateral acceleration, statistical values with different division number of wave frequencies were also scarcely varied as well as roll motion.

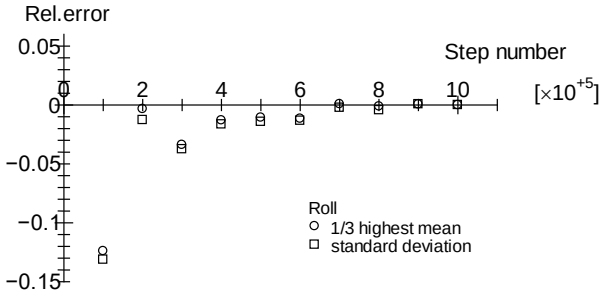

Fig. 12 Relative error of variance and 1/3 highest mean of roll and simulation time.

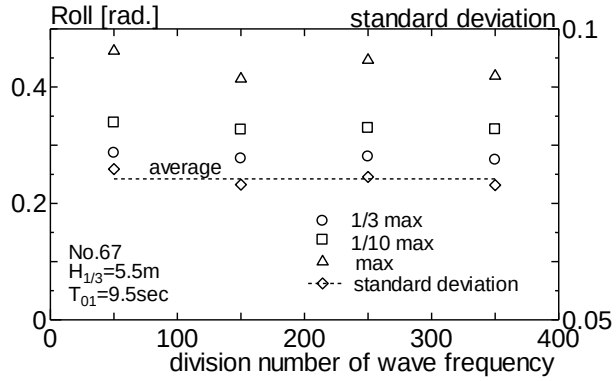

Fig. 13 Relation between statistical values of roll and the division number of wave frequencies.

5.3 Simulation and Experimental Results in Short-crested Irregular Waves

The simulated results of ship motions in short-crested irregular waves in the time domain have been compared with the experimental results to investigate the accuracy of calculation method.

Five cases of time domain simulation with initial phase of wave frequency and wave directions set by random numbers have been carried out and compared with the experimental results. As for wave condition, H_S and T_Z are 5.5m and 9.5s, respectively. Those simulated results of lateral acceleration are shown in Fig. 14. The simulated results are close to the mean value of 5 trials and indicate no effect of random phase of wave frequency and direction on the simulated results.

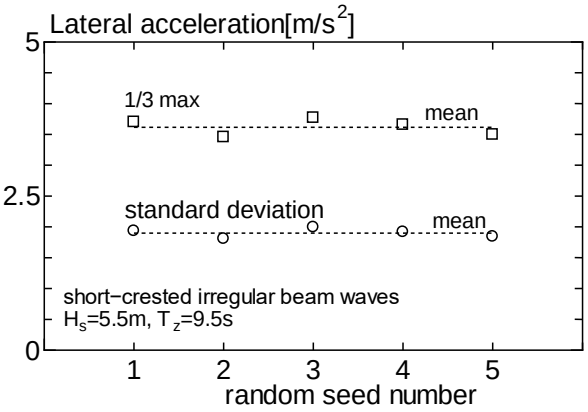

Fig. 14 Statistical values of simulated lateral acceleration of 5 trials.

Fig. 15 and 16 show the mean amplitude of highest one-third of roll motion and lateral acceleration and 95% confidence interval obtained by the simulation (5 trials) and model test (7 trials), respectively. As for roll motion, 95% confidence interval of simulation and experimental results overlap. This result indicates that this time domain simulation has sufficient accuracy to simulate ship motion in short-crested irregular waves. Although there is a difference of those results for lateral acceleration, the result of the time domain simulation is conservative estimation compared with the experimental results.

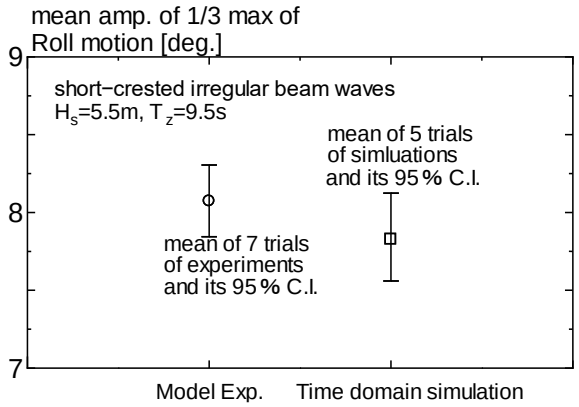

Fig. 15 Comparison of roll motion with 95% confidence interval between experimental and simulation results.

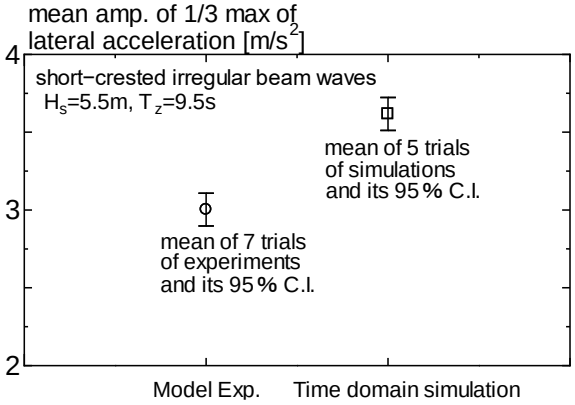

Fig. 16 Comparison of lateral acceleration with 95% confidence interval between experimental and simulation results.

The statistical values of the double amplitude distribution of lateral acceleration in the time domain simulation and relational formula of Rayleigh distribution were compared in Fig. 17. In Fig. 17, blue marks show the case of only wave-making damping coefficient (without viscous components) and red marks show the case of equivalent linearization of roll damping coefficient obtained by roll decay test. When the viscous component is not included in the roll damping, the statistical values coincide with the relational formula of Rayleigh distribution. On the other hand, the statistical values differ from that of Rayleigh distribution when viscous component is considered. This means that non-linear effect of roll damping on lateral acceleration appears in the time domain simulation.

By using the time history data of simulated lateral acceleration, the number n exceeding the threshold is counted and compared with the exceedance probability of the experiment. Fig. 18 shows the exceedance probability obtained from the direct counting method and variance value for the time domain simulation and the experiment. As for wave condition, H_s and T_Z are 7.5m and 9.5s, respectively. The exceedance probability of simulation by direct counting method agrees well with that of the experiment. However, the exceedance probability of the simulation by the direct counting method becomes to be smaller than that obtained from the variance value assuming Rayleigh distribution. In this case of time domain simulation, the exceedance probability from the variance value is evaluated to be conservative.

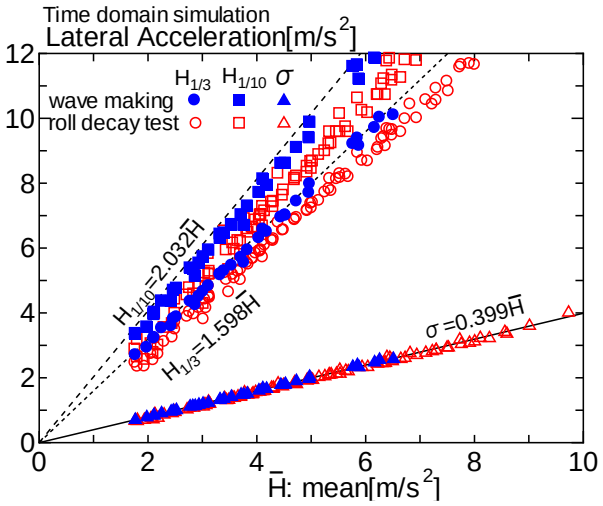

Fig. 17 Statistical values of lateral acceleration with roll damping obtained by roll decay test.

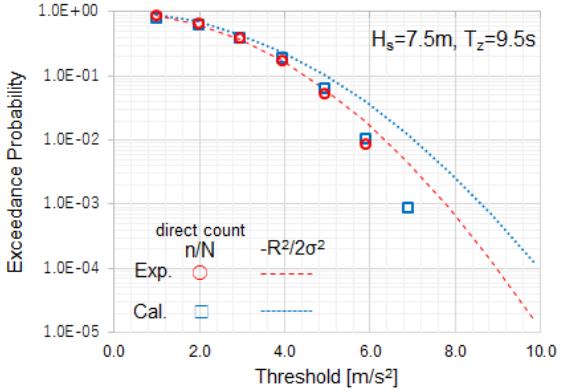

Fig. 18 Comparison of exceedance probability of simulation and experiment by direct counting method with Rayleigh distribution

5.4 Long-Term Probability by the Time Domain Simulation

The lateral acceleration in short-crested irregular beam waves was simulated in the time domain for wave scatter diagram of IACS No.34 where the frequency of wave occurrence exists. The short-term probability of lateral acceleration exceeding 9.81m/s^2 can be obtained from the variance value of simulated results. The long-term failure probability can also be obtained by using the short-term probability of lateral acceleration and wave scatter diagram. The long-term failure probability C obtained by

weighted average shown in the equation (3) is 0.0000168, that is smaller than 0.0002020 in the case of using the linear superposition of frequency response.

The average rate of stability failure per ship per year S_{DSA} as an index of DSA can be calculated with the long-term failure probability using equation (16) on the assumption that the ship encounters 1 wave per 10s.

$$S_{DSA} = 1 - (1 - 0.0000168)^{365\times24\times\frac{3600}{10}} = 1.00 \quad (16)$$

S_{DSA} is 1.00 for sample ship which is the same as the case obtained by the linear superposition of frequency response.

6. CONCLUSIONS

The trial calculation of DSA for excessive acceleration and model test have been carried out using the container ship based on CMV CHICAGO EXPRESS which caused an accident due to excessive acceleration. The concluding remarks can be written as below.

The ship motion in short-crested irregular waves was calculated by the linear superposition of frequency responses and was compared with the results of the model test. The results show this calculation method has a sufficient accuracy.

The lateral acceleration calculated by linear superposition method of frequency responses verifies the consistency with Level 2 vulnerability criterion.

Using above experimentally validated calculation method and wave scatter diagram of IACS No.34, DSA for excessive acceleration by calculating long-term failure probability has been done.

DSA using the time domain simulation was also carried out, and the assessment result is the same as that obtained by using the linear superposition method of frequency response.

7. ACKNOWLEDGMENTS

This study was carried out as a research activity of Goal-based Stability Criteria Project of Japan Ship Technology Association in the fiscal years of 2017, funded by the Nippon Foundation.

8. REFERENCES

Federal Bureau of Maritime Casualty Investigation, 2009, “Fatal accident on board the CMV CHICAGO EXPRESS during Typhoon “HAGUPIT” on 24 September 2008 off the coast of Hong Kong”, The investigation report 510/08.

SLF 54/INF.7, 2011, “Development of second generation intact stability criteria, a background study on seakeeping behaviour of container vessels in ballast condition”, IMO.

Hashimoto, N., Nagai, T. and Asai, T.,1994, “Extension of the Maximum Entropy Principle Method for Directional Wave Spectrum Estimation”, Proceedings of 24th Conference on Coastal Engineering, pp. 232-246.

SDC 3/WP. 5 Annex 2, 2016, “Draft amendments to part B of the IS code with regard to vulnerability criteria of Level 1 and 2 for the excessive acceleration failure mode”, IMO.

SDC 4/WP. 4 Annex 1, 2017, “Draft guidelines of direct stability assessment procedures for use with the second generation intact stability criteria”. IMO

Determination of Roll Damping for Empirical Measurements

Timothy Smith, *Naval Surface Warfare Center Carderock Division* timothy.c.smith1@navy.mil

ABSTRACT

Ship roll motion has non-linearity due to quadratic or cubic roll damping combined with cubic roll restoring moment. Roll damping while non-linear with respect to roll velocity also has dependence on roll angle and ship speed. Empirical roll damping measurements from free decay tests often have a biased mean and include the effects of other motions such as sway and heave. The roll damping values derived from these measurements typically follow from the basic assumption of a damped oscillator. This paper will explore and compare various methods of calculation of roll damping values from empirical data. While in theory these methods are equivalent, the study will show in practice the different methods do produce different values. The matching of calculation method with underlying assumption of roll damping form will be examined with respect to matching simulation roll decay results.

Keywords: *roll damping, seakeeping, log decrement*

1. INTRODUCTION

At model scale, free decay roll experiments can be made to measure roll damping. With free decay experiments, the model is excited in roll and then allowed to roll freely until the motion becomes small. The model rolls at the roll natural period. Experimentally exciting the model in roll will often induce a sway, heave, pitch, and yaw motion as well especially for large amplitude roll motions. Rudder action can also affect the roll decay. For these reasons special care is taken during the roll decay experiment to minimize these effects. The model is excited with a vertical impulse outboard near midships. This takes advantage of other motions requiring more excitation to produce a change, so roll will be excited with an impulse before the other motions can respond. Of course stiffer ships, like trimarans, will have an increased likelihood of exciting other motions because more excitation needs to be applied. The rudder angle is held constant during the decay experiment to reduce steering influence on roll. The excitation and rudder angle can be controlled more easily at zero speed, than trying to excite a moving model.

Other experimental methods, such as harmonic excited roll and forced rolling, have some advantages in measuring roll damping at large roll angle and at forward speed. Different analysis methods are needed for these experimental methods (Bassler et al., 2010, Handschel et al., 2014, Handschel et al., 2015). The analysis approaches discussed in this paper apply to free decay experiments.

Ship roll damping is known to be weakly non-linear with components from wave making, skin friction, eddy making, and lift. As a result, roll damping is dependent on roll amplitude and forward speed. Experimental measurements are the sum of these components; individual components are typically not measured. Roll damping can be expressed as quadratic with respect to roll rate. (Lewandowski, 2011)

The free roll decay data are analyzed assuming a linear damped spring-mass-damper system to represent roll. This assumption leads to the classic log decrement analysis of consecutive peaks to determine the damping coefficient (Karnopp, 1974). For a truly, linear system any pair of consecutive peaks will result in the same damping coefficient. However, ex-

perimental uncertainty can affect the determination of peak values and damping coefficient. Furthermore, the inherent non-linearity requires a nuanced approach to data analysis.

There are a number of approaches to analyze free decay that attempt to preserve the non-linearity and reduce uncertainty. These involve mean-to-peak (peaks measured from mean value), envelope (height) and curve fitting all or portions of the data set (Park et al., 2009, 2016, 2017). Finally, given the dependence on roll angle, the damping value needs to be associated with a roll angle. While each of these approaches produce the same damping coefficient with idealized linear data, it is possible to have different damping coefficients for the same data set depending on the analysis approach used. This paper discusses the advantages and disadvantages different approaches to free roll decay analysis.

2. NONLINEAR ROLL EQUATION

A means to determine ship roll damping is to conduct multiple free decay experiments of varying initial angle over a range of forward speeds including zero forward speed. Each free decay experiment is analyzed to determine dependency on roll angle. The dependency on ship forward speed is accommodated by testing over a range of speeds. The techniques described in this paper deal with roll angle dependency.

Roll damping is known to be weakly nonlinear with dependencies on roll angle and ship forward speed. Ikeda et al. (1978) has decomposed roll damping as relating to physical phenomenon such as skin friction, eddy making, wave making, and lift. The dependencies on roll angle and ship forward speed are a direct result of the phenomena that contribute to roll damping. To represent these nonlinearities, quadratic or sometimes cubic damping is added to the equations of motion (Vassilopoulos, 1971, Dalzell, 1978).

Roll stiffness can be represented with a cubic polynomial with the quadratic term set to zero resulting in a "Duffing" equation. The linear coefficient is the displacement time the metacentric height, GM. The cubic term is set to approximate the GZ curve. For roll angles where the slope of GZ curve equals GM, the cubic term does not play a noticeable role in the solution.

The single degree of freedom linear roll equation is a simple harmonic oscillator; Eqn 1.

$$(I_{44} + A_{44})\ddot{\varphi} + B_{44\_l}\dot{\varphi} + C_{44}\varphi = 0 \quad (1)$$

$$C_{44} = GMg\Delta \quad (2)$$

where I_{44} is the roll mass moment of inertia, A_{44} is the roll added mass, B_{44_l} is linear roll damping, and C_{44} is linear hydrostatic stiffness, GM is the metacentric height, g is the acceleration due to gravity, and Δ is the ship displacement.

Re-writing Eqn 1 in standard form results in Eqn 3 (Karnopp, 1974)

$$\ddot{\varphi} + 2\zeta\omega_n\dot{\varphi} + \omega_n^2\varphi = 0 \quad (3)$$

$$\omega_n = \sqrt{C_{44}/(I_{44} + A_{44})} \quad (4)$$

$$\zeta = B_{44\_l}/2\sqrt{C_{44}(I_{44} + A_{44})} \quad (5)$$

where ω_n is the undamped natural frequency and ζ is the damping ratio.

The free decay solution of which is given in Eqn 6:

$$\varphi = e^{-\omega_n\zeta t}\left(\frac{v_o + \omega_n\zeta x_o}{\omega_n\sqrt{1-\zeta^2}}\sin\omega_n\sqrt{1-\zeta^2}t + x_o\cos\omega_n\sqrt{1-\zeta^2}\,t\right) \quad (6)$$

where x_o and v_o are initial heel angle and roll velocity, respectively. The solution can also be written as a damped sine wave:

$$\varphi = e^{-\omega_n\zeta t}\sin\left(\omega_n\sqrt{1-\zeta^2}t + \varepsilon\right) \quad (7)$$

where ε is the phase angle used to match initial heel angle and roll velocity. Eqn 6 and 7 assume a zero mean heel angle. A non-zero mean heel angle, φ_o, can easily be added as seen in Eqn 8.

$$\varphi = \varphi_o + e^{-\omega_n \zeta t} \sin\left(\omega_n \sqrt{1-\zeta^2}\, t + \varepsilon\right) \quad (8)$$

Adding nonlinear damping and nonlinear stiffness in a single degree of freedom equation gives:

$$\ddot{\varphi} + 2\zeta\omega_n\dot{\varphi} + \beta\dot{\varphi}|\dot{\varphi}| + \omega_n^2\varphi + \gamma\varphi^3 = 0 \quad (9)$$

where the damping value is dependent on roll angle and forward speed and the stiffness values represent the GZ curve. β is the normalized quadratic damping and γ is the normalized cubic stiffness terms. Eqn 9 was solved with a fourth order Runge-Kutta method to provide roll decay data with known properties.

Experimental data from a free decay experiment will often have noise overlaid on the free decay caused by impulsive loading, steering, wave reflection, static heel, sensor error. To approximate that noise, φ_N, a sine wave (Eqn 9) was overlaid on the numerical solution to Eqn 8. A sine wave was selected rather than white noise as experience indicates signal noise is due to cross-coupling from impulsive loading and steering.

$$\varphi_N = \varphi_{o\_N} + \varphi_{A\_N}\sin(\omega_N t + \varepsilon_N) \quad (10)$$

The parameters of the sine wave, φ_{o_N}, φ_{A_N} and ω_N, are set nominal values; see Table 1.

3. FREE DECAY ANALYSIS BACKGROUND

The basis for all the free roll decay analysis approaches is the assumption of a linear spring-mass-damper system and its solution; Eqn 9. Traditionally, nonlinearity is addressed by analyzing the free decay data on a peak by peak basis. The damping coefficient is based on the change from one peak to the next. Lewandowski (2011) demonstrated a systems analysis approach using Hilbert filtering to determine the roll damping coefficients. Park et al. (2009) outlines the curve fitting approach which uses an optimization search method to determine coefficients for Eqn 7 resulting in the best fit of the entire data set. The best fit metric is a least squares error method.

The three basic approaches as outlined by Handschel et al. (2015) are: mean-to-peak, envelope, and curve fitting. Figure 1 shows a sample roll free decay time history with the peaks indicated. The equations for the three basic approaches use the indicated peak indices.

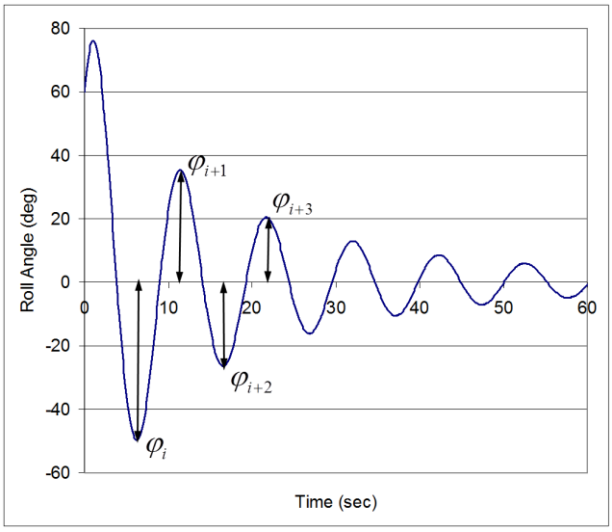

Figure 1. Sample Roll Free Decay.

The mean-to-peak approach measures peaks from the mean value. The mean value is from a recent calm water zero, average of the data set, or mean from the curve fit of the data set. The mean value is assumed constant throughout the roll decay. Then subsequent positive peaks and negative peaks are compared to determine the damping. The selection of mean value has a large effect on the analysis of small roll angles, where a non-zero mean value can be a large percentage of the peak. Generally, the curve fit mean value is the most accurate. Often damping values for roll angles less than a degree are ignored as the uncertainty becomes large and damping can be negative. The mean-to-peak approach is generally not recommended (Pawlowski, 2010; Handschel et al., 2015).

$$\zeta = \frac{1}{2\pi}\ln\left[\frac{\varphi_i}{\varphi_{i+2}}\right] \quad (11)$$

where φ_i and φ_{i+2} are consecutive same sign peaks and damping is associated with the average peak value.

The envelope method uses the height (positive peak to negative peak or negative peak to positive peak) as "peaks" for comparison. Handschel et al. (2015) refers to this as double amplitude with a "peak" as consecutive opposite sign peaks. This method avoids the entire question determining a mean value or having a moving mean value. Runs where this approach produces negative damping (later peaks larger than earlier peaks) indicate other forces are acting on the model and the data are suspect to begin with.

$$\zeta = \frac{1}{2\pi}\ln\left[\frac{|\varphi_i - \varphi_{i+1}|}{|\varphi_{i+1} - \varphi_{i+2}|}\right] \quad (12)$$

$$\bar{\varphi} = |\varphi_i + \varphi_{i+2} - 2\varphi_{i+1}| \quad (13)$$

The curve fit approach finds the damping value resulting from the best fit of a theoretical solution, often Eqn 7 to the data set. Park et al. (2009, 2016, 2017) fits the entire roll decay time history. This approach requires multiple data sets at different initial roll angles to account for roll angle dependence. This paper examines fitting of a single roll cycles as an alternative to the other peak methods. The curve fit approach is especially effective with data with very few peaks (critically damped).

Uncertainty of the roll damping estimate can be determined from the error of the linear curve fit to the roll damping data. The error associated with intercept and slope is the uncertainty in the linear and quadratic damping. Along similar lines, curve fitting the actual data, "cycle fit" approach, provides uncertainty of the roll damping at each cycle.

3.1 Experimental Data Pre-Conditioning

The free roll decay time history should have the mean value adjusted to remove any mean offset as peak magnitude can be referenced to the mean value. The mean value can simply be the average of the time history or found by fitting Eqn. 8 which includes a mean offset term.

It is also possible to fit a cubic polynomial through the peak in an effort to determine a more accurate peak value assuming the true peak value occurred between data samples. This was more important when model sample rates were 10-12 Hz. Now 50-100 Hz sample rates are more common and little accuracy is gained by curve fitting the peak.

4. RESULTS

To evaluate different analysis methodologies, free decay data with known nonlinearity was generated by using Eqn 9 for the four combinations of linear and nonlinear damping and stiffness.

Table 1 lists the coefficients used to generate the data sets and noise attributes. The time history was started from rest with an initial roll angle of 70 degrees to ensure cycles with nonlinear stiffness. Such large roll angles are impractical in experiments due to dangers of capsizing the model, introducing more noise and other nonlinearities associated with appendage (bilgekeel) exit/entrance. However, to demonstrate nonlinear behavior a large initial roll angle is acceptable.

Two noise signals were overlaid on the free decay data: constant offset and sinusoidal variation. The eight resulting time histories were analysed with all four analysis approaches to determine damping coefficients and roll frequency by cycle. The data plus noise were not pre-conditioned prior to analysis.

Table 1. Coefficients used for roll ordinary differential equation (Eqn 9) and noise (Eqn 10).

Coefficient	Units	Value
ω_n	rad/sec	0.613
ζ		0.050
β		0.18396
γ		-0.18800
ϕ_{O_N}; ϕ_{A_N}	deg	0.500
ω_N	rad/sec	0.09195

ε_N	deg	30.00

4.1 Linear Damping – Linear Stiffness

In this form, the equation is a simple harmonic oscillator; Eqn 1. In this context, linear damping is proportional to roll rate. The damping ratio is constant with respect to roll angle. The analytic solution is given by Eqn 6 with zero mean. The analysis approaches should return ζ.

With no noise, all of the approaches return the correct answer; see Figure 2. With the introduction of a mean offset as noise, the half and full cycle decrement approaches both had significant error as the peak amplitude approached the mean offset; see Figure 3. The estimated damping is either higher or lower depending on the sign of mean offset. The envelope and cycle fit approaches are not affected by the mean offset noise. When the noise is a varying mean, all of the approaches have scatter in the roll damping estimate at lower average roll angles; see Figure 4. The half-cycle decrement approach has error at even the largest roll angles. The envelope and cycle fit approaches have the least scatter. The nature of the scatter is typical of experimental data; indicating experimental noise is of the varying mean type. Figure 5 shows good prediction of roll frequency at all roll angles for all approaches regardless of noise.

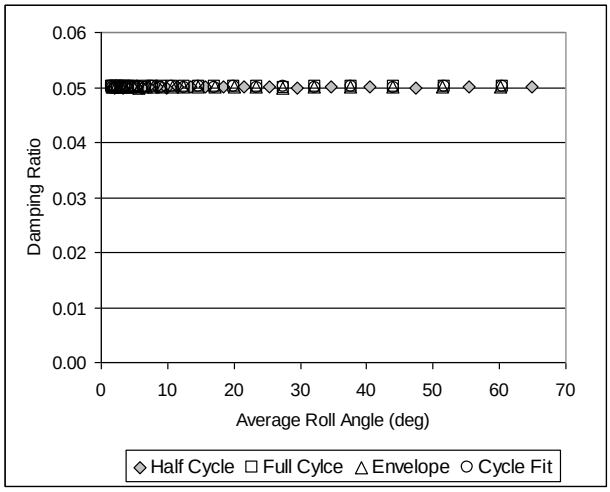

Figure 2. Damp Ratio for linear damping-linear stiffness and no noise.

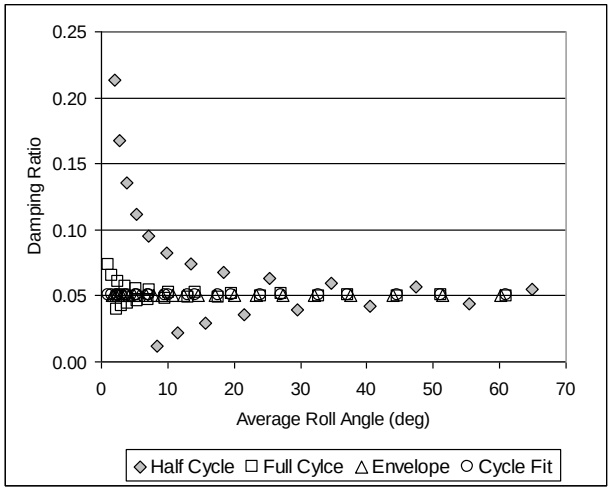

Figure 3. Damping Ratio for linear damping-linear stiffness and constant mean offset noise.

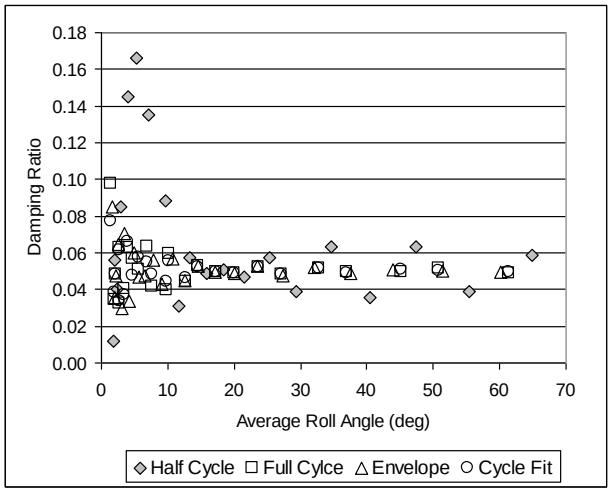

Figure 4. Damping Ratio for linear damping-linear stiffness and varying mean offset noise.

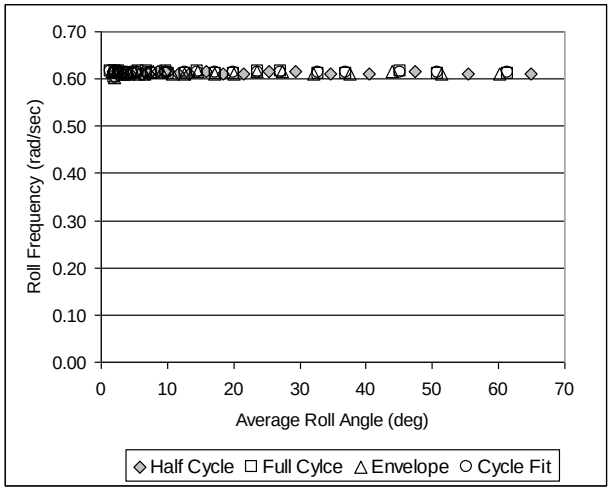

Figure 5. Roll Frequency for linear damping-linear stiffness and varying mean offset noise.

4.2 Linear Damping – Cubic Stiffness

This is the well-known "Duffing" equation with softening stiffness. The nonlinear stiffness does affect the free decay and appears as nonlinear damping at the larger roll angles. However, as the roll angles become smaller and enter the linear regime on the GZ curve, the damping ratio approaches the correct constant value; see Figure 6. Note the cycle fit approach is closer to the true value than the other log decrement approaches at larger roll angles. Figure 7 shows effect of nonlinear stiffness from Figure 6 and the same error response due to constant mean offset seen in Figure 3.

Figure 8 shows the effect of vary-ing mean noise. The results are similar to Fig-ure 4. The envelope and cycle fit approaches are closest to the correct value. The "softening stiffness" of the GZ curve results in reduced roll frequency at higher roll angle. As roll an-gles become smaller, the roll frequency ap-proaches the correct value; see Figure 9.

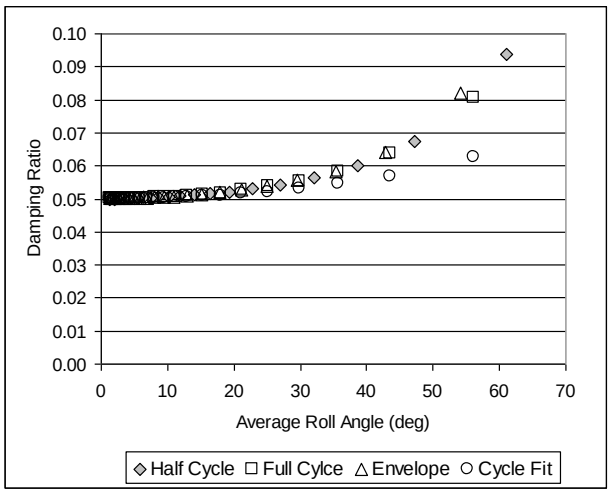

Figure 6. Damping Ratio for linear damping-cubic stiffness and no noise.

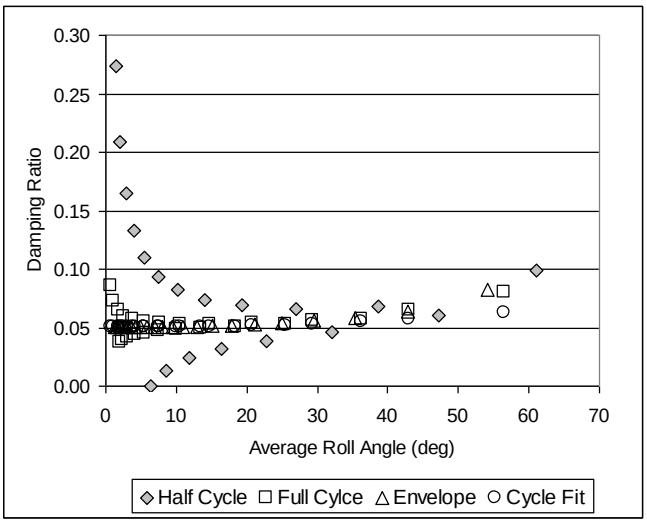

Figure 7. Damping Ratio for linear damping-cubic stiffness and constant mean offset noise.

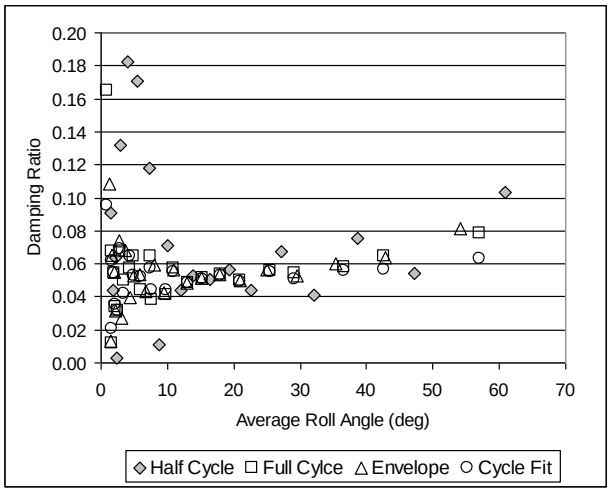

Figure 8. Damping Ratio for linear damping-cubic stiffness and varying mean offset noise.

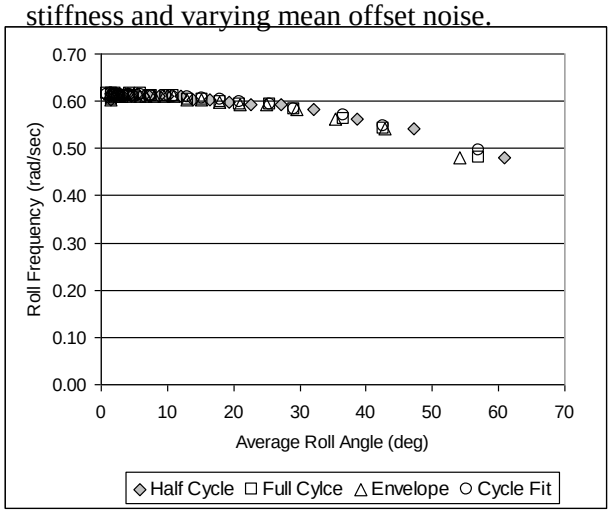

Figure 9. Roll frequency for linear damping-cubic stiffness and no noise.

4.3 Quadratic Damping-Linear Stiffness

This represents common seakeeping system of equations. In fact, even linear prediction tools with linear damping use some sort of iterative process calculating results at multiple roll angles to account for the nonlinear damping. For this equation, the damping coefficient is a linear function with respect to roll angle (Lewandowski, 2011). The Y-intercept is the linear damping ratio, ξ. The slope of the line is related to the quadratic damping term, $(8/3\pi)\omega\beta$ normalized critical damping for damping values less than 0.15 critical damping. The units of the slope is damping ratio per radian. With no noise, all the analysis approaches return the same result; see Figure 10. Park et al. (2017) shows this linear trend using initial roll angle on the curve fit rather than a cycle average roll angle.

The constant mean offset noise, Figure 11, shows half cycle decrement approach having the largest error. The data scatter is such that at the smaller roll angle range it is not possible to discern a quadratic part of the damping. Experimentally, the initial roll angle should be large enough to ensure some data with minimal data scatter.

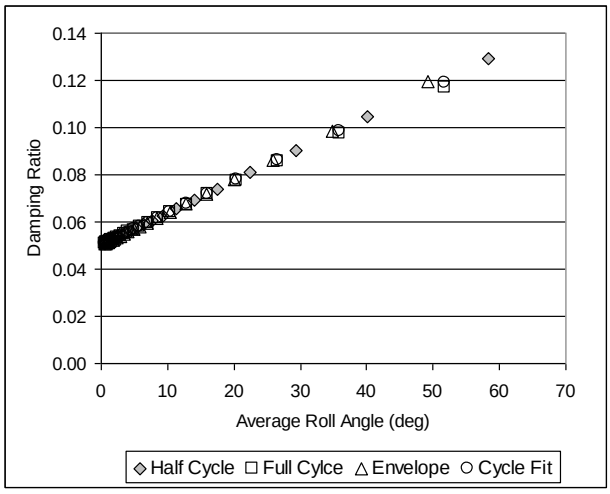

Figure 10. Damping Ratio for quadratic damping-linear stiffness and no noise.

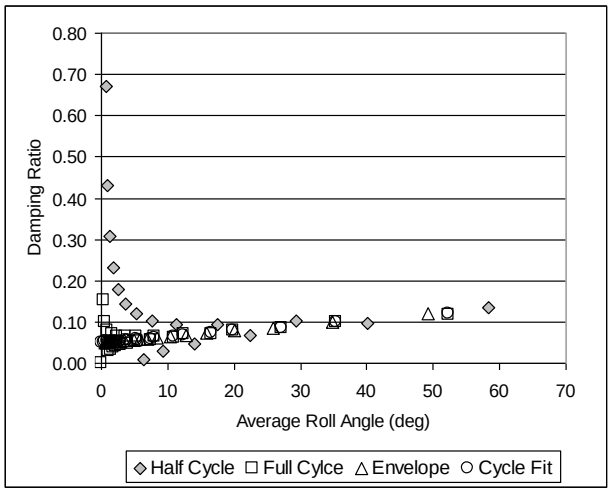

Figure 11. Damping Ratio for quadratic damping-linear stiffness and constant mean offset noise.

Figure 12 shows how the half cycle decrement approach is affected by a varying mean offset at large roll angles as well as smaller values. All approaches correctly estimate the roll frequency; see Figure 13.

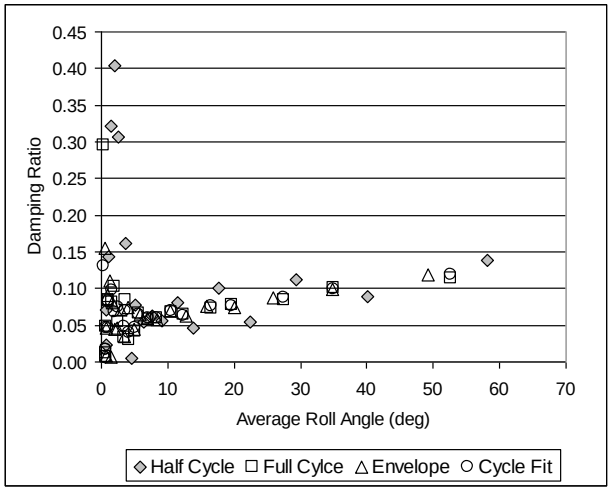

Figure 12. Damping Ratio for quadratic damping-linear stiffness and varying mean offset noise.

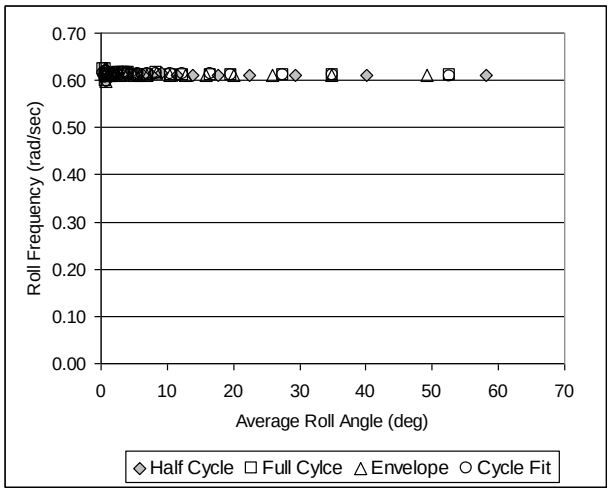

Figure 13. Roll frequency for quadratic damping-linear stiffness and varying mean offset noise.

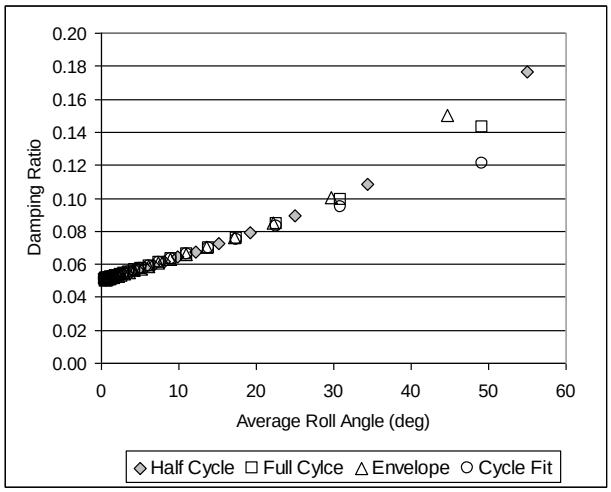

Figure 14. Damping Ratio for quadratic damping - cubic stiffness and no noise.

4.4 Quadratic Damping – Cubic Stiffness

This represents most "blended" seakeeping codes that use quadratic damping with body-exact hydrostatics and Froude-Krylov forces. The "no noise" case, Figure 14, shows the linear trend of quadratic damping at lower roll angles and superimposes the upward curve due to cubic stiffness at larger roll angles. Figure 14 is essentially the superposition of Figure 6 and Figure 10, and demonstrates the independence of damping and stiffness. Figure 15 shows the characteristic large error for the half and full cycle decrement approaches with constant mean offset noise. Figure 16 also shows larger error for half and full cycle decrement approaches, with more error for half cycle at large roll angles. Roll frequency in Figure 17 is nearly the same as Figure 9 as both have cubic stiffness.

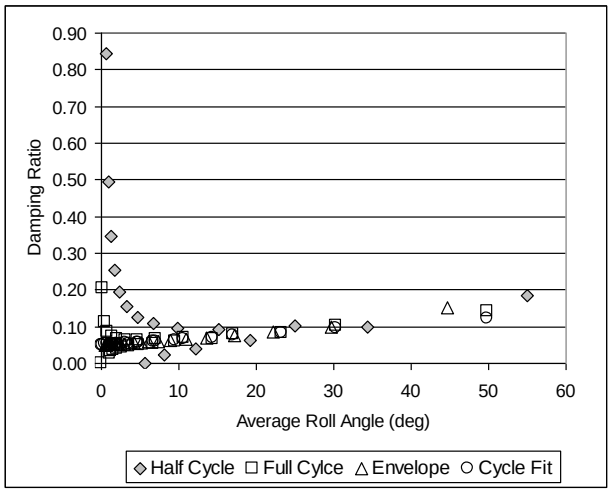

Figure 15. Damping Ratio for quadratic damping - cubic stiffness and constant mean offset noise.

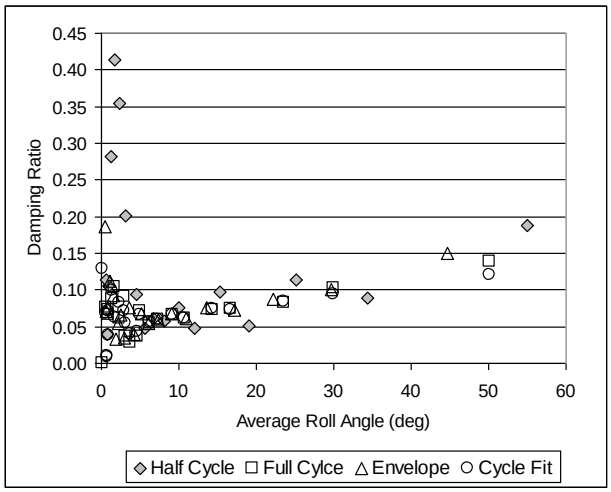

Figure 16. Damping Ratio for quadratic damping - cubic stiffness and varying mean offset noise.

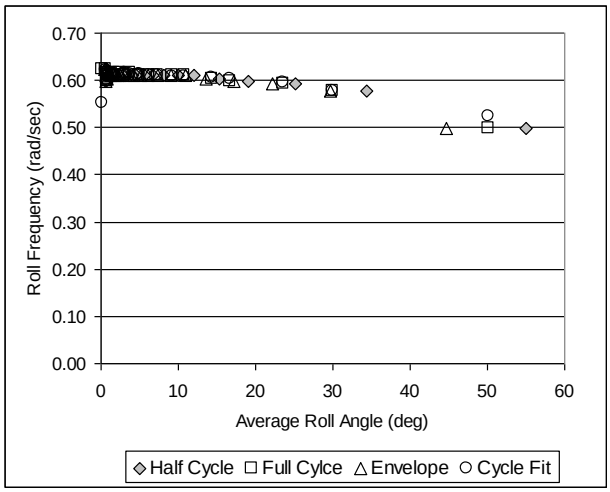

Figure 17. Roll frequency for quadratic damping - cubic stiffness and varying mean offset noise.

5. DISCUSSION

It is gratifying to know all examined methods are able to calculate the correct damping behavior with no noise. The addition of noise does makes the more traditional half and full cycle log decrement methods untenable. Even removal of the mean offset still produces scatter at the low roll angles. Even the envelope and cycle fit methods showed scatter at the low roll angles due to the varying mean offset.

Fitting the entire time history (Lewandowski, 2011; Park et al., 2017) promises to eliminate the scatter. With these approaches care must be taken to preserve the essential nonlinear quality of the data. The FREEVIB approach (Feldman, 1994; Lewandowski, 2011) is able to estimate both the linear damping term despite noise. Park et al. (2017) provides the best fit to linear harmonic oscillator equation and essentially linearizes the damping. Dependency on roll angle is addressed with analysing multiple time histories. Park et al. (2017) presents very little data below 10 degrees. Cycle curve fitting is to be preferred at it is more efficient with respect to data usage. The uncertainty estimation approach from Park et al. (2017) can still be applied on a per cycle basis with cycle curve fitting.

The roll frequency is well determined by all the methods over almost the entire roll angle range. This is a function locating the peaks with respect to time and not the peak magnitude. The peaks can easily be determined by a change in slope of the free decay time history. The peak determination is most prone to noise induced scatter when the roll angle approaches the noise level; at very small roll angles.

Given the nonlinear nature of roll damping, there needs to be a match between the simulation roll damping model and the empirical roll damping value used. This paper has focused on capturing the nonlinearities with the analysis method. However, if the simulation damping model is linear, what is needed from the experiment is an equivalent linear damping. In this case, fitting the entire (or large portion) of the time history with Eqn. 7 will produce equivalent linear damping. That value should not be associated with a specific roll angle, as linear damping assumes a constant damping value.

6. CONCLUSIONS

Four roll damping analysis approaches were evaluated on ability to correctly estimate roll damping for time histories with known nonlinearity and noise properties. For no noise, all the methods performed well. With the introduction of noise, the half and full cycle approaches exhibited much more error than the envelope or cycle fit approach. The half and full cycle decrement approaches are very dependent on determination of the mean value. The roll decay data should be de-meaned to minimize the error caused by a constant mean offset. Nevertheless, the half and full cycle log decrement methods should be avoided.

A varying mean also causes significant scatter in the damping ratio estimate. This scatter is minimized with the envelope or cycle fit approaches. Still once the roll oscillation amplitudes approach the amplitude of mean variation, rolling is no longer approximately sinusoidal. Roll damping estimates should be discarded for roll angles where the cycle roll frequency is not near the correct value. The change in cycle roll frequency indicates an unacceptable noise influence.

Additionally, an unacceptable noise influence is seen when the damping ratio is negative

as a result of noise causing peaks to not be decreasing. Peaks occurring later than this point should be discarded. Often this cutoff is arbitrarily set at 1.0-1.5 degrees, but the determination should be made on a run by run basis.

The linear damping ratio should be estimated by a linear curve fit of the larger roll angle data. Low roll angle data should be excluded from the curve fit, but used to verify the linear damping ratio estimate. This check is needed as large amplitude roll motion may have other nonlinearities or noise affecting it. And a curve fit stressing that portion of the data would be erroneous.

Initial roll angles for free decay experiments should be twice as than the expected significant single amplitude roll angle of interest with a maximum being the roll angle the bilge keels emerge from the water. This will ensure damping ratio measurements in the range of irregular seas rolling and with a higher signal to noise ratio. Once the bilge keels are out of the water, other nonlinearities need to be considered.

There should be a match in theory between the experimental analysis method and the simulation roll damping model. For instance, if the simulation uses linear damping, the experimental analysis method should produce an equivalent linear damping rather than a linear and quadratic term. The theoretical roll radiation damping should be deleted from the linear term to avoid double counting.

Analysis methods using the entire time history need to estimate both linear and nonlinear terms. A cycle approach is preferred more efficiently use the experimental data.

7. ACKNOWLEDMENTS

Dr. Joseph Klamo (Naval Post Graduate School) was instrumental in prompting this investigation into the differences in roll damping results produced by the analysis technique. Mr. Bradley Campbell suggested using a curve fitting technique to improve estimates of the mean value.

8. REFERENCES

Bassler, C.C., Reed, A.M., and Brown, A.J., 2010, "Characterization of Energy Dissipation Phenomena for Large Amplitude Ship Roll Motions," Proc. Of the 29th American Towing Tank Conference, Annapolis, MD, USA.

Dalzell, J.F., 1978, "A Note on the Form of Ship Roll Damping," Journal of Ship Research, Vol 22, No. 3, Sep 1978, pp. 178-185

Handschel. S., Fröhlich, M., and Abdel-Maksoud, M., 2014, "Experimental and Numerical Investigation of Ship Roll Damping by Applying the Harmonic Forced Roll Motion Technique," 30th Symposium on Naval Hydrodynamics, Hobart, Tasmania, Australia.

Handschel, S., Feder, D., Abdel-Maksoud, M., 2015, "Estimation of Ship Roll Damping – A Comparison of the Decay and the Harmonic Excited Roll Motion Technique for a Post Panamax Container," Proc. 12th Intl. Conf. on the Stability of Ships and Ocean Vehicles, Glasgow, UK, 19-24 June, page 475-488

Ikeda, Y., Y. Himeno, and N. Tanaka, 1978, "Components of Roll Damping of Ship at Forward Speed," Journal of the Society of Naval Architects of Japan, Vol. 143

Karnopp,B., 1974, "Introduction to Dynamics," Addison-Wesley, pp. 291-296.

Lewandowski, E., 2011, "Comparisonof Some Analysis Methods for Ship Roll Decay Data," Proc. of 11th Int. Ship Stability Workshop, Alexandria, VA, USA, 2011

Park, J. T., Hayden, D. D., Klamo, J., and Bishop, R. C., 2009, "Analysis Methodology of Roll Decay Data for Free-Running and Captive Model Tests," Proceedings of the 18th International Conference of Ship

and Shipping Research, Vol. 1, pp. 105-114, Messina, Italy.

Park, J. T., Turner, C. R., and Melendez, M. P., 2016, "Physical Properties and Roll Decay with Uncertainty Estimates for DTMB Model 5720, 23rd Scale R/V Melville," NSWCCD-80-TR-2016/018.

Park, J. T., Turner, C. R., and Melendez, M. P., 2017, "New Methodology in Analysis of Physical Properties and Roll Decay with Uncertainty Estimates for Surface-Ship Model Experiments," Proc. 30th American Towing Tank Conf., West Bethesda, USA, 3-5 October, 2017.

Pawlowski, M., 2010, "Approximation of the Non-Linear Roll Damping," Proc.of 11th Intl. Ship Stability Workshop, Wageningen, The Netherlands, 21-23 June 2010.

Vassilopoulos, L., 1971, "Ship Rolling at Zero Speed in Random Beam Seas with Nonlinear Damping and Restoration," Journal of Ship Research, Vol. 15, No. 4,

Ship Roll Damping Estimation: A Comparative Study of Different Roll Decay Tests

Adriana Oliva-Remola[0000-0002-0491-1456], *Universidad Politécnica de Madrid,* adriana.oliva@upm.es

Luis Pérez-Rojas[0000-0001-9027-8046], *Universidad Politécnica de Madrid,* luis.perezrojas@upm.es

H. R. Díaz-Ojeda[0000-0001-8045-0156], *Universidad Politécnica de Madrid,* hector.diaz@upm.es

ABSTRACT

Estimating ship roll motion precisely is still an unsolved problem today. The most common and easiest approach to estimate roll damping are decay tests. The performance of roll decays theoretically is simple, but in practice many parameters affect the results obtained from them. In particular, mechanical devices used to initially heel the ship may have a significant influence on the decaying curves, and thus the associated roll damping coefficients. In the present paper, three mechanical devices were used to carry out roll decays on a trawler fishing vessel. Obtained nonlinear damping and equivalent linear damping coefficients are compared.

Keywords: *roll damping; decay test; fishing vessels; nonlinear rolling; experimental techniques*

1. INTRODUCTION

Roll damping has gained importance in recent decades because of the international regulations under development, the Second Generation Intact Stability Criteria, see Bačkalov et al., (2016) and IMO (2016, 2017), and because of the increasing amount of ships that require a precise knowledge of its roll behavior due to their operability (Avalos et al., 2014). Despite undergoing continuous research studies, many unsolved questions remain, especially because of roll damping nonlinear behavior, which makes theoretical estimations of roll damping practically infeasible. Semi-empirical methods are available, such as the (Simplified) Ikeda Method, which is limited to cargo vessels of specific characteristics (Kawahara et al., 2012), or variants of the Ikeda Method in order to apply it to other ship types (Ali et al., 2004). Nevertheless, at large roll angles, these semi-empirical methods have been criticized for not being sufficiently accurate (Bassler, 2013). Therefore, experimental techniques are still used and recommended to predict roll damping (IMO, 2016).

Experimental techniques used to determine roll damping can be categorized mainly as decay, excited and forced roll tests (Wasserman et al., 2016, and ITTC, 2017). The present paper focuses on roll decay tests, which consist of inducing an initial heel to the ship model, releasing it allowing to roll freely, and then recording and analysing the transitory roll motion, e.g. the decaying oscillations. Among other techniques, roll decays have the advantage of being simple and not time-consuming. The main challenge in decay tests is that, for large ship models, producing an initial heel of more than 25 *deg* is difficult due to the significant moment required. Using proper mechanical devices may allow large heeling angles and fulfilling the required initial condition of zero roll angular velocity.

The aim of this paper is to systematically study different approaches to roll decays. First, a brief description of the roll motion model for decay tests is

reported. Second, the set-up used for each decay test technique is described, and the methodology of analysis to determine roll damping coefficients is illustrated. Then a case study of a trawler fishing vessel with no appendages or bilge keels is reported. Finally, some concluding remarks are provided.

2. MODELLING OF ROLL MOTION

The scope of roll decay tests is to determine the roll damping coefficients of the floating body under consideration. Roll decays are carried out by initially heeling the model up to a certain angle and then releasing it, allowing the ship to freely roll.

The dynamic model of a free roll motion at zero speed may be described by the 1-DOF (Degree of Freedom) nonlinear differential equation in calm water:

$$\ddot{\phi} + d\left(\dot{\phi}\right) + \omega_0^2 \cdot r\left(\phi\right) = 0 \qquad (1)$$

where:

- ϕ : $[rad]$ is the roll angle (dots represent derivatives with respect to (w.r.t.) time);
- $d\left(\dot{\phi}\right)$: $[s^{-1}]$ is the non-dimensional damping function, assumed to be dependent only on the instantaneous roll velocity ($\dot{\phi}$). This roll damping term is generally defined by the linear-quadratic-cubic damping model (ITTC, 2011):

$$d\left(\dot{\phi}\right) = 2 \cdot \mu \cdot \dot{\phi} + \beta \cdot \dot{\phi} \cdot \left|\dot{\phi}\right| + \delta \cdot \dot{\phi}^3 \qquad (2)$$

where μ $[1/s]$, β $[1/rad]$ and δ $[s/rad^2]$ are the linear, quadratic and cubic damping coefficients, respectively. Linear-quadratic ($\delta = 0$) or linear-cubic ($\beta = 0$) damping models may be considered as well, depending on the ship hull and on the presence of bilge keels.

- ω_0^2 : $[rad \cdot s^{-1}]$ is the undamped natural roll frequency, which is defined as:

$$\omega_0^2 = \frac{\Delta \cdot \overline{GM}}{J_{xx}^v} \qquad (3)$$

where Δ $[N]$ is the ship displacement, $\overline{GM}$ $[m]$ is the metacentric height w.r.t. the center of gravity of the ship (G), considering the vessel freely floating with displacement Δ, and J_{xx}^v $[kg \cdot m^2]$ is the total roll moment of inertia including the hydrodynamic added inertia;

- $r\left(\phi\right)$: $[nd]$ is the non-dimensional righting arm, which is equivalent to:

$$r\left(\phi\right) = \frac{\overline{GZ}\left(\phi\right)}{\overline{GM}} \qquad (4)$$

where $\overline{GZ}\left(\phi\right)$ $[m]$ is the hydrostatic roll righting lever w.r.t. G.

3. EXPERIMENTAL SET-UP

From the author's perspective, existing decay test methodologies may be categorized into the following types:

1. Only a roll moment is applied, without changing the ship model displacement;
2. A vertical force is applied, generating a roll moment, but changing the ship model displacement;
3. Pre-exciting the ship rolling a certain number of cycles and then releasing it. The ship model displacement is maintained.

In the present work, roll decays using the three types of tests cited above are performed. In the following, the technique used in each type is presented.

The main elements placed in the ship model are represented schematically in Figure 1. Translations and rotations of the vessel during the tests are measured using a commercial optical motion capture system "Optitrack Flex 3" (Optitrack, 2017).

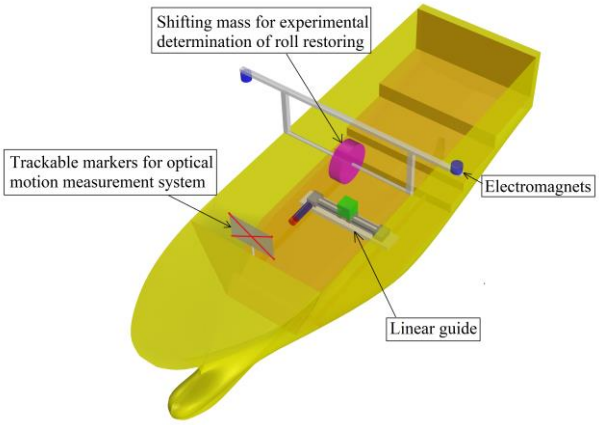

Figure 1 Set-up schematic representation.

3.1 Technique 1

The first technique consists of exerting a pure transversal moment on the ship model, which is the ideal concept of roll decays. A first approximation of this technique was used in (Bulian et al., 2009).

The system is schematically represented in Figure 2 and a picture of real experiments is shown in Figure 3. Two electromagnets are attached to the ship model and the moment is created thanks to equal and opposed vertical forces generated by the weights (see Figure 2: *weight 1* and *weight 2*). One peculiarity is that *weight 2* must be submerged to avoid disturbance of the water's surface because of the weight falling once released. For this reason, both weights do not have the same value, so for *weight 2* the buoyancy force should be accounted for. Additionally, the pulling rope of *weight 1* should be directed vertically. To this end, the transversal platform of *weight 1* could be moved.

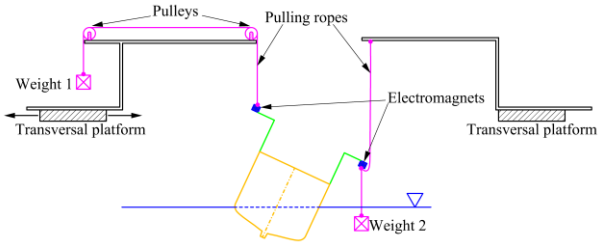

Figure 2 Schematic representation of Tech. 1.

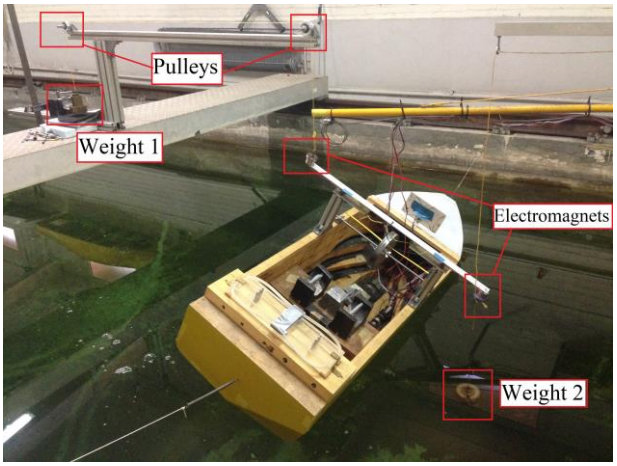

Figure 3 Experimental arrangement of Tech. 1.

3.2 Technique 2

This technique is the most common as it is the easiest to perform (Irvine et al, 2013, and el Moctar et al., 2012). As opposed to Technique 1, only one electromagnet is required, creating the roll moment using only one weight, as shown in Figure 4. The actual experimental arrangement is equivalent to the one illustrated in Figure 3, with the only difference being that the weight in the water (i.e. starboard side) is not present.

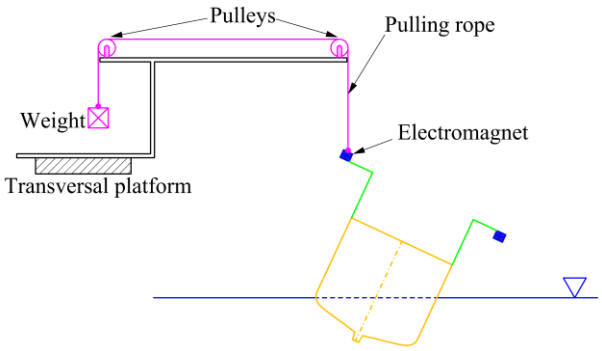

Figure 4 Schematic representation of Tech. 2.

3.3 Technique 3

The third technique was conceived to consider the so-called memory effects of the fluid (van't Veer et al., 2011). The memory effect concept is based on the idea that, if a system is not in a steady state, as roll decays the velocity field depends on one or more previous cycles as well as the roll motion itself.

This technique consists of pre-exciting the ship model by rolling the ship at the undamped roll natural frequency a certain amount of cycles up until it reaches the desired amplitude (i.e. decay test initial heel angle). It must be noted that if the ship model under analysis presents a nonlinear restoring (i.e. nonlinear righting arm curve), the undamped amplitude dependent roll oscillation frequency ($\omega_{0,eq}(A)$) should be considered (see Section 4), instead of the undamped roll natural frequency.

To pre-excite the ship, this technique was performed using an internal mass that moves through a linear guide, following a prescribed sinusoidal motion. This system was used by the authors to carry out excited roll tests, see (Oliva-Remola et al., 2018) and Figures 5 and 6. The guide is positioned near the centre of gravity of the ship model. The mass motion is controlled by an electrical engine connected to an encoder. The moving mass is initially placed at the centre of the guide and is allowed to move from the centre up to 90 *mm* on each side, which corresponds to the maximum transversal motion of the mass ($y_{m,\max}$), see Figure 5.

Using the linear guide, different forcing cases (FC) can be generated by changing the moving mass weight (m_m), and/or the maximum transversal motion of the mass. In the case study reported hereafter, the maximum transversal motion of the mass is kept constant and equal to 90 *mm*. Therefore, each forcing case has a moving mass weight associated with it.

When the mass oscillation frequency (ω_m) is the undamped amplitude dependent roll oscillation frequency $\omega_{0,eq}^2(A)$ after the transient state, a steady roll amplitude is reached. In this technique, this steady roll amplitude corresponds to the decay test's initial heel angle (A_0).

Therefore, carrying out decay tests with this technique requires us to fix the mass moving weight and the mass oscillation frequency. Knowing the roll response curve for each forcing case near the resonance zone (i.e. for each m_m), the peak resonance amplitude and frequency will determine the steady roll amplitude and the undamped amplitude dependent roll oscillation frequency.

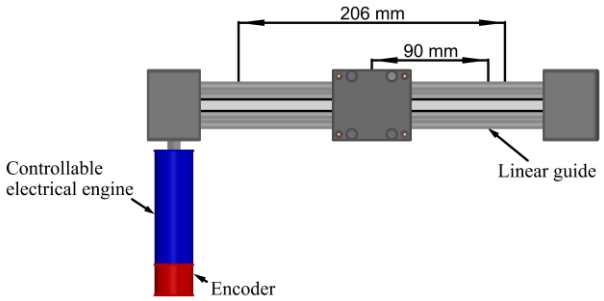

Figure 5 Details of the linear guide.

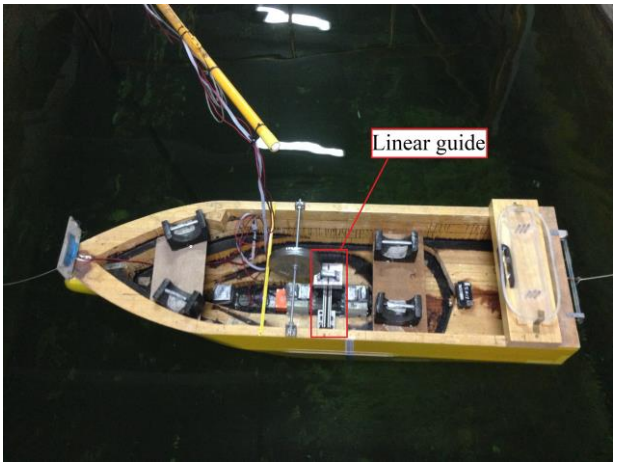

Figure 6 Experimental arrangement of Tech. 3.

4. METHODOLOGY OF ANALYSIS

Roll decays have been analysed using the procedure described in detail in Appendix 1 of (Bulian et al., 2009). This methodology considers non-linearities in restoring and damping terms, basically Eq. (1), and explicitly takes into account the amplitude-dependence frequency. In this study, the linear-cubic damping model was considered, (see Eq. (5))

and the non-linear restoring was calculated directly from the actual GZ curve, instead of obtaining the restoring coefficients from least square fitting.

The procedure is based on the logarithmic roll-decrement curve by approximating the nonlinear model of Eq. (1) by a linear equivalent model in a limited time window:

$$\ddot{\phi}+2\cdot\mu_{eq}(A)\cdot\dot{\phi}+\omega_{0,eq}{}^{2}(A)\cdot\phi=0\Big|_{\left[\tilde{t}-\frac{\Delta t}{2},\tilde{t}+\frac{\Delta t}{2}\right]} \quad (5)$$

$$\begin{cases}\mu_{eq}(A)=\mu+\dfrac{4}{3\pi}\cdot\beta\cdot\left(\tilde{\omega}(A)\cdot A\right)+\dfrac{8}{3}\cdot\delta\cdot\left(\tilde{\omega}(A)\cdot A\right)^{2}\\ \omega_{0,eq}^{2}(A)=\omega_{0}^{2}\cdot\dfrac{\int_{0}^{2\pi}r\left(\phi=A\cos(\alpha)\right)\cdot\cos(\alpha)\cdot d\alpha}{\pi\cdot A}\\ \tilde{\omega}(A)=\sqrt{\omega_{0,eq}^{2}(A)+\mu_{eq}{}^{2}(A)}\end{cases}$$

where $\mu_{eq}(A)$ is the equivalent linear damping coefficient and $\omega_{0,eq}^{2}(A)$ is the equivalent (undamped) roll natural frequency.

This methodology also allows us to aggregate data from different decay tests if they represent the same test case, allowing a robust estimation of roll damping coefficients.

Prior to analysing the decays using the aforementioned methodology, the raw measured data was filtered using an 8th order Butterworth low-pass filter with a normalized cut-off frequency of 0.125. Also, as with (Roberts, 1985), the roll decay envelope was corrected from possible bias, due to the presence of spurious effects.

5. CASE STUDY

5.1 Tested hull form

The hull used in the present work is a model of a trawler-fishing vessel at scale 1:20.667. Table 1 summarizes the main particulars of the ship and the details of the loading condition tested, and Figure 7 illustrates the body plan. The model was tested in bare hull condition, i.e. without rudder and without bilge keels.

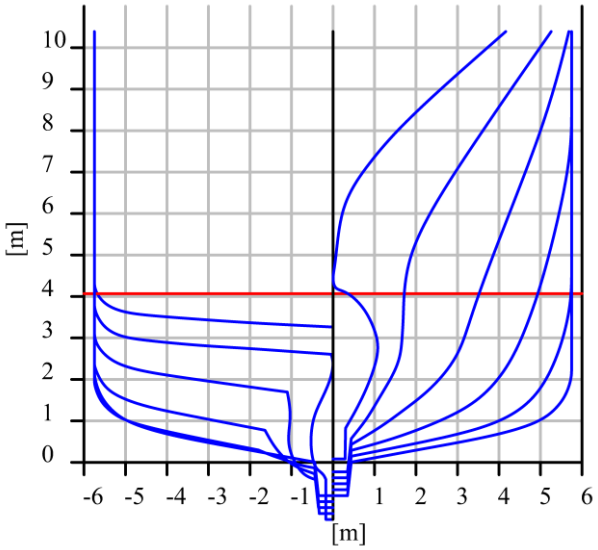

Figure 7 Body plan of the tested hull form.

Table 1 Main ship particulars. Model scale 1:20.667.

Length btw. perpendiculars, L_{pp} [m]	34.80
Length overall, LOA [m]	41.70
Breadth overall, B [m]	11.50
Draught, T [m]	4.07
Depth to upper deck, H [m]	11.94
Displacement, Δ [t]	973
Metacentric height, GM [m]	1.062
Natural roll frequency, ω_0 [rad/s]	0.750

The model displacement has been determined from directly weighing. The value of the metacentric height has been checked by means of inclining test, also reaching large heeling angles, using the system illustrated in Figure 1. The righting arm curves ($GZ(\phi)$ curve) determined from free trim hydrostatic calculations and experimentally measured ones are shown in Figure 8. The agreement between them is very good, which provides confidence in the determined metacentric height and the

reference geometry used for computations. The natural roll frequency was obtained by trial-and-error procedure performing roll decays at small angles of heel (less than 5 *deg*).

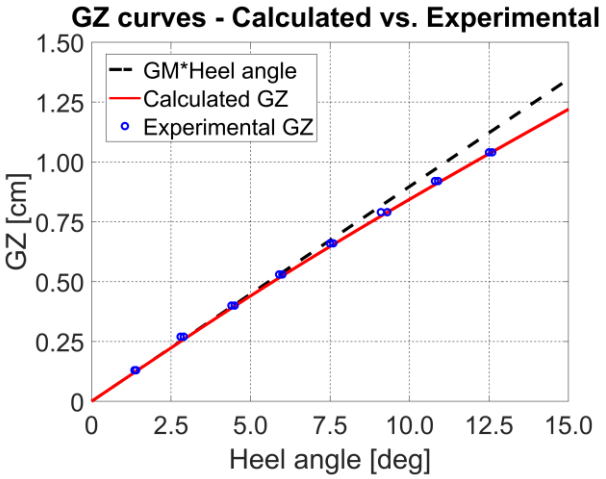

Figure 8 Comparison between experimental and calculated GZ curve of the ship model.

5.2 Decay test cases

Decay tests cases were selected considering the roll-response curves of the ship model obtained from internally excited tests using the moving mass, see (Oliva-Remola et al., 2018). The roll response curves, as a function of the normalized excitation frequency, and for each forcing case tested are shown in Figure 9.

Four forcing cases were selected to carry out the decay tests (i.e. FC01, FC03, FC05, FC07). The normalized peak amplitudes and peak resonance frequencies are associated with the decay tests' initial heel angles (for all the Techniques) and moving mass frequency (for Technique 3). Decay test cases, hereafter referred as FC, are reported in Table 2, as well as the associated moving mass weight for Technique 3.

In order to consider the influence of the fluid memory effects in Technique 3, for each decay test case two sets of mass cycles have been considered; the minimum number required to reach the steady roll amplitude (min. cyc) and a maximum number of 18 cycles, being equal for all decay test cases (max. cyc).

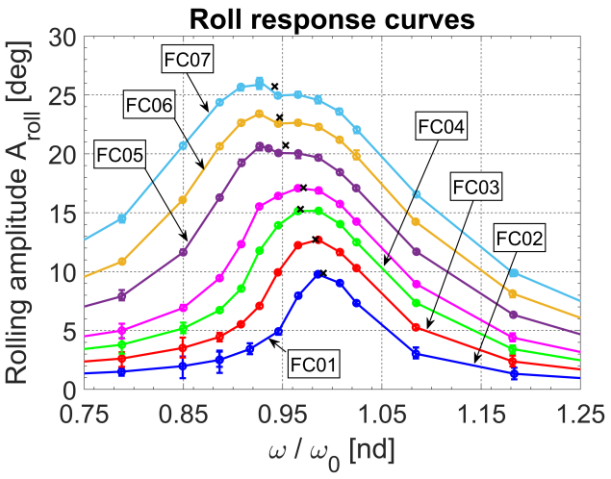

Figure 9 Experimental roll response curves from internally excited tests. Black cross marks represent the smoothed peaks. See Oliva-Remola et al. (2018).

Table 2 Decay tests cases.

FC	A_0 [*deg*]	m_m [*kg*]	ω_m / ω_0 [*nd*]	Cycles [min/max]
FC01	9.87	0.539	0.991	14/18
FC03	15.30	1.618	0.968	8/18
FC05	20.72	3.228	0.953	4/18
FC07	25.72	5.378	0.942	4/18

Three repetitions of each decay test case have been performed for each technique to increase the precision level of roll damping coefficients by increasing the total amount of experimental data points (more than 100).

5.3 Roll decay tests results

Experiments have been carried out in the ETSIN Towing Tank, which has dimensions of 100 *m* in length, 3.8 *m* breadth and 2.2 *m* depth. The ship model was placed transversally to the length of the towing tank at its mid-length. In this subsection, the characteristics of the measured roll decays are reported.

Table 3 Measured roll decay characteristics.

FC	*Tech.*	$\lvert A_0 \rvert$ [*deg*]	$\lvert A_1 \rvert$ [*deg*]	$\lvert A_0 \rvert - A_{0,mean}$ [%]
FC01	1	10.67	9.87	4.03
	2	10.04	9.40	-2.11
	3 (min)	10.09	9.22	-1.65
	3 (max)	10.23	9.30	-0.28
FC03	1	15.72	14.10	0.19
	2	15.32	13.52	-2.36
	3 (min)	15.73	13.33	0.28
	3 (max)	15.99	13.49	1.89
FC05	1	20.56	17.63	-1.63
	2	20.34	17.15	-2.68
	3 (min)	21.16	16.44	1.23
	3 (max)	21.54	16.61	3.08
FC07	1	25.88	20.95	-0.61
	2	25.19	20.05	-3.26
	3 (min)	26.63	19.20	2.27
	3 (max)	26.46	18.96	1.61

In Table 3, some characteristics of the roll decays are reported, aggregating data from the repetitions of the same decay tests case and technique. The characteristics shown are the absolute value of the initial heel angle ($\lvert A_0 \rvert$), the amplitude of the first peak considered for the analysis of roll decays ($\lvert A_1 \rvert$) and the difference as a percentage between the initial heel angle for each decay test technique and the mean initial heel angle for the decay test case. It should be noted that the first peak considered for the analysis is not equivalent to the initial heel angle, as the time instant when the ship model is released for Techniques 1 and 2 could not be known with enough confidence. Therefore, it was decided to start the analysis of decays from the second peak.

In all decay test cases, the minimum peak amplitudes considered were approximately 2 deg, except for Technique 3, FC05 (max) and FC07 (max), where the minimum amplitudes were of 5 *deg* and 4 *deg*, respectively. The reason is that, as the initial heel angles and the number of cycles were large, the model reflected waves that, eventually, affect the ship roll motion, as seen in Figure 10.

5.4 Determination and analysis of roll damping coefficients

Considering the experimental data and the analysis methodology shown in Section 4 and in Bulian et al. (2009), roll damping coefficients have been determined for each decay test case. In all cases, the linear-cubic damping model was considered, as the fitting of the other models (linear-quadratic-cubic or linear-quadratic) led to negative damping coefficients.

In Table 4, linear and cubic damping coefficients are reported for each decay test case, as well as the fitted (undamped) ship roll natural frequency. It is important to highlight that the cubic damping coefficient would be valid within the range of the experimental amplitudes for each forcing case.

In Figures 11, 12 and 13, the fitted coefficients for each forcing case are represented. Linear and cubic damping coefficients are reported adimensionalized by ω_0. The error bars reported in Figure 11 represent the difference between the fitted natural frequency and the mean fitted natural frequency, determined as the mean of the ω_0 values reported in Table 4. The error bars reported in Figures 12 and 13 represent the confidence intervals with a confidence level of 95% and have been calculated from the least square fitting of coefficients μ and δ, assuming a Gaussian distribution, and dividing (for μ) or multiplying (for δ) the confidence

intervals obtained by the fitted value of ω_0, neglecting uncertainties of ω_0. The coefficients for Technique 3 (max. cyc) and forcing cases 05 and 07 should be treated with care because

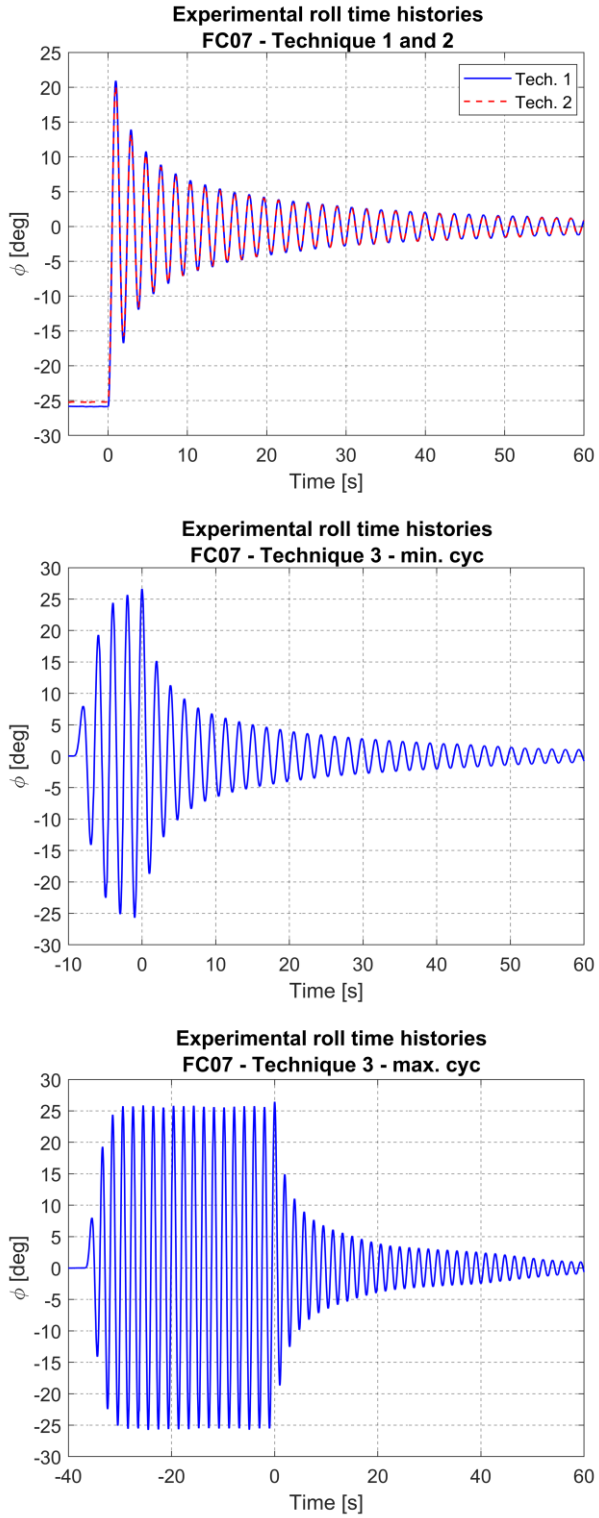

of the reflected waves (see Figure 10).

Figure 10 Roll decay histories. FC07.

From the results in Table 4 and Figure 11, it can be noted that the fitted roll natural frequency is always slightly larger than the imposed value. Nevertheless, the differences are very limited, with an average reduction of ω_0 of 0.352%.

From the results in Figures 12 and 13, it can be noted that differences of linear and cubic damping coefficients between the techniques are of the order of magnitude of the uncertainty of data for FC01, FC03 and FC05. If the results of Technique 3 (max. cyc) are omitted, FC07 succeeds in the same situation as for the other forcing cases. However, the cubic coefficients differ between them by more than 20%. It is important to point out that in general, the relative level of uncertainty is significant, between 4 to 10 % for μ and 2 to 12% for δ. This may be because of the data scattering, although during the decays analysis it did not appear to be significant, see Figure 14.

To consider a global quantity of the damping, the equivalent linear damping coefficient ($\mu_{eq}(A)$), see Eq. (6), has been calculated for two rolling amplitudes, namely 10 *deg* and 20 *deg*. The coefficients are represented in Figures 15 and 16. In these figures, the confidence intervals represent the ±1.96 Root Mean Square Error (*RMSE*), which is an approximation for 95% of the confidence interval of any new experimental value of $\mu_{eq}(A)$. The *RMSE* is defined as:

$$RMSE \simeq \sqrt{\frac{\sum_{k=1}^{N_{\exp}} \left(y_{\exp,k} - y_{fit,k} \right)^2}{N_{\exp} - n}} \qquad (6)$$

where $N_{\exp}$ is the total number of experimental data points, n the number of free parameters (i.e. = 2, for μ_{eq}), $y_{\exp,k}$ is the experimental data point and $y_{fit,k}$ is the fitted data point calculated from Eq. (6).

Table 4 Fitted coefficients for each decay case.

FC	Technique	ω_0 [*rad/s*]	μ [*1/s*]	δ [*s/rad²*]
FC01	1	3.414	0.0291	0.5829
	2	3.421	0.0263	0.6625
	3 (min)	3.417	0.0261	0.5878
	3 (max)	3.421	0.0294	0.5382
FC03	1	3.419	0.0280	0.5819
	2	3.418	0.0260	0.5976
	3 (min)	3.426	0.0278	0.6017
	3 (max)	3.417	0.0285	0.5733
FC05	1	3.419	0.0285	0.5623
	2	3.419	0.0266	0.5845
	3 (min)	3.425	0.0299	0.5713
	3 (max)	3.431	0.0291	0.5877
FC07	1	3.421	0.0303	0.5221
	2	3.421	0.0280	0.5668
	3 (min)	3.414	0.0270	0.6049
	3 (max)	3.427	0.0229	0.6537

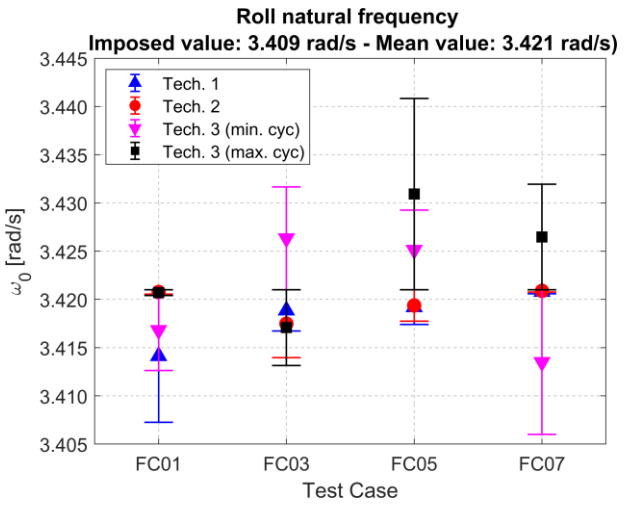

Figure 11 Fitted roll natural frequency (ω_0).

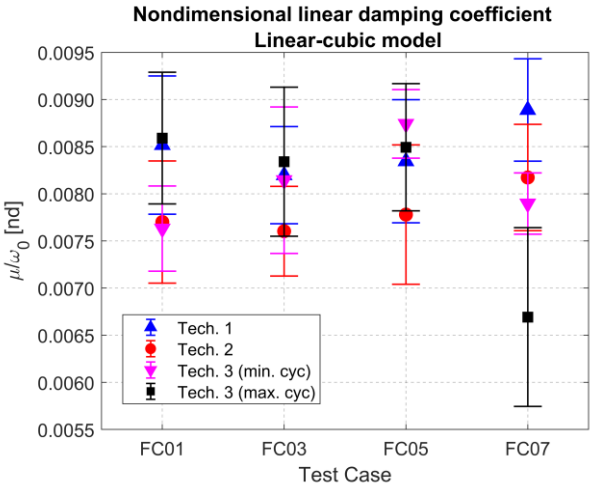

Figure 12 Non-dimensional linear damping coefficient (μ/ω_0).

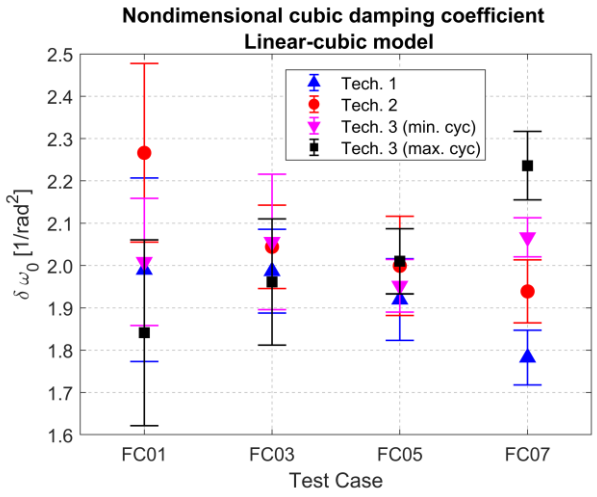

Figure 13 Non-dimensional cubic damping coefficient ($\delta \cdot \omega_0$).

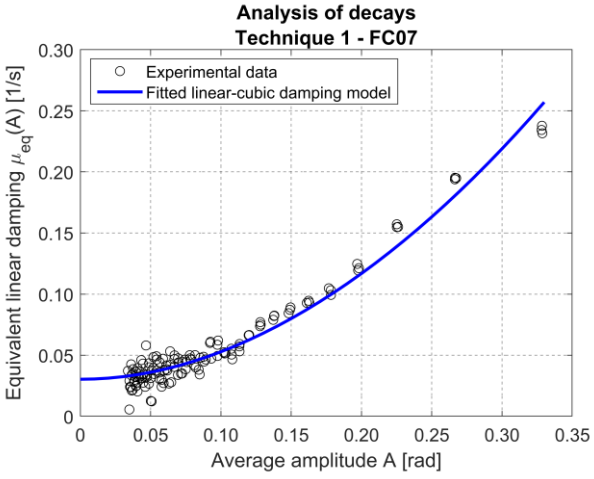

Figure 14 Decay test analysis. Tech. 1, FC07.

From Figures 15 and 16, the significant influence that the rolling amplitude has on the equivalent linear damping coefficient can be seen. It is evident especially when the damping model used is the linear-cubic.

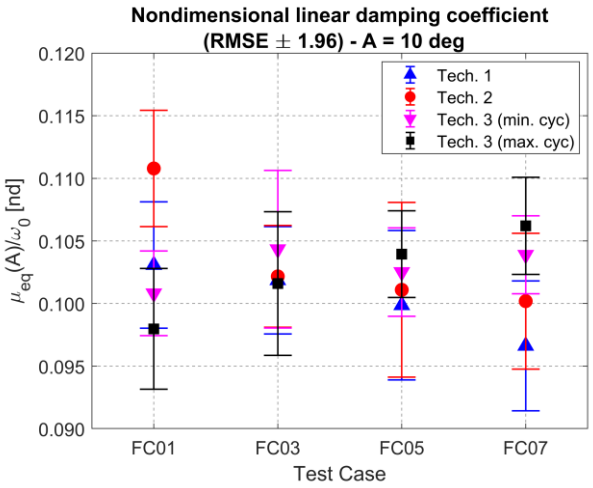

Figure 15 Dimensionless equivalent linear damping coefficient. Rolling amplitude: 10 *deg*.

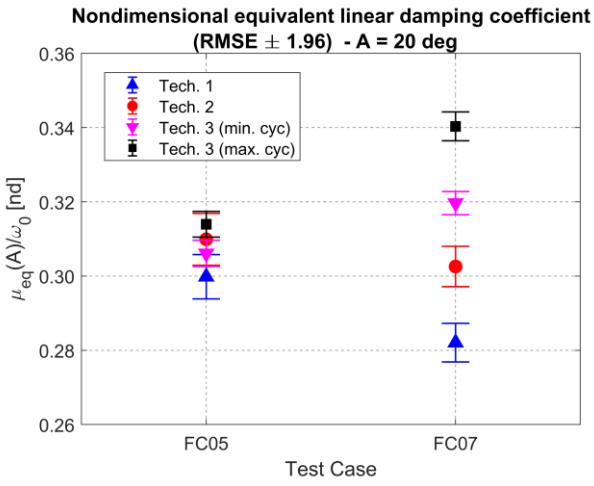

Figure 16 Dimensionless equivalent linear damping coefficient. Rolling amplitude: 20 *deg*.

It can also be found that the difference of $\mu_{eq}(A)$ among the three techniques are of the order of magnitude of the uncertainty levels, except for FC07. In FC07 the equivalent linear damping coefficient is slightly different for all techniques, differing between them by approximately 15% (without considering Technique 3 (max. cyc)). Therefore, it may be concluded that the uncertainties associated with the data recording (not considered in this study) and the analysis of decays dominate the different techniques for initial heel angles of decays around 20 *deg*. Thus, if damping coefficients for rolling amplitudes below 20 *deg* have to be determined, it may not be necessary to use complex techniques to carry out decay tests; using Technique 2 would be sufficient. However, if rolling amplitudes larger than 20 *deg* need to be studied, the above affirmation may not be reliable.

In line with the previous paragraph, it can be noted that the uncertainty levels, i.e. 95% confidence intervals, significantly reduce with the rolling amplitude. For 10 *deg* of roll amplitude, variations of linear equivalent damping reach 6%. Meanwhile, at 20 *deg*, the variations are around 2%.

6. FINAL REMARKS

In this study, different techniques have been implemented to determine roll damping coefficients. The techniques tested characterize the majority of decay test methodologies found in the literature. Additionally, for each technique four different initial heel angles have been tested.

The case study indicated that the non-linear damping coefficients determined using the different techniques are similar, showing differences of the order of magnitude of the uncertainty of the fitting procedure. The equivalent linear damping coefficient for different rolling amplitudes produced the same conclusion. However, it is important to highlight that the variation of the uncertainty levels dropped considerably at large angles of rolling.

In general, it seems that the uncertainty associated with data recording (not considered in the current study) and analysis dominate over differences between techniques. Hence, it may not be necessary to carry out complex decay tests, as pushing or pulling the ship model from one side, using a proper mechanical device, could be sufficient.

7. REFERENCES

Ali, B., Katayama, T., Ikeda, Y., 2004, "Roll damping characteristics of fishing boats with and without drift motion", International Shipbuilding Progress, Vol. 51(2,3), pp. 237-250.

Avalos, G. O.G., Wanderley, J. B.V., Fernandes, A. C., Oliveira, A. C., 2014, "Roll damping decay of a FPSO with bilge keels", Ocean Engineering, Vol. 87, pp. 111–120.

Bačkalov, I., Bulian, G., Cichowicz, J., Eliopoulou, E., Konovessis, D., Leguen, J.-F., Rosén, A., Themelis, N., 2016, "Ship stability, dynamics and safety: Status and perspectives from a review of recent STAB conferences and ISSW events", Ocean Engineering, Vol. 116, pp. 312-349.

Bassler, C.C., 2013, "Analysis and modelling of hydrodynamic components for ship roll motion in heavy weather", Ph.D. Thesis Virginia Tech. University, 2 May.

Bulian, G., Francescutto, A., Fucile, F., 2009, "Project HYD-III-CEH-5: Determination of relevant parameters for the alternative assessment of Intact Stability Weather Criterion on experimental basis", HYDROLAB Project. 22 November.

el Moctar, O., Shigunov, V., Zorn, T., 2012, "Duisburg Test Case: Post-Panamax Container Ship for Benchmarking", Ship Technology Research, Vol. 59(3), pp. 50-64.

IMO, 2016, "SDC4/5/1, SDC4/5/1/Add.1-Add.6. Report of the correspondence group. Part 1 to Part 7", 11 November. London, UK.

IMO, 2017, "SDC4/WP.4. Finalization of the Second Generation Intact Stability Criteria. Report of the Working Group. Part 1", 16 February. London, UK.

Irvine, M., Longo, J., Stern, F., 2013, "Forward Speed Calm Water Roll Decay for Surface Combatant 5415: Global and Local Flow Measurements", Journal of Ship Research, Vol. 57(4), pp. 202-219.

ITTC, 2011, "Numerical Estimation of Roll Damping. Recommended Procedure 7.5-02-07-04.5".

ITTC, 2017, "Stability in Waves Committee. Final Report and Recommendations", Proceedings of 28th ITTC, Vol. 1.

Kawahara, Y., Maekawa, K., Ikeda, Y., 2012, "A simple prediction formula of roll damping of conventional cargo ships on the basis of Ikeda's method and its limitation", Journal of Shipping and Ocean Engineering, Vol. 2(4), pp. 201-210.

Oliva-Remola, A., Bulian, G., Pérez-Rojas, L., 2018, "Estimation of damping through internally excited roll tests", Ocean Engineering. Vol. 160, pp. 490-506.

Optitrack, 2017, "Optitrack Flex 3", http://optitrack.com/ (accessed 01 March 2018).

Roberts, J., 1985, "Estimation of nonlinear ship roll damping from free-decay data", Journal of Ship Research, Vol. 29(2), pp. 127-138.

van't Veer, R., Fathi, F., 2011, "On the roll damping of an FPSO with riser balcony and bilge keels", The International Journal of Maritime Engineering, Vol. 153(2), pp. 125-135.

Wassermann, S., Feder, D.-F., Abdel-Maksoud, M., 2016, "Estimation of ship roll damping - A comparison of the decay and the harmonic excited roll motion technique for a post panamax container ship", Ocean Engineering, Vol. 120, pp. 371–382.

Numerical Study on the Scale Effect of Ship Roll Damping

Min Gu, *China Ship Scientific Research Center, Wuxi, China,* gumin702@163.com

Shuxia Bu, *China Ship Scientific Research Center, Wuxi, China,* bushuxia8@163.com

Chengsheng Wu, *China Ship Scientific Research Center, Wuxi, China,* cswu@163.com

Jiang Lu, *China Ship Scientific Research Center, Wuxi, China,* lujiang1980@aliyun.com

ABSTRACT

Ship roll damping is very important for the prediction of large amplitude roll motions, and the scale of the ship model could affect the result of roll damping. In order to investigate this effect, the roll damping with different model scales are numerically studied based on the RANS equation in calm water. Firstly, the free roll decay motions of different scales under different initial roll amplitudes are simulated using one two-dimensional ship section, and the influence of scale effect is studied. Secondly, taking three-dimensional ships as examples, the numerical simulation method is validated by the comparisons between experimental results and numerical simulation results under model scale, and the free roll decay motions under different scale factors of the three-dimensional ship are also simulated. It is found that the effects of different scales mainly due to the bilge keels, and scale ratio could affect the free roll decay motion and the roll damping coefficients, especially for large initial roll amplitude.

Keywords: *Roll damping, scale effect, RANS; free rolling*

1. INTRODUCTION

The large roll motions such as parametric roll, stability under dead ship condition and pure loss of stability are one of the critical risks for the safety when the ship sails in the seas, and the roll damping is essential to the accurate prediction of these large roll motions. However, the accurate prediction of ship roll damping is very difficult, except for high cost experiments. Therefore, a numerical method to predict the large roll damping with high accuracy is desirable.

Nowadays, the model to full-scale is based on the Froude law of similarity. In Froude-scaled model tests, the Reynolds number are different between model-scale and full-scale, which will affects the boundary layer of hull and flow separation. The large roll damping is strongly nonlinear, which has relationships with fluid viscosity and flow characteristics, such as the flow separation and vortex shedding. So the scale effect should be estimated.

For the calculation of roll damping, the Correspondence Group on Intact Stability regarding second generation intact stability criteria proposed that the roll damping could be calculated by roll decay/forced roll test or CFD simulation (United States & Japan, 2014). Although the model tests can predict the roll damping very well, it is costly and time-consuming and most of experimental data are limited to a certain frequency range and

particular geometry, which is impossible for the large-scale expansion of the application (Bass & Haddara, 1988; Blok & Aalbers, 1991).

For the accurate calculation of roll damping, the influence of viscosity must be considered. The CFD numerical simulation can consider different objects and its characteristics, which can also reduce the cost. With the development of CFD technology, the turbulent models have been improved, such as RANS equation and discrete vortex method. In addition, the fine structure of the flow field can also be analysed by CFD, so CFD could be widely used to predict roll damping. Forced roll method and free roll decay method are two main methods for the calculation of the roll damping.

In our previous studies (Min Gu, et al, 2015), the forced roll motions of one 2D ship section based on the methods of orthogonal design and variance analysis were carried out, in which different calculation parameters for the roll damping was analysed, and the free roll motions of one 3D containership were also carried out. Then the feasibility of CFD for the prediction of the roll damping was validated by taking one pure car carrier and one standard model 2792 as examples, in which two methods were used during numerical simulations: one is sliding interface method and another is dynamic overset grid method (Min Gu & Shuxia Bu, et al, 2016).

The aim of this paper is to study the scale effects of roll damping by dynamic overset grid method. The free roll decay curves of 2D ship section for different initial roll amplitudes under different model-scales are simulated based on the unsteady RANS equation, and the roll damping coefficients under different scales are compared. Then the scale effects for the standard model 2792 are also studied.

2. SHIP GEOMETRY

Two models are used in this paper. The first one is 2D ship section, and its principal particulars are shown in Table 1. The second one is the 2792 ship without bilge keel, which is one of the international standard model ship for dead ship stability provided by IMO second generation intact stability, and its principal particulars are shown in Table 2. The body plans and geometries are shown in Figure 1 and Figure 2.

Table 1 Principal particulars of the 2D section profile

Items	Model
Breadth: *B*	32.0m
Depth: *D*	28.0m
Mean draught: *T*	4.0m
Displ.: W	405260.0kg
Kxx	0.35B

Table 2 Principal particulars of the 2792 model

Items	Ship	Model
Length: L_{pp}	205.7m	3.165m
Mean draught: *T*	6.6m	0.102m
Breadth: *B*	32.0m	0.492m
Depth: *D*	20.2m	0.311m
GM	1.989m	0.0306m
Displ.: W	23986ton	87.34kg

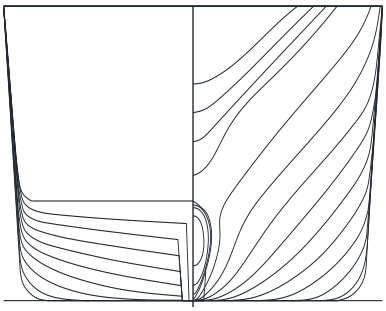

Figure 1 Lines of the ship 2792

Figure 2 Hull geometry of the ship 2792

3. EXPERIMENTS

The free roll decay experiments for the ship 2792 were carried out at the towing tank of

Wuhan University of Technology, as shown in Figure 3.

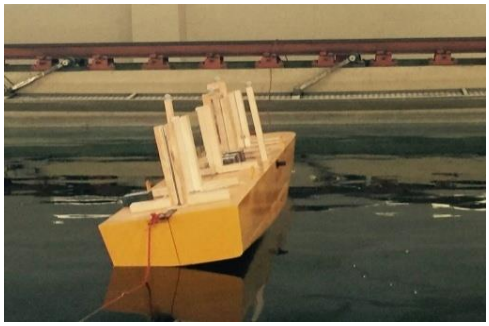

Figure 3 Ship 2792 model in the free roll decay model test

The roll decay curves were measured by a MEMS (Micro Electro-Mechanical System)-based gyroscope mounted on the ship model, and the initial roll angles are set as 10º, 20º and 25º, respectively.

4. COMPUTATION METHOD

All computations are performed by solving unsteady RANS equation. SST k-ω two-equation model is employed for the enclosure of the governing equations. The VOF method is adopted for the treatment of nonlinear free surface. The pressure-correction algorithm of SIMPLE type is used for the pressure-velocity coupling. The enhanced wall function is adopted based on the previous studies (Min Gu, et al, 2015).

In the simulations, the modes of roll, sway, and heave are free while other modes are constrained. For the 2D ship section, the profile of the computation domain is shown in Figure 4. The computational domain is separated into two main regions, background region and overset region, and each region is further divided into several small zones. The mesh in overlap region is refined to guarantee the data exchange between overset region and background region. The waterline plane region is refined to better capture the flow of free surface, and the body meshes around bilge keels are also refined in order to better capture the flow forms around the bilge keels, as shown in Figure 5.

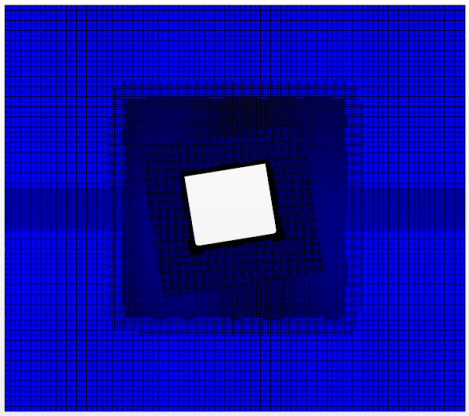

Figure 4 Computational domains of the 2D ship section

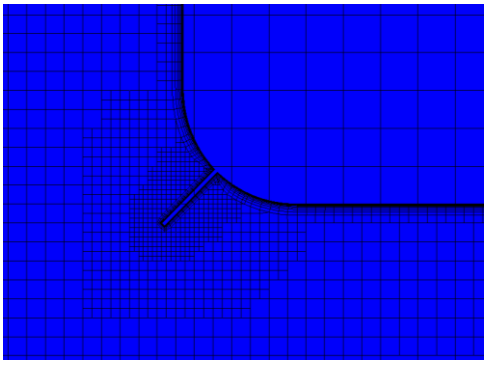

Figure 5 Meshes around bilge keels of the 2D ship section

For the ship 2792, the solution domains are shown in Figure 6, and the types of body meshes are shown in Figure 7. The numerical simulation method used was described in our previous paper (Min Gu & Shuxia Bu, et al, 2016).

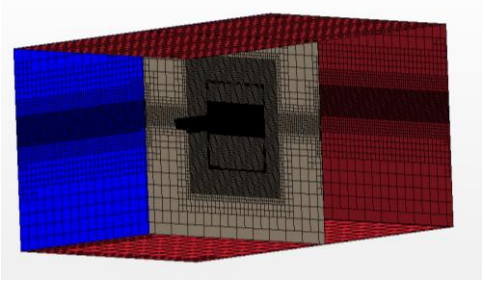

Figure 6 Computational domains of the ship 2792

Figure 7 Hull meshes of the ship 2792

For each model-scale, the mesh size growth rate is 1.3. On one hand, the setting of the thickness of the first grid should ensure the

smoothness of the grid. On the other hand, the value of y+ should guarantee to be located near 1. Since the difference between different scales is mainly in the difference of Re, which lead to the different thickness of the first gird layer. Except that, the setting of other meshes are according to the scale ratio. That is to say, the difference of mesh quantity is mainly due to the difference of the thickness of the first gird layer.

In order to compare the results of roll damping coefficients between different scales, the extinction curve should be expressed as the linear formula (1), which is the essential component of the roll damping.

$$\Delta\phi = A\phi_m \quad (1)$$

Where, $\Delta\phi$:decrement of roll decay curve and ϕ_m:mean swing angle of roll decay curve.

5. THE CALCULATION RESULTS AND ANALYSIS

5.1 Grid analysis

The grid analysis was done in our previous studies (Min Gu & Shuxia Bu, et al, 2016) by taking one pure car carrier as an example, and also validated by experimental results. Therefore, the same setting of computation domains and grid size are used in this paper.

5.2 Results of 2D ship section and analysis

For the 2D ship section, the free roll decay motions with three initial angular velocities and different scales are simulated. For the first initial velocity, the maximum roll amplitude is about 25º, as shown in Figure 8. In the figure, "Scale=1" represents the full-scale. "Scale=0.1" represents the scale of 1:10. In other words, the 2D ship section is scaled to 10% of the full-scale. Similarly, "Scale=0.05" represents the scale of 1:20; "Scale=0.02" represents the scale of 1:50; "Scale=0.01" represents the scale of 1:100. From the comparison results, it can be seen that there are certain differences for the free roll motion curves under different scale factors.

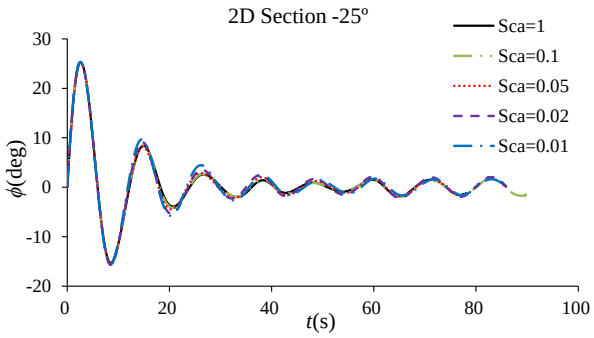

Figure 8 Comparisons of free roll decay curves with different scale factors (largest initial roll velocity)

The linear free roll decay coefficients can be obtained by linear fitting to each curves, as shown in Figure 9. The linear roll damping coefficients under different model-scales are compared with each other as shown in Figure 10. It can be seen from the diagram that the linear damping coefficient decreases sharply when the scale is too small. That is to say, the scale has great impact on the roll damping results when the model is too small.

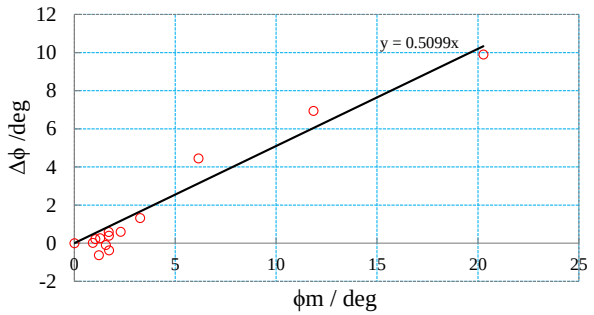

Figure 9 Fitting of linear roll damping coefficient

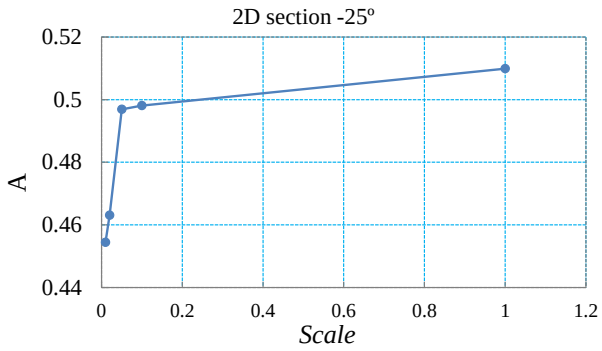

Figure 10 Comparisons of linear roll damping coefficients with different scale factors (largest initial roll velocity)

For the second initial velocity, the maximum roll amplitude is about 22º, and the

difference of free roll curves under different scale factors become smaller, as shown in Figure 11. For the third initial velocity, the maximum roll amplitude is about 12º, and there is almost no difference under different scale ratios, as shown in Figure 12.

The similar rules of scale effects on roll damping coefficient are also found when the maximum roll angle is 22º or 12º, as shown in Figure 13 and 14. However, the rules are not as obvious as that when the maximum roll angels is 25º. That is to say, the effects of model-scale on linear roll damping coefficients become obvious along with the increase of initial roll velocity. The effect of scale factor on roll damping coefficient is related to the initial roll amplitude.

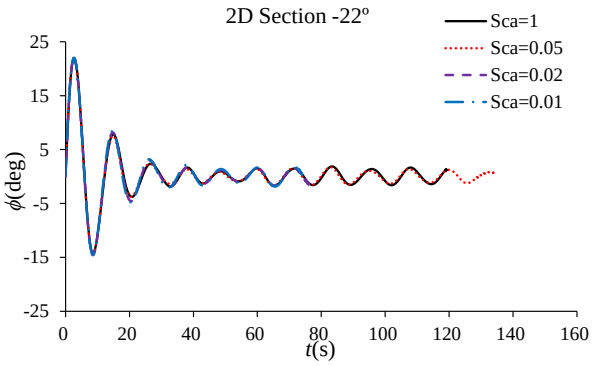

Figure 11 Comparisons of free roll decay curves with different scale factors (middle initial roll velocity)

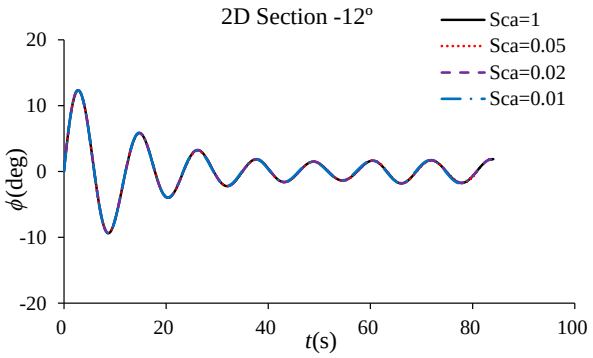

Figure 12 Comparisons of free roll decay curves with different scale factors (smallest initial roll velocity)

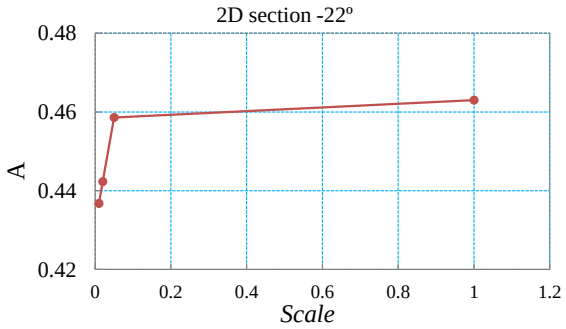

Figure 13 Comparisons of linear roll damping coefficients with different scale factors (middle initial roll velocity)

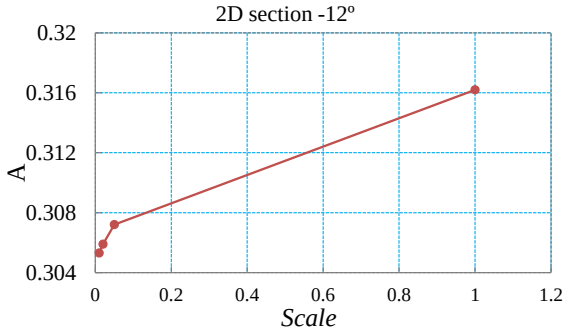

Figure 14 Comparisons of linear roll damping coefficients with different scale factors (smallest initial roll velocity)

The contours of velocity, as shown in Figure 15(a)-15(d), show evident formation and shedding of vortices near ship boundary in the process of rolling, especially near the bilge keel, which are related to roll damping. One scalar graph for the volume fraction of water is shown in Figure 16. The free surface can be clearly seen from the diagram, which demonstrates the ability of the proposed method in this paper to capture the free surface.

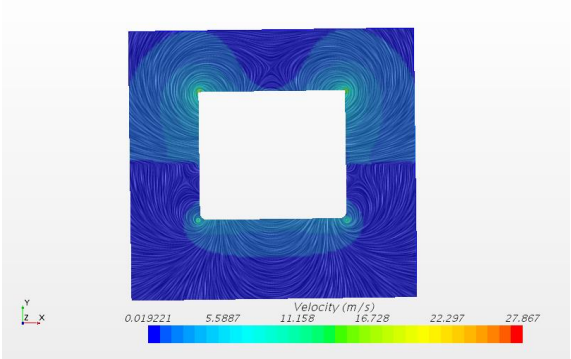

Figure 15(a) Velocity vector graph (t=0.0s)

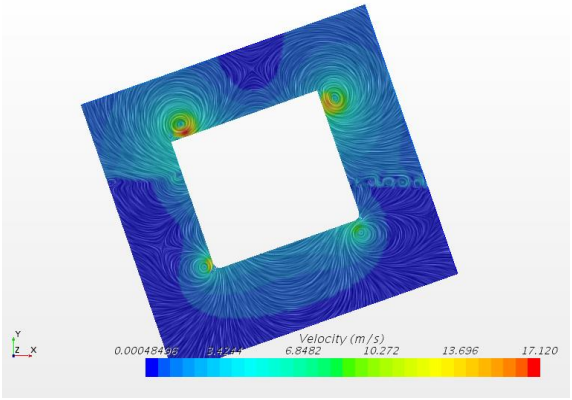

Figure 15(b) Velocity vector graph (t=1/4T)

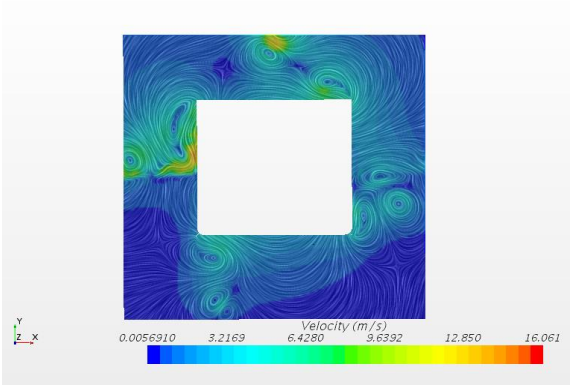

Figure 15(c) Velocity vector graph (t=1/2T)

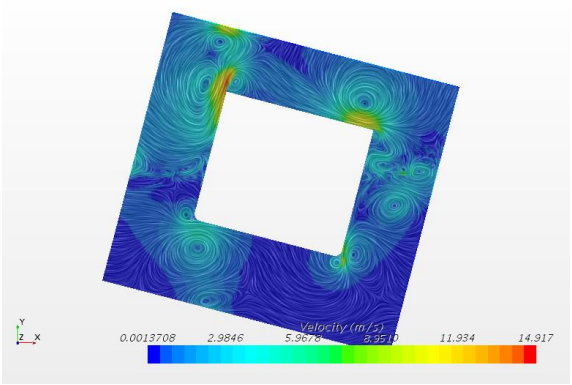

Figure 15(d) Velocity vector graph (t=3/4T)

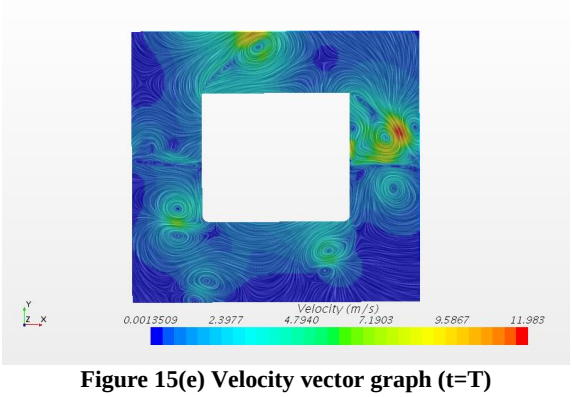

Figure 15(e) Velocity vector graph (t=T)

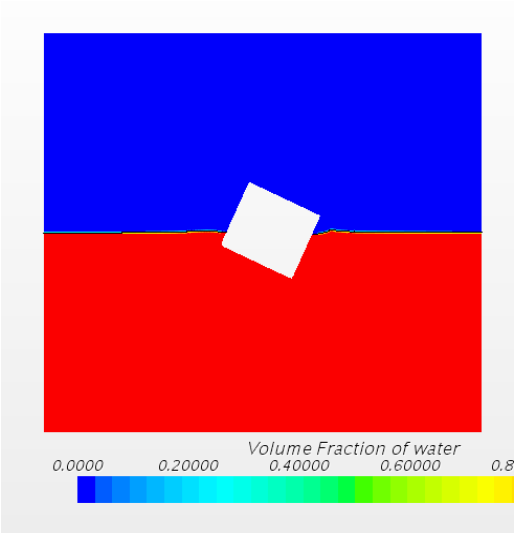

Figure 16 Scalar graph for free surface

5.3 Results of 2792 standard model and analysis

In order to verify the influence law obtained by the two dimensional section, the free roll decay motions are further simulated by taking 3D ships as examples. In our previous studies, the numerical simulation methods for free roll motions are carried out by taking one pure car carrier and 2792 standard model as examples. In current study, the 2792 standard model is chosen again.

The initial roll amplitude is set as 20º, and three scale factors are chosen, 0.0154, 0.154 and 0.769 respectively. For the scale of 0.0154, the model tests were conducted and the comparisons between numerical simulation results and experimental results are shown in Figure 17. It can be seen that the numerical simulation results are in good agreement with the model test results, which proves the reliability of the numerical simulation method.

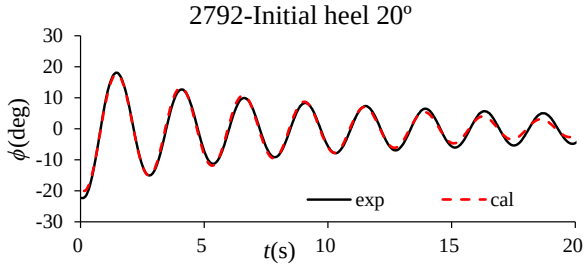

Figure 17 Free roll decay curves for 2792 (exp and cal)

Up to now, the comparisons between numerical simulations and real ship tests are not available due to the lack of real ships data. Therefore, the numerical simulation method validated by model tests is further extended to simulation of real ship. In the simulation, the y+ keeps almost the same, and the free roll decay curves at different scales are shown in Figure 18 and the comparison of roll damping coefficients is shown in Figure 19. From the curves, we can see that the effects of scale factor is not very obvious.

It is known that the percent of bilge keels roll damping is the largest in the total roll damping, and the formation and distribution of the vortices is very obvious near the bilge keels. However, the 2792 standard model ship does not have bilge keels, and the formation and shedding of the vortices around the hull are not obvious, as shown in Figure 20. Therefore, the influence of the scale ratio is not obvious, which can indirectly prove that the influence of scale ratio on the roll damping is mainly due to the effects of scale ratio on the bilge keel roll damping.

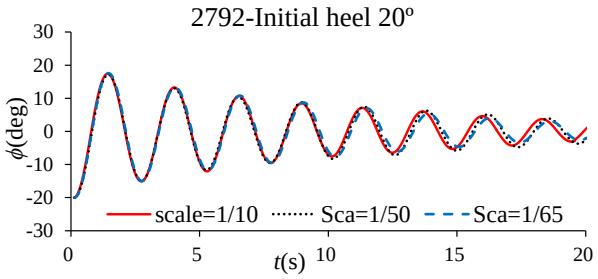

Figure 18 Free roll decay curves for 2792 with different scale factors

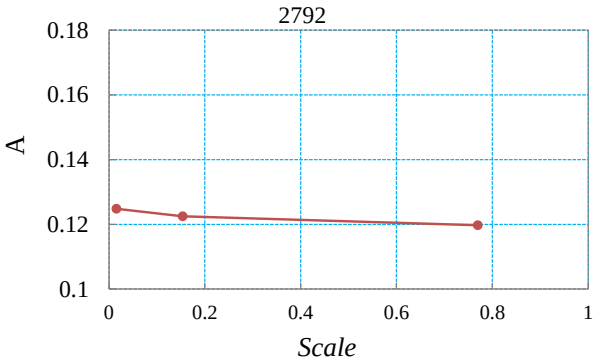

Figure 19 Linear roll damping coefficients along with scales.

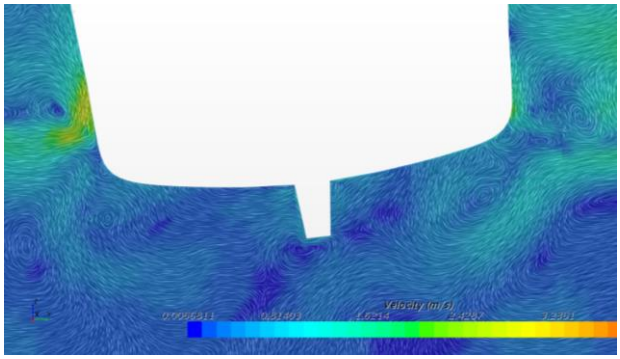

Figure 20 Vortices around the ship hull.

6. CONCLUSIONS

In this paper, taking one 2D ship section as example, the scale effects of roll damping are studied by comparing the linear roll damping coefficients under different scale factors. Then the influence of scale effects on roll damping are further validated by calculating the free roll decay motions of ship 2792 under different scales. The following remarks can be obtained:

(1) For the 2D ship section with bilge keels, the scale effects on roll damping coefficients are very obvious, especially for the large initial roll amplitude.

(2) For the ship 2792 without bilge keels, the scale effects can be ignored. The reason may be that the bilge keels roll damping is the most important part in the total roll damping, and the formation and shedding of the vortices around bilge keels are very obvious. That is to say, the influence of viscosity around bilge keels is the main reason for the scale effects of roll damping. However, this conclusion needs further study.

The validation of the current method is based on model test data, due to the lack of full scale ship data. On the one hand, full scale tests are essential, on the other hand, the uncertainty analysis should be carried out based on more model tests.

Considering that the urgent task is to develop a fixed set of methods and processes

for the numerical simulation of the roll damping based on the CFD method. The methods used in the paper have been validated by some experimental results, such as 4250TEU containership (Min Gu, et al, 2015), ship 2792 (Min Gu & Shuxia Bu, et al, 2016), one pure car carrier (Min Gu & Shuxia Bu, et al, 2016). In order to further validate our current method and form routine method for the numerical simulation of roll damping, the other ships with and without bilge keels, which have conducted free roll decay model tests are chosen, and the calculation works are still in process.

7. ACKNOWLEDGEMENTS

This research is supported by Ministry of Industry and Information Technology of China (No. [2016]26, [2017]614). The authors sincerely thank the above organization.

8. REFERENCES

Bass, D. W., and Haddara, M. R., 1988, "Non-linear Models of Ship Roll Damping", International Shipbuilding Progress, Vol. 35(401), pp. 5-24.

Bassler C.C., Reed A.M., 2009, "An Analysis of the Bilge Keel Roll Damping Component Model", 10th STAB, St. Petersburg, Russia. pp: 369-386.

Blok, J.J. and Aalbers, A.B., 1991, "Roll Damping Due to Lift Effects on High Speed Monohulls", FAST`91, Vol. 2, pp. 1331-1349.

Min Gu, Jiang Lu, Shuxia Bu, Chengsheng Wu, GengyaoQiu, 2015,"Numerical Simulation of the Ship Roll Damping", 12th STAB, Glasgow UK, pp:341-348.

Min Gu, Shuxia Bu, Gengyao Qiu, Ke Zeng, Chengsheng Wu, Jiang Lu, 2016, "Validation of CFD Simulation for Ship Roll Damping using one Pure Car Carrier and one Standard Model", 15th ISSW, Stockholm, Sweden, pp:165-172

ISCG (the Correspondence Group on Intact Stability), 2015, "Draft Explanatory Notes on the Vulnerability of Ships to the Parametric Roll Stability Failure Mode", IMOSDC3/INF.10, Annex 17.

Japan, 2011a, "Interim Verification and Validation Report on Simplified Roll Damping", IMO SLF 54/INF 12, Annex 7.

Japan, 2011b, "Additional Validation Data on Simplified Roll Damping Estimation for Vulnerability Criteria on Parametric Rolling", IMO SLF 54/INF 12, Annex 11.

Sweden, 2011, "Evaluation of Ikeda's simplified method for prediction of roll damping", IMO SLF 54/3/6.

United States and Japan, 2014, "Draft Guidelines of Direct Stability Assessment Procedures as a Part of the Second Generation Intact Stability Criteria, IMO SDC1/INF.8, Annex 27.

Accelerated HERM Technique by Induced Artificial Damping for Efficient Ship Roll Damping Estimation

Sven Wassermann, *Hamburg University of Technology (TUHH)* sven.wassermann@tuhh.de

Patrick Sumislawski, *Hamburg University of Technology (TUHH)* patrick.sumislawski@tuhh.de

Moustafa Abdel-Maksoud, *Hamburg University of Technology (TUHH)* m.abdel-maksoud@tuhh.de

ABSTRACT

A technique to reduce significantly the transient start process of the harmonic excited roll motion (HERM) is presented. The approach is based on Artificial Induced Damping (AID) which allows an acceleration of CFD simulations to estimate ship roll damping up to 80% with the same simulation setup but with a modified excitation moment. To determine the excitation moment, a newly developed roll damping prediction method for mono hulls is introduced. The application of the presented AID technique allows CFD engineers to estimate roll damping in a predefined simulation time.

Keywords: *roll damping, HERM, AID*

1. INTRODUCTION

Efficient simulations of ship motions in waves using the driven mass-spring-damper system are well known practice since several decades. Hydrodynamic forces and moments are calculated with potential theory based methods. While these methods are able to predict main energy dissipation in all other degrees of freedom, the estimation of damping for roll motion is still a weak point.

The Harmonic Excited Roll Motion (HERM) technique is established to estimate roll damping of ships, see Sugai & Yamanouchi (1963), Blume (1979) and Handschel & Abdel-Maksoud (2014). Compared to the decay technique, the estimation of roll damping for ships at higher speeds and for large roll amplitudes is possible. The roll motion is stationary, which means that effects at the starting phase will not influence the final results.

Weakly damped ships (damping ratio $\varphi_h/\varphi_a < 0.2$) which are excited to harmonic sine oscillations have a significant transient settling time (start process) before a stationary amplitude is reached, see Figure 1. However, to estimate nonlinear damping, a stationary state of the system is required. In this paper, a technique is presented to reduce the transient time significantly. The excitation moment is modified to induce an additional artificial damping which increases the total damping ratio. The characteristic of a sine oscillation is not affected. The amount of the additional induced damping force is known and will be subtracted during the post-processing from total damping of the system to estimate the unmodified ship roll damping.

For applying the HERM technique with Artificial Induced Damping (AID), a control algorithm will be introduced. Roll damping has to be roughly predicted to calculate the

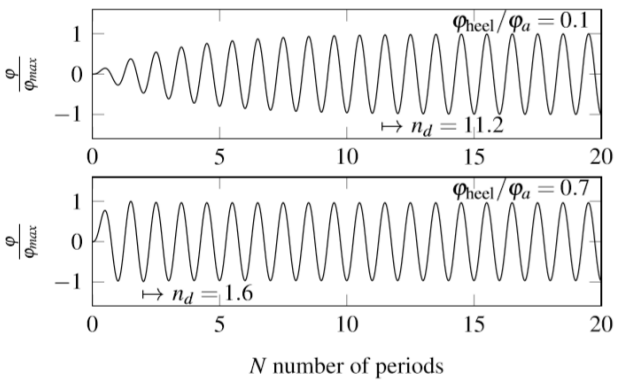

Figure 1 Number of periods n_d for transient time (start process) with 3% accuracy of the stationary amplitude for two different damping values

excitation moment. Therefore, an Artifical Neural Network (ANN) approach to approximate bare hull roll damping for mono hull ships was developed which is based on the four variables: roll amplitude, Froude number, the ratio of ship breadth to draft and the block coefficient. The initial data base to create the ANN is based on roll damping coefficients of 20 ships. To calculate bilge keel and frictional damping, force coefficient models are given.

CFD-HERM-simulations of the bench-marking containership DTC were carried out with and without AID. Using the same simulation setup but with a different excitation moment, time savings of 80% (4 instead 20 periods) were achieved for zero speed and 50% (3 instead 6 periods) for design speed. Results are discussed in detail.

2. APPROACH

2.1 HERM technique

Here, the harmonic excited ship motion is approximated as a one degree of freedom system around the longitudinal ship axis. The roll equation can be formulated based on Newton's second law. The inertia of the ship M_φ, the damping moment N_φ, restoring moment S_φ and the excitation moment F_E are usually formulated to achieve a balance between the rigid body moments and the external moment.

$$M_\varphi \frac{\partial^2 \varphi}{\partial t} + N_\varphi \left(\frac{\partial \varphi}{\partial t}\right) + S_\varphi(\varphi) = F_E(t) \qquad (1)$$

The HERM technique is carried out in the undamped natural frequency ω_0 which can be estimated e.g. with the determined frequency ω_d and the logarithmic decrement Λ of a decay test:

$$\omega_0(\varphi_a) = \frac{\omega_d(\varphi_a)}{\sqrt{1 - \left(\frac{\Lambda}{\pi}\right)^2}}. \qquad (2)$$

For sine harmonic oscillations, Equation (1) can be simplified for frequency ω_0 to:

$$\omega_0 N_{\varphi,e} \varphi_a = F_{E1,a} \qquad (3)$$

with

$$F_{E1,a} = M_\varphi \cdot f_1 = \rho V g \overline{GN} \varphi_h \qquad (4)$$

where $\overline{GN} = \overline{GZ}/sin\varphi_h$ and

$$M_\varphi = \frac{\rho V g \overline{GN}}{\omega_0^2}. \qquad (5)$$

The equivalent damping coefficient $N_{\varphi,e}$ can be expressed by a conservation of energy approach and estimated with e.g. a method based on the first Fourier coefficient of F_{E1} in phase with the roll velocity $D_{B,1}$, see Handschel & Abdel-Maksoud (2014),

$$N_{\varphi,e} = \frac{D_{B,1}}{\omega_0 \varphi_a}. \qquad (6)$$

Over a full roll cycle, the damping ratio $\frac{\varphi_h}{\varphi_a} = 2\zeta = \frac{N_{\varphi,e}}{M_\varphi \omega_0}$ yields to

$$\left(\frac{\varphi_h}{\varphi_a}\right) = \frac{N_{\varphi,e}\omega_0}{\rho V g \overline{GN}} = \frac{D_{B,1}}{\rho V g \overline{GN} \varphi_a}. \qquad (7)$$

The excitation force coefficient f_1 can be calculated with a predicted damping ratio for a specific roll amplitude φ_a with

$$f_1 = \omega_0^2 \varphi_a \left(\frac{\varphi_h}{\varphi_a}\right)_{\text{predicted}}. \qquad (8)$$

2.2 Artificial Induced Damping (AID)

To shorten the transient process in HERM simulations for weakly damped ships, roll damping has to be increased, see Figure 1. The idea behind the concept of Artificial Induced Damping (AID) is to modulate the excitation moment to induce additional damping of a

known value. An implementation based on a predicted velocity signal is given by Wassermann (2018). Here, the implementation based on a captured roll velocity $\dot{\varphi}$ signal is described. In Figure 2 (a) the block diagram of Equation (1) is given. The lower Figure (b) shows the AID concept based on a modified excitation moment:

$$F_{E2}(t) = M_\varphi \cdot [f_1 \sin(\omega_0 t) - f_2 \dot{\varphi}] \tag{9}$$

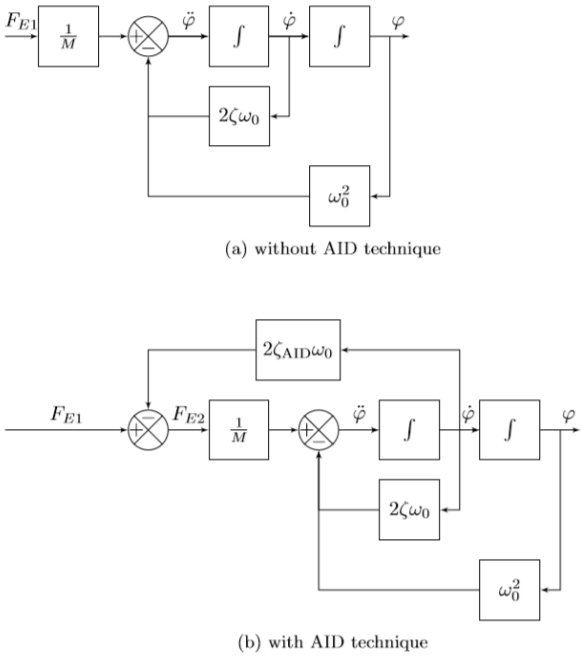

Figure 2 HERM block diagram w/o (a) and with (b) AID

with

$$f_1 = \omega_0 \varphi_a \left[f_2 + \omega_0 \left(\frac{\varphi_h}{\varphi_a} \right)_{\text{predicted}} \right] \tag{10}$$

and

$$f_2 = \omega_0 \left(\frac{\varphi_h}{\varphi_a} \right)_{\text{AID}} . \tag{11}$$

Due to the sinusoidal excitation moment, a sinusoidal roll velocity is created with

$$\dot{\varphi} = \varphi_a \omega_0 \cos(\omega_0 t) . \tag{12}$$

Equation (9) tends for stationary roll motions to

$$F_{E2}(t) = M_\varphi \cdot [f_1 \sin(\omega_0 t) - f_2 \varphi_a \omega_0 \cos(\omega_0 t)] . \tag{13}$$

Equation 13 can be generalized with

$$A \sin x + B \cos x = \cos\theta \sin x + \sin\theta \cos x \tag{14}$$

which yields to

$$\sqrt{A^2 + B^2} \sin(x + \theta). \tag{15}$$

This shows that the induced damping is not changing the sinusoidal characteristic of the system. The moment is phase-shifted by an angle θ.

Total roll damping

$$\left(\frac{\varphi_h}{\varphi_a} \right)_{\text{total}} = \left(\frac{\varphi_h}{\varphi_a} \right) + \left(\frac{\varphi_h}{\varphi_a} \right)_{\text{AID}} \tag{16}$$

can be determined with Equation 7 with $\varphi(t)$ and $F_{E1}(t)$. The subtraction of the known AID-part from the total damping part yields to the unmodified ship roll damping ratio.

3. VERIFICATION

3.1 Geometry and Test Setup

In the present paper CFD simulation results are presented for the post panamax container ship Duisburg Test Case (DTC, see el Moctar et al., 2012). Main dimensions are given in Table 2. The model is equipped with bilge keels, a propeller and a full spade rudder. The bilge keels are separated into five parts with a breadth of $0.008\,B_{WL}$. Especially the huge bow flare area as well as the transom stern is typical for this type

of ship. The model tests were carried out at Hamburg ship model basin (HSVA, Schumacher, 2010). A scale factor of 59.467 is applied.

Table 2 Main dimensions Duisburg Test Case (DTC) for full loading condition – scale factor 1:59.467

L_{WL}	6.0691 m
B_{WL}	0.8576 m
T	0.2354 m
KG	0.3992 m
C_B	0.6544
V	0.7887 m^3
i_{xx}	0.3967 B_{WL}
i_{yy}, i_{zz}	0.2447 L_{WL}

The concept of Artificial Induced Damping (AID) is proofed for two test cases, see Table 3. For AID, the total damping is quadrupled.

Table 3 Test setups for four CFD simulations with and without AID technique

		w/o AID	with AID	
Fr	T [s]	f_1	f_1	f_2
0.00	4.57	0.045	0.185	0.355
0.19	4.45	0.103	0.411	1.182

3.2 Numerical Simulation Method

The solver STAR-CCM+ is used to simulate the incompressible flow around the rolling ship. The finite-volume method solves the governing equations in integral form for mass and momentum, as well as for the volume fraction of water and air and equations for the turbulence model. The segregated iterative solution method is based on SIMPLE-algorithm.

The computational domain is divided into three regions. The ship region is shifted depending on the equation of motion results. To hold the model on course, a PID-controlled rudder is integrated, see Sumislawski et al. (2018). The rudder region is connected via a sliding interface to the ship region. The propeller is considered with a virtual disc force model. An outer region follows the translation of the ship region. An overset interface boundary condition is applied between the ship and the outer part of the grid (see Figure 3). The grid is unstructured and with trimmed hexahedral cells. For the RANSE simulations, a prism layer on the wall region exists. Local refinements are applied near the hull, the appendages and the free water surface. A volume of fluid (VOF) method is used to calculate the free water surface flow. The turbulence model k−ω-SST is used. The ship is able to move in all six degrees of freedom. Depending on whether simulations are performed with or without AID, the excitation moment definition of Equation 4 or 9 is used.

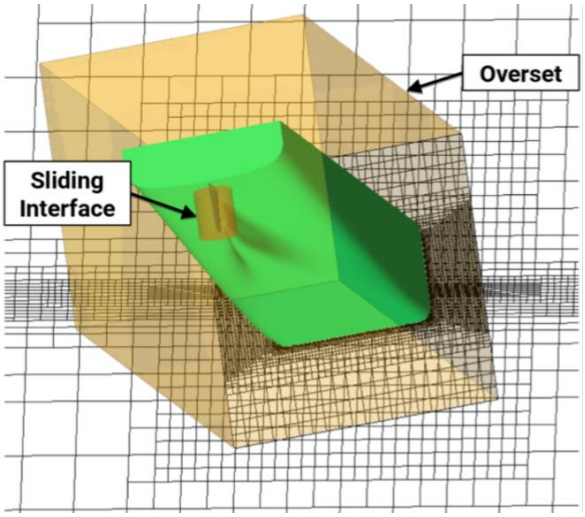

Figure 3 Application of the overset grid and sliding interface technique

3.3 Results

The comparison of damping values with and without AID technique and the required number of periods n_c to achieve a converged result are presented in Table 4.

Table 4 Comparison of roll damping results with and without AID technique

	w/o AID			with AID		
Fr	φ_a	φ_h/φ_a	n_c	φ_a	φ_h/φ_a	n_c
0.00	15.9	0.086	20	16.5	0.082	4
0.19	10.6	0.279	6	10.6	0.276	3

Using the same simulation setup, time savings of 80% (4 instead 20 periods) were achieved for zero speed and 50% (3 instead 6

periods) for design speed $Fr = 0.19$. Based on this study, the required number of periods for a converged result can be approximated with

$$n_c \approx \frac{-3}{2\pi\frac{\varphi_h}{\varphi_a}} ln\left(0.03\sqrt{1-\left(\frac{\varphi_h}{2\varphi_a}\right)^2}\right)+1\,. \quad (17)$$

Simulations with the AID technique show one further advantage. Due to the short simulation time, a PID-controlled rudder or the translation of the outer region are not necessary. DTC did not drift very much from course or got into a significant sway motion. However, this depends from the ship geometry and the motion setup.

4. APPLICATION

4.1 CFD simulation procedure

Compared to the simulation procedure described in Section 3.2., the setup is different in one point. Because the influence of rudder motions on roll damping can be significant (Sumislawski et al., 2018), the simulations were carried out with a fixed rudder. This is possible due to the short simulation time with the AID technique.

Previous simulations also showed that yaw and sway movements are very small. Moving the outer region is not necessary. Instead of the presented three region technique with overset grid, a one region technique with mesh morphing can be a suitable alternative.

4.2 Roll Damping Prediction

For roll damping prediction, here an approach presented by Wassermann (2017) is used. For the newly developed prediction method, a strategy based on a combination of machine-learning and semi-theoretical methods is adapted. It combines a black-box model for bare hull damping N_φ^{BH} and with gray-box models for bilge keel N_φ^{BK} and frictional damping N_φ^F. A short summary of the prediction method is given in the appendix. The damping ratio can be approximated with

$$\left(\frac{\varphi_h}{\varphi_a}\right)_{\text{predicted}} = \frac{\omega_0\left(N_\varphi^{BH}+N_\varphi^F+N_\varphi^{BK}\right)}{\rho V g \overline{GM}}\,. \quad (18)$$

4.3 Example with DTC

Roll damping is predicted for 5, 10, 15 and 20 degrees of three Froude numbers for DTC, see Table 5. AID parameters f_1 and f_2 are given as well as the roll period T_0. The target total roll damping ratio φ_h/φ_a is 0.35 which is a good compromise between a significant reduction of simulation time and the compliance with the condition $\omega_0 \approx \omega_d \approx \omega_p$. Here, ω_p is the damped natural frequency of the system described in Equation 1 with sinusoidal excitation moment. All simulations required $n_c = 6$ periods for a converged damping ratio result and a stationary roll amplitude.

Table 6 shows the roll amplitude and damping ratio achieved as well as the phase angle ϑ between excit. moment and roll angle.

Based on calculations with Equation 17, the application of the AID approach leads to a total simulation time reduction of 72% (72 instead of 257 roll cycles).

Table 5 Predicted parameters for roll simulations with AID technique, $\boldsymbol{\varphi_a}$ in [deg], $\boldsymbol{T_0}$ in [s]

Fr=0.00

φ_a	T_0	φ_h/φ_a	f_1	f_2
5	4.98	0.025	0.0486	0.4009
10	4.85	0.042	0.1025	0.3986
15	4.72	0.066	0.1627	0.3785
20	4.45	0.101	0.2441	0.3523

Fr=0.10

φ_a	T_0	φ_h/φ_a	f_1	f_2
5	4.82	0.062	0.0519	0.3751
10	4.67	0.085	0.1106	0.3570
15	4.54	0.114	0.1755	0.3269
20	4.43	0.150	0.2458	0.2833

Fr=0.19

φ_a	T_0	φ_h/φ_a	f_1	f_2
5	4.46	0.135	0.0606	0.3024
10	4.45	0.158	0.1218	0.2714
15	4.35	0.182	0.1912	0.2422
20	4.25	0.215	0.2670	0.2001

Table 6 Roll damping ratios estimated with AID technique, φ_a and ϑ in [deg]

Fr=0.00

φ_a	ϑ	φ_h/φ_a
4.99	88.3	0.026
9.97	88.1	0.043
14.88	85.9	0.067
19.57	91.1	0.109

Fr=0.10

φ_a	ϑ	φ_h/φ_a
4.85	91.1	0.072
9.61	94.3	0.097
14.06	93.5	0.136
18.50	89.8	0.177

Fr=0.19

φ_a	ϑ	φ_h/φ_a
4.29	101.4	0.182
8.71	96.7	0.205
12.73	98.4	0.237
16.64	98.4	0.279

5. CONCLUSIONS

Harmonic Excited Roll Motion (HERM) simulations with Artificial Induced Damping (AID) significantly reduce the necessary CPU time. Furthermore, the required simulation time can be predefined. Due to the shorter simulation times and the resulting smaller drift motions of the ship, simulation setups could be simplified and thus complex simulation techniques could be avoided. Damping coefficients can be estimated without the influence of a PID-controlled rudder which is required for applying roll damping coefficients in ship motion simulation methods.

6. ACKNOWLEDMENTS

This work is funded by the German Federal Ministry of Economics and Technology under the aegis of the BMWi-project *HERMes* within the framework program Schifffahrt und Meerestechnik für das 21. Jahrhundert. The authors would like to thank A. Schumacher from Hamburg Ship Model Basin (HSVA) for providing the experimental data.

7. REFERENCES

Blume, P., 1979, “Experimentelle Bestimmung von Koeffizienten der wirksamen Rolldämpfung und ihrer Anwendung zur Abschätzung extremer Rollwinkel”, Ship Technology Research / Schiffstechnik, Vol. 26, pp. 3-23 (in German).

el Moctar, B., Shigunov, V. and Zorn, T., 2012, “Duisburg Test Case: Post-Panamax Containership for Benchmarking”, Ship Technology Research/Schiffstechnik, 59/3.

Gadd, G.E., 1964, “Bilge keels and bilge vans”, Technical Report 64, National Physical Laoratory.

Handschel, S. and Abdel-Maksoud, M., 2014, “Improvement of the Harmonic Excited Roll Motion Technique for Estimating Roll Damping”, Ship Technology Research / Schiffstechnik, Vol. 61/3, pp. 116-130.

Ikeda, Y., Himeno, Y., Tanaka, N., 1978, ”A Prediction Method for Ship Roll Damping”, Report of the Department of Naval Architecture, University of Osaka Prefecture, No. 00405.

Kato, H., 1958, ”On the frictional resistance to the rolling of ships”, Journal of Zosen Kyokai, Vol. 102 (in Japanese).

Schumacher, A., 2010, “Rolldämpfungs-versuche mit dem Modell eines großen Containerschiffes - Teilvorhaben Mat-Roll“, Technical Report S 625/10, Hamburgische Schiffbau-Versuchsanstalt (in German).

Söding, H., 1991, ”Die Wirkung von Rolldämpfungsflossen abhängig von ihrem Einbauort”, Technical Report, University of Hamburg (in German).

Sugai, K. and Yamanouchi, Y., 1963, “A study on the rolling characteristics of ship by forced oscillation model experiments”, J. of the Soc. of Nav. Archit. of Jap. (in Japanese).

Sumislawski, P., Wassermann, S. and Abdel-Maksoud, M., 2018, "Rudder Influence on Roll Damping Estimation", Proceedings of the 13th Int. Conference on the Stability of Ships and Ocean Vehicles (STAB), Japan.

Wassermann, S., Work title: "Time-efficient Estimation of Damping Ratio ζ <0.1 for Driven Damped Harmonic Oscillations", will be published in 2018.

Wassermann, S., 2017, "Estimation of Ship Roll Damping for the Investigation of Extreme Roll Events", Verlag Schriftenreihe Schiffbau, 2017 (ISBN 978-3-89220-706-1).

8. APPENDIX

Prediction of frictionless bare hull damping N_φ^{BH}

The prediction of bare hull damping is based on an artificial neural network (ANN) approach which is used as an interpolation method of existing roll damping results estimated with model tests and CFD simulations for 20 modern ship hulls. Five inputs are required:

- ratio of ship's breadth to draft $\frac{B}{T}$
- block coefficient C_B
- Froude number Fr and
- roll amplitude φ_a $[rad]$.

The ANN has 5 hidden-layer nodes:

$$\frac{\varphi_{\text{heel}}}{\varphi_a} = 0.1036y + 0.116166,$$

where

$$y = -0.5512 - 0.8867x_1 + 0.2039x_2 + 1.694x_3 - 2.663x_4 + 0.416x_5$$
$$x_1 = ts(0.869 - 0.3655z_1 - 0.1669z_2 - 0.3751z_3 - 0.02166z_4)$$
$$x_2 = ts(-2.446 + 1.342z_1 - 0.07811z_2 + 0.855z_3 + 0.7062z_4)$$
$$x_3 = ts(-0.827 - 0.009079z_1 + 0.03348z_2 - 0.0262z_3 + 1.021z_4)$$
$$x_4 = ts(-1.114 + 0.03923z_1 + 0.06497z_2 + 0.2606z_3 + 0.6294z_4)$$
$$x_5 = ts(0.08154 + 0.4686z_1 + 0.2534z_2 + 0.03129z_3 + 0.9725z_4)$$

with the input nodes

$$z_1 = 2(\varphi_a - 0.087)/0.262 - 1,$$
$$z_2 = 2(\tfrac{B}{T} - 2.5)/2.5 - 1,$$
$$z_3 = 2(C_B - 0.5)/0.3 - 1,$$
$$z_4 = 2Fr/0.25 - 1.$$

The hyperbolic *t*angent *s*igmoid transfer function is defined as

$$ts(x) = \frac{2}{1 + e^{-2x}} - 1.$$

The roll damping coefficient is given by

$$N_\varphi^{BH} = \frac{\rho g \nabla \overline{GM}_T}{\omega_0} \cdot \left(\frac{\varphi_{\text{heel}}}{\varphi_a}\right).$$

Prediction of bilge keel damping N_φ^{BK}

The method is based on a force coefficient approach and is comparable to Gadd's (1964) and Ikeda's (1978) approach. The total roll damping due to bilge keels can be estimated from

$$N_\varphi^{BK} = N_\varphi^{BKP} + N_\varphi^{BKN} = k \cdot N_\varphi^{BKN}$$
$$= k \cdot \frac{8}{3\pi} \rho A_{BK} c_E r_{BK}^3 f^2 \omega \varphi_a cos(\alpha).$$

It is the sum of two parts: normal force bilge keel damping N_φ^{BKN} and hull-pressure damping due to bilge keels N_φ^{BKP}. N_φ^{BKP} is approximate with parameter k and reflects the interaction of the bilge keel vortices with the ship hull. k is determined based on CFD ship roll motion simulations. Because the bilge-keel moment approximation is based on the midship section, k also corrects the moment due to the variation of the bilge radii along the bilge keel length:

$$k = 1.5 + \varphi_a.$$

Bilge keel area:

$$A_{BK} = b_{BK} \cdot l_{BK}$$

Drag coefficient:

$$c_E = 0.43 \cdot \ln(KC)^2 - 4.44 \cdot \ln(KC) + 13.2$$

with KC-number

$$KC = \pi \frac{f r_{BK} \varphi_a}{b_{BK}}$$

Distance between the roll center and the bilge keel:

$$r_{BK} = \sqrt{(B/2)^2 + d^2} - \sqrt{2R_b^2} + R_b + \frac{b_{BK}}{2}$$

Bilge radius:

$$R_b = \sqrt{\frac{2BT \cdot (C_M - 1)}{\pi - 4}}$$

Midship coefficient (unless specified):

$$C_M = \frac{1}{1+(1-C_B)^{3.5}}$$

If the bilge keel is at right angles to the hull, $\cos(\alpha)$ can be approximated by:

$$\cos(\alpha) = \frac{x_R^2 - \left(r_{BK} - \frac{b_{BK}}{2}\right)^2 - R_b^2}{-2R_b\left(r_{BK} - \frac{b_{BK}}{2}\right)},$$

where

$$x_R = \sqrt{\left(\frac{B}{2} - R_b\right)^2 + (d - R_b)^2}.$$

The distance d from the keel to the roll axis can be calculated as

$$d = \frac{T + \overline{KG}}{2},$$

see Söding (1991). The factor f is a flow velocity increment factor taking the local effect of the hull shape into account. Factor f at the bilge is calculated based on 2D-BEM calculations (Söding, 1991) and results approximated using a feedforward artificial neural network. The input parameters of the neural network are, b_{BK}/R_b, the ratio of the bilge keel breadth to the bilge radius and, d/R_b the ratio of the roll axis height to the bilge radius. The neural network consists of 3 layers: an input layer with 2 nodes, a hidden layer of 7 nodes and an output with 1 target node.

$$f = 0.665y + 1.665,$$

where

$$\begin{aligned}
y = {} & (-0.1438 + 0.6467x_1 + 0.1234x_2 - 1.6522x_3 - 0.7120x_4 + \\
& 3.9170x_5 - 1.0484x_6 - 2.9389x_7) \\
x_1 = {} & ts(-5.2031 + 0.3190z_1 - 5.3609z_2) \\
x_2 = {} & ts(3.0012 + 1.2910z_1 - 3.1415z_2) \\
x_3 = {} & ts(-1.2944 + 0.2024z_1 - 0.4719z_2) \\
x_4 = {} & ts(-3.6227 - 0.0906z_1 - 3.9467z_2) \\
x_5 = {} & ts(-3.1864 - 2.0030z_1 + 0.1786z_2) \\
x_6 = {} & ts(1.0763 + 0.8498z_1 - 0.6800z_2) \\
x_7 = {} & ts(-6.2075 - 1.7691z_1 - 3.3647z_2)
\end{aligned}$$

and the input nodes are

$$z_1 = 0.87\frac{b_{BK}}{R_b} - 1.087,$$

$$z_2 = 0.105\frac{d}{R_b} - 1.105.$$

It will be assumed that effects due to forward speed on bilge keel damping cancel each other out. The approach can be used for all Froude numbers.

Prediction of frictional roll damping N_φ^F

The method presented is a preliminary study and a revision based on CFD simulation results of Ikeda's (1978) approach. The frictional damping part is approximated with

$$N_\varphi^F = \frac{1}{3\pi}\rho\bar{r}^3\varphi_a\omega S_F c_F \cdot [-2\sin(2\varepsilon_F) + \cos(2\varepsilon_F) + 3].$$

Frictional force coefficient:

$$c_{F0} = 1.328Re_F^{-0.5} + 0.016Re_F^{-0.114}$$

Roll Reynolds number:

$$Re_F = k_F\frac{\bar{r}^2\varphi_a^2\omega}{\nu} \quad \text{with}: \; k_F = \frac{1}{\varphi_a}$$

Forward velocity correction:

$$c_F = c_{F0}\left[1 + 0.79\cdot\frac{KC_L}{\varphi_a} - 0.022\left(\frac{KC_L}{\varphi_a}\right)^2\right]$$

$$KC_L = 2\pi\frac{U}{\omega L_{WL}} \quad \text{for}: \; 0 < \frac{KC_L}{\varphi_a} < 20$$

The frictional moment is not completely in phase by the roll velocity. A phase shift of angle ε_F exists.

$$\varepsilon_F = \bar{\varepsilon}_{F,BH} + \bar{\varepsilon}_{F,BK} = \left(\underbrace{-0.206}_{\bar{\varepsilon}_{F0,BH}} \underbrace{-0.18}_{\bar{\varepsilon}_{F,BK}}\right)\exp(Fr)$$

$\bar{\varepsilon}_{F,BK}$ is zero if the ship has no bilge keels.

Kato (1958) formulated an approximation for the wetted surface S_F:

$$S_F = L(1.7T + C_B B).$$

and determined $\bar{r}$ with

$$\bar{r} = \frac{1}{\pi}\left[(0.887 + 0.145C_B)\frac{S_F}{L} - 2\overline{OG}\right].$$

$\overline{OG}$ is the signed vertical distance between the water surface and the center of gravity, positive if the center of gravity is underwater.

Some remarks on EFD and CFD for ship roll decay

Hirotada Hashimoto, *Kobe University*, hashimoto@port.kobe-u.ac.jp

Tomoyuki Omura, *Kobe University*

Akihiko Matsuda, *National Research Institute of Fisheries Engineering*, amatsuda@fra.affrc.go.jp

Shota Yoneda, *Kobe University*

Frederick Stern, *The University of Iowa*, frstern@iowa.uiowa.edu

Yusuke Tahara, *National Maritime Research Institute*, tahara@nmri.go.jp

ABSTRACT

Firstly a purpose-built device was designed to obtain high-quality EFD data of ship roll decay motions. Then a model experiment was conducted for a slender ship using the new device with a high-quality gyroscope. Through analyses of the measured data, several important remarks on EFD were derived. Secondly URaNS CFD simulations of ship roll decay are performed and are compared with EFD results. From the comparisons, several remarks on the requirements for CFD to be considered in the development of guidelines annexed to the Second Generation Intact Stability Criteria discussed at IMO.

Keywords: *Roll decay, EFD, CFD, Validation, SGISC*

1. INTRODUCTION

In the second generation intact stability criteria (SGISC) discussed at the International Maritime Organization (IMO), roll damping estimation is required to assess vulnerability of ships to some of dynamic stability failure modes. An existing formula, so-called Ikeda's simplified method [Kawahara et al., 2009], is available for this purpose in the current draft, but it does not always give sufficient accuracy and also there is a limit of its applicable range. In the framework of the SGISC already agreed, Computational Fluid Dynamics (CFD) can be used as an alternative to the existing formula as well as model experiments. For the use of CFD as for the regulatory purposes, quantitative validation of CFD codes is required to guarantee their numerical results. In this regard, intensive studies are necessary to derive a standard procedure to obtain high-quality Experimental Fluid Dynamics (EFD) data that can be used for the quantitative validation of CFD simulation codes. Secondly, detailed guidelines for the appropriate use of CFD for roll damping estimation annexed to the SGISC is required.

For the quantitative validation of CFD methods, a purpose-built device was made to obtain high-quality EFD data of roll decay motions. Then a model experiment was conducted for a slender ship, known as the ONR-flare, using the new device with a top-quality optical fibre gyroscope. Through analyses of the measured data of roll decay at zero forward velocity started from several initial heel angles, some important remarks on EFD procedure and EFD analysis are derived. Then we simulate roll decay motions of the subject ship using an overset grids unsteady Reynolds-averaged Navier Stokes (URaNS) CFD solver. The CFD simulation is performed with the same condition as the model

experiment so that time histories of roll decay can be directly compared with EFD results.

The CFD simulations are also used to discuss the degree of freedom of ship motion to be solved in CFD computation. This is an important point to be described in the guidelines of CFD simulation of roll decay test for those who want to use CFD methods, as an alternative to a physical model experiment, to estimate the roll damping in the SGISC.

2. MODEL EXPERIMENT

2.1 Subject ship

In terms of the development of guidelines of EFD and CFD for roll decay tests to be annexed to SGISC, slender ships are reasonable to be selected as a subject ship because slender ships are prone to suffer stability failures due to the relatively small stability. In this study, a displacement-type slender body ship so-called the ONR-flare widely used for recent stability researches is selected as the subject ship. Principal particulars of the subject ship are shown in Table 1. This ship has a twin propeller and twin rudder system. In the model experiment, all appendages except for propellers are attached to be similar to actual conditions. Details of the ship hull and appendages can be seen in Fig.1.

Table 1 Principal particulars of ONR-Flare

	Actual	Scaled
Length between perpendiculars: L_{pp} (m)	154.0	3.305
Breadth: B (m)	18.78	0.403
Depth: D (m)	14.5	0.311
Draught: d (m)	5.415	0.116
Mass: m (kg)		85.4
Appendage: skeg, bilge keels, rudders propeller shafts, shaft brackets		

Fig.1 Ship hull and appendage

2.2 Experimental setup

A model experiment of roll decay was conducted at Marine Dynamic Basin of National Research Institute of Fisheries Engineering (NRIFE). Firstly, the height of ship hull at A.P., Midship and F.P. positions were measured to confirm that no difference from 3-D CAD data exists. Then, the design draught was carefully adjusted by using four draft gauges. From a viewpoint of comparisons with CFD, it is important to set the exact water line rather than the ship displacement because it has been confirmed in past CFD trials that a significant difference could occur in roll decay motion if the water line is changed. In particular, this difference becomes significant if a ship has transom stern and the gap between the transom stern and the water surface is small. Dummy weights having the same mass with the draught gauge were put at the same position of the draught gauges to keep the same displacement, heel and trim balance when conducting the model tests. The ship weight was measured before and after the experiment for each condition to confirm that there was no change of the ship weight during the experiment.

2.3 Experimental procedure

Roll decay tests were conducted in a sophisticated procedure to measure the high-quality data which can withstand the quantitative validation of CFD. In this procedure, a concern about the uncertainty via human handling is excluded by using a new purpose-built device. A long aluminium square pipe was attached to the ship model and the total weight and other particulars were adjusted including the attached long pipe. Then a certain initial heel angle is given to the ship model via the long square pipe as shown in Figs. 2-3. The square pipe can freely move in heave and pitch directions even being hold, so the change of ship attitude, due to the change of under-water ship volume and buoyancy balance, is allowed. The aluminium metal frame with rollers, to give an initial heel angle to the model through the square long pipe, can rotate at 5 degrees pitch and it is possible to repeat the same roll decay test from a fixed angle/attitude. By using this new apparatus, it is possible to separate the uncertainty of initial condition and the uncertainty of measurement system. It is necessary to release the heel constraint momentarily for roll decay tests. In the experiment, the aluminium frame can be shortly opened by the strong tension of connected rubber rope. Since the aluminium frame does not go back once opened due to the remained rubber tension, it does not prevent the ship roll motion at all. As the roll energy is consumed during the first swing, the square long pipe never reach to the initial angle and never hits the apparatus.

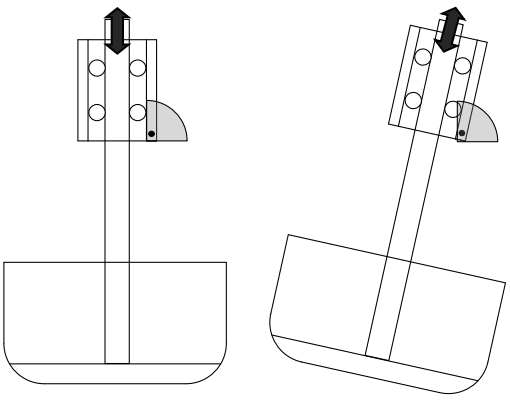

Fig.2 Schematic view of apparatus

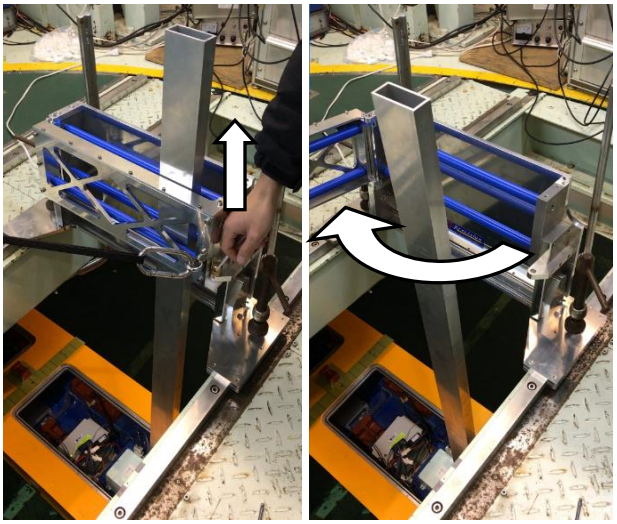

Fig.3 Opening mechanism of apparatus

Before the execution of roll decay test, the ship model is towed to the centre of the basin where the wave reflection effect can be ignored and then the roll decay test was executed after the state of water surface sufficiently settled down as shown in Fig.4. After the heel restraint is released, a subsequent roll decay motion is measured by an onboard gyroscope attached to the centre of ship gravity. Because the measured data is stored in the onboard microcomputer, cable handling is not necessary, which could adversely affect the roll decay motion. Here to minimize the zero value drift is very important for roll decay measurement. Because it is difficult to remove the time-dependent zero value shift appropriately, it makes the analysis to be quite difficult. In our experiment, one of most expensive top-quality optical fibre gyroscopes is used to solve this problem.

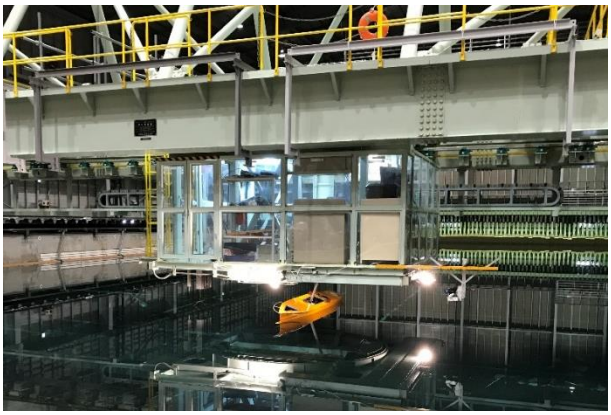

Fig.4 Overview of roll decay test

3. EFD RESULTS

3.1 Roll decay motion

For the use of CFD in the SGISC, the accuracy of CFD tools needs to be guaranteed by comparing with a model experiment, but it is required for a standard design loading condition only. For other possible loading conditions (with changes of metacentric height, roll moment of inertia, draught and trim), CFD simulation can be directly used without further experimental validation. To confirm the validity of this procedure, a model experiment of roll decay was conducted for three different conditions as shown in Table 2. Cond.1 is a full load condition as the standard condition, which was decided with the reference to a past free-running model experiment [Umeda et al., 2014]. Cond.2 has high-GM value, 1.5 times as large as Cond.1, but the same draught. Cond. 3 has the same GM with Cond.1 but smaller draught, about 10% smaller than the full load condition.

At the inclining test for GM measurement, a ballast weight on the upper deck was moved from the centreline to port and starboard directions. The weight was moved by two steps in each direction. The GM value was obtained as the result of linear curve fitting for six inclined angles including two-times zero measurement. In order to reduce the error by practitioners, two persons did the inclination test independently and the average value of two measurements is used as the final GM value. The ballast weight used for the inclination test was 500 g and the weight was moved by 25 mm pitch, and appropriate moving distances were decided so that 1 degrees of heel was sandwiched by the two steps. The heel angle was measured by an onboard gyroscope with no signal cables and the time-average value of heel angle is used for the GM analysis. In case the heel angle is beyond 1.5 degrees, the GM value does not increase linearly with respect to moving distance due to the nonlinearity of GZ curve. Therefore 1.0 degrees was used as the reference value for the GM measurement.

Table 2 Tested condition

Cond.	Draught d	Metacentric height GM	Initial heel ϕ_0
1	5.415 m	0.8 m	18.7
2	5.415 m	1.2 m	18.7
3	4.949 m	0.8 m	18.7

Firstly the repeatability of a roll decay test using the new apparatus was checked by repeating the roll decay test from the same initial heel angle. The comparisons of measured roll decay motions started from the starboard side (Left 1 & 2) and the port side (Right 1 & 2) are shown in Fig.5. The two curves independently conducted perfectly coincides with each other. This high repeatability implies that the uncertainty of the initial condition does not exist. The symmetricity was also confirmed as shown in Fig.6.

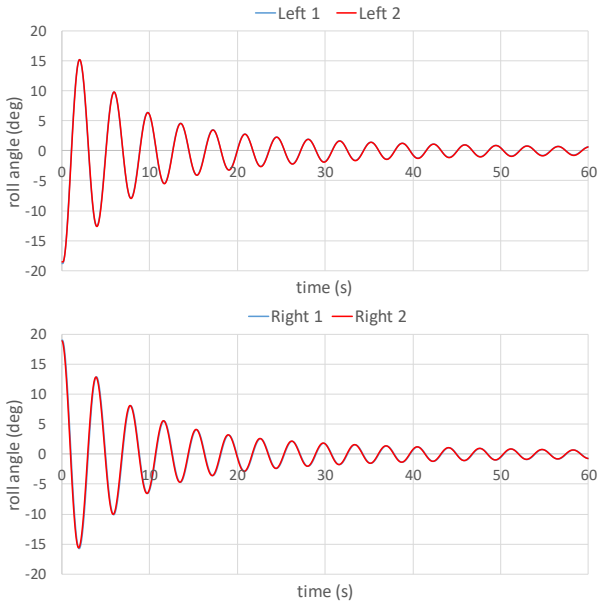

Fig.5 Repeatability check (Cond.1)

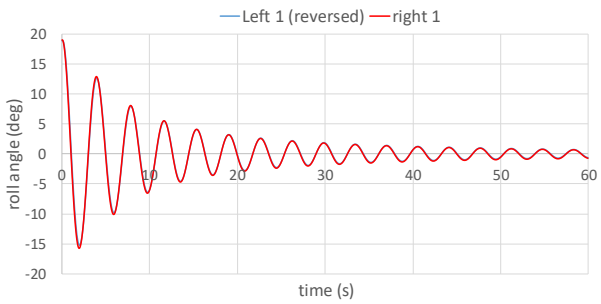

Fig.6 Symmetricity check (Cond.1)

The measured roll decay motions for three different loading conditions are drawn together in Fig.7. Because the subject ship has the large bilge keels and also several large-size appendages, the damping rate is relatively large as compared to general cargo ships. The roll period of each condition around 5 degrees is shown in Table 3. The decrease of roll period from Cond.1 to Cond.2 is inverse proportional to square root of GM as well known. The roll period of Cond.3 is same as Cond.1 even with the different draught, for this ship. Although the GM and draught values significantly differs among three conditions, the difference of roll angle decrement for each swing seems to be very small. This fact implies that the accuracy of the roll decay tests must be high enough to be able to measure such a small difference, which is essential for the quantitative validation of CFD.

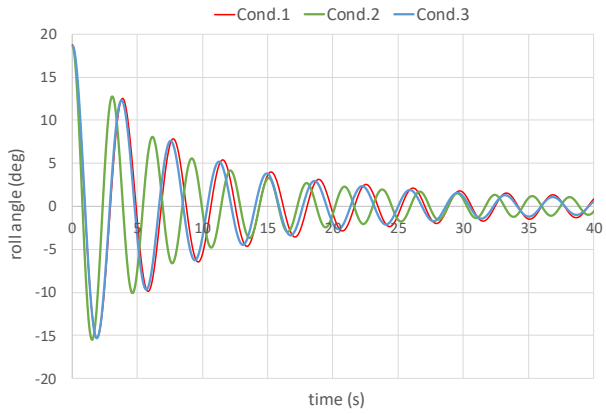

Fig.7 Measured roll decay motions for three loading conditions

Table 3 Roll period around 5 deg.

Cond.1	Cond.2	Cond.3
3.73 s	2.98 s	3.70 s

3.2 Extinction curve

In order to obtain roll damping coefficients from measured roll decay motions, the extinction curve is conventionally used. The procedure can be found in e.g. IMO MSC.1/Circ.1200 (2006). The extinction curve for all conditions are presented in Fig.8. For the drawing of these figures, initial heel angle is included as the 0th peak value. As a result, the extinction curves are not increasing monotonously with respect to mean swing, so it is difficult to approximate using a conventional 2nd order polynomial curve.

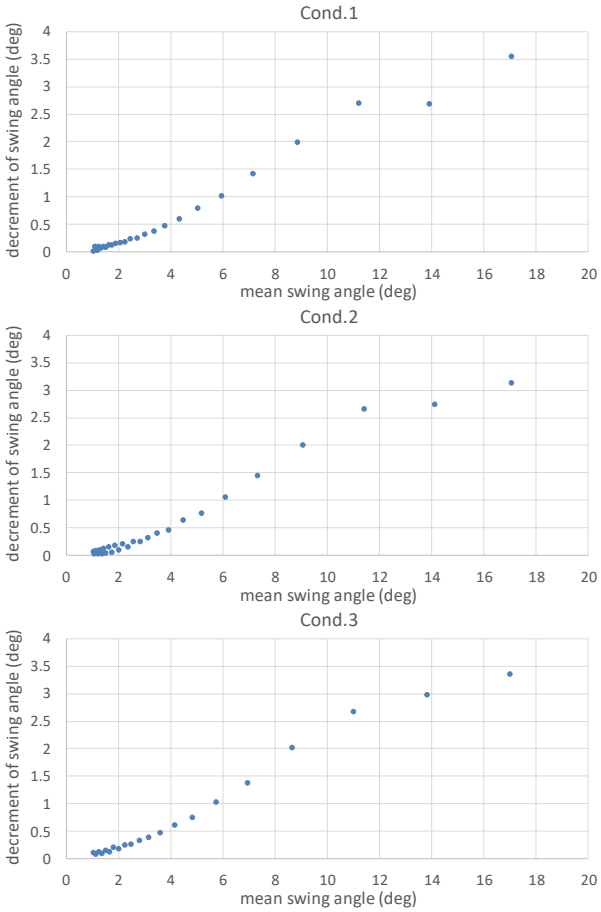

Fig.8 Extinction curves for different loading conditions

It is obvious that the first several half swings are regarded as abnormal because the roll decay started from the state of rest at certain initial heeling angle. In normal decay motions, the angular acceleration is not zero at each peak value. In addition, it was pointed out that the drag force on bilge-keels depends on the number of half swings in transient state. [Katayama et al., 2011] Therefore, several analyses of extinction curves are attempted to eliminate the inappropriate data for the anlysis. Here, the peak of each half swing data was removed in order from the 0th swing to 3rd swing. The extinction curves of each analysis are shown in Fig.9. Here the approximation

curve with linear and quadratic terms is drawn together.

Table 4 Analysis of extinction curve

	description
Analysis 1	Started from 0th half swing (=initial heel angle)
Analysis 2	Started from 1st half swing
Analysis 3	Started from 2nd half swing
Analysis 4	Started from 3rd half swing

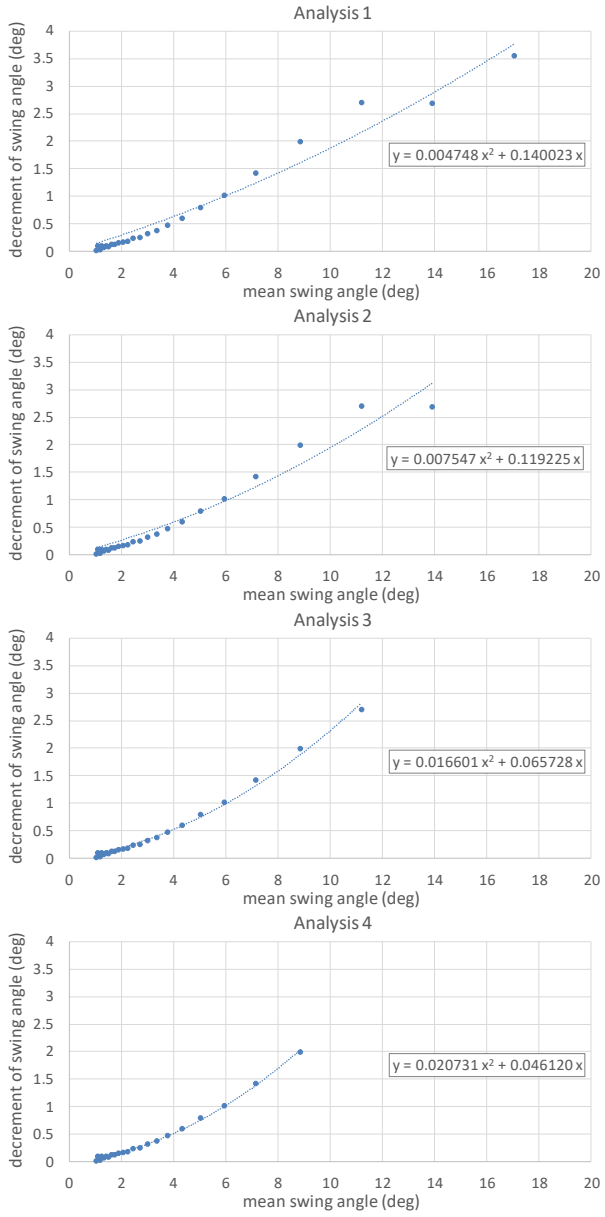

Fig.9 Extinction curves with different analysis methods (Cond.1)

These figures demonstrated that Analysis 1 and Analysis 2 are not appropriate in terms of curve fitting, so the 0th and 1st half swing must be removed in the analysis of roll extinction curves. The difference of Analysis 3 and Analysis 4 is not so significant compared to previous cases. To highlight this point, the extinction curves of each analysis are extrapolated to a large swing angle as shown in Fig.10. The error of Analysis 3 and Analysis 4 is about 13.7% at the mean swing angle of 20 degrees. This is not a negligibly small error, so we need to judge which result is more appropriate. For this judgement, a roll decay test from a large heel angle is necessary but it would get almost the same conclusion because the 0th and 1st half swings, which have very large decrement of swing angle when started from large heel angle, need to be eliminated as already discussed. To finalise this discussion, a forced roll test at large roll amplitude is expected. Although it is true that a forced roll test giving pure roll motion is slightly different from real ship motion during roll, sway-roll or heave-roll coupling effect on roll damping might be relatively small at large heel angle where wave-making and eddy-making components are dominant.

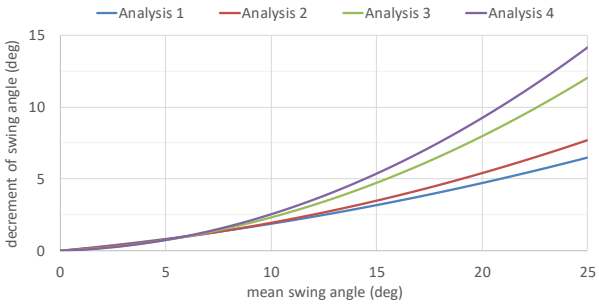

Fig.10 Extrapolated roll extinction curves (Cond.1)

3.3 Comparison with conventional method

Lastly, the influence of human intervention is investigated by comparing the measured roll decay motion using the purpose-built apparatus and those performed by human handling. The comparison of roll time history is shown in Fig.11. There is small difference of initial heel angle among them because the man cannot keep the exact heel angle. However, in general,

the difference of whole the curve among them seems to be reasonably small.

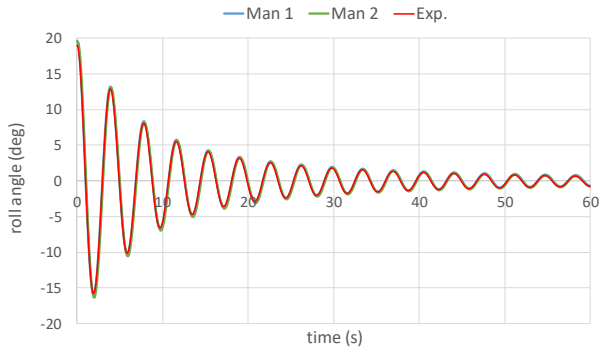

Fig.11 Comparision of roll decay with and without human intervention (Cond.1)

4. CFD RESULTS

4.1 CFD solver and grids

For the accurate prediction of friction and eddy-making components, which are major components of roll damping at low speed, CFD approach solving the Navier-Stokes equation, governing equation of viscous flow, is straightforward compared to conventional potential flow theories with empirical methods.

An URaNS solver, CFDShip-Iowa V4.5 [Huang et al., 2008] is used for this purpose. The latest applications of CFDShip-Iowa can be found in a literature [Stern et al., 2015]. CFDShip-Iowa is a block structured overset CFD solver designed for the applications to naval architecture and ocean engineering problems using either absolute or relative inertial non-orthogonal curvilinear coordinate system for arbitrary moving control volumes. Turbulence models include bended k-ε/k-ω based isotropic and anisotropic RaNS, and DES approaches with near-wall or wall functions. A single-phase level-set method is used for capturing complex free-surfaces. The SUGGAR [Noack, 2007] is used to handle the overset interpolation information.

The grids for the CFD test of roll decay are shown in Fig.12. The number of grid points is shown in Table 5. In order to obtain comparable results by CFD, all appendages in the experiment, i.e. skeg, bilge keels, rudders, propeller shafts and shaft brackets, are included in CFD. The numerical condition and selected models for CFD are listed in Table 6. These conditions were used for URaNS analysis for the subject ship of ONR-Flare in past study on the prediction of wave-induced hydrodynamic forces [Yoneda et al., 2016].

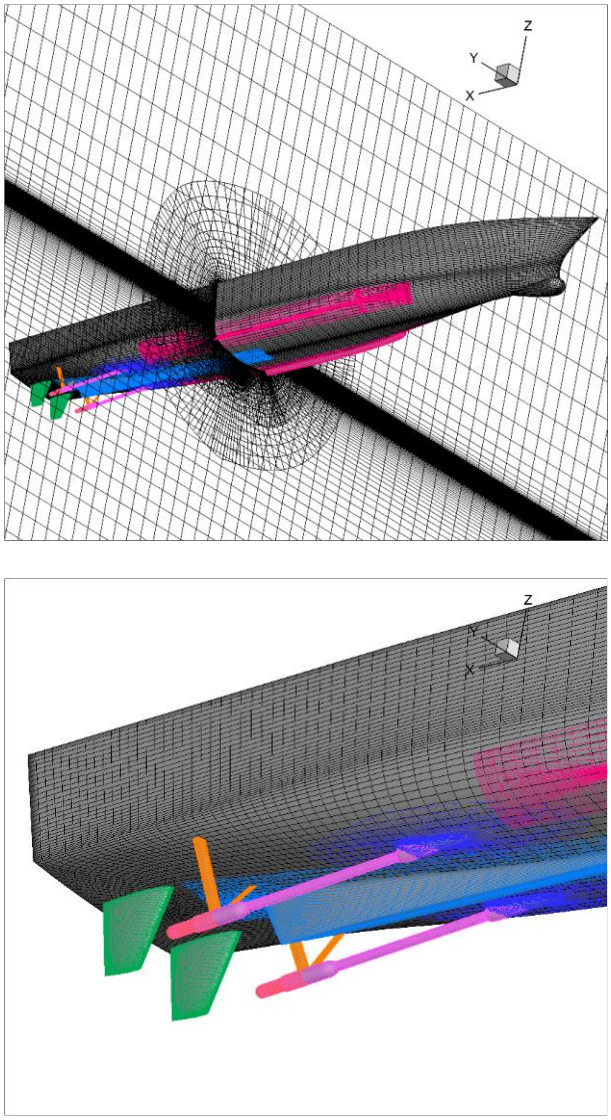

Fig.12 Grids around the full

Table 5 Number of grids

Hull	Background
3.29 M	0.89 M
Total 4.18 M	

Table 6 CFD condition

Reynolds number	1.053E+7
Time step	0.0145 s
Level set solver	Liner
Turbulence model	Blended k-ε/k-ω
Pressure solver	Projection
6DOF integration	2nd order implicit

CFDShip-Iowa has a function to give arbitrary prescribed body motion as a moving wall boundary problem. In addition, it allows to choose the degrees of freedom of motion to be solved in CFD. Therefore appropriate number of degree of freedom of ship motion, to be solved in cases of the prediction of roll decay motions of ships, can be investigated.

4.2 Roll decay motion

Roll decay motions corresponding to the EFD results shown in Fig.7 are simulated using CFD-Ship Iowa by solving 4 degrees of freedom (DOF) of sway, heave, roll and pitch. The influence of degrees of freedom of ship motion to be solved in CFD is discussed later. Although the same KG with EFD should be used in the CFD calculations, the exact KG value is not directly obtained from the inclining test. Therefore the height of centre of ship gravity used in CFD was determined by trial and error by repeating CFD inclining test until to find an appropriate height providing the same heel angle with EFD, for each condition. As the moment of inertia in air is hard to be measured in general, the moment of inertia for CFD calculations were also determined by trial and error, which provides the same natural roll period with the EFD result in small amplitude range.

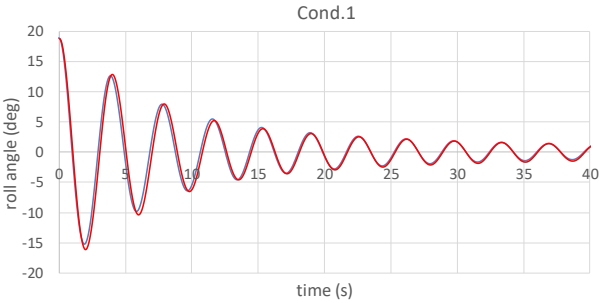

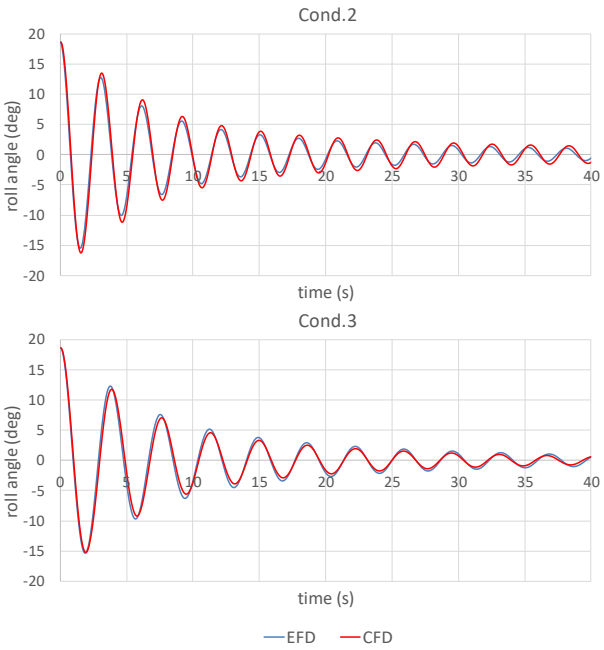

Fig.13 Comparison of roll decay motion between EFD and CFD

The comparison of roll decay motions for three loading conditions (Cond.1 to Cond.3) between EFD and CFD are shown in Fig.13. In the standard condition (Cond.1), the CFD result shows good agreement in terms of roll decay rate. The agreement becomes worse to some extent in Cond.3. The worst agreement between EFD and CFD is found in Cond.2 where the roll period is faster and the damping rate is smaller than other two conditions. The major reason of the disagreement in Cond.2 is presumed that the used CFD grids are not sufficiently fine for the shorter roll period in which the angular velocity becomes larger. In addition, the constant time step is used for all conditions, i.e. roll periods more precisely. Therefore it is preferable that the validation of CFD tools for the roll decay motions is done for the shortest roll period case if the initial heel angle is same. However, it could be acceptable to validate the CFD method only for standard loading condition if the required accuracy is not so high. For further discussion on this point, how much the error affects the vulnerability assessment in the SGISC should be investigated.

4.3 Roll extinction curve

To demonstrate the accuracy of estimated roll damping by CFD, the roll extinction curves are drawn in Fig.14. In the figures, 2nd order polynomial approximation curve is also shown. In the EFD results in Fig.8, the smallest roll damping was found in Cond.2 and the same result is obtained from the CFD result.

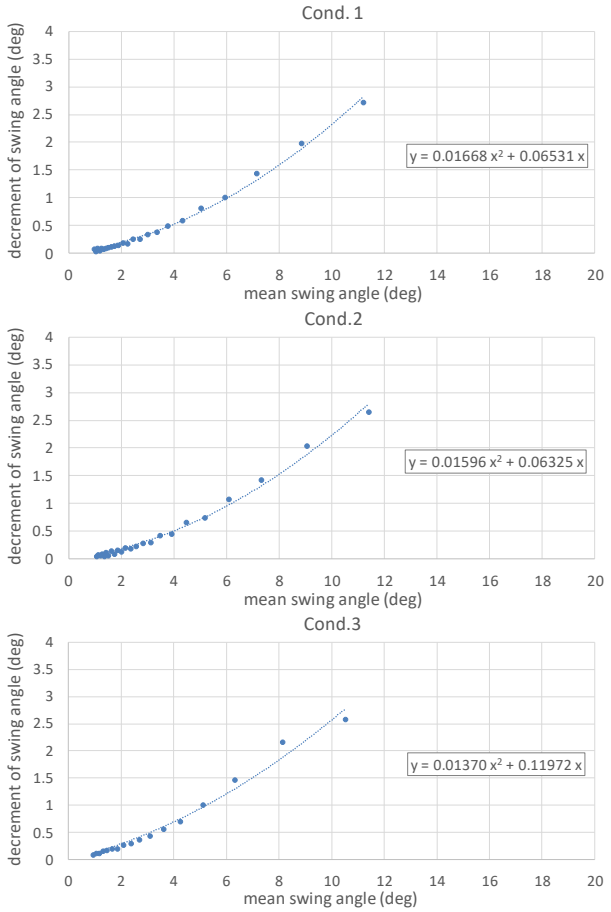

Fig.14 Extinction curves by CFD for three loading conditions (Analysis 3)

Then comparisons of the decrement of swing angle between EFD and CFD at 10 and 20 degrees of mean swing angle are presented in Table 8, which are obtained based on Analysis 3. The best agreement is found in Cond.1 and the errors are less than 0.3%. Similarly, a good agreement is also found in Cond.2 but the errors become slightly larger than Cond.1. This reason could be explained that the CFL number in Cond.2 is larger than that in Cond.1 in case the same hull grids are used for different draughts. The biggest errors about 7.74% are found at 10 degrees in Cond.3. However the decrement at 20 degrees agrees well. This difference of error comes from the degree of coincidence of polynomial curve fitting, so the range of mean swing angle should be carefully selected in cases it is used for regulatory purpose.

Table 7 Comparison of decrement of swing angle between EFD and CFD (Analysis 3)

Cond.1	Mean swing angle	
	10 deg	20 deg
EFD (deg)	2.317	7.955
CFD (Deg)	2.321	7.978
Error (%)	0.16	0.29
Cond.2	Mean swing angle	
	10 deg	20 deg
EFD (deg)	2.235	7.694
CFD (Deg)	2.229	7.649
Error (%)	-0.30	-0.59
Cond.3	Mean swing angle	
	10 deg	20 deg
EFD (deg)	2.383	7.820
CFD (Deg)	2.567	7.874
Error (%)	7.74	0.70

4.4 Influence of degrees of freedom

To discuss the appropriate selection of the degree of freedom of ship motion to be solved in CFD for roll decay motions, CFD runs solving different degrees of freedom of motions are executed for Cond.1, started from the same initial heel angle. The tested cases are shown in Table 8 and comparisons among four cases are shown in Fig. 15. Here the 4DOF calculation is same as the CFD result in Fig.13. From the result, it can be confirmed that 6DOF, 4DOF and 3DOF provide the quit similar result. In the contrary, 1DOF provides significantly different result, which shows much larger decay rate than other three cases. Therefore it is concluded that it is necessary to solve 3 DOF of sway-heave-roll motions or more degrees of freedom for the CFD simulation of roll decay motions. This is an important point to be included in the guidelines of CFD calculation of roll decay motions annexed to the SGISC.

Table 8 Degrees of freedom solved in CFD

	1DOF	3DOF	4DOF	6DOF
Surge	×	×	×	○
Sway	×	○	○	○
Heave	×	○	○	○
Roll	○	○	○	○
Pitch	×	×	○	○
Yaw	×	×	×	○

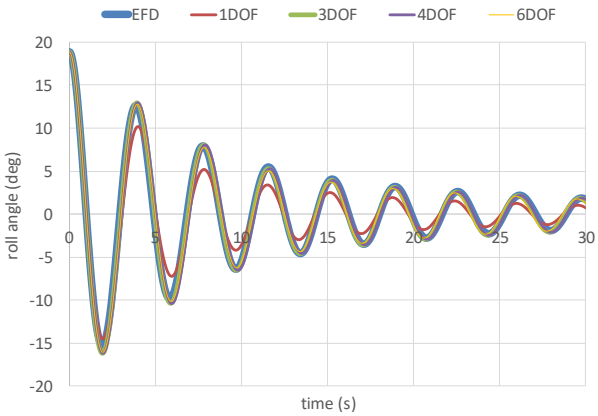

Fig.15 Influence of degrees of freedom to be solved on roll decay motion (Cond.1)

5. CONCLUSIONS

A purpose-built device was built to obtain high-quality EFD data of roll decay motions. Through analyses of the measured data, some important remarks regarding the experimental procedure and data analysis ways are derived. In addition, roll decay motions are predicted by URaNS simulation, which use the same conditions with the EFD. As a result, several important requirements for the CFD calculations and validations are derived. Those remarks on EFD and CFD of roll decay motions should be considered in the guidelines of alternative use of EFD and CFD in SGISC being developed at IMO.

6. ACKNOWLEDMENTS

This work was carried out as a research activity of Goal-Based Stability Criteria Project of Japan Ship Technology Research Association in the fiscal year of 2017, funded by the Nippon Foundation. This work was also supported by JSPS KAKENHI Grant number 17H03493.

7. REFERENCES

IMO, MSC.1/Circ.1200, ANNEX, 2006.

Kawahara, Y., Maekawa, K., Ikeda, Y., 2009, "A Simple Prediction Formula of Roll Damping of Conventional Cargo Ships on the Basis of Ikeda's Method and Its Limitation", Proceedings of the 10th International Conference on Stability of Ships and Ocean Vehicles, 387-398.

Umeda, N., Furukawa, T., Matsuda, A., Usada, S., 2014, "Rudder Normal Force during Broaching of a Ship in Stern Quartering Waves", 30th Symposium on Naval Hydrodynamics, 2014.

Yoneda, S., Hashimoto, H., Tahara, Y., Kobayashi, E., Umeda, N., Stern, F., 2016, "CFD-based captive tests for the wave-exciting force acting on a ship running in stern quartering waves", Proceedings of 3rd International Conference on Violent Flows.

Huang, J., Carrica, P. M. and Stern, F., 2008, "Semi-coupled air/water immersed boundary approach for curvilinear dynamic overset grids with application to ship hydrodynamics", International Journal for Numerical Methods in Fluids, 58(6), 591-624, 2008.

Katayama, T., Yoshioka, Y., Kakinoki, T., Ikeda, Y., 2011, "An Experimental Study on the Characteristics of Drag Force acting on a Flat Plate under Transitional and Irregular Oscillations", Journal of the Japan Society of Naval Architects and Ocean Engineers, 14, 55-62,(in Japanese).

Stern, F., Wang, Z., Yang, J. et al., 2015, "Recent progress in CFD for naval architecture and ocean engineering", Journal of Hydrodynamics, 27(1), 1-23.

Noack, R., 2007, "Enabling Large Amplitude and Relative Motions Through Overlapping Grids", Proceedings of 9th International Conference on Numerical Ship Hydrodynamics.

Characteristics of Bilge-keel Roll Damping Component for Shallow Draft

Toru Katayama, *Osaka Prefecture University*, katayama@marine.osakafu-u.ac.jp

Masaki Matsuoka, *Graduate Student*, *Osaka Prefecture University*, sxb03115@edu.osakafu-u.ac.jp

Kazuki Ikushima, *Osaka Prefecture University*, ikushima@marine.osakafu-u.ac.jp

ABSTRACT

Roll amplitudes of parametric roll in regular head waves are sometimes underestimated by motion calculations including Ikeda's roll damping prediction method, especially for the case of large roll amplitude caused by high wave height. In this case, generally ship has significant relative draft changing because of its heave and pitch. It may be said that the effects of change in relative draft on roll damping is significant. However, in Ikeda's prediction method, the bilge-keel component that is the largest component of total roll damping does not consider the draft effects.

In this study, the characteristics of the effects of draft on the bilge-keel component are investigated experimentally and numerically using a 2-dimensional model. And a prediction model of the draft effects of bilge-keel component for collecting the results of Ikeda's prediction method is proposed. Moreover, the calculated results by the proposed method are compared with some measured data including the effects of draft changing and its validity is confirmed.

Keywords: *Bilge keel component, Roll damping, Shallow draft, CFD*

1. INTRODUCTION

It is important to estimate the stability of vessel, especially roll, for its safety. However, it is not easy to estimate roll accurately, because viscous effects on roll damping affect significantly roll near its resonance frequency.

It is well known that there is a prediction method of roll damping proposed by Ikeda et al., (1978). However, it is pointed out by Tanaka et al.,(1981) that the method overestimate the roll damping when the method is applied to a ship with shallow draft, and the tendency is more significant as *KG* (height of the center of gravity) of the ship is lower. Furthermore, it is explained as reasons of overestimation that the interactions of waves made by hull and bilge keels decrease the wave making damping component and the free surface effects decrease the size of vortexes shed by bilge keels.

In the previous study (Katayama et al., 2017a), the characteristics of the roll damping of a ship with shallow draught and low *KG* is investigated, to improve the bilge-keel damping component of Ikeda's prediction method by multiplying a correction factor. However, that is not enough.

Ikeda's prediction method consists theoretical formulas and empirical formulas based on hydrodynamic phenomena with empirical coefficients according to measured data. Therefore, it may be significant to improve its empirical formula and coefficients. In this study, in order to improve the bilge-keel

damping component of Ikeda's prediction method, the characteristics of the correction coefficient f to take account of the increment of flow velocity at the bilge by hull shape is investigated by CFD (STAR-CCM+). First, the drag force acting on a bilge-keel attached on 2D cylinder with forced sinusoidal rolling is calculated by CFD and the results are compared with the measured results by Ikeda et al.,(1977). And the drag forces acting on bilge keels attached on 2D hull without free surface, which has systematically changed half breath to draught ratio (H_0=B/2d) and area coefficient (σ : area of section devided by Bd) is calculated by CFD, an improved f is proposed.

2. NORMAL-FORCE DAMPING OF BILGE KEEL OF IKEDA'S METHOD

In Ikeda's method, the bilge keel component B_{BK} of roll damping coefficient is divided into 2 components:

$$B_{BK} = B_N + B_S \tag{1}$$

where B_N is the normal force component due to the normal force acting on bilge keels and B_S is the hull pressure component due to the pressure on the hull surface created by the bilge keels.

The normal force component can be deduced from the experimental results of oscillating flat plates (Ikeda et al., 1976, 1978a). The drag coefficient C_D of an oscillating flat plate depends on the KC number (Keulegan Carpenter number). From the measurement of the drag coefficient C_D from free roll decay tests of an ellipsoid with and without bilge keels, and measured drag coefficients C_D of the bilge keels is in good agreement with the ones of the oscillating flat plates. The prediction formula for the drag coefficient of the normal force of a pair of the bilge keels proposed by Ikeda is the following:

$$C_D = 22.5\frac{b_{BK}}{\pi r\phi_a f} + 2.40 = \frac{22.5}{KC} + 2.40 \tag{2}$$

where b_{BK} is the breadth (or height) of the bilge keel, ϕ_a is roll amplitude, r is the distance from the roll axis to the hull surface attached on the bilge keel, and KC is Keulegan Carpenter number. In the case where form of a cross section is circle, f is 1.0. The equivalent linear sectional damping coefficient B'_N is:

$$B'_N = \frac{8}{3\pi}\rho r^3\omega\phi_a b_{BK} f^2 C_D \tag{3}$$

where ω is roll angular frequency, and f is a correction factor to take account of the increment of flow velocity at the bilge caused by hull form, determined from the experiments:

$$f = 1.0 + 0.3e^{-160(1-\sigma)} \tag{4}$$

where σ is area coefficient of the cross section (σ= area of section devided by Bd: B and d are breadth and draught.). In order to determine the empirical formula of f which is Eq.(4), the following experiment and analysis are carried out by Ikeda et al., (1977)(1979). For the comparison between predicted value and experimental ones, Ikeda et al., (1977)(1979) assumes that the roll damping coefficient B_{BK} due to bilge keels can be obtained by subtracting the damping for a naked hull from one for the hull with bilge keels, a forced roll tests in horizontal plane are carried out to avoid the free surface effects. And a formula of f is fitted by comparisons between predicted and measured value for four 2D models with various bilge radius shown in Table 1. As this table shows, half breadth to draught ratio H_0 of models is near 1.23 that is average value of cargo ships at that time.

Table 1 Particular of the 2D rectangle models used by Ikeda et al., 1977.

model	bilge radius	σ	H_0=B/2d	b_{BK}[m]
B	1.0cm	0.9970	1.250	0.005
C	2.0cm	0.9945	1.250	0.010
D	3.0cm	0.9890	1.250	0.010
E	Series 60 C_B=0.6, ss5	0.9770	1.232	0.010

*height of roll center: KG=d

3. DRAG FORCE OF BILGE-KEEL ATTCHED ON 2D-CYLINDER

3.1 Setup of CFD

There are various models available for turbulence model, such as the *k*-ε model, the *k*-ω model, and the Reynolds stress model (RSM). In this study, the *k*-ε model is employed based on Yildiz et al.,(2017b), because its calculation speed is fast and the flow separation point is clear and it is the tip of bilge-keel in this study (The flow separation means vortex shedding.) . The computational condition of CFD are shown in Table 1.

Fig.1 shows the computational model used in this study. There are two cell zones, the moving fluid zone (MFZ) and the remaining stationary zone (RSZ). MFZ is rotated with the hull around the roll axis in order not to disturb the region around the body. There is an interface between RSZ and MFZ to avoids cell-deforming issues. The both zones are connected using mesh overlaying technique. As a result of mesh division, the number of elements is 440,000. The boundary conditions are also shown in Fig.1. The circular outer boundary on RSZ is located far enough from the body, so that it can be assumed that the velocity and pressure field generated by the oscillating body are not affected by the outer boundary. The calculation domain is actually 3D and thickness of domain is thin in order to be fast calculation. The boundary condition of surfaces of two plates sandwiching the domain is free-slip. The boundary condition of cylindrical hull is non-slip. In this investigation, 2-dimensional behavior is to be discussed. To model 2-dimensional flow, very thin cells are employed and the number of mesh in depth direction is 1. There is no gravity. The calculated conditions of forced roll test are shown in Table 2.

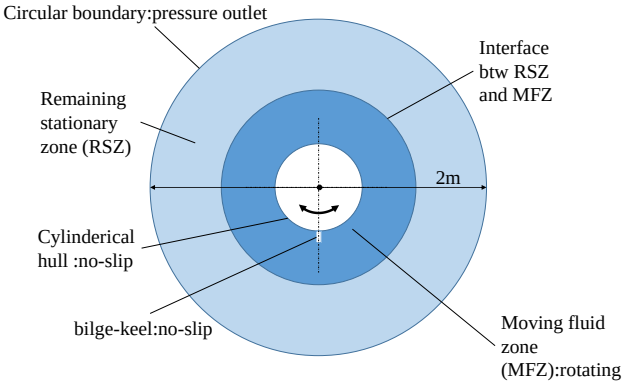

(a) Overall view

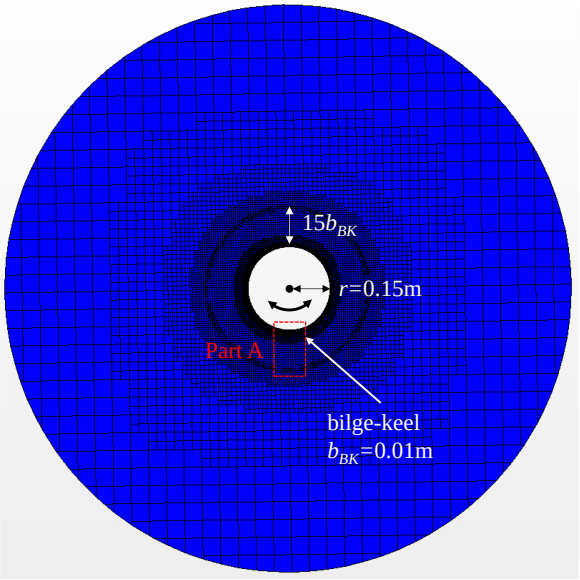

(b) Mesh divisions of moving fluid zone

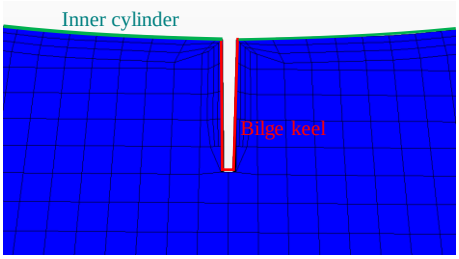

(c) Zoomed view near bilge-keel (part A)

Figure 1 Domain of calculation and 2D cylinder model with bilge keel.

Fig.1 also shows the bilge-keel of the cylindrical hull. The radius of the cylinder are r=0.15m. The bilge-keel is attached on a line

passing through the center of roll. The height and thickness of the bilge-keel are b_{BK}=0.01m and t_{BK}=0.001m. This analysis model is constructed based on the experiment conducted by Ikeda et al., (1976)(1978a).

MFZ is forced sinusoidal rolling and the normal force acting on the bilge-keel is calculated by integrating the pressure distribution on the bilge-keel.

Table 2 Computational condition of CFD.

numerical solver	implicit unsteady method
turbulent model	k-ε model
time discretization	2-order accuracy
inner iterations	5
minimum mesh size	0.001m
time steps	0.005s

Table 3 Condition of calculation of forced roll test.

roll period: Tr	1.0s
roll amplitude: ϕ_a	5.00, 8.59, 9.80, 11.39, 14.38, 20.00deg
$KC=\frac{\pi r\phi_a f}{b_{BK}}$ ($f=1$)	4.11,7.06, 8.06, 9.37 11.82, 12.90,16.44
total calculation cycles	5

Table 4 Particulars of a cylinder with bilge-keel.

radius: r	0.15m
size of bilge-keel: $b_{BK}\times t_{BK}$	0.01m×0.001m

3.2 Calculated result

The forced roll angle $\phi(t)$ is defined by

$$\phi(t)=\phi_a \sin\omega t \tag{5}$$

Here, $F(t)$ denotes the time history of the calculated force under a sinusoidal forced roll, and it can be expressed as Eq.6 by using Fourier series.

$$F(t)=F_0+\sum_{n=1}^{\infty}\{F_n \sin(n\omega t+\varepsilon_n)\} \tag{6}$$

Then, the equivalent linear amplitude of force component in proportion to roll angular velocity can be expressed as follow:

$$F=F_1 \sin(\varepsilon_1) \tag{7}$$

In the following sections, F is called the amplitude of drag.

The drag coefficient C_D is obtained from Eq.(8) with calculated drag acting on a bilge keel.

$$C_D=\frac{F}{1/2\rho S_{BK}(r\phi_a\omega)^2} \tag{8}$$

where S_{BK} is the projection area of bilge-keel, ϕ_a is roll amplitude, ω is roll angular frequency and F is amplitude of drag.

Fig.2 shows comparison between C_D proposed by Ikeda et al.(1976)(1978a) with measured data and the calculated results by CFD (shown by dot line). The calculated results are slightly bigger than Ikeda's empirical formula shown by solid line.

mark	b_{BK}×number	test method	model
○	1.0cm×1	free roll	ellipsoid
◎	1.0cm×2		
△	1.5cm×1		
□	0.7cm×1		
◇	0.9cm ×1	press.dif.	2D cylinder

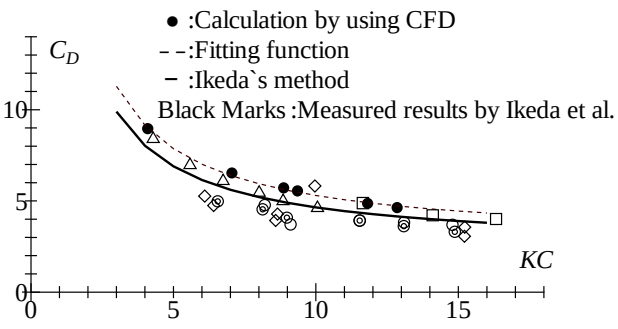

Figure 2 Comparison among the calculated drag coefficients of the bilge keel on a 2D cylinder by CFD, the empirical formula presented by Ikeda et al., (1976)(1978a) and the measured results by Ikeda et al., (1976)(1978a).

Ikeda et al., (1976)(1978a) obtains the drag acting on bilge keel by subtracting the damping of a naked hull from that of the hull with bilge keel based on the assumption that frictional damping component of the naked hull and the hull with bilge keels are the same. Fig.3 shows calculated shear stress on hull surface of a naked hull and the hull with bilge keel by CFD at the moment when roll velocity is maximum. This figure shows that these are not the same and it means that frictional damping components of the naked hull and the hull with bilge keel are not the same.

Therefore, the drag is re-obtained according to the analysis way of Ikeda et al., (1976)(1978a). Fig.4 shows the comparison between the re-obtained results (shown by dot dash line) and the results shown in Fig.2. This figure shows that the re-obtained drag coefficients is better agreement with Ikeda's results.

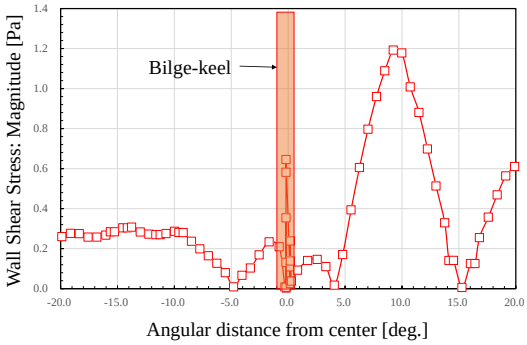

(a) with bilge keel.

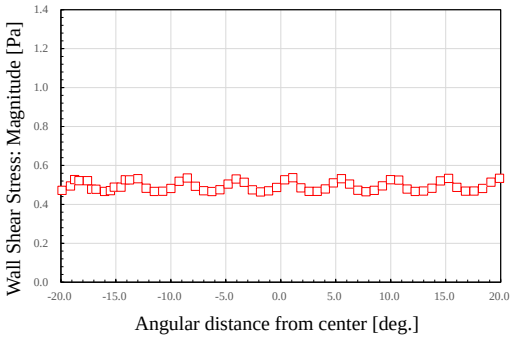

(b) without bilge keel.

Figure 3 Calculated shear stress distribution on the surface of 2D cylinder with or without bilge keel by CFD.

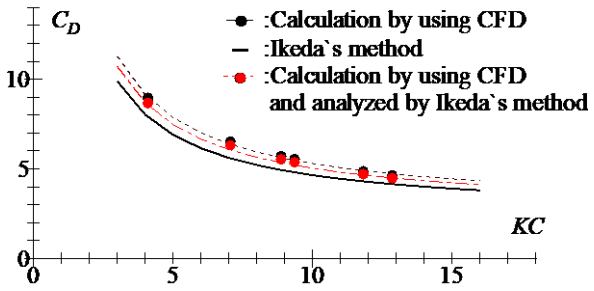

Figure 4 Comparison among the calculated drag coefficients of the bilge keel on a 2D cylinder according to Ikeda's analysis, the empirical formula presented by Ikeda et al., (1976)(1978a) and the measured results by Ikeda et al., (1976)(1978a).

4. EFFECT OF HULL FORM ON *f*

In the section 2, it has been explained how to obtain the correction factor *f*. In the discussion, *f* does not consider the effects of H_0 (: half breadth to draught ratio) and the free surface effects, but only σ (: area coefficient). In this section, in order to be applicable Ikeda's method in recent wide-breadth and shallow-draught ships, a forced roll test for these hull shapes is carried out using CFD. In the calculation, the effects of H_0 and σ on *f* are investigated to improve *f*.

4.1 Setup of CFD

Figure 5 shows a domain of calculation and a model. In this model, the rotating body is made by the upper semicircle and the lower half part. In lower half part, ship model under draft with bilge-keel is modelled. The bilge-keel is attached on a line passing through the center of roll. To investigate the effect of bilge keel and hull shape, the lower half is changed from the analysis model used in the previous section. The analysis model is very thin in thick direction as described in the same way as previous section. As a result of mesh division, the number of elements is 570,000. The gravity is not considered. The rolling motion is forcibly applied to the hull as same as the previous analysis. The *k*-ε model is also employed in this analysis as the turbulence model. The roll axis is the center of the circle. MFZ is forced sinusoidal rolling and the normal force acting on the bilge-keel is calculated by integrating the pressure distribution on the bilge-keel. Table 4 shows the particulars of model under draft and Table 5 shows the computational condition of CFD.

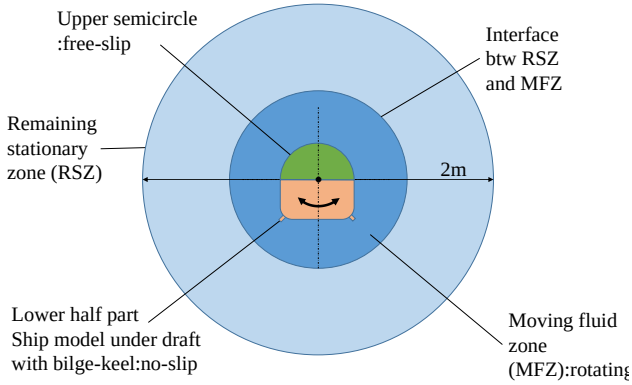

(a)Overall view

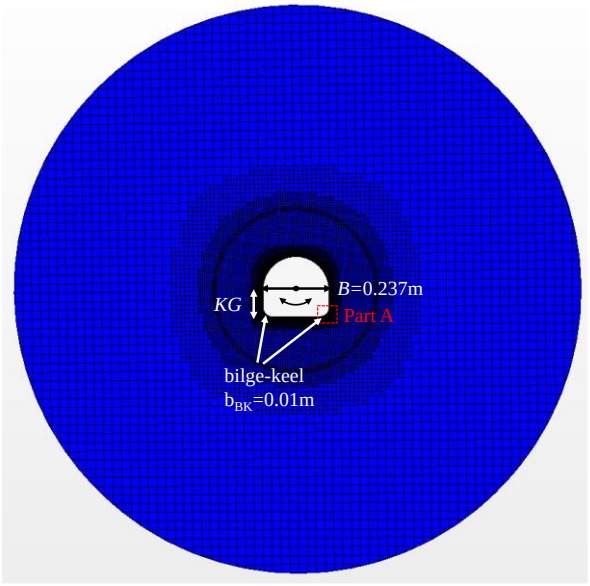

(b) Mesh division of overall model.

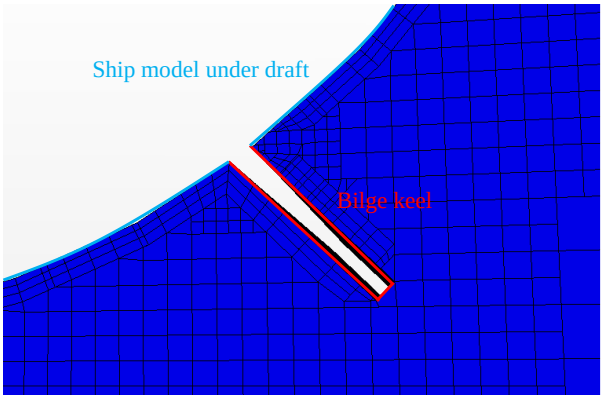

(c) Zoomed view of part A (near bilge keel).

Figure 5 Domain of calculation and a model with bilge keels at d = 0.096 m and H_0= 1.23.

Table 4 Particulars of 2D models.

length: L	0.05m
breadth: B	0.237m
draught: d	0.096, 0.072, 0.057, 0.042m
$H_0 = B/2d$	1.234, 1.645, 2.078, 2.821
area coefficient: σ	0.976, 0.968, 0.960, 0.946
r	0.138, 0.125, 0.118, 0.113m
bilge radius	0.035m
height of bilge keel	0.01m

Table 5 Computational condition of CFD.

roll period: Tr [s]		1.0
roll amplitude: ϕ_a [deg]		5.00, 8.59, 9.80 11.39, 14.38, 20.00
$KC = \frac{\pi r \phi_a}{b_{BK}}$	r=0.138	3.78, 6.50, 7.42, 8.62, 10.88, 15.14,
	r=0.125	3.41, 5.87, 6.70, 7.78, 9.82, 13.67,
	r=0.118	3.23, 5.55, 6.33, 7.36, 9.30, 12.93,
	r=0.113	3.09, 5.31, 6.06, 7.04, 8.89, 12.37
total calculation cycles		5

4.2 Characteristics of C_D and f

Fig.6 shows the calculated drag coefficients by CFD. A dotted line indicates the drag coefficient of the bilge keel on a 2D cylinder, and 4 marks indicate the drag coefficients of the bilge keels on 2D rectangles with the same bilge radius and 4 different H_0, whose area coefficient is not the same but almost same as shown in Table 4. From this figure, it is found that the drag coefficients of the bilge keels on 2D rectangles decrease according to increase of KC number as same as the drag coefficient of the bilge keel on a 2D cylinder, and the drag coefficients of the bilge keels on 2D rectangles decrease according to increase of H_0. Fig.7 shows the effects of roll period on the drag coefficient. From this figure, it is also found that there is not significant effects of roll period on C_D.

Fig.8 shows the correction factor obtained from Eq.6 by using data shown in Fig.6.

$$f = \sqrt{\frac{C_{D1}(KC)}{C_{D0}(KC)}} \qquad (9)$$

where $C_{D0}(KC)$ is the drag coefficient of bilge keel on a 2D cylinder shown in Fig.6, $C_{D1}(KC)$ is the drag coefficients of bilge keels on 2D rectangles shown in Fig.6, f is a correction factor of flow velocity at bilge caused by hull form. From this figure, it is noted that f increase according to decrease of H_0 and f is almost constant for change of KC number.

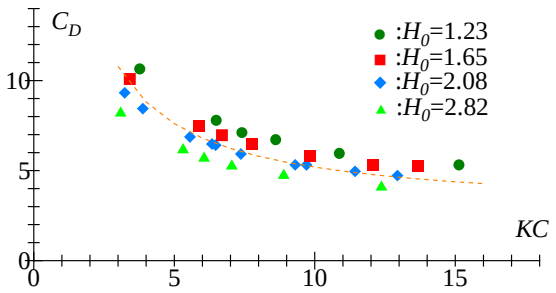

Figure 6 Comparison among the calculated drag coefficients of the bilge keels on a 2D cylinder by CFD shown by a dotted line and on 2D rectangles with the same bilge radius and 4 different H_0 shown by marks.

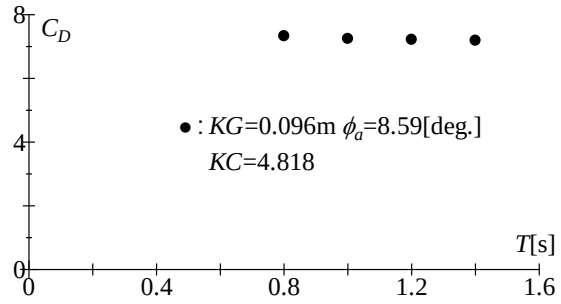

Figure 7 Effects of roll period on the drag coefficient at KC=4.818, ϕ_a=8.59 and H_0=2.078.

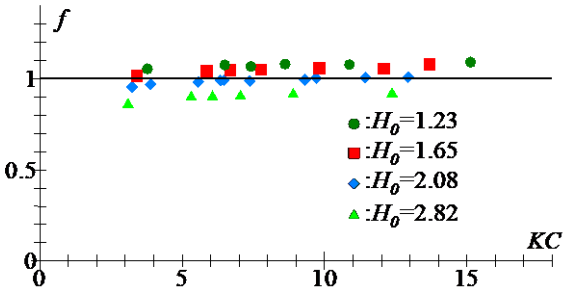

Figure 8 Correction factor f obtained from Eq.9.

4.3 Modification of *f*

From the results in the section 4.2, it is noted that the correction factor *f* has the effects of H_0. In this section, *f* is modified to take account the effects of H_0.

Fig.9 shows the correction factors *f* obtained from Eq.6 by using the calculated drag coefficients of the bilge keels on 2D rectangles shown in Table 6.

In the section 2, it is already explained how to decide Eq.4 which is the empirical formula of *f* by Ikeda et al., (1977)(1979). Eq.4 is fitted by comparisons between predicted and measured value for four 2D models with various bilge radius whose H_0 is near 1.23. Then, by using the calculated results shown in Fig.9, the ratios of *f* for various H_0 to *f* for H_0=1.23 are obtained, and the ratios are shown in Fig.10. From this figure, it is found that the ratio is constant in spite of area coefficient σ, and the relation between the ratio and H_0 is obtained from this figure, and the relation is shown in Fig.11 and the relation is expressed by the following formula.

$$g(H_0) = -0.1054H_0 + 1.1278 \tag{10}$$

where $g(H_0)$ is the correction factor of *f*, and $f \times g(H_0)$ is modified correction factor.

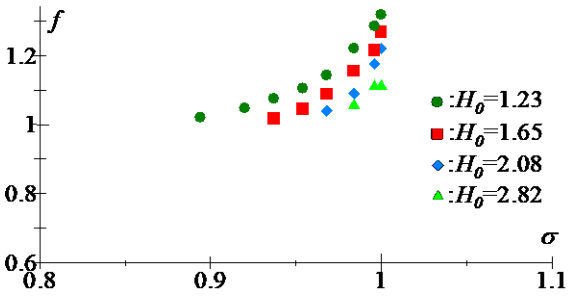

Figure 9 Correction factors *f* obtained from Eq.6 by using the calculated drag coefficient of the bilge keels on 2D rectangles at *KC*=6.50 shown in Table 6.

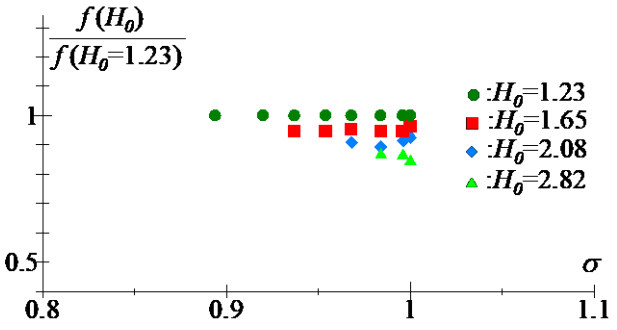

Figure 10 Ratios of *f* for various H_0 to *f* for H_0=1.23 obtained by using the data in Fig.9.

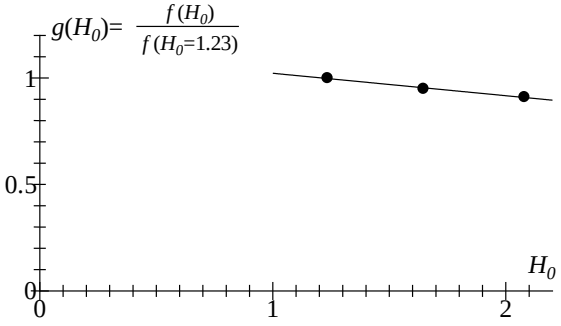

Figure 11 Relation between the ratio shown in Fig.10 and H_0 obtained by using Fig.10.

4.4 Modified Ikeda's method

In the subsection 4.3, the correction factor $g(H_0)$ of *f* is proposed as Eq.(10). In the process of obtaining $g(H_0)$, the effects of the water surface are not taken into account, and the height of roll center is *d*. In other words, it can be assumed that *d* denotes the height of roll center, if the water surface does not exist. By the way, in Ikeda's method, the height of roll center is expressed by *KG* generally, it means that the center of roll motion equation is defined as the center of gravity. Therefore, H_0 in Eq.7 is defined *B*/2*KG*, and Eq.7 is taken into account to Ikeda's method.

Fig.12 shows comparisons between the estimated bilge keel component by modified Ikeda's method and measured results by Katayama et al.,(2017a). In this figure, the results by Ikeda's original method are also shown. From this figure, the modified Ikeda's

method is slightly better than the original method. However, the modifications are not enough for larger roll amplitude, shallow draft and high *KG* cases, because the modifications do not consider the free surface effects. It is future works.

measured	original Ikeda's method	modified Ikeda's method
□	———	———

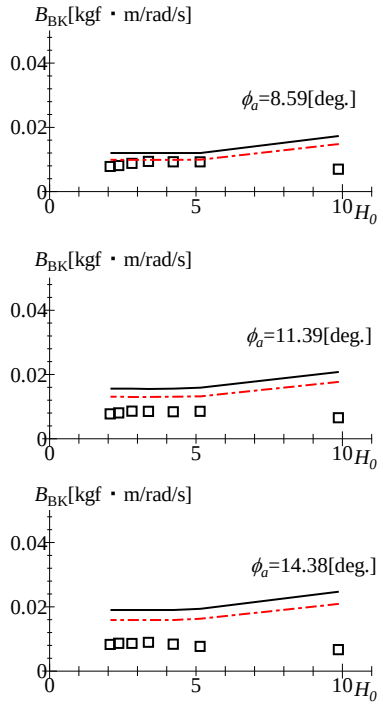

(a) *KG*=0.057m, *B*/2*KG*=2.079

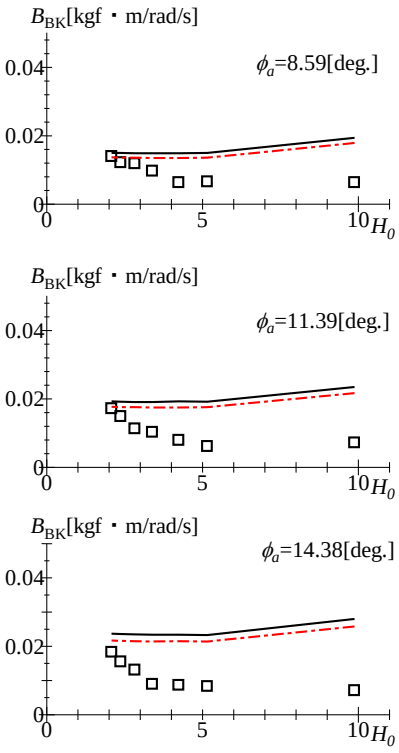

(b) *KG*=0.072m, *B*/2*KG*=1.646

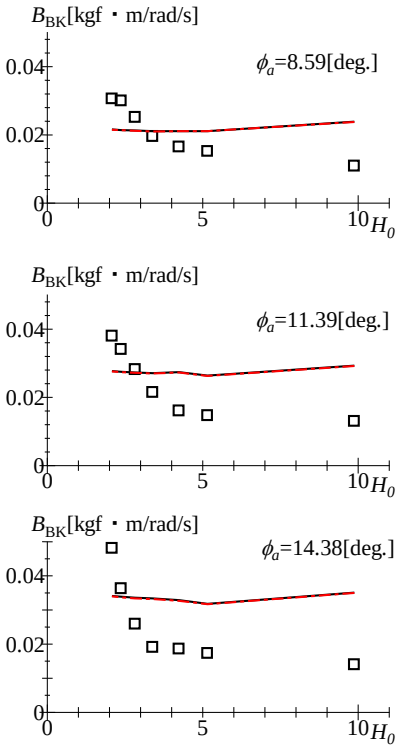

(c) *KG*=0.096, *B*/2*KG*=1.234

Figure 12 Comparisons between the estimated bilge keel component by modified Ikeda's method and measured results.

5. CONCLUSIONS

In this study, in order to improve bilge-keel damping component, the characteristics of the correction coefficient f to take account of the increment of flow velocity at the bilge by hull shape is investigated by CFD (STAR-CCM+). The following conclusions are obtained.

1. The calculated drag coefficients of the bilge keel on a 2D cylinder by CFD is slightly larger than the value of Ikeda's empirical formula regardless of KC number, however its characteristics is similar.

2. The drag coefficients of the bilge keels on 2D rectangles with the same bilge radius and 4 different H_0 decreases according to increase of KC number as same as the drag coefficient of the bilge keel on a 2D cylinder, and the drag coefficients of the bilge keels on 2D rectangles decrease according to increase of H_0. And the drag coefficients are not significant effects of roll period.

3. The correction factor f increases according to decrease of H_0. And f is almost constant for change of KC number.

4. In order to take account of the effects of H_0 on f, f is modified. And it is confirmed that the modified Ikeda's method is in better agreement with the measured results than the original method. However, the modifications are not enough for larger roll amplitude and shallow draft cases, because the modifications do not consider the free surface effects.

Acknowledgements Some parts of this research was carried out as joint research with Class NK

6. REFERENCES

Ikeda, Y., Himeno, Y., and Tanaka, N., 1976, "On Roll Damping Force of Ship -Effects of Friction of Hull and Normal Force of Bilge Keels", Journal of Kansai Society of Naval Architects, Japan, Vol. 161, pp.41-49.

Ikeda, Y., Himeno, Y., and Tanaka, N., 1978a, "On Roll Damping Force of Ship -Effects of Friction of Hull and Normal Force of Bilge Keels", Report of the Department of Naval Architecture, University of Osaka Prefecture, No.00401.

Ikeda, Y., Himeno, Y., Tanaka, N., 1978b, "A prediction method for ship roll damping", Report of the Department of Naval Architecture, University of Osaka Prefecture, No.00405.

Ikeda, Y., Komatsu K., Himeno Y. and Tanaka N., 1977, "On Roll Damping Force of Ship - Effects of Hull Surface Pressure Created by Bilge Keels", Journal of Kansai Society of Naval Architects, Japan, Vol. 165, pp.31-40.

Ikeda Y., Komatsu K., Himeno Y., Tanaka N., 1979, "On Roll Damping Force of Ship - Effects of Hull Surface Pressure Created by Bilge Keels", Report of Department of Naval Architecture, University of Osaka Prefecture, No. 00402.

Katayama, T., Matsuoka, M., 2017a, "Experimental Study on Bilge-keel Component of Roll Damping for Wide and Shallow Draught Vessel", Conference Proceedings the Japan Society of Naval Architects and Ocean Engineers, Vol.25, 2017, pp.255-259.

Tanaka N., Himeno, Y., Ikeda, Y., Isomura, K., 1981, "Experimental Study on Bilge-Keel Effect for Shallow-Draft Ship", Journal of Kansai Society of Naval Architects, Japan, Vol. 180, pp.69-75.

Yildiz, B., Katayama, T., 2017b, "Bilge keel–free surface interaction and vortex shedding effect on roll damping", Journal of Marine Science and Technology, Vol. 22, Number 3, pp.432-446.

Rudder influence on roll damping estimation

Patrick Sumislawski, *Hamburg University of Technology (TUHH)* patrick.sumislawski@tuhh.de

Sven Wassermann, *Hamburg University of Technology (TUHH)* sven.wassermann@tuhh.de

Moustafa Abdel-Maksoud, *Hamburg University of Technology (TUHH)* m.abdel-maksoud@tuhh.de

ABSTRACT

An established technique for investigating the roll damping of ships is the harmonic excited roll motion (HERM). HERM measurements of a free running model at forward speed require the use of a PID controlled rudder to keep the model course straight ahead. This PID set-up not only effects the yaw motion, but also influences the roll motion. The paper presents an efficient approach for quantifying and eliminating damping effects caused by the rudder while performing ship roll damping measurements. The impact of rudder forces on roll damping is determined analytically based on results from HERM measurements. Numerical simulations are used for validation of the rudder correction procedure. It will be shown that a rudder correction for HERM measurements is required.

Keywords: *Roll damping, Harmonic Excited Roll Motion (HERM) technique, Rudder*

1. INTRODUCTION

Forecasting ship motions in waves and predicting the occurrence of large roll motion amplitudes are a challenging task. In contrast to other degrees of freedom, the damping of roll motion is weak and thus a detailed investigation is necessary.

In the current study roll damping is estimated by applying a harmonic excitation of the roll motion (HERM). A free running ship model is excited by a sinusoidal moment, i.e. by two contrary rotating weights (see Blume, 1979 and Handschel et al., 2014). The HERM technique has a significant advantage over the decay technique when it comes to damping estimation at high model speed, as the number of investigated periods can be kept high for an accurate prediction.

In consequence of coupling effects, roll motion implies yaw motion and leads to a change of the model course. Using a PID set-up for the control of the rudder angle is a common way to keep the ship model on course. On the one hand, the resulting rudder forces affect yaw motion, and on the other hand, they have an undesirable influence on the roll motion. An overestimation of roll damping is presumed.

The simultaneous use of rudder for course keeping and for roll damping has often been discussed (e.g., Perez, 2005) but its influence on roll damping has not been studied in detail. This paper focusses on the estimation of rudder forces, the impact of rudder movements on roll damping and the development of an efficient approach for determining roll damping coefficients that are independent of the PID controlled rudder.

A detailed study on roll damping coefficients of the Duisburg Test Case (DTC) equipped with a spade rudder has been carried out at the Hamburg ship model basin (HSVA, Schumacher, 2010) and is used for validation in this investigation. The ship hull geometry is presented in Figure 1.

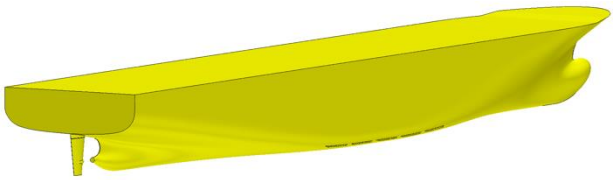

Figure 1: DTC hull geometry.

Table 1 shows the main dimensions of the examined ship in model scale.

Table 1: Main dimensions of Duisburg Test Case (DTC) with model scale $\boldsymbol{\lambda = 59.5}$, $\boldsymbol{T_\varphi}$ and $\boldsymbol{\overline{GM}}$ are valid for Fr = 0.0 measured with a small initial heeling angle.

L btw. perpendicular	L_{pp}	6.069m
Breadth	B	0.858m
Draught	D	0.235m
Vertical C.O.G.	$\overline{KG}$	0.399m
Metacentric height	$\overline{GM}$	0.023m
Block coefficient	c_B	0.654
Displacement volume	∇	$0.788m^3$
Froude number	Fr	0.104 / 0.191
Natural roll period	T_φ	4.85s

The study of HERM tests has shown that significant rudder angles were achieved during test runs. An example of roll, yaw and rudder motion is given in Figure 2. It can be observed that for a Froude number of 0.191 a roll amplitude of 10 degrees results in a rudder angle up to 5 degrees. The yaw angle is multiplied with a factor of 5.

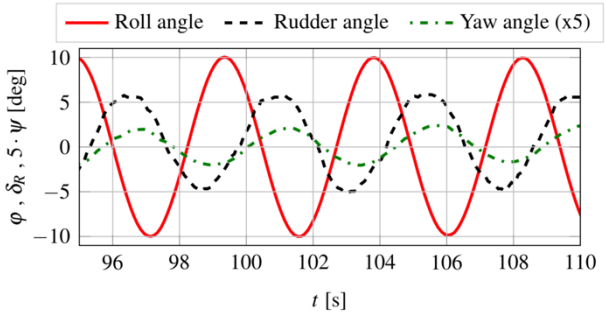

Figure 2: Results from model tests (Fr=0.191).

To investigate the impact of the rudder on roll damping, in the first step an overview of the theoretical background is presented. Subsequently HERM simulations of the post panamax container ship model DTC with and without a conventional PID-controller are carried out in order to study the rudder influence. Afterwards the approximation of rudder forces based on analytically calculated lift coefficients of the rudder is presented. Based on this model, the influence of the roll damping by the rudder will be determined and compared to the simulation results. It will be shown that the PID set-up can have significant influence on the roll damping values.

2. APPROACH

2.1 Roll damping

The equation of motion for roll can be simplified by considering one degree of freedom and taking Newton's second law into account:

$$M_\varphi \ddot{\varphi} + N_\varphi \dot{\varphi} + S_\varphi \varphi = M_{E,\varphi}. \qquad (1)$$

The ship's moment of inertia includes the influence of added mass and is represented by M_φ, the damping coefficient by N_φ and the restoring force coefficient by S_φ. The variable $M_{E,\varphi}$ stands for the external moment.

The time-dependent roll angle φ is expressed by a harmonic function

$$\varphi = \hat{\varphi}\, sin(\omega_e t + \nu) \qquad (2)$$

and the excitation moment $M_{E,\varphi}$

$$M_{E,\varphi} = \hat{M}_{E,\varphi}\, sin(\omega_e t). \qquad (3)$$

The phase angle ν is 90 degrees at resonance frequency. This simplifies equation 1 for the harmonic roll motion to:

$$\omega_e \hat{\varphi} N_\varphi = M_{E,\varphi}\,. \qquad (4)$$

Equating $M_{E,\varphi}$ with a static heel moment $M_{\varphi,h}$ leads to:

$$M_{E,\varphi} = M_{\varphi,h} = \varphi_h g \nabla \rho \overline{GM}\,. \qquad (5)$$

Transposing Equation 5 for the non-dimensional damping ratio of the static heel angle φ_h and the resulting roll amplitude $\hat{\varphi}$ yields to:

$$\frac{\varphi_h}{\hat{\varphi}} = \frac{N_\varphi \omega_e}{g \nabla \rho \overline{GM}}\,. \qquad (6)$$

Furthermore, it is assumed that the metacentric height remains constant over all Froude numbers and roll amplitudes.

An integration of the roll damping moment multiplied by the roll velocity yields to the damping energy within one period:

$$W_D = \int_0^{T_0} |N_\varphi \dot{\varphi} \dot{\varphi}\,| dt = N_\varphi \hat{\varphi}^2 \omega_e \pi. \qquad (7)$$

The roll damping coefficient is given as

$$N_\varphi = \frac{W_D}{\hat{\varphi}^2 \omega_e \pi}\,. \qquad (8)$$

The assumption that the damping energy must be compensated by the work done by the excitation moment leads to:

$$W_D = \int_0^{2\pi} M_{E,\varphi}\, d\varphi. \qquad (9)$$

For analysing W_D,the convergence of the roll amplitude, the phase angle and the damping coefficient for each roll period is used for indication of a steady state. HERM measurements and simulations are carried out in the ship's roll motion natural frequency ω_e, which is determined by decay tests.

2.2 PID controller

In order to keep the course of the model straight ahead, an active course keeping control is applied to the rudder using a proportional-integral-derivative (PID) controller. For this purpose, a rudder angle is calculated as a function of the yaw angle ψ as well as its derivative and integral value. Three coefficients are used for amplification: K_p for deviation of the course, K_i for the integral and K_d for the differential value. The rudder angle δ_R is defined using the following PID control function:

$$\delta_R = K_p\psi(t) + K_i \int_0^t \psi(\tau)d\tau + K_d \frac{d\psi(t)}{dt}. \qquad (10)$$

Within the framework of the present investigation, the control parameters are provided by HSVA.

2.3 Rudder Force Approximation

A rudder is a hydrofoil and normally placed behind the ship's propeller. It produces a transverse force and a steering moment. An approximation of the rudder's lift is necessary to describe the influence on the roll damping.
In general, the rudder lift L is described as a function of measured values from HERM tests: The rudder angle δ_R, roll motion velocity $\dot{\varphi}$, yaw motion velocity $\dot{\psi}$, model velocity v_M and the rotation rate n_p of the propeller:

$$L(t) = f\left(\delta_R, \dot{\varphi}, \dot{\psi}, v_M, n_p\right). \qquad (11)$$

The approximation procedure will be described in the following. Most of the outlined formulas have been given by Söding (1982 and 1986) based on the momentum theory and are summarised by Brix (1993) and Bertram (2012). The first step requires an estimation of the propeller slip stream v_A and the thrust coefficient C_{th}. The propeller open-water values for the thrust coefficient K_T are needed for interpolation as well as the wake fraction w:

$$v_A = v_M(1.0 - w), \qquad (12)$$

$$C_{th} = \frac{8}{\pi} \cdot \frac{K_T}{J^2} \qquad (13)$$

with the advance ratio $J = v_A/(n_p \cdot D_p)$. The propeller's diameter is defined by D_p. The axial velocity v_∞ at great distance from the propeller is given with:

$$v_\infty = v_A \cdot \sqrt{1.0 + C_{th}}. \qquad (14)$$

The corresponding radius of the propeller slip stream in the far field is defined using the propeller radius r_0:

$$r_\infty = r_0 \cdot \sqrt{\frac{1}{2} \cdot (1.0 + \frac{v_A}{v_\infty})}. \qquad (15)$$

Finally, the radius and axial velocity in the distance x from the propeller plane is calculated according to:

$$r_x = r_0 \frac{0.14\left(\frac{r_\infty}{r_0}\right)^3 + \frac{r_\infty}{r_0}\left(\frac{x}{r_0}\right)^{1.5}}{0.14\left(\frac{r_\infty}{r_0}\right)^3 + \left(\frac{x}{r_0}\right)^{1.5}}, \qquad (16)$$

$$v_x = v_\infty \left(\frac{r_\infty}{r_x}\right)^2. \qquad (17)$$

Moreover, due to turbulence effects, the slip stream radius is increased:

$$\Delta r = 0.15x \cdot \frac{v_x - v_a}{v_x + v_a}. \qquad (18)$$

According to the momentum theorem, an equation for the corrected stream velocity v_{corr} at the rudder is defined as follows:

$$v_{corr} = (v_x - v_a)\left(\frac{r_x}{r_x + \Delta r}\right)^2 + v_a. \qquad (19)$$

Using the corrected slip stream velocity v_{corr}, the angle of attack α_R and resulting velocity v_R may be approximated by:

$$v_R = \sqrt{v_{corr}^2 + \left(0.5\,\dot{\psi}\,cos\,\varphi\,L_{pp} + \dot{y} - \dot{\varphi}h_R\right)^2} \quad (20)$$

and

$$\alpha_R = \delta_R + tan^{-1}\left(\frac{0.5\,\dot{\psi}\,cos\,\varphi\,L_{pp} + \dot{y} - \dot{\varphi}h_R}{v_{corr}}\right). \quad (21)$$

The length between perpendiculars is denoted L_{pp}, the sway velocity $\dot{y}$ and the mean distance from rudder lift to the roll axis h_R. For small angles of α_R (< 15 degrees), the above-mentioned equation is simplified to the following equation:

$$\alpha_R = \delta_R + \frac{0.5\,\dot{\psi}\,cos\,\varphi\,L_{pp} + \dot{y} - \dot{\varphi}h_R}{v_{corr}}. \quad (22)$$

The above equation shows that the angle of attack consists of velocity components induced by sway $\dot{y}$, yaw $\dot{\psi}$ and roll motion $\dot{\varphi}$ as well as the rudder angle δ_R. Figure 3 describes the kinematics at the rudder for estimation of the effective rudder angle.

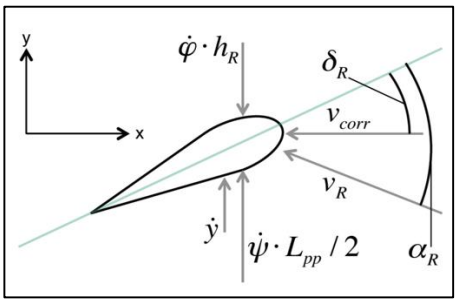

Figure 3: Estimation of effective rudder angle.

In order to correct only rudder forces due to the PID controlled rudder angle, linearity is assumed and components due to sway, yaw and roll motion are neglected, so that Equation 20 is simplified to:

$$\alpha_R = \delta_R. \quad (23)$$

The lift coefficient is dependent on the previously determined angle of attack α_R and may be approximated for small angles of attack by:

$$C_L = \frac{2\pi \cdot \Lambda(\Lambda+1)}{(\Lambda+2)^2} sin(\alpha_R) + C_q\, sin(\alpha_R)|\,sin(\alpha_R)|\,cos(\alpha_R) \quad (24)$$

with $C_q = 1.0$. The rudder's aspect ratio is denoted Λ.

Multiplying the lift coefficient with the stagnation pressure q and rudder area A_R yields to the lift:

$$L = C_L \cdot q \cdot A_R = 0.5 \cdot \rho \cdot v_R^2 \cdot C_L \cdot A_R \quad (25)$$

with

$$q = 0.5 \cdot \rho \cdot v_R^2. \quad (26)$$

Figure 4 shows an example that compares the lift of the rudder from later described numerical simulations and the analytical approximation. Both curves show a good correlation.

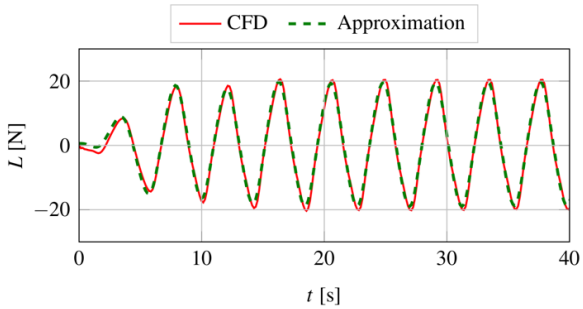

Figure 4: Comparison of rudder forces, CFD and approximation, Fr = 0.191.

Figure 5 illustrates the decomposition of the rudder lift calculated with the presented approximation method. The component of sway motion $\dot{y}$ is so small that it is neglected. Curve (I) is the sum of the lift from all components, whereas curve (II) represents the lift due to the rudder angle, curve (III) due to the yaw motion and curve (IV) due to the roll motion. The dominance of the lift caused by the rudder angle δ_R is clearly identified in this example.

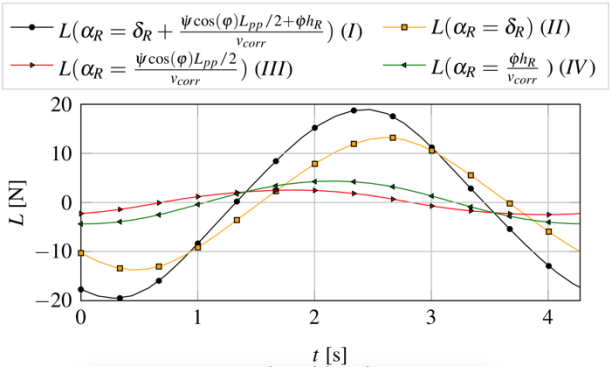

Figure 5: Comparison of lift components, Fr = 0.191.

2.4 Roll damping correction

In order to approximate the roll damping, the roll moment $M_R(t)$ caused by the rudder is described as the product of the previously introduced rudder lift L and the approximated distance between roll axis and rudder force h_R:

$$M_R(t) = L(t)h_R. \quad (27)$$

The distance h_R may be approximated by (Söding, 1991):

$$h_R = \frac{D + \overline{KG}}{2} - z_{rud}. \quad (28)$$

Here, the draught is denoted D, the vertical location of the center of gravity $\overline{KG}$ and the vertical location of the rudder's centroid z_{rud}. A correction of the damping coefficient due to the PID controlled rudder is realised by subtracting the rudder damping $N_{\varphi,rud}$ from the estimated roll damping N_φ:

$$N_{\varphi,corr} = N_\varphi - N_{\varphi,rud}. \quad (29)$$

Using Equations 7 and 8, the rudder damping over one roll period can be expressed as follows:

$$N_{\varphi,rud} = \frac{1}{\hat{\varphi}^2 \omega_e \pi} \int_0^{2\pi} M_R(t) d\varphi\,. \quad (30)$$

Now an equivalent excitation moment can be deduced, which is valid for frequencies near resonance and may be used in simulations without a PID set-up:

$$\widehat{M}_{E,corr} = N_{\varphi,corr} \cdot \hat{\varphi} \cdot \omega_e. \quad (31)$$

This corrected moment is necessary for HERM simulations without PID set-up in order to validate the procedure.

3. SIMULATION SETUP

Numerical simulations are carried out using the commercially available finite-volume method STAR-CCM+. Ship motions are realised by using an overset-technique. The background grid follows the overset grid in the horizontal plane while the overset grid is additionally allowed to heave, roll and pitch. Turbulent and viscous effects of the fluid are considered with the $k-\omega-SST$ turbulence model for solving the closure problem of the RANS equation.
The free surface is treated with a volume-of-fluid method. The propulsion is idealised by a volume-force method, which uses the propeller open-water values for the thrust and torque coefficients. The rudder movement is realised by a moving mesh with a sliding-interface technique within the overset mesh. Figure 6 illustrates the overset region and the rudder region. The appropriate mesh refinements ensure an adequate discretisation of the free surface within the overset mesh.

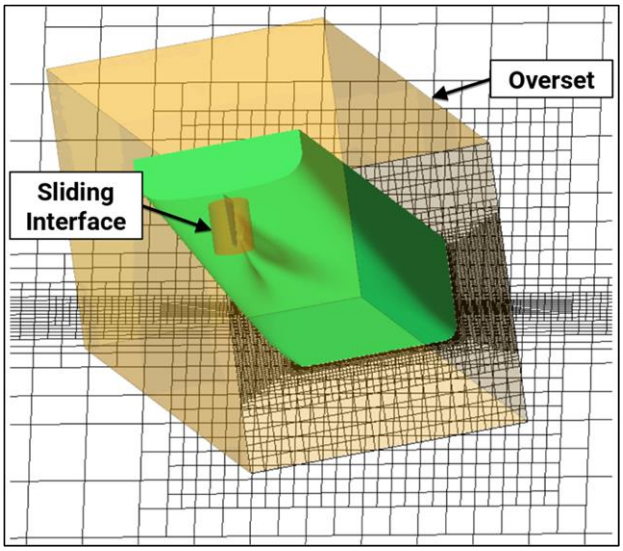

Figure 6: Computational grid.

Details of the mesh can be seen in Figure 7 for the stern of the computational model and a top view in Figure 8.

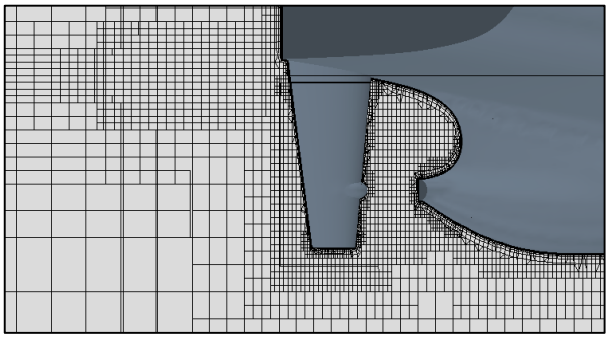
Figure 7: Computational grid (stern).

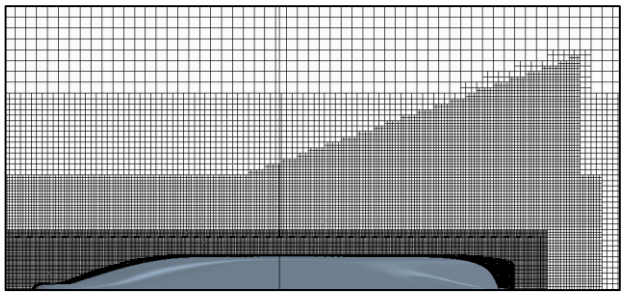

Figure 8: Computational grid (top view).

Studies on the time-step size have shown that satisfying results are achieved using around 1500 time-steps per period. The number of cells is primarily dependent on the investigated roll angle and amounts to approximately 3M.
The numerical domain is presented in Figure 9, which illustrates the extent of the domain and the type of boundary conditions. All boundaries are defined as inlet, except the boundary downstream. The extend of the domain is described depending on the wavelength λ_S of the ship's wave system, which is defined as follows:

$$\lambda_S = 2\pi Fr^2 L_{pp}. \qquad (32)$$

The bottom is eight wavelengths deep, so that shallow water effects are excluded. In order to avoid wave reflection at the boundaries, a wave damping zone is applied, starting at a distance of two wavelengths from each boundary.

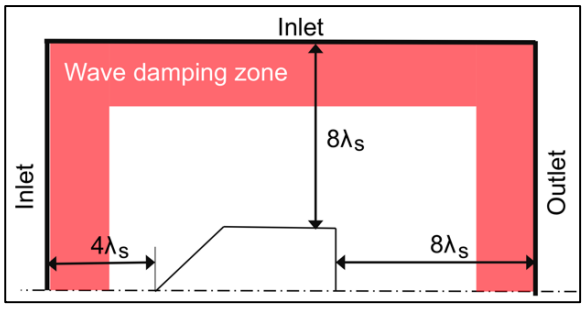

Figure 9: Extend of computational domain.

4. RESULTS

4.1 Comparison of simulations with model tests

This section deals with the validation of HERM simulations using experimental data for two different Froude numbers and the results from correction of the roll damping with regard to the PID-controlled rudder.
Figure 10 shows the time series of the excitation moment and roll angle as an example for all HERM simulations. The simulation can be divided into two stages: The transient growth of the roll amplitude and a steady state, where the roll amplitude remains constant. Simulations are carried out in close proximity to the ship's natural frequency, so that the phase shift between roll angle and excitation moment is nearly 90 degree.

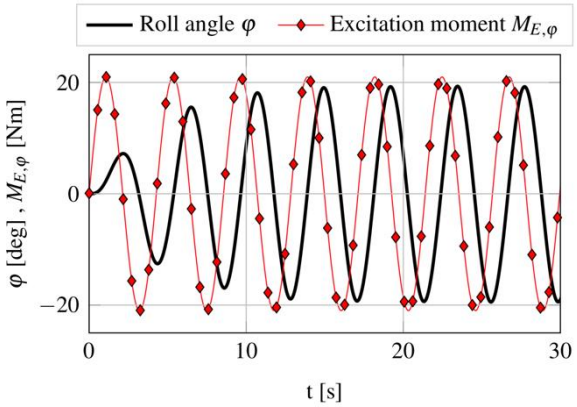

Figure 10: Excitation moment and roll angle in HERM simulation, Fr = 0.191.

An exemplary free surface elevation during a HERM simulation is shown in Figure 12. The model's Froude number is 0.191.

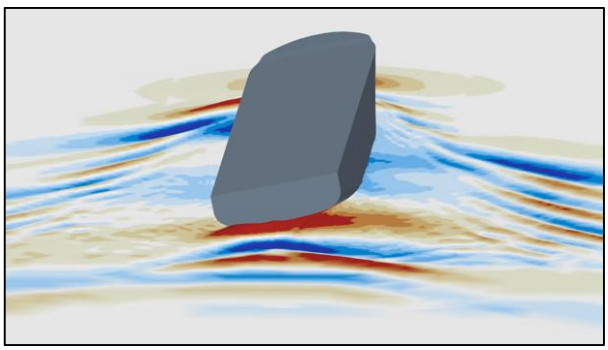

Figure 11: HERM simulation, free surface elevation.

A comparison of time series between numerical simulation (CFD) and experiments (EFD) for the roll φ, yaw ψ, and rudder δ_R angle is given in Figure 11. A good agreement can be observed for all reported motions.

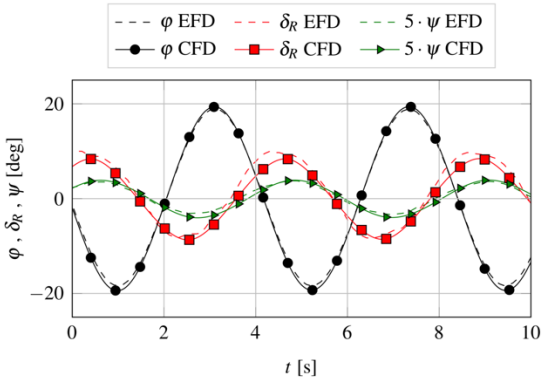

Figure 12: Time series of EFD and CFD HERM simulations, Fr = 0.191.

Results from HERM simulations and measurements are given in Figure 13.

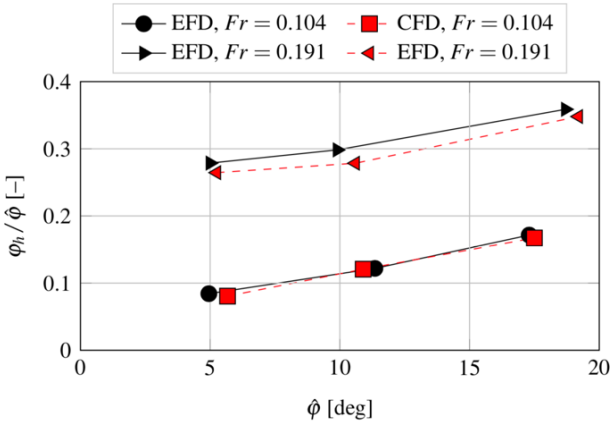

Figure 13: Comparison of EFD and CFD roll damping.

The measurement results correspond very well with numerical simulations, especially at the lower Froude number of 0.104. A moderate deviation of roll damping at the Froude number 0.191 is visible. The highest deviation occurs at a roll amplitude of 10 degrees and is about 6%. In summary, CFD results show a sufficient accuracy in comparison to experimental data.

4.2 Simulation with and without PID-controlled rudder

Figure 14 shows the roll damping over the roll amplitude at a Froude number of 0.104. The black curve (I) stands for HERM simulations with PID set-up and the green curve (II) for the prediction of corrected roll damping based on Equation 29. Additionally, the red curve (III) represents HERM simulations without PID set-up using the predicted excitation moment $M_{E,corr}$.

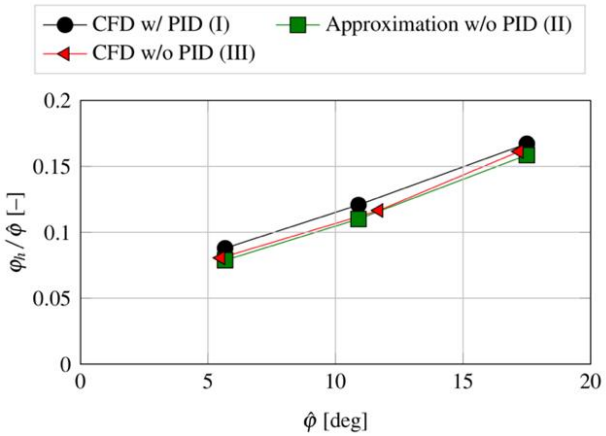

Figure 14: Corrected roll damping, Fr = 0.104.

The change of roll damping due to the PID control is small with slightly less than 10 percent. Figure 15 shows the results for a Froude number of 0.191. There is a clear difference between curve (I) with PID set-up and the other two curves without PID set-up.

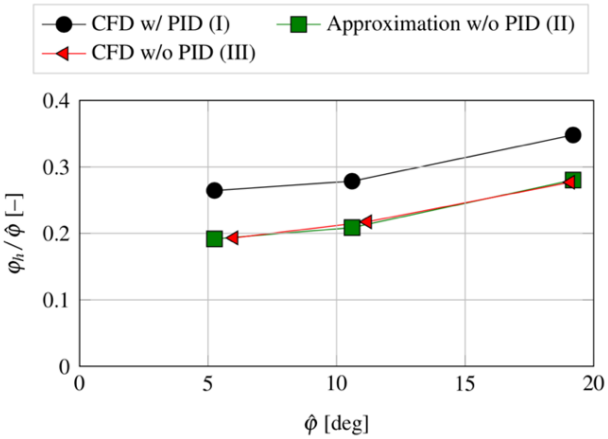

Figure 15: Corrected roll damping, Fr = 0.191.

In general, a considerable influence of the PID set-up on roll damping can be observed, which is significantly larger for higher Froude number. The analytical approximation (II) and the numerical simulation (III) are in good agreement. The presented analytical approach is suitable for the determination of the rudder influence with adequate accuracy with regard to the DTC hull.

As expected, the rudder influence is dependent on the model velocity. In order to quantify the influence of the rudder, results are summarised in Tables 2 and 3.

Table 2: Corrected roll damping, Fr = 0.104.

$\hat{\varphi}$	[deg]	5.6	10.9	17.5
$\hat{\psi}$	[deg]	0.15	0.3	0.4
$\hat{\delta}_R$	[deg]	2.5	3.1	3.8
$\varphi_h/\hat{\varphi}$ w/ PID	[-]	0.088	0.121	0.167
$\varphi_h/\hat{\varphi}$ w/o PID	[-]	0.082	0.110	0.159
Deviation	[%]	+8.5	+9.7	+5.2

Table 3: Corrected roll damping, Fr = 0.191.

$\hat{\varphi}$	[deg]	5.25	10.6	192
$\hat{\psi}$	[deg]	0.3	0.6	0.8
$\hat{\delta}_R$	[deg]	3.1	5.7	8.4
$\varphi_h/\hat{\varphi}$ w/ PID	[-]	0.264	0.279	0.348
$\varphi_h/\hat{\varphi}$ w/o PID	[-]	0.192	0.209	0.280
Deviation	[%]	+38.0	+33.5	+24.2

The rudder influence is of minor importance at a Froude number of 0.104, whereas a significantly increased influence due to rudder movements is observed at a Froude number of 0.191. In this case, the roll damping is over 30% higher with the use of a PID-controlled rudder. In all cases, yaw amplitudes are almost equal, whether a PID set-up is used or not.

To compare the total roll damping with the part of the rudder, a detailed analysis is performed. In this case, the percentage ratio of roll damping due to the rudder ($N_{\varphi,rud}$) is compared to the total roll damping (N_φ) for one period and is summed up in Table 4 for the Froude number of 0.191. Three set-ups of HERM simulations are chosen in order to outline the influence of the rudder stepwise:

V1: No PID control, yaw motion suppressed,
V2: No PID control, free motion, and
V3: With PID control, free motion.

Table 4: Percentage ratio of roll damping by the rudder, Fr = 0.191.

	$N_{\varphi,rud}/N_\varphi$ in %		
$\hat{\varphi}$	V1	V2	V3
5.25°	0.12	0.16	0.30
10.6°	0.10	0.14	0.31
19.2°	0.09	0.12	0.33

Without a PID controlled rudder, the difference between set-up V1 and V2 shows, that the roll damping caused by the rudder is slightly increased on the basis of the yaw motion. The percentage ratio rises significantly with the use of a PID controller (V3). About 30% of the overall roll damping can be traced back to the rudder. This underlines once more that the rudder has to be considered with respect to HERM measurements.

An example for the application of the presented method during HERM tests is shown for a Froude number of 0.191. On that account, roll and rudder angles as well as the roll damping with and without PID control for each period are shown in Figure 16.

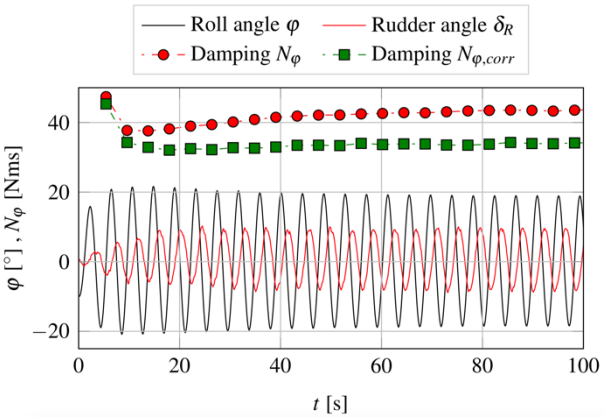

Figure 16: Roll damping correction in model test set-up.

5. CONCLUSION

The paper presents roll damping results for a modern container vessel and a detailed analysis of the rudder's impact on ship roll damping. The comparison of roll damping with and without a PID controlled rudder confirms that the rudder influence may not be neglected in analysis of HERM measurements. The results of HERM simulations using the Duisburg Test Case (DTC) have shown that roll damping is overestimated for the higher Froude number. A simple and efficient approach has been introduced in order to take the effect of a PID set-up into account. The correction of estimated roll damping yields to an increased accuracy with regard to the prediction of extreme roll motions. However, for a generalised conclusion the application for other ship and rudder types should be investigated further.

6. ACKNOWLEDMENTS

The work was funded by the German Federal Ministry for Economic Affairs and Energy under the aegis of the BMWi-project "HERMes" within the framework program "Schifffahrt und Meerestechnik für das 21. Jahrhundert". The authors would like to thank the cooperation partners in the project: Hamburg ship model basin (HSVA), Hoppe Marine and P. Döhle.

7. REFERENCES

Bertram, V., 2012, "Practical Ship Hydrodynamics", Elsevier Ltd., pp. 284-286.

Blume, P., 1979, "Experimentelle Bestimmung von Koeffizienten der wirksamen Rolldämpfung und ihrer Anwendung zur Abschätzung extremer Rollwinkel (in German)", Ship Technology Research / Schiffstechnik, Vol. 26, pp. 3-23.

Brix, J., 1993, "Manoeuvring Technical Manual (in German)", Seehafen Verlag GmbH, pp. 74-82.

Perez, T., 2005, "Ship Motion Control – Course Keeping and Roll Stabilisation Using Rudder and Fins", Springer Verlag.

Handschel, S. and Abdel-Maksoud, M., 2014, "Improvement of the Harmonic Excited Roll Motion Technique for Estimating Roll Damping", Ship Technology Research / Schiffstechnik, Vol. 61/3, pp. 116-130.

Schumacher, A., 2010, "Rolldämpfungs-versuche mit dem Modell eines großen Containerschiffes – Teilvorhaben Mat-Roll (in German)", Report at Hamburgische Schiffbau-Versuchsanstalt (HSVA), Germany.

Söding, H., 1982, "Prediction of ship steering capabilities", Ship Technology Research / Schiffstechnik, Vol. 29, pp. 3-29.

Söding, H., 1986, "Kräfte am Ruder (in German)", Handbuch der Werften XVIII, Hansa-Verlag, pp. 47-56.

Söding, H., 1991, "Die Wirkung von Roll-dämpfungsflossen abhängig von ihrem Einbauort (in German)", Technical Report, University of Hamburg.

Roll Damping Estimation for Small Planing Craft

Toru, Katayama, *Osaka Prefecture University,* katayama@marine.osakafu-u.ac.jp

Toshiya, Adachi, *Osaka Prefecture University,* syb03003@edu.osakafu-u.ac.jp

Tomohisa, Sawae, *Osaka Prefecture University*, tomohisa-sawae@mes.co.jp

ABSTRACT

As a roll damping prediction method, Ikeda's method is well-known. However, if it is applied to a small craft at planing condition, the method underestimates roll damping coefficient, because vertical lift component of roll damping is not taken into account. Then an estimation method of the component is proposed by Katayama et al.(2000). However, the method requires measured data of the craft or Savitsky's empirical formula. It takes cost to carry out measurement, and it is difficult to apply Savitsky's empirical formula to the hull form excepting the deep-V mono-hedron.

In this study, a prediction method of the vertical lift component which is applicable to a real hull is proposed. And it is confirmed that predicted results are in good agreement with measured ones.

Keywords: *Roll damping, planing craft, forced roll test*

1. INTRODUCTION

Roll is an important factor for safety of all kinds of ships. In order to estimate the characteristics of roll, the terms of motion equation, which are wave excitation, restoring, damping and inertia forces etc., play important roles, respectively. Therefore, it is necessary for roll estimation to know their characteristics correctly.

Ikeda's method is well-known as one of roll damping prediction method for displacement type vessels. In addition, Ikeda et al. (1990), (1998) proposes the prediction method that is improved to apply it to hard-chine type craft, and it is confirmed that it is in good agreement with measured results.

Lift component of roll damping is significant at high forward speed for any type of ships, and Ikeda's method includes a horizontal lift component which is caused by horizontal lift force caused by coupling sway velocity of hull from roll. However, for planing craft, its draft is extremely shallow compared with its breadth, the horizontal lift component is small, because its under water side projection area is generally small. On the other hand, the lift component due to a vertical lift force is significant for planing craft because of its large bottom projection area.

In the previous study, the roll damping of the small planing craft that is the hard-chine craft is measured by a forced roll test and it is compared with estimated results by Ikeda's method. Unfortunately, the comparison indicates that the measured results are larger than the estimated results. Because vertical lift component is dominant component of its roll damping according to increase in forward speed, and the component is not taken into account in Ikeda's method. Then the prediction method of the component is proposed. However, the method uses the measured data or empirical formula based on a prismatic planing surface and it is difficult to use it for the hull whose deadrise angle is not constant.

In this study, using some existing formulas which is applicable to the real hull, a prediction method of the component is proposed. And it is confirmed that the estimated results are in good agreement with measured ones at deep draught and large trim angle compared with general running attitude. Moreover, the characteristics of roll damping at around running attitude is experimentally investigated and the estimated results are also compared with measured results.

2. THE VERTICAL LIFT COMPONENT OF ROLL DAMPING

Typical planing craft has shallow draft compared with its breadth, then its under water side projection area is generally small when it runs at high forward speed, and accordingly the horizontal lift component is small.

On the other hand, its under water bottom projection area is large, the vertical lift force acting on bottom of craft is large and may play an important role in roll damping. Therefore, it is necessary to take the component due to vertical lift force into account. In the following section, the prediction method of the vertical lift component of roll damping for planing craft is proposed, and the comparison between the estimated and the measured results is shown.

2.1 Previous Prediction Method (Ikeda et al., 2000)

In this study, it is assumed that the planing craft is running at trim angle τ_1 [rad] and aft-draught d_{a1} [m] in calm water and it has only periodic roll around the center of gravity, and roll angle is written as follows,

$$\phi = \phi_a \sin \omega t \tag{1}$$

where ϕ [rad] is roll angle, ϕ_a [rad] is roll amplitude, and ω [rad/s] is roll circular frequency.

When roll angular velocity is maximum, a point $A(y, z)$ on a cross section which is shown in Fig.1 has vertical velocity v_x [m/s] as follows,

$$v_x = \phi_a \omega y \tag{2}$$

where y [m] is transverse distance between the center of gravity and point $A(y,z)$. When the planing craft has forward speed U [m/s], the buttock section including the point $A(y,z)$ gets attack angle $\alpha(y)$ [rad] for relative flow as shown in Fig. 2, and the angle can be calculated as follows,

$$\alpha(y) = \tan^{-1}\frac{v_x \cos\tau_1}{U - v_x \sin\tau_1} \approx \tan^{-1}\frac{v_x}{U} \approx \frac{\phi_a \omega y}{U} \tag{3}$$

Now, the running trim angle is τ_1 [rad], the vertical lift force acting on the craft is written by using the virtual trim angle $\tau(y)$ [rad] for relative flow, and it is written as follows,

$$\tau(y) = \tau_1 - \alpha(y) = \tau_1 - \frac{\phi_a \omega y}{U} \tag{4}.$$

For the planing craft, quantity of the vertical lift force significantly depends on trim angle. The sectional vertical lift force $f_L(y)$ [kg/s^2] (upword +) acting on the buttock line include the point $A(y, z)$ with the virtual attack angle $\tau(y)$ is written as follows,

$$f_L(y) = \frac{1}{2}\rho\, k_L(\tau_1)\tau(y)\, L_{WL}(y)\, U^2 \tag{5}$$

where $L_{WL}(y)$ and dy [m] are water a line length and a breadth of the buttock section, ρ [kg/m^3] is density of fluid, and $k_L(\tau_1)$ [1/rad] is a differential coefficient of the non-dimensional vertical lift coefficient $C_L(\tau_1)$. Therefore, the roll damping caused by the vertical lift force is written as follows,

$$
\begin{aligned}
M_{VL} &= -\int_{-\frac{B_{WL}}{2}}^{\frac{B_{WL}}{2}} f_L(y)\,y\,dy \\
&= \frac{\rho U^2}{2}\int_0^{\frac{B_{WL}}{2}} \{\tau(-y)-\tau(y)\}\,k_L(\tau_1)L_{WL}(y)\,y\,dy \\
&= \frac{\rho U^2}{2}\int_0^{\frac{B_{WL}}{2}} \left(\frac{2\phi_a\,\omega\,y}{U}\right)k_L(\tau_1)L_{WL}(y)\,y\,dy \\
&= B_{VL}\phi_a\omega
\end{aligned}
\tag{6}
$$

where B_{WL} [m] is the maximum breadth of the wetted surface of the craft at running condition. In the previous study, to simplify the term $k_L(\tau_1)L_{WL}(y)$, it is obtained by the following equation,

$$
\begin{aligned}
k_L(\tau_1)L_{WL}(y) &= \frac{C_L(\tau_1)}{\tau_1}\frac{S_{WA}}{B_{WL}} \\
&= \frac{2\times L(\tau_1, d_{a1})}{\tau_1\,\rho S_{WA}U^2}\frac{S_{WA}}{B_{WL}}
\end{aligned}
\tag{7}
$$

where $C_L(\tau_1)$ is the non-dimensional vertical lift coefficient of the craft at the trim angle τ_1 and the aft-draught d_{a1} in calm water, $L(\tau_1, d_{a1})$ [kgm/s^2] is the lift force acting on the craft and S_{WA} [m^2] is the wetted surface area at the running condition.

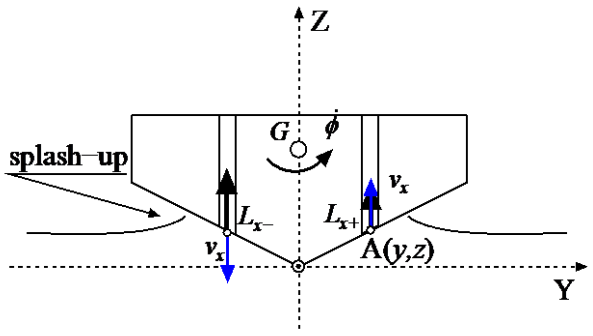

Fig. 1 A cross section at the moment when roll angular velocity is maximum.

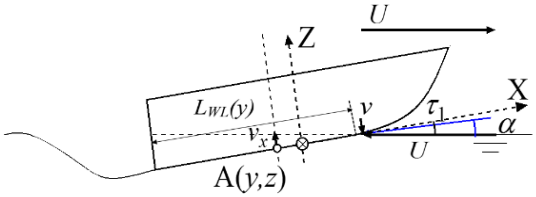

Fig. 2 A buttock section including the point *A*.

2.2 Present method

As an estimation method of hydrodynamic vertical lift force of the planing craft, Savitsky's empirical formula (Savitsky, 1964) is well-known, and the formula is used in the previous method introduced in the section 2.1. However, the empirical formula is made based on the prismatic planing surface and it is difficult to use it for the hull whose deadrise angle is not constant.

As other method, Payne's method (Payne, 1994) based on added-mass planing theory is also well-known and the method is able to use for the hull whose deadrise angle is not constant. Therefore, in this study, the method based on Payne's method is proposed.

First, roll damping acting on two dimensional cross sections shown in Fig. 3 is written as follows,

$$
M_{xVL} = L_{x-}l_{Rx} - L_{x+}l_{Rx} \tag{8}
$$

where L_{x-} and L_{x+} are vertical lift forces (up word +) acting left and right side of the cross section and l_{Rx} is a horizontal distance from the center of roll to action line of L_{x-} and L_{x+} and they are obtained by Smiley's empirical formula (Smiley, 1952) written as follows,

$$
l_{Rx} = E_2\frac{\pi}{4}\frac{b_x}{2} \tag{9}
$$

where b_x is the wetted breadth of the cross section considering the effect of splash-up. E_2 is 0.8 when the chine of the cross section is wetted (chine-wet), and 1.0 when the chine of the cross section is not wetted (chine-dry). The effects of splash-up is considered as 0.5π times of the draught of the cross section for still water surface that is known as Wagner's theoretical results (Wagner, 1932). L_{x-} and L_{x+} in Eq.(8) are written as follows,

$$
L_{x-} \text{ or } L_{x+} = -\frac{1}{2}U\cos\tau_1\frac{d}{dx}\left(m'_x v_x\right) \tag{10}.
$$

Eq.(10) is based on the momentum theory, and v_x is a velocity parallel to the cross section and it is written by the following formulae as the mean value for each side with the wetted breadth considering the effect of splash-up.

$$v_x = \begin{cases} v_{x-} = U\sin\tau_1 + \dfrac{b_x}{4}\phi_a\,\omega \quad (\text{for } L_{x-}) \\ v_{x+} = U\sin\tau_1 - \dfrac{b_x}{4}\phi_a\,\omega \quad (\text{for } L_{x+}) \\ \text{if } v_{x+} < 0 \text{ then } v_{x-} = 0. \end{cases} \tag{11}$$

The first term of Eq.(11) is caused by forward speed and the second term is caused by roll. In Eq.(10), m'_x is a vertical added-mass of the two dimensional cross section proposed by Payne, (1994) and it is written as follows,

$$m'_x = C_{m'x}\frac{\pi}{2}\rho\left(\frac{b_x}{2}\right)^2 f(A)$$
$$f(A) = \frac{1}{\sqrt{1+(KA)^2}} \tag{12},$$
$$K = \frac{1}{4} + \sqrt{\frac{2\beta_x}{\pi}}, \quad A = \frac{b_A^{\,2}}{S}$$

where b_A is the wetted width at the stern considering splash-up (b_A is the chine breath at the stern for chine-wet), S is the projected area of the planing wetted surface on the plane including the baseline, β_x is the deadrise angle of the cross section. $C_{m'x}$ for chine-wet or chine-dry are written as follows,

$$C_{m'x} = \left(1 + k\frac{z_{cx}}{b_x}\right)\left(1 - \frac{\beta_{Ex}}{2\pi}\right)^2$$
$$\text{where} \quad k = \begin{cases} 0 & \text{for chine-dry} \\ 2 & \text{for chine-wet} \end{cases} \tag{13},$$

where β_{Ex} is called effective deadrise angle and it is written as follows,

$$\tan\beta_{Ex} = \tan\beta_x / \cos\tau_1 \tag{14}.$$

z_{cx} is a length shown in Fig. 4 and it means the chine submergence below the chine which the splash-up first wets. Finally, the roll damping caused by the vertical lift force is written by integrating Eq.(8) from aft to fore as follows,

$$M_{VL} = \int_A^F M_{xVL}\,dx \tag{15}.$$

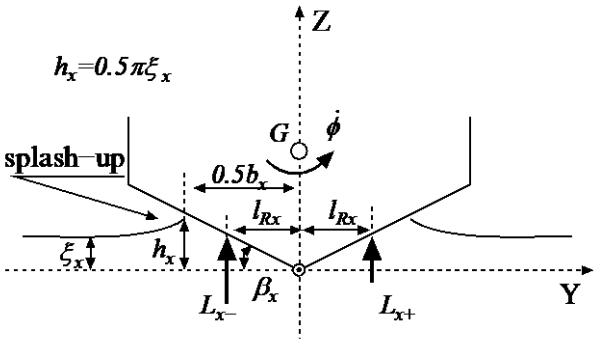

Fig. 3 Symbols expressing geometric relations among the water surface, a cross section of planing surface and vertical lift force on the cross section.

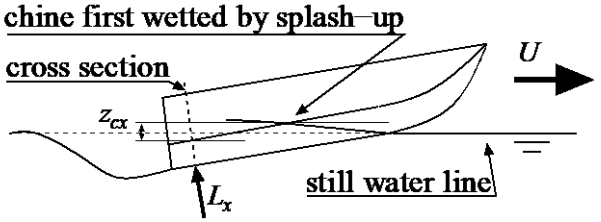

Fig. 4 Local chine submergence below the level at which "splash-up" first wets the chine.

2.3 Comparisons of results

Fig. 5 shows the comparisons among the results by the proposed method, the results by the present method and the measured results for the model shown in Fig. 6. The present method is also linear component for roll amplitude as same as the previous method and the results by the present method is similar to the results by the previous method. The estimation methods cannot show the effects of roll amplitude, though the estimated results are agreement with the measured results.

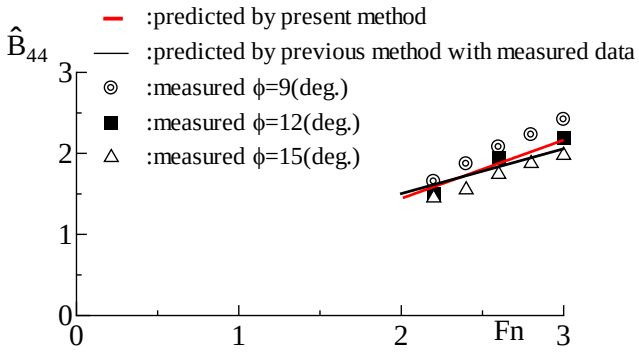

Fig. 5 Comparison of a roll damping coefficient between the measured and the estimated aft-draft 0.045 m, trim angle 4 deg and roll period 1.0 s.

3. CHARACTERISTICS OF ROLL DAMPING AROUND RUNNING ATTITUDE

In the chapter 2, it is confirmed that the results of the proposed estimation method of roll damping are in good agreement with the measured results. However, the measured data is at deep draught than general running draught, the vertical lift component of roll damping is dominant at that condition. Then in this chapter, roll damping around general running attitude is measured by a forced roll test and it is compared with the estimated results by the present method.

3.1 Ship model

The body plan and main particulars of the model which is used in this study are shown in Table 1 and Fig.6. It is a deep-V mono-hedron type hull.

Table 1 Principle particulars of the model.

Length: L_{OA}	1.000 m
Breadth: B	0.333 m
Depth: D	0.100 m
Draught: d	0.040 m
Ship weight: W	53.41 N
KG and the center of rotating motions	0.097 m
Deadrise angle: β	11.0 deg

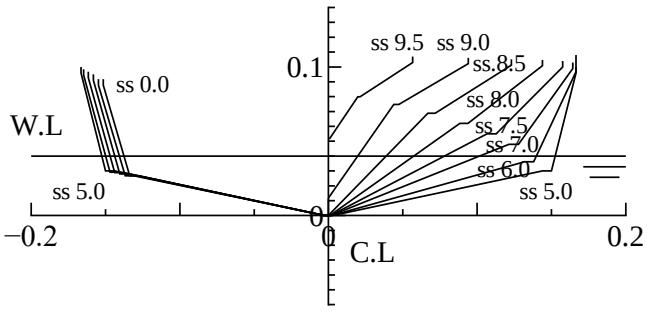

Fig. 6 Body plan of the model.

3.2 Experimental setup

In order to measure running attitude of the model, free running test is carried out. In the measurement, pitch and heave of the model are free shown in Fig. 7. The model is towed horizontally with constant speed in still water, and its trim angle and aft draught are measured. The towing point is at S.S.5 (L_{KC} =0.0 m: backward from the cross section of midship +). Table 2 shows experimental conditions. Fig.8 show the trim angle and the aft draught versus Froude number. From the results shown in Fig. 8, the attitudes of forced roll test are decided.

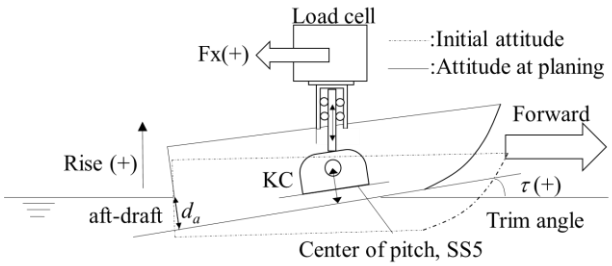

Fig. 7 Schematic view of free running model test.

Table 2 Conditions in free running model test.

forward speed: U [m/s]	1.0 to 10.0
initial aft-draught: d_{a0} [m]	0.040
initial trim angle: τ_0 [deg]	0.0
height of center of pitch from base line (up +): KC [m]	0.123
longitudinal position of center of pitch from ss5.0 (aft +): L_{KC}[m]	0

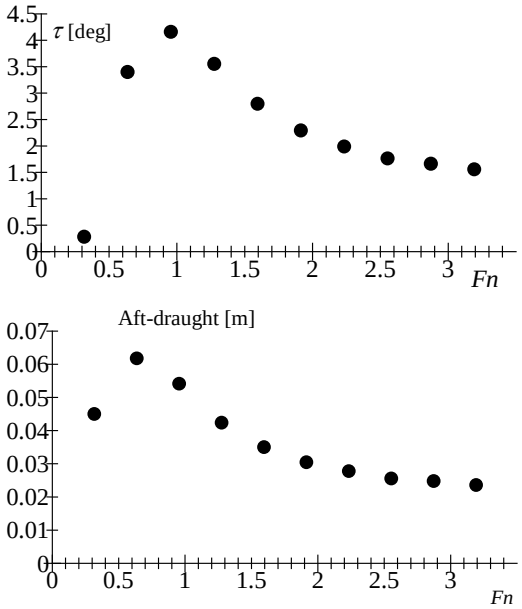

Fig. 8 Measured trim and aft-draught.

In this study, in order to obtain roll damping for the planing craft newly, a forced roll motion device is developed for the high-speed towing system of Osaka Prefecture University (Katayama et al., 2010) and the test was carried out with high forward speed. Fig. 9 and Fig. 10 show the forced roll device and the drawing of the test device.

In the measurement, the model is forced to roll periodically around an axis by sine swaying of the top of the center arm. When the sine swaying is expressed as,

$$y(t) = y_a \sin \omega t \qquad (16).$$

The periodic roll is obtained by the following equation,

$$\phi(t) = \sin^{-1} \frac{y(t)}{l} \approx \frac{y(t)}{l} = \frac{y_a}{l} \sin \omega t \qquad (17)$$

where y_a is sway amplitude, ω is the circular frequency of motion and l is shown in Fig.9. Under forced rolling, its roll motion and forced sway force are measured by synchronizing. Forced roll moment is obtained by the following equation.

$$M_T(t) = F(t) \times l \times \cos \phi(t) \qquad (18)$$

where $F(t)$ is measured sway force, $\phi(t)$ is measured roll motion. The uncoupled equation of motion to describe the forced roll motion in calm water can be written as,

$$(I_{44} + A_{44})\ddot{\phi} - B_{44}\dot{\phi} - C_{44}\phi = M_E \qquad (19)$$

where I_{44} donates the mass moment of inertia in the roll, A_{44} donates the added mass moment of inertia, B_{44} donates the roll damping coefficient, C_{44} donates the restoring moment coefficient, M_E donates the measured moment.
It can be determined by the total forced hydrodynamic roll moment using Fourier analysis which is written as follows,

$$(I_{44} + A_{44}) - \frac{C_{44}}{\omega^2} = \frac{2}{T\omega^2 \phi_a} \int_0^T M_E(t) \sin(\omega t) dt \qquad (20)$$

$$-B_{44} = \frac{2}{T\omega\phi_a} \int_0^T M_E(t) \cos(\omega t) dt \qquad (21)$$

where T is the roll period.

Moreover, the forced roll tests in the air is carried out and the moment is subtracted from the results with the draught at the same experimental condition, the forced roll hydrodynamic moment is obtained. The experimental conditions are shown in Table 3. In this experiment, the roll damping coefficient is measured not only at planing but also at semi-planing.

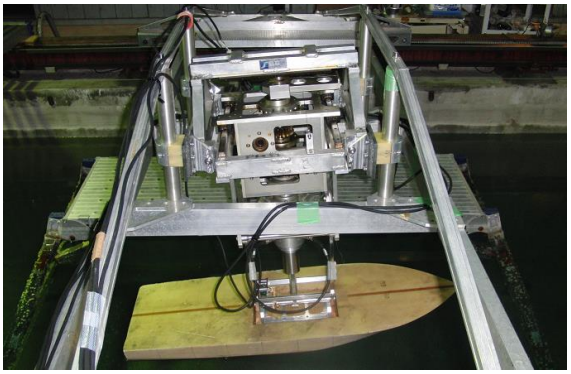

Fig. 9 Forced roll device and the model.

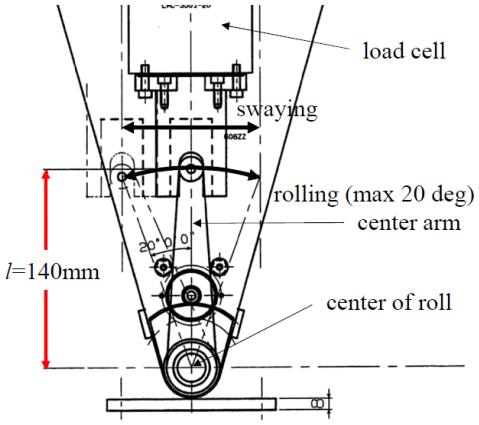

Fig. 10 Drawing of the forced roll test device.

Table 3 Conditions in the forced roll test at running attitude.

Froude number:Fn	0.9	2.2, 2.6	
trim angle:τ [deg]	4.0	1.5	2.0
aft draught:d_a [m]	0.055	0.023	0.027
roll amplitude:ϕ_a[deg]	3.0, 6.0, 9.0, 12.0, 15.0		
roll period:T [s]	1.0	0.6, 0.8, 1.0	

3.3 Results and discussions

Fig. 11 shows the effects of roll amplitude. In both of figures, measured roll damping coefficients at τ=2.0 deg do not change according to change in roll amplitude, but measured roll damping coefficients at τ=1.5 deg increase with increase in the roll amplitude. Since the roll damping component of the vertical lift has no effects of roll amplitude, it can be seen that the other components that have the effects of the roll amplitude increase.

Fig. 12 shows the effects of the roll frequency. Both the measured and the estimated roll damping coefficient are constant regardless of change in the roll frequency. Therefore, it can be said that the other component indicated previous paragraph do not have the effects of the roll frequency.

As the other components, the horizontal lift and the eddy making is supposed because the under water side projection area is increased according to decrease in the trim angle and they do not have the effects of the roll frequency and one of them has nonlinearity for the roll amplitude. Detailed investigations of this effects of the roll amplitude on roll damping are required and it is the future work.

Fig. 13 shows the effects of roll amplitude at semi-planing. The estimated roll damping coefficient is a good agreement with the measured. Both the measured and the estimated roll damping coefficient are constant regardless of change in roll the amplitude.

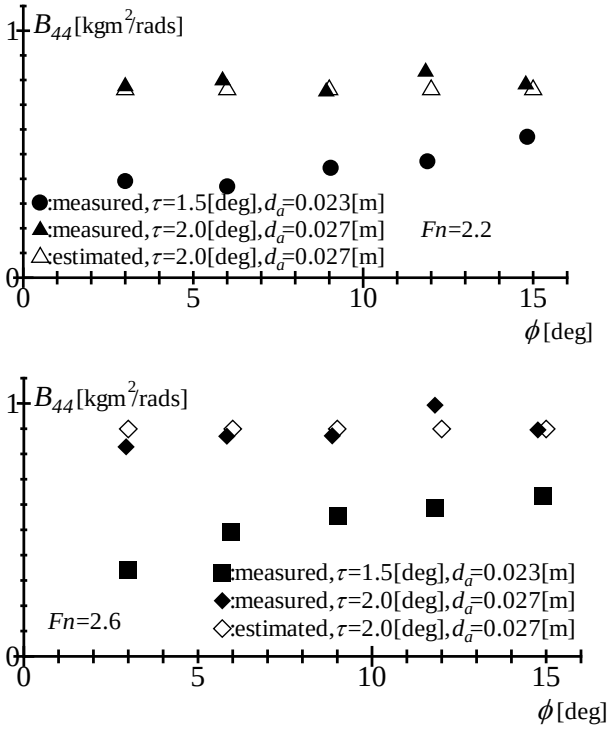

Fig. 11 Measured roll damping coefficients about the effects of the roll amplitude at T=1.0 s, Fn=2.2(upper), 2.6(lower).

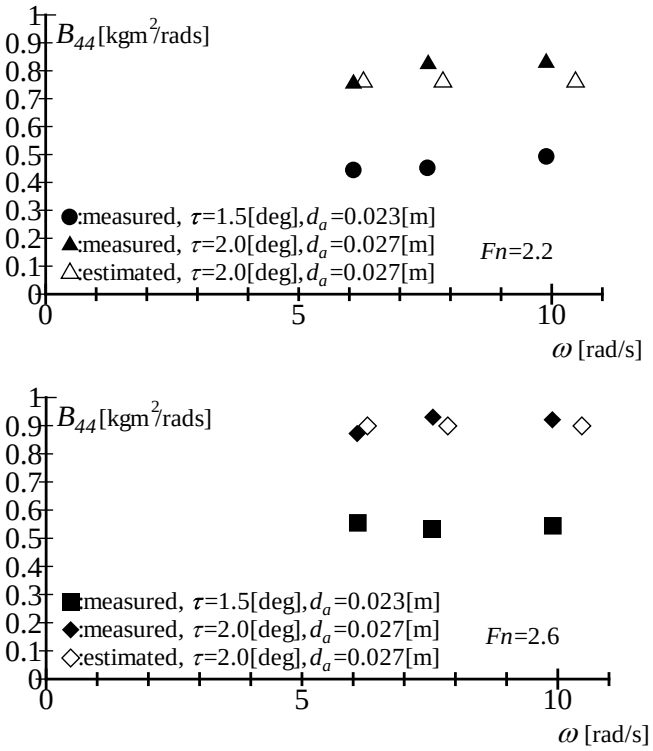

Fig. 12 Measured roll damping coefficients about the effects of the roll frequency at ϕ_a=9.0 deg, Fn=2.2(upper), 2.6(lower).

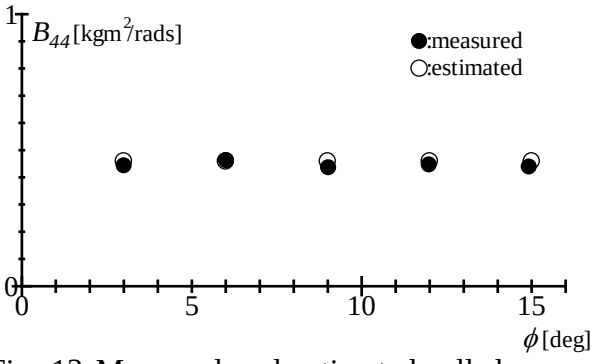

Fig. 13 Measured and estimated roll damping coefficients about the effects of the roll amplitude at T=1.0 s, τ=4.0 deg, d_a=0.055 m, Fn=0.9.

4. CONCULUSIONS

The roll damping of the high-speed planing craft is investigated and the following conclusions are obtained.

1. The estimation method of the vertical lift component of roll damping based on Payne's method is proposed
2. The effects of the roll amplitude, the roll period, and forward speed by this estimation method is investigated and estimated results is compared with measured results and its validity is confirmed.
3. The vertical lift component of the roll damping coefficient by proposed method does not have the effects of the roll amplitude. However, the effects of the roll amplitude on measured results appears when the trim angle becomes smaller than its general running trim angle.
4. In semi-planing, the effect of the roll amplitude is not observed.

5. REFERENCE

Ikeda, Y., Umeda, N., 1990, "A Prediction Method of Roll Damping a Hard-Chine Boat at Zero Forward Speed", Jour. of the Kansai Soc. of Naval Arch. Japan, No.213, pp.57-62.

Ikeda, Y., Umeda, N. and Tanaka, N., 1998, "Effect of Forward Speed on Roll Damping of a High-Speed Craft", Jour. of the Kansai Soc. of Naval Arch. Japan, No.208, pp.27-34.

Ikeda, Y., Katayama, T., 2000, "Roll Damping Prediction Method for a High-Speed Planing Craft", STAB, pp.1-16.

Ikeda, Y., Katayama, T., 2000, "Roll Damping Prediction Method for a High-Speed Planing Craft", STAB, pp.1-16.

Katayama, T., Taniguchi, T., Habara, K., 2010, "Tank Tests to estimate onset of Dynamic Instabilities of High-Speed Planing Craft", Transactions 2010, the Society of Naval Architects and Marine Engineers, pp.106-121.

Payne, Peter R., 1994, "Recent Developments in "Added-Mass" Planing Theory", Ocean Engineering, Vol.21, No.3, pp.257-309.

Savitsky, Daniel, 1964, "Hydrodynamic Design of Planing Hulls", Marine Technology, Vol.1, No.1, pp.71-95.

Smiley, Robert F., 1952, "A Theoretical and Experimental Investigation of the Effects of Yaw on Pressures, Forces, and moments during Seaplane Landing and Planing", NACA Technical Note 2817.

Wagner, H., 1932, "The Phenomena of Impact and Planing on Water", NACA translation 1366, ZAMM

APPENDIX CHECKING UNCERTAINTY OF FORCED ROLL TEST

In order to check the uncertainty of the test device, the measured data by forced roll test in the air is analyzed based on Eq.(A1) as the following.

$$\left(I_{44}+A_{44}\right)\phi_a\ \omega^2-C\phi_a=M_0\cos(\varepsilon) \quad \text{(A1)}$$

The roll moment of inertia is obtained from the following process. At first, the amplitude of roll moment related to roll angular acceleration or roll angle is obtained from Fourier Analysis written in Eq. (20).

Second, roll restoring moment is measured by inclining test at maximum roll angle with the same device. The amplitude of roll inertia moment is obtained from the amplitude of roll moment related to roll angular acceleration or roll angle by subtracting the roll restoring moment. Finally, roll inertia of moment is obtained by dividing the amplitude of roll inertia moment by the amplitude of roll angular acceleration. Table A1 shows the test condition and the results. The standard deviation of calibration is obtained by using least-square method. The difference between true value and mean value and the standard deviation to true value are small enough. Where true value is by calculated value because a weight whose density is constant, whose shape is known is placed at a known position.

Table A1 Conditions for checking uncertainty

Load cell	LMC-3501-20, KYOWA
Universal Recorder and Strain Measurement card	EDX-100 with CDV-40B, KYOWA
Potentiometer to measure roll motion	CPP-45 1kΩ, MIDORI PRECISIONS
Sampling frequency	100Hz
Low Pass Filter	30Hz
Range	500με
Calibration of the Load cell	
Weights [kg]	0.100, 0.200, 0.300, 0.500, 1.000, 1.500, 2.000
Calibration value of Load cell and its accuracy	Calibration value: 2.005×10^{-2} kg/με standard deviation: 9.994×10^{-4} kg/με
Calibration of potentiometer	
Roll angle [deg]	-23.0, -10.0, -5.0, 4.0, 9.0, 14.0, 19.0, 24.0
Calibration value of the potentiometer and its accuracy	Calibration value: 23.70 deg/V standard deviation: 3.679 deg/V
Forced roll test	
Roll amplitude, ϕ_a[deg]	3.2, 4.7, 6.3, 7.9, 9.5, 11.0, 12.4, 13.9, 15.5, 17.1
Roll period, T [s]	0.6
mean value, true value and standard deviation of measured results (true value: 5.664×10^{-3} kgm^2)	mean value: 5.613×10^{-3} kgm^2 standard deviation: 1.549×10^{-3} kgm^2

Dynamic Stability Analysis including Roll Motion in the Maneuvering Motion for a Damaged Surface Naval Vessel

Daehyuk, Kim, *Hyundai Heavy Industries* yaho@snu.ac.kr

Saeyong, Park, *Seoul National University* vexit@snu.ac.kr

Jongyeol, Park, *Seoul National University* hondea127@snu.ac.kr

Honggu, Yeo, *Seoul National University* hongnine@snu.ac.kr

Jeonghwa Seo, *Seoul National University* thamjang@snu.ac.kr

Shin Hyung, Rhee, *Seoul National University* shr@snu.ac.kr

ABSTRACT

The present study concerns a dynamic stability problem in ship maneuvering motion. A navy vessel, that is ONR Tumblehome, in damaged condition was employed. PMM tests were conducted to obtain hydrodynamic derivative terms for stability analysis based on maneuvering equations. Tests consist of static tests (static drift tests, static rudder tests, rudder drift tests) and dynamic tests (pure sway tests, pure yaw tests, yaw with drift tests). Because of the damaged condition, there was the biased term in all force and moment equations. Finally, dynamic stability was analyzed from the linearized equation and simulation results.

Keywords: *PMM(Planar Motion Mechanism), Damaged ship, Maneuvering, 4DOF, ONR tumblehome*

1. INTRODUCTION

Ship survivability after an accident is a critical issue in maritime safety. Survivability means the proper level of ability, i.e., damage control, stability and maneuverability with a damaged and flooded compartment or degraded ship performance. Maneuverability is the most important part. A vessel would have trouble to return to port safely if vessel can't keep maneuverability after the accident. Recently, the concept of survivability has been expanded to safe-return-to-port (SRtP), which refers to a ship's ability to continue operation for a brief period after an accident.

Especially SRtP problem in the case of naval vessels, it should focus on its maneuverability. As it can easily become the primary target of the attack, therefore, it must be able to avoid subsequent attacks from the enemy or terrorists and complete its mission or leave the battlefield.

To predict dynamic performances such as maneuverability of damaged naval ship is a complex problem. The dynamic performance of a ship in damage condition includes interaction with flooded water into the damaged compartment, thus few preliminary studies on damaged ship dynamics are available.

For naval vessels, requirements of stability and maneuverability in damage condition are more complicated than that of passenger ships. Generic naval vessels have a slender hull to

attain ability for missions, thus they are easy to lose transversal stability. In addition, the required level of maneuverability and seakeeping ability is higher than other non-combat vessels. The damaged naval vessel is vulnerable to enemy's attack, as a result, damaged naval vessel is easy to become the target of attack. Thus, it should be able to avoid successive attack from enemies and maintain its operation until escape from the battlefield.

The uniqueness of maneuverability of damaged naval vessel is the motivation of this study. A system-based method to estimate damaged ship maneuverability was developed from current method and studies on dynamics of damaged ships. A naval vessel with damaged compartment was designed based on regulations of survivability, and its maneuvering characteristics were examined by captive model tests and numerical simulations.

2. MANEUVERING MATHEMATICAL MODEL FOR DAMAGED VESSEL

2.1 Coordinate system

There are two different approaches to define the coordinate system of damaged ship: lost buoyancy and added weight approaches. The lost buoyancy method assumes although damaged compartment of ship flood, the hull only loses its buoyancy of the flooded compartment and the displacement, center of mass, and moment of inertia of the hull are unchanged. On the other hand, added weight method assumes the flooded water as the additional mass of the hull. As a result, the center of mass and moment of inertia should be obtained separately for the flooded condition. In this study, lost buoyancy method was adopted to analyze the ship motion in the damaged condition, for the convenience of model test setup and analysis.

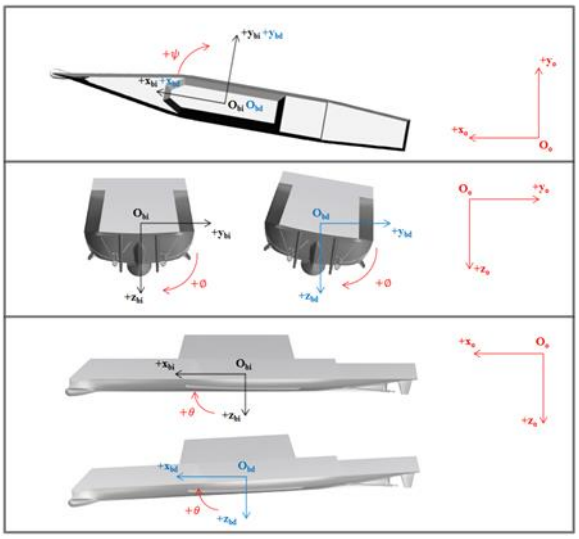

Figure 1 Body fixed the coordinate system in the intact and damaged conditions and the earth-fixed coordinate system

Figure 1 shows the coordinate system used in this study. The body-fixed coordinate system was defined as a right-handed coordinate system whose origin was located at the center of gravity of the hull. As lost buoyancy approach is used in this study, the center of gravity did not change due to the damage. Thus the origin of the body-fixed coordinate system was identical in the intact and damaged conditions. The x-axis and y-axis, however, were redefined to maintain parallel to the calm water surface plane, although the damaged hull had initial heel and trim.

2.2 Maneuvering mathematical model

In this study, the four degrees of freedom (4DOF) equations of motion, which consider surge, sway, roll, and yaw, were employed (see Eq. (1)). The right-hand side terms represent the hydrodynamic forces and moments acting on the whole ship according to Abkowitz's model (1980). Note that the forces and moments were treated as total ones acting on the whole ship and approximated by the third-order Taylor series expansions, rather than identifying them on the individual elements, i.e., hull, propeller, and rudder, and considering the interactions between them. In addition to Abkowitz's model where the terms affected by

asymmetry are eliminated in the equations of motion, the terms due to asymmetry were preserved to describe the asymmetric behavior of the ship while maneuvering. Those preserved terms were asymmetric and may not be differentiable at the origin, thus separately considered on the starboard and port sides, respectively.

$$
\begin{aligned}
m(\dot{u}-vr) &= X_0 + \begin{pmatrix} X_{w+}v_+^2 + X_{rr+}r_+^2 \\ X_{w-}v_-^2 + X_{rr-}r_-^2 \end{pmatrix} \\
&\quad + X_{vr}vr + X(\delta,u,v) \\
m(\dot{v}+ur) &= Y_0 + Y_{\dot{v}}\dot{v} + Y_{\dot{r}}\dot{r} \\
&\quad + \begin{pmatrix} Y_{v+}v_+ + Y_{vvv+}v_-^3 + Y_{r+}r_+ + Y_{rrr+}r_+^3 \\ Y_{v-}v_- + Y_{vvv+}v_+^3 + Y_{r+}r_+ + Y_{rrr+}r_+^3 \end{pmatrix} \\
&\quad + (Y_{vvr}v + Y_{vrr}r)vr + Y_{\phi}\phi + Y(\delta,u,v) \\
I_{xx}\dot{p} &= K_0 + K_{\dot{v}}\dot{v} + K_{\dot{r}}\dot{r} \\
&\quad + \begin{pmatrix} K_{v+}v_+ + K_{vvv+}v_-^3 + K_{r+}r_+ + K_{rrr+}r_+^3 \\ K_{v-}v_- + K_{vvv+}v_+^3 + K_{r+}r_+ + K_{rrr+}r_+^3 \end{pmatrix} \\
&\quad + (K_{vvr}v + K_{vrr}r)vr + K_{\phi}\phi + K_p p + K(\delta,u,v) \\
I_{zz}\dot{r} &= N_0 + N_{\dot{v}}\dot{v} + N_{\dot{r}}\dot{r} \\
&\quad + \begin{pmatrix} N_{v+}v_+ + N_{vvv+}v_-^3 + N_{r+}r_+ + N_{rrr+}r_+^3 \\ N_{v-}v_- + N_{vvv+}v_+^3 + N_{r+}r_+ + N_{rrr+}r_+^3 \end{pmatrix} \\
&\quad + (N_{vvr}v + N_{vrr}r)vr + N_{\phi}\phi + N(\delta,u,v)
\end{aligned}
\tag{1}
$$

The 4DOF motion variables (u, v, p, r) in the body-fixed coordinate system were transformed into position variables (x, y, φ, ψ) in the earth-fixed coordinate system using the following transformation matrix.

$$
\begin{bmatrix} \dot{x}_o \\ \dot{y}_o \\ \dot{\phi} \\ \dot{\psi} \end{bmatrix} = \begin{bmatrix} cos\psi & -sin\psi cos\phi & 0 & 0 \\ sin\psi & cos\psi cos\phi & 0 & 0 \\ 0 & 0 & 1 & 0 \\ 0 & 0 & 0 & cos\phi \end{bmatrix} \begin{bmatrix} u \\ v \\ p \\ r \end{bmatrix} \tag{2}
$$

3. EXPERIMENTAL SETUP

3.1 Test model

A scaled model of the hull, propellers, and rudders of ONR Tumblehome was used for the captive model tests and maneuvering simulations. The hull form has been used for many experimental and numerical studies on seakeeping and maneuverability of modern naval vessels (Araki et al., 2012; Sanada et al., 2013). Figure 2 shows the geometry of ONR Tumblehome model. It has design characteristics of a modern naval surface combatant, i.e., large sonar dome and bilge keels, twin-propellers and rudders, and a tumblehome superstructure.

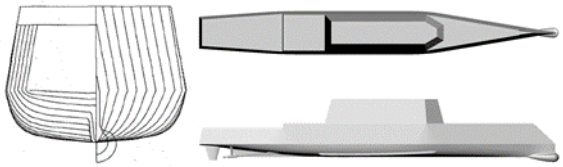

Figure 2 Geometry of ONR Tumblehome

The scale ratio of the model ship was 1/48.93, and its principal particulars are shown in Table 1. The test model, which is shown in Figure 3, was made of fiber-reinforced plastic. At station 19, an array of studs was attached for turbulence stimulation.

Table 1 Principal particulars of the model

Main Particulars		Model scale	Full scale
Length of waterline	L_{WL} (m)	3.147	154.0
Maximum beam of waterline	B_{WL} (m)	0.384	187.78
Draft	T (m)	0.112	5.494
Displacement	Δ	72.6 kg	8,507 ton
LCB	LCB aft of FP	1.625	NA
VGG (From Keel)	KG (m)	0.156	NA
Metacentric height	GM (m)	0.0422	NA
Moment of Inertia	K_{xx}/B	0.444	0.444
	K_{yy}/L_{WL}, K_{zz}/L_{WL}	0.246	0.25
Propeller diameter	D_P (m)	0.1066	NA

Figure 3 Photographs of the model ship used for testing (top) and its propellers and rudders (bottom)

The damaged compartment was determined by the US Navy regulations. Specification of regulations is shown in Table 2.

Table 2 Extent of damage in the United States Navy regulation

Waterline Length	Damage Extent
$L_{WL} < 30.5m$	The flooding of any compartment should not submerge beyond the margin line
$30.5m \le L_{WL} \le 91.5m$	Two flooded compartments
$L_{WL} > 91.5m$	Damage anywhere extending 15% of L_{WL} or 21 m, whichever is greater

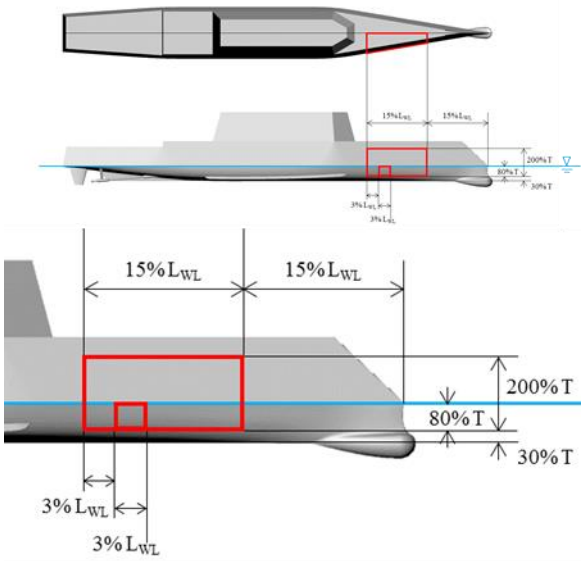

Figure 4 Extent and location of the damaged compartment for model ship

Figure 4 shows the extent and location of the damaged compartment. The length of a damaged compartment should be 15% of LWL, which corresponds to 23.1 m in the full scale and 0.472 m in the model. The width of the damaged compartment is set to be the lateral extent from the outmost bulkhead to the ship center line. The damage opening was assumed to be located below the waterline.

For ONRT in the full scale, LWL = 154 m, the longitudinal For captive model tests, a PMM device with maximum sway and yaw amplitudes of 0.45 m and 45°, respectively, was used. A six-axis load cell that can measure forces up to 500 N in the x-, y- and z-directions and moments up to 50 Nm in the x- and y-directions and 200 Nm in the z-direction was located at the center of mass of the test model. In the damaged condition, the ship's attitude was fixed at the initial heel and trim using a wedge.

Figure 5 shows the damage opening and top of the damaged compartment. The top of the damaged compartment was open to maintain atmosphere pressure in the compartment, as recommended by the ITTC (ITTC, 2017b). As the damage opening was located below the calm water surface, the air in the compartment was trapped and compressibility may affect the test results if the compartment did not have ventilation through the top.

Figure 5 Photographs of the damaged compartment

3.2 Test Facility and device

Model tests were carried out at the Seoul National University Towing Tank, which is 110 m in length, 8 m in width, and 3.5 m in depth. Figure 6 shows a schematic of the towing tank facility.

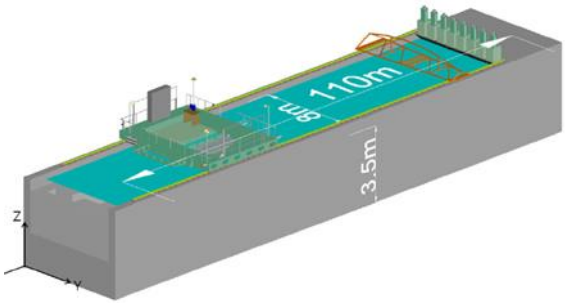

Figure 6 Schematic of Seoul National University Towing Tank

A towing carriage with a maximum speed of 5 m/s was set on the rails along the tank. The accuracy of towing speed was 0.78% of the input at the towing speed corresponding to Fn of 0.20.

3.3 Test conditions

Resistance, propeller open water (POW), and self-propulsion tests were conducted to identify the propeller revolution rate for the self-propulsion condition. Resistance and POW tests were conducted following the recommended procedure and guidelines of ITTC (ITTC, 2017c). In the POW test, the propeller revolution rate (n) was fixed to 16 rps, and the advance speed (u_o) was varied to achieve various advance ratio (J). The representative Reynolds number (Rn) at 0.7 R was 150,000.

Only the propeller revolution rate in the model scale was obtained from the self-propulsion tests, as the tests were intended to simulate maneuver in the model scale. For advance speed of captive model tests, Fn of 0.20 was chosen following previous maneuvering tests of the same vessel in the intact condition (Araki et al., 2012). Moreover, as this study considers a damaged ship, the tests were also conducted at a low advance speed, that is, Fn of 0.10.

Tables 3 and 4 show the model test conditions for the static and dynamic tests, respectively. To compare the results with those from the intact condition, non-coupled tests (static drift angle, pure sway, and pure yaw) were also conducted in the intact condition.

Table 3 Test conditions for the static tests

Test	Speed condition	Rudder angle	Drift angle
	Fn ($U/\sqrt{gL}$)	δ (deg.)	β (deg.)
Static drift	0.10, 0.20 (# 2)	-	-15° ~ +15° (# 15)
Static rudder	0.10, 0.20 (# 2)	-35° ~ +35° (# 15)	-
Rudder & drift	0.10, 0.20 (# 2)	-30° ~ +30° (# 6)	-15° ~ +15° (# 6)

Table 4 Test conditions for the dynamic tests

Test	Speed condition	Drift angle	Sway acc.	Yaw vel.
	Fn ($U/\sqrt{gL}$)	β (deg.)	$v_{dot}/(U^2/L)$	r/(U/L)
Pure sway	0.10, 0.20 (# 2)	-	0.02 ~ 0.47 (# 7)	-
Pure Yaw	0.10, 0.20 (# 2)	-	-	0.02 ~ 0.48 (# 7)
Yaw with drift	0.10, 0.20 (# 2)	-8° ~ +8° (#4)	-	0.08~0.31 (# 3)

4. MANEUVERING SIMULATION

4.1 Turning circle test

Turning circle maneuver simulation was performed in the intact and damaged conditions, and the results were compared with free-running test results (Sanada et al., 2013). The rudder deflection angle was 25° and Fn was 0.20. Figure 7 shows the simulation results. The turning circle diameter increased during starboard turning, because of the increased resistance and decreased advance speed.

Figure 8 and 9 show time histories of the ship speeds and the Euler angles from the turning circle maneuvering simulation. The ship speed decrease was larger during port turning, because of the water ingress/egress through the damage opening on the starboard side. In the damaged condition, the roll angle difference was smaller than that in the intact condition. Note that, however, the roll angles were much

smaller than those reported with the free-running model tests (Sanada et al., 2013).

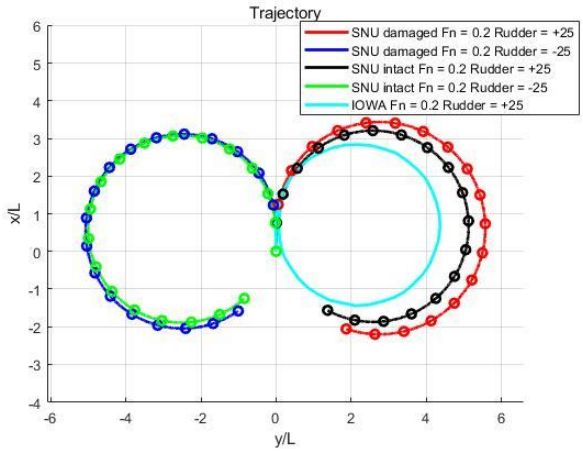

Figure7 Turning circle trajectories of maneuvering simulation and free-running tests

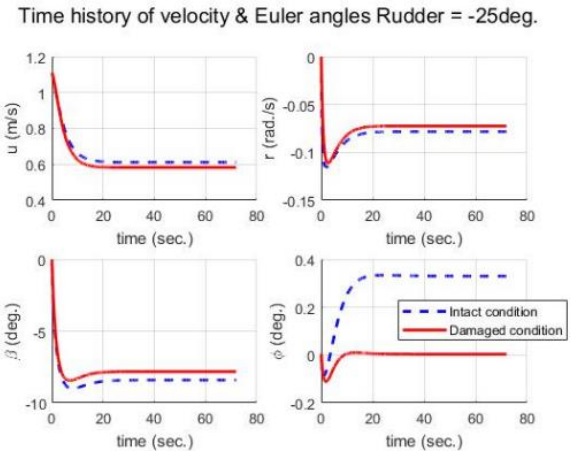

Figure 8 Time history of velocity and Euler angles in turning circle maneuvering simulation: port turning with δ of -25°

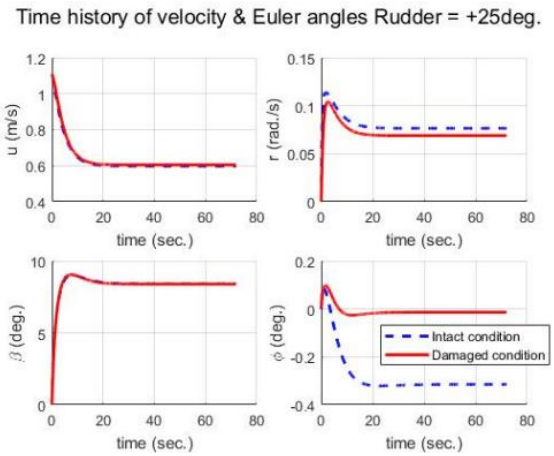

Figure 9 Time history of velocity and Euler angles in turning circle maneuvering simulation: starboard turning with δ of 25°

4.2 Zigzag test

Zigzag test simulations were performed at the rudder angles of -20°/+20° and Fn of 0.20. Figures 10 and 11 show the time histories of the rudder and heading angles of zigzag tests and the speeds and Euler angles, respectively. The rate of the rudder angle was based on the first order dynamics with a time constant of 0.3 s to reflect the operation of practical ships so the reactions of the hull appeared to have a slight time delay. The underestimation of the roll angle was also found in the zigzag test. The amplitude of the roll motion was 0.4°, while the maximum roll angle of 4° was reported in the free-running test of an intact model (Araki et al., 2012). In the zigzag maneuver, the roll motion reduces yaw checking ability, thus the underestimation of the roll motion resulted in short zigzag maneuvering periods, as reported in the comparisons of 4DOF mathematical model and free-running model tests (Araki et al., 2012).

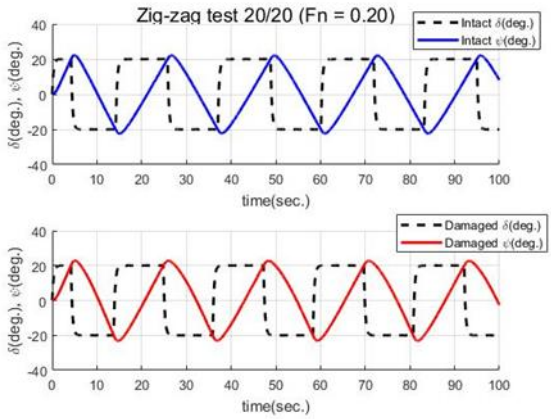

Figure 10 Time history of the rudder and heading angle of the zigzag test

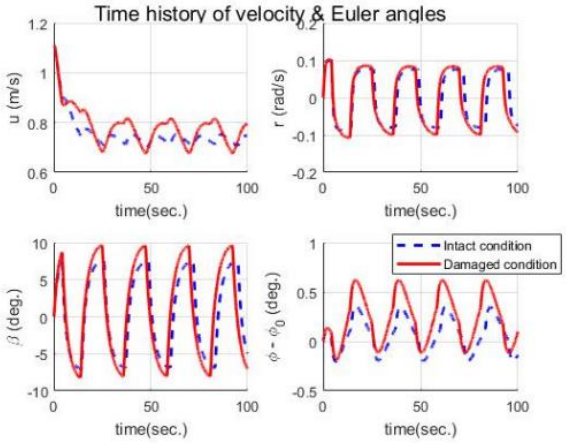

Figure 11 Time history of velocity and Euler angle of the zigzag test

5. CONCLUSION

In this study, we tested the use of a system-based method to assess the maneuverability of a damaged naval surface vessel. A conventional maneuvering mathematical model was reviewed and modified to take into account the asymmetry due to the initial flooding and attitude change of the damaged vessel. Then, captive model tests were conducted to obtain the maneuvering coefficients for the maneuvering mathematical model and maneuvering simulations were performed. A tumblehome ship model was used for these tests and its damaged compartment was designed based on current survivability regulations. The flooding was assumed to cause an initial heel and trim, and the dynamics of the damaged ship were analyzed via the lost-buoyancy approach.

The maneuvering simulations and free running test results didn't match well. In maneuvering simulation with the intact condition, the diameter of turning circle was bigger than a free running test. Also turning showed that roll motion of the model ship was smaller which is about 3degree in free running tests. As a result, results of maneuvering simulation with the damaged condition also unreliable. In other words, maneuvering simulation based on captive model tests has a limit to estimate a hydrodynamic characteristic of a real phenomenon.

In summary, the present study showed good agreement with the free-running model tests, but still contained disparity in terms of roll motion. By modifying and improving the maneuvering mathematical model, such disparity could be resolved.

6. ACKNOWLEDGMENTS

This research was supported by the IT R&D program of MOTIE/KEIT (Grant No. 100660329), National Research Council of Science & Technology (CMP-16-03-KISTI), grant by the Korea government, U.S. Office of Naval Research (ONR) and ONR Global as part of the Naval International Cooperative Opportunities in Science and Technology Program (NICOP) under the supervisions of Drs. Thomas Fu and Woei-Min Lin.

7. REFERENCES

Abkowitz, M. A., 1980 "Measurement of Hydrodynamic Characteristics from Ship Maneuvering Trials by System Identification. Society of Naval Architects and Marine Engineers, Jersey City, NJ.

Araki, M., Sadat-Hosseini, H., Sanada, Y., Tanimoto, K., Umeda, N. and Stern, F., 2012, "Estimating Maneuvering Coefficients Using

System Identification Methods with Experimental, System-based, and CFD Free-running Trial Data," Ocean Engineering, Vol. 51, pp. 63-84.

International Towing Tank Conference, 2017a, "Captive model test," ITTC Recommended procedures and Guidelines, 7.5-02-06-02, Lyngby, Denmark.

International Towing Tank Conference, 2017b "Model Tests on Damage Stability in Waves," ITTC Recommended procedures and Guidelines, 7.5-02-07-04.2, Lyngby, Denmark.

International Towing Tank Conference, 2017c "Propulsion / Bollard Pull Test," ITTC Recommended procedures and Guidelines, 7.5-02-03-01.1, Lyngby, Denmark.

Sanada, Y., Tanimoto, K., Takagi, K., Gui, L., Toda, Y., and Stern, F., 2013, "Trajectories for ONR Tumblehome Maneuvering in Calm Water and Waves." Ocean Engineering, Vol. 72, pp. 45-65.

A Solid Bulk Cargo-Sea-Ship Problem：Cargo Liquefaction

Lei Ju, Harbin Engineering University, Harbin, China, julei@hrbeu.edu.cn

Dracos Vassalos, Maritime Safety Research Centre, University of Strathclyde, Glasgow, UK,

d.vassalos@strath.ac.uk

Chunyang Wang, Harbin Engineering University, Harbin, China, wangchunyang007@foxmail.com

ABSTRACT

Recent problems with liquefied cargoes leading to serious loss of life are attracting attention by the international community. The liquefaction of mineral ores can result in cargo displacement and loss of ship stability, which has been a major cause of marine casualties. In the paper, the DEM liquefaction model is presented to capture the characteristics of the cargo from initial state to liquefied state. The interaction between cargo shift and the response of the 2D rectangular structure in regular waves is addressed. A parametric investigation is undertaken to identify the key parameters that trigger cargo liquefaction.

Keywords: *Solid bulk cargo; Cargo instabilities; Discrete element method*

1. INTRODUCTION

Over the past few years, the risk of cargo liquefaction on ship safety has risen sharply. The ship's motion and the engine vibration during passage may cause particle re-arrangement and compaction. The gaps between the particles become smaller in the process, with the corresponding pore pressure progressively increasing. As a result, the water holding ability of particles and the friction coefficient between cargoes decreases. In particular, the water in the interstellar spaces comes together to form a liquid layer that allows the cargo above to move relative to the cargo below — as if the two layers were part of a liquid, and hence the term 'liquefaction'. Such a transition during ocean carriage can cause a sudden loss of stability of the carrying vessel. In the last ten years, more than ten ships capsized and sank due to a loss of hull stability attributed to the cargo liquefaction (Ju et al., 2017; Ju et al., 2013). Especially, "STELLAR DAISY" and "EMERALD STAR" capsized due to cargo liquefaction in 2017. The above tragic accident is not the only one of its kind and unfortunately, it will not be the last unless immediate and comprehensive action is taken by the industry.

To address the granular material liquefaction phenomena, experimental works have been conducted by researchers. Liquefaction of granular materials in a rectangular container has also been experimentally investigated (Koromila et al., 2013). The experiments indicate that homogeneous cargo loading can lead to substantial loss of stability after cargo liquefaction. Even at small dynamic stresses on particles with sufficient periods of vibration, the cargoes will lose effective stress and reach a state of failure (Unno et al., 2006; Ju et al., 2016).

Most of the methods for liquefaction are based on the effective stress model to establish a constitutive equation. This lacks the study of discrete characteristics of cargo flow. Cargoes like iron ore and nickel ore behave like soils. Thus, the DEM modelling approach is widely used in the solid bulk cargo analysis (Spandonidis et al., 2013; Spandonidis et al., 2016; Ju et al., 2017; Ju et al., 2018).

The particles interact with each other and also, with the ship hold in waves in a comprehensive manner, which is a cargo-sea-ship problem and cannot be investigated separately. With this in mind, a simulation approach based on an adapter that couples a DEM code and a CFD code is applied to identify the key parameters that trigger cargo liquefaction. This approach will provide a better understanding of the coupled interaction between solid bulk cargoes and ship vessels, which could possibly support a suitable regulatory framework for assessing the ship stability so that decision making during the design, loading and transport could be effective to avoid the ship capsize and casualties.

2. NUMERICAL MODELS

Prediction for ship response in waves due to cargo liquefaction needs to address two problems simultaneously including 1) Liquefaction and particle movement; 2) Ship response in waves.

The commercial software, Particle Flow Code (PFC) is based on DEM, which simulates the movement of granular particles and the interaction between particles. Some assumptions are specified before using the DEM to address the liquefaction problem: 1) In PFC, particles are assumed to be spheres. If one sphere is regarded as one particle of the cargo, it is difficult to initialize the hypothetical porosity of particles, the size distribution and monitor the pore water pressure. Therefore, each sphere is regarded as a hypothetical assembler of particles, including many solid particles, water and air; 2) The radius of the particle can be scaled with the elastic-plastic strain to change the size at the end of every time-step according to the stress on the particles based on the UBCSAND model; 3) Various friction coefficients can be used to represent various moisture contents. Based on the assumptions above, the DEM liquefaction model can predict the cargo flow, deformation, and liquefaction phenomenon. Some validations are presented in the following section. However, the interaction between water, air and solid skeleton are neglected, which may decrease the accuracy of the prediction.

To predict the ship response in waves due to cargo shift, the regular wave is generated using the paddle wave generating method based on ANSYS Fluent software. Navier-Stokes equation, Volume of Fluid (VOF) method and dynamic meshing method are solved to establish a two-dimensional wave tank with a wave-absorbing method employed to absorb the wave energy. An adapter coupling ANSYS Fluent and PFC is developed to simulate the interaction between cargo movement and ship motion, which allows transferring data during the coupled calculations without any changes in the source of the simulation code.

2.1 Contact Force and Stress

The force acting on each sphere due to interaction with all its neighbouring particles is calculated based on the Rolling Resistance Linear Model (PFC help manual). The internal force and moment (F_c and M_c) act at the contact location in an equal and opposite sense on the two pieces.

$$F_c = F^l + F^d, \qquad M_c = M_r \tag{1}$$

The dynamic stress of each particle is defined. For granular assemblies in a dynamic regime, a definition of a mean stress tensor is more disputable. A consistent definition must involve not only contact forces between particles, but also inertia effects of grains subjected to dynamic effects (Fortin et al., 2003). Stress is defined as follows (François Nicot, 2013):

$$\langle\sigma_{ij}\rangle = \frac{1}{V}\sum_{c=1}^{N_c} f_i^c l_j^c + \frac{1}{3V}\sum_{p\in V}\left(\varepsilon_{ijk}M_k^p\right) + \frac{1}{3V}\sum_{p\in V} J_p\left((\Omega^p)^2\delta_{ij} - \Omega_i^p\Omega_j^p\right) \tag{2}$$

V: the representative elementary volume (REV)

f_i^c: the contact reaction force

l_j^c: the branch vector joining the centre of the particles in contact

ε_{ijk}: the Levi-Civita symbol
M_k^p: the moment imbalance for particle 'p'
J_p: the moment of inertia for particle 'p'
Ω^p: the angular velocity for particle 'p'

2.2 Elastic-plastic Strain

According to the dynamic stress calculated above, the elastic-plastic strain of each particle can be obtained based on UBCSAND model (Ju et al, 2016). The elastic behavior, which occurs within the yield surface, is controlled by two parameters expressed in terms of the elastic bulk modulus K_B^e and the elastic shear modulus k_G^e as shown below:

$$K_B^e = k_B^e P_A (\frac{p'}{P_A})^{me} \quad K_G^e = k_G^e P_A (\frac{p'}{P_A})^{ne} \quad (3)$$

p' : the mean effective stress
P_A : the reference stress (usually equal to 100kPa)
k_B^e: the bulk modulus numbers
k_G^e: the shear modulus numbers
me: the elastic exponent
ne : the shear exponent

The plastic behavior which occurs outside the yield surface is controlled by the hardening rule, given as:

$$dsin\phi_{mob} = 1.5K_G^p \left(\frac{p}{P_A}\right)^{np} \frac{P_A}{P_m} (1 - \frac{sin\phi_{mob}}{sin\phi_{peak}} R_f)^2 d\lambda \quad (4)$$

$d\lambda$: the plastic strain increment multiplier
np: the plastic shear modulus exponent
ϕ_{mob}: the mobilized friction angle, which is defined by the stress ratio
ϕ_{peak}: the peak friction angle
R_f: the failure ratio n_f/n_{ult}, ranging from 0.5 to 1.0

2.3 Soil Water Characteristic Curve

SWCC is the basis for estimating the dynamic analysis of unsaturated soils. The most common model to describe the hydraulic behavior of unsaturated soils is the model of Van Genuchten relationship (Galavi et al., 2010). Van Genuchten function is a three-parameter equation and relates the saturation to the suction pore pressure head $\emptyset_p$.

$$S(\phi_p) = S_{res} + (S_{sat} - S_{res})[1 + (g_a|\phi_p|)^{g_n}]^{g_c} \quad (5)$$

$$\phi_p = -p_w/(\rho_w * g) \quad (6)$$

S_{res}: the residual saturation which describes the part of water that remains in soil even at high suction heads
S_{sat}: the saturation when the pores are filled with water

With the elastic-plastic strain of each particle, the development of the degree of saturation can be updated. With an increasing degree of saturation, the contact properties (friction coefficient) will be identified. The corresponding friction coefficient will be set on the contact pieces. Since (ship) cargo liquefaction will go through a longer-term process during carriage, the pore water pressure can be calculated according to the Soil Water Characteristic Curve (SWCC), which relates to the water content or degree of saturation to pore water pressure.

Table 1 Coupled Model Input Parameters.

	Symbol	Description
Deformation parameters	$\varphi_p(\circ)$	Peak friction angle
	$\varphi_{cv}(\circ)$	Constant volume friction angle
	k_B^e	Elastic bulk modulus
	k_G^e	Elastic shear modulus
	k_G^p	Plastic shear modulus
	me, ne	Elastic bulk, shear modulus index
	np	Plastic shear modulus index
	R_f	Failure ratio
	P_A	Atmospheric pressure
Hydraulic parameters	g_a, g_n, g_c	Empirical parameters
	n_{sat}	Saturation when the pores are filled with water
	n_{res}	Residual saturation when the part of water remains at high suction heads
	MC	Initial moisture content
	Poro_initial	Initial porosity
Contact model parameters	*emod*	Effective modulus
	kratio	Stiffness ratio
	fric	Friction coefficient
	rfic	Rolling resistance coefficient
	dp_nratio	Normal critical damping ratio
	dp_sratio	Shear critical damping ratio
	dpmod	Dashpot mode

2.4 Model Input Parameters

The model input parameters include three parts: deformation parameters, hydraulic parameters, and contact model parameters, as shown in Tab. 1. According to contact force and moment, the particle movement will be updated according to Newton's second law. During the same time step, in calculating the stress on the particles, the strain of particles will be identified based on the UBCSAND model. With the development of the degree of saturation, the pore water pressure and contact model parameter, particularly the friction coefficient at various moisture contents (degree of saturation), will be updated. Therefore, cargo displacement due to cargo liquefaction can be regarded in a holistic manner which can offer the unique capability to model the liquefaction problem.

3. CONTACT PROPERTIES

The moisture content of a cargo is vitally important to transportation safety. As a matter of fact, the cargo in nature contains certain moisture more or less and it is the moisture that leads to cargo shift, which results in a large angle of heel, although the moisture in the cargo is not visibly wet in appearance. ClassNK conducted the laboratory experiment that the behavior of the nickel ore stored in the container was observed by inclining the container statically up to the maximum inclined angle of 50 degrees (Fig. 1). At low moisture content (MC), nickel ore shows great inertia. Along with the increasing of MC, nickel ore begins to show the characters of fluid. According to the assumption above, MC of the cargo is described by correspondent friction coefficient. The static incline test is simulated by PFC2d software to identify the contact properties of nickel ore at various MC (Fig. 1). With the quantitative comparison of numerical results with experimental data, by changing the friction coefficient of the particle, the state of the cargo inside the container is compared with the experimental data from ClassNK to identify the relation between the friction coefficient and MC.It can be seen that the granular particle flow shows a good agreement with nickel ore flow.

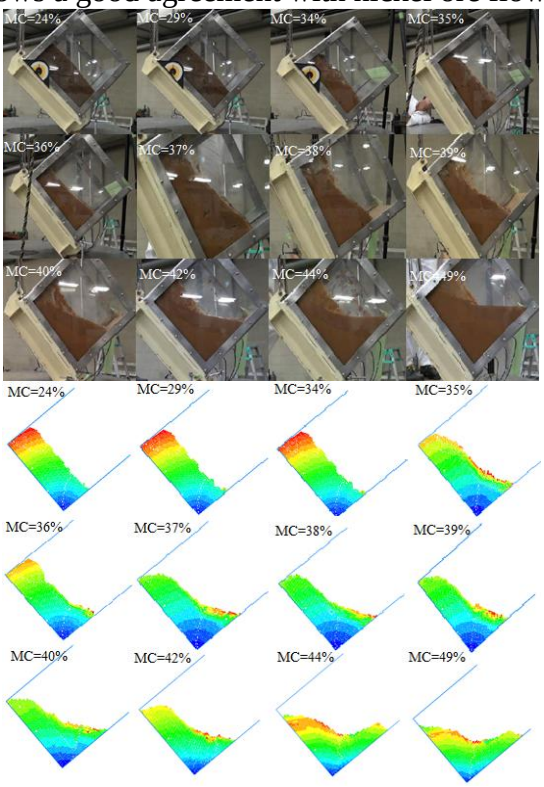

Figure 1 Appearance of nickel ore sample (ClassNK, 2011) and granular particles inclined at 50° (Blue color reflects that displacement of the particle is small during incling).

4. NUMERICAL VALIDATION

4.1 Simple Shear Test

Cuomo Sabatina (2016) conducted simple shear tests on the unsaturated soil and saturated soil. The soil specific gravity (Gs) is equal to 2.55. Two experimental tests with saturated condition and unsaturated condition were conducted, as shown in Tab. 2.

Table 2 Experimental tests for simple shear.

condition	Test	e	$\sigma_v', \sigma - u_a$ (kPa)
Saturated	CL	2.02	76
Unaturated	CL	1.66	100

CL=Constant vertical Load; e is void ratio; σ' is the vertical effective stress

Table 3 Coupled model input parameters for shear test.

Parameters	Symbol	Saturated soil (Simple shear)	Unsaturated soil (Simple Shear)	saturated soil (Cyclic Shear)	Liquefaction (a)
Deformation parameters	$\varphi_p(\circ)$	34.7	34.8	33	33
	$\varphi_{cv}(\circ)$	32	32	32	32
	k_B^e	5e8	5e10	1e5	5e5
	k_G^e	0.25e8	0.25e10	1e5	1e5
	k_G^p	5e8	5e10	5e4	1e5
	me, ne, np	0.5	0.5	0.5	0.5
	R_f	0.7-0.98	0.7-0.98	0.7-0.98	0.98
	P_A	76kPa	100kPa	100kPa	100kPa
Hydraulic parameters	g_a, g_n, g_c	0.5, 1.23, -0.624	0.5, 1.23, -0.624	5.0, 2.0, -1.0	5.0, 2.0, -1.0
	n_{sat}	0.721	0.721	1.0	1.0
	n_{res}	0.337	0.337	0.0	0.0
	MC(%)	51.9	51.9	100	50
	Poro_initial	0.668	0.624	0.5	0.5
Contact model parameters	emod	1e5	1e5	1e5	1e5
	kratio	2.0	2.0	2.0	2.0
	fric	0.8	0.99	0.005	0.8
	rfic	0.8	0.99	0.02	0.6
	dp_nratio	0.2	0.2	0.2	0.2
	dp_sratio	0.2	0.2	0.2	0.2
	dpmod	3	3	3	3

In the simple shear test, spin velocity is 0.01*L (m/s), L is the length of the shearing specimen. and the samples in PFC are shown in Fig. 2. The model parameters used in the simulation are given in Tab. 3. As shown in Fig. 3, when shearing to a certain extent, the specimens lose shear strength, which causes destruction. The simulation data shows good agreement with experimental data.

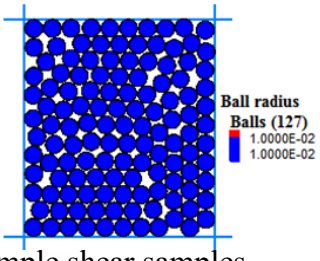

Figure 2 Simple shear samples.

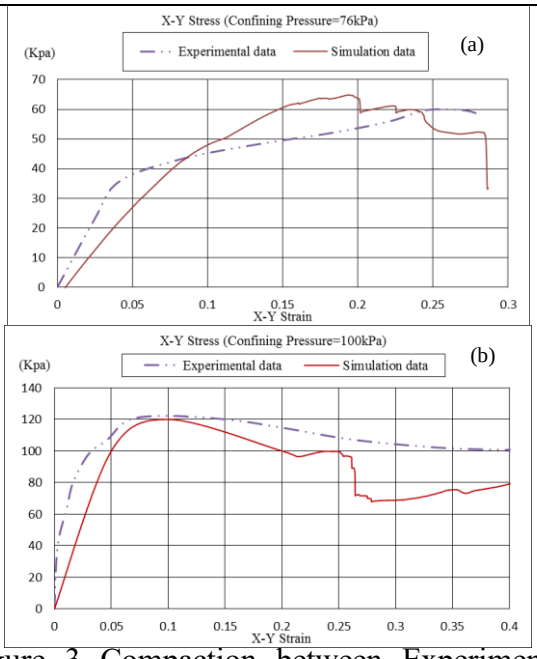

Figure 3 Compaction between Experimental results and simulation results. Simple Shear: (a) Saturated soil; (b) Unsaturated soil.

4.2 Cyclic Shear Test

The model parameters used in cyclic shear test are given in Tab. 3. Fig. 4 presents the typical stress path and stress-strain response for a simulation with cyclic stress ratio (CSR=shear stress/vertical effective stress) of 0.08 and vertical effective stress of 100 kPa. A gradual drop of vertical effective stress is observed from an initial value of 100 kPa with the application of cyclic shear until it reaches σ'_{vc}, a value of about 50kPa followed by a sudden overall drop of σ'_{vc} during the last two cycles. This is associated with the development of relatively large shear strains during the last two cycles of loading. Based on the DEM liquefaction model, at a constant of confining pressure (100kPa) and initial degree of saturation of 100%, specimen gradually is sheared and the effective stress decreases. When the shear modulus decreases to some extent, the shear strain suddenly becomes obvious, especially at the last several shearing cycles, which is similar to the experiment phenomenon, indicating shear failure. Compared to the experimental results, this further shows that the modelling approach presented in the paper is suitable for addressing the cyclic behavior of the specimen, and the liquefaction behavior of cargoes.

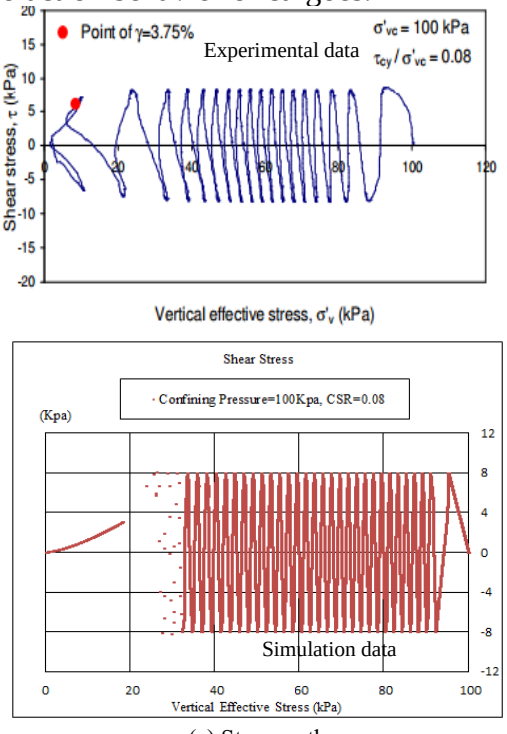

(a) Stress path

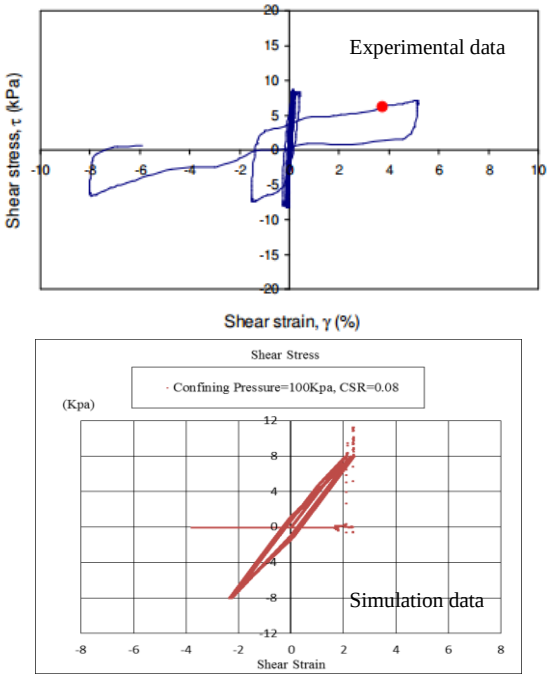

(b) shear stress-strain response

Figure 4 Results from cyclic laboratory DSS testing of Fraser River sand for CSR (τ/σ') of 0.08 (Wijewickreme et al. 2005).

5. LIQUEFACTION TEST

5.1. Hypothetical Property of A Cargo

Given a hypothetical property of a cargo (see Tab. 3), we can identify what factors such as amplitude, frequency or moisture trigger cargo liquefaction. During the carriage, the cargoes may experience compaction. Although the moisture content does not change, the degree of saturation increases during the compaction. Therefore, according to the relation between moisture content and degree of saturation, the friction coefficient related to DoS is calculated.

$$\mathrm{DoS} = \mathrm{MC} * \mathrm{r(s)}/(\mathrm{e} * \mathrm{r(w)})$$

$$n=e/(1+e)$$

DoS: degree of saturation
MC: moisture content
r(s): unit weight of the particle
r(w): unit weight of water
n: porosity
e: void ratio

In fact, when the degree of saturation increases, the friction coefficient and rolling

friction coefficient decrease. Therefore, the relation of friction coefficient to the degree of saturation should be identified by the experimental approach before the assessment of cargo liquefaction. Two fitting equations are presented to describe the relation between the friction coefficient and rolling friction coefficient and the degree of saturation according to the simulation data and the equation above from ClassNK, which can be implemented into the DEM liquefaction model.

$$fric = \begin{cases} 0.9 & (0 \le DoS \le 48\%) \\ 0.8 & (48\% \le DoS \le 69\%) \\ 599492 * e\text{^}(-18.95 * DoS) & (69\% \le DoS \le 100\%) \end{cases}$$

$$rfric = \begin{cases} 0.6 & (0 \le DoS \le 71\%) \\ -8.0 * DoS + 6.45 & (71\% \le DoS \le 80\%) \\ 0.02 & (80\% \le DoS \le 100\%) \end{cases}$$

fric: friction coefficient
rfric: rolling friction coefficient

5.2 Time Domain Analysis

The Hexapod tests conducted by consulting firm MARIN of Australia (TWG, 2013) as shown in Fig. 5, which showed that at high moisture contents, cracks will occur in the cargo surface. Free surface apparent in the corners of the ship hold can be shaped after shaking.

Figure 5 Iron ore piles before and after a sea state test (TWG report, 2013).

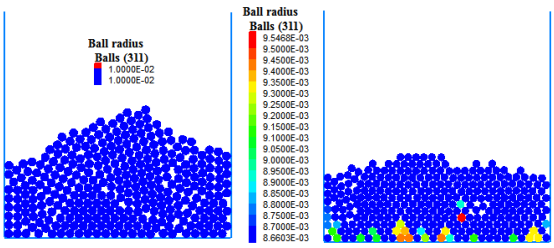

Figure 6 Iron ore piles before and after roll motion.

The DEM liquefaction model is used to simulate the whole process of liquefaction in a 2D rectangular structure (0.2m*0.2m) as shown in Fig. 6. As seen from the simulation results and compared with Fig. 5, this model used in the paper can fully describe the liquefaction phenomenon from the initial state to liquefied state.

Roll oscillation of a 2D rectangular structure (0.2m*0.2m) with an amplitude of 0.3rad and frequency of 1HZ is investigated to identify the influence of the structure motion on cargo shift, especially to address the liquefaction phenomenon. From Fig. 7 shown below, the cargoes close to the wall are liquefied first (small size). When cargoes liquefy, they have enough space to move, resulting in more severe collisions. As seen in Fig. 8, taking one ball with ID 106 in consideration, the degree of saturation increases to 100% from an initial degree of 50% at 20s. At 50s, the liquefied percent reaches 100%, which means all of particles liquefy. The fluctuation force due to cargo shift on the container increases suddenly.

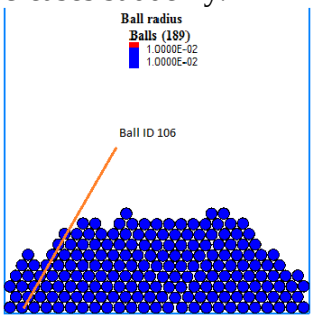

(a) Initial state of pile

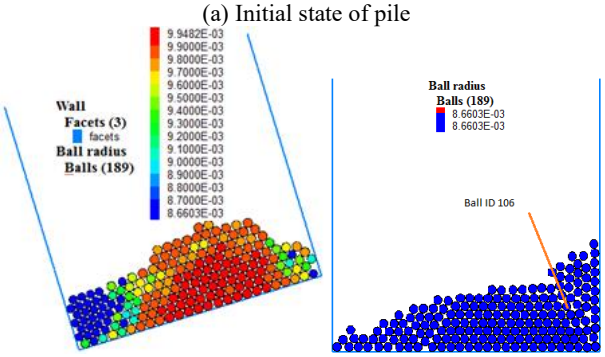

(b) Partial liquefied state (c) Full liquefied state

Figure 7 Liquefaction process in roll motion.

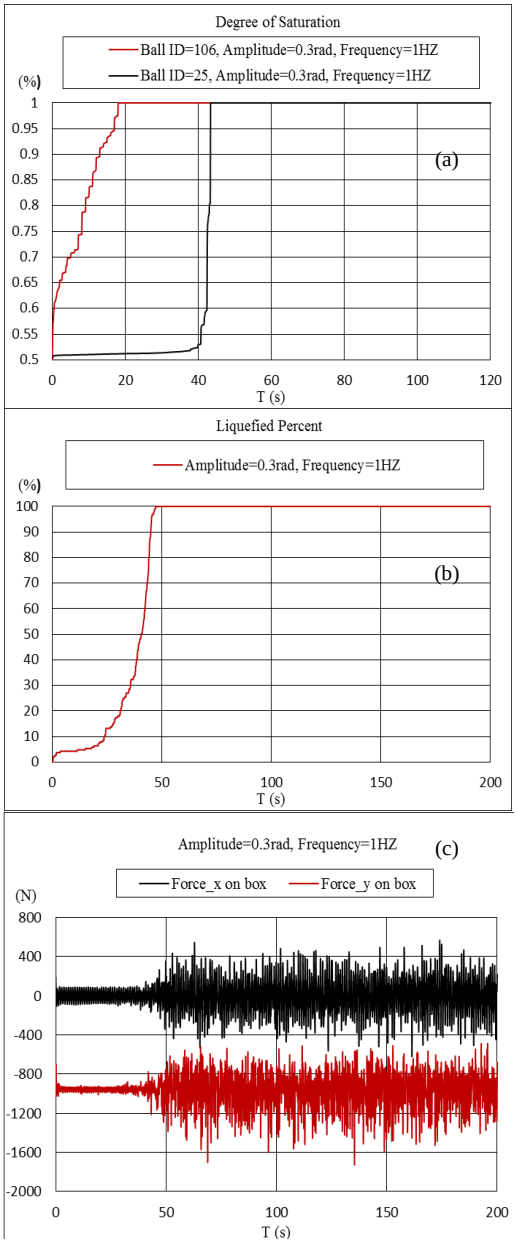

Figure 8 Development of (a) degree of saturation (ball id =106, 25), (b) liquefied percent, and (c) fluctuation forces on container.

6. PARAMETRIC INVESTIGATION

A parametric investigation is undertaken to identify the key parameters that trigger cargo and ship instabilities. On the XY plane appears 726 particles with the density of 1642.865kg/m3 and the radius of 0.002m. Two cases are carried out for the purpose of determining the effect of shifting cargo on the structure. The first is to change the moisture content of the cargo with the wave amplitude fixed at 0.02 m and the frequency at 6.75 rad/s (case 1). The second is to change the wave frequency with moisture content fixed at 49% and amplitude at 0.02m (case 2). The key findings are as follows:

Case 1: The maximum roll angle of the structure is approximately 18°at the moisture content level of 49%, which shows that the cargo has a high probability to flow with higher initial MCs (Fig. 9). The development of the roll angle at the MC level of 37% and the MC level of 40% is almost the same. This means that the roll motion of the structure is not affected by the displacement of the cargo containing low moisture content; Case 2: For the structure itself, the resonant frequency is 6.75rad/s. Therefore, for the wave frequency above or below the resonant frequency, the response of the structure is not obvious (Fig. 10). Especially for the wave frequency values of 5.93 rad/s, the peak roll angle is no more than 5°.

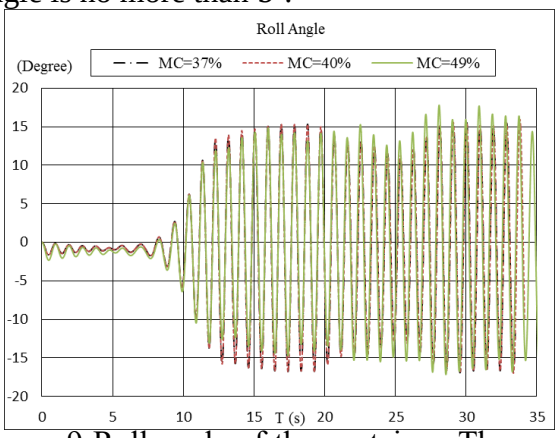

Figure 9 Roll angle of the container. The wave apmlitude is 0.02m, the frequency is 6.753rad/s and the MC is varied as 37%, 40% and 49% .

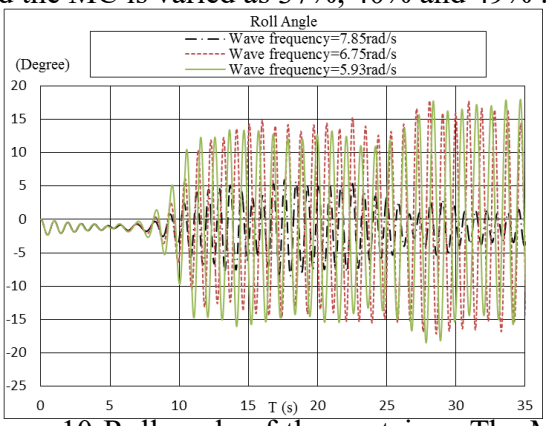

Figure 10 Roll angle of the container. The MC is 49%, the wave amplitude is 0.02m and the wave frequency is varied as 7.85rad/s, 6.75rad/s and 5.93rad/s (right).

Based on the parametric investigation above, the UBCSAND liquefaction model is activated to investigate the coupled simulation of 2D rectangular structure motion and cargo shift exposed to regular waves (Tab. 4). Two cases are tested using this method. The initial degree of saturation of the cargo is 50% and the validation properties of the cargo in Tab. 3 will be used.

Table 4 Parameters of linear wave for liquefaction.

T (s)	ω (rad/s)	λ (m)	H (m)
0.93	6.76	1.35	0.027
0.93	6.76	1.35	0.04

As shown in Fig. 11a, When the calculation time reaches 10s, the wave spreads to the container, causing the container to roll. The roll angle of the 2D structure shows irregularity as to the interaction between cargo shift and ship motion in waves. The roll angle of the container ranges from -10° to 10° with wave height of 0.04m, while the roll angle of the container ranges from -5° to 10° with wave height of 0.027m. This means that cargoes move to one side of the container and create a large moment to resist the righting moment of the container — resulting in a small heel. As we can see from Fig. 11b, when the wave height is 0.027m, the liquefied percentage reaches 90% at 25s. When the wave height is 0.4m, the liquefied percentage reaches 90% at 20s, which indicates that the external energy input has a great influence on cargo liquefaction. When cargoes liquefies completely (100% liquefied percentage), the moment due to cargo shift shows a fluctuation around a fixed value of 0.8N.m and the roll angle fluctuates around a value of 2.5°. However, for the wave height of 0.04m, the fluctuation of the roll angle is close to the balance point of 0°. This can be explained by how energy input like waves will accelerate the liquefaction most definitely, but not always decrease the stability of the ship. Therefore, it can be concluded that energy input has a great influence on liquefaction and is proportional to the liquefaction rate. But, as for the ship stability, this depends on a combination which includes cargo shift and the ship response in waves.

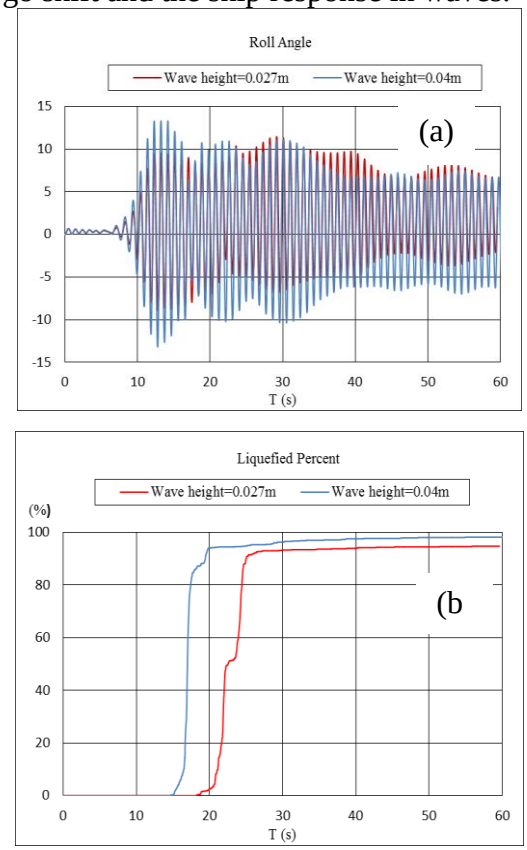

Figure 11 Development of (a) roll angle; (b) liquefied percent versus wave height

7. CONCLUSIONS

A DEM liquefaction model was developed to address the liquefaction phenomenon. The DEM combined with the UBCSABND model can effectively capture the cyclic shear behavior, liquefaction phenomena. Based on the assumptions, the validations were carried out to confirm the accuracy of the DEM liquefaction model. Time domain analysis of cargo liquefaction was conducted to identify the evolution of the degree of saturation of each particle, liquefied percentage for all particles, liquefaction zone and the fluctuation forces on the ship hold. The response of a 2D container in waves due to cargo shift, to address the liquefaction phenomenon, has been simulated by the method developed. The method provides a better understanding of the liquefaction phenomenon, identification, and quantification of the controlling parameters.

8. ACKNOWLEDMENTS

This work was supported by the National Key Research and Development Program of China [2016YFE0202700], and the National Natural Science Foundation of China (NSFC) [Grant Nos. 51639004, 51579054], and the Fundamental Research Funds for the Central Universities [HEUCFM180111].

9. REFERENCES

Cuomo S., Moscariello M. and Foresta V., 2016. Simple shear test son unsaturated soils. Procedia Engineering, 158, 122-127.

ClassNK, 2011. Guidelines for the Safe Carriage of Nickel Ore.

Fortin J., Millet O. and Saxcé G. de., 2003. Construction of an averaged stress tensor for a granular medium. European Journal of Mechanics A/Solids, 22, 567–582.

François Nicot, Nejib Hadda, Mohamed Guessasma, Jerome Fortin and Olivier Millet, 2013. On the definition of the stress tensor in granular media. International Journal of Solids and Structures, 50, 2508–2517.

Galavi V., 2010. Groundwater flow, fully coupled flow deformation and undrained analyses in PLAXIS 2D and 3D. Internal report from PLAXIS BV.

Ju L., Xue Y. Z., Vassalos D., Liu Y. and Ni B.Y., 2017. Numerical investigation of rolling response of a 2D rectangular hold, partially filled with moist bulk cargo. Ocean Eng. 142, 348–362.

Ju L., Vassalos D. and Jin W., 2013. Rolling motion of Newtonian and non-Newtonian fluids in a ship hold. 5th International Maritime Conference on Design for Safety.

Ju, L., Vassalos, D. and Boulougouris, E., 2016. Numerical assessment of cargo liquefaction potential. Ocean Eng. 120, 383–388.

Ju L., Vassalos D., Wang Q., Wang Y. K. and Liu Y., 2018. Numerical investigation of solid bulk cargo liquefaction, Ocean Eng. 159, 333-347.

Koromila, I.A., Spandonidis, C.C. and Spyrou, K.J., 2013. Experimental investigation of cargo liquefaction and impact on the stability of a bulk – carrier. Proc. 13th Int. Ship Stability Workshop.

PFC Help Manual, 2016, ITASCA Consulting Group, Inc.

Spandonidis C.C. and Spyrou K.J., 2013. Micro-scale modeling of excited granular ship cargos: A numerical approach. Ocean Engineering, 74, 22–36.

Spandonidis C.C. and Spyrou, K.J., 2016. Coupled vessel-dry-granular-cargo roll dynamics in regular beam seas. Ocean Engineering, 120, 238-245.

TWG report, 2013. Iron Ore Technical Working Group Submission for Evaluation and Verification

Unno T., Kazama M., Sento N. and Uzuoka R., 2006. Cyclic shear behavior of unsaturated volcanic sandy soil under various suction conditions. The 4th International Conference on Unsaturated Soils, ASCE.

Wijewickreme, D., Sriskandakumar, S. and Byrne, P., 2005. Cyclic loading response of loose air-pluviated Fraser River sand for validation of numerical models simulating centrifuge tests. Canadian Geotechnical Journal, 42:2, 550-561.

Local stability and bifurcation analysis of the softening Duffing equation by numerical computation

Yuu Miino, *Tokushima University*, c501647001@tokushima-u.ac.jp

Tetsushi Ueta, *Tokushima University*, ueta@tokushima-u.ac.jp

Hiroshi Kawakami, *Tokushima University*, h.kawakami@384.jp

Atsuo Maki, *Osaka University*, maki@naoe.eng.osaka-u.ac.jp

Naoya Umeda, *Osaka University*, umeda@naoe.eng.osaka-u.ac.jp

ABSTRACT

In the field of ship stability, the softening Duffing equation is used for the ship capsizing problem. However, most of the researches for this system have used the approximation methods. In this paper, we investigate this system by using the legacy numerical methods. We define the proper Poincaré map to analyze the system and confirm the general definitions of the asymptotic stability, the stable and unstable manifolds, and the local and global bifurcations. Finally, we calculate the 2-dimensional bifurcation diagram of the system and observe the changes of the basin of attraction in the state space.

Keywords: *the softening Duffing equation, numerical computation, local stability, local bifurcation, global bifurcation*

1. INTRODUCTION

In the research field of ship stability, so far, the softening Duffing equation has been utilized because of its similarity to the ship roll equation of motion in beam seas (e.g. Virgin (1987)). This system is very simple but as the hardening Duffing system is, the certain parameter combination generates the chaotic behavior (e.g. Nayfeh and Sanchez (1988); Kan and Taguchi (1991)). However, as pointed out by Kan and Taguchi, this chaotic behavior is not actually remarkable in softening system comparing with the hardening system. On the other hand, after heteroclinic bifurcation, fractal metamorphoses can be observed on the safe basin boundary (e.g. Kan and Taguchi (1990, 1991)). This starting point of the safe basin corrosion can be considered as one of the bifurcation stages to ship catastrophic capsizing. Therefore, a lot of researchers has shown the results on the heteroclinic point existing in this system by using the approximation method such as Melnikov's method (e.g. Kan and Taguchi (1990, 1991); Falzarano et al. (1992); Spyrou et al. (2002); Wu and McCue (2008); Maki et al. (2010, 2014)). The equation dealt with here is a 2nd order ordinary differential equation about ship roll motion in beam seas and corresponds to a nonlinear non-autonomous dynamical system. It is difficult to analytically solve this system since the system is a nonlinear system; therefore, the approximation methods have been utilized for obtaining the local bifurcation parameter set (e.g., Nayfeh and Sanchez (1989); Maki et al. (ared)). However, most of the relating researches have used the approximation method such as the perturbation technique, the av-

eraging method, the harmonic balance and so on; and there are few studies researching the characteristics of the system by using the numerical method, as is mentioned by Kawakami (1984) or Yoshinaga et al. (1997). Thus, we try to analyze the softening Duffing equation by the numerical method. We evaluate the local stability of the solution orbit by adopting the traditional method for the nonlinear systems. We define the proper Poincare map of the solution orbit and derive the variational equation. We introduce the characteristic equation whose characteristic multipliers imply the occurrence of the local bifurcation phenomena; and we suggest the method to compute the parameter set raising the local bifurcation. We explain the topological structure of stable and unstable manifolds that can cause the global bifurcation phenomena: homoclinic bifurcation or heteroclinic bifurcation; and we also suggest the method to obtain the parameter set raising the global bifurcation. Finally, we reveal the bifurcation diagram calculated by the proposed method and consider the relationship between the capsizing and the bifurcations.

2. SYSTEM DESCRIPTION

Let us consider the softening Duffing equation described by

$$\frac{d^2x}{dt^2} + k\frac{dx}{dt} + x - x^3 = B_0 + B\cos\Omega t, \quad (1)$$

where, $t \in \boldsymbol{R}$ is the time, $x \in \boldsymbol{R}$ is the state variable, and k, B_0, B and Ω are the parameters. x and y correspond to the roll angle of the ship and its angular velocity. In this study, assume that $k > 0$. We rewrite the system (1) into two first-order differential equations by defining a new variable $y := dx/dt$:

$$\begin{aligned} \frac{dx}{dt} &= y, \\ \frac{dy}{dt} &= -ky - x + x^3 + B_0 + B\cos\Omega t. \end{aligned} \quad (2)$$

We use vector notation $\boldsymbol{x} := (x, y) \in \boldsymbol{R}^2$ below. Let $\boldsymbol{\varphi}(t, \boldsymbol{x})$ be the solution of the system (2)

$$\boldsymbol{\varphi}(t, \boldsymbol{x}) := \boldsymbol{x}(t), \quad \boldsymbol{x}_0 := \boldsymbol{\varphi}(0, \boldsymbol{x}) = \boldsymbol{x}(0). \quad (3)$$

The solution satisfying

$$\boldsymbol{x}(t + L) = \boldsymbol{x}(t), \quad {}^{\forall}t \in \boldsymbol{R}, \quad (4)$$

is called a periodic orbit with period L.

3. PERIODIC ORBIT AND ITS ASYMPTOTIC STABILITY

Let us define the Poincaré map which replaces the solution of the system (2) with a discrete map:

$$T : \boldsymbol{R}^2 \to \boldsymbol{R}^2; \quad \boldsymbol{x}_0 \mapsto \boldsymbol{x}(L_{\min}), \quad (5)$$

where $L_{\min}$ is a minimum value of L and, in this case, is defined as $2\pi/\Omega$ which corresponds to the period of $\cos\Omega t$ in dy/dt. $\boldsymbol{x}^*$ is called a fixed point of T if it satisfies

$$T(\boldsymbol{x}^*) = \boldsymbol{x}^*, \quad (6)$$

and $\boldsymbol{x}^*$ is called an l-periodic point of T if it satisfies

$$T^l(\boldsymbol{x}^*) = \boldsymbol{x}^*, \quad (7)$$

where l is called the period of $\boldsymbol{x}^*$. Fixed and l-periodic points of T correspond to the periodic orbits of the system (2). In this study, a periodic orbit corresponding to an l-periodic point is called an l-periodic orbit. The asymptotic stability of a periodic orbit is in accord with the asymptotic stability of a corresponding to periodic point.

The variational equation of the Poincaré map about $\boldsymbol{x}^*$ is

$$\boldsymbol{\xi}_{i+1} = DT(\boldsymbol{x}^*)\boldsymbol{\xi}_i, \quad (8)$$

where

$$DT(\boldsymbol{x}^*) := \frac{\partial T}{\partial \boldsymbol{x}_0}(\boldsymbol{x}^*). \quad (9)$$

The characteristic multipliers $DT(\boldsymbol{x}^*)$ measure the asymptotic stability of $\boldsymbol{x}^*$. We obtain two multipliers from $DT(\boldsymbol{x}^*)$ since its dimension is two; let us label them as μ_1 and

μ_2 and assume $\mu_1 < \mu_2$. If all multipliers of $DT(\boldsymbol{x}^*)$ have absolute values less than unity, $\boldsymbol{x}^*$ is asymptotically stable (we label it ${}_0D^l$). If any multipliers of $DT(\boldsymbol{x}^*)$ have absolute values more than unity, $\boldsymbol{x}^*$ is unstable. Moreover, we can classify the unstable periodic points into three types based on the multipliers. If $-1 < \mu_1 < 1 < \mu_2$, $\boldsymbol{x}^*$ is directly unstable (we label it ${}_1D^l$). If $\mu_1 < -1 < \mu_2 < 1$, $\boldsymbol{x}^*$ is inversely unstable (we label it ${}_1I^l$). If $|\mu_1| > 1, |\mu_2| > 1$, $\boldsymbol{x}^*$ is completely unstable (we label it ${}_2D^l$). Subscript of each symbol shows the number of the unstable dimensions of $\boldsymbol{x}^*$. From the Liouville's formula, the system (2) cannot show ${}_2D^l$ if $k > 0$.

4. BIFURCATION PHENOMENA

4.1 LOCAL BIFURCATIONS

For the fixed point and periodic point, their asymptotic stability might change if we perturb some parameters. This kind of changes is called local bifurcation altogether (e.g., Kawakami (1984)). The multipliers satisfy $^{\exists}i$, $|\mu_i| = 1$ when the local bifurcation arises. There are three types of local bifurcations: tangent, period-doubling and Neimark-Sacker bifurcation, they occur with $\mu = 1$, $\mu = -1$ and $\mu = e^{i\theta}$, respectively. In a two-dimensional system, Neimark-Sacker bifurcation arises together with the completely unstable solution, however, the system (2) cannot generate it if $k > 0$ from the Liouville's formula. Thus, the system (2) cannot arise Neimark-Sacker bifurcation. In this paper, we use the symbols G^l and I^l to express the bifurcation sets of tangent and period-doubling bifurcation, respectively.

4.2 GLOBAL BIFURCATIONS

For a fixed point $\boldsymbol{x}^*$, there exist two T-invariant curves $\alpha(\boldsymbol{x}^*)$ and $\omega(\boldsymbol{x}^*)$, they are, at $\boldsymbol{x}^*$, tangent to the eigenvectors of μ_1 and μ_2. These curves are called unstable and stable manifolds and we also call them α-branch and ω-branch, respectively. If $\boldsymbol{x}^*$ is directly unstable, these branches are defined as

$$\begin{aligned} \alpha(\boldsymbol{x}^*) &:= \left\{ \boldsymbol{x} \in \boldsymbol{R}^2 \mid \lim_{k\to\infty} T^{-k}(\boldsymbol{x}) = \boldsymbol{x}^* \right\}, \\ \omega(\boldsymbol{x}^*) &:= \left\{ \boldsymbol{x} \in \boldsymbol{R}^2 \mid \lim_{k\to\infty} T^{k}(\boldsymbol{x}) = \boldsymbol{x}^* \right\}. \end{aligned} \tag{10}$$

Assuming that P and Q are saddles, $\alpha(P)$ and $\omega(Q)$ intersect each other in some cases. These intersections are called doubly asymptotic point. The point is also called a homoclinic point if P and Q are identical, and if not, the point is also called a heteroclinic point. The appearance and disappearance of the doubly asymptotic point are well known as the bifurcation phenomenon, which is called a global bifurcation. The bifurcation which generates the homoclinic point is called homoclinic bifurcation and the bifurcation which generates the heteroclinic point is called heteroclinic bifurcation. For global bifurcation analysis, we use the method mentioned by Yoshinaga et al. (1997), whose method computes the bifurcation parameter set by using Newton's method.

5. RESULT OF ANALYSIS

In this section, we investigate the bifurcation set of the system (2) in B-B_0 plane. Let the parameters be $k = 0.05$, and $\Omega = 1$. We chose the value of the parameter k from the result of the experiment practiced by Kan and Taguchi (1990), which measured the parameter values by using a model ship. From another result by Kan and Taguchi (1991), we chose the large parameter range of B_0 and B for calculating a bifurcation diagram.. Figure 1 shows the bifurcation diagram in parameter plane B-B_0.

Near $B = B_0 = 0$, a stable 1-periodic orbit appears with a small amplitude, as shown in Fig. 2 (a). This orbit comes from the completely stable equilibrium point with $B = B_0 =$

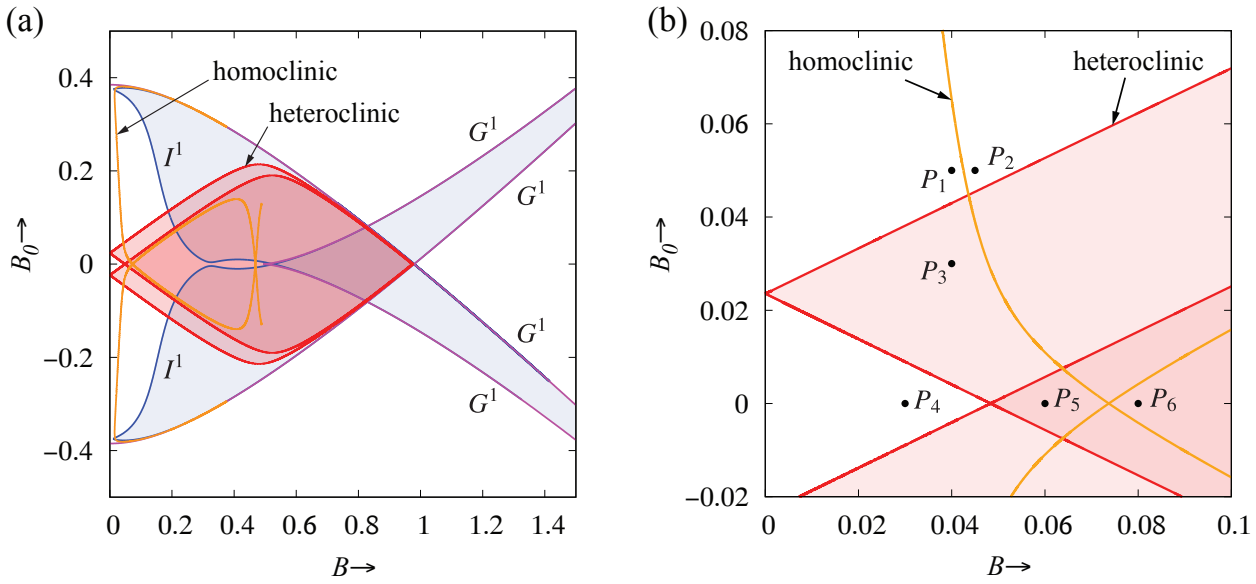

Figure 1: Bifurcation diagram of the system (2) in B-B_0 plane with $k = 0.05, \Omega = 1$. (a) $B \in [0 : 1.5]$ and $B_0 \in [-0.5 : 0.5]$, and (b) $B \in [0 : 0.1]$ and $B_0 \in [-0.02 : 0.02]$. The system (2) includes heteroclinic points if the parameters are in the red shaded region.

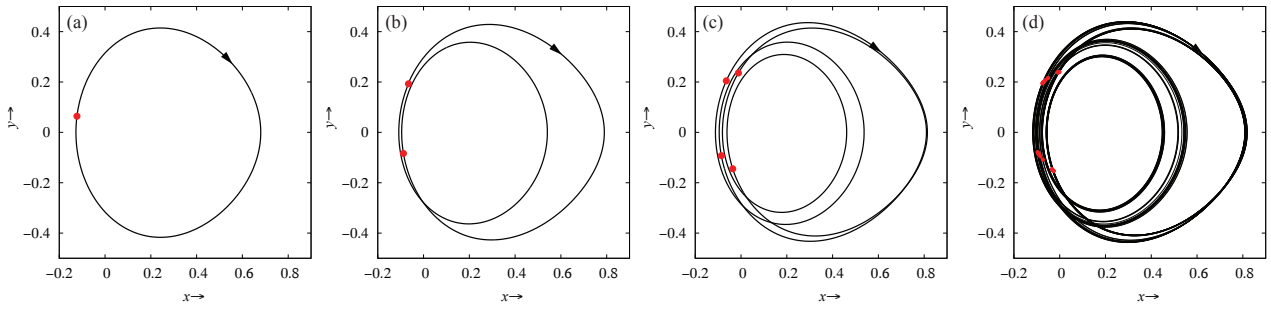

Figure 2: Phase portraits of the system (2) with $k = 0.05$, $\Omega = 1$, $B_0 = 0.2$, and (a) $B = 0.15$, (b) $B = 0.16$, (c) $B = 0.165$, (d) $B = 0.1655$. (Red points: Poincaré map.)

0, that is, the time-periodic function in dy/dt perturbs the equilibrium point and makes it a periodic orbit. This 1-periodic orbit becomes unstable by undergoing the period-doubling bifurcation I^1, and at the same time, stable 2-periodic orbit emerges, as shown in Fig. 2 (b). As B increases from here, the solution orbit takes the period-coubling cascade and finally gets chaotic, as shown in Fig. 2 (c)-(d). However, the system (2) rarely shows stable attractors if we choose the parameters in the region enclosed by I^1. This is because there exist homoclinic points in the region.

Orange and red curves in Fig. 1 labeled as homoclinic and heteroclinic are the homoclinic and the heteroclinic bifurcation sets. Setting the parameters in theses sets, the stable and unstable manifolds are tangent to each other, as shown in Fig. 3 (a) and (b). Figure 4 shows the basin boundary before and after the global bifurcations arise. Between the points P_1 and P_2, there is a homoclinic bifurcation set. Undergoing this bifurcation, the basin boundary gets a little fuzzy, as shown in the windows labeled as P_1 and P_2 in Fig. 4. On the other hand, between the points P_1 and P_3, there is a heteroclinic bifurcation set. Comparing with the case of P_1, the basin boundary with P_3 also gets fuzzy and slightly changes its shape. As a remarkable change, the black region stretches to the

upper left. This is because the stable manifold of a ${}_1D_1^1$ stretches to the upper left under the influence of the occurrence of the heteroclinic bifurcation, as shown in the window labeled as P_3 in Fig. 5. In other words, this bifurcation breaks the basin boundary. For the points P_4, P_5, and P_6, the similar phenomena arise. Setting the parameters at the point P_4, there are no doubly asymptotic points in the state space. Conversely, setting the parameters at the point P_5, there exist many heteroclinic points; and the basin of attraction with this parameter is eroded, as shown in the window labeled as P_5 in Fig. 4.

In the red shaded region enclosed by the heteroclinic bifurcation set, the calculation to obtain the homoclinic bifurcation set suddenly stop at some points. The potential reason of this stopping is that the unstable degree of the saddle ${}_1D_0^1$ or ${}_1D_1^1$ becomes too large.

6. CONCLUSION

We have investigated the softening Duffing equation by using the legacy numerical methods. We have defined the proper Poincaré map to analyze the system and have confirmed the general definitions of the asymptotic stability, the stable and unstable manifolds, and the local and global bifurcations. We have mentioned the previous method to solve the bifurcation problem that mainly based on Newton's method. We have finally calculated the 2-dimensional bifurcation diagram of the system and have observed the changes of the basin of attraction in the state space. For the future work, we should consider the method to avoid the suddenly stop of the numerical computation.

7. References

Falzarano, J. M., Shaw, S. W., and Troesch, A. W., 1992. Application of global methods for analyzing dynamical systems to ship rolling motion and capsizing. *International Journal of Bifurcation and Chaos*, 2(01):101–115.

Kan, M. and Taguchi, H., 1990. Capsizing of a ship in quatering seas (part 2-chaos and fractal in capsizing phenomenon). *Journal of the Japan Society of Naval Architects and Ocean Engineers*, 168:211–220.

Kan, M. and Taguchi, H., 1991. Capsizing of a ship in quartering seas-part 3 chaos and fractal in asymmetric capsise equation. *Journal of the Japan Society of Naval Architects and Ocean Engineers*, 169:1–13.

Kawakami, H., 1984. Bifurcation of periodic responses in forced dynamic nonlinear circuits: Computation of bifurcation values of the system parameters. *IEEE Transactions on circuits and systems*, 31(3):248–260.

Maki, A., Umeda, N., and Ueta, T., 2010. Melnikov integral formula for beam sea roll motion utilizing a non-hamiltonian exact heteroclinic orbit. *Journal of marine science and technology*, 15(1):102–106.

Maki, A., Umeda, N., and Ueta, T., 2014. Melnikov integral formula for beam sea roll motion utilizing a non-hamiltonian exact heteroclinic orbit: analytic extension and numerical validation. *Journal of Marine Science and Technology*, 19(3):257–264.

Maki, A., Virgin, L. N., Umeda, N., Ueta, T., Miino, Y., and Kawakami, H. (to be prepared). On the loss of stability of periodic oscillations and its relevance to ship capsize.

Nayfeh, A. and Sanchez, N., 1988. Chaos and dynamic instability in the rolling motion of ships. In *Symposium on Naval Hydrodynamics, 17th*, pages 617–630.

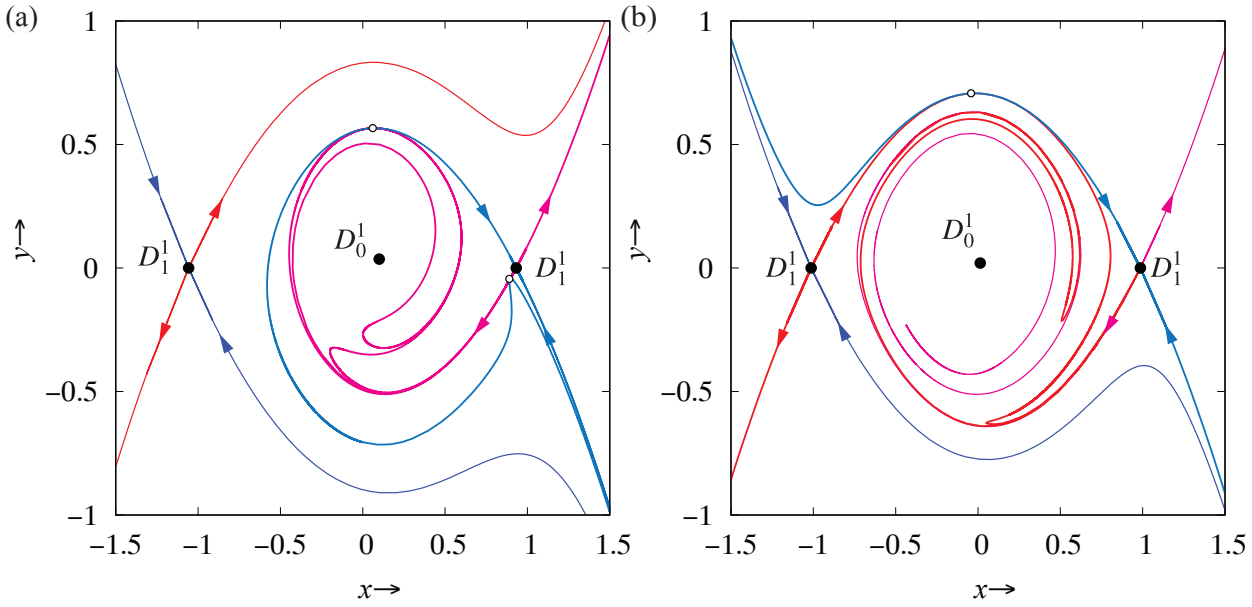

Figure 3: Stable and unstable manifolds of (a) the homoclinic tangency with $B_0 = 0.1$ and $B = 0.035825$, and (b) the heteroclinic tangency with $B_0 = 0.013817$ and $B = 0.02$.

Nayfeh, A. H. and Sanchez, N. E., 1989. Bifurcations in a forced softening duffing oscillator. *International Journal of Non-Linear Mechanics*, 24(6):483–497.

Spyrou, K., Cotton, B., and Gurd, B., 2002. Analytical expressions of capsize boundary for a ship with roll bias in beam waves. *Journal of ship research*, 46(3):167–174.

Virgin, L., 1987. The nonlinear rolling response of a vessel including chaotic motions leading to capsize in regular seas. *Applied Ocean Research*, 9(2):89–95.

Wu, W. and McCue, L., 2008. Application of the extended melnikov's method for single-degree-of-freedom vessel roll motion. *Ocean Engineering*, 35(17-18):1739–1746.

Yoshinaga, T., Kitajima, H., Kawakami, H., and Mira, C., 1997. A method to calculate homoclinic points of a two-dimensional noninvertible map. *IEICE Trans. Fundamentals*, E80-A(9):1560–1566.

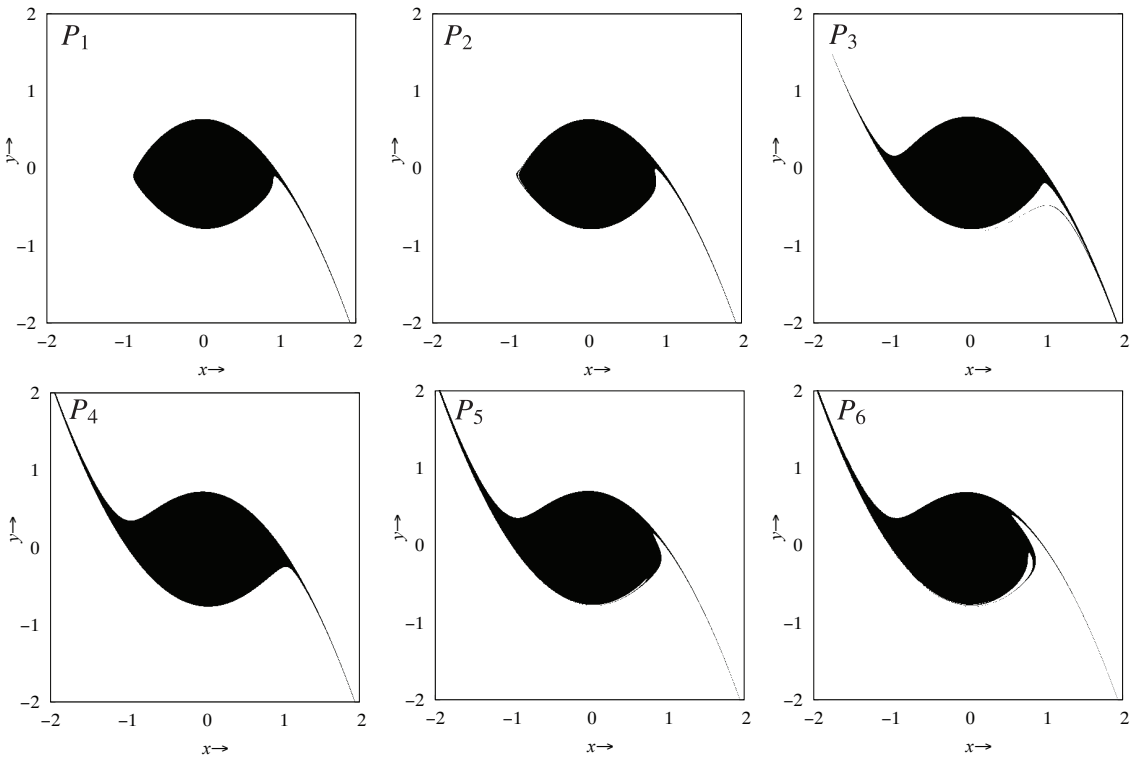

Figure 4: Basin of attraction in x-y plane with each parameter. (Black: not capsizing, white: capsizing.)

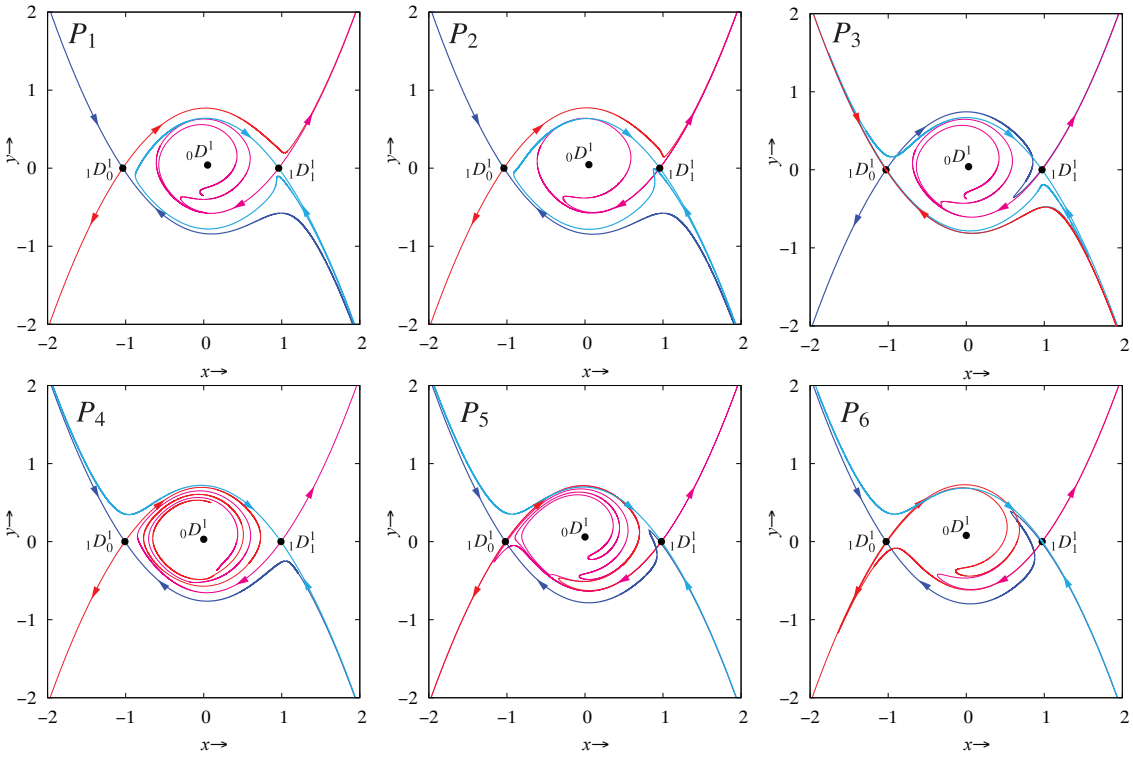

Figure 5: Stable and unstable manifolds with the parameters in Fig. 4.

Characteristics of Roll with Drift at Rest in Regular Beam Waves for Small Planing Craft

Toru, Katayama, *Osaka Prefecture University*, katayama@marine.osakafu-u.ac.jp

Mina, Adachi, *Mitsui O.S.K. Lines*, mina.adachi@molgroup.com

Mai, Kankaku, Student, *Osaka Prefecture University*, szb03054@edu.osakafu-u.ac.jp

ABSTRACT

The characteristics of roll in regular beam waves at rest for a small planing craft is investigated experimentally, and improvement of a strip method with Ikeda's roll damping prediction method is proposed. From the comparison between calculated and measured results, it is confirmed that the calculation overestimates roll amplitude at the condition where wave encounter period is shorter than its natural roll period, especially. The reasons of overestimation are investigated and it is confirmed that the coupling roll moment from swaying cannot be ignored for small planing craft for shorter wave period than its natural roll period. Because the natural roll period is shorter than that of a conventional displacement type vessel and its resonant wavelength is short comparing with its breadth, therefore its sway can not follow orbital motion of wave, coupling viscous roll moment from sway becomes significant.

Keywords: *Small hard chain craft, Roll, Damping, Viscous effects, Coupling motion*

1. INTRODUCTION

In general, sea trial is conducted at calm sea condition to avoid the effects of winds and waves on its results. However, it is difficult to ignore their effects on small craft as compared to their effects on conventional displacement type vessel. Therefore, it is necessary to correct the effects by using measured sea condition when sea trial is conducted.

In our research group, a simplified method to obtain wave spectrum by using measured roll of small boat without forward speed is investigated. The reason why roll is used is because a small boat drifts generally in beam sea, and it is confirmed by full scale measurements in real sea. The simplified method requires the response amplitude operator of the small boat whose roll is measured. Then, it is considered to use a strip method (: Ordinary Strip Method by Tasai et al., 1969) with Ikeda's roll damping prediction method (Ikeda et al.,1990), in order to estimate RAO of roll. However, it is confirmed by Katayama et al.,(2016) that OSM with Ikeda's method overestimates roll of small boat at the condition where wave encounter period is shorter than its natural roll period.

In this study, the characteristics of roll in regular beam sea without forward speed of a scale model are investigated experimentally, and improvement of OSM with Ikeda's method is considered. As a result, it is found that phase delay of sway to wave is drastically changed in shorter wave period than natural roll period. The change in phase delay means that its sway can not follow orbital motion of wave. Finally, it causes relative velocity around hull and the relative velocity makes the coupling viscous roll moment from sway. It is one of reasons of overestimation that OSM with Ikeda's method does not include the effects.

2. CHARACTERISTICS OF ROLL IN REGULAR BEAM SEA AT REST

2.1 Object Ship

Table 1 and Fig.1 show the principle particulars and a photograph of a model. Height of the center of gravity KG and natural roll period T_n are obtained from inclining test and free decay test, respectively.

Table 1 Principal particulars of model.

scale	1/11
overall length: L_{OA} [m]	1.130
breadth: B [m]	0.316
deadrise angle: β [deg]	20
draught: d [m]	0.055
ship weight: W [N]	70.89
height of the center of gravity: KG [m]	0.089
natural roll period: T_n [s]	0.68

Figure 1 Photograph of model.

2.2 Measuring device and coordinate system

Fig.2 shows a schematic view of experiment and its coordinate system. A model is fixed surge and yaw, and its roll, sway (drift), heave and pitch are free. Wave height is measured with a servo type wave height meter attached to model basin. Data is measured with 100Hz of sampling frequency. Wave height is small enough to avoid nonlinearity of roll for wave height (see Appendix).

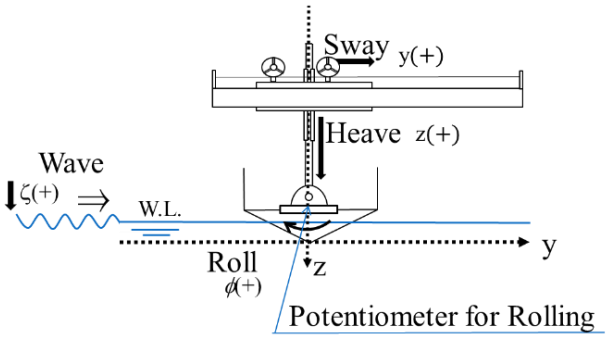

Figure 2 Schematic view of motion measurement with fixed surge and yaw from the behind of hull.

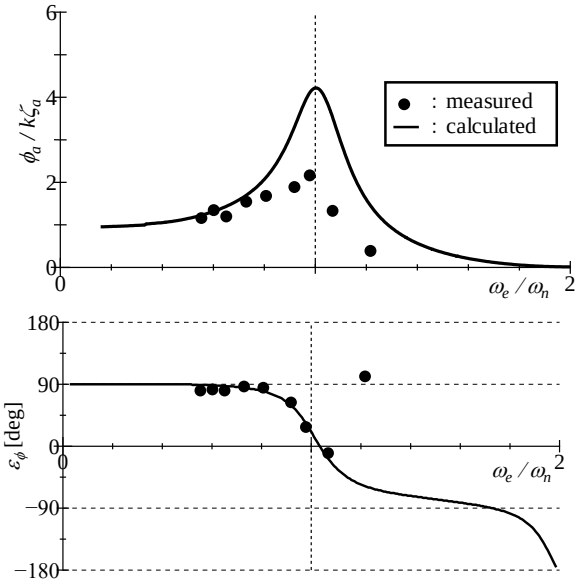

Figure 3 Comparisons of roll amplitude and phase delay to incident waves obtained by motion measurement and OSM with Ikeda's method at H_w=0.017m.

2.3 Measured results

Fig.3 shows the measured and the estimated results of non-dimensional roll amplitude and phase delay to incident waves. The estimation method is OSM with Ikeda's method. The horizontal axis of this figure is the ratio of roll circular frequency to natural roll circular frequency ω_e/ω_n. The dotted line shows natural roll period. This figure shows that the estimation method overestimates at the condition where wave encounter period is shorter than natural roll period.

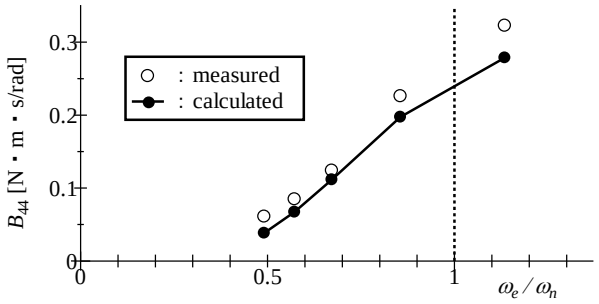

Figure 4 Roll damping coefficient B_{44} obtained by forced roll motion test and Ikeda's method.

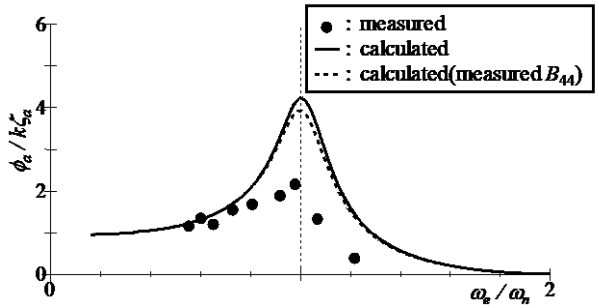

Figure 5 Comparison of RAO of roll obtained by motion measurement, OSM with Ikeda's method and OSM with measured roll damping by forced roll test.

3. CAUSE OF OVERESTIMATION

As a cause of the overestimation, Roll damping and coupled viscous effects from sway to roll is investigated.

3.1 Roll damping

A forced roll test is carried out to obtain roll damping. The model is made sinusoidal roll around the center of gravity, and forced roll moment and roll displacement are measured. Amplitude of forced roll is 5.0deg and its periods are 0.60, 0.80, 1.00, 1.20, 1.40s. Roll damping coefficient B_{44} is obtained from dividing the roll moment at the moment when roll angular velocity is maximum by the maximum roll angular velocity.

Fig.4 shows measured and estimated roll damping coefficient B_{44}. This figure shows that the estimated results is smaller than the measured results.

Fig.5 shows the estimated results by using the measured B_{44}. Modified estimation is slightly better than the original estimation.

3.2 Coupling viscous effects from sway to roll

Ikeda et al., (1982) indicates that the viscous effects on roll under coupling sway-roll in wave is completely different from the effects under single roll, if relative fluid velocity caused by sway and orbital motion of wave is significant compared with relative fluid velocity caused by roll.

Fig.6 shows the measured and the estimated results of non-dimensional sway amplitude and phase delay to incident waves. The horizontal axis of this figure is same as Fig.3. This figure shows that sway amplitude is 1 and phase delay is 90deg when ω_e/ω_n smaller than 0.8, on the other hand, when ω_e/ω_n larger than 0.8, sway amplitude becomes small according to increase in ω_e/ω_n. This means that sway does not follow orbital motion of wave, and it makes the relative fluid velocity that may affect the viscous effects on roll. Generally, length of significant waves for conventional displacement type vessels is much longer than ship breadth. In this situation, sway follows orbital motion of wave, and coupled viscous effects on roll from sway is not significant. However, relative fluid velocity caused by sway and orbital motion of wave is significant, when sway does not follow orbital motion of wave as shown in Fig.6.

Fig.7 shows relative fluid velocities at keel of midship section caused by roll only and by roll, sway and orbital motion of wave at the moments when ship is upright and when ship has maximum roll angle under rolling. The horizontal axis of this figure is same as Fig.3. This figure shows that there are relative fluid velocities caused by sway and orbital motion of wave.

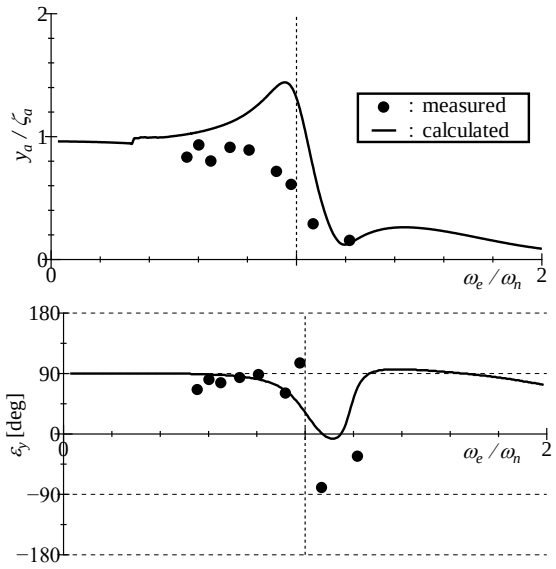

Figure 6 Comparison of sway amplitude and phase delay to incident waves obtained by motion measurement and OSM with Ikeda's method at H_w=0.017m.

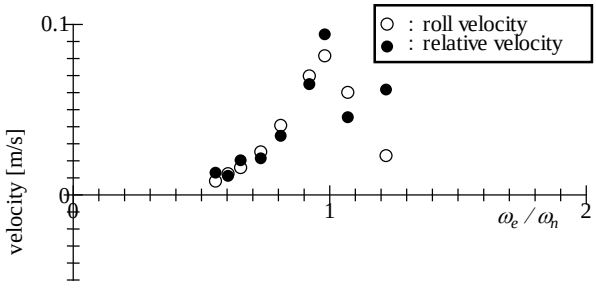

at the moments when ship is upright

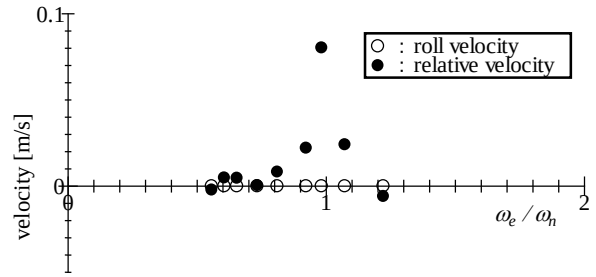

at the moment when ship has max. roll angle

Figure 7 Relative fluid velocities at keel of midship section calculated by only roll motion (: roll velocity) and including coupling effect of sway and orbital motion obtained from Fig.3 and Fig.6.

In order to measure the hydrodynamic roll moment that is the viscous effects on roll caused by coupling sway-roll in wave at the condition show in Fig.7, a forced coupling sway-roll test is carried out. The model is forced sinusoidal roll around the center of gravity, and forced roll moment and roll displacement are measured. Fig.8 shows a schematic view of forced motion test and its coordinate system. A model is fixed three arms. Arm 1 and Arm 2 are made the parallel sway that has same amplitude and phase. And when all Arms do the same motion, a model sway. When only Arm 3 moves, a model roll. When motion of Arm 3 is different from motions of Arm 1 and Arm2, a model makes a coupling motion of sway and roll. Forced sway force is measured with the strain gages attached to Arm 1 and Arm 2. Forced roll moment around roll center is measured with the strain gage attached to Arm 3. Roll damping moments with the coupling effect of sway is obtained as a component in proportion to roll angular velocity, and another component in proportion to roll angular acceleration is also obtained from measured forced roll moment. Table 3 shows experimental conditions of the forced roll test. The measurement at the same condition shown on Table 3 is also carried out in the air to subtract inertia force or moment.

Fig.9 shows roll damping with and without the coupling effects of sway and orbital motion of wave at roll period T=0.70s as a sample. This figure shows that the coupling effects change roll damping.

Fig.10 shows estimated results by using measured roll moment (damping and another component) by the forced coupling sway-roll test. The estimated results is better than the results of OSM with Ikeda's method.

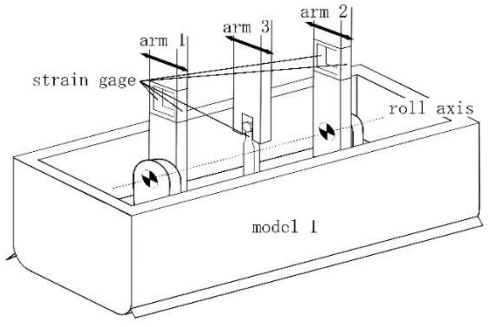

Figure 8 Schematic view of sway-roll coupled forced motion test.

Table 2 Conditions of sway-roll coupled forced motion test.

period[s]	0.50, 0.60, 0.70, 0.80
roll amplitude [deg]	5.0
sway amplitude [m]	0.05, 0.07, 0.10, 0.12
phase delay of sway to roll [deg]	0, 45, 90, 135, 150, 180, 270, 315

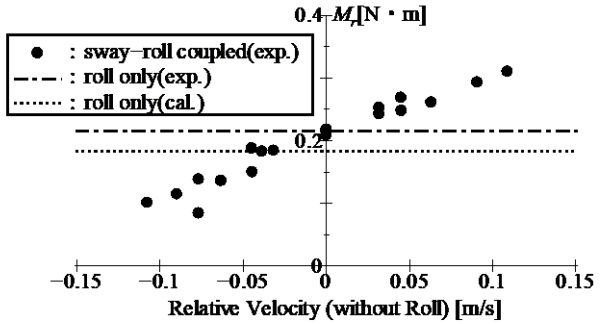

Figure 9 Roll damping moments with and without the coupling effects of sway and orbital motion of wave for the condition shown in Fig.3 and Fig.6.

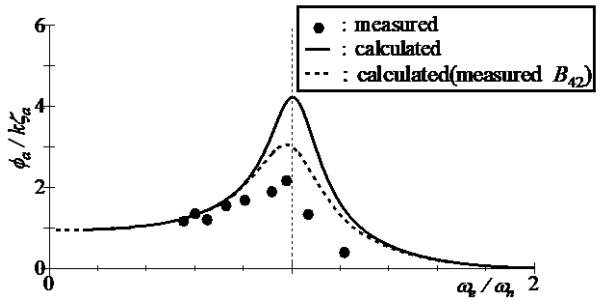

Figure 10 Comparison of RAO of roll obtained by motion measurement, OSM with Ikeda's method and OSM with Ikeda's method and measured roll moment by the sway-roll coupled forced motion test.

3.3 Wave exciting roll moment

Ikeda et al., (1992) indicates that the measured wave exciting roll moment acting on a small hard-chine craft is much smaller than the estimated ones by OSM with Ursell-Tasai method of Lewis form section and close-fit method. And their result is different from the result that wave exciting roll moment can be calculated accurately if a sectional hull form is expressed correctly in the case of a general cargo ship by Fujino et al.,(1983).

Fig.11 shows comparison between measured and estimated wave exciting moments. From this figure, it is found that the measured results are much smaller than the estimated results by OSM. In OSM, Ursell-Tasai method of Lewis form section is used, and the diffraction potential is not solved strictly, it seems one of reasons for the difference of wave exciting moment. Because, generally, it is difficult to apply the radiation potential to wave exciting roll moment instead of the diffraction potential at the wave length not long enough to compare with breadth of ship. Then the results calculated by the other strip methods (: STFM by Slvensen et al., 1970 and NSM) are also shown in the same figure. STFM uses close-fit method and solve the diffraction potential directly. On the other hand, NSM uses close-fit method, however the diffraction potential is not solved strictly. As the results, STFM, which uses close-fit method and solves the diffraction potential, is better agreement with the measured results.

Fig.12 shows comparison among measured RAO of roll, calculated results by OSM with Ikeda's method and OSM with Ikeda' method, measured roll moment by the sway-roll coupled forced motion test and measured wave exciting roll moment. This figure shows that the results of OSM with Ikeda's method are improved by using the measured wave exciting roll moment.

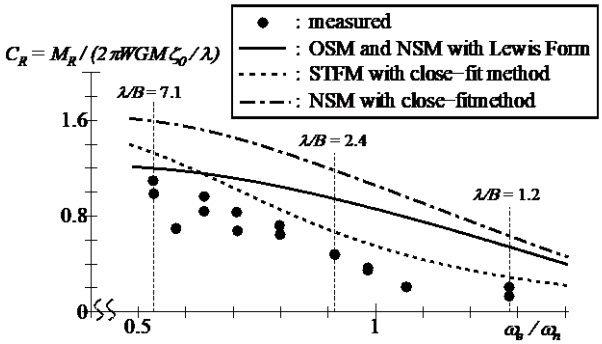

Figure 11 Comparison of wave exciting moment obtained by measurement, OSM, NSM and STFM.

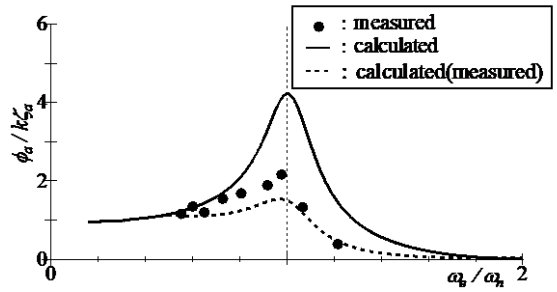

Figure 12 Comparison of RAO of roll obtained by motion measurement, OSM with Ikeda's method and OSM with Ikeda' method, measured roll moment by the sway-roll coupled forced motion test and measured wave exciting moment.

4. CONCLUSIONS

In this study, the characteristics of roll motion in regular beam sea without forward speed of a scale model are investigated experimentally, and improvement of OSM with Ikeda's method is considered. The following conclusions are obtained.

1. The estimation method overestimates at the condition where wave encounter period is shorter than natural roll period.

2. Estimated roll damping by Ikeda's method is slightly smaller than the measured one.

3. It is necessary for small planing craft to include roll damping with the coupling effects of sway and orbital motion of wave.

4. Measured wave exciting roll moment is smaller than the results by OSM. And it is confirmed that the estimated results is corrected by using measured moment.

REFERENCES

Fujino, M., Sakurai, K., 1983, "On the evaluation of Wave Exciting Roll Moment by the Strip Method", Journal of the Society of Naval Architects of Japan, Vol. 152, pp. 125-137.

Ikeda, Y., Kawahara, Y., Yokomizo, K., 1992, "A Study on Roll Characteristics of Hard-chine Craft", Journal of the Kansai Society of Naval Architects, Japan, No.218, pp.215-227.

Ikeda, Y., Miki, H., 1982, "A Rational Treatment of Viscous Effect on Roll and Sway Coupled Motion", Journal of the Kansai Society of Naval Architects, Japan, No.187, pp.25-31.

Ikeda, Y., Umeda, N., 1990, "A Prediction Method of Roll Damping of a Hardchine Boat at Zero Forward Speed", Journal of the Kansai Society of Naval Architects, Japan, Vol.213, pp.57-62.

Katayama, T., Adachi, M., 2016, "Study on Roll Motion with Drift in Regular Beam Waves for Small Planing Craft at Dead Ship Condition", Conference proceedings, the Japan Society of Naval Architects and Ocean Engineers, Vol.22, pp.69-72.

Slvensen, N., Tuck, E.O., Faltinsen, O., 1970, "Ship Motions and Sea Loads", Transactions, Society of Naval Architectures and Marine Engineers, 78, pp.250-287.

Tasai, F., Takagi, M., 1969, "Theory and Calculation of Ship Response in Regular Waves (in Japanese), Proc. Symposium on Seakeeping, the Society of Naval Architects of Japan, pp.1-52.

APPENDIX

EFFECTS OF WAVE HEIGHT ON ROLL AMPLITUDE

Roll amplitudes for systematically changed wave height at the natural roll period are measured, in order to investigate the maximum limit of wave height where roll amplitude is linear for wave height. Experimental method is the same as the method explained in Chapter 2. Fig.A1 shows the measured results. The horizontal dot dash line shows the roll angle where the chine is on the water surface in calm water. This figure shows that roll amplitude increases according to increases of wave height and it is in proportion to wave height at the wave height smaller than about 1.9 cm.

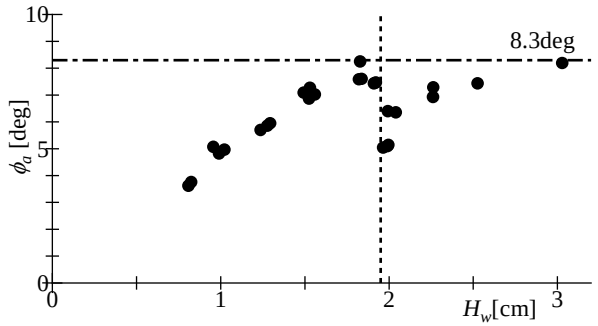

Figure A1 Roll amplitude in regular beam sea without forward speed at d=0.055m.

Experimental Assessment of the Wind Force Impact on the Roll Back Angle

Arman ARIFFIN, *ENSTA Bretagne, LBMS EA 4325, Brest, France*

arman.ariffin@ensta-bretagne.org

Mohd Naim AWANG, *Politeknik Ungku Omar, Perak, Malaysia*

mnaim@puo.edu.my

Hayati ABDULLAH, *UTMLEAD, Universiti Teknologi Malaysia, Malaysia*

hayatiabdullah@utm.my

Shuhaimi MANSOR, *Faculty of Mechanical Engineering, Universiti Teknologi Malaysia, Malaysia*

shuhaimi@mail.fkm.utm.my

Jean-Marc LAURENS, *ENSTA Bretagne, LBMS EA 4325, Brest, France*

jean-marc.laurens@ensta-bretagne.fr

ABSTRACT

Revision of 2008 IS Code started in 2001 gave an opportunity to maritime researchers and industries to analyse and scrutinise the intact stability code. The heeling angle is calculated by balancing the heeling moment and the hydrostatic restoring moment. The heeling moment is due to the action of the wind on the superstructure and the hydrodynamic force of reaction exerted on the hull. Around this equilibrium angle, a regulatory rolling motion calculated from the geometrical data of the ship and its GM is applied. A sudden gust of wind is then applied when the vessel starts its half roll period in the direction of the wind. The criterion applies to the maximum roll angle that the vessel will reach. The principle of this regulatory calculation is to be conservative and to be verified without resorting to complex hydrodynamic computation or tests on models which are very difficult to implement. In this paper, the proposal for direct assessment of dead ship condition was presented. two models were tested in the Low-Speed Wind Tunnel of the Universiti Teknologi Malaysia for two models: a simple academic shape and the DTMB 5415. The experimental setup is presented in this paper. The results were obtained for several wind velocities and initial heel angle. As expected, the code's results are more conservative than the experimental results. Finally, an illustrative result is presented to verify whether the experimental results could provide additional margin during the ship design process.

Keywords: *second generation intact stability, weather criterion, GZ curve, roll back angle*

1. INTRODUCTION

During the Concept Design Stage for a ship, the stability characteristic is crucial to be finalised before the other aspects such as damage stability, hydrodynamics, endurance and exterior design take in place. The stability of a ship is compulsory to abide with the International Code on Intact Stability 2008 (2008 IS Code). This 2008 IS Code is based

on the best "state-of-the-art" concepts available at the time the Code was developed. Since the design technology for modern ships is rapidly evolving, 2008 IS Code should be revised continuously and re-evaluated as necessary. In generally, 2008 IS Code consists of two main criteria. First is the criteria regarding righting lever curve properties as stated in (IMO 2009) Ch 2 Paragraph 2.2 and second is the severe wind and rolling criterion (also known as weather criterion) as stated in (IMO 2009) Ch 2 Paragraph 2.3.

The concepts in naval architecture known as buoyancy and stability were founded on the roots of Archimedes' principle. Indeed, the development of ship stability as a science occurred very late in the 18th century with two different approaches based on the introduction of the metacentre and the righting moment as stated by Francescutto (Francescutto 2016). These approaches were developed by Bouguer and Euler respectively.

The revision of the 2008 IS Code started in 2001 with a critical analysis submitted by the Italian delegation to the IMO concerning the need for updating and tuning some coefficients of the weather criterion, given its excessive weight in determining the limiting VCG for ships with large values of the beam to draught ratio. This was considered an opportunity to "shake up" the 2008 IS Code foundations and place them on a more physical basis through the development of new performance-based criteria originally intended to replace the old criteria. After much comprehensive discussion and thorough debates in the IMO and several conferences, it was subsequently decided that the five major possible stability failures modes should be individually addressed (Belenky et al. 2009; Francescutto 2007; Peters et al. 2011).

An alternative assessment of the weather criterion is the guideline for model experiment setup and test procedure for determining the wind heeling lever, l_{w1} and the angle ϕ_1 (IMO MSC.1/Circ.1200 2006).

2. COMPARISON THE IMO RULES AND THE NAVAL RULES FOR THE WEATHER CRITERION

The principles of calculating the weather criterion for both the IMO rules and Naval Rules are almost similar. The variant between both rules are presented in Table 1.

Table 1 Comparison on the weather criterion for the IMO and the Naval rules

Criteria	IMO Rules	Naval Rules
Wind heeling arm (WHA) i. Velocity	26ms^{-1} or 50.54 knots	100 knots
ii. Curve	Constant with heel angle	Cosine square with heel angle
Angle of stable heel	16° (calculated from l_{w1})	20° (calculated from WHA)
Ratio between capsizing and restoring energy (A_2/A_1) based on lw$_2$ (gust)	≥ 1	nil
Ratio between capsizing and restoring energy (A_2/A_1) based on *WHA* (100 knots)	nil	≥ 1.4
Roll windward due to beam wave	Variable based on ship characteristic	25°

The calculation for Wind Heeling Arm (WHA) is different in the IMO and Naval Rules. For the IMO, the calculation of WHA or wind heeling levers (l_{W1}) is constant at any heel angle (Part A, Ch 2, Para 2.3.3) (IMO 2009). For the Naval Rules, the WHA is calculated

based on wind velocity. The calculation for obtaining the WHA is shown in Table 2.

Table 2 Formula for wind heeling arm of the IMO and Naval Rules Criteria

Criteria	IMO rules	Naval rules
Wind heeling arm, (l_{W1}) (l_{W2} = 1.5 l_{W1})	$\frac{P.A.Z}{1000.g.\Delta}$	$\frac{0.0195.V^2.A.Z.cos^2\phi}{1000.\Delta}$

Where:
P = wind pressure of 504 Pa,
A = projected lateral area (m^2),
Z = vertical distance from the centre of A to the centre of the underwater lateral area,
Δ = displacement (t),
g = gravitational acceleration of 9.81 (ms^{-1}),
V = wind velocity (knots),
ϕ = heel angle (degrees).

The coefficient 0.0195 is derived from the combination of physical constants and the unit used for wind speed (Luquet et al. 2015). It uses 1 nautical miles = 1852 km where:

$$WHA = \frac{1}{2}.\frac{\rho Cy}{g}.(\frac{1852}{3600})^2 = 0.0195 \quad (1)$$

Where:
ρ = density = 1.29 kg/m^3,
Cy = coefficient for y-axis = 1.12,
g = gravitational acceleration of 9.81 (ms^{-1}).

To determine the effect of heel angle, there are two approaches to estimate the aerodynamic effect, either by considering that the wind velocity is constant and that the inclined projected area decreases relatively or that the wind velocity decreases relatively and that the projected area is constant.

In civil industry, an important problem in modelling winds in urban areas concerns the estimation of drag induced by a group of buildings with different densities. However, in contrast to bulk drag coefficients based on the total drag on an obstacle, the sectional drag coefficient requires knowledge of the detailed vertical profiles of the drag force and mean velocity within the building canopy. These are difficult to obtain experimentally, and information about drag coefficient, $C_D(z)$ is therefore scarce (Santiago et al. 2008). A wind tunnel test was conducted and obtained the C_D for a group of buildings. The C_D obtained from this experiment was around 1.15 (Hagishima et al. 2009).

To the author's best knowledge, there is no statement mentioned in the literature regarding the cosine square used in Naval Rules. For the authors, the cosine square originates from the velocity where V_{actual} = Vcos ϕ. Since the calculation of the WHA has the velocity square, the cosine square has appeared in the WHA for Naval Rules.

3. DEVELOPMENT OF THE MODELS

3.1 Model Description

Two models were used for the experimental work. The first model is an academic container ship geometry referred as "ASL shape" in the rest of the paper. The second model is a research ship model, the well know DTMB 5415 (Molgaard 2000). The 5415 DTMB model is widely used for the research study in seakeeping (Begovic et al. 2013; Jones & Clarke 2010; Yoon et al. 2015).

The main particulars of ASL shape are given in Table 3 and for the 5415 DTMB shape in Table 4. The body plan and perspective view for "ASL shape" is shown in Figure 1. The body plan and perspective view for "5415 shape" is shown in Figure 2.

Table 3 Main particulars of ASL shape

Ship model	Ship	Model
LOA, (m)	140	1.400
BOA, (m)	20	0.200
Draft, (m)	12	0.120
Displacement, (tonnes)	26,994	0.027
VCG, (m)	10	0.10
LCG, (m)	70.037	0.70
KM, (m)	10.206	0.10
GM, (m)	0.206	0.002

Table 4 Main particulars of 5415 shape

Ship model	Ship	Model
LOA, (m)	153.3	1.533
BOA, (m)	20.54	0.205
Draft, (m)	6.15	0.061
Displacement, (tonnes)	8,635	0.0086
VCG, (m)	7.555	0.076
LCG, (m)	70.137	0.70
KM, (m)	9.493	0.09
GM, (m)	1.938	0.014

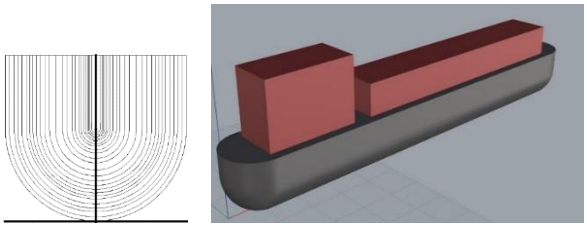

Figure 1 Body plan (left) and perspective view (right) of the ASL shape

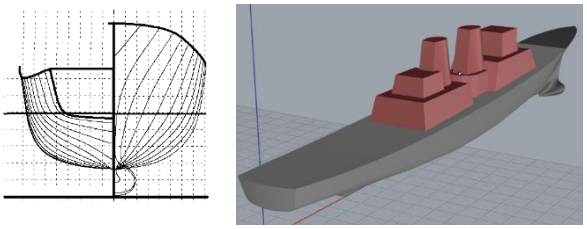

Figure 2 Body plan (left) and perspective view (right) of the 5415 shape

3.2 Model Verification

To determine the correct centre of gravity, inclining tests were performed. The inclining test is a procedure which involves moving a series of known weights, normally in transverse direction and measuring the resulting change in the equilibrium heel angle of the ship. By using this information and applying basic naval architecture principles, the ships' vertical centre of gravity is determined from the GM. We also verified that the natural roll period is as expected. Two devices were used for the data recording, first is the Ardu Flyer device and smartphone (Djebli et al. 2016). The GZ Curve for both ASL and 5415 DTMB shape as shown in Figure 4.

(a)

(b)

Figure 3 Complete build ship models (a) ASL shape (b) 5415

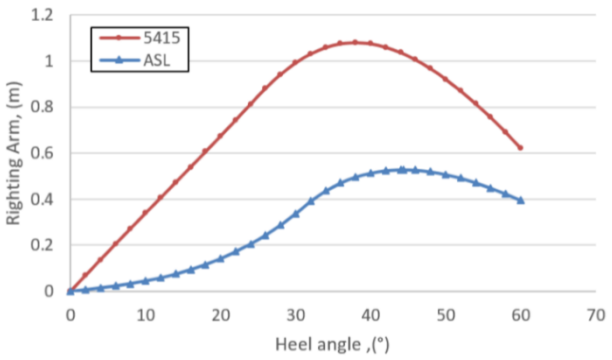

Figure 4 The GZ curves for the ASL shape and 5415 shape

4. UTM'S LOW-SPEED WIND TUNNEL SPECIFICATION

The wind tunnel test is the commonly used method in research works as reported in the literatures (Ariffin et al. 2016; Mantari et al. 2011; A. D. Wnęk et al. 2010; Blendermann 1994; Noor & Mansor 2013; Abdullah et al. 2013) . The wind tunnel method is commonly used for reasons of safety and economy. Model scale tests are cheaper and offer a controlled environment. However, it can be difficult to obtain an accurate simulation of the atmosphere and geometric characteristics of the ship. There are three important components in the wind tunnel which are known as the test section, fan motor and settling chamber. The general arrangement of the wind tunnel is shown in Figure 5.

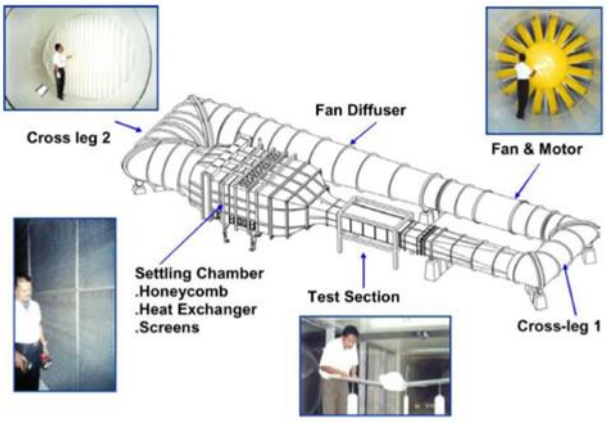

Figure 5 General arrangement of the UTM's Low-Speed Wind Tunnel

The main laboratory facility is the state-of-the-art low-speed wind tunnel with a maximum speed of 288 km/h. The wind tunnel has an excellent flow quality with 2.0 m (W)×1.5 m (H)×5.8 m (L) test section size. It has a flow uniformity of less than 0.15%, a temperature uniformity of less than 0.2˚C, a flow angularity uniformity of less than 0.15° and a turbulence level of less than 0.06%. This facility, the first of its kind in Malaysia, became operational in June 2001. The wind tunnel is housed inside the Aeronautical Engineering Laboratory building. The wind tunnel is furnished with a compressed air facility for general purpose applications. The test section is connected to the wind tunnel control room via a metal structure platform (Noor & Mansor 2013).

5. TEST RIG DESIGN

Dealing with air in the test section is the norm in a wind tunnel experiment. Meanwhile, dealing with water in the test section requires additional precaution because the instrument underneath the test section floor is not designed to be watertight. In this experiment, a water tank of the dimensions (length x width x height) 1600mm x 400mm x 240mm was constructed using 8mm glass. The water tank joints were properly sealed to avoid any water leakage. For safety reasons, a small watertight curtain was located underneath the dummy test section platform to collect any water leakage. To prevent the models from moving transversally, a rod with a diameter of 4mm (see Figure 6) held both the ASL shape and 5415 shape. The rod was located at the centre of buoyancy (*CoB*). For the ASL shape, the *CoB* location was at 6.88 cm from the keel, and for the 5415 shape, the position was at 3.66cm from the keel. The superstructures above the waterline for both models are shown in Figure 7 and Figure 8. To avoid the wind velocity from accelerating at the water tank, a spoiler was used to create a good velocity profile. The height of the spoiler was at the same level as the water tank to avoid any obstruction. The concept drawing of the test rig is shown in Figure 9.

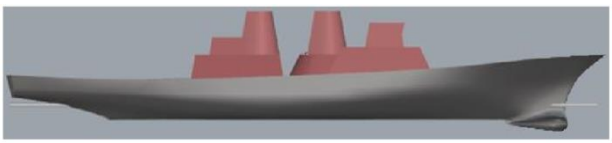

Figure 6 Location of longitudinal rod on model 5415

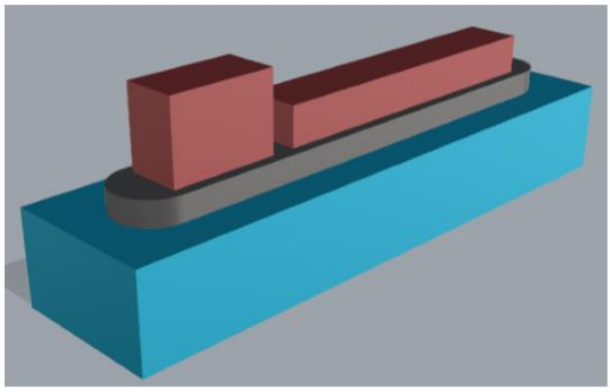

Figure 7 The superstructure above water line for the ASL shape

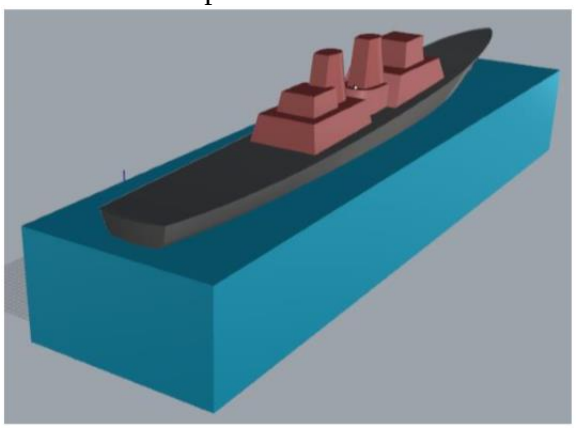

Figure 8 The superstructure above water line for the 5415 shape

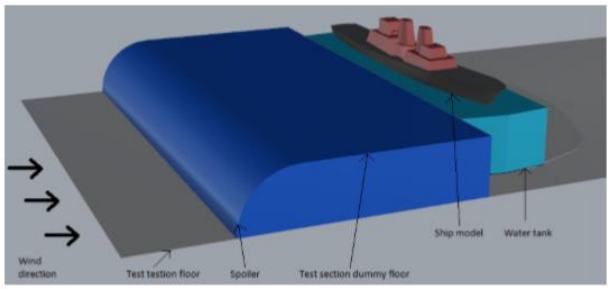

Figure 9 Perspective view of the test rig

The spoiler used in the test section is shown in Figure 10. The spoiler was attached to the test section floor and the dummy test section floor. During the test, the wind velocity was controlled from the control room. The control room faced the test section to allow emergency action to be taken rapidly. At the same time, an electronic pressure sensor (Figure 11) was used to measure the static pressure and dynamic pressure. Since the wind velocity was the main concern in this test, a secondary instrument, a micro-manometer, was used to measure the wind velocity in the wind tunnel. The velocity profile in the test section needed to be verified before the test was conducted. A set of tubes was used to measure the static and dynamic pressure (Figure 12). Each tube was placed vertically at each distance of 2.5mm to obtain the boundary layer. Only the velocity profile was obtained and verified; the model was balanced before being placed in the water tank. The model was balanced with a set of loads and an accelerometer. The accelerometer contained sensors and a battery. All loads and sensors were placed correctly and firmly to avoid any disturbance during the experimental work. The height of the ballasting weight placed in the hull was also considered to make sure the model presented the correct *GM* and natural roll period. The longitudinal rod used on both models was not to penetrate the hull model. It was to avoid any risk of leakage during the experiment. Therefore, the rod was properly glued at both the fore and aft of the model. At the water tank, a "double L" plate was used to prevent the longitudinal rod from moving in a transverse direction. With this plate, the model was allowed to float freely and have the correct centre of buoyancy every time it heeled. The plate was located at the fore (Figure 13) and aft (Figure 14) of the water tank. It was fixed to the dummy floor test section. A rollback angle ($\varphi 2^*$) measure was performed for all the models. The definitions of ($\varphi 1$) and ($\varphi 2^*$) are shown in Figure 15.

Figure 10 Side view of test section with spoiler and dummy test section floor

Figure 11 TSI Electronic pressure sensor model 9565-P

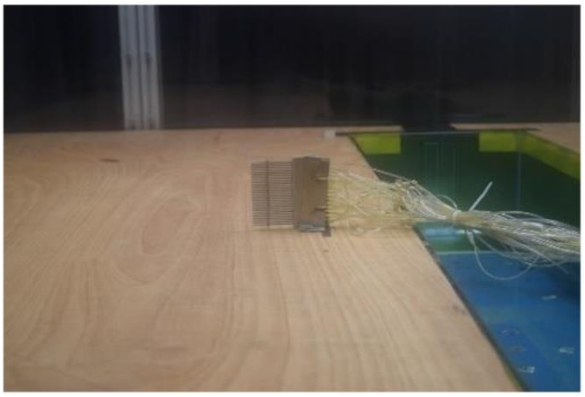

Figure 12 A set of tubes used to collect static and dynamic pressure

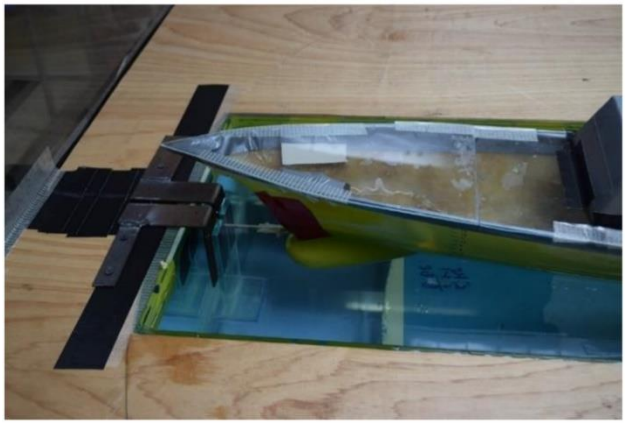

Figure 13 Rod location to the fore of the model

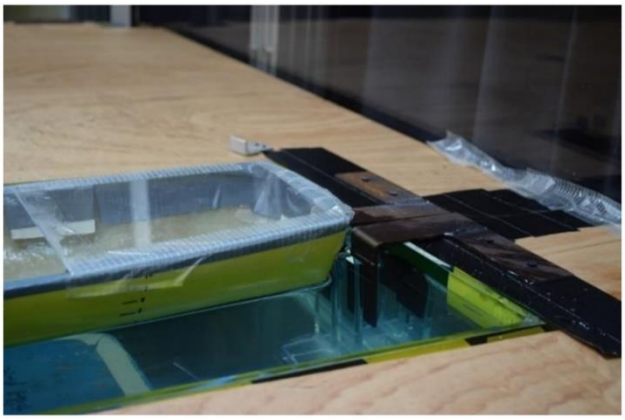

Figure 14 Rod location to the aft of the model

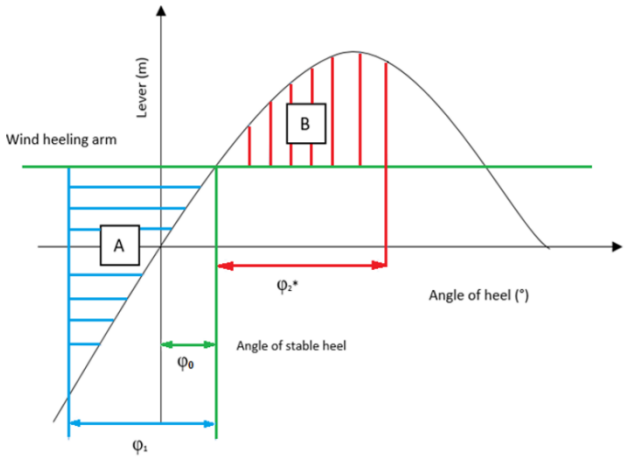

Figure 15 Definition used in this experiment

6. RESULTS AND DISCUSSIONS

6.1 Natural Roll Period Verification

The results for the natural roll period test were compared with several methods. Each method was well established and had been widely used in the naval architecture domain. In this research, three main methods were used. The first was the calculation method based on formulae using General Hydrostatic (GHS) software, second was the simulation method using the Fine Marine software and third was the experimental result prior to the wind tunnel test. The details of the pre-test results for the ASL shape are shown in Table 5 and Figure 16. The details of the pre-test results for the 5415 shape is shown in Table 6 and Figure 17.

The natural roll period simulation for the ASL and 5415 shapes was slightly different. The 5415 shape was more sensitive due to the time step calculation. For the ASL shape, the time step value used was 0.015s and the 5415 shape used the time step value of 0.005s. Both said time steps and shapes showed the same results as the time step of 0.001s. Indeed, small time steps should be selected for accurate prediction, and fixed time steps should be preferred to adaptive schemes.

Table 5 Results for pre-test of the ASL shape

Method	Natural roll period (seconds)
Formula:	
IMO	3.6198
WEISS formula	3.5373
Benford, 1991	3.3490
Simulation	
Fine Marine	3.3750
Experimental	
Prior to wind tunnel test	3.4815

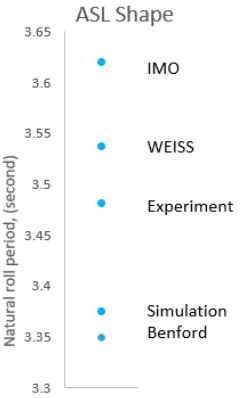

Figure 16 Comparison of natural roll period test for the ASL shape

Table 6 Results for pre-test of the 5415 shape

Method	Natural roll period (seconds)
Formula:	
IMO	1.1214
WEISS formula	1.1844
Benford, 1991	1.1213
Simulation	
Fine Marine	1.1750
Experimental	
Prior to wind tunnel test	1.1102

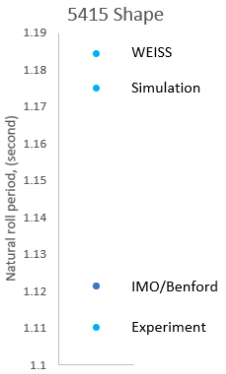

Figure 17 Comparison of natural roll period test for the 5415 shape

6.2 Roll Back Angle (ϕ_{2*}) versus Roll to Windward (ϕ_1)

Figure 18 shows the roll back angle (ϕ_{2*}) versus roll to windward (ϕ_1) for the ASL shape for the wind velocity range of 2 m/s to 4 m/s. Figure 19 shows the roll back angle (ϕ_{2*}) versus roll to windward (ϕ_1) for the 5415 shape. In the absence of damping, the results should be like a swing where ϕ_{2*} follows ϕ_1.

The straight lines in Figure 18 and Figure 19 represent an equal energy dispersal and absorption (theoretical value) both leeward and windward. The ASL shape shows that the experimental results diverged from the theoretical values and the 5415 shape shows that it converged to the theoretical value. In fact, the ASL shape had a rounded hull and is imposed to null damping. The ASL shape has more damping because of the work done by the wind heeling arm which is considered. This phenomenon is not present for the 5415 shape because the GZ curves for both ASL and 5415 shapes are different. Referring to Figure 4, the 5415 shape has a linear GZ curve from 0 to 30° and the ASL shape has a non-linear curve from 0 angle. Therefore, the area under the wind heeling arm contributed a significant influence to the roll back angle. Figure 20 shows the roll back angle (ϕ_{2*}) versus roll to windward (ϕ_1) for the ASL with bilge keel configuration for the wind velocity range of 2.3 m/s to 2.4 m/s. The results suggest a far more complex

behaviour where the hydrostatic force shape plays an important roll.

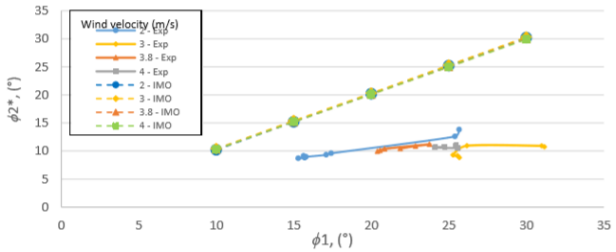

Figure 18 Rollback angle (ϕ_{2*}) vs roll to windward (ϕ_1) for the ASL shape

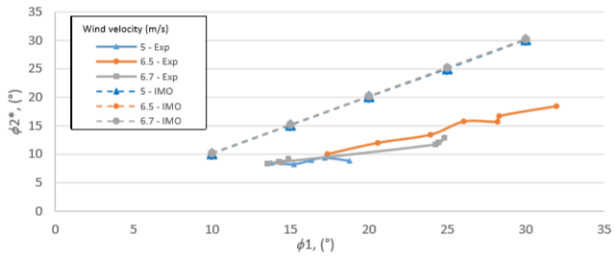

Figure 19 Rollback angle (ϕ_{2*}) vs roll to windward (ϕ_1) for the 5415 shape

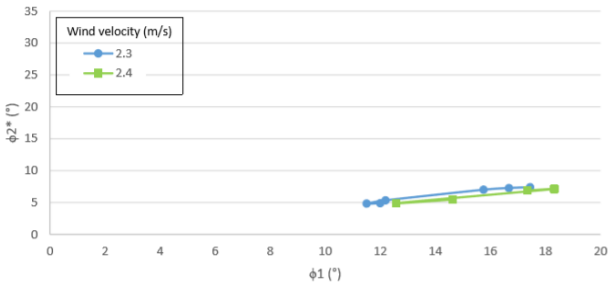

Figure 20 Rollback angle (ϕ_{2*}) vs roll to windward (ϕ_1) for ASL with bilge keel configuration

7. CONCLUSIONS

Experimental work on the evaluation of the weather criterion in the wind tunnel test is possible. The wind tunnel is not designed to be waterproof. Therefore, additional safety precautions are required to minimise the risk of water splash that may cause critical damage to equipment or tools underneath the test section. For the first rule concerning the weather criterion, which is an angle of stable heel, the experimental result for the ASL shape shows a higher value than GHS. For the 5415 shape, the experimental result shows a lower value than GHS. This phenomenon is explained by the drag coefficient of the tested shapes. For the second rule in the weather criterion, which is an area under the curve, both shapes show the experimental results are less conservative than GHS. Therefore, this may allow more margin for ship designers during the design stage.

The drag coefficient is possible to be measured using the test rig presented in this paper. The heel response of the wind force could be translated from the hydrostatic solver based on the GZ curve where the moment is equal to the GZ times the displacement of a tested shape.

8. ACKNOWLEDGEMENTS

The authors would like to acknowledge the support of the Government of Malaysia, Universiti Teknologi Malaysia, the Government of the French Republic, and the Malaysian- France University Centre (MFUC).

9. REFERENCES

A. D. Wnęk et al., 2010. Numerical and experimental analysis of the wind forces acting on LNG carrier. In *V European Conference on Computational Fluid Dynamics-ECCOMAS CFD 2010*. Lisbon, Portugal, pp. 14–17.

Abdullah, H., Ariffin, A., and Hassan, M.Y., 2013. Exhaust Gas-Superstructure Interactions Onboard Ships with Side Exhaust. In *Engineering Conference*. Kuching, Sarawak, Malaysia.

Ariffin, A., Mansor, S., and Laurens, J.-M., 2016. Conduction of a wind tunnel experiment to investigate the ship stability weather criterion. In *15th International Ship Stability Workshop*. Stockholm, Sweden.

Begovic, E. et al., 2013. Experimental assessment of intact and damaged ship motions in head, beam and quartering seas. *Ocean Engineering*, 72, pp.209–226.

Belenky, V., Bassler, C.C., and Spyrou, K.J., 2009. Dynamic Stability Assessment in Early-Stage Ship Desgin. In *International Conference on Stability of Ships and Ocean Vehicles*. pp. 141–154.

Blendermann, W., 1994. Parameter identification of wind loads on ships. *Journal of Wind Engineering and Industrial Aerodynamics*, 51(3), pp.339–351.

Djebli, M.A. et al., 2016. The application of smartphone in ship stability experiment The Application of Smartphone in Ship Stability Experiment. *Journal of Marine Science and Application*.

Francescutto, A., 2016. Intact stability criteria of ships – Past , present and future. *Ocean Engineering*, 120, pp.312–317..

Francescutto, A., 2007. The Intact Ship Stability Code: Present Status and Future. In *Proceedings of the 2nd International Conference on Marine Research and Transportation, Naples, Italy, Session A*. pp. 199–208.

Hagishima, A. et al., 2009. Aerodynamic parameters of regular arrays of rectangular blocks with various geometries. *Boundary-Layer Meteorology*, 132(2), pp.315–337.

IMO, 2009. *International Code of Intact Stability, 2008*, London.

IMO MSC.1/Circ.1200, 2006. *Interim Guidelines for Alternative Assessment of the Weather Criterion*

Jones, D. a. and Clarke, D.B., 2010. *Fluent Code Simulation of Flow around a Naval Hull: the DTMB 5415*, Victoria, Australia.

Luquet, R. et al., 2015. Aerodynamics loads on a heeled ship. *12th International Conference on the Stability of Ships and Ocean Vehicles*, (June), pp.14–19.

Mantari, J.L., Ribeiro e Silva, S., and Guedes Soares, C., 2011. Intact stability of fishing vessels under combined action of fishing gear, beam waves and wind. *Ocean Engineering*, 38(17–18), pp.1989–1999..

Molgaard, A., 2000. *PMM-test with a model of a frigate class DDG-51*, Lyngby, Denmark.

Noor, A.M., and Mansor, S., 2013. Measuring Aerodynamic Characteristics Using High Performance Low Speed Wind Tunnel at Universiti Teknologi Malaysia. *Journal of Applied Mechanical Engineering*, 3(1), pp.1–7..

Peters, W.S. et al., 2011. On Vulnerability Criteria for Parametric Roll and Surf-riding. In *International Ship Stability Workshop*. pp. 1–6.

Santiago, J.L. et al., 2008. Variation of the sectional drag coefficient of a group of buildings with packing density. *Boundary-Layer Meteorology*, 128(3), pp.445–457.

Yoon, H. et al., 2015. Benchmark CFD validation data for surface combatant 5415 in PMM maneuvers – Part I: Force/moment/motion measurements. *Ocean Engineering*, 109, pp.705–734.

Second generation calculation method for use in the inclining experiment

Kristian Bertheussen Karolius, *Maritime Safety Research Centre* kristian.karolius@strath.ac.uk

Dracos Vassalos, *Maritime Safety Research Centre* d.vassalos@strath.ac.uk

ABSTRACT

The vertical centre of gravity (VCG) is paramount in assessing intact and damage stability being the baseline for any condition of loading. It is well known that the *Classical* method used to calculate the VCG is limited by assuming an unchanged metacentre position and may produce error prone results. An alternative method, namely the *Polar* method, will be presented in this paper. Possible implications inherent in the *Classical* method on stability performance and safety will be assessed utilising the attained index A. The study clearly highlights the accuracy and flexibility of the *Polar* method and demonstrates the importance of correct VCG calculation as even minor errors in the order of millimetres may translate into extensive weights and moments compromising stability and safety.

Keywords: Stability, Safety, Inclining experiment, Lightweight, VCG, Calculation method

1. INTRODUCTION

The centre of gravity of a vessel and specifically its vertical centre of gravity (VCG) is paramount for assessing intact and damage stability performance, being the baseline for any condition of loading. It is also affecting other important aspects such as vessel motion behaviour through the rolling period, hence linked to the new second generation intact stability criteria (IMO, 2016). The VCG is utilised in most intact and damage stability legislation through enforcing requirements to the GZ righting curve. It can therefore also be regarded as a safety baseline.

It is a well-known fact that the so called *Classical* method, in which the VCG is calculated following inclining experiments, has its limitations on performance in terms of applied heel angle magnitude, applied loading condition and accuracy for certain hull forms. This is due to the assumption made of unchanged metacentre position when the vessel is heeled. As a result of the limiting assumptions

in the *Classical* calculation method, more accurate and flexible calculation methods have been proposed. A detailed study on such methods has been presented by Karolius & Vassalos (2018a), highlighting possible limitations inherent in the *Classical* method whilst demonstrating due flexibility and higher accuracy through the use of the new methods.

A second study by Karolius & Vassalos (2008b) has also been presented, but with higher focus on design implications in terms of stability and cargo carrying capacity. In this paper, focus will be on the *Polar* method. The method derivation will be outlined and its accuracy and superiority over the *Classical* method will be highlighted through a technical inclining experiment utilising a completely box-shaped vessel, enabling first principle calculations. The paper will further assess possible implications on stability performance and subsequent safety resulting from incorrect

VCG calculations using the *Classical* method based on the two vessels showing highest errors from the initial study by Karolius & Vassalos (2018a).

Assessment of possible stability implications is achieved by identifying the ensuing false safety resulting from calculating incorrect VCG using the *Classical* method, hence impact on the attained index A as set out in SOLAS Reg. II-1/7-8 (IMO, 2009). By performing calculations for both actual lightweight VCG and calculated lightweight VCG from the technical inclining experiment, the false safety can be identified, highlighting the importance in achieving a correct VCG value following the inclining experiment for a safe vessel design.

2. BACKGROUND

2.1 The inclining experiment

Before vessel stability in any condition of loading can be assessed, the initial lightweight condition needs to be identified using the inclining experiment. All other loading conditions are created using the lightweight condition as a basis, applying loads in terms of cargo, crew, consumables and other equipment, and checked against given stability criteria. As such, it can be considered to be the main stability reference and measure of loading capacity for a vessel. Any errors in determining the lightweight particulars will be a consequential error on all other loading conditions that are to be assessed against relevant intact and damage stability criteria.

SOLAS Reg. II-1/5 (IMO, 2009) requires every passenger ship, regardless of size, and every cargo ship above 24 meters in length, to be inclined upon its completion or following any design alterations affecting stability. High-speed and light-craft have similar requirements found in the HSC Code Reg. II/2.7 (IMO, 2000), and in Torremolinos Reg. III/9 (IMO, 1977 as amended), for fishing vessels. Even smaller recreational craft above 6 meters in length have equivalent requirements in ISO standard 12217-2 (ISO, 2013).

Passenger vessels are further required by SOLAS to be inclined every 5 years if lightweight surveys identify a weight change above a given threshold limit. Evolution of the lightweight is very common, as most vessels are refurbished and converted through their operating-life. The inclining experiment report is subject for approval by flag administration and class and comprise approval of the vessel's lightweight particulars which is needed for the purpose of stability approval and its control. The approval establishes the stability baseline setting limiting constraints on the vessels loading conditions, thus ensuring safe operations.

2.2 Classical method assumptions

The validity of the *Classical* method is based on the assumption of unchanged position of the metacentre when the vessel is heeled. This is illustrated in Figure 1.

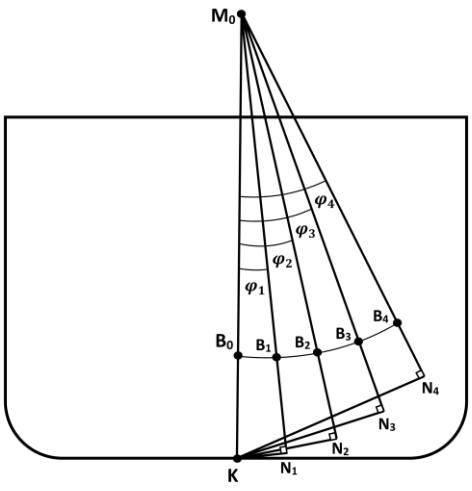

Figure 1. Assumption of unchanged metacentre position.

The position of the metacentre can be represented by the metacentre-radius (BM) given by (1):

$$BM = \frac{I_{XX}}{\nabla} \quad (1)$$

were I_{XX} = second moment of the waterplane area, and ∇ = displaced volume.

The vessel displaced volume is constant during the incline and the change in the position of the metacentre is, therefore, proportional to the change in the second moment of the waterplane area and, consequently, the waterplane area itself. A more realistic movement of the metacentre with increased waterplane area is illustrated in Figure 2. The assumption in the *Classical* method, however, relates to smaller heel angles, and may hold to an acceptable level for more traditional hull forms. In an attempt to ensure the correct application of the *Classical* method, various requirements have been set out in the 2008 IS Code Part B Ch. 8 and Annex I (IMO, 2008).

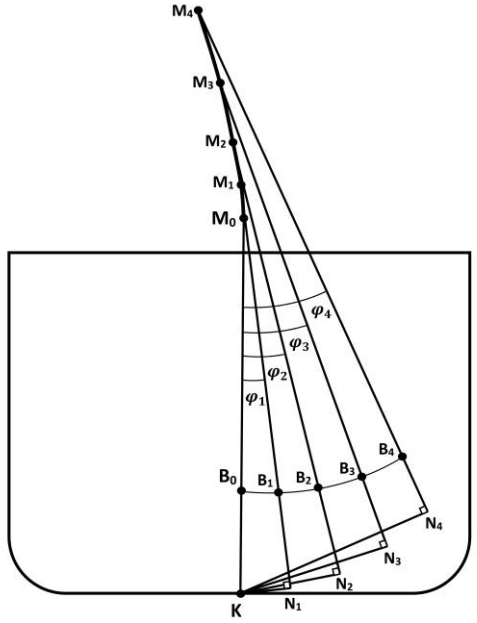

Figure 2. More realistic movement of metacentre position.

Most vessels have today various design features that may result in higher change in the waterplane area than should be accepted even for smaller heel angles. This is the main reason for the *Classical* method being subjected to scrutiny and debate. Such design features may include:

- Chine lines and knuckles
- Large fore- and aft flare
- Misc. appendages
- Large change in trim during heel
- Other unconventional hull forms

The reason for the assumption in the *Classical* method is to utilise a simplified trigonometric relationship as illustrated in Figure 3, which facilitates a formula for VCG to be derived using (2-7). The assumption further enables the use of upright hydrostatics in the calculation of GM for every weight shift.

$$\tan(\varphi) = \frac{G_0 G_\varphi}{G_0 M_0} \tag{2}$$

$$G_0 M_0 = \frac{G_0 G_\varphi}{\tan(\varphi)} \tag{3}$$

$$G_0 G_\varphi = \frac{wd}{\Delta} \tag{4}$$

$$GM = G_0 M_0 = \frac{wd}{\Delta \tan(\varphi)} \tag{5}$$

$$\tan(\varphi) = \frac{r}{L} \tag{6}$$

$$VCG = KM - GM \tag{7}$$

were w = inclining weight, d = movement distance, Δ = displacement, r = pendulum reading, and L = pendulum length. Remaining parameters are explained using figure 3.

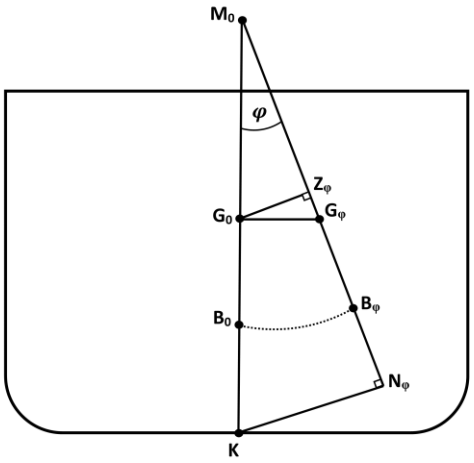

Figure 3. Simplified trigonometric relationship for deriving the Classical formula for GM.

2.3 Implications on stability

The waterplane area may increase or decrease depending on heel magnitude and which specific design features are emerged or submerged during the incline. This can be addressed as two specific cases:

Case 1: Increase in waterplane area:

$$BM_0 < BM_\varphi \quad (8)$$

$$GM_0 < GM_\varphi \quad (9)$$

$$VCG_0 > VCG_\varphi \quad (10)$$

Case 2: Decrease in waterplane area:

$$BM_0 > BM_\varphi \quad (11)$$

$$GM_0 > GM_\varphi \quad (12)$$

$$VCG_0 < VCG_\varphi \quad (13)$$

By using the *Classical* method, Case 1 will overestimate vessel stability, thus producing a lower VCG value than is the actual case, while Case 2 will underestimate the vessel stability leading to a higher VCG than is the actual case. Moreover, the VCG is utilised in most intact and damage stability legislation through enforcing requirements on the GZ righting curve. The GZ curve is represented by (14) and it is clear that any error in VCG will lead to subsequent errors in the GZ curve and hence incorrect assessment against relevant stability criteria.

$$\mathrm{GZ}(\varphi) = KN(\varphi) - VCG\sin(\varphi) \quad (14)$$

Another way to illustrate possible implications on stability, a traditional VCG stability limit curve can be used as shown in Figure 4.

Figure 4. Stability limit curve.

The limit curve serves as the safe operational envelope for a vessel and represents the operational conditions for which the relevant intact and damage stability requirements are fulfilled. The black curve represents the limit curve prepared using the lightweight VCG, as obtained from the *Classical* method. For the sake of argument, an error of 1% underestimation in VCG is assumed. The actual curve is then represented by the stapled line as the underestimation of the lightweight VCG has resulted in a more lenient operational limit. This clearly shows that a vessel may be operating in an unsafe area if the lightweight VCG is underestimated, presenting false safety to the operators.

3. THE POLAR METHOD

The *Polar* method was presented in the study by Karolius & Vassalos (2018a), and is derived utilising the line through point (x, y) represented in polar coordinates, i.e. polar line (PL), illustrated in Figure 5. The representation in polar coordinates is seen in (17) and is derived using (15) and (16).

$$\mathrm{a} = y + \frac{x}{\tan(\varphi)} \quad (15)$$

$$\mathrm{z} = a \cdot \sin(\varphi) \quad (16)$$

$$\therefore \quad z = \left(y + \frac{x}{\tan(\varphi)}\right)\sin(\varphi)$$

$$= y\sin(\varphi) + \frac{x\sin(\varphi)}{\tan(\varphi)}$$

$$= x\cos(\varphi) + y\sin(\varphi)$$

$$z = x\cos(\varphi) + y\sin(\varphi) \quad (17)$$

If corrected for actual KN and HZ values for each weight shift using (18), the line will pass through the point (x, y) for any arbitrary weight shift from the neutral position, i.e. Inclining weights in initial position. Further, knowing that the x-coordinate is equal to TCG, and the y-coordinate equal to VCG as represented by (19) and (20) respectively, equation (21) is obtained.

$$z = KN - HZ \quad (18)$$

$$x = TCG \quad (19)$$

$$y = VCG \quad (20)$$

$$KN - HZ = TCG\cos(\varphi) + VCG\sin(\varphi) \quad (21)$$

Using equation (21) and solving for VCG and TCG, we get equations (22) and (23).

$$VCG = \frac{TCG\cos(\varphi) - KN + HZ}{\sin(\varphi)} \quad (22)$$

$$TCG = \frac{-VCG\sin(\varphi) + KN - HZ}{\cos(\varphi)} \quad (23)$$

The method takes advantage of the fact that both VCG and TCG need to be located on the PL line in the initial condition and to be kept constant in this position for each individual weight shift, i.e. the initial VCG_0 and TCG_0 are kept constant on this line, while the overall system TCG is shifted a distance G_0G_i for each shift i as represented by (24) and (25).

$$TCG_0 = TCG_i \quad (24)$$

$$VCG_0 = VCG_i \quad (25)$$

There are, as a result, two equations to derive the two unknown parameters and by using (22) and (23), and following some deduction, (24) results in a solution for VCG given by (26) and (25) in a solution for TCG given by (27) in their most general form:

$$VCG = \frac{(KN_i - HZ_i)\cos(\varphi_0) - (KN_0 - HZ_0)\cos(\varphi_i)}{\cos(\varphi_0)\sin(\varphi_i) - \sin(\varphi_0)\cos(\varphi_i)} \quad (26)$$

$$TCG = \frac{(KN_i - HZ_i)\sin(\varphi_0) - (KN_0 - HZ_0)\sin(\varphi_i)}{\cos(\varphi_i)\sin(\varphi_0) - \sin(\varphi_i)\cos(\varphi_0)} \quad (27)$$

The equations can further be simplified using the trigonometric relations in (28) and (29) and knowing that the heeling arm in the neutral position HZ_0 needs to be zero, this results in (30) and (31).

$$\cos(\varphi_0)\sin(\varphi_i) - \sin(\varphi_0)\cos(\varphi_i) = \sin(\varphi_i - \varphi_0) \quad (28)$$

$$\cos(\varphi_i)\sin(\varphi_0) - \sin(\varphi_i)\cos(\varphi_0) = \sin(\varphi_0 - \varphi_i) \quad (29)$$

$$VCG = \frac{(KN_i - HZ_i)\cos(\varphi_0) - (KN_0)\cos(\varphi_i)}{\sin(\varphi_i - \varphi_0)} \quad (30)$$

$$TCG = \frac{(KN_i - HZ_i)\sin(\varphi_0) - (KN_0)\sin(\varphi_i)}{\sin(\varphi_0 - \varphi_i)} \quad (31)$$

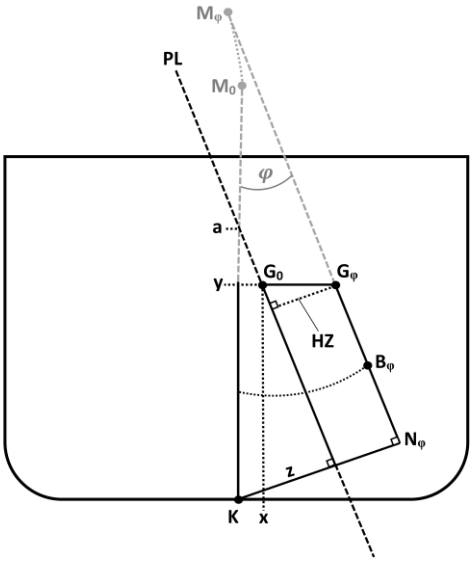

Figure 5. Main parameters of the Polar method.

The *Polar* method can in theory be used to calculate VCG directly for any arbitrary shift from the neutral position, but to account for

other sources of errors, it is recommended to utilise a least square linear regression similar to that of the *Classical* method, by plotting the denominator against the numerator and calculating the regression slope.

4. VALIDITY ASSESSMENT

4.1 Approach

For assessing the mathematical validity and accuracy of the *Classical* and *Polar* calculation methods, a technical inclining experiment has been performed using a completely box shaped vessel, enabling first principles calculations. The main particulars of the box shaped vessel are seen in table 1, and the lightweight particulars of the vessel are seen in table 2.

Table 1. Main particulars of box shaped vessel.

Vessel type	L_{BP} [m]	B [m]	D [m]	T [m]
Box-shape	100	40	40	10

Table 2. Lightweight particulars of box shaped vessel.

Para.	Δ [tonnes]	LCG [m]	TCG [m]	VCG [m]
Val.	392400	50.00	0.00	12.00

The technical inclining experiment has been performed using small heel angles of 4° in line with the IMO requirements and larger heel angles of 10° to clearly show the limitation of the *Classical* method when it comes to larger heel angles. Both calculation methods have been applied using a least squares linear regression, and 8 weight shifts.

4.2 Result

The result from the technical inclining experiment is presented in table 3. It is clear that the *Classical* method is highly dependent on the heel angle magnitude, and will produce result with increasing errors with increasing heel angle. This finding is in line with the earlier studies by Karolius & Vassalos (2008a-b). It is further shown that the *Polar* method produce exact results with no errors compared to the actual VCG value.

Table 3. Validity assessment results.

	Classical		Polar	
Heel [°]	4	10	4	10
$VCG_{calculated}$ [m]	11.97	11.84	12.00	12.00
VCG_{actual} [m]	12.00	12.00	12.00	12.00
Error [%]	0.21	1.34	0.00	0.00
Error [mm]	25.36	161.29	0.00	0.00

5. STABILITY AND SAFETY ASSESMENT

5.1 Approach

For most vessels, it is the damage stability requirements that is governing and limits the operational envelope. For the sake of illustrating possible implications on stability, the probabilistic damage stability requirements in accordance with SOLAS Reg. II-1/7-8 (IMO, 2009) have been utilised. The attained index A for the operational VCG and the corrected VCG have been calculated, making it possible to gauge the impact of incorrect VCG calculation using (32).

$$Risk = 1 - A \tag{32}$$

Knowing the ensuing risk, this allows obtaining a measure of false safety inherent in the vessel as a result of the inaccurate VCG calculated using the *Classical* method

5.2 Test vessels

The test vessels used in the following for assessing possible implications on stability performance comprise one *RoPax* and one *Container* vessel. These are the two vessels identified in the study by Karolius & Vassalos (2018a) to have highest underestimated VCG values corresponding to Case 1 explained in Section 2.3 above. The vessels main particulars

are presented in table 4, and the corrected VCG values are presented in table 5.

Table 4. Test vessels utilised in the study.

Vessel type	L_{BP} [m]	B [m]	D [m]	C_B [m]
RoPax	195.3	25.8	14.8	0.79
Cont. vessel	320.00	48.20	27.20	0.76

Table 5. Corrected VCG values.

Vessel	VCG [m]	Correction [mm]	VCGcorr [m]
RoPax	13.171	41.478	13.213
Cont. vessel	17.228	60.813	17.288

5.3 Results

Table 6 presents the false safety inherent in the vessel as a result of the inaccurate VCG calculated using the *Classical* method. For both vessels, an error in safety estimation of around 3% is seen due to the error in VCG. The table further presents the difference in number of capsize cases and it is seen that the *RoPax* vessel has 6 additional capsize cases not accounted for due to the error in VCG. This corresponds to a 7.5% error in estimated capsize cases. The *Container* vessel has 37 additional capsize cases, corresponding to a 4% error in estimation.

Table 6. Underestimated VCG translated to overestimated probabilistic damage stability performance, i.e. false safety.

Vessel	LW case	A	Risk = 1-A	Capsize cases
RoPax	VCG [m]	0.725	0.275	74
	VCG_{corr} [m]	0.717	0.283	80
	Difference [%]	1.11	2.83	7.50
Cont. Vessel	VCG [m]	0.711	0.289	896
	VCG_{corr} [m]	0.702	0.298	933
	Difference [%]	1.28	3.02	3.96

6. CONCLUDING REMARKS

As can be seen from the technical inclining experiment, the *Classical* method is highly dependent on heel angle magnitude and may produce unacceptable errors that could affect stability performance. The additional measures imposed by IMO are unnecessary when applying the *Polar* method, as no reference is made to the metacentre in the equation. The *Polar* method produce accurate results for any floating position, in terms of draught, heel magnitude and initial heel as they utilise actual KN values corresponding to each floating position. This reduces the possibility of making mistakes and can therefore be considered more reliable and flexible than the *Classical* method.

As the Classical calculation method was developed in the late 17th century (Hoste, 1693) when detailed software models were not available, the limiting assumptions makes sense as it enables upright hydrostatics to be utilised. Today, however, the strife is towards higher accuracy and there exists a range of tools for this purpose, making such simplifications and requisite assumptions obsolete.

The results further highlight the importance of achieving correct VCG value following the inclining experiment for a safe vessel design, as even minor errors in the order of millimetres may translate into extensive weights and moments compromising safety. The most common argument for maintaining the *Classical* method is that the errors are small and insignificant in comparison with other sources of errors, but the validity of this argument can be questioned.

Considering the results from this study, the industry should be more critical when applying the *Classical* method and it may even be time to replace it with better and more flexible calculation methods. It is at least important for the industry to know that there are other more reliable alternatives to the *Classical* method and should be accounted for in the regulations and guidelines in use today.

7. REFERENCES

Hoste, Paul., 1697, "Théorie de la Construction des Vais-seaux" ("Theory of the Construction of Vessels"), Arisson & Posule, Lyon.

International Maritime Organization, 2016, SDC 3/WP.5, Development of Second Generation Intact Stability Criteria. Report of the Working Group, London, UK.

International Maritime Organization, 2009, "Reg. II-1/5 of SOLAS Consolidated Edition 2009", as adopted in IMO Res. MSC 216(82)), 2006.

International Maritime Organization, 2008, "Part B Annex I of the International Code on Intact Stability 2008", as adopted in IMO Res. MSC.267(85), 2008.

International Maritime Organization, 2000, "Reg. II/2.7 of the International Code of Safety for High- Speed Craft Code, 2008 Edition", as adopted in IMO Res. MSC.97(73)

International Maritime Organization, 1977, "Reg. III/9 of the Torremolinos International Convention for the Safety of Fishing Vessels, as modified by the 1993 Protocol (SFV/Torremolinos Convention)".

International Organization for Standardization, 2013, "ISO 12217-2:2013 – Small craft – Stability and buoyancy assessment and categorization".

Karolius, Kristian and Vassalos, Dracos, 2018a, "Tearing down the wall – The inclining experiment", Ocean Engineering Vol. 148, pp 442-475.

Karolius, Kristian and Vassalos, Dracos, 2018b, "Weight and buoyancy is the foundation in design: Get it right", IMDC 2018: 13th International Marine Design Conference.

Calculation of Restoring Moment in Ship roll motion through Numerical Simulation

S. S. Kianejad, *Australian Maritime College, Australia,* seyed.kianejadtejenaki@utas.edu.au

Hossein Enshaei, *Australian Maritime College, Australia,* hossein.enshaei@utas.edu.au

Jonathan Duffy, *Australian Maritime College, Australia,* j.duffy@utas.edu.au

Nazanin Ansarifard, *Australian Maritime College, Australia,* nazanin.ansarifard@utas.edu.au

ABSTRACT

Accurate calculation of restoring moment, virtual mass moment of inertia and damping moment increases accuracy of a ship's dynamic stability simulation. The current methods of approximating the roll restoring moment are based on hydrostatic calculations. These methods overlook dynamic conditions and the effects of pressure distribution around the body. In the current study, a CFD approach is adopted based on a harmonic excited roll motion method to investigate roll motion characteristics and calculate the restoring moment in dynamic conditions. This investigation considers multiple degrees of freedom (DOF) at different Froude numbers, bare-hull and fully appended conditions. The results show that the restoring moment in dynamic condition is larger than static condition.

Keywords: *Restoring moment, damping moment, moment of inertia, CFD, harmonic excited roll motion.*

1. INTRODUCTION

A ship in the rough sea condition experiences non-linear translational and rotational motions. These motions change the performance of the ship, and decrease safety. There is a greater concern regarding roll motion compared to other motions because the damping and restoring moments which resist against the roll motion increment, are lower.

Capsizing of a ship can occur both in resonant and non-resonant conditions (Wawrzyński and Krata, 2016). The non-resonant capsizing can occur in two different situations; when a ship experiences a large roll motion in a seaway and is also acted upon by gusty wind, and in surf-riding and broaching phenomena. The external forces and moments induced by regular waves at a specific frequency can excite the resonance condition. Capsizing in the resonance condition can occur due to two different phenomena of synchronous and parametric roll, where the encounter frequency is equal and two times of the ship's natural roll frequency, respectively. The parametric roll is most probable to arise in some types of ships like container ship in head sea condition when the wavelength is equal to the ship length. While all ship types may be subjected to the synchronous rolling in beam sea conditions. This condition is very dangerous since, small external forces and moments can impose a large roll angle.

In order to investigate a ship's motions, there are generally three approaches including

experiments, CFD and equation based methods. Direct investigation of different failure modes of dynamic stability is time-consuming, therefore, most studies have been conducted using the equation based methods. The accuracy of these methods depends on several hydrodynamic coefficients like mass and added mass moment of inertia, damping and restoring. However, the magnitude and effects of restoring moment at resonance condition is much larger than the other parts. Thus, computing the precise magnitude of the restoring part is essential.

In this regard, Neves (2002), Neves et al. (2002), Holden et al. (2007) used a 3-DOF non-linear model to investigate the effects of heave, pitch and roll motions on the restoring moment. Although this model was simpler than 6-DOF, the computation time of forces and coupled motions was significant. Oh et al. (2000) found that the effects of heave and pitch motions on righting arm are small, hence modelling of the coupled heave, pitch and roll motions could be simplified. They used a 1-DOF model by adding the coupled heave and pitch motions effects on the restoring moment, which was approximated by a third order fitting polynomial equation. In the case of regular waves, Bulian et al. (2006) introduced a 1.5-DOF model based on a quasi-static approach, where the half DOF is related to the coupled heave and pitch motions. They estimated the righting arm at different angles based on the height and position of the wave crest regarding the ship's length using polynomial fitting function and Fourier series. In case of irregular waves, they introduced Grim's effective wave to estimate the righting moment which provides a conservative approximation. Vidic (2011), Dunwoody (1989) assumed a linear relation between changes of metacentric height (GM) of a ship in the calm water and wave conditions based on the wave height. Silva et al. (2005) proposed that the restoring moment can be predicted accurately by computing the pressure distribution over the wetted surface area, however, this requires long running simulations. They suggested a fifth-order nonlinear polynomial function instead of a direct calculation of the righting arm; however, it may not be feasible for some types of ships. Song et al. (2013) developed a 1-DOF method to predict the parametric roll that used a GM spectrum considering the coupled heave and pitch motions. The variation of righting arm was estimated by combining the righting arm in the calm water and the fluctuation of the GM. The GM spectrum was computed regarding the heave motion, pitch motion and wave elevation.

What is apparent according to the literature, a ship in the parametric roll and dead ship condition experiences the resonance condition where the roll angle increases over the time. The existing methods of predicting the restoring moment fail to take into account the influence of dynamic pressure on the ship's hull. Adding the dynamic pressure to the hydrostatic pressure improves calculation of the restoring moment in the dynamic conditions. To replicate the harmonic roll motion of a ship in these conditions, a harmonic excited roll motion (HERM) technique is used. In this study a model of a container ship is excited to compute the restoring moment using CFD simulations. Additionally, the effects of appendages, forward speed and number of degrees of freedom (DOF) on the roll restoring moments at a frequency close to the natural frequency of model are investigated.

2. SHIP GEOMETRY

A model of a Post-Panamax containership in bare and fully appended conditions was used. The appendages are rudder, propeller and bilge keels. The five bilge keels were installed on either side of the model in the middle section. The model was utilized for benchmarking at Hamburg ship model basin and more

information about the model can be found in (Moctar et al., 2012). A snapshot of the model is shown in Figure 1 and main particulars of the model and ship are presented in Table 1.

Table 1 Main characteristics of model and full-scale ship

Main dimension	Full scale	Model
L_{pp} [m]	355	5.97
L_{wl} [m]	360.91	6.07
B_{wl} [m]	51	0.86
D [m]	14	0.24
C_B	0.6544	0.65
V [m^3]	165868.5	0.79
KM [m]	25.05	0.42
GM [m]	1.37	0.02
KG [m]	23.68	0.39
T_0 [s]	38.17	4.95
I_{xx} [m]	20.25	0.34
I_{yy} [m]	88.19	1.48
I_{zz} [m]	88.49	1.49

Figure 1 Hull geometry of the Post-Panamax container ship

3. NUMERICAL MODELLING

The present simulations were conducted by commercial RANS solver STAR-CCM+ and details of the selected approach are presented in the following sections. The model was excited in various conditions as presented in Table 2 to investigate the influence of several parameters on the roll motion characteristics. The fully appended (Full) and bare hull models were excited under a 25 Nm roll exciting moment at a frequency of 1.4 Rad/s and different Froude numbers (Fn.). The degrees of freedom (DOF) of the model was varied from only roll (R) motion to 6DOF. In the Table 2 heave, pitch and sway motions are shown by H, P and S, respectively.

Table 2 Test conditions to calculate the restoring moment in dynamic condition.

Case No.	Fn.	Excitation frequency (Rad/s)	DOF	Model condition	Roll exciting moment (Nm)
1	0	1.4	R	Full	25
2	0	1.4	RH	Full	25
3	0	1.4	RP	Full	25
4	0	1.4	RS	Full	25
5	0	1.4	6DOF	Full	25
6	0	1.4	6DOF	Bare	25
7	0.1	1.4	R	Full	25
8	0.1	1.4	RH	Full	25
9	0.1	1.4	RP	Full	25
10	0.1	1.4	RS	Full	25
11	0.1	1.4	6DOF	Full	25
12	0.1	1.4	6DOF	Bare	25
13	0.19	1.4	R	Full	25
14	0.19	1.4	RH	Full	25
15	0.19	1.4	RP	Full	25
16	0.19	1.4	RS	Full	25
17	0.19	1.4	6DOF	Full	25
18	0.19	1.4	6DOF	Bare	25

3.1 Governing equations and physics modelling

The incompressible averaged continuity and momentum equations in terms of tensor form and based on Cartesian coordinates were adopted to conduct simulations as follows (Ferziger et al., 1997):

$$\frac{\partial(\rho\bar{u}_i)}{\partial x_i} = 0 \tag{1}$$

$$\frac{\partial(\rho\bar{u}_i)}{\partial t} + \frac{\partial}{\partial x_j}(\rho\bar{u}_i\bar{u}_j + \rho\overline{u_i'u_j'}) = -\frac{\partial\bar{p}}{\partial x_i} + \frac{\partial\bar{\tau}_{ij}}{\partial x_j} \tag{2}$$

$$\bar{\tau}_{ij} = \mu\left(\frac{\partial\bar{u}_i}{\partial x_j} + \frac{\partial\bar{u}_j}{\partial x_i}\right) \tag{3}$$

The indices of i and j determine the flow direction of x and y-axes. ρ and μ are density and viscosity, $\bar{\tau}_{ij}$ and $\rho\overline{u_i'u_j'}$ reflect the mean viscous stress tensor and the mean Reynolds

stress tensor, respectively. $\overline{u}_i$ and $\overline{P}$ demonstrate the time-averaged velocity and pressure. The solver uses finite volume method to simulate the flow around the model and to link the continuity and momentum equations utilizes a predictor-corrector method. The realizable k–ε turbulence model was adopted to reduce the uncertainty of the stress tensor. This type of turbulence model is precise and economical in terms of time compared to other types of turbulence models (Tezdogan et al., 2015). In order to capture the free surface changes, the "volume of fluid" (VOF) was adopted and mesh size at that region was reduced to solve the interface between two phases of the water and air. The solver uses a segregated flow model to solve the continuity and momentum equations in an uncoupled condition and the second order upwind scheme and the Simple algorithm was utilized to discretize the governing equations. The dynamic fluid body interaction (DFBI) approach was employed to consider the effects of forces on the model like a real sea condition. Courant number (CFL) was used to determine the time step. The magnitude of Courant number was selected less than one for each cell to have numerical stability.

3.2 Meshing structure

An overset mesh method was used to simulate the model motions. It includes the overset and a background region. The overset region is connected to the model and has motions in the same direction of the model inside of a stationary background region (Field, 2013). The cell size of the overset region was set small enough to capture the flow separation, eddy, boundary layer and wave generation over harmonic roll motion. Four types of meshers were used to generate the mesh including trimmed, prism layer, surface and automatic surface repair. The trimmed mesher was used to generate high-quality mesh and the prism layer was utilized to create perpendicular prismatic cells close to the model surface to capture the velocity changes and boundary layer. Three volumetric control zones were considered to reduce the size of cells, especially around the model and free surface to resolve sophisticated flow characteristics. An overlap volumetric control zone was used to match the cell size in the background and overset regions and minimize the possibility of solution divergence. An illustrations of the computational mesh are shown in Figure 2.

3.3 Boundary and initial conditions

Proper selection of the initial and boundary conditions reduces the simulation time and increases precision of the results. The upstream, top, bottom and lateral boundaries were set as velocity inlet, while the outlet boundary was set as pressure outlet to prevent any backflow. Determining the lateral, top and bottom boundaries as velocity inlet removes the velocity gradient due to the interaction between the walls and flow and directs the current towards the outlet boundary condition. Therefore, using such boundary conditions reduces the size of the flow domain. The magnitude of velocity for both the initial and boundary conditions was set according to the flat wave condition. The initial outlet boundary was set as hydrostatic pressure.

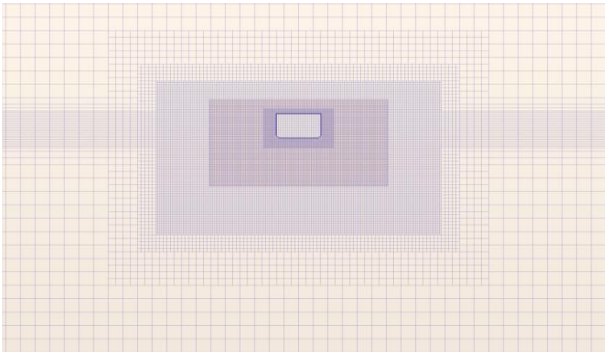

Figure 2 Cross section of the computation mesh

3.4 Methodology

The roll motion equation of a ship is governed by Newton's second law:

$$(I_{44}+\delta I_{44})\frac{\partial^2\varphi}{\partial t^2}+N_{44}\frac{\partial\varphi}{\partial t}+S_{44}\varphi=M_{E44}(t) \qquad (4)$$

Where the roll mass and added mass moment of inertia coefficients are I_{44} and δI_{44} respectively. N_{44} is roll damping coefficient, S_{44} reflects the roll restoring coefficient and M_{E44} is an external roll exciting moment. Upon simulation of the fluid field around the body, exerted forces and moments on the body were computed in the earth-fixed coordinate system. The forces and moments were transferred into the body local coordinate system, which was set at the centre of gravity. In the following step, the velocity and acceleration of body were computed by solving the motion's equations and transferred back to the earth-fixed coordinate system to locate the body (Simonsen et al., 2013). For a range of frequencies lower and close to the resonance frequency, the exciting moment and the virtual roll moment of inertia (mass moment plus added mass moment of inertia) contribute to increase the roll motion, while the damping and restoring moments oppose the roll motion. Whereas, for a range of frequencies higher than the resonance frequency and at large roll angles the actions of these terms are different. The exciting moment at high frequency acts on the model quicker, which means that when the model experiences a larger roll angle, the exciting moment acts in a reverse direction due to the large generated phase shift between the roll motion and exciting moment. Therefore, the restoring, damping and exciting moments oppose the moment of inertia to reduce the roll angle.

The excitation frequency is very close to the natural roll frequency of model (the natural frequency of the model is 1.38 Rad/s). By computing the virtual mass moment of inertia based on (Kianejad et al., 2017), damping moment by (Handschel and Abdel-Maksoud, 2014) and knowing the exciting moment over different roll angles, the restoring moment is extracted. According to Kianejad's method, the angular acceleration is maximized at a maximum roll angle while the angular velocity is zero (damping moment will be negligible), the added mass moment of inertia is calculated by the equation below:

$$\delta I_{44}=\frac{M_{E44}(t)-S_{44}\varphi}{\frac{\partial^2\varphi}{\partial t^2}}-I_{44} \qquad (5)$$

Where, the restoring moment was calculated from the hydrostatic calculation and considering a quasi static condition at the maximum roll angle. The mass moment of inertia is the model characteristic and the acceleration is calculated by the simulations. The damping moments were computed based on the energy conservation method independently using harmonic excited roll motion (HERM) technique (Handschel and Abdel-Maksoud, 2014). In one cycle of the roll motion where the start-up effects are vanished, the work done by the exciting moment is equal to the dissipated damping energy, and the roll damping can be calculated by equation below:

$$N_{44}\frac{\partial\varphi}{\partial t}=\frac{M_{E44}(t)\sin\vartheta}{\omega\varphi_a}\frac{\partial\varphi}{\partial t} \qquad (6)$$

Where ω is frequency and φ_a is maximum roll angle over one cycle of the roll motion. ϑ reflects the phase shift between the roll exciting moment and roll angle. Deducting damping, virtual mass moment of inertia terms from the exciting moment yields the residual moment, which is the restoring moment as follows:

$$S_{44}\varphi=M_{E44}(t)-(I_{44}+\delta I_{44})\frac{\partial^2\varphi}{\partial t^2}-N_{44}\frac{\partial\varphi}{\partial t} \qquad (7)$$

The numerical method was used to investigate the impact of effective parameters (different degrees of freedom, different Froude numbers and appendages) on the roll motion characteristics and hydrodynamic coefficients.

3.5 Mesh study

A mesh study was carried out for three mesh configurations to study the influence of each of them on the roll motion characteristics. In this section, the model was exposed to a 5.5 Nm roll exciting moment at a frequency of 1.39 Rad/s, which is close to the natural roll frequency of the model. The resistance of the model at a forward speed of 1.54 m/s was computed to choose the proper mesh configuration that could precisely calculate pressure and shear forces. The mesh configurations with 2.6, 3.6 and 5.8 million cells were considered. The increment for the cells was mainly focussed on the overset region to refine the quality of mesh. The initial and boundary conditions were the same while the number of mesh cells varied. The results of the simulations are compared with experimental data (Handschel and Abdel-Maksoud, 2014) shown in Table 3. The numerical simulations were performed considering the model free in 6DOF to replicate the physical model scale tests. Overall, the simulation results have larger values than the experimental values. It was found that the 5.8 million cells produces the most reliable results and provides the best correlation with the experimental data. The y+ value of the fine mesh configuration at Froude number 0.19 is 5 (**Error! Reference source not found.**). This magnitude of y+ and using realizable k–ε can reliably calculate shear forces on the model. The maximum roll angle and drag have 2.64% and 2.42% difference with experimental measurement, respectively. It shows this numerical approach has capability to simulate the roll motion accurately. Hence, it was used to simulate the roll motion characteristics in further simulations.

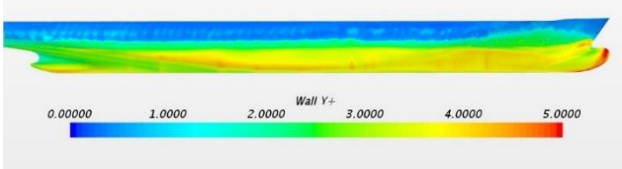

Figure 3 The y+ value of the model at Fn=0.19.

4. RESULTS AND DISCUSSION

4.1 Roll motion characteristics

The time histories of the roll, angular velocity, angular acceleration and roll moment for the bare and fully appended (Full) models are presented in

Figure 4 to Figure 7. The magnitude of exciting moment was 25 Nm at a frequency of 1.4 Rad/s where Froude number changes from 0 to 0.19. The fully appended model was simulated in different degrees of freedom (DOF) to investigate the effect of each degree on the roll motion characteristics. It can be seen in Figure 4 to Figure 7 that equipping the model with appendages and increasing the forward speed reduce the roll motion characteristics. Both appendages and forward speed increase the pressure difference between two sides of the hull and create a larger moment which impede the roll motion. The impact of appendages is more dominant at a larger roll angle because of the higher induced angular velocity and moment. Reduction of the maximum roll angle as a result of increasing the forward speed is depicted in Figure 4, and it is clear that reduction is more significant at Fn=0.19. At Froude number zero, considering the model free in only roll motion (R) experiences smaller roll motion characteristics, while increasing the DOF of the model such as being free in roll and heave (RH) slightly increases the roll motion characteristics. Considering the model free in roll and pitch (RP) and roll and sway (RS) conditions, increase the roll angle, however, the maximum roll angles

Table 3 Mesh convergence study and comparing by experimental measurement.

	Exp.	5.8 million	Difference	3.6 million	Difference	2.6 million	Difference
Roll	14.42	14.8	2.64%	15	4.02%	15.7	8.88%
Roll Moment	-	42.44	-	44.5	-	50	-
Acceleration	-	0.52	-	0.53	-	0.55	-
Velocity	-	0.36	-	0.37	-	0.38	-
Drag	26.46	27.1	2.42%	28.14	6.35%	30.5	15.27%

are still smaller than 6 DOF conditions. Increasing the forward speed reduces the pitch and sway motions, and subsequently, their contribution on the maximum roll angle. The contribution of different motions at Froude number 0.1 and 0.19 are similar as shown in Figure 4, while the model at 6DOF still experiences larger roll angle.

When the phase shift between the exciting moment and roll angle is near to 90 degrees, the model experiences larger roll motion. Increasing the forward speed reduces the phase shift (Figure 4). Hence, the roll motion characteristics decrease for the higher froude numbers. Although, the fully appended model free in 6 DOF experiences larger phase shift compared to the bare hull model and closer to 90 degrees, it generates smaller roll motion characteristics. Because the appendages create a moment to resist development of the roll angle. For the model free in roll and sway (RS) there is a smaller phase shift compared to the other DOF conditions. On the other hand, the coupled roll-pitch (RP) motion has larger phase shift.

As shown in Figure 5 and Figure 6 the angular velocity and acceleration of the models under the same roll exciting moment are identical for the first cycle at different forward speeds. However, in the following cycles, where both amplitudes increase, rising the forward speed decreases the amplitude of angular velocity and acceleration. It is also shown that the reduction at higher speed is more significant. The bare and fully appended models free in 6 DOF have larger angular velocity and acceleration compared to the other cases. The model free in coupled roll-pitch (RP) and coupled roll-sway (RS) generate larger angular velocity and acceleration compared to the model free in a single roll and the coupled roll-heave (RH) conditions. The roll moment is a function of acceleration and varies in different cycles according to the angular acceleration. The effects of DOF on the roll moment are shown in Figure 7. The amplitude of the roll moment varies about 20 percent from the single to 6DOF conditions. Decreasing the DOF decreases the amplitude of roll motion characteristics. Therefore, the simulation results are underestimated and cannot be applied for a real sea condition. It makes inevitable to extend our investigation up to 6DOF.

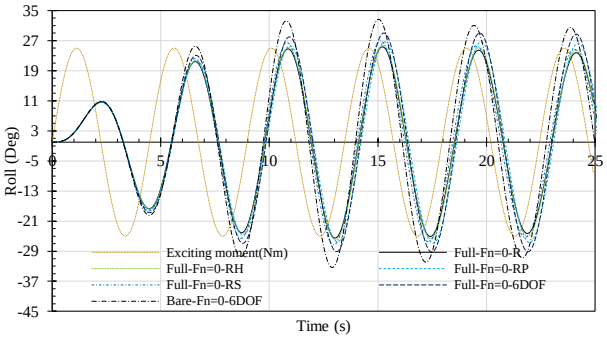

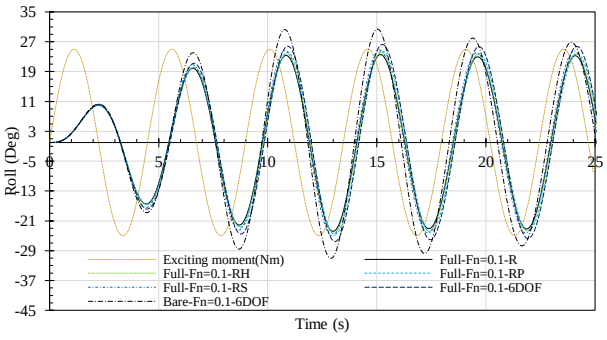

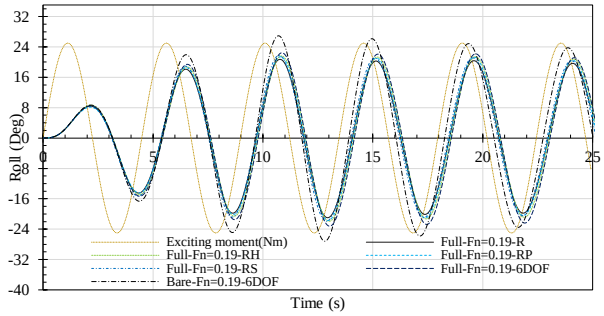

Figure 4 The roll angle trajectory under 25 Nm exciting moment at a frequency of 1.4 Rad/s, different Froude numbers (Fn.) and DOF.

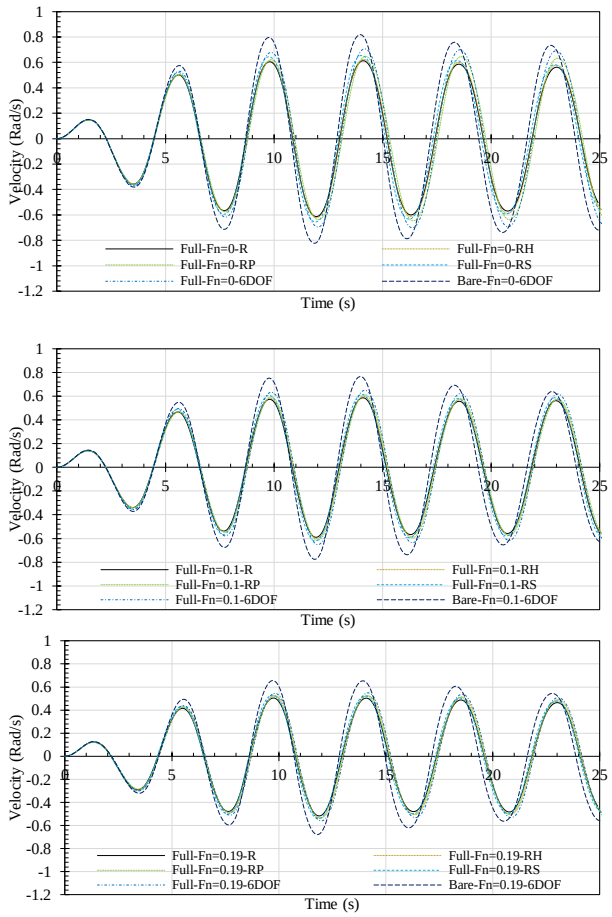

Figure 5 The angular velocity trajectory under 25 Nm exciting moment at a frequency of 1.4 Rad/s, different Froude numbers (Fn.) and DOF.

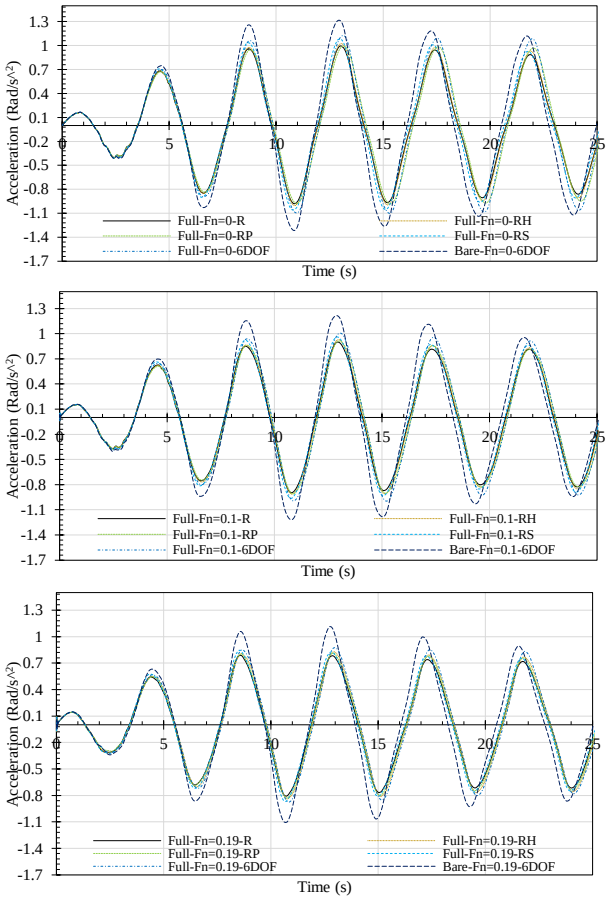

Figure 6 The angular acceleration trajectory under 25 Nm exciting moment at a frequency of 1.4 Rad/s, different Froude numbers (Fn.) and DOF.

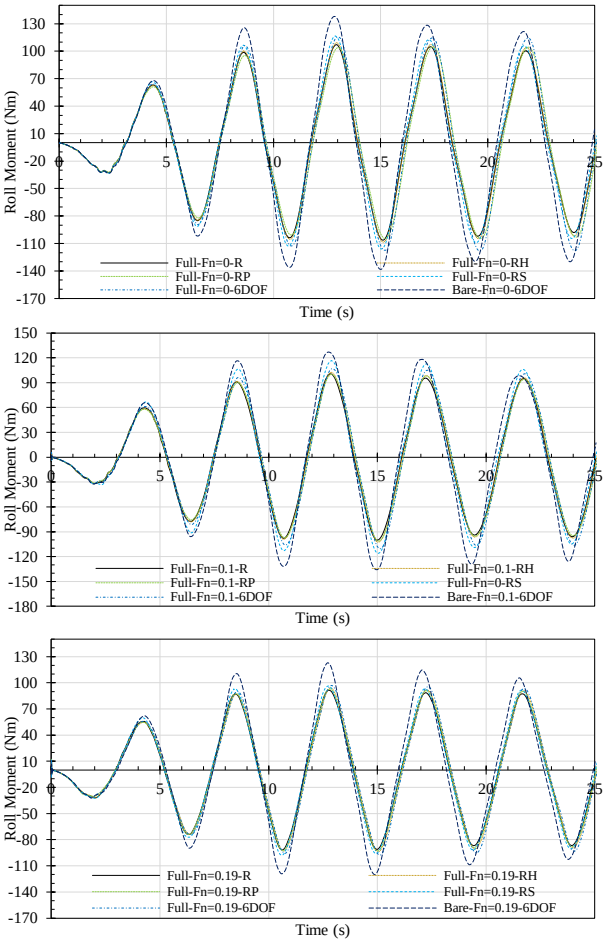

Figure 7 The roll moment trajectory under 25 Nm exciting moment at a frequency of 1.4 Rad/s, different Froude numbers (Fn.) and DOF.

4.2 Flow visualisation

Variation of vorticity magnitude in the middle section of the bare and fully appended models considering free in 6DOF at different forward speed are presented in Figure 8. The contours are recorded at about zero angle because the angular velocity and associated vorticity is in the maximum condition. It can be seen that at zero forward speed, the bilge keels generate larger vorticity compared to the bare hull model and changes the pressure distribution between two sides of the hull. Increasing the forward speed expands the vorticity along and across the hull. However, the magnitude of vorticity for the fully appended model is still larger than the bare hull. It means, the pressure differences between two sides of the fully appended model is larger at higher Froude numbers.

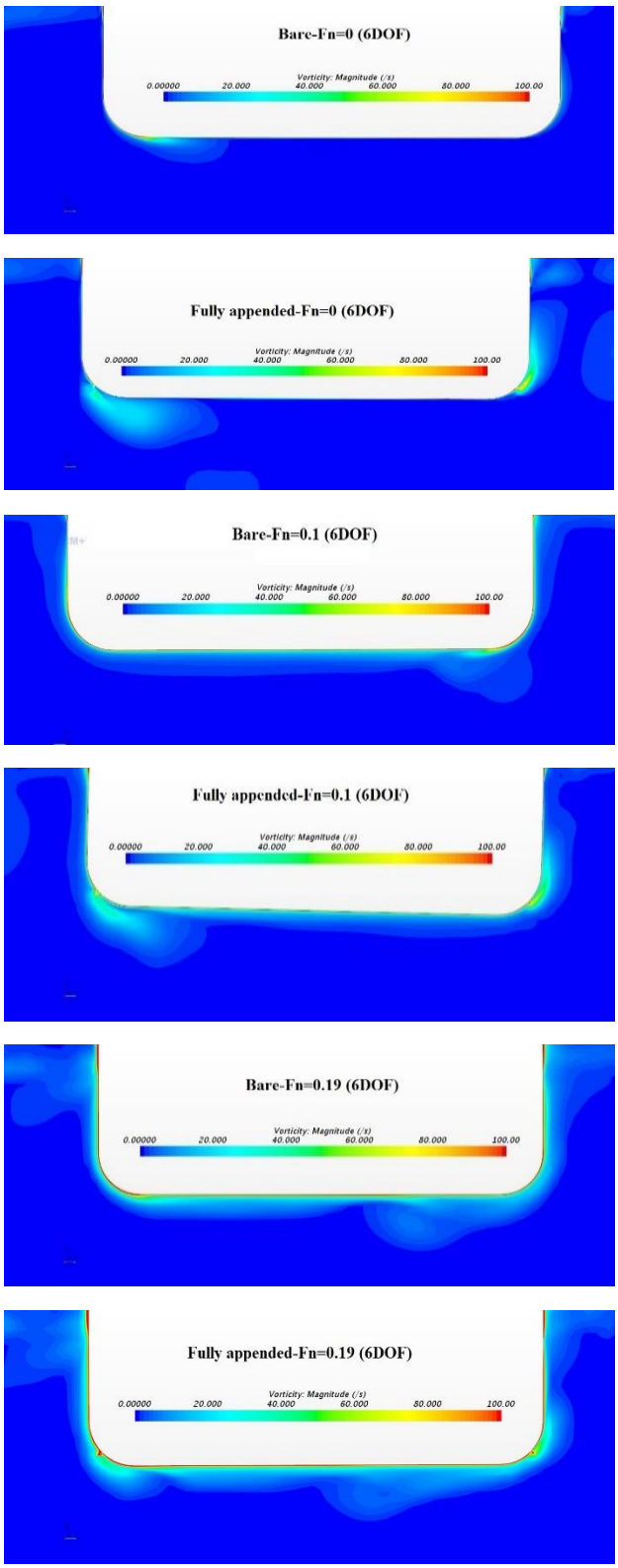

Figure 8 Comparison of the vorticity magnitude for the bare and fully appended models at different Froude numbers.

4.3 Magnitude of the roll inertia, damping and restoring moments

Variation of the mass and added mass moment of inertia, damping and restoring moments over different roll angles for both bare and fully appended models at different forward speeds and DOF are shown in Figure 9. The amplitude of exciting moment was 25 Nm at a frequency of 1.4 Rad/s. The negative sign was considered for the roll exciting moment and total mass moment of inertia (mass and added mass moment of inertia) because they collaborate to increase the roll motion and decrease the ship safety. On the other hand, the positive sign was considered for damping and restoring moment which oppose the roll motion development. The restoring moment has the largest value in all conditions. The mass moment of inertia has the second larger magnitude greater than the added moment of inertia. The damping moment has the smallest value, but it is an important parameter at a resonance frequency to counteract the roll motion increment. At the same time, there is a close interdependence between moments.

At the zero forward speed, the magnitude of dynamic restoring moment is larger than the static restoring moment at small roll angles due to the larger angular velocity and added dynamic pressure. Under the same exciting moment, the bare-hull model free in 6DOF experiences a larger virtual mass moment of inertia compared to the fully appended model, while it has smaller damping and restoring moments. Because the appendages by creating separation, increases the vorticity and reduces the acceleration or deceleration of fluid during roll motion (Figure 8). The appendages also generate a moment in opposite direction of the roll motion, causing the maximum roll angle to decrease. The coupled roll-pitch (RP) condition generates a larger damping and virtual moment of inertia due to the larger phase shift, while, the restoring moment remains smaller than the other DOF. The coupled roll-sway (RS) has the smaller damping moment with large restoring and virtual moment of inertia due to the smallest phase shift. It can be seen in Figure 9 that constraining the model free in 1 and 2 DOF reduces the magnitude of virtual mass moment of inertia significantly while increases the damping moment. On the other hand, the magnitude of restoring moment decreases slightly. Therefore, the magnitude of the contributor moments to increase the roll angle were declined and model in lower DOF experiences smaller roll motion characteristics.

The magnitude of restoring moment at higher speed for the small roll angle is relatively smaller than the zero forward speed conditions. Because the incoming flow reduces the pressure difference between two sides of the model. On the other hand, the magnitude of restoring moment at higher speed for the larger roll angles is relatively larger than the zero forward speed condition. The main reason of increase in pressure difference is due to the speed of flow which extend the separation and vorticities along the model. As can be seen from Figure 9, increasing forward speed increases the damping moment and reduces the virtual moment of inertia. The reduction in added moment of inertia at higher Froude number is significant and as result, the model experiences smaller roll motion. By increasing forward speed, the magnitude of virtual moment of inertia and damping moment varies for different DOF conditions. The coupled roll-heave (RH) has the larger damping and virtual moment of inertia. The results show that the restoring moment and damping moment for the fully appended model free in 6DOF at higher Froude number is larger than the bare hull model, while, the fully appended model has smaller virtual moment of inertia.

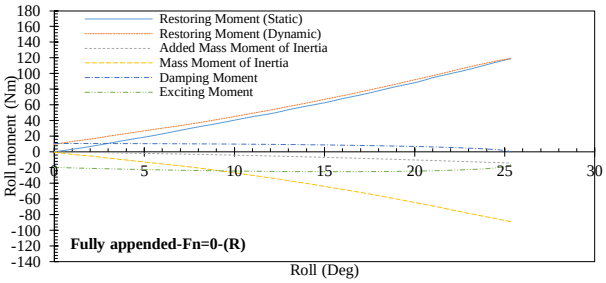
Restoring Moment (Static)
Restoring Moment (Dynamic)
Added Mass Moment of Inertia
Mass Moment of Inertia
Damping Moment
Exciting Moment
Roll moment (Nm)
Roll (Deg)
Fully appended-Fn=0-(R)

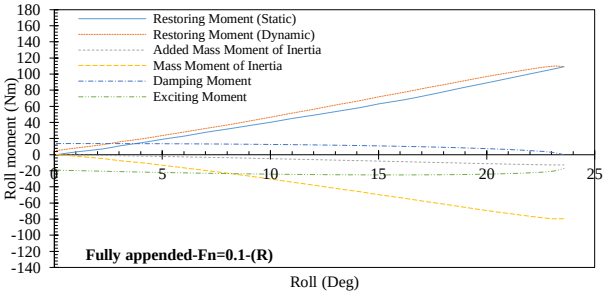
Restoring Moment (Static)
Restoring Moment (Dynamic)
Added Mass Moment of Inertia
Mass Moment of Inertia
Damping Moment
Exciting Moment
Roll moment (Nm)
Roll (Deg)
Fully appended-Fn=0.1-(R)

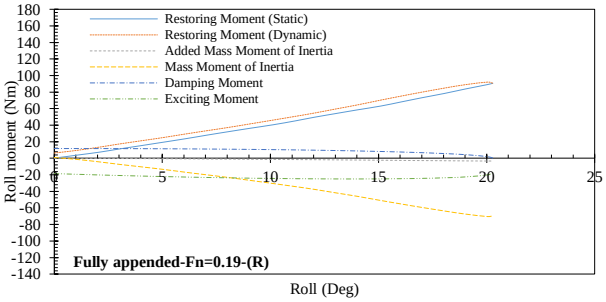
Restoring Moment (Static)
Restoring Moment (Dynamic)
Added Mass Moment of Inertia
Mass Moment of Inertia
Damping Moment
Exciting Moment
Roll moment (Nm)
Roll (Deg)
Fully appended-Fn=0.19-(R)

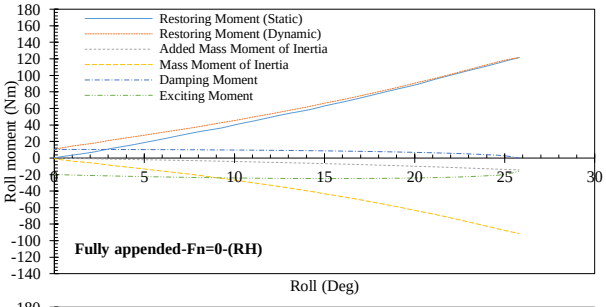
Restoring Moment (Static)
Restoring Moment (Dynamic)
Added Mass Moment of Inertia
Mass Moment of Inertia
Damping Moment
Exciting Moment
Roll moment (Nm)
Roll (Deg)
Fully appended-Fn=0-(RH)

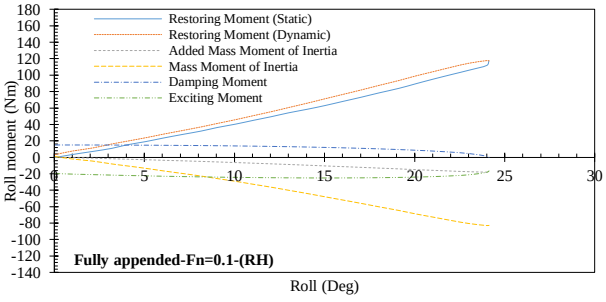
Restoring Moment (Static)
Restoring Moment (Dynamic)
Added Mass Moment of Inertia
Mass Moment of Inertia
Damping Moment
Exciting Moment
Roll moment (Nm)
Roll (Deg)
Fully appended-Fn=0.1-(RH)

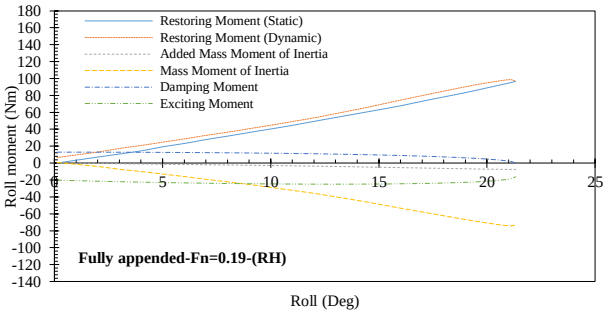
Restoring Moment (Static)
Restoring Moment (Dynamic)
Added Mass Moment of Inertia
Mass Moment of Inertia
Damping Moment
Exciting Moment
Roll moment (Nm)
Roll (Deg)
Fully appended-Fn=0.19-(RH)

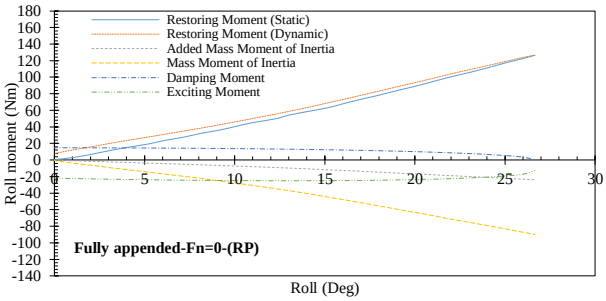
Restoring Moment (Static)
Restoring Moment (Dynamic)
Added Mass Moment of Inertia
Mass Moment of Inertia
Damping Moment
Exciting Moment
Roll moment (Nm)
Roll (Deg)
Fully appended-Fn=0-(RP)

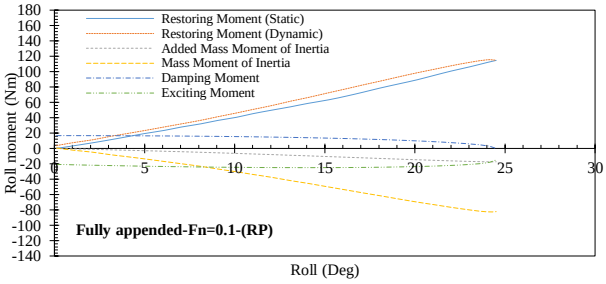
Restoring Moment (Static)
Restoring Moment (Dynamic)
Added Mass Moment of Inertia
Mass Moment of Inertia
Damping Moment
Exciting Moment
Roll moment (Nm)
Roll (Deg)
Fully appended-Fn=0.1-(RP)

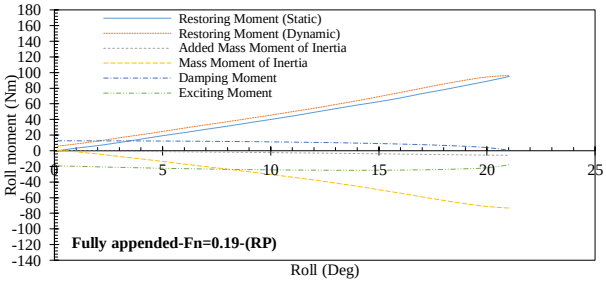
Restoring Moment (Static)
Restoring Moment (Dynamic)
Added Mass Moment of Inertia
Mass Moment of Inertia
Damping Moment
Exciting Moment
Roll moment (Nm)
Roll (Deg)
Fully appended-Fn=0.19-(RP)

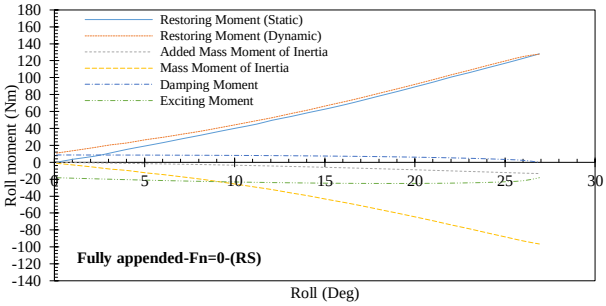
Restoring Moment (Static)
Restoring Moment (Dynamic)
Added Mass Moment of Inertia
Mass Moment of Inertia
Damping Moment
Exciting Moment
Roll moment (Nm)
Roll (Deg)
Fully appended-Fn=0-(RS)

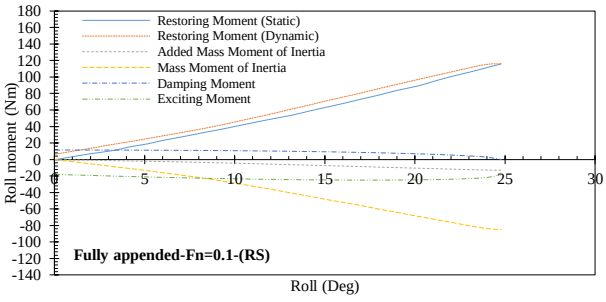
Restoring Moment (Static)
Restoring Moment (Dynamic)
Added Mass Moment of Inertia
Mass Moment of Inertia
Damping Moment
Exciting Moment
Roll moment (Nm)
Roll (Deg)
Fully appended-Fn=0.1-(RS)

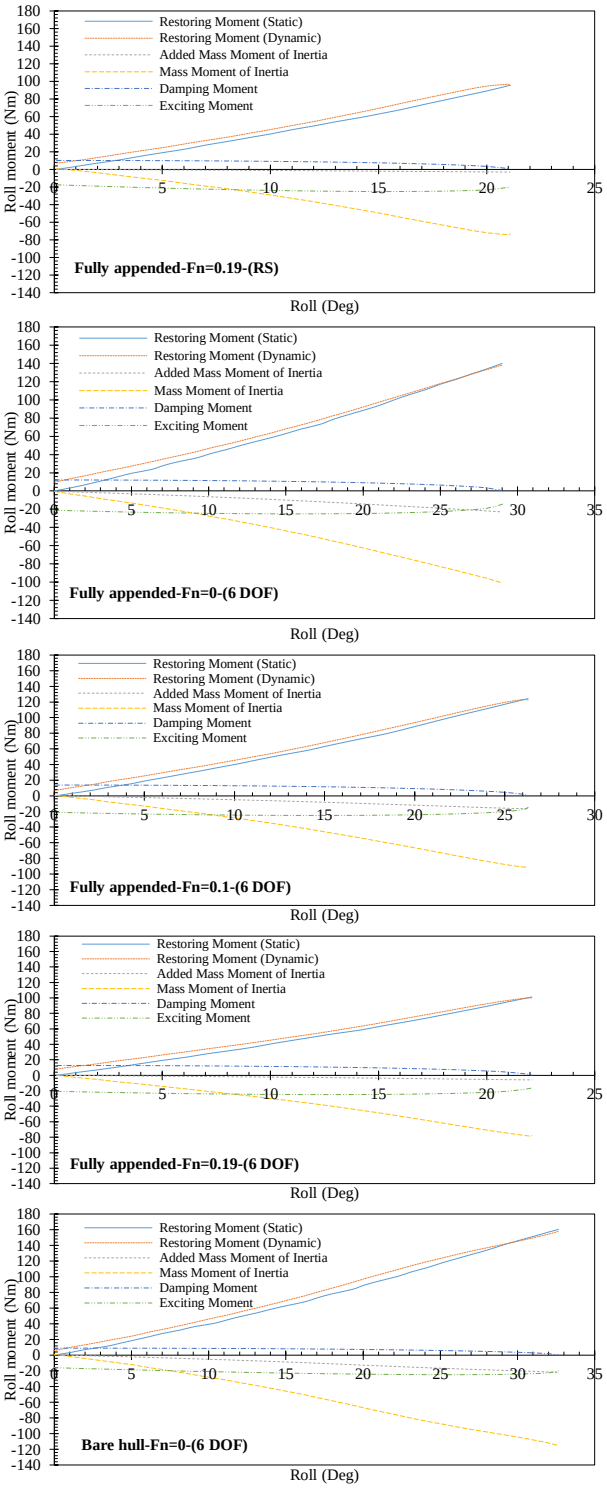

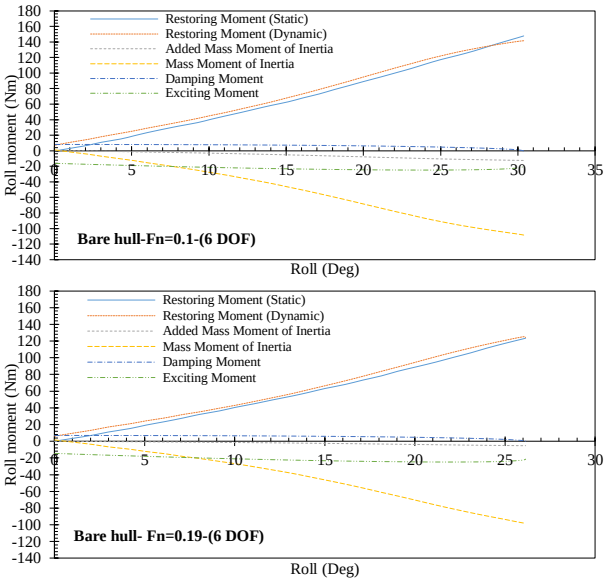

Figure 9 The variation of different roll moments versus the roll angle under 25 Nm exciting moment at a frequency of 1.4 Rad/s, bare and fully appended models, different Froude numbers and DOF conditions.

5. CONCLUDING REMARKS

CFD simulations were carried out to study the roll motion characteristics and to calculate the restoring moment over different roll angles in dynamic conditions. It was found that the appendages reduce the peak values of the motion characteristics, while they increase the phase shift between the exciting moment and roll trajectory. Increasing the forward speed reduces both maximum roll angle and phase shift. Decreasing the DOF decreases the motion characteristics.

The computed restoring moment in dynamic condition was larger than the static condition. That is especially about small roll angle, due to the angular velocity being at a highest value and dynamic pressure adds up to the hydrostatic pressure. The appendages increase the pressure difference between two sides of the model by generating the vorticity, therefore, the restoring moment of the fully appended condition is larger than the bare hull condition. Increasing DOF increases the magnitude of restoring

moment and the sway motion specifically has the greater contribution among other motions.

Increasing the Froude number increases the damping moment while reduces the added moment of inertia. The reduction of added moment of inertia is considerable at the highest Froude number, which is the main reason for smaller roll angle.

6. REFERENCES

BULIAN, G., FRANCESCUTTO, A., and LUGNI, C., 2006, "Theoretical, numerical and experimental study on the problem of ergodicity and 'practical ergodicity'with an application to parametric roll in longitudinal long crested irregular sea" Ocean engineering, 33**,** 1007-1043.

DUNWOODY, A. B., 1989, "ROLL OF A SHIP IN ASTERN SEAS--METACENTRIC HEIGHT SPECTRA", Journal of ship research, 33.

FERZIGER, J. H., PERIC, M., and LEONARD, A., 1997, "Computational methods for fluid dynamics", AIP.

FIELD, P. L., 2013, "Comparison of RANS and Potential Flow Force Computations for the ONR Tumblehome Hullfrom in Vertical Plane Radiation and Diffraction Problems", Virginia Tech.

HANDSCHEL, S. and ABDEL-MAKSOUD, M., 2014, "Improvement of the Harmonic Excited Roll Motion Technique for Estimating Roll Damping", Ship Technology Research, 61**,** 116-130.

HOLDEN, C., GALEAZZI, R., RODRÍGUEZ, C., PEREZ, T., FOSSEN, T. I., BLANKE, M., and DE ALMEIDA SANTOS NEVES, M., 2007, "Nonlinear container ship model for the study of parametric roll resonance", Modeling, identification and control, 28**,** 87-103.

KIANEJAD, S., ENSHAEI, H., and RANMUTHUGALA, D., 2017, "Estimation of added mass moment of inertia in roll motion through numerical simulation", PACIFIC 2017 International Maritime Conference, 1-15.

MOCTAR, O. E., SHIGUNOV, V., and ZORN, T., 2012, "Duisburg Test Case: Post-panamax container ship for benchmarking", Ship Technology Research, 59**,** 50-64.

NEVES, M. A., 2002, "On the excitation of combination modes associated with parametric resonance in waves", Proceedings of the 6th International Ship Stability Workshop.

NEVES, M. A., PÉREZ, N., and LORCA, O., 2002, "Experimental analysis on parametric resonance for two fishing vessels in head seas", Proceedings of the 6th International Ship Stability Workshop.

OH, I., NAYFEH, A. and MOOK, D., 2000, "A theoretical and experimental investigation of indirectly excited roll motion in ships", Philosophical Transactions of the Royal Society of London A: Mathematical, Physical and Engineering Sciences, 358**,** 1853-1881.

SILVA, S., SANTOS, T., and SOARES, C. G., 2005, "Parametrically excited roll in regular and irregular head seas", International Shipbuilding Progress, 52**,** 29-56.

SIMONSEN, C. D., OTZEN, J. F., JONCQUEZ, S., and STERN, F., 2013, "EFD and CFD for KCS heaving and pitching in regular head waves", Journal of Marine Science and Technology, 18**,** 435-459.

SONG, K.-H., KIM, Y., and PARK, D.-M., 2013, "Quantitative and qualitative analyses of parametric roll for ship design and operational guidance", Proceedings of the Institution of Mechanical Engineers, Part M: Journal of Engineering for the Maritime Environment, 227**,** 177-189.

TEZDOGAN, T., DEMIREL, Y. K., KELLETT, P., KHORASANCHI, M., INCECIK, A., and TURAN, O., 2015, "Full-scale unsteady RANS CFD simulations of ship behaviour and performance in head seas due to slow steaming", Ocean Engineering, 97**,** 186-206.

VIDIC-PERUNOVIC, J., 2011, "Influence of the GZ calculation method on parametric roll prediction", Ocean Engineering, 38**,** 295-303.

WAWRZYŃSKI, W. and KRATA, P., 2016, "On ship roll resonance frequency", Ocean Engineering, 126**,** 92-114.

Quantifying Ship's Dynamic Stability through Numerical Investigation of Weight Distribution

Hossein Enshaei, *Australian Maritime College, Australia*, hossein.enshaei@utas.edu.au

S. S. Kianejad, *Australian Maritime College, Australia*, seyed.kianejadtejenaki@utas.edu.au

ABSTRACT

The Roll resonance can occur both in the parametric roll and dead ship condition, where the roll angle increases and endangers safety of the ship. The effects of loading conditions and weight distributions on the aforementioned phenomena are unknown. This study uses CFD method to investigate the effects of loading conditions, different vertical centre of gravity (VCG) and roll moment of inertia on dynamic stability. A model of a container ship is excited by a roll exciting moment at different frequencies and Froude numbers. The effects of VCG and loading conditions on the dynamic stability are compared against hydrostatic characteristics for the similar conditions. It was found, their effects in the static condition are more significant than the dynamic condition.

Keywords: *Weight distribution, VCG, roll moment of inertia, CFD, harmonic excited roll motion.*

1. INTRODUCTION

Investigating ships intact stability is required by the safety of life at sea (SOLAS) convention at different loading conditions. The restoring arm is calculated in different loading conditions to make sure there is a "sufficient restoring moment" over a range of roll angles to fulfil the criteria enforced through the intact stability code (ISC). These requirements are achieved in a static condition. Investigating intact stability of a ship in static condition is far from reality specially when the ship is exposed to waves and wind at sea. Second generation of intact stability criteria (SGISC) was proposed by IMO in recent years, which defines a set of failure modes associated with potentially dangerous dynamic stability phenomena in waves. These phenomena are parametric roll, pure loss of stability, surf-riding and broaching, dead ship condition and excessive accelerations. As a result, the ship may undergo cargo loss or crew injuries despite of fulfilling the required stability criteria because of poor dynamic stability. On the other hand, a ship may fulfil the static stability criteria marginally, but being quite safe due to an acceptable dynamic stability at sea, which could potentially increase the overall displacement.

The roll resonance can be experienced in some of the failure modes, such as parametric roll and dead ship condition, wherein the ship experiences an incremental roll angle, and in the worst scenarios a large roll angle can capsize the ship. The parametric roll occurs mostly in the head and bow sea conditions, when an encounter frequency is two times the ship's roll natural frequency. In the quartering and beam sea conditions, resonance occurs if the encounter frequency matches the ship' roll natural frequency (Bassler et al., 2011).

Study of the parametric roll based on theoretical methods was started by Kerwin (1955), Paulling and Rosenberg (1959) where they used linear and weakly nonlinear Mathieu equations at a range of frequencies close to natural frequency. They found that generated

roll angle in the head sea at an encounter frequency of two times natural frequency was larger than the other frequencies. Soliman and Thompson (1992) considered only roll motion, whereas Oh et al. (2000) took in to account the coupled pitch and roll motions in their investigations and results were justified experimentally. Although the parametric roll occurs both in head and following waves, but is more probable in the head waves. Considering a model free in heave, pitch and roll motions provides a better insight in simulation of the parametric roll (Shin et al., 2004) because the model experiences these motions simultaneously in encountering head waves.

Neves et al. (1999) suggested a 3DOF method, where the pitch and heave motions were coupled and the output was an input to a 1DOF nonlinear roll motion's equation. The heave and pitch motions were solved simultaneously and the outcomes were used to analyse the occurrence of parametric roll at two different frequencies; twice and equal roll natural frequencies. e Silva and Soares (2013) suggested a 3DOF (heave, roll and pitch) and a 5DOF (sway, heave, roll, pitch and yaw) numerical models in time domain condition. These numerical simulations have been deployed at a frequency of twice the roll natural frequency using a 3D panel code. That is brought into the time domain by tuning the impulse response functions method. Munif and Umeda (2000), and Matusiak (2003) utilized six degrees of freedom (6-DOF) models for numerical simulations in time domain. In the case of following and quartering sea the encountered frequency was kept equal to the roll natural frequency, while in the case of head and bow sea the encountered frequency was twice the roll natural frequency. In more recent study, a 4DOF coupled non-linear motion equation was suggested by Ahmed et al. (2010), where irregular waves, nonlinear restoring moment, instantaneous wetted surface, hydrodynamic forces and moments, and diffraction at a frequency twice the roll natural frequency were taken into account. Prediction of the parametric roll occurrence in the irregular wave is more intricate but realistic, while recognizing the physics of parametric roll could be carried out by numerical and experimental simulations in the regular waves. A 1DOF simulation was performed by Bulian and Francescutto (2007) in long-crested head waves using the concept of Grim's effective wave amplitude at a resonance frequency. They proposed a framework to consider hydrostatic restoring variations in the wave at different situations.

A study by Ribeiro e Silva and Guedes Soares (2000) has shown that both linear and non-linear methods can be utilized to investigate the parametric roll in the regular head waves at a resonance frequency. It was observed that accuracy of the roll angle prediction under wave-induced parametric roll was not satisfactory, because the linear method fails to take into account the deck submergence effect and non-linear damping term. Nevertheless, the nonlinear numerical model of Ribeiro e Silva and Guedes Soares (2000) addresses the weaknesses of the linear method in the regular head waves. The numerical simulations of this method had a good agreement with the experimental measurements having limited responses and the time domain simulations of roll motion in longitudinal regular waves. To address the deficiencies of non-linear method, a coupled 5DOF (sway, heave, roll, pitch and yaw) model was suggested by Ribeiro e Silva and Guedes Soares (2009) to simulate the time domain responses of a ship at a resonance frequency in long-crested irregular waves. The model has been developed further to a six DOF using a semi-empirical equation for surge motion (Schumacher et al., 2016). Umeda et al. (2016) conducted 5DOF numerical simulations to predict the parametric roll in oblique waves with low forward speed at a frequency twice the roll natural frequency. The obtained results were in good agreement with experimental data.

Several studies have been conducted to investigate the parametric roll and dead ship condition phenomena. However, the impacts of weight distributions on dynamic stability have not been investigated. In this study, the effects of different loading conditions and weight distributions on the roll motion characteristics

including the roll angle and the roll angular acceleration are studied using CFD simulations. A model of a post panamax container ship is excited at different roll excitation frequencies and Froude numbers to simulate the occurrence of resonance in the parametric roll and dead ship condition. Moreover, vertical centre of gravity (VCG) and roll moment of inertia as a result of weight distributions are also considered. Finally, the results from dynamic stability are compared with hydrostatic calculations.

2. SHIP GEOMETRY

To investigate the effects of weight distributions on the roll motion characteristics, a fully appended model of a post panamax container ship (DTC) with scale factor 59.467 was used. The appendages are rudder, propeller and five segments bilge keels which were set on either side of the model in the parallel section. The model was used for benchmarking purposes to calculate resistance and roll damping and more details of the model can be found in (Moctar et al., 2012). A 3D sketch of the model is shown in Figure 1 and main particulars of the model in two loading conditions are presented in Table 1.

3. NUMERICAL MODELLING

The CFD simulations are conducted to investigate the effects of loading condition, Froude number, VCG and roll moment of inertia over a range of frequencies close to resonance frequency on roll motion characteristics as presented in Table 2. The model is excited by a 15 Nm sinusoidal roll exciting moment free in 6DOF. They were conducted for two loading conditions at their relevant resonance frequencies for different Froude numbers (cases 1 to 6), and the results are compared against the hydrostatic calculations. The hydrostatic calculation is performed using Auto Hydro software. In the second attempt, the impact of VCG on the roll motion was investigated over a range of frequencies close to the resonance frequency while the roll moment of inertia was kept constant. That is performed to study the effects of VCG on both dynamic and hydrostatic conditions (cases 7 to 14). Finally, the dynamics of roll motion was studied by changing the roll moment of inertia (I) while VCG is kept constant (cases 15 to 20).

Figure 1 3D sketch of the post Panamax container ship

Table 1 Main particulars of the model in two loading conditions

Main dimension	Loading condition 1	Loading condition 2
L_{pp} [m]	5.97	5.97
L_{wl} [m]	6.07	6.07
B_{wl} [m]	0.86	0.86
D [m]	0.24	0.21
C_B	0.65	0.63
V [m^3]	0.79	0.65
KM [m]	0.42	0.44
GM [m]	0.02	0.08
KG [m]	0.39	0.36
T_0 [s]	4.49	2.56
K_{xx} [m]	0.34	0.33
K_{yy} [m]	1.48	1.61
K_{zz} [m]	1.49	1.61

3.1 Governing equations and physics modeling

An unsteady Reynolds-Averaged Navier-Stokes approach was selected to resolve the governing equations using a commercial CFD software STAR-CCM+. Considering no external forces the averaged continuity and momentum equations in the Cartesian coordinate system are as follows (Ferziger et al., 1997):

Table 2 Test conditions to study the effects of different loading conditions and weight distributions on the roll motion

Case No.	Loading condition	Froude No.	VCG (m)	Roll moment of inertia (Kg.m^2)	Roll excitation frequency (Rad/s)
1	1	0.00	0.3983	91.7	1.40
2	1	0.10	0.3983	91.7	1.40
3	1	0.19	0.3983	91.7	1.40
4	2	0.00	0.3595	69.1	2.45
5	2	0.10	0.3595	69.1	2.45
6	2	0.19	0.3595	69.1	2.45
7	1	0.00	0.3983	91.7	1.30
8	1	0.00	0.3983	91.7	1.50
9	1	0.00	0.4023	91.7	1.30
10	1	0.00	0.4023	91.7	1.40
11	1	0.00	0.4023	91.7	1.50
12	1	0.00	0.3943	91.7	1.30
13	1	0.00	0.3943	91.7	1.40
14	1	0.00	0.3943	91.7	1.50
15	1	0.00	0.3983	96.29	1.30
16	1	0.00	0.3983	96.29	1.40
17	1	0.00	0.3983	96.29	1.50
18	1	0.00	0.3983	87.12	1.30
19	1	0.00	0.3983	87.12	1.40
20	1	0.00	0.3983	87.12	1.50

$$\frac{\partial(\rho\bar{u}_i)}{\partial x_i}=0 \quad (1)$$

$$\frac{\partial(\rho\bar{u}_i)}{\partial t}+\frac{\partial}{\partial x_j}(\rho\bar{u}_i\bar{u}_j+\rho\overline{u_i'u_j'})=-\frac{\partial\bar{p}}{\partial x_i}+\frac{\partial\bar{\tau}_{ij}}{\partial x_j} \quad (2)$$

$$\bar{\tau}_{ij}=\mu(\frac{\partial\bar{u}_i}{\partial x_j}+\frac{\partial\bar{u}_j}{\partial x_i}) \quad (3)$$

In these equations, i and j are the indices which reflect the direction of the flow. ρ and μ demonstrate the density and viscosity of the flow. Time averaged velocity and pressure are $\bar{u}_i$ and $\bar{P}$. $\bar{\tau}_{ij}$ is the mean viscous stress tensor and $\rho\overline{u_i'u_j'}$ is the Reynolds stress tensor. The solver is based on a finite volume method and the continuity and momentum equations were linked by a predictor-corrector approach. A turbulence model is required to complete the RANS equations and to address the uncertainty of the stress tensor. In this study, the SST-kω was used which blends the k-ε turbulence model for far field and the k-ω model for near the ship model. The volume of fluid (VOF) method was selected to simulate the free surface. This method can be used to simulate the flows with various phases. The solver uses a segregated flow model to resolve the continuity and momentum equations in an uncoupled condition. The SIMPLE algorithm was selected for the simulations and a second order upwind scheme was used to discretise the convection terms. A dynamic fluid body interaction (DFBI) method was used to estimate the ship's motions and the acting forces and moments similar to a ship condition at sea. Courant number (CFL) was used to specify a suitable time step to reduce the simulation time while maintaining the same accuracy. The selected time step was smaller than one to ensure the numerical stability.

Selecting an appropriate and independent size of the domain reduces the simulation time and increases the accuracy of the results. In this study, the inlet boundary was placed one Lpp upstream of the model, while the outlet was places three Lpp downstream of the model. The top boundary and remaining boundaries are located 0.5 Lpp and one Lpp from the model respectively, to avoid boundary effects on the simulation results.

3.2 Mesh generation

An overset mesh technique was adopted to generate a volume mesh. There are two regions in this method including overset and background regions shown in Figure 2. The overset region surrounds and holds the model and moves with the model inside the background region. The advantage of this method is reduction of the total number of cells, because of reduction of the cells size within the overset region to capture the boundary layer, flow separation, vorticity and generated wave when the model is moving. Four meshers were utilised to generate the mesh such as trimmed, prism layer, surface and automatic surface repair. The trimmed mesher generates a high quality mesh and the prism layer generates several inflation layers using hexahedral prisms on the model surface to capture the boundary layer. The surface remesher improves the surface quality to generate a better volume mesh. The automatic surface repair mesher was used to remove a possible geometry problem. Mesh refinement was performed to increase the number and quality of the cells to capture the complex flow characteristics at the free surface and around the model. The size of cells in the overset region is smaller than the background region and therefore, an overlap volumetric block was used to match the size of the cells between the two regions (Kianejad et al., 2017).

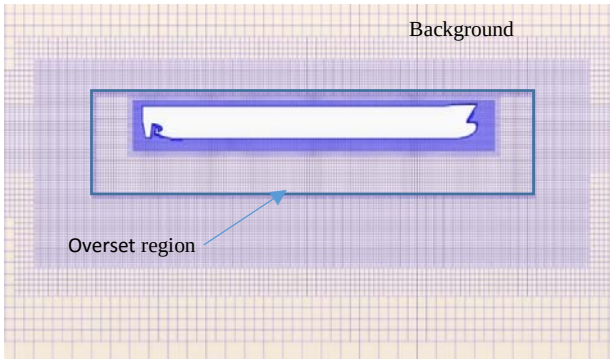

Figure 2 2D section of the mesh around the model

3.3 Boundary and initial condition

To increase the accuracy of the simulations and to decrease the simulation time, a suitable initial and boundary conditions were chosen. The two opposite boundaries of the domain at the x-direction were set as inlet (positive x-direction) and outlet (negative x-direction). The outlet boundary condition was set as hydrostatic pressure outlet to avoid any backflow. The remaining boundaries including inlet, top, bottom and lateral sides were set as velocity inlet to avoid velocity gradient resulting from interactions between the flow and walls. The initial velocity of the flow at all boundaries except the outlet were set as velocity of flat wave to direct the flow to the outlet boundary to minimise flow reflection. For the outlet boundary, the initial hydrostatic pressure of flat wave was chosen. The model was set as a no-slip wall condition for calculating the motions and moments.

3.4 Mesh study

It is necessary to determine the level of uncertainty to improve the reliability of the simulation results. In this study, a verification method proposed by Stern et al. (2001) is used. The numerical uncertainty U_{SN}, consists of iterative convergence uncertainty, U_I, grid-spacing uncertainty, U_G and time-step uncertainty, U_T in equation below:

$$U^2_{SN} = U^2_I + U^2_G + U^2_T \tag{4}$$

Since these simulations were conducted in a calm water condition, the uncertainty of the U_I is negligible. Moreover, the selected time step based on the Courant number was small enough to minimize the time-step uncertainty. The grid-spacing as a major source of the uncertainty was investigated by applying a 5.5 Nm roll external exciting moment at a frequency of 1.3 rad/s. Three different mesh configurations with a refinement ratio of $r_G = \sqrt{2}$ were considered as shown in Table 3. The grid uncertainty for

different configurations was performed based on Richardson extrapolation (Jin et al., 2016). The variation of simulation results for the cases of coarse (S_3), medium (S_2) and fine (S_1) configurations are calculated by:

$$\varepsilon_{G32} = S_3 - S_2 \tag{5}$$

$$\varepsilon_{G21} = S_2 - S_1 \tag{6}$$

$$R_G = \varepsilon_{G21} / \varepsilon_{G32} \tag{7}$$

Table 3 The number of mesh in different configurations.

	Background	Overset	Total
Fine (S_1)	2,473,043	3,306,135	5,779,178
Medium (S_2)	1,862,000	2,869,103	4,731,103
Coarse (S_3)	967,207	2,236,488	3,203,695

The numerical convergence ratio was calculated using equation 6. Four typical conditions could be expected as follows: (i) monotonic convergence ($0<R_G<1$), (ii) oscillatory convergence ($R_G<0$; $|R_G|<1$), (iii) monotonic divergence ($R_G>1$), and (iv) oscillatory divergence ($R_G<0$; $|R_G|>1$). In cases (iii) and (iv) the numerical uncertainty cannot be computed. In case (ii) uncertainty can be computed based on bounding error with upper limit (S_U) and lower limit (S_L) using the equation below:

$$U_G = \left|\frac{1}{2}(S_U - S_L)\right| \tag{8}$$

In the case of (i), the generalized Richardson extrapolation should be adopted to compute the numerical error $\delta^*_{RE_{G1}}$ and the order of accuracy P_G is shown in the equations below:

$$\delta^*_{RE_{G1}} = \frac{\varepsilon_{G21}}{r_G^{p_G} - 1} \tag{9}$$

$$p_G = \frac{\ln(\varepsilon_{G32} / \varepsilon_{G21})}{\ln(r_G)} \tag{10}$$

A correction factor C_G defined by the equation below, determines the method of uncertainty calculation.

$$C_G = \frac{r_G^{p_G} - 1}{r_G^{p_{Gest}} - 1} \tag{11}$$

If the C_G value is near to 1, then the solutions are close to the asymptotic range. The numerical error δ^*_{SN}, benchmark result Sc and the uncertainty U_{GC} can be calculated by the following set of equations:

$$\delta^*_{SN} = C_G \times \delta^*_{RE_{G1}} \tag{12}$$

$$S_C = S - \delta^*_{SN} \tag{13}$$

$$U_{GC} = \begin{cases} (2.4(1-C_G)^2 + 0.1)\,|\,\delta^*_{RE_{G1}}\,| & \leftrightarrow |1-C_G| < 0.125 \\ |1-C_G|\,|\,\delta^*_{RE_{G1}}\,| & \leftrightarrow |1-C_G| \geq 0.125 \end{cases} \tag{14}$$

If the value of C_G is much greater than 1, the solutions are away from the asymptotic range and numerical uncertainty should be calculated by:

$$U_{GC} = \begin{cases} (9.6(1-C_G)^2 + 1.1)\,|\,\delta^*_{RE_{G1}}\,| & \leftrightarrow |1-C_G| < 0.125 \\ (2\,|1-C_G| + 1)\,|\,\delta^*_{RE_{G1}}\,| & \leftrightarrow |1-C_G| \geq 0.125 \end{cases} \tag{4}$$

The results of numerical simulations for each mesh configuration and the magnitude of uncertainty for grid-spacing are presented in Table 4. It is apparent that the uncertainty in the roll angular velocity and angular acceleration is more than the uncertainties in the roll angle and roll moment. Resistance calculations were also conducted in different mesh configurations and the results were validated against experimental measurement (Handschel and Abdel-Maksoud, 2014). Overall, a good correlation was found to conclude that the numerical approach is reliable to compute pressure and shear forces reasonably accurate. Therefore, based on these results, further simulations were performed using the fine mesh configuration.

4. RESULTS AND DISCUSSIONS

This section discusses the results obtained from simulations investigating the impact of three influential parameters associated with weight distributions.

Table 4 Mesh convergence study for different configurations

Amplitude	Exp.	S_1	S_2	S_3	R_G	$\delta^*_{RE_{G1}}$	U_G (%S_1)
Roll angle (°)	14.52	14.08	13.50	12.00	0.39	-0.37	5.84
Roll moment (Nm)	-	44.59	42.22	30.00	0.19	-0.57	2.88
Angular acceleration (Rad/s^2)	-	0.45	0.42	0.38	0.49	-0.02	10.62
Angular velocity (Rad/s)	-	0.32	0.30	0.26	0.41	-0.01	8.73
Drag (N)	26.46	25.91	25.35	24.40	0.59	-0.80	6.98

4.1 Impact of loading conditions

The variation of roll angle and roll acceleration in two loading conditions and three Froude numbers are shown in Figure 3. The roll exciting moment was set at 15 Nm at the resonance frequencies. It was observed that increasing the forward speed decreases the amplitude of roll motion characteristics, consisting of the roll angle and the angular roll acceleration. The roll angle variations measured for the loading condition 1 is greater because of smaller restoring moment.

The product of displacement and metacentric height (Δ*GM) for both conditions at different roll angles is shown in Figure 4. It is apparent that product for the loading condition 2 is more than two times of the loading condition 1. Therefore, the responses of the models in these loading conditions are different at their own resonance condition at sea. The natural frequency of the model in the loading condition 1 and 2 are about 1.4 and 2.45 rad/s, respectively. The model in loading condition 2 experiences about 15 degrees of roll angle, while the model in loading condition 1 experiences about 24 degrees. That is while both models were excited by the same exciting moment (15 Nm) at their own resonance frequencies. It appears that in the dynamic condition, the model at loading condition 2 is safer because developing smaller roll angle, about 63% of the loading condition 1. In contrast, the generated acceleration of the loading condition 2 is 1.75 times higher than the loading condition 1. Despite of better stability in loading condition 2, a larger angular acceleration is unfavourable for the motion sickness and damage to the cargo and lashing equipment in terms of excessive acceleration.

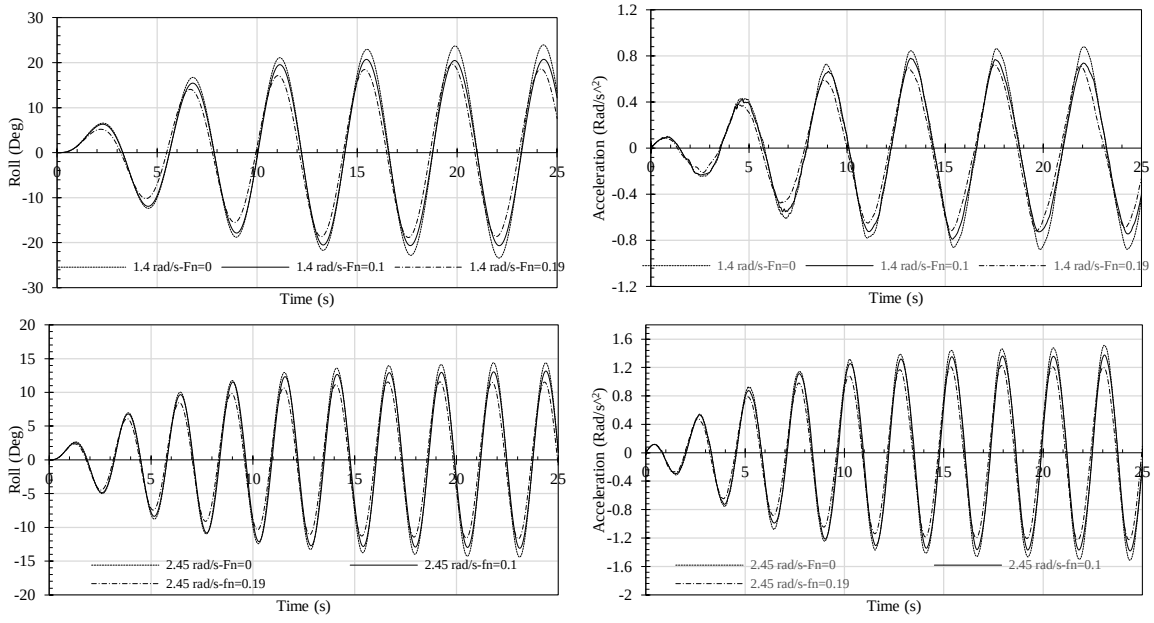

Figure 3 Time traces of the roll angle and acceleration at three frequencies and two Froude numbers (Fn). Top figures are loading condition 1 and bottom figures are loading condition 2.

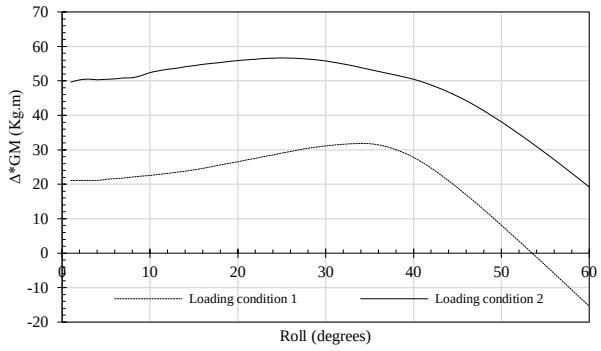

Figure 4 Product of Δ*GM for loading conditions 1&2

4.2 Impact of VCG

The loading condition 1 was selected to investigate the effects of cargo distributions for a same displacement over the static and dynamic stability of the ship. The investigation was limited to change of VCG by only ± 1% over three frequencies close to the resonance frequency, because larger changes of VCG changes the resonance frequency. Figure 5 shows the results of this investigation by recording the roll angle and angular acceleration while comparing them at various VCGs.

The top row depicted in Figure 5 (VCG=0.3983 m) is used for benchmarking and the largest roll angle recorded is 24 degrees at resonance frequency of 1.4 rad/s. It is also apparent that angular acceleration for 1.4 and 1.5 rad/s have a similar amplitude, which confirms that increasing the excitation frequency increases the angular acceleration. In the middle row of Figure 5 (VCG=0.3943 m) the maximum roll angle recorded is 21.7 degrees at the frequency of 1.5 rad/s, 2.3 degrees lower than the maximum roll angle for the top row, which accounts for 10% variation. However, reducing the VCG by 1% increases the metacentric height by about 20%. Figure 6 shows the comparison from a static stability perspective, where decreasing the VCG increases both metacentric height and resonance frequency. The bottom row of Figure 5 shows the condition where the VCG is increased by 1%. That has caused a shift in the resonance frequency to 1.3 rad/s. The maximum roll angle recorded is 1.5 degrees (6% variation) higher than the maximum roll angle of the original condition (VCG=0.3983 m). The maximum roll angle for a frequency of 1.5 rad/s decreases in the following cycles, because it is getting far from the resonance frequency. It is obvious that increasing the VCG causes a 20% decrease in the metacentric height shown in Figure 6. Therefore, variation of the VCG, influences the static stability more than two times compared to the dynamic stability. The angular accelerations on the right side of Figure 5 confirm a similar behaviour to the roll angles by illustrating the same patterns and the comparable amplitudes. For the same roll angle close to resonance frequency, the model excited by a higher frequency generates larger roll angular acceleration.

4.3 Impact of roll moment of inertia

Roll moment of inertia as a result of weight distribution is another factor which influences the dynamic stability of a ship, but the hydrostatic calculation ignores this effect. This section intends to show the influence of the roll moment of inertia on dynamic stability at a range of frequencies close to resonance frequency while the displacement remains constant. The magnitude of the roll moment of inertia was changed by ± 5% to investigate its effects on the maximum roll angle and the angular acceleration. The roll angle and roll angular acceleration trajectories over different frequencies and roll moment of inertias are shown in Figure 7. While the model's responses in the first cycle are similar, the differences become apparent in the following cycles. The top row in Figure 7 is used as a benchmark for the other two rows having different moment of inertia. The results of middle row show that decreasing the roll moment of inertia by 5% increases the magnitude of the resonance frequency and decreases the amplitude of roll

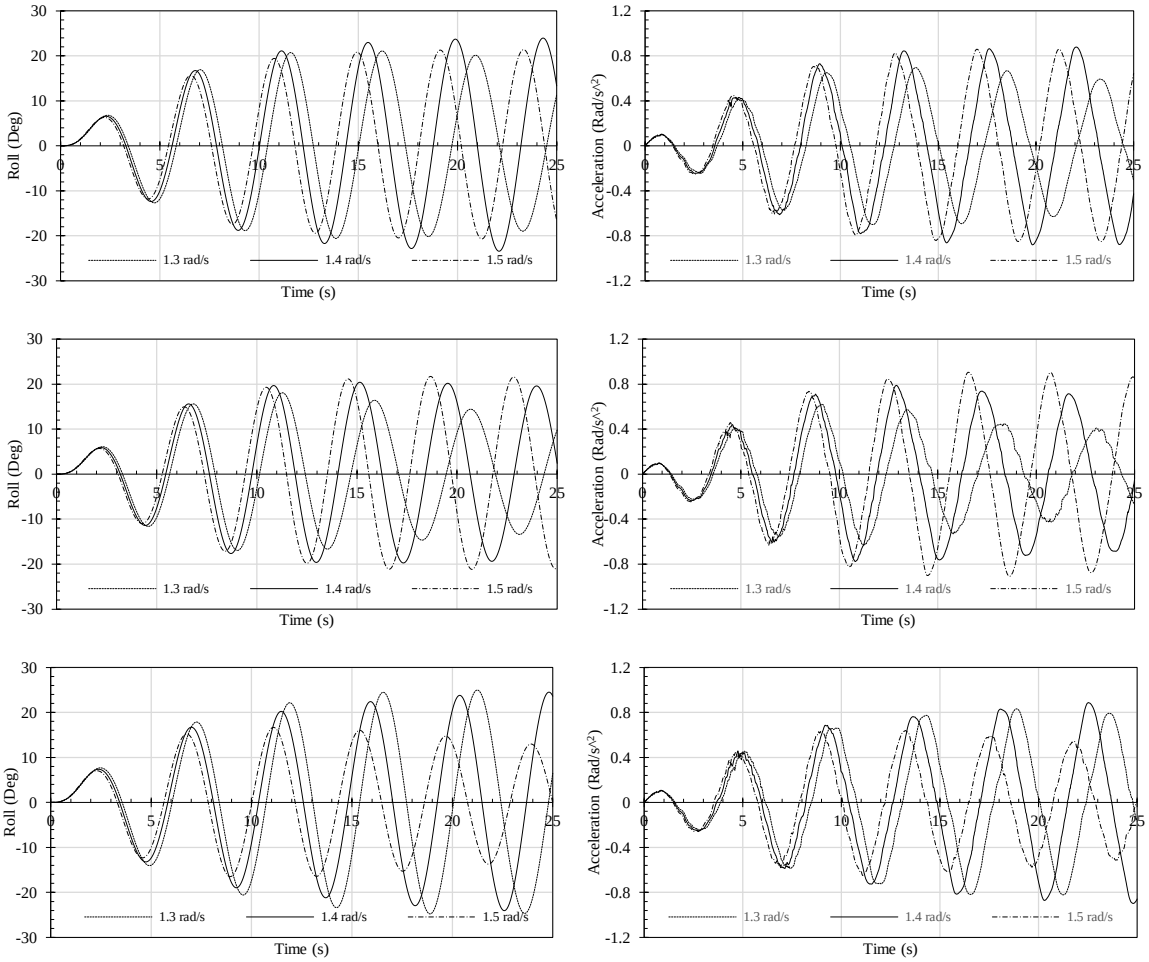

Figure 5 Time traces of the roll angle and angular acceleration in loading condition 1 over three range of frequencies and I=91.7 Kg.m^2. From top down VCG is 0.3983m, 0.3943m and 0.4023m.

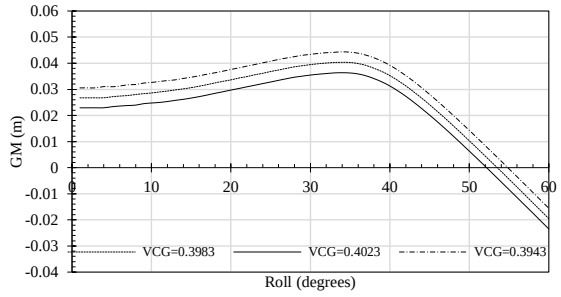

Figure 6 GM values of the loading condition 1 for different VCGs

angle by 1.5 degrees to become 22.5 at the frequency of 1.4 rad/s. The maximum roll angle also decreases for the frequency of 1.3 rad/s, because of getting far from resonance frequency.

Although the maximum roll angle was recorded at a frequency of 1.4 rad/s, the maximum angular acceleration is at the frequency of 1.5 rad/s. Increasing the magnitude of the roll moment of inertia for the bottom row in Figure 7 slightly decreases the resonance frequency and increases the maximum roll angle about 1.5 degrees for frequencies of 1.3 and 1.4 rad/s in comparison to the benchmark. In this case, the excitation frequency of 1.5 rad/s generates smaller roll angle, because it is far from the resonance frequency. In contrast, the induced acceleration for the frequency of 1.5 rad/s is larger than the frequency of 1.3 rad/s.

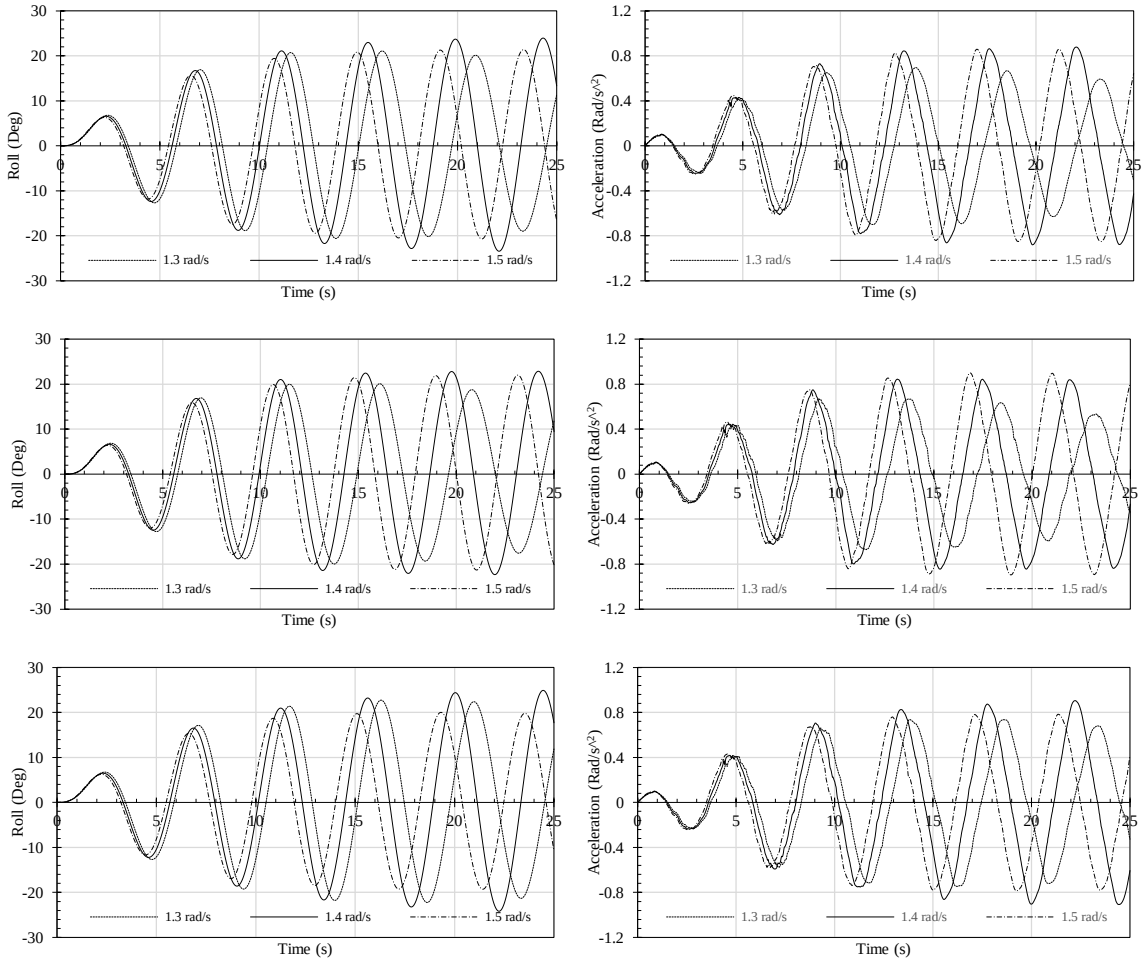

Figure 7 Time traces of the roll angle and acceleration in loading condition 1 over three range of frequencies considering VCG=0.3983m. From top down I=91.7 Kg.m^2, I=87.12 Kg.m^2, I=96.29 Kg.m^2.

5. CONCLUSION

Variation in cargo loadings and weight distributions changes the dynamic stability of a ship. In this study, numerical simulations using CFD method were carried out to investigate the impacts of loadings and weight distributions on both static and dynamic stability. It was found that variations in the loading condition changes the static ship stability significantly, while its effect on dynamic stability (maximum imposed roll angle) is not as much under the same external roll exciting moment. Changing 1% of the VCG, changes the restoring moment (hydrostatic condition) and maximum roll angle (dynamic condition) by 20% and 9%, respectively. Variation of the roll moment of inertia by 5% for the same loading condition changes the maximum roll angle about 7%, while the hydrostatic calculation fails to consider the effects of the roll moment of inertia.

A ship at sea is exposed to a dynamic condition and hydrostatic calculations is insufficient for assessment of a ship stability. It was found that changing the loading condition and weight distribution has less influence on dynamic stability than perceived by the static stability.

The scope of this study was limited in terms of ship's type to a containership. These findings lay the groundwork for future research into dynamic stability to further explore the impact of influential parameters at resonance frequency.

6. REFERENCES

AHMED, T., HUDSON, D. & TEMAREL, P., 2010, "An investigation into parametric roll resonance in regular waves using a partly non-linear numerical model", Ocean Engineering, 37**,** 1307-1320.

BASSLER, C. C., BELENKY, V., BULIAN, G., FRANCESCUTTO, A., SPYROU, K. & UMEDA, N., 2011, "Review of available methods for application to second level vulnerability criteria, Contemporary ideas on ship stability and capsizing in waves", Springer.

BULIAN, G. & FRANCESCUTTO, A., 2007, "On the effect of stochastic variations of restoring moment in long-crested irregular longitudinal sea", International Shipbuilding Progress, 54**,** 227-248.

E SILVA, S. R. & SOARES, C. G., 2013, "Prediction of parametric rolling in waves with a time domain non-linear strip theory model", Ocean Engineering, 72**,** 453-469.

FERZIGER, J. H., PERIC, M. & LEONARD, A., 1997, "Computational methods for fluid dynamics", AIP.

HANDSCHEL, S. & ABDEL-MAKSOUD, M., 2014, "Improvement of the Harmonic Excited Roll Motion Technique for Estimating Roll Damping", Ship Technology Research, 61**,** 116-130.

JIN, Y., CHAI, S., DUFFY, J., CHIN, C., BOSE, N. & TEMPLETON, C., 2016, "RANS prediction of FLNG-LNG hydrodynamic interactions in steady current", Applied Ocean Research, 60**,** 141-154.

KERWIN, J., 1955, "Note on rolling in longitudinal waves", Int Shipbuild Prog, 2**,** 597-614.

KIANEJAD, S., ENSHAEI, H. & RANMUTHUGALA, D., 2017, "Estimation of added mass moment of inertia in roll motion through numerical simulation", PACIFIC 2017 International Maritime Conference, 1-15.

MATUSIAK, J., 2003, "On the effects of wave amplitude, damping and initial conditions on the parametric roll resonance", Proceedings of the 8th International Conference on Stability of Ships and Ocean Vehicles, Madrid, Spain, 341-348.

MOCTAR, O. E., SHIGUNOV, V. & ZORN, T., 2012, "Duisburg Test Case: Post-panamax container ship for benchmarking", Ship Technology Research, 59**,** 50-64.

MUNIF, A. & UMEDA, N., 2000, "Modeling extreme roll motions and capsizing of a moderate-speed ship in astern waves", Journal of the Society of Naval Architects of Japan, 2000**,** 51-58.

NEVES, M., PÉREZ, N. & VALERIO, L., 1999, "Stability of small fishing vessels in longitudinal waves", Ocean Engineering, 26**,** 1389-1419.

OH, I., NAYFEH, A. & MOOK, D., 2000, "A theoretical and experimental investigation of indirectly excited roll motion in ships", Philosophical Transactions of the Royal Society of London A: Mathematical, Physical and Engineering Sciences, 358**,** 1853-1881.

PAULLING, J. & ROSENBERG, R., 1959, "On unstable ship motions resulting from nonlinear coupling", Journal of Ship Research, 3**,** 36-46.

RIBEIRO E SILVA, S. & GUEDES SOARES, C., 2000, "Time domain simulation of parametrically excited roll in head seas", Proceedings of the 7th International Conference of Ships and Ocean Vehicles (STAB'2000), Launceston, Tasmania, Australia, 652-664.

RIBEIRO E SILVA, S. & GUEDES SOARES, C., 2009, "Parametric Rolling of a Container Vessel in Longitudinal Waves", Proc. 10th Int'l Conf. Stability of Ships & Ocean Vehicles.

SCHUMACHER, A., E SILVA, S. R. & SOARES, C. G., 2016, "Experimental and numerical study of a containership under parametric rolling conditions in waves", Ocean Engineering, 124**,** 385-403.

SHIN, Y., BELENKY, V., PAULLING, J., WEEMS, K., LIN, W., MCTAGGART, K., SPYROU, K. J., TREAKLE, T. W., LEVADOU, M. & HUTCHISON, B. L., 2004, "Criteria for parametric roll of large containerships in longitudinal seas", Transactions-Society of Naval Architects and Marine Engineers, 112**,** 14-47.

SOLIMAN, M. S. & THOMPSON, J., 1992, "Indeterminate sub-critical bifurcations in parametric resonance", Proceedings of the Royal Society of London A: Mathematical, Physical and Engineering Sciences, The Royal Society, 511-518.

STERN, F., WILSON, R. V., COLEMAN, H. W. & PATERSON, E. G., 2001, "Comprehensive approach to verification and validation of CFD simulations-Part 1: methodology and procedures", Transactions-American Society of Mechanical Engineers Journal of Fluids Engineering, 123**,** 793-802.

UMEDA, N., SAKAI, M., FUJITA, N., MORIMOTO, A., TERADA, D. & MATSUDA, A., 2016, "Numerical prediction of parametric roll in oblique waves", Ocean Engineering, 120**,** 212-219.

Motion Characteristics of a Spar-Buoy with Ring-Fin Motion Stabilizer

Toru, Katayama, *Osaka Prefecture University*, katayama@marine.osakafu-u.ac.jp

Yusuke, Yamamoto, *Osaka Prefecture University*, sxb03137@edu.osakafu-u.ac.jp

ABSTRACT

The main topics of this paper is the motion characteristics of a spar-buoy. Motion measurements for the spar-buoy with and without a ring-fin motion stabilizer in currents and waves are carried out at the circular water channel and the towing tank of Osaka Prefecture University, in order to investigate the characteristics of its motion. Motion amplitude of the spar-buoy with the stabilizer is much smaller than the results of the spar-buoy without the stabilizer, however, the spar-buoy with the stabilizer causes the inclination that means a time average value of motion and the inclination becomes larger according to increase in wave height at long wavelength. On the other hand, from the results in currents, the inclination of the spar-buoy with the stabilizer is much smaller than the results of the spar-buoy without the stabilizer, however, it is found that there is possibility it to have multi-balanced-inclinations for higher current velocity than the designed current velocity. The mechanism of these unexpected phenomena are investigated, and it is indicated that their occurrence can be avoided to optimize cross-section form of the stabilizer to change its characteristics of hydrodynamics.

Keywords: *Spar-Buoy, Motion Stabilizer, Hydrodynamic force*

1. INTRODUCTION

The diversification of energy into renewable resources is being promoted in recent years. Renewable energy in the ocean have also attract attention, and offshore wind is also one of them. When an offshore wind power generator is installed, it is required to observe the continuous wind condition at the hub height of wind turbine on the installed sea area for one year to estimate the capacity of power generation.

As a wind observation device for shallow water area with low installation cost and environment impacts, Doppler Lidar on a floating platform is considered. However, a floating platform causes motion by waves, winds and currents, and it affects the accuracy of measurement.

In our research group, low motion floating platforms is continuously considered and developed. As one of them, a spar-buoy with ring-fin motion stabilizer for shallow water area is proposed by Katayama et al. (2015). And its performance has been confirmed by a 1/20.23 scale model test at the towing tank of Osaka Prefecture University and 1/2.5 scale model test in real sea is also carried out at Sagami Bay in Japan in 2014 and its performance has been confirmed.

In this study, the motion characteristics of a spar-buoy with the ring-fin motion stabilizer is investigated by using 1/20.32 scale model and its performance is improved. Motion amplitude of the spar-buoy with the stabilizer is much smaller than one of the spar-buoy without the stabilizer, however, the spar-buoy with the stabilizer causes the inclination that is

time average value of motion and it becomes larger according to increase in wave height at long wavelength. On the other hand, from the results in currents, the inclination of the spar-buoy with the stabilizer is much smaller than the results of the spar-buoy without the stabilizer, however, it is found that there is possibility it to have multi-balanced-inclinations for higher current velocity than the designed current velocity. The mechanism of these phenomena are investigated, and it is indicated that their occurrence can be avoided to optimize cross-section form of the stabilizer to change its characteristics of hydrodynamics.

2. MODEL AND CORDINATE SYSTEM

Fig.1 shows schematic views of the buoy with the motion stabilizer and coordinate system. The earth fixed coordinate system is defined as O-$X_0Y_0Z_0$, and the body fixed coordinate system is defined as O-$x_0y_0z_0$. H is water depth, h_0 is the distance from the sea bottom to O, $U(Z_0)$ is the velocities of tidal current, T_w and ζ_w are period and amplitude of regular waves.

Fig.2 shows a figure of the ring-fin motion stabilizer. The angles of arms and fins (θ_{Arm} [deg] and θ_{Fin} [deg]) can be changed. And zero value of the angles are defined as the condition where they are perpendicular to the center pipe of the spar buoy. Table 1 shows the principal particulars of the model.

Table 1 Principal particulars of the ring-fin with flat section motion stabilizer.

θ_{Arm} [deg]	θ_{Fin} [deg]	lever: l_f [m]	area of the fin: S_{Fin} [m^2]	R [m]	r [m]
10	4.7	0.4009	0.07541	0.4163	0.3865
			0.1580	0.4312	0.3716
20	13.8	0.3912	0.07550	0.3967	0.3661
			0.1510	0.4120	0.3508
30	23	0.3807	0.07548	0.3668	0.3353
			0.1507	0.3825	0.3196
7.92	6.0	0.4431	0. 1231	0.4649	0.4209

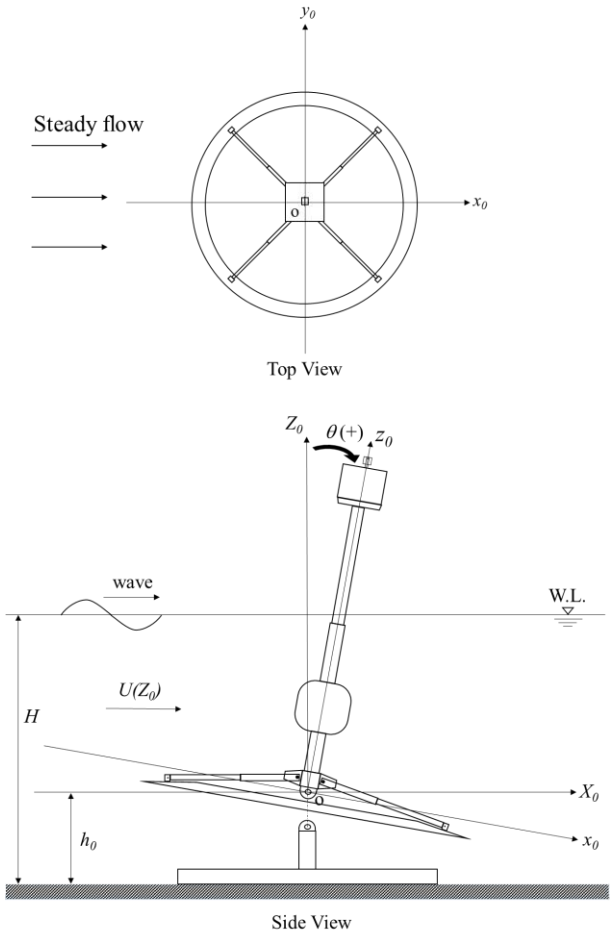

Fig.1 Schematic top and side view of the buoy with the ring-fin motion stabilizer and coordinate system.

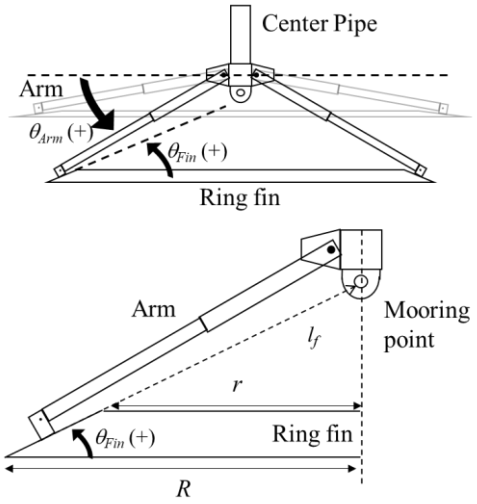

Fig.2 Schematic side view of the ring-fin motion stabilizer.

3. PERFORMANCE IN STEADY FLOW

3.1 Motion measurement

Motion measurement in steady flow is carried out at the circular water channel of Osaka Prefecture University (size of observation section: 6m in length, 1.5m in breadth, 1.09m in depth). Table 2 shows the conditions of measurement in steady flow. The range of flow velocity is 1.0~3.0kts in the real scale. The initial inclination is given to the buoy, and the measurements for the buoy with the motion stabilizer are carried out. The motion is taken by a video camera (AVTGigE camera (GE1050)) and it is analyzed with a motion capture software (TEMA, Photron).

Fig.3 shows the measured results of the buoy with the motion stabilizer at θ_{Arm}=7.92deg in steady flow. This figure shows two equilibrium angles of inclination at higher flow velocity than 0.30m/s (about 2.7kts in real scale). One of angles is almost zero, which means upright. And the other is downstream inclination and it increases according to increase of flow velocity. It indicates the possibility of occurrence of the jumping phenomenon that the equilibrium inclination is changed by small disturbance.

Table 2 Condition of the experiment.

flow velocity: U [m/s]	0.114～0.342
initial incline of pitching [deg]	-20, 0, 40

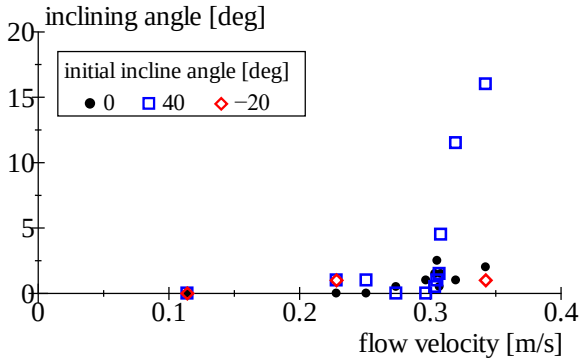

Fig.3 Measured inclination of spar-buoy in steady flow.

3.2 Hydrodynamic forces measurement

Hydrodynamic force acting on the buoy with the motion stabilizer at θ_{Arm}=10, 20, 30deg in steady flow are measured at the circular water channel of Osaka Prefecture University, in order to clarify the cause of two equilibrium inclinations. Measurements of hydrodynamic forces of the strut and arms is also carried out, and the hydrodynamic forces acting on the fin are obtained from subtracting the hydrodynamic forces acting on the strut and arms from the hydrodynamic forces acting on the buoy with the motion stabilizer.

Fig.4 shows the moment coefficient C_M calculated with Eq.(1).

$$C_M = \frac{M_{yo}}{0.5\rho S_{Fin} U^2 l_f} \tag{1}$$

where S_{Fin} is surface area of the ring-fin, l_f is the length from the mooring point of the buoy (shown in Fig.2) to the center of gravity of the fin. In this figure, coefficients at different flow velocity are shown. The results show that the

coefficients are almost same when the inclination and the arm angle are decided, even if flow velocity or surface area is different.

Fig.5 shows pitching moments acting on ring-fin motion stabilizer at θ_{Arm}=10deg and center pipe whose directions are anticlockwise and clockwise in Fig.1, respectively. The point of intersection of these lines indicates equilibrium inclination in steady flow. At U=0.342m/s, these are three equilibrium inclinations. Multiple equilibrium inclinations appear, because the pitching moment acting on ring-fin has the maximum value at around θ=0deg and approaches a constant value after rapidly decreasing for inclining downstream.

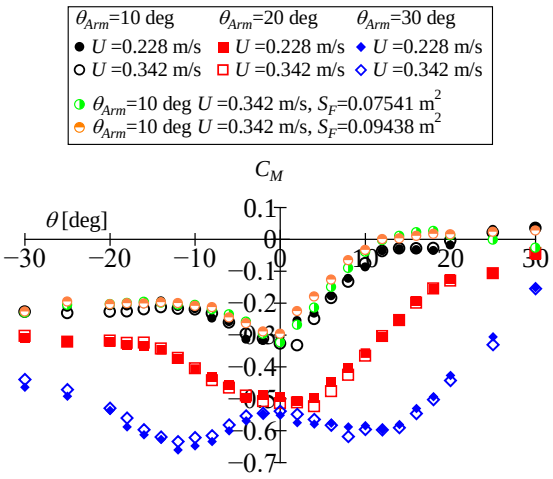

Fig.4 Measured moment coefficient of the ring-fin motion stabilizer without arms in steady flow.

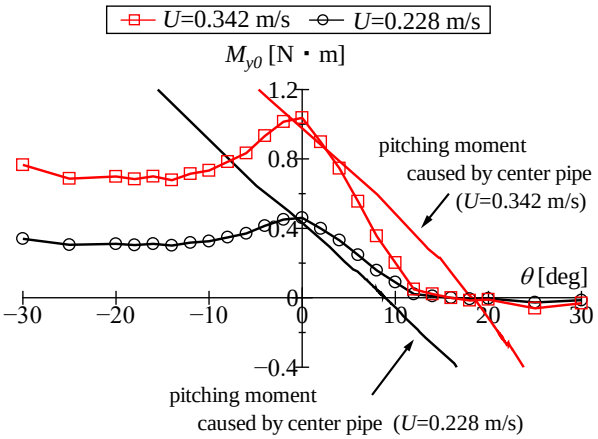

Fig.5 Moments acting on center pipe and ring-fin motion stabilizer at θ_{Arm}=10 deg and U=0.228, 0.342 m/s.

3.3 Characteristics of hydrodynamic force of ring-fin

It is supposed that the ring fin stabilizer generate significant pitching moment at the part of upstream and downstream sides. Then, the simple model of Eq.(2) is proposed, which consist of two flat plates of upstream and downstream sides as shown in Fig.6.

$$M = F_{D1} l_a \sin(-\theta_{Arm} + \theta) - F_{D2} l_a \sin(\theta_{Arm} + \theta) + F_{L1} l_a \cos(-\theta_{Arm} + \theta) - F_{L2} l_a \cos(\theta_{Arm} + \theta) \quad (2)$$

where F_D and F_L are drag and lift forces acting on a fin, and l_a, θ_{Arm} and θ are shown in Fig.6.

Fig.8 shows the calculated moment coefficients with Eqs.(1) and (2) by using the drag and lift coefficients of flat plate shown in Fig.7. From this figure, it is confirm that the simple model can explain the characteristic of moment acting on ring-fin with flat section shown in Fig.4.

From detailed investigation for the calculated results by the simple model, it is found that the characteristics of pitching moment which has the maximum value at around θ=0deg and approaches a constant value after rapidly decreasing for inclining downstream is caused by the characteristics of lift coefficient which is stall angle. For example shown in Fig.9, in the case of θ_{Arm}=20deg shown in Fig.8, the pitching moment rapidly decreases according to increase of θ from θ =0deg, because lift coefficient of aft fin does not increase compared with decreasing of lift coefficient of fore fin. If the absolute values of increasing and decreasing of lift coefficient of aft and fore fins according to increasing of θ, the pitching moment is constant. In order to change the characteristics of pitching moment which has the maximum value at around θ=0deg and approaches a constant value after rapidly decreasing for inclining downstream, it is required to delay stall angle.

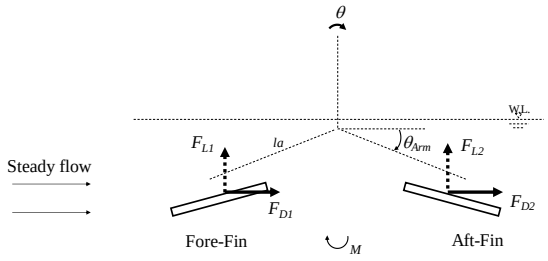

Fig.6 Simple model of ring-fin.

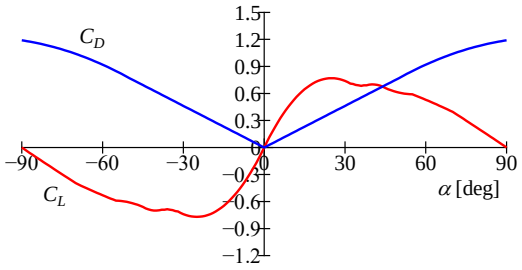

Fig.7 Drag and lift coefficients of flat plate for the simplified calculation model of ring-fin motion stabilizer without arms.(Ortiz et al., 2015)

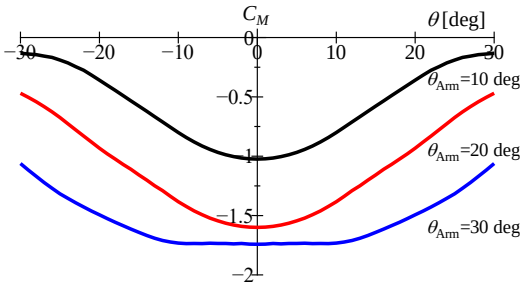

Fig.8 Calculation of moment coefficient of simplified model of ring-fin.

3.4 Effects of cross-sectional shape

As one of ways to avoid multiple equilibrium inclination, to change characteristics of pitching moment acting on ring-fin motion stabilizer shown in Fig.5 is investigated by using CFD (STAR-CCM+).

In order to validate results of CFD, flow field around a 2D flat plate in uniform flow as shown Fig.10 is calculated. Table 3 shows the condition of CFD. Fig.11 shows the comparisons between the calculated results and the experimental results shown in Fig.7, and it is confirmed that both of them are in good agreement.

In order to realize the characteristics of pitching moment of stabilizer mentioned in the section 3.3, kite section wings whose surface area is constant is considered as shown in Fig.12 and Table 4. Fig.13 shows the calculated result of drag and lift force acting on the wings. Drag force acting on each wing is almost same, on the other hand, lift force acting on each wing is different ratio of increase with increasing attack angle. Hydrodynamic forces acting on wing is changed by changing in *l*/*L*.

By using the simple model shown in Fig.6, pitching moment acting on ring-fin with 2D kite section for downstream is investigated. Fig.14 shows the calculated results at downstream inclination. This figure shows the rapid slope of pitching moment at *l*/*L* =1/4 for downstream inclination is disappeared.

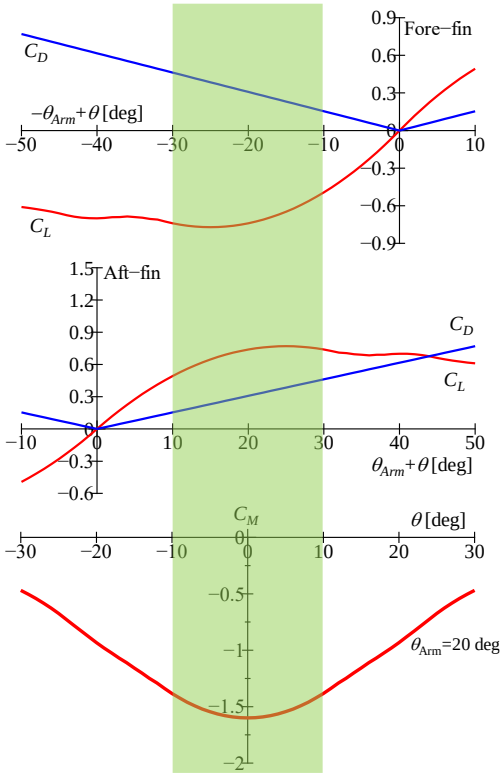

Fig.9 Calculated moment coefficient caused by Simplified calculation model of ring-fin motion stabilizer without arms in case of arm angle 20 deg.

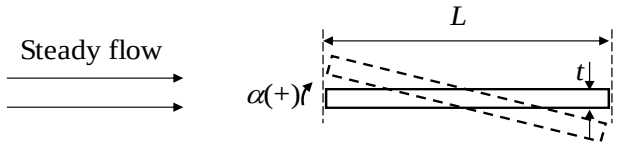

Fig.10 Schematic view of 2D flat plate which is used in CFD.

Table 3 Principal particulars of 2D wing with flat section and calculation condition of CFD.

L [m]	α [deg]	t [m]
0.123	0~24	0.001
mesh size [m]		0.002
flow velocity [m/s]		0.342
numerical solver		unsteady method
turbulent model		k-ε model
inner iterations		5
object surface condition		non-slip

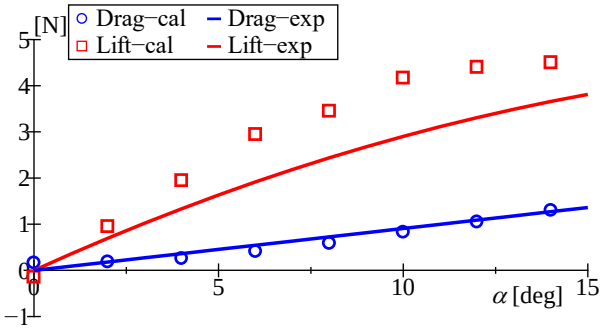

Fig.11 Calculated lift force of 2D flat plate by CFD.

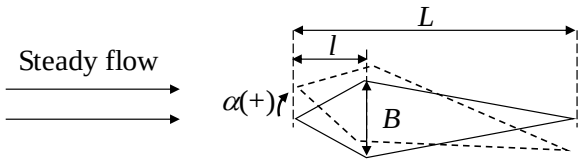

Fig.12 Schematic view of 2D wing with kite section which is used in CFD.

Table 4 Principal particulars of 2D wing with kite section.

L [m]	B [m]	L [m]	l/L
0.0684	0.01206	0.0171	1/4
		0.0342	1/2
		0.0513	3/4

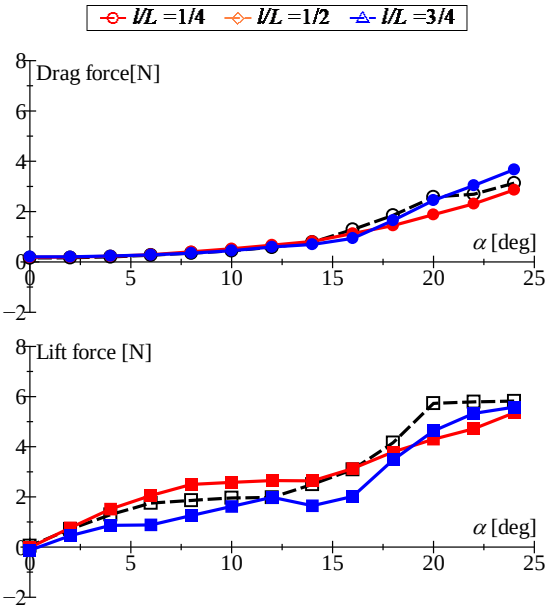

Fig.13 Calculated drag, lift of 2D wing with CFD.

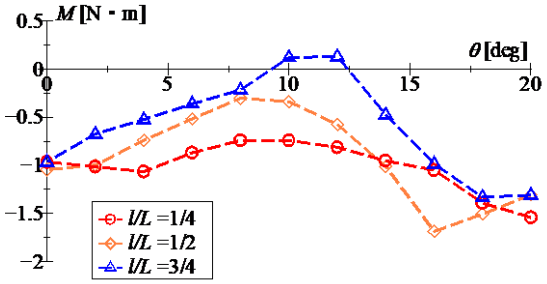

Fig.14 Calculated moment at downstream inclination caused by Simplified calculation model of ring-fin motion stabilizer without arms.

4. MODEL TEST IN REGULAR WAVE

4.1 Motion measurement

Motion measurement in regular wave is carried out at the towing tank of Osaka Prefecture University (length 70m, breadth 3m, depth 1.53m). The model is installed at 9m from the wave maker, motion measurement in regular wave is carried out by using the same measurement devices as the section 3. The experimental conditions are shown in Table 5 and 6.

Fig.15 shows time average value and amplitude of the measured pitch of the buoy with motion stabilizer at θ_{Arm}=7.92deg in regular wave. If wave height is constant, the time average value and amplitude of pitch are almost same regardless of wave periods, and if wave period was constant, the time average value increases in proportion to increase of wave height, and amplitude increases also according to increase wave height.

Moreover, motion measurement for ring-fin with flat section at θ_{Arm}=10deg and with rhomboid section is carried out. Table 7 shows principal particulars of ring-fin with rhomboid section motion stabilizer. Fig.16 shows time average value of the measured pitch.

Table 5 Condition of measurement in regular waves at constant wave height.

wave height:H_w [m]	wave period:T_w [s]
0.123	1.11, 1.33, 1.55, 1.77, 2.00, 2.22, 2.44

Table 6 Condition of measurement in regular waves at constant wave period.

wave period:T_w [s]	wave height:H_w [m]
2.00	0.0492, 0.0738, 0.0984, 0.123, 0.147, 0.172

Table 7 Principal particulars of ring-fin with rhomboid section motion stabilizer.

θ_{Arm} [deg]	θ_{Fin} [deg]	surface area of the fin : S_F [m^2]	lever : l_f [m]
10	4.42	0.13208	0.403361

4.2 Wave excitation force acting on the buoy

Wave excitation force acting on the fixed upright buoy with motion stabilizer in regular wave at constant wave period shown in Table 6 are measured at the towing tank of Osaka Prefecture University. Measurement of wave excitation force acting on center pipe with arms is also carried out, and the wave excitation force acting on ring-fin is obtained from subtracting the wave excitation force acting on center pipe with arms from wave excitation force acting on the fixed upright buoy.

Fig.17 shows time average value of measured horizontal (or surge) force acting on the fixed upright buoy. The time average value of the force acting on the fixed upright buoy and center pipe with arms is almost same regardless of wave height. On the other hand, time average value of the force acting on ring-fin increases in upstream of wave according to increase in wave height. Unfortunately, this results cannot explain the result of Fig.16. The cause of the time average value of pitch cannot be understood. Further investigation is required.

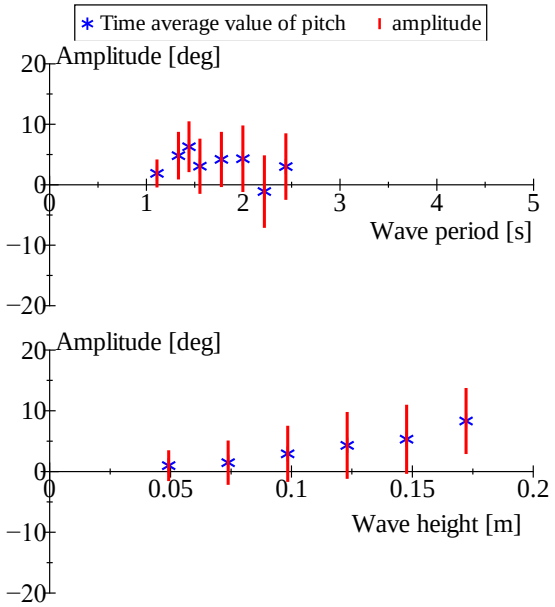

Fig.15 Amplitudes of the measured pitch of spar-buoy with ring-fin motion stabilizer in regular waves. (upper figure: Table 5, lower figure: Table 6)

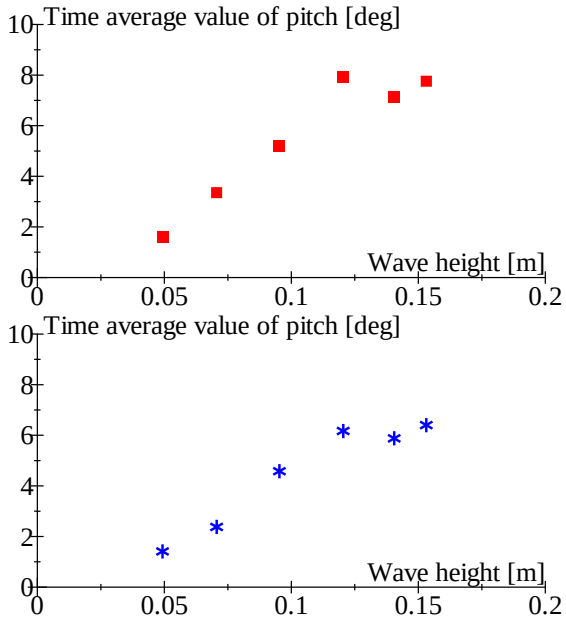

Fig.16 Time average value of the measured pitch of spar-buoys at Table6. (upper figure: flat section motion stabilizer, lower figure: rhomboid section motion stabilizer)

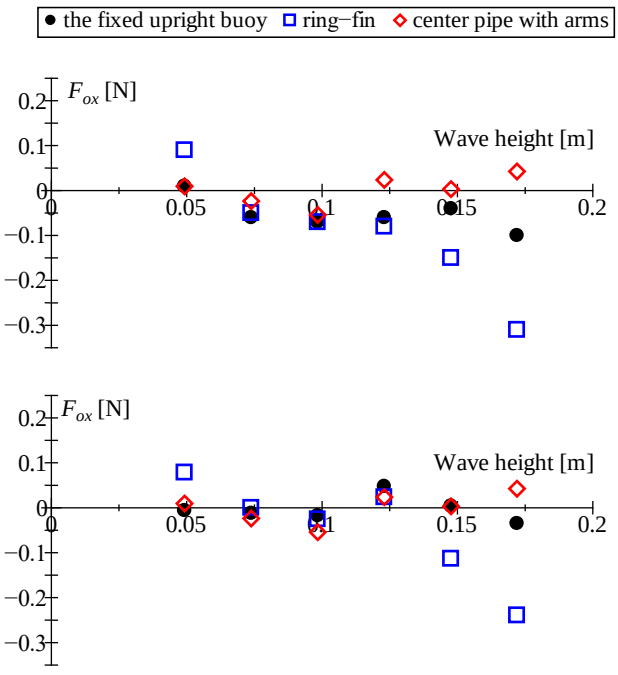

Fig.17 Time average value of the measured horizontal force. (upper figure: flat section at θ_{Arm}=10deg, lower figure: rhomboid section)

5. CONCLUTION

In this study, in order to improve the performance of ring-fin motion stabilizer, motion measurement in steady flow and regular wave are carried out and their characteristics are investigated. And the following conclusions are obtained.

1. In steady flow, it is found that multiple equilibrium inclination appears at 0.30m/s and more, and it is caused by the hydrodynamic forces acting on ring-fin.

2. The characteristic of hydrodynamic force acting on ring-fin can be explained by a simple model. By changing the cross-section of ring-fin , the characteristic of the hydrodynamic forces acting on motion stabilizer can be changed. The cross-section shape which is kite type with thinned outside can make the gradient of pitch moment for downstream inclination small.

3. In regular wave, the time average value of pitch increases according to increase of wave height. Unfortunately, the cause of the time average value of pitch cannot be cleared.

6. REFERENCES

Katayama, T., Hashimoto, K., Asou, H., Komori, S., 2015, “Development of a motion stabilizer for a Shallow Sea Area Spar Buoy in Wind, Tidal Current and Waves”, Journal of Ocean and Wind Energy, The International Society of Offshore and Polar Engineers, Vol. 2, No. 3, 2015, pp.182-192.

Ortiz, X., Rival, D., Wood, D., 2015, “Forces and Moments on Flat Plates of Small Aspect Ratio with Application to PV Wind Loads and Small Wind Turbine Blade”, Energies, Vol.4, Issue 4, pp.2438-2453.

Overview of the Development of a Series of Cabin-suspended Ships Governed by Different Motion Control Algorithms

Jialin Han, Specially Appointed Researcher, *Institute of Industrial Science, The University of Tokyo*

jialinhan.com@gmail.com

Daisuke Kitazawa, Associate Professor, *Institute of Industrial Science, The University of Tokyo*

dkita@iis.u-tokyo.ac.jp

Teruo Maeda, *OPD Research Centre* t-maeda@theia.ocn.ne.jp

Hiroshi Itakura, Technical Staff, *Institute of Industrial Science, The University of Tokyo*

itakura@iis.u-tokyo.ac.jp

ABSTRACT

A series of cabin-suspended ships has been developed since 2008. The main focuses were placed on the motion reduction of the cabin and the wave-energy extraction by means of various motion control algorithms. The approaches can be divided into two categories: ship and/or suspension structure modifications, and their control system development. Comparing to a traditional rigid ship body, the significant feature of a cabin-suspended ship is its suspensions, which are mounted in-between the cabin part and the hull part. Owing to the expansion/compression movement of the suspensions, the motion of the cabin can be recognized from that of the hull. Oil dampers, stepping motors or brushed DC motors were adopted in different model ships. A passive control system, a semi-active control system and an active control system were developed, respectively. An overview of the development of the cabin-suspended ships is given in details. The evolution of the ship structure and the control systems, as well as the effectiveness of each ship type are demonstrated. The lengths of the model ships are 1.6 m and 3.28 m, respectively. Those ships are either in shape of a trimaran or a catamaran. Towing tank tests at regular head waves and beam waves were carried out. The heave, pitch and roll motions of the cabin were observed and evaluated. The motion attenuation and elimination of each model ship is evaluated by comparing the cabin's motion at a control mode to that at a free mode and a rigid mode, respectively. Energy absorption by the generators and energy consumption by the motors are demonstrated when a semi-active control system and an active control system are adopted, respectively. In the end, comparisons on the average motion response of the cabin among six model ships are discussed, the possible applications, the issues need to be dealt with and the future plan of the proposed ships are summarized.

Keywords: *Motion Control, Skyhook Control, Suspension System, Ride Comfort, Catamaran*

1. INTRODUCTION

Marine vessels, which use fossil fuels as the main power source, have been rapidly developed since the second industrial revolution. The design of a vessel mainly depends on its usage. For instance, cargo vessels would pursue large loading capacity and low operation cost, while passenger ships and ferries turn to require high ride comfort and short travel time. In 2011 additional requirements concerning to the greenhouse gases (GHG) emission have been proposed in accordance with the amendments of the Annex VI of International Maritime Organization's pollution prevention treaty (MARPOL). In 2012, guidelines concerning to Energy Efficiency Design Index (EEDI) were issued. Those treaties require the existing ships to reduce about 30% of GHG emission by 2030 and the new ships to obtain the International Energy Efficiency Certificate (IEEC) before their initial survey (IMO, 2011).

Given this, technologies and researches on improving energy efficiency, developing waste heat recovery systems and design of low-emission ships have drawn great attentions. Here, the main concern is given to the latter one, especially for the smaller ships other than ocean-going vessels. The technologies and proposals for reducing GHG emission and improving ride comfort are focused.

Smaller ships are normally used as passenger ships, ferries, fishing boats, sailboats, leisure boats and so on. For those ship types, which have short travel distance, one of the alternative power sources of fuel oil can be electricity. The first battery-powered passenger/car ferry, namely Ampere, has been put in operation since 2015 in Norway. It was reported that the ship is zero GHG emission and could cut costs by 30% (ShaHan, 2015). Hybrid electric propulsion has been proposed to reduce fuel oil consumption of the existing ships. In order to use both fuel oil and electricity, and to drive the propulsion system at the optimum point, the engine system are required to be reengineered (Dedes et al., 2012).

It is known that utilizing suspension systems to isolate vibration has reached great success in automotive industries. However, the applications of such technique on ships are rare. In 1990, a cabin-suspended passenger ship, named HSCC VOYAGER, was built and put in operation in Shimonoseki-Kokura-Yahata route in Japan. The results of its sea trials showed that about 75% of the roll and pitch of the cabin were reduced comparing to the twin-hull (Kihara et al., 1991). In 2012 and 2014, several sea trials of two cabin-suspended ships were unveiled by Velodyne Marin® and Nauti-craft Pty Ltd, respectively (Velodyne, 2012; Nauti-craft, 2014). The video of those sea trials presented great stability and high level of ride comfort of the suspended cabin. The mechanical energy of the cabin was converted into heat by the damping systems. In the Japan International Boat Show 2018, a concept boat produced by Nauti-craft Pty Ltd and Yanmar Co., Ltd was exhibited. It was reported that the boat has achieved certain level of energy absorption while using a hydraulic suspension system to improve stability (Yanmar, 2018). However, converting the aborted energy into electricity was not achieved yet.

Inspired by the ride quality improvement and energy saving techniques widely used in the land vehicles, the authors have proposed and tested a series of cabin-suspended ships since 2008. On the one hand, feasibility of converting the mechanical energy of the oscillating cabin into electrical energy was investigated, on the other hand, proper control algorithms aiming to eliminate the motion of the cabin at the most were sought.

In this paper, an overview of those cabin-suspended ships is given. The ships were named Wave Harmonizer (WHzer). Seven types model ship have been made and investigated, in which one type was not finished yet. The motion response of the cabin

and the energy production of the control systems in six types are demonstrated in details. Here, the positive and negative values of the energy production represent energy absorption and energy consumption, respectively.

2. STRUCTURE AND CONTROL SYSTEMS

The development of the WHzers started in 2008. The evolution of the prototypes involves the ship structures and the corresponding control systems. The ship structures can be divided into three parts: the cabin part, the hull part and the conjunction part, while the control systems are categorised as: passive control system, semi-active control system and active control system.

2.1 Type-1 and Type-2

The first prototype of the WHzers, named WHzer-1 or Type-1, was in shape of a trimaran. It consisted of three planning hulls and one submerged float. The buoyance was mainly provided by the submerged float. Three sets of suspension were mounted between the cabin's deck and the planning hulls (Lu, 2010). WHzer-2 was a catamaran, which had two sets of suspension on each planning hull (Tsukamoto, 2010). The details of the ship structures and components are given in Figure 1 and Figure 2, respectively.

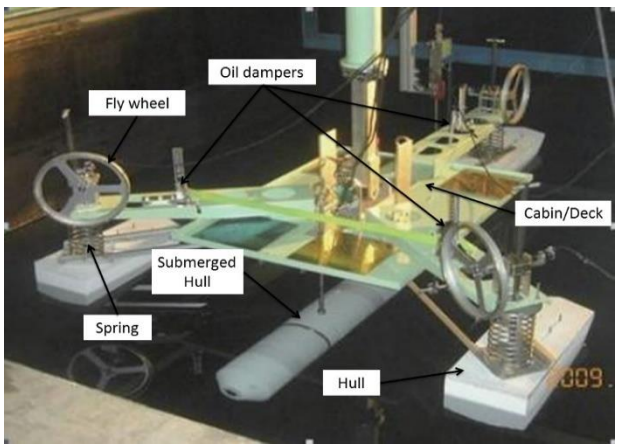

Figure 1 Structure and components of WHzer-1. The research was conducted during 2008-2010.

For WHzer-1 and WHzer-2, the components of the conjunction part included compression springs, rack-pinions and mechanical linkages. The control system was comprised of oil dampers and fly-wheels.

The degrees of freedom (DOFs) of the suspended cabin depended on the structure of the mechanical linkages, and were discussed on a basis of using the hull part as a reference. For instance, if heave distinction between the cabin part and the hull part can be sustained while the hull part is excited vertically, it is regarded that one DOF of the cabin (heave) is obtained. Such estimation of the DOF can be extrapolated to other motion modes. As a result, the cabin of WHzer-1 had three DOFs: heave, pitch and roll, while that of WHzer-2 had two DOFs: heave and pitch.

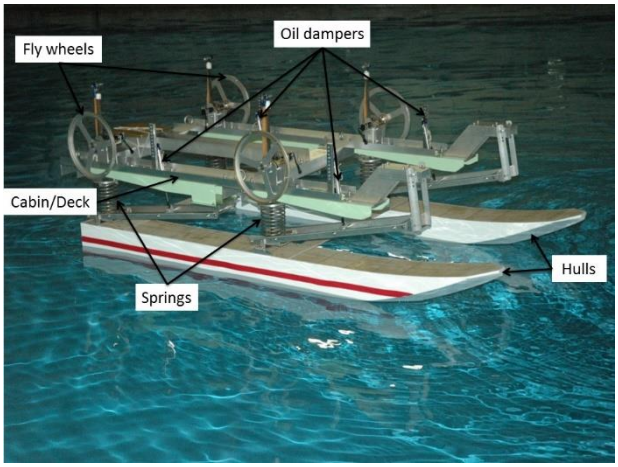

Figure 2 Structure and components of WHzer-2. The research was conducted during 2010-2011.

The motion responses of the cabin in WHzer-1 and WHzer-2 were modified by tuning the damping coefficient of the oil dampers and the moment of inertia of the flywheels. Hereby, the motion control system was regarded as passive.

2.2 Type-3 and Type-4

The cabin part and the conjunction part of WHzer-3 were as same as those of WHzer-2. The main modification was the shape of the hull part and the algorithm of the control system. One structural keel with a breadth of 0.03m was mounted into each hull to increase buoyance. The oil dampers and the flywheels were removed. A new passive control system, which consisted of a stepping motor and an electric circuit, was developed (Figure 3). One control system was used for the front two suspensions, while the other was for the rear two suspensions. By doing so, the tuning operation of the damping coefficient became easier and for the first time, the energy production of the control system was experimentally investigated.

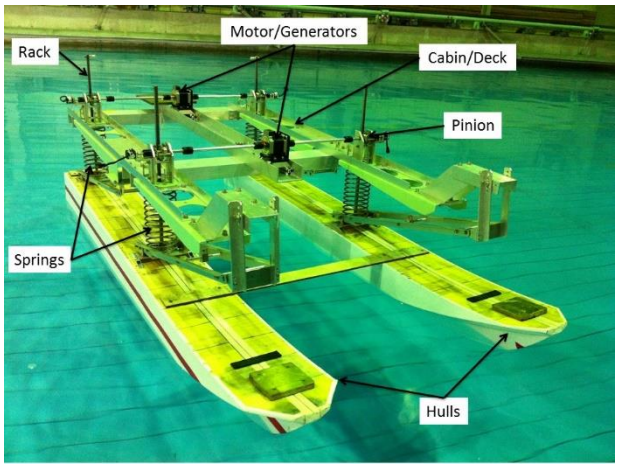

Figure 3 Structure and components of WHzer-3. The research was conducted during 2011-2012.

The structure of WHzer-4 was as same as that of WHzer-3. The major progress was given to the development of a semi-active motion control system (Han, 2013).

As shown in Figure 4, dual stepping motors were placed in the front and rear of the deck near the cabin's centre longitudinal line, respectively. At each end of the centre line on the deck, a y-z axis acceleration sensor, produced by Murada Electronics with part number of SCA1020-D02-1, was used to collect the local vertical acceleration. This signal was then sent back to a local semi-active control system. Whether or not a control force should be exerted is determined by whether or not reduction of the local vertical velocity of the cabin can be achieved consequently. In this control system, the stepping motors were activated only as generators. Owing to the braking torque of the stepping motors, electricity was produced and the rotational speed of the motors was reduced, hence the local vertical velocity of the cabin was slowed down.

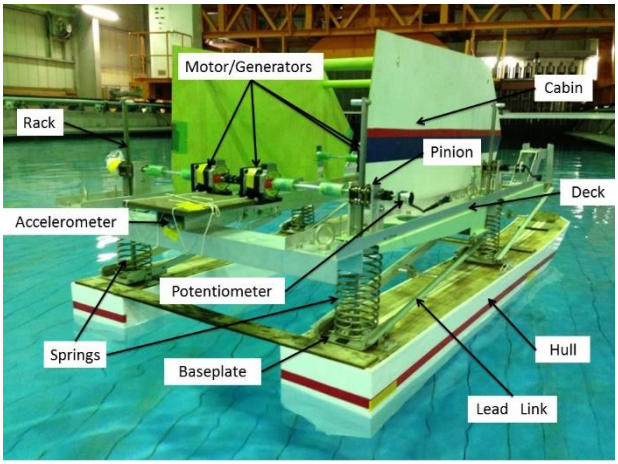

Figure 4 Structure and components of WHzer-4. The research was conducted during 2012-2013.

The suspended cabin of WHzer-3 and WHzer-4 had two DOFs: heave and pitch. The towing tank tests were implemented at regular head waves.

2.3 Type-5

In early 2013, two displacement hulls were made (Figure 5), and a hydrodynamic force experiment was conducted. The development of the prototype of type-5 with a semi-active control system was paused due to a time conflict with the development of WHzer-6.

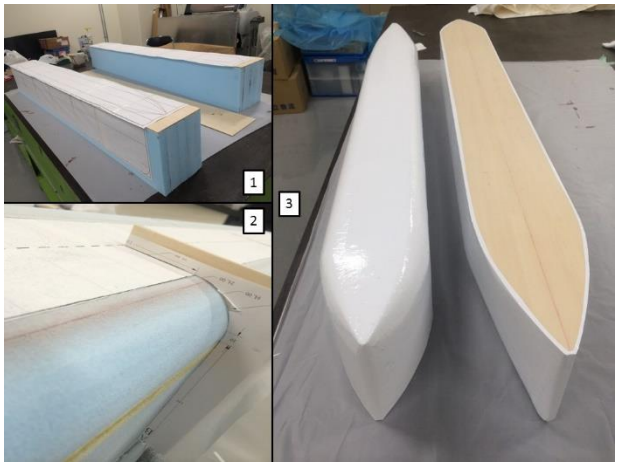

Figure 5 Steps of producing the displacement hulls. The research was conducted in 2013.

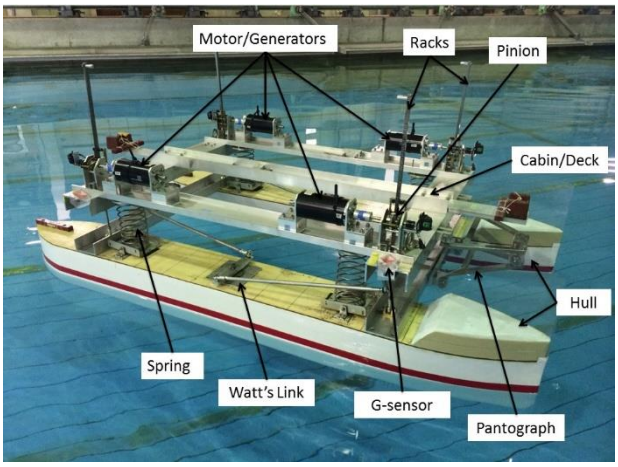

Figure 6 Structure and components of WHzer-6. The research was conducted during 2013-2014.

2.4 Type-6 and Type-7

A new conjunction part and a cabin part were proposed and designed in later 2013. WHzer-6 was formed by combining those two parts with the twin-hull developed in WHzer-5. The structure and the components of the ship are given in Figure 6.

The conjunction part consisted of two pantographs, two sets of Watt's links and four modified rack-pinions. The pantographs were attached at the front and the rear of the ship. One end of a pantograph was fit to the cabin's deck, while the other end to a bridge frame that connecting the two hulls. The Watt's links were mounted between the cabin and the twin-hull in a way that one for each hull. The middle joint of a Watt's link was fixed on a hull, while its two ends were bolted at the bottom of the cabin's deck near the front and rear compression springs, respectively. The rack-pinion units were modified to reduce the twist of the gear mesh caused by the roll distinction between the cabin and the twin-hull.

The cabin had three DOFs: heave, pitch and roll. The tank experiments were implemented at regular head waves and beam waves. (Han et al., 2015).

An active control system was developed for WHzer-6. The system consisted of a Motor/Generator (M/G), an accelerometer and a Proportional (P) controller. Known that one suspension was taken in charge of one active control system, hence, there were four sets of active control systems in total. The M/Gs were coreless brushed DC motors produced by Maxon Motor with part number of 353300. The local vertical acceleration of the cabin, above each compression spring, was collected by an accelerometer. The integrated signal of the acceleration, which means the local vertical velocity, was sent to the P controller. The aim of this P controller was to sustain the local vertical velocity at zero.

It should be mentioned that the exerted control force by each P controllers was relayed only on the local vertical velocity. The interaction among the four P controllers were regarded as external disturbance which was not discussed specifically.

WHzer-7 was in length of 3.28 *m*. The components of its conjunction part were similar to those of the WHzer-6 except the size was enlarged. The twin-hull was designed in a more practical way. Two 80 lbs bow mount trolling motors and a 24 volt power supply were adopted in the propulsion system. A gear head with reduction ratio of 3.7 was combined to each M/G. The structure and components of the

WHzer-7 are given in Figure 7. Tank tests and sea trials were implemented in 2016 (Han et al., 2017).

Figure 7 Structure and components of WHzer-7. The research was conducted during 2015-2016.

2.5 Quarter Model and Equations of Motion

The control force, either provided by passive control system, semi-active control system or active control system, was acted on the cabin part and the hull part as action-reaction pairs. A simplified quarter model of the ship is shown in Figure 8. The equations of motion of the quarter model shown in Fig. 8 are:

$$M_s\ddot{Z}_s = -k_s(Z_s - Z_u) - F_s \tag{1}$$

$$\begin{aligned}&(M_u + a_{33})\ddot{Z}_u \\ &= E_3 - k_w Z_u - C_w\dot{Z}_u + k_s(Z_s - Z_u) + F_s\end{aligned} \tag{2}$$

where a_{33} is the heave added mass, E_3 is the wave exciting force, F_s is the control force.

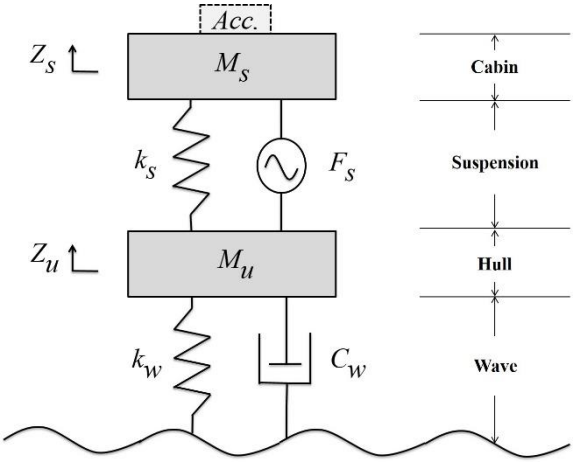

Figure 8 Schematic diagram of a quarter model of the ships with suspension systems.

The control force can be expressed in two ways according to the control algorithms. For a passive control system, the force is a product of the damping coefficient and the relative velocity of the cabin and the hulls, as given in Eq. (3); for a semi-active control system or an active control system, it is a function of the gain of the controller, the cabin's velocity and/or acceleration, as given in Eq. (4).

$$F_s = C(\dot{Z}_s - \dot{Z}_u) \tag{3}$$

$$F_s = F_s(gain, \dot{Z}_s, \ddot{Z}_s) \tag{4}$$

The damping coefficient of an oil damper C_o is determined by its specification, while that of the electrical damper C_e is determined by the arrangement of the RLC circuit being adopted. For Type-3, only a loading resistant was employed in the RLC circuit, thus the C_e can be estimated by

$$C_e = \frac{K_e K_t}{r^2(R_w + R_L)} \tag{5}$$

in which, K_e, K_t and R_w represent the M/G's back electromotive force constant, torque constant and winding resistance, respectively; r is the radius of the pinion, R_L is the loading resistance.

2.6 Summary

The specification of the model ships are given in Table 1. The sprung mass indicates the sum of the mass of the cabin part and half mass of the conjunction part, while the unsprung mass includes the mass of the hull part and half mass of the conjunction part.

Table 1 Specification of the model ships

WHzer	1	2	3	4	6	7
Length (m)	1.6	1.6	1.6	1.6	1.6	3.28
L_{pp} (m)	1.5	1.4	1.5	1.5	1.6	3.28
Breadth (m)	1.2	0.8	0.83	0.83	0.83	2.1
Draft (m)	0.14	0.127	0.129	0.129	0.11	0.4
Sprung Mass (kg)	12.6	20.8	26	26	31.9	611
Unsprung Mass (kg)	1.2	8.2	10.7	10.7	13.1	326
Spring Constant (N/m)	120	527	615	615	615	6890
Control System	Passive	Passive	Passive	Semi-active	Active	Active

The evolution of the WHzers can be summarized as follow. WHzer-1 and WHzer-2 adopted passive control systems, which included oil dampers and flywheels, to modify the motion of the cabin. WHzer-3 equipped two passive control systems which included stepping motors and RLC circuits. The energy harvesting ability was evaluated for the first time. WHzer-4 employed two semi-active control systems, which were comprised of dual stepping motors and PI controllers. The control system was aimed to reduce the absolute vertical velocity of the cabin, meanwhile investigated the amount of wave energy that can be absorbed. WHzer-5 had two displacement hulls. The hydrodynamic force test of the hulls was done. WHzer-6 owned four active control systems, which consisted of coreless brushed DC motors and P controllers. The aim is to sustain the cabin's vertical velocity above each compression spring at zero. WHzer-7 had similar control systems to the WHzer-6. The size of WHzer-7 was larger and gearheads were employed.

3. EVALUATION ON MOTION RESPONSE AND ENERGY PRODUCTION

3.1 Evaluation Method

The dimensionless heave, pitch and roll motions of the cabin are depicted with respect to the ratio of the wave length to the length between perpendiculars. When the ships were towed at a forward speed of 1.5 *m/s*, the wave length of encounter was used to calculate the length ratios. In this way, the effectiveness of the control algorithms on the motion reduction and energy production, regardless of the forward speed variation, can be distinguished readily.

In the following figures, η, k and L_{pp} represent the incident wave amplitude, wave number and the length between perpendiculars, respectively, while λ and λ_e represent wave length and wave length of encounter, respectively.

In deep water, wave length of encounter is defined as the wave length as seen from a ship, which can be written as

$$\lambda_e = \frac{gT_e^2}{2\pi} \tag{6}$$

where T_e means wave period of encounter.

Motion responses at the rigid mode and/or the free mode are employed as references. At the rigid mode, the cabin and the hulls are rigidly connected which firms a rigid body ship. At the free mode, the damping coefficient of the suspensions is approximate zero.

Terms used to evaluate the motion modification of the cabin are defined as follow. If a motion at a control mode is smaller than

that at the free mode, the motion modification by the control system is called attenuation; if it is smaller than that at the rigid mode, it is called elimination. Both attenuation and elimination can be called reduction.

3.2 Type-1 and Type-2

A series of towing tank tests of WHzer-1 was carried out in 2010. The investigation was given to the heave, pitch and roll motion of the cabin and the three planning hulls, respectively. The test conditions varied in terms of towing speed, damping coefficient, clutch force, wave frequency and wave propagation angle.

The maximum moment of inertia of a flywheel was controlled by a clutch. This clutch connected the flywheel to the pinion of a rack-pinion unit. Above a given clutch force, the flywheel and the clutch would spinning at different speeds and cause slipping. This setting was used to smooth the movement of the cabin, and prevent it from jerking with the incident waves.

Typical results of the heave and pitch of the cabin are given in Figure 9. In which, C_o represents the damping coefficient of the oil damper. It is seen that at zero forward speed, the heave and pitch at the free mode and the passive control mode were similar, although heave attenuation of the cabin is occasionally observed. Comparing the control mode to the rigid mode, a significant peak of the pitch is observed. It implies that the damping coefficient of 130 *Ns/m* might be too weak to eliminate the pitch motion. At the forward speed of 1.5 *m/s*, elimination of the heave and pitch are only obtained at few wave conditions.

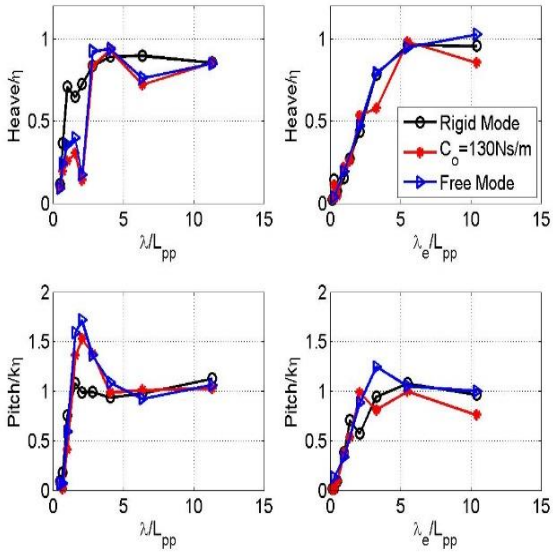

Figure 9 Heave and pitch response of the cabin of Type-1. Left: $v = 0m/s$; right: $v = 1.5m/s$.

Generally, the effectiveness of the passive control system on motion elimination is not clearly observed. But, the development and test of WHzer-1 provided the authors valuable information and perspectives on the development of the next type of the cabin-suspended ship.

Towing tank tests of WHzer-2 were implemented in 2011 at regular head waves. The focus was placed on the heave and pitch motion modification of the cabin as well as that of the twin-hull. The test conditions varied in terms of towing speed, damping coefficient and clutch force.

Comparisons among two damping coefficients and the rigid mode are shown in Figure 10. At the zero forward speed, the heave elimination by the passive control system is seen at few cases in short wave conditions, while at others it is barely observed. Moreover, the pitch motion is slightly exacerbated at the control mode. At the forward speed of 1.5 *m/s*, elimination of the heave and pitch are observed at most of the wave conditions. The results also show that the stronger the damper the more the contribution on motion reduction.

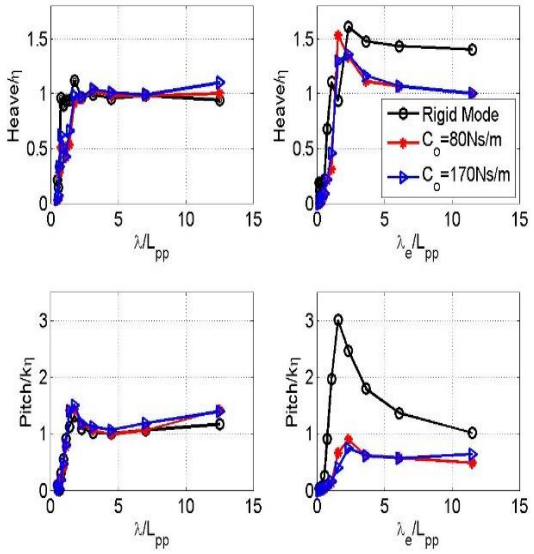

Figure 10 Heave and pitch response of the cabin of Type-2.

The development and the test of WHzer-2 provided the authors promising potential on the motion elimination of the suspended cabin. It also suggested that catamaran might be a suitable ship type for further investigations.

3.3 Type-3 and Type-4

The passive control system of WHzer-3 was tested in regular head waves in 2012. The damping coefficient was tuned by varying the load resistance of the RLC circuit. The tank test results under two damping coefficients and the free mode are given in Figure 11. In which, C_e represents the electrical damping coefficient. It is observed that the control system attenuates the heave and the pitch of the cabin in a basis that the stronger the damping coefficient, the more the attenuation.

The amount of the time-averaged electrical energy flowed through the control system is estimated by

$$P_{cs} = \frac{1}{nT}\int_0^{nT} V(t)I(t) + I(t)^2 R_w dt \qquad (7)$$

in which, nT is a duration with wave period of T and an integer of n, $V(t)$ and $I(t)$ represent the motor terminal voltage and the electric current, R_w represents winding resistance of the motor. Positive and negative values of P_{cs} indicate the amount of the time-averaged energy that flows out of and flows into the control system, respectively. In other words, the positive or negative sign of P_{cs} tells the energy is harvested or consumed accordingly. It should be pointed out that in Eq. (7) the energy consumed by the winding resistant is compensated by the second term in the right side of the equation. By doing so the error brought by the motor selection can be eliminated.

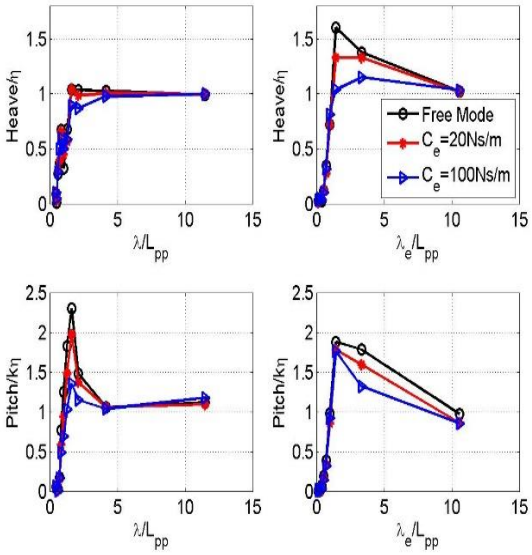

Figure 11 Heave and pitch response of the cabin of Type-3.

The time-averaged energy carried by the wave crest per meter seen from the ship in deep water condition is defined by

$$P_{wv} = \frac{1}{32\pi}\rho g^2 H^2 T - \frac{1}{16}\rho g H^2 v\cos\beta \qquad (8)$$

in which, P_{wv} is the time-averaged energy of encounter, ρ and g represent the water density and the acceleration of gravity, H is wave height and v is the velocity of the ship, β is the encounter angle between the direction of the wave propagation and ship's heading.

The wave energy capture width ratio (CWR) is defined by the ratio of P_{cs} to the

product of the hull width and P_{wv}. Typical results of the energy production are given in Figure 12. The upper sub-figures represent the amount of the time-averaged energy that has been absorbed. The peaks of the absorbed energy are seen when the wave length or the wave length of encounter approaching to the length between perpendiculars. It also shows that the amount of energy and the corresponding CWR with C_e of 20 *Ns/m* are generally larger than that at 100 *Ns/m*.

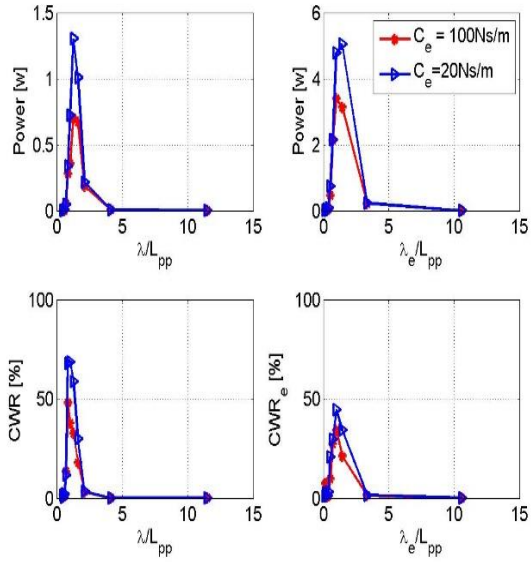

Figure 12 Energy production of the passive damping system of Type-3.

A series of towing tank tests of WHzer-4 was implemented in 2013. P gain and I gain of the semi-active motion controller were tuned in the tests. Typical results of the heave and pitch motion response of the cabin are given in Figure 13, the corresponding energy production is depicted in Figure 14.

In Figure 13, it is observed that attenuation of the heave and pitch of the cabin are achieved. However, the elimination are only obtained at short waves, for instance when the wave length is less than the length between perpendiculars. In Fig.14, the peak of the energy harvesting at zero forward speed is found near the λ/L_{pp} of 1, while that at the forward speed of 1.5 m/s is seen near the λ_e/L_{pp} of 1.5. The peaks of the CWR are about 30%.

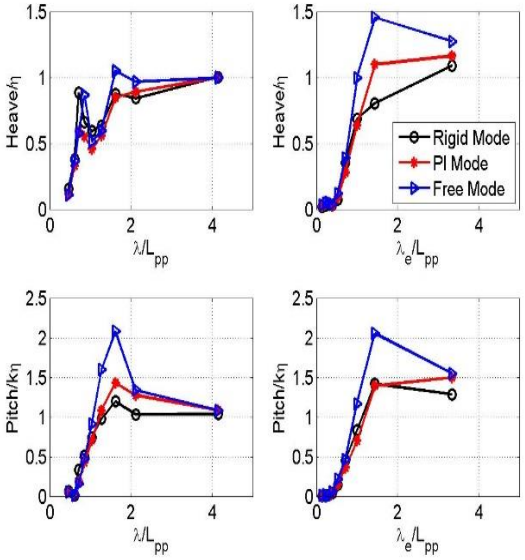

Figure 13 Heave and pitch response of the cabin of Type-4.

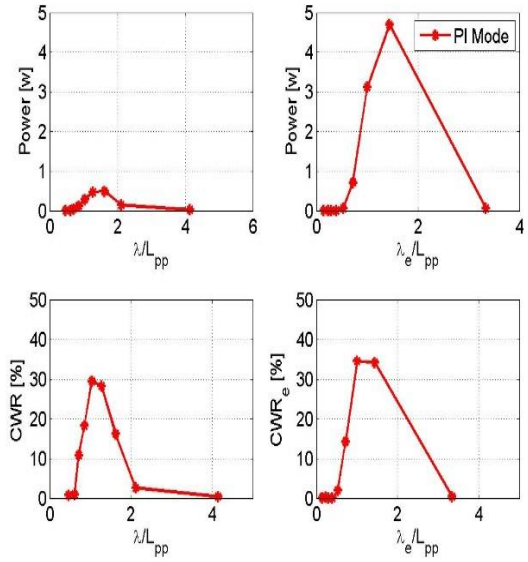

Figure 14 Energy production of the semi-active damping system of Type-4.

3.4 Type-6 and Type-7

The energy harvesting mode and the motion reduction mode of the control system in the WHzer-6 and WHzer-7 were operated and discussed separately. In the section, only the motion reduction mode, which is also called the skyhook mode, is demonstrated. In this mode, the M/Gs were activated only as motors. Energy was consumed to drive the motors exerting control force.

The towing tank tests of WHzer-6 were carried out in 2014. Gains of the P-controller were tuned at varies regular head waves and beam waves. A group of typical results of the cabin's motion and the corresponding energy production of the control system are given in Figure 15 and Figure 16, respectively.

In Figure 15, attenuation and elimination of the heave and pitch of the cabin are achieved at both towing speeds. Specifically, significant reduction of the resonance of the heave and the pitch are observed.

In Figure 16, the amount of the time-averaged energy and the corresponding CWR are depicted. It shows that along with the growth of the wave length, the amount of energy consumed by the control system is increasing accordingly. The peaks of the CWR are observed at the condition where the resonances of the cabin are eliminated at the most. The CWRs are about -250% and -220% at zero forward speed and at the forward speed of 1.5 *m/s*, respectively.

The results of the motion modification and the energy production at the beam wave conditions are given in Figure 17 and Figure 18, respectively. Those tests were only implemented at zero towing speed.

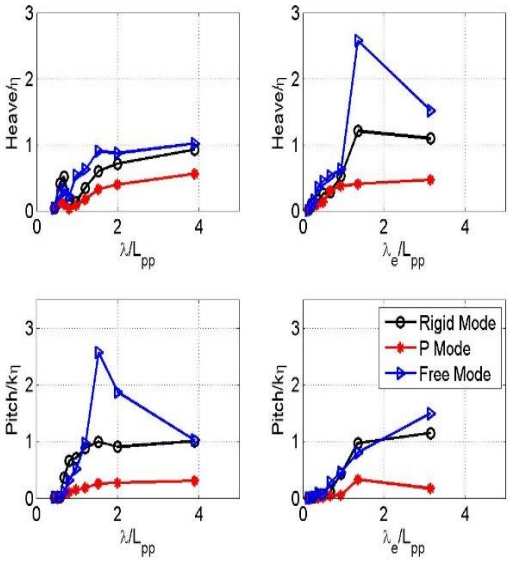

Figure 15 The heave and pitch response of the cabin of Type-6.

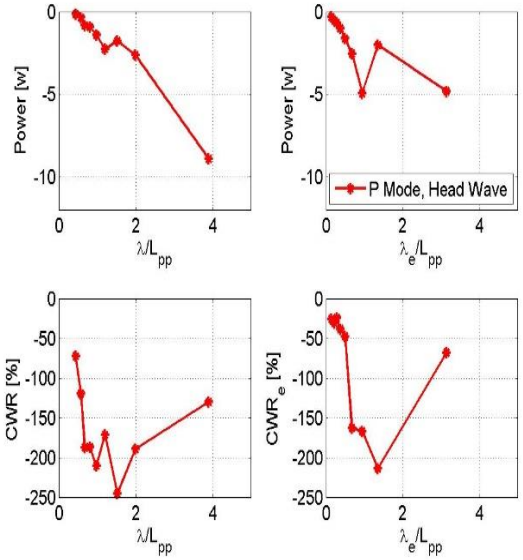

Figure 16 Energy production of the active control system of Type-6.

In Figure 17, significant attenuation and elimination of the heave of the cabin are observed, while that of the roll is only seen at the λ/L_{pp} of 3.8. When the wave length gets longer, the roll of the cabin at the control mode is approaching that at the rigid mode, however, the roll at the free mode is substantially increased.

In Figure 18, at short waves, although the amount of consumed energy is little, the CWR reaches up to -800%. This might be partly caused by the measurement error and partly by the true consumption increase of the control system. It is suggested this case should be repeated if possible in the future, so as to gather the proper value of the energy consumption. At other wave conditions, the CWR is about -200%, which means approximate twice of the energy carried by the wave crest with the same width of the twin-hull is consumed.

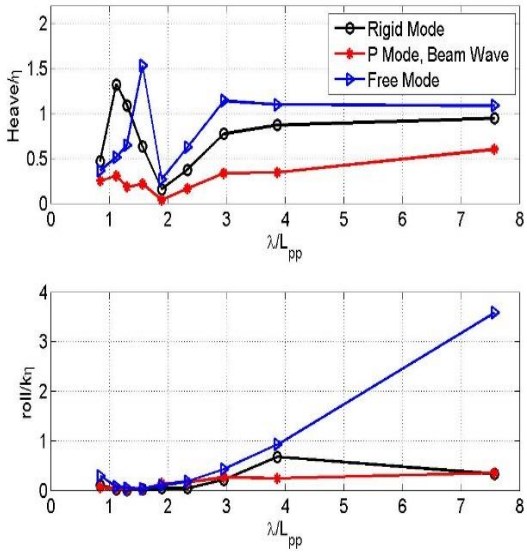

Figure 17 Heave and roll motion of the cabin of Type-6 at beam wave condition.

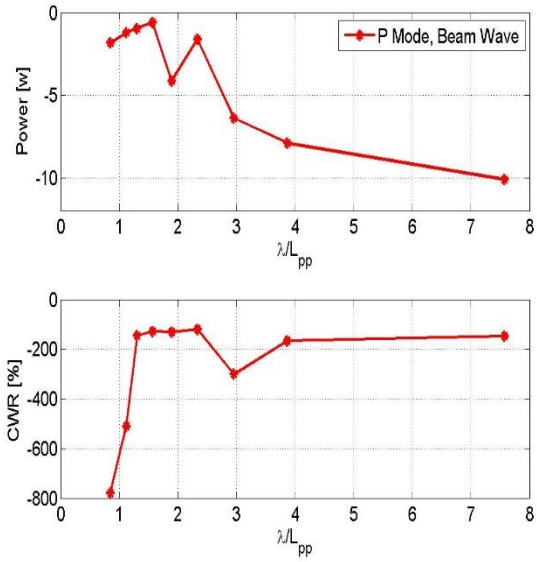

Figure 18 Energy production of the active control system of Type-6 at beam wave condition.

Tank test of Type-7 was implemented in 2016 at three regular waves. At which the accelerations of the cabin were regarded as sufficient to activate the active control system. The motion responses of the cabin at head waves and beam waves are given in Figure 19, while the corresponding energy productions are depicted in Figure 20.

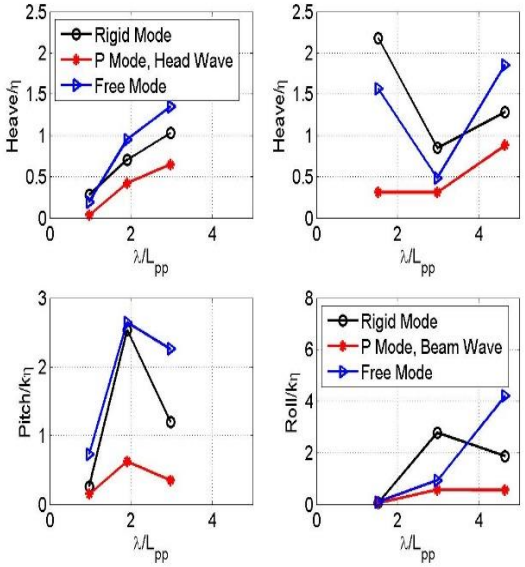

Figure 19 Heave, pitch and roll motion of the cabin of Type-7 at head wave and beam wave condition.

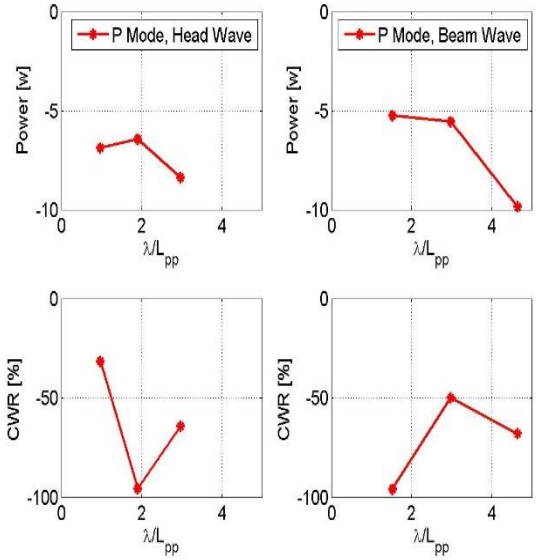

Figure 20 Energy production of the active control system of Type-7 at head wave and beam wave.

In Figure 19, the attenuation and elimination of the heave and pitch at the head waves and those of the heave and roll at the beam waves are achieved, especially on the peaks of the pitch and the roll motion.

In Figure 20, the amount of the time-averaged energy consumption increases along with the growth of the wave length, and the peak of the consumption is about 10 *Watt* at the

beam wave condition when the wave length is approximate 4.5 times of the length between perpendiculars. The peak of the CWRs are about -100%, which means the energy consumption of the control system is almost as same as the energy carried by the wave crest with the same width of the twin-hull.

4. DISCUSSION

4.1 Effectiveness Evaluation

Average reference ratio is proposed when making comparisons among the WHzer's prototypes with respect to the motion modification of the cabin under different control scenarios.

For each type of the WHzers, the wave conditions tested at the control mode, the rigid mode and the free mode are the same, which is regarded as a wave package. Let the weight factor of each wave condition be 1, then the mean value of the dimensionless motion responses at a mode (free mode, rigid mode or control mode) is treated as the average motion response of the mode at the wave package.

The average rigid reference ratio and the average free reference ratio are defined as the ratio of the average motion response at a control mode to that at the rigid mode and the free mode, respectively. The neutral ratio is 1. The less the ratio, the higher the effectiveness of the control system. Comparisons among the average reference ratios are given in Tables 2-4.

It is seen that all the prototypes of the WHzers have reached certain attenuation on the cabin's motion judging by the fact that the average free reference ratios are less than 1. However, from WHzer-1 to WHzer-4 the pitch of the cabin is exacerbated slightly as seen that the average rigid reference ratios are larger than 1 but less than 1.1.

Table 2 Average reference ratio at head wave conditions with zero forward speed.

	Average Rigid Reference Ratio		Average Free Reference Ratio	
WHzer-	heave	pitch	heave	pitch
1	0.72	1.09	0.92	0.92
2 80Ns/m	0.79	1.04	-	-
3 100Ns/m	-	-	0.58	0.66
3 20Ns/m	-	-	0.99	0.87
4	0.89	1.06	0.88	0.81
5	-	-	-	-
6	0.47	0.24	0.38	0.18
7	0.54	0.28	0.44	0.2

Table 3 Average reference ratio at head wave conditions with forward speed of 1.5 m/s.

	Average Rigid Reference Ratio		Average Free Reference Ratio	
WHzer-	heave	pitch	heave	pitch
1	0.95	0.96	0.95	0.95
2 170Ns/m	0.73	0.25	-	-
2 80Ns/m	0.73	0.27	-	-
3 100Ns/m	-	-	0.42	0.49
3 20Ns/m	-	-	0.93	0.9
4	1.09	0.99	0.78	0.75
5	-	-	-	-
6	0.51	0.23	0.3	0.2
7	-	-	-	-

At the forward speed of 1.5 *m/s*, in Table 3 all the ratios are less than 1, except for the averaged rigid reference ratio of WHzer-4. It tells that the active motion control system adopted in WHzer-6 and WHzer-7 have strong ability on motion elimination of the cabin. At head wave conditions, the average rigid reference ratios of pitch are less than 0.3,

which implies in average more than 70% of pitch motion is reduced comparing to the rigid body ship, meanwhile that reduction of heave is more than 55%.

At beam wave conditions, in Table 4 the average rigid reference ratios of heave and roll are less than 0.75 and 0.26, respectively, which tell that in average more than 25% of heave and more than 74% of roll are reduced.

Table 4 Average reference ratio at beam wave conditions with zero forward speed.

	Average Rigid Reference Ratio		Average Free Reference Ratio	
WHzer-	heave	roll	heave	roll
6	0.74	0.16	0.81	0.63
7	0.39	0.25	0.38	0.23

4.2 Application and Future Plan

Based on the test results mentioned in section 3, at a given wave condition, especially near the ship's resonance frequency, one may notice that the motion responses of the cabin at the free mode are generally larger than that at a control mode and the rigid mode. It addresses a risk of equipping suspensions on ships in a way that once the control system fails or breaks down, the passengers, equipment and the ship itself may be exposed in an extreme oscillation condition. To reduce the risk, fail-safe strategy of the control system is required.

In present study the redundancy of the four control systems may reduce such risk. If one of the four systems fails, the rest three may still work normally and sustain certain motion attenuation or reduction of the cabin.

To explore the possibility and feasibility of utilizing suspensions to benefit the wave energy harvesting and ride comfort improvement, the authors have tested several algorithms. It is suggested that the control strategy should vary along with the usage of a WHzer. For the stability-oriented ships, such as ferries and passenger ships, skyhook mode of the controller should be adopted; for the speed-oriented ships, such as rescue boat and coast guard boat, the skyhook mode may improve its maximum speed by attenuating the slamming; for maintenance ships which need transport personals or equipment between the ship and offshore structures, absolute position control of the cabin could be developed to keep the cabin at a specific height above the sea surface so as to provide a safe connection between the plants; for the energy-saving purpose, a proper speed of the ship should be chosen to harvest wave energy at the most; moreover, in the case that a ship is in port, the energy harvesting mode could be activated to generate and store electrical energy.

An issue that was not mentioned and hardly to be observed in the motion response figures is the inclination of the cabin while weights are loaded or unloaded apart from the centre of gravity of the cabin. To solve the problem, inclination control system is proposed and developed as an outer loop of the skyhook control circuit. Another prototype, called WHzer-8, was tested with inclination control in 2017. The results of the tank test and sea trial will be summarized in the near future.

5. CONCLUSIONS

The evolution of seven types of cabin-suspended ship, the WHzers, is demonstrated. Typical results of the towing tank tests are given. Comparisons among the motion responses of the cabin and the corresponding energy production of the control system are discussed.

The results show that along with the evolution of the ships, the effectiveness of the control system is improved. For WHzer-1 and WHzer-2, knowledge of the motion response of the suspended cabin is gained, which provides valuable perspective on designing the following types. For WHzer-3 and WHzer-4, the wave energy capture width ratio is obtained

in 30% ~ 50%. Especially, when a ship sustains a forward speed of 1.5 *m/s*, the amount of the absorbed time-average energy increases dramatically. It shows an important merit of the WHzers comparing to the existing wave energy converters which do not run on the waves. However, the ride comfort improvement of those two prototypes is not significant. Development of Type-5 was paused and not finished yet. For WHzer-6 and WHzer-7, elimination of the heave, pitch and roll of the cabin is sustainable. The average reduction of the roll motion is more than 74%, while that of pitch is more than 70% and the correlated heave reduction is above 20%. The energy consumption by the control system of the two prototypes are about twice and one time of the energy carried by the wave crest with the same width of the twin-hull, respectively.

Usage divergence of the WHzers may require the control algorithms to be flexible, and a fail-safe system should be developed before its first free running sea trial. To meet the needs of running the WHzers in real sea, the authors intend developing more precise control systems and improving the robustness of the suspension systems.

6. ACKNOWLEDMENTS

The authors are sincerely grateful, to Mr. Yukitsugu Hirota for the suggestions and comments on the control system design and the simulation program development. The authors would also like to express the deepest gratitude to the Sasakawa Scientific Research Grant from the Japan Science Society (Grant Number: 25-731), to Grant-in-Aid for Challenging Exploratory Research from JSPS (Grant Number: 25630399), and to the New Energy and Industrial Technology Development Organization (NEDO).

7. REFERENCES

Chenliang Lu, 2010, “A comfortable boat with suspensions absorbing wave power”, Master’s thesis, the University of Tokyo.

Cynthia ShaHan, 2015, “World’s first all-electric battery-powered ferry”, https://cleantechnica.com/2015/06/13/worlds-first-electric-battery-powered-ferry/

Daisuke Tsukamoto, 2012, “Basic research on a wave energy absorbing and motion-controlled ship”, Master’s thesis, the University of Tokyo.

Eleftherios K. Dedes, Dominic A. Hudson, Stephen R. Turnock, 2012, “Assessing the potential of hybrid energy technology to reduce exhaust emissions from global shipping”, Energy Policy, Vol.40, pp.204-218.

IMO, 2011, “Amendments of the annex of the protocol of 1997 to amend the international convention for the prevention of pollution from ships, 1973, as modified by the protocol of 1978 relating therteo”, ANNEX19.

Jialin Han, 2013, “Research on a new semi-active motion-controlled ship by harvesting wave energy”, Master’s thesis, the University of Tokyo.

Jialin Han, Daisuke Kitazawa, Takeshi Kinoshita, Teruo Maeda, Hiroshi Itakura, 2017, “ Motion response analysis of a cabin-suspended ship governed by a velocity feedback control system”, Conference Proceedings JASNANO, Vol.25, pp.217-221.

Jialin Han, Teruo Maeda, Daisuke Kitazawa, Takeshi Kinoshita, 2015, “Towing test and motion analysis of a motion-controlled ship – based on an application of skyhook theory”, Proceeding of the 12th International Conference on the stability of

Ships and Ocean Vehicles, Vol.2, pp.879-888.

Kazuyuki Kihara, Chikafusa Hamada, Shigeki Ohnaka, Tooru Kitamura, 1991, "Development of a 200 passenger Hi-Stable Cabin Craft", The Japan Society of Naval Architects and Ocean Engineers, 81, pp.57-69.

Nauti-craft Pty Ltd., 2014, http://www.nauti-craft.com/

Yanmar Co., Ltd, 2018, https://www.yanmar.com/global/news/2018/03/08/39663.html

Velodyne Marine, 2012, http://www.velodynemarine.com/

Influence of Trimaran Geometric Parameters on Intact and Damaged Ship Stability

W. Scott Weidle, *NSWC Carderock Division* william.weidle@navy.mil

ABSTRACT

Recently the trimaran ship has captured interest among designers and stakeholders. A multi-hull continuum is introduced to explain intact stability of trimarans between that of a monohull and catamaran. Next, a series of trimaran configurations are modeled in CAD with subdivision and analysed according to USN deterministic stability criteria at intact and damaged conditions. The allowable KG is determined for each variation. A response surface model is estimated for allowable KG as a function of center hull length to beam, side hull beam to draft, transverse position, and displacement for use as a rule of thumb measure and optimization constraint.

Keywords: *trimaran, ship, stability, intact, damaged*

1. INTRODUCTION

A "trimaran" is a type of hull form within a larger set of hull forms called "multi-hulls." In a broad sense, the term "multi-hull" vessel was defined for this paper as a continuum of vessels between a monohull and catamaran. (Weidle, 2017) Using this definition, a monohull can be considered as a vessel with center hull and infinitesimally small side hulls and a catamaran is considered as a vessel with two side hulls and infinitesimally small center hull. Trimaran vessels are "in-between" a monohull and catamaran on this multi-hull continuum where the center hull and side hulls each contribute a portion of the total displacement. Figure 1 is a graphical representation of the multi-hull vessel continuum with the monohull on the lower left, catamaran on the upper right, and trimaran linearly in-between.

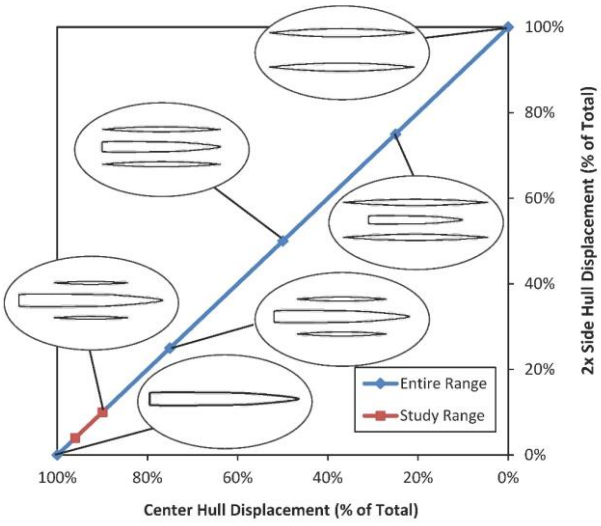

Figure 1 Multi-Hull Continuum

Previous works by Andrews and Zhang (1995, 2004a, 2004b) have found that trimarans with each side hull contributing 2-5% of the total displacement to be an optimal zone, for resistance performance, where benefits of the monohull are seen with high heel angle before deck submergence as well as benefits of the catamaran with high righting arm values. This range is plotted in red (Figure 1) where two side hulls contribute 2 to 10% of the total displacement and the center hull contributes 98 to 90% of the total displacement. This range of trimaran vessels on the multi-hull continuum under intact and damaged conditions was the focus of my thesis (Weidle, 2017) and is summarized in this paper. The transverse quasi-static stability was analyzed for several key geometric parameters.

1.1 Influential Geometric Parameters

In general, increasing draft is recommended over increasing the waterplane area for improved stability. This increases the displacement of each side hull to a reasonable minimum of 3 – 5% of total displacement, in the deep condition, while maintaining resistance performance. (Andrews, 2004a) (Andrews and Zhang, 1995) Additionally, the side hull will remain in the water for larger heel angles. Also, Andrews notes that critical stability problems occur in the damaged condition, and thus should be a principal factor in choosing the size and configuration of the side hulls.

"Specifics of damage buoyancy and stability of multi-hull ships, as compared with monohulls, are due to: the presence and configuration of their cross-structure; subdivision of both hulls and cross-structure into watertight compartments and their ratios; specifics of principal dimensions of individual hulls." (Multi-Hull Ships, Dubrovsky, p. 89) Four transverse extent conditions are recommended for assessing damage stability: (1) center hull only; (2) side hull plus associated cross-structure; (3) center hull, cross-structure and 1 side hull; and (4) complete transverse extent of ship. (Andrews, 2004a) It is also noted that for flooding in center hull only, improvements are made by increasing side hull displacement and lowering center of gravity (CoG). Also, longitudinal subdivision is necessary in the center hull to preserve transverse stability. Any additional flooding in the side hull reduces buoyancy and waterplane area, with no CoG change causing adverse effects to stability. Conversely, increasing the length of the side hull and adding bulkheads in the side hull minimizes this effect, meeting criteria.

Also, conveniently, ballasting the side hulls provides an automatic way of meeting damage criteria; the heel is controlled after damage because the sea cannot flood into tanks that are already full, possibly allowing for heel in the opposite direction. Andrews and Zhang (1995) concludes, "With this radical [trimaran] hull form the criteria for satisfactory stability must be re-examined." "Trimaran stability assessment is a much more complex task than that for monohulls and catamarans. There are many variables which affect the final stability characteristics, and a small change in a single variable may result in quite different stability qualities."

1.2 Stability Criteria

Deterministic criteria to assess stability for United States Navy (USN) surface ships was used as outlined in the current Naval Seas Systems Command (NAVSEA) technical publication (2016). A quasi-static approach which evaluates the righting arm, GZ, was used as a function of heel angle. Additionally, USN stability criteria was compared to those published by the UK MoD (2014), which comply with NATO Allied Naval Engineering Publication (ANEP). (2017) Published criteria from NAVSEA and UK MoD are very similar and were used in this paper. (Weidle, 2017)

1.3 Thesis Motivation and Objective

Compared to monohulls, there has been limited research concerning the assessment of both intact and damaged stability of trimarans. The trimaran vessel has demonstrated significantly different stability qualities than an equivalent monohull; however, the investigations examining the effect of design changes on the trimaran's stability qualities compared to monohulls are small at this point for the intact ship and even smaller for the damaged vessel subject to flooding. Trimaran vessels have only recently been examined for issues related to stability. The intact trimaran vessel has been investigated for instability in longitudinal waves (Bulian et al, 2011) and for general stability qualities encountered during early-stage design. Single naval trimaran ship configurations have been evaluated for intact and damage stability. (Andrews, 1995)

(Ordonez, 1995) However, at the time of publication, no other research was found to examine the stability qualities for a series of damaged trimaran vessels subject to flooding to understand the influence of the geometric parameters.

The general perspective for many monohull forms has been that a lower CoG and large metacentric height (GM) benefit ship stability; however, ship motions are often unfavorable for crew. For monohulls, in general, an increased beam increases the transverse metacentric height (GM_T). For a trimaran, the transverse separation, beam, and distribution of displacement for each hull are important factors influencing GM_T. How do these different geometries affect the stability and what behavior does a damaged trimaran, subject to flooding, exhibit? This thesis examined trimaran stability qualities in both intact and damaged conditions using a series of trimaran hull forms with varying geometric configurations in a Design of Experiments (DoE) approach. The relationships between geometry changes in the trimaran hull-form to intact and damaged stability qualities are observed.

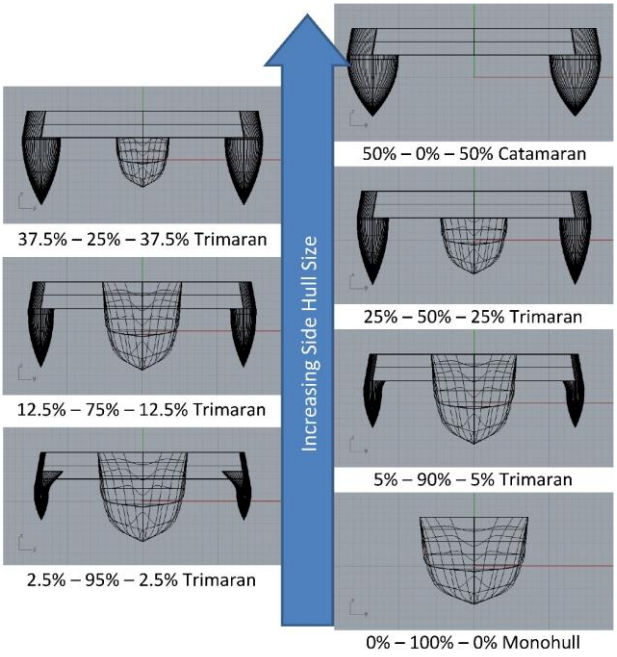

Figure 2 Generated Multi-Hulls

2. MULTI-HULL INTACT STABILITY COMPARISON

The stability advantages of trimarans compared to other multi-hull ships were examined from a quasi-static viewpoint in heel. A series of intact hull forms were generated along the multi-hull continuum, shown in Figure 1. Starting from a parent center and side hull, geometrical similar scaling (geosim) of the principal dimensions (length, beam, and draft) at the waterline was used to vary the distribution of displacement between the center and side hulls, maintaining:

Total displacement (saltwater):	3,500 mt
Initial waterplane (WP) area:	1,100 m^2
Wet Deck Clearance (WDC):	3.0 m AWL
Freeboard (FB):	6.6 m AWL
Side Hull Transverse Position (SH_Y):	13.5 m

The floating plane hydrostatic characteristics were calculated at the design displacement with a CoG corresponding to level heel and trim at the design draft line. Figure 2 shows the body view of the generated multi-hull forms.

2.1 Quasi-static Assessment in Heel

The change in waterplane (WP) area from level to 55 degrees heel for each multi-hull is plotted in Figure 3. The WP area plots show how the trimaran ships exhibit behavior in between the monohull and the catamaran with

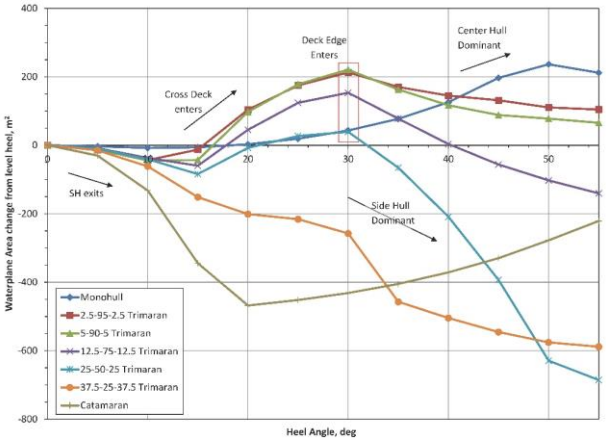

Figure 3 Change in WP Area

displacement distribution for increasing heel angles.

The righting arm, GZ, exhibits the same behavior and is plotted in Figure 4 showing the positive range of stability for each multi-hull. The monohull has the greatest range of positive stability and the smallest maximum GZ; while the catamaran has the smallest range of positive stability and the largest maximum GZ. The trimaran falls in-between where larger side hulls exhibit behavior like the catamaran and smaller side hulls exhibit behavior like the monohull. The GZ values and A1 area under the GZ curve up to the angle of downflooding are also examined. USN published criteria specifies 70 deg or less at intact condition. (NAVSEA, 2016) At 70 degrees of heel, trimarans with relatively small side hulls, 2.5% to 5% each, have advantages of larger GZ and A1 area over a monohull with a higher angle of vanishing stability. A strong trend is exhibited between side hull displacement and area, A1, when bounded by the downflood angle, when deck edge submerges, and angle of vanishing stability as shown in Figure 6.

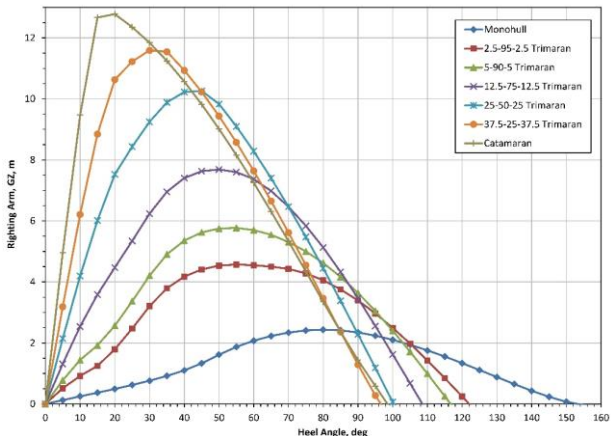

Figure 4 Change in GZ with Heel Angle

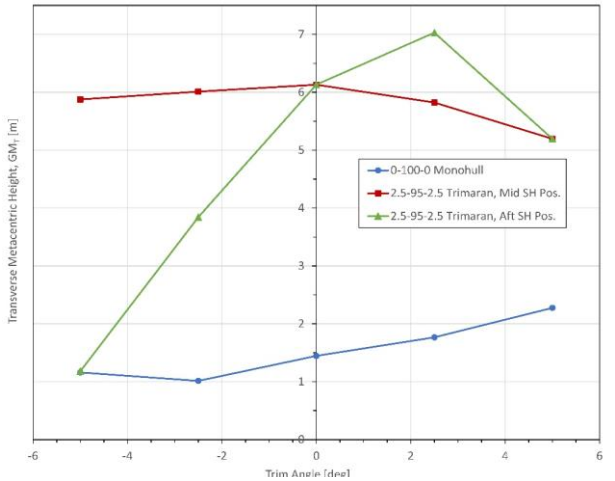

Figure 5 Change in GM_T with Trim Angle

For the monohull, the deck edge submerged at a larger heel angles around 50 degrees; in contrast to the trimarans which submerge at 30 degrees of heel.

2.2 Quasi-Static Assessment With Trim and Heel

The stability and dynamic motion of an intact ship can be further assessed in a quasi-static manner by a thorough examination of the hydrostatic properties at trim and heel angles. Using quasi-static methods some of the results found in more advanced hydrodynamic simulations can be achieved. This method is practical for use in early-stage ship design projects (Belenky and Bassler, 2010) and is employed here to analyze the monohull and 2.5% - 95% - 2.5% trimaran discussed previously, shown in Figure 2.

The GM_T at level heel is examined, shown in Figure 5. The monohull and trimaran with mid side hull (SH) position has little change in GM_T with trim angle compared to the trimaran with aft SH position which exhibits a substantial, non-linear trend with trim angle. The side hull's WP area is substantially reduced at -5 degrees, bow down trim such that GM_T is

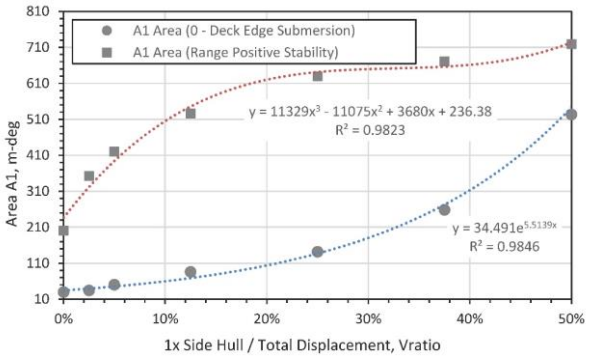

Figure 6 A1 and SH Disp Correlation

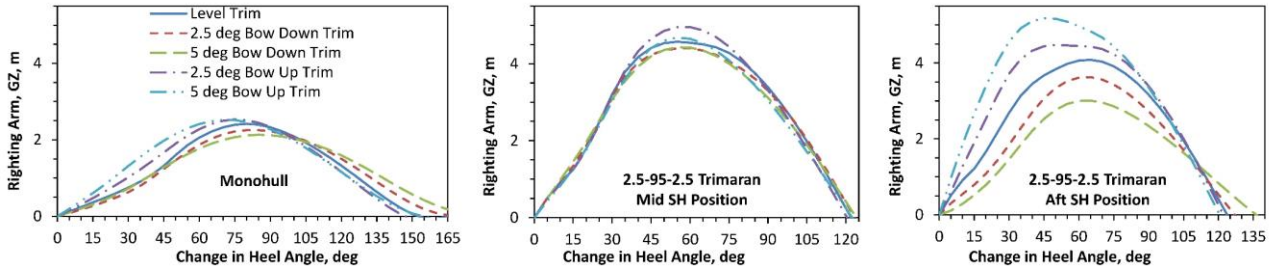

Figure 7 Change in GZ with Trim and Heel

equal to that of the monohull. This suggests that the trim angle may have an effect on the transverse stability of the trimaran with aft SH position.

Next, the effect of heel angle on the righting arm, GZ, and WP area is examined at different trim angles. The GZ curve is plotted against heel angle up to point of vanishing stability in Figure 7. These plots further show how the trim angle affects the trimaran with aft SH position more than the monohull and trimaran with mid SH position. Also note that both the mid and aft SH position trimarans have a substantially higher maximum GZ then the monohull.

2.3 Intact Stability Conclusions

The quasi-static examinations and intact stability analysis for multi-hulls along the continuum provided useful insights that will guide the next investigation of this thesis. First the side hull displacement range, Vratio from 2% to 5%, identified by Andrews (2004a) is confirmed by Figure 4. In this range the angle of vanishing stability is high, exhibiting monohull behavior; and the maximum righting arm (GZ) is relatively high, exhibiting catamaran behavior. Secondly, the effect of side hull longitudinal position is observed to have an effect on intact transverse stability at all trim angles and should be considered.

3. TRIMARAN STABILITY STUDY

The objective of this second study was to build upon the observed trends from the first intact stability study and examine the effects of additional trimaran hull form geometric parameters on transverse intact and damaged stability. The results were used to generate a stability response surface model (RSM) from trimaran hull form parameters for use as rule-of thumb in early-stage ship design. While the focus of this second study was to examine the damaged condition, the intact conditions during normal operations and overhaul, towing and decommissioning (OTD) were also examined. Certain ratios between hull dimensions and properties have a noticeable effect on stability qualities, as noted by Dubrovsky (2001, p. 89) and Andrews. Most notably the vertical center of gravity to depth ratio, KG/D, depth to draft ratio, D/T, length to beam ratio, L/B, beam to draft ratio, B/T, Vratio, and the position of the side hull transversely, SH_Y were examined. Additionally, the longitudinal position (SH_X) was examined for effects on trim and list angle during damage conditions.

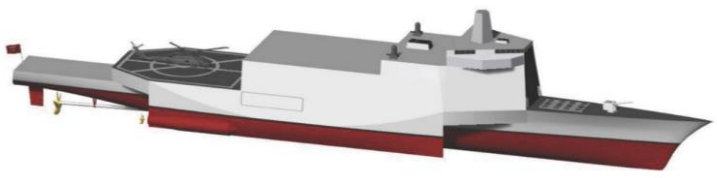

Figure 8 Isometric View of Concept

3.1 Design Concept

A multi-mission frigate concept (Figure 8) previously developed by Virginia Tech students was used as baseline for the series of trimaran hulls. (Manzitti et al, 2016) The principal characteristics are listed in Table 1.

Table 1 Concept Principal Characteristics

Length Overall, LOA [m]	150
Beam Overall, BOA [m]	24.9
Depth Overall, D [m]	11.6
Center Hull Length at Waterline, L_{CH} [m]	143
Side Hull Length at Waterline, L_{SH} [m]	64
Wet Deck Clearance [m]	3.7
Cross Deck Height [m]	3.0
Full Load Weight [mt]	3,780
Vertical Center of Gravity, KG [m]	5.9

3.2 Design Variables

Using the frigate design concept as a starting point, a series of 26 subdivided trimaran models were generated. The principal and coupled effects of side hull beam to draft ratio, $(B/T)_{SH}$, longitudinal side hull position relative to midships, SH_X, transverse side hull position relative to centreline, SH_Y, center hull length to beam ratio $(L/B)_{CH}$, and Vratio on the intact and damaged stability response were examined through a multi-stage DoE approach. The design variables (DVs) and values used in the design of experiments (DoE) are listed in Table 2.

Table 2 Design Variable Values for DoE

$(L/B)_{CH}$	12.7	14.2	15.6
Vratio (Δ_{SH}/Δ)	0.02	0.03	0.04
$(B/T)_{SH}$	0.42	0.61	1.16
SH_X / L_{CH}	0.073 (L2)		0.276 (L1)
SH_Y / L_{CH}	0.063 (T1)	0.080 (T2)	0.098 (T3)

3.3 Assumptions

The hull form length of each design was kept constant at 143 m to maintain transverse bulkhead locations and longitudinal subdivision. Additionally, displacement was kept constant at 3,780 mt to focus on the primary geometric parameters. Center hull beam at waterline (B) was determined by the specified $(L/B)_{CH}$ ratio. The center hull draft, T, was adjusted to achieve the center hull displacement distribution, $\Delta_{CH}/\Delta = 1\text{-}2\Delta_{SH}/\Delta$. Similarly, each side hull maintained constant length, while B and T were adjusted uniformly to achieve displacement distribution, Vratio.

Each hull form configuration had the same subdivision, arrangement, and downflood points (X, Y) located on the main/weather deck. The total displacement was changed proportionally with an increase in cross structure volume. The percent increase of cross structure was calculated from the baseline hull and applied to structures weight (1,311 mt). This weight was added to the design displacement and used for stability analysis. The KGa/D ratio was determined iteratively by determining the maximum, allowable KG which fulfills all stability criteria. The deckhouse was assumed to be a non-watertight space and was not included in intact or damaged stability analyses.

3.4 Intact and Damaged Stability Model

A quasi-static analysis was employed as a least resource intensive method for adequate intact and damaged stability results to inform a rule-of-thumb approaches used in early-stage ship design. The hydrostatic properties were determined for discrete heel angles and the stability qualities were assessed numerically. For damaged conditions, the ship was balanced to determine hydrostatic equilibrium. A lost buoyancy approach, free to sink and trim as a function of heel angle was employed as specified by NAVSEA for flooding in free communication with the sea. (NAVSEA, 2016)

The subdivided, trimaran hull form was modeled as closed polysurface compartments in CAD software, Rhinoceros. Then using the Orca3D plug-in, stability qualities and USN published criteria (NAVSEA, 2016) were evaluated for intact and damaged conditions. Orca3D is a suite of tools, providing powerful naval architectural design and analysis capabilities in a 3D CAD environment. (DRS, 2017) To account for reduced permeability in machinery compartments, engines equivalent to

Table 3 KGa/D Results: Worst Damaged Condition

Hull	$(B/T)_{SH}$	Vratio	$(L/B)_{CH}$	SH_X		SH_Y	KGa/D
1	0.64	0.04	14.16	L2		T2	0.51
1a	1.16	0.04	14.16	L2		T2	0.56
1b	0.42	0.04	14.16	L2		T2	0.47
2	0.64	0.04	14.16	L2		T1	0.41
3	0.64	0.04	14.16	L2		T3	0.73
4	0.64	0.04	14.16	L1		T2	0.53
5	0.64	0.04	14.16	L1		T1	0.41
6	0.64	0.04	14.16	L1		T3	0.75
7	0.64	0.04	15.60	L2		T2	0.47
8	0.64	0.04	15.60	L2		T1	0.35
9	0.64	0.04	15.60	L2		T3	0.53
10	0.64	0.03	15.60	L2		T2	0.46
11	0.64	0.03	15.60	L2		T1	0.35
12	0.64	0.03	15.60	L2		T3	0.50
13	0.64	0.02	14.16	L2		T2	0.45
14	0.64	0.02	14.16	L2		T1	0.37
15	0.64	0.02	14.16	L2		T3	0.53
16	0.64	0.03	14.16	L2		T2	0.47
17	0.64	0.03	14.16	L2		T1	0.38
18	0.64	0.03	14.16	L2		T3	0.56
19	0.64	0.02	12.70	L2		T2	0.58
20	0.64	0.02	12.70	L2		T1	0.48
21	0.64	0.02	12.70	L2		T3	0.69
22	0.64	0.03	12.70	L2		T2	0.63
23	0.64	0.03	12.70	L2		T1	0.47
24	0.64	0.03	12.70	L2		T3	0.71

15% of the volume at the centroid were modeled at bulkheads 32, 62, and 92. Similarly, missile like components, equivalent to 15% of the compartment volume were modeled at bulkhead 20. 100% permeability was assumed for all other spaces for simplicity in modelling Figure 10 shows the compartments with reduced permeability.

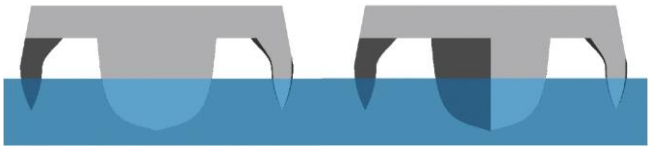

Figure 9 Asymmetric, Transverse Damage Extents Subject to Flooding

Beam-wind heeling arm amplitude was determined using a 2m strip method to integrate the wind pressure on the hull and deckhouse above the waterline. Two asymmetric, transverse extents shown in Figure 9 were evaluated. Using a 15 % damage length longitudinal extend, ten damage conditions were evaluated. Altogether, 20 damaged conditions were evaluated per hull form configuration. The worst of the intact and damaged conditions was determined for each hull. For compartments with side hull components below the bulkhead deck two transverse asymmetric extents are evaluated: ½ CH +SH and SH only. Damage is considered vertically from the keel up to the bulkhead deck for all conditions. Trends were observed and relationships between DVs and stability metrics were developed, noting key designs with excellent stability.

3.5 Relationships

First, the effect of $(B/T)_{SH,}$ on KGa/D is investigated for hulls 1, 1a, and 1b listed in Table 3 and shown in Figure 11. An increase in $(B/T)_{SH}$ decreases the KGa for the intact condition. This is because the limiting criterion is A1/A2>1.4, in which the shallower draft at

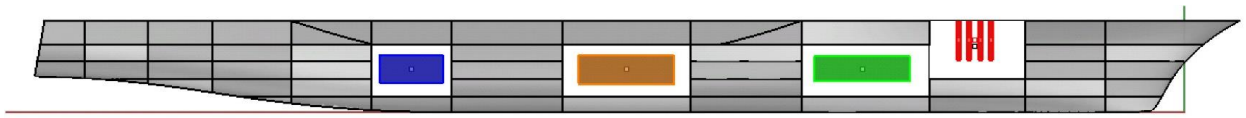

Figure 10 Engine and VLS components in 85% Permeable Spaces

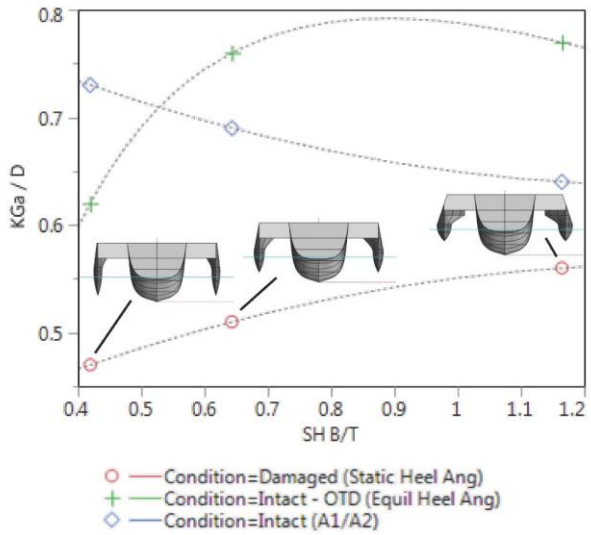

Figure 11 $(B/T)_{SH}$ Relationships

high $(B/T)_{SH}$ adversely effects KGa. In contrast, the KGa increases with an increase in side hull B/T for intact-OTD, and damaged conditions. This is because in those conditions, the limiting criteria are the equilibrium and static heel angle respectively. These criteria are most affected by beam.

Next, the effect of side hull longitudinal position, SH_X, on KGa/D is investigated through six side hull positions. As shown in Figure 12, the KGa increases from aft L1 to mid L2 SH position for intact conditions, however for damaged conditions minimal effect is present. Upon this understanding, SH_X was dropped from the remainder of the DoE. Despite a minimal effect seen from quasi-static methods evaluating the transverse stability, the effect SH_X should be included for dynamic methods to capture its effect on longitudinal stability in both intact and damaged conditions. Because a manual approach was taken to accomplish the stability analysis a reduced number of points are used for the DoE. Given this sparse DoE, the data and results should only be used for rule-of-thumb and initial guidance early-stage design.

Given the previous results, the major effects of $(L/B)_{CH}$, side hull displacement and transverse position on KGa/D are investigated through 19 hull form variations. As expected the side hull transverse location, SH_Y, has the most effect on the KGa/D ratio followed by $(L/B)_{CH}$ and Vratio for intact and damaged conditions.

Given that the baseline design concept had a KG/D ratio of 0.5, this value was set as a threshold with which to determine hulls that passed or failed the stability criteria. 10 of the 19 hull forms examined at the mid L2 SH position failed in the intact and/or damaged conditions (KG > KGa). Except for on hull form, the limiting condition with the least KGa/D was the damaged criterion: list angle < 15 deg. All of the variations with side hulls at the inner T1 SH position failed as well as those at mid T2 SH position except for those with smaller $(L/B)_{CH}$ or larger Vratio. In general, it was observed that the side hull geometry dominates the stability assessment result when placed further from the center hull transversely; conversely, the center hull geometry dominates when the side hull is closer to the center hull.

3.6 Response Surface Model

Using the KGa/D results from executing the DoE through the stability model, statistical relationships were developed to guide rule-of thumb processes and early-stage design efforts. First, functions for intact and damaged conditions were fit to the three hull forms with varying $(B/T)_{SH}$ in Figure 11. Next using the 19 hull form data, KGa/D as a function of SH_Y/L_{CH}, $(L/B)_{CH}$, and Vratio for intact and damaged conditions were determined. The damaged condition limited each hull, so combining those equations for KGa/D as function of $(B/T)_{SH}$,

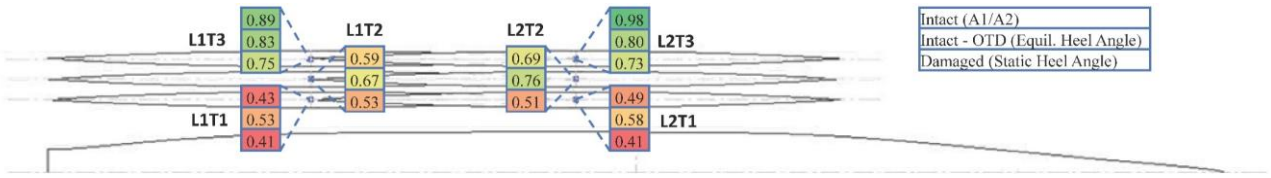

Figure 12 Side Hull Positions Examined in DoE

SH_Y/ L_{CH}, $(L/B)_{CH}$, yields a comprehensive Equation 1. The effect of SH_X was not significant enough for inclusion. This response surface model (RSM) has good R Squared and RMSE values; however, to maintain valid results given the sparse DoE, care should be taken not to extrapolate the variable values beyond the bounds in Table 4.

$$\frac{KG_a}{D}\left(\left(\frac{B}{T}\right)_{SH},\frac{SH_Y}{L_{CH}},\left(\frac{L}{B}\right)_{CH},\frac{\Delta_{SH}}{\Delta}\right) = 3.91842$$
$$+0.29637\left(\frac{B}{T}\right)_{SH} - 0.11088\left(\frac{B}{T}\right)^2_{SH}$$
$$-5.0862\frac{\Delta_{SH}}{\Delta} - 0.61314\left(\frac{L}{B}\right)_{CH} + 24.8936$$
$$+88.23142\frac{SH_Y}{L_{CH}}\frac{\Delta_{SH}}{\Delta} + 0.89659\frac{SH_Y}{B_{CH}}$$
$$\mathbf{+0.02215\left(\frac{L}{B}\right)^2_{CH} - 58.22412\left(\frac{SH_Y}{L_{CH}}\right)^2} \quad (1)$$

Table 4 Variable Bounds for KGa/D RSM

Variable	Min	Max
$(B/T)_{SH}$	0.40	1.16
SH_Y/ L_{CH}	0.063	0.098
$(L/B)_{CH}$	12.7	15.6
Vratio	0.02	0.04

4. APPLICATION TO SHIP DESIGN

Surface combatants in navies across the globe are employing more capable topside weapons, radars, and other sensors on surface ships for increased coverage. These systems are often heavier than the systems they're replacing and are often mounted high in the top-level superstructure and on the mast for maximum coverage. Placing too many of these systems in these areas will increase the KG. Having a KGa estimate at the concept stage will guide the design towards a stable ship from the start. The derived function in Equation 1 provides such a rule of thumb, first approach when determining the KGa for a small surface combatant, trimaran ship displacing close to 3,780 mt during early-stage design. Coupled with displacement, the KG is an important parameter to be considered; not only for adequate stability, but for seakeeping performance as well.

While the trimaran exhibits high righting arm, GZ, and good stability behaviour, as shown in Figure 7, the GM_T can be high enough to change ship motions from an equivalent monohull in similar sea states. These ship motion changes can impact operational limits for launch and recovery of helicopters and small boats as well as have adverse effects on crew. The seakeeping performance should also be assessed when considering trimaran and monohull forms.

5. CONCLUSIONS

With one small exception, the worst damaged condition determined the KGa for each hull variation and an overall function was established in Equation 1. For these damage conditions the criterion list angle<15 degrees determined the KGa. This is somewhat concerning given the results Peters and Wing (2009) found where the list angle for a damaged monohull shows poor correlation with dynamic stability results. Performing a similar analysis for a trimaran hull form would enable further insight regarding the usefulness of the list angle criterion as a measure of stability.

Several tasks for additional work to expand and enhance this thesis are recommended. Adding more trimaran hull form configurations to the DoE would increase the applicability of the RSM and its use in early-stage design. The density of points should be increased in areas where contours aren't well defined in the RSM. Applying probabilistic methods to compare damaged monohull and trimaran vessels would aid in the understanding of their differences in terms of dynamic stability and criteria to use.

6. ACKNOWLEDMENTS

I would like to thank my committee chair and advisor, Dr. Alan Brown, for his willingness to work with me remotely to converge on the thesis presented here. Also, many thanks to my colleague and committee member, Dr. Chris Bassler, who encouraged me to start my thesis and whose door was always open for discussion. Additional thanks to Dr. Stefano Brizzolara for joining my committee and his readiness to support.

7. REFERENCES

Andrews, D.J., 2004a, "Architectural Considerations in Trimaran Ship Design" UCL, RINA, Design and Operation of Trimaran Ships, London, UK

Andrews, D.J., 2004b, "Multi-Hulled Vessels", Chapter 46, Ship Design and Construction, Lamb, T. (ed), SNAME, New Jersey

Andrews, D.J. and J.W. Zhang, 1995, "Trimaran Ships – The Configuration for the Frigate of the Future" Naval Engineers Journal

Belenky, V., C. Bassler, and K. Spyrou, 2009, "Dynamic Stability Assessment in Early-Stage Ship Design," 10th International Conference on Stability of Ships and Ocean Vehicles, pp. 141-154, St. Petersburg

Belenky, V. and C. Bassler, 2010, "Procedures for Early-Stage Naval Ship Design Evaluation of Dynamic Stability: Influence of the Wave Crest," *Naval Engineers Journal,* 122(2), pp.93-106

Brown, A.J., 2015 "Multi-Objective Design of a Trimaran Surface Combatant," International Maritime Design Conference (IMDC), Tokyo, Japan

Bulian , G., A. Francescutto and F. Fucile, 2011, Study of trimaran stability in longitudinal waves, Ships and Offshore Structures, 6:4, 265-271, DOI: 10.1080/17445302.2010.507494

DRS Technologies, Inc., 2017, "Orca3D Help," orca3d.com/wp-content/uploads/2015/help, Accessed 4 Sept 2017

Dubrovsky, V.A., 2004, Ships with Outriggers, Backbone Publishing Company, Fair Lawn, NJ

Dubrovsky V.A. and A.G. Lyakhovitsky, 2001, Multi-Hull Ships, Backbone Publishing Company, Fair Lawn, NJ

MoD, 2014, Defence Standard 02-900 Part 4, Safety and Environmental Protection, Ship, Chapter 3: Stability

Manzitti, T., K. Neild, L. Pomeroy, M. Sweet, H. Thompson, 2016, "Design Report Frigate Trimaran (FFGT2)," Ocean Engineering Design Project, Department of Aerospace and Ocean Engineering, Virginia Tech, Blacksburg, VA

Naval Sea Systems Command (NAVSEA), 2016, Design Practices And Criteria For U.S. Navy Surface Ship Stability And Reserve Buoyancy, Technical Publication T9070-AF-DPC-010/079-1, U.S. Navy

NATO Standardization Agency (NSA), 2017, Naval Ship Code. Allied Naval Engineering Publication, ANEP-77, Ed. F, ver.2. Brussels

Peters, A.J., and D. Wing, 2009, "Stability Criteria Evaluation and Performance based criteria development for damaged Naval Vessels" 10th International Conference on Stability of Ships and Ocean Vehicles, pp. 155-170, St. Petersburg

Weidle, W.S., 2017, "Influence of Trimaran Geometric Parameters on Intact and Damaged Ship Stability," Master's Thesis, Department of Aerospace and Ocean Engineering, Virginia Polytechnic Institute and State University, Blacksburg, VA

A framework for investigating the potential for operational measures in relation to intact stability

Hans Liwång, *KTH Royal Institute of Technology*, liwang@kth.se

Anders Rosén, *KTH Royal Institute of Technology*, aro@kth.se

ABSTRACT

Operational safety measures are an important aspect of a holistic safety approach for intact stability. With the aim to facilitate and further investigate potential operational measures this research aims to describe a framework for prioritizing intact stability issues suitable for being addressed with operational safety measures. The proposed framework identifies that there are different potentials and uncertainties in relation to operational safety measures dependent on the operation type under study. It is demonstrated that there is not one solution that facilitates operational measures and the reliability of potential measures varies.

Keywords: *Probabilistic and risk-based assessment; intact stability; operational stability management; reliability; safety measures*

1. INTRODUCTION

Engineering approaches to improve safety are developed under the assumption that there is a link between the technical solutions implemented and the safety level during operation. There is also a link between how the ship is operated and the safety level during operation. However, this second link is often hidden to engineers because traditional engineering approaches and tools typically do not describe how risk decisions taken on-board affect safety (Kuo, 2007). As discussed within the intact stability community and at previous conferences, operational guidance or limitations are an important aspect of a holistic safety approach for intact stability. However, such operational measures also introduce new uncertainties.

With the aim to facilitate and further investigate potential operational measures this paper proposes a framework for prioritizing intact stability issues suitable for being addressed with operational safety measures and for discussing how sufficient safety can be achieved. Focus is put on pin-pointing uncertainties and how they affect the reliability of the safety efforts.

A safety level is here understood in the same way as presented in the Formal Safety Assessment (FSA) IMO (2013). FSA is an approach that investigates the risk level (and thus implicitly the safety level) in ship operations. The risk investigated in the FSA is the final risk during operation independent on whether the safety barrier is implemented in technology, crew training or operations.

2. THEORY AND METHOD

Here safety is understood as the “ability of individuals or organisations to deal with risks and hazards so as to avoid damage or losses yet still achieve their goals” (Reason, 2000). Reason also describes that effective safety work requires informed participants that can operate close to unacceptable danger without passing over the edge.

Particularly in areas with few but severe incidents, it is difficult to develop safety measures from negative outcomes (historic in-

cidents) (Kuo, 2007). The traditional approach to safety in maritime design and operation is to implement prescriptive regulations. Such regulations are suitable for routine activities but devolve responsibility and innovation which makes them less suitable for new developments (IMO, 1994, Kuo, 2007). In a dynamic world prescriptive codes should be complemented with an effective safety culture. An effective culture knows that hazards and threats will not go away, "they anticipate the worst and equip themselves to cope with it" (Reason, 2000). However, according to Parker et al. (2006) a desirable safety culture does not just emerge, it is a result of many aspects, particularly: formal regulations and processes; competence and training; and shared risk awareness throughout the organisation.

Risk is a common approach for measuring the absence of safety. Risk is typically defined as a function of the probability of an incident and the resulting consequences. Which type of consequences to measure depend on the case studied. The FSA focus on fatalities and serious injured (IMO, 2013). The aim with risk management is most often to avoid unnecessary risks with cost effective measures (IMO, 2013). The FSA focus on the safety during operation including both proactive and reactive measures for risk reduction as illustrated by the bow tie diagram in Figure 1.

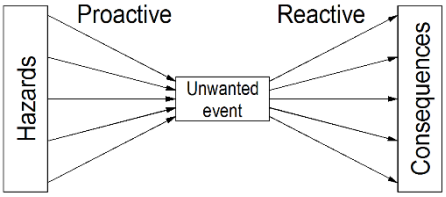

Figure 1 Bow tie diagram showing that risk controls can be applied proactively and reactively, developed from (Rausand & Bouwer Utne, 2009).

The bow tie diagram in Figure 1 show that there could be safety issues that can be eliminated long before the event with design measures, but also closer to the event and also after the unwanted event. In this work *operational safety measures are understood as measures that during operations reduce the probability of unwanted events and or the consequences of unwanted events*. Operational measures here include operational guidance and operational limitations as discussed within the work with the second generation intact stability criteria (Peters et al., 2011, Umeda & Francescutto, 2016).

Safety can be increased with different types of measures. Möller and Hansson (2008) describe four principles for engineering safety measures according to Table 1. Often, systems are designed with a combination of the principles and some applied approaches can be said to belong to more than one principle (Möller & Hansson, 2008). The principles in Table 1 will here be used to categorize different types of safety measures in general and in relation to the *reliability of the safety system, i.e., the ability of the total set of safety measures to maintain a suitable level of safety (successful performance) during operation*[1].

Table 1 Principles for engineering safety (Möller & Hansson, 2008).

#	Principle
(1)	Inherently Safe Design, which means that potential hazards or threats are excluded
(2)	Safety Reserve, safety factors or safety margins
(3)	Safe Fail, systems that fails safely
(4)	Procedural Safeguards, procedures and training is used to enhance safety

2.1 Acceptable safety level

Bačkalov et al. (2015) states that "the likelihood of an intact stability failure is typically required to be at acceptable probability levels, which can be very low". Acceptable probabilities for incidents are for example presented by Bačkalov (2012) and Peters (2010). They both explicitly assumes a relationship between the safety level and the probability of capsize as defined by the probability of reaching a specific heel angle. Such a relationship is not straight

[1] The definition developed from Andrews and Moss (2002b).

forward as exemplified for cruise ships by Hinz (2015).

Acceptable incident probabilities assumed by Bačkalov (2012) is once in 20 years of operation for river-sea ships, but he also states that "an appropriate safety level ... is open to discussion". The approach assumes that the probability of a specific heel angle is proportional to the risk posed by capsizing. There could be different reactive solutions affecting the resulting safety level. Bačkalov (2012) also illustrates how such a probability can be used to calculate the safety level introduced by a rule (more formal and complete assessments include IMO (2008a, 2008b) on damage stability). Also Peters (2010) discusses tolerable risk in relation to intact stability. The approach defines a maximum probability for the ship to reach a specific heel angle (capsize angle) based on British levels of acceptable risk. The maximum allowable probability for large heel angles is by Peters calculated to be $1 \cdot 10^{-4}$.

The FSA define negligible number of fatalities in relation to societal risk and individual risk, risks below that level do not need to be reduced further. For accidents with multiple fatalities societal risk is the most relevant measure (Pedersen, 2010, Skjong, 2009). Negligible societal risk is a function of the value the activity presents to the society and IMO (2013) describes that the negligible level should be calculated based on acceptable Potential Loss of Life given by the number of occupational fatalities per Gross National Product and the economic value of the activity. The negligible risk level is given by the number of fatalities and the upper limit of the number of fatalities, i.e. the maximum number of persons on-board. For details of the calculations see IMO (2013) and Skjong (2009).

Therefore, if the fatalities associated with a capsize is known the maximum probability of capsize can be calculated. If the capsize probability is lower than that there are no safety reasons for reducing it further. How the probability of capsize level corresponds to a maximum annual large heel angle probability (such as discussed by Peters (2010)) depends on the system's recoverability after large heel angles.

However, also for operations with negligible levels of capsize risk may it be suitable to improve intact stability. One example of other reasons for introducing operational measures and intact stability knowledge on-board is presented by Huss (2016). Huss' example illustrates the power of operational measures with the aim to increase the quality of service for Pure Car and Truck Carriers (PCTC).

2.2 The second generation intact stability criteria

The work in regard to the second generation intact stability criteria is based on three alternative assessment procedures: Level 1 vulnerability assessment, Level 2 vulnerability assessment; and Direct stability assessment. Compliance with Level 1, 2 or the Direct stability assessment fulfils the requirements of the intact stability criteria. It is also proposed that alternatively, ship-specific operational limitations or operational guidance can be developed for conditions failing to fulfil the criteria (Peters et al., 2011, Umeda & Francescutto, 2016).

The work within the second generation intact stability criteria so far has focused on "passive" safety measures described by the level 1 and 2 assessments (Bačkalov et al., 2015). These are typically *Principle (2) Safety Reserve* as defined by Table 1. However, the operational environment and the operation itself is not static, this may lead to that safe passive design measures need to be far reaching in order to exclude unsafe operations. This is the reason for introducing operational limitations or operational guidance within the second generation intact stability criteria.

2.3 Operational aspects of safety

The personnel need to be able to take informed decisions. This includes avoiding surprises in operation (Cleary, 1975), such as sudden loss of stability without prior large ship motions (Mata-Álvarez-Santullano & Souto-Iglesias, 2014). Stensson and Jansson (2014) call this needed awareness of safety issues *edge awareness*, i.e., the awareness needed to take informed decisions to avoid accidents.

From Reasons (2000) definition of safety it follows that operations without incidents is not a proof of safe operation. Especially for these types of rare events discussed here. Also, crews sometimes are underestimating risks in dangerous situations where they have been successful in the past (Schröder-Hinrichs et al., 2012). Therefore, other types of feedback are needed to distinguish between safe and unsafe operation. The traditional prescriptive regimes typically do not inform the crew enough (Kuo, 2007). An operational measure regime must therefore be designed to inform the crew.

Operational limitations prescribe safe combinations of aspects such as sea state, heading and speed and operational guidance dynamically introduce limitations (Bačkalov et al., 2015). This typically aims towards avoiding hazards, i.e., an operational version of *Principle (1) Inherently Safe Design* (Table 1) that could be called *Inherently Safe Operations*.

Principle (4) Procedural Safeguards (Table 1) in regard to ship safety can be exemplified by, but are not limited to, prepared procedures for the crew if the ship is experiencing cargo shift or other risk driving events. Typical *Principle (3) Safe Fail* (Table 1) equipment on ships include lifesaving equipment, such as survival suites, life vests and life rafts, that can save crew and passengers if there is an accident. However, such equipment typically does not save the operation, the cargo or the ship.

Increased system reliability is another form of *Principle (3) Safe Fail* (Table 1) and can be achieved with redundancy, segregation and diversity (Möller & Hansson, 2008). Redundancy and segregation are important concept in designing for intact stability. However, typical engineering redundancy and segregation require the operational conditions to be within the design conditions and therefore the diversity of the concept can be low. Operational measures introduce other possibilities than designed engineering solutions and therefore increase the diversity of the safety system, i.e., solutions that "avoid common cause failures" (Möller & Hansson, 2008). They have the power to change the operational conditions. This means that such safety measures add reliability, i.e., reduces uncertainty to the systems as a whole even though there are uncertainties in the measure itself (Andrews & Moss, 2002a, Möller & Hansson, 2008). Operational measures are specifically important for operations with large uncertainties where procedural safeguards are ineffective (Oltedal, 2018).

3. DATA AND ANALYSIS

To widen the understanding of the risks in relation to intact stability Table 2 presents 36 intact stability incidents at sea.

Table 2 is not a complete list of incidents and therefore not intended to be used for calculating probabilities or frequencies. The list is in this study used to highlight:

- the different types of conditions and different stability failure modes that lead to an intact stability incident,
- the often severe consequences that follow with an intact stability incident, and
- the large variations in the operational conditions.

The aim here is to discuss qualitative aspects of intact stability risk. Most of the incidents described are serious accidents, i.e., leading to one or more fatality, damage to the vessel that interrupt the service or vessel lost (IMO, 2008b).

Table 2 Example of intact stability incidents at sea and documented causes. Documented or investigated in academic publications within the stability community (AIBN, 2016, Bass & Wong, 1994, Borlase, 2002, BSU, 2009, France et al., 2002, Guldhammar, 1986, Hofman & Bačkalov, 2007, Hua & Rutgersson, 1994, Huss, 2016, Kan et al., 1986, Kluwe & Krüger, 2007, Kure & Bang, 1975, MAIB, 2016, Marón et al., 2006, Mata-Álvarez-Santullano & Souto-Iglesias, 2014, NTSB, 2006, Pérez Rojas et al., 2007, Pérez Rojas et al., 2006, Sadakane, 2000, Sagarra & Puig, 1997, Shin, 1997, Swedish Accident Investigation Authority, 2008, Taguchi et al., 2015, Taguchi et al., 2003, Taylan, 2005, Umeda et al., 2006, van Walree & de Kat, 2006, Vorobyov & Sizov, 2006).

Year	Ship	Ship type	Crew + Passengers	Fatalities	Other consequences	Sea state	Down flooding	Over loaded/loaded incorrect	Cargo shift	Water on deck	Rudder forces	Free surface in tanks	Technical. error	Parametric rolling*	Forced oscil. low damping*	Flaw due to design	Poor stab. in design cond.	Stab. sensitive to waves*	Limited knowledge
2000	Ryuho Maru No.5	Fishing vessel	18	14	Ship lost	Moderate	X	X	X	X	X								
2014	Viking 7	Pleasure craft	7	1	Boat damaged	Moderate	X	X								X			
1990	Straits Pride II	Fishing vessel	6	3	Ship lost	Severe	X		X	X									
1987	Herald of free enterprise	RoPax	≈590	193	Ship lost	Moderate	X			X									
2001	Arctic Rose	Fishing vessel	15	15	Ship lost	Severe	X			X		X							
1982	Akebono Maru	Fishing vessel	33	32	Ship lost	Severe	X			X	X								
1974	MFV Gaul	Fishing vessel	36	36	Ship lost	Severe	X												
2006	-	Fishing vessel	-	-	Ship lost	Severe													
2007	-	Fishing vessel	-	-	Ship lost	Severe		X		X								X	
2004	Enrique el Morico	Fishing vessel	>2	1	Ship lost	Severe		X		X									
2004	O Bahía	Fishing vessel	10	10	Ship lost	Severe		X		X									
<1997	-	General cargo	14	0	Ship lost	Calm		X											
2015	Hoegh Osaka	PCTC	24	0	1 injured, cargo and ship damaged	Calm		X											
2006	Lady D	Passenger vessel, small	25	5	4 injured	Moderate		X									X		
2006	Cougar Ace	PCTC	-	0	Cargo and ship damaged	Moderate		X											
<2000	-	Tanker, Chem.	-	-	Ship lost	Moderate			X	X	X	X					X		
1993	-	Fishing vessel	>1	>1	Ship lost	Severe			X	X									
1980	Zenobia	RoRo	≈140	0	1 injured, cargo and ship damaged	Calm			X		X		X						
1988	Vinca Gorthon	RoRo	≈14	0	Ship lost	Moderate			X										
1980	Zenobia	RoRo	≈140	0	-	Severe			X										
2006	Finnbirch	RoRo	14	2	Ship lost	Severe			X								X	X	
1993	Jan Heweliusz	RoPax	-	55	Ship lost	Severe			X										
2003	-	Sailboat	12	7	Ship lost	Severe										X	X		
1950	SS Fidamus	General cargo	-	-	Ship lost	Severe				X							X	X	
1951	SS Irene Oldendorff	General cargo	-	-	Ship lost	Severe				X							X	X	
<1975	Edith Terkol	Tanker, small	>2	≥1	Ship lost	Moderate								X					
2008	-	PCTC	-	0	-	Moderate								X					
<2016	-	Large PCTC	-	0	-	Severe								X					
1998	-	Container, post panamax	-	0	800 containers lost or destroyed	Severe								X					
1981	RF2	Rescue Boat	6	6	Boat damaged	Severe										X			
1976	Rechitsa	General cargo	-	-	Ship lost	Severe													X
2013	No.38 Sankyo Maru	Tug boat	3	2	Ship lost	Severe					X					X			
2004	Nuevo Pilín	Fishing vessel	>5	5	Ship lost	Severe											X	X	
2008	Chicago Express	Container	35	1	5 injured	Severe									X				
1969	-	Tanker, LPG	>17	17	Ship lost	Severe										X	X		
1950	MV Lohengrin	General cargo	-	-	Ship lost	Severe											X	X	
		Total:	**>1174**	**>408**		**Number of incidents:**	**8**	**9**	**9**	**13**	**5**	**2**	**1**	**4**	**1**	**5**	**9**	**7**	**1**
		Median:	**14**	**3**															

*) The causes of the accidents are summarized based on the accident descriptions studied. The five intact stability failure modes: dead ship condition, parametric rolling, pure loss of stability, surf riding/broaching and excessive accelerations were not found to be suitable categories for describing the causes of the accidents.

The 36 incidents in Table 2 add up to more than 408 fatalities. The median number of persons on-board is 14 and the median number of fatalities per accident is 3 (13 and 6 respectively if the ship capsized or sunk). In all but 11 cases the ship was lost as a result of the accident.

The incidents described in Table 2 can all most often be contributed to a combination of causes and for many of the accidents the cause is uncertain.

Many of the incidents in Table 2 (approximately 20 out of 36) are cases were the operational condition and ship state was not according to design. For example, vessels that are over loaded and/or operated in heavy weather with hatches open potentially in combination with forces from fishing gear (Mata-Álvarez-Santullano & Souto-Iglesias, 2014). Cargo shift is also common in Table 2. These conditions lead to a poor recoverability after large heel angles.

For cargo vessels the cargo and ship status is generally changed under controlled circumstances (often at port). There is a potential for a high level of internal and external control. Therefore, a high level of detail in the data on the ship status is possible. On the other hand, vessels such as fishing vessels are an example of an operation where the ship status is changed at sea dynamically without external control which lead to large uncertainties. The conditions are described by Mata-Álvarez-Santullano (2015) who show that, in stability accidents involving Spanish fishing vessels from 2008 to 2014, more than 75% of the accidents can be contributed to lack of safety culture, lack of safety awareness or lack of training. The investigation also show that the stability regulation does not give enough support for operational stability management for these kind of operations.

The difference in potential control over the ship's loading condition produce different conditions for safety work, different reliability of the passive safety designed into the craft, and different reliability as well as different need for operational safety measures. However, knowledge on safe operations, based on knowledge about the vessel's limitations and weaknesses (edge awareness) could increase the reliability of the crew decisions taken on-board in relation to intact stability especially for ships and vessels that relatively often operate beyond the operational conditions defined during the design. Therefore, operational safety measures can be an effective approach to reach acceptable levels of safety, especially for operations with large uncertainties.

4. PROPOSED FRAMEWORK AND DISCUSSION

As described in Section 2.1 the probability of capsize need to be low, how low depends on what other (reactive) safety measures are implemented. Also, it is here argued that based on Table 2 the conditions for operational measures differs between ship types as a result of different types of operations and different conditions for implementing the measures on-board. Therefore, it is here proposed that there is an important distinction between a ship's general likelihood for intact stability incidents such as large roll motions (*vulnerability* to intact stability failures) and if the ship at a specific situation will not, when it experience an intact stability incident, return to a safe mode (*recoverability* after intact stability failures). Vulnerability is then typically a result of ship design whereas recoverability can be a result of ship design as well as operational aspects such as decisions taken on-board in relation to loading or unclosed hatches. Figure 2 present a framework distinguishing between the ships vulnerability and recoverability to stability incidents including the data from Table 2.

In relation to operational measures the framework aims to serve as a tool for differentiating between different types of operational safety measures. As identified among the top half of the incidents in Table 2 the safety intro-

duced by design measures can deteriorate by lower control of ship condition (large uncertainties) and the resulting operations outside the design conditions.

The second-generation intact stability rules mainly investigate the vulnerability to intact stability failure for ships operating within the operational conditions. However, as shown in Section 2 the safety level is by IMO primarily assessed in number of fatalities and injured. Therefore, the ships recoverability to intact stability failure as well as other life saving measures need to be included if the safety effects of high vulnerability to intact stability failure is to be assessed. It is still not identified that high vulnerability alone is enough to introduce a safety problem according to IMOs definitions of safety (as can be seen for the incidents with high recoverability in Figure 2).

Ships with high recoverability and high vulnerability (A-3 in Figure 2) includes for example modern PCTC with high possible control and specialized hull forms (that lead to vulnerability to specific intact stability failure modes) and superstructures that can contribute to high recoverability after large heel angles (Hofman & Bačkalov, 2007). For such ships high-end on-board simulations can be an effective way of supporting the master's decisions about routing as well as manoeuvres to avoid intact stability incidents. However, as mentioned above, such on-board operational guidance is not necessarily needed to meet IMO's safety level ambitions according to the FSA and should if that is the case not be mandatory. The operational safety measures are motivated by the aim to increase effectiveness and quality of service, i.e. with the aim to reduce injuries to personnel and damages to cargo during the incident. Suitable operational measures for these ships need to be ship specific and supported by support tools, i.e., operational guidance. Therefore, the exchange of stability knowledge between the design phase and the development of stability management support systems, as described by (Huss, 2016), should be facilitated by the IMO rules.

For ships with high control and standard configuration (A-1 in Figure 2) standard operational safety measures is enough.

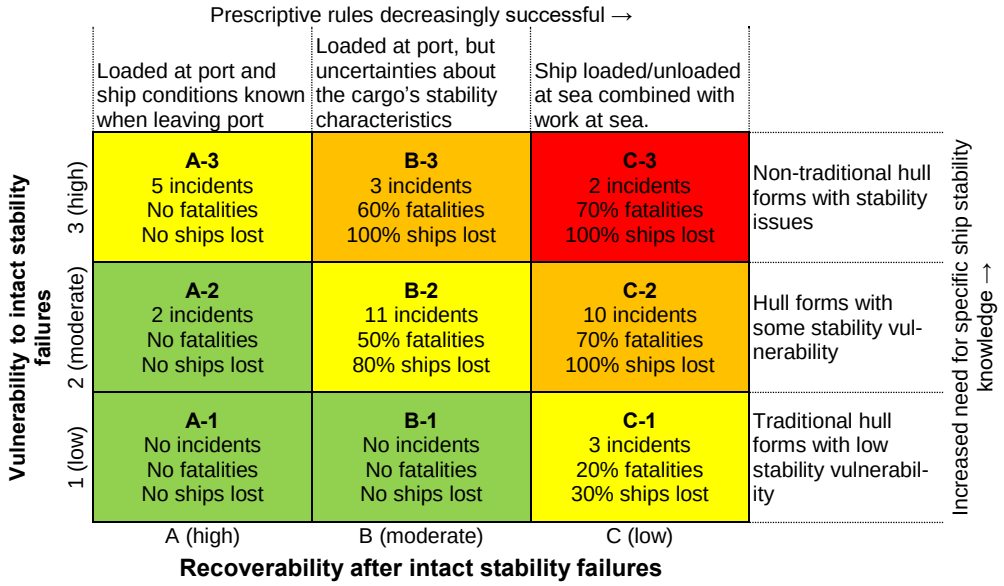

Figure 2 Framework for identifying severity of stability incidents as a function of recoverability and vulnerability. The incident data from Table 2 are distributed to their respective categories and the average percentage of fatalities in relation the number of persons on-board and percentage of ships lost is given for each category based on the data in Table 2.

For ships with moderate recoverability and moderate to high vulnerability (B-2 and B-3 in Figure 2) the effective approach could be found in dealing with the recoverability uncertainties in regards to the cargo. This typically, given the examples in Table 2, include identifying the dynamic characteristics of the cargo and putting effort into tending to the problems before or while the cargo is loaded on-board. This could include efforts such as to a larger extent inspect how cargo is secured in trailers and containers, improve cargo lashing and limit the amount of cargo taken on-board for specific cargos. In total this means that the stability uncertainties introduced by the cargo is reduced. Only after such uncertainties are reduced can operational guidance, such as on-board stability simulations be reliable.

For ships with low recoverability and moderate to high vulnerability (C-2 and C-3 in Figure 2) the uncertainty in relation to the effectiveness of engineering solutions is high (because the conditions defined during design cannot be assumed to be valid). The effective approach is most likely found in making sure that risk drivers, such as open hatches and overloading, are reduced, especially in situations when the ship is more vulnerable to intact stability incidents. In such situations decisions support, such as operational guidance, can be ineffective as a result of the limited possibility to take in the information presented by such support (Oltedal & Lützhöft, 2018). Identifying and tending to risk drivers is a work that has to be performed by the whole crew by strengthening risk knowledge and risk awareness onboard thru safety management. Operational safety measures are a precondition for safe operations for this type of ships. Specific knowledge and risk management could be the primary choice for safety assurance (compare with the UK Safety Case approach for the offshore industry (Kuo, 2007) and the risk based approach for the Norwegian offshore industry (Rausand & Bouwer Utne, 2009)).

For ships with low control and standard configuration (C-1 in Figure 2) the potential for operational safety measures is high in terms of safety and effectiveness. However, the operational measures do not need to be ship specific (are not cost effective to develop).

The framework captures the different types of accidents covered in Table 2 and also articulate how the different conditions and varying uncertainties affect the consequences of the incidents, the need for operational measures and also the requirements on the measures. The framework therefore identifies that strengthening the on-board competence should be a prioritized operational safety measure approach that also increases the reliability of the safety work as it affects operational aspects that cannot be affected by design. However, this cannot be done without further knowledge about the human factors aspects involved including aspects such as safety management and human element aspects (Kuo, 2007, Oltedal & Lützhöft, 2018).

A wider understanding of the terms for operational measures is needed, especially in relation to a ship's recoverability after intact stability incidents. They cannot be judged in the same way as passive engineering solutions for safety. Such a view takes away the strength of safety solutions in the ship operation. However, the acceptable level of uncertainty varies between types of ships and especially with the ship's recoverability after stability incidents.

The work within the second-generation intact stability criteria has so far mainly considered vulnerability and has only to a limited extent considered a ship's actual recoverability after large heel angles and how that recoverability affects the risk level. This means that the relation to the safety level is not fully investigated and the operational aspects of the recoverability not fully understood. Such operational aspects include the knowledge about the potential of, and need for, operational safety measures. If the list in Table 2 is representative the potential for operational measures is high and should not be limited to operational limitations and operational guidance as defined by

the forms so far discussed within the intact stability community.

The vulnerability can largely be classified based on ship dynamics. However, the tools available for investigating the recoverability are not as developed and the recoverability is largely a function of the specific ship conditions at the time of the incident. Therefore, in order to categorize a ship's recoverability more work, and multi-disciplinary studies, is needed especially in relation to operational stability management and safety culture during challenging operational situations. It is likely that intact stability recoverability must be addressed with regulations both in relation to ship dynamics and in relation safety management.

5. CONCLUSIONS

The work with the framework identifies that there are different potentials and uncertainties in relation to operational safety measures. Therefore, there is not one solution that facilitates operational measures and the reliability of potential measures varies. The work within the second generation intact stability criteria has so far mainly considered vulnerability and has only to a limited extent considered a ship's recoverability to large heel angles and how that recoverability affects the risk level. This means that the relation between a ship's intact stability vulnerability and the safety level is not fully investigated because the recoverability is not fully understood. Therefore, in order to categorize a ship's recoverability more work is needed especially in relation to challenging operational conditions.

6. ACKNOWLEDMENTS

This research has been financially supported by the Swedish Mercantile Marine Foundation (Stiftelsen Sveriges Sjömanshus) and the Swedish Transport Administration (Trafikverket) which are both gratefully acknowledged.

7. REFERENCES

AIBN, 2016, "Report on marine accident - Capsizeing of Viking 7, LG8351, Northwest of Mehamn on 6 July 2014 (Report Marine 2016/10)". Lillestrøm: Accident Investigation Board Norway.

Andrews, J. D. and Moss, T. R., 2002a, "Common cause failures", Reliability and risk assessment, (Second ed.), Professional Engineering Publishing Limited, London, pp. 267-285.

Andrews, J. D. and Moss, T. R., 2002b, "An introduction to reliability and risk assessment", Reliability and risk assessment, (Second ed.), Professional Engineering Publishing Limited, London, pp. 1-20.

Bačkalov, I., 2012, "A probabilistic analysis of stability regulations for river-sea ships", 11th International Conference on the stability of ships and ocean vehicles (STAB 2012), Athens, pp. 67-77.

Bačkalov, I., Bulian, G., Rosén, A., Shigunov, V., and Themelis, N., 2015, "Ship stability and safety in intact condition through operational measures", 12th International Conference on the Stability of Ships and Ocean Vehicles (STAB 2015), Glasgow, UK, pp. 159-173.

Bass, D. W. and Wong, C., 1994, "The capsizing of the F.V. 'Straits Pride II'; a study of the dynamics of paravanes", Fith International Conference on Stability of Ships and Ocean Vehicles (STAB 1994), Melbourne, FL.

Borlase, G. A., 2002, "Research opportunities identified during the casualty analysis of the fishing vessel Arctic Rose", 6th International Ship Stability Workshop (ISSW 2002), New York.

BSU, 2009, "Fatal accident on board the CMV Chicago Express during Typhoon "Hagupit" on 24 September 2008 off the

coast of Hong Kong". Hamburg: Bundsstelle für Seeunfalluntersuchung.

Cleary, W. A. J., 1975, "Marine Stability Criteria", International Conference on Stability of Ships and Ocean Vehicles (STAB 1975), Glasgow, pp. 1-17.

France, W., Treakle, T., and Moore, C., 2002, "Head-sea parametric rolling and its influence on container lashing systems", 6th International Ship Stability Workshop (ISSW 2002), New York, NY.

Guldhammar, H. E., 1986, "Analysis of a self-righting test of a rescue boat", Third International Conference on Stability of Ships and Ocean Vehicles (STAB 1986), Gdansk, pp. 165-175.

Hinz, T., 2015, "Risk analysis of a stability failure for the dead ship condition", 12th International Conference on the Stability of Ships and Ocean Vehicles (STAB 2015), Glasgow, pp. 799-807.

Hofman, M. and Bačkalov, I., 2007, "Cougar Ace: the tipping point". The Naval Architect, Vol. April, pp. 10-11.

Hua, J. and Rutgersson, O., 1994, "A study of the dynamic stability of a RO-RO ship in waves", 5th International Conference on Stability of Ships and Ocean Vehicles (STAB 1994), Melbourne, FL.

Huss, M., 2016, "Operational stability beyond rule compliance", 15th International Ship Stability Workshop (ISSW 2016), Stockholm.

IMO, 1994, "International code of safety for high-speed craft (HSC Code, MSC.36 (63))". London: International Maritime Organization.

IMO, 2008a, "FSA - Cruise ships, Submitted by Denmark (MSC 85/17/1)". London: International Maritime Organization.

IMO, 2008b, "FSA - RoPax ships, Submitted by Denmark (MSC 85/17/2)". London: International Maritime Organization.

IMO, 2013, "Revised guidelines for formal safety assessment (FSA) for use in the IMO rule-making process (MSC-MEPC.2/Circ.12)". London: International Maritime Organization.

Kan, M., Saruta, T., and Okuyama, T., 1986, "Model experiments on capsizing of a large stern trawler", Third International Conference on Stability of Ships and Ocean Vehicles (STAB 1986), Gdansk, pp. 107-111.

Kluwe, F. and Krüger, S., 2007, "Using full-scale capsizing accidents for the validation of numerical seakeeping simulations", 9th International Ship Stability Workshop (ISSW 2007), Hamburg.

Kuo, C., 2007, "Safety management and its maritime application", The Nautical Institute, London.

Kure, K. and Bang, C. J., 1975, "The ultimate half roll", International Conference on Stability of Ships and Ocean Vehicles (STAB 1975), Glasgow, pp. 1-12.

MAIB, 2016, "Report on the investigation into the listing, flooding and grounding of Hoegh Osaka Bramble Bank, The Solent, UK on 3 January 2015 (REPORT NO 6/2016)". Southampton: Marine Accident Investigation Branch.

Marón, A., Carrillo, E., Valle, J., Prieto, M. E., Gutiérrez, C., and Taboada, M., 2006, "Investigation on the capsizing of a small fishing vessel in following seas", 9th International Conference on the Stability of Ships and Ocean Vehicles (STAB 2006), Rio de Janeiro.

Mata-Álvarez-Santullano, F., 2015, "Main contributing factors to the stability accidents in the Spanish fishing fleet", 12th International Conference on the Stability of

Ships and Ocean Vehicles (STAB 2015), Glasgow, pp. 653-660.

Mata-Álvarez-Santullano, F. and Souto-Iglesias, A., 2014, "Stability, safety and operability of small fishing vessels ". Ocean Engineering, Vol. 79, pp. 81-91.

Möller, N. and Hansson, S. O., 2008, "Principles of engineering safety: Risk and uncertainty reduction". Reliability Engineering & System Safety, Vol. 93(6), pp. 798-805.

NTSB, 2006, "NTSB Determines Insufficient Stability Caused Lady D to Capsize in Baltimore Harbor". Washington, DC: National Transportation Safety Board.

Oltedal, H. A., 2018, "Setting the stage for maritime safety management". In H. A. Oltedal & M. Lützhöft (Eds.), Maritime safety management, Routledge, Abingdon, pp. 1-15.

Oltedal, H. A. and Lützhöft, M., 2018, "The human contribution". In H. A. Oltedal & M. Lützhöft (Eds.), Maritime safety management, Routledge, Abingdon, pp. 71-90.

Parker, D., Lawrie, M., and Hudson, P., 2006, "A framework for understanding the development of organisational safety culture". Safety Science, Vol. 44(6), pp. 551-562.

Pedersen, P. T., 2010, "Review and application of ship collision and grounding analysis procedures". Marine Structures, Vol. 23(3), pp. 241-262.

Pérez Rojas, L., López Pavón, C., Pérez Arribas, F., and Martín Landaluce, A., 2007, "On the experimental investigation on the capsizing of small fishing vessels", 9th International Ship Stability Workshop (ISSW 2007), Hamburg.

Pérez Rojas, L., Pérez Arribas, F., Zamora Rodríguez, R., and Guerrero y Pacheco, A., 2006, "On the accidents of small fishing vessels", 9th International Conference on the Stability of Ships and Ocean Vehicles (STAB 2006), Rio de Janeiro.

Peters, A., 2010, "Tolerable capsize risk of a naval vessel", 9th International Ship Stability Workshop (ISSW 2010), Wageningen.

Peters, W., Belenky, V., Bassler, C., Spyrou, K., Umeda, N., Bulian, G., and Altmayer, B., 2011, "The second generation intact stability criteria: An overview of development". Transactions - Society of Naval Architects and Marine Engineers, Vol. 121.

Rausand, M. and Bouwer Utne, I., 2009, "Risikoanalyse - teori og metod [Risk analysis -theory and method]", Tapir Akademiske Forlag, Trondheim.

Reason, J., 2000, "Safety paradoxes and safety culture". International Journal of Injury Control and Safety Promotion, Vol. 7(1), pp. 3-14.

Sadakane, K., 2000, "On the stability of a small coastwise tanker capsized in turning", 7th International Conference on the Stability of Ships and Ocean Vehicles (STAB 2000), Launcheston.

Sagarra, R. M. and Puig, J. O., 1997, "Analysis of a general cargo ship lost in front of the Catalonia coast", 6th International Conference on the Stability of Ships and Ocean Vehicles (STAB 1997), Varna, pp. 303-313.

Schröder-Hinrichs, J.-U., Hollnagel, E., and Baldauf, M., 2012, "From Titanic to Costa Concordia—a century of lessons not learned". WMU Journal of Maritime Affairs, Vol. 11(2), pp. 151-167.

Shin, C. I., 1997, "Experimental investigation on capsizing of a purse seiner in beam seas", 6th International Conference on the

Stability of Ships and Ocean Vehicles (STAB 1997), Varna, pp. 113-120.

Skjong, R., 2009, "Regulatory framework". In A. D. Papanikolaou (Ed.), Risk-based ship design, Springer-Verlag, Berlin, pp. 97-151.

Stensson, P. and Jansson, A., 2014, "Edge awareness: A dynamic safety perspective on four accidents/incidents", 5th International Conference on Applied Human Factors and Ergonomics (AHFE), Kraków.

Swedish Accident Investigation Authority, 2008, "Handelsfartyget FINNBIRCHs förlisning mellan Öland och Gotland, den 1 november 2006 (Rapport RM 2008:03) [The foundering of the ship FINNBIRCH between Öland and Gotland, 1 November 2006 (Report 2008:03)]". Stockholm: The Swedish Accident Investigation Authority.

Taguchi, H., Haraguchi, T., Minami, M., and Houtani, H., 2015, "An investigation into the capsizing accident of a pusher tug boat", 12th International Conference on the Stability of Ships and Ocean Vehicles (STAB 2015), Glasgow, pp. 903-910.

Taguchi, H., Ishida, S., Watanabe, I., Sawada, H., Tsujimoto, M., Yamakoshi, Y., and Ma, N., 2003, "A study on factors related to the capsizing accident of a fishing vessel "Ryuho Maru No.5"", 8th International Conference on the Stability of Ships and Ocean Vehicles (STAB 2003), Madrid, pp. 49-57.

Taylan, M., 2005, "Anatomy of a capsize: Then and now", 8th International Ship Stability Workshop (ISSW 2005), Istanbul.

Umeda, N. and Francescutto, A., 2016, "Current state of the second generation intact stability criteria - achievements and remaining issues", 15th International Ship Stability Workshop (ISSW 2016), Stockholm.

Umeda, N., Hori, M., Aoki, K., Katayama, T., and Ikeda, Y., 2006, "Experimental investigation on capsizing and sinking of a cruising yacht in wind", 9th International Conference on the Stability of Ships and Ocean Vehicles (STAB 2006), Rio de Janeiro.

van Walree, F. and de Kat, J. O., 2006, "Forensic research into the loss of ships by means of a time domain simulation tool ", 9th International Conference on the Stability of Ships and Ocean Vehicles (STAB 2006), Rio de Janeiro.

Vorobyov, Y. L. and Sizov, V. G., 2006, "The transverse stability and rolling of a vessel loaded by elastically movable cargo ", 9th International Conference on the Stability of Ships and Ocean Vehicles (STAB 2006), Rio de Janeiro.

An Investigation into the Capsizing Accident of a Purse Seiner in Hauling a Fishing Net

Harukuni Taguchi, *National Maritime Research Institute* taguchi@nmri.go.jp

Takako Kuroda, *National Maritime Research Institute* tkuroda@nmri.go.jp

ABSTRACT

This paper outlines a technical investigation into an accident of a typical Japanese purse seiner, which capsized and foundered during hauling fishing net operation in the Sea of Japan in December 2014. In order to clarify the detailed process and mechanism of the accident, stability of the vessel at that time was calculated and based on the situation at the accident, downward force acting on the starboard side of the vessel, which was induced by movement of a shoal of fish inside the net and amount of shipped water on a working deck were estimated. Furthermore, effect of empty condition of a port side water ballast tank due to an equipment failure on the accident was examined.

Keywords: *Accident investigation, purse seiner, capsizing, hauling fishing net, heel due to movement of a shoal of fish*

1. INTRODUCTION

A typical Japanese purse seiner "Genpuku-maru No.1" capsized and foundered during hauling fishing net operation in the southwest part of the Sea of Japan on 24 December 2014. The accident claimed 5 lives out of 20 crews on board. The Japan Transport Safety Board (JTSB) had investigated this accident. The results of the investigations were compiled into an investigation report and it was submitted to the Minister of Land, Infrastructure, Transport and Tourism and publicized in July 2016 (JTSB, 2016).

As a technical part of the investigation, National Maritime Research Institute analysed the process of the capsizing. In the course of analysis stability of the vessel and heeling moment at the accident were estimated with influences of hauling fishing net operation and shipping water around the stern part taken into account. And utilising the estimation results a mechanism of the capsizing was examined. Based on the technical investigation and so on the JTSB concluded the probable causes of the accident and issued remarks in order to prevent similar accidents.

In this paper main points of the technical investigation are presented.

2. OUTLINE OF THE ACCIDENT

2.1 Summary of the Accident

"Genpuku-maru No.1", which engaged in purse seine fishery with 4 colleague vessels, capsized during side-hauling work with 19 crew members lined up on its starboard side. Figure 1 shows position of each vessel at the accident. In Figure 1 "Vessel A" indicates "Genpuku-maru No.1" . "No.13" and "No.17" are vessels equipped with fish-luring lights and "No.67" and "No.68 are vessels for transporting catch.

According to survivors the accident occurred as follows.

1) A large shoal of fish inside the fishing net

suddenly moved toward the bottom about five minutes after starting side-hauling work and the vessel started to heel.

2) The heel angle increased gradually and as freeing ports on the starboard bulwark were immersed outside water started to flow backward onto the upper deck.
3) When the surface of water flowed through the freeing ports almost reached the starboard edge of working deck around amidships, shipping water around the stern part occurred.
4) The shipped water depth on the starboard side of working deck around amidships reached 0.3-0.4 meters and the heel angle increased further.
5) Shipping water around the stern part occurred again and then the vessel capsized about one minute after starting to heel.

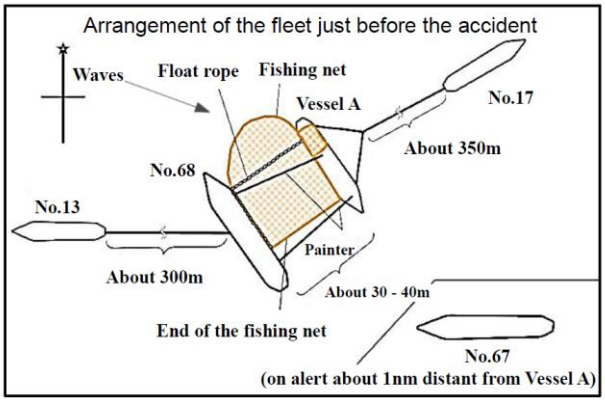

Figure 1 Arrangement of the vessels concerned at the accident (JTSB, 2017).

Table 1. Wind and Sea Conditions at the Accident.

Average wind speed	about 10 m/s
Wind direction	WNW
Significant wave height	about 2.0 m ~ 2.5 m
Wave direction	WNW

The wind and sea conditions at the time of the accident are summarised in Table 1. "Genpuku-maru No.1" was supposed to encounter wind and waves from 30-40 degrees starboard stern.

2.2 Capsized Purse Seiner

"Genpuku-maru No. 1" (L = 48.50 m, B = 8.10 m and D = 3.31 m) constructed in 1990 was a typical Japanese purse seiner of 135 gross tonnage. The general arrangement of the vessel is shown in Figure 2. Above the upper deck the working deck was set up at height of 0.40-0.65 meters to facilitate workability of crews.

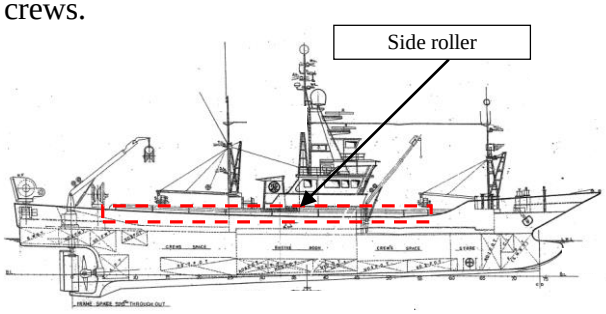

Figure 2 General arrangement of "Genpuku-maru No.1".

3. EXAMINATION OF CAPSIZING PROCESS AND MECHNISM

According to the above mentioned situation at the accident it is presumed that "Genpuku-maru No.1" capsized whilst the heel angle determined from quasi static balance between the up-righting moment of the vessel and the heeling moment acting on it increased gradually. In order to clarify the detailed process and mechanism of the capsizing, stability of the vessel at that time was calculated and based on the situation at the accident, the downward force acting on the starboard side of the vessel, which was induced by the movement of a shoal of fish inside the fishing net and the amount of shipped water on the working deck were estimated. Furthermore effect of empty condition of a port side ballast water tank due to failure of a water injection valve on the accident was examined.

3.1 Original Stability at the Accident

Table 2 summarises the estimated loading condition of the vessel at the beginning of side-

hauling work, which is based on the design condition in hauling fishing net operation modified with the amount of the fuel oil and fresh water loaded at the accident. As for the fishing net only the hauled part of it with the water retentive ratio of 40% (Inoue, 2009) is included. Although at the accident the port side ballast water tank was empty due to the equipment failure, in the usual practice it had been filled up before hauling fishing net operation. A supposed loading condition with the filled up port side ballast water tank at the accident is also indicated in Table 2.

Table 2. Loading conditions at the accident. The actual port side ballast water tank was empty.

Port Side Ballast Water Tank	Empty (actual)	Full (supposed)
Displacement: W (t)	482.28	488.47
Vertical C.G.: KG (m)	2.99	2.99
Longitudinal C.G.: mid-G (m)	-3.43	-3.66
Free surface effect: GG_0 (m)	0.03	0.03

For the both loading conditions stability calculation was carried out on trim free condition. In the calculation all the free surface effects of tanks were taken into account. Figure 3 shows the righting lever curves and Table 3 shows the estimated draft, trim, metacentric height and maximum righting lever.

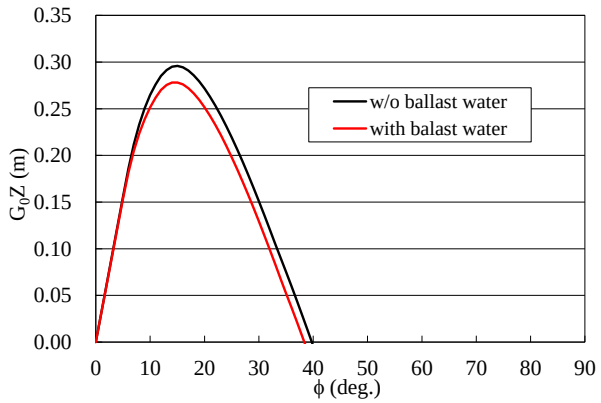

Figure 3 Righting lever curves at the accident.

At the beginning of side-hauling work the estimated maximum righting lever is 0.30 meters at the heel angle of about 15 degrees. From Figure 3 and Table 3 it is noticed that the filled up port side ballast water tank increases the trim by stern and decreases the stability of the vessel overall. And in this condition it was confirmed that the vessel complied with the requirements of the Japanese stability criteria for fishing vessels. However the vessel in this condition seems to comply with not all the requirements of the recommendatory IMO stability criteria regarding righting lever curve properties for fishing vessels.

Table 3. Draft, trim, metacentric height and maximum righting lever at the accident.

Port Side Ballast Tank	Empty (actual)	Full (supposed)
Mean draft: d (m)	2.86	2.87
Trim by stern: τ (m)	0.59	0.70
Metacentric height: G_0M (m)	1.78	1.75
Maximum righting lever: GZ_{max} (m)	0.30	0.28

3.2 Stability and Heeling Moment at the Accident

According to the situation explained in section 2.1 the stability and heeling moment at three phases of the accident were estimated and the capsizing process was examined.

(1) At the Beginning of Side-Hauling Work.

In this section the situation just before the accident, namely at the beginning of side-hauling work, is examined. Stability at this situation was already estimated in section 3.1. And at that time heeling moments due to the wind force and the towing forces by colleague vessels (Figure 1) acted on the capsized vessel and they were supposed to keep acting during the accident.

The wind heeling moment was estimated with similar method as the IMO weather criterion. In the estimation wind pressure at 10 m/s was used and the difference in encounter angle, beam wind for the criterion and quartering wind at the accident, was taken into account.

At the accident in the usual practice, a colleague vessel ("No.17" in Figure 1) towed the port side of the capsized vessel to keep its relative position to the fishing net on the starboard side appropriately. And as shown in Figure 1 the colleague vessel ("No.68") on the opposite side of the net connected with the capsized vessel by ropes at bow and stern was also towed by the other colleague vessel ("No.13"). Utilising data of towing forces of the colleague vessels and attached positions of ropes the heeling moment due to this practice was estimated under an assumption that all vessels concerned were rigidly connected.

As the result the estimated wind heeling moment is 2.66 tf-m and the heeling moment due to towing by colleague vessels is estimated to be 24.60 tf-m. And both heeling moments were presumed to act in the port side down direction, the opposite direction of capsizing. The detailed data used to estimate these heeling moments is shown in the JTSB investigation report (2016, JTSB).

(2) Before Occurrence of Shipping Water.

In this section the following situations before the occurrence of first shipping water are examined.

1) Due to the heeling moment induced by the movement of fish inside the net freeing ports on the bulwark were immersed and outside water flowed backward onto the upper deck.
2) The surface of water flowed through the freeing ports almost reached the starboard edge of working deck around amidships.

No information on the downward force acting on the starboard side of the vessel, which was induced by the movement of a shoal of fish inside the net, was available. Therefore based on the presumption that at the accident the up-righting moment of the vessel and the heeling moment acting on it were quasi statically balanced, the downward force due to the movement of fish was estimated backward by trial and error.

Table 4 shows conditions used in the trial and error estimation. In Table 4 C.L.-G indicates the lateral deviation of the centre of gravity from the centre line. The downward force induced by the movement of fish inside the net, F_{net} was presumed to vertically act at the position of side roller (Figure 1) through the net. This induces same influence on stability of the vessel as hanging outboard cargo on its side. Therefore the displacement and position of the centre of gravity vary with magnitude of F_{net} (Morita, 1985).

Table 4. Examined conditions with variation of the downward force induced by the movement of fish inside the net, F_{net}.

Condition F_{net} (tf)	W (t)	KG (m)	mid-G (m)	C.L.-G (m)	GG_0 (m)
25.0	507.28	3.19	3.27	0.185	0.03
30.0	512.28	3.23	3.24	0.220	0.03
33.0	515.28	3.25	3.22	0.240	0.03
33.5	515.78	3.26	3.22	0.244	0.03
34.0	516.28	3.26	3.22	0.247	0.03
35.0	517.28	3.27	3.21	0.254	0.03

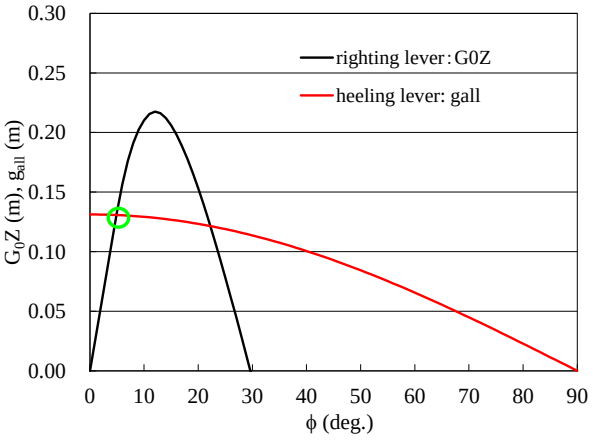

Figure 4 Righting lever and heeling lever curves at the condition of F_{net} = 25.0 tf.

Two examples of calculation result for the conditions in Table 4 are shown in Figure 4 and Figure 5. Black lines show the righting lever with free surface effects of tanks taken into account, G_0Z. And the total heeling lever, g_{all}, due to the wind force, the towing forces by colleague vessels and the starboard downward force induced by the movement of fish in the

net are shown in red lines. And as a part of g_{all}, the heeling lever to the starboard side due to the movement of fish in the net, g_{net} is calculated with equation (1).

$$g_{net} = F_{net} \cdot l_{net} \cos\phi / W \quad (1)$$

where l_{net} is the transverse distance from the centre line to the point of application of the downward force, ϕ is the heel angel, W is the displacement of the vessel.

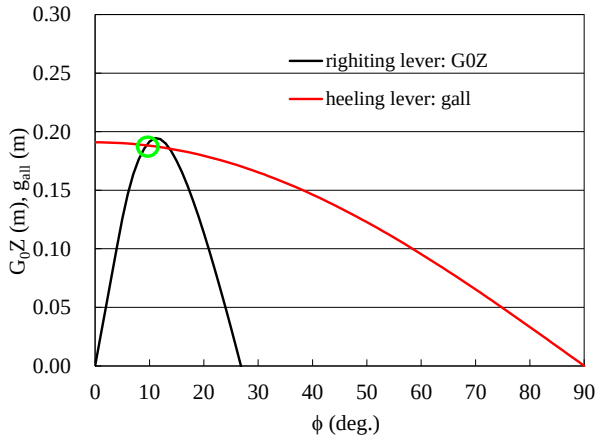

Figure 5 Righting lever and heeling lever curves at the condition of F_{net} = 33.5 tf.

In Figure 4 and Figure 5 the angle of first intercept between the righting lever and heeling lever curves, ϕ_e, is the steady heel angle in the case the heeling moments due to the wind force, the towing forces by colleague vessels and the downward force due to the movement of fish were assumed to act statically. Table 5 shows the estimated steady heel angle and the angle of the working deck edge immersion around amidships, ϕ_{WD}.

Table 5. Calculation results.

Condition F_{net} (tf)	ϕ_e (deg)	ϕ_{WD} (deg.)
25.0	4.9	9.9
30.0	6.8	9.7
33.0	8.9	9.5
33.5	9.5	9.5
34.0	10.3	9.5
35.0	-	9.4

With above mentioned calculation results the first situation, where freeing ports on the bulwark were immersed in the first stage of the accident was examined. As a result, it is clarified that if the heeling moment due to the downward force of 25.0 tf, induced by the movement of fish is assumed to act on the vessel, the steady starboard heel angle reaches the angle of freeing ports immersion, 4.9 degrees (Table 5 and Figure 4). As the downward force was presumed to act at the position of side roller, which is higher than the original C.G. of the vessel, the resultant vertical C.G. with the downward force of 25.0 tf reaches 3.19 meters, 0.20 meters higher than its original (Tables 2 and 4) and the stability is reduced. As shown in Figure 4 at this situation the estimated maximum righting lever is reduced to 0.22 meters at the heel angle of about 12 degrees and the estimated starboard heeling lever at the up-righting position reaches 0.13 meters.

As the result of examination of the second situation, it is clarified that if the downward force of 33.5 tf, induced by the movement of fish is assumed to act on the vessel, the steady heel angle reaches the angle of working deck edge immersion, 9.5 degrees (Table 5 and Figure 5). The resultant vertical C.G. with the downward force of 33.5 tf becomes 3.26m, 0.07 meters higher than its previous situation, and the stability is reduced further. At this situation the estimated maximum righting lever is reduced to 0.20 meters at the heel angle of about 11 degrees and the estimated heeling lever at the up-righting position is increased to 0.19 meters. Moreover in this situation the bulwark top heights from the water line at the starboard amidships and the aft end are estimated to be 1.07 meters and 1.60 metres respectively.

(3) <u>After Occurrence of Shipping Water.</u>

It was explained that the first shipping water around the stern part occurred when the surface of flowed water through the freeing ports almost reached the starboard edge of

working deck around amidships. However the only available information on the shipped water was that its depth around the bottom of bulwark at S.S. 3 was presumed to be 0.35 meters. Based on this information the weight and the centre of the shipped water were estimated. In the estimation it was assumed that the shipped water formed horizontal surface at heel angle of 9.5 degrees, corresponding to the angle of the starboard working deck edge immersion. And change of its depth along longitudinal direction and transverse direction was calculated based on the trim at that condition and the height of working deck.

Table 6 summarises the estimated the shipped water. The estimated weight of shipped water is 7.00 tf and its vertical centre of gravity is estimated to be 3.92 meters. Compared to the condition just before the occurrence of the first shipping water, corresponding to the one with F_{net} = 33.5 tf in Table 4, with this shipped water the C.G. of the vessel is raised by 0.01 meters and the maximum up-righting lever becomes lesser than 0.20 metres. Moreover with the additional heeling moment M_{sw}, the resultant heeling lever increases to 0.23 meters at the up-righting position and exceeds the maximum up-righting lever. As the result quasi static balance between the up-righting moment of the vessel and the heeling moment acting on it cannot be attained. Therefore after the first shipping water occurred it is presumed that the heel angle kept to increase and the vessel capsized.

Table 6. Shipped water on the working deck.

Weight: w_{sw} (t)	7.00
Vertical C.G.: KG_{sw} (m)	3.92
Transverse C.G.: C.L.-G_{sw} (m)	3.53
Heeling moment: M_{sw} (tf-m)	24.4
Heeling lever: g_{sw} (m)	0.05

3.3 Effect of the Port Side Ballast Water Tank Condition on the Accident

The port side ballast water counteracts the starboard side downward force due to the movement of fish. If the port side ballast water tank is supposed to be filled up, the heeling lever to the starboard side due to the downward force g_{net} is reduced by the heeling lever due to the port side ballast water, g_b, as indicated in equation (2).

$$g_{net} - g_b = (F_{net} \cdot l_{net} - w_b \cdot l_b)\cos\phi / W \qquad (2)$$

where w_b is the weight of ballast water and l_b is the transverse distance from the centre line to the centre of the tank.

Table 7. Effect of port side ballast water at the condition of F_{net} = 33.50 tf.

Port Side Ballast Tank	Empty (actual)	Full (supposed)
Displacement: W (t)	515.78	521.97
Vertical C.G.: KG (m)	3.26	3.26
Longitudinal C.G.: mid-G (m)	-3.22	-3.44
Transverse C.G.: C.L.-G (m)	0.244	0.241
Free surface effect: GG_0 (m)	0.03	0.03
Steady heel angle: ϕe (deg.)	9.5	6.7

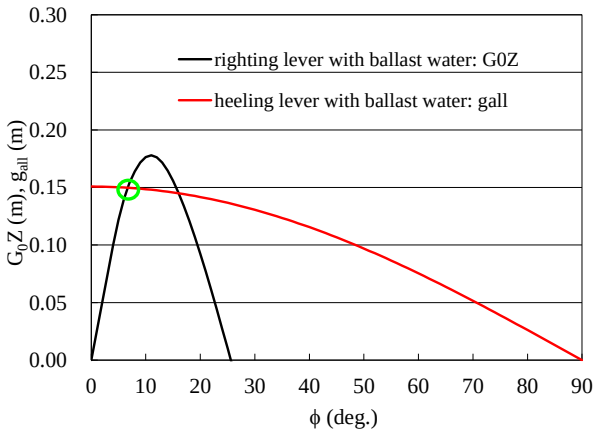

Figure 6 Righting lever and heeling lever curves with ballast water at the condition of F_{net} = 33.5 tf.

As mentioned above at the condition just before the occurrence of first shipping water, where the heel angle was presumed to reach

9.5 degrees, the heeling lever without the port side ballast water is estimated to be 0.19 meters at the up-righting position (Figure 5). If the port side water ballast tank is supposed to be filled up at this condition (Table 7), the heeling lever is offset by 21 % and reduced to 0.15 meters. And compared to the maximum up-righting lever with the filled up ballast water tank, the reduced heeling lever becomes smaller by 16 % and the resultant steady heel angle is reduced to 6.7 degrees (Table 7 and Figure 6). Moreover with the filled up port side ballast water tank the bulwark top heights from the water line at the starboard amidships is estimated to be 1.26 meters, higher by 0.19 meters than that at the accident. Therefore in the condition at the accident it is considered that the filling up port side ballast water tank enhances the safety of the vessel with reducing the starboard heel angle and raising the limiting height for shipping water.

3.4 Capsizing Process and Mechanism

Capsizing Process.

From the examination explained above, the capsizing process in this accident could be summarised as follows.

1) At the beginning of side-hauling work, the vessel without filling up the port side water ballast tank was subjected to the wind heeling moment of 2.66 tf-m and the heeling moment of 24.60 tf-m due to towing by colleague vessels, both acted in the port side down direction, opposite to the capsizing.
2) When the heeling moment due to the downward force of 25.0 tf, induced by the movement of fish in the net acted on the vessel, the starboard heel angle reached 4.9 degrees. At this situation the freeing ports on the bulwark were immersed and outside water flowed backward onto the upper deck.
3) Just before the occurrence of the first shipping water, the downward force due to the movement of fish reached 33.5 tf and the starboard heel angle increased to 9.5 degrees, the angle of the working deck edge immersion.
4) Due to the first shipping water outboard water of 7.00 tf shipped on the working deck and its depth reached 0.35 meters at around the bottom of bulwark at S.S. 3. The shipped water induced additional heeling moment and the total heeling moment exceeded the maximum up-righting moment. At this situation the heel angle kept to increase and after the second shipping water occurred the vessel capsized.

Capsizing Mechanism.

Based on the above mentioned process the capsizing mechanism in this accident could be explained as follows. Without filling up the port side water ballast tank the action of the starboard downward force induced by the movement of fish in the net and the occurrence of the shipped water on the working deck made the stability of the vessel reduced and caused the heeling moment to exceed the maximum up-righting moment. As the results the starboard heel angle kept increased and the vessel capsized.

4. CONCLUSIONS

With the technical investigation mentioned in this paper and so on, the JTSB had concluded the probable causes of the accident and issued remarks on safety measures to owners of purse seiner in order to prevent similar accidents (JTSB, 2016). The main points of the remarks are as follows. In order to prevent similar accident, it is necessary for purse seiner owners to consider appropriate counter measures in case of large heel due to the action of downward force induced by movement of fish in a net and train their crews. They are also demanded to instruct their crews to maintain equipment which might affect stability of purse seiner, i.e. ballast water tanks and fishing cranes, in good condition and to fix failure of such equipment before engaging in fishing operation.

5. ACKNOWLEDMENTS

The authors would like to express their sincere gratitude to Mr. Masafumi Ichikawa, who was the maritime accident investigator of the JTSB in charge of this accident, for his substantial contribution to the technical investigation. Discussion with him and suggestion from him were very valuable to analyse the capsizing process.

6. REFERENCES

Inoue, Y., 2009, “Technical Problem on the Purse Seine Fishery and Toward Improvement of it - Issue on Fishing Net Size -, Journal of Fishing Boat and System Engineering Association of Japan, Vol.83, pp.37-42 (in Japanese).

Japan Transport Safety Board, 2016, "Fishing Vessel GENPUKU MARU No.1 Capsizing", Marine Accident Investigation Report, MA2016-7-1 (in Japanese).

Japan Transport Safety Board, 2017, “JTSB Annual Report 2017”, pp.80.

Morita, T., 1985, “Theory of Ship Stability - Basis and Application -”, Kaibun-do, pp. 178-179 (in Japanese).

On the applicability of real time stability monitoring for increasing the safety of fishing vessels

Marcos Míguez González, *GII, University of A Coruña, Spain* mmiguez@udc.es

Lucía Santiago Caamaño, *GII, University of A Coruña, Spain* lucia.santiago.caamano@udc.es

Vicente Díaz Casás, *GII, University of A Coruña, Spain* vdiaz@udc.es

ABSTRACT

Stability-related accidents are among the main sources of fatalities within fishing, and crew lack of training, together with the absence of simple stability-related guidance onboard, have been stated as their main cause. Simplified guidance systems have been proposed as a possible solution to this problem. The authors have developed their own alternative, based on the linking of a stability guidance system with a methodology for estimating the vessel *GM*. In this work, the performance of this method, based on the analysis of the roll motion, will be tested during a fishing campaign onboard a mid-sized trawler, showing very promising results.

Keywords: *Fishing vessels, intact stability, stability monitoring, guidance systems, sea trials.*

1. INTRODUCTION

Fishing is well known for being one of the most dangerous industrial sectors in many countries. One of the main causes of a large percentage of the casualties occurring in fishing are stability related accidents, which in many occasions lead to the capsizing of the vessel (Jensen et al., 2014). It is generally accepted that one of the main causes for this large accident rate is the crew lack of training in stability matters, together with the absence of objective information which could contribute to a proper evaluation of the stability-related risk.

The use of simplified stability guidance systems has been proposed by different authors as an appropriate way to try to improve the safety of medium and small fishing vessels, by providing the crews with simple and easy to understand stability related information. These systems, which have to be easy to use, to understand and inexpensive to install and maintain, are normally based on simplified diagrams and colour codes. Then, from a series of simplified loading conditions, an estimation of the risk level of the vessel in a given situation is provided.

Some examples include the Womack matrix (Womack, 2003), the Wolfson stability guidance (Scarponi, 2017) or the approaches from the Norwegian Maritime Directorate (Wolfson Unit, 2004) or CENTEC in 2010 (Rodrigues et al., 2012). Other alternatives, such as the one from the Icelandic Administration (Viggosson, 2009), are not strictly speaking guidance systems, but could be included within the methods aimed at reducing stability-related accidents in fishing vessels.

Although the performance of some of these approaches has shown to be very good, as the Icelandic case, most of the aforementioned systems still rely on the subjective appreciation of the crew, and also have the drawback of losing simplicity as the size of the vessel increases, thus minimizing their performance.

The analysis of roll motion in real time to determine the stability characteristics of the vessel in real time, together with some type of linked guidance system, has been stated by different authors as an alternative to overcoming the aforementioned issues. The first proposal by Koyama dates from the 1982 (Koyama, 1982), and it consisted on a pendulum that measured roll period, which was then processed by an onboard computer able to compute roll motion RMS and generate an alarm if necessary. In Köse et al. (1995), the authors propose an expert system fed by different sensors, including accelerometers, pressure transducers, radar and Loran-C, with the objective of avoiding capsizing, especially due to stability failures in waves.

More recently, Terada et al. (2016), propose an autoregressive procedure and a general state space modelling for estimating the vessel metacentric height (*GM*), testing the system with good results using both scale model tests and real sea trials of a containership, although the system was not tested in small vessels.

Following these approaches, the authors have been developing their own proposal (Santiago Caamaño et al., 2018a), with the objective of linking a simplified stability guidance system (Míguez González et al., 2012), with a methodology for estimating the vessel *GM* (Míguez González et al., 2017), and which could overcome the main drawbacks of the aforementioned proposals (need for crew interaction, complexity and accuracy of the obtained results).

In this work, a study of the performance of the aforementioned method for estimating the vessel metacentric height, will be presented. This method is based on the analysis of the roll motion spectrum, which is obtained through Fast Fourier Transform (FFT) of the vessel roll motion time series, on a sequential way.

In previous works (Míguez González et al., 2017), the authors have validated the accuracy of this methodology using roll motion data obtained from a nonlinear roll model, under the effect of irregular beam waves and gusty winds, obtaining promising results.

In order to evaluate how does the proposed system behave in a more realistic scenario, data from sea trials corresponding to a fishing campaign of a medium sized pair stern trawler, where stability data have been manually monitored on a continuous basis, will be used.

2. SIMPLIFIED STABILITY GUIDANCE SYSTEM

2.1 System overview

The proposed simplified stability guidance system is based on the one previously developed by the authors (SKIPPER, Míguez González et al. (2012)), and which had a major drawback, consisting on the need for crew interaction for determining the vessel stability level.

In order to try to solve this issue, an additional module has been added to the current version, which has the main objective of minimizing the need for manual input of data within the system. In this module, vessel metacentric height is obtained after the estimation of natural roll frequency (applying the methodology described in the next section). From it, an Stability Index (SI), computed by evaluating the mandatory vessel intact stability criteria (IMO, 2012), is determined. This SI is then used for displaying, using a colour bar, the stability level of the vessel to the crew in a simple and understandable way.

In Figure 1, an screenshot of this system is included. This new module is described more in detail in Santiago Caamaño et al. (2018a).

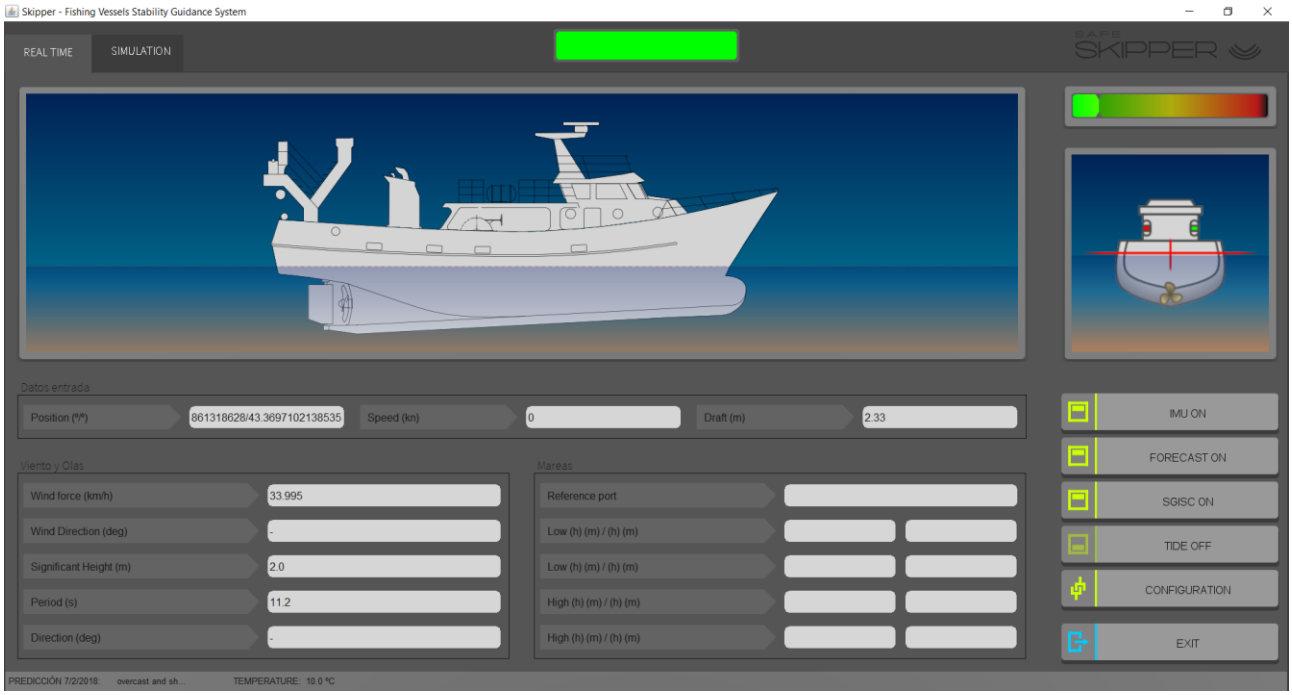

Figure 1. Simplified stability guidance system. Real time module.

2.2 Natural roll frequency estimation methodology

In order to estimate the natural roll frequency of the vessel in real time, a methodology based on the analysis of the vessel roll motion (Figure 2), which is described in detail in Míguez González et al. (2017), has been applied.

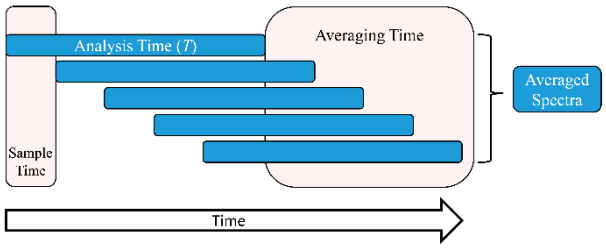

Figure 2. Proposed methodology Míguez González et al. (2017).

This method relies on the assumption that the peak frequency of the vessel roll spectrum coincides with its natural roll frequency. In order to set up a methodology for the real time analysis of this spectrum, and taking into consideration that subsequent spectra may differ from the previous or following ones, a sequential method has been proposed.

So, the resulting roll spectrum will be obtained after averaging, for a given time (known as "averaging time"), the roll spectra obtained by applying FFT for subsequent overlapped time segments of length "analysis time", obtained for a given "sample time".

After the averaging, and in order to increase the frequency resolution of the obtained spectrum (which only depends on the length of the time series under analysis, the "analysis time"), a smoothing process is done, applying a parametric model based on the superposition of three Gaussian functions.

Once these smoothed roll spectrum has been obtained and its peak frequency determined (which is assumed to coincide with the vessel natural roll frequency), the vessel metacentric height is estimated by applying the Weiss formula,

$$GM = \frac{{k_{xx}}^2 \omega_0^2}{g} \quad (1)$$

where GM is the transversal metacentric height, k_{xx} the roll gyradius ($k_{xx} \approx 0.4 \cdot B$), ω_0 is the natural roll frequency, which coincides with the

roll spectrum peak frequency, and g is the constant of gravity.

3. SEA TRIALS

In order to check the performance of the proposed methodology, a sea trial onboard a medium sized stern trawler, has been carried out. In order to do so, a complete fishing campaign has been monitored, including vessel motions, loading condition, heading and speed, and prevailing meteorological conditions, and these data have been used to test the proposed methodology for the estimation of vessel stability in real time.

The vessel under analysis is a medium sized pair stern trawler, which will be described in the following section, based in La Coruña port and which fishes on a daily basis together with her sistership in the coastal waters of Galicia, in Northwest Spain.

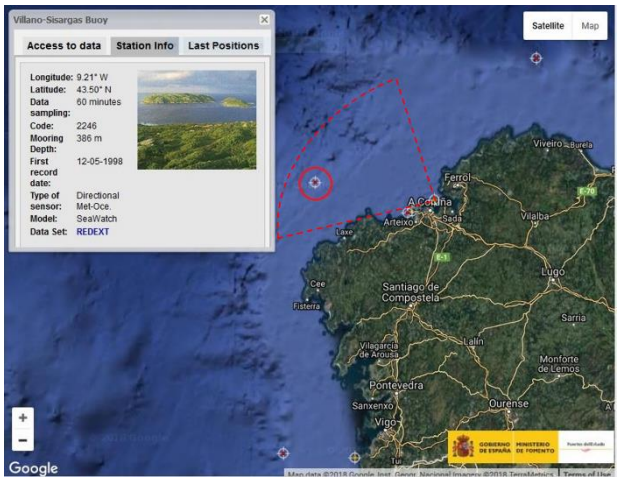

Figure 3. Sea trial area and SeaWatch buoy position.

The fishing ground in this case was in the vicinity of the Villano – Sisargas SeaWatch buoy, moored 35 miles off La Coruña port. Fishing area is highlighted with the red dashed line in Figure 3, while the red circle shows the buoy position.

Vessel motions have been measured by using an Xsense IMU, while speed, heading and route/location were obtained by using GPS. Regarding prevailing wave and wind conditions, hourly data from Villano-Sisargas buoy have been provided by Puertos del Estado, including, among others, significant wave height, peak period and mean wave direction, and mean wind speed and direction.

3.1 Test vessel

The vessel under analysis is a pair stern trawler, very similar to the one analysed in Míguez González et al. (2017), where the natural roll frequency estimation methodology was tested using roll motion data from a 1 degree of freedom nonlinear mathematical model. The main characteristics of the ship are included in Table 1. Its hull sections, together with an image of the vessel, are shown in Figure 4 and 5.


Figure 4. Test vessel. Photo courtesy of José R. Montero.

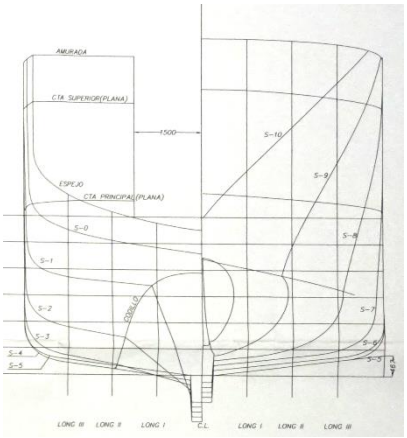

Figure 5. Test vessel: hull sections.

Table 1. Test vessel: main characteristics.

Overall Length	30.70 m

Length Between Perpendiculars	25.20 m
Beam	8.00 m
Depth	3.60 m
Design Draft	3.55 m
Displacement	504 t

3.2 Trial conditions

The whole fishing campaign lasted for a total of 19 hours, including 3 hours of sailing to the fishing ground, 10 hours of fishing and 6 hours of sailing back to port. In order to have a comparative value to check the performance of the natural roll frequency estimation methodology, the loading condition of the vessel during the whole campaign has been manually monitored, including tank filling levels, approximate fish weight and location, situation and weight of fishing nets and other equipment and number of people onboard. Ship lightweight has been obtained from the vessel compulsory inclining experiment, included in the stability booklet. In this work, a roll time series corresponding to 2h 5' has been analysed to test the proposed methodology. This situation corresponds to a condition with no fish in holds, with the vessel trawling together with her sistership at reduced speed, in slight starboard beam to quartering forward seas and lateral port wind, with a 67 % of fuel remaining and a 100 % of the rest of the consumables.

Table 2. Test series parameters.

Mean Draft	3.225 m
Trim	1.750 m
Displacement	469 t
Metacentric Height (*GM*)	0.385 m
Roll Gyradius ($k_{xx} = 0.4 \cdot B$)	3.2 m
Natural Roll Frequency (ω_0)	0.607 rad/s
Natural Roll Period	10.35 s
Average Heading	247º
Mean Vessel Speed	1.72 knt
Mean Significant Wave Height	0.9 m
Mean Wave Peak Period	10.25 s
Mean Wave Direction	322.5º
Mean Wind Speed	1.29 m/s
Mean Wind Direction	154º

In Table 2, vessel conditions during this period, together with mean wind and wave data, are presented. Natural roll frequency has been obtained by applying the Weiss formula using the vessel metacentric height estimated for this loading condition and the roll gyradius.

3.3 Natural roll frequency estimation results

The roll motion of the vessel during these 2h 5' is reported in Figure 7. As it can be appreciated in this figure, and due to the slight values of wind and waves, maximum roll amplitude does not reach large values.

In addition to this, and near the time instant 3000 s, it can be observed a change in the vessel heel angle, which goes from around 1 degree to starboard side to 0.5 degrees to port side. This fact is explained due to a modification of the two trawling vessels heading, which lead to a slight reduction of the net tension. Considering that the vessel under analysis is the one trawling at the port side of the couple (Figure 6), and that it had an initial heel angle of 2.5 degrees to port while not fishing, the reduction of the net tension reduced the heeling to the starboard side induced by the net.

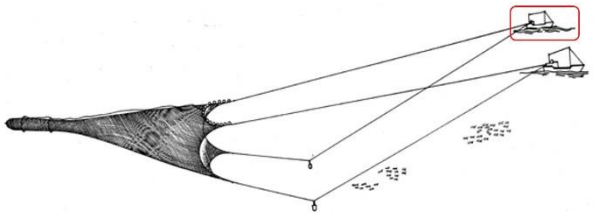

Figure 6. Pair trawling (FAO, 2008). Situation of the test vessel is highlighted.

In order to estimate the natural roll, frequency of the vessel, the already presented methodology has been applied to this roll motion time series. Considering the similarities between the ship studied in Míguez González et al. (2017) and the one tackled in this case, the same parameters have been used.

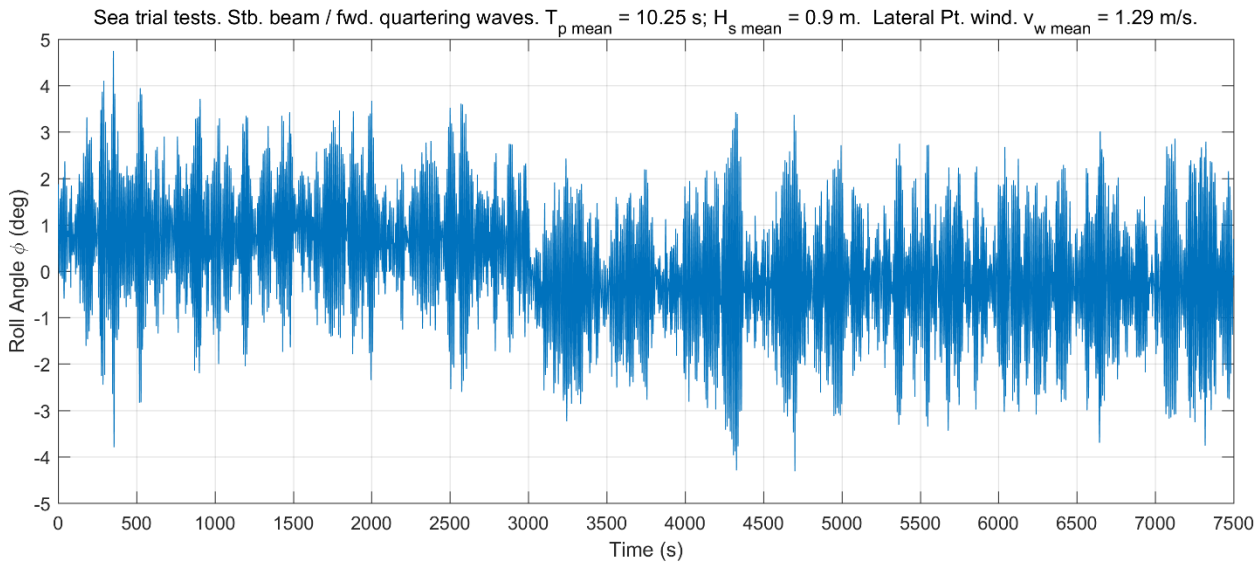

Figure 7. Analysed roll motion time series.

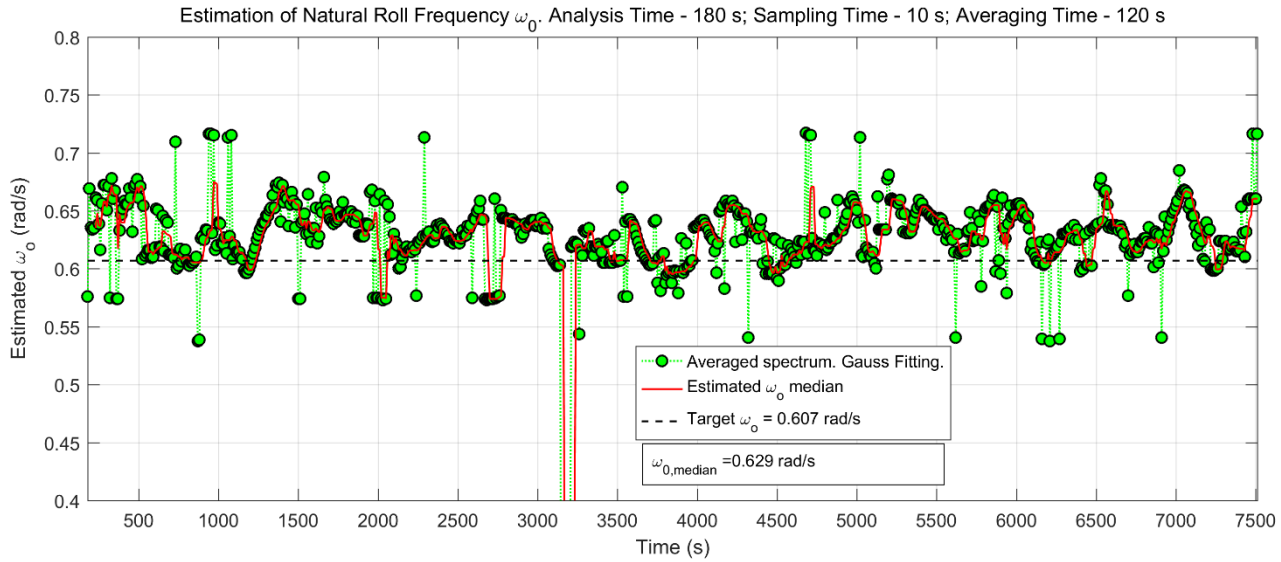

Figure 8. Natural roll frequency estimation results.

The "analysis time", which has to provide a minimum resolution for the method and also has to be small enough as to detect possible changes in the loading condition, has been taken as 180 seconds. A "sample time" (determined by the possible modifications of the natural roll frequency) of 10 seconds has been selected. And finally, the "averaging time", which represents the "memory" of the system, and which has to be long enough as to not being affected by short term estimations, but while trying not to hide changes in the loading condition, has been taken as 120 seconds.

The obtained results are shown in Table 3 and Figure 8, where green dots represent the natural roll frequency estimations at each analysis step, the red line represents the median of the last six estimations and the dashed black line is the manually computed target value for the natural roll frequency.

If the loading condition is considered to be constant during the whole time series, and the median of the estimations is taken as the representative value, a final estimated natural roll frequency of $\omega_{0\,est} = 0.629$ rad/s has been obtained, which is equivalent to an estimated metacentric height of $GM_{est} = 0.413$ m. This

results in a deviation from the manually computed value of less than an 8 %, as shown in Table 3. If 5 % percentile and 95 % percentile are taken into account to study the deviation of the estimations from the target value along the whole time series, ω_0 deviations are within the range [-5.1 %, +9.89 %], and subsequent *GM* deviations are within the range [-9.95 %, +20.76 %].

Table 3. Estimation results.

Target Natural Roll Frequency	0.607 rad/s
Target Metacentric Height	0.385 m
Estimated ω_0 Median ($\omega_{0\ est}$)	0.629 rad/s
Estimated *GM* from $\omega_{0\ est}$ (GM_{est})	0.413 m
5 % Percentile Estimated ω_0 ($\omega_{0\ est\ 5\%}$)	0.576 rad/s
95 % Percentile Estimated ω_0 ($\omega_{0\ est\ 95\%}$)	0.667 rad/s
Estimated *GM* from $\omega_{0\ est\ 5\%}$ ($GM_{est\ 5\%}$)	0.346 m
Estimated *GM* from $\omega_{0\ est\ 95\%}$ ($GM_{est\ 95\%}$)	0.464 m

From these results, it can be observed that underpredictions in *GM* are kept under a reasonable value (a 10 %). However, for the case under analysis, the system has a tendency to overpredicting the vessel *GM*, while still keeping the 95 % of the estimations under a 20 % from the target value. This same situation has been already observed in the results obtained in Míguez González et al. (2017) for the mathematical model, where *GM* deviations where in the range of [-9.10 %, +17.80 %]. Although including a safety margin over the prediction is always a possible solution if this deviation is kept constant in all possible environments, the analysis of the whole fishing campaign, together with carrying out some more tests in more severe weather conditions, are necessary to accurately determine the deviation range and then to set up this safety increment.

In fact, the need of testing in more severe weather conditions is also necessary to accurately determine the source of the observed error, especially the influence of external excitations on the estimated roll spectra. In the case under analysis and due to the near absence of waves and wind, the obtained roll spectra are not heavily influenced by external excitations, and the main error source should then come from the use of the Weiss formula for the estimation of roll inertia (Santiago Caamaño et al., 2018b).

Another conclusion from the analysis of the obtained data, is that the effect of nets while fishing don´t seem to have a clear influence on the predictions, and that the methodology works reasonably well, even while trawling, at least under the wind and wave conditions present at the time of the study.

Finally, as it can be observed in Figure 8 near the time instant 3000 s, and coinciding with the moment where the vessel heading is changed, the obtained estimations are very far from the target value. This fact is possibly due to the effect of rudder forces acting during that period, which largely modify the rolling pattern of the vessel. However, taking into consideration that this type of manoeuvres are usually short time ones, the use of an outlier detection algorithm could be applied to remove these points from the data fed into the guidance system, avoiding the generation of false alarms.

4. CONCLUSIONS

In this paper, the performance of a methodology for the estimation of the vessel metacentric height in real time while in operation, based on the computation of the roll motion spectrum and, from it, on the estimation of the vessel natural roll frequency, has been tested in a real environment.

In order to do so, the authors have monitored a fishing campaign of a medium sized pair stern trawler, in waters off the port of A Coruña, Spain, obtaining all the relevant data regarding the motions, route, speed, loading condition and prevailing sea state and wind during the whole length of this campaign.

The roll motion time series of 2h 5’ corresponding to a trawling manoeuvre have

been used, in this paper, to analyse the performance of the aforementioned methodology for making estimations of the vessel initial stability parameters (*GM*), showing good results, even under the effect of fishing nets.

However, obtained estimations are generally over predicting the desired target value, which could lead to the undesirable effect of overestimating the vessel stability. This fact is still an open issue.

Although the use of a safety margin could be a possible solution, it is necessary to analyse the behaviour of the system in a more severe sea state, in order to analyse whether these differences remain constant or increase when external excitations become more relevant.

5. ACKNOWLEDGEMENTS

The authors would like to thank Puertos del Estado for providing the wave and wind data used in this work (Puertos del Estado, Ministerio de Fomento, Gobierno de España, www.puertos.es).

6. REFERENCES

FAO, 2018, "Fishing Techniques. Midwater pair trawling", Technology Fact Sheets, Fisheries and Aquaculture Department, Food and Agriculture Organization of the United Nations, Rome, Italy.

IMO, 2012, "Cape Town Agreement of 2012 on the Implementation of the Provisions of the Torremolinos Protocol of 1993 Relating to the Torremolinos International Convention for the Safety of Fishing Vessels, 1977", International Maritime Organization, London, UK.

Jensen, O.C., Petursdottir, G., Holmen, I.M., Abrahamsen, A. and Lincoln, J., 2014, "A review of fatal accident incidence rate trends in fishing", International Maritime Health, 65 (2), pp. 47-52.

Köse, E., Gosine, R. G., Dunwoody, A. B., and Calisal, S. M., 1995, "An Expert System for Monitoring Dynamic Stability of Small Craft", IEEE Journal of Oceanic Engineering, Vol 20, 1, pp. 13-22.

Koyama, T., 1982, "On a Micro-Computer Based Capsize Alarm System", Proceedings of the 2nd International Conference of Stability of Ship and Ocean Vehicles, Tokyo.

Míguez González, M., Bulian, G., Santiago Caamaño, L., and Díaz Casás, V., 2017, "Towards real-time identification of initial stability from ship roll motion analysis", Proceedings of the 16th International Ship Stability Workshop (ISSW 2017), Belgrade, Serbia, pp. 221-230.

Míguez González, M., Caamaño Sobrino, P., Tedín Álvarez, R., Díaz Casás, V., Martínez López, A., and López Peña, F., 2012, "Fishing vessel stability assessment system", Ocean Engineering, Vol. 41, pp. 67-78.

Rodrigues, J. M., Perera, L. P., and Guedes Soares, C., 2012, "Decision support system for the safe operation of fishing vessels in waves", Maritime Technology and Engineering, Taylor & Francis Group, London, pp. 153-161.

Santiago Caamaño, L., Míguez González, M., and Díaz Casás, V., 2018a, "Improving the safety of fishing vessels trough roll motion analysis", Proceedings of the 37th International Conference on Ocean, Offshore and Arctic Engineering (OMAE2018), Madrid, Spain.

Santiago Caamaño, L., Míguez González, M., and Díaz Casás, V., 2018b, "On the feasibility of a real time stability assessment for fishing vessels", Ocean

Engineering, Vol. 159, pp. 76-87.

Scarponi, M., 2017, "Use of the Wolfson stability guidance for appraising the operational stability of small fishing vessels", Proceedings of the 16th International Ship Stability Workshop (ISSW 2017), Belgrade, Serbia, pp 213-220.

Terada, D., Tamashima, M., Nakao, I. and Matsuda, A., 2016, "Estimation of the metacentric height by using onboard monitoring roll data based on time series analysis", Proceedings of the 15th International Ship Stability Workshop (ISSW 2016), Stockholm, Sweden, pp. 209-215.

Viggosson, G., 2009, "The Icelandic Information System on Weather and Sea State Related to Fishing Vessels ´ Crews and Stability", Proceedings of the World Fishing Exhibition, Vigo, Spain.

Wolfson Unit, 2004, "Research project 530. Simplified presentation of FV stability information. Phase 1. Final report", Report No.1773, University of Southampton, Southampton, UK.

Womack, J., 2003, "Small commercial fishing vessel stability analysis: Where are we now? Where are we going?", Marine Technology, Vol. 40, 4, pp. 296-302.

Direct estimation of natural roll frequency using onboard data based on a Bayesian modeling procedure

Daisuke Terada, *National Defense Academy* dterada@nda.ac.jp

Hirotada Hashimoto, *Kobe University* hashimoto@maritime.kobe.ac.jp

Akihiko Matsuda, *Japan Fisheries Research and Education Agency* amatsuda@affrc.go.jp

Naoya Umeda, *Osaka University* umeda@naoe.eng.osaka-u.ac.jp

ABSTRACT

Understanding the natural frequency of roll motion is important for safely navigating a vessel at sea as this knowledge can help the vessel avoid dangerous situations, e.g., harmonic roll resonance and parametric roll resonance. Analyzing onboard monitoring roll data can help gain an insight into this aspect. This paper introduces a novel procedure to estimate the natural frequency of roll motion using onboard monitoring data. This method is based on a Bayesian modeling procedure employing the Markov chain Monte Carlo method. The effectiveness of the proposed procedure was verified using the results of onboard experiments conducted on a fisheries research vessel.

Keywords: *bivariate autoregressive model, MAICE, Hamiltonian Monte Carlo method, random walk Metropolis–Hastings algorithm*

1. INTRODUCTION

Understanding the natural frequency of roll motion is important for safely navigating a vessel at sea as this knowledge can help the vessel crew to avoid dangerous situations, e.g., harmonic roll resonance and parametric roll resonance. Terada et al. (2016) reported that the natural frequency of such motion can be estimated indirectly; however, the procedure to calculate the parameters is complex.

In the present study, an attempt was made to resolve this problem and a novel procedure to estimate the natural frequency of roll motion using onboard monitoring data was proposed. Our past research focused on the 2nd–order linear ordinary differential equation. Further, any external disturbance was assumed stochastic, because sea waves can be considered stochastic. Thus, the basic equation is extended to a stochastic dynamical system driven by a colored noise sequence. After the system is transformed into state–space representation, it is discretized based on an analytical solution. Note that whitening of the colored noise sequence is necessary. According to Yamanouchi (1956), a discrete autoregressive (DAR) process was applied to meet this requirement. Thus, the system is expressed as a bivariate AR model, a type of time series model. Since the AR coefficients contain information of the basic equation, the natural frequency f can be estimated from the relations of the AR coefficients and the f values obtained from an eigenvalue of a state transition matrix in the state–space expression. Terada et al. (2016)first estimated the AR coefficients and then estimated the eigenvalue of a state transition matrix based on the down hill simplex method (Nelder and Mead (1965)), which a type of nonlinear optimization method. Finally, f was calculated from the estimated eigenvalue based on a genetic algorithm (Ishida et al. (1997)). Thus, this procedure yields an indirect estimation.

Therefore, herein we attempted to directly estimate f from the bivariate AR coefficients based on a Bayesian modeling procedure employing both the Hamiltonian Monte Carlo (HMC) method (Duane et al. (1987)) and the random walk Metropolis–Hastings (RM–MH) algorithm (Brooks et al. (2012)). The effectiveness of the proposed procedure was verified by using the results of the experiments conducted onboard a fisheries research vessel. The experimental findings are comprehensively described herein.

2. RELATIONSHIP BETWEEN THE LINEAR STOCHASTIC DYNAMICAL SYSTEM AND TIME SERIES MODEL

The relationship between a linear stochastic dynamical system and a time series model was reported by Terada et al. (2016).

Consider the following linear roll motion equation:

$$\ddot{\phi}(t)+2\alpha\dot{\phi}(t)+\omega^2\phi(t)=u(t), \qquad (1)$$

where $\phi(t)$ is the roll angle of the ship, α is the damping coefficient, $\omega(=2\pi f)$ is the natural angular frequency, f is the natural frequency, and $u(t)$ is an external disturbance. Here, $u(t)$ is treated as a stochastic process; however, it does not satisfy the assumption of a white noise sequence, as the characteristics of the roll motion change with the frequency characteristics of external disturbances, e.g., waves and winds.

Equation 1 can be expressed in the vector form as follows:

$$\dot{\mathbf{x}}_t=\mathbf{K}\mathbf{x}_t+\mathbf{B}\mathbf{u}_t. \qquad (2)$$

where

$$\mathbf{x}_t=\left[\dot{\phi}(t),\phi(t)\right]^T,\mathbf{u}_t=\left[u(t),0\right]^T,$$

$$\mathbf{K}=\begin{pmatrix}-2\alpha & -\omega^2\\ 1 & 0\end{pmatrix},\ \mathbf{B}=\begin{pmatrix}1 & 0\\ 0 & 0\end{pmatrix}.$$

A discrete model for an analytic solution of the linear dynamical stochastic model can be written in Equation 2:

$$\mathbf{x}_n=\mathrm{EXP}\left[\mathbf{K}\Delta t\right]\cdot\mathbf{x}_{n-1}+\mathbf{B}\mathbf{u}_n. \qquad (3)$$

where

$$\mathbf{A}\equiv\mathrm{EXP}\left[\mathbf{K}\Delta t\right]$$
$$=\frac{e^{a\Delta t}}{b}\times$$
$$\begin{pmatrix}b\cos b\Delta t+a\sin b\Delta t & -\left(a^2+b^2\right)\sin b\Delta t\\ \sin b\Delta t & b\cos b\Delta t-a\sin b\Delta t\end{pmatrix},$$

and $\mathbf{x}_n=\left[\dot{\phi}_n,\phi_n\right]^T$. Here, a and b are the real and imaginary parts of the eigenvalue of $\mathbf{K}$, respectively. Moreover, $\mathbf{B}\mathbf{u}_n$ is a two–dimensional colored noise sequence, which is obtained from the stochastic integral. This colored noise term must be transformed into a white noise sequence to deal with the problem stochastically. For this purpose, the DAR process proposed by Yamanouchi (1956) is employed. In Equation 3, let

$$\varepsilon_n\equiv\mathbf{B}\mathbf{u}_n. \qquad (4)$$

Then, suppose that ε_n can be approximated by the following m–th order DAR process:

$$\varepsilon_n=\sum_{i=1}^{m}\mathbf{D}_i\varepsilon_{n-i}+\mathbf{w}_n,\quad(\varepsilon_n=\mathbf{w}_n\ \text{ for } i=0), \qquad (5)$$

where $\mathbf{w}_n$ is a 2×2 Gaussian white noise sequence with $N(0,\mathrm{diag}(\sigma_1^2,\sigma_2^2))$ and $\mathbf{D}_i$ is a 2×2 AR coefficient matrix. The following relation is evident.

$$\begin{cases}\varepsilon_n=\mathbf{x}_n-\mathbf{A}\mathbf{x}_{n-1},\\ \varepsilon_{n-1}=\mathbf{x}_{n-1}-\mathbf{A}\mathbf{x}_{n-2},\\ \quad\vdots\\ \varepsilon_{n-m}=\mathbf{x}_{n-m}-\mathbf{A}\mathbf{x}_{n-m-1}.\end{cases} \qquad (6)$$

Therefore, by substituting Equations 6 into Equation 5, the following two–dimensional $(m+1)$–th order bivariate AR model can be obtained:

$$\mathbf{x}_n=\sum_{i=1}^{m+1}\mathbf{C}_i\mathbf{x}_{n-i}+\mathbf{w}_n. \qquad (7)$$

Here, $\mathbf{C}_i$ $(i = 1, \cdots, m+1)$ is the bivariate AR coefficient matrix, which is expressed as follows:

$$\begin{cases} \mathbf{C}_1 = \mathbf{D}_1 + \mathbf{A}, \\ \mathbf{C}_2 = \mathbf{D}_2 - \mathbf{D}_1\mathbf{A}, \\ \quad \vdots \\ \mathbf{C}_m = \mathbf{D}_m - \mathbf{D}_{m-1}\mathbf{A}, \\ \mathbf{C}_{m+1} = -\mathbf{D}_m\mathbf{A}. \end{cases} \tag{8}$$

Hence, the elements of $\mathbf{A}$ and $\mathbf{D}_i$ can be estimated using the Markov Chain Monte Carlo method (Brooks et al. (2012)) after fitting the bivariate AR model. In this case, the real and imaginary parts $\{a, b\}$ of the eigenvalue of $\mathbf{K}$ are considered as the hyper–parameter of $\mathbf{A}$; they can be estimated using the RW–MH algorithm. Moreover, the real part and imaginary parts $\{a, b\}$ of the eigenvalue of $\mathbf{K}$ and the unknown parameters $\{\alpha, f\}$ satisfy the following relations.

$$\begin{cases} \alpha = -a \\ f = \sqrt{a^2 + b^2}/2\pi \end{cases} \tag{9}$$

Consequently, f can be directly estimated from the real and imaginary parts $\{a, b\}$ of the eigenvalue of $\mathbf{K}$.

3. ESTIMATION OF PARAMETERS

3.1 Preprocessing

In the preprocessing for the estimation of f, spectral analysis is performed based on the AR modeling procedure using the minimum AIC (Akaike Information Criterion) estimation (MAICE) method proposed by Akaike (1973). The peak frequency of the estimated spectrum with respect to the roll angle is used as the initial value of the hyper–parameter, which comprises the real and imaginary parts $\{a, b\}$ of the eigenvalue of $\mathbf{K}$.

3.2 Parameter estimation based on Markov chain Monte Carlo

The RW–MH algorithm is used to estimate the hyper–parameters $\{a, b\}$ as follows:

$$\begin{cases} a = \theta_a^t + e_a \\ b = \theta_b^t + e_b \end{cases} \tag{10}$$

Here, e_* (* is a or b) follows a Gaussian distribution. The acceptance of the state is same as in the ordinary MH algorithm.

For the parameters, the d–dimensional parameter vector θ is considered:

$$\theta = \left(\mathbf{A}_{(1,1)}, \cdots, \mathbf{A}_{(2,2)}, \mathbf{D}_{1\,(1,1)}, \cdots, \mathbf{D}_{M+1\,(2,2)}\right)^{\mathrm{T}}. \tag{11}$$

Now, assume a step size ε and a repetition number L for the path integral in the Leapfrog method in the HMC method. Then, the algorithm can be written as follows.

1. Set the initial values of $\theta^{(1)}$, ε, L, and the maximum sampling step T_{max}. Further set $t = 1$.
2. Perform the RW–MH algorithm, and obtain the hyper–parameters.
3. Reproduce the d–dimensional normal random number $\mathbf{p}^{(t)}$. This $\mathbf{p}^{(t)}$ is used in the next step.
4. Obtain the state $\theta^{(p)}$ and $\mathbf{p}^{(p)}$ based on the Leapfrog method.
5. If r, the rejection ratio, satisfies the requirement of probability $\min(1, r)$, the state is accepted. Then set $\theta^{(t+1)} = \theta^{(p)}$. Otherwise, set $\theta^{(t+1)} = \theta^{(t)}$.
6. If $T_{max} = t$, stop.
7. As $t = t + 1$, return to step 2.

In this calculation, $\varepsilon = 1.0^{-6}$, $L = 100$, $T_{max} = 10^4$, and the burn–in period$= 5000$. Noted that in this section, the meaning of ε is different from the meaning of the notation in Section 2.

The natural frequency can be evaluated using the relations shown in Equation 10 based on the estimated hyper–parameters $\{a, b\}$.

4. ONBOARD EXPERIMENTS

Onboard experiments were performed to examine the effectiveness of the proposed procedure. The sample ship was "Taka–maru", a fisheries research vessel belonging to Japan Fisheries Research and Education Agency. Table 1 presents the principal dimensions of Taka–maru and Fig.1 shows the general arrangement of Taka–maru. The vessel followed an octagonal route, and the time series for the parameter estimation measured using a micro electro mechanical systems(MEMS) type gyro sensor at a sampling interval of 0.5 s. The experimental sea area is the Tateyama Bay off. The measurement time for one experiment was 240 s. The experimental conditions are summarized in Table 2. Hereafter, the symbol * stands for numerals 1–8, and Data * refers to Case *. In Table 2, the direction is defined according to a geographic coordinate system; the wave characteristics were observed by ship officers. This table summarizes that the ship encountered waves from various directions. Figs.2 show the measured time series. In these figures, the black and red lines indicate the roll rate and the roll angle, respectively. The roll rate and roll angle are large in the beam sea (Figs.2(d) and 2(h), respectively), and small in the head sea and the following sea (Figs.2(c) and 2(f), respectively). In general, these variables depend on the wave height and wave period. Further, Fig.2(g) shows that the roll rate and roll angle are small. This is explained by the influence of the wave height as the wave height was 1.0 m.

Table 1: Principal dimensions of Taka-maru

Length between perpendiculars: L	25.0m
Breadth: B	5.2m
Mean draft: d	1.7m
Block coefficient: C_b	0.442
Metacentric height: GM	0.52m

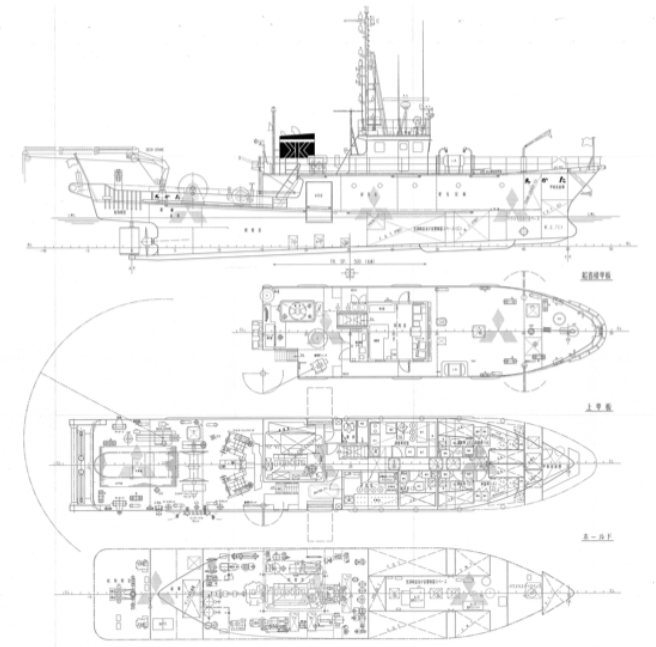

Figure 1: General arrangement of Taka–maru

Table 2: Experimental conditions

Date	Nov. 29, 2012	
Data num.	Ship speeds [knots = 0.514 m/s]	Ship course [deg.]
1	4.0	330
2	4.0	15
3	4.0	60
4	4.0	105
5	4.0	150
6	4.0	195
7	4.0	240
8	4.0	285
Wave	Height[m]	1.2 → 1.0
	Period[s]	4.0 ∼ 5.5
	Direction[deg.]	145 ∼ 180
Sampling	interval[s]	0.5

5. RESULTS AND DISCUSSION

5.1 Spectral analysis

First, the characteristics of the frequency domain are explained based on the results of spectral analysis by employing the MAICE method. In the AR modeling procedure, the AR model from the 1st order to the 50th order was used to fit the time series. The best model order determined by the AIC is summarized along with the value of the AIC in Table 3. Stable estimation can be performed since the best model in each dataset exists in the set range. Figs.3 show an example of the spectral analysis. In particular, the figure shows the results for Case 1. The top left figure indicates the power spectrum with respect to the roll rate, the top right and bottom left figures indicate the cross spectrum with respect to the roll rate and the roll angle, and the bottom right figure indicates the power spectrum with

respect to the roll angle. In these figures, the black line indicates the real part of the spectrum and the red line indicates the imaginary part of the spectrum. This result shows that a smoothness cross spectrum is obtained. Fig.4 shows the spectral density of the roll angle. In this figure, the horizontal axis indicates the frequency, and the vertical axis indicates the spectral density. Further, each colored line indicates the results corresponding to the case number under the experimental conditions. This figure shows that the results for the beam sea in Fig.2(d) indicated by the blue line and in Fig.2(h) indicated by the gray line are large and are the unimodal spectral density. In general, the roll motion of the ship hardly depends on the frequency characteristics of external disturbances, e.g., waves and winds (Kobylinski and Kastner (2003)). It can be confirmed that the peak frequency for each case is in the range 0.170 to 0.192 Hz. Thus, it is considered that f exists within this range. On the contrary, for Cases 1–3, the results exhibit bimodal spectral density because the bottom of the ship was exposed to air during navigation in the following seas. Noted that these cases represent a singular situation.

Table 3: Best model order.

Case num.	Model order	AIC
1	20	-7384.9
2	10	-7565.5
3	8	-7651.0
4	10	-7509.1
5	18	-7331.0
6	20	-7527.7
7	31	-7525.7
8	20	-7371.9

5.2 Estimation of the natural frequency

Although both the natural frequency and roll damping coefficient can be estimated using the proposed procedure, only the results for the estimated natural frequency are presented herein. Since the estimates are obtained as realizations, the maximum a posteriori (MAP) is used to evaluate the results. Figs.5 show the histogram of the realizations. Figs.5(a)–(h) show the results for Cases 1–8, respectively. These figures show that each histogram follows a closed distribution and has a mode. This indicates that the calculation is stable, resulting in successful estimation. In this study, the mode of the histogram is used as the MAP. Comparisons of the MAPs of the estimates and the peak frequency values calculated from the spectrum with respect to the roll angle are summarized in Table 4. Each estimated MAP of f is less than the peak frequency, except for Case 5, and the MAPs range is from 0.160–0.189 Hz. However, slight discrepancies are also seen for each MAP. To determine the cause of this discrepancy, it is necessary to confirm convergence of another parameter.

Table 4: Comparison of the estimated natural frequency and the peak frequency calculated from the spectrum with respect to the roll angle.

Case num.	MAP (Hz)	Peak (Hz)
1	0.173	0.184
2	0.189	0.192
3	0.188	0.188
4	0.164	0.172
5	0.195	0.192
6	0.170	0.170
7	0.160	0.170
8	0.174	0.182

6. CONCLUSIONS

In this study, a novel procedure to estimate the natural frequency of roll motion using onboard monitoring data was introduced. The proposed method is based on a Bayesian modeling procedure. Data of onboard experiments were used to verify the proposed procedure. The findings can be summarized as follows:

1. The histograms of the estimates of the natural frequency follow closed distributions with modes.
2. Thus, the mode can be used as the MAP to evaluate the estimates.
3. The estimation calculation is stable, and successful estimation is realized.
4. However, each MAP shows slight discrepancies.

Therefore, in the future, it is necessary to confirm the convergence of another parameter. Moreover, by analyzing other data on the natural frequency during navigation, it is necessary to verify the reliability of the proposed procedure.

7. ACKNOWLEDGEMENTS

This work was supported by JSPS KAKENHI Grant Number JP15H02327 and JP17K06978.

8. REFERENCES

Akaike, H. (1973). Information theory and an extension of the maximum likelihood principle. In Petrov, B. N. and Caski, F., editors, Proceedings of the 2nd International Symposium on Information Theory, pages 267–281. Akadimiai Kiado, Budapest.

Brooks, S., Gelman, A., Jones, G., and Meng, X. L. (2012). Handbook of Markov Chain Monte Carlo. Chapman & Hall.

Duane, S., Kennedy, A. D., Pendleton, B. J., and Roweth, D. (1987). Hybrid monte carlo. Physics Letters B, 195(2):216–222.

Ishida, R., Murase, H., and Koyama, S. (1997). Fundamental theories and application programs for genetic algorithms by personal compute (in Japanese). MORIKITA PUBLISHING Co., Ltd.

Kobylinski, L. and Kastner, S. (2003). Stability and safety of ships, volume 1. ELSEVIER.

Nelder, J. A. and Mead, R. (1965). A simplex method for function minimization. Computer Journal, 7:308–313.

Terada, D., Hashimoto, H., and Matsuda, A. (2016). Estimation of parameters in the linear stochastic dynamical system driven by colored noise sequence. In Proceedings of the 47th ISCIE International Symposium on Stochastic Systems Theory and Its Applications, volume 2016, pages 125–131.

Yamanouchi, Y. (1956). On the analysis of ships'oscillations as a time series (in japanese). Journal of zosen kyokai, 99:47–64.

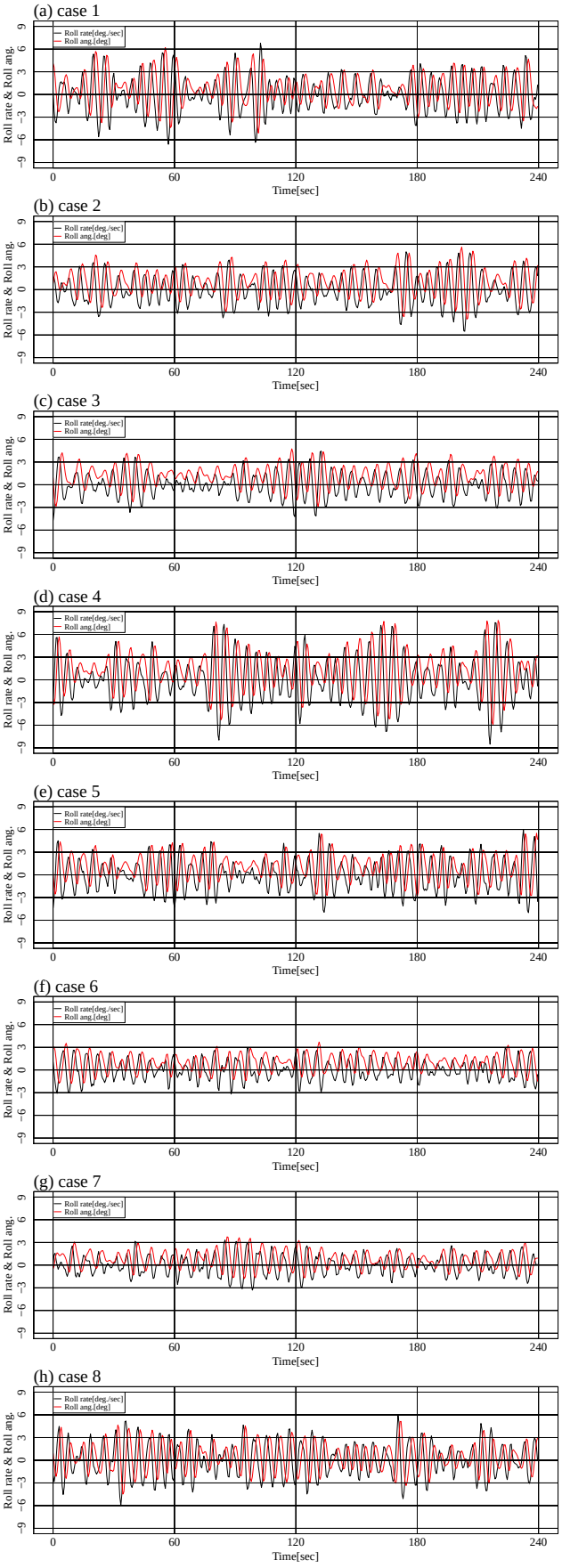

Figure 2: Measured time series.

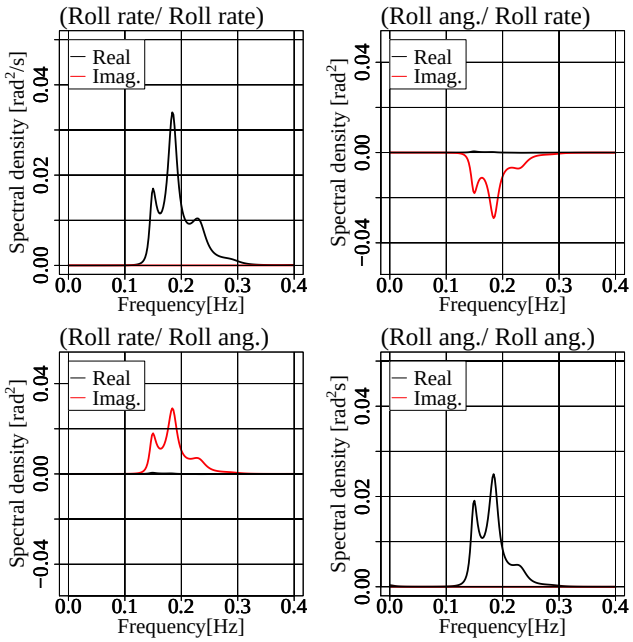

Figure 3: Example of the spectral analysis.

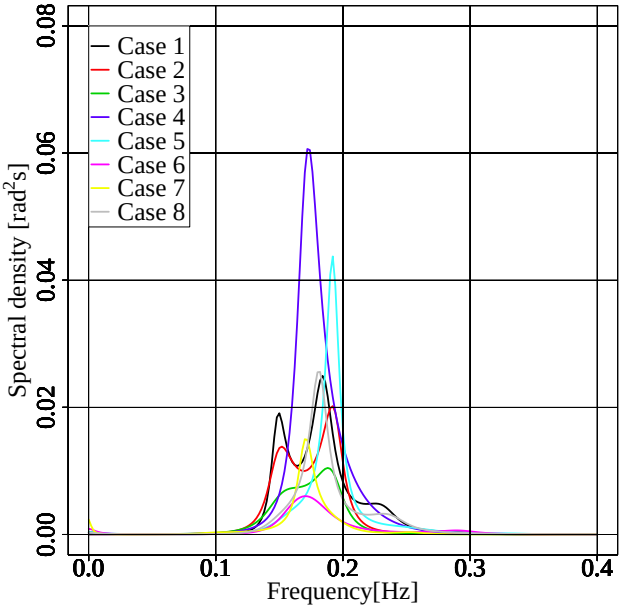

Figure 4: Estimated power spectrum with respect to the roll angle.

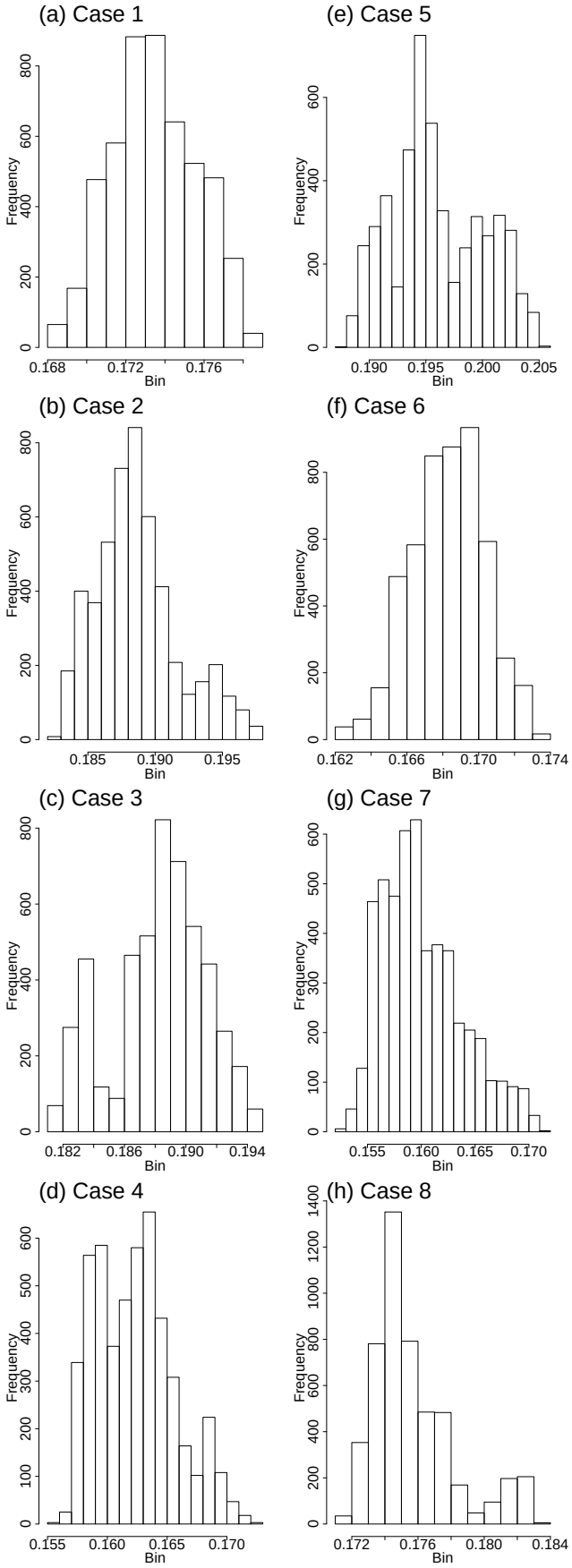

Figure 5: Histogram of the estimated natural frequency.

Approximation of capsize probability using a Roll Excedence (RE) probability with a threshold chosen in roll phase plane

Romain Macé, DGA Hydrodynamics, romain.mace@intradef.gouv.fr
Jean-Yves Billard, French Naval Academy (École Navale), jean-yves.billard@ecole-navale.fr
Guillaume Lannel, DGA Hydrodynamics, guillaume.lannel@intradef.gouv.fr
Jean-François Leguen, DGA Hydrodynamics, jean-françois.leguen@intradef.gouv.fr

ABSTRACT

A Monte-Carlo method has been applied on a French frigate submitted to a fixed Pierson Moskowitz spectral sea state $S(\omega)$, performed until either capsize or maximum duration of *20.000 s*. Among the complete set of simulations performed, signals that end in capsize were classed by duration and used for computing the probability to capsize in a duration comprised between *0* and *t* seconds, that might be approximated by an exponential formula. Comparison is proposed with the evaluation of Roll Excedence (RE) probability determined on simulations where no capsize occur.

Keywords: *Monte-Carlo, roll excedence, attraction basin.*

1. INTRODUCTION

For a ship in given loading conditions, having given heading and speed and on a given sea state, her probability of capsize gives a precise evaluation of the meteorological risks encompassed by the ship. The determination of this probability is of major concern and remains an open problem. Methods like Monte-Carlo give a good evaluation of this probability at a very large computation cost but its high computational cost is not compatible with many applications of capsize risk assessment.

Probability of roll excedence can be evaluated rapidly and used to define a global probability of capsize for the all life cycle of the ship. Unfortunately, the correlation between those two approaches is not straightforward. In the present paper, a method of correlation based on the definition of the attraction basin is proposed. As Maki (2017) compare capsize risk including Monte-Carlo method, this paper try to use numerical simulation of a ship in waves instead of analytical results.

2. SHIPS AND NUMERICAL TOOLS

2.1 The ships

The ship considered in the present paper is a French frigate designed in the seventies and out of duty for several years.

The righting arm of this ship is preesented on figure 1 where the characteristic vanishing stability angle has been defined. It can be seen on the figure that the *GZ* value remains quite linear up to 30°.

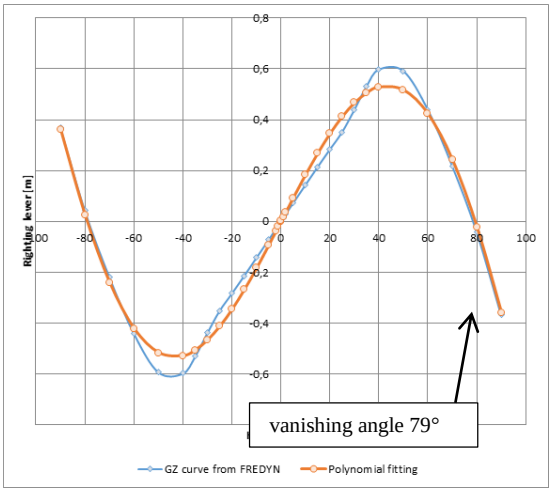

Figure 1: Righting arm curve of the GLG

2.2 The numerical code, FREDYN

Computations are performed using FREDYN V14, a time domain computational code developed by MARIN in the frame of the CRNAV. More details on the codes are given for example in Ypma (2012).

For sea state representation, FREDYN allows the definition of a repetition time in which the wave train should not repeat. In all our computations, this duration has been set to *50.000 s* when the longest computation duration was equal to *20.000 s*.

3. CAPSIZE PROBABILITY

3.1 Capsize probability defined by Monte-Carlo computations

To define the capsize probability on a given time, N_{total} computations of *20.000 s* have been conducted on a rough sea state ($H_s = 11$ *m*, $T_p = 9.5$ *s* Pierson Moskowitz spectrum). For each computation, the sea state is described by *80* wave components with a different set of phase angles given rise to N_{total} different time representation having the same statistical properties. Each computation can either end before *20.000 s* by the capsizing of the ship or end after *20.000 s* of computation. In each case the computation time is retained. For these computations the ship is in beam seas conditions at zero speed with sway and yaw motions frozen.

The sea state has been chosen to conduct to numerous capsizes in a time shorter than the ordered computation time. The probability of survival, PS_t for a given duration $t < 20.000$ *s*, is given by the ratio of the number N_t of simulations which have not ended before the time t due to the capsize of the ship over the total number of simulations performed, $N_{total} = 1.000$ in our study. The capsize probability is then defined as:

$$PC_t = 1 - PS_t = 1 - \frac{N_t}{N_{total}} \qquad (1)$$

As shown by Belenky (2007) the time evolution of PC obeys an exponential law (risk):

$$PC = 1 - e^{-\alpha t} \qquad (2)$$

The value of α is determined by a least square method based on the simulation points. On figure 2 the probability of capsize has been plotted as a function of time. Dots represent the values of the probability PC_t and the curve is the exponential fit of those points, PC. The main interest of this formulation is that the probability of capsize is described by only one parameter, α_s, which is also the tangent at $t = 0$ *s* to the curve.

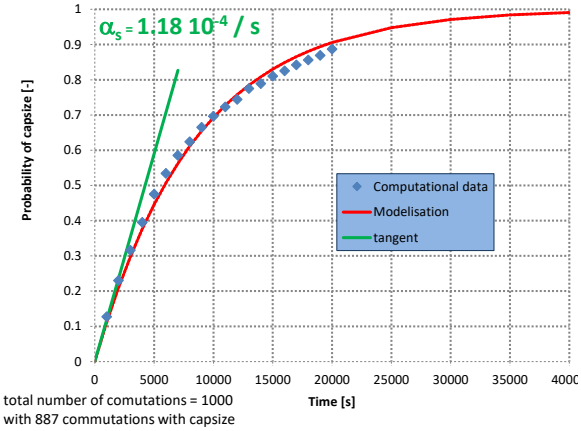

Figure 2: Evolution of capsize probability of the frigate as function of time

This curve can be also constructed versus the number of roll cycles experienced by the ship to allow a direct comparison with the roll excedence probability described hereafter.

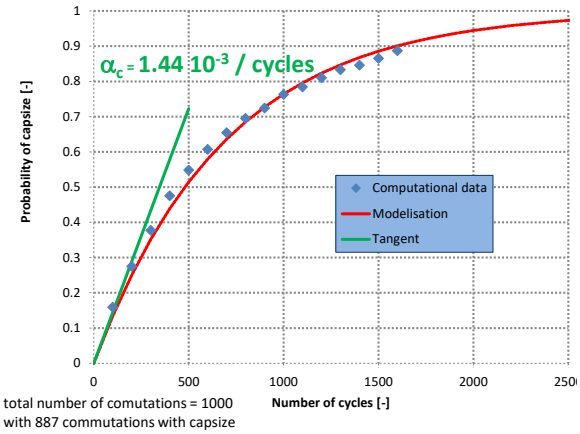

Figure 3: Evolution of capsize probability of the frigate as function number of roll cycle

For this second probability curve the abscissa is in number of cycles. In average, one cycle is equal to the mean period of roll cycle (here *12.5 s* to be compared to the natural roll period at small angle in calm water of the ship, *13.75 s* modified by the shorter period of the sea state). As it is demonstrated theoretically by Belenky (2007) this second curve is more or less a re-scaling of the first one by the mean period. From both curves, the tangent at *t=0 s* give the probability by cycle or by second. The ratio between α_c and α_s is 2% close to the mean period.

3.2 Probability of roll excedence

To define the probability of roll excedence, the simulations without capsize are cumulated. Besides, the maxima and minima of rolls are determined independently and post treated using a method described by Derbanne (2008), allowing the drawing of figure 4 where the probability of roll excedence has been plotted as function of the roll angle value. A confidence interval has been associated to the curve (the probability to be outside the two limits is 10%).

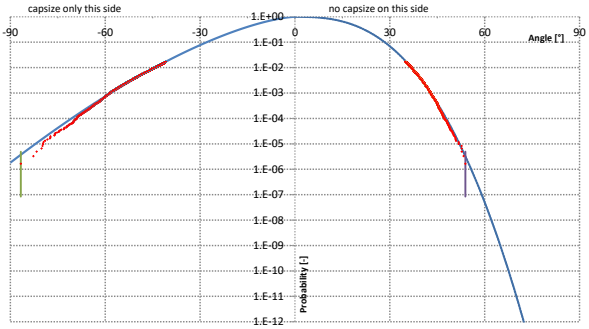

Figure 4: Curve of roll excedence and associated confidence interval

This curve gives the probability of excedence on the next wave, it is then a probability evaluated on a very short duration of the order of magnitude of the next roll oscillation of the ship. In addition to the high cost of computation, the used of the probability of excedence of the vanishing angle seems too optimistic. A capsize can then be defined as an excedence of a given value, the safety roll angle. From a statistical point of view a ship that exceeds hers safety roll angle can be considered as lost. Then, the values of maximum roll angles observed in the dynamic simulations before capsize shall be of the same order of magnitude to the safety roll angle which is determined in still water conditions.

As the procedure of determination of the probability of roll excedence is quite short this can be used efficiently in the determination of the long-term probability of capsize of the ship.

The link between the probability of roll excedence and the parameter α_c issued of the Monte-Carlo method must now be studied. A link using the attraction basin of the ship is proposed.

4. PHASE PLANE AND ATTRACTION BASIN

4.1 General

The determination of the attraction basin makes use of a one degree of freedom roll equation:

$$A\ddot{\varphi} + B\dot{\varphi} + C(GZ(\varphi)) = 0 \qquad (3)$$

The two terms, *A* and *B* are identified from a numerical extinction test performed with FREDYN, *GZ(φ)* is a polynomial approximation of the *GZ* curves (see figure 1).

Thus the area of the attraction basin can be computed and phase curves (un-damped equation) with chosen initial $(\varphi, \dot{\varphi})$ conditions have been added, on figure 5.

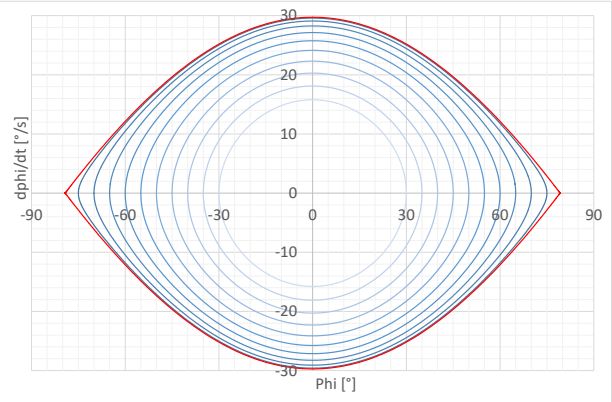

Figure 5: attraction basin and phase curves

4.2 Phase trajectories before capsize

The sample of simulations that end on a capsize is retained and the last roll cycle of each simulation is plotted on the phase plane, figure 6.

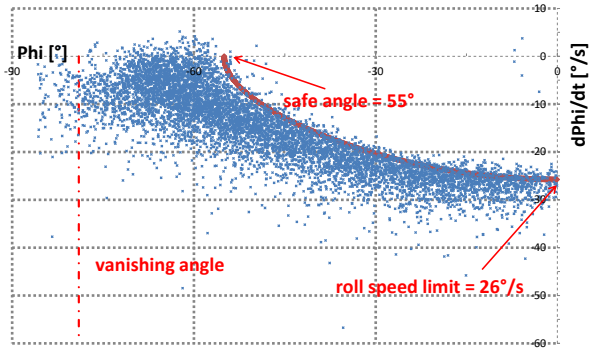

Figure 6: phase trajectories before capsize

It can be seen on the figure that all the cycles leading to capsize are situated over a safe region limited by a curve to be defined by a statistical procedure, on each angular sectors of *5°* the limit chosen to keep *95%* the dots out of the safe domain. From a statistical point of view most of the simulations that lead to capsize are outside of this limit.

4.3 Phase trajectories during safe periods

For this approach, the sample of simulations that do not capsize are retained and plotted in the phase plane, figure 7.

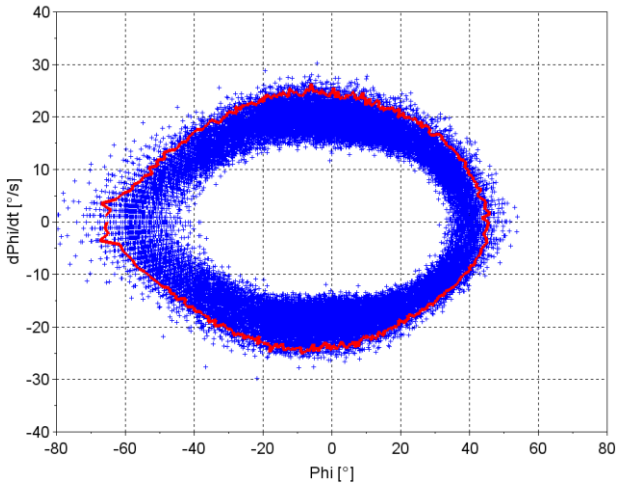

Figure 7: phase trajectories during safe periods

As shown in the previous paragraph a safe area inside the curve can be defined (for all angular sectors, *99.95%* of dots are below the safe limit, in red in the figure 7).

4.4 Boundary of the safe area of the attraction basin

Comparison of the safe areas define either using the envelop of the capsize cycles or using the envelop of the largest safe roll angles give an equivalent value of the maximum roll rate the ship can experience without capsize, *26°/s*. These curves have been superimposed, figure 8, on the graph of figure 5. As the three curves are similar, we decided to define the safe roll angle, φ_s, as the maximum roll angle of a phase trajectory in still water reached at $(\varphi_s, 0°/s)$ from *(0°,26°/s)* initial condition.

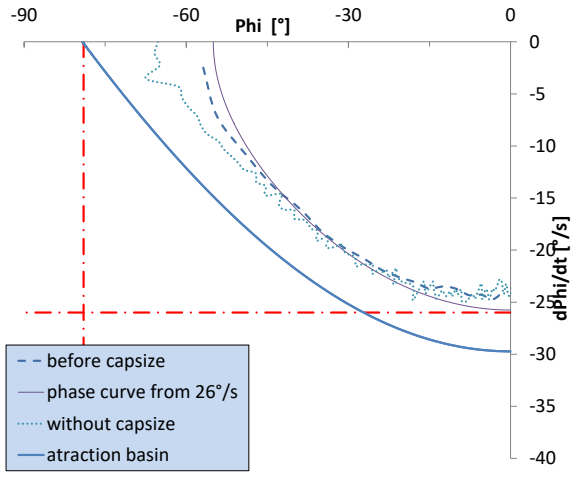

Figure 8: definition of safe roll angle

The value of the probability of excedence for the safety roll angle is now compared with the value of α_c issued from the Monte Carlo probability curve. On figure 4, the safe angle *(55°)* have a probability of $1.26\ 10^{-3}$ similar to the probability of capsize obtain by Monte-Carlo approximation, $1.44\ 10^{-3}$, per cycles.

Table 1: ratios of safe domain

Full attraction basin		Safe domain		safe / full
$\varphi_{max,basin}$ [°]	79	$\varphi_{max,safe}$ [°]	55	70%
$\left(\frac{d\varphi}{dt}\right)_{max,basin}$ [°/s]	30	$\left(\frac{d\varphi}{dt}\right)_{max,saf}$ [°/s]	26	87%
Area A_{basin} [$deg^2.s^{-1}$]	8481	Area A_{safe} [$deg^2.s^{-1}$]	4941	58%

5. CONCLUSIONS

The probability of capsize of a frigate has been determined by a Monte Carlo procedure. To be able to realize rapid computations, it is proposed a method that enables to evaluate the value of this probability from a probability of excedence determined in non-capsizing computations.

It is shown that a good correlation is obtained between the samples of capsized computations and non-capsized ones, which allows to define of a safe roll angle from the area of the attraction basin or from a fraction of the maximum roll rate.

More computations are required to verify that the value obtained is the same on other ships, that the value is not sea state dependant and that this value is not modified for different headings for which strong coupling may exist between the different movements of the ship. Work is in progress to verify those previous points.

6. ACKNOWLEDMENTS

The authors want to acknowledge the financial support French navy and DGA and the valuable discussions during the meetings of CRNAV and ISSW.

7. REFERENCES

Belenky, V., Sevastianov, N. B., 2007, "Stability and Safety of Ships: Risk of Capsizing", the Society of Naval Architects and Marine Engineers, Second Edition (2007).

Maki, A., Estimation method of the capsizing probability in irregular beam seas using non-Gaussian probability density function, Journal of Marine Science and Technology (2017) 22:351–360.

Ypma E., Harmsen E., 2012, "Development of a New Methodology to Predict the Capsize Risk of Ships", Proceedings of STAB 2012, pp. 1-10.

Derbanne, Q., Leguen J.-F., Dupau, T., Hamel, E., 2008, "Long-Term Non-Linear Bending Moment Prediction", Proceedings of OMAE 2008.

The effects of Hullform Geometric change on probability of Capsize

Andrew Peters, *QinetiQ, Haslar Marine Technology Park* (*UK*) AJPETERS@qinetiq.com
Charles Pope - *QinetiQ, Haslar Marine Technology Park* (*UK*)

ABSTRACT

The current quasi-static stability criteria used by the UK MoD are largely based on the Sarchin and Goldberg work published in 1962. These criteria ensure a level of stability performance when both intact and damaged. The inherent level of safety in these criteria and the link to the dynamic performance of the vessel in waves is now being investigated.

During the vessel design process the choices made on the geometric hull form have an effect on the overall dynamic stability performance. A methodology has been developed to evaluate the dynamic stability performance of naval vessels intact in wind and waves whilst performing a systematic variation of geometric hull parameters while keeping the area under the GZ curve to 70 degrees constant. This study has shown that whilst keeping the same GZ curve stability characteristics between vessels that the dynamic stability assessment has shown differences in stability performance with the geometric variations. This paper compares the dynamic performance against the vessel geometric variations and discusses the effect on the stability performance.

Key words: Geometric variations, Naval Standards, FREDYN, Numerical Simulation, Time Domain Simulation, Intact Stability

1. INTRODUCTION

The UK Royal Navy currently uses static based stability criteria, UK MoD 2013, to measure the performance of a vessel. The current Sarchin and Goldberg based criteria are the foundation of the standard used by the UK MoD, defined in Defence Standard 02-900 (DefStan) and MAP 01-024. The inherent level of safety in these criteria and the link to the dynamic performance of a vessel in waves is little known.

A study has been performed with the aim to isolate the effect on the probability of loss (defined as the probability of exceeding a 70 degrees roll angle), based solely on geometric changes to a vessel. Therefore, the static stability condition of each geometric change to the vessel has been systematically altered so that the area under the GZ curve up to 70 degrees remained constant. The area of GZ to 70 degrees has been selected as a potential new criteria for the Naval Ship Code and is based upon dynamic stability based studies performed by the Co-operative Research Navies (CRN) working group, Harmsen 2012. A modern frigate hullform from the recent CRN stability investigations was scaled to provide the smaller baseline hullform for the geometric changes. The baseline hullform was scaled in 3

dimensions; from the baseline, 6 new vessel variants were created making 7 vessels for the analyse.

For each vessel variant based on the geometry change applied, the overall Probability of loss was calculated using Time domain simulations and compared against the Naval Ship Code (NSC), vessel particulars and other static based stability criteria, Sarchin & Goldberg 1962.

Calculating the probability of loss (exceeding 70 degrees roll in this study) can be conducted with modern computational tools, such as FREDYN, which can model the motions of a vessel in extreme wind and waves. However, there are many areas of uncertainty that are inherent in the calculations that require careful consideration.

In order to accurately calculate the probability of loss of a naval vessel, a simulation tool is required to examine all possibilities of sea state and operational loading conditions to provide assessment of all realistic operational scenarios. The numerical simulation program FREDYN (De Kat et al 2002, MARIN 2011) was developed by the Maritime Research Institute Netherlands (MARIN) for the Cooperative Research Navies working group and continues to be applied extensively to both intact and damaged ships.

The FREDYN time-domain program is able to take account of nonlinearities associated with drag forces, wave excitation forces, large-angle rigid-body dynamics and motion control devices. The FREDYN program permits investigations into the dynamics of intact and damaged vessels operating in realistic environments.

The baseline hullform has been scaled in 3 dimensions, so that the length between perpendiculars (LBP) is 105 metres; from this 6 vessel variants were created based on the following geometric changes.

- Scaling in the X direction only, to lengths of 95 and 115 metres, keeping displacement constant.
- Scaling in the Y direction only, keeping L/B ratio constant for the 95 and 115 metre vessel lengths and displacement remaining constant.
- Altering the displacement based on a constant L/Disp. ratio for the 95 and 115 metre vessel lengths.

In total there were 7 vessels, a letter designation has been given to each vessel with its geometric changes, as shown in Table 1-1.

Table 1-1 Vessel geometric variations

Variant	Geometric description
A	Baseline hullform (LBP 105m)
B	Length decrease (95m)
C	Length increase (115m)
D	Beam and length decrease (L/B ratio remains constant to base hullform)
E	Beam and length increase (L/B ratio remains constant to base hullform)
F	Displacement and length decrease (L/Disp. Ration remains constant to base hull form)
G	Displacement and length increase (L/Disp. Ration remains constant to base hull form)

FREDYN Time domain simulations for each vessel were conducted in the following operating conditions.

- 7 headings (001, 030, 060, 090, 120, 150, 179 degrees).
- One speed of 17 knots.

- Significant wave heights and periods selected from the Bales wave scatter diagram (significant wave heights ranging from 4.5 to 17.5 metres and mean wave periods ranging from 6.8 to 15.4 seconds).
- Minimum of 10 wave realisations per case.
- One load condition per vessel.

From each vessel variant based on the geometry change applied, the overall probability of loss was calculated. This was achieved by analysing the FREDYN simulation output using an envelope peaks over threshold (EPOT) methodology incorporated by the LORELEI software tool developed with CRN. The EPOT methodology, detailed in Ypma 2011 and Ypma 2013, produces a theoretical probability of loss for an individual single sea state and heading combination. It is important to understand and define what is meant by a loss/capsize event; this is based on the roll angle exceeding a critical angle of 70 degrees in this study. The results from the LORELEI software were then compared against the geometric variations, the NSC and other static based stability criteria.

2. MODELLING APPROACH

2.1 Geometry creation

The creation of 7 different vessel variants, including the baseline hullform, has been produced from the geometric and parametric changes as shown in Table 1-1. Figure 2-1 shows 2D plan and profile views of the geometric changes.

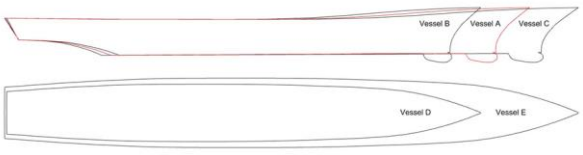

Figure 2-1: Vessel variants

Vessels F and G (displacement variants) have not been presented as these used the same geometry as vessels B and C, these two vessels variants were based on loading condition change. The draughts are only altered accordingly to match the L/Disp. ratio to the baseline hullform (vessel A).

The models were created in the software package Paramarine™ with indicative hull form coefficients in order to create a set of modern representative hullform models.

2.2 Loading condition

To produce a baseline loading condition for vessel A the data from the original modern frigate parent form where also scaled. Table 2-1 shows a comparison of the principle dimensions and hydrostatics between the parent modern frigate and baseline vessel A.

Table 2-1 Hullform Parameters

Hydrostatics	Modern frigate	Vessel A
LBP (m)	123.00	105.00
Beam at amidships (m)	16.220	13.787
Max depth (m)	12.010	10.209
Draught at AP (m)	4.490	3.817
Draught at FP (m)	4.490	3.817
Displacement (tn)	3984.4	2446.9
LCG (m)	59.925	50.933
VCG (m)	6.500	5.340
Gm. (m)	1.223	1.223
L/B ratio	7.583	7.616
L/Disp. Ratio	0.031	0.043
Area under GZ curve up 70º (m/rad)	0.545	0.585

Paramarine™ was used for generating the loading cases for each vessel and to perform the static stability analysis. The calculated loading condition for vessel A was used as the baseline loading condition for this study. To produce a loading condition for vessels B to E, each vessel was systematically adjusted with a level trim and displacement within Paramarine™. This allowed the longitudinal centre of gravity (LCG) to move accordingly and for the vessel to alter draught to achieve the displacement requirements.

Vessel F and G within Paramarine™ were also systematically adjusted to create a level trim and with a required displacement. However, the displacement has been calculated based on the same L/Disp. ratio calculated for vessel A. Paramarine™ adjusted the draught of the vessel to achieve the displacement and the LCG moves accordingly.

The aim was to produce each vessel with the same area under the GZ curve up to 70 degrees. This was done by manually altering the vertical centre of gravity (VCG) of each vessel until the area under the curve matched. Loading conditions were generated and all models were checked for compliance with the intact Def Stan 02-900 stability criteria.

Figure 2-2 shows the comparison of the GZ curves for each vessel.

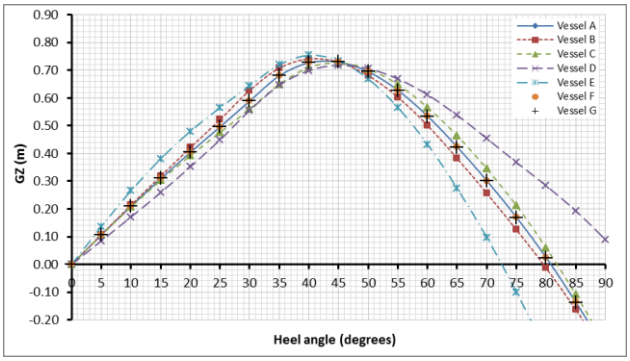

Figure 2-2 GZ curve comparison

The original parent modern frigate used within FREDYN for previous CRN studies had appendages fitted (rudders, bilge keel and stabilizer fins). For this study the same appendages have been fitted to each of the variant vessels. To capture the appropriate roll damping for each vessel, the length of the bilge keels were scaled accordingly for each of the vessel lengths while the chord of the bilge keels remained constant. Powering characteristics, roll damping and natural roll periods were all

selected based on data for the parent vessel to ensure realistic vessel motions were obtained for all the variant vessels.

3. SIMULATION DETAILS

3.1 Simulation setup

The FREDYN simulation analysis simulated sea state conditions from a sea state 5 upwards using height and wave period information from a wave Scatter table. For this study a matrix of different mean wave periods (T1) and significant wave heights (Hs) were chosen (64 wave height/period combinations). Waves were modelled in the simulation using a Pierson-Moskowitz spectrum as this is an open ocean wave spectra and representative of the operational environments for vessels of this type to ships of this type. FREDYN's default autopilot settings have been shown to be suitable for vessels of this type including the parent vessel and so were used for vessel course keeping for all of the vessel variants in the study.

Long crested seas were used in all the simulations. A summary of the wave definitions used in the simulations, derived using the World Meteorological Organisation sea state code as guidance, is seen in Table 2-2:

Table 2-2 Simulation wave definitions

Significant wave height (Hs) (m)	Mean wave period (T1) (s)								
	6.8	7.5	8.4	9.5	10.6	11.6	12.6	13.9	15.4
4.5	✓	✓	✓	✓	✓	✓	✓	✓	✓
5.5		✓	✓	✓	✓	✓	✓	✓	✓
6.5		✓	✓	✓	✓	✓	✓	✓	✓
7.5				✓	✓	✓	✓	✓	✓
8.5				✓	✓	✓	✓	✓	✓
9.5				✓	✓	✓	✓	✓	✓
10.5					✓	✓	✓	✓	✓
11.5						✓	✓	✓	✓
12.5							✓	✓	✓
13.5							✓	✓	✓
14.5								✓	✓
15.5								✓	✓
16.5									✓
17.5									✓

Initially 10 one-hour simulations were run for each wave height and period modelled, each with a different wave realization. Dependent on the resulting probability of loss, up to an additional 90 simulations are run for each case. Each vessel was simulated with RPM set for 17 knots in clam water. Seven headings were simulated, from stern to head seas (001, 030, 060, 090, 120, 150, 179 degrees in FREDYN).

The original procedure for using FREDYN simulations to calculate a probability of vessel loss was developed by McTaggart 2002. The PCAPREF method, adopted by the CRN working group, was largely based upon the method described fully in his paper and was used for evaluating capsize risk of intact ships in random seas. This approach for predicting ship capsize risk combined the time domain simulation program FREDYN with probabilistic input data for wave conditions and ship operations (speed and heading). More recent studies with the CRN group have shown that for other frigate types there may be a need for a greater number of simulations to produce statistically reliable results of probability of

loss. The current methodology uses a peaks over threshold methodology as it has been found to produce better fidelity of results, as the roll motion peaks during the whole simulation are used in the calculation of the capsize probability rather than just the maximum roll angle in each simulation.

This 'Envelope Peaks Over Threshold' (EPOT) methodology, Campbell and Belenky 2010, uses the FREDYN program to look at the potential vessel loss in up to different 100 seaway realisations. The EPOT method considers the roll peaks from the entire time history rather than just the largest roll values, which is the case for the original CRN PCAPREF method. This provides significantly more data from which distributions of roll angles can be determined and consequently the calculation of the probability of exceeding a defined roll angle limit can be made. This leads to improved short term capsize predictions over that of the original CRN PCAPREF method.

In order to generate sufficient data for reliable statistics to be obtained FREDYN must be executed multiple times for each speed, heading and wave combination, using different random seeds to generate the wave time history. In order to avoid wasting processor time calculating more exact capsize probabilities in waves, where the capsize probability does not contribute significantly to the overall probability, a staged approach to the number of simulations was adopted. A method was adopted that incrementally increases the number of simulations according to the actual calculated capsize risk. For each wave, 10 simulations is initially required. From these 10 simulations, the hourly capsize probability was determined using the method detailed below and compared to the threshold values. If the calculated capsize probability was less than the 10 run simulation threshold then no more simulations were necessary and the output from the Gumbel fitted capsize probability was output. Otherwise 10 more simulations were run and the capsize probability calculated again, this time using the highest 50 envelope roll angles of all 20 simulations. If the calculated probability was less than the 20 simulation threshold, no more simulations were necessary. Otherwise, it continued to 30 simulations and so on. Once 100 simulations were completed, regardless of the capsize risk, no further simulations were required and the capsize risk and fitted Gumbel data are calculated and output.

For each FREDYN output file it is necessary to extract the roll motion peak data (both positive and negative) from the time history trace. This approach results in peaks which are not strictly independent of each other, as it includes both positive and negative peaks of the same roll cycle. In order to extract independent data, it is necessary to determine an envelope of the peaks. This leaves a set of envelope peaks and their amplitudes for each FREDYN simulation. An example roll trace, roll peaks and envelope peaks are shown in Figure 3-1, Peters et al 2010.

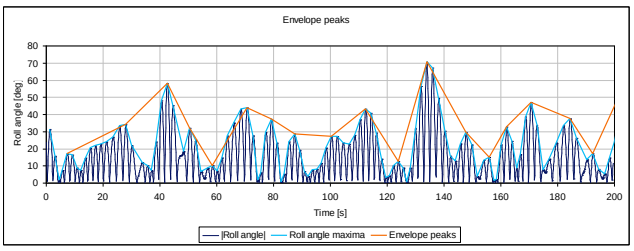

Figure 3-1 : Envelope peaks

Once the envelope peaks have been determined for all the individual FREDYN simulations, these can be combined into one data set and sorted in ascending order. Using

this set of sample data, the probability of a randomly selected envelope peak being larger than the amplitude of a particular sample can be directly determined. In the majority of cases there will be insufficient data to extrapolate to the actual angle of loss, so a suitable distribution needs to be fitted to the data. The Gumbel distribution represents the distribution of maxima well if the underlying sample data are normal. Experience has shown that using a selection of the highest envelope peaks alone for the distribution fitting gives the most reliable results, as the Gumbel distribution is not appropriate for the distribution of lower roll angles. Having defined the Gumbel distribution, the probability of an envelope peak exceeding the angle of loss can be calculated, however this gives only the per-peak probability of loss. To provide meaningful statistics this is then extrapolated to give a per-hour probability of loss. In order to reduce the calculated data to a more manageable size, the likelihood of encountering waves can be incorporated to weight the overall probability of capsize by using the wave statistics from a wave scatter table or equivalent. In a similar fashion to the wave probability weighting, it is possible to determine the probability for each speed (17kts) or heading (001-179 degs). The final hourly capsize risk can be calculated using the combined speed and heading probability. The annual probability of loss can then be calculated in a similar manner to the extrapolation from a per-envelope-peak risk of loss to the annual probability of loss. This methodology is further detailed in Ypma 2013. The CRN working group created a new tool, LORELEI, to apply this EPOT methodology to simulated non-linear roll response.

The FREDYN data was analysed by this envelope peaks over threshold (EPOT) method to evaluate the probability of loss of each speed, heading and wave case to produce an overall probability of loss of the vessel.

4. RESULTS

The following probability of loss results are presented for each vessel, with comparison against a number of intact stability criteria's and ship particulars (LBP, L/B ratio and L/Disp. ratio). Table 4-1 shows each vessel designation and a description of the geometric change for that vessel while Table 4-2 shows the probabilities of loss for each vessel.

Table 4-1: Vessel designation and geometric description

Vessel designation	Geometric description
A	Baseline hullform (LBP 105m)
B	Length decrease (95m)
C	Length increase (115m)
D	Beam and length decrease (L/B ratio remains constant to base hullform)
E	Beam and length increase (L/B ratio remains constant to base hullform)
F	Displacement and length decrease (L/Disp. Ration remains constant to base hull form)
G	Displacement and length increase (L/Disp. Ration remains constant to base hull form)

Table 4-2: Vessel probability of loss value

Vessel	No. of Simulations	Probability of Loss
A	11790	0.0004395
B	12328	0.0007425
C	11360	0.0001278
D	12028	0.0009048
E	11320	0.0002284
F	12100	0.0004978
G	11150	0.0002152

All vessels modelled within this study were set with an area under the GZ curve to 70 degrees of 0.585m/rads. All cases passed both the NSC static stability criteria of a minimum area of 0.38m/rads and the CRN derived tolerable risk boundary point of $3x10^{-3}$. Even with the significant geometry changes all vessels had a lower probability of loss, highlighting that the comparison between the NSC GZ area criteria and the probability of loss performance of a vessel in a dynamic environment remains good for this type of vessel.

4.1 PCAP comparison to area under the GZ curve to 70 degrees

The first plot, Figure 4-1 compares the Probability of Loss value for each vessel against its area under the GZ curve to 70 degrees. Although all vessels have the same area under the curve, it is felt that this plot shows the performance range of each geometry change based on the same static stability parameters.

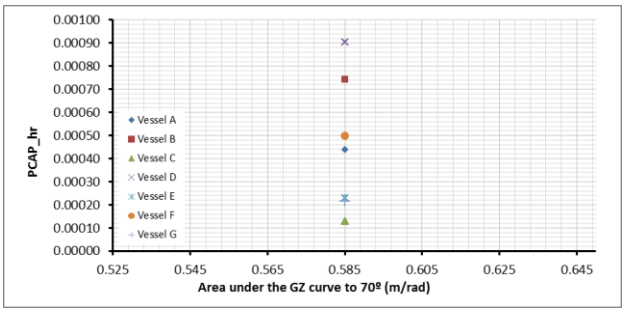

Figure 4-1: PCAP vs. Area under GZ curve to 70 degrees

It is very clear from Figure 4-1 that vessel A (baseline) is in the middle of the data point range and that an increase in vessel length only, exhibits an improved probability of loss

performance, a decrease in vessel length slightly increases the probability of loss. Vessel's D and E are the length and beam combination geometry changes, where vessel D shows the highest probability of loss. With vessel E's increase in length and beam compared to D, it shows an improved probability of loss. Vessel C with the length increase only, still shows the better probability of loss performance which could be due to the wider beam and transom inducing more surf riding and broaching behavior. Investigation is underway to identify if there is increased surfriding seen in the simulations.

Both vessel's F and G (displacement and Length changes) show a similar trend, a higher probability of loss for the length and displacement decrease and a lower Probability of loss for the length and displacement increase from vessel A. However, Figure 4-1 shows that vessel F has a closer probability of Loss performance to vessel A rather than vessel's B and D, which may suggest that a small displacement change at shorter vessel lengths has a larger effect on vessel performance, due to the reduction in probability of Loss. Vessel G has a very similar performance to vessel E with a lower probability of loss than the baseline vessel, both of which are increases in vessel length compared to the baseline.

4.2 PCAP comparison to vessel particulars

Figure 4-2, Figure 4-3 and Figure 4-4 show a comparison of the probability of loss of each vessel against LBP, L/B ratio and L/Disp. ratio.

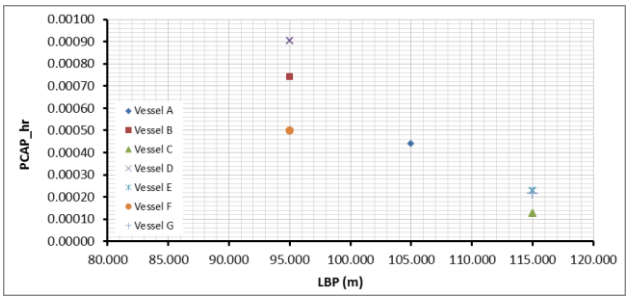

Figure 4-2: PCAP vs. LBP

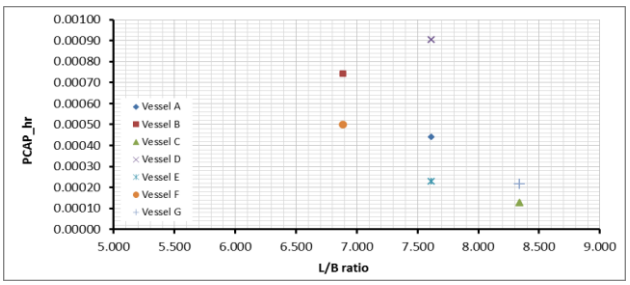

Figure 4-3: PCAP vs. L/B ratio

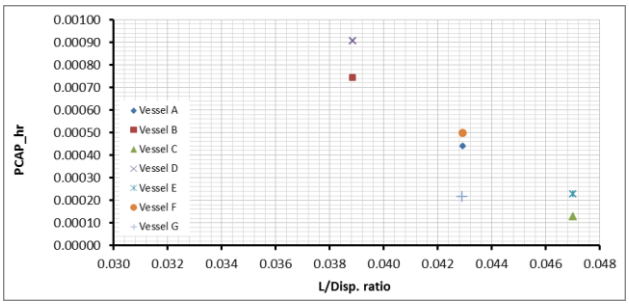

Figure 4-4: PCAP vs. L/Disp. ratio

From all three of these plots it's clear that there appears a trend between the results vessel A, B and C. Although a limited data set, this indicates that if the vessel's area under the curve remains constant then a longer more slender ship would have a better dynamic stability performance based on the results of probability of loss (probability of exceeding 70 degrees roll).

The same trends are also seen throughout these plots for the remaining vessels and that the decrease in beam along with a decrease in

length produce the highest probability of loss results. With the current data set it is currently unclear if the length and beam changes show the same trend. A suggestion for further study would be to have multiple changes of beam on vessel's A, B and C. It is also shown that a small change in beam for the shorter vessel length has a greater effect on probability of loss than just a greater length change.

5. CONCLUSIONS

It has been shown that following this methodology and using a suitable time-domain code that the dynamic stability performance of a vessel due to geometric variations can be evaluated while keeping area under GZ to 70 degrees constant. With any geometry modification to a ship the stability characteristics may differ from the original design. However, for this study the aim was to understand the effects of systematic geometry changes have on the performance of a vessel in a dynamic environment by the measure of its probability of loss in a seaway. This was done by making systematic geometric variations while maintaining the static stability characteristics of the area under the GZ curve to 70 degrees for each vessel.

Overall the study has shown that even with the same stability characteristics between vessels, once subjected to a dynamic stability assessment there are differences in dynamic performance due to the geometric differences as demonstrated by the probability of loss values. However, all probability of loss values are within the same order of magnitude of 10^{-4}, the level of risk between the geometric changes are seen to change by multiple times, but these numbers are very small. So it may be concluded that although significant geometric changes have been applied, the performance difference may not be classed as significant in terms of the probability of loss measure when the GZ area remains constant. It is acknowledged that the EPOT methodology has been further developed for assessing probability of vessel loss during this study, Campbell, et al (2016) and Smith and Zuzick (2105) with the application of Generalized Pareto Distribution (GPD) and statistical validation of the EPOT method. The effect of these changes should be investigated in future but initial expectations are the performance comparison between these hullform variants would remain.

6. ACKNOWLEDGEMENTS

The authors would like to gratefully acknowledge the permission granted by QinetiQ, UK MoD and CRN Navies for allowing the publication of the findings from the investigation.

7. REFERENCES

Bales, S. L, Lee W.T and Voelker J.M, Standardised wind and wave environments for NATO operational areas, DTNSRDC Report SPD-0919-01.

Campbell, B, and Belenky, V, 2010,"Assessment of Short Term Risk with Monte-Carlo Simulation", 11th International Ship Stability Workshop Proceedings.

Campbell, B., Belenky, and Pipiras, V., 2016 "Application of the Envelope Peaks over Threshold (EPOT) Method for Probabilistic Assessment of Dynamic Stability, in Ocean Engineering, Vol. 120, pp. 298-304

De Kat, J.O., Peters A.J., 2002, "Damage Stability of Frigate Sized Ships", International Maritime Association of the Mediterranean Conference, Crete.

Ewing, J., 1974, Some results from the Joint North Sea Wave Project of interest to engineers, First international symposium on the dynamics of marine vehicles in waves, IMechE.

Harmsen, E.,2012 "Intact Risk assessment Phase 3 – Regression and criterion proposal", DMO Report to NSSWG.

Hasselmann K. et al., 1973, "Measurements of wind-wave growth and swell decay during the Joint North Sea Wave Project (JONSWAP)". Ergnzungsheft zur Deutschen Hydrographischen Zeitschrift ReiheA(8) (Nr. 12): 95

Marin, FREDYN.,2011 – "A computer program for the simulation of a steered ship in extreme seas and wind", User's Manual Version 10.3, Part I – Intact Hull.

Peters A, Walby, T, and Wing, D., 2010, "Dynamic stability and safety criteria Phase 3", QinetiQ/10/01921, A, UK RESTRICTED, QinetiQ Proprietary.

Peters, A.,2010 "Tolerable Capsize Risk of a Naval Vessel", Proceedings of the 11th International Ship Stability Workshop.

Sarchin, T.H. and Goldberg, L.L., 1962 Stability and Buoyancy Criteria for US Naval Surface Ships, Transactions SNAME.

Smith, T. and Zuzick, A., 2015, "Validation of Statistical Extrapolation Methods for Large Motion Prediction," Proc. 12th Intl. Conf. on Stability of Ships and Ocean Vehicles, Glasgow, UK.

United Kingdom Defence Standard 02-900, 2013, General Naval Standard Part 1: Ship Safety & Environmental Protection, Issue 1

United Kingdom Maritime Acquisition,2010 Publication No 01-024, Stability of Surface Ships Part 1 Conventional Ships, Issue 4.

Ypma, E.,2011 Capsize Risk Analysis, PCap2011 Tool Design, MARIN.

Ypma, E, LORELEI., 2013 Capsize Risk Analysis application, User Manual for version 2.0.0, MARIN.

Non-Gaussian PDF of ship roll motion in irregular beam sea and wind conditions

-Comparison between theory and experiment-

Atsuo, MAKI, *Osaka University* maki@naoe.eng.osaka-u.ac.jp

Naoya, UMEDA, *Osaka University* umeda@naoe.eng.osaka-u.ac.jp

Akihiko, MATSUDA, *NRIFE* amatsuda@fra.affrc.go.jp

Hiroki, YOSHIZUMI, *Osaka University* hiroki_yoshizumi@naoe.eng.osaka-u.ac.jp

ABSTRACT

Ship transverse stability in beam seas has long been a significant concern to naval architects. Estimating roll motion remains important for practical risk assessments. However, this problem is not simple, due to the nonlinear equations of motion. A theoretical method for estimating the roll response and capsizing probability has been proposed, but this method has only been correlated by Monte Carlo simulations. Therefore, in this study, model experiments for a subject ship, which exhibited a strong nonlinearity exhibited in the GZ curve, were conducted at National Research Institute of Fisheries Engineering. The results from this study correlated the proposed theory.

Keywords: *Beam seas, Non-Gaussian probability density function, Capsizing probability*

1. INTRODUCTION

Ship transverse stability in beam seas has long been a significant concern to naval architects. Estimating roll motion remains an important theme for practical risk assessment. Although much research has been conducted in this field, theoretical assessments of roll behavior in random beam seas remains difficult due to the nonlinear components in the ship roll equation. A key characteristic of roll motion is that the restoring moment has zero crossing at the angle of vanishing stability, which limits theoretical predictions. Thus far, some methods have been presented to address this (e.g., Umeda et al., 1991 or Belenky, 1993). For instance, Belenky (1993) applied the piecewise linear approach whereby the restoring curve is first piecewise linearized, and the analytical solution is then obtained in each segment. Then, the capsizing probability was calculated. Paroka et al. (2006) and Maeda et al. (2012) validated this theory experimentally. Maki (2013 and 2017) proposed a method for calculating ship motion and capsizing probability using a non-Gaussian probability density function (PDF). Kougioumtzoglou and Spanos (2015) and Chai and Naess (2015) reported results for a vessel rolling in irregular seas using the path integration (PI) method and found a good correlation with Monte Carlo simulation (MCS) results. Recently, a comparison of the stochastic averaging (Dostal, 2012) and PI methods was presented (Chai et al., 2017).

As stated, Maki proposed a method for calculating the PDF of roll response following Kimura (1998). These results produced were in good agreement with MCS results from

previous work. This procedure had been extended to include the estimation of the capsizing probability (Maki, 2017), and the capsizing probability for the linear damping coefficient case was strongly correlated with the MCS results. However, this method had not been tested experimentally. Therefore, in this study, model experiments using hypothetical ship CEHIPAR2792 (Gabriele et al., 2010) with almost sinusoidal characteristics in the GZ curve were conducted at the National Research Institute of Fisheries Engineering (NRIFE). These results were compared with theoretical predictions from the current method and correlated that this method is capable of predicting the roll behavior to some extent despite the presence of nonlinear restoring terms. Furthermore, the authors newly proposed the non-Gaussian PDF in which the nonlinear damping term is explicitly taken into account (Maki et al., 2018), and its results are correlated with the experimental results.

2. FORMULATION

2.1 Equation of motion

The authors first outline the theory used in this study. The original method was applicable for irregular waves with a steady wind condition (Maki, 2013 and 2017). In this study, it is extended to include irregular beam wind and wave situations.

The one degree of freedom (DoF) roll equation for motion in irregular beam seas and wind is generally given as

$$\begin{aligned}&\ddot{\phi}+\alpha\dot{\phi}+\beta\dot{\phi}\left|\dot{\phi}\right| \\ &+\frac{W}{I_{xx}}\left(GM\,\phi+GZ_3\phi^3+GZ_5\phi^5\right) \\ &=M_{wind}(t)+M_{wave}(t)\end{aligned} \tag{1}$$

where t: time, ϕ: ship roll angle, α: linear damping coefficient, β: quadratic damping coefficient, W: ship weight, I_{xx}: moment of inertia in roll (including added moment of inertia), GM: metacentric height, GZ_i: ith component of GZ polynomial fit, M_{wave} (t): time-dependent roll moment induced by wind (normalized by I_{xx}), and M_{wind} (t): time-dependent roll moment induced by irregular waves (normalized by I_{xx}). In this study, the overdot denotes the differentiation with respect to time t.

The equation for wind moment is given as

$$M_{wind}(t)=\frac{1}{2I_{xx}}\rho_{air}C_mA_LH_C\left(U_w+U(t)\right)^2 \tag{2}$$

where ρ_{air}: air density, U_w: mean wind velocity, $U(t)$: time-varying wind velocity, C_m: drag coefficient of wind pressure, A_L: hull side area, and H_C: height of the center of the wind force from the center of hydrodynamic reaction force. Here the higher-order term of the time-varying component, $U^2(t)$, is neglected and given as

$$\left(U_w+U(t)\right)^2\approx U_w^2+2\,U_w\cdot U(t) \tag{3}$$

Then, Eq. (2) can be linearized as follows:

$$M_{wind}(t)\approx M_{winds}+M_{windv}(t) \tag{4}$$

where

$$\begin{cases}M_{winds}\equiv\dfrac{1}{2I_{xx}}\rho_{air}C_mA_LH_CU_w^2 \\ M_{windv}(t)\equiv\dfrac{1}{I_{xx}}\rho_{air}C_mA_LH_CU_w\cdot U(t)\end{cases} \tag{5}$$

The wind velocity is modeled with the Davenport spectrum and is given as

$$S_{wind}=4K\frac{U_w^2}{\omega}\frac{X_D^2}{\left(1+X_D^2\right)^{4/3}} \tag{6}$$

where K and X_D are defined as

$$\begin{cases} K = 0.003 \\ X_D = 600\dfrac{\omega}{\pi U_w} \end{cases} \tag{7}$$

The time-varying wind velocity can be estimated using the following equation:

$$U(t) = \sum\nolimits_{N_{wind}} \Delta S_{wind} \cos\left(\omega_i t + \varepsilon_i\right) \tag{8}$$

where

$$\Delta S_{wind} \equiv \sqrt{2 S_{wind}\, \Delta\omega_{wind}} \tag{9}$$

Due to the steady component of wind moment, the heel inclination ϕ_b was induced, and this angle can be calculated by solving the following algebraic equation

$$\begin{aligned} &\frac{W}{I_{xx}}\left(GM\,\phi_b + GZ_3\,\phi_b^3 + GZ_5\,\phi_b^5\right) \\ &-M_{winds} = 0 \end{aligned} \tag{10}$$

Following this, the origin of roll is shifted, and newly defined ϕ has the origin at the shifted position (ϕ -ϕ_b is redefined as ϕ). The roll motion around the shifted equilibrium point can then be represented by the following equation:

$$\begin{aligned} &\ddot{\phi} + \alpha\dot{\phi} + \beta\dot{\phi}\left|\dot{\phi}\right| + \frac{W}{I_{xx}}\left(GM'\phi + GZ_2'\phi^2\right. \\ &\left. + GZ_3'\phi^3 + GZ_4'\phi^4 + GZ_5'\phi^5\right) \\ &= M_{windv}(t) + M_{wave}(t) \end{aligned} \tag{11}$$

where the restoring coefficients with apostrophes, e.g., *GM'*, indicate the restoring coefficients for the shifted equation of motion due to steady wind conditions. The roll moment due to irregular waves is then calculated by using the effective wave slope coefficient γ, and wave slope $\Theta(t)$, given as

$$M_{wave}(t) = \frac{W \cdot GM'}{I_{xx}}\gamma\,\Theta(t) \tag{12}$$

where wave slope is calculated for a given spectrum using the following equation:

$$\Theta(t) = \sum\nolimits_n \frac{\omega_n^2}{g}\Delta S_{wave}\cos\left(\omega_n + \varepsilon_n\right) \tag{13}$$

where

$$\Delta S_{wave} \equiv \sqrt{2 S_{wave}\left(\omega_n\right)\Delta\omega_{wave}} \tag{14}$$

Then, the equation of motion used in this study is derived as

$$\begin{aligned} &\ddot{\phi} + \alpha\dot{\phi} + \beta\dot{\phi}\left|\dot{\phi}\right| + \omega_0^2\left(\phi + \frac{GZ_2'}{GM'}\phi^2\right. \\ &\left. + \frac{GZ_3'}{GM'}\phi^3 + \frac{GZ_4'}{GM'}\phi^4 + \frac{GZ_5'}{GM'}\phi^5\right) \\ &= \sum\nolimits_{N_{wave}} \frac{\gamma\,\omega_0^2\omega_n^2}{g}\Delta S_{wave}\cos\left(\omega_n + \varepsilon_n\right) \\ &+ \frac{\rho_{air} C_m A_L H_C U_w}{I_{xx}} \\ &\times \sum\nolimits_{N_{wind}} \Delta S_{wind}\cos\left(\omega_i t + \varepsilon_i\right) \end{aligned} \tag{15}$$

In this study, the ITTC (International Towing Tank Conference) spectrum (Eq. 16) is applied and given as

$$\begin{aligned} S_{wave}(\omega) &= 0.11\frac{(2\pi)^4 H_{1/3}^2}{T_{01}^4\omega^5} \\ &\times\exp\left[-0.44\frac{(2\pi)^4}{T_{01}^4\omega^4}\right] \end{aligned} \tag{16}$$

In Eq. 16, the coefficients are defined as

$$\begin{cases} G_1 \equiv \omega_0^2 \\ G_i \equiv \omega_0^2 GZ'/GM_i' \;(i > 2) \end{cases} \tag{17}$$

$$\begin{cases} a_n \equiv \dfrac{\gamma \omega_0^2 \omega_n^2}{g} \Delta S_{wave} \\ b_n \equiv \dfrac{\rho_{air} C_m A_L H_C U_w}{I_{xx}} \Delta S_{wind} \end{cases} \tag{18}$$

Finally, the following equation is obtained:

$$\begin{aligned} &\ddot{\phi} + \alpha \dot{\phi} + \beta \dot{\phi} \left| \dot{\phi} \right| \\ &+ G_1 \phi + G_2 \phi^2 + G_3 \phi^3 + G_4 \phi^4 + G_5 \phi^5 \\ &= \sum\nolimits_{N_{wave}} a_n \cos\left(\omega_n t + \varepsilon_n\right) \\ &+ \sum\nolimits_{N_{wind}} b_n \cos\left(\omega_n t + \varepsilon_n\right) \end{aligned} \tag{19}$$

2.2 Non-Gaussian distribution

To obtain the roll response for Eq. (19), the following equivalent linearization procedure is applied (e.g., Caughey, 1963 [2]). Initially, the equivalent linearized equation of motion is given as (Sakata et al., 1979) (Sakata et al., 1980) (Kimura et al., 1998)

$$\ddot{\phi} + \alpha_e \dot{\phi} + g_e \left(\phi - \phi_e\right) = f\left(t\right), \tag{20}$$

where α_e: equivalent damping coefficient, g_e: equivalent linear stiffness and a_e: equivalent shift of the restoring force defined as

$$a_e \equiv g_e \phi_e, \tag{21}$$

The equivalent forcing function can now be defined as

$$f_e\left(t\right) = f\left(t\right) + a_e, \tag{22}$$

From this, the following equation is obtained:

$$\ddot{\phi} + \alpha_e \dot{\phi} + g_e \phi = f_e\left(t\right) \tag{23}$$

To estimate the unknown coefficients g_e and a_e, the error function is defined as

$$\begin{aligned} w \equiv &\left(\alpha_e \dot{\phi} + g_e \phi\right) - \left(\alpha \dot{\phi} + \beta \dot{\phi} \left| \dot{\phi} \right| \right. \\ &\left. + G_1 \phi + G_2 \phi^2 + G_3 \phi^3 + G_4 \phi^4 + G_5 \phi^5 \right) \end{aligned} \tag{24}$$

The minimum condition of $E[w]$ in terms of the least square fit is finally given as

$$\begin{aligned} \alpha_e &= \alpha + \beta \frac{\mathrm{E}\left[\dot{\phi}^2 \left| \dot{\phi} \right| \right]}{\mathrm{E}\left[\dot{\phi}^2\right]} \\ a_e &= \left(\mathrm{E}[\phi] \sum\nolimits_{n=2}^{5} G_n \mathrm{E}\left[\phi^{n+1}\right] \right. \\ &\quad \left. - \mathrm{E}\left[\phi^2\right] \sum\nolimits_{n=2}^{5} G_n \mathrm{E}\left[\phi^n\right] \right) \\ &\quad / \left\{ \mathrm{E}\left[\phi^2\right] - \left(\mathrm{E}[\phi]\right)^2 \right\} \\ g_e &= G_1 + \left(\sum\nolimits_{n=2}^{5} G_n \mathrm{E}\left[\phi^{n+1}\right] \right. \\ &\quad \left. - \mathrm{E}[\phi] \sum\nolimits_{n=2}^{5} G_n \mathrm{E}\left[\phi^n\right] \right) \\ &\quad / \left\{ \mathrm{E}\left[\phi^2\right] - \left(\mathrm{E}[\phi]\right)^2 \right\} \end{aligned} \tag{25}$$

where E denotes the expected value. The first equation in (Eq. 25) simply represents the well-known equivalent damping expression.

The expectations in Eq. (25) can be obtained by solving following a differential equation concerning with the expectations (Sakata et al. 1979), which is given as

$$\begin{cases} \dot{\mathrm{E}}[\phi] = \mathrm{E}\left[\dot{\phi}\right] \\ \dot{\mathrm{E}}\left[\dot{\phi}\right] = -\alpha_e \mathrm{E}\left[\dot{\phi}\right] - g_e \mathrm{E}[\phi] + \mathrm{E}\left[f_e\right] \\ \dot{\mathrm{E}}\left[\phi^2\right] = 2\,\mathrm{E}\left[\phi \dot{\phi}\right] \\ \dot{\mathrm{E}}\left[\phi \dot{\phi}\right] = \mathrm{E}\left[\dot{\phi}^2\right] - \alpha_e \mathrm{E}\left[\dot{\phi}\right] - g_e \mathrm{E}\left[\phi^2\right] \\ \qquad + \mathrm{E}\left[\phi f_e\right] \\ \dot{\mathrm{E}}\left[\dot{\phi}^2\right] = -2\alpha_e \mathrm{E}\left[\dot{\phi}^2\right] - 2 g_e \mathrm{E}\left[\phi \dot{\phi}\right] \\ \qquad + \mathrm{E}\left[\dot{\phi} f_e\right] \end{cases} \tag{26}$$

In the case of stationary condition, the above differential equation becomes the simultaneous equation be solved:

$$\begin{aligned} -g_e \mathrm{E}[\phi] + a_e &= 0 \\ \mathrm{E}[\dot{\phi}^2] - g_e \mathrm{E}[\phi^2] + \mathrm{E}[\phi f] + a_e \mathrm{E}[\phi] &= 0 \\ -2\alpha_e \mathrm{E}[\dot{\phi}^2] + \mathrm{E}[\dot{\phi} f] &= 0 \end{aligned} \tag{27}$$

where $\mathrm{E}[\phi f]$ and $\mathrm{E}[\dot{\phi} f]$ are calculated using the following equations:

$$\begin{aligned} \mathrm{E}[\phi f] &= \int_0^\infty H_{12}(k) R(k) dk \\ \mathrm{E}[\dot{\phi} f] &= \int_0^\infty H_{22}(k) R(k) dk \end{aligned} \tag{28}$$

Furthermore, the following condition is also obtained in stationary condition.

$$\mathrm{E}[\dot{\phi}] = 0 \quad \text{and} \quad \mathrm{E}[\phi\dot{\phi}] = 0 \tag{29}$$

In Equation (29), H_{12} and H_{22} are the components of the impulse response function **H** given in Eq. (23).

$$\mathbf{H} = \begin{bmatrix} H_{11} & H_{12} \\ H_{21} & H_{22} \end{bmatrix} \tag{30}$$

Each component, H_{ij} (i, j=1, 2), has following form:

$$\begin{aligned} H_{11} &= e^{-\alpha_e t/2}\left(\frac{\alpha_e}{2\omega_h}\sin\omega_h t + \cos\omega_h t\right) \\ H_{12} &= \frac{e^{-\alpha_e t/2}}{2\omega_h}\sin\omega_h t \\ H_{21} &= \frac{e^{-\alpha_e t/2} g_e}{2\omega_h}\sin\omega_h t \\ H_{22} &= e^{-\alpha_e t/2}\left(\cos\omega_h t - \frac{\alpha_e}{2\omega_h}\sin\omega_h t\right) \end{aligned} \tag{31}$$

where ω_h is defined as

$$\omega_h = \sqrt{g_e - \alpha_e^2/4} \tag{32}$$

Furthermore, $R(k)$ in Eq. (28) represents the autocorrelation function concerned with the external force $f(t)$. Assuming that the wind and wave moments are not correlated, and using simple analytical integration, Eq. (28) can be given as

$$\begin{aligned} &\int_0^\infty H_{12}(k) R(k) dk \\ &= \sum\nolimits_{N_{wave}} \frac{a_n^2\left(\alpha_e^2/4 + \omega_h^2 - \omega^2\right)}{\left(\alpha_e^2/4 + \omega_h^2 + \omega^2\right)^2 - 4\omega_h^2\omega^2} \\ &+ \sum\nolimits_{N_{wind}} \frac{b_n^2\left(\alpha_e^2/4 + \omega_h^2 - \omega^2\right)}{\left(\alpha_e^2/4 + \omega_h^2 + \omega^2\right)^2 - 4\omega_h^2\omega^2} \end{aligned} \tag{33}$$

$$\begin{aligned} &\int_0^\infty H_{22}(k) R(k) dk \\ &= \sum\nolimits_{N_{wave}} \frac{\alpha_e a_n^2 \omega^2}{\left(\alpha_e^2/4 + \omega_h^2 + \omega^2\right)^2 - 4\omega_h^2\omega^2} \\ &+ \sum\nolimits_{N_{wind}} \frac{\alpha_e b_n^2 \omega^2}{\left(\alpha_e^2/4 + \omega_h^2 + \omega^2\right)^2 - 4\omega_h^2\omega^2} \end{aligned} \tag{34}$$

Once $\mathrm{E}[\phi f]$ and $\mathrm{E}[\dot{\phi} f]$ have been evaluated, Eq. (27) can be solved by numerical iteration, such as the Newton method. Although some moment properties can be evaluated, the shape of the distribution remains unknown. The Gaussian distribution is not applicable for this problem, since the restoring components have strong nonlinearity. Kimura et al. (1998) introduced the non-Gaussian distribution to overcome this, which is given as

$$p_\phi(\phi; d) = C \exp\left[-d\int_0^\phi GZ(\xi) d\xi\right] \tag{35}$$

where $GZ(\phi)$ is defined as

$$GZ(\phi) \equiv \sum_{n=1}^{5} G_n \phi^n \tag{36}$$

If the external force has a white noise spectrum, this result is rigorously equal to the analytical solution of the Fokker–Planck equation (Caughey, 1963 [1]).

The two unknown parameters, C and d, in Eq. (35) can be determined from the following condition:

$$\begin{cases} \int_{\phi_{VN}}^{\phi_{VP}} p_{\phi}(\phi;d)\,d\phi = 1 \\ \int_{\phi_{VN}}^{\phi_{VP}} \phi^2 p_{\phi}(\phi;d)\,d\phi = \mathrm{E}\left[\phi^2\right] \end{cases} \tag{37}$$

where ϕ_{VP} and ϕ_{VN} indicate the two vanishing angles of the restoring moment. Now, we assume that the roll rate is normally distributed, given as

$$p_{\dot{\phi}}(\dot{\phi}) = \frac{1}{2\pi E\left[\dot{\phi}^2\right]} \exp\left(-\frac{\dot{\phi}^2}{2E\left[\dot{\phi}^2\right]}\right) \tag{38}$$

The joint PDF can then be given as

$$p_1(\phi,\dot{\phi}) = p_{\dot{\phi}}(\dot{\phi}) \cdot p_{\phi}(\phi;d) \tag{39}$$

Following Maki (2017), the exceedance probability and the capsizing probability can be estimated once the distribution is fully obtained (a detailed explanation for this is omitted here).

3. EXPERIMENTAL VALIDATION

In this study, an experiment was conducted at NRIFE to test the proposed theory. CEHIPAR2792 (Gabriele et al, 2010) was the subject ship, and its key properties are listed in Table 1. The restoring curve and its fifth-order polynomial fit are also plotted in Fig. 2. The fitting equation for the GZ curve is given as

$$GZ(\phi) = 1.308\phi - 1.734\phi^3 + 0.08601\phi^5 \tag{40}$$

Table 1 Key properties of CEHIPAR2792

Items	*Values*
Ship weight: W	23,993 *ton*
Natural roll period: T_{ϕ}	20.42 *s*
Effective wave slope: γ	0.8998
Metacentric height: GM	2.014 *m*
Roll damping coefficient: α	0.02008
Roll damping coefficient: β	0.4505
Drag coefficient: C_m	1.000
Hull side area: A_L	6631 m^2
Height of the center of the wind pressure: H_C	15.72 *m*

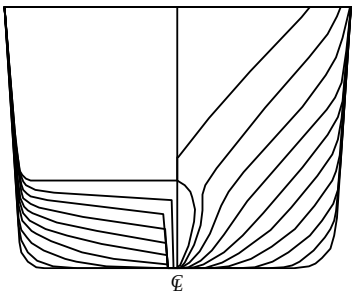

Figure 1 Body plan of the subject ship.

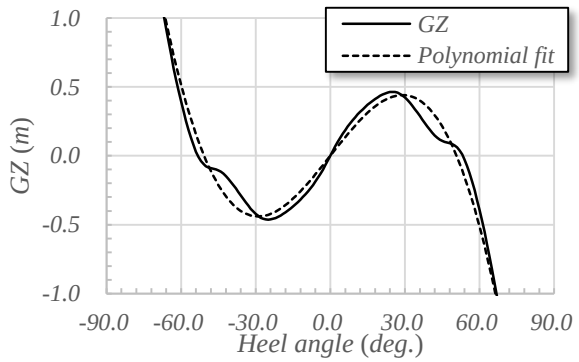

Figure 2 Restoring curve and the associated polynomial fit.

Free-roll experiments were conducted at NRIFE to obtain the damping coefficients. The obtained extinction curve is shown in Fig. 3, which was fitted with quadratic and linear damping coefficients given as

$$\Delta\phi = 0.02500\,\phi_m + 0.01048\,\phi_m^2 \tag{41}$$

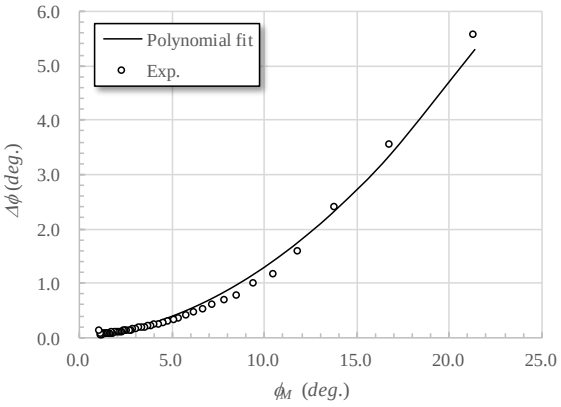

Figure 3 Extinction curve and the associated polynomial fit.

Before considering the probabilistic results, the validation results from the one DoF motion equation in regular beam sea conditions are presented. The theoretical results based on the averaging method were obtained to achieve this. In regular wave conditions, the equation of motion is given as

$$\begin{aligned}&\ddot{\phi} + \alpha\dot{\phi} + \gamma\dot{\phi}^3 \\ &+c_1\phi + c_3\phi^3 + c_5\phi^5 = B\cos\,\omega t\end{aligned} \tag{42}$$

where the parameters c_1, c_i and B are defined as

$$\begin{cases} c_1 = \dfrac{W\cdot GM}{I_{xx}} \\ c_i = \dfrac{W\cdot GZ_i}{I_{xx}}\ (i = 3 \text{ and } 5) \\ B = \pi\,\omega_0^2\gamma\,k\,\zeta_a \end{cases} \tag{43}$$

In Eq. 42, the phase term for the external wave moment is omitted for brevity.

Since the theoretical analysis uses an averaging technique here, it is difficult to use the absolute function in the roll damping expression. Therefore, the damping term can be replaced by a cubic polynomial expression for the damping curve, which is given as

$$\Delta\phi = 0.05696\,\phi_m + 0.0004720\,\phi_m^3 \tag{44}$$

According to Fig. 4, the cubic polynomial fit functions well, and there is not a large discrepancy between the quadratic and cubic expression.

To apply the averaging method, a small value parameter ε was introduced to Eq. (42), and the following equation was obtained:

$$\begin{cases} \dot{\phi} = p \\ \dot{p} = -\omega^2\phi + \\ \quad +\varepsilon\left[-\alpha\,p - \gamma\,p^3 - \left(c_1 + \omega^2\right)\phi\right. \\ \quad \left. -c_3\,\phi^3 - c_5\,\phi^5 + B\cos\,\omega t\right] \end{cases} \tag{45}$$

The following solution is now assumed:

$$\begin{cases} \phi = A\cos\left(\omega t + \psi\right) \\ \dot{\phi} = -A\omega\sin\left(\omega t + \psi\right) \end{cases} \tag{46}$$

The newly-introduced parameters, A and ε, are slowly varying functions with respect to time t. By substituting in the terms from Eq. (46) and averaging in one roll period, differential equations for the averaged system were finally obtained and given as

$$\begin{cases} \dot{A} = -\varepsilon\left(\nu\dfrac{A}{2} + \beta\dfrac{3A^3}{8} + B\dfrac{\sin\psi}{2\omega}\right) \\ \dot{\psi} = \varepsilon\left(c_1\dfrac{1}{2\omega} + c_3\dfrac{3A^2}{8\omega} + c_5\dfrac{5A^4}{16\omega}\right. \\ \quad \left. -\dfrac{\omega}{2} - B\dfrac{\cos\psi}{2A\omega}\right) \end{cases} \tag{47}$$

If the sole interest now is the stationary solution of Eq. (47), then the following condition must be considered:

$$\begin{cases} \dot{A} = 0 \\ \dot{\psi} = 0 \end{cases} \tag{48}$$

This becomes a fifth-order polynomial equation with respect to A^2, which enables numerical methods, such as Bairstow's method, to be applied.

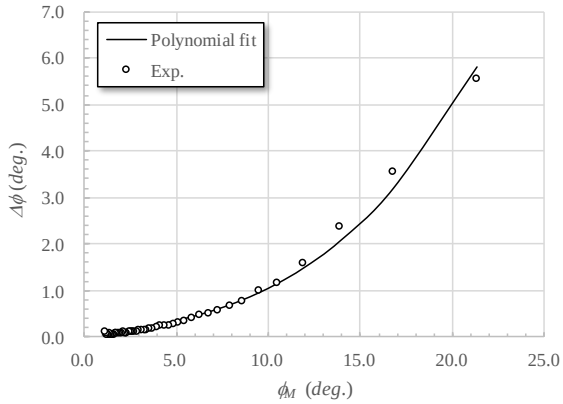

Figure 4 Damping curve and the associated polynomial fit.

Figures 5-7 compare the experimental and theoretical roll response results. Notably, the folding behavior of the response amplitude was clearly observed in the theoretical results and the experimental results. These results can be found in Francescutto et al. (1994). Even for wave steepness values of 0.01, that is small wave height, the nonlinearity of the response curve was observed due to the soft spring characteristics in the restoring curve. The theoretical results qualitatively agree with the experimental results. However, there are non-negligible discrepancies between the experiments and the theoretical results, which could be due to two limitations: first, the limitation of the one DoF roll motion equation. Obviously, roll, sway, and yaw modes are typically coupled, but this is ignored here for theoretical purposes. Second, and importantly, the experimental method may be another limitation. The bow and stern were softly moored by wires to maintain the zero yaw angle in our beam sea experiments conducted at NRIFE. However, the wire might affect the roll motion like a spring, which may particularly affect the low-frequency region. Further investigations and improving the experimental methods are required and will be the subject of our future work.

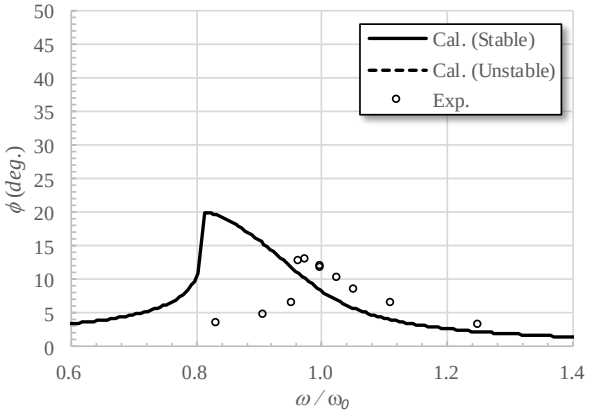

Figure 5 Roll response curve where H/λ=0.01.

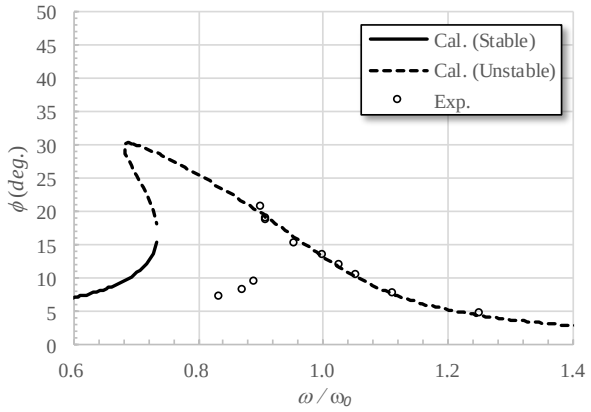

Figure 6 Roll response curve where H/λ=0.02.

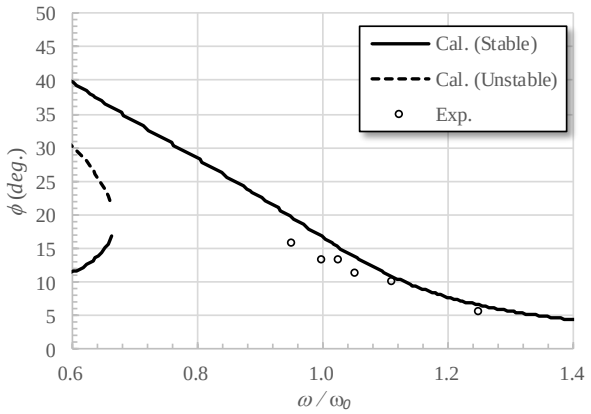

Figure 7 Roll response curve where H/λ=0.03.

From the above regular wave results using the nominal averaging method, the one DoF roll motion model was partly validated in regular beam sea conditions. Therefore, the discussion is advanced to the main topic, which is the irregular condition case. The proposed

theory shown in the previous section is now utilized for estimating the response in irregular beam sea conditions.

Initially, we compared the roll PDF between experimental results and theoretical calculations (Fig. 8). Wind was not generated in these, and only the irregular beam wave was considered. Because of the limitation of the one DoF model, MCSs show a slight discrepancy in the roll estimation. However, a qualitative agreement was achieved from a practical view. As for the theoretical results, the results obtained from the proposed method and the linear method are shown in Fig. 8. The theoretical results and MCSs do not fully agree. In particular, the PDF takes a larger value for large roll angles in the proposed method. Therefore, it is considered that the proposed method may underestimate the damping.

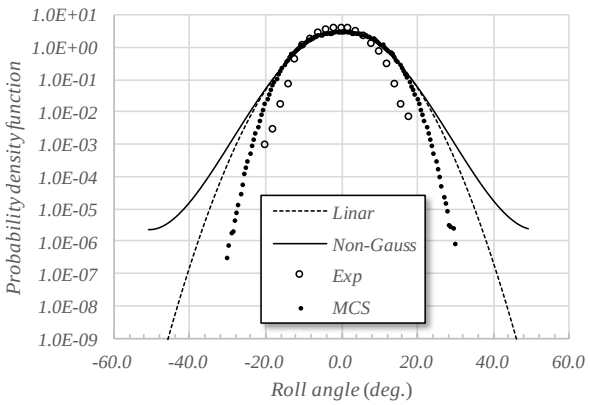

Figure 8 Comparison of the roll PDF measured in experiments and predicted by theory where T_{01}=20.83s and $H_{1/3}$=19.67 m.

Next, the results in the irregular beam wind and waves condition are shown. The steady heel moment acts on the hull in irregular wind conditions as shown in the first line in Eq. (5). The experimental measurements of heel angle as a function of wind velocity are shown in Fig. 9. These data were collated from Tsutsumi (2014). These experiments were conducted to obtain the probability of capsizing in the presence of irregular beam wind and wave conditions. As the subject ship used in this study has a low probability of capsizing in upright conditions in calm water, the experiments were conducted with an initial heel angle to increase this probability.

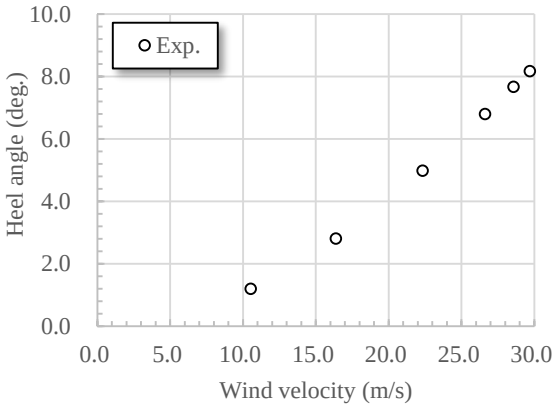

Figure 9 Heel angle due as a function of wind velocity.

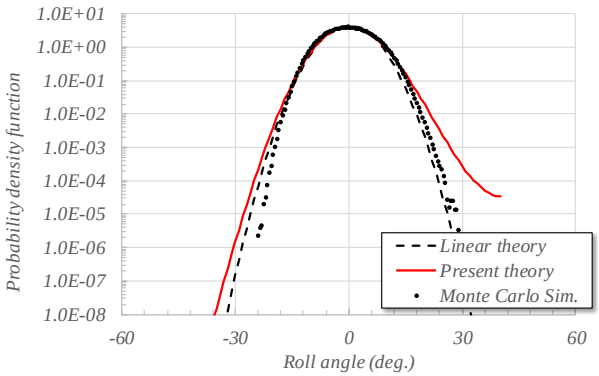

Figure 10 Roll PDF with an initial heel angle of 0 deg, where T_{01}=16.48 s, $H_{1/3}$=11.04 m and U_w=23.85 m/s.

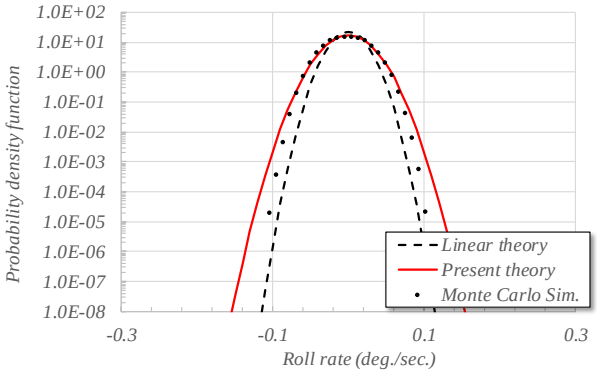

Figure 11 Roll rate PDF with an initial heel angle of 0 deg, where T_{01}=16.48 s, $H_{1/3}$=11.04 m and U_w=23.85 m/s.

Figures 10-11 compare the roll and roll rate PDF with an initial heel angle of 0 deg, whereby MCS and theoretical results are plotted. Since the calculation shown in Fig. 8 was obtained for only the wave condition, the

PDF result exhibits symmetricity. However, Fig. 10 shows clear asymmetry in the PDF at particularly large roll angles, which is a strong contrast to the result from Fig. 8. This is because wind was not generated in Fig. 8, which only represents the wave condition. There is also a discrepancy in the predicted roll rate in Fig. 11. As stated, this discrepancy could be due to the underestimation of roll damping.

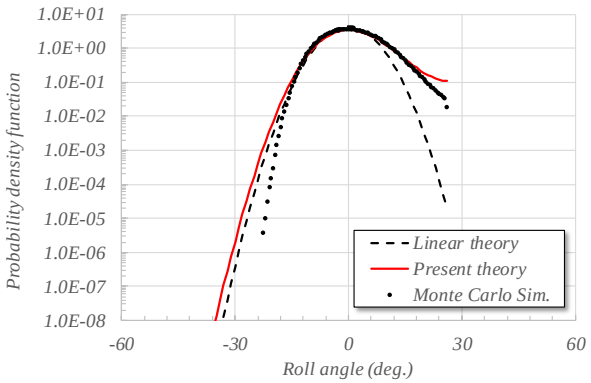

Figure 12 Roll PDF with an initial heel angle of 7 deg, where T_{01}=16.48 *s*, $H_{1/3}$=11.04 *m* and U_w=23.85 *m/s*.

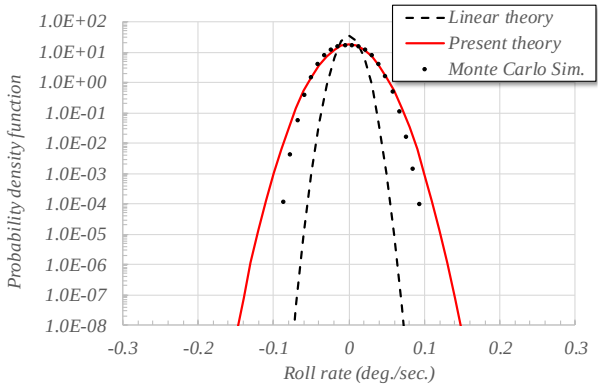

Figure 13 Roll rate PDF with an initial heel angle of 7 deg, where T_{01}=16.48 *s*, $H_{1/3}$=11.04 *m* and U_w=23.85 *m/s*.

Figures 12–13 compare the MCSs and the theoretical results with an initial heel angle of 7 deg. Under these conditions, the PDF clearly shows the non-Gaussian behavior at large roll angles. In particular, its tendency can be easily observed in the vicinity of the vanishing roll angle. The roll and roll rate results from the proposed method also show a good agreement with the MCS results. In such conditions, the linear calculation could obviously completely fail to predict the PDF. Therefore, the results from this show a large discrepancy with the MCS results.

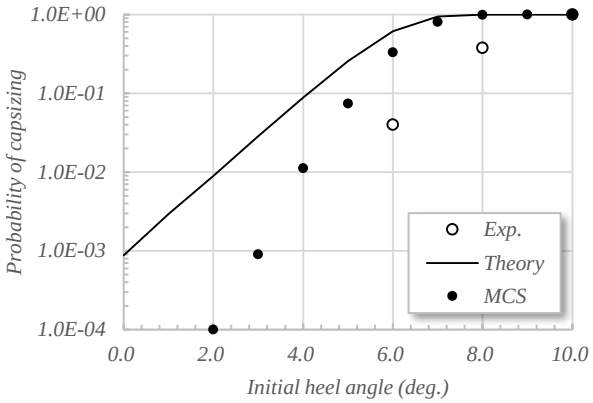

Figure 14 Probability of capsizing when T_{01}=16.48 *s*, $H_{1/3}$=11.04 *m* and U_w=23.85 *m/s*.

Finally, the capsizing probability results are given in Fig. 14. The x axis is the initial heel angle, and the y axis is the capsizing probability for a one-hour period of exposure at the given wind and wave conditions. In this figure, the experimentally obtained capsizing probability from Tsutsumi (2014) is also plotted. Initially, there is a discrepancy between the experimental and MCS results. As stated, it could be due to the limitation of the one DoF model and the effect of wires at the stern and bow. In particular, the effect of wires should be checked in our future work. However, this discrepancy does not appear to be very large from a practical point of view. Although there are clear disagreements between the proposed method and MCS, the proposed method still appears to be able to qualitatively predict the capsizing probability. Further improvements of the proposed method are required to provide quantitative evaluations, fill existing gaps, and achieve quantitative predictions.

4. NEW CALCULATION METHOD

The present theory is based on two basic assumptions: 1) roll and roll rate are independent, and 2) the roll rate follows a Gaussian process. However, these two

assumptions could not be satisfied in a larger nonlinear damping case. The present discrepancy between the theoretical and MCS results is then caused by these two assumptions. Therefore, we introduced a non-Gaussian PDF that considers nonlinear damping (Maki et al., 2018), which is given as

$$p_2(\phi,\dot{\phi};d) = C\exp\left\{-d\left[\alpha H + \frac{8\beta}{9\pi}(2H)^{3/2}\right]\right\} \quad (49)$$

where

$$H = \frac{1}{2}\dot{\phi}^2 + \int_0^{\phi} GZ(\xi)\,d\xi \quad (50)$$

A detailed explanation is given in Maki et al. (2018), and the results are shown in Fig. 15. Note that the wave condition is the same as in Fig. 8. The proposed method shows better correlation with MCSs (Fig. 15). Its application to estimation of capsizing probability is our future task.

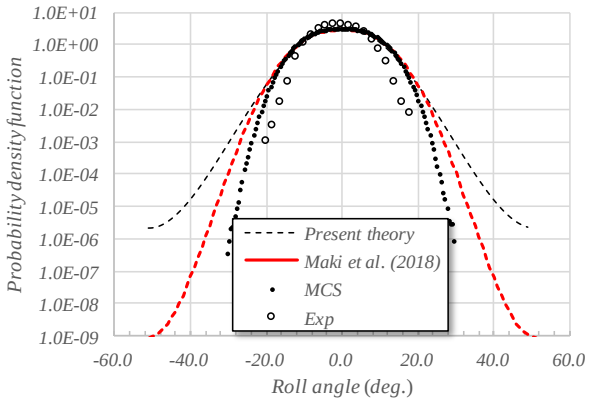

Figure 15 Comparison of the roll PDF between experimental results and two theoretical predictions with T_{01}=20.83 *s* and $H_{1/3}$=19.67 *m*.

5. CONCLUDING REMARKS

Although thus far it has been proposed that the method for predicting the capsizing probability in waves, which is based on the work of Kimura, had only been correlated with MCS. Therefore, here we used experimental results in NRIFE to test the present method.

1. The original methodology was extended by proposing an estimation method for irregular wind and wave conditions.
2. To test the one DoF roll equation used in this study, a beam sea test in regular waves was conducted. Due to the strong nonlinearity in the restoring curve of the subject ship, folding behavior was observed in response amplitude curve of roll. The theoretical calculations conducted using the nominal averaging method. The results showed the qualitative agreement with the experimental results.
3. The theoretical method was correlated with experiments in irregular wind and wave conditions, which also confirmed that the non-Gaussian PDF is reliable. However, further improvements in the theory are essential to achieve quantitative estimates, which is the goal of our future work.
4. For the above purpose, the authors proposed the non-Gaussian distribution in which the nonlinear damping term is explicitly taken into account, and its results were correlated with the experimental results. Its application for the estimation of capsizing probability is highly desired.

6. ACKNOWLEDGMENT

This work was supported by a Grant-in-Aid for Scientific Research from the Japan Society for Promotion of Science (JSPS KAKENHI Grant number 15H02327). The authors would like to thank Enago (www.enago.jp) for English language review.

7. REFERENCES

Belenky, V.L., 1993, "A Capsizing Probability Comparison Method," Journal of Ship Research, Vol. 37, pp.200-207.

Belenky, V.L., 1994, "Piecewise linear method for the probabilistic stability assessment for

ship in a seaway," 5th International Conference on Stability of Ship and Ocean Vehicle, Melbourne, Florida, USA, 5.

Bulian, G., Francescutto, A., and Fucile, F., 2010, "An Experimental Investigation in the Framework of the Alternative Assessment for the IMO Weather Criterion," Proceedings of the HYDRALAB III Joint User Meeting.

Chai, W. and Naess, A., 2015, "Stochastic Dynamic Analysis and Reliability of a vessel rolling in random beam seas," Journal of ship research, Vol. 59, pp.113-131.

Chai, W., Dostal, L, Naess, A., and Leira, B.J., 2017, "A Comparative Study of the Stochastic Averaging Method and the Path Integration Method for Nonlinear Ship Roll Motion in Random Beam Seas," Journal of Marine Science and Technology, Published Online.

Caughey, T.K., 1963 [1], "Derivation and Application of the Fokker-Planck Equation to Discrete Nonlinear Dynamic Systems Subjected to White Noise Random Excitation," The Journal of the Acoustical Society of America, Vol. 35, No.11, pp.1683-1692.

Caughey, T.K., 1963 [2], "Equivalent Linearization Techniques," The Journal of the Acoustical Society of America, Vol. 35, No.11, pp.1706-1711.

Dostal, L, Kreuzer, E., and Namachchivaya, S.N., 2012, "Non-Standard Stochastic Averaging of Large-Amplitude Ship Rolling in Random Seas," Proceedings of the Royal Society A, Published Online.

Francescutto, A. and Naito, S., 2004, "Large Amplitude Rolling in a Realistic Sea," International Shipbuilding Progress, Vol. 51, No.2/3, pp.221-235.

Francescutto, A., Contento, G., and R. Penna, 1994, "Experimental evidence of strong nonlinear effect of rolling motion of a destroyer in beam seas", Proc. of 5th International Conference on Stability of Ships and Ocean Vehicles", Melbourne, Florida, USA, Vol.1

Kimura, K., and Morimoto, T., 1998, "Estimation of Non-Gaussian Response Distribution of a Nonlinear System Subjected to Random Excitation (Application to Nonwhite Excitation with Nonrational Spectrum (In Japanese)," Journal of the Japan Society of Mechanical Engineers, Vol.64, No.617, pp.1-6.

Kougioumtzoglou, L.I., and Spanos, P.D., 2014, "Stochastic Response Analysis of the Softening Duffing Oscillator and Ship Capsizing Probability Determination via a Numerical Path Integral Approach," Probabilistic Engineering Mechanics, Vol. 35, pp.67-74.

Maeda, E., Kubo, T., and Umeda, N., 2012, "Theoretical Methodology for Quantifying Probability of Capsizing for a Ship in Beam Wind and Waves and Its Numerical Validation," Journal of the Japan Society of Naval Architects and Ocean Engineers, Vol. 15, pp.227-235.

Maki, A., 2013, "Stochastic Research on Roll Motion of Surface Combatants in Irregular Beam Seas (in Japanese)," Technical Report of Technical Research and Development Institute, Ministry of Defense, No.7127.

Maki, A., 2017, "Estimation method of the capsizing probability in irregular beam seas using non-Gaussian probability density function," Journal of Marine Science and Technology, Vol.22, pp.351-360.

Maki, A., Sakai, M., and Umeda, N., 2018, "Estimating a non-Gaussian probability density of the rolling motion in irregular beam seas," Journal of Marine Science and

Technology (to be reviewed).

Paroka, D., Ohkura, Y., and Umeda, N., 2006, "Analytical Prediction of Capsizing Probability of a Ship in Beam Wind and Waves," Journal of Ship Research, Vol. 50, No.2, pp.187-195.

Sakata, K. and Kimura, K., 1979, "The Use of Moment Equations for Calculating the Mean Square Response of a Linear System to Non-Stationary Random Excitation," Journal of Sound and Vibration, Vol. 67, No.3, pp. 383-393.

Sakata, K., Kimura, K.,1980, "Calculation of the non-stationary mean square response of a non-linear system subjected to nonwhite excitation," Journal of Sound and Vibration, Vol. 73, No.3, pp.333-343.

Umeda, N. and Yamakoshi, Y., 1991, "Assessment for Probability of Ship Capsizing due to Pure Loss of Stability in Quartering Seas (in Japanese)," Journal of the Society of Naval Architects of Japan, Vol. 169, pp.15-25.

Tsutsumi, Y., Umeda, N., Kawaida, D. and Matsuda, A., 2014, Probability of Ship Capsizing in Beam Wind and Waves–Comparison between Model Experiment and Numerical Simulation, Proceedings of the 7th Asia–Pacific Workshop on Marine Hydrodynamics in Naval Architecture, Ocean Technology and Subsea Technology, Russia, 2014

A Method for the Prediction of Extreme Roll Suitable for Nonlinear Time-Domain Realization

Wenzhe Xu, *University of Michigan* wenzhe@umich.edu

Kevin J. Maki, *University of Michigan* kjmaki@umich.edu

ABSTRACT

In this paper we present a method that produces time-domain realizations of a nonlinear process and its excitation in a time window that contains the extreme of the response in a longer time window. The ability to analyse the system in the time domain near the extreme value offers the possibility to perform high-fidelity numerical simulation or experimental observation of the extreme response. The Duffing equation is studied with nonlinear stiffness as a surrogate for a generic nonlinear ship response. Posteriori analysis of the extreme response is done via the linear and nonlinear transformation from response to forcing using a neural network.

Keywords: *Extreme value, Design-Loads Generator, Duffing Equation*

1. INTRODUCTION

Extreme ship responses, such as loads, roll angle, and slamming pressure, are governed by nonlinear physical processes. Numerical evaluation of ship responses through solution of Navier-Stokes equations or nonlinear potential flow are very expensive relative to the length of time that is required to find extreme responses if the codes were used in a brute-force Monte Carlo manner. This means these numerical tools cannot be used in Monte-Carlo simulations with the goal of characterizing the extreme response directly. Experimental measurements have similar limitations. They are expensive, require specialized facilities, and are subject to difficulties in scaling or extrapolating results from model scale to full scale. Due to the expense of numerical nonlinear-numerical solvers and experiments it is not possible to directly observe multiple extreme responses, and as such it is required to extrapolate from a limited time-window of observation to the extreme in a longer time-window of interest. A great body of literature is focused on this step, see for example Belenky et al. (2010, 2013, 2016); Gaidai et al. (2016); Naess and Gaidai (2008a, 2009); Naess et al. (2010).

A strategy to allow for time-domain evaluation of the extreme response is to build a suitable nonlinear model that is simple enough for Monte-Carlo simulation but sufficiently complex to capture the important nonlinearity of the process. For example single degree-of-freedom models capture important nonlinear physics and are suitable for analytical and numerical investigation (Maki, 2017; Belenky et al., 2016).

The ultimate goal of this work is to employ unsimplified nonlinear analysis, via experiment of fully nonlinear numerical simulation of ship responses, to observe extrema that are predicted by extrapolation. We call this a *posteriori* analysis of the extreme. It is necessary to prescribe tailored sea environments that lead to extreme responses. The current authors have built a framework (Xu et al., 2018) for *posteriori* analysis built upon the Design-Loads Generator (Alford and Troesch, 2009; Alford et al., 2011). The objective of this paper is to present the Design-Loads Generator as a method to produce environments that lead to extreme responses, and to analyse the role of process nonlinearity in the accuracy of the time-domain realizations of

the extreme. To do this a Duffing oscillator with nonlinear response is studied.

2. DUFFING OSCILLATOR

A Duffing oscillator is used as a surrogate nonlinear dynamic system for a generic ship response. The dynamics of a Duffing oscillator is governed by the following second-order Ordinary Differential Equation (ODE) with nonlinear stiffness term.

$$\frac{d^2x}{dt^2} + \delta\frac{dx}{dt} + \alpha x + \beta x^3 = f(t) \tag{1}$$

where δ is the damping coefficient, α is the linear stiffness coefficient, and β is the nonlinear stiffness coefficient.

To better relate this Duffing problem with ship hydrodynamics, the exciting force is chosen to be a Gaussian process. To deterministically simulate the system, a finite Fourier representation of this process is used. This is natural for the description of water-waves.

$$f(t) = \sum_{i=1}^{N} a_i \cos(2\pi f_i t + \phi_i) \tag{2}$$

where $a_i = \sqrt{2S(f_i)\Delta f}$, $S(f)$ is the force power spectral density function, and ϕ_i is a random variable uniformly distributed on $[-\pi, \pi]$.

Using $\tau = t\sqrt{\alpha}, \gamma = \sum a_i, \sigma_i = f_i/\sqrt{\alpha}, y = x\alpha/\gamma$, $\eta = \delta/(2\sqrt{\alpha})$, and $\varepsilon = \beta\gamma^2/\alpha^3$, a dimensionless form of the Duffing equation is written as

$$\frac{d^2y}{d\tau^2} + 2\eta\frac{dy}{d\tau} + y + \varepsilon y^3 = \sum_{i=1}^{N} \frac{a_i}{\gamma} \cos(2\pi\sigma_i\tau + \phi_i). \tag{3}$$

The force has the following wide-banded constant spectrum.

$$S(\sigma) = \begin{cases} S_0 & 0 \le \sigma \le 1 \\ 0 & \text{otherwise} \end{cases} \tag{4}$$

We seek to determine the distribution of the extreme response during an observation time window T_L. Care is taken such that the self repeating period from the deterministic force series ($\frac{1}{\Delta f} = \frac{1}{N}$) is longer than T_L (plus several natural period to cancel the effect of initial conditions).

The Duffing equation with different degree of nonlinearity is studied by varying the nonlinear stiffness term over the range 5,000 < ε < 9,000. The damping is set of η = 0.5, the number of Fourier components is N = 800, and the length of the exposure window is T_L = 500. Monte Carlo Simulations are conducted using the `ode45` solver from MATLAB.

A typical time series for ε = 9,000 is shown in Figure 1. In this figure, the threshold of when the nonlinear stiffness term is equal to the linear stiffness term is shown with different colors. The blue portion of the time history is for linear term being greater than the nonlinear $\frac{\varepsilon y^3}{y} = \frac{\beta x^3}{\alpha x}$ < 1, and the red is for the opposite case. In order to quantify the relative role of nonlinearity the fraction of time in which $\frac{\varepsilon y^3}{y} = \frac{\beta x^3}{\alpha x}$ > 1 is measured for each Monte-Carlo simulation. The percentage of time in which this is true is listed in Table 1 and presented for different values of nonlinear stiffness parameter ε. We carry forward most analysis on ε = 5,000 and 9,000.

ε	$T(\varepsilon y^3/y > 1)/T_L$
5,000	11.11%
6,000	13.89%
7,000	16.41%
8,000	18.69%
9,000	20.75%
10,000	22.61%

Table 1 Nonlinear duration for different values of ε

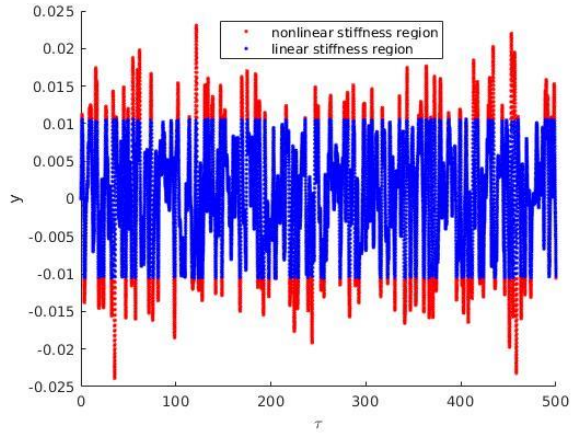

Figure 1 One realization of $y(\tau)$ with nonlinear stiffness coeff. ε = 9,000

Another way to visualize the nonlinearity in the system is to inspect the response spectrum. Figure 2 shows the response spectrum with different ε calculated using `pwelch` from MATLAB.

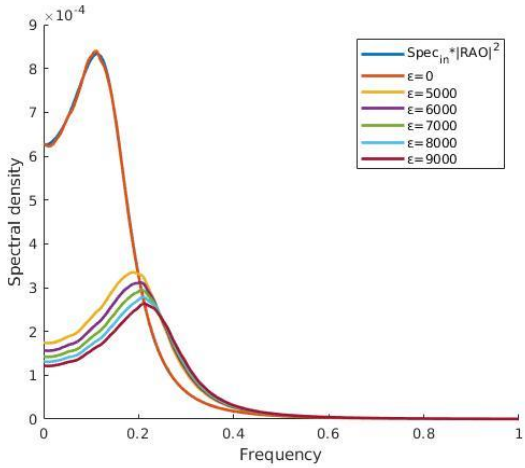

Figure 2 Response spectrum using `pwelch` from MATLAB with ε = 0 (with linear theory), 5,000, 6,000, 7,000, 8,000, and 9,000.

There are many studies in estimating extreme values of a random process during an exposure window. A method using the distribution of positive maxima and order statistics theory is briefly reviewed here. Consider the continuous random process $y(\tau)$ with a time window T_L. If $y(\tau)$ is a Gaussian process, the probability density function (PDF) of its positive maxima is also a random variable denoted by Ξ and is given by Cartwright and Longuet-Higgins (1956) ($0 \le \xi < \infty$):

$$f_{\Xi}(\xi) = \frac{\left(2/\sqrt{m_0}\right)}{1+\sqrt{1-\epsilon^2}}\left[\frac{\epsilon}{\sqrt{2\pi}}\exp\left\{-\frac{1}{2\epsilon^2}\left(\frac{\xi}{\sqrt{m_0}}\right)^2\right\} + \sqrt{1-\epsilon^2}\left(\frac{\xi}{\sqrt{m_0}}\right)\exp\left\{-\frac{1}{2}\left(\frac{\xi}{\sqrt{m_0}}\right)^2\right\} \times\left\{1-\Phi\left(-\frac{\sqrt{1-\epsilon^2}}{\epsilon}\frac{\xi}{\sqrt{m_0}}\right)\right\}\right] \tag{5}$$

where $\epsilon = \sqrt{1-m_2^2/(m_0 m_4)}$ (different from ε, which is the nonlinear stiffness coeff.) is the bandwidth parameter of $y(\tau)$ spectrum, and m_i is the ith moment of the spectrum. The PDF is normalized by the 0th spectral moment ($\frac{\Xi}{\sqrt{m_0}} = H$) to form the following PDF of H ($0 \le h < \infty$):

$$f_H(h) = \frac{2}{1+\sqrt{1-\epsilon^2}}\left[\frac{\epsilon}{\sqrt{2\pi}}\exp\left\{-\frac{h^2}{2\epsilon^2}\right\} + \sqrt{1-\epsilon^2}\,h e^{-h^2/2}\left\{1-\Phi\left(-\frac{\sqrt{1-\epsilon^2}}{\epsilon}h\right)\right\}\right] \tag{6}$$

And the corresponding cumulative distribution function (CDF) of H is

$$F_H(h) = \frac{2}{1+\sqrt{1-\epsilon^2}}\left[-\frac{1}{2}(1-\sqrt{1-\epsilon^2}) + \Phi(h/\epsilon) - \sqrt{1-\epsilon^2}\exp\left\{-\frac{\eta^2}{2}\right\} \times\left\{1-\Phi\left(-\frac{\sqrt{1-\epsilon^2}}{\epsilon}h\right)\right\}\right]. \tag{7}$$

The expected number of positive maxima during T_L is given by Ochi (1973):

$$n = \frac{T_L}{2}\left(\frac{1+\sqrt{1-\epsilon^2}}{\sqrt{1-\epsilon^2}}\right)\sqrt{\frac{m_2}{m_0}} \tag{8}$$

If n positive maxima samples are observed $(h_1, \cdots, h_n)$, they can be ordered into a sequence $(z_1 \le \cdots \le z_n)$. The largest positive maxima (extreme value) Z_n is a random variable, which

has the following PDF, called extreme value PDF. The samples are assumed to be independent.

$$f_{Z_n}(z_n) = n f_H(z_n)[F_H(z_n)]^{n-1} \tag{9}$$

Figure 3 shows the distribution of positive maxima and extreme value PDF for the linear case ($\varepsilon = 0$) computed from Equations 6, 7, 8, and 9. Also shown in this figure are the histograms from 2,000 Monte Carlo Simulations (MCS). Note the strong agreement between the theory and the observation. This is expected because the theoretical results are based on a Gaussian assumption and indeed the response $y(\tau)$ is a Gaussian process filtered by a linear ODE from a Gaussian force.

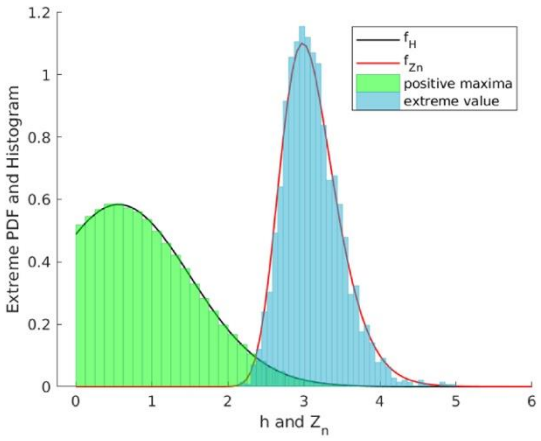

Figure 3 Normalized histogram of positive maxima and extreme values compared with theoretical prediction with Gaussian assumption ($\varepsilon = 0$)

Figure 4 shows the same thing but for the nonlinear cases of ε = 5,000, and 9,000. Note the large differences, in particular for the extreme value distribution. When the nonlinear stiffness coefficient ε becomes sufficiently large, the nonlinear ODE produces a non-Gaussian response even though the input force is Gaussian. The difference between theory and MCS in Figure 4 is due to the Gaussian response assumption made in deriving the theory.

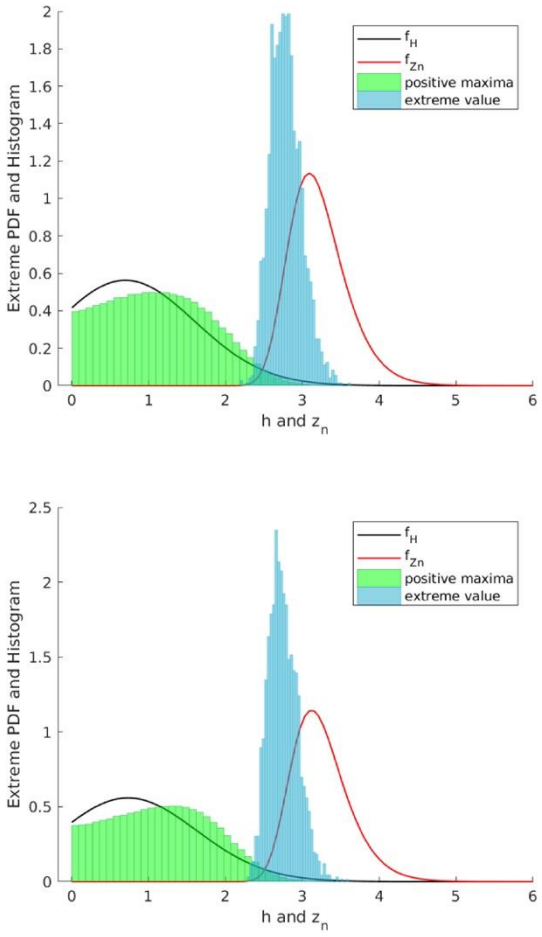

Figure 4 Normalized histogram of positive maxima and extreme values compared with theoretical prediction with Gaussian assumption (top ε = 5,000, bottom ε = 9,000).

A better estimate of the extreme value distribution can be determined using the empirical PDF and CDF for the positive maxima and number of samples estimated from MCS. By doing so there is no need to assume that the response is Gaussian, and the numerical PDF and CDF of the positive maxima can be used directly in the order-statistics Equation 9. Figure 5 compares this numerical extreme value PDF prediction and histograms for ε = 5,000 and 9,000, respectively. Equation 9 assumes independent events. The strong agreement between the numerical extreme-value PDF and the MCS histogram suggests that this is a safe assumption for this problem. We note that there are other sophisticated methods using peak-over-threshold to generate extreme PDF (Belenky et al. (2010); Naess and Gaidai

(2008b)). For this simple ODE we are able to perform enough MCS to generate the distribution of the positive maxima with enough accuracy to form the extreme-value PDF using the order-statistics formula.

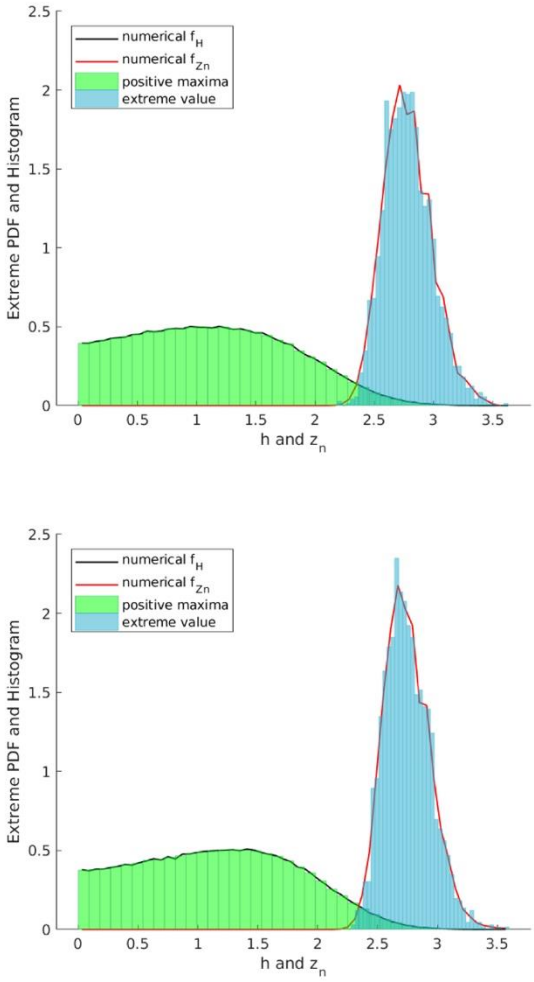

Figure 5 Normalized histograms of positive maxima and extreme values with numerical PDF (top ε = 5,000, bottom ε = 9,000).

3. TIME DOMAIN RESPONSES VIA THE DLG

It is cost prohibitive, if not impossible, to directly simulate dynamic systems during a long time window T_L using high-fidelity numerical tools like CFD. For example, ship operation in a storm lasts from hours to days, and lifetime of a fixed platform is decades. Moreover, to investigate the extreme-value distribution, realizations of many different random environments must be simulated. Hence, it is only possible to use CFD for a short time window T_s ($T_s \ll T_L$). In general the expensive nonlinear numerical tools should only be used where it is needed, that is for the most extreme nonlinear responses. Here we seek to generate a practically infinite number of independent sea environments that allow for deterministic short-time window MCS to be conducted. This short-time Monte Carlo Simulation will provide not only the extreme value distribution, but also time-domain information on how and why the extreme events develops and perhaps leads to system failure.

To understand the cost of MCS for rare events, we recall the scaling for a Gaussian process. For the asymptotic analysis for a Gaussian process, when measuring the rareness in terms of standard deviation $\sqrt{m_0}$ (*e.g.* $3\sqrt{m_0}, 4\sqrt{m_0}, \cdots$), the time window length T_L for a $N\sqrt{m_0}$ event grows as $O(e^{N^2})$. The Design Loads Generator (DLG) method (Alford et al. (2011) and Kim (2012)) is able to generate a time ensemble by giving Fourier phases near the extreme event. All that is required is the response spectrum and the exposure window or number of encounters. The cost does not scale with the rareness $N\sqrt{m_0}$ and the short time window T_s only depends on the characteristics of the dynamic system. This scale-invariant approach is thus highly attractive to simulate rare events.

The DLG method is reviewed briefly. Consider the response process $y(\tau)$ in Fourier representation.

$$y(\tau) = \sum_{i=1}^{N} b_i \cos(2\pi\sigma_i\tau + \phi_i) \qquad (10)$$

Where b_i are evaluated from its response spectrum and ϕ_i must not be uniformly distributed on $[-\pi, \pi]$ for non-Gaussian response. This deterministic process achieves the extreme value z_n at the moment τ_* with extreme phases φ_i.

$$2\pi\sigma_i\tau_* + \phi_i = \varphi_i \tag{11}$$

$$z_n = \frac{1}{\sqrt{m_0}} \sum_{i=1}^{N} b_i \cos(\varphi_i) \tag{12}$$

Where the extreme value has been nondimensionalized by $\sqrt{m_0}$. The phases of the extreme are random variables. Alford et al. (2011) employs a random number generator with the independent and non-identical distributed assumption to generate a random phase vector $(\tilde{\varphi}_1, \cdots, \tilde{\varphi}_N)$, that results in the following extreme value.

$$\tilde{z}_n = \frac{1}{\sqrt{m_0}} \sum_{i=1}^{N} b_i \cos(\tilde{\varphi}_i) \tag{13}$$

The resultant PDF $f_{\tilde{Z}_n}(\tilde{z}_n)$ differs from the target extreme value PDF $f_{Z_n}(z_n)$ with close mean ($E[\tilde{Z}_n] \approx E[Z_n]$) but larger variance ($Var[\tilde{Z}_n] > Var[Z_n]$). A filter-based Acceptance and Rejection method is used by Kim (2012) to tailor the phase set $(\tilde{\varphi}_1, \cdots, \tilde{\varphi}_N)$ such that the extreme value PDF $f_{Z_n}(z_n)$ is achieved. The outline of this algorithm is shown below.

1. Generate a phase vector $(\tilde{\varphi}_1, \cdots, \tilde{\varphi}_N)$ from the random number generator and a random number u from the uniform distribution $U(0,1)$.

2. Calculate the corresponding extreme value $\tilde{z}_n$ and evaluate the PDF's at this value ($f_{Z_n}(\tilde{z}_n)$ and $f_{\tilde{Z}_n}(\tilde{z}_n)$).

3. If $u \leq f_{Z_n}(\tilde{z}_n)/cf_{\tilde{Z}_n}(\tilde{z}_n)$, which factor c is large enough to ensure $\frac{f_{Z_n}(\tilde{z}_n)}{cf_{\tilde{Z}_n}(\tilde{z}_n)} < 1$, accept the tailored phase vector $(\tilde{\varphi}_1, \cdots, \tilde{\varphi}_N)$. Otherwise, reject and go to the first step.

4. Repeat the procedure until a sufficient number of phase angle vectors are generated.

Figure 6 shows a time ensemble of response series from 2,000 MCS simulations shifted the extreme to $\tau - \tau_* = 0$. Figure 7 presents a histogram from their extreme values along with the 2,000 DLG phase sets. These 2,000 DLG phase sets produce a time ensemble, shown in Figure 8. Note the difference in the ensemble from the DLG responses. The DLG produces many realizations in which the maximum occurs after or before the focusing time. As the rareness of the design event increases, *i.e.* increasing T_L, this effect becomes smaller. See Figure 8 where DLG response ensembles are plotted for increasing rareness.

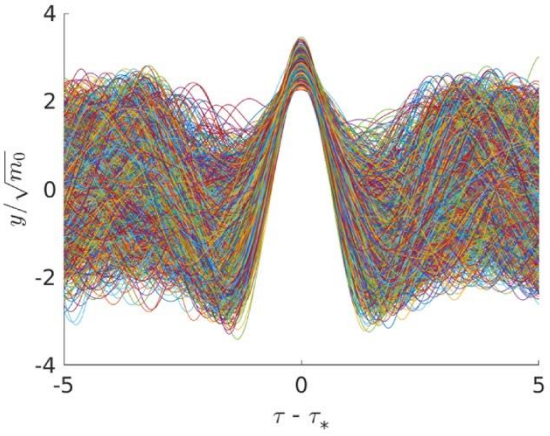

Figure 6 Response resemble by shifting the extreme moment to origin from MCS (ε = 9,000)

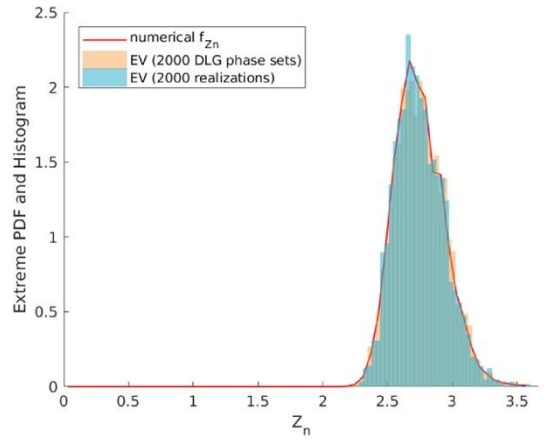

Figure 7 Normalized response histogram from 2,000 unfiltered DLG phase sets at $2.67\sqrt{m_0}$ (ε = 9,000)

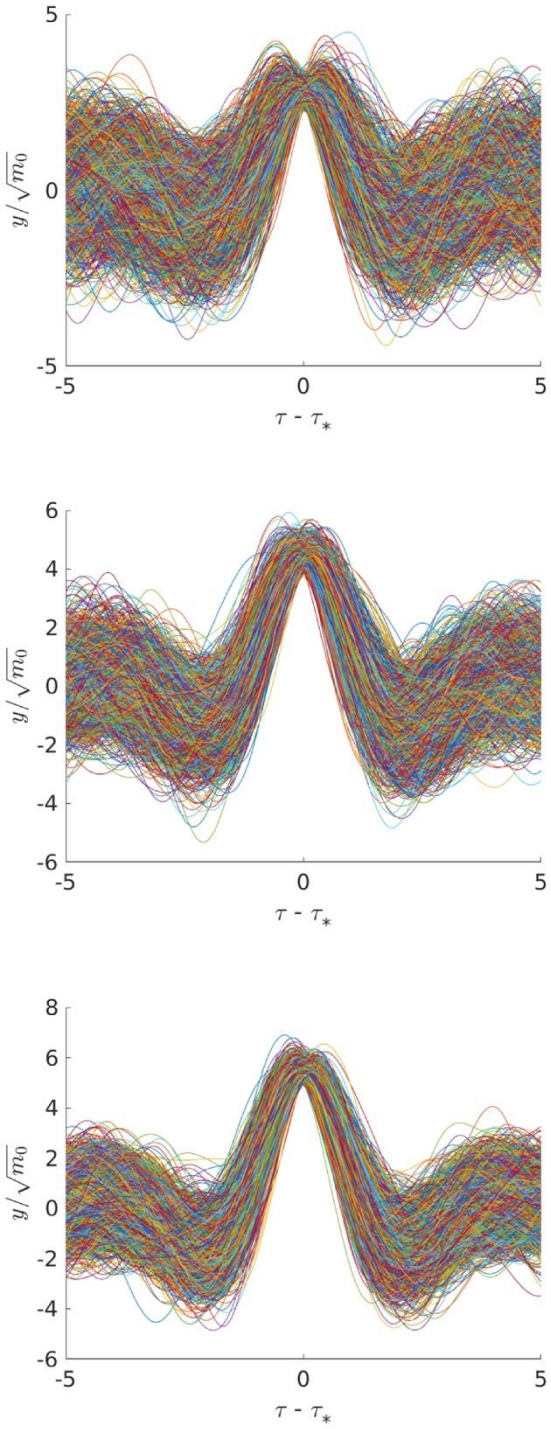

Figure 8 Response ensemble from 2,000 unfiltered DLG phase sets at 2.67 $\sqrt{m_0}$, 4.36$\sqrt{m_0}$, and 5.30$\sqrt{m_0}$ (ε = 9,000)

By adding another filter to reject those phase vectors that fail to produce local maxima in time, this filtered DLG phase sets have a time ensemble, shown in Figure 9. The normalized extreme-value histogram using the filtered DLG phase sets is shown in Figure 10.

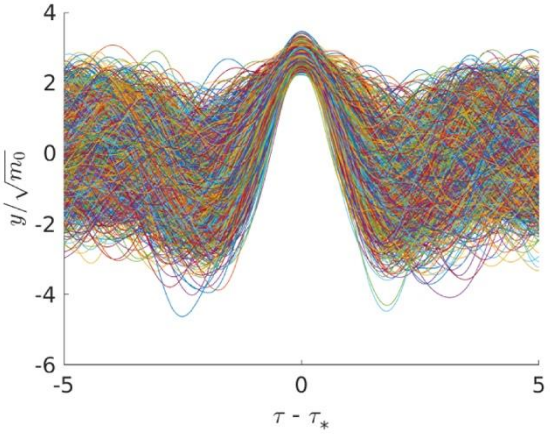

Figure 9 Response ensemble from 2,000 Filtered DLG phase sets at 2.67$\sqrt{m_0}$ (ε = 9,000)

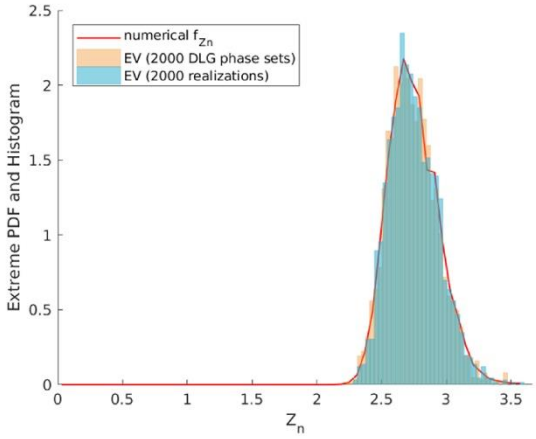

Figure 10 Normalized response histogram from 2,000 Filtered DLG phase sets at 2.67$\sqrt{m_0}$ (ε = 9,000)

Another way to compare the DLG response time histories to the MCS is to use a contour plot as shown in Figure 11. In this figure color corresponds to number of occurrences. The top is for the MCS, and the bottom is for the filtered DLG responses.

The remaining task is to recreate force environment for each DLG phase set, which is discussed in the next section.

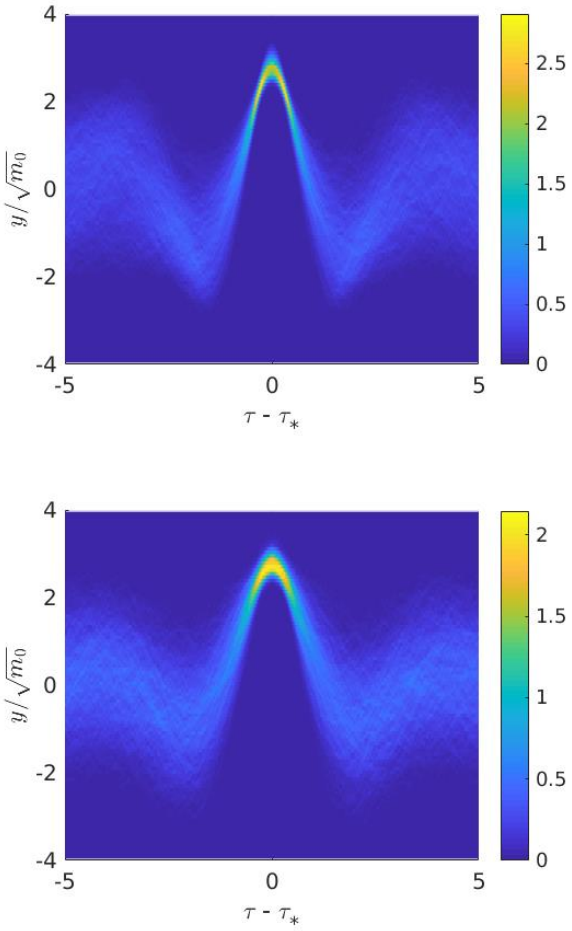

Figure 11 Evolution of response histogram by shifting the extreme moment to origin from MCS, ε = 9,000 (top MCS, bottom Filtered DLG phases)

4. NEURAL NET FOR TIME-DOMAIN FORCING

Once the response time series near the extreme is given from Filtered DLG phase, one may be interested in observing the system in the extreme state. This is now possible using experiment or nonlinear numerical simulation. Simulation of this short window T_s is helpful to answer the questions such as what factors contribute most to the observed extreme event, such as water on deck, emergence of control surfaces from the water, etc. To construct a T_s window, a time-domain force needs to be provided to the simulation solver. If the differential equations governing the dynamic are known a priori, the target response may be inserted into the left-hand side of Equation 3 to generate the needed force for the simulation. However, if the differential equations are unknown, or only the linearized equations are known, providing the force leading to target extreme response is challenging for nonlinear systems. The final target of this work is to generate a sea environment that leads to an extreme ship response. In that case the extreme-response phases must be transferred to the phases of the wave-maker. Here a data-driven method using Neural Networks is proposed to relate the response phases to the forcing (or wave-maker) phases for a general nonlinear system.

Neural networks are widely used for many problems, and can perform well especially when a large amount of data is available. The technique has been applied in many supervised learning problems, such as regression and classification. It has also been used in unsupervised learning problems, such as clustering. The success of fitting generally nonlinear data provides neural networks with the potential to identify the relationship between response and forcing (of wave making) for the dynamical system.

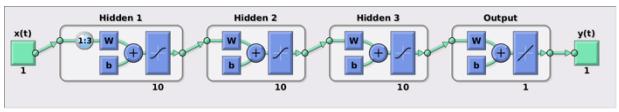

Figure 12 Net architecture (three hidden layer, 10 neurons each, delay order 3)

In the Duffing problem a time-delay network is selected and used to characterize the dynamic system. In the training stage, the parameters of the net are determined by nonlinearly fitting the output time series given the input time series. The net developed in this work has one input layer, three hidden layers, and one output layer. This simple architecture is shown in Figure 12. The nonlinear function this net represents maps the time-delay input (oscillator response) $\mathbf{x}[k] = (x[k], x[k-1], \cdots, x[k-d])^T$ to the system output (exciting force) $\tilde{\mathbf{f}}[k] = \tilde{f}[k]$ in the following nonlinear function.

$$\tilde{\mathbf{f}}[k] = \mathbf{W_4}(\mathbf{W_3}h(\mathbf{W_2}h(\mathbf{W_1}\mathbf{x}[k]+\mathbf{b_1})+\mathbf{b_2})+\mathbf{b_3})+\mathbf{b_4} \quad (14)$$

Where d is the delay order, and h is a nonlinear function, called the activation function. One example of h can be

$$h(a) = \frac{2}{1+e^{-2a}} - 1 \quad (15)$$

Given one realization, sliding the input window ($d = 3, k = 1, 2, \cdots$) generates a training set with input-output pair ($\mathbf{x}[1] \rightarrow \mathbf{f}[1], \mathbf{x}[2] \rightarrow \mathbf{f}[2], \cdots$). The training procedure solves the model parameter $\mathbf{W}$ and $\mathbf{b}$ by minimizing the difference between the prediction $\tilde{\mathbf{f}}[k]$ and the target $\mathbf{f}[k]$. After training, the net is able to generate output time series given any new input series.

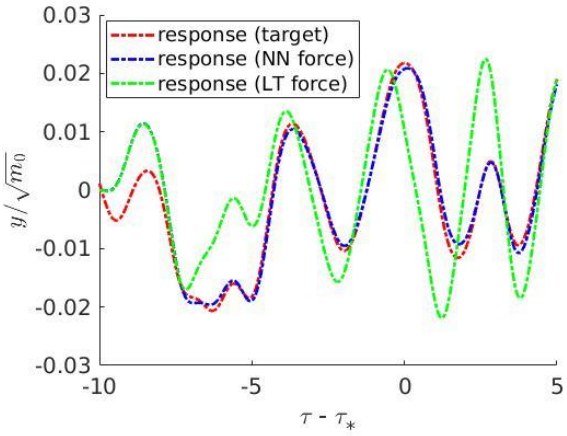

Figure 13 response during short-window T_s, ε = 9,000 (one of Filtered DLG target response, response under NN force, response under linear force)

Figure 13 shows an example of how the neural net improves the response. In this figure the red line is the target response time history from a single filtered DLG phase set vector. Without the neural net, the forcing phase can be determined using the transfer function (LT) from the linearized Duffing equation. Note the large differences between the target response and the short-time MCS using forcing phases form the linear transfer function. The result using the neural net to determine the force phases is shown in the blue line. Note the large improvement over LT phase result.

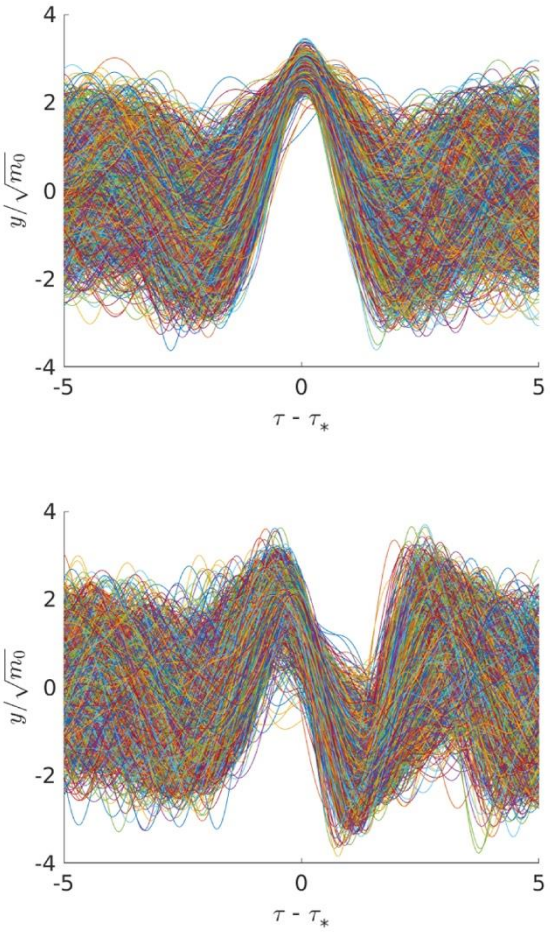

Figure 14 Response ensemble, ε = 9,000 (top NN force, bottom linear force)

Ensembles of 2,000 responses are shown in Figure 14. On the top of this figure the time series using the neural net are shown, and the bottom the linear transfer function is used. Note the strong difference in the response, especially post extreme ($\tau - \tau_* > 0$). The ensembles are shown in histogram form as a function of time with the contour plots in Figure 15. Compare the top of Figure 15 to the bottom of Figure 11. It is clear that the neural net force significantly improves the prediction of the force for short-time MCS.

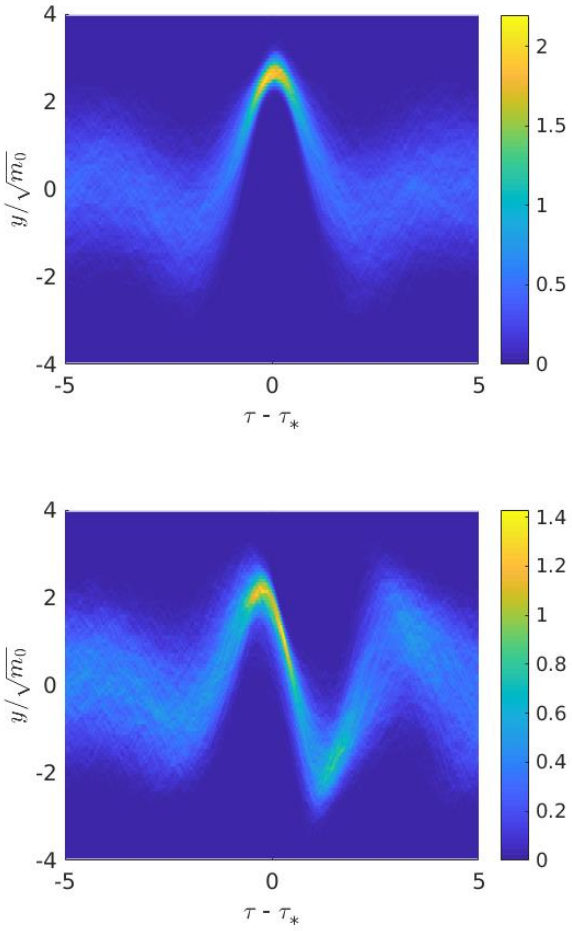

Figure 15 Evolution of response histogram, ε = 9,000 (top NN force, bottom linear force)

5. CONCLUSIONS

In this paper, the Duffing equation with large nonlinear stiffness is studied to illustrate the effect from nonlinear behaviour on the extreme response in a given time window of exposure. The distribution of the extreme positive maxima of the system response is determined with a numerical estimate of the process PDF and CDF and order-statistics. The numerical estimate of the extreme value PDF matches the Monte Carlo Simulation results well.

The DLG method is used to generate time histories of responses that match the extreme value PDF. For purposes of posteriori time-domain evaluation of the extreme, it is shown that for a general nonlinear system there is a need to transfer the extreme response to the forcing leading to the extreme response. For a linear system the transfer function can be used, but for a nonlinear system this process leads to a marked shift in the resulting time-domain realizations. In this work a neural network is employed to develop a relationship between the response and the forcing. The resulting time-domain realizations that are generated with the neural-net phases show strong agreement with the target DLG response time-histories.

6. REFERENCES

Alford, L.K., Kim, D.H. and Troesch, A.W., 2011. Estimation of extreme slamming pressures using the non-uniform Fourier phase distributions of a design loads generator. *Ocean Engineering*, *38*(5-6), pp.748-762.

Alford, L.K. and Troesch, A.W., 2009. Generating extreme ship responses using non-uniform phase distributions. *Ocean Engineering*, *36*(9-10), pp.641-649.

Belenky, V., Bassler, C., Dipper, M., Campbell, B., Weems, K. and Spyrou, K., 2010. Direct assessment methods for nonlinear ship response in severe seas. In *Proc. of ITTC Workshop on Seakeeping, Seoul, Korea*.

Belenky, V.L., Glozter, D., Pipiras, V. and Sapsis, T.P., 2016. On the Tail of Nonlinear Roll Motions. In *Proceedings of the 15th International Ship Stability Workshop* (pp. 109-114).

Belenky, V., Pipiras, V., Kent, C., Hughes, M., Campbell, B. and Smith, T., 2013. On the Statistical Uncertainties of Time-domain-based Assessment of Stability Failures: Confidence Interval for the Mean and Variance of a Time Series. In *Proc. 13th Int'l. Ship Stability Workshop* (pp. 251-258).

Cartwright, D. and Longuet-Higgins, M.S., 1956. The statistical distribution of the maxima of a random function. *Proc. R. Soc.*

Lond. A, *237*(1209), pp.212-232.

Chai, W., Dostal, L., Naess, A. and Leira, B.J., 2017. A comparative study of the stochastic averaging method and the path integration method for nonlinear ship roll motion in random beam seas. *Journal of Marine Science and Technology*, pp. 1-12.

Gaidai, O., Storhaug, G. and Naess, A., 2016. Extreme value statistics of large container ship roll. *Journal of Ship Research*, *60*(2), pp.92-100.

Kim, D.H., 2012. Design Loads Generator: Estimation of Extreme Environmental Loadings for Ship and Offshore Applications.

Maki, A., 2017. Estimation method of the capsizing probability in irregular beam seas using non-Gaussian probability density function. *Journal of Marine Science and Technology*, *22*(2), pp.351-360.

Naess, A. and Gaidai, O., 2008. Monte Carlo methods for estimating the extreme response of dynamical systems. *Journal of Engineering Mechanics*, *134*(8), pp.628-636.

Naess, A. and Gaidai, O., 2008. Monte Carlo methods for estimating the extreme response of dynamical systems. *Journal of Engineering Mechanics*, *134*(8), pp.628-636.

Næss, A. and Gaidai, O., 2009. Estimation of extreme values from sampled time series. *Structural Safety*, *31*(4), pp.325-334.

Naess, A., Gaidai, O. and Batsevych, O., 2010. Prediction of extreme response statistics of narrow-band random vibrations. *Journal of engineering mechanics*, *136*(3), pp.290-298.

Ochi, M.K., 1973. On prediction of extreme values. *Journal of Ship Research*, *17*(1).

Xu, W., Filip, G., Maki, K. J., 2018. A method for the prediction of extreme ship responses using design-event theory and computational fluid dynamics. In: 32nd Symposium on Naval Hydrodynamics. Hamburg, Germany.

Evaluation of an Improved Critical Wave Groups Method for the Prediction of Extreme Roll Motions

Panayiotis A. Anastopoulos, *Department of Naval Architecture and Marine Engineering, National Technical University of Athens, Greece*, panasto@central.ntua.gr

Kostas J. Spyrou, *Department of Naval Architecture and Marine Engineering, National Technical University of Athens, Greece*, k.spyrou@central.ntua.gr

ABSTRACT

The paper proposes an improved formulation of the "critical wave groups" method for calculating the probability of extreme roll responses in beam seas. The new approach employs irregular waveforms for identifying "critical" wave events that cause slight exceedance of a given roll angle threshold for a number of initial conditions of the vessel at the instant of the group encounter. The probability of any exceedance of that threshold is estimated by the probability of encountering any wave sequence higher than the determined critical. The accuracy and the efficiency of the method are tested against Monte Carlo simulations of roll motion.

Keywords: *wave group, probability, instability, roll, dynamics, resonance, rare events*

1. INTRODUCTION

Addressing simultaneously the rarity and the nonlinearity of extreme behaviour represents a state-of-art scientific challenge in stochastic mechanics. However the interest is not only theoretical; because in the process of developing rigorous criteria against ship capsize, one is confronted with this challenge. It is well known that, providing reliable estimates for the statistics of events with extremely low probabilities using standard tools, such as time domain simulations, suffers from a number of deficiencies. First, the accuracy of a "direct counting" definition of probability becomes questionable when dealing with events that are rarely realized. At the same time, due to the eventually softening character of restoring and the associated possibility of system escape, the stationary qualities of ship rolling can be assumed only in an approximate sense (e.g. Roberts & Vasta, 2000). On the other hand, a practical solution can seemingly be obtained by applying the so called "principle of separation" which can be applied in various ways disassembling the ship response problem into sub-problems. One possibility is to separate the "non-rare" from the "rare" part. The objective of the former could be to determine the distribution of the initial conditions that can lead to the occurrence of extreme events. As for the "rare" part, it can target the conditional probability of extreme events, given that specific initial conditions are met. The above concept of separation has been demonstrated in several studies and different techniques have been developed regarding its implementation for ship stability assessment (e.g. Belenky et al., 2012, Campbell et al., 2016, Mohamad & Sapsis, 2016; and others).

Based on the same principle, the "critical wave groups" method quantifies instability tendency through a calculation of the probability of encountering any wave group that could provoke the instability. Hence, the

separation is applied for distinguishing a deterministic part which is, in general, easily handled computationally by using, in deterministic context, a mathematical model of ship motion; from a probabilistic one, which involves calculations of the wave field only, targeting the probability of encountering critical waves. In the original formulation of the method, regular wave trains had been employed in the deterministic part, in order to identify height thresholds for the critical waveforms (Themelis & Spyrou, 2007). Then, in the probabilistic part, the probability of encountering any group exceeding the specified height thresholds was calculated using distributions of wave heights and periods derived from spectral methods. Recently, the "critical wave groups" method was implemented using irregular wave group excitations (Anastopoulos & Spyrou, 2017). These "irregular groups" were derived as the expected wave group forms per given sea state.

In the present paper we investigate how the assumption of zero initial conditions (i.e. $\varphi_0 = 0$ and $\dot{\varphi}_0 = 0$) of the vessel at the instant of a group encounter, adopted in Anastopoulos & Spyrou (2017), affects the deduced probability figures. At the same time, our effort towards improving the deterministic part of the "critical wave groups" method is continued by modifying the method developed by Anastopoulos et al. (2016) to construct the expected wave groups of a sea state, given that their periods vary within a specific range. In this context, we propose a new formulation of the "critical wave groups" calculation scheme and its performance for predicting extreme roll motions in beam seas is tested against the original one of Themelis & Spyrou (2007). To evaluate the impact of the probabilistic part, height and period distributions are derived directly from simulations of the wave field and the results are compared with those obtained when the same distributions are derived from the theoretical wave envelope process (spectral methods). Finally, we demonstrate that the method can effectively produce response statistics in the tail region, where the accuracy of Monte Carlo simulations is disputable.

2. THE "CRITICAL WAVE GROUPS" METHOD

In the field of ocean and coastal engineering, wave groups are traditionally considered as sequences of waves with heights exceeding a certain preset level and slightly varying periods (Masson & Chandler, 1993, Ochi, 1998). Despite that several threshold-based definitions have been utilized in the past to study wave groupiness measures, one would argue that, from a ship dynamics perspective, critical wave groups are sequences of waves which are sufficiently high to provoke instabilities.

2.1 Mathematical formulation

Let us assume that we are interested in estimating the probability that a vessel exceeds a roll angle threshold φ_{crit}. The key idea of the "critical wave groups" method is to first identify the wave events that cause the exceedance and then, calculate the probability of encountering them. The essence of the approach is presented below:

$$p\left[\varphi > \varphi_{crit}\right] = \sum_k \underbrace{p\left[\varphi > \varphi_{crit} \middle| \left(\bigcup_j wg_{k,j}, ic_k \right) \right]}_{=1} \times p\left[\bigcup_j wg_{k,j}, ic_k \right] \quad (1)$$

where $wg_{k,j}$ is a wave group event with characteristics j, determined for the k^{th} set of initial conditions $(\varphi_0, \dot{\varphi}_0)$ of the vessel at the moment of the encounter. Therefore, the problem reduces to the estimation of the second term in eq. (1):

$$p\left[\bigcup_j wg_{k,j}, ic_k \right] = \sum_k p\left[\bigcup_j wg_{k,j} \middle| ic_k \right] \times p\left[ic_k \right] \quad (2)$$

For sufficiently large roll angle thresholds we assume that "critical" (or worse) wave group occurrences are rare events and thus, statistically independent from each other. This enables us to rewrite the conditional probability in eq. (2) using the following transformation rule, known as "De Morgan's law":

$$p\left[\bigcup_j wg_{k,j}\middle|ic_k\right]=1-p\left[\overline{\bigcup_j wg_{k,j}}\middle|ic_k\right]=$$

$$1-p\left[\bigcap_j \overline{wg}_{k,j}\middle|ic_k\right]=1-\prod_j\left(1-p\left[wg_{k,j}\middle|ic_k\right]\right) \quad (3)$$

where the overbar denotes the complement of an event. Eventually, the calculation of the last probability in eq. (3) is decomposed in two parts: a purely deterministic one, focused on the identification of the so called "critical" wave groups, i.e. those wave successions leading to only slight exceedance of φ_{crit}; and a probabilistic part to calculate the probability of encountering any wave group higher than the determined critical. As realized, the accuracy of the method depends explicitly on the shape of the critical wave groups which are in fact height thresholds for the wave events that result in $\varphi > \varphi_{crit}$.

A significant challenge in eq. (3) is to ensure that wave groups that provoke exceedance of φ_{crit} form a set of mutually exclusive and collectively exhaustive events. To avoid possible overlaps in the calculations, it is convenient to identify wave groups with respect to their run length j, which is the number of consecutive heights exceeding a critical threshold:

$$p\left[wg_{k,j}\middle|ic_k\right]=$$

$$p\left[\bigcup_m\left\{\mathbf{H}_j>\mathbf{h}_{cr,j},\mathbf{T}_j\in T_{cr,m}\right\}\middle|ic_k\right] \quad (4)$$

where $\mathbf{H}_j=\{H_1,...,H_j\}$ and $\mathbf{T}_j=\{T_1,...,T_j\}$ are vectors of random variables referring respectively to the heights H_n and periods T_n of an individual wave group event with run length j $(1\le n\le j)$, $\mathbf{h}_{cr,j}=\{h_{cr,1},...,h_{cr,j}\}$ is a deterministic vector for the heights of a critical wave group with run length j and $T_{cr,m}$ is the m^{th} range $(m=1,2,...,M)$ within which the critical periods $\mathbf{t}_{cr,j}=\{t_{cr,1},...,t_{cr,j}\}$ are considered to vary. In this way, for a given run length j, critical height thresholds are determined for each of the $T_{cr,m}$ segments which have been used to discretize the whole range of periods that could be met in a real sea (Themelis & Spyrou, 2007). The width of the period segments T_w is a key parameter which controls the probability of encountering a critical wave episode and should reflect the extent up to which period variations are truly responsible for the occurrence of instabilities.

2.2 Construction of realistic wave groups

Modelling of wave successions as Markov chains has been one of the most successful approaches in wave group theory. Kimura (1980) was the first to elaborate on wave group statistics assuming that wave heights and related periods are Markov processes. Ever since the concept has been tested several times against numerical simulations and real wave field measurements with remarkable success (e.g. Stansell et al., 2002).

Anastopoulos et al. (2016) extended the Markovian model of Kimura (1980) developing a method for the systematic construction of irregular wave group profiles, characterized by high probability of occurrence. Later, it became apparent that the construction algorithm needed to be modified since the produced waveforms had periods varying only in the vicinity of the mean period of the assumed sea state (Anastopoulos & Spyrou, 2017). Thus, here we have revised the method of Anastopoulos et al. (2016) to determine critical wave events in terms of the expected wave groups with periods varying in a defined range $T_{cr,m}$, given a sea state. Again, the height h_c and the period t_c of the highest wave of the

group are utilized to initiate the following iterative scheme:

$$\overline{t_n} = \frac{1}{p_{T_n}} \int_{T_{cr,m}} t_n f_{T_n|H_{n-1},T_{n-1}}\left(t_n|h_{n-1},t_{n-1}\right) dt_n \qquad (5)$$

where

$$p_{T_n} = \int_{T_{cr,m}} f_{T_n|H_{n-1},T_{n-1}}\left(t_n|h_{n-1},t_{n-1}\right) dt_n \qquad (6)$$

$$\overline{h_n} = \int_0^\infty h_n f_{H_n|T_n,H_{n-1},T_{n-1}}(h_n \,|\, t_n,h_{n-1},t_{n-1}) dh_n \qquad (7)$$

Now, consider that we are interested in generating a sequence of j wave group heights with related periods in a range of interest $T_{cr,m}$. Assuming that h_c and t_c occupy the n^{th} position in the sequence ($1 \le n \le j$), forward application of eqs. (5) to (7) will provide the heights and periods of the waves succeeding the initial (highest) one. The "most expected" past outcomes are identified by applying the same procedure backwards in time. The calculation of the conditional expectation in eq. (5) precedes that of eq. (7) so as to take into account the correlation between the height and the period of a predicted wave. The kernels of the integrals are the transition probability density functions (PDFs) of the Markovian process and details regarding their derivation are given in Anastopoulos et al. (2016).

The final step is to construct the continuous-time counterpart of a generated sequence. To this end, we opt for a representation of water surface elevation η of the form:

$$\eta\left(x,t\right) = \sum_{i=0}^{5j} a_i f_i\left(x,t\right) \qquad (8)$$

Then, the objective is to determine the coefficients a_i so that eq. (8) satisfies a set of geometrical constraints which ensure that the shape of the produced waveform is compatible with the predictions of eqs. (5) and (7). The number of terms kept in eq. (8) naturally depends on the run length j and it is selected so that the uniqueness of the solution is guaranteed. In our earlier studies the f_i basis functions of the expansion had been modelled by wavelets and they were derived from the application of the Karhunen-Loève theorem (Sclavounos, 2012). Here, aiming at reducing the computational cost due to the solution of the Karhunen-Loève eigen-problem, we employ Fourier basis functions, i.e. trigonometric functions. Another advantage of this approach is that closed forms for the a_i parameters are readily available from the existing literature (e.g. Nathan, 1975). It should be noted however that the truncation order in eq. (8) is lower than the originally recommended ($6j$) since it was recently observed that desired waveforms could be generated even if the constraints for the time instants of zero down-crossings were removed. More details on this part of the construction process can be found, e.g. in Anastopoulos & Spyrou (2016).

2.3 Equation of roll motion

To determine a set of critical wave groups, time-domain simulations are performed using the following simple uncoupled equation, written in terms of the relative roll angle φ:

$$\left(I_{44} + A_{44}\right)\ddot{\varphi} + D\left(\dot{\varphi}\right) + g\Delta GZ\left(\varphi\right) = M\left(t\right) \qquad (9)$$

with I_{44} and A_{44} being the roll moment of inertia and the added moment of inertia, respectively, Δ is the ship displacement, g is the gravitational acceleration and D is the damping moment:

$$D\left(\dot{\varphi}\right) = B_1\dot{\varphi} + B_2\dot{\varphi}\left|\dot{\varphi}\right| \qquad (10)$$

The restoring arm in still water is given as:

$$GZ\left(\varphi\right) = C_1\varphi + C_3\varphi^3 \qquad (11)$$

The energy spectrum of the wave induced moment is estimated from the water surface elevation spectrum $S_{\eta\eta}$ using the roll response amplitude operator (RAO):

$$S_{MM}(\omega) = \left|RAO(\omega)\right|^2 S_{\eta\eta}(\omega) \tag{12}$$

Dividing eq. (9) by $I_{44} + A_{44}$ we finally obtain:

$$\ddot{\varphi} + b_1\dot{\varphi} + b_2\dot{\varphi}\left|\dot{\varphi}\right| + c_1\varphi + c_3\varphi^3 = m(t) \tag{13}$$

2.4 Solution to the rare sub-problem

The probability of encountering dangerous wave groups with certain specifications, as in eq. (4), is calculated by once again employing the concept of Markov chains, according to the following procedure (Themelis & Spyrou, 2007):

$$p\left[wg_{k,j}\middle|ic_k\right] = p_1 \times p_2 \tag{14}$$

where

$$p_1 = \iint_{T_{cr,m}} f_{T_n,T_{n-1}|\mathbf{H}_n}\left(t_n, t_{n-1}\middle|\mathbf{h}_n > \mathbf{h}_{cr,n}\right) dt_n dt_{n-1} \tag{15}$$

$$p_2 = \int_{h_{cr,n}}^{+\infty}\int_{h_{cr,n-1}}^{+\infty} f_{H_n,H_{n-1}}(h_n, h_{n-1})\, dh_n dh_{n-1} \tag{16}$$

In the context of spectral methods, Tayfun (1993) observed that a bivariate Gaussian distribution is a good approximation for the PDF of successive wave periods, appearing in eq. (15), given the associated heights $\mathbf{H}_n = \{H_n, H_{n-1}\}$ exceed a certain level $\mathbf{h}_{cr,n} = \{h_{cr,n}, h_{cr,n-1}\}$. For the distribution of two consecutive wave heights $f_{H_n,H_{n-1}}$ in eq. (16) Kimura (1980) proposed the bivariate Rayleigh distribution.

2.5 Solution to the non-rare sub-problem

Attempts to validate the "critical wave groups" method have been based mostly on the assumption that the ship has zero initial conditions $(\varphi_0, \dot{\varphi}_0) = (0,0)$ when approached by a wave group (e.g. Anastopoulos & Spyrou, 2017, Shigunov et al., 2012). Although this can somehow be acceptable from a ship roll dynamics perspective (Rainey & Thompson, 1991), the matter needs to be thoroughly investigated. However, the idea of treating probabilistically the initial conditions via the computation of the second term in eq. (2) had already been demonstrated in Themelis & Spyrou (2008). In their study, the joint PDF of initial conditions had been modelled by a Gaussian distribution and by further assuming that the roll angle and velocity are independent random variables. In the following section, the distribution of initial conditions is estimated directly from Monte Carlo simulations of roll motion using eq. (13). To evaluate the assumptions of Gaussianity and independence, the obtained empirical distribution is compared with a bivariate Gaussian distribution that is fitted to the generated data.

3. RESULTS AND DISCUSSION

In this section, the "critical wave groups" method is applied to an ocean surveillance ship, with main parameters listed in Table 1, to predict the probability of exceedance for a number of roll angle thresholds φ_{crit}. For comparison reasons, the method is implemented using first regular and then irregular wave group excitations. In both cases the results are tested against Monte Carlo simulations of roll motion. To assess the performance of the approach when spectral methods are employed, desired distributions in eqs. (15) and (16) are also estimated using simulations of the wave field (Anastopoulos & Spyrou, 2017).

The ship is assumed to operate in a sea state described by the modified Pierson-Moskowitz

spectrum with significant wave height $H_S = 3\text{m}$ and peak period $T_P = 11\text{s}$:

$$S_{\eta\eta}(\omega) = \frac{5.058 g^2 H_S^2}{\omega^5 T_P^4} \exp\left[-\frac{5}{4}\cdot\left(\frac{\omega_P}{\omega}\right)^4\right] \quad (17)$$

were ω_P is the peak frequency. The wave induced moment was modelled using eq. (12) and the roll response amplitude operator (RAO) of the vessel is given in Su (2012).

Table 1: Main ship parameters

Parameter	Dimensional value
$I_{44} + A_{44}$	5.540×10^7 kg·m^2
Δ	2.056×10^6 kg
B_1	5.263×10^6 kg·m^2/s
B_2	2.875×10^6 kg·m^2
C_1	3.167 m
C_3	–2.513 m

For the simulation of a stationary and ergodic Gaussian wave field, the following model was adopted (St. Denis & Pierson, 1953):

$$\eta(t) = \sum_n \sqrt{2 S_{\eta\eta}(\omega_n)\, d\omega}\cos(\omega_n t + \varepsilon_n) \quad (18)$$

where ε_n are random variables uniformly distributed over [0,2π), ω_n are the frequencies of the wave components and $d\omega$ is the frequency resolution. In total, 175132 waves were analyzed from a set of 16 records of 24 hours. Statistics of roll motion were collected without assuming the ergodic property for the roll response (for a discussion on the egodicity problem see Belenky et al., 1998). As a corollary, the analysis was made on a set of approximately $3\cdot10^6$ short-duration realizations, sampled at a fixed time instant $t_s = 150\text{s}$. Regarding the construction of irregular wave group shapes, the transition probabilities in eqs. (5) to (7) were calculated according to the method described in Anastopoulos et al. (2016) with the only difference that the necessary correlation parameters were estimated from the generated wave data. In this way, the efficiency of the Markov model for determining the expected wave height and period sequences is enhanced.

In Figure 1, the joint PDF of roll angle and velocity, as obtained from the Monte Carlo simulations, is compared with a bivariate Gaussian distribution that was fitted to the generated data. The standard deviation of roll angle was $\sigma_1 = 6.4\,\text{deg}$, while for the velocity it was $\sigma_2 = 6.3\text{deg}$. The correlation between these two random variables was estimated using Pierson's parameter and was found zero. Although this does not necessarily imply statistical independence, one could argue that in a first approximation it is sufficient to consider the joint distribution of roll angle and velocity as the product of the respective marginal distributions (Themelis & Spyrou, 2008).

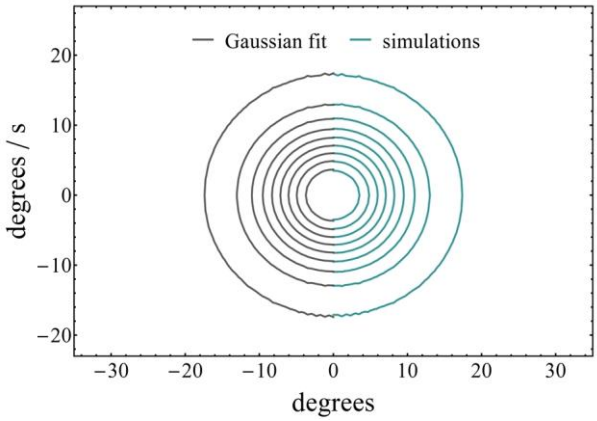

Figure 1: Joint PDF of roll response obtained from simulations (right half) and Gaussian fit (left half).

From Figure 1 it is evident that ship response exhibits an almost Gaussian behaviour and this is attributed to the rarity of extreme events. In other words, nonlinearity is not visible in the statistics because the dynamical system spends most of the time close to the stable equilibrium which contributes the main probability mass of the response PDF (Belenky et al., 2016). Finally, considering that any state of the system

$(\varphi_0, \dot{\varphi}_0)$ can be regarded as the time evolution of an initial state $(\varphi_0, \dot{\varphi}_0)$, the solution of the non-rare sub-problem coincides with the derived response distribution. Hence, the fitted Gaussian PDF was selected to compute the second term in eq. (2), although the parameters of the fitted distribution could have been estimated with fair accuracy using a much smaller number of simulations.

3.1 Regular wave groups

Below we present the results of the "critical wave groups" method when regular wave groups with $j \leq 5$ are utilized and for two cases of critical period range widths $T_w = 1$s and $T_w = 2$s . Critical wave groups were determined for 81 cases of initial conditions of the vessel, spanning the domains [-16deg, 16deg] and [-16deg/s, 16deg/s] with a fixed step. The probability of exceedance P_e was calculated for several roll angle thresholds within the stability range of the vessel (0-64deg). In Figure 2, crosses indicate that critical wave groups were determined only for zero initial conditions $(\varphi_0, \dot{\varphi}_0)$ and probabilistic calculations were carried out using wave distributions obtained from simulations of the wave field. Circles and rectangles refer to the synthesized solutions of the non-rare and rare sub-problems when distributions of heights and periods in eqs. (15) and (16) are estimated from simulations (CWGM sim.) and spectral methods (CWGM sp.), respectively. The results of Monte Carlo simulations (MC sim.) are overlaid on the same plots (solid lines).

The selection of an appropriate grid of initial conditions is a matter of importance for the implementation of the method. Since eq. (3) requires statistical independence of the critical wave groups, its application could be valid only for intermediate and large roll angle thresholds. The limits of application are manifested by the "problem of rarity" which for the case of MC sim. becomes obvious beyond the limit of 30 degrees, as shown in Figure 2. Consequently, the "critical wave groups" scheme is applied for relatively lower thresholds to also test its performance against the results obtained from the simulations. With the first estimate corresponding to a 20 degrees roll angle threshold, initial conditions up to 16 degrees were included.

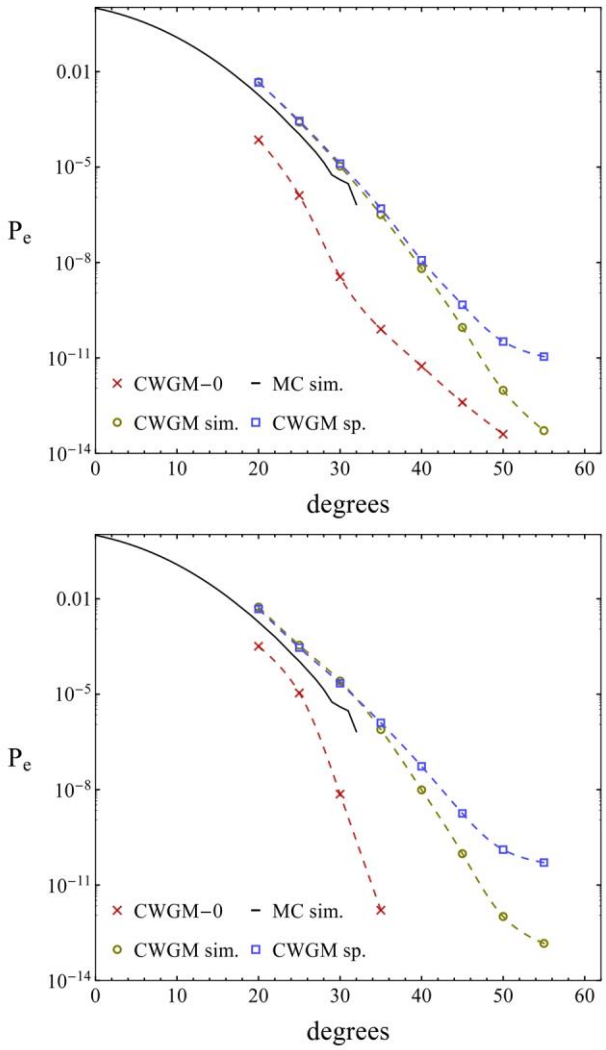

Figure 2: Probability of exceedance using regular wave groups with $T_w = 1$s (upper panel) and $T_w = 2$s (lower panel).

As illustrated in Figure 2, the synthesized solution of the method (CWGM sim. and CWGM sp.) extends the estimates of the Monte Carlo simulations up to the region of extreme responses. However, the predictions below 30 degrees are an order of magnitude greater than those of the simulations and the same trend continues up to 40 degrees. Thus, we would assume that the method generally overestimates the probability of exceedance when regular

wave groups are utilized. Moreover, it should be noted that the "problem of rarity" is not completely solved in the case of CWGM sim. because wave distributions were empirically estimated from limited data. The amount of generated data becomes even smaller for exceptionally high waves and thus, sample estimates naturally deviate from the "true" population values. This justifies why CWGM sim. predicts lower probability levels than the CWGM sp. scheme in the tail region. Hence, the deviation of the CWGM sp. and the CWGM sim. curves of Figure 2, for roll angles above 35deg, can lead to the conclusion that the spectral method is more effective. Another advantage of the CWGM sp. approach is that the PDFs in eqs. (15) and (16) exist in closed forms which makes them more attractive for practical applications.

From Figure 2 it is obvious that the simplified approach CWGM-0 consistently underestimates the probability of exceedance. This fact, along with the sensitivity of the results to the selection of T_w, were reported also in our previous study (Anastopoulos & Spyrou, 2017), where the same ship model was studied, yet for a different sea state. It is interesting to note, however, that the effect of T_w becomes weaker when more initial conditions $(\varphi_0, \dot{\varphi}_0)$ are taken into account. To interpret why the deviations between respective curves for $T_w = 1\text{s}$ and $T_w = 2\text{s}$ are limited to the region of extreme responses, we shall refer to the work of Boccotti (2000). According to data collected from real wave field measurements, period variations tend to asymptotically vanish in the limit of infinitely high waves. Therefore, when the tolerance for the detection of resonant phenomena is relaxed ($T_w = 2\text{s}$), the probability of occurrence of large waves is artificially increased.

3.2 Irregular wave groups

In Figure 3 the results of the "critical wave groups" method with irregular wave groups are displayed using the same parameters as before ($j \le 5$, $T_w = 1\text{s}$ & $T_w = 2\text{s}$). For this application, critical wave groups were identified so that exceedance of a roll angle threshold was always recorded during the encounter of the highest wave. In this way, waves succeeding the highest one were excluded from the probability calculations and the occurrence of instabilities was explicitly related to the characteristics of the highest wave which uniquely defines the structure of a realistic wave group (Anastopoulos et al., 2016).

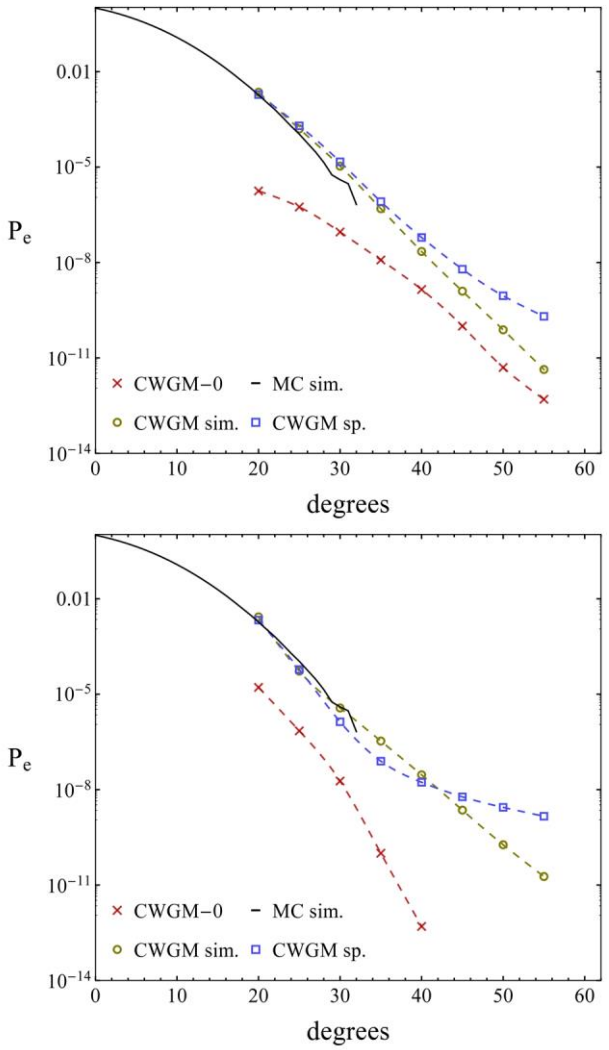

Figure 3: Probability of exceedance using irregular wave groups with $T_w = 1\text{s}$ (upper panel) and $T_w = 2\text{s}$ (lower panel).

From Figure 3 we see that for moderate roll angle thresholds the results of the new approach are almost identical with the Monte Carlo estimates. In the tail region, the predictions extend smoothly from the non-rare

part for both the examined cases of the T_w parameter. The success of the approach is possibly due to the wave groups' construction method which naturally avoids producing wave groups with unusual specifications because they are very unlikely to be encountered. With this feature not being present in the case of regular waveforms, unnaturally high trains may be utilized for a given period. Since their probability of occurrence is really low, they affect mostly the tail of the response distribution. Similarly to the case of regular wave groups, the rarity of extreme events is more effectively treated when spectral methods are employed. Again, it is confirmed that treating the initial conditions in a probabilistic context is an essential part of the current methodology.

4. CONCLUSIONS

In this study an improved "critical wave groups" calculation scheme was developed further and it was applied for predicting the probability of large-amplitude roll motions in beam seas. The method separates ship roll response into sub-regions with distinct dynamics which are studied individually. Extreme ship motions are analyzed under the influence of realistic wave group excitations and critical, for ship stability, wave events are determined for a number of initial conditions of the vessel. The tail of the response distribution is obtained by calculating the probability of encountering such events conditioning on the initial conditions at the moment of the encounter. To complete the solution, the distribution of initial conditions, assumed concerning mostly the linear region of the GZ curve, was approximated by a Gaussian model that was fitted to a set of data derived from a limited number of time-domain simulations. Comparisons with pertinent Monte-Carlo simulations of roll motion demonstrate the good potential of the approach in terms of efficiency and accuracy although the use of many initial conditions imposes a time penalty. Regarding the shape of design wave groups, it is revealed that considering only the most expected representatives of a given sea state may be adequate for producing reliable results since they extend smoothly the Monte Carlo estimates. The implementation of the method using fewer cases of initial conditions to alleviate the computational burden is a topic of future research.

5. REFERENCES

Anastopoulos, P.A., Spyrou, K.J., Bassler, C.C., and Belenky, V.L., 2016, "Towards an Improved Critical Wave Groups Method for the Probabilistic Assessment of Large Ship Motions in Irregular Seas", Probabilistic Engineering Mechanics, Vol. 44, pp. 18-27.

Anastopoulos, P.A., and Spyrou, K.J., 2016, "Ship Dynamic Stability Assessment Based on Realistic Wave Group Excitations", Ocean Engineering, Vol. 120, pp. 256-263.

Anastopoulos, P.A., and Spyrou, K.J., 2017, "Evaluation of the Critical Wave Groups Method for Calculating the Probability of Extreme Ship Responses in Beam Seas", Proceedings of the 16th International Ship Stability Workshop, Belgrade, Serbia, pp. 131-138.

Belenky, V.L., Degtyarev, A.B., and Boukhanovsky, A.V., 1998, "Probabilistic Qualities of Nonlinear Stochastic Rolling", Ocean Engineering, Vol. 25(1), pp. 1-25.

Belenky, V.L., Weems, K.M., Bassler, C.C., Dipper, M.J., Campbell, B.L., and Spyrou, K.J., 2012, "Approaches to Rare Events in Stochastic Dynamics of Ships", Probabilistic Engineering Mechanics, Vol. 28, pp. 30-38.

Belenky, V.L., Glozter, D., Pipiras, V., and Sapsis, T.P., 2016, "On the Tail of Nonlinear Roll Motions", Proceedings of the 15th International Ship Stability Workshop, Stockholm, Sweden, pp. 109-114.

Boccotti, P., 2000, "Wave Mechanics for Ocean Engineering", Book, Elsevier, Oxford, England, ISBN: 978-0-444-50380-0.

Campbell, B.L., Belenky, V.L., and Pipiras, V., 2016, "Application of the Envelope Peaks Over Threshold (EPOT) Method for Probabilistic Assessment of Dynamic Stability", Ocean Engineering, Vol. 120, pp. 298-304.

Kimura, A., 1980, "Statistical Properties of Random Wave Groups", Proceedings of the 17th International Coastal Engineering Conference, Sydney, Australia, pp. 2955-2973.

Masson, D., and Chandler, P., 1993, "Wave Groups: A Closer Look at Spectral Methods", Coastal Engineering, Vol. 20, pp. 249-275.

Mohamad, M.A., and Sapsis, T.P., 2016, "Probabilistic Response and Rare Events in Mathieu's Equation under Correlated Parametric Excitation", Ocean Engineering, Vol. 120, pp. 289-297.

Nathan, A., 1975, "Trigonometric Interpolation of Function and Derivative Data", Information and Control, Vol. 28(3), pp. 192-203.

Ochi, M., 1998, "Ocean Waves: The Stochastic Approach", Book, Cambridge University Press, Cambridge, England, ISBN: 978-0-521-01767-1.

Rainey, R.C.T., and Thompson, J.M.T., 1991, "The Transient Capsize Diagram – A New Method of Quantifying Stability in Waves", Journal of Ship Research, Vol. 35(1), pp. 58-62.

Roberts, J.B., and Vasta, M., 2000, "Markov Modelling and Stochastic Identification for Nonlinear Ship Rolling in Random Waves", Philosophical Transactions of The Royal Society A: Mathematical, Physical and Engineering Sciences, Vol. 358(1771), pp. 1917-1941.

Sclavounos, P.D., 2012, "Karhunen–Loève Representation of Stochastic Ocean Waves", Proceedings of the Royal Society A, Vol. 468(2145), pp. 2574-2594.

Shigunov, V., Themelis, N., and Spyrou, K.J., 2012, "Critical Wave Groups vs. Direct Monte-Carlo Simulations for Typical Stability Failure Modes of a Container Ship", Proceedings of the 11th International Conference on Stability of Ships and Ocean Vehicles, Athens, Greece, pp. 11-20.

Stansell, P., Wolfram, J., and Linfoot, B., 2002, "Statistics of Wave Groups Measured in the Northern North Sea: Comparisons between Time Series and Spectral Predictions", Applied Ocean Research, Vol. 24(2), pp. 91-106.

St. Denis, M., and Pierson, W.J., 1953, "On the Motions of Ships in Confused Seas", Transactions of SNAME, Vol. 61, pp. 280-332.

Su, Z., 2012, "Nonlinear Response and Stability Analysis of Vessel Rolling Motion in Random Waves Using Stochastic Dynamical Systems", Ph.D. Thesis, Texas A&M University.

Tayfun, M.A., 1993, "Joint Distributions of Large Wave Heights and Associated Periods", Journal of Waterway, Port, Coastal and Ocean Engineering, Vol. 119(3), pp. 261-273.

Themelis, N., and Spyrou, K.J., 2007, "Probabilistic Assessment of Ship Stability", Transactions of SNAME, Vol. 115, pp. 181-206.

Themelis, N., and Spyrou, K.J., 2008, "Probabilistic Assessment of Ship Stability Based on the Concept of Critical Wave Groups", Proceedings of the 10th International Ship Stability Workshop, Daejeon, Korea, pp. 115-125.

On Confidence Intervals of Mean and Variance Estimates of Ship Motions

Vladas Pipiras, *University of North Carolina at Chapel Hill*, pipiras@email.unc.edu
Dylan Glotzer, *University of North Carolina at Chapel Hill*, dglotzer@live.unc.edu
Vadim Belenky, *Naval Surface Warfare Center Carderock Division*, vadim.belenky@navy.mil
Michael Levine, *Naval Surface Warfare Center Carderock Division*, michael.d.levine@navy.mil
Kenneth Weems, *Naval Surface Warfare Center Carderock Division,* kenneth.weems@navy.mil

ABSTRACT

The paper describes several approaches to construct confidence intervals for the mean and variance (or standard deviation) of a stationary process, from its sample in a finite observation window. The focus is on the processes arising with ship motions, through computer simulators or qualitative models, that could represent ship roll, pitch and yaw dynamics, bending moments, etc. The considered approaches are based on either estimation of the so-called long-run variance of the process and its square, or self-normalization. The degenerate case of the zero long-run variance is also considered, with ways to recognize it from data. The approaches are illustrated on synthetic processes from (non-)linear random oscillators, and the loads data from Large Amplitude Motion Program.

Keywords: *Mean, Variance, Confidence Intervals, Stationarity, Long-Run Variance, Self-Normalization, Degenerate, (Non-)Linear Random Oscillator, Bandwidth.*

1. INTRODUCTION

The goal of this paper is to present several approaches to constructing confidence intervals for the mean and variance of a stationary process, from its sample in a finite observation window. The focus is on the processes arising with ship motions, through computer simulators or qualitative models, that could represent ship roll, pitch and yaw dynamics, bending moments, etc. A key difficulty in the construction is the need to account for the temporal dependence in the process.

The need of computing confidence interval for roll variance estimate, first appeared when the practical non-ergodicity of nonlinear roll response was encountered. It raised the question of whether the difference between two variance estimates is caused by practical non-ergodicity or it can be explained by the natural variability of an estimate, computed over a finite sample. The technique used in Belenky (2004) accounted for dependence of the data points within the record but used the assumption of normal distribution for computing the variance of the variance estimate.

One of the results of this study was that the utility of assessing statistical uncertainty with confidence interval was appreciated in its own value (Belenky and Weems, 2008). While the assumption of normality remained, the evaluation of confidence interval of an ensemble estimate was attempted.

Further developments led to abandoning the assumption of normality for computation of variance of the variance estimate and for formal derivation of the variance of an ensemble estimate (Belenky, *et al.*, 2013, 2015).

ITTC (2017) also considered a confidence interval of a single significant amplitude and offered recommendation to cutting the estimate of auto-covariance function (the estimate of auto-covariance function loses accuracy for large lags due to the decreasing volume of data).

Two approaches to confidence intervals are considered in this work: the first one is based on estimation of the so-called long-run variance, which is associated with the variance of the sample mean of the process, and the second one is based on the idea of the so-called self-normalization, which does without the need to estimate the long-run variance. Both of these approaches are well known in the Statistics literature but likely less so in Naval Architecture, especially in the case of self-normalization. Some aspects of these approaches are also somewhat specific to the processes of interest in Naval Architecture, especially those that exhibit cyclical patterns (such as e.g. roll motion). In addition to the two approaches above, we also discuss the "degenerate" case when the long-run variance is zero, which requires separate treatment.

The rest of the paper is organized as follows. Sec. 2 concerns confidence intervals for the mean, and Sec. 3 concerns those for the variance (and standard deviation). The degenerate case is considered in Sec. 4. Simulations results are presented in Sec. 5. Conclusions and acknowledgements are found in Secs. 6 and 7.

2. CONFIDENCE INTERVALS FOR MEAN

Let $\{X_t\}_{t\in\mathbb{R}}$ be a stationary process of interest, and $\mu(X) = \mathbb{E}X_t$ be its constant mean. Suppose that the process X_t is observed in the time window $t \in [0,T]$. It is then natural to estimate the true mean $\mu(X)$ through the sample mean

$$\bar{X}_T = \frac{1}{T}\int_0^T X_s\, ds. \qquad (1)$$

The question addressed in this section is that of how to set a confidence interval associated with this sample mean estimate. We also note that, in practice, a process would typically be given through a discrete- rather than continuous-time sample, in which case the integral in Eq. (1) and others below need to be replaced by their discrete analogous.

2.1 Approach based on estimation of long-run variance

To construct a confidence interval associated with $\bar{X}_T$, we need to know its sampling distribution. By the Central Limit Theorem, this distribution is expected to be approximately normal for large T, with mean $\mathbb{E}(\bar{X}_T)$ and variance $Var(\bar{X}_T)$. For the mean of $\bar{X}_T$, we have $\mathbb{E}(\bar{X}_T) = \mu(X)$, which is the true mean of interest. For the variance of $\bar{X}_T$, we have

$$Var(\bar{X}_T) = Cov\left(\frac{1}{T}\int_0^T X_s\, ds, \frac{1}{T}\int_0^T X_v\, dv\right)$$

$$= \frac{1}{T^2}\int_0^T\int_0^T Cov(X_s, X_v)\, dsdv$$

$$= \frac{1}{T^2}\int_0^T\int_0^T Cov(X_{s-v}, X_0)\, dsdv$$

$$= \frac{1}{T^2}\int_{-T}^T (T-|u|)Cov(X_u, X_0)\, du, \qquad (2)$$

where we used the stationarity to write $Cov(X_u, X_v) = Cov(X_{u-v}, X_0)$, made a change of variables $s - v = u, v = v$, and then integrated over v to get a single integral in Eq. (2). Thus, $T \cdot Var(\bar{X}_T) \approx \int_{-\infty}^{\infty} \Gamma_X(u)\, du$ where $\Gamma_X(u) = Cov(X_u, X_0)$ is the auto-covariance function of the process. Summarizing, by the Central Limit Theorem, we thus expect that

$$\bar{X}_T \approx \mathcal{N}\left(\mu(X), \frac{\Pi(X)}{T}\right), \qquad (3)$$

where $\mathcal{N}(\mu, \sigma^2)$ refers to a normal distribution with mean μ and variance σ^2, and

$$\Pi(X) = \int_{-\infty}^{\infty} \Gamma_X(u)\, du. \qquad (4)$$

The quantity $\Pi(X)$ is known as the *long-run variance* of the process X_t.

Based on Eq. (3), a normal approximate confidence interval for $\mu(X)$ is then

$$\left(\bar{X}_T - \frac{z_\alpha\sqrt{\widehat{\Pi}(X)}}{\sqrt{T}}, \bar{X}_T + \frac{z_\alpha\sqrt{\widehat{\Pi}(X)}}{\sqrt{T}}\right), \quad (5)$$

where z_α is a normal critical value for the desired confidence level α (e.g. $z_\alpha = 1.96$ for $\alpha = 95\%$) and $\widehat{\Pi}(X)$ is some estimate of the long-run variance $\Pi(X)$.

Note that the confidence interval (5) requires an estimate $\widehat{\Pi}(X)$ of the long-run variance $\Pi(X)$. There is a considerable literature in Statistics on developing suitable estimators of the long-run variance, going back at least to Parzen (1956), in connection to estimation of a spectral density. Time-domain approaches for discrete time series are studied in the seminal paper by Andrews (1991). Here, in the continuous-time setting, we refer to the work of Lu and Park (2014).

Thus, the long-run variance is commonly estimated in the literature as

$$\widehat{\Pi}(X) = \int_{-T}^{T} K\left(\frac{u}{B_T}\right)\hat{\Gamma}_X(u)du, \quad (6)$$

where B_T (smaller than the sample size T) is referred to as a *bandwidth*, K is a function, known as a *kernel function*, which is symmetric, satisfies $K(0) = 1$ and may have additional properties, and $\hat{\Gamma}_X(u)$ is the sample auto-covariance function defined as, for $u \in [0, T]$,

$$\hat{\Gamma}_X(u) = \frac{1}{T}\int_0^{T-u}(X_{s+u} - \bar{X}_T)(X_s - \bar{X}_T)ds. \quad (7)$$

Examples of kernels K include a truncated (or box) kernel $K(x) = 1$ for $x \in [-1,1]$, and $= 0$ otherwise, for which $\widehat{\Pi}(X) = \int_{-B_T}^{B_T}\hat{\Gamma}_X(u)du$; or the Bartlett (or triangle) kernel $K(x) = (1 - |x|)$ for $x \in [-1,1]$, and $= 0$ otherwise; and others.

The choice of a bandwidth B_T is often made based on the following "optimality" principle. One can show (Lu and Park, 2014) that the bias of the estimator $\widehat{\Pi}(X)$ decays to 0 with increasing T approximately as

$$\mathbb{E}\widehat{\Pi}(X) - \Pi(X) \approx -K_\nu\Lambda_\nu(X)B_T^{-\nu}, \quad (8)$$

where a constant $K_r = lim_{x\to 0}(1 - K(x))/|x|^r$ is related to the kernel function, ν is the largest integer r for which $K_r < \infty$ (e.g. $\nu = 1$ for the Bartlett kernel) and a constant $\Lambda_\nu(X) = \int_{-\infty}^{\infty}|u|^\nu\Gamma_X(u)\,du$ depends on the underlying process X_t. Similarly, the variance of the estimator $\widehat{\Pi}(X)$ decays to 0 with increasing T approximately as

$$\mathbb{E}\left(\widehat{\Pi}(X) - \mathbb{E}\widehat{\Pi}(X)\right)^2 \approx 2\Pi(X)^2\|K\|_2^2 B_T/T, \quad (9)$$

where $\|K\|_2^2 = \int_{-\infty}^{\infty}K(x)^2\,dx$. The "optimal" bandwidth $B_{opt,T}$ is chosen as to minimize the so-called mean square error of $\widehat{\Pi}(X)$, defined as

$$\mathrm{MSE}\left(\widehat{\Pi}(X)\right) = \mathbb{E}\left(\widehat{\Pi}(X) - \Pi(X)\right)^2, \quad (10)$$

which can be shown to be equal to

$$\left(\mathbb{E}\widehat{\Pi}(X) - \Pi(X)\right)^2 + \mathbb{E}\left(\widehat{\Pi}(X) - \mathbb{E}\widehat{\Pi}(X)\right)^2.$$

Substituting here the expressions from Eqs. (8) and (9), and then minimizing with respect to B_T leads to

$$B_{opt,T} = \left(\frac{\nu K_\nu^2\Lambda_\nu(X)^2}{\|K\|_2^2\Pi(X)^2}T\right)^{1/(2\nu+1)}. \quad (11)$$

The difficulty with using the optimal bandwidth $B_{opt,T}$, however, is that it depends on the quantities $\Lambda_\nu(X)$ and $\Pi(X)$ involving the characteristics of the underlying process X_t. One of these quantities, $\Pi(X)$, is even the one we are trying to estimate! At least two approaches have been taken to "get around" this issue:

- Data-driven method,
- Model-driven method.

In the model-driven method, a model would be fitted to data and the constants $\Lambda_\nu(X)$ and

$\Pi(X)$ for the optimal bandwidth be calculated based on this model. The fitted model itself does not necessarily have to be "perfect" but rather is expected to capture some key properties of the data. For processes related to ship motions that exhibit cyclical behaviour, we have been fitting a linear oscillator with white noise excitation (see Sec. 5 below), and computing constants based on these.

In the data-driven method, the idea is to use kernel based estimators of $\Pi(X)$ (as defined in Eq. (6)) and $\Lambda_\nu(X)$(defined as in Eq. (6) but replacing $\hat{\Gamma}_X(u)$ with $|u|^\nu\hat{\Gamma}_X(u)$) with some crude preliminary choice of the bandwidth B_T, for example, $B_T = \sqrt{T}$ or that based on a practical "decorrelation" time (that is, the time beyond which the envelope of the sample auto-correlation function of the process becomes smaller than some prescribed value, e.g. 0.05).

2.2 Approach based on self-normalization

The self-normalization approach allows constructing confidence intervals for the mean without estimating the long-run variance. The unfamiliar reader might be surprised that this is possible at all! In fact, there is some "price" to pay: the confidence intervals will *not* be based on normal distribution and, on average, they tend to be slightly larger. The self-normalization method goes back at least to Lobato (2001) and is summarized nicely in Shao (2015).

To explain the approach, we need a slightly stronger result than the Central Limit Theorem expressed through Eq. (3). By the so-called Functional Central Limit Theorem, it is expected that, for $z \in [0,1]$,

$$\frac{1}{\sqrt{T}}\int_0^{Tz}\big(X_s - \mu(X)\big)\,ds \;\approx \sqrt{\Pi(X)}W(z), \quad (12)$$

where $W(z), z \in [0,1]$, is a standard Wiener process (with the term "standard" referring to $\mathbb{E}W(1)^2 = 1$). Note that by setting $z = 1$, Eq. (12) can also be written as

$$\sqrt{T}(\bar{X}_T - \mu(X)) \approx \sqrt{\Pi(X)}W(1), \quad (13)$$

which is just another way to express the Central Limit Theorem in Eq. (3).

Now, set

$$N_T^2 = \int_0^1 \left(\frac{1}{\sqrt{T}}\int_0^{Tz}(X_s - \bar{X}_T)\,ds\right)^2 dz \quad (14)$$

and note that the quantity inside the square can be expressed as

$$\frac{1}{\sqrt{T}}\int_0^{Tz}\big(X_s - \mu(X)\big)\,ds - z\sqrt{T}(\bar{X}_T - \mu(X)).$$

The Central Limit Theorems in Eqs. (12) and (13) then suggest that

$$N_T^2 \approx \Pi(X)\int_0^1 (W(z) - zW(1))^2\,dz. \quad (15)$$

The key observation now is that both Eqs. (13) and (15) involve the same long-run variance $\Pi(X)$, which would cancel out by taking the ratio. That is, we expect that

$$\sqrt{T}\frac{\bar{X}_T - \mu(X)}{N_T} \approx \frac{W(1)}{\left(\int_0^1 (W(z) - zW(1))^2 dz\right)^{1/2}} =: U_0. \quad (16)$$

This leads to an approximate confidence interval for the mean given by

$$\left(\bar{X}_T - \frac{u_\alpha N_T}{\sqrt{T}}, \bar{X}_T + \frac{u_\alpha N_T}{\sqrt{T}}\right), \quad (17)$$

where u_α is a critical value from the distribution of U_0 for the desired confidence level α. Some critical values for $(U_0)^2$ are tabulated in Lobato (2001). For example, for $\alpha = 90\%$, these yield $u_\alpha = \sqrt{28.31} = 5.32$.

As indicated above, the last point also indicates a potential price to pay. The critical values for U_0 are larger than those for the standard normal, potentially leading to larger confidence intervals. This happens only "potentially," since the relationship between $\sqrt{\hat{\Pi}(X)}$ in the normal confidence interval (5) and N_T in the confidence interval (17) is a

priori not clear. In fact, note that the long-run variance $\Pi(X)$ that $\widehat{\Pi}(X)$ estimates, is deterministic, whereas N_T is random. A relationship as $N_T > \sqrt{\widehat{\Pi}(X)}$ can only be quantified in probabilistic terms.

3. CONFIDENCE INTERVALS FOR VARIANCE

We now turn to estimation of the constant variance

$$\sigma^2(X) = \mathbb{E}(X_t - \mathbb{E}X_t)^2 = \mathbb{E}(X_t^2) - (\mathbb{E}X_t)^2$$

of a stationary process $\{X_t\}_{t\in\mathbb{R}}$. Suppose again that the process X_t is observed in the time window $t \in [0, T]$. It is then natural to estimate the true variance $\sigma^2(X)$ through the sample variance

$$s_T^2 = \frac{1}{T}\int_0^T (X_s - \bar{X}_T)^2\, ds. \qquad (18)$$

The question addressed in this section is that of how to set a confidence interval associated with this sample variance estimate.

Note that a simple-minded approach would be to treat the sample variance in Eq. (18) just as the sample mean of $(X_s - \bar{X}_T)^2$ or, after an approximation, of $(X_s - \mathbb{E}X_s)^2$, and then just apply the approaches outlined in Sec. 2 with X_s replaced by $(X_s - \bar{X}_T)^2$. In fact, this is precisely what is suggested in Sec. 3.2 below for the self-normalization approach, with some justification. For the approach based on the long-run variance (Sec. 3.1 below), on the other hand, a natural bivariate extension of the approach of Sec. 2.1 can be provided that makes no such approximation.

3.1 Approach based on estimation of bivariate long-run variance

Note that the true variance $\sigma^2(X)$ can be expressed as

$$\sigma^2(X) = g(\mathbb{E}X_t, \mathbb{E}(X_t^2)) = g\left(\mathbb{E}\mathbf{X}_t^{(2)}\right), \qquad (19)$$

where $g(x_1, x_2) = x_2 - x_1^2$ is a deterministic function and the notation

$$\mathbf{X}_t^{(2)} = (X_t, X_t^2) \qquad (20)$$

represents a bivariate process consisting of the process itself and its square. Similarly, we can express the sample variance as

$$s_T^2 = g(\bar{X}_T, \overline{X_T^2}) = g\left(\bar{\mathbf{X}}_T^{(2)}\right), \qquad (21)$$

where the bars refer to sample means. The idea now is that the developments of Sec. 2.1 can essentially be repeated for the bivariate process $\mathbf{X}_t^{(2)}$ and its bivariate sample mean $\bar{\mathbf{X}}_T^{(2)}$, and then the functions g of these quantities for the variances be dealt with by using the so-called delta method. The following provides some details.

As in Eq. (3), we expect that

$$\bar{\mathbf{X}}_T^{(2)} \approx \mathcal{N}\left(\mathbb{E}\mathbf{X}_t^{(2)}, \frac{\mathbf{\Pi}(\mathbf{X}^{(2)})}{T}\right), \qquad (22)$$

where $\mathcal{N}(\boldsymbol{\mu}, \boldsymbol{\Sigma})$ refers to a multivariate normal distribution with mean vector $\boldsymbol{\mu}$ and covariance matrix $\boldsymbol{\Sigma}$. Here,

$$\mathbf{\Pi}\left(\mathbf{X}^{(2)}\right) = \left(\pi_{jk}(\mathbf{X}^{(2)})\right)_{j,k=1,2} \qquad (23)$$

is a 2×2 long-run variance matrix of the bivariate process with entries defined as

$$\pi_{jk}\left(\mathbf{X}^{(2)}\right) = \int_{-\infty}^{\infty} \Gamma_{X^j,X^k}(u)\, du, \qquad (24)$$

where $\Gamma_{X^j,X^k}(u) = Cov\left(X_u^j, X_0^k\right)$ is the (cross) auto-covariance function at time lag u. Note that the diagonal entries of the matrix are just the long-run variances of the univariate processes X_t and X_t^2. In a matrix form, one can also write

$$\mathbf{\Pi}\left(\mathbf{X}^{(2)}\right) = \int_{-\infty}^{\infty} \Gamma_{\mathbf{X}^{(2)}}(u) du, \qquad (25)$$

where $\Gamma_{\mathbf{X}^{(2)}}(u) = \left(\Gamma_{X^j,X^k}(u)\right)_{j,k=1,2}$.

The long-run variance matrix $\mathbf{\Pi}(\mathbf{X}^{(2)})$ can be estimated similarly as in Eq. (6), namely,

$$\hat{\mathbf{\Pi}}(\mathbf{X}^{(2)}) = \int_{-T}^{T} K\left(\frac{u}{B_T}\right) \hat{\Gamma}_{\mathbf{X}^{(2)}}(u)du, \quad (26)$$

where, for $u \in [0,T]$,

$$\hat{\Gamma}_{\mathbf{X}^{(2)}}(u) = \frac{1}{T}\int_0^{T-u} \left(\mathbf{X}_{s+u}^{(2)} - \bar{\mathbf{X}}_T^{(2)}\right)' \left(\mathbf{X}_s^{(2)} - \bar{\mathbf{X}}_T^{(2)}\right) ds$$

is the sample auto-covariance function matrix, with the prime indicate a transpose of the row vector.

An optimal bandwidth, based on a principle similar to that described in Sec. 2.1, is given by

$$B_{opt,T} = \left(\frac{\nu K_\nu^2\left(\Lambda_\nu(X)^2 + \Lambda_\nu(X^2)^2\right)}{\|K\|_2^2(\Pi(X)^2 + \Pi(X^2)^2)} T\right)^{\frac{1}{2\nu+1}} \quad (27)$$

(Lu and Park, 2014). In practice, it could be evaluated by using the same two methods, data-driven and model-driven, discussed in Sec. 2.1.

Having an estimate of the long-run variance matrix, we can now construct approximate normal confidence intervals for the variance as follows. By the delta method, it follows from Eqs. (19), (21) and (22) that

$$s_T^2 \approx \mathcal{N}\left(\sigma^2(X), \frac{V(\sigma^2)}{T}\right), \quad (28)$$

where

$$V(\sigma^2) = \nabla g(\mathbb{E}\mathbf{X}_t^{(2)})\, \mathbf{\Pi}(\mathbf{X}^{(2)}) \nabla g(\mathbb{E}\mathbf{X}_t^{(2)})' \quad (29)$$

with $\nabla g(x_1, x_2) = (\partial g/\partial x_1, \partial g/\partial x_2) = (-2x_1, 1)$. In practice, the latter quantity is estimated as

$$\hat{V}(\sigma^2) = \nabla g(\bar{\mathbf{X}}_T^{(2)})\, \hat{\mathbf{\Pi}}(\mathbf{X}^{(2)}) \nabla g(\bar{\mathbf{X}}_T^{(2)})' . \quad (30)$$

Finally, based on Eq. (28), an approximate normal confidence interval for the variance $\sigma^2(X)$ is set as

$$\left(s_T^2 - \frac{z_\alpha\sqrt{\hat{V}(\sigma^2)}}{\sqrt{T}}, s_T^2 + \frac{z_\alpha\sqrt{\hat{V}(\sigma^2)}}{\sqrt{T}}\right), \quad (31)$$

where z_α is a normal critical value for the desired confidence level α

Another application of the delta method also yields confidence intervals for the standard deviation $\sigma(X)$ as

$$\left(s_T - \frac{z_\alpha\sqrt{\hat{V}(\sigma^2)}}{2s_T\sqrt{T}}, s_T + \frac{z_\alpha\sqrt{\hat{V}(\sigma^2)}}{2s_T\sqrt{T}}\right). \quad (32)$$

Alternatively, one could also just take the square roots of the boundary points of the confidence interval in Eq. (31).

3.2 Approach based on self-normalization

As noted in the beginning of Sec. 3, to set a confidence interval for the variance by using the self-normalization approach, the method described in Sec. 2.2 is applied to the process $(X_s - \bar{X}_T)^2$ instead of the process X_s. This effectively assumes that in the self-normalization approach, working with $(X_s - \bar{X}_T)^2$ is the same, in the asymptotic sense for large T, as working with $(X_s - \mathbb{E}X_s)^2$. Some justification for this in a similar setting can be found in Lobato (2001), Sec. 3.

4. DEGENERATE CASE

The discussion in Sec. 2.1 assumes implicitly that the long-run variance $\Pi(X) \neq 0$. What happens in the case when $\Pi(X) = 0$? This case is known as degenerate (e.g. Lee (2010)). Having zero long-run variance is quite plausible for processes associated with oscillatory systems, since their auto-covariance function exhibits naturally an oscillating pattern and thus can integrate to 0.

In the degenerate case, we expect that

$$\int_0^t (X_s - \mu(X))\, ds = V_t - V_0, \qquad (33)$$

where V_t is a stationary process. To avoid mathematical technicalities, we shall not provide a rigorous proof of Eq. (33). But the idea is the following, which should be evident to those familiar with the spectral analysis of stationary processes. In the spectral domain, the degenerate case $\Pi(X) = 0$ is equivalent to the spectral density of the process X_s being 0 at the zero frequency. The effect of integration of the process as on the left-hand side of Eq. (33) translates in the spectral domain to the division of the spectral density by the frequency squared. This operation in most cases would not lead to a stationary process because in that case the resulting spectral density would not be integrable around the zero frequency. But in the case when the original spectral density is zero at the zero frequency, one does expect integrability and hence Eq. (33).

We now turn to interesting consequences of Eq. (33). Note that it implies

$$T(\bar{X}_T - \mu(X)) = V_T - V_0. \qquad (34)$$

In particular, the convergence rate of the sample mean is no longer $\sqrt{T}$ as in Eq. (13) but rather T. Moreover, $V_T - V_0$ does not need to follow a normal distribution. We next explain how Eq. (34) can be used to construct confidence intervals for the mean $\mu(X)$.

Since dependence between V_T and V_0 is expected weak for large T, Eq. (34) implies that

$$T(\bar{X}_T - \mu(X)) \approx V_0' - V_0, \qquad (35)$$

where V_0' is an independent copy of V_0. An approximate (not necessarily normal) confidence interval for the mean can then be constructed as

$$\left(\bar{X}_T - \frac{\widehat{t_\alpha}(V_0' - V_0)}{T}, \bar{X}_T + \frac{\widehat{t_\alpha}(V_0' - V_0)}{T}\right), \qquad (36)$$

where $t_\alpha(V_0' - V_0)$ denotes the $(1+\alpha)/2$ quantile of $V_0' - V_0$ and the hat its estimator. In practice, the value $(-V_0)$ can be estimated as the sample mean of $\int_0^t (X_s - \bar{X}_T)\, ds$, $t \in [0, T]$, and then removed from $V_t - V_0$ to obtain a realization of V_t. The latter realization can then be used to estimate the corresponding quantile of $V_0' - V_0$. More specifically, we use resampling from the realization of V_t to obtain a sample of the values $V_0' - V_0$, from which we then select the desired quantile.

We also note that from a practical perspective, a decision needs to be made on whether the underlying process is in the degenerate case or, equivalently, whether the integrated process $\int_0^t (X_s - \mu(X))\, ds$ can be viewed stationary. This can be achieved by using one of the so-called unit root tests (see Sec. 6 below for an illustration).

Finally, we also note that the discussion above concerns the case of estimating the mean. Turning to estimation of the variance, recall that it involves estimation of the mean of the square process X_t^2. If X_t exhibiting cyclical behavior can be expected to belong to the degenerate case, this is not expected for the square process X_t^2. For example, if X_t is a Gaussian (normal) process, then the auto-covariance function of the square process is $\Gamma_{X^2}(u) = 2(\Gamma_X(u))^2$ and $\Pi(X^2) = \int_{-\infty}^{\infty} \Gamma_{X^2}(u)\, du \neq 0$. If X_t falls into the degenerate case but X_t^2 does not, the confidence interval for $\sigma^2(X)$ can be constructed as

$$\left(s_T^2 - \frac{z_\alpha \sqrt{\widehat{\Pi}(X^2)}}{\sqrt{T}}, s_T^2 + \frac{z_\alpha \sqrt{\widehat{\Pi}(X^2)}}{\sqrt{T}}\right) \qquad (37)$$

in the case of long-run variance estimation, where $\widehat{\Pi}(X^2)$ estimates the long-run variance of the square process X_t^2. This is because the rate of convergence of $\bar{X}_T$ is not $\sqrt{T}$ but T.

5. SIMULATION RESULTS

We shall illustrate here the approaches of Secs. 2 and 3 on several simulated processes. Our goal is not to perform an exhaustive study but rather to make several instructive observations.

We generate processes from a random oscillator model with white noise excitation, satisfying

$$\ddot{X}_t + 2\delta\dot{X}_t + r(X_t) = s \cdot Z_t, \qquad (38)$$

where $\delta > 0$ is a damping parameter, $r(x)$ is a restoring force (stiffness) and Z_t is a white noise excitation with strength s. We consider the linear case for which $r(x) = \omega_0^2 x$ with a natural frequency ω_0, and a piecewise linear (PWL) case with

$$r(x) = \begin{cases} \omega_0^2 x, & \text{if } |x| \le x_m, \\ -k\omega_0^2(x - s(x)x_m) + s(x)\omega_0^2 x_m, & \text{if } |x| > x_m, \end{cases}$$

where $s(x) = sign(x)$, x_m is referred to as the knuckle point (separating the linear and nonlinear regimes) and $k > 0$ enters into the negative slope of the nonlinear part.

For the linear case, we take $\delta = 0.15$, $\omega_0 = 0.6$ and $s = 1$. For the PWL case, we take $\delta = 0.09$, $\omega_0 = 0.6$, $k = 0.1$, $x_m = \pi/6$ and $s = 0.07$. Moreover, $T = 50$ and the observations are gathered at sampling rate 0.1.

Figs. 1-4 present 95% confidence intervals in vertical lines with sample mean estimates in circles for the mean in 100 independent runs. The true mean (here, zero) is indicated by a horizontal line. The different cases (linear and PWL, long-run variance and self-normalization approaches) are indicated in captions.

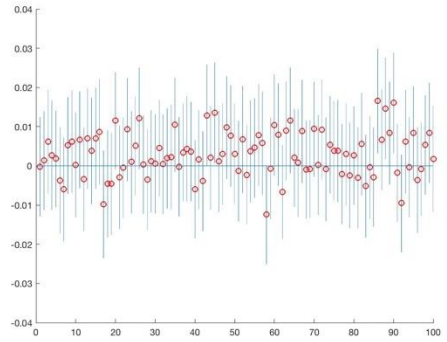

Figure 1: Confidence intervals for the mean in the linear case based on estimation of the long-run variance (data-driven method).

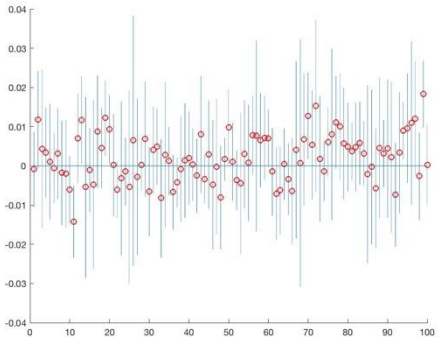

Figure 2: Confidence intervals for the mean in the linear case based on the self-normalization approach.

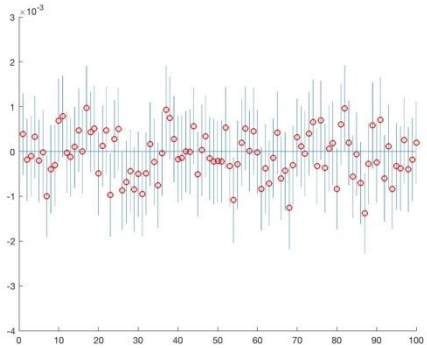

Figure 3: Confidence intervals for the mean in the PWL case based on estimation of the long-run variance (data-driven method).

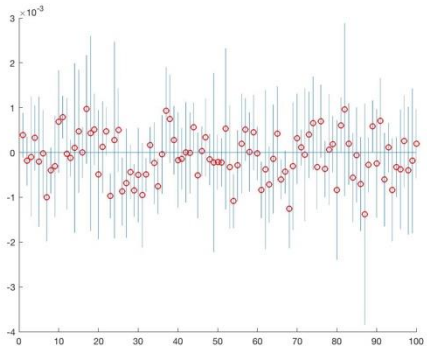

Figure 4: Confidence intervals for the mean in the PWL case based on the self-normalization approach.

Several observations can be made from Figs. 1-4. First, the methods generally seem to perform well (with about 95% of confidence intervals containing the true mean). The approach based on self-normalization tends to produce slightly larger confidence intervals on average. (For better comparison, the y-axis limits in Figs. 1 and 2, and Figs. 3 and 4 are the same.)

Figs. 5-8 provide similar plots when estimating the standard deviation. The same conclusions can be drawn.

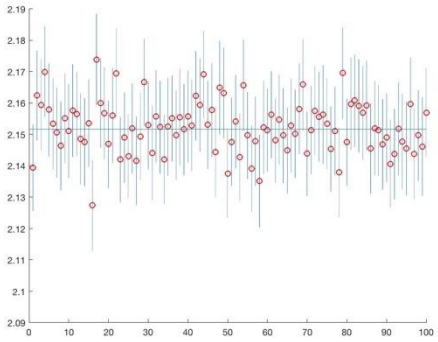

Figure 5: Confidence intervals for the standard deviation in the linear case based on estimation of the long-run variance (data-driven method).

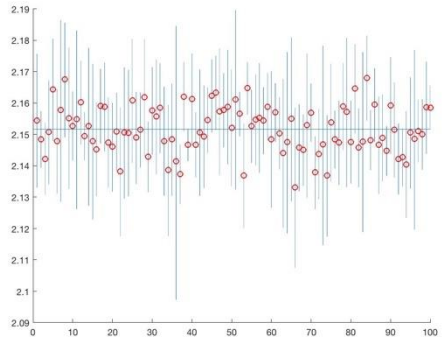

Figure 6: Confidence intervals for the standard deviation in the linear case based on the self-normalization approach.

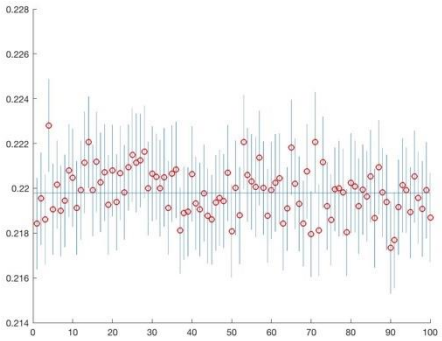

Figure 7: Confidence intervals for the standard deviation in the PWL case on based estimation of the long-run variance (data-driven method).

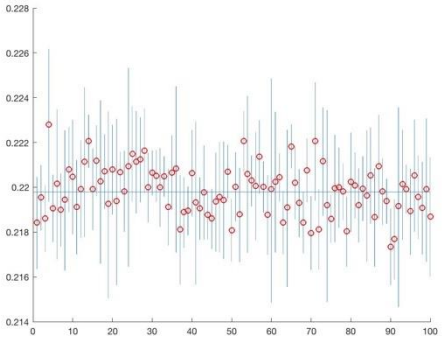

Figure 8: Confidence intervals for the standard deviation in the PWL case based on the self-normalization approach.

6. APPLICATION

We illustrate here the proposed methodology on the data generated by a high-fidelity ship motion simulation code (more specifically, Large Amplitude Motion Program or LAMP of Lin and Yue (1991)). The data in question concerns loads at a particular point of a ship. The time plot of the data is depicted in Fig. 9. The duration of the record is $T = 819$ seconds (with the first 20 seconds discarded), and we consider a sampling rate ranging from $\Delta = 0.02$ to $\Delta = 0.16$. We are interested in providing confidence intervals for the mean and the standard deviation of the underlying process.

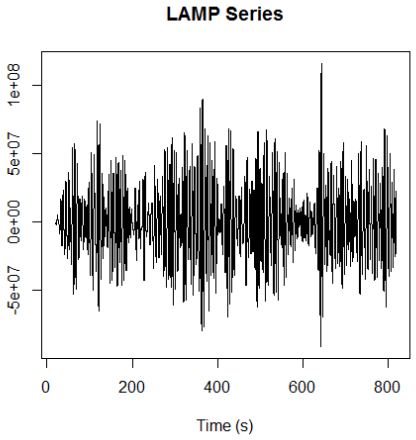

Figure 9: Process data simulated from LAMP.

As a first step, we need to decide whether the data suggest the degenerate case. As discussed in Sec. 4, the degenerate case is associated with the fact that the process $\int_0^t (X_s - \mu(X))\, ds$ is stationary (and vice-versa, the non-degenerate case with the process being non-stationary). The time plot of the sample analogue of the process, namely, the discrete version of $\int_0^t (X_s - \bar{X}_T)\, ds$ is given in Fig. 10. To see whether the non-degenerate case can be assumed, we postulate it as a null hypothesis to be tested. We use the well-known augmented Dickey-Fuller (ADF) test for the null hypothesis - see e.g. Chapter 3 in Pfaff (2008). The test statistic value is -24.3202, and the critical value is -2.58 at $\alpha = 1\%$ (-1.95 at $\alpha = 5\%$). Based on these values, we reject the null hypothesis, i.e. conclude that the data is consistent with the degenerate case.

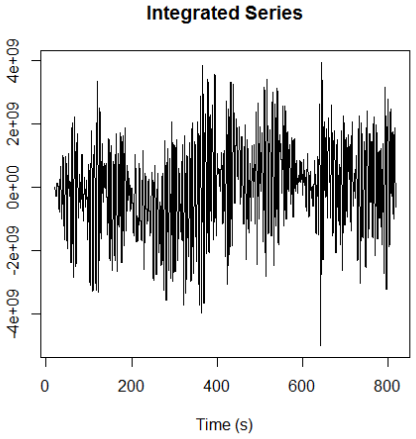

Figure 10: Integrated LAMP process.

Proceeding with the method proposed in the degenerate case, the sample mean of the process with $\Delta = 0.02$ (the smallest available) is 313739.6 and the corresponding 95% confidence intervals for the mean for several choices of Δ are shown in Fig. 11.

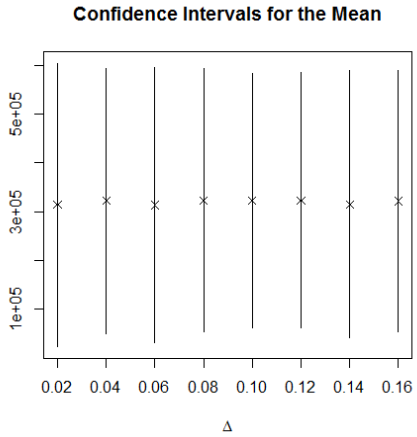

Figure 11: Confidence intervals for the mean from the LAMP series for different sampling rates.

To construct confidence intervals for the standard deviation for the LAMP series, we need only look at the squared series to estimate its long-run variance (see the end of Sec. 4). The squared series and its integrated series

(after removing the mean) are plotted in Figs. 11-12. The ADF test gives a test statistic value of -2.3433; as expected, we consider the squared series to be non-degenerate and proceed with the methods proposed in Sec. 3.

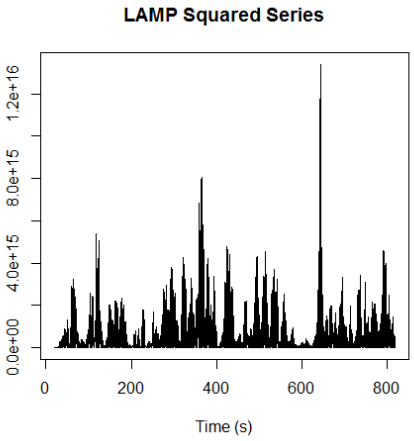

Figure 12: Squared LAMP process.

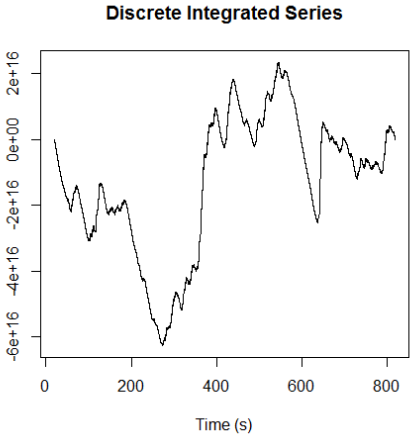

Figure 13: Integrated squared LAMP process.

The sample standard deviation of the process with $\Delta = 0.02$ (the smallest available) is 28119779 and the corresponding 95% confidence intervals for the standard deviation for several choices of Δ are shown in Figs. 14-15, when estimating the long-run variance and using self-normalization. The intervals using self-normalization are slightly smaller here.

Note from Figures 11, 14-15 that our results are roughly invariant to fine sampling rates Δ. On the other hand, one should obviously expect the results to change as Δ becomes larger and larger. In our experience, this happens for Δ around $T_m/4$, where T_m is the modal period of the oscillation associated with the frequencies at which the spectrum is largest.

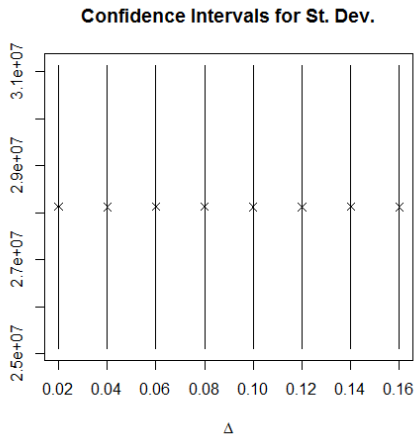

Figure 14: Confidence intervals for the standard deviation from the LAMP series for different sampling rates, based on estimation of the long-run variance.

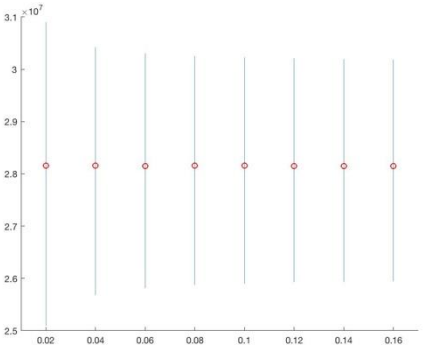

Figure 15: Confidence intervals for the standard deviation from the LAMP series for different sampling rates, based on the self-normalization approach.

7. CONCLUSIONS

In this work, several approaches were considered to set confidence intervals for the mean and variance of a stationary process. The first approach was based on estimation of the so-called long-run variance, through

consideration of an optimal window size (bandwidth) to include sample auto-covariances. The second approach was based on the so-called self-normalization approach, for which the long-run variance does not need to be estimated. Both methods were examined on a simulated and real data. A separate approach was also suggested for the case of zero long-run variance, along with methods to detect it from data.

8. ACKNOWLEDGEMENTS

The work described in this paper has been funded by the Office of Naval Research (ONR) under Dr. Woei-Min Lin and by NSWCCD Independent Applied Research (IAR) program. The work was carried out during a sabbatical stay of the first author at NSWCCD facilitated by NSWCCD Sabbatical and Summer Faculty Program under Dr. Jack Price, who also managed the IAR program.

9. REFERENCES

Andrews, D.W.K., 1991, "Heteroskedasticity and autocorrelation consistent covariance matrix estimation", Econometrica, Vol. 59, pp. 817-858.

Belenky, V.L., 2004, "On Risk Evaluation at Extreme Seas", Proc. 7th Intl. Ship Stability Workshop, Shanghai, P. R. China, pp. 188-202.

Belenky, V. and Weems, K.M., 2008, "Procedure for Probabilistic Evaluation of Large Amplitude Roll Motions", Proc. Osaka Colloquium on Seakeeping and Stability of Ships, Osaka, Japan, pp. 241-248.

Belenky, V., Pipiras, V., Kent, C., Hughes, M., Campbell, B., and T. Smith, 2013, "On the Statistical Uncertainties of Time-domain-based Assessment of Stability Failures: Confidence Interval for the Mean and Variance of a Time Series", Proc. 13th Intl. Ship Stability Workshop, Brest, France, pp. 251-258.

Belenky, V., Pipiras, V., and Weems, K., 2015, "Statistical Uncertainty of Ship Motion Data", Proc. 12th Intl. Conf. on Stability of Ships and Ocean Vehicles STAB 2015, Glasgow, UK.

ITTC, 2017, "Single Significant Amplitude and Confidence Interval for Stochastic Process", 28th International Towing Tank Conference, Wuxi, China, Recommended Procedure 7.5-02-07-01.4, Revision 00.

Lee, J., 2010, "Long-run variance estimation for linear processes under possible degeneracy", Journal of Economic Theory and Econometrics, Vol. 21, pp. 1-22.

Lin, W. M. and Yue, D. K. P., 1991, "Numerical solutions for large amplitude ship motions in the time-domain", Proceedings of the 18th Symposium on Naval Hydrodynamics, Ann Arbor, pp. 41–66.

Lobato, I. N., 2001, "Testing that a dependent process is uncorrelated", Journal of the American Statistical Association, Vol. 96, pp. 1066-1076.

Lu, Y. and Park, J.Y., 2014, "Estimation of long run variance of continuous time stochastic process using discrete sample", Preprint.

Parzen, E., 1957, "On consistent estimates of the spectrum of a stationary time series," Annals of Mathematical Statistics, Vol. 28, pp. 329-348.

Pfaff, B., 2008, "Analysis of Integrated and Cointegrated Time Series with R", Springer Science & Business Media.

Shao, X., 2015, "Self-normalization for time series: a review of recent developments", Journal of the American Statistical Association, Vol. 110, pp. 1797-1817.

Extended Fast Ship Motion Simulations for Stability Failures in Irregular Seas

Kenneth Weems, *NSWCCD (Naval Surface Warfare Center Carderock Division)*, kenneth.weems@navy.mil
Vadim Belenky, *NSWCCD (Naval Surface Warfare Center Carderock Division)*, vadim.belenky@navy.mil

ABSTRACT

The use of time-domain numerical simulations for the development and testing of probabilistic models of stability failures in random, irregular seas requires a challenging combination of speed and accuracy. To begin with, the simulation must be fast enough to observe a statistically significant number of failure or near failure events, which can then be tested against the probabilistic estimates based on extreme value theory or a wave group approach. The simulation must then be accurate and complete enough to capture the physical behavior that drives the event. Of particular importance are the body-nonlinear hydrostatic and Froude-Krylov forces, which are critical for large-amplitude roll motion and may also play a significant role in the surge and sway forces involved in surf-riding and broaching.

This paper presents a 6-DOF volume-based evaluation of the body-nonlinear Froude-Krylov and hydrostatic pressure forces, which retains the inseparability of hydrostatic and Froude-Krylov forces and the effects of large-amplitude relative motion along the length of a ship. Diffraction and radiation forces are presented with coefficients and other simplified models are used for maneuvering and rudder forces, thrust, and resistance. The implementation of the method requires a minimum number of evaluations of the incident wave so it can run at a fraction of the computation cost of traditional surface pressure integration schemes.

Keywords: *Seakeeping, Nonlinear Restoring, Froude-Krylov Forces*

1. INTRODUCTION

The use of time-domain numerical simulations for the investigation of stability failures and other rare events in random, irregular seas requires a challenging combination of speed and accuracy. The rarity of such events requires an extremely long set of simulations in order to observe a statistically significant number of events, while the complexity of the physics precludes the use of excessively simple models.

Hybrid time-domain simulation codes, which generally combine a body-nonlinear calculation of the hydrostatic and Froude-Krylov forces with a potential-flow solution of the wave-body hydrodynamic disturbance forces (radiation, diffraction, etc.) and theoretical or semi-empirical models of viscous and lift forces, have become the principal tool for simulating non-linear ship motion in irregular waves. These tools provide a reasonable compromise between accuracy and speed, and they can readily generate hundreds or thousands of hours of motion data for different realizations of ocean waves. However, they are still far too slow to develop a reliable stochastic model of an extreme event in irregular seas, which may require millions of hours of simulation for each seaway and operating condition.

This has led to the development of extrapolation methods that attempt to

characterize the probability of rare events from limited motion data (see, for example, Belenky *et al.* 2015 and Campbell *et al.* 2015). However, the development, testing, and validation of such methods require extremely large simulation data sets of motions in extreme conditions. To create such data sets, it is necessary to have a simulation capability that captures the problem's essential physics in at least a qualitative sense while running fast enough to produce hundreds of thousands or even millions of hours of data for a ship in a given irregular sea condition (Smith and Zuzick 2015).

In terms of essential physics, the body-nonlinear restoring (hydrostatic) and incident wave (Froude-Krylov) forces are of particular importance. These forces are critical for large-amplitude roll motions and may also play a significant role in the surge and sway forces involved in surf-riding and broaching. France *et al.* (2003) described how these forces were key to describing parametric roll, while Spyrou *et al.* (2014) and others have linked the change of roll stability in waves to large roll events and capsizing in pure loss-of-stability events. While it is relatively straightforward to calculate these forces via direct pressure integration, they can be computationally expensive: they require a very large number of evaluations of the incident wave, and a very large number of component frequencies are required for a statistically valid representation of the irregular wave field for long simulations (Belenky 2011).

To provide a fast but complete calculation of the body-nonlinear Froude-Krylov and hydrostatic pressure forces, a sectional, volume-based evaluation has been developed that retains the inseparability of hydrostatic and Froude-Krylov forces and the effects of large-amplitude relative motion along a ship's length (Weems and Wundrow 2013, Weems and Belenky 2015). Implementing the method requires a minimum number of evaluations of the incident wave, so it can run at a fraction of the computational cost of traditional surface pressure integration schemes.

The calculation was originally implemented in a 3-DOF (heave-roll-pitch) hybrid numerical method incorporating ordinary differential equation (ODE) like models for wave-body perturbation forces. A series of numerical studies demonstrated that the non-linear restoring curve and vertical motion in regular and irregular waves well matches that of the LAMP potential-flow based code (Weems and Belenky 2015).

The 3-DOF volume-based hybrid method has been used to produce a very large number of realizations of irregular sea responses, including a statistically significant number of stability failures, for validating schemes to extrapolate extreme motion responses (Weems *et al.* 2016). Figure 1 shows a sample set of 20 records of the roll response for the ONR Tumblehome ship at a low GM condition (GM=1.5m) in large (Sea State 8) steep stern quartering waves. The seaway is modeled by 220 wave components to provide a statistically independent wave representation over each 30-minute realization. The total calculation time for these 20 realizations was about 7 seconds on a single processor laptop computer. 2,000,000 realizations comprising 1,000,000 hours of data can be generated in a day or so on a modest sized cluster.

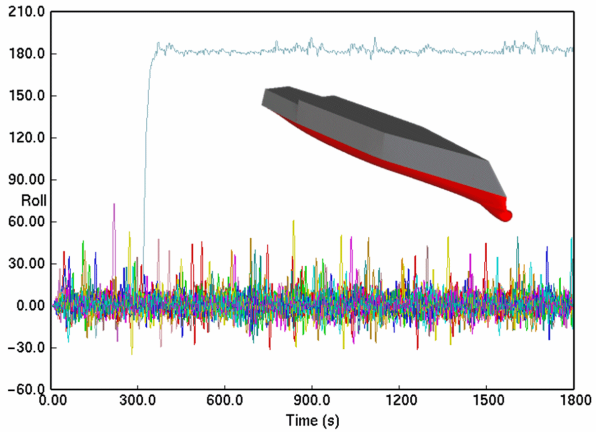

Figure 1: Roll motion for 20 realizations of ONR Tumblehome hull in steep Sea State 8.

The implementation is now being extended to 6-DOF by integrating surge-sway-yaw models for surf-riding and broaching. The resulting system will consider the body-

nonlinear hydrostatic and Froude-Krylov effects on both lateral and vertical motion in waves.

2. COORDINATE SYSTEMS

The formulation and implementation of the simulation considers three coordinate systems:

- Global – Earth-fixed system
- Ship-fixed – System that stays fixed to the ship, moving with its 6-DOF motion
- Local – System that moves with the ship's lateral motion (surge-sway-yaw) but whose X-Y plane stays in global X-Y plane.

In part because of the hybrid nature of the implementation, different forces are computed in different coordinate systems. The local system provides and important link between the 3-DOF horizontal and vertical models and the 6-DOF system.

3. VOLUME-BASED HYDROSTATICS AND FROUDE-KRYLOV FORCES

3.1 Formulation

The core of the present method is the rapid evaluation of the non-linear wave forcing and restoring forces, which is summarized here but described in detail in Weems and Belenky (2015). These forces are generally computed by integrating the incident wave and hydrostatic pressure over the instantaneous wetted hull surface (in the global frame):

$$\mathbf{F}_{FK+HS}(t) = -\rho \iint_{S_B(t)} \left(\frac{\partial \phi_0(x,y,z,t)}{\partial t} + gz \right) \hat{\mathbf{n}}\, ds \qquad (1)$$

$\partial\phi_0(x,y,z,t)/\partial t$ is the pressure of the undisturbed incident wave field and $S_B(t)$ is the instantaneous wetted portion of the hull surface up to the incident wave waterline $\eta(x,y,t)$.

This expression can be expensive to evaluate by pressure integration as it generally involves a large number of evaluations of the incident wave. To provide a much faster calculation, a volume-based calculation scheme has been developed, which requires a minimal number of incident wave evaluations. As it is imperative that the scheme captures the effect of the longitudinal variation of the relative motion, Equation (1) is expressed as the sum of incremental forces calculated on a set of incremental sections distributed along the ship's length:

$$\mathbf{F}_{FK+HS}(t) = \sum_i^n -\rho \iint_{\delta S_B(x_i,t)} \left(\frac{\partial \phi_0}{\partial t} + gz \right) \hat{\mathbf{n}}\, ds \qquad (2)$$

Within each section, a Taylor series expansion (neglecting higher-order derivatives) and the dynamic free surface boundary condition can be used to approximate the distribution of the incident wave pressure as:

$$\begin{aligned} \frac{\partial \phi_0(x,y,z,t)}{\partial t} \cong & -g\eta(x_0,y_0,t) \\ & - g \frac{\partial \eta(x_0,y_0,t)}{\partial x}(x-x_0) \\ & - g \frac{\partial \eta(x_0,y_0,t)}{\partial y}(y-y_0) \\ & + \frac{\partial^2 \phi_0(x_0,y_0,\eta,t)}{\partial t \partial z}(z-\eta) \end{aligned} \qquad (3)$$

Using an overbar to designate the mean or nominal value of the elevation, etc. for a section, the force can be written as:

$$\begin{aligned} \mathbf{F}_{FK+HS}(t) \cong \sum_i^n \iint_{\delta S_B(x_i,t)} & (\rho g \overline{\eta} - gz \\ & + g\overline{\frac{\partial \eta}{\partial x}}(x-x_0) + g\overline{\frac{\partial \eta}{\partial y}}(y-y_0) \\ & + \overline{\frac{\partial^2 \phi_0}{\partial z \partial t}}(z-z_0))\hat{\mathbf{n}}\, ds \end{aligned} \qquad (4)$$

Gauss's theorem can then be applied in order to define the sectional force as an integral of the gradient of the approximated pressure field over the incremental volume. This results in a

volume-based formula for the sectional incident wave and restoring force:

$$\begin{aligned}\mathbf{F}_{FK+HS}(t) \cong & \sum_{i}^{n} \rho g \delta V(x_i,t)\hat{\mathbf{k}} \\ & - \rho g \delta V(x_i,t)\overline{\frac{\partial \eta}{\partial x}}\hat{\mathbf{i}} \\ & - \rho g \delta V(x_i,t)\overline{\frac{\partial \eta}{\partial y}}\hat{\mathbf{j}} \\ & + \rho g \delta V(x_i,t)\overline{\frac{\partial^2 \phi_0}{\partial z \partial t}}\hat{\mathbf{k}}\end{aligned} \quad (5)$$

$\delta V(x_i,t)$ is the instantaneous volume of the submerged portion of the i^{th} section up to the incident wave surface. The first term in Equation (5) is the familiar buoyancy term, but with the volume integrated up to the incident wave surface. The second and third terms are longitudinal and side forces from the gradient of the incident wave pressure field, evaluated in terms of the incident wave slope. The final term can be considered to be a "correction" to the vertical incident wave force, using a linear approximation of the exponential decay of the incident wave pressure field with depth.

Similar expressions for the roll and moments can be derived:

$$\begin{aligned}Mx_{FK+HS}(t) \cong & \sum_{i}^{n} \rho g \delta V(x_i,t) y_{CV}(x_i,t) \\ & - \rho g \delta V(x_i,t)\overline{\frac{\partial \eta}{\partial y}} z_{CV}(x_i,t) \\ & + \rho g \delta V(x_i,t)\overline{\frac{\partial^2 \phi_0}{\partial z \partial t}} y_{CV}(x_i,t)\end{aligned} \quad (5)$$

$$\begin{aligned}My_{FK+HS}(t) \cong & \sum_{i}^{n} -\rho g \delta V(x_i,t) x_{CV}(x_i,t) \\ & + \rho g \delta V(x_i,t)\overline{\frac{\partial \eta}{\partial x}} z_{CV}(x_i,t) \\ & - \rho g \delta V(x_i,t)\overline{\frac{\partial^2 \phi_0}{\partial z \partial t}} x_{CV}(x_i,t)\end{aligned} \quad (6)$$

$x_{cv}(x_i,t)$, $y_{cv}(x_i,t)$, and $z_{cv}(x_i,t)$ are coordinates for the center of the instantaneous submerged volume for the i^{th} section up to the incident wave waterline. The yaw moment can be computed from the sectional lateral forces as:

$$\begin{aligned}Mz_{FK+HS}(t) & \\ = \sum & -\rho g \delta V(x_i,t)\overline{\frac{\partial \eta}{\partial y}}(x_i - x_{cg})\end{aligned} \quad (7)$$

With these formulae, the body-nonlinear Froude-Krylov and hydrostatic restoring forces can be computed with a single evaluation of the incident wave elevation and its derivatives per section. The only major assumption in the derivation of these formulae is the Taylor series expansion of the incident wave pressure, which assumes that the wave slope is constant over the beam and the incremental length of each section. This assumption should be quite reasonable for waves, or wave components in an irregular sea model, that are longer than two times the beam, but the linear approximation of the sinusoidal wave profile will become inaccurate for shorter waves. The expansion considers the vertical pressure gradient to be, at most, linear with depth, so the wave is also assumed to be long compared to the draft of the ship; therefore, any implementation of the $\partial^2\phi_0/\partial z \partial t$ term must carefully treat short waves or wave components. For now, this term is neglected.

3.2 Implementation

The implementation of these volume-based formulae in a time-domain numerical code requires calculating the submerged volume (up to the incident wave) and volume center for a set of ship hull sections at each time step. To expedite the calculation, the sectional volume calculations were implemented using an approach similar to the Bonjean curves used for classic stability analysis. Prior to starting the simulation, a set of x=constant stations are cut through the hull, and the volume and volume moments for the $y>0$ half of the hull section are pre-computed for 0 heel up to each station offset point.

At each time step of a simulation (or heel angle of a restoring curve calculation), the Froude-Krylov and hydrostatic restoring forces for each section are computed by:

1. finding the waterline intersections on each side of the ship,
2. interpolating precomputed volume and center up to the waterline points,
3. correcting for the incremental triangles between the waterline and the centerline (see Figure 2).

Further details of the implementation can be found Weems and Belenky (2015).

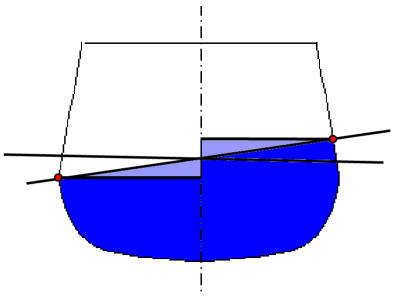

Figure 2: Sample sectional volume calculation for ONR Topsides Series Tumblehome hull.

The sectional forces and moments are then integrated along the ship's length to get the total forces and moments. The procedure is very fast, since it requires only a single evaluation of the incident wave elevation and its derivatives for each station at each time step.

The sectional volume calculations are done in the local coordinate system, and consider only the vertical motion of the section relative to the incident wave surface. The lateral motion (surge-sway-yaw) is only considered when evaluating the incident wave elevation and slope at each section.

4. ADDED MASS AND DAMPING

In the initial implementation of the 6-DOF code, added mass is considered by a constant linear coefficient presented in a standard 6x6 matrix form, which can readily be included on the left-hand side of the equations of motion in the usual way.

Heave, roll, and pitch damping are computed in the ship-fixed frame using constant linear coefficients and the instantaneous roll rate at each step. Optional higher-order roll damping terms are also available. Horizontal damping is included in the maneuvering model described below.

Damping due to appendages – such as rudders, bilge keels, and anti-rolling fins – can be included with global damping coefficients or in appendage force models (see below). Active rudder roll stabilization and anti-rolling fins are not in the code but could readily be added within the time-domain structure.

At the present time, frequency dependent added mass and damping associated with the wave radiation problem is not included. While this is adequate for the qualitative accuracy required for the validation of extrapolation procedures, it is insufficient for the quantitative accuracy required for direct assessment. For this purpose, frequency-dependent coefficients or convolutions based on impulse response functions (IRFs) are being considered but have not yet been implemented. For efficiency, such coefficients or IRFs would be pre-computed using a potential-flow based program such as LAMP (Shin *et al.* 2003).

5. MANEUVERING FORCES

In the context of the 6-DOF code, maneuvering forces are those associated with the ship's steady and unsteady surge, sway, and yaw motion, and are the result of thrust and resistance, hull lift and cross-flow drag, and rudder forces. Their initial implementation here is based on the 3-DOF surf-riding and broaching model of Spyrou (see, for example, Spyrou *et al.* 2007) adapted to the framework of the 6-DOF code.

These forces/moments are evaluated in the local coordinate system and are based on the ship's surge, sway, and yaw rates in the horizontal plane.

5.1 Thrust and Resistance

Propeller thrust and ship resistance are computed from the ship's forward speed in the horizontal plane (u) and propeller rotation rate (n) as:

$$Thr(u,n) = \tau_1 n^2 + \tau_2 nu + \tau_3 u^2 \quad (8)$$

$$Res(u) = r_1 u + r_2 u^2 + r_3 u^3 \quad (9)$$

Where τ_n and r_n are specified coefficients. The propeller rate is constant and is set based on calm water speed, although a speed controller could be easily implemented, as could alternative models.

5.2 Hull Forces

The forces due to hull lift, etc. are computed using standard force derivatives as:

$$F_y = Y_v v\bar{u} + Y_r r\bar{u} + Y_{vv} v|v| + Y_{rr} r|r| + Y_{vr} v|r| \quad (10)$$

$$M_z = N_v v\bar{u} + N_r r\bar{u} + N_{rr} r|r| + N_{rrv} vr^2/\bar{u} + N_{vvr} v^2 r/\bar{u} \quad (11)$$

Here, $\bar{u}$ is an optional speed scaling term computed as the ratio of the instantaneous surge speed to the nominal surge speed corresponding to the force derivatives.

These force/moment derivatives can be measured experimentally or estimated using approximate formulae such as those found in PNA (1989). As part of the present research effort, CFD simulations are being used derive these coefficients (Weems *et al.* 2018).

A roll moment M_x can be calculated by assuming a vertical center of side force F_y or by deriving equivalent roll moment coefficients.

5.3 Rudder and Appendage Forces

Rudder forces have been implemented in two different ways. The first follows traditional force derivatives:

$$F_y = Y_\delta \delta \bar{u}^2 \; ; M_z = N_\delta \delta \bar{u}^2 \quad (12)$$

The second method follows the LAMP appendage model and computes the rudder force by:

1. Evaluate the inflow vector to the rudder due to 6-DOF ship motion and, optionally, orbital wave velocity
2. Compute the effective inflow speed and angle of attack from the velocity vector and rudder deflection
3. Compute the lift and induced drag forces from inflow speed, angle of attack, planform area, and specified or computed lift and drag coefficients
4. Apply the vector lift/drag force at fin position.

The former method provides compatibility with purely ODE models, while the second is more complete and provides more accurate coupling with vertical motions. With both models, the rudder deflection can be scheduled for a turn, etc. or controlled by a PD autopilot:

$$\delta(\psi, \dot{\psi}) = -k_p(\psi - \psi_0) - k_d \dot{\psi} \quad (13)$$

Separate models for forces due to other appendages such as bilge keels and anti-rolling fins have not been implemented but could easily be added following the second rudder force model described above.

6. CROSS-VALIDATION APPROACH

The cross-validation problem appears when different codes or calculation approaches need to be compared. The most straightforward method is comparing the statistics of simulation results, as has been done for the present approach in Weems and Belenky (2015), but it may be difficult to understand the root and importance of what differences there are. For,

indeed, there will be always some discrepancy – caused by differences in geometry presentation, details of numerical implementation, etc. So, in order to demonstrate that both codes reproduce the same physics, one could try to compute some basic characteristic of the relevant problem that reflects its underlying physics.

Considering nonlinear roll, the first characteristic that comes to mind is a backbone curve, which is a trace of the natural frequency of a system with increasing response amplitude (Shin, *et al.* 2003). However, the backbone curve is essentially a characteristic of a 1-DOF dynamical system, so it may not be so basic for a multi-DOF dynamical system. The consideration of what is basic enough for a dynamical system described by a code leads to the somewhat unexpected introduction of a new object, described in the next subsection.

6.1 Concept of Hydrodynamically-Driven Dynamical System (HDDS)

The volume-based model of ship motion has an important property: minimum degrees of freedom. For a ship with a generic hull form (symmetry relative to the centerline, but no symmetry relative to the mid-ship section), a volume-based code can naturally reproduce three degrees of freedom: heave, roll, and pitch. What does "naturally" mean? As described in the previous section, the volume-based algorithm allows a full account of the inseparability of nonlinear Froude-Krylov and hydrostatic forces, which is a major driver for nonlinear phenomena in ship motions. It comes with the price, however. Roll can no longer be modeled separately – even in calm water. The smallest number of degrees of freedom that can be reproduced without introducing artificial constraints is two: pitch and heave. To verify the nonlinear properties of roll, all three degrees of freedom must be considered.

This creates a methodological problem, as almost all nonlinear phenomena associated with the roll motions of ships were studied for single DOF dynamical systems; most instruments were originally developed for models of dynamical systems described by a single ODE. The application of these tools to 3-DOF dynamical system with inseparable Froude-Krylov forces requires a certain amount of caution, as such a dynamical system is essentially a different model. Formally, it is a system of ordinary differential equations, but the restoring and excitation terms are inseparable and related. This model is called a "hydrodynamically-driven dynamical system" or HDDS.

The volume-based calculation described here is, perhaps, the simplest implementation of a HDDS, and is physically equivalent to the LAMP code with its perturbation potential calculation turned off (LAMP-0). Inclusion of diffraction and radiation brings memory to the HDDS, making the dynamical problem even more complex.

The simplest possible HDDS reproducible with volume-based calculations and LAMP-0 is heave-pitch motions without damping or excitation. Thus, comparison between LAMP-0 and volume-based calculations is to be first done with this very basic dynamical system. While favorable comparison does not constitute validation, an unfavorable comparison would indicate the presence of a significant problem.

6.2 Formulation of the Simplest HDDS

As was noted above, the simplest HDDS describes heave and pitch without damping in calm water:

$$\begin{cases} \ddot{\zeta} + f_{\zeta}(\zeta,\theta) = 0 \\ \ddot{\theta} + f_{\theta}(\zeta,\theta) = 0 \end{cases} \tag{14}$$

Where f_ζ and f_θ are restoring terms:

$$f_{\zeta}(\zeta,\theta) = \frac{\rho g\left(V_0 - V(\zeta,\theta)\right)}{M + A_{33}} \tag{15}$$

$$f_{\theta}(\zeta,\theta) = \frac{\rho g V(\zeta,\theta)}{I_{MY} + A_{55}} \times \left(\left(LCB(\zeta,\theta) - LCG\right)\cos\theta + \left(KB(\zeta,\theta) - KG\right)\sin\theta\right) \tag{16}$$

Where V_0 is initial volumetric displacement, M is the mass, I_{MY} is a moment of inertia, and A_{33} and A_{55} are respective added masses. The rest of hydrostatic parameters are expressed as:

$$V(\zeta,\theta)=\int_{-L/2}^{L/2}\int_{0}^{d(x,\zeta,\theta)} b(x,z)dzdx \tag{17}$$

$$LCB(\zeta,\theta)=\frac{1}{V(\zeta,\theta)}\times \int_{-L/2}^{L/2}\int_{0}^{d(x,\zeta,\theta)} xb(x,z)dzdx \tag{18}$$

$$KB(\zeta,\theta)=\frac{1}{V(\zeta,\theta)}\times \int_{-L/2}^{L/2}\int_{0}^{d(x,\zeta,\theta)} zb(x,z)dzdx \tag{19}$$

$$d(x,\zeta,\theta)=(x-LCG)\theta+d_0-\zeta \tag{20}$$

Here, d_0 is the draft corresponding to the initial volumetric displacement V_0.

6.3 Linearization of the Simplest HDDS

Consider the linearization of HDDS (14), with the intention of using the closed-form solution for verification:

$$\begin{cases}\ddot{\zeta}+c_{33}\zeta+c_{35}\theta=0\\ \ddot{\theta}+c_{53}\zeta+c_{55}\theta=0\end{cases} \tag{21}$$

The c coefficients are expressed through respective derivative of the restoring functions (15) and (16):

$$c_{33}=\rho g\frac{A_{WP}}{M+A_{33}} \tag{22}$$

$$c_{53}=\rho g\frac{A_{WP}(LCG-LCF)}{I_{MY}+A_{55}} \tag{23}$$

$$c_{35}=\rho g\frac{A_{WP}(LCG-LCF)}{M+A_{33}} \tag{24}$$

$$c_{55}=\rho g\frac{GM_LV_0+A_{WP}(LCG-LCF)^2}{I_{MY}+A_{55}} \tag{25}$$

A_{WP} is the area of the waterplane and GM_L is the longitudinal metacentric height.

6.4 Linear Solution of the Simplest HDDS

As the system (21) is linear, it has closed-form solution:

$$\begin{aligned}\zeta(t)&=\zeta_{A1}\cos(\omega_1 t-\phi_{\zeta 1})+\\ &\quad\zeta_{A2}\cos(\omega_2 t-\phi_{\zeta 2})\\ \theta(t)&=\theta_{A1}\cos(\omega_1 t-\phi_{\theta 1})+\\ &\quad\theta_{A2}\cos(\omega_2 t-\phi_{\theta 2})\end{aligned} \tag{26}$$

ζ_{A1}, ζ_{A2}, θ_{A1}, θ_{A2}, $\varphi_{\zeta 1}$, $\varphi_{\zeta 2}$, $\varphi_{\theta 1}$, and $\varphi_{\theta 2}$ are arbitrary solution constants depending on the initial conditions $\zeta_0,\dot{\zeta}_0,\theta_0,\dot{\theta}_0$.

$$\omega_{1,2}=\left(0.5(c_{33}+c_{55})\mp\sqrt{0.25(c_{33}-c_{55})^2+c_{35}c_{53}}\right)^{0.5} \tag{27}$$

$$\zeta_{A1,2}=\frac{1}{\kappa_{2,1}-\kappa_{1,2}}\times\sqrt{(\kappa_{2,1}\zeta_0-\theta_0)^2-\left(\frac{\kappa_{2,1}\dot{\zeta}_0-\dot{\theta}_0}{\omega_{1,2}}\right)^2} \tag{28}$$

$$\theta_{A1,2}=\kappa_{1,2}\zeta_{A1,2} \tag{29}$$

$$\phi_{\zeta 1,2}=\arctan\frac{\kappa_{2,1}\dot{\zeta}_0-\dot{\theta}_0}{\omega_{1,2}(\kappa_{2,1}\zeta_0-\theta_0)} \tag{30}$$

$$\phi_{\theta 1,2}=\phi_{\zeta 1,2} \tag{31}$$

The coefficients κ_1 and κ_2 are defined as:

$$\kappa_{1,2}=\frac{\omega_{1,2}^2-c_{33}}{c_{35}}=\frac{c_{53}}{\omega_{1,2}^2-c_{55}} \tag{32}$$

6.5 Verification and Cross-Validation

Detailed consideration of the linear solution may seem to be redundant, but Equation (26) has a property making it important for cross-validation. While generally being bi-harmonic, the solution becomes mono-harmonic for special combinations of initial conditions:

$$\left.\begin{aligned}\kappa_1\zeta_0 &= \theta_0\\ \kappa_1\dot{\zeta}_0 &= \dot{\theta}_0\end{aligned}\right\} \Rightarrow \begin{cases}\zeta(t) = \zeta_{A1}\cos(\omega_1 t - \phi_{\zeta 1})\\ \theta(t) = \theta_{A1}\cos(\omega_1 t - \phi_{\theta 1})\end{cases} \quad (33)$$

$$\left.\begin{aligned}\kappa_2\zeta_0 &= \theta_0\\ \kappa_2\dot{\zeta}_0 &= \dot{\theta}_0\end{aligned}\right\} \Rightarrow \begin{cases}\zeta(t) = \zeta_{A2}\cos(\omega_2 t - \phi_{\zeta 2})\\ \theta(t) = \theta_{A2}\cos(\omega_2 t - \phi_{\theta 2})\end{cases} \quad (34)$$

Equations (33) and (34) establish limitations for the initial conditions and allow two sets of initial conditions to be found that produce mono-harmonic solutions with frequencies ω_1 and ω_2, respectively.

This property can be used for a first verification. This part of verification may be considered successful if the code reproduces a single harmonic response with expected frequency when the initial conditions are set in accordance with Equation (33) or (34). For this verification, the initial displacements or pitch angles must be small enough for the motions to remain in the linear domain.

The cross-validation may then be performed by systematically increasing an initial displacement or rate, running both codes, and observing the frequency of the response. Computation of the response frequency can be done by finding instances of zero-crossing, and calculating periods and frequencies with averaging at the last step. Such an approach allows the evaluation of confidence intervals to account for random error caused by numerical inaccuracies due to time resolution, etc.

Figures 3 and 4 shows the results of such calculations for the frequencies ω_1 and ω_2, respectively for the ONR Tumblehome configuration. LAMP-0 results are plotted in red and results from the volume-based simulations are plotted in blue. The dashed lines show the boundaries of the confidence intervals.

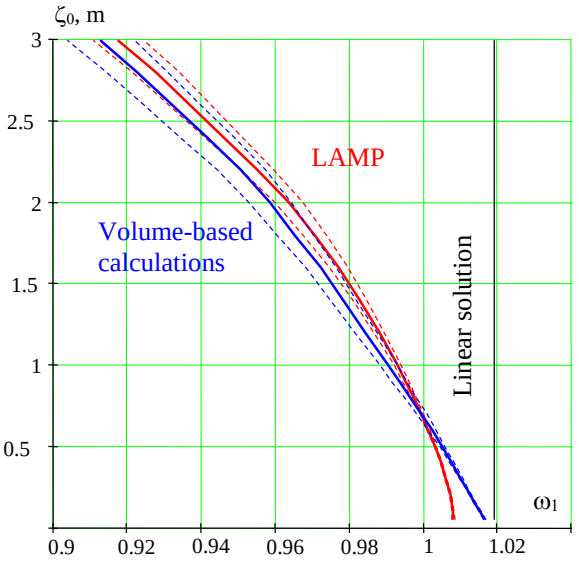

Figure 3: Single-frequency response as a function of initial heave displacement for ω_1.

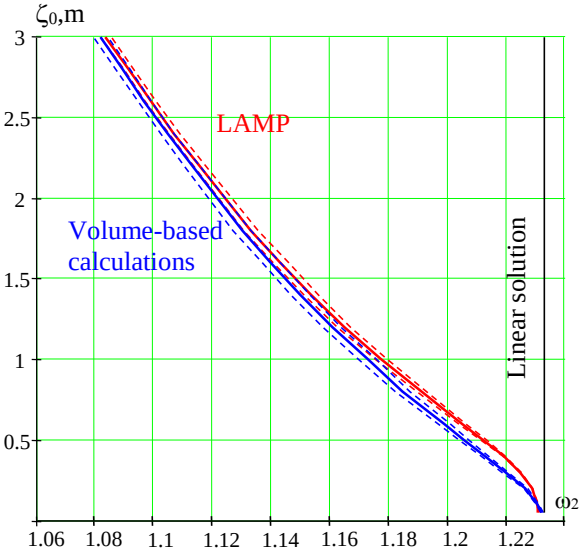

Figure 4: Single-frequency response as a function of initial heave displacement for ω_2.

While some initial discrepancy can be seen for the frequency ω_1 in Figure 3, the similarity of the dependence of the frequency on the initial heave displacement is remarkable, even when the motions were in the substantially nonlinear region. One should also note how quickly the response has diverged from the linear solution.

The identical character of the dependence of the natural heave/pitch frequency on the initial

heave may be used as a proof of a similar nonlinearity being reproduced by both codes. This can be taken as one element of successful cross-validation.

7. CONCLUSIONS AND FUTURE WORK

The practical analysis of stability failures, such as capsizing or extreme roll angle, in irregular seas requires extrapolation techniques that can characterize the probability of these rare events from a relatively short amount of time-domain data. At the same time, the development and testing of such extrapolation methods requires an ability to create very large data sets. There is, therefore, a requirement for very rapid numerical simulations that can capture, at least qualitatively, the principal physical phenomenon of the events. The very large data sets of irregular sea ship motion generated by such methods would allow the direct observation of rare events or near events and provide a basis for building and testing probabilistic models.

As part of developing such a numerical simulation, a very fast calculation method has been developed for the body-nonlinear hydrostatic restoring and incident wave (Froude-Krylov) forcing, which has been identified as a principal contributor to parametric roll and pure loss-of-stability events. The calculation method uses volume-based formulae for the forces and moments on a series of hull stations, and is far faster than traditional methods based on integrating pressure over the hull surface.

The method had previously been implemented in a 3-DOF (heave, roll, pitch) hybrid simulation tool that incorporates simple, coefficient-based models for wave-body hydrodynamics and viscous damping. In this form, it has been successfully evaluated against more advanced simulation tools and extensively used in the development and validation of methods for predicting the probability of large roll motions and capsizing in irregular waves.

The method has now been combined with ODE-based models of non-linear surge, sway, and yaw to create a 6-DOF model for analyzing extreme roll motion due to surf-riding and broaching. Future work will include the continued development and testing of the extended code in order to verify that the method provides a qualitatively accurate representation of 6-DOF ship motions in large waves.

As part of the on-going testing of the approach, this paper has considered the problem of cross-validation – comparisons to another code modeling the same physical phenomena. Detailed consideration of the cross-validation problem led to introduction of a new concept of mathematical modeling of ship motion – the hydrodynamically driven dynamical system (HDDS). These dynamical systems, which are, at some level, described by ODE, have their restoring and excitation terms resulted from numerical integration over the ship surface (or volume). As a result, the restoring and excitation are inseparable and cannot be expressed in closed form.

The simplest possible HDDS describes pitch and heave in calm water. The single harmonic form of this solution can be used to demonstrate that natural frequencies of the results of two different codes are the same, showing an example of one item of the cross-validation between the volume-based calculations and LAMP-0. Other elements of cross-validation remain to be determined.

8. ACKNOWLEDGEMENTS

The work described in this paper has been funded by the Office of Naval Research under Dr. Woei-Min Lin, and a Naval Surface Warfare Center's Independent Applied Research project under Dr. Jack Price. The authors greatly appreciate their support.

The authors are also very grateful for the help of Prof. Kostas Spyrou of the National Technical University of Athens for his assistance in the development and application of

nonlinear models for surge, sway, and yaw in large seas.

9. REFERENCES

Belenky, V.L., 2011, "On Self-Repeating Effect in Reconstruction of Irregular Waves", Chapter 33 of Contemporary Ideas on Ship Stability, edited by M.A.S. Neves, V. L. Belenky, J. O. de Kat, K. Spyrou, and N. Umeda, Springer, pp. 589-598.

Belenky, V., Weems, K., and Lin, W.-M., 2015, "Split-time Method for Estimation of Probability of Capsizing Caused by Pure Loss of Stability," Proceedings of 12th International Conference on Stability of Ships and Ocean Vehicles (STAB 2015), Glasgow, UK.

Campbell, B., Belenky, V., and Pipiras, V., 2015, "Statistical Extrapolation in the Assessment of Dynamic Stability in Irregular Waves", Proceedings of 12th International Conference on Stability of Ships and Ocean Vehicles (STAB 2015), Glasgow, UK.

France, W.M, Levadou, M, Treakle, T.W., Paulling, J.R., Michel, K., and Moore, C., 2003, "An Investigation of Head-Sea Parametric Rolling and its Influence on Container Lashing Systems", Marine Technology, Vol. 40, No. 1, pp. 1-19.

Lewis, Edward (Editor), 1989, Principles of Naval Architecture, Society of Naval Architects and Marine Engineers, Vol. 3.

Shin, Y.S., Belenky, V., Lin, W.-M., Weems, K., and Engle, A., 2003, "Nonlinear Time Domain Simulation Technology for Seakeeping and Wave-Load Analysis for Modern Ship Design", SNAME Transactions, Vol. 111.

Smith, T., and Zuzick, A., 2015, "Validation of Statistical Extrapolation Methods for Large Motion Prediction", Proceedings of 12th International Conference on Stability of Ships and Ocean Vehicles (STAB 2015), Glasgow, UK.

Spyrou, K., Tigkas, I., and Chatzis, A., 2007, "Dynamics of a Ship Steering in Wind", Journal of Ship Research, Vol. 51, No. 2, pp. 160–173.

Spyrou, K.J., Belenky, V., Reed, A., Weems, K., Themelis, N., and Kontolefas, I., 2014, "Split-Time Method for Pure Loss of Stability and Broaching-To", Proceedings of 30th Symposium on Naval Hydrodynamics, Hobart, Tasmania, Australia.

Weems, K. and Belenky, V., 2015, "Rapid Ship Motion Simulations for Investigating Rare Stability Failures in Irregular Seas", Proceedings of 12th International Conference on Stability of Ships and Ocean Vehicles (STAB 2015), Glasgow, UK.

Weems, K., Belenky, V., and Campbell, B., 2016, "Validation of Split-time Method with Volume-Based Numerical Simulation", Proceedings of the 15th International Ship Stability Workshop, Stockholm, Sweden.

Weems, K., Belenky, V., and Spyrou, K., 2018, "Numerical Simulations for Validating Models of Extreme Ship Motions in Irregular Waves", Submitted to 32nd Symposium on Naval Hydrodynamics, Hamburg, Germany.

Weems, K. and Wundrow, D., 2013, "Hybrid Models for Fast Time-Domain Simulation of Stability Failures in Irregular Waves with Volume-Based Calculations for Froude-Krylov and Hydrostatic Force", Proceedings of 13th International Ship Stability Workshop, Brest, France.

Extreme-Value Properties of the Split-Time Metric

Vadim Belenky, *Naval Surface Warfare Center Carderock Division*, vadim.belenky@navy.mil
Kenneth Weems, *Naval Surface Warfare Center Carderock Division,* kenneth.weems@navy.mil
Vladas Pipiras, *University of North Carolina at Chapel Hill,* pipiras@email.unc.edu
Dylan Glotzer, *University of North Carolina at Chapel Hill,* dglotzer@live.unc.edu

ABSTRACT

The paper describes recent developments in the split-time method for estimating the probability of capsizing or large roll angle in random, irregular ocean waves. The split-time method separates a nonlinear and practically not observable problem into two problems of lesser complexity: non-rare and rare. The non-rare problem is associated with an upcrossing of an intermediate level that can be statistically characterized from a sample of practical size. The rare problem is a computation of a "metric," which is a value specific to the considered mode of stability failure and expressing an instantaneous "distance to trouble." For capsizing in waves, a suitable metric is the difference between the roll rate at the instant of upcrossing and the smallest roll rate at that instant of time that leads to the capsizing of the ship following the upcrossing. The metric value is computed using motion perturbation analysis that incorporates the changing physics of the stability failure that otherwise would not be included in any simulation sample of practical size. Theory devised from a piecewise linear model suggest an exponential tail of the metric distribution. A statistical study is presented that confirms that theoretical prediction.

Keywords: *Capsizing, Probability, Split-Time Method*

1. INTRODUCTION

The split-time method associates capsizing with a random variable, referred to as a "metric", exceeding a certain value (Belenky, *et al.* 2016). For capsizing in waves, the metric is essentially the difference between the roll rate at the instant of upcrossing of a certain intermediate roll level and the critical roll rate, computed at this instant.

$$y_i = 1 + \dot{\phi}_{Ui} - \dot{\phi}_{Ci}\,; \quad i = 1,\ldots,N_U \qquad (1)$$

$\dot{\phi}_{Ci}$ is the critical roll rate calculated for the i^{th} upcrossing, and $\dot{\phi}_{Ui}$ is the roll rate observed at the i^{th} upcrossing. The critical roll rate is computed using a series of simulations starting from the instant of upcrossing, perturbing the roll rate at upcrossing until capsizing is observed (see Fig. 1). These calculations can be carried out using an advanced hydrodynamic code with 3 to 6 degrees of freedom and including of diffraction and radiation via a body-linear solution of the wave-body interaction problem (Weems and Belenky, 2017).

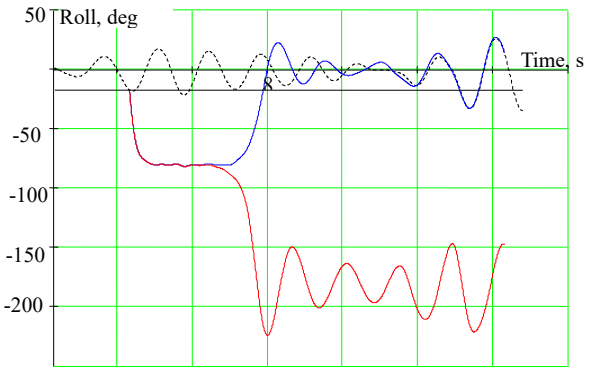

Figure 1: Perturbed and unperturbed roll motions calculated with LAMP-2 / IRF option (Weems and Belenky, 2017).

Belenky *et al.* (2016) used the generalized Pareto distribution (GPD) to model the tail of the distribution for the metric y and then calculating the probability of capsizing as $P(y>1)$. Weems, *et al.* (2016) reported satisfactory statistical validation with 3-DOF (heave, roll, pitch) simulations incorporating a volume-based calculation of the body-nonlinear restoring, which were fast enough to observe capsizing in realistic sea state and loading condition.

2. TAIL OF THE DISTRIBUTION

The application of GPD is based on the second extreme value theorem, which states that essentially any tail above a certain threshold can be approximated with GPD (see, *e.g.* Coles, 2001). The GPD has two parameters: shape ξ and scale σ, and approximates the tail above the threshold μ with the following pdf:

$$f(y)=\begin{cases}\dfrac{1}{\sigma}\left(1+\xi\dfrac{y-\mu}{\sigma}\right)^{-\left(1+\frac{1}{\xi}\right)}; \\ \quad if \quad \mu<y, \quad \xi>0, \quad or \\ \quad\quad \mu<y<\mu-\dfrac{\sigma}{\xi}, \quad \xi<0 \\ \dfrac{1}{\sigma}\exp\left(-\dfrac{y-\mu}{\sigma}\right) \quad ; \\ \quad if \quad \mu<y, \ \xi=0\end{cases} \qquad (2)$$

If the shape parameter ξ is positive, the tail is referred to as "heavy" and extends to infinity. If the shape parameter ξ is negative, the tail is referred to as "light" and has an upper bound y_U, expressed as

$$y_U=\mu-\frac{\sigma}{\xi} \qquad (3)$$

The probability of exceedance of the upper bound is zero. The lowest infinite tail in the GPD family is exponential tail when ξ=0, see Fig 2.

The parameters ξ and σ,are estimated from the data using the maximum likelihood method. These estimates are random numbers; they reflect the random nature of the collected sample and "drive" the statistical uncertainty of the final result – probability of capsizing.

The type of the tail may have a physical reason. Belenky *et al.* (2016a) studied the tail of an oscillator with softening stiffness and found that the tail of solution and its peaks should be heavy. What type of tail does the capsizing metric have?

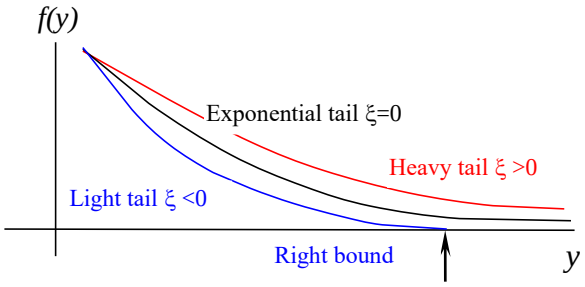

Figure 2 Heavy and light tails

3. PIECWISE LINEAR SYSTEM

A model, based on single DOF ordinary differential equation (ODE) with piecewise linear stiffness, was originally developed for the calculation of probability of capsizing (Belenky, 1993), see Fig. 3. It has seen a number of applications in the analysis of nonlinear (Paroka and Umeda, 2006; Paroka, *et al.* 2006) and has further evolved into the split-time method, in which a numerical code has taken the place of piecewise linear ODE.

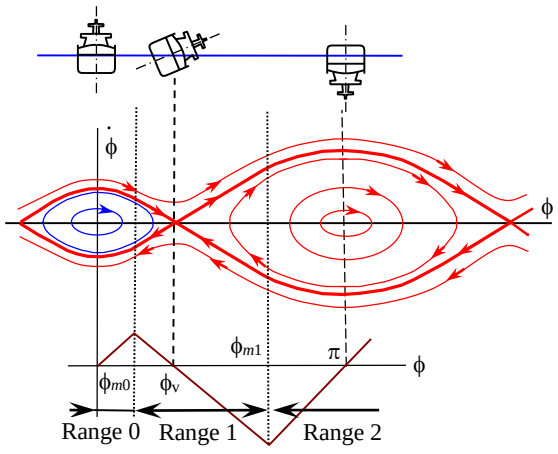

Figure 3 Piecewise linear dynamical system

The piecewise linear dynamical system (PWL) remains an important tool for theoretical research, and may help to answer the question on the type of the tail for metric:

$$\ddot{\phi}+2\delta\dot{\phi}+\omega_0^2 f_L(\phi)=f_{E\phi}(t) \qquad (4)$$

Where δ is a linear damping coefficient, ω_0 is natural frequency, f_L is piecewise linear restoring, shown in Fig. 3 and $f_{E\phi}$ is an excitation that is assumed to be stationary ergodic normal stochastic process.

Consider a general solution of the PWL system after roll just has up-crossed the level ϕ_{m0}, which is the boundary between range 1 and range 0, shown in Fig. 3.

$$\phi = Ae^{\lambda_1 t} + Be^{\lambda_2 t} + p_1(t) \qquad (5)$$

Where p_1 is a particular solution, λ_1 and λ_2 are eigenvalues and A and B are arbitrary constants. One of these eigenvalues is positive while the other is negative:

$$\begin{aligned} \lambda_1 &= -\delta + \sqrt{\omega_\phi^2 k_{f1} + \delta^2} > 0 \\ \lambda_2 &= -\delta - \sqrt{\omega_\phi^2 k_{f1} + \delta^2} < 0 \end{aligned} \qquad (6)$$

k_{f1} is the slope coefficient for Range 1 taken with opposite sign. Whether the capsizing occurs is determined by the sign of the arbitrary constant A (all other terms in equation 5 are limited).

$$A = \frac{\left(\dot{\phi}_U - \dot{p}_{01}\right) - \lambda_2\left(\phi_{m0} - p_{01} - \phi_V\right)}{\lambda_1 - \lambda_2} \qquad (7)$$

$\dot{\phi}_U$ is the roll rate at the instant of upcrossing, p_{01} and $\dot{p}_{01}$ are values of the particular solution and its derivative at the instant of upcrossing. The critical roll rate is associated with a zero-value of the arbitrary constant A

$$\dot{\phi}_C = \lambda_2\left(\phi_{m0} - p_{01} - \phi_V\right) + \dot{p}_{01} \approx -\lambda_2\phi_V \qquad (8)$$

Further details, including why the approximation makes sense, are available from (Belenky, *et al.* 2016). As the critical roll rate (8) is a constant, the metric (1) is a function of a single random argument: the roll rate at instant of upcrossing $\dot{\phi}_U$

$$y = 1 + \dot{\phi}_U - \dot{\phi}_C \qquad (9)$$

If the upcrossings are rare, the probability density function (pdf) of $\dot{\phi}_U$ can be approximated with a Rayleigh distribution (see *e.g.* Leadbetter, *et al.* 1983, p. 201):

$$pdf\left(\dot{\phi}_U\right) = \frac{\dot{\phi}_U}{\sigma_{\dot{\phi}}^2} \exp\left(-\frac{\dot{\phi}_U}{2\sigma_{\dot{\phi}}^2}\right) \quad \dot{\phi}_U > 0 \qquad (10)$$

Where $\sigma_{\dot{\phi}}$ is a standard deviation of roll rates for range 0, *i.e.* without influence of crossings.

From the GPD perspective, the Rayleigh distribution is associated with the GPD having a zero shape parameter, $\xi = 0$, that is, the exponential distribution. This fact is expected and well-known to researchers familiar with the mathematical side of Extreme Value Theory. For example, in the case of a standard normal distribution, which has a similar exponential-like tail as the Rayleigh distribution, such a result in the parallel form of the limiting extreme value distribution (namely, the Gumbel distribution, instead of the exponential) is proved in de Haan and Ferreira (2007), Example 1.1.7.

FITTING EXPONENTIAL DISTRIBUTION

An attempt to fit exponential tail has been described by the authors in (Belenky, *et al.* 2013). Initial validation attempt have shown an overestimation of the true values. Perhaps the procedure of finding the threshold can be rectified by applying more robust methods.

3.1 Goodness-of-fit test

If u is a candidate threshold, a goodness-of-fit test can be used to assess whether the observations y_i above the threshold u follow an exponential distribution. The traditional Kolmogorov-Smirnov (KS) goodness-of-fit is not best for this purpose since the sample size is potentially small and since the parameter of the exponential distribution is unknown (and

thus needs to be estimated). The KS test and its critical values have been modified for the exponential distribution by Stephens (1974). The proposed goodness-of-fit test for the exponential distribution proceeds as follows.

Let $x_j, j = 1, \dots, n$, be the positive peaks $y_i - u$ of the observations above the threshold, which need to be tested for the exponential distribution, the latter forming the null hypothesis H_0. Suppose that x_j are in ascending order. The test statistic for the null hypothesis is defined as

$$D^* = \left(D - \frac{0.2}{n}\right)\left(\sqrt{n} + 0.26 + \frac{0.5}{\sqrt{n}}\right), \qquad (11)$$

where $D = max\{D^+, D^-\}$ with

$$D^+ = \max_{j=1,\dots,n}\left|\frac{j}{n} - z_j\right|, \; D^- = \max_{j=1,\dots,n}\left|z_j - \frac{j-1}{n}\right|,$$

$$z_j = 1 - e^{-\frac{x_j}{\bar{x}}}, \; \bar{x} = \frac{1}{n}\sum_{j=1}^{n} x_j. \qquad (12)$$

The critical values for the test statistic D^* were tabulated by Stephens (1974). For example, for the significance levels 5%, 10%, 20% and 30%, they are given by 1.094, 0.99, 0.88 and 0.795, respectively.

For a range of candidate thresholds, the test statistic D^* could then be computed and a p-value of the test for the exponential distribution be calculated. Since Stephens (1974) tabulated critical values for only a few significance levels, the p-value can be taken as the significance level whose critical value is the largest but still smaller than D^*. A final threshold can be selected as the largest u above which the thresholds have their associated p-value larger than certain significance level. A significance level of 5% seems reasonable but it has been found that for the extrapolation to work, it should be larger, say 10% or above. That is, for the thresholds above the selected one, we should be more certain that the exponential distribution provides an adequate fit. In the figures presented below, results are reported for a range of significance levels.

3.2 Prediction error criterion

A prediction error criterion to select a threshold for the extrapolation with an exponential distribution can be found in Mager (2015). This method is based on the following principle. Let $y_{n,n} \leq \cdots \leq y_{1,n}$ be the order statistics of the observations y_i. A threshold u will be chosen as $u = y_{k+1,n}$ and thus is associated with the $(k+1)th$ largest observation and the index k (or $k+1$). For this $u = y_{k+1,n}$, let also $x_{i,k} = y_{i,n} - u, i = 1, \dots, k$.

The focus of the method is on the so-called mean squared prediction error defined as

$$\Gamma(k) = \frac{1}{k}\sum_{i=1}^{k} E\left(\frac{\hat{x}_{i,k} - Ex_{i,k}}{\sigma_i}\right)^2. \qquad (13)$$

Here, ${\sigma_i}^2 = Var(x_{i,k})$ and $\hat{x}_{i,k}$ is the estimated value of $x_{i,k}$ according to, in our case, the exponential model. These and other quantities will be specified below. But the basic idea behind threshold selection is to choose k which minimizes an estimate of $\Gamma(k)$.

To estimate $\Gamma(k)$, it is first expressed as

$$\Gamma(k) = \frac{1}{k}\sum_{i=1}^{k} E\left(\frac{\hat{x}_{i,k} - x_{i,k}}{\sigma_i}\right)^2 + \frac{2}{k}\sum_{i=1}^{k}\frac{Cov(\hat{x}_{i,k}, x_{i,k})}{{\sigma_i}^2} - 1, \qquad (14)$$

where the equality is proved in Mager (2015), Lemma 4.2. The estimator of $\Gamma(k)$ is then defined as

$$\hat{\Gamma}(k) = \frac{1}{k}\sum_{i=1}^{k}\left(\frac{\hat{x}_{i,k} - x_{i,k}}{\hat{\sigma}_i^2}\right)^2 + \frac{2}{k}\sum_{i=1}^{k}\frac{\widehat{Cov}(\hat{x}_{i,k}, x_{i,k})}{\hat{\sigma}_i^2} - 1, \qquad (15)$$

where hats indicate the estimators. The index $\hat{k}$ for the threshold selection is chosen as that minimizing $\hat{\Gamma}(k)$ over some range of values k. Mager (2015) suggests using the range $[\min(40, 0.02n), 0.2n]$.

To conclude the description of the method, it is necessary to specify the various quantities in the definition of $\hat{\Gamma}(k)$. Under the exponential model, the distributions of the order statistics $x_{i,k}$ are well-known for the exponential model (e.g. Embrechts *et al.* (2013), Example 4.1.5). In particular, with details omitted here, one can show that

$$\sigma_i{}^2 = \sigma^2 \sum_{j=i}^{k} \frac{1}{j^2} \approx \sigma^2 \frac{1}{k}\left(\frac{k+1}{i} - 1\right), \qquad (16)$$

where σ is the mean parameter of the exponential distribution and the approximation is that used by Mager (2015). This quantity can then naturally be estimated through

$$\sigma_i{}^2 = \hat{\sigma}^2 \frac{1}{k}\left(\frac{k+1}{i} - 1\right), \qquad (17)$$

where $\hat{\sigma} = \frac{1}{k}\sum_{i=1}^{k} x_{i,k}$. The estimator $\hat{x}_{i,k}$ of $x_{i,k}$ is defined as follows. One can think of $x_{i,k}$ as the $(1 - \frac{i}{k+1})th$ quantile of the exponential distribution. But for this distribution, this quantile is $-\sigma \log(\frac{i}{k+1})$, which suggests using

$$\hat{x}_{i,k} = -\hat{\sigma} \log(\frac{i}{k+1}). \qquad (18)$$

One can also show (with details omitted) that $Cov(\hat{x}_{i,k}, x_{i,k}) \approx \frac{\sigma^2}{k}\left(\log(\frac{i}{k+1})\right)^2$, suggesting the use of

$$\widehat{Cov}(\hat{x}_{i,k}, x_{i,k}) = \frac{\hat{\sigma}^2}{k}\left(\log(\frac{i}{k+1})\right)^2. \qquad (19)$$

Substituting these quantities into the definition of $\hat{\Gamma}(k)$ leads to the expression

$$\hat{\Gamma}(k) = \hat{\sigma}^{-2} \sum_{i=1}^{k} \left(\frac{k+1}{i} - 1\right)^{-1} \left(x_{i,k} + \hat{\sigma} \log(\frac{i}{k+1})\right)^2 + \frac{2}{k} \sum_{i=1}^{k} \left(\frac{k+1}{i} - 1\right)^{-1} \left(\log(\frac{i}{k+1})\right)^2 - 1, \qquad (20)$$

which also appears in Mager (2015), bottom of p. 64.

4. NUMERICAL TESTS

4.1 Performance indicators

An extrapolation is successful if it predicts the "correct" result, which is the result that would be obtained from a larger dataset where capsizing was actually observed. Testing or validation of an extrapolation technique requires a larger data set that is used to estimate rate of capsizing via direct observation. The latter is taken as the "true" value" to be compared to the estimate extrapolated from a small dataset that may not contain actual capsizes. As both the "true" value and the extrapolated estimates are random variables, they considered equal when their confidence intervals overlap. Repeating the extrapolation for a number of different small data sets (usually 50 or 100) allows the evaluation of the percentage of successful extrapolations, which defines a passing rate (Smith and Zuzick 2015).

Besides the passing rate, the assessment of the performance of different methods of approximation of the distribution tail can be done with:

$$CD = \log \frac{\hat{E}\lambda_U}{\hat{\lambda}_T} \qquad (21)$$

$$RB = \frac{\hat{E}\lambda_E - \hat{\lambda}_T}{\hat{\lambda}_T} \qquad (22)$$

Where, $\hat{E}\lambda_U$ is the upper boundary of extrapolated estimates averaged over the considered extrapolation data sets, $\hat{E}\lambda_E$ is the most probable extrapolated estimate averaged over considered datasets, and $\hat{\lambda}_T$ is the true value estimated from capsizing observations.

The CD value (CD stands for "conservative distance") expresses, in a sense, the practicality of the extrapolation. The upper boundary of the extrapolated estimate is likely to be used for the final answer, to keep the whole procedure conservative. If the upper boundary is too far from the "true" value, the result may be too conservative to be practical. The CD-value shows, on average, by how many orders of magnitude the upper boundary exceeds the true value.

The RB performance indicator (RB, stands for "relative bias") may be helpful to understand what contributes to the inaccuracy. Problems may come from imperfections in the fit of the exponential distribution, so the extrapolation will "miss" the target. However, the extrapolation still may be recognized as successful due to the confidence interval being wide enough to cover the true value.

If the fit is good, the most probable extrapolated estimate may be close to the true value, but there could be simply an insufficient volume of data, resulting in too much statistical uncertainty of the fit. The combination of small RB and large CD points towards this scenario.

4.2 Source of data and results

The "true" value data was taken from Weems, *et al*. (2016) for simulations of the ONR tumblehome top configuration (Bishop, *et al*, 2005) in extreme seas with a significant wave height of 9 m and modal period of 14 s. The ship's heading relative to the direction of wave propagation was varied from 30 to 70 degrees while the speed was fixed at 6 knots. The results, including passing rate, conservative distance (CD) and relative bias (RB), are summarized in Table 1. Extrapolations are performed with both methods of fitting exponential tail: prediction error criterion and goodness-of-fit test. The latter method was repeated for *p*-values from 0.1 to 0.5.

Table 1 Comparison for different exponential tail fit methods

Heading, deg	"True" estimate of capsizing rate, 1/s	Number of capsizings	Predication error criterion			Goodness of fit		
						α=0.1		
			Passing rate	*CD*	*RB*	Passing rate	*CD*	*RB*
35	4.71E-09	12	0.94	1.41	1.20	1.00	1.42	0.32
40	1.70E-08	12	0.98	1.71	5.64	0.92	1.33	2.88
45	7.20E-08	51	0.98	1.35	3.20	0.98	0.95	0.66
50	9.89E-08	7	1.00	1.23	2.64	0.98	1.14	1.79
55	3.25E-07	69	1.00	0.75	0.77	0.98	0.76	0.61
60	2.49E-07	176	0.98	0.88	1.31	0.92	0.89	1.11
65	1.13E-07	80	0.90	1.12	2.82	0.92	0.99	1.54
70	8.48E-09	6	0.98	1.75	7.96	0.86	1.67	7.81

Table 1 Comparison for different exponential tail fit methods (cont.)

Heading deg	Goodness of fit											
	α =0.2			α =0.3			α =0.4			α =0.5		
	Passing rate	*CD*	*RB*	Passing rate	*CD*	*RB*	Passing rate	*CD*	*RB*	Passing rate	*CD*	*RB*
35	1.00	1.75	1.03	1.00	1.84	1.58	1.00	1.90	1.87	1.00	1.98	2.92
40	0.98	1.65	3.93	1.00	1.75	4.16	1.00	1.80	4.68	0.98	1.81	5.11
45	0.98	1.19	1.12	0.96	1.28	1.47	0.98	1.34	1.57	0.98	1.36	1.87
50	1.00	1.27	1.63	1.00	1.32	1.78	1.00	1.36	1.73	1.00	1.38	1.76
55	0.98	0.84	0.30	0.98	0.88	0.31	0.98	0.90	0.30	0.98	0.91	0.29
60	0.98	0.97	0.69	0.96	1.01	0.72	0.96	1.03	0.70	0.96	1.04	0.69
65	0.98	1.16	1.56	1.00	1.21	1.38	0.96	1.22	1.46	0.96	1.24	1.26
70	0.96	1.82	7.07	0.98	1.85	5.45	1.00	1.88	5.37	0.98	1.89	4.52

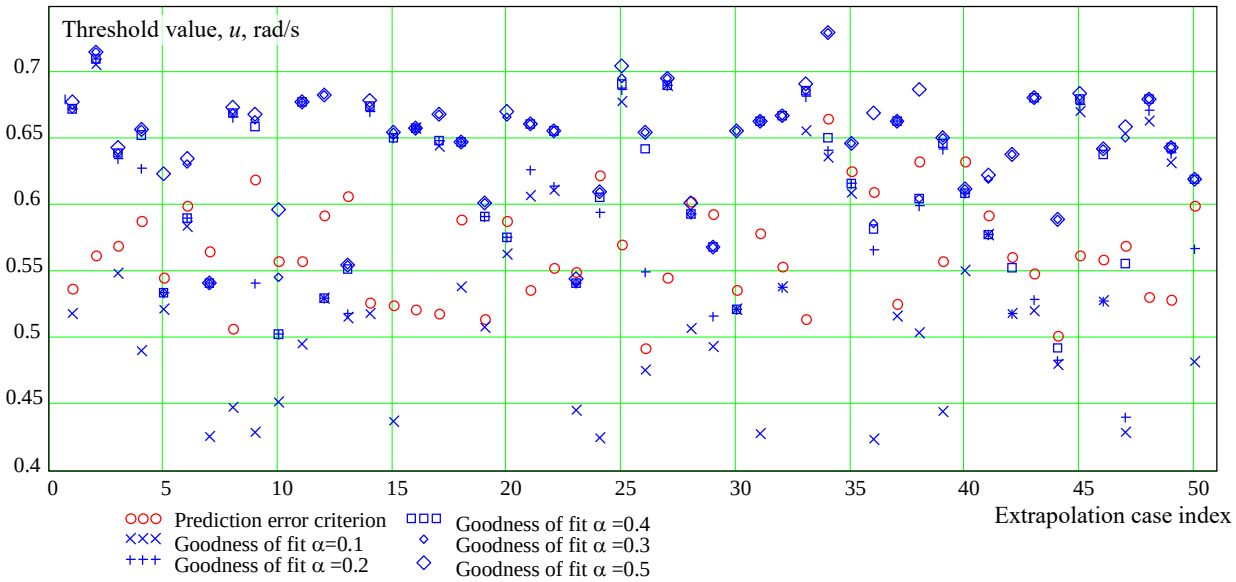

Figure 4: Threshold values obtained with different fit methods for heading 45 deg.

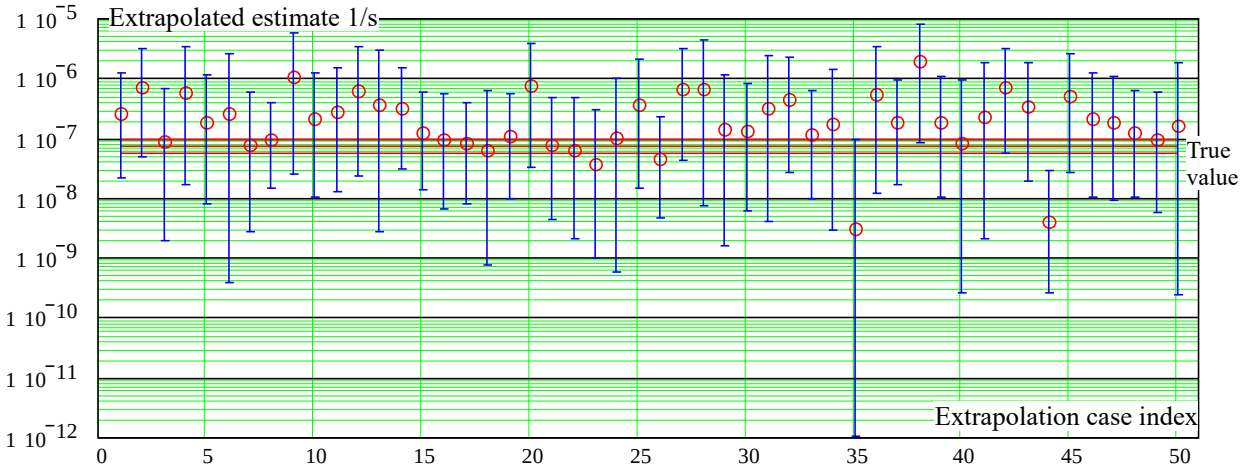

Figure 5: Extrapolation with prediction error method for heading 45 deg. Passing rate 0.98 *CD*=1.35 *RB*=3.2.

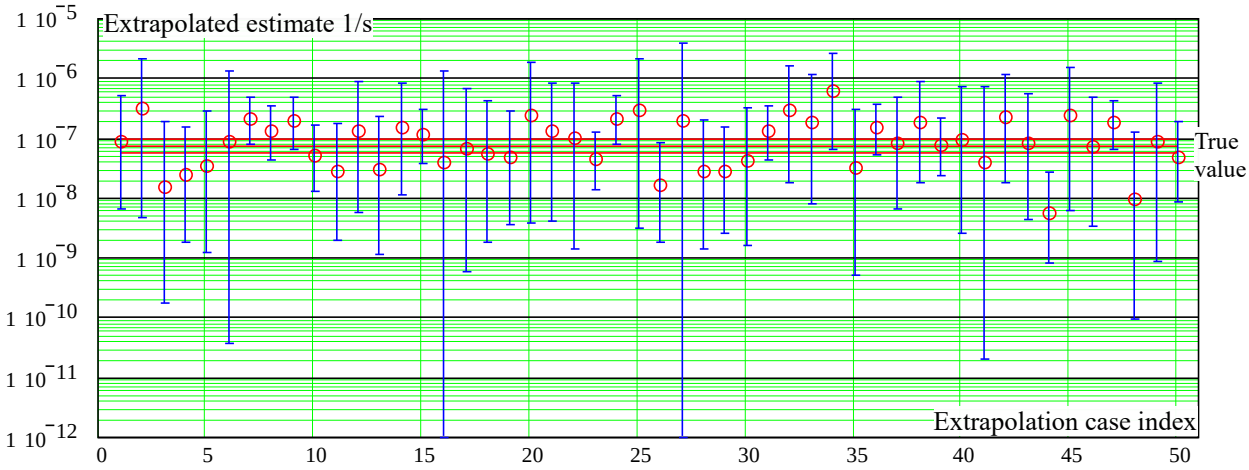

Figure 6: Extrapolation with goodness-of-fit method with α=0.1 for heading 45 deg. Passing rate 0.98 *CD*=0.95 *RB*=0.66.

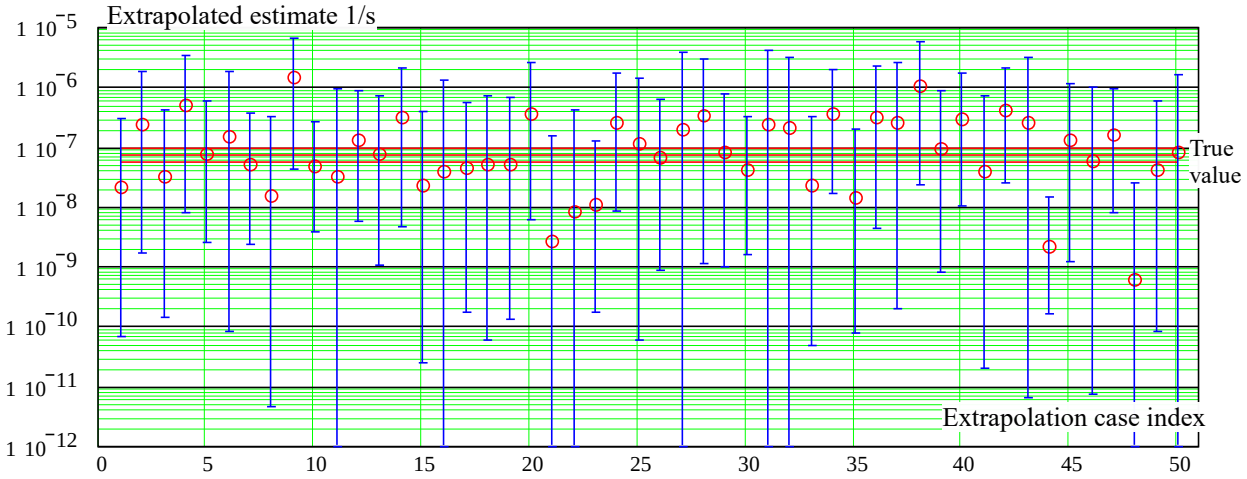

Figure 7: Extrapolation with goodness-of-fit method with α =0.3 for heading 45 deg. Passing rate 0.96 *CD*=1.28 *RB*=1.47.

Table 2 Characteristics of threshold for heading 45 degrees

Value	Prediction error criterion	Goodness of fit				
		α=0.1	α =0.2	α =0.3	α =0.4	α =0.5
Mean, rad/s	0.565	0.536	0.599	0.621	0.641	0.648
Standard deviation, rad/s	0.039	0.08	0.065	0.056	0.046	0.041

Figures 4 through 7 shows intermediate and final results for the relative heading of 45 degrees, which is stern quartering seas. Figure 4 shows the thresholds that have been chosen by both methods: predication error criterion and goodness-of-fit test with different α-values. Increasing α-value obviously increases the threshold, (to be more precise, the fit implies a higher threshold). Thresholds chosen by prediction error criterion are on average between the goodness of fit thresholds with p-values of 0.1 and 0.2, see Table 2.

The estimates of standard deviation in Table 2 suggest that the prediction error criterion provides, on average, a more stable threshold. However, the performance indicators in Table 1 do not support this impression. Figures 8 and 9 plot the performance indicators for 45 degrees heading.

Figures 8 and 9 seem to indicate that the goodness of fit method with α=0.1 provides superior performance. Other headings, however, do not always support this determination. The best performance is highlighted in green in Table 1. Sometimes the prediction error criterion method seems to be better in terms of conservative distance, though only marginally.

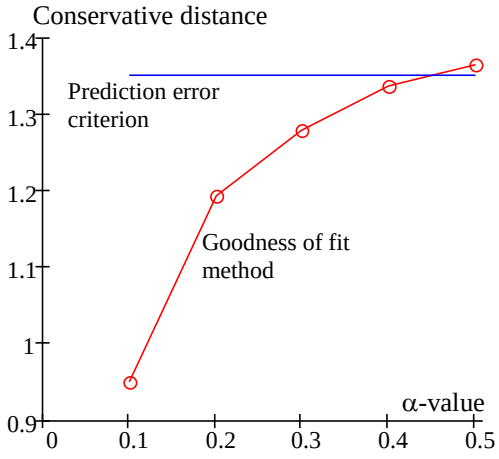

Figure 8 Conservative distance (CD) vs. α-value

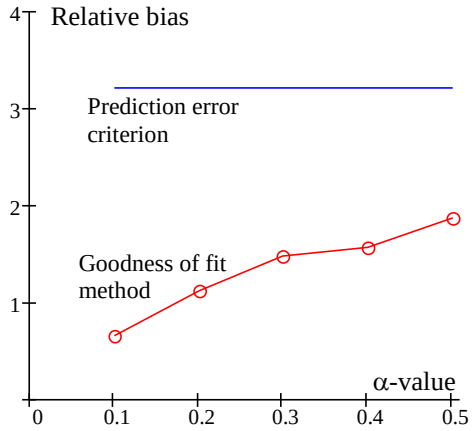

Figure 9 Relative bias (RB) vs. α -value

As far as the passing rate is concerned, all cases except one do have the passing rate equal to or above 0.9. So the error predication criterion method and goodness-of-fit with α-value 0.2 and above will pass the statistical validation as described by Smith and Zuzick (2015). The complete understanding of the performance issues of exponential tail fitting still lies ahead.

5. CONCLUSIONS

Theoretical consideration of the tail of the capsizing metric distribution suggested its exponential character. Two methods of fitting exponential tails were considered in this paper: prediction error criterion and goodness-of-fit test method. Limited statistical validation has confirmed that both methods produce a valid approximation of the distribution tail of the capsizing metric.

Performance analysis, however, has not yet determined which method is superior. Two performance indicators were used: conservative distance and relative bias. Further studies will probably need to include some measure of demand: how far the extrapolation target was from the threshold.

6. ACKNOWLEDGEMENTS

The work described in this paper has been funded by the Office of Naval Research (ONR) under Dr. Woei-Min Lin and by NSWCCD Independent Applied Research (IAR) program.

The participation of Prof. Pipiras was facilitated by NSWCCD Sabbatical and Summer Faculty Program under Dr. Jack Price, who also managed the IAR program.

7. REFERENCES

Belenky, V. L., 1993, "A Capsizing Probability Computation Method", Journal of Ship Research, Vol. 37, pp. 200- 207.

Belenky, V., Weems, K., and Pipiras, V., 2013, "Split-time Method for Calculation of Probability of Capsizing Due to Pure Loss of Stability", Proceedings of the 13th International Ship Stability Workshop, Brest, France, pp. 70-78.

Belenky, V., Glotzer, D., Pipiras, V., Sapsis, T. 2016a, "On the Tail of Nonlinear Roll Motions" Proceedings of the 15th International Ship Stability Workshop, Stockholm, Sweden, pp. 109-114.

Belenky, V., Weems, K., and Lin, W.M., 2016, "Split-time Method for Estimation of Probability of Capsizing Caused by Pure Loss of Stability" in Ocean Engineering, Vol. 122, pp.333-343.

Bishop, R. C., W. Belknap, C. Turner, B. Simon, and J. H. Kim, 2005, "Parametric Investigation on the Influence of GM, Roll damping, and Above-Water Form on the Roll Response of Model 5613." Report NSWCCD-50-TR-2005/027.

Coles, S., 2001, An Introduction to Statistical Modeling of Extreme Values, London, Springer-Verlag.

De Haan, L. and Ferreira, A., 2007, Extreme Value Theory: An Introduction, Springer Science & Business Media.

Embrechts, P., Klüppelberg, C., and Mikosch, T., 2013, Modelling Extremal Events: For Insurance and Finance, Springer Science & Business Media.

Mager, J., 2015, "Automatic threshold selection of the peaks over threshold method", Master's Thesis, Technische Universitat Munchen.

Paroka, D., Okura, Y., Umeda, N., 2006, "Analytical prediction of capsizing probability of a ship in beam wind and waves", Journal of Ship Research, Vol. 50, No. 2, pp. 187-195.

Paroka, D. and Umeda, N., 2006, "Capsizing probability prediction of the large passenger ship in irregular beam wind and waves: comparison of analytical and numerical methods", Journal of Ship Research, Vol. 50, No. 4, pp. 371-377.

Leadbetter, M. R., Lindgren, G, Rootzen, H. 1983, *Extremes and Related Properties of Random Sequences and Processes*, Springer Series in Statistics, Springer-Verlag, New York-Berlin.

Smith, T. C., and Zuzick, A., 2015, "Validation of Statistical Extrapolation Methods for Large Motion Prediction", Proceedings of 12th International Conference on Stability of Ships and Ocean Vehicles (STAB 2015), Glasgow, UK.

Stephens, M. A., 1974, "Edf statistics for goodness of t and some comparisons", Journal of the American Statistical Association, Vol. 69, No. 347, pp. 730-737.

Weems, K., Belenky, V., and Campbell, B., 2016, "Validation of Split-time Method with Volume-Based Numerical Calculations", Proceedings of the 15th International Ship Stability Workshop, Stockholm, Sweden, pp. 103-108.

Weems, K. and Belenky, V., 2017, "Including Diffraction and Radiation into Probabilistic Description of Capsizing", Proceedings of the 16th International Ship Stability Workshop, Belgrade, Serbia, pp. 117-123.

Application of Flooding Simulation for a Detailed Analysis of SOLAS Damage Stability Results

Daniel Lindroth, *NAPA* daniel.lindroth@napa.fi

Pekka Ruponen, *NAPA* pekka.ruponen@napa.fi

Markus Tompuri, *NAPA* markus.tompuri@napa.fi

ABSTRACT

Probabilistic damage stability calculations in SOLAS Chapter II-1 use simplified methods for defining the intermediate stages and phases of flooding. Consequently, cross-flooding and progressive flooding through A-class fire proof boundaries are studied independently, although in reality these often occur simultaneously. A more realistic flooding process can be calculated using time-domain simulation. This paper presents an approach, where a limited group of individual cases from the conventional SOLAS damage stability results are selected for further analysis. This aims at improving the attained subdivision index. The applied case selection method, as well as sample results with a large passenger ship design are presented.

Keywords: *Damage stability; Flooding simulation; Progressive flooding; Passenger ship; SOLAS*

1. INTRODUCTION

The first international damage stability regulations were developed after the sinking of the Titanic in 1912. These requirements were based on a combination of floodable length and margin line criteria. Over the past century, both damage stability criteria and computing capacity have evolved significantly, and nowadays thousands of damage scenarios can easily be calculated. Consequently, deterministic checks have mainly been superseded by probabilistic approaches. The current regulatory trend is towards first principle tools, with more realistic modelling of physics.

Over the years, several tools for time-domain flooding simulation has been developed, as described in Papanikolaou (2007). Yet, the use of these tools in a regulatory context has been mainly limited to cross-flooding studies, Ruponen et al. (2012). Recently, the use of flooding simulation in regulatory analyses was discussed in Ruponen and Lindroth (2016), and a new concept of simulation based safety assessment was introduced by Dafermos and Papanikolaou (2016).

Simulation of all the cases within the probabilistic damage stability framework is still quite time-consuming. Therefore, a new approach, where a limited number of cases are selected for re-analysis with a time-domain flooding simulation is studied.

2. CALCULATION METHODS

2.1 Conventional Approach

Normal damage stability calculations for SOLAS Ch. II-1 are done by applying the lost buoyancy method for the flooded compartments. In addition, for sequential flooding computation, at least two intermediate

filling phases are calculated for each stage, IMO (2008).

Non-watertight flooding boundaries, which are still strong enough to seriously restrict the flow of water, need to be considered in the conventional calculations, IMO (2008). These structures are limited to A-class fire rated boundaries, but further details on how these structures are to be considered in the calculations is not provided in the Explanatory Notes. As a result, the industry standard approach for considering the effects of A-class structures is conservative. In practice, all possible combinations of intact and collapsed A-class boundaries and the resulting alternative paths for progressive flooding are studied independently. From these combinations, the one giving the smallest s-factor is used for the case in question in the evaluation of the attained subdivision index (A-index), IMO (2006). Especially for multi-zone damages, the number of alternative combinations can thus become enormous, as described in Ruponen and Lindroth (2016).

Lemoine et al. (2013) suggested an approach, where more realistic sequences of progressive flooding are defined manually. However, considering the increase in computing capacity, time-domain flooding simulation is now a viable option. In simulation each A-class structure (typically a door) either remain intact, are leaking or collapse from the floodwater pressure.

In addition, cross-flooding can result in intermediate flooding stages. The simplified method described in IMO Resolution MSC.362(92), IMO (2013), is used for calculation of the cross-flooding time. Due to the limitations of this method, simultaneous cross-flooding in different zones cannot be properly evaluated.

2.2 Flooding Simulation

The regulatory damage stability analyses in SOLAS are based on the righting lever (GZ) curve. Consequently, a quasi-static approach is needed so that the s-factor, representing the survivability, can be evaluated for each time step.

The flooding rates through the modelled openings are calculated from Bernoulli's equation, and all water levels are assumed to be horizontal. The ship motions are quasi-static, and the righting lever curve is calculated at every time step.

A pressure-correction method with implicit scheme is used for calculation of the hydrostatic pressures in the flooded rooms and the flow rates in the openings. This approach has proven to be suitable for complex flooding scenarios. The details of the applied method are given in Ruponen (2007).

2.3 S-factor Calculation with Simulation

Simulation provides results as functions of time. Therefore, it is essential to define the threshold times for applying the s-factor formula for intermediate stages and for the final condition, as given in Table 1. In addition, s-final is always applied to the last time step.

Table 1 Application of the s-factor in the analysis of simulation results

time	s-factor	explanation
< 60 s	none	transient flooding
≥ 60 s and < 600 s	intermediate	progressive flooding
≥ 600 s (or equilibrium)	final	slow progressive flooding

2.4 Righting Lever Curve

The s-factor, which in SOLAS is used to represent the survivability level, is calculated from the properties of the GZ curve, IMO (2006). Therefore, the calculation of this curve is of special interest.

The conventional SOLAS approach treats the flooded rooms as lost buoyancy, whereas simulation uses a constant amount of floodwater for the progressive flooding during the GZ curve calculation. Therefore, the GZ curves with the two methods are not identical even if the equilibrium condition for the flooding stage is the same. These differences and their impact have been extensively discussed, along with practical examples, by Ruponen et al. (2018).

3. MODELLING PRINCIPLES

3.1 General

The same 3D model of the ship should be used both for conventional SOLAS damage stability calculations, and for the more detailed analyses using flooding simulation. Therefore, the detailed 3D model, including the doors and other openings in the bulkheads, needs to be prepared first. The 3D model for SOLAS calculations can then automatically be generated from the more detailed model by applying some simplifications.

3.2 Modelling for Simulation

All cross-flooding devices need to be modelled for both simulation and conventional calculations. However, for simulation of progressive flooding through collapsing A-class structures, modelling only the relevant doors and hatches in these structures should be sufficient. The full-scale studies in EU FP7 project FLOODSTAND indicate that the doors are much weaker than the A-class bulkheads around them, Jalonen et al. (2017). The up and down-flooding routes, such as staircases, escape trunks and lifts, should be modelled as separate rooms, extending vertically through the decks.

Special attention needs to be paid on the default status (is it open or closed) of the non-watertight doors, since this can have a notable effect on the time-to-flood, Ruponen (2017). Especially open doors leading to staircases allow for a faster up-flooding, whereas open doors on transverse A-class bulkheads result in a faster equalization of the heeling.

Compartments in way of the damage extent are treated as lost buoyancy, since the same approach is applied in the conventional SOLAS calculations.

3.3 Modelling for Conventional Analysis

A complete 3D model for simulation purpose will contain most of the doors in the ship on all decks within the watertight hull. With such a large number of openings of different types, some simplification is needed when the openings are converted to A-class boundaries for the conventional SOLAS calculations. For example:

- unobstructed openings and doors, such as corridors, can be modelled by directly connecting the rooms to flood simultaneously
- A-class doors can be replaced as A-class boundaries for generation of alternative flooding stages

A detailed modelling of A-class structures is necessary in the subdivided part of the ship. However, evaluating the effect of doors on the bulkhead deck and above is not feasible using the conventional approach. Therefore, to simplify this while remaining on a conservative side, these openings can be converted to unprotected openings instead that will limit the

range of stability, and nullify the s-factor when submerged.

With the help of these simplifications and assumptions, the simulation openings in the 3D model can automatically be converted to suit the conventional damage stability calculations.

4. DETAILED ANALYSIS METHOD FOR SOLAS RESULTS

4.1 Objectives

The main objective of the detailed analysis for the selected damage cases is to check if the ship actually would survive these with a sufficient reserve stability or not. Therefore, the selected cases should have a potential to increase the attained subdivision index (A-index).

4.2 Selection of Cases for Simulation

The cases with the best potential to increase the attained subdivision index are the ones with the highest coefficient:

$$c_i = (1 - s_i) p_i v_{m,i} w_i \quad (1)$$

where s_i is the determining s-factor for the case i, p_i is the probability of the damage and $v_{m,i}$ accounts for the possible horizontal watertight subdivision. The weight coefficient w_i accounts for the probability of the initial condition for case i.

In practice this means that damages with a very small probability p_i or cases with s_i close to 1.0 are not relevant for a further analysis using simulation, since the potential increase of the A-index is small.

Especially cases, where the s-factor during an intermediate flooding stage is nullified when the heel angle is larger than 15° should be re-calculated with time-domain simulation, since the statutory approach can be very conservative. The simulation can capture the progressive flooding behaviour during the intermediate flooding phases realistically, thus avoiding the unrealistic flooding stages with an extensive heel angle. If asymmetric flooding is equalized rapidly, it is still possible to obtain s = 1.0.

On the other hand, cases where the final stage determines the s-factor do not have much potential for improving the A-index, since both calculations methods usually result in the same final equilibrium condition.

In this study, the following criteria were applied for the selection of the cases that were re-analysed using simulation:

- s-factor < 0.98
- First stage (with only the damaged rooms flooded) is not the most critical one
- The ship has positive range of stability, and the steady heel angle is less than 20° in the most critical flooding stage

The selected cases are then sorted based on the highest potential for increasing the A-index, equation (1). Following this, a certain number of cases (e.g. 100) can be re-analysed using flooding simulation, and the improvement to the A-index can be calculated based on the new s-factor from the simulation results.

5. CASE STUDY

5.1 Model and Conventional Results

The presented method for a more detailed analysis of SOLAS damage stability results using flooding simulation is demonstrated with a slightly modified version of the large passenger ship design presented in Kujanpää and Routi (2009). Most notably, a double skin

was added to the engine room compartments following the current practice after the Costa Concordia accident. The ship and the applied subdivision are illustrated in Figure 1.

In principle all A-class boundaries were modelled, apart from smaller rooms that were combined to adjacent rooms for simplification. All doors between the rooms were modelled, and the initial status (open/closed) for each door was selected based on the assumed normal operational condition. All WT doors were considered to be closed.

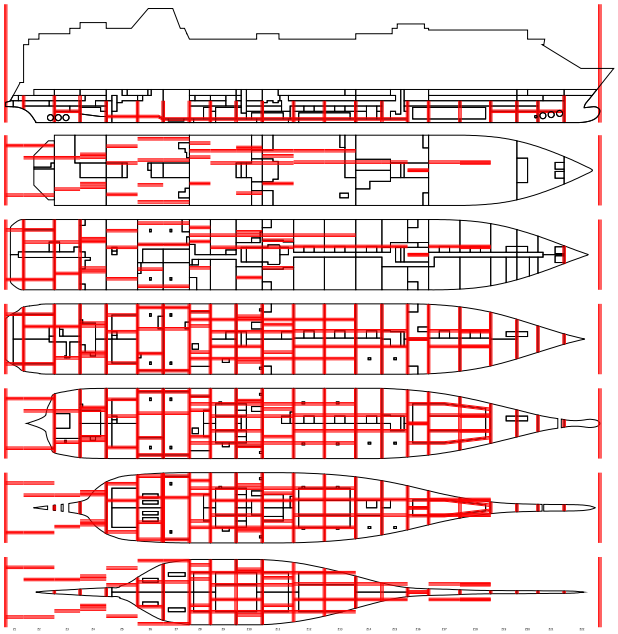

Figure 1 Applied subdivision of the studied large passenger ship

In all calculations, the upper limit of the buoyant hull is two deck heights above the bulkhead deck level.

In order to decrease the number of alternative intermediate flooding stages due to A-class structures with the conventional calculation, only the primary vertical connection (staircase) and up-flooding through escape trunks are considered in each WT compartment. In the flooding simulations however, all modelled routes are considered. Despite of these simplifications, the number of alternative A-class combinations was very high (in some cases over 3000), and consequently only 1, 2 and 3 zone damages were calculated.

For simplicity, immersion of the evacuation routes is not considered. In practice, this is one reason for an s-factor being nullified, but in reality evacuation could successfully be carried out before the routes are flooded.

A summary of the conventional SOLAS Ch. II-1 probabilistic damage stability results is shown in Table 2.

Table 2 Results for the conventional SOLAS calculations (1, 2 and 3 zone damages)

Attained subdivision index	0.7958
Sum of probabilities	0.9120

5.2 Impact of Simulation on the A-index

A total of 150 cases with the highest potential to improve the A-index were re-analysed using time-domain flooding simulation. A constant time step of 5.0 s was used, and the righting lever curve (and s-factor) were calculated at each time step.

A summary of the results is visualized in Figure 2. The achieved increase in the A-index was 0.0529 (i.e. 6.65%). Most notably, for 32 of the re-analysed cases the s-factor was increased from 0 to 1. Only in 10 cases did the simulation also result in an s-factor equal to zero.

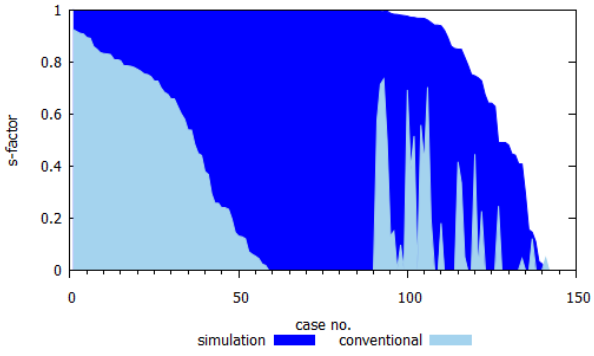

Figure 2 Visualization of the s-factor improvement for the 150 individual simulated cases

The total potential increase in the A-index for the selected 150 cases was 0.0634, of which 83.5% was achieved by the re-analysis using flooding simulation.

5.3 Examples of Detailed Results

In general, the cases, where a significant improvement of the s-factor was obtained with simulation can be divided into two categories:

- The small s-factor from the conventional SOLAS calculation results came from an unrealistic intermediate stage due to the A-class structures
- The initial heeling is larger than 15°, but simulation confirms a rapid equalization of the asymmetric flooding

An example case with an extensive progressive flooding through multiple A-class structures is presented in Figure 3. The simulated development of the heeling angle is shown in Figure 4, and the corresponding results with the conventional SOLAS calculation are presented in Figure 5. When comparing the Figures 4 and 5, it is obvious that there are unrealistic alternative intermediate flooding stages coming from the A-class structures.

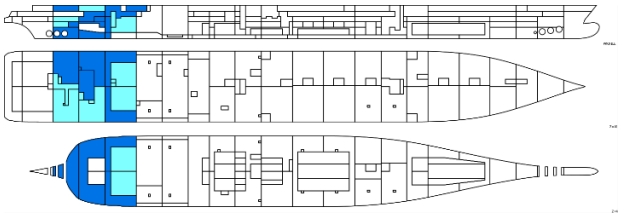

Figure 3 Example case a), the darker filled rooms are the initially damaged ones, and the lighter filling represents progressively flooded rooms

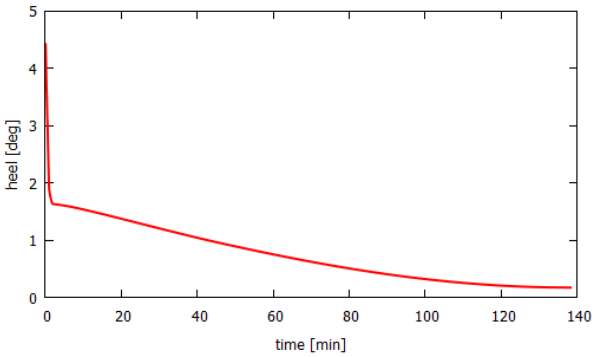

Figure 4 Simulated heel angle for the example a) with slow progressive flooding

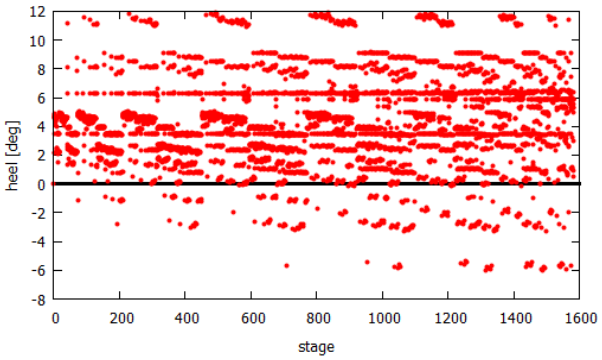

Figure 5 Visualization of heel angles for different flooding stages in the SOLAS calculation for example a)

Figure 6 presents another case, example b), with a rapid equalization of a large initial heel due to flooding. In the SOLAS calculation the s-factor for this case is nullified since during an intermediate stage heel angle exceeds 15°. However, simulation shows that equalization is rapid, Figure 7, and in the final equilibrium condition the heeling is less than 7°, resulting in that the s-factor in reality equals to 1.

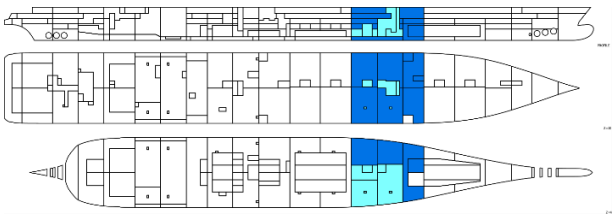

Figure 6 Example case b), the darker filled rooms are the initially damaged ones, and the lighter filling represents progressively flooded rooms

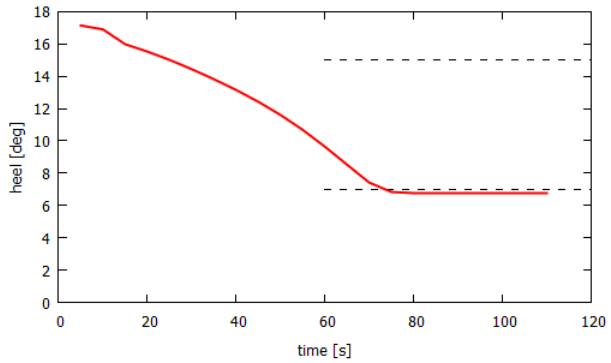

Figure 7 Simulated heel angle for example b); the dashed lines mark the heel limits in s-factor calculation

There are also a lot of alternative flooding stages in the conventional SOLAS calculations with very large heel angles, Figure 8. This is an example of a case, where simulation is actually faster to calculate.

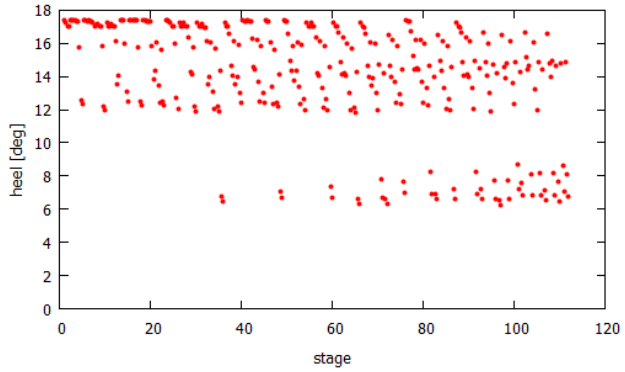

Figure 8 Visualization of heel angles for different flooding stages in SOLAS calculation for example b)

Time-domain flooding simulation allows for a more detailed, and realistic, assessment of the intermediate stages of flooding. These results can be used to better understand and improve the design, e.g. by further equipping it with blow-out panels and down-flooding hatches.

5.4 Computational Performance

With a rather complex inner geometry of the studied ship design, and a large number of A-class doors converted from the simulation model, the conventional calculation with up to 3-zone damages resulted in over 90 000 flooding stages to calculate for three draughts. The calculation time for this was about a day.

The computation time for simulation of the selected 150 cases was about 160 min. In this study a business laptop (Intel® Core™ i7-7820HQ @ 2.9GHz with 24GB of RAM) was used for performing the calculations.

6. CONCLUSIONS

The presented approach offers a possibility to re-evaluate SOLAS damage cases by using a simulation method that accurately reflects the progress of floodwater inside the ship. Applying this method can provide an increased A-index by giving a more accurate picture of the true survivability of the ship.

In several cases the simulation provides a clear advantage since the conventional method gives overly conservative results. Especially for passenger ships with a complex inner geometry, some alternative flooding stages due to A-class structures can be unrealistic. On the other hand, simulation also enables a realistic assessment of flooding progression through the modelled openings, including leaking through and collapsing of closed doors.

For the cases with hundreds of alternative A-class stages, simulation can even enable faster computation times. Thus for ships with a dense internal non-watertight subdivision, simulation of all damage cases for SOLAS index calculation might actually be a feasible option in the future.

Combination of traditional and novel approaches enables a more accurate assessment of the survivability of a ship after a damage. The presented approach allows for the flexibility of the conventional SOLAS calculation, as well as the robustness of simulation for complex flooding scenarios.

7. REFERENCES

Dafermos, G., Papanikolaou, A., 2016. On the Survivability of ROPAX and Cruise Ships - A new approach to differences in design, Proceedings of the 6th Conference on Design for Safety, 28-30 November 2016, Hamburg, Germany, pp. 34-39.

IMO, 2006, "Adoption of Amendments to the International Convention for the Safety of Life at Sea, 1974, as amended", Resolution MSC.216(82).

IMO, 2008, "Explanatory Notes to the SOLAS Chapter II-1 Subdivision and Damage Stability Regulations", Resolution MSC.281(85).

IMO, 2013. "Revised Recommendation on a Standard Method for Evaluating Cross-Flooding Arrangements", Resolution MSC.362(92).

IMO, 2017. "Revised Explanatory Notes to the SOLAS Chapter II-1 Subdivision and Damage Stability Regulations", Resolution MSC.429(98).

Jalonen, R., Ruponen, P., Weryk, M., Naar, H. and Vaher, S., 2017. "A study on leakage and collapse of non-watertight ship doors under floodwater pressure", Marine Structures, Vol. 51, pp. 188-201.

Kujanpää, J., Routi, A-L., 2009. "Concept Ship Design A", FLOODSTAND Deliverable D1.1a.

Lemoine, L., Mahé, F., Morisset, N., Bertin, R., 2013. "Interpretation and Design Implications of Probabilistic Damage Stability Regulation", ISSW2013, Brest, France, pp.214-227.

Papanikolaou, A.D., 2007. "Review of Damage Stability of Ships Recent Developments and Trends", Proceedings of the 10th Int. Symposium on Practical Design of Ships and Other Floating Structures (PRADS 2007), Houston, U.S.A.

Ruponen, P., 2007. Progressive Flooding of a Damaged Passenger Ship, Doctoral Dissertation, Helsinki University of Technology, TKK Dissertations 94.

Ruponen, P., Queutey, P., Kraskowski, M., Jalonen, R., and Guilmineau, E., 2012. "On the calculation of cross-flooding time", Ocean Engineering, Vol. 40, pp. 27-39.

Ruponen, P. and Lindroth, D., 2016. "Time-Domain Simulation for Regulatory Flooding Analysis" PRADS 2016 - Proceedings of the 13th International Symposium on PRActical Design of Ships and Other Floating Structures, 4-8 September 2016, Copenhagen, Denmark.

Ruponen, P., 2017. "On the effects of non-watertight doors on progressive flooding in a damaged passenger ship", Ocean Engineering, Vol. 130, pp. 115-125.

Ruponen, P., Manderbacka, T., Lindroth, D., 2018. "On the calculation of the righting lever curve for a damaged ship", Ocean Engineering, Vol. 149, pp. 313-324.

Study on the Floodwater Dynamics and its Effects on the Damaged Ship Motion

Shuxia Bu, *China Ship Scientific Research Center, Wuxi, China* bushuxia8@163.com

Min Gu, *China Ship Scientific Research Center, Wuxi, China* gumin702@163.com

Jiang Lu, *China Ship Scientific Research Center, Wuxi, China* lujiang1980@aliyun.com

Ke Zeng, *China Ship Scientific Research Center, Wuxi, China* 398638829@qq.com

ABSTRACT

The motion responses of damaged ship are affected not only by external wave excitations, but also by internal liquid loads of water flooding. The floodwater dynamics are very important to predict ship motion under the damaged condition. In this paper, in order to investigate the effect of floodwater dynamics on damaged ship motion, the numerical simulation method is studied based on the unsteady RANS equations combined with the VOF method by taking one damaged compartment as an example. The accuracy of the numerical simulation method is verified by one exist model test and the floodwater dynamics of different opening shapes are studied. Then the large roll motion of one damaged ship is studied considering the effects of inflow and outflow of water through damaged opening based on the three dimensional time domain potential theory and viscous flow theory. The results show that the floodwater dynamics are related with the damaged opening shapes, and the motions of damaged ship are significantly influenced by the flooding water dynamics.

Keywords: *damaged ship motion, floodwater dynamics, different damaged opening shapes, air compressibility*

1. INTRODUCTION

The performance of damaged ship in waves is influenced not only by the external excitation of waves, but also by the internal loads of the fluid flow and sloshing. At the same time, the dynamic characteristics of the liquid flow are also affected by the motion of the ship. The liquid flowing into the ship will change the ship mass and buoyancy, as well as the internal and external exchange of wave mass and energy, which will lead to the internal sloshing and the ship motion. Obviously, the fluid flowing into the compartment has a significant effect on ship stability and safety, even lead to the capsizing of ship.

For the study of damage dynamics, some research methods have also been developed. Jasionowski & Vassalos (2001) developed a time domain numerical simulation method for damaged ship based on the potential theory, in which the inflow and outflow of water through the openings is determined by the modified empirical Bernoulli`s equation. The motion responses for one RoRo ship calculated by this method are in good agreement with model tests. Umeda & Kamo (2004) analyzed the theoretical modeling of damaged ship by multiple time scale expansion, in which the interaction between slow and fast motion can be taken into account. They also studied the motion responses of one pure car carrier with

multiple decks. The research showed that it is difficult to predict the survivability of damaged ship based on the static assumption even in calm water. Spanos & Papanikolaou (2007) analyzed the capsizing time of one damaged Ro-Pax in waves by nonlinear hydrodynamic method, and the statistical simulation method is used to consider the change and uncertainty of the viscous parameters. The ship motions are solved by linear potential flow theory and nonlinear FK forces, and the flow problem is solved by the quasi static method based on the Bernoulli equation. van Walree et al. (2007) analyzed the capsizing problem of one towed fishing boat by this method. In addition, the shallow water equation is also used to simulate the physical characteristics of the internal flow inside the compartment. Chang et al. (1998) calculated the dynamic characteristics of the internal flow. Santos et al. (2006, 2008) studied the motions of one damaged RoPax in random waves and compared with the model tests. In this method, the ship motion is solved in time domain, and the partial differential equation is used to describe the characteristics of water accumulation on the main deck. This improved model can display the nonlinear characteristics of the flow inside the compartment.

Valanto (2007) reports the studies of HSVA and TUHH on Estonia accidents. The Rolls program is used to simulate the ship motion in waves. The sloshing of internal liquid in car deck is considered, and a possible sinking scene is deduced by analyzing the possible form of motion.

The authors of this paper has analyzed the restoring moments of one damaged RoRo ship, and the motion responses of the damaged ship are also simulated by 4DOF (sway-heave-roll-pitch) coupled mathematical models.

CFD simulation method can simulate the dynamic characteristics of flow very well. It is a common method for studying the process of the water inflow and outflow through damaged openings, as well as the internal liquid flow and sloshing. Cho et al. (2006) analyzed the influence of compartment geometry opening, the internal layout and the air compressibility on the flow. Nabavi et al. (2006) analyzed the influence of damaged geometric parameters on the discharge rate of water flow on deck, and the results are compared with model tests. The results show that the longitudinal waves will lead to the fluctuation of the discharge coefficient. Gao & Vassalos (2011) analyzed the hydrostatic characteristics of the section of one damaged barge by forced and free motions. Strasser (2010), Gao (2011) simulated the transient and progressive flooding of a damaged barge in clam water. Cho (2006) simplified the compartment of Estonia, and conducted a systematically research on the damaged flow of different opening shapes. In the model tests, six different opening shapes are selected, and the influence of the internal compartment layout and air compressibility are studied. These model tests are also one of the common used data for the study of damaged flow.

In this paper, we also use this kind of model. Firstly, the numerical simulation method for ingress and egress of this model are studied, and the calculated results of inlet 1 are compared with the model tests of Cho (2006). Secondly, the parametric roll of C11 containership is calculated by an in-house three dimensional panel method, which is validated by model tests. Finally, the influence of the fluid inflow through damaged openings on the parametric roll is studied, assuming the damaged compartment is one part of the C11 containership.

2. DAMAGED FLOW CALCULATION

2.1 Calculation model

The shape of the calculation model is shown in Figure 1, and the particular parameters are shown in table 1.

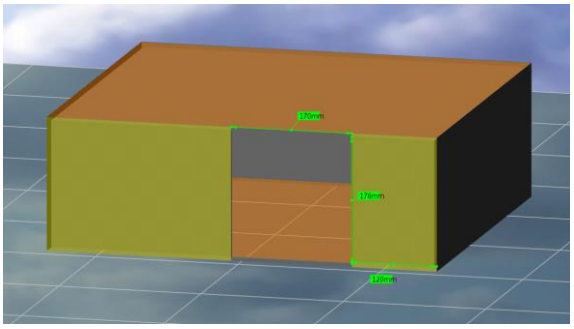

Figure 1 Geometry of damaged compartment

Table 1 Main particulars of the compartment

	Values	Unit
Length	0.55	m
Breadth	0.515	m
Height	0.186	m
Draft	0.13	m
Damaged length	0.17	m
Damage side	Starboard	Starboard

2.2 Computation domain and mesh

The commercial CFD software is used in the numerical simulation, and computation domain is divided into two regions, as shown in Figure 2.

The boundaries of the fluid domain include the following parts: the front boundary which is about 3.0Lpp from the bow of the model; the back boundary which is about 3.0Lpp from the stern of the model; the side boundaries which are about 3.0B from the sides of the model; the top boundary which is about 1.0d above the waterline; the bottom boundary which is about 2.0d below the waterline; the model outer surface of the compartment; the opening of the compartment.

The boundaries of the second computation domain consist of the following two parts: the model inter surface of the compartment and the opening of the compartment.

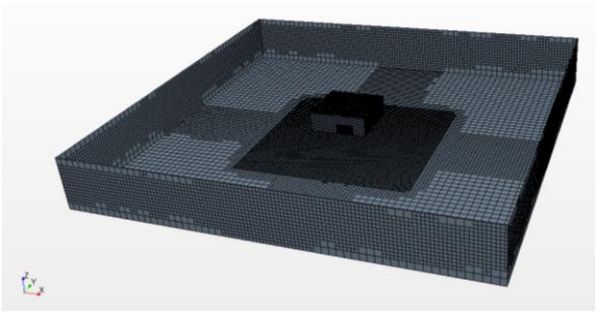

Figure 2 Meshes of computation domain

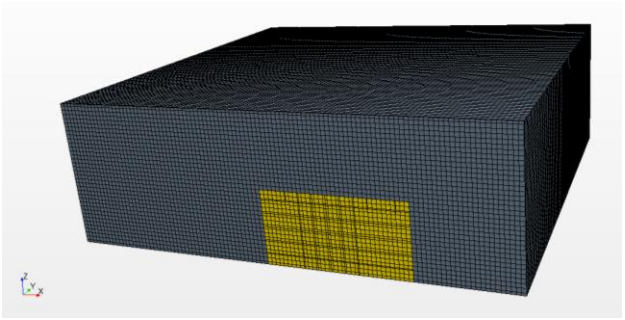

Figure 3 Meshes of compartment surface

The growth rate of mesh sizes in the computation domain is 1.3. The meshes of the second computation domain is shown in Figure 3, and the density is kept constant in this domain. The meshes around waterline and compartment are refined.

2.3 Computation method analysis

A single factor rotation method is used to study the calculation method for the inflow of fluid into the damaged compartment.

Firstly, the boundaries of the computational domain are studied by comparing the results of two calculation cases. In the case 1 (cal-1), the front, back and bottom boundaries are all velocity inlet conditions. In the case 2 (cal-2), the front, back and bottom boundaries are all wall conditions.

Secondly, the wall function is studied by comparing the results of case 2 and case 3 with experimental results. The enhanced wall function is used in the “cal-2” and the standard wall function is used in the “cal-3”.

Thirdly, the mesh quantity is studied by comparing the calculation results of case 3, case 4 and case 5.

In the calculation, the damage opening is located on one side; the X axis is along the longitudinal direction; the positive Y axis points to portside; the heave motion is along the Z axis. The force in the Z direction represents the compartment vertical loads induced by floodwater, and this value can indirectly reflect the mass of floodwater inside the compartment. X moment represents the roll moment imposed on the compartment, and Y moment represents the pitch moment on compartment.

The comparison results of the forces in y and z directions, and the moments in x and y directions, show that the results of case 5 are in good agreement with the results of model tests, as shown in Figure 5-8. Other comparison results are shown in the appendix. Therefore, the calculation method used in "Cal-5" is used for the following simulation and analysis.

The flooding process of inlet 1, as shown in Figure 9, indicates that the floodwater entered the compartment violently with a high flow velocity in the beginning. Then the fluid reached the opposite of the opening, and fluid will roll and crush at this time. The nonlinear characteristics are very obvious.

Table 2 Comparisons of computation cases

	Cases	Cal-1	Cal-2	Cal-3	Cal-4	Cal-5
Boundary condition	Front	velocity inlet	wall	wall	wall	wall
	Back	velocity inlet	wall	wall	wall	wall
	Top	pressure outlet	pressure outlet	pressure outlet	pressure outlet	pressure outlet
	Bottom	velocity inlet	wall	wall	wall	wall
	Sides	symmetry	wall	wall	wall	wall
Mesh quantity		1,350,000	1,350,000	1,350,000	1,250,000	870,000
Boundary function		high y+ wall	high y+ wall	low y+wall	low y+wall	low y+wall

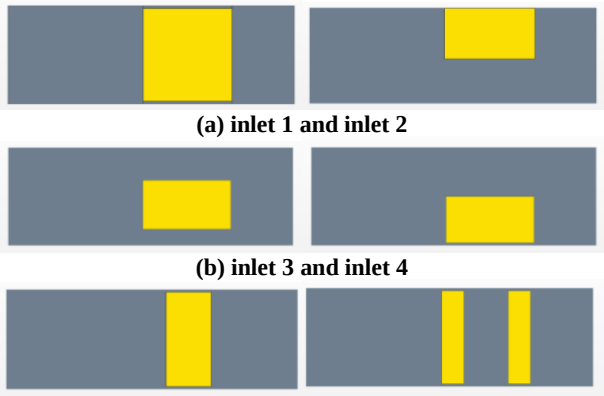

(a) inlet 1 and inlet 2

(b) inlet 3 and inlet 4

(c) inlet 5 and inlet 6

Figure 4 Damaged opening dimensions

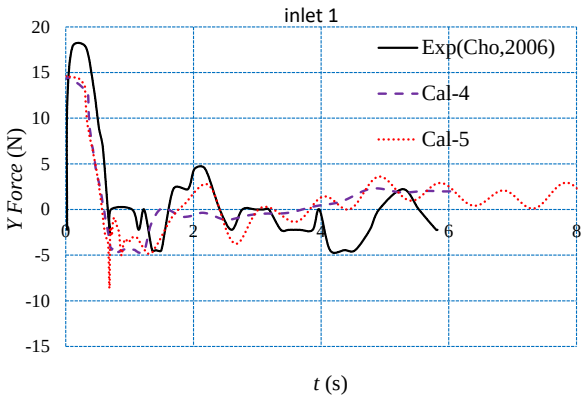

Figure 5 Comparison of forces in y direction

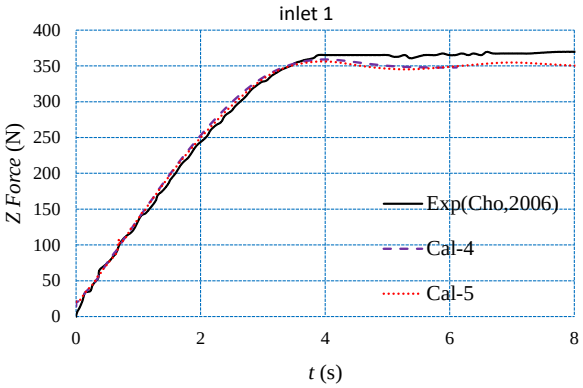

Figure 6 Comparison of forces in z direction

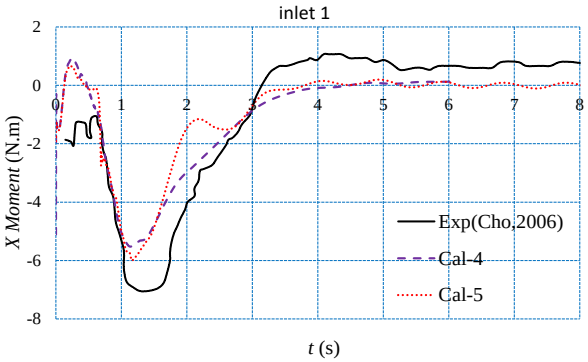

Figure 7 Comparison of moments in x direction

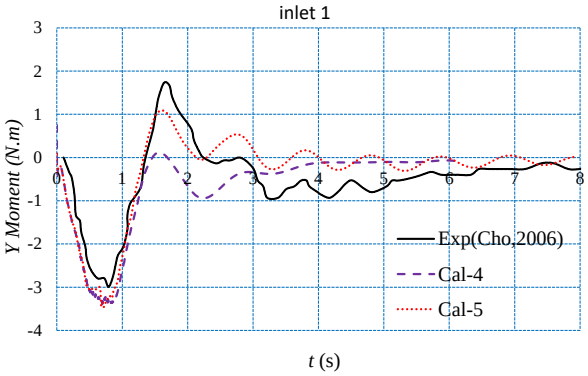

Figure 8 Comparison of moments in y direction

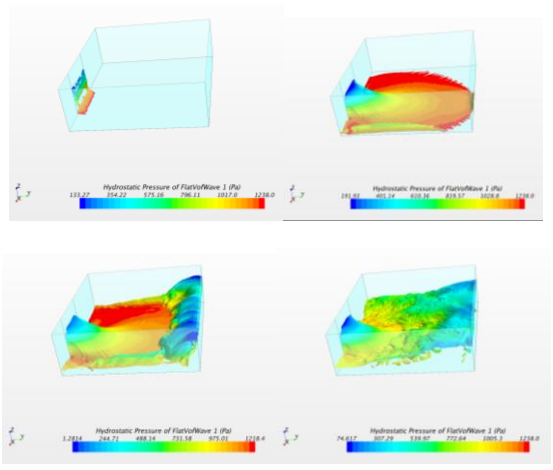

Figure 9 Flooding process of inlet 1

2.4 Comparative study

The other inlets are also calculated sequentially based on the calculation method for inlet 1, as shown in Figures 10-12. It can be seen from the comparison curves that the flooding process of inlet 1 which has the largest opening area is the fastest. The speed of inlet 2 is the slowest, because this opening is above the waterline. For the roll moment, it start to be positive and then becomes negative. Finally, it reaches equilibrium. These characteristics are basically consistent with the dynamic characteristics of the flow. In the initial stage of the flow process, the water accumulates at the entrance side, then accumulates in the opposite direction of the entrance, and finally reaches equilibrium, as shown in Figure 9. For the pitch motion, as it is mainly caused by the rotation of floodwater, the amplitude of pitch moment is relatively small compared with roll moment.

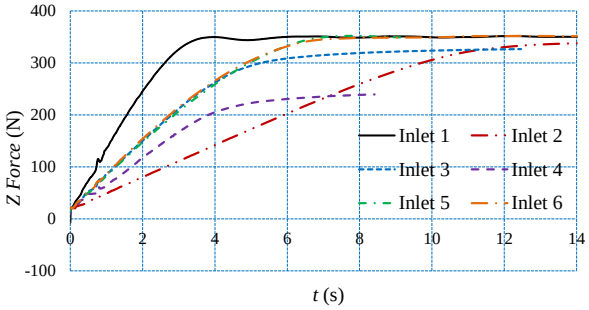

Figure 10 Comparison of forces in vertical direction

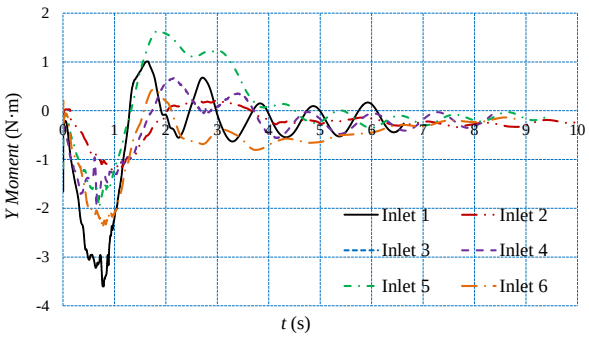

Figure 11 Comparison of moments in pitch motion

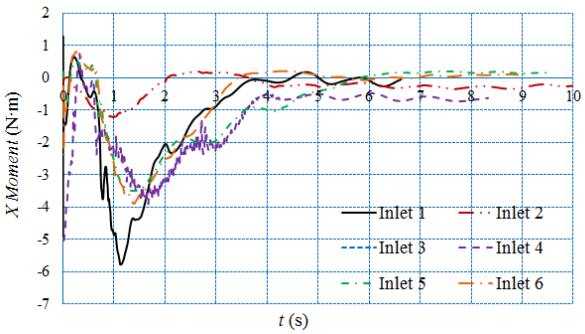

Figure 12 Comparison of moments in roll motion

3. LARGE AMPLITUDE MOTION

3.1 Computation method and model

Taking C11 containership as an example, the main particular is shown in table 3 and the hull geometry is shown in Figure 13. This ship has experienced a very serious parametric roll accident in 1998, and now it is one of the international standard study model for parametric roll. The model tests of parametric roll in regular waves were carried out in CSSRC seakeeping basin, and the model test photos were shown in Figure 14.

Table 3 Principal particulars of C11 containership (Scale 1/65.5)

Items	Values	Items	Values
Length: (L_{pp})	262m	Mean draught (T)	11.8m
Breadth (B)	40m	Block coefficient (C_b)	0.566
Depth (D)	24.45m	Natural roll period: (T)	24.5s
Metacentric height (GM)	1.9m	Pitch radius of gyration: (k_{yy})	0.24L_{pp}

Figure 13 Hull geometry of C11 containership

Figure 14 Ship model in the free running experiment

3.2 Computation method

A mixed source method using both transient Green functions and Rankine sources has been developed for the calculations of large amplitude roll motion. In this method, the fluid domain is split into two domains as shown in Figure 15. The inner fluid field (I) problem is solved by Rankine sources within the domain enclosed by the wetted body surfaces S_b, one part of the free surface S_f near the body (S_{f1}), and an outer control surface S_C. The transient Green functions are used to solve the problem in the outer fluid field (II), which are distributed over control surface, where S_∞ is the imaginary surface at infinity.

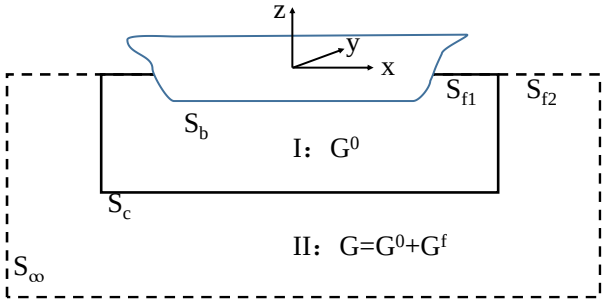

Figure 15 Mixed source formulation of panel method

The coupled heave-roll-pitch mathematical model expressed as formula (1) is used to calculate ship motions in regular head seas.

$$\left(M_{ij}+A_{ij}\right)\ddot{x}_i+\begin{cases}B_{ij}\dot{x}_i & \text{heave, pitch}\\ N_1\dot{x}_4+N_3\dot{x}_4\dot{x}_4{}^3 & \text{roll}\end{cases}=F_i^{FK}+F_i^{H}+F_i^{DF}\quad i=3,4,5 \tag{1}$$

where M_{ij}: the mass or moment inertia; A_{ij}: added mass or added inertia; B_{ij}: roll damping; x_i: the displacement in i direction; N_1, N_3: the

linear and cubic roll damping coefficient, which can be obtained from model tests or experience formulas; F^{FK+H}: the FK forces and hydrostatic forces are calculated by integrating the incident wave pressure around the instantaneous wetted hull surface; F^{DF}: diffraction forces calculated the same as radiation forces.

3.3 Results and validations

The three dimensional time domain panel method is used to calculate the parametric roll in regular waves.

In order to study the effects of water inflow on the large amplitude roll motion, the parametric roll of intact ship under different wave conditions are firstly simulated. The results are shown in Figure 16-17, and one of the time history curves are shown in Figure 18-19. It can be seen that the calculation results are in good agreement with experimental results, which can also prove the reliability of the three-dimensional time domain method.

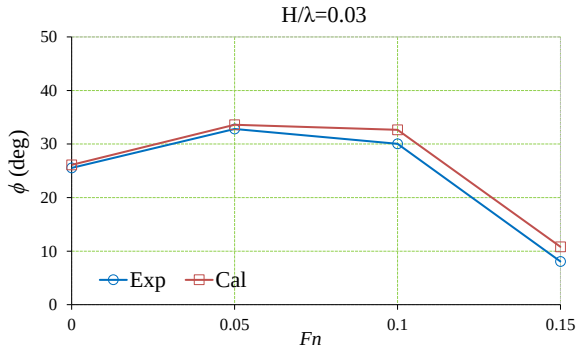

Figure 16 Comparison of roll amplitudes (H/λ=0.03)

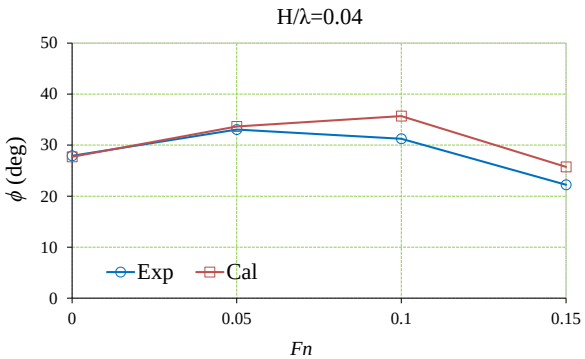

Figure 17 Comparison of roll amplitudes (H/λ=0.04)

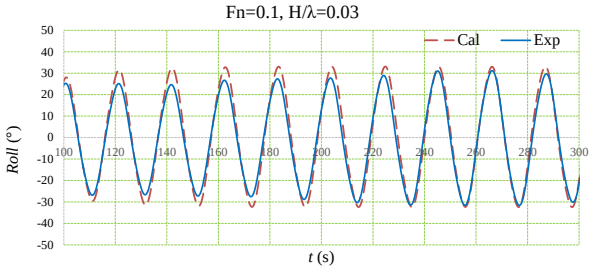

Figure 18 Comparison of roll motion time history records (Fn=0.1, H/λ=0.03)

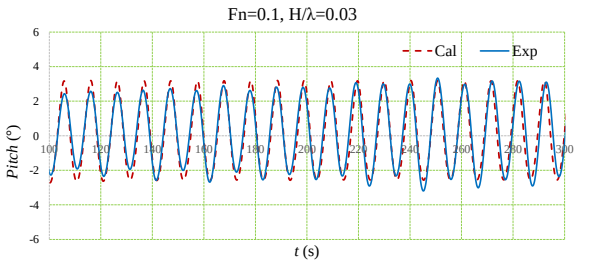

Figure 19 Comparison of pitch motion time history records (Fn=0.1, H/λ=0.03)

4. INFLUENCE OF FLOODWATER ON LARGE AMPLITUDE MOTION

4.1 Mathematical model and numerical method

When the ship is damaged, the floodwater can be treated as one part of the hull. On this assumption, the mathematical model can be written as Eq.(2). Besides, it can also be treated as one independent part, and the mathematical model is written as Eq.(3). In this paper, the influence of floodwater on large amplitude motion are analyzed by these two methods separately. In the simulation, the loads induced by the floodwater and the change of water amount are calculated by CFD, and the scale is 77.7. The ship motions are calculated by the three dimensional time domain panel method.

Method-1 (Ime-1):

$$\begin{aligned}&\left(M_{ij}+A_{ij}+M_w(t)_{ij}\right)\ddot{x}_i\\&+\begin{cases}\dot{M}_w(t)\dot{x}_i+B_{ij}\dot{x}_i & \text{heave, pitch}\\ \dot{M}_w(t)\dot{x}_4+N_1\dot{x}_4+N_3\dot{x}_4\dot{x}_4^3 & \text{roll}\end{cases}\\&=F_i^{FK}+F_i^{H}+F_i^{H-Mw}+F_i^{DF}\end{aligned}\qquad(2)$$

Method-2 (Ime-2):

$$\begin{aligned}&\left(M_{ij}+A_{ij}\right)\ddot{x}_i\\&+\begin{cases}B_{ij}\dot{x}_i & \text{heave, pitch}\\ \dot{M}_w(t)\dot{x}_4+N_1\dot{\phi}_4+N_3\dot{\phi}_4\dot{\phi}_4^3 & \text{roll}\end{cases}\\&=F_i^{FK}+F_i^{H}+F_i^{DF}+F_i^{EXT}\end{aligned}\qquad(3)$$

where $M_w(t)$: mass of floodwater; $\dot{M}_w(t)$: velocity of floodwater mass; F_i^{H-Mw} : restoring moment caused by floodwater inside the compartment, F_i^{EXT} : liquid load due to the motion of floodwater inside the compartment.

4.2 Results and analysis

The ship is assumed to be sailing in heading seas with forward speed Fn=0.1. The time history curves shown in Figure 20 and Figure 21 are motion responses of the damaged ship assuming that the damaged compartment is located at the *x*=-70m and *x*=90m, separately. The "intact" in the curves stands for the intact state. The "Ime=1" and "Ime=2" in the curves stand for the motions that are calculated by mathematical model 1 and model 2, respectively.

The results show that the time history calculated by method 2 is more violent than the results calculated by method 1 during initial stage. This is because the method 1 consider the influence of floodwater through the change of water amount, while the method 2 consider the force and moment directly, which also appear to be violent due to the high hydrostatic pressure across the opening during the initial several minutes. The parametric roll disappeared when damaged compartment located at *x*=-70m, while the roll amplitudes are enlarged when damaged compartment located at *x*=90m. This means that the effects of floodwater on motion responses are related to the location of damaged compartment.

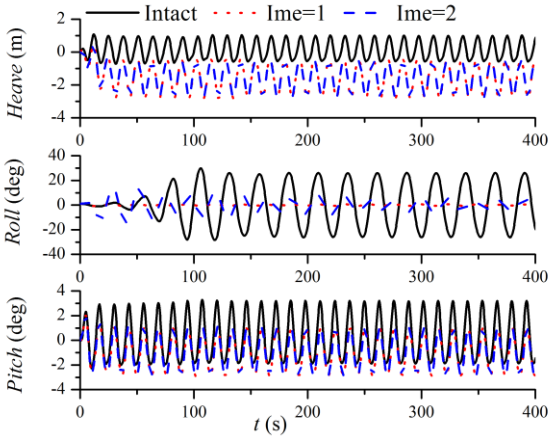

Figure 20 Comparison of time history when damaged opening located at x=-70m

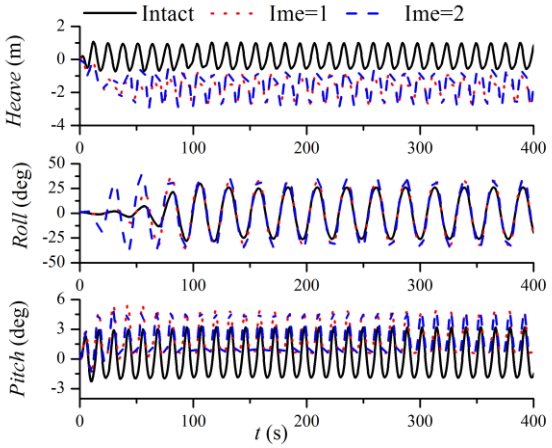

Figure 21 Comparison of time history when damaged opening located at x=90m

Different longitudinal positions are selected, and the calculation results of the roll amplitudes are shown in the Figure 22. From the calculation results, it can be seen that the the roll amplitudes were related to the longitudinal location of damaged compartment, which is similar to the passive anti-roll tank.

The results of heave and pitch motion at different positions are also compared as shown in Figure 23 and Figure 24, and the results of two methods are basically the same. When the water flowed into compartment, the increase of water amount will cause sinkage and trim of ship. The sinkage and trim due to water accumulation inside the hull are shown in Figure 25 and Figure 26.

No matter which method is applied, the final volume of floodwater inside the

compartment calculated by these two methods should be the same. Method 2 is used to further compare the effect of different openings on the large amplitude motion. The calculation results are shown in Figure 27. Although different openings have different effects on the initial stage of ship, the loads imposed on the compartment are basically the same when it reaches to the steady state. Therefore, the influence of different opening forms on the stability of the ship is basically the same.

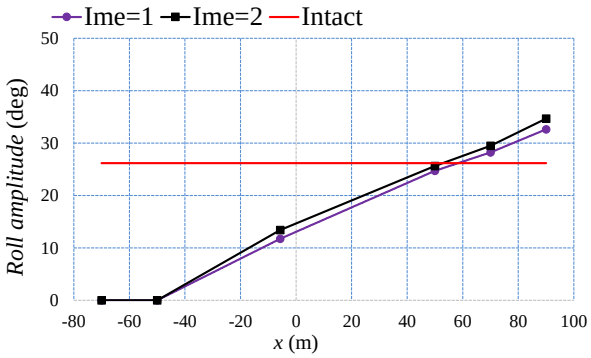

Figure 22 Comparison of roll amplitudes by different methods.

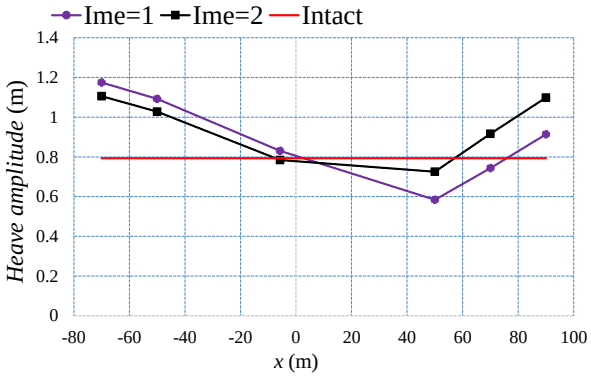

Figure 23 Comparison of heave amplitudes by different methods.

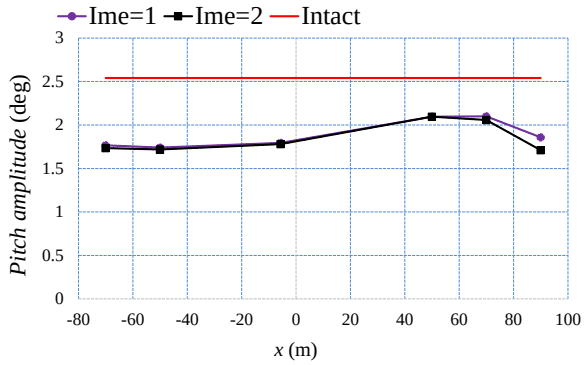

Figure 24 Comparison of pitch amplitudes by different methods.

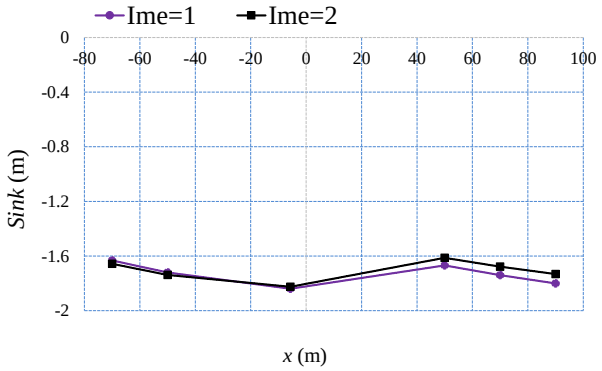

Figure 25 Comparison of ship sink by different methods.

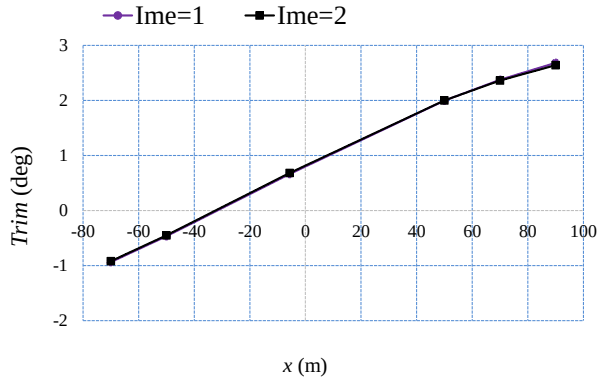

Figure 26 Comparison of ship trim by different methods.

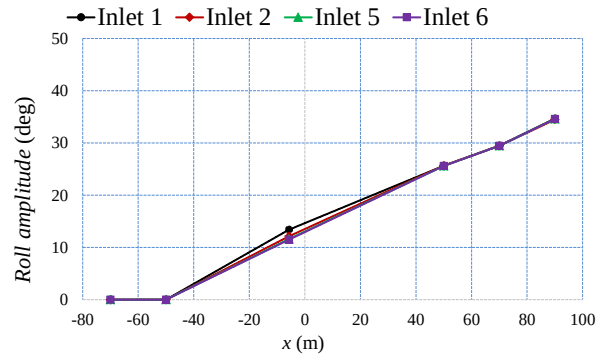

Figure 27 Comparison of roll amplitude of different inlets.

5. CONCLUSIONS

In this paper, the flooding process of dynamics characteristics of floodwater are studied by CFD numerical simulation method, and the influence of different opening forms on the large amplitude motion of C11 containership are also analyzed. The following remarks con be obtained:

(1) In the initial stage, the forces/moments induced by the floodwater are related to the

shape of the damaged opening, and the nonlinear characteristics are very obvious.

(2) The influence of the damaged floodwater on the ship large amplitude motion is related to the longitudinal position of the opening.

(3) The water accumulation inside the compartment will cause the sinkage and trim of ship, and the ship will reach a new equilibrium when the inflow and outflow of water through damaged opening reaches a stable stage.

In this paper, we only consider the influence of damage compartment influx on ship motion. In the future, we plan to consider the time domain coupling between damaged compartment influent and the ship large amplitude motion.

6. REFERENCES

Jasionowski, A. and Vassalos, D., 2001, "Numerical modelling of damage ship stability in waves", Proceedings of 5th International Workshop on Stability and Operational Safety of Ships, Trieste, pp.b7.3.1-7.3.7

Umeda, N., Kamo, T., and Ikeda, Y., 2004, "Some remarks on theoretical modeling of damaged stability", Marine Technology, 41(1), pp. 45-49.

Spanos, D. and Papanikolaou, A., 2007, "On the time to capsize of a damaged RoRo/passenger ship in waves", Proc. 9th ISSW, Hamburg, Germany.

van Walree, F., de Kat, J.O., and Ractliffe, A.T., 2007, "Forensic research into the loss of ships by means of a time domain simulation tool", International Shipbuilding Progress, 54(4), pp.381-407.

Chang, B.C. and Blume, P., 1998, "Survivability of damaged Ro-Ro passenger vessels-ship technology research", Schiffstechnik, 45(3). pp. 105-117.

Santos, T.A. and Soares C.G., 2006, "Study of the dynamics of a damaged passenger Ro-Ro ship", Proc. 9th STAB, Rio de Janeiro, Brazil, P012.

Santos, T.A. and Soares, C.G., 2008, "Study of damaged ship motions taking into account floodwater dynamics", Journal of Marine Science and Technology, 13(3), pp. 291-307.

Valanto, P., 2007, "New research into the MV ESTONIA disaster", Proc. 9th ISSW, Hamburg, Germany.

Bu, S.X., Gu, M., and Lu, J., "Time domain prediction of the damaged ship motion in waves", Shipbuilding of China (accepted).

Cho, S.K., Hong, S.Y., and Kyoung, J.H., 2006, "The numerical study on the coupled dynamics of ship motion and flooding water", Proc. 9th STAB, Rio de Janeiro, Brazil, P061.

Nabavi, Y, Calisal, S.M., Akinturk A., and Klaptocz, V., 2006, "A computational investigation of the three dimensional geometric parameters' effects on the discharge rate of a ship opening", Proc. 9th STAB, Rio de Janeiro, Brazil, P088.

Gao, Q. and Vassalos, D., 2011, "Numerical study of the roll decay of intact and damaged ships", Proc. 12th ISSW, Washington D.C., pp. 277–282.

Gao, Z., Gao, Q., and Vassalos, D., 2011, "Numerical simulation of flooding of a damaged ship", Ocean Engineering, 38(14), pp. 1649-1662.

7. APPENDIX

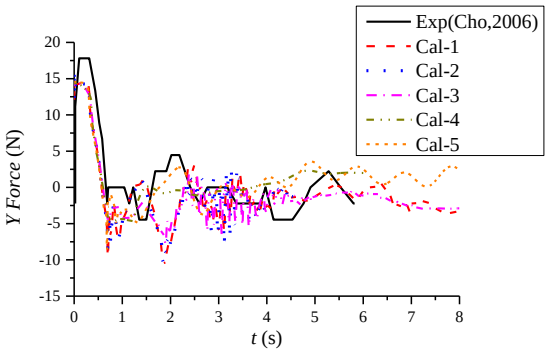

Figure 28 Comparison of forces in y direction with different calculation methods

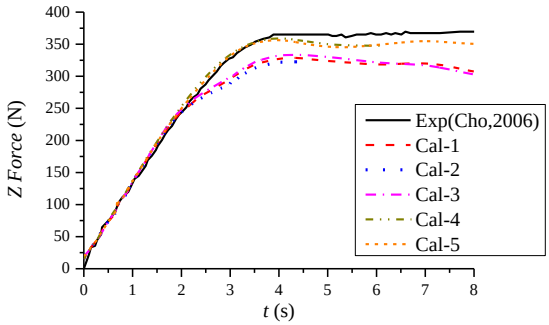

Figure 29 Comparison of forces in z direction with different calculation methods

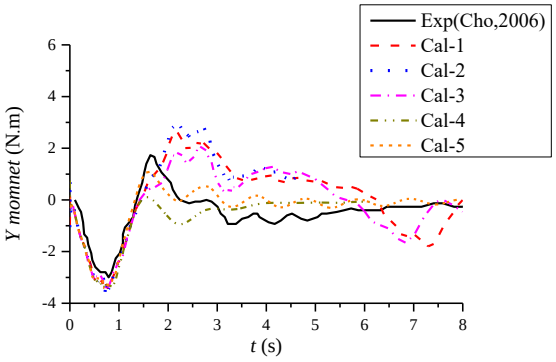

Figure 30 Comparison of moments in y direction with different calculation methods

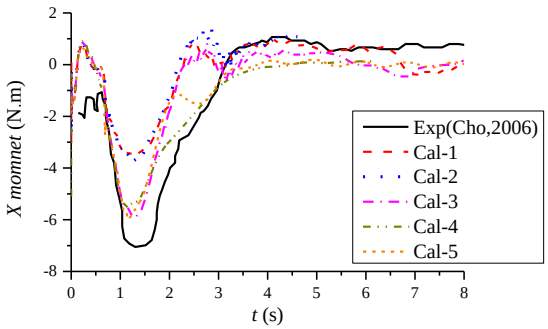

Figure 31 Comparison of moments in x direction with different calculation methods

Risk-based positioning of Flooding Sensors to reduce Prediction Uncertainty of Damage Survivability

Kristian Bertheussen Karolius, *Maritime Safety Research Centre*, kristian.karolius@strath.ac.uk

Jakub Cichowicz, *Maritime Safety Research Centre*, jakub.cichowicz@strath.ac.uk

Dracos Vassalos, *Maritime Safety Research Centre*, d.vassalos@strath.ac.uk

ABSTRACT

From the perspective of the design-stage evolution of damage stability, it is recognised that only certain combinations of damaged compartments will result in critical flooding cases with high risk of vessel loss. This knowledge may be utilised to identify optimised location of flooding sensors for the purpose of survivability prediction during actual flooding casualties. It is the aim of this paper to demonstrate the methodology for determining optimal sensor positions based on the identification of critical damage cases and associated flood-water propagation paths. The study confirms that a significant proportion of damage cases and relevant compartments are not critical, hence, focus should rather be placed on the critical, high-risk, areas to enable high accuracy prediction where it matters.

Keywords: *Flooding sensors, Damage stability, Prediction technique, Critical damage cases*

1. INTRODUCTION

The trend of increasing vessel size and complexity makes it challenging for the crew to accurately assess the extent of flooding casualty and to make fully informed decisions. The introduction of flooding sensors in compartments below the bulkhead deck as required by SOLAS Reg. II-1/22-1 (IMO, 2009) for passenger vessels aims at reducing this uncertainty and assisting the crew in decision making. The regulatory measures provide only minimum requirements for flooding detection systems with limited relevance for robust emergency management systems. Current research at the Maritime Safety Research Centre of the University of Strathclyde aims at adopting the concept of Dynamic Barrier Management (Astrup et al., 2016) through increased use of sensors and analytics for predicting the outcome of an actual flooding incident and to provide a decision support tool in emergencies (Karolius et al. 2017).

Recent research shows that predicting the evolution of flooding process purely based on flooding sensors is possible, but is highly dependent on sensor type, position and density (Ruponen et al. 2010, 2017a & 2017b). A high-density array of flooding sensors has shown to increase the accuracy of flooding assessment and compartment coverage but such dense network of sensors may be impractical or even not be feasible at all. On the other hand, the result of standard damage stability assessment demonstrates that only certain combinations of damaged compartments will result in critical high-risk cases leading to vessel loss. This knowledge may be utilised to identify locations for flooding sensors accounting for such high-risk cases enabling optimal position in terms of risk coverage and making sure the survivability assessment is delivered rapidly and with high accuracy. It is the aim of this paper to present the methodology for assessing the position of sensors by determining optimal locations based on the identification of critical damage cases and associated flood-water propagation paths.

The evaluation is carried out in two steps. Firstly, the initial assessment is performed to identify critical damages; it utilises probabilistic damage stability calculations in accordance with SOLAS Reg. II-1/6-8 (IMO, 2009) and the well-known p & s factors. As a first step, progressive flooding through openings is considered, resulting in a stepped GZ curve, an approach more realistic than is currently mandated by the regulations. As a second step, the identified critical damage cases are investigated in time-domain simulations to assess impact of dynamic factors, such as waves, on the flooding process and to identify a cut-off limit for high risk cases and flood-water propagation paths, which may be used for optimal risk-based positioning of sensors.

2. BACKGROUND

2.1 Current regulations and use of flooding sensors

Safety of passenger ships has traditionally attracted considerable attention because of their ever-increasing size, complex subdivision and large number of passengers carried. To account for this, a range of safety measures and safety systems have been implemented to improve safety and assist crew in decision making in high-risk incidents with inherent high uncertainty. In particular, the most recent developments resulted in significant (if not a step) change in the approach to damage stability and flooding response. Among the pivotal advancements are the IMO's regulations for Safe Return to Port (SRtP) (IMO, 2009). Although the regulations mainly focus on redundancy of on-board systems, they also provide guidance for what should be available for decision making post damage based on flooding extent and residual stability. As a result, on-board stability loading computers must be capable of providing operational information to the Master for safe return to port after a flooding incident as required by SOLAS Reg. II-1/8-1.3 (IMO, 2009). Moreover, flooding detection systems are incorporated with flooding sensors in watertight spaces below the bulkhead deck as required by SOLAS Reg. II-1/22-1 (IMO, 2009). However, a major shortcoming of the IMO requirements is that the SRtP flooding scenarios are deterministic and limited to single watertight compartments. In realistic scenarios and real flooding emergencies it is essential to determine the actual damage extent and produce a reliable estimate of the time available for safe evacuation and abandonment. Hence, the decision support tools for emergency flooding management systems must be far more robust than those required by the regulations.

2.2 Recent innovative use of flooding sensors

Recent, more advanced developments comprise flooding detection systems utilising flooding sensors for breach estimation in combination with time-domain simulations for real-time survivability assessment (Ruponen et al., 2010, 2012, 2015 & 2017a-b) and (Varela et al., 2007, 2011 & 2014). The latter studies do not account for sensor positioning in their developments, nor utilise sensors for detecting breach size; this is done by manual input. In the former studies, the authors utilise flooding sensors to estimate the breach size and have considered sensor positioning and its influence on detection accuracy. Their studies clearly highlight the need to use flood level sensors rather than limit switches for accurate breach estimation as well as sufficient sensor density for accurate and fast survivability assessment. Their involvement in the EU project FLOODSTAND (Jalonen et al., 2012) a few years earlier resulted in improved recommendations for positioning of flooding sensors (IMO, 2014). In brief, these guidelines recommend two flood sensors in each watertight compartment, one on each side of the ship to ensure fast detection.

The sensor layout required by the current IMO regulations as set out in guidance note MSC.1/Circ.1291 (IMO, 2008), focuses on compartments above a certain size limit, i.e. those that either have a volume in cubic metres larger than the ship's moulded displacement per centimetre immersion (at deepest subdivision draught), or have a volume in excess of 30 cubic metres.

2.3 Alternative take on sensor use: Pathway monitoring

Resistance to flooding and capsize is highly ship specific. Every vessel design has a unique subdivision and watertight integrity that will govern their survival capability in flooding incidents. Deciding on sensor layout purely based on compartment size alone will therefore be suboptimal, especially if the sensors are utilised for more advanced flooding prediction assessment as mentioned in 2.2. In general, larger compartments will accumulate more flood-water, which in many scenarios may lead to critical situations, but it is not always the case. Even if a damage resulted in flooding and deterioration of the vessel residual stability, the flooding may reach steady state and not necessarily cause loss of the ship. It is for cases not reaching steady state due to progressive flooding where high accuracy prediction is important as there will be a gradual deterioration over time, and possible capsize. More specifically, high accuracy prediction is needed to determine whether steady state will be reached and, if not, what is the likely time for the ship to sink/capsize? Smaller compartments on their own seldom result in high risk cases, but they may act as propagation paths to larger, critical, compartments initially not affected by the flooding casualty. Monitoring of these compartments would therefore be valuable for fast detection and accurate prediction, i.e. *pathway monitoring*.

Requiring sensors solely on compartment size, rather than on identified critical compartments and associated flood sequences in the progressive stages is certainly a flawed strategy. Investigating a specific vessel in the design stage, enables identification of combinations of damaged compartments, including progressively flooded compartments and their associated flood-water propagation paths that will result in vessel loss. The objective is to fit the high-risk compartments and associated flood paths with more sensors allowing for more efficient targeted positioning. Giving more focus to the actual cases likely to lead to vessel loss will achieve a higher risk coverage, faster detection and better accuracy.

3. CRITICALITY ASSESSMENT

As mentioned in the introduction, both a static and dynamic assessment have been applied for identification of critical damage cases, each described in the following sections. It is important to highlight that the models used for both assessments were identical in terms of compartmentation and openings.

3.1 Static damage assessment

Initially, a static assessment has been performed in the stability software NAPA using the probabilistic approach of SOLAS (2009) Reg. II-1/6-8. Generating all SOLAS damages for up to 7-zones, enabled calculation of the well-known p & s factors from the probabilistic framework. A detailed model was established with all openings represented as geometric objects rather than points. This enabled progressive flooding through the openings if submerged in the final stage utilising the calculation method WEPROGR2 (NAPA, 2018). Each damage was represented with an initial stage, i.e. initial damage extent, and a progressive stage, i.e. compartments progressively flooded as a result of submerged openings.

For every stage of equilibrium, new openings are checked and additional rooms added to the progressive flooding sequence. The approach accounted for all watertight doors closed and watertight, and all other doors as open and unprotected, enabling progressive flooding. In total, 661 openings were used. As all non-watertight openings were considered as progressive flooding points with relevant connections, weathertight points were added to the life-boat deck for assessment of the range criteria of the regulations. The model and internal openings are illustrated in figure 1.

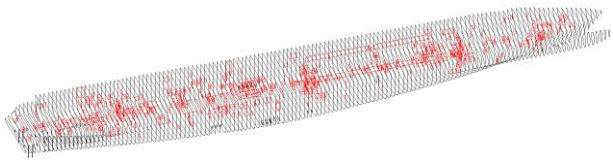

Figure 1 – NAPA model with internal openings

The inclusion of evacuation arrangements and control stations were further omitted as the requirement for including these are intended to assess the risk beyond damage stability and floatability, which is of interest in survival assessment. A flooding prediction system should give the status of the ship as a result of damage, providing assistance in decision making (i.e. to evacuate or stay onboard) and possible active measures to implement. In this study, the important aspect is therefore the identification of critical cases in terms of survivability and floatability only, and the effect on the vessel's ability to work as lifeboat as set out in SRtP requirements. Following probabilistic damage assessment, the s-factor could be used for categorising all cases into 3 categories as is illustrated in figure 2, using the relation (1 - s).

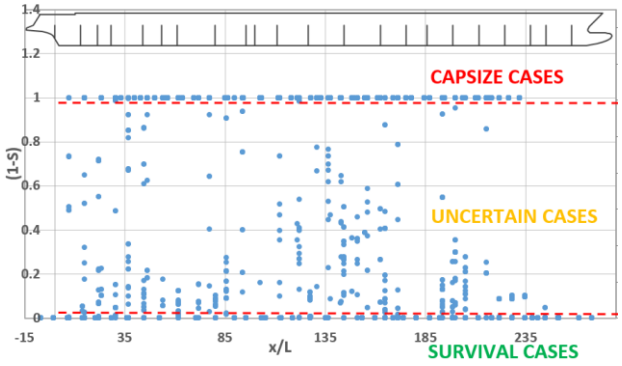

Figure 2 – Initial categorisation of static damage cases, (1-s) diagram

Cases with s = 0 were considered as capsize cases as they either capsize statically, or have insufficient residual stability margin and would not survive in waves. Cases with s = 1 were considered survival cases with sufficient residual stability margin for surviving in waves. The remaining cases with 0 < s < 1, uncertain in terms of survival in waves, were all checked in the dynamic damage assessment described in section 3.1 for identifying the cut-off limit for critical cases as is illustrated in figure 3.

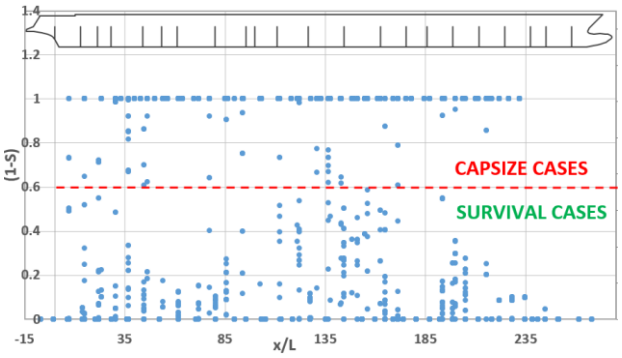

Figure 3 – Illustration of cut-off limit for critical loss scenarios

3.2 Dynamic damage stability assessment

As a vessel operates in a highly dynamic environment, such effects need to be accounted for when assessing its survival resistance to flooding incidents. In this study, time-domain simulation was conducted by the sea-keeping simulator PROTEUS3 (Jasionowski, 2001) for the cases where 0 < s < 1.

A conservative approach was followed with simulation runs in beam seas and random waves of 7 m significant wave height (H_S). Openings were given relevant collapse heads and discharge coefficients enabling a more realistic progressive flooding than was achieved in the static assessment. The model for the dynamic assessment is shown in figure 4.

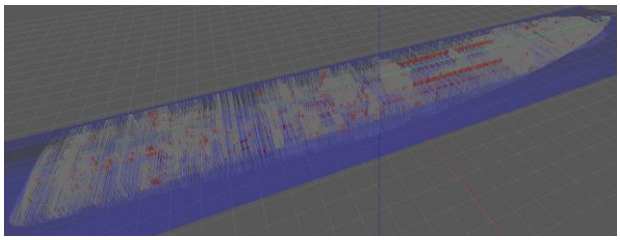

Figure 4 – Proteus3 model with internal openings

The capsize criteria followed the ITTC guidelines (ITTC, 2011), i.e.:

- instantaneous roll angle exceeds 30 degrees, or;
- the 3-minute average heel exceeds 20 degrees.

SOLAS damages in the stability software NAPA are generated using a zonal approach by applying a series of subdivision boundaries. Replication of the NAPA damages for the numerical simulations would involve generating large shell openings in the affected area leading to transient capsize in many cases. To overcome this, and to dampen the transient effect, only 1/3rd of the aft- and fore-most zones were included in the damage. The compartments missing out due to this reduction were added to the damage definition manually with the help of a compartment-connection table. An example for one specific deck is given in figure 5 for a 4-zone damage. As a result of only including 1/3rd of the aft- and fore-most zones, several smaller compartments as marked red in the figure are not included in the damage. Consequently, the damage case is not identical to the corresponding NAPA case.

As a solution, these rooms were accounted for by adding them in a connection table in the time-domain software tool.

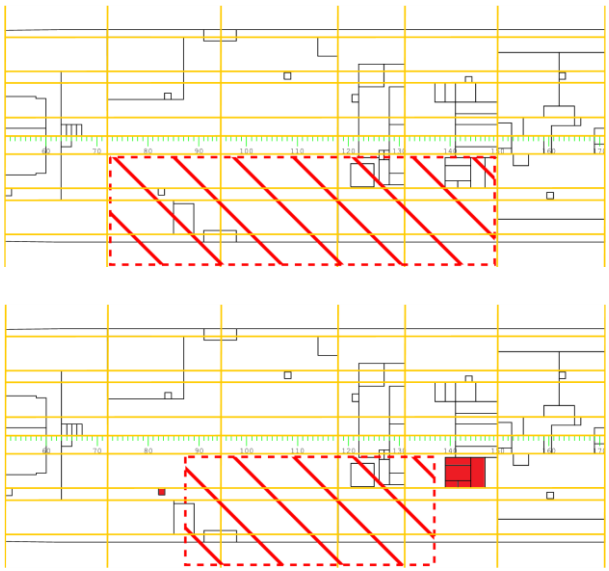

Figure 5 – Reduction in damage length to damp the effects of transient flooding

3.3 Sample vessel

The vessel used in the assessment is a large modern cruise vessel of 100,000 GT, currently in operation. The vessel main particulars are presented in table 1, including loading condition, D_S, used in the calculations.

Table 1. Vessel and loading particulars.

Parameter	Value [des.]
Length between perp., L_{BP}	273.00 [m]
Breadth, B	36.00 [m]
Depth (height of main deck), D	21.00 [m]
Gross tonnes, GT	100000 [tonnes]
Displacement, Δ	52565 [tonnes]
Draught, T	8.30 [m]
Trim, Tr	0.00 [m]
Metacentric height, GM	2.60 [m]
Vertical centre of gravity, KG	18.00 [m]

The vessel WT arrangement and current sensor layout in accordance to MSC.1/Circ.1291 is presented in Figure 6. A total of 52, and 94 sensors are fitted in dry spaces and tanks respectively.

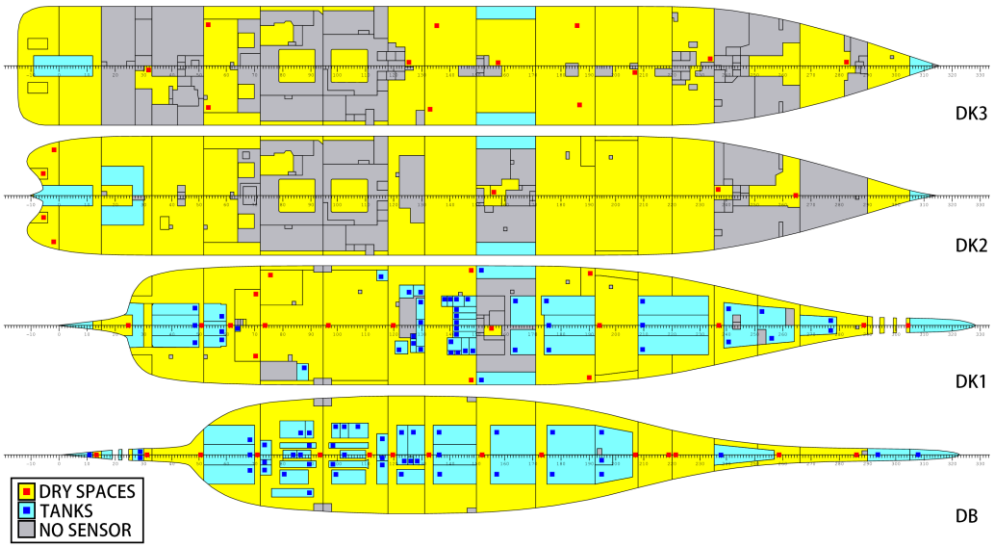

Figure 6 – Arrangement of flooding sensors according to IMO guideline.

4. COMPARTMENT RATING

An initial approach was to use the well-known p(1-s) diagram as seen in figure 7 to identify critical cases and areas of the ship. This proved not to be detailed enough for the purpose of this study as the diagram may provide false criticality for certain cases comprising high number of zones.

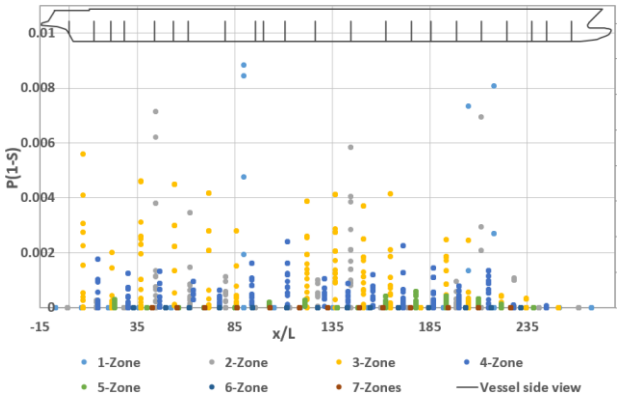

Figure 7 – P1S diagram illustrating damage cases in terms of risk along ship length

It is noteworthy that as each damage case is graphically represented using the mid position of the damage length, hence the marker position does not necessarily match the location of the critical compartments.

This can be illustrated with the help of a 4-zone damage centred at midship. This damage may be shown to be highly critical due to its inclusion of the engine room. The engine room, however, is located further aft than the x-coordinate from the p(1-s) diagram, and as such, the criticality position is deceptively presented at midship, while in reality, the critical compartment (the engine room) lies further aft. For a more detailed representation of critical areas, each compartment has been assigned a criticality metric as described in the following. Firstly, it is recognised that all the capsize cases have a survival index s = 0. This enables representing the risk from flooding by the p-factor alone, as in (1):

$$Risk = p(1-s) \rightarrow Risk = p \qquad (1)$$

Each compartment can be given a risk rating based on all critical damage cases it is taking part in, by summing up relevant p-factors as in (2):

$$Risk_{Comp_k} = \sum_i^n p_{dam_i} \qquad (2)$$

Were, n = number of damage cases i, resulting in flooding of compartment k.

5. METHODOLOGY SUMMARY

The following summarises the methodology applied for identification of critical cases, and subsequent compartment rating.

1. Assessment of static cases from NAPA:

   a. Remove all cases with s = 1 (these cases have sufficient residual stability margin to survive in waves.)

   b. Disregard all cases s = 0 (many of these cases capsize or sink in still water, and the remaining are assumed to capsize in waves due to insufficient residual stability margin)

2. For all cases with 0 < s < 1, use time-domain simulations (PROTEUS3) to assess survivability in waves. This will identify a cut-off limit for critical dynamic capsize cases.

3. Compartment criticality rating:

   c. Calculate the criticality rating for individual rooms (by summing p-factors of the relevant damage cases) and rank the rooms accordingly.

   d. Screen all capsize cases and identify critical flood pathways. Identify common or partly-common flood pathways.

   e. Recommend sensor positioning.

6. RESULTS

6.1 Identification of critical capsize cases

The static calculations up to 7-zone damages resulted a total of 5564 different damage cases. The assessment was carried out at single loading condition (the summer load-line loading condition D_S). This is recognised as the worst damage stability loading condition of SOLAS. It is further shown that passenger ships normally operate around this condition most of the time (eSafe, 2017). Of all the damage cases, a total of 1568 cases resulted in s = 1, indicating survival, and 3450 cases resulted in s = 0, indicating capsize. This left 546 cases with marginal survival factor, i.e. 0 < s < 1. The results have already been presented graphically in figure 2 in section 3.1.

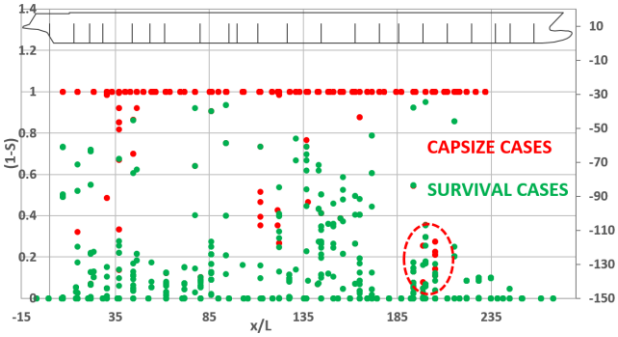

Figure 8 – Identified capsize cases in the uncertain region of the (1-P) diagram.

Due to the stochastic nature of the wave environment, the situation is not as black and white as presented in figure 3. Instead of a clear cut-off limit, there is a transition area for which neither capsize nor survival is definitive. This transition area, as shown in figure 8, may be related to the so-called capsize band (Vassalos et al. 1998), where the same flooding case may result in either capsize or survival if simulated a number of times. There will also be differences between a static and dynamic approach due to the dynamic effects incorporated in the time-domain simulations. This is particularly true in the transient stage, which is not covered by the static assessment method. Several of the capsize cases marked in red in the lower right corner of figure 8 are transient capsize cases.

Of the 546 identified cases with 0 < s < 1, 108 cases have been identified as capsize cases following the dynamic assessment. In total, there were 3558 capsize cases which can be used in the compartment risk rating (including the initial s = 0 cases). It is noteworthy that the large number of capsize cases is mainly due to the extensive damage extents considered in the calculations. Of the total amount of capsize cases, 1690 are located on port side, while 1868 are located on starboard side. This difference is due to asymmetries in the vessel internal subdivision and openings arrangement.

6.2 Compartment rating

Having identified all capsize cases, these where then used in the compartment rating. Rating of the compartments (by means of relation (2)) is presented in the bar chart presented in figure 9. The rating can further be separated between initial and progressive stages as shown in figures 10 and 11, respectively. Due to the high number of compartments, the compartment names are not presented in the figures.

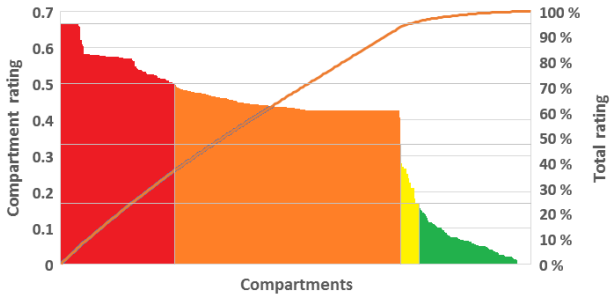

Figure 9 – Compartment risk rating: All stages

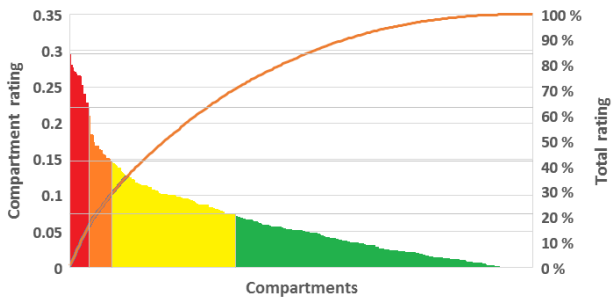

Figure 10 – Compartment risk rating: Initial stages

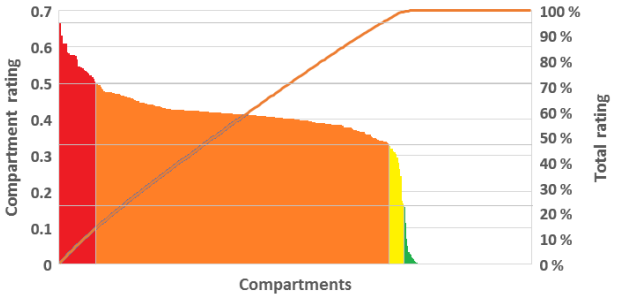

Figure 11 – Compartment risk rating: Progressive stages

The compartment have been represented graphically with colour coding corresponding to criticality. Table 2 shows the scales for criticality and corresponding colour coding. Figures 12 and 13 show the results for initial and progressive stages plotted on the deck layout.

Table 2. Colour coding for compartment criticality.

Risk/Criticality	Range	Colour
Very high	75% < Risk < 100%	Red
High	50% < Risk < 75%	Orange
Low	25% < Risk < 50%	Yellow
Very low	0% < Risk < 25%	Green

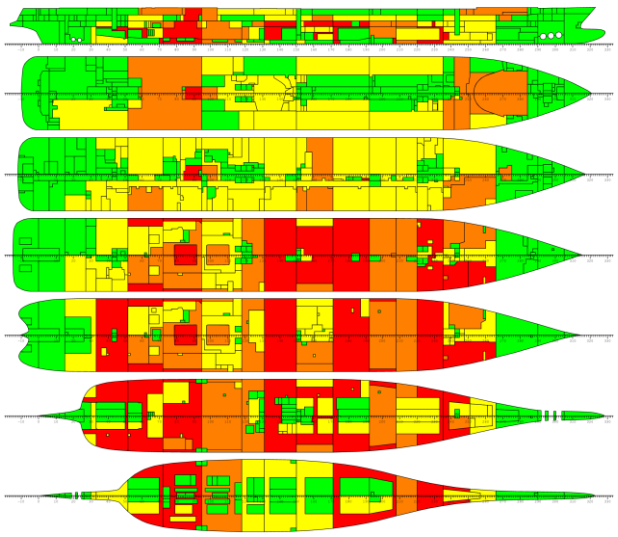

Figure 12 – Graphical representation of the compartment risk rating: Initial stage

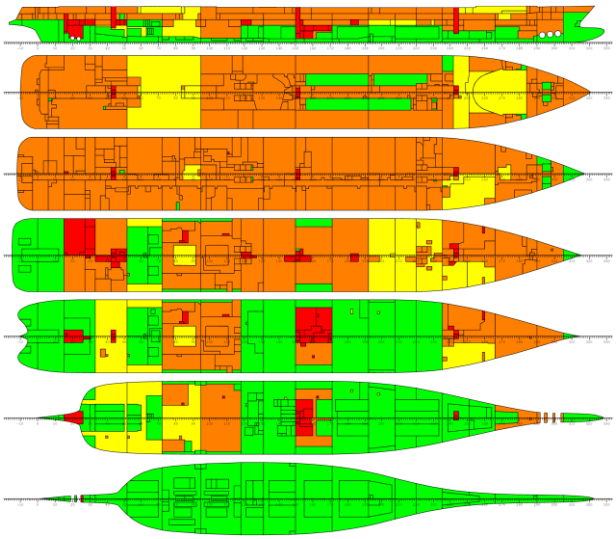

Figure 13 – Graphical representation of the compartment risk rating: Progressive stage

Figures 12 and 13 show the clear distinction between compartment criticality in the initial and progressive stages of flooding. In the initial stage, many of the critical compartments lie in the mid region of the vessel around the waterline. They also tend to be larger compartments in line with the IMO guidelines. In case of progressive stages of flooding (Figure 13), there are several smaller compartments (specifically stairwells, elevator shafts, and vertical escape shafts) that are given the highest risk rating. Interestingly, the large, upper, compartments are shown to be of secondary criticality despite being a direct cause (due to their size) for capsize when flooded. This is because the larger compartment in the upper decks are flooded in the progressive stages through the smaller compartments, acting as flood-water pathways. The smaller compartments are therefore taking part in a higher number of critical cases.

6.3 Optimised flooding sensor position

The results of compartment rating show clearly that the criticality information can be utilised in optimised positioning of the flooding sensors. In the case of compartments for which IMO requires installation of the sensors, their number and location can be analysed in detail in order to increase accuracy of flooding detection. Furthermore, additional sensors could be installed inside the compartments not covered by the IMO requirements but scoring high in the criticality rating. This should enable controlling of critical spaces and flooding pathways not only for flooding detection but also for monitoring of the flooding progress during actual casualties. Finally, openings belonging to the critical flooding pathways should also be monitored in order to allow for better assessment of the extent of the progressive flooding.

7. CONCLUDING REMARKS

The study presented here outlines the methodology for risk-based positioning of flooding sensors aiming at reducing uncertainty in the assessment of survivability of damaged ships. The study confirms that the extent of a damage case or geometrical properties of the compartments alone are insufficient criteria for the positioning of the flooding sensors for the accurate estimate of survivability during flooding casualties. The regulatory requirements should be also complemented by the systematic, risk-based rating to determine critical spaces and flooding pathways. This should lead to targeted and efficient sensor positioning.

The results also show that the same compartment may have different criticality rating in the initial and progressive stages of flooding. For this reason, these stages should be ranked separately as smaller compartments may form critical flooding paths to larger rooms (through up- and cross-flooding) and should also be fitted with sensors for early warning of capsize. Separating initial stage, and progressive stage may also help identifying sensor type and position. Specifically, the following can be taken into account:

- Initially damaged compartments below waterline: Flooding sensors for initial estimate of the damage extent, i.e. breach detection.

- Initially damaged compartments above waterline: Alternative sensor types for vertical breach detection.

- Progressively flooded compartments: Pathway monitoring for assessing survivability and watertight integrity.

- Openings: Status of the openings forming the critical flooding pathways should be closely monitored (e.g. open/close status, leaking, hydrostatic head build-up).

8. FUTURE DEVELOPMENTS

Similar approach for compartment rating should be implemented with survivability assessment by time-domain simulations. Random non-zonal damage cases can be sampled using Monte Carlo sampling directly from damage accident statistics. Sufficiently large damage sample (5000-10000) should ensure convergence to the zonal model (i.e. as used in static simulations). In this approach the criticality would also reflect random sizes of the openings and impact of environment on the progressive flooding. Time-domain simulations are particularly important for the inherently stochastic problem of detecting and monitoring critical flooding pathways.

Further work is also needed to verify if the proposed approach (i.e. criticality-driven sensor positioning) provides higher risk coverage and more robust survivability prediction.

9. REFERENCES

Astrup O.C., Wahlstrøm A.M., King T., 2015, "A framework Addressing Major Accident Risk in the Maritime Industry", Wmtc2015 – SNAME.

International Maritime Organization (IMO), 2008, "Guidelines for Flooding Detection Systems on Passenger Ships" MSC.1/Circ.1291, 9 December 2008.

International Maritime Organization (IMO), 2009, "Safety of Life at Sea" (SOLAS) Reg. II-1/22-1, guidance in MSC.1/Circ.1291.

International Maritime Organization (IMO), 2009, "Safety of Life at Sea" (SOLAS) Reg. II-1/6-8, explanatory notes in MSC.281(85).

International Maritime Organization (IMO), 2009, "Safety of Life at Sea" (SOLAS) Reg. II-1/8-1.3, explanatory notes in MSC.1/Circ.1369 and guidance in MSC.1/Circ.1400.

International Maritime Organization (IMO), 2009, "Safety of Life at Sea" (SOLAS) Safe Return to Port (SRtP) Reg. II-1/8-1, II-2/21 and II-2/22, explanatory notes in MSC.1/Circ.1369 and guidance in MSC.1/Circ.1400.

International Maritime Organization (IMO), 2014, "Guidelines for Flood Sensor Placement and Technical Requirements", SDC2/INF.6, submitted by Finland.

Jalonen R., Ruponen P., Jasionowski A., Maurier P., Kajosaari M., Papanikolaou A., 2012, "FLOODSTAND - Overview of Achievements", Proceedings of the 11th International Conference on Stability of Ships and Ocean Vehicles, STAB2012, Athens, Greece, 2012, pp. 819–829.

Jasionowski, A., 2001, "An Integrated Approach to Damage Ship Survivability Assessment", PhD Thesis, Glasgow, UK.

Joint industry project eSAFE, 2017, report No. D1.2.1, Rev. 5.0, "Analysis of onboard data with regards to probabilities of initial draughts".

Karolius K.B., Vassalos D., 2017, "How to buy time following a flooding incident – intelligent quantification of emergency response measures", Proceedings of the 16th International Ship Stability Workshop, 5-7 June 2017, Belgrade, Serbia, pp. 67-72.

NAPA Ltd., 2018 "NAPA for Design Manuals".

Penttilä P., Ruponen P., 2010, "Use of Level Sensors in Breach Estimation for a Damaged Ship", 5th International Conference on Collision and Grounding of Ships, 2010, pp. 80-86.

Ruponen, P., Larmela, M. and Pennanen, P., 2012, "Flooding Prediction Onboard a Damaged Ship", Proceedings of the 11th International Conference on the Stability of Ships and Ocean Vehicles 23-28 September 2012, Athens, Greece, pp. 391-400.

Ruponen, P., Lindroth, D., Pennanen, P., 2015, "Prediction of Survivability for Decision Support in Ship Flooding Emergencies", Proceedings of the 12th International Conference on the Stability of Ships and Ocean Vehicles 14-19 June 2015, Glasgow, UK, pp. 987-997.

Ruponen, P., Pulkkinen, A., and Laaksonen, J., 2017b, "A method for breach assessment onboard a damaged passenger ship", Applied Ocean Research 64 (2007), pp. 236-248.

Takkinen E., Ruponen P., Pennanen P., 2017a, "Required Flooding Sensor Arrangement for Reliable Automatic Damage Detection", Smart Ship Technology, 24-25 January 2017, London, UK.

The International Towing Tank Conference (ITTC), Recommended Procedures and Guidelines, 2011, "Numerical Simulation of Capsize Behaviour of Damaged Ships in Irregular Beam Seas", Doc. No. 7.5-02 -07-04.4, Rev. 00.

Varela, J.M. and Guedes Soares C., 2007, "A Virtual Environment for Decision Support in Ship Damage Control", IEEE Computer Graphics and Applications, 27(4):58-69.

Varela, J.M., Cacho, A.J., Guedes Soares, C., 2011, "Virtual Environments for simulation and study of maritime scenarios", Marine Technology and Engineering, Taylor & Francis Group, London, ISBN 978-0-415-69808-5, pp. 719-740.

Varela, J.M., J.M.Rodrigues., Guedes Soares, C., 2014, "On-board Decision Support System for Ship Flooding Emergency Response", Procedia Computer Science Volume 29, 2014, pp. 1688-1700.

Vassalos, D., Jasionowski, A., Dodworth, K., Allan, T, Matthewson, B and Paloyannidis, P: "Time-based Survival Criteria for Ro-Ro Vessels", RINA Spring Meeting, 1998.

Complementing SOLAS framework with a probabilistic description for the damage extent below water

Gabriele Bulian, *University of Trieste*, gbulian@units.it

Mike Cardinale, *Fincantieri SpA*, mike.cardinale@fincantieri.it

Alberto Francescutto, *University of Trieste*, francesc@units.it

George Zaraphonitis, *National Technical University of Athens*, zar@deslab.ntua.gr

ABSTRACT

SOLAS damage stability regulations do not embed a probabilistic description for the damage extent below water. A "worst case approach" is therefore used for the s-factor when there are horizontal subdivision boundaries below water. This can lead to the underestimation of the ship survivability, and it prevents an effective assessment of the effect of horizontal subdivision boundaries below water. To make a step forward, this paper presents a "u-factor", derived from statistical analysis of accidents data, which can be embedded in the SOLAS framework to account for horizontal subdivision boundaries below water, avoiding the need for the "worst case approach".

Keywords: *collision; damage stability; extent of damage; flooding probability; IMO; SOLAS; zonal approach..*

1. INTRODUCTION

Damage stability regulations from the International Maritime Organization (IMO), in the framework of the International Convention for the Safety of Life at Sea (SOLAS), assess the ship safety level through the attained subdivision index. The attained subdivision index is determined by combining the probability of flooding of each possible (group of) compartment(s) with the conditional survivability measured through the s-factor (IMO, 2018). However, from the perspective of probabilistic modelling, present SOLAS is, unfortunately, not complete.

In fact, in assuming damages due to collision, SOLAS embeds probabilistic models for the longitudinal position of damage, for the damage length and for the damage penetration, which lead to the present formulations for p-factor (SOLAS/II-1/B-1/7-1/1.1) and for r-factor (SOLAS/II-1/B-1/7-1/1.2). The embedded probabilistic models are basically a variation of those originally developed in the framework of the project "Harmonisation of Rules and Design Rationale (HARDER)" (Lützen 2001, 2002). SOLAS also embeds a probabilistic model regarding the distribution of the vertical position of the upper limit of damage above the waterline, which corresponds to the v-factor (SOLAS/II-1/B-1/7-2/6.1). Information on the development of the v-factor have been provided by Lützen (2001, 2002) and Tagg et al. (2002).

However, present SOLAS framework does not embed any probabilistic description for the distribution of the vertical extent of damage below water. To compensate for this missing element, a "worst case approach" is then used in SOLAS for the determination of the s-factor when there are horizontal subdivision boundaries below water (SOLAS/II-1/B-1/7-2/6.2; MSC.281(85) (IMO, 2008)). Such conservative approach is based on the

combination of the v-factor with the minimum s-factor considering all the possible damages involving different horizontal boundaries below the waterline. By its very nature, the use of this "worst case approach" leads, in general, to an underestimation of the actual ship survivability, and it may also lead to a misinterpretation of the effect of horizontal subdivision boundaries below water. In addition, the lack of a complete probabilistic modelling for the vertical extent of damage in the SOLAS framework prevents the development of a consistent non-zonal approach for collision damages if this is to be based only on the assumptions underlying present SOLAS (see Bulian et al. (2016) for a description of a non-zonal approach in case of grounding damages).

In order to address the identified limitation of the present SOLAS framework, this paper presents a "u-factor", derived from statistical analysis of accidents data, which can be embedded in the SOLAS framework to account for horizontal subdivision boundaries below water, avoiding the need for the use of present "worst case approach". In the following, first, the accidents data analysis with consequent modelling of the damage extent below water is presented. Afterwards, the proposed "u-factor" is introduced and an explanation is provided of how it can be readily and seamlessly embedded in the present SOLAS framework, thus avoiding the use of the "worst case approach". The developed approach is then applied on a sample vessel, and the effect of the introduction of the developed "u-factor" on the attained subdivision indices (partial and global) is assessed. Some concluding remarks are finally provided.

2. ACCIDENTS DATA ANALYSIS AND PROBABILISTIC MODELLING OF DAMAGE EXTENT BELOW WATER

Scope of the analysis presented herein is to provide a probabilistic modelling for the damage extent below water, starting from collision accidents data. To this end, use is made of data from the HARDER accidents database as updated in the "GOAL Based Damage Stability (GOALDS)" project (Bulian & Francescutto, 2010; Mains, 2010; IMO, 2012).

In the following, first, an overview is given of the database used for the analysis. Then, the statistical analysis and associated probabilistic modelling are presented.

2.1 Overview of the database

The GOALDS database contains, among others, data regarding damage characteristics as recorded from collision accidents (Bulian & Francescutto, 2010; Mains, 2010; IMO, 2012). The GOALDS database is the result of the update of the previous HARDER database, which was used for the development of SOLAS2009 (Lützen, 2001, 2002).

For consistency with the present SOLAS approach, data from the database have been used after a series of "filtering", in accordance with the approach used during GOALDS (Bulian & Francescutto, 2010; IMO, 2012). Filtering levels as used in GOALDS are summarised in Table 1, while more information can be found in the cited references. Herein, in particular, data filtered at "filtering level 05" have been used as starting basis for the present study.

With specific reference to the present study, the available dataset contains information regarding the ship length between perpendiculars, the ship breadth and the ship draught before casualty, as well as information regarding damage length, damage penetration, vertical distance from baseline to the lowest point of the damage and maximum vertical damage height measured up from the lowest point. Not all accidents entries are complete in all data, leading to a general fragmentation of the information. It is also recalled that, according to Bulian & Francescutto (2010) and

IMO (2012), following also the HARDER approach, in the statistical analysis of damages due to collision, multiple breaches from the same accident were considered as separate breaches. For consistency reasons, the same approach has been followed also in the present analysis.

Table 1. Short description of filtering levels of GOALDS database.

Filt. level	Short description
01	Extraction of collision accidents using the field "Nature of Casualty".
02	Removal of some cases identified as inconsistent.
03	Removal of cases which were explicitly reported as not being ship-ship collisions.
04	Removal of accidents for which it could be identified that the lower limit of damage was above the waterline.
05	Removal of cases where the damaged vessel could be identified as the striking one on the basis of the longitudinal position of damage.

From the available data, some further filtering was carried out in this study to arrive at the final dataset used in the analysis. First, a series of additional checks were carried out regarding the reported draught before casualty. A series of recorded damages were found to report inconsistent data (IDs: 47, 532, 580, 621, 665, 1170, 1186, 3001) and it was therefore decided to omit them from the subsequent analysis.

Implicitly, present SOLAS framework assumes that breaches due to collision are always crossing the waterline (IMO, 2008), i.e. that the breach has the upper limit above the actual calculation waterline and the lower limit below the actual calculation waterline. As a result, the transversal section of a collision damage can be represented as shown in Figure 1. In the figure, $z_{UL,p}$ and $z_{LL,p}$ represent the vertical coordinates of the upper and of lower limit of potential damage, respectively. The coordinate $z = 0m$ is conventionally assumed to correspond to the ship bottom. The coordinate z^* corresponds to the waterline at which the potential damage penetration $L_{y,p}$ is measured. It is herein assumed that z^* coincides with the ship draught d . The coordinates indicated as $x_{min,p}$ and $x_{max,p}$ correspond to the aft and forward limit, respectively, of the potential damage in longitudinal direction. Herein, similarly to Bulian et al. (2016), the wording “potential” is used to indicate that, in principle, the damage can extend also outside the vessel limits.

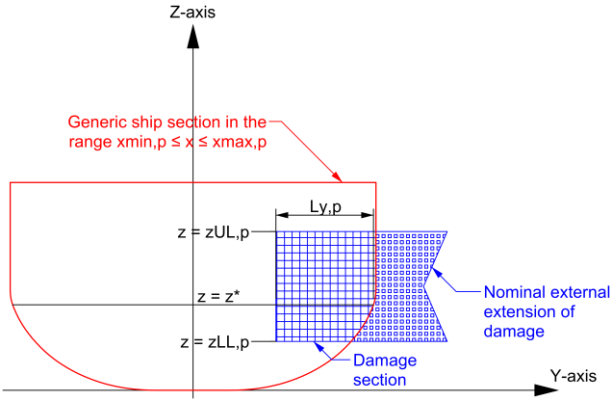

Figure 1. Representative transversal section with variables characterising a collision damage.

Since the SOLAS damage is assumed to be always crossing the waterline, it follows that $z_{LL,p} \le d \le z_{UL,p}$. For consistency with this assumption, as a final filtering, only cases with sufficient data to unambiguously identify that the damage was crossing the waterline have been retained in the analysis. The necessary data for performing the check that the damage was crossing the waterline are: the ship draught before casualty, the vertical distance from baseline to the lowest point of the damage and the maximum vertical damage height measured up from the lowest point. This final filtering led to a total set of data comprising 152 entries.

Since damage distributions in present SOLAS are common to passenger and cargo vessels, the analysis considers data from both types of ships.

An overview of the distribution of main ship characteristics (length between perpendiculars L_{ship}, breadth B, ship draught before casualty T) from the considered set of data is reported in Figure 2.

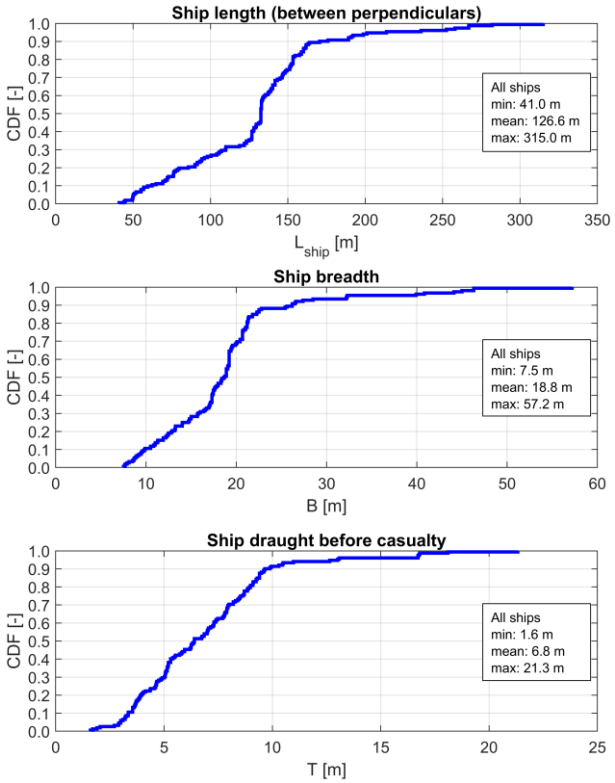

Figure 2. Cumulative distribution (CDF) of main ship characteristics for the analysed dataset.

2.2 Comparison between v-factor and accidents data

In order to check whether the available dataset can be considered to be a sufficiently consistent source of information for developing a model for the vertical extent of damage below water, a first check is carried out considering the vertical extent of damage above water. According to SOLAS, the cumulative distribution of the vertical position of upper limit of potential damage above the waterline, i.e. the vertical extent of potential damage above water ($h_{aw,p} = z_{UL,p} - d$), corresponds to the v-factor. Since no information is available in the database regarding the total height of the vessel, it is not possible to directly differentiate between damages which could have potentially extended above the maximum height of the vessel, which are hence limited by the maximum height of the vessel, and damages which are instead not affected by this limitation (Lützen, 2001, 2002; Tagg et al., 2002). As a result, the analysis is herein carried out assuming that the fraction of cases for which the upper limit of damage is limited by the total height of the vessel is sufficiently small to be neglected. This basically corresponds to assuming the equivalence between $z_{UL,p}$ and z_{UL} when data are analysed. Results from the comparison between available data and v-factor are shown in Figure 3. In the figure z_{UL} is the measured vertical position of upper limit of damage, and T, as indicated before, is the reported ship draught before casualty.

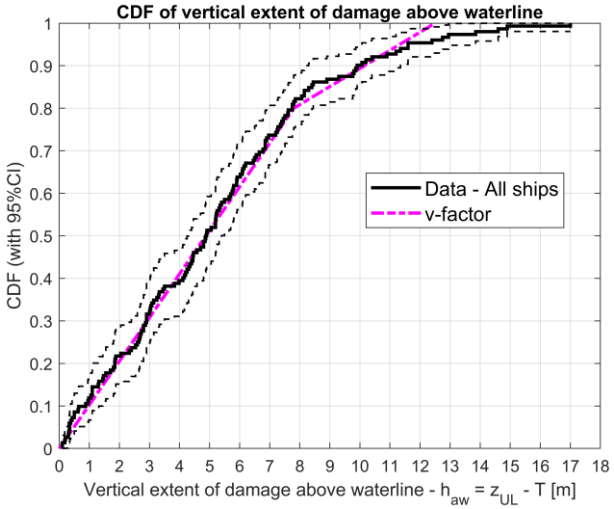

Figure 3. Comparison between v-factor from SOLAS and cumulative distribution of vertical extent of damage above water as obtained from the accidents database. CDFs are reported with corresponding 95% confidence intervals.

From the comparison in Figure 3, it can be noticed that the SOLAS v-factor represents a good approximation of the distribution obtained from the accidents database. The v-factor seems to slightly underestimate the occurrence of very high damages above the waterline (approximately 4% of the cases extend above the maximum 12.5 m limit assumed through the v-factor).

Overall, it can therefore be concluded that there is a good agreement between the database and the probabilistic model embedded in the v-factor, and this provides some confidence in the use of the database for the development of a probabilistic model for the extent of damage below water, as described in the next section.

2.3 Statistical analysis and probabilistic modelling

In order to develop a probabilistic model for the extent of damage below water, first an exploratory data analysis was carried out, which led to the derivation of some main outcomes.

Some dependence was observed between the nondimensional vertical position of lower limit of damage, z_{LL}/T, and the ship draught T. However, this dependence was not monotonic with respect to T, and it was concluded that a simplified modelling where z_{LL}/T is independent of the ship draught could sufficiently represent the available data.

It was also observed that the nondimensional extent of damage below water, $h_{bw}/T=(T-z_{LL})/T$, was basically independent of the dimensional vertical extent of damage above water, $h_{aw}=z_{UL}-T$. The same of course holds for z_{LL}/T because $z_{LL}/T=1-h_{bw}/T$. It was therefore concluded that a simplified modelling could be developed, where the dimensionless vertical position of the lower limit of damage from ship bottom, z_{LL}/T, is statistically independent of the dimensional vertical extent of damage above water. The cumulative distribution of this latter quantity, as said, corresponds to the v-factor.

Accidents data, instead, showed a dependence between the dimensionless extent of damage below water h_{bw}/T and the dimensionless damage penetration L_y/B. In particular, there was a clear tendency for h_{bw}/T to increase as L_y/B increases, indicating that damages characterised by larger (dimensionless) penetrations are also associated with larger (dimensionless) extent of damage below water. However, in order to develop a sufficiently simple approach which could be directly embedded in the existing SOLAS zonal framework, this statistical dependence has been neglected in the model presented hereinafter.

From the observation of the available data it was concluded that the distribution of z_{LL}/T could be sufficiently well approximated by a linear trapezoidal probability density function (PDF), with corresponding quadratic cumulative distribution (CDF), having the following general form:

$$\begin{cases} PDF(\zeta_{LL}) = f_0 + 2\cdot(1-f_0)\cdot\zeta_{LL} \\ CDF(\zeta_{LL}) = f_0\cdot\zeta_{LL} + (1-f_0)\cdot\zeta_{LL}^2 \\ \\ f_0\in[0,2] \quad ; \quad \zeta_{LL}=\dfrac{z_{LL}}{T}\in[0,1] \end{cases} \tag{1}$$

The free parameter f_0 is linked to the mean value $\mu_{\zeta_{LL}}$ of $\zeta_{LL}=z_{LL}/T$ as follows:

$$\begin{cases} \mu_{\zeta_{LL}} = E\{\zeta_{LL}\} = \dfrac{2}{3}-\dfrac{f_0}{6} \Leftrightarrow f_0 = 4-6\cdot\mu_{\zeta_{LL}} \\ f_0\in[0,2] \quad ; \quad \mu_{\zeta_{LL}}\in\left[\dfrac{1}{3};\dfrac{2}{3}\right] \end{cases} \tag{2}$$

where $E\{.\}$ indicates the usual expected value operator.

The analysis of data led to an estimated average value $\hat{\mu}_{\zeta_{LL}}$, and corresponding 95% confidence interval, as reported in Table 2.

Table 2. Estimated expected value of dimensionless vertical position of lower limit of damage, all ships.

Number of samples	152
Estimated mean $\hat{\mu}_{\zeta_{LL}}$	0.428
95% confidence interval	[0.384,0.472]

Taking into account (2) and the result in Table 2, it was considered sufficiently accurate to set:

$$f_0 = 1.4 \left(\Leftrightarrow \mu_{\zeta_{LL}} = 13/30 = 0.433 \right) \quad (3)$$

Figure 4 compares the distribution of the dimensionless vertical position of lower limit of damage according to the developed model, and that obtained from the accidents database.

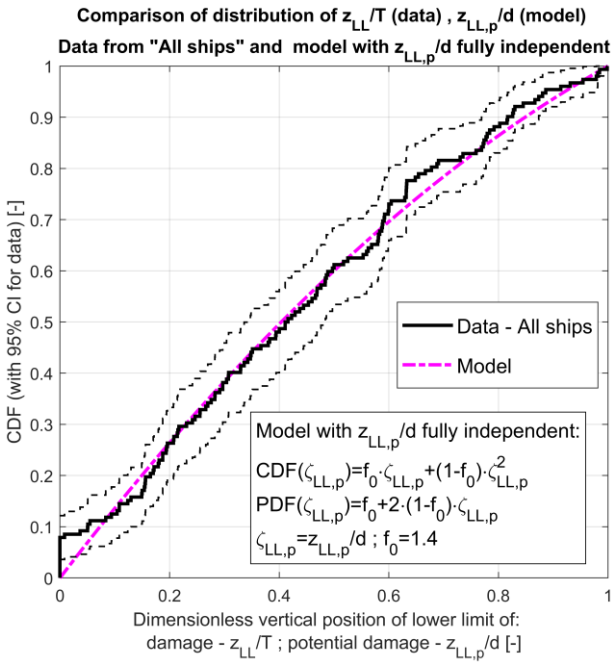

Figure 4. Comparison of distribution of dimensionless vertical position of lower limit of damage between developed model and available accidents data.

Results in Figure 4 indicate that the developed model, despite its simplicity, accurately represents the available data.

3. EMBEDDING OBTAINED RESULTS IN THE SOLAS FRAMEWORK: THE U-FACTOR

The "fully independent" probabilistic model for the lower limit of collision damage, as developed in the previous section, can potentially be used to readily and seamlessly update the existing SOLAS framework, by avoiding the use of the "worst case approach" which is presently embedded in the determination of the s-factor in presence of horizontal subdivisions below water (SOLAS/II-1/B-1/7-2/6.2).

This can be conveniently accomplished by defining a new factor, which can be used similarly to the existing v-factor (SOLAS/II-1/B-1/7-2/6.1), and which, together with the p-factor, r-factor and v-factor, allows the determination of the probability of flooding of a (group of) compartment(s) in presence of combined longitudinal, transversal and horizontal subdivision, when horizontal subdivision boundaries are above and/or below the considered calculation waterline.

This factor, herein referred to, for simplicity, as "u-factor", corresponds to the cumulative distribution function (CDF) of the vertical position of the lower limit of potential damage from the ship bottom (see (1) and (3)), and it has therefore the following expression:

$$\begin{cases} u(z) = f_0 \cdot \dfrac{z}{d} + (1 - f_0) \cdot \left(\dfrac{z}{d} \right)^2 \\ f_0 = 1.4 \quad ; \quad z \in [0, d] \end{cases} \quad (4)$$

The above expression for the u-factor assumes that the vertical position of the ship bottom is conventionally placed at $z = 0m$.

The use of the u-factor, in combination with standard SOLAS factors "p", "r" and "v" will be explained herein through some example applications making reference to the representative geometry reported in Figure 5. The figure reports (half of) a notional transversal section, with combined horizontal and longitudinal subdivision. In addition, it is assumed that the geometry in Figure 5 represents the transversal section of a zone extending between two generic coordinates x_1 and x_2, with corresponding p-factor from SOLAS/II-1/B-1/7-1 being $p(x_1, x_2)$.

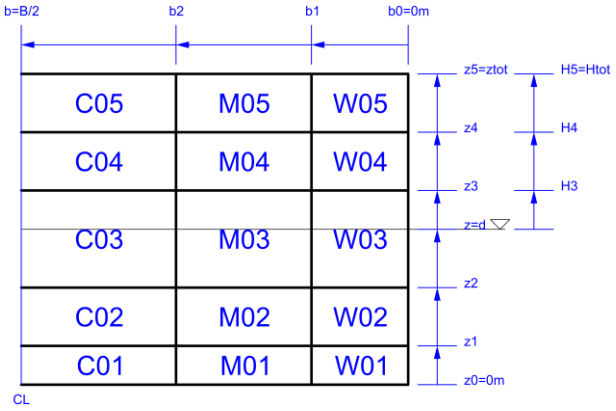

Figure 5. Example geometry for the description of the use of the u-factor.

In general, the probability of flooding of a (group of) compartment(s) in presence of horizontal subdivision boundaries below the considered waterline can be determined by the usual application of p-factor (SOLAS/II-1/B-1/7-1/1.1), r-factor (SOLAS/II-1/B-1/7-1/1.2) and v-factor (SOLAS/II-1/B-1/7-2), with a further multiplicative term which is determined on the basis of the u-factor defined in (4).

As a first example, the probability of flooding only the compartment W03 is considered, which can be calculated as:

$$\begin{aligned}&\Pr\{\text{flooding W03}\} = \\ &= \Pr_{side} \cdot p(x_1, x_2) \cdot r(x_1, x_2, b_1) \cdot \\ &\quad \cdot v(H_3 = z_3 - d) \cdot \\ &\quad \cdot (1 - u(z_2))\end{aligned} \tag{5}$$

In equation (5), $\Pr_{side}$ is the probability that the damage occurs to the specified side and, according to SOLAS framework, it can be taken as 0.5 for each side. Alternatively, if the side of the vessel is deterministically fixed, then $\Pr_{side}$ is to be taken equal to 1.0 for the considered side, and 0.0 for the other. The term $(1-u(z_2))$ represents the probability that the lower limit of damage is above the horizontal subdivision boundary corresponding to the bottom of W03, and which is placed at $z = z_2$. It shall be reminded that damages are assumed to always cross the waterline. Therefore, the probability that the lower limit of the (potential) damage is above the waterline is zero.

As a second example, the probability of flooding, at the same time, compartments W02, W03 and W04 is considered, which can be calculated as follows:

$$\begin{aligned}&\Pr\{\text{flooding W02} \wedge \text{W03} \wedge \text{W04}\} = \\ &= \Pr_{side} \cdot p(x_1, x_2) \cdot r(x_1, x_2, b_1) \cdot \\ &\quad \cdot \left(v(H_4 = z_4 - d) - v(H_3 = z_3 - d)\right) \cdot \\ &\quad \cdot \left(u(z_2) - u(z_1)\right)\end{aligned} \tag{6}$$

In this case, the term $\left(u(z_2) - u(z_1)\right)$ represents the probability that the lower limit of the (potential) damage is within z_1 and z_2.

As a final example, the probability of flooding W01, W02, W03, W04 and W05, is considered, which can be determined as follows:

$$\begin{aligned}&\Pr\left\{\begin{matrix}\text{flooding W01} \wedge \text{W02} \wedge \\ \wedge \text{W03} \wedge \text{W04} \wedge \text{W05}\end{matrix}\right\} = \\ &= \Pr_{side} \cdot p(x_1, x_2) \cdot r(x_1, x_2, b_1) \cdot \\ &\quad \cdot \left(1 - v(H_4 = z_4 - d)\right) \cdot \\ &\quad \cdot u(z_1)\end{aligned} \tag{7}$$

In this case $u(z_1)$ represents the probability that the lower limit of (potential) damage is below the upper limit of compartment W01, which is placed at $z = z_1$.

Similar expressions are obtained when, instead of determining the probability of flooding of (groups of) W_j compartments, the interest is on the determination of the probability that also inner M_j compartments (see Figure 5) are involved in the damage. In this case it is sufficient to substitute $r(x_1, x_2, b_1)$ in (5)-(7) with $\left(r(x_1, x_2, b_2) - r(x_1, x_2, b_1)\right)$ in accordance with the standard SOLAS zonal approach. Similarly, when the interest is on the probability of damaging up to central C_j compartments (see

Figure 5), then $r(x_1, x_2, b_1)$ in (5)-(7) is to be substituted by $1-r(x_1, x_2, b_2)$. Similar formulations can be applied for any other particular case.

Finally, the introduction of the u-factor allows to avoid the use of the "worst case approach" (SOLAS/II-1/B-1/7-2/6.2) for the determination of s-factor in presence of horizontal subdivision below waterline. In fact, in the limits of the SOLAS approximations and of the approximations embedded in the model underlying the u-factor, the u-factor now allows to determine a specific probability of flooding for each damage case, also in presence of horizontal subdivision boundaries below the waterline. This is instead not possible within the present SOLAS framework.

As a result, for each generic calculation draught, the corresponding partial attained index can be determined simply as:

$$A_c = \sum_i \Pr_{side,i} \cdot (prvu)_i \cdot s_i \quad \text{with} \quad c = l, p, s \qquad (8)$$

where the summation is extended to all damage cases for the considered calculation draught. The term $\Pr_{side,i} \cdot (prvu)_i$ is the probability of flooding for the i-th damage case as determined by the damage side probability $\Pr_{side,i}$ and corresponding appropriate combination of p-factor, r-factor, v-factor and u-factor. The term s_i is the s-factor calculated for the considered damage case. Accordingly, there is no longer need to define a "minimum s-factor" as it is instead presently done in SOLAS/II-1/B-1/7-2/6.2, and the possible presence of horizontal subdivision boundaries is now consistently accounted for in the determination of the attained index.

4. APPLICATION

In order to assess the effect of the introduction of the developed probabilistic model for the lower limit of damage through the u-factor, an application was carried out on a sample vessel. The vessel used in the calculations is a panamax cruise ship with subdivision length of approximately 230m, carrying a number of persons onboard in the range of 2000, and with a required index R=0.77 according to SOLAS2009. The vessel is characterised by having horizontal subdivision boundaries below the waterline.

In the application, the partial attained subdivision indices $A_c\ (c = l, p, s)$ and the global attained subdivision index $A = 0.2 \cdot A_l + 0.4 \cdot A_p + 0.4 \cdot A_s$ have been calculated according to two approaches. On the one hand, calculations were carried out according to standard SOLAS, using, therefore, the "worst case approach". On the other hand, calculations were done by using the SOLAS zonal approach supplemented with the u-factor developed herein.

Based on the obtained results, the increase of attained indices as given by the introduction of the u-factor has been determined. Figure 6 reports the increase of partial attained indices for the three calculation draughts ($\delta A_l, \delta A_p, \delta A_s$) and the corresponding increase of the global attained index (δA).

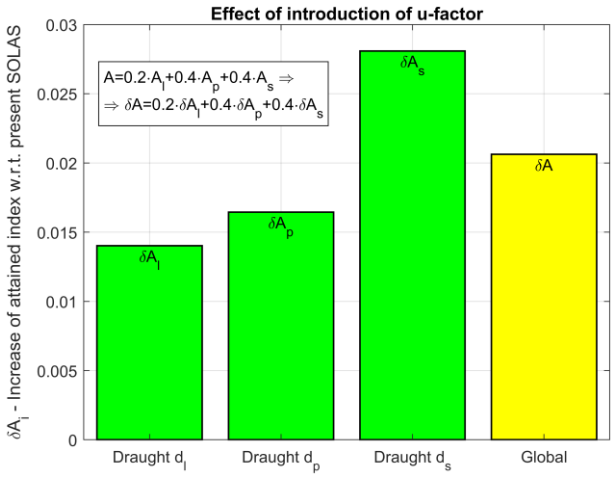

Figure 6. Assessment of the introduction of u-factor: increase of A-indices with respect to standard calculations based on present SOLAS.

Results in Figure 6 show an increase of all attained indices. Qualitatively, this is of course an expected result. In fact, in case of damage

cases limited by horizontal subdivision boundaries below water, the present SOLAS methodology uses the "worst case approach" for the determination of s-factor, whereas the introduction of the proposed u-factor leads to a fair weighting of the s-factors according to the probabilities of flooding the corresponding (group of) compartment(s). Eventually, quantitatively, for the considered sample vessel, the introduction, through the u-factor, of a probabilistic model for the lower limit of potential damage has a clear impact on the attained indices.

5. CONCLUSIONS

Present SOLAS damage stability regulation embeds probabilistic models for the longitudinal position, the length, the transversal penetration and the vertical extent above water, of collision damage. The corresponding models represent the bases for the derivation of SOLAS p-factor, r-factor and v-factor. However, although in SOLAS the damage is assumed to be crossing the waterline, and although it is recognised that the damage can have different extents below water, no probabilistic model is embedded in the regulation in this respect. As a result, it is not possible, within present SOLAS, to actually determine the probability of flooding a (group of) compartment(s) when there is a horizontal subdivision boundary below the waterline.

To cope with this limitation, SOLAS uses a "worst case approach", often referred to as "damages of lesser extent", for the calculation of the s-factor, where the minimum s-factor is considered among all the possible damages involving different horizontal subdivision boundaries below the waterline.

However, although practical, this approach is not probabilistically sound, and when horizontal subdivision boundaries below water are present, this approach leads, in general, to an underestimation of the actual ship survivability. Moreover, the use of such an approach may also lead to a misinterpretation of the effect of horizontal subdivision boundaries below water.

To address this problem, the paper has presented the development of a probabilistic model addressing the extent of collision damages below water, with a view to a link with the existing SOLAS framework.

The model was developed on the basis of damage characteristics from the GOALDS accidents database. Consistently with present SOLAS regulation, which uses harmonized probabilistic models of damage characteristics for passenger and cargo ships, data from all ships were considered in the analysis.

Simplifications have been introduced in the modelling, in order to allow a potential simple and straightforward introduction in the existing SOLAS zonal framework. According to the developed probabilistic model, a new u-factor has been defined, which corresponds to the cumulative distribution of the vertical position, from the ship bottom, of the lower limit of damage below water. This new u-factor can potentially be used, together with existing SOLAS p-factor, r-factor and v-factor in order to consistently calculate the probability of flooding a (group of) compartment(s) also in presence of horizontal subdivision boundaries below the waterline. The use of the u-factor is very similar to that of the v-factor, and the introduction of the u-factor in the existing SOLAS formulation is straightforward. In this respect, examples have been shown on how to determine the probability of flooding of (group of) compartment(s) accounting for horizontal subdivision boundaries both above and below the waterline.

The developed methodology has been tested on a sample cruise ship. Qualitatively, results indicated the expected increase of all attained indices (partial and global). Eventually, quantitatively, for the considered sample vessel, the introduction, through the u-factor, of a probabilistic model for the lower limit of

potential damage had a clear impact on the attained indices.

Eventually, the developed u-factor could provide a complement to the existing SOLAS framework, making it a truly fully probabilistic one. This could lead to a more consistent estimation of the ship survivability level, by avoiding the underestimation of ship survivability as obtained by the present application of the "worst case approach" for the s-factor in presence of horizontal subdivision boundaries below water. Moreover, the extension of the existing SOLAS framework with the introduction of a consistent probabilistic model for the extent of damage below water may also lead to a better, more properly informed interpretation of the effect of horizontal subdivision boundaries below water on the overall performance of the ship in damaged condition. In addition, the introduction of a probabilistic model for the lower limit of damage allows the implementation of a non-zonal approach for collision damages.

6. ACKNOWLEDMENTS

This work was carried out in the framework of the project "eSAFE – enhanced Stability After a Flooding Event – A joint industry project on Damage Stability for Cruise Ships". The funding partners of eSAFE are: Carnival Corporation Plc, DNV GL, Fincantieri, Lloyd's Register, Meyer Werft, RINA Services, Royal Caribbean Cruises Ltd. and STX France. The financial support from the eSAFE funding partners is acknowledged. The information and views as reported in this paper are those from the authors and do not necessarily reflect the views of the eSAFE Consortium.

7. REFERENCES

Bulian, G., Francescutto, A., 2010, "Exploratory data analysis of ship-ship collision data from the updated GOALDS database", Department of Mechanical Engineering and Naval Architecture, University of Trieste, Project GOALDS (GOAL based Damage Stability) - Grant Agreement 233876, 30 August.

Bulian, G., Lindroth, D., Ruponen, P., Zaraphonitis, G., 2016, "Probabilistic assessment of damaged ship survivability in case of grounding: development and testing of a direct non-zonal approach", Ocean Engineering, Vol. 120, pp. 331-338.

IMO, 2008, "Resolution MSC.281(85) – Explanatory Notes to the SOLAS Chapter II-1 Subdivision and Damage Stability Regulations", 4 December

IMO, 2012, "Document SLF55/INF.7 – The GOAL based Damage Stability project (GOALDS) – Derivation of updated probability distributions of collision and grounding damage characteristics for passenger ships", Submitted by Denmark and the United Kingdom, 14 December.

IMO, 2018, "International convention for the Safety of Life at Sea (SOLAS)", Consolidated Edition as of 2018

Lützen, M., 2001, "Ship Collision Damages", PhD Thesis, Department of Mechanical Engineering, Technical University of Denmark, December.

Lützen, M., 2002, "Damage Distributions", HARDER Document 2-22-D-2001-01-4, 29 July.

Mains, C., 2010, "WP3 Database of damage characteristics - File: GOALDS-database-rev3.xls", Germanischer Lloyd, Project GOALDS (GOAL based Damage Stability) - Grant Agreement 233876.

Tagg, R., Bartzis, P., Papanikolaou, A., Spyrou, K., Lützen, M., 2002, "Updated vertical extent of collision damage", Marine Structures, Vol. 15, pp. 475–498.

Life-Cycle Flooding Risk Management of Passenger Ships

Dracos Vassalos, Maritime Safety Research Centre, d.vassalos@strath.ac.uk

Georgios Atzampos, Maritime Safety Research Centre, georgios.atzampos@strath.ac.uk

Jakub Cichowicz, Maritime Safety Research Centre, jakub.cichowicz@strath.ac.uk

Donald Paterson, Maritime Safety Research Centre, d.paterson@strath.ac.uk

Kristian B. Karolius, Maritime Safety Research Centre, kristian.karolius@strath.ac.uk

E. Boulougouris, Maritime Safety Research Centre, evangelos.boulougouris@strath.ac.uk

Tor Svensen, Maritime Safety Research Centre, tor.e.svensen@strath.ac.uk

Kevin Douglas, Royal Caribbean Cruises Ltd, kevindouglas@rccl.com

Henning Luhmann, Meyer Werft GmbH & Co.KG, henning.luhmann@meyerwerft.de

ABSTRACT

The paper describes the background and provides the rationale and the framework to embrace the whole spectrum of measures (design, operational and emergency response) for improving the damage survivability of existing and newbuilding passenger vessels. Damage control, evacuation, Life-Saving Appliances, rescue and crisis management are all topics attracting a great deal of attention but how all this fits in and is accounted for? How are these being addressed during the design stage and how effective are they post-accident in a way that this can be quantified and accounted for in calculating life-cycle risk? Developments to address these questions are still embryonic. This represents a step change both in the mind-set of naval architects and in safety legislators but the impact of having in place such a framework will be immense and mostly positive. Zero-risk tolerance is a goal but rendering modern passenger ships into lifeboats is certainly within reach. An attempt to delve in this direction is presented in this paper by presenting a life-cycle framework of de-risking flooding risk.

Keywords: *Damage stability, flooding risk, vulnerability management, life-cycle risk, safety assessment*

1. INTRODUCTION

Recent disasters in the passenger ship industry serve to demonstrate that a proper framework and process for risk mitigation of large-scale accidents in the marine industry is lacking (e.g. MS Costa Concordia, MS Norman Atlantic). Despite considerable advances in science and technology, leading to unique capabilities to design ships and offshore assets to high level of safety (passive means of risk reduction), development to address management of residual risk during ship operation and in emergencies is still embryonic. As a result, the last line of defence in safety provision (damage control, emergency response, crisis management, escape, evacuation and rescue) is dealt with haphazardly and hence ineffectively. This is particularly true in large-scale accidents, where failure nowadays might include ships and assets of such proportions that the potential impact on human life and the environment can completely re-shape or indeed eradicate the whole industry. Therefore, the need to address these issues systematically and methodologically is paramount. This should involve all means for risk mitigation and control during accidents, with on-board or shore-based decision support systems for emergency response and crisis management as well as effective means of evacuation and rescue. Moreover, as safety affects everything on-board a ship and is affected by anything, an attempt to rank and assign merit to any such measure in a

way that this is accounted in the risk evaluation and decision making will lead to step changes in maritime safety, mostly positive.

This paper is an attempt to pave this way forward by presenting a holistic, methodological approach of risk reduction / mitigation during design, operation and in emergencies.

In the specific case of flooding risk, a multi-phase, multi-level process is demonstrated, encompassing design, operation and emergency response phases of life-cycle risk management.

2. BACKGROUND

Every time there is a collision/grounding accident involving passenger ships, their vulnerability to flooding is exposed. Societal outcry follows and industry and academia "buckle up", delving for design improvements to address the Achilles heel of this ship type, namely damage stability. However, any such improvements are targeting mainly new buildings, which comprise a small minority of the existing fleet. Therefore, state-of-the-art knowledge on damage stability is all but wasted, scratching only the surface of the problem and leaving thousands of ships with severe vulnerability, that is likely to lead to further (unacceptably high) loss of life. This problem is exacerbated still further, today more rapidly, as the pace of scientific and technological developments is unrelenting, thus raising understanding and capability to address damage stability improvements of newbuildings cost-effectively, in many ways not previously considered. As a result, SOLAS (Safety of Life at Sea) is becoming progressively less relevant and unable to keep up with this pace of development. This has led to gaps and pitfalls, which not only undermine safety but also inhibit progress.

Moreover, lack of retrospectively applied legislation (supported by what is commonly known as the Grandfather Clause) is not the only reason for damage stability problems with passenger ships. Tradition should share the blame here. In the quest for damage stability improvement, design (passive) measures have traditionally been the only means to achieve it in a measurable/auditable way (SOLAS 2009, Ch. II-1). However, safety affects everything on-board a ship and is affected by myriad of factors relating to engineering and management: people, processes, technology, organisation and environment. In this respect, they also reflect in rules, regulations, codes of practice and internal procedures; these could be passive, active, removable, non-removable, endogenous, exogenous, etc. One way of demonstrating this holistic approach to safety pre- and post-accident is through the "bow-tie" diagram (Figure 1). In these, all measures to prevent, control or mitigate flooding risk as act as "barriers" that need to be evaluated, monitored and cost-effectively managed through the life cycle (King, et al., 2015).

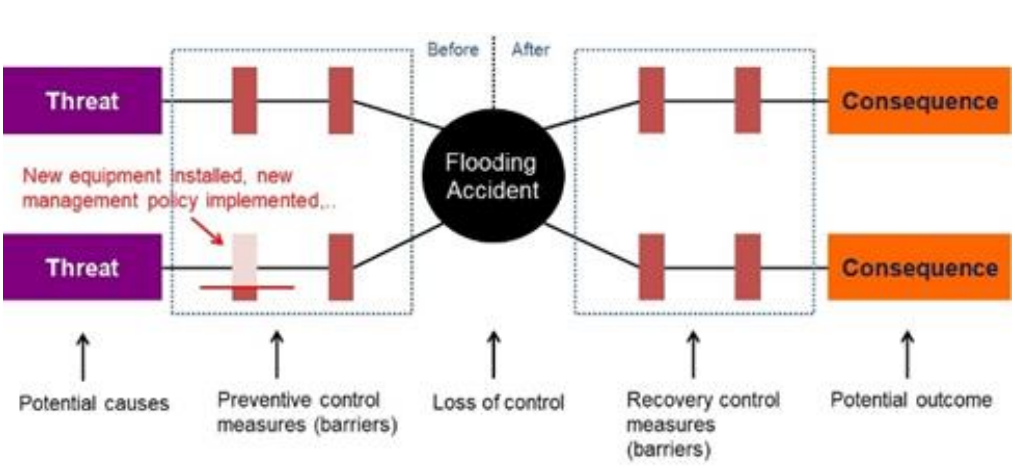

Figure 1: Barrier Management Concept

In principle, therefore, the consequences from inadequate damage stability can also be reduced by other (non-design) means, for example operational (active) measures, which may be considerably more cost-effective in reducing loss of life. The question is: why do we limit choice only to design solutions? There are three main reasons for this. The first relates to the traditional understanding that operational measures safeguard against erosion of the design safety envelop (possible increase of residual risk over time). The second derives from lack of measurement and verification of the risk reduction potential by any active measures. The third is a consequence of the second, namely the absence of a life-cycle risk-based regulatory framework to facilitate and guide the whole process. In simple terms, what is needed is the means to account for risk reduction by operational measures as well as measures that may be taken during emergencies. Such risk reduction may then be considered alongside (though ultimately instead) of risk reduction deriving from design measures. With this in place, new measures for risk reduction (operational and in emergencies) will be considered in addition to design measures. Therefore, what needs to be demonstrated and justified is the level of risk reduction and a way to account for it, the latter by adopting a formal process and framework and by taking requisite steps to institutionalise it.

3. BASIC CONCEPTS

3.1 Ship vulnerability

"Vulnerability" is a word being used extensively in the naval sector (Ball & Calvano, 1994) but not so in merchant shipping in so far as damage stability is concerned; Vulnerability is, of course, used in the second generation intact stability criteria with specific definition provided in SDC 5, par. 1.2 (IMO, 2016).

The way this term has been used by MSRC relates to "the probability that a ship may capsize or sink within a certain time when subjected to any feasible flooding scenario." As such, vulnerability contains (and provides) information on every parameter that affects ship damage stability (Vassalos, 2012). A simple example is provided next.

Figure 2 indicates that there are 3 possible flooding cases, following collision, of known (available statistics) frequency and calculable (available "tools") probability of surviving, say 3 hours. With this information at hand, vulnerability to collision flooding of this simple example is:

$$\mathbf{0.5 \times 0.72 + 0.35 \times 0.01 + 0.15 \times 0.99 = 51.2\%}$$

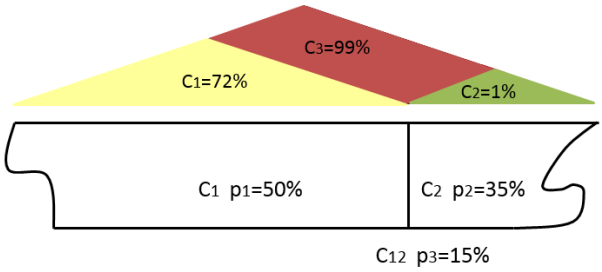

Figure 2: Vulnerability to Collision Flooding

3.2 Vulnerability in ship design

The vulnerability to flooding of passenger ships is well documented through a number of accidents claiming many lives (e.g. MS Estonia). Such vulnerability relates in many cases to Water on Deck (WoD), that is flooding into large, undivided cargo spaces, leading often to rapid capsize of the ship. Whilst for this ship type design vulnerability is well understood, for cruise ships a similar mode of loss has been brought to light as recently as the early 2000s (Vassalos, et al., 2005). The latter case relates to the service corridor on the subdivision deck, which acts as conduit for floodwater to spread along the ship, leading to down flooding through deck openings / stairwells and ultimately to sinking / capsize of the ship. Figures 3 and 4 provide typical results demonstrating such vulnerability in the design of RoPax and Cruise vessels, respectively.

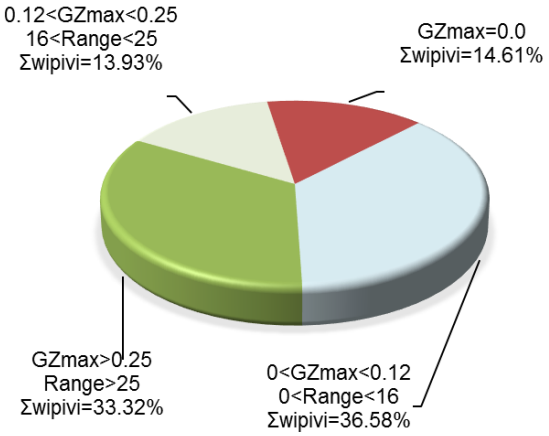

Figure 3: Design Vulnerability (Watertight Integrity – typical RoPax)

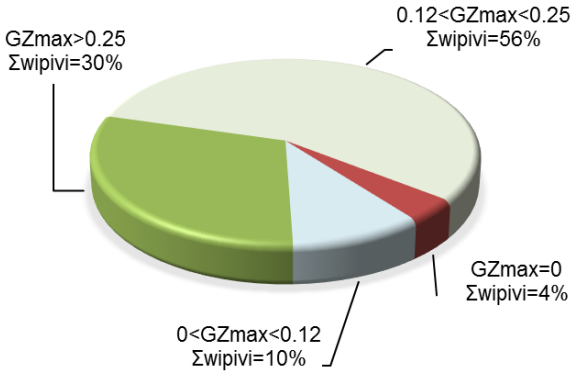

Figure 4: Design Vulnerability (Watertight Integrity - typical Cruise Ship)

3.3 Vulnerability in operation

A threat that exacerbates further the design vulnerability to flooding of passenger ships, probably at the heart of many catastrophes, is vulnerability in operation. This is an issue that has been attracting serious attention at IMO over many years and new legislation is now in place (IMO, June 2006). It aims to address the fact that passenger ships are operated with a number of Watertight (WT) doors open, thus worsening considerably the design vulnerability of these ships, SOLAS II-1/15. Figures 5 and 6 demonstrate this rather emphatically by considering the well-known Estonia case (Jasionowski, 2011), as designed and as operated at the time of her loss. In the latter case (because of open WT doors), the vulnerability of the vessel was at 68%; 3.5 times higher than her design vulnerability of 19%.

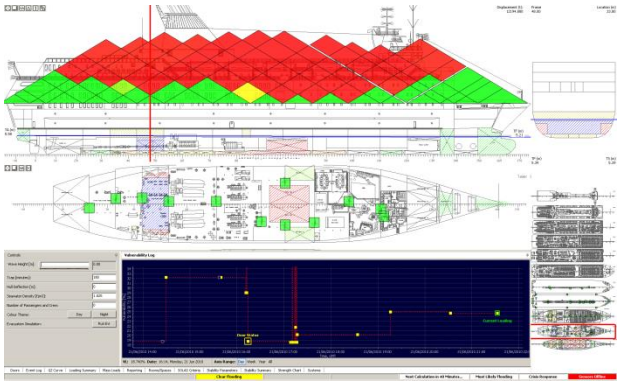

Figure 5: MV Estonia - Design Vulnerability

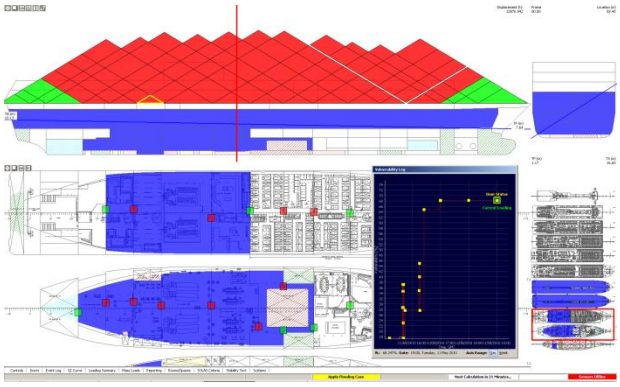

Figure 6: MV Estonia - As Operated at the Time of her Loss

4. LIFE-CYCLE FLOODING RISK ASSESSMENT

Traditionally, regulations (e.g. SOLAS, Ch. II-1), focus on built-in solutions, identified normally during the design phase. Active/interventional measures considered during operation or emergency response phases, whilst fuelling debates on their risk reduction potential, has never been actually measured or verified, as explained in the foregoing. These cover many areas and measures such as Damage Control, Decision Support Systems for Crisis Management, Evacuation, LSA, Escape and Rescue.

A framework that facilitates assignment of risk merit to every risk control measure is key to life-cycle risk management. A life-cycle perspective facilitates a holistic approach to damage stability, encompassing risk control options for all three phases and accounting for each by using, for example, IMO cost-effectiveness criteria. This, however, assumes that the risk reduction potential of all such measures is known and, as explained earlier, this is where there is a big gap in this approach that needs to be overcome before such a process can be formalised and adopted. This constitutes the kernel of the work to be undertaken. With this perspective in mind, Figure 7 presents, in a form of flowchart, a "pipeline" comprising different phases and levels of a life-cycle vulnerability assessment approach, which is elaborated further in the following sections. The levels referred to in this figure relate to the fidelity of the tools being used to address specific requirements during the life-cycle, namely static or quasi-static, time-domain numerical simulation tools and high-fidelity tools such as Computational or Experimental Fluid Dynamics. Such approach is justified as different design stages (concept, preliminary, detail), require different tools that best satisfy the constraints and objectives in the design process. For example, watertight subdivision, general dimensioning of internal arrangements, initial positioning of ship systems, evacuation routes and arrangements would require low-fidelity, fast and accurate tools.

On the other hand, modelling transient, progressive and cross- flooding processes in extreme sea states with the view to identify loss-scenarios post-casualty demands robust and versatile tools (e.g., time-domain simulation tools). At the extreme, in cases where the detail offered by the most advanced Computational Fluid Dynamic and Experimental Fluid Dynamic tools will make a difference, use of these (Level 3 tools) is justified. In fact, use of Level 2 and 3 tools will also be required for verification purposes (for example approval of Alternative Design and Arrangements); this would apply to all three life-cycle phases. More detail is provided in the following by addressing each phase separately.

Figure 7: Multi-Phase, Multi-Level process for life-cycle-flooding risk management

5. PHASE 1: DESIGN PHASE

Decisions made during the design phase shape safety over the whole life cycle. In this respect, use of advanced tools and exploiting knowledge in all forms at the design stage is most effective and, hence, highly desirable. This may be done incrementally, with simpler tools at the initial stages, then progressively introducing more advanced tools as design matures. In this respect, the design phase may be addressed in three levels namely, static vulnerability assessment, dynamic vulnerability assessment and verification and approvals as outlined in the following.

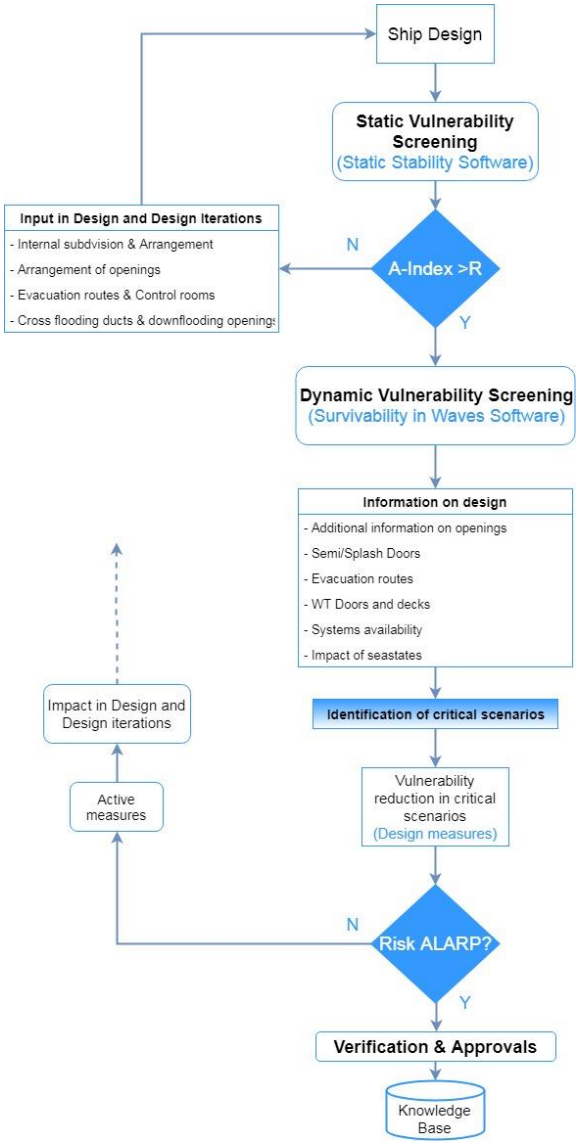

Figure 8: Design Phase

5.1 Static Vulnerability Screening

As highlighted in Figure 8, this relates to using industry standard damage stability software to undertake probabilistic damage stability calculations leading to assessing Index A for rule compliance. This entails generating damage scenarios from flooding (presently only collision) events deriving from SOLAS-related accident statistics. In the process, design vulnerabilities may be identified to support and guide decision-making concerning initial subdivision or other watertight/weather-tight arrangements and openings. Downflooding and cross-flooding arrangements and constraints set by evacuation routes and other access as well as performance requirements are also considered. Assuming that all key design vulnerabilities are accounted for through this process, then the output from it also provides key input for vulnerability monitoring during the operational phase as well as for damage control and emergency response. The latter, however, has yet to be proven and demonstrated. Hence, at present, existing static damage stability software should better be utilised for design iterations and decision support only at the concept stage.

5.2 Dynamic Vulnerability Assessment

For more in-depth information on the mechanics of the flooding process and filtering of scenarios for critical scenarios identification, time-domain flooding simulations need to be used. Such methodology, utilising dynamic stability assessment tools, for example PROTEUS (Cichowicz & Vassalos, 2009), allows for addressing the whole flooding process (see Figure 8 and Figure 9). Damage breach generation should lead to the same initial flooding scenarios, irrespectively of the static or dynamic nature of the calculations (Luhmann, et al., 2018). Screening of critical scenarios with the aid of numerical time-domain simulations accounts for the impact of the operating environment (wind, waves, current) as well as of the floodwater progression in the ship internal spaces, including interactions between sea-floodwater-ship in a continuously evolving dynamic environment. Investigating systematically the ensuing results allows for identification and ranking of design vulnerabilities, e.g. large undivided spaces and horizontal or vertical openings that lead to large/progressive flooding; similar to the static vulnerability assessment but now properly considering the physics of the problem at hand. These provide the right focus for vulnerability reduction (design solutions) or vulnerability mitigation (damage control, WTD management), based on cost-effectiveness or indeed other owner or designer criteria. What is most important to understand is that, through experience, design vulnerabilities are limited in modern passenger ship designs. As a result,

vulnerability screening ends up with a handful of critical scenarios, where the survivability of the vessel is compromised (see Figure 9). Such vulnerabilities are normally linked with behaviour of the ship in extreme damages and environments, again unrelated to static/quasi-static behaviour in calm water. Importantly, this analysis provides a set of properly-defined critical scenarios with potential for loss of the ship and, ultimately, loss of life. Hence, realistic target scenarios are identified for "de-risking" the vessel, either by suitable design solutions or by emergency response measures, as explained in the following. In this respect, the link between design and operation (including emergencies) is formally addressed and the benefit is clearly obvious (Jasionowski, 2009).

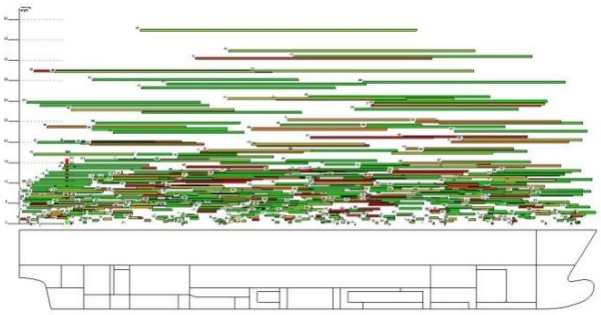

Figure 9: Typical collision scenarios considered in numerical simulation for vulnerability screening (Monte Carlo sampling of collision accident statistics)

5.3 Vulnerability reduction (design measures / options)

Using a range of tools, from simple static calculations of stability and vulnerability to numerical time-domain simulations, feasible design changes with vulnerability reduction potential are examined to address problems identified in Level 2.

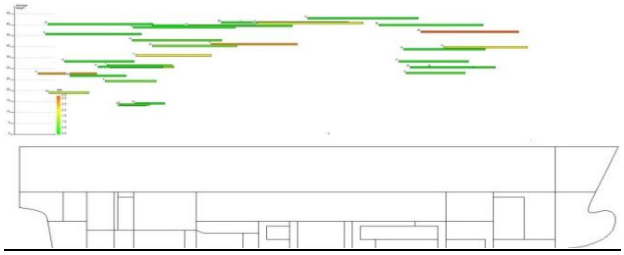

Figure 10: Typical results following vulnerability screening, demonstrating regions of vulnerability in design (critical scenarios)

Design changes may vary from simple internal modifications such as the installation of additional doors, introducing chamber doors, removing / relocating openings as well as rendering parts of decks watertight through structural modifications. Ultimately, changes in main dimensions or loading conditions for newbuildings or external modifications for existing vessels, such as ducktail or sponsons, could be investigated, The impact on the overall vulnerability of each option is assessed (with regard to safety and cost) and all implications critically examined. For example, some of these design options may inherently present additional benefits, such as increased GM margins, increased deadweight capacity and reduced fuel consumption or drawbacks, such as additional weight, increased fuel costs and reduced access in addition to direct costs (see for example Figure 11). Therefore, targeted optimisation exercises may be needed.

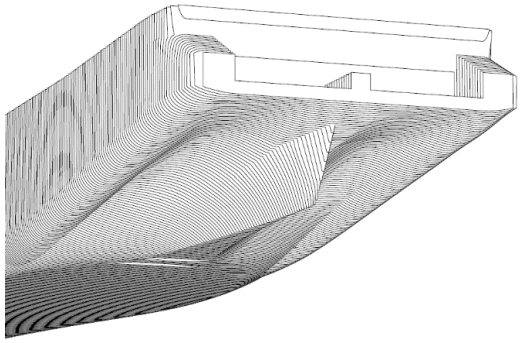

Figure 11: Complex external modifications (Ducktail, Sponsons, Skeg)

More advanced time-domain simulations tools afford knowledge leading to forensically

examining the flooding process in critical scenarios and, hence leading to solutions for preventing progressive flooding and hence saving the ship. Figure 12, for example, indicates frequencies (through a colouring scheme) of floodwater propagation through various openings on the subdivision deck, hence identification of critical openings concerning floodwater propagation in critical scenarios. Similarly, Figure 13 relates to examining strength of semi-watertight (splash type doors) and of the windows when immersed during progressive flooding.

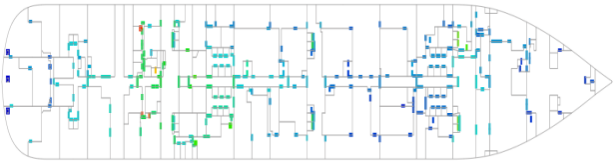

Figure 12: Vulnerability screening (identification of focal areas/details for improved survivability)

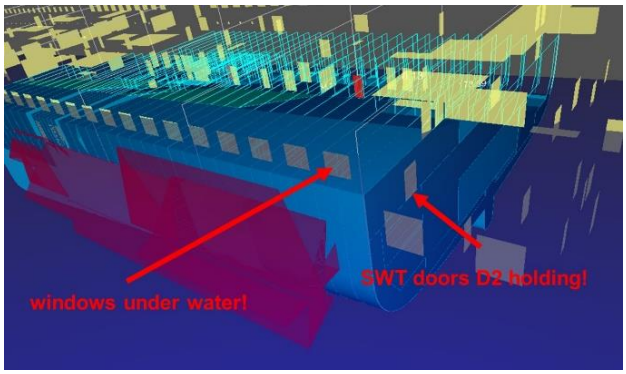

Figure 13: Vulnerability screening (identification of design detail for improved survivability) (Vassalos & Guarin, 2009)

Decision-making concerning choice, based on cost-effectiveness of design or other measures for risk reduction, follows an established process at the International Maritime Organisation (IMO, 2008) based on cost-effectiveness, targeting risk levels As Low As Reasonably Practicable (ALARP – Figure 14).

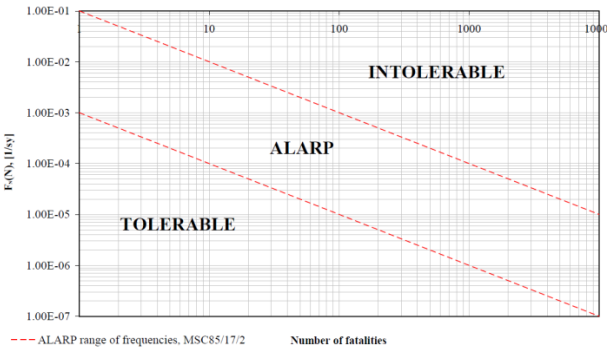

Figure 14: Decision Parameters and Risk Acceptance Criteria

5.4 Verification and Approvals

Whilst considerable work has been undertaken by the International Towing Tank Conference (ITTC 2002, 2005, 2008) to develop a process to validate and verify numerical time-domain simulation tools addressing intact and damage stability, there has been limited uptake by the industry, with a few notable exceptions (e.g., Oasis of the Seas, using model experiments, ITTC proceedings 2009). The reason for this derives partly from the fact that the scientific community pursuing damage stability has not managed to achieve critical mass with most of the work addressing damage stability by performing time-domain numerical simulations taking place at MSRC, NTUA (Papanikolaou, 2008) and MARIN (de Kat, 2015).The second derives from an uncharacteristic inertia by the maritime industry to adopt numerical simulation work as part of safety performance verification in the design stage. This, in turn incentivises further investment for developing requisite tools and the syndrome of "chicken and egg" reigns. For the passenger ship industry and for the leading operators safety is the foundation of their business with many investing demonstrably towards safety improvement of their fleet. The responsibility therefore lies with the regulators, designers and academia.

A clear example of such initiatives being taken by industry is the eSAFE Project (Luhmann, 2016). In this project, PROTEUS has been used as the platform for undertaking numerical time-domain simulations in a seaway

as the basis for developing a new survivability factor (s-factor) for cruise ships. In principle, the eSAFE numerical experiments played a similar role to the physical experiments performed in the HARDER and GOALDS projects. Within fact, results from numerical simulations were used as the basis to derive formulations for the probability of survival (local and ship levels). CFD models have then been developed and used to verify the numerical simulation results (Figure15). This is the first-ever attempt where verification at this level of detail has been undertaken. As a result, various problems surfaced regarding effort and time but also the realisation that whilst serious and concerted effort might be required to develop a verification platform for damage survivability, this is not only feasible but also highly desirable (Ruth, et al., 2017). In this particular case, verification does not address only the numerical tools per se but also the use of such tools to estimate Index A by the Direct Method (Vassalos, 2015). In addition, verification should also address the use of numerical simulations (as an alternative to the SOLAS 2009 prescribed calculations) of damage survivability based on the guidelines for use of alternatives as described in "Alternative Design and Arrangements"(IMO,2013). In this respect, it is encouraging to see that the EC has recently invited proposals for research in this very area (EC, 2018).

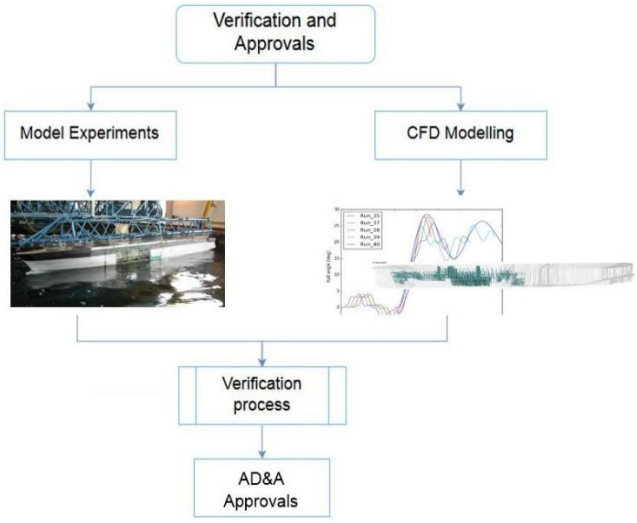

Figure 15: Level 3: Verification and Approvals

6. PHASE 2: OPERATIONAL PHASE

Operation is the longest phase in the ship life-cycle, during which changes take place, which have a direct impact on risk. Therefore, risk must be monitored and reviewed to ensure changes in design / operation are reflected in the way risk is managed. This sounds straightforward in so far as changes take place in tangible, hence measurable, ship and environmental parameters, e.g., draft levels, loading condition, fluid tank levels, even watertight door status as well as prevailing wind and wave conditions. There are many other significant parameters and conditions, however, for example changing the ship master, improving navigational equipment, and so on, which affect safety significantly and unarguably. Amazingly, the impact of the majority of these changes on safety cannot, at present, be measured and hence monitored as we have not yet devised a way to assign risk credit/value to such changes. Notwithstanding this, monitoring what can be measured and is known to be KPI for safety (in this case flooding risk in real time) is a step in the right direction (this is depicted in Figure 16). The saying that if "we can measure it we can improve it" applies equally well here. This is further explained next.

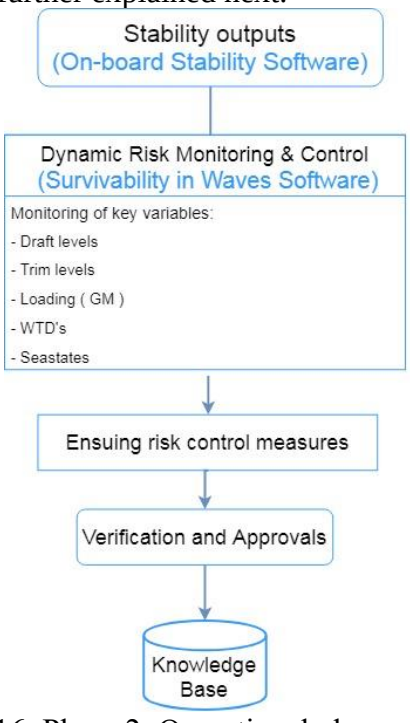

Figure 16: Phase 2: Operational phase

6.1 Dynamic risk monitoring and control

In the operational phase the main stability parameters are derived via on-board loading computer programs. These may be used as inputs in a dynamic stability assessment platform (e.g., PROTEUS) and subjected to further monitoring with respect to impact from WTDs, sea states and the actual operational loading of the vessel. The output, for example ship vulnerability as defined in the foregoing, could be monitored, providing all requisite information for effective management of the flooding risk. The emphasis here is on preparedness and being in a position of readiness to respond to an emergency. An additional advantage for operators relates to having all main ship systems, including safety systems, modelled as part of the Safe Return to Port requirements (IMO, 2010). More specifically, there are clear benefits derived in using ship systems effectively as well as having a platform in place to train new crew in the use of ship systems.

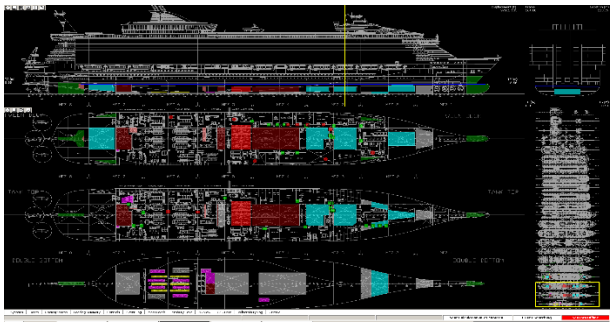

Figure 17: on-board loading computer

6.2 Vulnerability mitigation measures

Vulnerability mitigation entails the use of operational measures, such as training, counter-ballasting, procedures and policies. Counter ballasting, in particular, will require knowledge of the residual functionality of the related systems in each one of the scenarios in question, to enable action being taken as appropriate. This, in turn, may suggest modelling and availability analysis of such systems, and preparing crew operating manuals. Alternatively, some degree of automation (decision support) may be required to render the operation effective and time-efficient (Vassalos & Jasionowski, 2013).

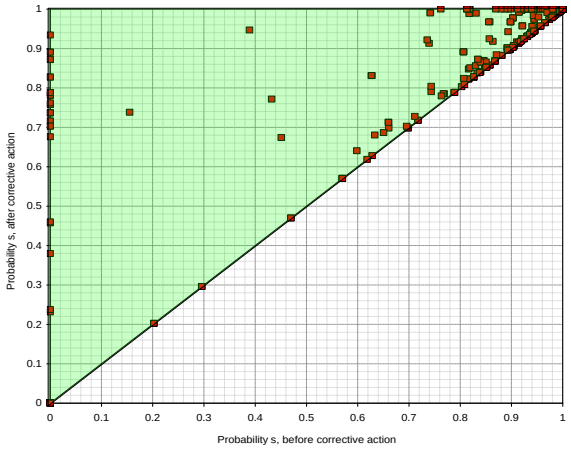

Figure 18: Counter-ballasting capacity post-casualty (typical example)

Once all requisite or possible actions had been taken, there will be a limited number of scenarios for which the probability of the ship capsizing/sinking will still be high, even if the risk of the ship is tolerable, as derived from applicable regulations. These scenarios constitute the emergency scenarios and are examined in the following phase, namely the emergency response phase.

7. PHASE 3: EMERGENCY RESPONSE PHASE

The emphasis, in this phase, is on ensuring that in any of the critical scenarios where ship stability is compromised, the ship will remain upright and afloat, with all safety systems available, for sufficient time to ensure safe evacuation of all the people on-board.

However, similar to the operational phase most of the key elements affecting emergency response are not measurable/auditable, thus not providing any guidance to the operator in his strive to adopt cost-effective means to mitigate and control flooding risk in this vital last phase. This may entail, for example, introducing a Safety Centre, new LSA, a Decision Support

System for crisis management, emergency response teams and emergency response drills. Furthermore, new technologies are explored to enhance situational awareness and guidance of evacuees during emergencies, interventional measures to restore stability post damage and so on. Unfortunately, none of these are assigned a risk credit. Therefore, there is no incentive to introduce/improve any of the above.

Even for procedures included in the regulations (SOLAS, 2009), for example mustering and abandonment, the guidelines are too high level (IMO, 2016), they address irrelevant scenarios and in many cases they are unable to address the real problem. Abandonment time of 30 minutes in the rules with ships having 10,000 people on-board is a clear indication that the regulations have become irrelevant. More importantly, they undermine safety.

In order to manage the emergency response efficiently many aspects need careful attention. Primarily, setting a process in place and implementing it through rigorous verification and training.

This entails undertaking a risk assessment of all emergency scenarios aiming to identify potential design alternatives / refinements and/or operational arrangements to ensure that people stay safely on-board or all persons will be able to abandon the vessel safely. This involves assessing and verifying the functionality and performance of all escape, evacuation and rescue systems / processes (Vassalos, 2015). The verification itself will involve estimation of Time To Capsize (TTC, typical example Figure 20) in each pertinent scenario as well as advanced evacuation analysis (Time To Evacuate – TTE, typical example, Figure 21) not only as defined in MSC.1/Circ.1533 (IMO, 2016) but more importantly in those pertinent extreme flooding scenarios that derive as a result of the process described in the foregoing.

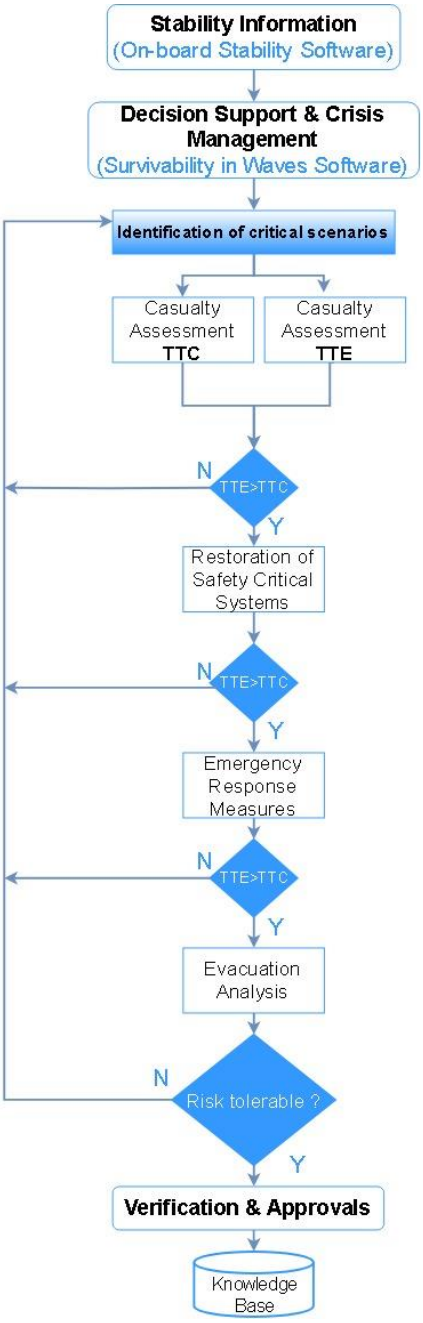

Figure 19: Phase 3: Emergency Response phase

The probability mass function of the event of capsizing in a time within which a number of passengers fail to evacuate, conditional on serious flooding occurring, can be estimated from the CDF of Time To Capsize (for example, Figure 20) and the evacuation/abandonment completion curve, as it is demonstrated in Figure 21.

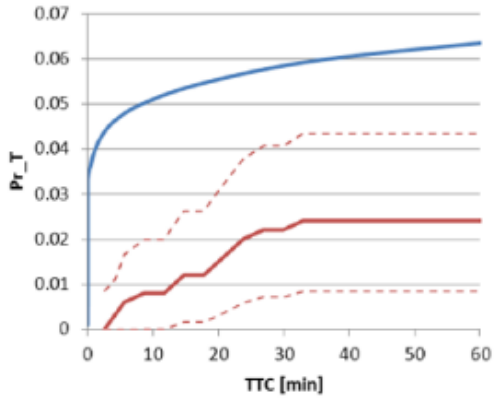

Figure 20: Time To Capsize estimation curve (typical example) (GOALDS, 2009-2012)

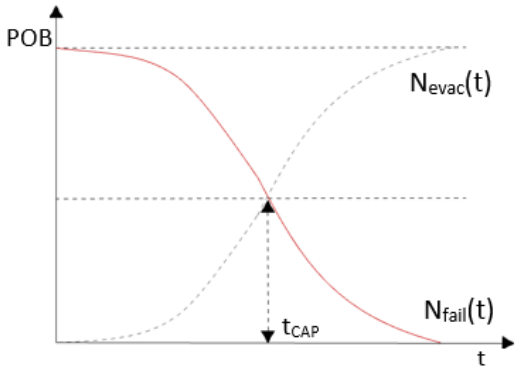

Figure 21: Time To Evacuate completion curve (typical example)

However, as the current rules address only day and night scenarios unrelated to the extreme scenarios being discussed here, the whole evacuation process might need to be considered as an alternative system and be subject to approval through the rule for equivalents.

The impact of failures on active components, sub-systems and auxiliaries, including power generation and supply can be examined through advanced modules of PROTEUS (Cichowicz & Vassalos, 2009). Suggestion of options for recovering such systems, includes manual actions by the crew. At this stage, operability of systems can be ascertained by systems segregation, redundancy and/or active recovery of affected components and sub-systems. These are examined in time-efficient manner with the view to facilitating the identification of optimal ship systems concepts and arrangements (Figure 22).

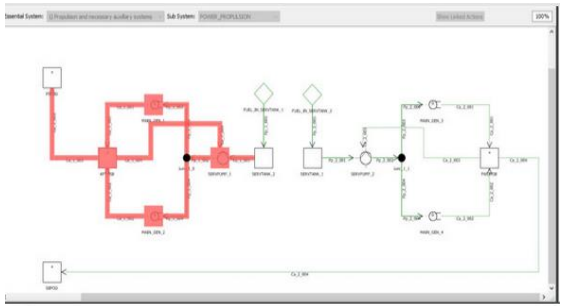

Figure 22: System availability screening example. Safety at Sea/Brookes Bell, safety consultants in Glasgow have developed unique expertise in this latter area with a number of applications in modern cruise liners in the records (Douglas et al, 2011).

As a last line of defence, various emergency response systems can be utilised with the view to mitigating potential risks. For instance, counter ballasting systems for the compensation of heel angles due to asymmetric flooding can be implemented. Alternatively, active systems enabling damage stability recovery could be considered. During project GOALDS (GOALDS, 2009-2012) inflatable cylinders deployed on the sides of the ship were suggested. (NTUA-SDL & SSRC, 2009). Latterly, the application of a Decision Support System (DSS) with intelligent foam technology (Flooding Containment System -FCS) injecting highly expandable foam in critical flooded compartments for flooding prevention and stability recovery (Vassalos, et al., 2016) is proving to be a very effective means from both cost and performance perspectives (Figure 23). Application to all the ships considered to date, leads to three or higher compartment standard, an unparalleled improvement by any other means. This is highly encouraging, demonstrating that technical and other solutions will surface once we have a framework ion place that support and credits novel/alternative risk control options, irrespective of the nature of any such measure of improving ship damage stability and survivability.

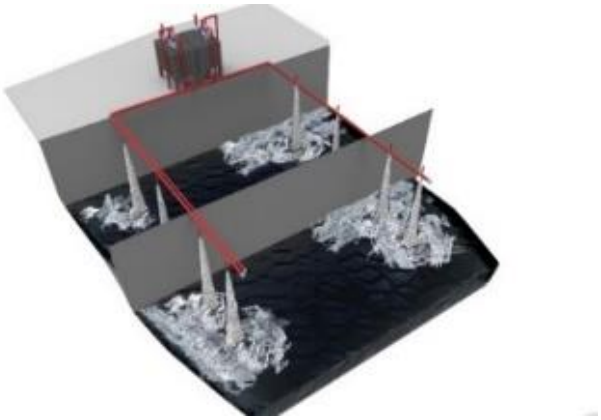

Figure 23: Flooding Containment System illustration (Atzampos, et al., 2017)

In this respect, FCS would constitute the last line of defence, aiming to ensure that the vessel remains upright and afloat in all extreme scenarios or, at the very least, it ensures sufficient time for the safe evacuation of all the people on-board. This is ascertained through evacuation analysis, entailing mustering and ship abandonment where the human and LSA system performance is accounted for through the utilisation of advanced evacuation tools, Figure 24 (Vassalos, 2009).

Throughout the process described in the foregoing, information and knowledge derived through the use of advanced numerical simulation tools as well as through the process of verification will form useful input during design iterations, during the operational life of the ship and, of course, when it matters, in emergencies.

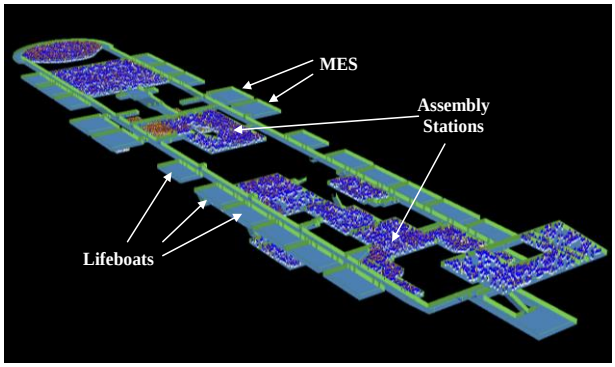

Figure 24: Evacuation analysis simulation (typical example)

Following verifications and approvals, the ensuing knowledge and know-how acquired through the operational and emergency response phases is transferred and stored into the knowledge base for future utilisation in design and through the life-cycle altogether.

8. CONLCUDING REMARKS

1. Building on the knowledge and understanding of damage stability fundamentals, a process has been elucidated to address the vulnerability to flooding of passenger ships from a life-cycle perspective and with focus on operational and emergency response measures alongside the more traditional design measures, hence application on existing ships is also being addressed.
2. In addition, considering the level of detail available during different stages in the various life-cycle phases of the vessel, a multi-level approach has been presented to facilitate use of different "tools" and knowledge base to be used on a "fit for purpose" basis. In principle, there is no need to use a sledge hammer to break a nut and conversely one cannot fly without wings.
3. The life-cycle process delineates the identification of emergency scenarios and describes a systematic procedure of de-risking the people on-board by a series of design and operational measures (including emergencies) and a rational means for decision-making based on cost-effectiveness.
4. The process is holistic and equally suited to newbuildings and existing ships by addressing the whole life cycle.
5. What now remains is to institutionalise this and use it as the driving mechanism to create and sustain safety culture, leading to a process of continuous safety improvement.

9. ACKNOLEDGEMENTS

The authors would like to express their gratitude to Royal Caribbean Cruises Ltd and their partnership for offering them the opportunity and the incentive to delve deeper and deeper into the fascinating subject of damage stability, leading to a de-risking process that is likely to have a huge impact on maritime safety.

10. REFERENCES

Atzampos, G., Vassalos, D., Paterson, D., and Boulougouris, E., 2017, "A New Era of Fishing Vessel Safety Emerges". Belgrade, International Ship Stability Workshop.

Ball, R. and Calvano, C., 1994, "Establishing the fundamentals for a surface ship survivability design discipline". Naval engineering Journal, 106(1), pp. 71-74.

Cichowicz, J. and Vassalos, D., 2009, "Probabilistic assessment of post-casualty availability of ship systems". St Petersberg, International Conference on Stability of Ships and Ocean Vehicles.

De Kat, J., 2015, "Dynamic stability of ships - design and operation". Glasgow, International conference on the ship stability of ships and ocean vehicles- STAB.

EC, 2018. "Horizon 2020, Marine Accident Response, H2020-MG-2-2-2018", Brussels: EC.

GOALDS, 2009-2012, "Goal-Based Damage Stability". Glasgow: European commission Project FP7 .

IMO, 2006, "Guideline on Alternative Designs and Arrangements for SOLAS, Chapter II-1 & III, MSC/Circ.1212", London: IMO.

IMO, 2008, "Formal Safety Assessment for Cruise Ships, MSC 85/17/1". London, IMO.

IMO, 2010, "SRtP requirements, MSC.1/Circ1369", London: International Maritime Organisation.

IMO, 2013, "Guidelines for the Approval of Alternatives and Equivalents", MSC.1/Circ.1455, London: IMO.

IMO, 2016, "Guidelines for evacuation analysis for new and existing passenger ships", MSC.1/Circ 1533. London: IMO.

IMO, 2016, SDC 5, "Sub-Committee on ship design and construction, 4rth session", London: International Maritime Organisation.

IMO, June 2006, "Resolution MSC.216(82), Amendments to the international convention for the Safety Of Life At Sea 1974", London: International Maritime Organisation.

ITTC, 2002, Proceedings of the 23rd ITTC – Volume II, "Extreme ship motions and Capsizing". Venice, International Towing Tank Conference.

ITTC, 2005, Proceedings of the 24th ITTC- Volume II , "Stability in waves". Edinburgh, International Towing Tank Conference.

ITTC, 2009, Proceedings of 25th ITTC – Volume II, "Stability in waves". Fukuoka, International Towing Tank Conference.

Jasionowski, A., 2009, "Study of the specific damage stability parameters of Ro-Ro passenger vessels according to SOLAS 2009 including WoD calculations",EMSA study. Glasgow, SSRC.

Jasionowski, A., 2011, "Decision support for ship flooding crisis management". Ocean engineering, Volume 38, pp. 1568-1581.

King, T., Welter, C., and Svensen, T., 2015, "Stability Barrier Management for Large Passenger ships". Glasgow, International conference on the stability of ships and

ocean vehicles.

Luhmann, H., 2016.,"Presentation on Damage stability of Cruise Ships - eSAFE Project". Germany: EMSA, SeaEurope Workshop.

Luhmann, H., Olufsen, O., Atzampos, G., and Bulian, G., 2018, Summary report, JIP project eSAFE -D.4.3, Papenburg.

NTUA-SDL and SSRC, 2009, "Optimisation procedures, GOAL based Damaged Stability project WP4.1", Athens: GOALDS.

Papanikolaou, A., 2008, "Benchmark study on numerical codes for the prediction of damage ship stability in waves". Daejeon, International Ship Stability Workshop.

Paterson, D., Atzampos, G., Vassalos, D., and Boulougouris, E., 2017, Impact of wave statistics on ship survivability. Belgrade, Serbia, International Ship Stability Workshop.

Ruth, E., Caldas, A., and Olufsen, O., 2017, "Results from Validation", JIP eSAFE WP3 D3.2.2", Hovik.

SOLAS, 2009, "Safety of Life at Sea". London: IMO.

Vassalos, D., 2009, "Risk Based ship Design". 1 ed. Athens: Springer.

Vassalos, D., 2012, "Damage Stability of Passenger Ships- Notions and Truths". Athens, International Conference on the stability of ships and ocean vehicles.

Vassalos, D., 2015, "Damage stability of cruise ships - evidence and conjecture". Glasgow, Ship Stability Conference.

Vassalos, D. et al., 2016, "An Alternative system for damage stability enhancement, Design & Operation of Ferries & Ro-Pax Vessels". London,UK, RINA.

Vassalos, D. and Guarin, L., 2009, "Designing for damage stability and survivability- Contemporary developments and Implementation". Glasgow, Ship Science and Technology.

Vassalos, D., Jasionowski, A., and Guarin, L., 2005, "Passenger Ship Safety - Science Paving the Way", Istanbul: Proceedings of the 8th International Ship Stability Workshop.

Vassalos, D., and Jasionowski, A., 2013, "Emergency Response in Ship Flooding Casualties". Brest, International Ship Stability Workshop.

Rebooting SOLAS – Impact of Drafts on Damage Survivability of Cruise Ships

Donald, Paterson, Maritime Safety Research Centre, d.paterson@strath.ac.uk
Dracos, Vassalos, Maritime Safety Research Centre, d.vassalos@strath.ac.uk
Georgios, Atzampos, Maritime Safety Research Centre, georgios.atzampos@strath.ac.uk
E.Boulougouris, Maritime Safety Research Centre, evangelos.boulougouris@strath.ac.uk
Jakub, Cichowicz, Maritime Safety Research Centre, jakub.cichowicz@strath.ac.uk
Henning, Luhmann, Meyer Werft GmbH & Co.KG, henning.luhmann@meyerwerft.de

ABSTRACT

The prevailing probabilistic damage stability concept, as outlined within SOLAS 2009 for passenger ships, calculates the Attained Subdivision Index based upon three loading conditions which combine to form a theoretical draft range for a given vessel. To each of these loading conditions a weighting factor is then applied to account for the probability that a vessel will be operating at or near any of these drafts at the time of collision, should one occur. Currently the weighting factors are applied in a 'one-size-fits-all' manner, with the same weightings to be applied in the case of cargo vessels and passenger vessels despite the fact that these ship types are known to have very different tendencies when it comes to the nature of their operation. This in turn calls into question the suitability of these weightings with regards to what degree they in fact reflect the operational profile of the vessels covered by the standard. With this in mind, the present paper aims to investigate the suitability/accuracy of the currently assumed draft weighting factors with regards to cruise vessels. This study is conducted using operational loading condition data sourced from 18 ships and spanning up to a period of two years in some cases. On the basis of this data, draft probability distributions are derived and new weighting factors are formed specifically pertaining to cruise ships and the nature of their operation. Finally an assessment is conducted looking into the impact of the newly derived weighting factors on the magnitude of the Attained Subdivision Index and recommendations are made on how best to implement them.

Keywords: *SOLAS Chapter II-1; Damage stability; Draft distribution; Operational data; Attained Index; Survivability*

1. INTRODUCTION

The current IMO instrument for assessing the damage stability performance of passenger vessels and dry cargo ships is that which is outlined in SOLAS Chapter II-1, Res. MSC.216(82) (IMO, 2006), referred to herein as SOLAS 2009. Upon entering into force this brought about an end to the age of deterministic requirements on passenger vessel subdivision based on what were widely considered to be anachronistic means of damage stability evaluation. This included such elements as the floodable length and margin line criteria which had existed within the rules for well over half a century and were starting to show their age.

Instead, the more traditional prescriptive requirements were cast aside in favour of the probabilistic approach to damage stability assessment. With regards to methodology this was nothing new and in fact rules based on this approach were already in place within the mandatory requirements for dry cargo ships in Chapter II-1, part B-1 from 1992 along with the seldom used though highly innovative alternative regulations for passenger ships, Res. A.265(VIII) from 1973. Instead, SOLAS 2009 had the effect of harmonising damage stability assessment under one common and rational methodology.

Unfortunately, however, a fully probabilistic approach has never been realised and there remains a requirement to supplement the criteria with a number of prescriptive rules. In this respect, SOLAS 2009 is neither a design nor a performance-based standard, but instead a hybrid, relying on a combination of both probabilistic and deterministic elements. In addition, designers are still required to adhere to a number of prescribed modelling methodologies, many of which bring back some of the shortcomings of the deterministic approach.

One of the most predominant examples of this concerns the assumptions made regarding the assumed draft range and respective weighting factors defined within SOLAS 2009. The underlying concept behind the probabilistic approach to damage stability is simple, and one that is based upon the probability of a vessel surviving collision damage in waves. This probability is then used as an objective measure of ship's safety in the damaged condition and is represented within the rules by the Attained Subdivision Index, A (2). This index is formed on the basis of three partial indices calculated with respect to three drafts assumed to be representative of the operational draft range of the vessel. To each of these indices a weighting factor is then applied which does not vary with regards to ship type and which is intended to account for the likelihood that the vessel will be operating near or at any of these drafts at the time of collision (4). In this respect, the weighting factors can be viewed as a representation of the vessels' operational profile and it is this deduction in combination with a number of other observations that present cause for concern.

Firstly, the means by which the current weighting factors were determined remains somewhat unclear as there is little that can be found in literature on their derivation. Consequently, the current weighting factors appear, at least on the surface, to be completely unsubstantiated. This in turn calls into question the accuracy of these weighting factors with respect to how representative they are of the operational profiles of the vessels covered by the standard. Even if the above is disregarded, the "one-size-fits-all" approach currently in place would appear to be a gross over simplification. The current regulation assumes in essence that RoPax, Dry Cargo and Cruise vessels are operated according to the same operational profile despite the fact that these ship types are known to have very different tendencies when it comes to the nature of their operation. In order to substantiate such an assertion one must first be able to show that there is adequate correlation between the loading behaviours of each of these ship types, which intuitively speaking is unlikely to be the case. In this respect, even if it was found that these values are accurate for any one of the vessel types covered by the standard, confirmation of that fact would subsequently indicate that they were inaccurate for the others.

It is understood that within any technical standard there will always be elements of assumption, generalisation and simplification, particularly where there are areas of uncertainty stemming from either a lack of information or knowledge, but also in an effort to achieve broad applicability. The latter gives rise to a somewhat paradoxical situation between what are two conflicting objectives, namely to achieve broad levels of applicability whilst also ensuring that the standard sufficiently captures the complexities of scattered reality. As such, generalisation must be attained in a balanced way that ensures any simplifications made don't undermine the fundamental purpose of the regulation which rests upon the ability to accurately assess and measure ship survivability. In fact, a number of studies have been conducted in which certain aspects of the current SOLAS 2009 regulation have been challenged with a view to improving the prescribed assumptions. This includes such studies as the joint research project eSAFE where proposals were made regarding more accurate calculation of cruise ship survivability (Luhmann et al, 2018). In addition the assumed sea state distribution behind the SOLAS s-factor has also been challenged with a view to better accounting for the impact of operational

environment on ship survivability (Paterson et al, 2017). Building on this, it is important that where circumstances permit us to reduce uncertainty or to replace any of these simplifying assumptions with more accurate information, not only should we do so, but such efforts should be actively encouraged.

It is with this in mind that the present paper investigates to what degree the currently assumed draft weightings reflect the true operational profile of cruise vessels, which is a particular class of vessel for which the suitability of SOLAS 2009 has already previously come under question (Vassalos, 2015). This is achieved through analysis of operational loading condition data sourced from a total of 18 cruise vessels and over a time frame spanning in some cases up to two years. Drawing on this analysis a further study is conducted in which weighting factors more representative of the manner in which cruise vessels are operated are derived and their impact on the magnitude of the Attained Index is measured. This is conducted with a view to satisfying two objectives. Firstly, an attempt is made in order to provide a more appropriate means of assessing cruise vessel survivability within the design stage and with the understanding that uncertainty at this stage calls for certain assumptions to be made. And secondly, proposals are made in order to provide a simplified assessment for vessels that are already in operation and where sufficient data is available in which to constrain the assessment allowing for a more straightforward approach to be taken.

2. BACKGROUND

The survivability of a vessel following collision damage that has led to hull breach and subsequent flooding is dependent on a number of factors, none more so than the loading condition of the vessel. The manner in which a vessel is loaded effects greatly its ability to withstand the effects of flooding, with draft and trim influencing important parameters such as freeboard and reserve buoyancy, and the centre of gravity affecting the vessel's restoration properties. As touched upon within the introduction, SOLAS 2009 assumes a draft range based on three values defining the lower and upper limits of an assumed draft range along with consideration of an intermediate condition, each of which are defined as follows:

- Light service draft - dl: Service draft corresponding to the lightest anticipated loading and associated tankage, including ballast as required for adequate stability and immersion. In the case of passenger ships, dl also includes a full complement of passengers and crew on board.

- Deepest subdivision draft – ds: corresponds to the Summer Load Line draft of the ship.

- Partial subdivision draft – dp: this is estimated by the service draft with the addition of 60% of the difference between the light service draft and the deepest subdivision draft.

$$dp = dl + 0.6 \cdot (ds - dl) \qquad (1)$$

A partial Attained Index is then calculated at each of these draft values and the Attained Index is formed as the weighted sum of these indices according to the formula below:

$$A = \sum_{j=1}^{J} \sum_{i=1}^{I} w_j \cdot p_i \cdot s_i \qquad (2)$$

Where,

$j =$ The loading condition under consideration.

$J =$ The total number of loading conditions considered in the calculation of A, usually three drafts covering the operational draft range of the vessel.

$w_j =$ A weighting factor applied to each intial draft.

i = Represents each compartment or group of compartments under consideration for loading condition j.

I = The total number of all feasible damage scenrios involving flooding of individual compartments or groups of adjacent compartments.

p_i = The probability that, for loading condition j, only the compartment or group of compartments under consideration are flooded, disregarding any horizontal subdivision.

s_i = Accounts for the conditional probability of survival following flooding of the compartment or group of compartments under consideration for loading condition j weighted by the probability that the space above a horizontal subdivsion may not be flooded.

The weighting factors represent the time t spend in each loading condition T as provided below.

$$w_{dl} = P(t|T_{dl}) = 0.2 \quad (3a)$$

$$w_{dp} = P(t|T_{dp}) = 0.4 \quad (3b)$$

$$w_{ds} = P(t|T_{ds}) = 0.4 \quad (3c)$$

$$\sum_{j=1}^{3} w_j = w_{dl} + w_{dp} + w_{ds} = 1 \quad (3d)$$

$$A = 0.2 \cdot A_{dl} + 0.4 \cdot A_{dp} + 0.4 \cdot A_{ds} \quad (4)$$

The mandated level of safety is dictated by the Required Subdivision Index, R, which is determined predominantly by the passenger and lifeboat capacity of the vessel and to a lesser extent by the subdivision length. So long as a vessel possesses an Attained Index greater than or equal to the Required Index it is deemed safe from a regulatory perspective.

The partial Attained Index values are also used in order to form the vessel's limiting GM envelope, Figure 1. GM limits are determined as those required such to satisfy the following conditions at each calculation draft:

- A≥0.9R in the case of passenger vessels
- A≥0.5R in the case of dry cargo ships.

These conditions have been set in order to ensure a certain level of safety is maintained across the entire draft range. However, the question remains as to why this was not set as A≥R. Currently, the Attained Index for a given loading condition can fall short of the requirements by 10% in the case of passenger vessels and more shockingly by 50% in the case of dry cargo vessels, so long as the deficit in Attained Index is made up for by another loading condition. If we consider this with regards to the GM limit curve, it enables the limits to be manipulated in such a manner as to apply a more stringent limit on a draft at which the vessel will rarely operate or that is limited by intact stability requirements such as the lower draft often is, and then allows a relaxation on the GM limitation around the design draft where the vessel is likely to be more vulnerable to damage and where GM margins are tighter.

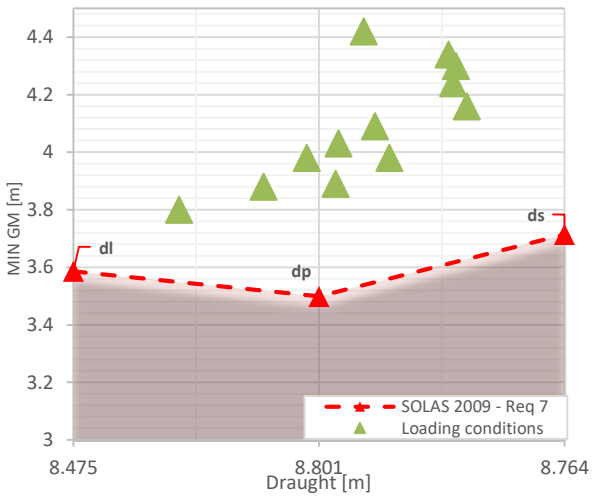

Figure 1: Limiting GM curve, three loading conditions (typical example for cruise ship).

3. WEIGHTING FACTOR DERIVATION METHODOLOGY

In the development of new draft weighting factors that are more reflective of the manner in which cruise vessels are operated, loading condition data from a total of 18 cruise vessels has been sourced. This data contains in some cases up to two years of operational loading information from a range of cruise vessels that provide ample coverage of the fleet demographic both with regards to size and age.

The information obtained has been processed accordingly in order to yield draft probability distributions, both ship-specific and in a generalised format with consideration of all vessel data.

Due to the large variance in size between the vessels contained within the test group, it was imperative to process the data in a uniform way though normalising the draft distributions. Two sets of results are obtained; in the first, the data are normalised with respect to the actual operational draft range of the vessels, whilst in the second, with regards to the SOLAS 2009 assumed draft range. Generally, normalisation scales all numeric variables in the range [0, 1]. The lightest draft (DL) will reflect the zero value whilst unity the highest draft (DS) of the non-dimensional data set, respectively. A linear scaling to unit range approach was performed from the family of linear transformation techniques for data normalisations applicable to unbiased data sets pertaining to small noise tendencies. The generalised formula for the max-min normalisation is indicated below.

$$\widehat{x_i} = \frac{x_i - \min(x_i)}{\max(x_i) - \min(x_i)} \qquad (5)$$

Where, x_i is taken as the mean value ($\overline{x_i}$) between the respective aft and fore draft of each vessel. This was essential as the sample data varied largely with regards to operational trim.

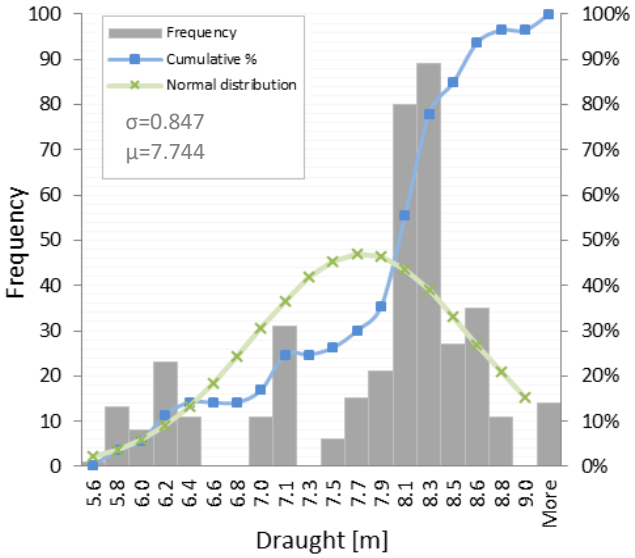

Figure 2: Statistical presentation of mean drafts under consideration covering all sample ships.

Translating equation (5) with respect to drafts yields the following:

$$T_{new} = \frac{\overline{T_i} - \min(T_i)}{\max(T_i) - \min(T_i)} \qquad (6)$$

Where, $\max(T_i), \min(T_i)$ represent the maximum and minimum operational drafts and $\overline{T_i}$ the mean draft.

The frequencies of the normalised draft ranges are apportioned within the specific value of the normalisation range spanning from 0 to 1. Consequently, the sum of all frequencies coincides with the total number of drafts for each case. An inverse normalisation is considered to identify the actual values of the drafts that reflect each increment within the range [0, 1]. This provides a clear picture of the draft distribution of the vessels by also determining the lightest and deepest subdivision drafts. The drafts are utilised for the derivation of the partial Attained subdivision Indices for the different types of draft probability distributions that are investigated. The following formulation is obtained by altering equation (6):

$$T_{new} = Range \times T_{max} - Range \times T_{min} + T_{min} \qquad (7)$$

Where, Range is the value of the normalised draft representing each increment.

4. OPERATIONAL DISTRIBUTION OF DRAFTS

4.1 Ships in Operation

The operational loading condition data from the range of cruise vessels has been utilised in order to generate a number of different draft probability distributions. In the first case, the data from each vessel has been non-dimensionalised with respect to their operational draft range. Through doing so it is possible to assess the manner in which cruise vessel behave in operation as opposed to the manner in which SOLAS 2009 assumes. The distribution yielded in this case is presented in Figure 3 below. Here we see that cruise vessels have a tendency to operate towards the upper region of their draft range with limited time having been spent towards the lower end. It should also be noted that, in the majority of cases, the vessels' operational draft range was found to be much narrower than that assumed within SOLAS 2009. As such, it is important to consider that the distribution shown below corresponds to minimal variance in draft and is over a draft range that is relatively speaking towards the upper portion of the assumed SOLAS 2009 draft range.

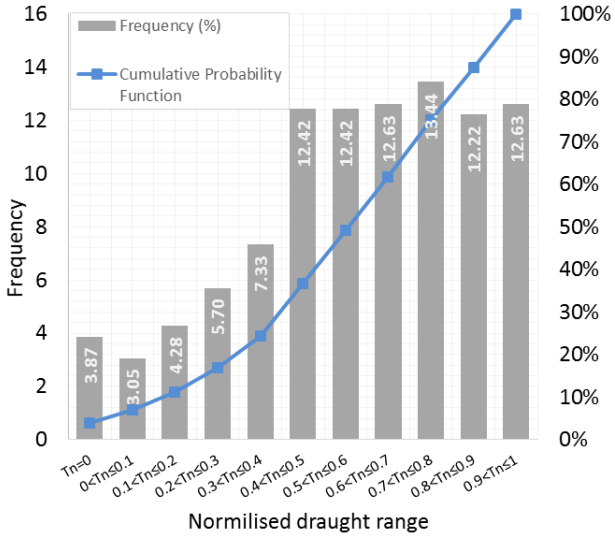

Figure 3: Draft distribution based on the operational draft range - operational profile for all ships (global statistics).

In light of the previous, it has been found that as a simplified means of assessing/monitoring survivability once a vessel has entered operation, a one draft approach to calculating the Attained Index could be taken. In such a case, the Attained subdivision Index would be calculated using the highest recorded draft value within the vessels' loading condition history, weighed with a factor of 1 and using actual trim, fluid GM and respective KG values, as shown in the following:

$$A = w \cdot A|T_{DS} \tag{8}$$

$$A = 1 \cdot A_{DS} \tag{9}$$

Such a simplified approach is made possible due to two reasons; firstly, the availability of information within the operational phase, which would otherwise be an unknown within the design stage, enables the problem to be substantially constrained. Secondly, as cruise vessels operate within a minimal draft range, the magnitude of the Attained Index calculated has little sensitivity with regards to the number of drafts considered within its calculation. This in turn allows for only one draft to be considered whilst producing accurate results. This last point is further substantiated within the next section where sensitivity analysis is performed. By the time at which a vessel has entered operation, design risk is more or less fixed and as such Attained Index calculation of this kind is unlikely to impact design. However, it could foreseeably be used as a simple monitoring tool, in line with such proposals as outlined in (Vassalos et al, 2018) for measuring operational risk and allowing risk information to be used in order to guide decision making and enhance safe operation.

4.2 Ships within the Design Stage

Unlike vessels that are in operation, those within the design stage suffer from a lack of operational data which produces a greater amount of uncertainty and calls for assumptions to be made. However, certain steps can be taken in order to ensure that the draft weighting factors are more representative of cruise vessel operation in general. With this in mind, an

additional draft distribution has been generated, this time having non-dimensionalised the draft data of each vessel with regards to their respective SOLAS 2009 assumed draft ranges. The resultant distribution, shown in figure 4, illustrates more predominantly the tendency of cruise vessels to operate towards the upper portion of their draft range. Though there are however incidents, albeit infrequently, where the lower end of the draft range is also utilised.

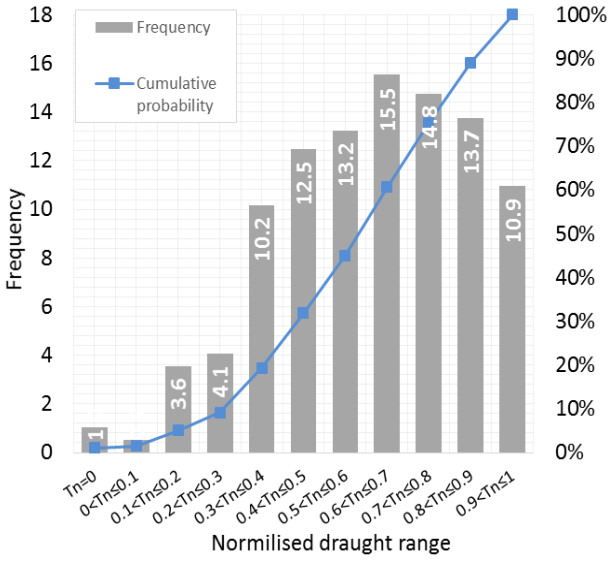

Figure 4: Draft distribution – operational profile for all ships with regards to SOLAS drafts (global statistics)

When deciding upon which draft values and associated weighting factors would be most suitable for the calculation of the Attained Index it was recognised that both the upper and lower ends of the draft range would need to be catered for. This is despite the fact that, in theory, a one draft approach similar to that proposed for vessels in operation would suffice with regards to accurate calculation of the Attained Index. However, in contrast with the operational phase where the primary interest would be safety monitoring within the vessels permissible operational limits, during the design stage not only must the safety level be calculated but also the operational limitations defined. Furthermore, these limitations need to cover all foreseeable eventualities in order to account for uncertainty and as such must consider a wider, more versatile draft range than that found during operation. For this reason it is proposed that during the design stage a two draft approach is utilised corresponding to the non-dimensional drafts 0.15 and 0.65 based upon the SOLAS 2009 assumed draft range. The weighting of these drafts is identified through summing the individual frequencies within each draft increment, resulting in weighting factors of 0.1 and 0.9 respectively (Figure 7).

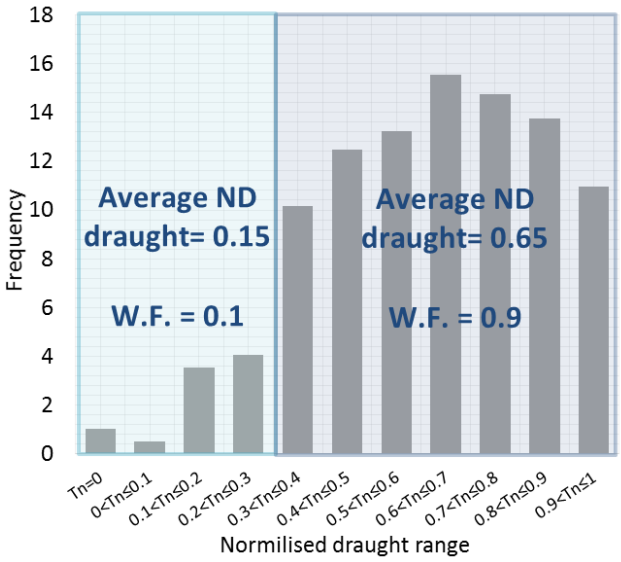

Figure 5: Draft distribution based on SOLAS 2009 drafts. Two drafts with weighting

Thus, the Attained Subdivision Index, equation (2) and (4), can be translated to the following

$$A = \sum_{j=1}^{2} w_j \cdot A|T_j \tag{10}$$

$$A = 0.1 \cdot A_{0.15} + 0.9 \cdot A_{0.65} \tag{11}$$

Where, $A_{0.15}$ and $A_{0.65}$ are the partial Attained Indices for the two normalised drafts. The calculation of the two draft values to be considered is achieved through re-dimensionalising the draft values 0.15 and 0.65 as shown:

$$T_n = (T_{ND} \cdot T_{range}) + d_l \tag{12}$$

Where,

T_n draft(s) to be considered in the calculation of the Attained subdivision Index.

T_{ND} non-dimensional draft values taken from the draft distribution, defined as 0.15 and 0.65, respectively.

T_{range} the vessel draft range according to SOLAS 2009.

d_l the lightest service draft as defined in SOLAS 2009.

It is then proposed to base GM limit curve upon these two draft values with the requirement to satisfy the condition A≥R in order to prevent areas of vulnerability within the draft range. For draft values spanning below non-dimensional draft 0.15 it is recommended that the GM limit continue uniformly. For non-dimensional drafts above 0.65 it is recommended that the GM limit be projected at the same slope formed between the two calculation drafts as shown in Figure 6.

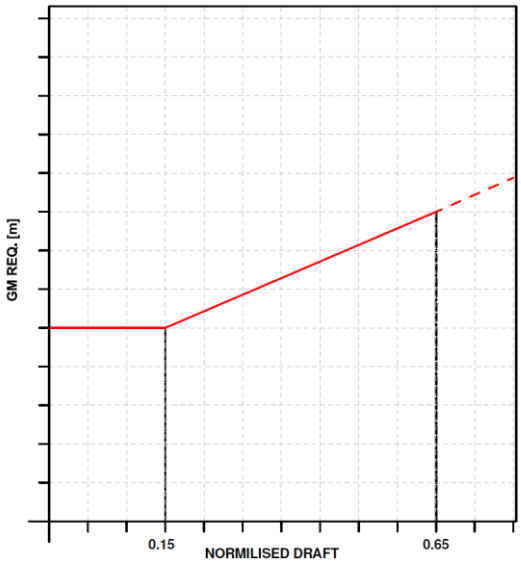

Figure 6: Ship-specific draft distribution

For the purpose of assessing the impact of trim, it is deemed appropriate to conduct a trim sensitivity analysis. In this respect, the trim is assessed according to ±0.25%L and ±0.5%L along with level trim. The final Attained Index should be taken as the lowest Attained index obtained in either case.

4.3 Ship Specific Operational Distributions

The third manner in which the data has been utilised is in order to generate ship specific draft distributions. In this case, ship specific loading condition information was utilised in order to generate draft probability distributions for each vessel, an example of which is shown in Figure 7. The reason for this was primarily to gauge the correlation between the trends witnessed for each vessel and in order to perform a sensitivity analysis on the Attained Index with regards to using the ship specific draft distributions and the more generalised approach previously outlined.

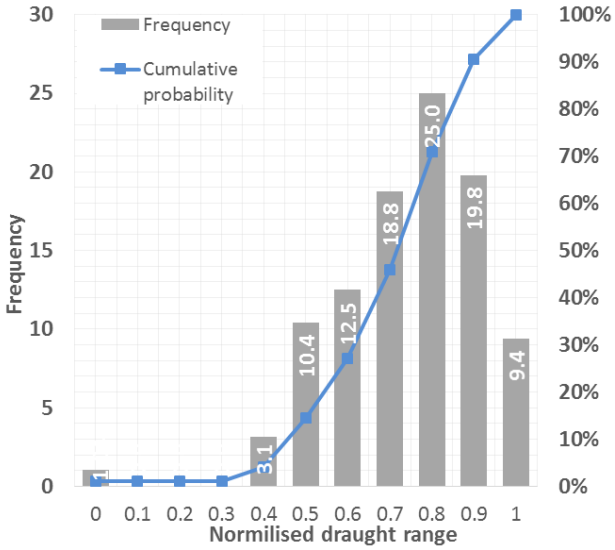

Figure 7: Ship-specific draft distribution

5. DRAFT DISTRIBUTION SENSITVITY ANALYSIS

Following on from the previous section, the various draft probability distributions derived have been assessed in order to identify the sensitivity of the Attained Index with regards to the distribution employed within its calculation. Focus in this case has been placed upon those distributions generated with respect to the vessels' actual operational draft range and with a view to assessing the impact on Attained Index with consideration of the following:

- All draft increments within the draft distribution weighted according to the global statistics.
- The two draft Attained Index calculation Approach as elaborated in the previous for vessels within the design stage.
- All draft increments within the draft distribution weighted according to ship specific draft probability distributions.
- The one draft approach suggested in the previous for vessel within operation.
- The SOLAS 2009 draft weighting values.

For each of the above conditions the Attained Index of one of the vessels from which the operational data was sourced has been calculated. Where ship specific draft distributions have been considered, these have each been applied to the same vessel but with consideration of their unique weighting factors. The results of this process are highlighted below in Figure 8. Observation of the results demonstrates firstly that there is little sensitivity in the magnitude of the Attained Index with regards to using the generalised draft probability distribution over the ship-specific variant. In addition, there is also little sensitivity with regards to the number of drafts considered within the calculation of the Attained Index, having shown less than 1% variance in either case.

The primary reason for the observed lack of sensitivity is due to the fact that cruise vessels operate within a very narrow draft range and as such the change in condition of the vessel across its draft range is minimal. There is however a considerable difference between the results found using the newly derived weighing factors and those currently in place within SOLAS 2009. Here we observe that SOLAS 2009 appears to underestimate considerably the survivability of a SOLAS 90 vessel which from a safety perspective is positive but it also indicates that operator/designer is being over penalised, this is highlighted further in Figure 9.

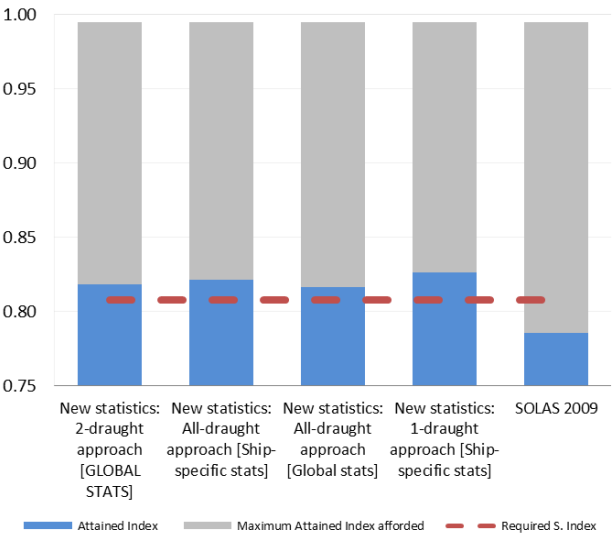

Figure 9: Comparison of impact assessment on Attained subdivision Index for a typical cruise ship complying with SOLAS0 90'.

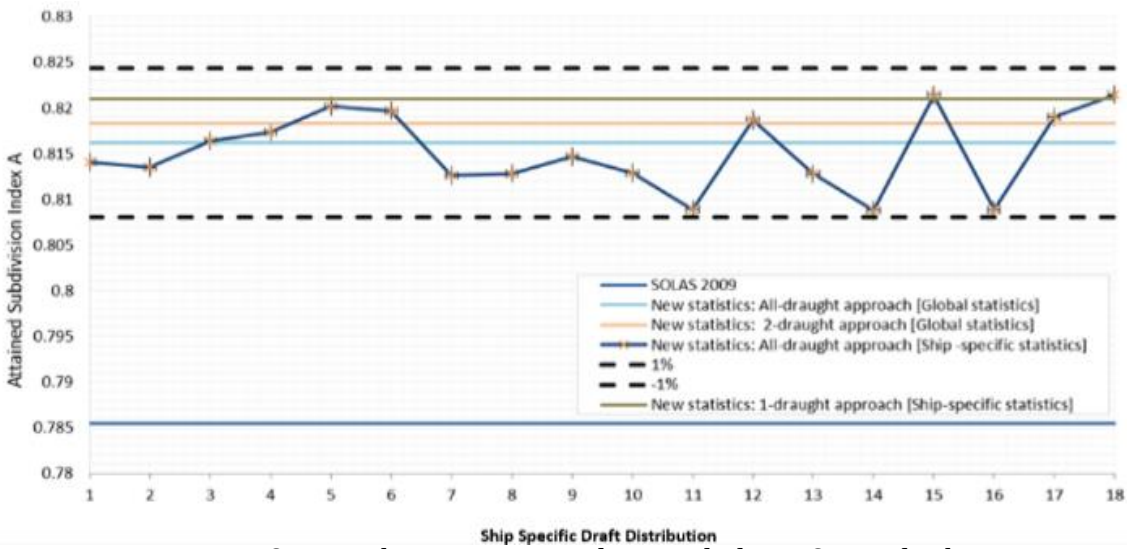

Figure 8: Draught sensitivity analysis including 18 sample ships

The reason for the disparity in the Attained Index value calculated according to SOLAS 2009 in contrast with those calculated using the newly derived weighting factors stems from several reasons. Firstly, the weighting factors used within SOLAS 2009 overestimate the time cruise vessels operate within the lower to mid draft range. Secondly, the draft range assumed within SOLAS 2009 is too wide and in fact cruise vessels operate within a much narrower range. Furthermore, it was observed that in the majority of cases the sample vessels were operating with a considerable GM margin which gives rise to a large discrepancy between the design and operational risk. Regarding the latter, it should be noted that the SOLAS 2009 Attained Index has been calculated using the vessel's exiting GM limit curves which have been formed on the basis of the requirements of SOLAS 90'. For this reason it can be observed that the vessel falls short of the Required Index in Figure 9.

6. CONTINIOUS STABILITY MONITORING FOR SHIPS IN OPERATION

The availability of operational loading condition data opens the doors to continuous stability monitoring with very high potential. Particularly, it can enable identification of high risk practices that lead to reduction of stability and establishment of techniques appropriate for maximisation of the GM margin. Additionally, continuous monitoring would enable monitoring of GM margin erosion and facilitate life-cycle stability management (GM).

Figures 11 and 12 below demonstrate the operational profile of two cruise ships. In the first case, observation of the results shows that the vessel in its worst operational condition still has a minimum of 0.21m GM in excess of the requirement. Therefore, it stands to reason that an Attained subdivision Index based on the GM limiting curve would underestimate the safety level of the vessel under consideration. While the requirement for a GM limit cannot be disputed, the use of A=R as the limiting curve criteria can be challenged.

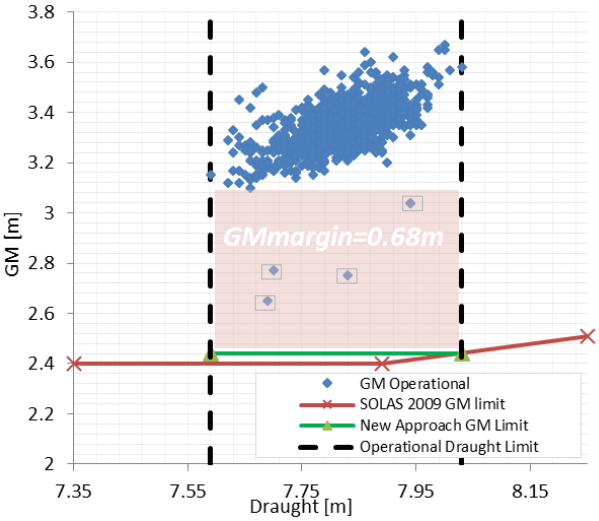

Figure 10: Limiting GM curves using new and old approach with illustration of operational loading conditions accumulated over two years for a typical large cruise ship.

In theory, a new GM limit based on the actual operational profile of the vessel could be used in order to provide a more accurate and, as it turned out as shown in Figure 11, a larger Attained subdivision Index value. This being said, a GM value of 2.6 meters would produce a higher Attained Index and redefine the GM limit as 2.6 meters across the draft range of the vessel whilst the vessel is not penalised with regards to its operation. In the second case, the cruise ship is over-penalised having an average GM margin of 1.32 meters resulting to lower survivability and therefore, as expected, an underestimated level of safety.

Further to the information above, Figure 12 below highlights the relationship between the non-dimensional draft data for all vessels against their respective GM margin. This shows that in some cases there is a large gap between the GM limit and the operational GM but also highlights that some vessels operate very closely to their GM limit. In consideration of the foregoing, continuous stability monitoring can be advantageous as it can give prominence to unfavourable trends and provide guidance to cost-effective actions that can enhance stability and hence safety.

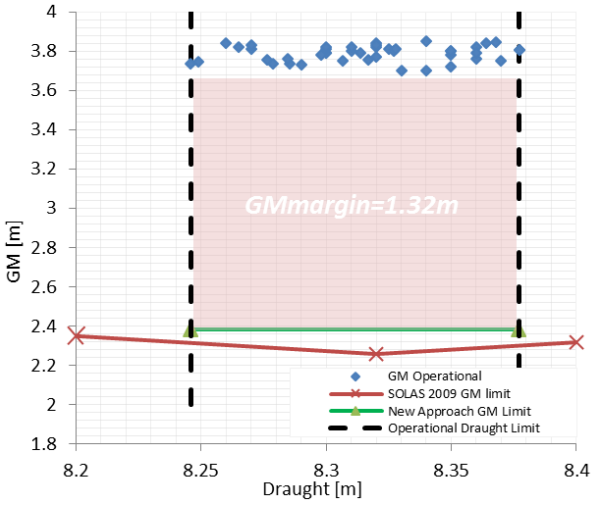

Figure 11: Limiting GM curves using new and old approach with illustration of operational loading conditions of a typical cruise ship.

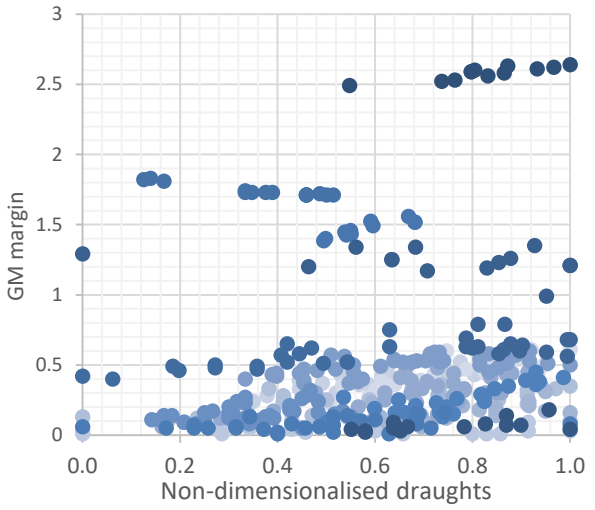

Figure 12: GM margin [m] versus non-dimensionalised draft overview of sample cruise ships.

7. CONCLUSIONS

On the basis of the foregoing study and the results presented, the following concluding remarks can be made:

- The weighing factors used within the SOLAS 2009 framework appear not to reflect the nature of operation of cruise vessels and subsequently underestimate the Attained subdivision Index (safety level).

- The use of real loading condition (draft) data can be employed to generate weighting factors based upon draft probability distributions that represent the true operational profile of the vessels.

- In the case of existing ships, a one-draft approach to calculating the Attained Index has been identified, which will simplify calculations significantly whilst resulting in higher Attained Index that better reflects cruise ship operation.

- For assessment of cruise vessels during the design stage it is recommended to use a two draft approach with appropriate weighting factors formed on the basis of cruise vessel specific loading condition data and which is ultimately more reflective of the operational profile of cruise vessels.

8. ACKNOWLEDGEMENTS

The authors would like to express their gratitude to all the partners in eSAFE project for their constructive criticism and help in the undertaking of this research and the Cruise Ship Safety Forum for funding this very important research.

9. REFERENCES

IMO, 2009. SOLAS - International Convention for the Safety of Life at Sea. London: IMO.

Luhmann, H., Olufsen, O., Atzampos, G., and Bulian, G., 2018. “Summary report”, project eSAFE -D.4.3, Papenburg: Meyer Werft.

Paterson, D., Atzampos, G., Vassalos, D., and Boulougouris, E., 2017. “Impact of wave statistics on ship survivability”. Belgrade, Serbia, ISSW.

Vassalos, D., Atzampos, G., Cichowicz, J. Paterson D. , Karolius, K., Boulougouris, E., Svensen, T., Douglas, K., Luhmann, H., 2018, "Life-cycle flooding risk management of passenger ships", STAB, Kobe, Japan.

Vassalos, D. 2015, "Damage stability of cruise ships – evidence and conjecture". Proceedings of the 12th international conference on the stability of ships and ocean vehicles, STAB, Glasgow, UK

Vassalos, D. York, A., Jasionowski, A., Kanerva, M., and Scott, A. 2007, "Design implications of the new harmonised probabilistic damage stability regulations". International shipbuilding progress, pp. 339-361

Vassalos, D. Jasionowski, A., and Guarin, L. 2005, "Passenger ship safety – science paving the way". Proceedings of the 8th International Stability Workshop, Istanbul, Turkey.

Vassalos, D. 2014, "Damage stability and survivability – 'nailing' passenger ship safety problems". Journal of ships and offshore structures. pp 237-256.

STAB 2018 Kobe Japan

ClassNK

TSUTOMU NAKAUCHI FOUNDATION

KOBE CONVENTION BUREAU

Office of Naval Research Science & Technology

ISBN 000-000-00000-0-0